

12TH INTERNATIONAL BEAM INSTRUMENTATION CONFERENCE

IBIC2023

September 10-14, 2023
Saskatoon, Canada
Lightsource.ca/IBIC2023

The Canadian Light Source (CLS) is proud to host the 12th annual IBIC conference. This event brings together the world's beam instrumentation community to explore the physics and engineering challenges of beam diagnostic and measurement techniques for particle accelerators.

PROCEEDINGS

Scientific Program Committee

Tonia Batten, CLS, Canada, Chair
Willem Blokland, SNS/ORNL, USA
Lorraine Bobb, Diamond, UK
Peter Forck, GSI, Germany
Dave Gassner, BNL, USA
Nicolas Hubert, Soleil, France
Kevin Jordan, JLAB, USA
Changbum Kim, PAL, Korea
Prapong Klysubun, SLRI, Thailand
Patrick Krejcik, SLAC, USA
Thibaut Lefevre, CERN, Switzerland
Yongbin Leng, NSRL/USTC, China
Shengli Liu, Fermilab, USA; TRIUMF, Canada
Hirokazu Maesaka, SPring-8, Japan
Sergio Marques, LNLS, Brazil
Kenichiro Sato, J-PARC, Japan
Victor Scarpine, Fermilab, USA
Volker Schlott, PSI, Switzerland
Adriana Wawrzyniak, Solaris, Poland
Carsten Welsch, UOL, UK
Kay Wittenburg, DESY, Germany
Junxia Wu, IMP, China
Junhui Yue, IHEP, China

Local Organizing Committee (CLS)

Tonia Batten
Grant Bilbrough
Michael Bree
Shawn Carriere
Darren Hunter
Ginette LaVoie, Chair
Adam Leontowich
Sandra Ribeiro
Michael Smith
Robby Tanner
Dustin Wasyliw
Glen Wright

JACoW Editors

Michael Bree, CLS, Canada - Editor in Chief
Darren Hunter, CLS, Canada – Scientific Secretariat
Grzegorz Kowalski, GSI, Germany
Christine Petit-Jean-Genaz, CERN (Ret.), Switzerland
Volker RW Schaa, GSI (Ret.), Germany
Ana Štajminger, ELI, Czech Republic

Canadian Light Source | Centre canadien de rayonnement synchrotron
City of Saskatoon
DISCOVER SASKATOON
TOURISM SASKATCHEWAN CANADA
innovation SASKATCHEWAN

Preface
Group Photo

CONFERENCE ORGANIZATION

Hosted by
Canadian Light Source Inc. (CLS)

Supported by
City of Saskatoon, Tourism Saskatchewan,
Discover Saskatoon, Innovation Saskatchewan

Student grant Program Supported by
Bergoz Instrumentation
Busch Vacuum Technics Inc.
Dimtel, Inc.
Cern Courier

Chair Organizing Committee	**Tonia Batten, CLS**
Chair Scientific Program Committee	**Tonia Batten, CLS**
Chair Local Organizing Committee	**Ginette LaVoie, CLS**

LOCAL ORGANIZING COMMITTEE

Tonia Batten, CLS (OC Chair), Ginette LaVoie, CLS, Sandra Ribeiro, CLS, Shawn Carriere, CLS, Mike Bree, CLS, Glen Wright, CLS, Adam Leontowich, CLS, Robby Tanner, CLS, Michael Smith, CLS, Grant Bilbrough, CLS, and Darren Hunter, CLS

SCIENTIFIC PROGRAM COMMITTEE

Tonia Batten, CLS (SPC Chair), Dave Gassner, BNL, Vic Scarpine, FNAL, Kevin Jordan, JLab, Sergio Rodrigo Marques, LNLS, Willem Blokland, ORNL, Shengli Liu, TRIUMF, Kenchiro Sato, J-PARC, Changbum Kim, PAL, Yong-bin Leng, NSRL and USTC, Hirokazu Maesaka, SPring-8, Junxia Wu, Institute of Modern Physics, Prapong Kylsubun SLRI, Junhui Yue, IHEP, Peter Forck, GSI, Thibaut Lefevre, CERN, Kay Wittenburg, DESY, Lorraine Bobb, Diamond, Volker Schlott, PSI, Adriana Wawrzyniak, Solaris, Nicolas Hubert, Soleil, and Patrick Krejcik, SLAC

EDITORIAL BOARD

Mike Bree, CLS (Chair), Tonia Batten, CLS, Darren Hunter, CLS, Christine Petit-Jean-Genaz, CERN, Volker RW Schaa, GSI

JACoW INTERNATIONAL TEAM

Mike Bree, CLS (Editor-in-Chief), Christine Petit-Jean-Genaz, CERN, Volker RW Schaa, GSI, Ana Štajminger, ELI, Grzegorz Kowalski, GSI, Darren Hunter, CLS

STUDENTS WITH GRANTS

Alec Clapp, Royal Holloway Univ. of London and Diamond
Christophe Lannoy, CERN – EPFL
Nicolas Vallis, PSI and Ecole Polytechnique Federale de Lausanne
Hong Shuang Wang, SINAP and Chinese Academy of Science
Ruizhe Wu, NSRL and USTC
Xing Yang, SINAP
Xuhui Tang, IHEP, Chinese Academy of Science
Jonas Lamaack, Univ. of Hamburg
Philipp Niedermayer, GSI

CONFERENCE OVERVIEW

IBIC is a fruitful and successful gathering of the world's beam instrumentation community and it is dedicated to exploring the physics and engineering challenges of beam diagnostic and measurement techniques for particle accelerators.

The 12th International Beam Instrumentation Conference, IBIC 2023, was hosted by the Canadian Light Source and held in Saskatoon, Canada between September 10th and 14th 2023.

IBIC 2023 included overall

- 38 invited and contributed talks,
- 2 tutorials,
- 114 posters, and a
- 3-day long vendor exhibition with 9 exhibitors that could be visited during the conference.

In total, 182 participants coming from 18 countries got together during the conference.

The Organizing Committee warmly thank all the participants for their enthusiastic contribution to IBIC 2023.

Contents

Preface i
Organization & Overview . . . iii
Contents . . . v

Papers 1
MO2I02 – Fast Orbit Feedback for Diamond-II . . . 1
MO2C03 – Coupled Bunch Mode Zero Correction within the Orbit Feedback Bandwidth . . . 7
MO2C04 – SOLEIL New Platform for Fast Orbit Feedback . . . 11
MO3C03 – Development of the SLS 2.0 BPM System . . . 15
MO3C04 – A MTCA Based BPM-System for PETRA IV . . . 19
MO3C05 – Canadian Light Source Beam Position Visualization Tool . . . 24
MOP001 – Current Status of the HESR Beam Instrumentation . . . 29
MOP002 – MiniBEE - Minibeam Beamline for Preclinical Experiments . . . 34
MOP004 – Design and Study of Cavity Quadrupole Moment and Energy Spread Monitor . . . 37
MOP007 – Experimental Verification of the Coherent Diffraction Radiation Measurement Method for Longitudinal Electron Beam Characteristics . . . 41
MOP008 – Consideration of Beam Instrumentation for SOLARIS Linac Upgrade . . . 45
MOP009 – A Snapshot of CERN Beam Instrumentation R&D Activities . . . 49
MOP010 – Diagnostics for a High Emittance and High Energy Spread Positron Source . . . 54
MOP011 – Safety Considerations for Shield Door Control Systems . . . 59
MOP013 – Expansion of the MTCA Based Direct Sampling LLRF at MedAustron for Hadron Synchrotron Applications . . . 63
MOP018 – Beam-diagnostic and T0 System for the mCBM and CBM Experiments at GSI and FAIR . . . 66
MOP019 – First Test with MicroTCA Based Cavity BPM Electronics for the European XFEL and FLASH . . . 70
MOP022 – Replacement of the Single-Pass BPM System with MicroTCA.4-based Versatile Electronics at SPring-8 . . . 74
MOP023 – The Conceptual Design Study for New BPM Signal Processing System of J-PARC (MR) . . . 78
MOP026 – A Novel BPM Mechanical Center Calibration Method Based on Laser Ranging . . . 82
MOP030 – Developments of 4GSR BPM Electronics . . . 87
MOP031 – A Study Into the Long-Term Stability of Front End X-Ray Beam Position Monitor Support Columns at Diamond Light Source . . . 90
MOP032 – One Dimensional Beam Position Monitor Prototype using Incoherent Cherenkov Diffraction Radiation . . . 94
MOP033 – 1L Target Harp Diagnostic Display Tool . . . 99
MOP036 – A New Approach for Canadian Light Source Future Orbit Correction System Driven by Neural Network . . . 102
MOP037 – Tune Feedback at the Canadian Light Source . . . 106
MOP038 – Development of an Active Beam-Stabilization System for Electrofission Experiments at the S-Dalinac . . . 111
MOP039 – Transverse Multi-Bunch Feedback Detector Electronics Using Direct Sampling Analog-to-Digital Converters for the Synchrotron Radiation Source PETRA IV . . . 115
MOP041 – Modified Fast Orbit Feedback Controller for Disturbance Attenuation in Long Straights for Diamond-II . . . 119
MOP043 – Using Lag Compensator in Orbit Feedback . . . 123
MOP044 – "Instantaneous" Lifetime Measurement in Storage Ring with Top-Up Injection . . . 125
MOP045 – Robust Emittance Measurements . . . 127
MOP046 – Measurement of Slice Emittance with Deflecting Cavity and Slit . . . 129
TU1I01 – Beam Instrumentation Challenges for High-Energy and Low-Emittance Beam at SuperKEKB . . . 131
TU1I02 – Beam Instrumentation Performance During Commissioning of the ESS Normal Conducting LINAC . . . 136
TU1C03 – An Experimental Setup for PIXE Analysis in a Medical Cyclotron at TENMAK-NUKEN . . . 142
TU2I02 – First Direct Measurement of Electron and Positron Bunch Characteristics during Positron Capture Process at the Positron Source of the SuperKEKB B-Factory . . . 146
TU2C03 – Sub-20 fs Synchronization Between Mode-Locked Laser and Radio Frequency Signal . . . 151
TU3I01 – Commissioning of the LCLS-II Machine Protection System for MHz CW Beams . . . 154
TU3C02 – FPGA Architectures for Distributed ML Systems for Real-Time Beam Loss De-Blending . . . 160
TU3C03 – Collimator Scan Based Beam Halo Measurements in LHC and HL-LHC . . . 164
TU3I04 – Comparison of Different Bunch Charge Monitors Used at the ARES Accelerator at DESY . . . 169
TU3C05 – Low Intensity Beam Current Measurement of the Associated Proton Beam Line at CSNS . . . 174
TUP002 – Development of Bunch Position Monitors to Observe Sudden Beam Loss of SuperKEKB Rings . . . 179
TUP004 – Detector Response Studies of the ESS Ionization Chamber . . . 183
TUP005 – Commissioning the Beam-Loss Monitoring System of the LCLS Superconducting Linac . . . 187

TUP006 – Simulation and Shot-by-Shot Monitoring of Linac Beam Halo . . . 191
TUP007 – Use of the ISAC-II Flight Time Monitors toward Automated Tuning . . . 195
TUP009 – Bunch Length Measurement System Downstream the Injector of the S-DALINAC . . . 200
TUP010 – Intermediate Frequency Circuit Components for Integration of on-Chip Amplifier With THz Detectors . . . 204
TUP011 – Geometry Study of an RF-Window for a GHz Transition Radiation Monitor for Longitudinal Bunch Shape Measurements . . . 209
TUP012 – First Measurements of an Electro-Optical Bunch Arrival-Time Monitor Prototype with PCB-Based Pickups for ELBE . . . 214
TUP014 – Design and Test of a Prototype 324 MHz RF Deflector in the Bunch Shape Monitor for CSNS-II Linac Upgrade 219
TUP021 – Development of the RF Phase Shifter with Femtosecond Time Delay Resolution for the PAL-XFEL Laser System 222
TUP022 – Characterisation of Cherenkov Diffraction Radiation Using Electro-Optical Methods . . . 226
TUP023 – Application of a Camera Array for the Upgrade of the AWAKE Spectrometer . . . 230
TUP026 – Bunch Compressor Monitors for the Characterization of the Electron Bunch Length in a Linac-Driven FEL . 235
TUP027 – Microbunching of Thermionic Cathode RF Gun Beams in the Advanced Photon Source S-Band Linac . . . 240
TUP028 – Collimator Irradiation Studies at the Advanced Photon Source . . . 245
TUP029 – A Hybrid Approach to Upgrade Hardware for the Proton Storage Ring Fast Kicker . . . 250
TUP031 – Beam Test of a Harmonic Kicker Cavity . . . 254
TUP034 – Axial Cryogenic Current Comparator (CCC) for FAIR . . . 259
TUP035 – Multi-Tile Zinc-Oxide-Based Radiation-Hard Fast Scintillation Counter for Relativistic Heavy-Ion Beam Diagnostics: Prototype Design and Test . . . 263
TUP036 – Cryogenic Current Comparators as Low Intensity Diagnostics for Ion Beams . . . 268
TUP037 – Charge Measurement with Resonators at ARES . . . 273
TUP038 – BCM System Optimization for ESS Beam Commissioning through the DTL Tank4 . . . 277
TUP041 – APS Upgrade Radiation Safety Beam Current Interlock . . . 281
TUP042 – Nano-Amp Beam Current Diagnostic for Linac-to-ESA (LESA) Beamline . . . 285
TUP044 – The Digital Signal Processing Chain of the CERN LIU BWS . . . 288
TUP045 – Real Time Momentum Spread Measurement of the CERN Antiproton Decelerator Beam . . . 293
TUP046 – Status of the RFSoC-based Signal Processing for Multi-bunch and Filling Pattern Feedbacks in the SLS 2.0 297
WE1C03 – THz Antenna-Coupled Zero-Bias Schottky Diode Detectors for Particle Accelerators . . . 301
WE2C02 – Software Defined Radio Based Feedback System for Transverse Beam Excitation . . . 306
WE2C03 – Beam Instrumentation Hardware Architecture for Upgrades at the BNL Collider-Accelerator Complex and the Future Electron Ion Collider . . . 308
WE3I01 – Gas Jet-Based Fluorescence Profile Monitor for Low Energy Electrons and High Energy Protons at LHC . . 312
WE3C02 – Development of a Precise 4d Emittance Meter Using Differential Slit Image Processing . . . 318
WE3C03 – Radiation Hard Beam Profile Monitors for the North Experimental Beamlines CERN . . . 321
WEP001 – Non-invasive Profilers for the Cold Part of ESS Accelerator . . . 326
WEP002 – Study of Visible Synchrotron Radiation Monitor on SOLEIL Booster . . . 331
WEP005 – Effect of Incoherent Depth of Field for Bean Halo Measurement with the Coronagraph in SuperKEKB . . . 335
WEP006 – Development of Pepper-pot Emittance Monitor for High-intensity Ion Beam Accelerated by RIKEN AVF Cyclotron . . . 339
WEP007 – Beam Profile Measurement using Helium Gas Light Emission and BEPM for Superheavy Element Search Experiment . . . 343
WEP011 – A Preliminary Design of Bunch-by-bunch 3D Positions Measurement . . . 347
WEP013 – Quality Assurance of Proton Beam Profile Using Phosphor Screen and TE-Cooled CMOS Camera . . . 350
WEP014 – Measuring Electromagnet Polarity Using Magnetic Remanence . . . 354
WEP015 – Synchrotron Light Monitor for the Advanced Photon Source Booster Synchrotron . . . 358
WEP016 – Beamline for Time Domain Photon Diagnostics at the Advanced Photon Source Upgrade . . . 363
WEP017 – Electron Beam at the Advanced Photon Source Linac Extension Area Beamline . . . 368
WEP018 – Simulation of Oscillating Arm Wire Monitor Mechanics Driven by a Stepper Motor . . . 373
WEP019 – Study of Single Wire Scanner Monitor for FETS-FFA Test Ring . . . 377
WEP020 – Performance Evaluation of GAGG+ and Tungsten Carbide Blades in an X-ray Pinhole Camera . . . 382
WEP021 – 100Hz X-ray Beam Profile Measurements from a Transmissive CVD Diamond Detector . . . 387
WEP022 – Target Multiwire for the Fermilab Booster Neutrino Beamline . . . 392
WEP023 – Progress on an Electron Beam Profile Monitor at the Fermilab Main Injector . . . 395
WEP024 – A Simulation of the Photoionization of H^- Together With the Subsequent Tracking of the Liberated Electrons 400
WEP025 – A Study of the Gain of Microchannel Plates in the Ionization Profile Monitors at Fermilab . . . 405

WEP027 – Status of Gas Sheet Monitor for Profile Measurements at FRIB . . . 410
WEP028 – LANSCE High Density Emittance Instrumentation System . . . 413
WEP029 – LANSCE QAC/DAQ Wire Scanner Instrumentation Upgrade . . . 415
WEP030 – First Results for a 50 MeV Beam Induced Fluorescence Monitor for Beam Profile Measurements . . . 418
WEP031 – Image Acquisition System for the Injection Dump at the Spallation Neutron Source . . . 421
WEP033 – A Schottky Tune Meter for the Fermilab Mu2E Delivery Ring . . . 425
WEP034 – Effect of Longitudinal Beam-Coupling Impedance on the Schottky Spectrum of Bunched Beams . . . 428
WEP035 – Statistical Properties of Schottky Spectra . . . 433
WEP036 – Study of Non-destructive BPM-Based Energy Measurement of the Canadian Light Source Linac . . . 438
WEP042 – Implementation of Transimpedance Analog Front-End Card for Los Alamos Neutron Science Center Accelerator Wire Scanners . . . 442
WEP043 – Upgrade of the ELBE Timing System . . . 446
WEP046 – Progress on Distributed Image Analysis from Digital Cameras at ELSA using the RabbitMQ Message Broker 449
TH1I01 – LCLS-II Timing System and Synchronous Bunch Data Acquisition . . . 453
TH1I02 – A Novel Cavity BPM Electronics for SHINE Based on RF Direct Sampling and Processing . . . 458
TH2C03 – Analysis of the Transverse Schottky Signals in the LHC . . . 462

Appendices **467**
List of Authors . . . 467
List of Institutes . . . 474
Participants List . . . 483
Sponsors . . . 486
Exhibitors . . . 487

ISBN: 978-3-95450-236-3 ISSN: 2673-5350 doi:10.18429/JACoW-IBIC2023-MO2I02

FAST ORBIT FEEDBACK FOR DIAMOND-II

I. Kempf *, M. Abbott, L. Bobb, G. B. Christian, Diamond Light Source, Oxfordshire, UK
G. Rehm, Helmholtz-Zentrum für Materialien und Energie, Berlin, Germany
S. Duncan, University of Oxford, Oxford, UK

Abstract

The electron beam stability is critical for 4th generation light sources. As opposed to 10 % of beam size up to 140 Hz at Diamond, advances in detector speed and resolution at Diamond-II increase the stability requirements to 3 % up to 1 kHz. This paper presents a novel control methodology for the fast orbit feedback at Diamond-II, which will stabilise the beam using two arrays of 252 slow and 144 fast correctors and 252 beam position monitors at 100 kHz. In contrast to existing approaches that separate slow and fast feedback loops, our approach is based on a two-matrix factorisation called the generalised singular value decomposition (GSVD), which decouples the system into 144 two-input modes controlled by slow and fast magnets and 108 modes controlled by slow magnets only. The GSVD-based controller is implemented in the existing Diamond storage ring using a centralised communication architecture, such as planned for Diamond-II. We present results from the Diamond storage ring and simulation, which confirm that the proposed approach meets the target specification for Diamond-II.

INTRODUCTION

The fast orbit feedback (FOFB) at Diamond Light Source (Diamond) attenuates disturbances of the electron beam in the storage ring. Disturbance sources include ground and girder vibrations, power supply and RF noise, and transients induced by insertion device (ID) gap changes. At Diamond, the FOFB uses 173 electron beam position monitors (BPMs) measuring both horizontal and vertical positions, and 172 vertical and 172 horizontal correctors to perform global orbit correction of the electron beam at 10 kHz. The FOFB reduces the root-mean square (RMS) deviation of the electron beam to within 10 % of the beam size up to a closed-loop bandwidth of 140 Hz, i.e. the frequency at which disturbances are attenuated by 3 dB. For Diamond-II, advances in beamline technology require the closed-loop bandwidth to be increased to 1 kHz, while the new multi-bend achromat lattice will reduce the beam size [1], resulting in the increased beam stability requirements summarised in Table 1 (top).

To meet these requirements, the FOFB hardware and software for Diamond-II have been redesigned, increasing the specifications as shown in Table 1 (bottom). Firstly, the sampling frequency is increased to 100 kHz and the overall latency reduced to 100 µs. Secondly, the number of BPMs is increased to 252. Finally, to achieve the 1 kHz closed-loop bandwidth, the open-loop bandwidth, i.e. the overall corrector bandwidth, is increased from 500 Hz to ≥ 5 kHz by introducing two types of correctors: 252 slow correctors producing a deflection of 1 mrad, and 144 fast correctors producing a deflection of 20 µrad [1].

Table 1: Top: Beam size, relative and absolute orbit stability requirements at standard straight source points. Bottom: FOFB specifications. Tables adapted from Ref. [1].

Parameter	Diamond	Diamond-II
Beam size H/V	123 µm/3.5 µm	30 µm/4 µm
Rel. stability	10 % up to 100 Hz	3 % up to 1 kHz
Abs. stability H/V	12 µm/0.35 µm	0.9 µm/0.12 µm
Closed-loop BW	140 Hz	≥ 1 kHz
Latency	700 µs	≤ 100 µs
BPMs	173	252
Correctors	172	252 slow/144 fast

H: horizontal, V: vertical, BW: bandwidth

While using two types of correctors allows the closed-loop bandwidth to be increased, it prohibits the existing FOFB control algorithm to be reused, which is based on diagonalising the dynamics using the modal decomposition and controlling the single-input single-output (SISO) modal dynamics. Although extensions of modal decomposition have been proposed in [2, 3], they leave the decoupling process unspecified for systems with fewer fast than slow correctors. For Diamond-II, we propose a joint design method based on the generalised singular value decomposition (GSVD) [4] to decouple the system into sets of two-input single-output (TISO) and SISO systems. It can be shown that the generalised modal decomposition of a system with two corrector types is closely related to the modal decomposition of a system with one corrector type, which allows techniques to be carried over to the system with two corrector types, including regularisation gains that account for a large condition number of the orbit response matrix (ORM).

Based on the assumption that the bandwidths of the slow and fast correctors differ significantly, other approaches split the control problem into two separate feedback loops: one feedback loop for the slow correctors that may be operated at a lower sampling/actuation frequency, and a separate feedback loop for the fast correctors. Such a separation is implemented in most synchrotrons that use separate sets of slow and fast correctors [5–7], but interactions at intermediate frequencies can require the introduction of a frequency deadband between the slow and fast loops [8]. Depending on the disturbance spectrum, this approach can lead to significant performance degradation [6]. One common way

* Corresponding author: idris.kempf@eng.ox.ac.uk. Also at University of Oxford. This work was supported in part by Diamond Light Source and in part by the Engineering and Physical Sciences Research Council (EPSRC) with a Collaborative Awards in Science and Engineering (CASE) studentship.

Content from this work may be used under the terms of the CC-BY-4.0 licence (© 2023). Any distribution of this work must maintain attribution to the author(s), title of the work, publisher, and DOI

ISBN: 978-3-95450-236-3 ISSN: 2673-5350 doi:10.18429/JACoW-IBIC2023-MO2I02

Content from this work may be used under the terms of the CC-BY-4.0 licence (© 2023). Any distribution of this work must maintain attribution to the author(s), title of the work, publisher, and DOI

to avoid introducing a frequency deadband is to subtract the predicted effect of the slow correctors from the feedback signal for the fast correctors [5]. Another solution is to periodically subtract the DC gain from each fast corrector (individually) and to import these values into the slow feedback loop, thereby shifting the low-frequency action from the fast correctors to the slow correctors [9]. However, this approach neglects the coupling between slow and fast correctors and relies on a SISO analysis of the combined slow and fast loops. As in the case of systems with one corrector type, large condition numbers of the ORM limit the closed-loop bandwidth [10], and neglecting the coupling may require further reduction of controller gains [11]. None of these approaches – the frequency deadband method [5], the periodic DC method [9], or combinations of those [11, 12] – provide a means of jointly investigating the stability, performance and robustness properties of the combined feedback loops.

This paper presents the controller design for Diamond-II using preliminary corrector models, and summarises the GSVD-based controller [13]. To estimate the FOFB performance at Diamond-II, predictions of the Diamond-II disturbance [14] are used for obtaining worst-case estimates of the beam displacement. To validate these theoretical expectations, the algorithm is implemented and tested on the existing Diamond storage ring.

DIAMOND-II CONTROLLER DESIGN

Background: The Existing System

The electron beam dynamics at Diamond are modelled by a cross-directional system with one corrector type [10]:

$$y(s) = Rg(s)u(s) + d(s), \tag{1}$$

where $R \in \mathbb{R}^{n_y \times n_u}$ is the ORM, $s \in \mathbb{C}$ the Laplace variable, $u(s) \in \mathbb{C}^{n_u}$ are the corrector currents (inputs), $y(s) \in \mathbb{C}^{n_y}$ the BPM signals (outputs) and $d(s) \in \mathbb{C}^{n_y}$ the disturbances. The coupling between the planes is negligible so the horizontal and vertical orbit corrections are treated as separate control problems. The stable transfer function $g(s) \in \mathbb{C}$ captures the temporal dynamics of the correctors and is modelled as $g(s) := a/(s+a)\mathrm{e}^{-\tau_d s}$, where $a := 2\pi \times 700\,\mathrm{rad\,s^{-1}}$ is the magnet bandwidth and $\tau_d := 900\,\mu\mathrm{s}$ the time delay [10]. At Diamond, the controller is designed in modal space, i.e. the thin singular value decomposition (SVD) $R = U\Sigma V^{\mathrm{T}}$ is substituted in Eq. (1) and decoupled as $\hat{y}(s) = \Sigma g(s)\hat{u}(s) + \hat{d}(s)$, where $\hat{y}(s) := U^{\mathrm{T}}y(s)$, $\hat{u}(s) := V^{\mathrm{T}}u(s)$, $\hat{d}(s) := U^{\mathrm{T}}d(s)$. In modal space, the multi-input multi-output (MIMO) control problem is simplified to n_y decoupled SISO problems.

The Diamond-II System

For Diamond-II, the beam will be monitored by $n_y = 252$ BPMs, with primary BPMs located upstream and downstream of each ID. The front-end X-ray BPMs are integrated into the 100 kHz data stream so that primary (electron) BPMs can be substituted for front-end X-ray BPMs by providing the corresponding ORM, increasing the fault tolerance and allowing source point control of bending magnet beamlines. The FOFB will use $n_s = 252$ slow correctors with a bandwidth of ~ 200 Hz and $n_f = 144$ fast correctors with a bandwidth of ~ 8 kHz. The electron beam dynamics for the system with two corrector types are

$$y(s) = R_s g_s(s)u_s(s) + R_f g_f(s)u_f(s) + d(s), \tag{2}$$

where $R_s \in \mathbb{R}^{n_y \times n_s}$, $R_f \in \mathbb{R}^{n_y \times n_f}$, $n_y = n_s = 252$ and $n_f = 144$. The preliminary corrector models $g_s(s)$ and $g_f(s)$ include the frequency responses of the DAC, ADC, signal processing filters, power supplies, magnets, and copper vessel for slow correctors and stainless steel vessel for fast correctors, resulting in 2nd- and 3rd-order transfer functions. Note that since $n_s = n_y$, the FOFB can also be operated using slow correctors only, or fast correctors substituted for slow ones.

To reduce the latency in the FOFB loop, the FOFB communication network will be changed from a distributed topology to a centralised topology [1], and the centralised controller is planned to be implemented on the FPGA of a White Rabbit switch v4 (WRSv4). The time delay of $g_{(\cdot)}(s)$ is assumed to be 100 µs, which is a worst-case upper bound of the latency estimates for Diamond-II. The latency estimate includes 39.35 µs for signal processing (DAC, ADC, BPM), 8 µs for communication, 20 µs for FOFB computations, and 30 µs to account for uncertainty in the fast corrector model.

Decoupling the Diamond-II System

Analogous to the SVD for systems with one corrector type, the GSVD [4] factorises R_s and R_f as

$$R_s = X\begin{bmatrix}\Sigma_s & 0\\ 0 & I\end{bmatrix}U_s^{\mathrm{T}}, \qquad R_f = X\begin{bmatrix}\Sigma_f\\ 0\end{bmatrix}U_f^{\mathrm{T}}, \tag{3}$$

where $X = [x_1 \ldots x_{n_y}] \in \mathbb{R}^{n_y \times n_y}$ with $\det(X) \neq 0$, is the shared matrix of generalised output modes, $\Sigma_{(\cdot)} = \mathrm{diag}(\sigma_{(\cdot),1}, \ldots, \sigma_{(\cdot),n_f}) > 0$ with $(\cdot) = \{\mathrm{s}, \mathrm{f}\}$ are the matrices of generalised singular values that satisfy $\sigma_{\mathrm{s},i}^2 + \sigma_{\mathrm{f},i}^2 = 1$, and $U_{(\cdot)} \in \mathbb{R}^{n_{(\cdot)} \times n_{(\cdot)}}$ with $U_{(\cdot)}^{\mathrm{T}}U_{(\cdot)} = I$ are the matrices of generalised input modes. In contrast to the standard singular values that measure the gain in the direction of the singular vectors, the generalised singular values measure the relative gain of slow and fast correctors in the direction of x_i. It can be shown that the matrices X and $R = [R_s\ R_f]$ share the same standard singular values and left singular vectors [13], relating the modal decomposition to the generalised modal decomposition. For Diamond-II, the condition numbers are $\kappa(X) = 4404$ for the vertical and $\kappa(X) = 2371$ for the horizontal planes, and the generalised singular values satisfy $1 < \kappa(\Sigma_s) < 2$ and $1 < \kappa(\Sigma_f) < 2$.

Substituting the GSVD in Eq. (2) and left-multiplying with X^{-1} decouples the system with two corrector types as

$$\tilde{y}(s) = \begin{bmatrix}\Sigma_s & 0\\ 0 & I\end{bmatrix}g_s(s)\tilde{u}_s(s) + \begin{bmatrix}\Sigma_f\\ 0\end{bmatrix}g_f(s)\tilde{u}_f(s) + d(s), \tag{4}$$

where $\tilde{y}(s) := X^{-1}y(s)$, $\tilde{u}_{(\cdot)}(s) := U_{(\cdot)}^{\mathrm{T}}u_{(\cdot)}(s)$ and $\tilde{d}(s) := X^{-1}d(s)$. The decoupled systems shows that for $n_f < n_s =$

ISBN: 978-3-95450-236-3 ISSN: 2673-5350 doi:10.18429/JACoW-IBIC2023-M02I02

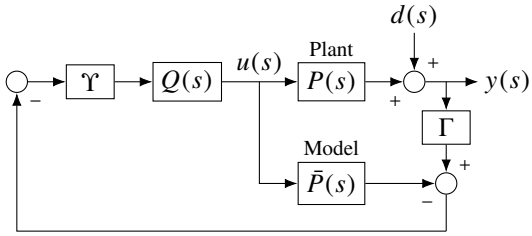


Figure 1: IMC structure in original space with additional compensators Υ and Γ.

n_y, only a subset of the disturbances is attenuated by slow and fast correctors, i.e. those lying entirely in $\text{span}(x_1, \ldots, x_{n_f})$.

TISO and SISO Controllers

Equation (4) reads row-wise as $\tilde{y}_i(s) = \tilde{P}_i(s)\tilde{u}_i(s) + \tilde{d}_i(s)$, where for $i \in \mathcal{I}_{\text{tiso}} := \{1, \ldots, n_f\}$, $\tilde{P}_i(s) := [\sigma_{s,i} g_s(s), \sigma_{f,i} g_f(s)]$, $\tilde{Q}_i(s) := [q_{s,i}(s), q_{f,i}(s)]^T$, and $\tilde{u}_i(s) := [u_{s,i}(s), u_{f,i}(s)]^T$, and for $i \in \mathcal{I}_{\text{siso}} := \{n_f + 1, \ldots, n_s\}$, $\tilde{P}_i(s) := g_s(s)$, $\tilde{Q}_i(s) := q_{s,i}(s)$, and $\tilde{u}_i(s) := \tilde{u}_{s,i}(s)$. Although any control approach including PID control could be applied, the internal model control (IMC) structure is used [15], which is naturally amenable to time delays and also used at Diamond. The IMC structure is shown in is shown in Fig. 1 in original space, where Υ and Γ are matrices that will be considered in the following section. For the remainder of this paper, the plant model is assumed to be accurate, i.e. $P_i(s) = \bar{P}_i(s)$ and $\tilde{P}_i(s) = \tilde{\bar{P}}_i(s)$, so that the control inputs are $\tilde{u}_i(s) = -\tilde{Q}_i(s)\tilde{d}_i(s)$. Substituting in the row-wise dynamics yields $\tilde{y}_i(s) = \big(1 - \tilde{P}_i(s)\tilde{Q}_i(s)\big)\tilde{d}_i(s)$. First, the desirable closed-loop dynamics are defined as

$$\tilde{y}_i(s) = \big(1 - T_{(\cdot)}(s)\big)\tilde{d}_i(s) \quad \text{for } i \in \mathcal{I}_{(\cdot)}, \tag{5}$$

for $(\cdot) = \{\text{tiso}, \text{siso}\}$ and where the complementary sensitivities must satisfy $T_{(\cdot)}(0) = 1$ for a zero steady-state error. Secondly, the controller structure is simplified as $\tilde{k}_{(\cdot),i} \times f_{(\cdot)}(s)$ for $(\cdot) = \{\text{s}, \text{f}\}$, so that equating Eq. (5) and the row-wise dynamics yields

$$q_{(\cdot)}(s) := \tilde{k}_{(\cdot),i} T_{(\cdot)}(s) / g_{(\cdot)}(s), \tag{6}$$

for $(\cdot) = \{\text{s}, \text{f}\}$ and where $T_s(s) := T_{\text{siso}}(s)$ and $T_f(s) := T_{\text{tiso}}(s) - T_{\text{siso}}(s)$, and $\tilde{k}_{s,i} := 1/\sigma_{s,i}$ and $\tilde{k}_{f,i} := 1/\sigma_{f,i}$ for $i \in \mathcal{I}_{\text{tiso}}$, and $\tilde{k}_{s,i} = 1$ for $i \in \mathcal{I}_{\text{siso}}$. The controller in Eq. (6) splits the control effort between slow and fast correctors and is also referred to as mid-ranging controller [16].

For Diamond-II, the corrector models $g_s(s)$ and $g_s(s)$ are 2nd- and 3rd-order transfer functions with a time delay of $\tau_d = 100\,\mu\text{s}$, so the complementary sensitivities are chosen as $T_{(\cdot)}(s) := \omega_{(\cdot)}/(s + \omega_{(\cdot)}) \times H_{2,(\cdot)}(s)e^{-s\tau_d}$, where $(\cdot) = \{\text{tiso}, \text{siso}\}$ and $H_{2,(\cdot)}(s)$ is a second-order Butterworth filter [15] with a cutoff frequency of 500 Hz for SISO and 10 kHz for TISO systems.

Tuning for Expected Disturbances

The controller is tuned based on the estimated power spectral density (PSD) of the disturbance for Diamond-II, which

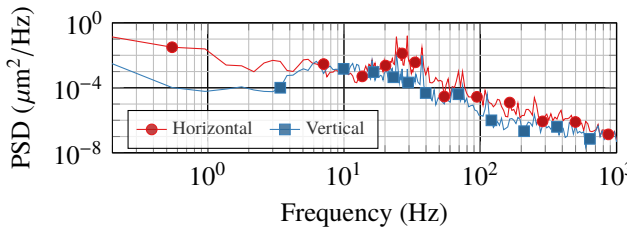


Figure 2: Estimated power spectral density (PSD) of the uncorrected vertical disturbance for Diamond-II at the upstream primary BPM on the first standard straight [14].

is shown in Fig. 2 for the upstream primary BPM on the first standard straight [14]. The PSD includes contributions from ground vibrations, girder motion, power supply ripple and RF noise.

The closed-loop bandwidth of the slow correctors, ω_{siso}, is limited by rate constraints of the power supplies, but must be chosen high enough to deliver low-frequency disturbance attenuation across all n_y directions. According to Fig. 2, the PSD drops by several orders of magnitude above 100 Hz, so ω_{siso} is chosen as $\omega_{\text{siso}} = 2\pi \times 100\,\text{rad}\,\text{s}^{-1}$. Note that if ω_{siso} is chosen larger than the open-loop bandwidth of $g_s(s)$, the controller will result in large corrector gains above the open-loop bandwidth.

Although a large ω_{tiso} yields a large overall closed-loop bandwidth, in the presence of large time delays it can cause disturbances to be amplified by a large sensitivity peak, i.e. large values of $S_{\max} := \max_\omega |S_{\text{tiso}}(\text{j}\omega)|$. Moreover, large ω_{tiso} may cause disturbances at high frequencies (i.e. above the closed-loop bandwidth) to be amplified, and make the controller prone to instabilities [15]. A bandwidth of 1 kHz for $S_{\text{tiso}}(s)$ results in $S_{\max} = 6\,\text{dB}$ at 5 kHz, so the bandwidth is reduced to 600 Hz ($\omega_{\text{tiso}} = 2\pi \times 2\,\text{krad}\,\text{s}^{-1}$), giving $S_{\max} = 4.12\,\text{dB}$ at 2.2 kHz. Note that with a time delay of 70 µs instead of 100 µs, the peak could be reduced to 2.4 dB, or the closed-loop TISO bandwidth increased to 1 kHz with $S_{\max} = 4.12\,\text{dB}$.

Structure in Original Space

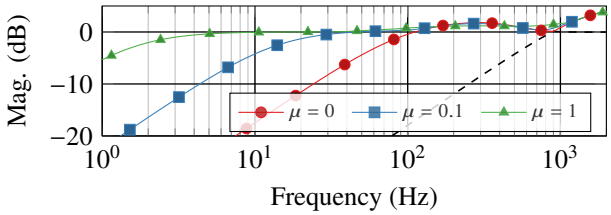
After designing the TISO and SISO controllers for the decoupled systems, the modal controllers in Eq. (6) are concatenated and mapped back to original space to obtain the control inputs as $u_{(\cdot)}(s) = -Q_{(\cdot)}(s)d(s)$ with $Q_{(\cdot)}(s) := K_{(\cdot)}q_{(\cdot)}(s)$ and $K_{(\cdot)} := U_{(\cdot)}\tilde{K}_{(\cdot)}X^{-1}$. Substituting the control inputs in Eq. (2) yields the closed-loop dynamics in original space:

$$y(s) = \Big(I - IT_{\text{siso}}(s) - X_{\text{tiso}}X^{-1}T_f(s)\Big)d(s), \tag{7}$$

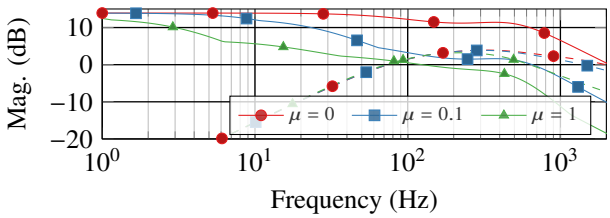
where $X_{\text{tiso}} := \big[x_1, \ldots, x_{n_f}, 0, \ldots, 0\big]$. Since $\kappa(X) = \kappa(R) \gg 1$, the inverse X^{-1} in $K_{(\cdot)}$ produces large controller gains in directions associated with the small singular values of R. Moreover, the term associated with the $n_f < n_s$ fast correctors in Eq. (7) amplifies certain disturbance directions when X is not orthogonal.

Content from this work may be used under the terms of the CC-BY-4.0 licence (© 2023). Any distribution of this work must maintain attribution to the author(s), title of the work, publisher, and DOI

ISBN: 978-3-95450-236-3 ISSN: 2673-5350 doi:10.18429/JACoW-IBIC2023-MO2I02



(a) MIMO sensitivity.



(b) MIMO controller gains.

Figure 3: Minimum (dashed) and maximum singular values of the sensitivity $S(\mathrm{j}\omega)$ for different values of μ (a), and controller gains for slow and fast (dashed) correctors (b).

In original space, two compensators, $\Upsilon \in \mathbb{R}^{2n_y \times n_y}$ and $\Gamma \in \mathbb{R}^{n_y \times n_y}$, are added to the IMC structure in Fig. 1, where $P(s) := [R_s g_s(s)\ R_f g_f(s)]$, $Q(s) := \mathrm{diag}(Q_s(s), Q_f(s))$, and $u(s) := [u_s(s)^T\ u_f(s)^T]^T$. The compensator $\Upsilon := [I\ \Upsilon_f^T]^T$ with $XX^{\dagger}_{\mathrm{tiso}}$ only applies to the case $n_f < n_s$ and projects $d(s)$ onto $x_1, \ldots, x_{n_f}$ for the TISO systems [13].

The compensator Γ reduces the controller gain and is defined as $\Gamma := (XX^T + \mu I)^{-1} XX^T$, where $\mu \in \mathbb{R}_{\geq 0}$ is a regularisation parameter [13]. With Υ and Γ, the closed-loop dynamics are $y(s) = S(s)d(s)$, where the sensitivity $S(s)$ is

$$S(s) := I - P(s)Q(s)\Upsilon(I + (\Gamma - I)P(s)Q(s)\Upsilon)^{-1}\Gamma. \quad (8)$$

The effect of Γ on the minimum and maximum singular values of $S(\mathrm{j}\omega)$ is shown in Fig. 3a for $\mu = \{0, 0.1, 1\}$. The maximum singular values of the transfer functions from $d(s)$ to $u_s(s)$ and $u_f(s)$ are shown in Fig. 3b. As μ increases, the overall bandwidth decreases, but the minimum singular values (dashed) remain unchanged. It can be shown that the bandwidth is reduced for higher modes of $R = [R_s\ R_f]$ that satisfy $\sigma_i^2 \ll \mu$. As most of the disturbances are input disturbances, most of the disturbances occur within the lower order modes, which justifies the use of the compensator Γ [13]. For Diamond-II, μ is chosen as $\mu = 0.1$, yielding a fast corrector demand of 276 mA and 92 mA in the horizontal and vertical direction up to 1 kHz, which is below the maximum demand of 920 mA.

Expected Performance

Although the PSDs from Fig. 2 can be used to design the TISO and SISO controllers, they lack the phase information that is required to describe the spatial distribution across the storage ring needed for the MIMO analysis. However, an upper bound on the amplitude spectral density (ASD) $|Y_i(\omega_k)|$ – the square root of the PSD – at BPM i can be obtained from

$$|Y_i(\omega_k)| \leq \sum_{j=1}^{n_y} |S_{ij}(\omega_k)||D_j(\omega_k)|, \quad (9)$$

where $S_{ij}(\omega_k)$ refers to row i and column j of $S(\cdot)$ in Eq. (8) and $D_j(\omega_k)$ to the disturbance at BPM j. Another upper bound is $|Y_i(\omega_k)| \leq \|Y(\omega_k)\|_2 \leq \|S(\omega_k)\|_2 \|D(\omega_k)\|_2$, though this is always equally or more conservative than the bound in Eq. (9).

In addition, the performance can be estimated with simulations that use disturbances obtained from sampling the ASDs in Fig. 2 with a random phase. Although these simulations do not yield strict upper bounds, they also lack the phase information, so that simulations can be interpreted as an additional measure of worst-case performance.

The integrated beam motion (IBM) up to 1 kHz, i.e. the square root of the integral of the PSD, is summarised for all primary BPMs in Table 2. The results show that the upper bound from Eq. (9) yields a conservative estimate that is more than two times larger than the attenuation expected from simulations. However, except for the primary BPMs of the long straight in the vertical direction, the upper bound is below the target deviation, indicating that the Diamond-II specifications are met. For the long straights, the IBM is up to 0.04 µm above target for the upper bound, but below target in simulations. Since the PSD lacks phase information, the Diamond-II disturbance does not reflect the characteristic modal distribution caused by input disturbances and the regularisation significantly impacts the controller performance. However, given that most of the Diamond-II disturbances are input disturbances, it can be expected that the targets will also be met on the long straights.

TESTS ON THE EXISTING DIAMOND STORAGE RING

As part of the FOFB design for Diamond-II, the GSVD-based controller has been implemented and tested on the existing Diamond storage ring. The aim of these experiments is to evaluate the controller in practice, i.e. investigate the FOFB with $n_f < n_s$ and model uncertainty, and to test new FOFB configurations, such as the centralised topology used at Diamond-II. The control system is implemented on a VadaTech AMC540 – a board combining a Xilinx Virtex-7 FPGA with two Texas Instruments (TI) DSPs [17] – and interfaced with the FOFB communication network. The existing 24 computing nodes from all the cells in the storage ring are bypassed, and the communication network reconfigured to form the centralised topology used at Diamond-II. The FPGA on the AMC540 is used for signal routing, and the DSPs are used to produce the corrector inputs for the horizontal and vertical directions. During tests with the AMC540, the time delay is increased from 700 µs to 900 µs and the communication network additionally broadcasts setpoints for the correctors.

As the FOFB at Diamond uses only one corrector type, a subset of $n_u = 160$ correctors and $n_y = 96$ BPMs is selected

Content from this work may be used under the terms of the CC-BY-4.0 licence (© 2023). Any distribution of this work must maintain attribution to the author(s), title of the work, publisher, and DOI

ISBN: 978-3-95450-236-3 ISSN: 2673-5350 doi:10.18429/JACoW-IBIC2023-MO2I02

Table 2: Targets and expected IBMs up to 1 kHz for Diamond-II at upstream (US) and downstream (DS) primary BPMs on long straights (LS), mid straights (MS), and standard straights (SS). All values are in µm. The disturbance corresponds to FOFB disabled, and the bound is obtained from Eq. (9).

	Horizontal						Vertical					
	LS US	**LS DS**	**MS US**	**MS DS**	**SS US**	**SS DS**	**LS US**	**LS DS**	**MS US**	**MS DS**	**SS US**	**SS DS**
Disturbance	0.64	0.72	0.45	0.48	0.6	0.61	0.25	0.25	0.21	0.2	0.22	0.21
Target	1.20	1.20	0.90	0.90	0.97	0.97	0.23	0.23	0.14	0.14	0.18	0.18
Bound	0.53	0.41	0.21	0.25	0.2	0.48	0.24	0.27	0.11	0.07	0.13	0.11
Simulation	0.16	0.18	0.06	0.07	0.04	0.11	0.15	0.20	0.07	0.03	0.07	0.06

and represented as in Eq. (2) with $g_s(s) = g_f(s) = g(s)$ and $\tau_d = 900\,\mu s$. The correctors are divided into $n_s = 96$ "slow" and $n_f = 64$ "fast" correctors, and the controller is designed using the GSVD-based approach with $\omega_{tiso} = 2\pi \times 176\,rad\,s^{-1}$ and $\omega_{siso} = 2\pi \times 50\,rad\,s^{-1}$. With this choice of parameters, the sensitivity overshoot is 3.4 dB at 300 Hz.

The GSVD-based controller is compared with a "standard" IMC controller that controls the same $n_y = 96$ BPMs and $n_s = 96$ correctors, but with all n_u correctors tuned to a closed-loop bandwidth of $2\pi \times 176\,rad\,s^{-1}$. All algorithms are evaluated on the storage ring at 300 mA beam current and with wigglers disabled.

The horizontal IBMs measured at BPM 1 are compared in Fig. 4, which also shows the disturbance recorded before the experiments (with FOFB disabled) and the corresponding simulated attenuation. As expected from the lower SISO bandwidths, the GSVD-based controller performs worse than the standard controller, but the results show that both controllers yield similar closed-loop bandwidths. The performance differences between standard and GSVD-based controllers are within 0.01 µm for frequencies below 10 Hz, and decrease for higher frequencies, which is in line with theoretical expectations. Comparing the simulation with the real-world results, the simulations perform slightly worse in the horizontal plane, but better in the vertical plane. The differences could be caused by various factors, including model uncertainty or time varying disturbance spectra.

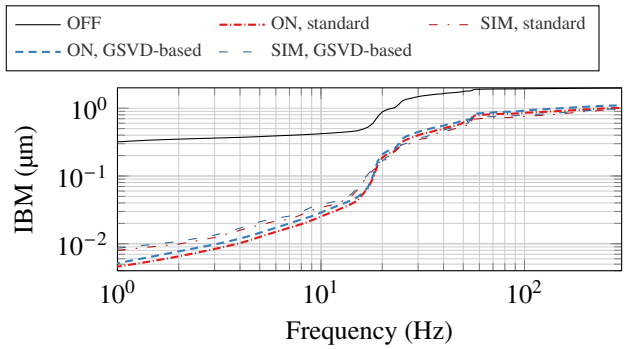


Figure 4: Measured (OFF, ON) and simulated (SIM) horizontal IBM for BPM 1 of the Diamond storage ring with FOFB disabled, standard and GSVD-based IMC.

CONCLUSION

In this paper we have proposed a joint control method for the FOFB at Diamond-II that will use slow and fast correctors. The performance of our method was evaluated using PSD estimates of the disturbance at Diamond-II. We calculated a worst-case upper bound that meets the performance criteria except for the primary BPMs in the long straight that exceed the target by 0.002 µm (0.9 %) in the vertical plane. However, simulations using sampled disturbance show that this upper bound may be conservative. Once the fast correctors are prototyped, the actuator dynamics and the latency will be updated, which is likely to result in better performance estimates.

To demonstrate our algorithm in practice, we integrated a new computing node in the existing storage ring and implemented a GSVD-based controller, splitting the control effort onto designated slow and fast correctors. The results from tests on the storage ring showed that although only a subset of the correctors covered the full bandwidth, the performance of the controller with two corrector types was nearly as good as the one with one corrector type, and that the simulations accurately reflect experimental measurements.

Even though the simulation and real-world results proved the feasibility for Diamond-II, several research questions remain. The mid-ranging approach requires inverting $g_s(s)$ and $g_f(s)$, but for Diamond-II the fast correctors may be such that $g_f(0) = 0$. The mid-ranging approach may therefore result in undesirable integrating behaviour for the fast correctors. To avoid this problem, one solution would be to invert only parts of $g_f(s)$ and quantify the resulting performance loss. Alternatively, one could combine the generalised modal decomposition with a $\mathcal{H}_2$ or $\mathcal{H}_\infty$ controller design [15], which may also reduce the sensitivity peaks.

While upper bounds showed that most performance requirements for Diamond-II are met, simulations using sampled Diamond-II data and tests on the existing facility showed that these upper bounds are conservative. To obtain less conservative bounds, future research could extend the disturbance data using phase information, e.g. by aggregating the different disturbance sources and modelling their spatial impact onto the storage ring.

Content from this work may be used under the terms of the CC-BY-4.0 licence (© 2023). Any distribution of this work must maintain attribution to the author(s), title of the work, publisher, and DOI

ISBN: 978-3-95450-236-3 ISSN: 2673-5350 doi:10.18429/JACoW-IBIC2023-MO2I02

REFERENCES

[1] M. G. Abbott *et al.*, "Diamond-II technical design report," Diamond Light Source, Tech. Rep., Aug. 2022. https://www.diamond.ac.uk/Home/News/LatestNews/2022/14-10-22.html

[2] S. R. Duncan and W. Heath, "The robustness of multi-array cross-directional control systems," in *Proc. Contr. Sys. Conf.*, Stockholm, Sweden, Sep. 2010, pp. 180–185.

[3] S. Gayadeen, S. R. Duncan, and W. P. Heath, "Design of multi-array controllers for electron beam stabilisation on synchrotrons," in *Proc. Amer. Contr. Conf. (ACC'13)*, Washington, DC, USA, Jun. 2013, pp. 1201–1206. doi:10.1109/ACC.2013.6579999

[4] G. H. Golub and C. F. Van Loan, *Matrix Computations*, 4th ed. The Johns Hopkins Univ. Press, 2013.

[5] N. Hubert, L. Cassinari, J. C. Denard, A. Nadji, and L. Nadolski, "Global Fast Orbit Feedback System Down to DC using Fast and Slow Correctors," in *Proc. Eur. Workshop Beam Diagn. Instrum. Part. Accel. (DIPAC'09)*, Basel, Switzerland, May 2009, pp. 27–31. https://jacow.org/d09/papers/MOOC01.pdf

[6] C. Steier, E. Domning, T. Scarvie, and E. Williams, "Operational Experience Integrating Slow and Fast Orbit Feedbacks at the ALS," in *Proc. Eur. Part. Accel. Conf. (EPAC'04)*, Lucerne, Switzerland, Jul. 2004, pp. 2786–2788. http://jacow.org/e04/papers/THPLT141.pdf

[7] E. Plouviez and F. Uberto, "The Orbit Correction Scheme of the New EBS of the ESRF," in *Proc. of Int. Beam Instrum. Conf. (IBIC'16)*, Barcelona, Spain, Sep. 2016, pp. 51–54. doi:10.18429/JACoW-IBIC2016-MOPG09

[8] C. Schwartz and L. Emery, "Compensating the Frequency Deadband of the APS Real-Time and DC Transverse Orbit Correction Systems," in *Proc. Part. Accel. Conf. (PAC'01)*, Chicago, IL, USA, Jun. 2001, pp. 1234–1236. https://jacow.org/p01/papers/TPAH001.pdf

[9] L. H. Yu, S. Krinsky, O. Singh, and F. J. Willeke, "The Performance of a Fast Closed Orbit Feedback System with Combined Fast and Slow Correctors," in *Proc. Eur. Part. Accel. Conf. (EPAC'08)*, Genoa, Italy, Jun. 2008, pp. 3315–3317. https://jacow.org/e08/papers/THPC140.pdf

[10] S. Gayadeen and S. R. Duncan, "Discrete-time anti-windup compensation for synchrotron electron beam controllers with rate constrained actuators," *Automatica*, vol. 67, pp. 224–232, May 2016. doi:10.1016/j.automatica.2016.01.037

[11] E. Plouviez, F. Epaud, F. Farvacque, and J. M. Koch, "Optimisation of the SVD treatment in the fast orbit correction of the ESRF storage ring," in *Proc. Int. Beam Instrum. Conf. (IBIC'13)*, Oxford, UK, Sep. 2013, pp. 694–697. https://jacow.org/IBIC2013/papers/WEPC13.pdf

[12] E. Plouviez, F. Epaud, J. M. Koch, and M. B. Scheidt, "The new fast orbit correction system of the ESRF storage ring," in *Proc. Eur. Workshop Beam Diagn. Instrum. Part. Accel. (DIPAC'11)*, Hamburg, Germany, May 2011, pp. 215–217. https://jacow.org/DIPAC2011/papers/MOPD74.pdf

[13] I. Kempf, P. J. Goulart, and S. Duncan, "Control of Two-Array Cross-Directional Systems using the Generalised Singular Value Decomposition," *arXiv*, 2023. doi:10.48550/arXiv.2308.08631

[14] I. P. S. Martin *et al.*, "Orbit Stability Studies for the Diamond-II Storage Ring," in *Proc. Int. Part. Accel. Conf. (IPAC'22)*, Bangkok, Thailand, Jul. 2022, pp. 2602–2605. doi:10.18429/JACoW-IPAC2022-THPOPT017

[15] M. Morari and E. Zafiriou, *Robust Process Control*, 1st ed. Prentice-Hall, 1989.

[16] B. J. Allison and A. J. Isaksson, "Design and performance of mid-ranging controllers," *J. Proc. Contr.*, vol. 8, no. 5, pp. 469–474, Oct. 1998. doi:10.1016/S0959-1524(98)00012-2

[17] VadaTech, *Xilinx Virtex-7 FPGA AMC with dual TI DSP (AMC540)*, 4FM737-12, 2019.

Content from this work may be used under the terms of the CC-BY-4.0 licence (© 2023). Any distribution of this work must maintain attribution to the author(s), title of the work, publisher, and DOI

ISBN: 978-3-95450-236-3 ISSN: 2673-5350 doi:10.18429/JACoW-IBIC2023-MO2C03

COUPLED BUNCH MODE ZERO CORRECTION WITHIN THE ORBIT FEEDBACK BANDWIDTH *

P. Kallakuri†, A. Brill, J. Carwardine, L. Emery and N. Sereno
Argonne National Lab, Lemont, USA

Abstract

The fast orbit feedback (FOFB) bandwidth for Advanced photon source upgrade (APS-U) will be DC-1 kHz and the synchrotron frequency will be between 100-560 Hz. This frequency overlap places coupled bunch mode 0 (CBM0) induced horizontal orbit motion inside the orbit feedback bandwidth, potentially affecting our ability to achieve beam stability goals. Longitudinal feedback kicker is not strong enough to damp CBM0 oscillations. We developed new beam-based feedback method to suppress CBM0 oscillations with low level RF phase as actuator. It uses existent FOFB framework with no changes to the feedback algorithm. Effectiveness of this method is verified using present APS operations lattice where synchrotron frequency is outside orbit feedback bandwidth. In the present work, low alpha lattice is created to emulate APS-U setting where synchrotron frequency is inside the orbit feedback bandwidth. Experiments with this lattice successfully demonstrated CBM0 correction within orbit feedback bandwidth. Combined operation of orbit feedback and CBM0 correction is stable, and CBM0 oscillations are damped. We achieved better orbit motion suppression and corrector drive efforts are reduced as well.

INTRODUCTION

The target bandwidth of the Advanced Photon Source Upgrade (APS-U) Fast Orbit Feedback (FOFB) is DC-1000 Hz where the synchrotron tune will be between 100-560 Hz. This overlap places Coupled Bunch Mode 0 (CBM0) induced horizontal position offsets within the FOFB bandwidth range, affecting APS-U goals for beam stability. Large storage-rings such as APS would need longitudinal feedback system with high kick voltage capability for CBM0 suppression. APS-U longitudinal feedback kicker is not strong enough to damp CBM0 oscillations. We developed new orbit to RF phase feedback method using existent orbit feedback framework with no additional processing hardware requirements [1]. It operates at the Low Level RF (LLRF) signal level of the main RF system and does not require high kick voltages. Based on synchrotron oscillation theory [2, 3], we derived relationship between beam position deviation at dispersive BPMs and RF phase noise that represents the open loop dynamics of our feedback configuration. An analytical model is devised for the coupling mechanism of synchrotron oscillations to transverse orbit through dispersion. It allows an energy-induced component to be extracted from the measured orbit which is derivative of the RF phase error. Using this the orbit feedback controller generates a RF phase control signal as another drive signal in the orbit feedback algorithm. Experiments conducted at the present APS storage ring using 7 GeV operations lattice and APS-U prototype fast orbit feedback controller [4, 5] demonstrated the effectiveness of this method at damping coupled bunch mode zero oscillations.

In the above experiments [1] the synchrotron frequency (2.2 kHz) and orbit feedback bandwidth (920 Hz) are well separated. We continued our study using low-alpha lattice configuration developed to mimic APS-U setting where, synchrotron frequency (60 Hz) is within the orbit feedback bandwidth (90 Hz). We would be able to study the interaction of both feedbacks more clearly in this setup. The storage-ring energy is set to 6 GeV and low momentum compaction factor of $3.6 \cdot 10^{-06}$ is used to get synchrotron frequency to around 60 Hz. Orbit feedback with 1.5 kHz sampling rate used for APS operations is termed as Real Time Feedback (RTFB) [6]. Experiments with low-alpha lattice are conducted using RTFB system so that we would be able to use 38 fast correctors and 154 BPMs around the ring. With the prototype system we could only use 3 fast correctors and 12 BPMs in 2 sectors that is not adequate to deal with larger noise seen in low-alpha lattice. Details of our experimental setup with RTFB controller, closed loop performance of orbit to RF phase feedback, and results from the simultaneous operation of RTFB and CBM0 correction with low alpha lattice are presented in next sections.

EXPERIMENTAL SETUP

Closed loop schematic of RTFB together with orbit to RF phase feedback is shown in Figure 1. RTFB controller hardware only allows use of total 160 BPMs (4 per sector) for orbit feedback computations. We used 154 BPMs for beam position measurements. Orbit feedback uses 38 horizontal fast correctors, and orbit to RF phase feedback is integrated into RTFB framework by repurposing fast corrector (S40A:H3) analog drive signal as phase drive. DAC output channel of S40A:H3 is connected to LLRF system [7] phase input. The cavity phase loop bandwidth is adequately greater than the synchrotron oscillation frequency. So the RF system is considered as simple gain term in the feedback model. PID_rtfb controller is used orbit correction and PID_rfPh controller is used for CBM0 correction. Same feedback algorithm that generates corrector power supply set-points is used for phase drive. Phase computations are incorporated as additional row in Inverse Response Matrix (IRM) dot product. Horizontal BPM position vector **x** is

* Work supported by the U.S. Department of Energy, Office of Science, under Contract No. DE-ACO2-O6CH11357.
† pkallakuri@anl.gov

Content from this work may be used under the terms of the CC-BY-4.0 licence (© 2023). Any distribution of this work must maintain attribution to the author(s), title of the work, publisher, and DOI

ISBN: 978-3-95450-236-3 ISSN: 2673-5350 doi:10.18429/JACoW-IBIC2023-MO2C03

Content from this work may be used under the terms of the CC-BY-4.0 licence (© 2023). Any distribution of this work must maintain attribution to the author(s), title of the work, publisher, and DOI

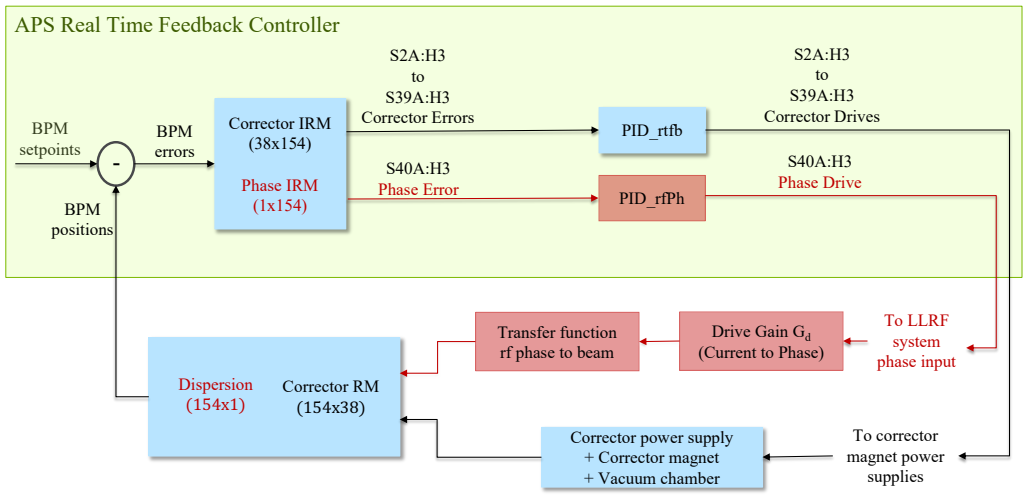


Figure 1: Experimental setup for simultaneous operation of RTFB and orbit to RF phase feedback using APS RTFB system.

obtained from 154 BPMs. Phase error is calculated as dot product of measured orbit and weighted dispersion vector *Phase_IRM* as defined in Eq. (1). α_c is the momentum compaction factor, ω_{rf} is RF angular frequency, and η is the dispersion vector.

$$Phase_IRM = \frac{180}{\pi}\frac{1}{G_d}\frac{\omega_{rf}\alpha_c}{\eta\cdot\eta}\eta \qquad (1)$$

Drive gain $G_d = \frac{1}{13}$ is to convert phase drive in amperes to RF phase set-point in degrees. Phase IRM (1x154) computed from Eq. (1) and Corrector IRM (38x154) obtained from orbit response matrix are concatenated as 39x154 IRM used in the experiments. For beam-based studies we used 6 GeV low alpha lattice with storage-ring current of 14 mA in 24 bunch operation and 24 mA in 48 bunch operation. Relatively low currents are used since it was very difficult to inject into this lattice. So, beam loading is negligible.

ORBIT TO RF PHASE FEEDBACK FOR CBM0 CORRECTION

First step in our experiments is to establish LLRF phase set-point control from RTFB controller in open loop, and then verify the stability of orbit to RF phase feedback and suppression of synchrotron frequency magnitude in closed loop. For open loop measurements S40A:H3 drive signal is the input, and beam phase response is the output. Figure 2 shows the step input to phase drive, and measured beam phase response. Input step of 20 A resulted in 1.6° change in RF phase response confirming drive gain $G_d = \frac{1}{13}$. Large 360 Hz noise from klystron power supply is seen in the steady state RF phase.

CBM0 Correction in Closed Loop Operation

After testing the open loop drive setup, studies are conducted with closed loop orbit to RF phase feedback configuration using 1x154 phase IRM. The storage ring configuration for this test is 24 bunches, 14 mA, 6 GeV low alpha lattice with synchrotron frequency at 60 Hz. Closed loop

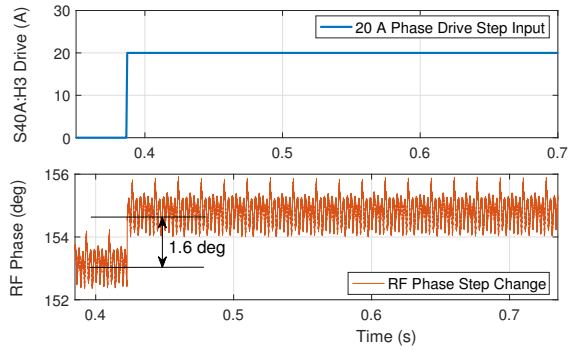


Figure 2: Open loop phase step response measured for 20 A input step amplitude.

is stable with negative proportional gain and we achieved suppression around synchrotron frequency. We tested K_p gains in the range -0.01 to -0.06, the beam was unstable beyond -0.06. Motion at 360 Hz.

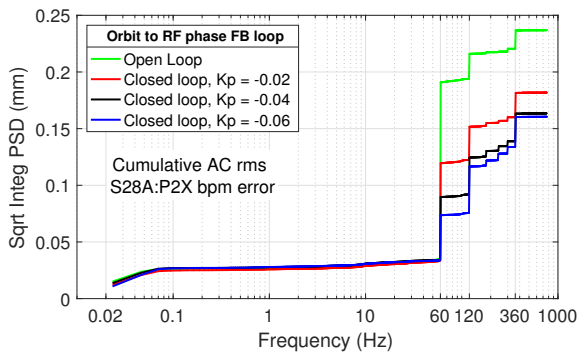


Figure 3: Orbit motion measured in open loop, and closed loop with different proportional gain values.

Figure 3 shows square root integrated Power Spectral Density (PSD) of BPM error for open loop and closed loop with different K_p gain values. Orbit motion suppression at synchrotron frequency (60 Hz) is observed when the feedback is ON. Increase in proportional gain resulted in more suppression at synchrotron frequency.

ISBN: 978-3-95450-236-3 ISSN: 2673-5350 doi:10.18429/JACoW-IBIC2023-MO2C03

REAL TIME FEEDBACK WITH COUPLED BUNCH MODE ZERO CORRECTION

Next step in our experiments is to study interaction between CBM0 correction and RTFB during the simultaneous operation of both feedbacks.The test configuration is 6 GeV low alpha lattice with 48 bunches and 24 mA storage-ring current. Synchrotron frequency 60 Hz is within the orbit feedback bandwidth of 90 Hz emulating APS-U settings.

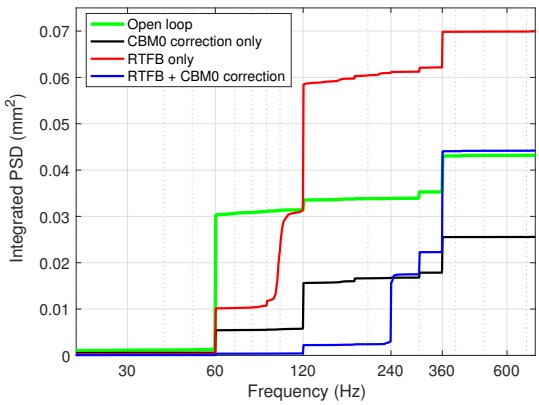


Figure 4: Comparison of cumulative mean square orbit motion at S28A:P2X BPM for different feedback configurations.

Closed loop with unified 39x154 IRM is stable with proportional controllers. For RTFB we used K_p gains in the range 0.01 to 0.03, and for orbit to RF phase feedback we used K_p gains in the range -0.01 to -0.05. For individual operation optimum performance is achieved with maximum permissible K_p gains in each case. For simultaneous operation we tuned the gains together for optimum performance. For RTFB $K_p = 0.02$, and for CBM0 correction $K_p = -0.03$ are the optimal gains. The angle between dispersion and betatron closed orbits with 154 BPMs are in the range $83 - 97°$ which is comparable to 440 BPMs case shown in Ref. [1].

We are working on a simulation study to further understand whether this near orthogonality is inferring complete decoupling when both corrections has a frequency overlap. BPM noise response data is measured for different feedback configurations: open loop, CBM0 correction only $K_p = -0.05$, RTFB only $K_p = 0.03$, RTFB $K_p = 0.02$ + CBM0 correction $K_p = -0.03$. Integrated PSD of BPM error in different feedback configurations is shown in Figure 4. Open loop orbit motion shows significant spike at 60 Hz, which is suppressed in all three closed loop configurations: RTFB only, CBM0 correction only, and RTFB + CBM0 correction. During individual operation, orbit to RF phase feedback and RTFB are correcting respective energy and betatron components at synchrotron frequency which resulted in partial suppression at 60 Hz. High frequency motion beyond 90 Hz is amplified during RTFB only operation. Motion at 120 Hz is amplified when only CBM0 correction is used. With both feedbacks running together we got significant suppression at 60 Hz due to the combined effect. Also, high frequency motion amplified by individual feedback operation is attenuated up to ≈220 Hz. Motion at 360 Hz is not suppressed by orbit to RF phase feedback. Perturbation at 360 Hz is in phase with RF phase modulation whereas perturbation at synchrotron tune is 90° out of phase. So, we would need large controller gains to affect 360 Hz which could be beyond the stability limit of synchrotron frequency damping.

BPM responses are measured at all 154 BPMs around the storage-ring to analyze envelope of the orbit motion. Figure 5 shows power spectral density plots of measured BPM errors in open loop and different closed loop configurations. All BPM responses showed similar frequency response pattern, while BPMs in the high dispersion area has larger magnitudes compared to others. Individual operation of RTFB or CBM0 correction partially suppressed 60 Hz and frequencies beyond 90 Hz are amplified. During combined

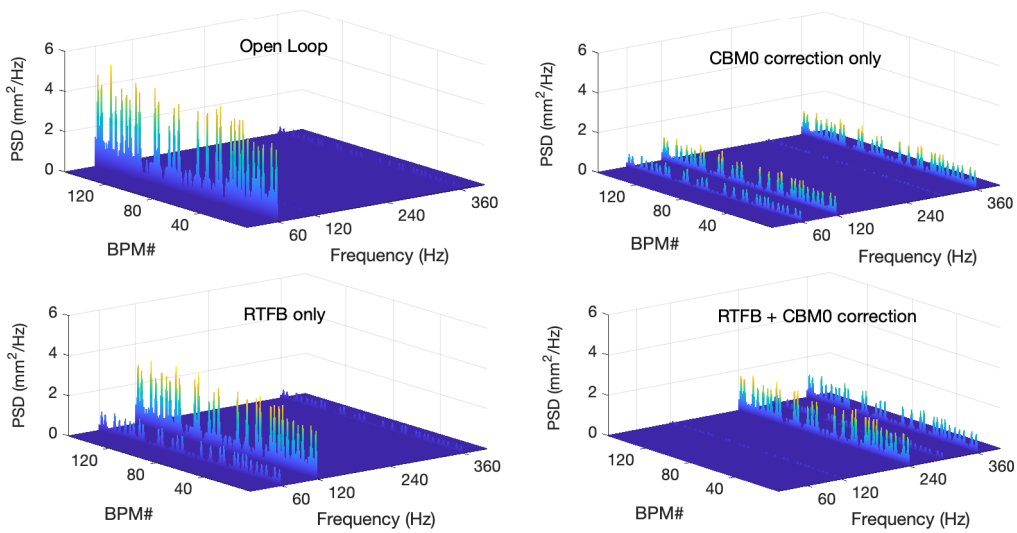


Figure 5: PSD of BPM errors at all 154 BPMs around the storage ring. Comparison of responses in open loop and different closed loop configurations.

Content from this work may be used under the terms of the CC-BY-4.0 licence (© 2023). Any distribution of this work must maintain attribution to the author(s), title of the work, publisher, and DOI

ISBN: 978-3-95450-236-3 ISSN: 2673-5350 doi:10.18429/JACoW-IBIC2023-MO2C03

operation significant suppression at 60 Hz and better orbit motion suppression up to 240 Hz is achieved. APS RF system has noise at 360 Hz and other 60 Hz harmonics. These frequencies have larger amplitudes in low alpha lattice configuration. Hence narrow resonant increase of noise at 60 Hz harmonics is seen when high frequency motion is amplified during individual and combined feedback operation.

Analysis of Feedback Control Efforts

Feedback control effort is the input to the actuator from the dynamic controller to perform necessary correction. Reduction in control efforts is beneficial to the feedback operation.The corrector and phase drive signals in our case indicate the control efforts. In order to analyze the drive efforts of both feedbacks we used cumulative mean square of phase and 38 corrector drive signals. Integrated PSDs of drive signals during individual operation of each feedback and combined operation of both feedbacks are shown in Figure 6. Drive magnitudes during individual operation

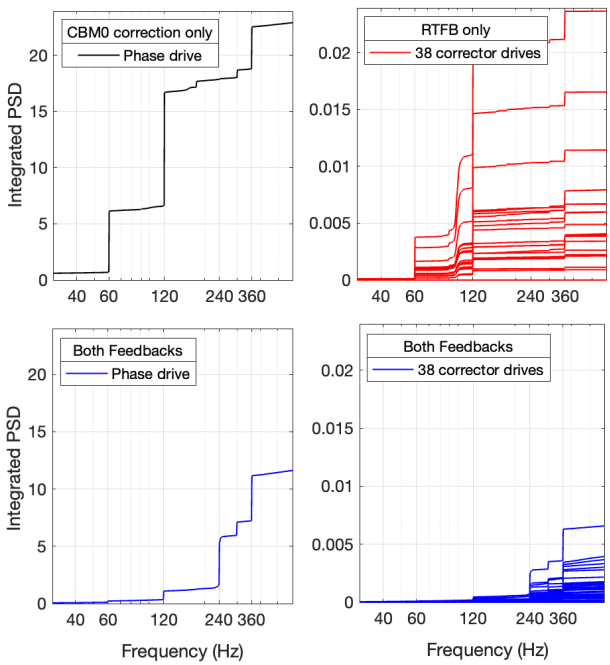


Figure 6: Comparison of drive efforts of each feedback individual operation with drive efforts in simultaneous operation.

are larger compared to simultaneous operation. During individual operation the feedbacks see large error at synchrotron frequency which results in more drive effort as the feedback keeps trying to correct the error. When CBM0 correction and orbit feedback are operated together both energy and betatron components are corrected simultaneously, and the error will be small. As a result phase and corrector drive magnitudes for frequencies below 120 Hz are significantly reduced in combined operation, and drive magnitudes up to Nyquist frequency are also less compared to respective individual operations. From these results we can say that the combined operation is aiding in control effort reduction of both feedbacks.

CONCLUSIONS

We successfully demonstrated CBM0 correction within the orbit feedback bandwidth. We used 6 GeV low-alpha lattice that provides a test setup where synchrotron frequency (60 Hz) is within the RTFB bandwidth (90 Hz) similar to APS-U configuration. First, we established LLRF phase set-point control from RTFB controller open loop and then verified the stability in closed loop. Orbit to RF phase feedback loop is stable and we achieved suppression around synchrotron frequency. Closed loop operation with both feedbacks using unified corrector and phase IRM is stable with proportional controllers. During individual operation, orbit to RF phase feedback and RTFB are correcting respective energy and betatron components at synchrotron frequency which resulted in partial suppression at 60 Hz. Orbit feedback was effective at reducing motion at synchrotron frequency, but did so at the expense of increasing broadband rms motion beyond the open-loop level. This was consistent with previous RTFB operating experience. Running CBM0 correction on its own also reduced motion at synchrotron frequency and without increasing the broadband rms motion. The combination of CBM0 correction and RTFB was significantly more effective than RTFB alone over all frequency bands from DC to 360 Hz. Feedback drive efforts are also reduced during combined operation of RTFB and CBM0 correction.

ACKNOWLEDGEMENTS

We are grateful to U.Wienands for the valuable insights. We wish to thank T. Berenc, S. Xu, S. Shoaf, R. Blake, H. Bui, and T. Madden for helping with experiments; V. Sajaev for the help with low alpha lattice setup.

REFERENCES

[1] P. Kallakuri, A. Brill, J. Carwardine, and N. Sereno, "Coupled bunch mode zero correction using orbit measurements and RF system phase feedback", in *Phys. Rev. Accel. Beams*, vol. 25, pp. 082801, 2022. doi:10.1103/PhysRevAccelBeams.25.082801

[2] W. Ormond and T. Rogers, "Synchrotron Oscillation Driven by RF Phase Noise", in *Proc. PAC'97*, Vancouver, Canada, May 1997, paper 4V038, pp. 1822–1824. https://jacow.org/pac97/papers/pdf/4V038.PDF

[3] H. Wiedemann, *Particle Accelerator Physics, 4th ed.*, Springer, 2015, ISBN: 978-3-319-30759-6.

[4] N. Sereno *et al.*, "Beam Stability R&D for the APS MBA Upgrade", in *Proc. IPAC'15*, Richmond, VA, USA, May 2015, pp. 1167–1169. doi:10.18429/JACoW-IPAC2015-MOPWI011

[5] P. S. Kallakuri, A. R. Brill, J. Carwardine, and N. Sereno, "Closed Loop Modeling of the APS-U Orbit Feedback System", in *Proc. NAPAC'19*, Lansing, MI, USA, Sep. 2019, pp. 683–686. doi:10.18429/JACoW-NAPAC2019-WEPLM11

[6] J. Carwardine and F. Lenkszus, "Real-time orbit feedback at the APS", in *Proc. BIW'98*, Palo Alto, CA, USA, May 1998.

[7] J. J. Song *et al.*, "Review of the APS SR RF Systems", in *Proc. APAC'98*, Tsukuba, Japan, Mar. 1998, paper 6D036, p. 767.

Content from this work may be used under the terms of the CC-BY-4.0 licence (© 2023). Any distribution of this work must maintain attribution to the author(s), title of the work, publisher, and DOI

ISBN: 978-3-95450-236-3 ISSN: 2673-5350 doi:10.18429/JACoW-IBIC2023-MO2C04

SOLEIL NEW PLATFORM FOR FAST ORBIT FEEDBACK

R. Bronès†, A. Bence, J. Bisou, N. Hubert, D. Pédeau, G. Pichon
Synchrotron SOLEIL, Gif-sur-Yvette, France

Abstract

SOLEIL is upgrading its Fast Orbit Feedback platform to withstand coming obsolescence of electronic BPM and future evolutions of the machine. This new platform has to be compatible with current boundary devices such as BPM electronics or corrector power supplies, but it also shall evolve to interface future versions of these systems. A MTCA based platform was designed and installed. It is integrated in the control system by mean of a OPCUA server, and care has been taken to seamlessly toggle the closing of the feedback loop on the former or new FOFB platform. This paper will present the first tests and results conducted to commission this new system.

CONTEXT AND SPECIFICATIONS

SOLEIL is working on upgrading its accelerators to the fourth generation of synchrotron. SOLEIL II will bring outstanding performances, with a new beam lattice, renewed systems and cutting-edge technics. As presented in [1], the renewal of BPM electronics will be conducted prior to the long shutdown and machine upgrade. The current Fast Orbit FeedBack (FOFB) system, which is strongly embedded in these electronics, is to be ported on a new platform.

The evolution of the FOFB spreads on several years and must follow the numerous modifications and improvements that will bring SOLEIL II. The roadmap for this system can be summarized in Table 1, while evolutions of key points are underlined in Table 2.

Table 1: FOFB Roadmap

	Evolution	Impact
2024	FOFB running on new platform	Same performances
2025	Added features	Faster lattice identification.
2026	New BPM electronics	Loop latency reduced, data rate increased, correction bandwidth increased
2028	SOLEIL II, new PSC	Loop latency reduction, dimension reduction, SOLEIL II performances
2028 +	New correction algorithm	Increased performances

Table 2: FOFB Performances Evolution

	Actual FOFB	Future FOFB
# BPM	122	180~200
# Corrector	50 H & V	44~60 H & V
Data rate	10 kHz	100 kHz
Correction BW	200 Hz	1 kHz
Loop Latency	350 µs	100 µs
Stability	10 % of beam size 20 µm H ; 0.8 µm V	2-3% of beam size 50 nm H & V

† romain.brones@synchrotron-soleil.fr

FOFB NEW PLATFORM INSTALLATION

A versatile platform was elaborated and is presented in [1]. We will detail last additions and comment on the installations.

Hardware Platform

The basis of the platform is a MTCA chassis, equipped with a SOC-FPGA board that host a SFP-FMC. The overall system is composed of five of these chassis, connected in a star topology. For denomination: a Central Node connected to four Cell Nodes. Communication between these nodes is a simple custom packet protocol, encapsulated in Ethernet frames and transported over optical fibers at 10 Gbps. This network was installed in the first months of 2023. Three full duplex fiber pairs are layed between Central and Cell Nodes, with one used and two as spare links.

The Cell Nodes are installed near BPM electronics in four different cells. For now they are connected as data spy to the running communication ring transporting the position data. After the upgrade of the BPM electronics, each Cell Node will be connected directly to a subset of them. Position data are grabbed, before being packeted and forwarded to the Central Node.

Correction packets are received back and transmitted to Power Supply Controller (PSC). A 1.25 Mbps RS422 UART link connects a Cell Node to each PSC. This limits the link length to 80 m and great care has been taken to position the Cell Nodes, each one serving PSCs in its own cell cabinet and to three neighbour cells. Current PSC can only receive command from one driver. We selected and installed very simple RJ45-CAT6 cables, each one transporting 4 differential pairs. To ease commutation from actual drivers (BPM electronics) to Cell Nodes, electromechanical relays were temporarily installed to toggle the differential lines from one driver to the other. Each relay can toggle 2 differential pairs. All relays are powered from a central location, activated by a single switch lever. Switched off relays connect the PSC to the BPM electronics. For the new platform tests, we simply have to toggle the lever to switch on all relays and connect PSC to the Cell Nodes. This feature was well received and shortened greatly the set-up times for dedicated machine shifts. Ultimately, relays will be removed.

To provide the RS422 UART commands to each PSC, Cell Nodes are equipped with a custom made RTM board named CACTUS. These very simple boards receive LVCMOS single-ended signals from the AMC FPGA and translate it to RS422 pairs, transported to RJ45 outlets, allowing us to put eight outlets on the RTM, hence providing signals to eight groups of four PSCs. Except from the MTCA management, no other functionality is

Content from this work may be used under the terms of the CC-BY-4.0 licence (© 2023). Any distribution of this work must maintain attribution to the author(s), title of the work, publisher, and DOI

ISBN: 978-3-95450-236-3 ISSN: 2673-5350 doi:10.18429/JACoW-IBIC2023-MO2C04

Content from this work may be used under the terms of the CC-BY-4.0 licence (© 2023). Any distribution of this work must maintain attribution to the author(s), title of the work, publisher, and DOI

embedded on the CACTUS. These board will be decommissioned with the PSC and replaced with a new interface compatible with SOLEIL II new PSC.

FPGA Firmware

Fast or interface-specific functionalities are supported by the FPGA matrix present on the AMC. From the position data grabbing to the correction command sending, the data passes through FPGA logic blocs: Ethernet core, BPM communication decoder, correction computation, UART for PSC, etc. The overall firmware project is built with the help of FWK, the framework provided by DESY MSK. This framework allows to separate functionalities in deployable blocs, organized and versioned to prepare two slightly different systems: Central and Cell Nodes firmware. Further features of this framework are an easier integration with software control and process script to rebuild. This will keep the firmware project clean and allow further evolutions.

The Cell Nodes grab the position data exchanged on the BPM dedicated network. Every 100 µs (10 kHz), 122 positions packets are exchanged, composed of (1) the BPM identification, (2) X and Y position data and (3) a frame number incremented at each iteration. Each Cell Node selects around ¼ of these packets and forwards these to the Central Node. On the way back 100 correction packets are received from the Central Node, composed of (1) the PSC identifier, (2) the correction data and (3) the same frame number used to compute this correction. Each Cell nodes selects in the stream the correction data for the PSC it is connected to and forward it with the proper format on the correct output interface. The latency from the position packet departure to Central Node to the corrector packet reception has been measured on field with a maximum value of 4.5 µs.

The Central Node receives and aggregates all the positions data from the Cell Nodes. The correction processing scheme is kept identical to the previous implementation [2]: (1) Remove reference orbit to get the position error at each BPM, (2) space change from BPM position errors to PSC correction errors using the inverted response matrix, obtained from singular value decomposition and corrected with Tikhonov Regularization and (3) filter corrections signals with a 8 Hz low-pass filter given in Eq. (1), before broadcasting corrections to the Cell Nodes. Note that with the closed-loop, perturbations will be attenuated by the inverse of this correction filter.

$$H(z)=\frac{64}{4096-4075z^{-1}} \quad (1)$$

Data can be captured before and after the correction processing chain. On user demand, a few tens of seconds of data can be captured and pushed in a dedicated DDR memory for the on-board software. A sine waveform generator is also added on the data path. It can add a sine waveform, with programmable frequency, phase, amplitude and offset to the correction signal. These features are heavily used for the systems tests and commissioning. The global data processing scheme in the Central Node is pictured in Fig. 1.

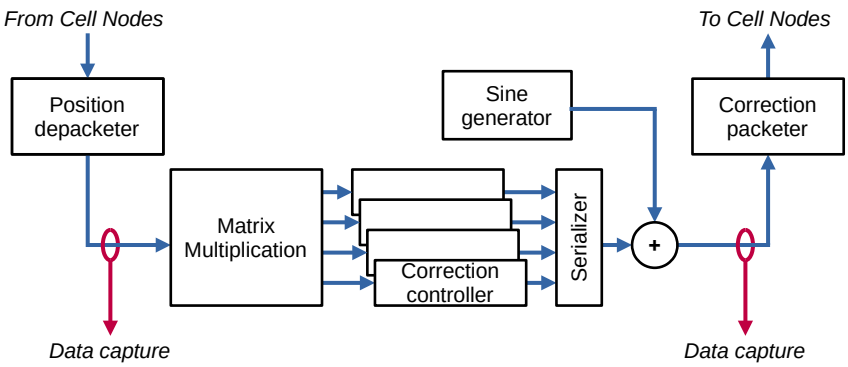


Figure 1: Overview of data processing inside the Central Node.

On-board Software

The FPGA-SOC provides a CPU which is running a Linux distribution built by Yocto. Regular operation can be performed: SSH connection, NFS mount, configuration scripting, logging, etc. To access the FPGA bloc functions programmed, we use a ChimeraTK generic server, which access FPGA register using Linux UIO and run an OPCUA server to provide access to remote control. The available FPGA registers are automatically understood by the software with a MAP files generated alongside the firmware. This feature allows name access to registers, from the OPCUA server. Identically, it is possible to access from python scripts and prompt with a ChimeraTK DeviceAccess python bindings. This features proved to be very helpful to conduct tests.

Integration in the Control System

SOLEIL II control system will still be Tango. Control of the new platform must initially be compliant with current Matlab Script and GUI, with features and access tools gradually added. Base access to the on board functionalities will use a Tango Server / OPCUA client which will bring registers up to the Tango Level. Expert users or applications will be built over this server.

ISBN: 978-3-95450-236-3 ISSN: 2673-5350 doi:10.18429/JACoW-IBIC2023-MO2C04

NEW IDENTIFICATION FEATURES

With the on-board sine generation and the local data capture, it is now possible to conduct easily identification of the system.

Transfer Function Identification

This identification aims at measuring the frequency response, or Transfer Function (TF) from the PSC command to the BPM Fast Acquisition (FA, 10 kHz) data output. This identification is performed open-loop, the correction algorithm is disabled and outputs zeros and a sine waveform is generated for a single PSC. Data is captured for several frequencies in the band of interest, capture length is stretched to be able to record at least 100 periods of the sine.

Data capture and sine generator are synchronized on the same clock reference. The sine generator is composed of a 16 bits Numerically Controlled Oscillator with a programmable phase increment Φi. Equation (2) shows ν_{sin} the normalized frequency to the data-rate which will be used for frequency analysis, preventing scalloping losses. Equation (3) shows how for each capture, we compute the complex Discrete Time Fourier Transform (DTFT) of all the BPM position at ν_{sin} before dividing it by the PSC DTFT. With this, we have the TF gain and phase of the selected PSC to every BPM, at each frequency point captured.

$$f_{sin} = f_{datarate}\,\Phi_i \;/\; 2^{16} \;\rightarrow\; \nu_{sin} = \Phi_i \;/\; 2^{16} \tag{2}$$

$$TF_{m,n}(\nu_{sin}) = \frac{DTFT\left[bpm_n\right](\nu_{sin})}{DTFT\left[psc_m\right](\nu_{sin})} \tag{3}$$

Each BPM has a different TF gain, depending on the Orbit Response Matrix (ORM). As we are interested in the overall shape of the TF, we first select the ten most significant TF and further normalize each one by its value at a given frequency (210 Hz) before aggregating the data by mean. The result is displayed on the Bode plot in Fig. 2. It shows an expected drop at 1.5 kHz coming from the notch filter, and a constant delay of 354 µs and 332 µs for X and Y planes respectively. We suspect that this difference comes from the vacuum chamber geometry at the corrector magnets location, resulting in a different latency from Eddy currents.

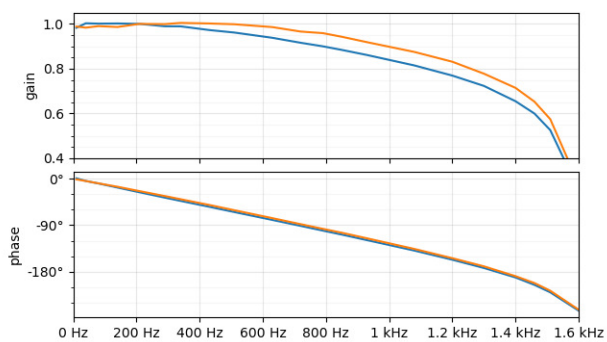


Figure 2: Bode plot of the measured TF. Blue and orange are one horizontal and one vertical PSC respectively.

Orbit Response Matrix Identification

This identification aims at measuring the ORM of the fast corrector magnets to BPM. Usually, this is performed by taking each of the PSC and apply a constant current step. ORM coefficients are deduced from the position difference induced on each BPM. Another approach, presented in [3] is to apply sine waveforms and perform a frequency analysis. This brings the possibility of frequency multiplexing to quicken the measure.

We tried this latter approach with our new platform. PSC in both planes were randomly selected by group of ten. One sine waveform is allocated and generated simultaneously by each PSC, from 223 Hz to 423 Hz, with 20 Hz gaps. For each group, 1.5 seconds of position data is captured. The measure has been repeated 4 times, with different groups and frequency distributions, allowing us several identifications for further corrections. For each capture, the DTFT at the ten sine frequencies are computed. We used a Blackman window on the data to reduce frequency leaking from one sine to the other, but in the future a better selected frequency gap will be used to minimize the leaking.

Two corrections are applied to the DTFT result before obtaining the ORM coefficients: (1) the phase is corrected by the identified constant delay, different to each plane, leading to real values. And (2) the module is corrected by estimating the TF shape on the measurement frequency band, for each PSC. Indeed, the results showed a ±2 % module variation over the 200 Hz, different for each PSC. Once these corrections done, we observe the repeatability over the four repetitions in Fig. 3. We hope to improve this by performing a better identification of the TF shape for each PSC.

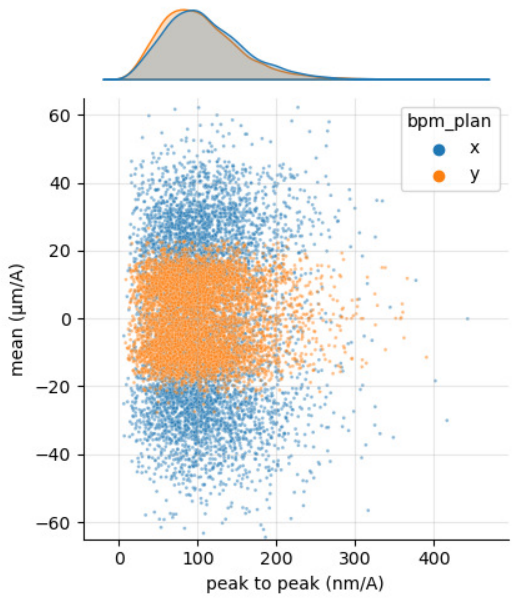


Figure 3: ORM measured coefficients. Each point is a PSC to BPM coefficient, its location gives the mean and peak to peak values from the 4 measure repetition. The error distribution is given for convenience.

Content from this work may be used under the terms of the CC-BY-4.0 licence (© 2023). Any distribution of this work must maintain attribution to the author(s), title of the work, publisher, and DOI

ISBN: 978-3-95450-236-3 ISSN: 2673-5350 doi:10.18429/JACoW-IBIC2023-MO2C04

Content from this work may be used under the terms of the CC-BY-4.0 licence (© 2023). Any distribution of this work must maintain attribution to the author(s), title of the work, publisher, and DOI

MACHINE TEST RESULTS

A few machine shifts have been dedicated to test the new platform correction. After some struggles with the corrector algorithm gain, we succeeded in closing the loop and achieving similar orbit stability compared to the previous system. We measured performances by assessing the integrated position PSD, and measuring the FOFB efficiency.

Position PSD

Figure 4 shows the power spectral density and its integration over the frequency band, for the mean orbit over all BPMs, obtained from the FA data. These signals are measured with a 5 mA beam stored, only one plane is shown for clarity. We can see that same performances are reached with the new platform. Sharp eyes can observe a slightly increase of the resonance crossover frequency. This comes from a small latency reduction obtained with our new platform. Indeed, the computation on the Libera starts after a waiting time of 60 µs after the loop iteration start, whereas the new platform starts the correction as soon as all position are received, which is around 30 µs after the loop iteration start.

The FOFB running on the new platform has been kept on while the beam was accumulated up to 450 mA without any issues.

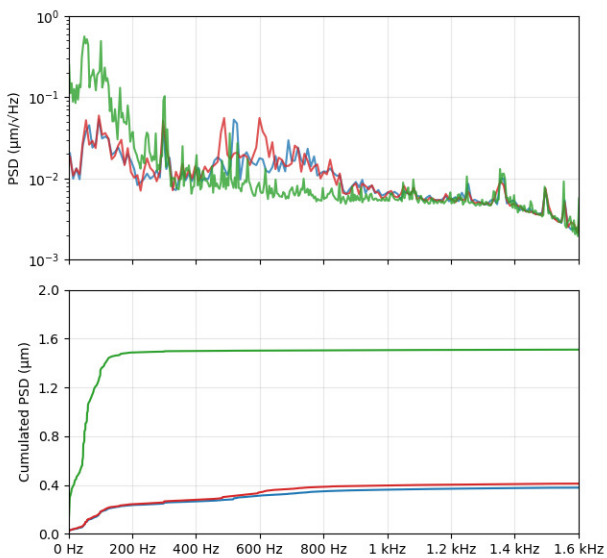


Figure 4: Position PSD and integrated PSD, for x plane. Green is FOFB off, blue and red is FOFB running on new and old platform respectively. Measured with a 450 mA stored beam.

FOFB Efficiency

This measure uses the on-board sine generator to add a sine wave on one selected PSC. The position orbit is then captured with and without the FOFB running. As for the TF identification, we compute the DTFT of the mean position over all BPM at the PSC sine wave frequency, only the module is kept. We consider efficiency as the ratio of the mean orbit oscillation with and without the FOFB running. By repeating this measure at several PSC frequencies, we have the efficiency over the band of interest, as plotted in Fig. 5. It shows an attenuation factor of 5 at 100 Hz and a resonance crossover frequency at 400 Hz. Comparison to previous system efficiency is not possible as that one is outdated. The new platform allows a very quick way to make this measurement, whereas the previous method required disabling a PSC in the correction algorithm and driving it with an analog external generator, which would takes too many time.

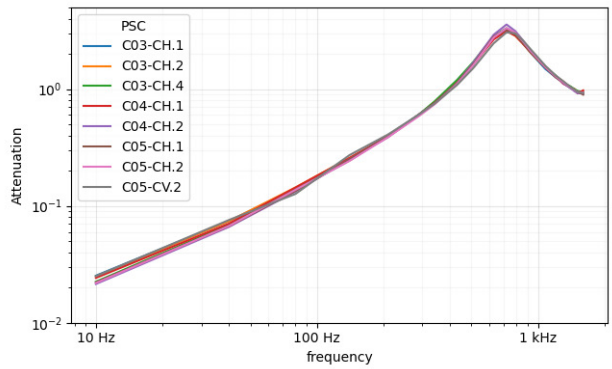


Figure 5: FOFB efficiency for several PSC.

FUTURE STEPS

Integration to the Control System is still to be deployed and tested. This will allow SOFB and FOFB interaction which is mandatory for nominal operation. With this last addition, the new platform will be selected for operation, with the possibility to fall back to the previous system for the first few weeks.

CONCLUSION

The new FOFB platform based on MTCA was installed at SOLEIL and has reached the actual performances. This new platform unlocks new identification features that will be used to improve daily operations, diagnostic and correction scheme.

ACKNOWLEDGEMENTS

We would like to thank S. Zhang, Y.M. Abiven and F. Bouvet from SOLEIL for their work or views on the project. We equally thank C. Guemues, L. Butkowski, B. Dursun, J. Georg and M. Killenberg from DESY for their help with FWK and ChimeraTK.

REFERENCES

[1] R. Broucquart and N. Hubert, "Fast Orbit Feedback Upgrade at SOLEIL", in *Proc. IBIC'22*, Kraków, Poland, Sep . 2022, pp. 339-342. doi:10.18429/JACoW-IBIC2022-TUP42

[2] N. Hubert, L. Cassinari, J. Denard, A. Nadji, and L. S. Nadolski, "Global Fast Orbit Feedback System Down to DC using Fast and Slow Correctors", in *Proc. DIPAC'09* Basel, Switzerland, May 2009, paper MOOC01, pp. 27-31.

[3] Z. Marti *et al.*, "Fast Orbit Response Matrix Measurements at ALBA", in *Proc. IPAC'17*, Copenhagen, Denmark, May 2017, pp. 365-367. doi:10.18429/JACoW-IPAC2017-MOPAB102

ISBN: 978-3-95450-236-3 ISSN: 2673-5350 doi:10.18429/JACoW-IBIC2023-MO3C03

DEVELOPMENT OF THE SLS 2.0 BPM SYSTEM

B. Keil, R. Ditter, F. Marcellini, G. Marinkovic, J. Purtschert, M. Rizzi,
M. Roggli, D. Stephan, X. Wang, Paul Scherrer Institut, Villigen, Switzerland

Abstract

After more than 20 years of operation, the storage ring of the Swiss Light Source (SLS) will be replaced. The new ring called SLS 2.0 will have 40 times higher brilliance, thanks to an innovative low-emittance magnet lattice and a beam pipe with smaller aperture. For SLS 2.0, the ageing SLS RF beam position monitor (BPM) electronics will be incrementally replaced for the whole accelerator, including linac, booster, transfer lines and storage ring. This contribution presents the development status and latest prototype test results of the SLS 2.0 BPM system, including pickups, mechanics, and electronics.

INTRODUCTION

Machine and Beam Parameters

Table 1 shows the parameters of the SLS 2.0 [1] compared to the present SLS ("1.0") ring. The nominal beam energy for user operation will be slightly increased from 2.4 GeV to 2.7 GeV, which is already supported by the SLS 1.0 full energy booster synchrotron that is re-used for SLS 2.0, as well as the linac and linac-to-booster transfer line. The booster-to-ring transfer lines will be modified, including a new magnet lattice and additional BPMs for improved control of the more critical injection process.

Table 1: SLS Storage Ring Beam Parameters

Parameter	Units	SLS 1.0	SLS 2.0
Circumference	m	288	
Beam Current	mA	400	
Injection Charge	nC	~0.15	
Beam Energy	GeV	2.4	2.7
Main RF	MHz	499.637	499.654
Harmonic No.	#	480	
Hor. Emittance	pm	5030	131-158
Vert. Emittance	pm	5-10	10
Ring BPMs	#	75	136

BPM REQUIREMENTS AND TYPES

Table 2 shows the BPM requirements for the SLS 2.0 storage ring, with an expected minimal beam size of $\sigma \geq 5$ µm at the BPMs, where <0.05 µm desired electronics RMS noise from 0.1 Hz to 1 kHz translates to 1% of this beam size. Like SLS 1.0, SLS 2.0 will operate in top-up injection mode at 400 mA with typ. 2-3 mA (max. 4 mA) periodic current variation within a few minutes. 430-460 of 480 successive RF buckets are typically filled with approximately the same charge, with ~10% charge variation between buckets, excluding an optional so-called "cam-shaft" bunch in the bunch gap with ~3-5 times higher charge. For the linac, booster and transfer lines operated with single bunches of ~0.15 nC at 3 Hz injection rate, the position resolution requirement is also <50 µm, aiming at <10 µm/week long-term drift of the averaged position readings in the booster-to-ring transfer line for negligible variations of bunch charge transfer efficiency to the ring.

Table 2: SLS 2.0 Storage Ring BPM Position Measurement Requirements

Parameter	Goal
RMS Noise, 0.1 Hz-1 kHz, 400 mA	0.05 µm
RMS Noise, 0.1 Hz-0.5 MHz, 400 mA	1 µm
RMS Noise, 1 Bunch, 0.15 nC	50 µm
Electronics Drift (400 mA Top-Up)	0.1 µm/h 0.4 µm/week 1 µm/year
Overall Drift (incl. Cables/Mechan.)	0.25 µm/h 1 µm/week 2.5 µm/year
Beam Current Dependence	0.02 µm/mA

Table 3: SLS 1.0 / 2.0 BPM Types

Location	Type	geom. factors kx/ky [mm]
Linac & Transfer Lines	Resonant Stripline	various
Booster	Button	8.3/7.7
SLS 1.0 Ring	Button	16.7/14.3
SLS 2.0 Ring	Button	7.1/7.2

Table 3 shows a list of BPM types used in SLS. Booster and storage ring have button BPMs with four diagonal electrodes. Linac and transfer lines have so-called resonant stripline BPMs, generating a decaying 500 MHz sine signal which can be processed by the normal storage ring BPM electronics also working at 500 MHz. The beam position is calculated by the BPM electronics from the button/stripline signal voltage amplitudes A, B, C and D (upper outer, upper inner, lower inner and lower outer button/stripline) for the horizontal (X) and vertical (Y) plane with the common approximation formulas

$$X = k_x * (A-B-C+D)/(A+B+C+D)$$
$$Y = k_y * (A+B-C-D)/(A+B+C+D)$$

Storage Ring Beam Pipe

Figure 1 shows the cross section of the SLS 1.0 storage ring beam pipe in blue and the smaller SLS 2.0 pipe in orange. The latter has an octagonal shape, usually with 18 mm aperture. While the SLS 1.0 pipe is made of stainless steel, SLS 2.0 uses a NEG-coated copper pipe. However, at the BPMs and their adjacent horizontal and vertical orbit corrector dipole magnets, the pipe is made of stainless

Content from this work may be used under the terms of the CC-BY-4.0 licence (© 2023). Any distribution of this work must maintain attribution to the author(s), title of the work, publisher, and DOI

ISBN: 978-3-95450-236-3 ISSN: 2673-5350 doi:10.18429/JACoW-IBIC2023-MO3C03

steel, with, with a ~5 µm copper coating (to reduce impedance) and ~0.5 µm NEG coating like in the surrounding solid copper pipe, where the button electrodes are only NEG coated but not copper coated.

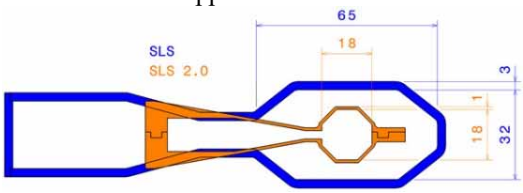


Figure 1: SLS 2.0 beam pipe (yellow) compared to the previous SLS pipe (blue), with dimensions in [mm].

BPM MECHANICS

The inner beam pipe aperture at the SLS 2.0 BPMs and correctors is tapered from the nominal 18 mm to 21 mm, thus shielding BPMs and correctors from synchrotron radiation, reducing beam-induced temperature variations and mechanical position drift (see Fig. 2).

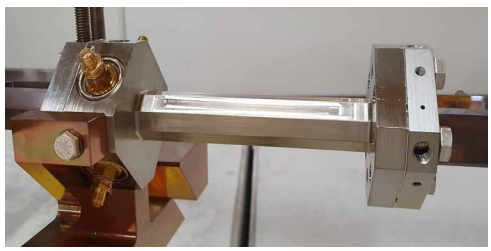


Figure 2: SLS2 BPM storage ring block with corrector magnet beam pipe.

The combined BPM/corrector beam pipe block has flanges to the surrounding copper beam pipe, and a dedicated rigid mechanical support for the BPM block, aiming at keeping the BPM position stable, while the softer surrounding copper pipe can float. The SLS 2.0 storage ring will have 136 BPMs overall. 115 of them have an adjacent horizontal and vertical corrector magnet to be used by the global fast orbit feedback (FOFB). The beam pipe at the corrector magnets is only 0.5 mm thick, compared to 2 mm for SLS 1.0, reducing eddy currents and improving the FOFB bandwidth.

The mechanical supports of the BPM blocks are double steel plates with a sealed compound of balsawood and viscoelastic glue in between that damps vibrations. The upper part of the BPM support is a water-cooled copper alloy block (CuCrZr), aiming at reducing the beam-induced temperature variation and thus thermal drift of the BPM block when the ring is filled from 0 mA to 400 mA. The expected remaining beam-induced power dissipation for the combined BPM/corrector beam pipe is ~2.6 W due to stray synchrotron radiation, and ~1 W losses due to the beam pipe impedance, assuming 400 mA and 9 ps worst-case bunch length (that is several times larger during normal user operation). Additional temperature sensors will enable feedforward correction of any remaining temperature-induced position drift of the BPM block.

Button Electrode Design

Figure 3 shows the cross section of the SLS 2.0 storage ring button BPM at one electrode (left) and the button electrode before insertion into the steel BPM block (right). The electrode (red) with 6.5 mm diameter and 0.25 mm gap to the BPM block is round and symmetric towards the beam pipe surface, with a radial asymmetry of the part going through the borosilicate glass dielectric (dark blue), thus suppressing higher-order modes (HOMS) in the electrode. The TIG welding of the buttons into the BPM block is done at the upper side between the steel (grey) and outer button (light blue) body that is also made from steel. The electrode has an SMA male connector (red/orange/yellow), where a female-to-female connector is screwed from the outside, using RF cables with SMA male connectors.

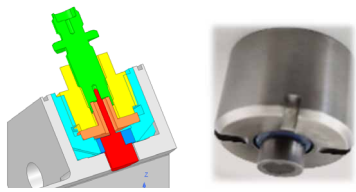


Figure 3: SLS 2.0 storage ring button BPM electrode.

While the SLS 1.0 storage ring BPMs use Molybdenum button electrodes with brazed Al_2O_3 dielectric, the SLS 2.0 ring will have Inconel® electrodes with a borosilicate glass dielectric. Although Molybdenum has better thermal and electrical conductivity, we chose Inconel for several reasons. Firstly, the Swiss company that produces the buttons (designed by PSI) uses Inconel for nearly all their other borosilicate glass feedthroughs, mainly for non-RF industry applications in harsh environments, with proven mechanical robustness. Secondly, simulations showed that the expected Inconel button temperature for worst-case SLS 2.0 beam conditions (400 mA, 9 ps bunch length, 3rd harmonic cavity inactive) is 51.8 °C (for ~0.4 W power dissipation per button), which is only 11 °C higher than Molybdenum. The resulting simulated mechanical stress of the borosilicate glass is only 15% higher and well below any critical threshold. Last but not least, we exposed buttons in the lab to thermal stress (much higher than during production, beam operation and bake out procedures) without causing any vacuum leaks.

Production Status and Offset Measurements

About 25% of the BPM blocks have been produced so far, and one of twelve sectors of the SLS 2.0 beam pipe has been assembled, including 12 BPMs, where all BPMs passed all vacuum tests. The button electrodes were sorted by their transfer impedance which was measured before welding, thus reducing the resulting position offset from tens of microns without sorting to typically <1 µm with sorting. In addition, we estimated the beam position offset after welding using the Lambertson method, where the RF asymmetry of the BPM electrodes and general geometry is measured with a 4-port RF network analyzer. Combined with future pre-beam calibration of RF cables and BPM electronics, we aim for an overall position offset uncertainty of < 100 µm for SLS 2.0 beam commissioning.

Content from this work may be used under the terms of the CC-BY-4.0 licence (© 2023). Any distribution of this work must maintain attribution to the author(s), title of the work, publisher, and DOI

ISBN: 978-3-95450-236-3 ISSN: 2673-5350 doi:10.18429/JACoW-IBIC2023-MO3C03

BPM ELECTRONICS

The SLS 2.0 BPM electronics is based on the so-called DBPM3 platform that was developed at PSI and is already used for cavity BPMs at SwissFEL [2]. The platform has a generic back-end with a Xilinx/AMD Zynq UltraScale+ (ZynqU+) MultiProcessing System-on-Chip (MPSoC), combined with accelerator-specific RF front-end modules (RFFEs) with integrated ADCs. The RFFEs are inserted at the rear side of the 19" DBPM3 unit (see Fig. 4). The MPSoC has a 2-core 32-bit CPU ("RPU") for real-time signal processing in addition to the programmable logic (PL) of the chip, and a 4-core 64-bit CPU ("APU") running Linux and an EPICS7 IOC for easy control and readout of the BPM system.



Figure 4: DBPM3 BPM electronics unit for SLS 2.0 with front-to-rear ventilation, redundant fans, and redundant power supply.

RF Front-End and ADC

For SLS 2.0, each DBPM3 unit has three RFFEs, one per BPM. Figure 5 shows a simplified block schematics of the RFFE. It has four SMA beam signal inputs, as well as an SMA output providing two mono-frequent "pilot tone" signals with adjustable frequencies and amplitudes.

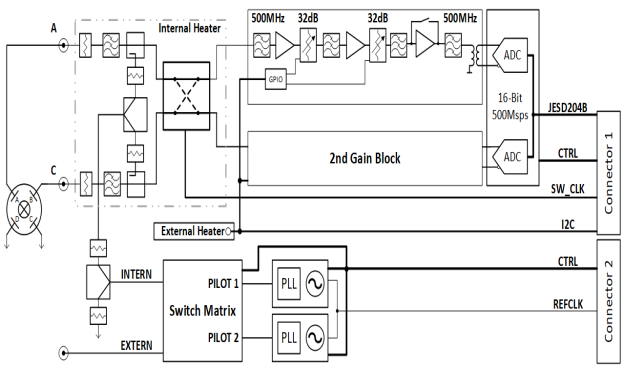


Figure 5: DBPM3 RF Front-End electronics with integrated 2-channel 16-bit 500 MS/s JESD204B ADC.

The pilot signals will be recombined with the four SLS 2.0 BPM beam signals close to the beam pipe, using a so-called "pilot combiner box", with four ~2 m long RF cables from the pickup to the pilot combiner box, and five 20-36 m long RF cables from the pilot combiner box to the electronics racks: One cable delivers the pilot tone from the DBPM3 unit to the pilot combiner box, and four cables with the combined beam/pilot signals go back to the DBPM3 unit in the electronics racks located in the SLS technical gallery. This setup enables pilot-tone-based compensation of beam position drift and low-frequent noise caused by cables and electronics. The DBPM3 RFFE performs low pass and bandpass filtering and amplification/attenuation with 63 dB overall dynamic range for the incoming beam/pilot signals. In addition to the support of an external beam-pilot signal combiner, the DBPM3 RFFE also has an additional internal beam-pilot signal combiner on the RFFE PCB, close to the SMA inputs. The user can select for each of the two generated pilot tones if it goes to the internal combiner (used e.g. for pre-beam tests and calibration of the electronics after production), or to the external combiner, or both. The DBPM3 RFFE also has two 2x2 crossbar switches close to the SMA beam signal inputs, where the switch swaps the RFFE channels used for the input signals of opposite BPM button electrodes. This enables suppression of gain asymmetries and drift of the RFFE channels by sufficiently fast switching (and digital uncrossing of ADC output signals in the ZynqU+).

ADCs and Digital Signal Processing

The present DBPM3 RFFE prototype for SLS 2.0 uses two dual-channel 16-bit 500 MSPS JESD204B ADCs. Digital down-converters (DDCs) in the ZynqU+ MPSoC process the beam and the two pilot signals simultaneously in separate DDC channels. The DDC, implemented at PSI, decimates and lowpass filters the ADC data in three successive stages with decreasing data rates and bandwidth. For the tests presented in this paper, we used an ADC sample rate of ~433 MSPS, thus enabling an integer fraction of ADC samples both for the storage ring and booster that have slightly different revolution frequencies. The ADC data was decimated to ~1 MSPS (beam revolution frequency) with ~0.5 MHz bandwidth, to 20 kSPS with 3.3 kHz bandwidth, and to 20 SPS with 11 Hz bandwidth. The DDC data rates, filters and filter bandwidths can be reprogrammed during operation using a Python GUI.

Drift Suppression

The ZynqU+ provides beam position readings calculated only from the beam signal (representing the real beam position in the accelerator), from the pilot signals (result is ideally zero, with a small offset mainly due to electronics and cable drift), and from the difference of both. This difference represents the beam position, but suppresses measurement errors caused by drift of the insertion loss / gain of each BPM channel, including all components downstream of the beam/pilot signal combiner, including the ADCs. The 2x2 crossbar switches serve the same purpose, thus supporting two different methods of drift suppression. The pilot tones provide the additional benefit of including RF cable induced drifts. It also enables easy pre-beam tests and calibration of the cables before 1st SLS beam, as well as monitoring cable attenuation and general health during beam operation and after maintenance shutdowns.

In addition to these active drift suppression approaches, we plan to sort all SLS 2.0 BPM RF cables from beam pipe to electronics by measured time of flight (TOF) and attenuation, and then install cables with similar TOF and attenuation for each BPM. Combined with a common thermal isolation of these cables, we thus aim at reducing cable-

Content from this work may be used under the terms of the CC-BY-4.0 licence (© 2023). Any distribution of this work must maintain attribution to the author(s), title of the work, publisher, and DOI

ISBN: 978-3-95450-236-3 ISSN: 2673-5350 doi:10.18429/JACoW-IBIC2023-M03C03

Content from this work may be used under the terms of the CC-BY-4.0 licence (© 2023). Any distribution of this work must maintain attribution to the author(s), title of the work, publisher, and DOI

induced beam position drift by equalizing cable properties and related drift for each BPM.

BEAM TEST RESULTS

Booster and Transfer Lines

We tested the DBPM3 electronics in the SLS 1.0 booster that has similar BPM signal level and geometry factor like the SLS 2.0 storage ring. The measured turn-by-turn single bunch turn-by-turn position resolution was <40 µm RMS at 0.15 nC, thus meeting our goal of <50 µm for booster and SLS 2.0 ring. For the SLS 1.0 transfer line resonant striplines, we measured <10 µm single bunch resolution at 0.15 nC, thanks to the larger signal levels and matched signal spectrum. We improved the single-bunch noise performance by feeding only ADC data near the beam signal peaks into the DDCs, zeroing all other ADC samples near the noise level (not using pilot tones here). This optional function is implemented in programmable logic and can run continuously at the full ADC sample rate, with adjustable signal level and pre-/post peak sample counts, thus improving position resolution for all DDC decimation stages of the booster BPMs.

Storage Ring

For tests of the new DBPM3 electronics with the SLS 1.0 storage ring beam, we installed a DBPM3 unit with two RFFEs in a prototype SLS 2.0 rack that is water-cooled and has an active temperature stabilization. The RFFEs received signals from two unused SLS 1.0 storage ring BPMs, where their four button signals were going to a 4x RF combiner. The sum signal was then combined with the pilot output signal of a DBPM3 RFFE. The combined beam/pilot signal was split 4 times to the four signal inputs of the RFFE, using only short (<20 cm) cables for our first tests to characterize the electronics alone. This setup simulates a centered beam with a signal spectrum similar to the real SLS beam (at ~400 mA beam current and the usual bunch filling pattern). We used the SLS 2.0 storage ring geometry factors to calculate the beam positions. So far, we only used one pilot tone, with a frequency offset of 0.531 MHz (0.5 times the beam revolution frequency of 1.04 MHz plus 10 kHz) above the beam signal frequency of ~499.637 MHz. The ADC sample rate was ~433 MS/s, the crossbar switching frequency ~130 kHz, both synchronized to the accelerator main RF. As shown in Figs. 6 and 7, the measured noise and 24 hour drift of the present DBPM3 prototype meets SLS 2.0 requirements.

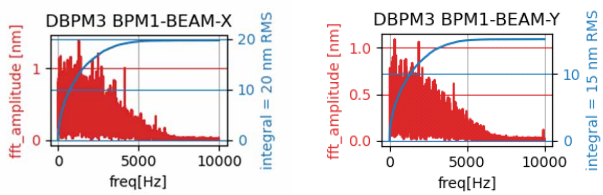


Figure 6: 20 nm horizontal (X) and 15 nm vertical (Y) RMS beam position noise of DBPM3 (0.001-3.3 kHz bandwidth, 50% ADC full scale, one pilot tone active, same signal level as beam signal).

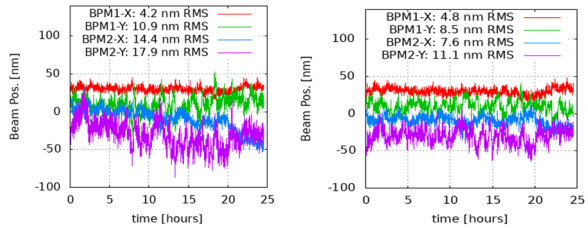


Figure 7: Horizontal and vertical beam position drift of two DBPM3 RFFEs (11 Hz bandwidth) over ~24 hours, using the pure beam signal (left side, no pilot-based drift suppression), and the pilot subtracted from the beam signal position (right side), with one data point every ~30 seconds.

SUMMARY AND OUTLOOK

The SLS 2.0 BPM system design and first electronics prototype test results at SLS 1.0 were presented. The present basic ZynqU+ firmware and software will be extended, supporting presently unused hardware features like the integrated temperature regulation of the RFFEs using 14 heating zones. The signal processing will also be improved, including the digital suppression of crossbar switching noise and balancing of signal levels and phases of the different RFFE channels. Long-term measurements with larger quantities are needed to investigate if the performance of present prototypes is reached reliably for every single BPM and large quantities over longer time scales, where only two prototypes of the latest RFFE version were available during two weeks for the results presented in this paper.

The "dark time" during which SLS 1.0 is replaced by SLS 2.0 starts 1.10.2023. For 1st SLS 2.0 beam in January 2025, we will equip only the SLS 2.0 ring mainly with the present 1st generation of DBPM3 electronics, keeping the old SLS 1.0 DBPM1 electronics for linac, booster, transfer lines and some uncritical ring BPMs. We intend to install a 2nd DBPM3 generation in the ring during a 2nd shorter dark time in Q1/2026, then moving the 1st generation to the linac, booster and transfer lines, thus finally replacing all DBPM1 systems. This incremental upgrade is aiming to reduce risks and get experience with production and operation of DBPM3 gen. 1, allowing to improve and optimize DBPM3 gen. 2 for highest ring performance.

ACKNOWLEDGEMENTS

The authors would like to thank all contributing colleagues from the SLS 2.0 project team for their support with the design, production, procurement, installation and test of the mechanical and electrical BPM system components and related infrastructure.

REFERENCES

[1] A. Streun *et al.*, "SLS 2.0, the Upgrade of the Swiss Light Source", in *Proc. IPAC'22*, Bangkok, Thailand, June 2022, pp. 925-928. doi:10.18429/JACoW-IPAC2022-TUPOST032

[2] B. Keil *et al.*, "First Application of a Multiprocessing System-on-Chip BPM Electronics Platform at SwissFEL", in *Proc. IBIC'22*, Krakow, Poland, September 2022, pp. 245-248. doi:10.18429/JACoW-IBIC2022-TUP12

ISBN: 978-3-95450-236-3 ISSN: 2673-5350 doi:10.18429/JACoW-IBIC2023-MO3C04

A MTCA BASED BPM-SYSTEM FOR PETRA IV

G. Kube, H.-T. Duhme, J. Lamaack, F. Schmidt-Föhre, K. Wittenburg
Deutsches Elektronen-Synchrotron DESY, Germany
A. Bardorfer, L. Bogataj, M. Cargnelutti, P. Leban, M. Oblak, P. Paglovec, B. Repič
I-Tech, Solkan, Slovenia

Abstract

The PETRA IV project at DESY aims to upgrade the present PETRA III synchrotron into an ultra low-emittance source. The small emittances translate directly into much smaller beam sizes, thus imposing stringent requirements on the machine stability. In order to measure beam positions and control orbit stability to the level of 10% of beam size and divergence, a high resolution BPM system will be installed which consists of 788 individual monitors with the readout electronics based on MTCA.4. In order to fulfil the long-term drift requirement (< 1 µm over 7 days), several analog, digital and SW parts were taken from the Libera Brilliance+ and a new RTM module has been developed to be used as BPM electronics RF frontend (RFFE). In addition, its analogue RF switch matrix used for long-term stabilization was separated and placed close to the BPM pickup, hence enabling an additional drift stabilization of the acquired RF input signals against environmental and other impact along the RFFE cables. At present, a fully populated MTCA crate with 6 AMC boards for the readout of 12 BPMs is installed at PETRA III and is extensively being tested. This contribution summarizes the latest beam measurements, showing the achieved performance of the BPM system.

INTRODUCTION

The PETRA IV project at DESY (Hamburg, Germany) aims at the construction of a diffraction limited ultra–low emittance light source operating at 6 GeV [1, 2]. The PETRA IV storage ring will be built in the existing PETRA III tunnel, thus inheriting the original 8-fold symmetry of the former PETRA collider. The accelerator lattice is based on a modified hybrid six-bend achromat (H6BA) cell and, taking advantage of the 2.3 km circumference, it provides electron beams with 20 pm rad emittance. The facility layout is shown in Fig. 1, the PETRA IV design operational parameters are summarized in Table 1.

Table 1: PETRA IV Main Parameters

Parameter	Value
energy	6 GeV
circumference	2304 m
emittance	20 pm rad
rel. energy spread	0.91×10^{-3}
momentum compaction	3.3×10^{-5}
$\beta_{x,y}$ at IDs	2.2 m, 2.2 m

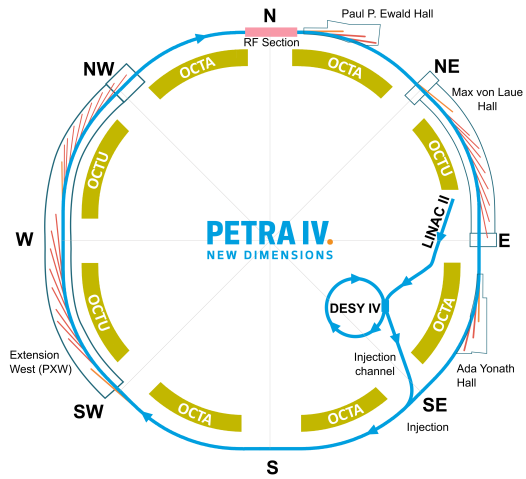


Figure 1: Layout of the PETRA IV facility.

The small beam emittances translate directly into much smaller beam sizes of about 7 µm horizontally and 3 µm vertically at the insertion device source points, thus imposing stringent requirements on the machine stability. In order to measure beam positions and control orbit stability to the level of 10% of beam size and divergence, a high resolution BPM system will be installed which consists of 788 individual monitors with the readout electronics based on MTCA.4 as technical platform.

In the beam commissioning phase of a storage ring, the BPM accuracy is essential. Before any beam accumulation in the ring will be possible, the BPM measurement accuracy must satisfy the requirements for the beam-based alignment (BBA) procedure, i.e. offset errors between the magnetic axes of the nearby quadrupoles and the electric centers of the BPMs must be identified. These offsets comprise alignment tolerances as well as electric and electro-mecanical offsets

Table 2: Readout electronics specifications. The single bunch / turn resolution holds for 0.5 mA bunch current, the closed orbit one for 1 kHz bandwidth, the beam current dependency for a 60 dB range with centered beam, and the long term stability should be measured over 6 days and a temperature span of ±1°C within a stabilized rack.

Requirement	Value
single bunch / single turn	< 10 µm
closed orbit resolution	< 100 nm (rms)
beam current dependence	±2 µm
long term stability	< 1 µm

Content from this work may be used under the terms of the CC-BY-4.0 licence (© 2023). Any distribution of this work must maintain attribution to the author(s), title of the work, publisher, and DOI

ISBN: 978-3-95450-236-3 ISSN: 2673-5350 doi:10.18429/JACoW-IBIC2023-MO3C04

Content from this work may be used under the terms of the CC-BY-4.0 licence (© 2023). Any distribution of this work must maintain attribution to the author(s), title of the work, publisher, and DOI

and are discussed elsewhere. After commissioning and in the user operating phase when orbit and optics corrections are complete, BPM resolution and beam stability are of greatest importance. In this case all random errors that change over time are of relevance. These errors are mainly affected by the BPM readout chain which will be covered in this report, the corresponding specifications are summarized in Table 2.

In order to fulfil the requested long-term drift requirement for PETRA IV, the specific machine geometry with the infrastructure distributed in the former experimental halls has to be taken into account, resulting in long cable lengths between monitor and readout electronics. With these long cables it is not guaranteed that cable routing will be in a perfectly stabilized temperature and humidity environment, thus affecting the BPM position readings [3, 4]. Therefore, in order to fulfil the requested long-term drift stability the BPM cable paths have to be stabilized in addition. Different drift compensation schemes are available and reviewed in Refs. [5, 6], the most popular one is the well proven concept of crossbar switching [7, 8] which stabilizes the analogue RF frontend part of the system. Another concept which has gained in popularity in recent years is the pilot tone (PT) compensation method where a sinusoidal PT signal with fixed frequency close to the carrier is injected in the signal chain. This signal is used as reference for calibration and compensation, see e.g. Refs. [9–12].

A series of test measurements at PETRA III indicated that the PT method works well with a homogeneous fill pattern, however the compensation was less effective for few bunch mode operation due to an overlap of PT and beam signals in the frequency domain [13]. According to this finding and following the discussion in Ref. [6], for PETRA IV it was decided to extend the standard crossbar switching method and come up with the idea of external crossbar switching where the analogue switching part is separated from the readout electronics and brought as close as possible to the BPM pickup, thus stabilizing also the cable paths. Based on this idea, DESY and the company *I-Tech* started a cooperation within the PETRA IV Technical Design Report (TDR) phase with the objectives to develop and test a MTCA.4 based BPM system with the extended stabilization scheme. The external crossbar switching method was tested successfully on a prototype at DESY. In a series of measurements performed at PETRA III with a modified Libera Brilliance+ (LB+) [14] and external switching matrix it was demonstrated that this concept works well and that the performance of the modified setup fulfils the specifications, see Refs. [15, 16]. Afterwards the readout electronics was ported to be compatible with the MTCA.4 standard, the prototype system evaluation under laboratory tests is described in Ref. [17].

This contribution summarizes the results from first beam measurements at PETRA III. A fully populated MTCA crate with 6 AMC boards for the readout of 12 BPMs is presently installed in the machine and extensively being tested. In the subsequent section a brief description of the MTCA.4 based readout system will be given, and afterwards the status of the investigations at PETRA III is presented.

SYSTEM DESCRIPTION

The signal chain of two BPMs together with their related electronic boxes (containing the 4x4 RF crossbar switch *Libera XBS FE* together with analog RF signal conditioning circuits) and RF frontend cabling is shown in Fig. 2. The signals from two BPMs are processed by an analog/digital RTM and a digital AMC board. It is planned to use a maximum of 6 modules per crate, corresponding to 12 BPMs. The AMC board serves as signal interface between MTCA backplane and the outer world as well as for the incoming raw BPM data from the four 2-channel ADCs on the RTM module. The COTS AMC board (CAENels FMC2ZUP) is optionally planned to be replaced by a specialized version, currently under development at DESY.

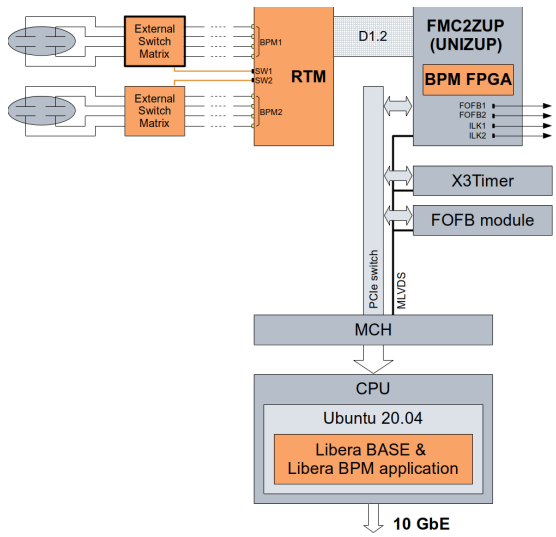


Figure 2: BPM system building blocks and interconnections. Courtesy: I-Tech.

The RTM board developed by I-Tech holds the analog RFFE of both BPMs from the signal cable output of the two external switching boxes up to the analog/digital backend of the ADC data chain together with additional glue logic for the control of the ADCs, up to two external switching boxes, and a couple of internal sensors. The encapsulation of the longest RF signal path between the *Libera XBS FE* and the ADC on the RTM module ensures a maximum of low-perturbation RF input signal integrity up to the digital domain.

Specialized turn-by-turn data streams at bunch revolution frequency (f_0 ~130.1 kHz) for the fast orbit feedback (FOFB) connect each BPM module inside the crate over a specialized data aggregation backplane (star topology) with a dedicated FOFB data aggregation module. Central timing signals are delivered to the boards via a timer module (X3Timer) using clock and trigger lines on the backplane according to the MTCA standard. BPM channel related interlock alarm signals (ILK) can be produced by each AMC module. BPM-related software and firmware required for configuration, status evaluation and data management of all BPM channels inside the MCTA crate is distributed on each

ISBN: 978-3-95450-236-3 ISSN: 2673-5350 doi:10.18429/JACoW-IBIC2023-MO3C04

of the RTMs and AMCs as well as on the crate CPU. All data exchange between CPU and distinct BPM modules are accomplished over high-speed PCIe connections.

Besides the Linux OS, the CPU software hosts the common control system specific data infrastructure as well as BPM-specific software parts. The BPM-specific application core (libera-ebpm, Libera Base and libera kernel) contains the specific crate configurations, the BPM-specific adaption layer (libera-mci) and an adapted interface to the DOOCS control system. It is completed by less execution time critical functional software blocks for the BPM application of all channels inside the crate.

Time critical functional blocks for the BPM application are implemented inside the application-specific parts of the programmable logic FPGA firmware on each AMC board for fast execution. In addition, minimal housekeeping data is acquired from several onboard sensors for long-term operation safety under typical environmental conditions. A small micro controller on the RTM serves for RTM-specific low-level board control purposes.

Each BPM channel is able to deliver basic data structures: (1) a local slow acquisition (SA) beam position information in a continuous 10 Hz data stream; (2) a fast acquisition (FA) data structure acquired on-demand (i.e. externally triggered) at 10 kHz; (3) ADC raw data blocks sampled at approximately 117 MHz; (4) turn-by-turn (TbT) data blocks which alternatively can be derived via digital down conversion (DDC) or time domain processing (TDP) at bunch revolution data rate f_0; (5) a special MultiTbT data structure which will be available for dedicated operating conditions that profit from segmentation of the TbT acquisition window. For first turn steering during the commissioning phase, either TbT or single pass data can be utilized, the latter ones having the advantage of an improved signal-to-noise ratio.

In order to test the new readout system, a fully populated MTCA crate was installed in PETRA. The signals of 12 BPMs were split and fed to both, the existing PETRA III *Libera Brilliances* and the new MTCA based system, hence allowing a direct comparison of their performance. Figure 3 shows the installation of the new readout system in the accelerator.

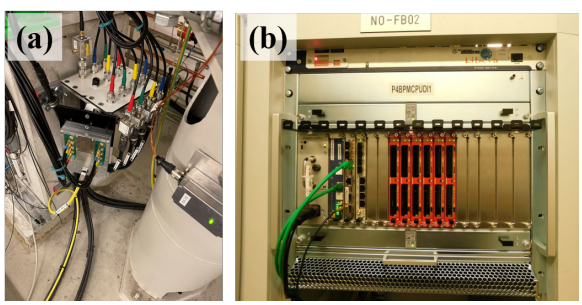


Figure 3: BPM readout system installation in PETRA III: (a) *Libera XBS FE* crossbar switch matrix installation in the tunnel and patch panel for signal splitting; (b) MTCA crate in the electronics cabinet equipped with 6 AMC boards, MCH, CPU, timing and fan module.

MEASUREMENTS

A series of measurements was performed at PETRA III using 480 bunches with 120 mA stored beam current during top-up operation, a similar mode is also planned for PETRA IV. For each BPM under test the data paths described before were investigated. As an example, Fig. 4 shows the horizontal power spectral density (PSD) derived from the FA data path using a BPM close to an undulator. Besides the influence of the notch filter at 3.3 kHz which is implemented in all *Liberas*, the influence of the top-up injection in PETRA III is clearly visible and can be eliminated by gating-out the injection. Nevertheless, a number of characteristic frequency lines is still present which consist mainly of higher harmonics of 50 Hz.

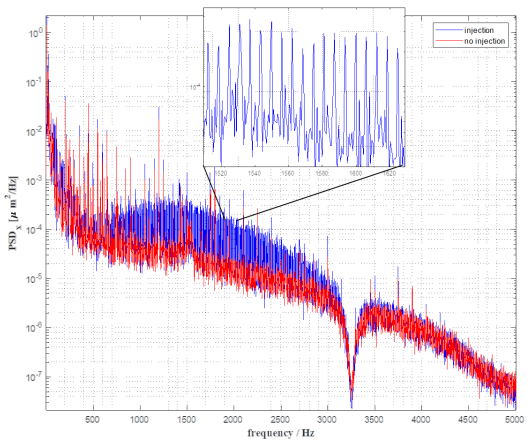


Figure 4: Horizontal power spectral density, derived from the FA data path at 10 kHz sampling rate. The blue curve was recorded under standard operational conditions. The detail enlargement shows a series of frequency lines equally spaced by 6.25 Hz. This frequency is characteristic for the top-up injection in PETRA III. For the red curve the injection was gated-out.

As can be concluded from this but also from other measurements using different data paths, the beam stability in PETRA III is not sufficient to explore the resolution limits of the readout electronics. Hence, in order to get rid of the beam jitter it was decided to exclude one of the BPMs under test from the orbit measurement and place 2 four-way splitters in the signal paths behind 2 pickup antennas. The output cables from one splitter were connected to the MTCA system, the signals from the other one to a *Libera Brilliance* under test. After the installation in September 2023 a new series of measurements was performed, investigating only a single BPM with beam jitter cancellation.

Figure 5 shows the horizontal PSD based on FA data together with the closed orbit resolution as function of bandwidth. As can be seen, the PSD is free from spurious lines except the one at about 3.5 kHz, mainly caused due to downmixing of a crossbar switching frequency. The rms resolution for the bandwidth from DC to 1 kHz amounts to 70 nm (monitor constant K_x = 10 mm). Assuming a constant of K_x

Content from this work may be used under the terms of the CC-BY-4.0 licence (© 2023). Any distribution of this work must maintain attribution to the author(s), title of the work, publisher, and DOI

ISBN: 978-3-95450-236-3 ISSN: 2673-5350 doi:10.18429/JACoW-IBIC2023-MO3C04

Content from this work may be used under the terms of the CC-BY-4.0 licence (© 2023). Any distribution of this work must maintain attribution to the author(s), title of the work, publisher, and DOI

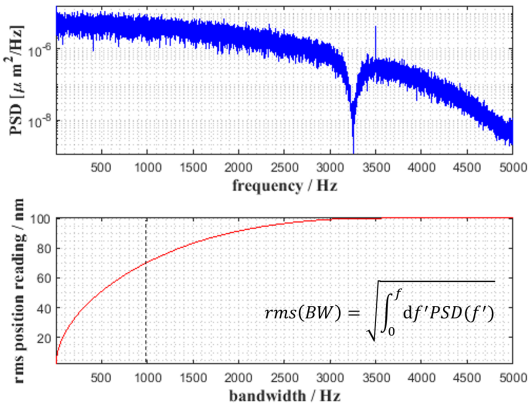


Figure 5: Horizontal power spectral density and closed orbit resolution as function of bandwidth, derived from the FA data path for the BPM with beam jitter cancellation. The monitor constant is K_x = 10 mm.

= 7.1 mm which is the case for the PETRA IV standard arc BPMs, the resolution is about 50 nm which is well below the specification of < 100 nm according to Table 2. The measured resolution is comparable to the one from a *Libera Brilliance+* [15], indicating that their system performances are equivalent.

Using the TbT data stream instead of FA data, the rms resolution in the requested bandwidth up to 1 kHz is well reproduced. Moreover, this data stream is also available from the existing PETRA III *Libera Brilliances*, hence allowing a direct comparison of both systems. Assuming again a monitor constant of 10 mm, the rms resolution in the full bandwith from DC to $f_0/2$ amounts to 1 µm for the *Libera Brilliance*, and to 300 nm for the new MTCA based system, thus demonstrating the performance improvement.

In order to investigate the long term stability, the SA data path with 10 Hz sampling rate is of importance. For the time being the measurement period was set to only 1.5 days, later on it will be extended to the required 6 days according

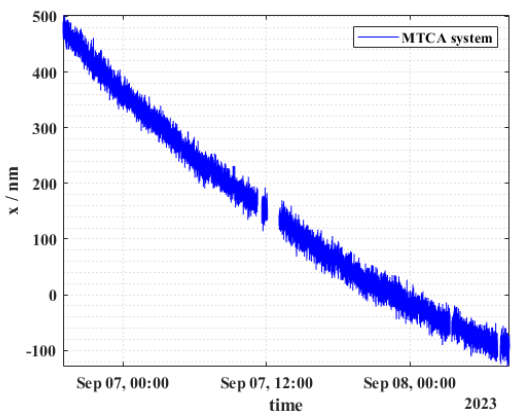


Figure 6: Horizontal position readings acquired from the SA data path with the MTCA based system and monitor constant K_x = 10 mm. Gaps in the data indicate periods where the beam was lost.

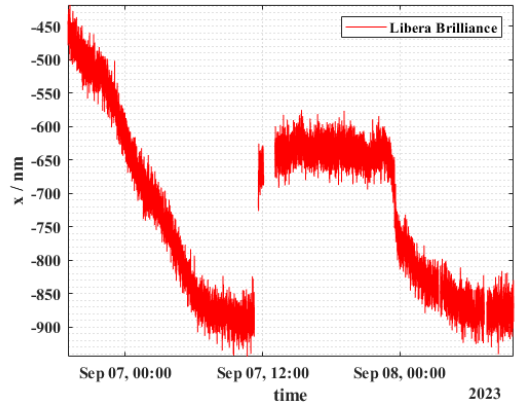


Figure 7: Horizontal position readings acquired from the SA data path with a *Libera Brilliance* under the same conditions than in Fig. 6.

to Table 2. As can be seen in Fig. 6 the horizontal position readings show a smooth drift which is in the order of 600 nm. Figure 7 shows a simultaneous measurement but with a *Libera Brilliance*, indicating a drift of about 1.35 µm. From the comparison it is clear that the drift behaviour of the MTCA based system is smaller, especially the external crossbar switching seems to cope better with sudden environmental changes as in the case of a beam loss where the heat load in the tunnel changes on a short timescale. Nevertheless, the remaining drift in the MTCA based long term measurement has to be minimized. From the experience with the proof-of-principle setup described in Refs. [15, 16] it is assumed that this drift is caused by the measurement setup itself and not by the readout electronics. Especially the signal cables between 4-way splitter and crossbar switching matrix are uncompensated and therefore extremely sensitive to any kind of variations. However, this needs to be proven and will be topic of upcoming investigations.

SUMMARY AND OUTLOOK

This paper summarizes first performance evaluations of a MTCA based BPM readout system relying on the concept of external crossbar switching at PETRA III. The system is continuously in operation since end of 2022 without any downtime. For a measurement exploiting the resolution limit of the electronics it is evident to exclude any kind of beam jitter. Under this condition it is demonstrated that the new system fulfils the closed orbit resolution specification for PETRA IV, indicating the performance improvement compared to the existing *Libera Brilliance* based PETRA III system.

While the long term stability of the new system is better compared to the *Libera Brilliance* and below the specification limit of < 1 µm, the measured drift behaviour suggests an influence of the uncompensated signal path as it was experienced at earlier stages using a proof-of-principle setup.

In the next step this long term drift behaviour will further be investigated and improved, and the readout system will be tested in view of the remaining specifications in Table 2.

ISBN: 978-3-95450-236-3 ISSN: 2673-5350 doi:10.18429/JACoW-IBIC2023-MO3C04

REFERENCES

[1] C.G. Schroer *et al.*, "PETRA IV: upgrade of PETRA III to the Ultimate 3D X-ray microscope", Conceptual Design Report PUBDB-2019-03613, DESY, Germany. doi:10.3204/PUBDB-2019-03613

[2] R. Bartolini *et al.*, "Status of the PETRA IV Machine Project", in *Proc. IPAC'22*, Bangkok, Thailand, Jun. 2022, pp. 1475–1478. doi:10.18429/JACoW-IPAC2022-TUPOMS029

[3] G. Rehm and C. Bloomer, "Impact of Relative Humidity on EBPM Readings", talk presented at 2nd Diagnostics Experts of European Light Sources Workshop (DEELS'15), Cerdanyola del Vallès, Spain, June 2015. https://indico.cells.es/event/22/.

[4] N. Hubert, "Test of BPM Cables vs Humidity and Temperature", talk presented at 6th Diagnostics Experts of European Light Sources Workshop (DEELS'19), Grenoble, France, June 2019. https://indico.cern.ch/event/789811/.

[5] G. Rehm, "Review of BPM Drift Effects and Compensation Schemes", presented at the IBIC'22, Kraków, Poland, Sep. 2022, paper MO3I1, unpublished.

[6] F. Schmidt-Foehre, G. Kube, and K. Wittenburg, "Comparison of Two Long Term Drift Stabilization Schemes for BPM Systems", in *Proc. IBIC'21*, Pohang, Korea, Sep. 2021, pp. 145–149. doi:10.18429/JACoW-IBIC2021-MOPP36

[7] U. Mavrič, "Innovative RF Design Unites Benefits of Multiplexed and Multi-channel System", in *Proc. 4th Beam Instrumentation Workshop (BIW'04)*, Knoxville, TN, USA, May 2004, pp. 373–378.

[8] A. Kosicek, "Libera Electron Beam Position Processor", in *Proc. 21st Particle Accelerator Conf. (PAC'05)*, Knoxville, TN, USA, May 2005, paper RPAT093, pp. 4284–4286.

[9] J. Mead *et al.*, "NSLS-II RF Beam Position Monitor Comissioning Update", in *Proc. 3rd Int. Beam Instrumentation Conf. (IBIC'14)*, Monterey, CA, USA, Sep. 2014, paper WECYB2, pp. 500–504.

[10] G. Brajnik, S. Carrato, S. Bassanese, G. Cautero and R. De Monte, "Pilot tone as a key to improving the spatial resolution of eBPMs", in Proc. AIP Conf., vol. 1741, p. 020013, 2016. doi:10.1063/1.4952792

[11] M. Cargnelutti, S. Bassanese, G. Brajnik, S. Cleva, R. De Monte, and P. Leban, "Stability Tests with Pilot-Tone Based Elettra BPM RF Front End and Libera Electronics", in *Proc. 7th Int. Beam Instrumentation Conf. (IBIC'18)*, Shanghai, China, Sep. 2018, pp. 289–292. doi:10.18429/JACoW-IBIC2018-TUPB13

[12] G. Brajnik and B. Repič, "Current Status of Elettra 2.0 eBPM System", presented at *Libera Workshop 2021*.

[13] G. Kube, "BPM Studies in view of PETRA IV", presented at *15th Libera Online Workshop*, June 17, 2020.

[14] Libera Brilliance+, https://www.i-tech.si/products/libera-brilliance-3/.

[15] G. Kube *et al.*, "Tests of the New BPM Long Term Drift Stabilization Scheme Based on External Crossbar Switching at PETRA III", in *Proc. IBIC'21*, Pohang, Korea, Sep. 2021, pp. 123–127. doi:10.18429/JACoW-IBIC2021-MOPP30

[16] G. Kube *et al.*, "Upgrade of the BPM Long Term Drift Stabilization Scheme Based on External Crossbar Switching at PETRA III", in *Proc. IBIC'22*, Kraków, Poland, Sep. 2022, pp. 395–398. doi:10.18429/JACoW-IBIC2022-WEP08

[17] P. Leban *et al.*, "Preliminary Evaluation of the MTCA.4 BPM Electronics Prototype for the PETRA IV Project", in *Proc. IBIC'22*, Kraków, Poland, Sep. 2022, pp. 399–402. doi:10.18429/JACoW-IBIC2022-WEP09

Content from this work may be used under the terms of the CC-BY-4.0 licence (© 2023). Any distribution of this work must maintain attribution to the author(s), title of the work, publisher, and DOI

ISBN: 978-3-95450-236-3 ISSN: 2673-5350 doi:10.18429/JACoW-IBIC2023-MO3C05

CANADIAN LIGHT SOURCE BEAM POSITION VISUALIZATION TOOL

M. A. Bree*, T. D. Batten, C. W. Stevens, J. M. Vogt
Canadian Light Source, Saskatoon, Canada

Abstract

The Canadian Light Source orbit correction system acquires, collates, and publishes storage ring beam centroid position information from 48 beam position monitors (BPMs) at a rate of 1000 samples per second. We present a "Beam Position Visualization Tool" that computes and displays dynamic Fast Fourier Transforms (FFTs) and Cumulative Power Spectral Densities (CPSDs) for all BPMs in real-time using full resolution data. The computed FFTs and CPSDs can be plotted in various combinations and in waterfall plots that allow visualization of changes over long periods of time. In addition, correlations between all BPM channel combinations are computed and ranked. Data from any two BPM channels can be selected for plotting in two dimensions wherein correlations are visually apparent. Computed CPSDs are further binned and archived for further analysis. Preliminary results from the Beam Position Visualization Tool have proven useful in identifying storage ring beam position noise at the Canadian Light Source.

INTRODUCTION

The Canadian Light Source (CLS) is a third generation synchrotron commissioned in 2005 that now supports 22 operational beamlines. The storage ring orbit correction (OC) system was upgraded in November 2021 to replace obsolete hardware and support new diagnostic capabilities [1]. The original Beam Position Monitors (BPMs) and associated Bergoz electronics are unchanged but new high speed D-tAcq analog-to-digital converters (ADCs) [2] feed beam position data via fiber optic cables to an OC host computer running Scientific Linux 7. The OC host uses the BPM data as input to the orbit correction algorithm to compute and send setpoints to the orbit corrector magnets (OCMs) over dedicated private Ethernet networks. The OC system uses the Experimental Physics and Industrial Control System (EPICS) [3] for configuration and control.

Many new features were built into the new OC system to facilitate specific diagnostic requirements such as hardware status. One such feature, called "beam position broadcast", publishes a data stream consisting of the beam positions read at all OC BPMs. Since the data stream protocol is connectionless and static, its usage by clients is completely decoupled from the OC system. Future diagnostic tools can be implemented using the data stream without modifying, interrupting, or otherwise interacting with the running OC system in any way.

* michael.bree@lightsource.ca

This paper covers two general topics:

- *Beam Position Broadcast*, which publishes BPM data.
- *Beam Position Visualization Tool*, which is an example of a client that consumes the published BPM data.

BEAM POSITION BROADCAST

The new OC system uses four D-tAcq ACQ435ELF ADCs to read BPM values of the X (horizontal) and Y (vertical) beam centroid positions at 48 locations around the CLS storage ring. The BPMs are read at 1000 Hz, and each reading (sample) is three bytes. Using four bytes per sample results in a data rate of 384,000 bytes/s (plus protocol overhead) to transmit all 96 channels.

Publishing the beam position data in some form allows clients external to the OC system to process the information as they see fit, independently of OC operation. The CLS uses the EPICS control system and one possible mechanism for publishing beam position data is via EPICS Process Variables (PVs). EPICS clients can connect to PVs via a TCP-based protocol and can receive (and transmit) data via PVs over the control system network. However, the 1000 Hz update rate is high for EPICS (although there are techniques to mitigate this). More important, though, was the desire to not burden the real-time OC host computer that publishes the BPM data stream with hosting EPICS PVs for full resolution BPM data; and to not require data consumers (clients) to support EPICS. Therefore, EPICS was not used to publish the BPM data stream.

System Architecture

The User Datagram Protocol (UDP) [4] was chosen to publish the BPM data stream. UDP is a lightweight, connectionless protocol that minimizes the burden on the OC host computer which has as its primary task running the orbit correction algorithm and sending updates to the OCMs. A dedicated CPU core on the OC host was assigned to transmit the data stream on a configurable network interface. The data stream is transmitted on a private network to keep it off the control system network. It is sent to the broadcast address which allows any number of clients to independently receive it with no impact on the transmitting OC host. For example, the beam visualization tool described later in this paper is a data stream client that runs on a separate computer which is connected to the private network. The tool is a pure Python program that receives the BPM data stream directly, processes it, and publishes its results as EPICS PVs. The overall system architecture is illustrated in Fig. 1.

Content from this work may be used under the terms of the CC-BY-4.0 licence (© 2023). Any distribution of this work must maintain attribution to the author(s), title of the work, publisher, and DOI

ISBN: 978-3-95450-236-3 ISSN: 2673-5350 doi:10.18429/JACoW-IBIC2023-MO3C05

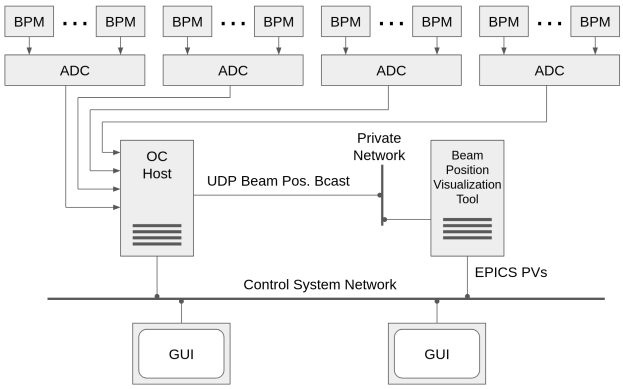


Figure 1: System Architecture. Each of the 4 ADCs supports 12 BPMs. The OC host transmits the BPM data stream on a private network on which multiple clients can receive it. Processed results are published as EPICS PVs on the control system network where they may be accessed by screens and graphical user interfaces (GUIs).

BPM Data Stream Protocol

Each transmitted frame consists of a 20-byte header as shown in Fig. 2. Typically, clients read the header of each

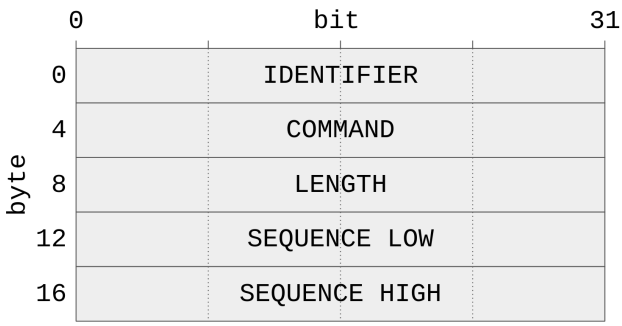


Figure 2: BPM data stream protocol frame header structure.

received frame, and immediately reject any frame that does not contain the 32-bit identifier. Next they can read the 32-bit length field which indicates the number of bytes in the frame and reject any frame with a size that does not match. They may optionally check the 64-bit sequence number as frame delivery and frame order is not guaranteed by UDP[1]. Finally, the 32-bit command is read and the frame processed accordingly. Currently, the protocol consists of two commands:

- **BPM_Position:** The frame contains sequential 32-bit numbers, each representing the calibrated voltage read by a BPM ADC.
- **BPM_Meta:** The frame contains a JavaScript Object Notation (JSON) string consisting of a human readable dictionary specifying the index, name, and volt-to-metre conversion factor for each channel. The dictionary also contains the current sampling rate. Such dictionaries are easily parsable by high level languages such as Python.

The OC host transmits a **BPM_Position** frame each time the BPMs are read (1000 Hz). Also, it sends a **BPM_Meta** whenever the meta data change, or once per second otherwise.

This protocol simplifies client implementation. For example, clients need not be EPICS aware as they would be had EPICS been chosen to publish the BPM data.

BEAM POSITION VISUALIZATION TOOL

Dynamic Fast Fourier Transforms

After the new OC system was commissioned, a project was launched to use the new BPM data stream to dynamically compute and display the Fast Fourier Transforms (FFTs) and Cumulative Power Spectral Densities (CPSDs) of all 96 BPM channels. A pure Python multi-threaded program reads the data steam and waits for the next **BPM_Meta** frame that when received allows the program to dynamically configure itself. It then sends subsequent BPM samples from **BPM_Position** frames to worker threads, one for each channel. By monitoring the frame sequence numbers, missing data can be detected and FFT computations suspended until the data stream resumes.

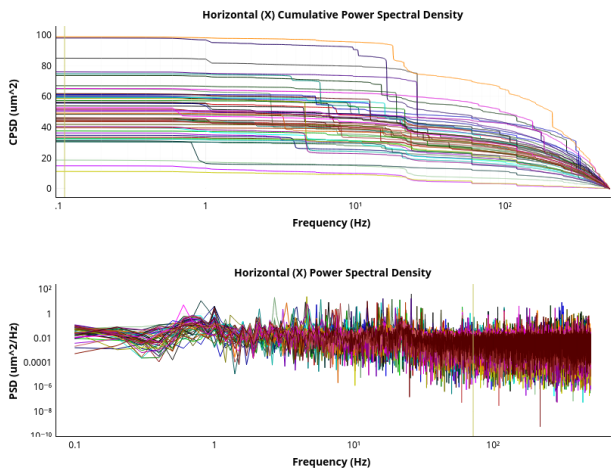


Figure 3: CPSDs and FFTs for all 48 horizontal BPM channels [1]. 60 Hz noise can be seen in the CPSDs for all channels. Other large spikes affect only individual BPMs or small groups of BPMs. Any combination of channels may be selected for plotting.

The Python `multiprocessing` module is used for each worker, ensuring true parallel processing. Each worker adds each beam position sample to 10,000 element First-In-First-Out (FIFO) memory buffers for FFT computations. This produces a FFT from 0.1 to 500.0 Hz at 0.1 Hz resolution. At some configurable interval computations are performed using the FIFOs as input and the resulting FFTs are published as EPICS waveform PVs.

[1] In 1.5 years of continuous operation no missing or out of sequence frames have been detected.

Content from this work may be used under the terms of the CC-BY-4.0 licence (© 2023). Any distribution of this work must maintain attribution to the author(s), title of the work, publisher, and DOI

ISBN: 978-3-95450-236-3 ISSN: 2673-5350 doi:10.18429/JACoW-IBIC2023-MO3C05

Content from this work may be used under the terms of the CC-BY-4.0 licence (© 2023). Any distribution of this work must maintain attribution to the author(s), title of the work, publisher, and DOI

The FFTs are integrated from the Nyquist frequency (500 Hz) back to DC resulting in CPSDs which are also published as EPICS waveform PVs.

A GUI (Fig. 3 and first presented in Ref. [1]) was developed to display the dynamically computed FFTs and CPSDs. The dynamic display makes it easy to see transient noise, and noise that affects single BPMs and multiple BPMs. For example, in Fig. 3, 60 Hz noise is discernible in all BPMs.

Data Archiving

The CPSDs are further summed into five large frequency bins: 0.1-1 Hz, 1-10 Hz, 10-100 Hz, and 100-500 Hz. Each of these values is published at a configurable interval (currently once per second) as an EPICS scalar PV. This results in 480 PVs (i.e., 5 per channel) suitable for archiving.

Dynamic Waterfall Plots

Another visualization technique is to treat each FFT for a BPM as a row in an image with pixel intensity corresponding to FFT amplitude. The resulting images illustrate noise as a function of time on the vertical axis and frequency on the horizontal axis. A new row is added to the top of the image each time a new FFT is calculated, and the bottom row (based on a configurable time span) is removed. Thus the image scrolls downward, leading to the *waterfall* name. Some interesting results are shown in Figs. 4 and 5. These images were collected with orbit correction in operation and with typical user-mode ring current. At the present time, sources of noise revealed by this new visualization tool are under investigation.

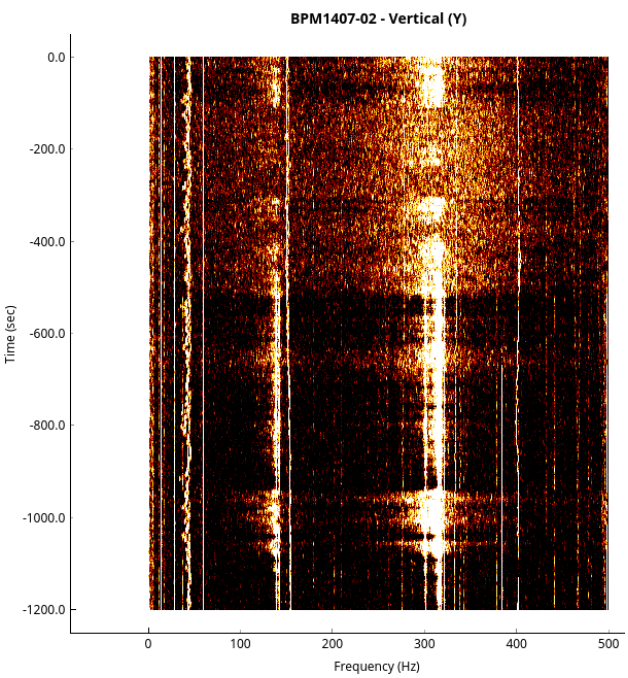


Figure 4: Intermittent noise across a wide frequency spectrum.

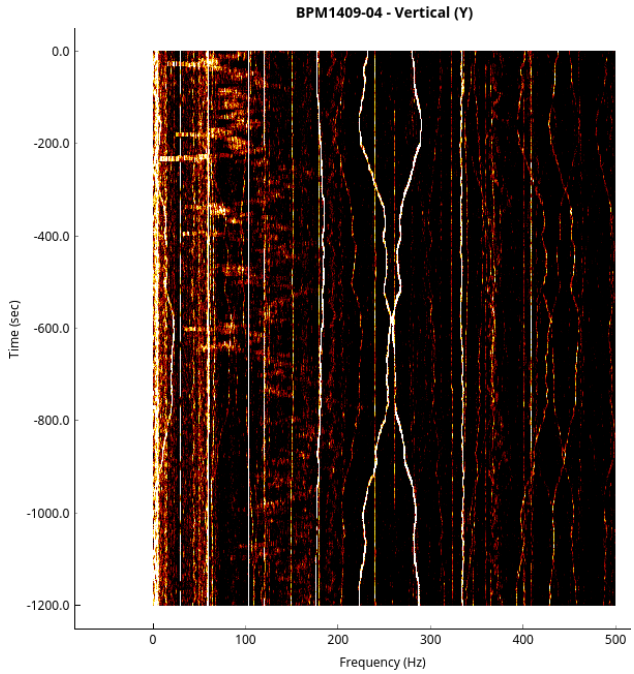


Figure 5: Narrowband noise that slowly drifts in frequency between 200 Hz and 300 Hz.

Position Visualization

The tool uses the BPM data stream to plot data from pairs of BPM channels as pixels on an X-Y grid. The grid is divided into bins, and a bin "hit count" is incremented each time a measured position falls within it. As data is acquired, an image appears with pixel intensity proportional to the hit count, resulting in probability density function of beam position. An example is shown in Fig. 6.

Bin hits can be optionally aged out, and the pixel takes on the behaviour of a phosphorous screen with persistence. What appears is a dynamically changing image of beam position, updated at 1000 pixels per second. When the X and Y channels of the same BPM are chosen, the pixels represent the actual measured beam centroid position at the BPM. Examples are illustrated in Figs. 7 and 8.

Channel Correlation

The tool computes the correlation between all combinations of the 96 beam position channels over sliding time windows of configurable duration. The pairs with the highest correlation are displayed on a GUI from which they can be selected for plotting.

Machine Learning

The CLS is researching the potential application of machine learning techniques to orbit correction [5]. A Python client was written to gather and store full resolution beam position data from the BPM data stream for training the neural network. Users can now gather beam position data whenever and for whatever duration they want.

ISBN: 978-3-95450-236-3 ISSN: 2673-5350 doi:10.18429/JACoW-IBIC2023-MO3C05

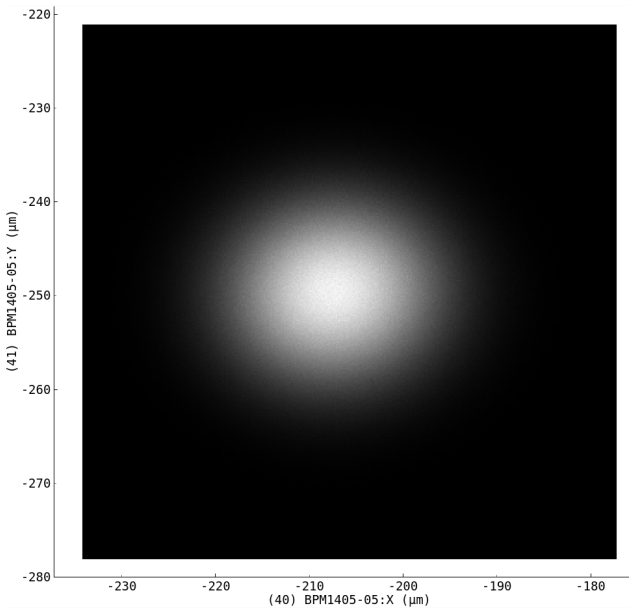


Figure 6: Image of beam position at BPM1405-05 with aging disabled. All recorded positions are kept and the pixel intensity reflects the total number of observations in the corresponding bin. The image represents the beam position probability density function over a period of time.

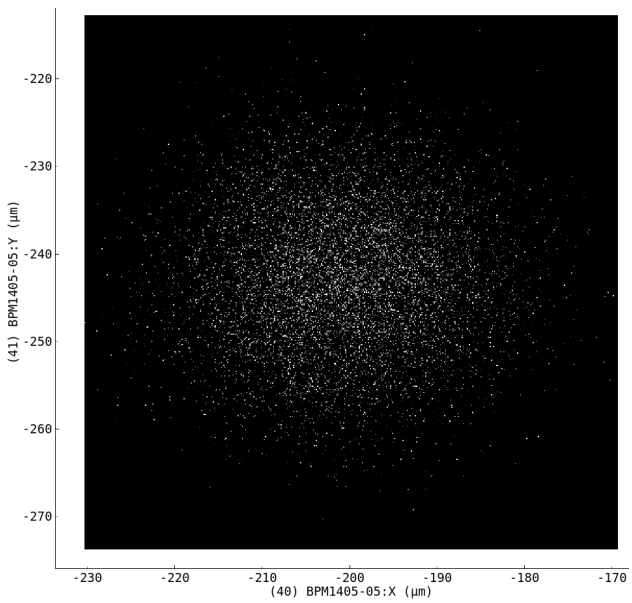


Figure 7: Image of beam position at BPM1405-05 with aging enabled. That is, position observations are discarded after a configurable period of time. The dynamic image is updated at 1000 pixels per second.

FUTURE WORK

The data stream could be expanded to include full rate orbit corrector magnet (OCM) setpoints. This would include potential commands such as **OCM_Setpoint** and **OCM_Meta**. These are analogous to the **BPM_Position** and **BPM_Meta** commands described above except that they would describe the OCM setpoints computed by the OC system and the OCM metadata respectively. This additional data, along with the beam position information, has the potential to facilitate external tools to characterize the performance of the complete OC system. There are many possibilities for analysis of the streamed data. For example unexpected beam behaviour such as clustering or deviation from other reference measurements could be detected and flagged.

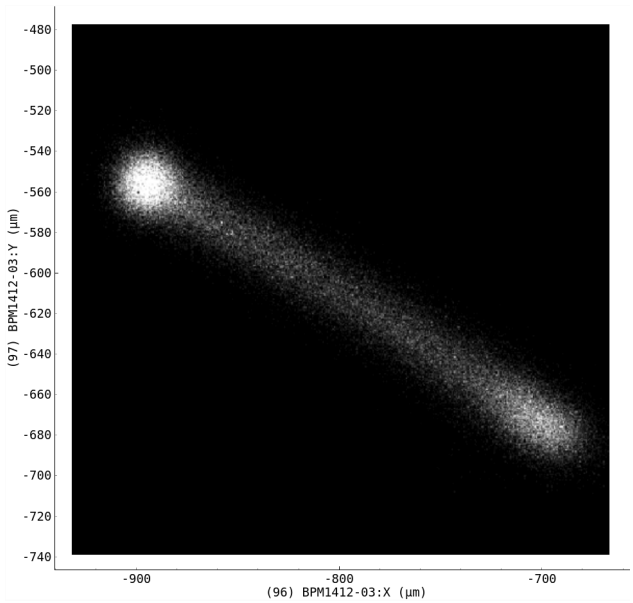


Figure 8: Beam motion at BPM1412-03 during injection with ring current at 3.4 mA.

CONCLUSION

The beam position broadcast feature has facilitated new visualization and analysis tools after the deployment of and without affecting the in-production orbit correction system. The extremely simple protocol allows anyone with interest to receive and analyze the BPM data stream (e.g., with simple Python) with no risk or impact on the orbit correction system.

The results have provided new insights and views of the CLS beam position characteristics that are still being evaluated. The archived CPSD values have proven useful for correlating changes in beam noise to other events, including modifications to the orbit correction algorithm. Likewise data gathered from the BPM data stream has facilitated studies such as machine learning initiatives.

ACKNOWLEDGEMENTS

Research at the CLS is funded by the Canada Foundation for Innovation, the Natural Sciences and Engineering Research Council of Canada, the National Research Council of Canada, the Canadian Institutes of Health Research, the Government of Saskatchewan, Western Economic Diversification Canada, and the University of Saskatchewan.

Content from this work may be used under the terms of the CC-BY-4.0 licence (© 2023). Any distribution of this work must maintain attribution to the author(s), title of the work, publisher, and DOI

ISBN: 978-3-95450-236-3 ISSN: 2673-5350 doi:10.18429/JACoW-IBIC2023-MO3C05

REFERENCES

[1] T. D. Batten, M. A. Bree, and J. M. Vogt, "Orbit Correction Upgrade at the Canadian Light Source", in *Proc. 11th Int. Beam Instrum. Conf. (IBIC'22)*, Kraków, Poland, Sept. 2022, pp. 485-487. doi:10.18429/JACoW-IBIC2022-WEP34

[2] D-tAcq ACQ435ELF 32 Channel Simultaneous Digitizer, https://www.d-tacq.com/acq435elf.shtml

[3] Experimental Physics and Industrial Control System (EPICS), https://epics.anl.gov

[4] User Datagram Protocol (UDP), https://www.ietf.org/rfc/rfc768.txt

[5] S. Saadat and M. J. Boland, "A New Approach for CLS Future Orbit Correction System Driven by Neural Network", presented at IBIC'23, Saskatoon, Canada, Sept. 2023, paper MOP036, this conference.

Content from this work may be used under the terms of the CC-BY-4.0 licence (© 2023). Any distribution of this work must maintain attribution to the author(s), title of the work, publisher, and DOI

ISBN: 978-3-95450-236-3 ISSN: 2673-5350 doi:10.18429/JACoW-IBIC2023-MOP001

CURRENT STATUS OF THE HESR BEAM INSTRUMENTATION

C. Böhme, Forschungszentrum Jülich, Germany
A. Halama, V. Kamerdzhiev, G. Koch, K. Laihem, K. Reimers
GSI Helmholtzzentrum für Schwerionenforschung, Darmstadt, Germany

Abstract

The High Energy Storage Ring (HESR), within the FAIR project, will according to current planning, provide antiproton beams for PANDA and heavy ion beams for i.a. the SPARC experiment. Manufacturing for most of the envisaged beam instrumentation devices in vacuum is completed and testing is well underway. The overall status update of the beam instrumentation devices is presented, with a focus on the test-bench results of the BPMs. In addition, the planned future timeline of the HESR beam instrumentation is briefly reported.

INTRODUCTION

The HESR, part of the Facility of Antiproton and Ion Research in Europe (FAIR) in Darmstadt, Germany, is dedicated to the field of antiproton and heavy ion physics. The envisaged energy range is 0.8 GeV to 14 GeV for antiprotons and 0.17 GeV/a to 5 GeV/a for heavy ions [1]. The ring will be a racetrack design with a length of 574 m. The foreseen beam instrumentation within the modularized start version is:

63	Diagonally Cut Beam Position Monitors (BPM)
118	Beam Loss Monitors (BLM)
2	Beam Current Transformers (BCT)
2	Ionization Beam Profile Monitors (IPM)
1	In-gap particle measurement
1	Schottky Pick-up
1	Phase Pick-up
1	Dynamical Tune-meter
5	Viewer
2	Scraper

BPM SYSTEM

The pick-up design is based upon the diagonally cut shoebox design of the COSY BPMs [2]. The design was shown in detail in [3]. While 62 BPMs will have the inner diameter of 89 mm, one is designated to be located closely after the injection septum, where the beam pipe has a diameter of 150 mm. Therefore, this BPM has to have a larger diameter to not limit the aperture at this place. This one has still to be designed and the production is not planned for the near future.

In the bend sections of the synchrotron, between the dipole magnets, different configurations of quadrupole, sextupole and steering magnets are foreseen, with at least one quadrupole magnet but a different secondary magnet being in place. In order to save as much longitudinal space as possible, the BPM is build in the single vacuum chamber serving through all these devices. But for each configuration a different length of the vacuum chamber, 1585 mm, 1249 mm, or 1180 mm, is needed. In addition, in the straight sections, these restrictions do not apply, therefore a 450 mm long vacuum chamber is used there. But the BPM pick-ups itself are identical in each configuration. All these different length vacuum chamber have to fit on the test stand.

Signal Chain

Within the FAIR project, the standard signal chain consists of the A110 pre-amplifier [4], which features an amplification range of +60 dB to -60 dB. For the readout and calculation of the beam position the LIBERA Hadron [5] was chosen. It features an extension for orbit control, which has been adapted to the FAIR magnet control units (ACU). As an extension to the original plan, the orbit control extension units have been ordered for the HESR as well. As an addition to the FAIR standard, taking the low expected signal for the HESR into account, an additional low-noise head amplifier of 20 dB, will be used directly on the vacuum feedthroughs in front of the A110 pre-amplifiers. It is foreseen to use the same head-on amplifiers in other parts of FAIR with expected low signal, e.g. the high energy beam transport (HEBT) beamlines.

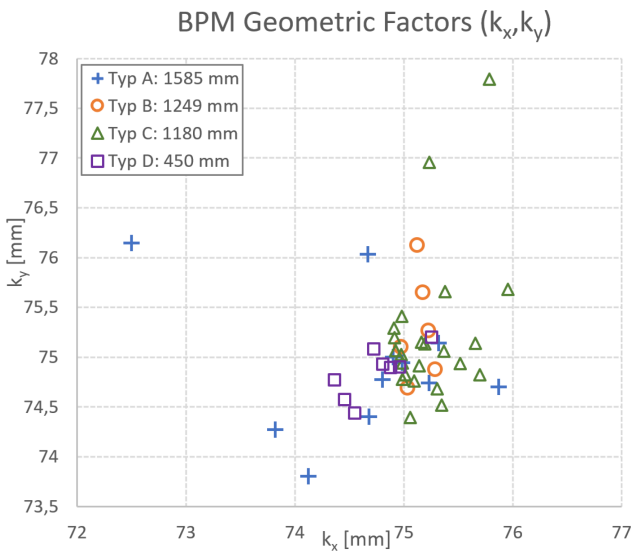


Figure 1: Overview of the measured geometric factors of the HESR BPMs. Notable spread and outliers result from the real statistical characteristic of the individual BPM, systematic errors on the test bench as well as measurement uncertainties. The standard deviations of the geometrical factors are $k_x = 0.55$ mm and $k_y = 0.66$ mm.

Content from this work may be used under the terms of the CC-BY-4.0 licence (© 2023). Any distribution of this work must maintain attribution to the author(s), title of the work, publisher, and DOI

ISBN: 978-3-95450-236-3 ISSN: 2673-5350 doi:10.18429/JACoW-IBIC2023-MOP001

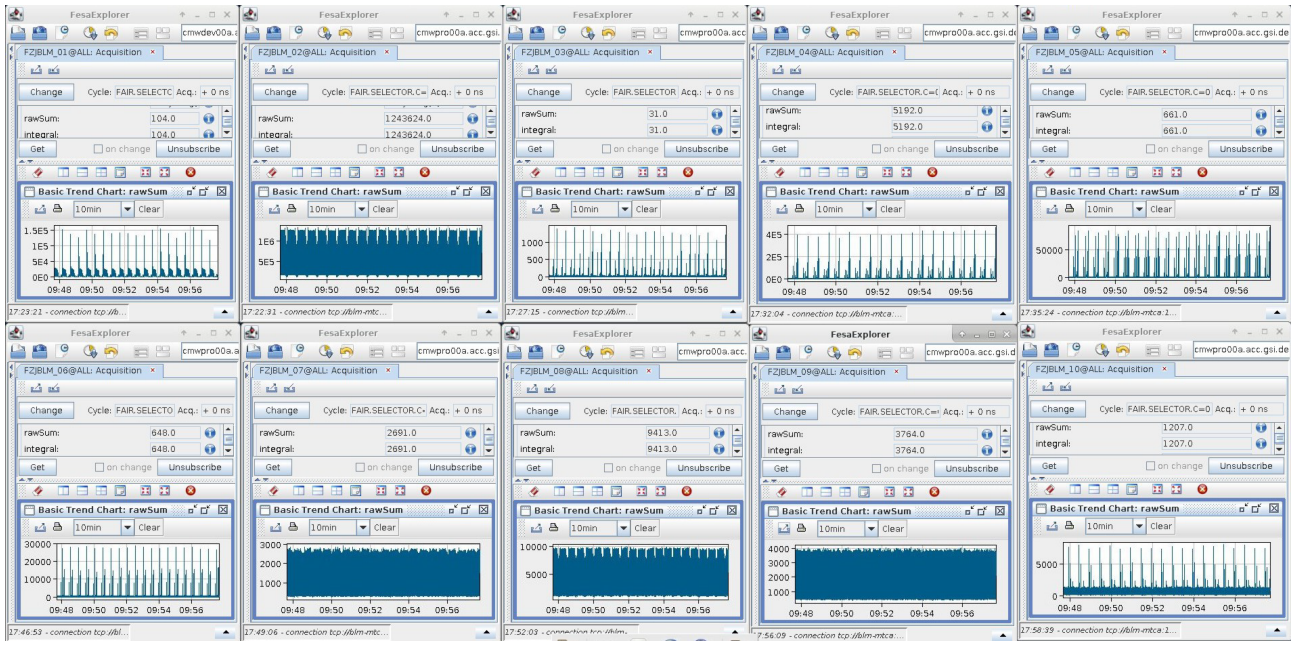


Figure 2: Overview of the BLM loss rate of the installed HESR BLMs at the COSY synchrotron for testing. The GUI is not the final GUI for HESR, but only for testing with the FESA explorer.

BPM Testing

Of the 62 envisaged 89 mm BPMs, 47 have been tested, the so far test results are shown in Fig. 1. An additional 14 recently received from production to be tested in the near future. That leaves one BPM to be delivered. Every BPM is tested using a wire test bench to check general electrical functionality and determine the linear coefficients and electrical offsets per plane. The test bench is fitted with µ-meter precision linear drives and optical micrometers for moving the wire and determining the precise position. In every BPM two highly precise measured reference markers are added during manufacturing, which deliver a reference for the wire positioning. The signals are amplified by head amplifiers and the A110, before being digitized by a Spectrum 16-bit 250 MHz ADC card. The whole measurement process, including the positioning of the wire, control of the gain of the A110, the ADC signal readout, and writing the measured values to a file is done with LabView.

The initial concept of performing tests at the test bench did only include centering the wire using the xy-arrangement of optical micro-meters to determine a suitable homing position. Drifts and mishaps during start up of a measurement run may ruin an entire measurement cycle, as a permanent unspecified shift from the geometrical center may occur in such circumstances. Endeavours to include the optical micrometer readings for the evaluation of the entire measurement run yielded an increased robustness and the means to mitigate such shifts have been performed. Concerns over some results lead to a photogrammetric investigation to determine the optical micro-meters rotation and shifts. It has been concluded that the optical micro-meters in the lower box are rotated by 1.4° for one and 0.5° for the second device and for the upper box 0.6° and 0.03°. The statistical uncertainty of these values is estimated around 0.1°. Comparing electrically and optically derived positional wire positions indicate a tilting behaviour for every position of the meander path of the linear drive assembly through the BPM while measuring. Although the linear drives allow for sub micro-meter motion, the examinations showed, the actual wire position should not be taken from raw set-values of the linear drives but the optical micro-meter readings should be favored.

While the mechanical tolerances for the parts of the BPM directly involved in the measurement process, such as the pick-up electrodes, have been specified with tolerances lower than 2/100 mm, the mechanical deviations have an impact on both, the electrical zero position in regards to the mechanical zero position, and the geometrical factors used for the calculation of the position of the particle beam. An additional source for spread of the additive coefficients may be explained by a large contribution of mechanical deviations in the electrical signal feedthroughs of the BPM because of their varying parasitic capacity. An analysis of 10 feedthroughs and their effects on signal strength against their individual capacitance indicates strong correlation as well as a spread in capacitance in the entire tested set that would accommodate a good part of the noted distribution of the electrical centers. The expected values for the BPMs have been presented in [6]. There simulations resulted in k=73.52 mm and for the offset to 0.7 mm.

Theoretical models have shown a weak but noticeable coupling between the vertical and horizontal measurement plane of BPM electrodes. A more realistic approach to convert the electrical signals to beam position would be to append a linear term for each decoupled case:

$$x_{beam} = x_0 + k_{xH} \cdot DOS_H + k_{xV} \cdot DOS_V$$

Content from this work may be used under the terms of the CC-BY-4.0 licence (© 2023). Any distribution of this work must maintain attribution to the author(s), title of the work, publisher, and DOI

ISBN: 978-3-95450-236-3 ISSN: 2673-5350 doi:10.18429/JACoW-IBIC2023-MOP001

and y_{beam} analogous respectively. The terms k_{xV} and k_{yH} are small and could naivly be omitted and even will be for the simplicity with the Libera Hardron implementation. Yet one can include a correction calculation within the control system software to transform $xy_{beam-naiv}$ to $xy_{coupled}$ using a predetermined 2x2 matrix for each BPM.

BEAM LOSS MONITOR

For machine commissioning, routine operation and further beam optimization detailed beam loss data is very valuable. Unlike other accelerators, the HESR BLM data will not be used for an automated machine protection, as the stored total beam energy will not be high enough to damage the machine. Along the ring 118 BLMs will be used, of which 20 have been so far delivered by GSI, mainly for testing purposes.

The BLM consists of a BC-400 plastic scintillator and a Hamamatsu photomultiplier (PMT). This solution is favored over e.g. an ion chamber type loss monitor because of the low expected loss rates. The design was presented in detail at [7]. It was developed by GSI and will be used in other parts of FAIR as well, e.g. the HEBT.

For the readout of the BLMs a µTCA system will be used utilizing scaler/counter SIS8800 and RTM discriminator SIS8980 from Struck Innovative Systeme GmbH. Both cards are connected to each other via the µTCA backplane and provide 16 channels per card. The BLM PMTs will be powered individually utilizing a multichannel HV system in order to be able to compensate for the properties of the individual BLM detector and the individual location.

FESA Control Test System

In order to have a Front-end Software Architecture (FESA) control system operational for development and testing, a stripped down test system was installed by Cosylab d.d. at COSY. As a functioning system the control and readout of the BLM system was implemented and can be used in addition to the COSY BLM system with additional BLMs, with its GUI shown in Fig. 2. Besides this test setup, the system is also designed as a reference for further FESA development and testing.

IONIZATION BEAM PROFILE MONITOR

Ionization Beam Profile Monitors (IPM) have been built and tested in cooperation with the GSI since 2007 [8], becoming a very valuable instrument in beam diagnostics at COSY and GSI [9]. Based on the experiences, a similar device is under development for the HESR. Depicted in Fig. 3, it is being designed in a size that would not only fit the HESR but also in the HEBT. Because of the delicate nature of the microchannel plates and the importance of the system, 2 systems will be installed, providing one backup system in case of failure. Unlike other systems the side electrodes of the E-field-box are connected individually, thus giving a greater control over the E-field and eliminating the need of resistors within the vacuum. Parts of that wiring is shown in Fig. 3. Within the HESR and HEBT an amount of 17 devices is foreseen, although some of them shall provide only one plane-measurments.

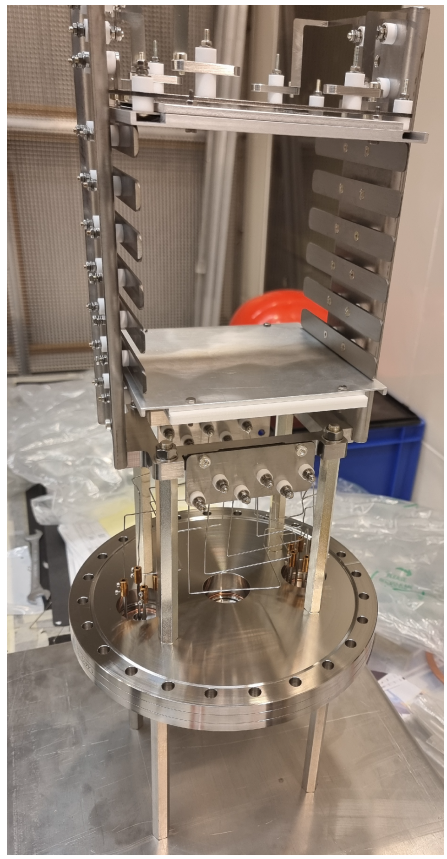


Figure 3: The ready mounted vacuum part of the IPM. On top a module with a MCP stack and a phosphor screen will be mounted. The E-field-box with its 6 field flattening electrodes is visible. On the bottom, covered with a protective shield during mounting, a fine mesh will be installed, which flattens the electric field but lets through UV light for calibration purposes. The UV light will be generated by a lamp mounted outside the vacuum, right behind the vacuum window in the lower CF flange.

The first of series device is being build at the Research Center Jülich with the setup being almost complete, some in-vacuum wiring has still to be done. The manufacturing of the vacuum chamber, after facing some delays, has just been completed, with vacuum-testing still to be done.

VIEWER

There will be 6 viewers installed in the HESR. One in the injection beamline. Within the HESR ring, one will be installed at the beginning and end of each telescope and an additional one directly after the injection septum magnet. The ring viewers consist of a scintillation screen mounted at 45°. They will be moved by a pneumatic drive and, as a speciality at the HESR, if the viewer is not used a RF cage will be moved into its place. This is done in order to minimize the overall impedance of the ring. If the RF

Content from this work may be used under the terms of the CC-BY-4.0 licence (© 2023). Any distribution of this work must maintain attribution to the author(s), title of the work, publisher, and DOI

ISBN: 978-3-95450-236-3 ISSN: 2673-5350 doi:10.18429/JACoW-IBIC2023-MOP001

Content from this work may be used under the terms of the CC-BY-4.0 licence (© 2023). Any distribution of this work must maintain attribution to the author(s), title of the work, publisher, and DOI

cage is in its operational position, a second pneumatic drive will move RF fingers in their position to ensure an optimal electrical conduction. Before moving the RF cage out, these springs will be pulled back. A RF cage before being mounted onto the system is shown in Fig. 4.

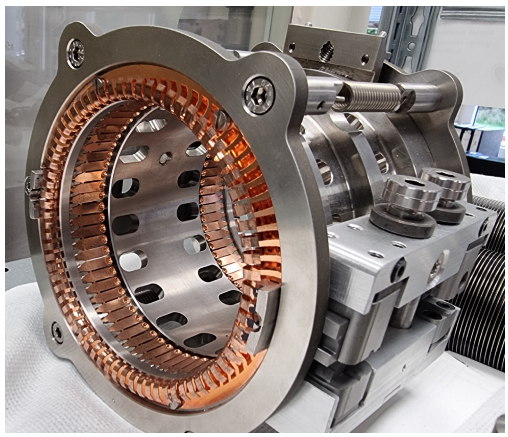


Figure 4: RF cage that is being moved into position if the vievers are not used. Once in its position the Copper-Beyllium springs will be moved outwards to insure a good electric conductivity. This is done in order to minimize the overall impedance of the storage ring.

SCRAPER

The scraper system is shown in Fig. 5. There will be 2 scraper systems installed in the HESR. Each system consists of 2 vertical and 2 horizontal jaws. Each jaw contains 10 copper rods which are placed in an alternating manner and are each 25 mm in diameter. This layout ensures a particle will be slowed down by at least 50 mm of material while the structure will have a minimal effect on the RF impedance while being in its out position. Each jaw can move in further than the middle of the beam pipe, in order to allow the scraping of a non-centered region. In order for the jaws not accidentally touching each other, they have been placed in succession. The manufacturing and testing of these devices is completed.

PHASE PICK-UP

The in-vacuum part of the Phase Pick-Up will be a non-split BPM. This is derived from the construction layout of the regular BPMs and will be manufactured directly after all regular BPMs have been manufactured. The readout of the Phase Pick-Up still has to be defined.

BEAM CURRENT

For beam current measurements, two commercially available Bergoz transformers will be used. One NPCT and one FCT have already been delivered and the site acceptance test was successfully performed.

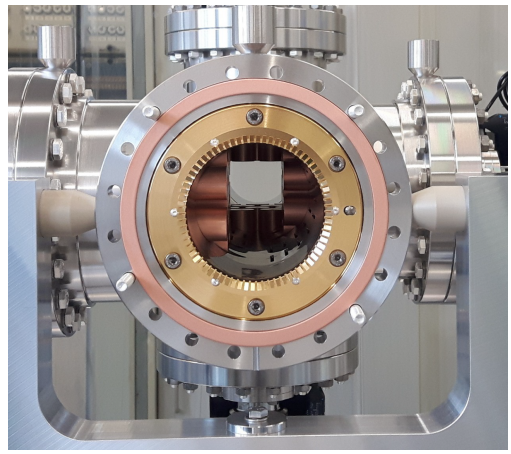


Figure 5: Look into the scraper in the beam plane. The 4 jaws from top, bottom, and the sides are partially moved in [10].

OUTLOOK

To the present day, 61 of 63 of the BPM pick-ups have been produced and delivered. The measurement of the BPMs on the test stand is also well underway, as well as the calculation of the individual geometrical factors and offsets, which has been done for 47 so far. The beam current transformers and the scrapers are completely manufactured and tested. The viewers are partly manufactured, while their vacuum chamber manufacturing is delayed, and therefore their overall completion. For the IPM, the first of series is almost completed, with vacuum tests and about half of the in-vacuum wiring still to be done.
Because of the recent desicions of the FAIR council, the stepwise approach for the completion of FAIR will be pursued [11]. The first step (Early Science: ES) includes the Super-FRS using beams from the existing SIS18 and will be possible from 2028, followed by First Science (FS), which provides beams from the SIS100 for NUSTAR and and atomic physics (APPA) experiments. This will be followed by the First Science Plus (FS+) step, in which beams will be extracted to the CBM cave. After these steps the rest of the Modularized Start Version of FAIR, which includes the antiproton part, the p-bar target, the Collector Ring (CR), and the HESR, will be realized. Therefore further developments of other HESR beam instrumentation, like the measurement of the amount of trapped particles in the injection gap, or the beam damping, have been postponed.

REFERENCES

[1] J. Hetzel, “The High Energy Storage Ring (HESR) at FAIR”, *ESRW’22*, Geneva, Switzerland.

[2] R. Maier *et al.*, “Non-Beam Disturbing Diagnostics at COSY-Jülich”, *EPAC’90*, Nice, France, June 1990, p. 800.

[3] C. Böhme *et al.*, “Status Overview of the HESR Beam Instrumentation”, in *Proc. IBIC’18*, Shanghai, China, Sep. 2018, pp. 26–28. doi:10.18429/JACoW-IBIC2018-MOPA01

ISBN: 978-3-95450-236-3 ISSN: 2673-5350 doi:10.18429/JACoW-IBIC2023-MOP001

[4] "Amplifier 110", Instrumentation Technologies d.o.o., https://www.i-tech.si/products/amplifier-110/.

[5] "Libera Hadron", Instrumentation Technologies d.o.o., https://www.i-tech.si/products/libera-hadron/.

[6] A. J. Halama, C. Boehme, V. Kamerdzhiev, F. Klehr, and S. Srinivasan, "Numerical Comparative Study of BPM Designs for the HESR at FAIR", in *Proc. IBIC'16*, Barcelona, Spain, Sep. 2016, pp. 608–611. doi:10.18429/JACoW-IBIC2016-WEPG01

[7] P. Boutachkov *et al.*, "Commissioning of the Beam Loss Monitoring system for the HADES beam-line at GSI", in *Proc. IBIC'19*, Malmö, Sweden, Sep. 2019, pp. 74–77. doi:10.18429/JACoW-IBIC2019-MOPP006

[8] T. Giacomini, P. Forck, J. G. De Villiers, J. Dietrich, and D. A. Liakin, "Ionization Profile Monitors - IPM @ GSI", in *Proc. DIPAC'11*, Hamburg, Germany, May 2011, paper TUPD51, pp. 419–421.

[9] V. Kamerdzhiev *et al.*, "Results of Electron Cooling Beam Studies at COSY", in *Proc. RuPAC'10*, Protvino, Russia, Sep.-Oct. 2010, paper WECHZ04, pp. 156–160.

[10] R. Tölle, IKP, Forschungszentrum Jülich, private communication.

[11] J. Blaurock, H. Simon, O. Boine-Frankenheim, and P. Spiller, "FAIR completion of construction works, towards commissioning and first science", presented at the IPAC'23, Venice, Italy, May 2023, paper THYD1, to be published. https://www.ipac23.org/preproc/pdf/THYD1.pdf

Content from this work may be used under the terms of the CC-BY-4.0 licence (© 2023). Any distribution of this work must maintain attribution to the author(s), title of the work, publisher, and DOI

ISBN: 978-3-95450-236-3 ISSN: 2673-5350 doi:10.18429/JACoW-IBIC2023-MOP002

MiniBEE - MINIBEAM BEAMLINE FOR PRECLINICAL EXPERIMENTS*

J. Reindl†, A. Rousseti, J. Neubauer, G. Datzmann[1], G. Dollinger
Universität der Bundeswehr München, Neubiberg, Germany
G. Kourkafas, J. Bundesmann, A. Dittwald, A. Denker[2], Helmholtzzentrum Berlin, Berlin, Germany
[1]also at Datzmann Interact & Innovate GmbH, Munich, Germany
[2]also at Berliner Hochschule für Technik, Berlin, Germany

Abstract

Spatial fractionated radiotherapy using protons, so-called proton minibeam radiotherapy (pMBT) was developed for better sparing of normal tissue in the entrance channel of radiation. Progressing towards clinical use, pMBT should overcome current technical and biomedical limitations. This work discusses a preclinical pMBT facility, currently built at the 68.5 MeV cyclotron at the Helmholtz Zentrum Berlin. The goal is to irradiate small animals using focused pMBT with a sigma of 50 µm, a high peak-to-valley dose ratio at center-to-center distance as small as 1 mm and beam current of 1 nA. A first degrader defines the maximum energy of the beam. Dipole magnets and quadrupole triplets transport the beam to the treatment room while multiple slits properly form the transverse beam profiles. A high magnetic field gradient triplet lens forms the minibeams in front of the target station and, scanning magnets are used for a raster scan at the target. An additional degrader, positioned close before the focusing spot and the target, further reduces the energy, forming a spread-out Bragg peak. A small animal radiation research platform will be used for imaging and positioning of the target.

INTRODUCTION

Radiation therapy (RT) aims to maximize the delivered dose in the tumor while minimizing the dose to the normal tissues [1]. Proton beams can contribute to that goal due to their advantageous physical properties [2]. They deposit low dose at the entrance and the maximum dose is deposited in a well-defined range, based on their initial energy. Additional methods of protecting the healthy tissues are the temporal and spatial fractionation. The concept of Spatially Fractionated Radiation Therapy (SFRT) is the fragmentation of dose in space creating at the entrance a periodical pattern of regions with high (peak) and low (valley) doses [3]. Proton minibeam radiation therapy (pMBT) is an innovative treatment method which exploits the advantages of proton beams and spatial fractionation [4, 5]. Minibeams have a transverse beam size (σ) in the submillimeter range and they are delivered with an interdistance, which is called center-to-center (ctc) distance, in the millimeter range in order to cover the tumor laterally. In this way, the created alternated pattern of peaks and valleys in the entrance spares the healthy tissues. When proton beams transverse the matter they broaden due to multiple Coulomb scattering (MCS) ending up to cover the tumor homogeneously (see Fig. 1).

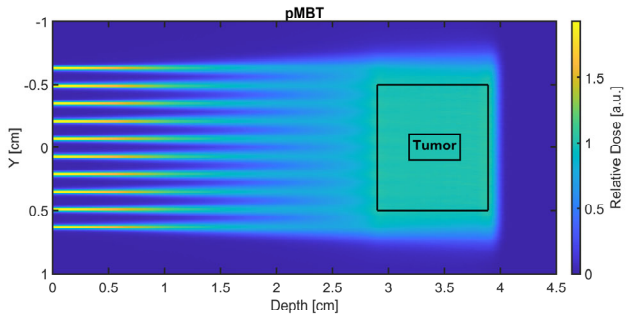


Figure 1: Simulated dose distribution of pMBT applying 68 MeV proton minibeams (σ =98 µm and ctc = 1.4 mm) in a water phantom assuming a tumor in 2.9 - 3.9 cm depth. The spread-out Bragg peak (SOBP) was obtained by positing a range shifter close to the phantom.

The in-vivo studies conducted so far have highlighted the superiority of pMBT over conventional RT. One of the first proof-of-principle experiments, in which the right ear of the mice were irradiated with a broad proton beam or with an array of 16 minibeams (σ=180 µm and with ctc=1.8 mm), showed that the acute side effects can be bypassed [6]. Another important in-vivo experiment investigated the dependence of side effects to the σ of the beam [7]. Also in this case, the right ear of the mice were irradiated with an array pattern of proton minibeams with different σ and the same ctc. The results showed that better sparing can be achieved with smaller beam sizes. Furthermore, a study in which rats with RG2 glioma were irradiated with pMBT or conventional RT schemes showed that rats irradiated with minibeams had better survival rate and less side effects [8]. All the aforementioned results gave a prominence to pMBT over conventional RT due to the better sparing of healthy tissue. However, the biological mechanisms underlying that phenomenon are not clear yet. A preclinical pMBT facility can contribute to intense and systematic research and tissue sparing effects have to be demonstrated on various tissues and beam settings in order to fully investigate the aspects and prospects of pMBT. In this paper we describe the concept of a preclinical proton minibeam radiotherapy facility for small animal irradiation at the Helmoholtz-Zentrum in Berlin (HZB) [9].

BEAMLINE DESIGN

The proposed beamline concept should fulfill some constraints related to the beam energy, the beam energy degra-

* Work supported by German Ministry of Defence BMVg
† Judith.reindl@unibw.de

Content from this work may be used under the terms of the CC-BY-4.0 licence (© 2023). Any distribution of this work must maintain attribution to the author(s), title of the work, publisher, and DOI

ISBN: 978-3-95450-236-3 ISSN: 2673-5350 doi:10.18429/JACoW-IBIC2023-MOP002

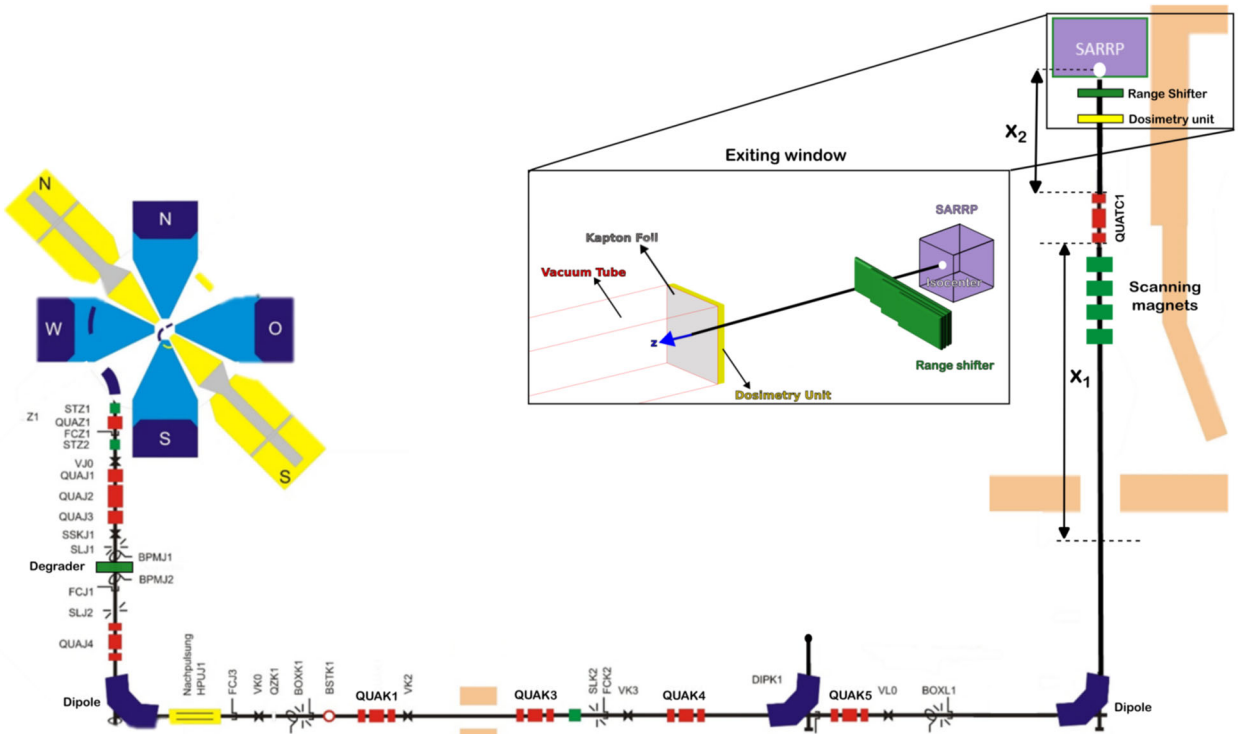


Figure 2: Layout of the pMBT beamline design at HZB. The beam goes from the left downwards to the right and upwards. Quadrupoles are shown in red, dipoles in blue and steerers in green.

dation and the beam dimensions in the target in order to be suitable for preclinical experiments in animals. The proposed beamline design is demonstrated in Fig. 2. The cyclotron at HZB generates a 68 MeV proton beam which has a maximum penetration depth ~ 4 cm (in water), appropriate for small animal experiments. The energy can be degraded by a "Hybrid range shifter system" in a twostep process. Firstly, the beam energy, as extracted from the cyclotron will be reduced by a degrader, defining the maximum penetration depth. Then, a range shifter placed a closed to the target will further degrade the energy, creating a SOBP to fully cover the tumor. After the first energy degrading, the beam can be transported towards the target room by using a set of two 90° dipole magnets and four quadrupole triplets (QUAK1, QUAK3, QUAK4, QUAK5). Downstream of the second dipole magnet a focusing system is situated consisting by one quadrupole triplet (QUATC1), with high magnetic field gradient, and two drift lengths ($x1$, $x2$). The drift length $x1$ is the distance between the focus plane of the second 90° dipole magnet and the QUATC1 and $x2$ is the distance between the QUATC1 and the isocenter. In order to achieve the demagnification of the beam's size, the drift length $x1$ is almost five times larger compared to $x2$ ($x1 \approx 5\,x2$). Upstream of the QUATC1, two sets of scanning magnets are placed aiming to have raster-scanning application of the minibeams in the target. In the last part of the beamline, the beam is extracted by the exiting window, which consists of the vacuum tube and a Kapton foil. Right after there is a dosimetry unit and then the beam transverse a few cm of air and its energy is further degraded, when it is necessary, until the target. For the accurate positioning and imaging of the animal, a small animal radiation research platform (SARRP, Xstrahl GmbH, Ratingen, Germany) will be used. The suggested beamline aims to generate proton pencil minibeams with a transversal size of σ=50 μm, ctc ~ 1 mm, for raster-scanning application and beam current ~ 1 nA.

BEAMLINE SIMULATION

In this work, we performed preliminary beamline simulations for the presented minibeam beamline concept (see above). All the simulations have been done using Trace 3-D [10], which is a first-order beam dynamic code. The starting point of the simulations, named "SLJ1", is after the beam extraction from the cyclotron (see Fig. 2). The beam parameters at SLJ1 are know from measurements that have been already conducted in HZB. The measurements have been performed at a current of 22 nA, but more than 100 nA are easily available with the same beam parameters. The beam is transported from SLJ1 until the isocenter, which is located in the SARRP, using only the 90° dipole magnets and the quadrupole triplets, as it is illustrated in Fig. 3. In Table 1 the transversal beam parameters (beam size: σ and beam divergence: σ′) are presented for

Content from this work may be used under the terms of the CC-BY-4.0 licence (© 2023). Any distribution of this work must maintain attribution to the author(s), title of the work, publisher, and DOI

ISBN: 978-3-95450-236-3 ISSN: 2673-5350 doi:10.18429/JACoW-IBIC2023-MOP002

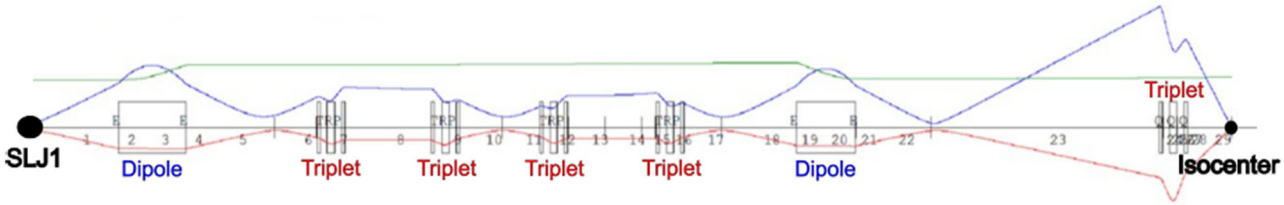


Figure 3: Beamline simulations in Trace 3-D: The simulations include only the magnetic elements (dipole magnets and triplets) starting after the beam extraction from the cyclotron (SLJ1) until the isocenter (SARRP).

both SLJ1 and the isocenter. These preliminary results demonstrate that the suggested setup can achieve a beam size demagnification of ~ 1/4 in the isocenter in both axes.

Table 1: Beam Parameters at SLJ1 and at the Isocenter

	SLJ1	Isocenter
σ_x	800 µm	220 µm
σ_y	480 µm	118 µm
σ'_x	3.67 mrad	9.83 mrad
σ'_y	1.19 mrad	4.84 mrad

CONCLUSION

The presented beamline concept can properly reduce the beam size in the isocenter by a factor of ~4. In the next steps, the slits should be positioned to properly shape the transversal phase spaces to meet the desired beam parameters. In addition, it is crucial to study the effects of the degrader in the beam current and the beam size. For all these purposes, programs which also include Monte Carlo simulations are going to be used to properly simulate the beam transport and its interaction with materials. The results will contribute to a fully comprehensive investigation of the beamline and finally, to the construction of the MiniBEE facility.

REFERENCES

[1] Radiation Oncology Physics: A Handbook for Teachers and Students, IAEA, Vienna, Austria, 2005.

[2] R.R. Wilson, "Radiological use of fast protons," *Radiology*, vol. 47, no. 5, pp. 487–491, 1946. doi:10.1148/47.5.487

[3] J.A. Laissue, H. Blattmann, and D.N. Slatkin, "Alban Köhler (1874-1947): Erfinder der gittertherapie," *Zeitschrift für Medizinische Physik,* vol. 22, no. 2, pp. 90–99, 2012. doi:10.1016/j.zemedi.2011.07.002

[4] O. Zlobinskaya *et al.,* "Reduced side effects by proton microchannel radiotherapy: Study in a human skin model", *Radiat. Environ. Biophys.*, vol. 52, no. 1, pp. 123–133, 2013. doi:10.1007/s00411-012-0450-9

[5] Y. Prezado and G. R. Fois, "Proton-minibeam radiation therapy: A proof of concept", *Med. Phys.,* vol. 40, no. 3, p. 031712, 2013. doi:10.1118/1.4791648

[6] S. Girst *et al.,* "Proton Minibeam radiation therapy reduces side effects in an in vivo mouse ear model", *Int. J. Radiat. Oncol. Biol. Phys.,* vol. 95, no. 1, pp. 234–241, 2016. doi:10.1016/j.ijrobp.2015.10.020

[7] M. Sammer *et al.,* "Proton Pencil minibeam irradiation of an in-vivo mouse ear model spares healthy tissue dependent on beam size," *Plos One*, vol. 14, no. 11, 2019. doi:10.1371/journal.pone.0224873

[8] Y. Prezado *et al.,* "Tumor control in RG2 glioma-bearing rats: A comparison between Proton Minibeam therapy and standard proton therapy," Int. J. Radiat. Oncol. Biol. Phys, vol. 104, no. 2, pp. 266–271, 2019. doi:10.1016/j.ijrobp.2019.01.080

[9] A. Denker *et al.,* "Status of the HZB Cyclotron", in Proc. Cyclotrons'1), Cape Town, South Africa, Sep. 2019, pp. 253-255. doi:10.18429/JACoW-CYCLOTRONS2019-TUC02

[10] K.R. Crandall, Trace 3-D Documentation, Los Alamos National Laboratory, Los Alamos, NM, USA, 1987.

Content from this work may be used under the terms of the CC-BY-4.0 licence (© 2023). Any distribution of this work must maintain attribution to the author(s), title of the work, publisher, and DOI

ISBN: 978-3-95450-236-3 ISSN: 2673-5350 doi:10.18429/JACoW-IBIC2023-MOP004

DESIGN AND STUDY OF CAVITY QUADRUPOLE MOMENT AND ENERGY SPREAD MONITOR*

Q. Wang, Q.Y. Dong, L.T. Huang
Dalian Institute of Chemical Physics, Chinese Academy of Sciences, Dalian, China
Q. Luo†
NSRL, University of Science and Technology of China, Hefei, China

Abstract

A nondestructive method to measure beam energy spread using the quadrupole modes within a microwave cavity is proposed. Compared with a button beam position monitor (BBPM) or a stripline beam position monitor (SBPM), the cavity monitor is a narrow band pickup and therefore has better signal-to-noise ratio (SNR) and resolution. In this study, a rectangular cavity monitor is designed. TM220 mode operating at 4.76 GHz in the cavity reflects the quadrupole moment of the beam. The cavity plans to be installed behind a bending magnet in Dalian Coherent Light Source (DCLS), an extreme ultraviolet FEL facility. In this position, the beam has a larger dispersion, which is beneficial to measure the energy spread. A quadrupole magnet, a fluorescent screen, and a SBPM with eight electrodes is installed near the cavity for calibration and comparison. The systematic framework and simulation results are also discussed in this paper.

INTRODUCTION

Energy spread is an important parameter that reflects the quality of the beam. Especially in linear accelerators used as storage rings and collider injectors, ensuring a good energy spread of the beam can improve injection efficiency and maintain beam stability. Therefore, real-time and high-resolution measurement of energy spread needs to be achieved.

The most widely used method for energy spread measurement at present is to insert a fluorescent screen or an OTR after bending magnets. By measuring the generated light spot, the transverse distribution of the beam can be determined, and the energy spread is capable to be obtained based on the principle that different energy electrons have different turning radius [1]. However, this intercepting method is unsuitable for real-time measurement or feedback control. Therefore, a nonintercepting energy spread monitor is required.

A feasible nondestructive method is using stripline beam position monitor (SBPM) [2–4]. SBPM is installed at positions with high value of dispersion function, allowing extraction of the beam's quadrupole moment to obtain the energy spread. The sensitivity of this method is influenced by the angle of electrodes.

* Work supported by the National Key Research and Development Proram of China No.2022YFA1602201, the International Partnership Program of the Chinese Academy of Sciences Grant No. 211134KYSB20200057 and the STCF Key Technology Research Project.
† email address: luoqing@ustc.edu.cn

In order to achieve the energy spread measurement with high-resolution, this paper proposes the method of RF resonant cavity. Similar to SBPMs, cavities can also measure the quadrupole moment, thus obtaining the energy spread. Compared to SBPMs, cavities have higher signal-to-noise ratio (SNR), enabling better quadrupole moment resolution, which can also be confirmed in the position measurement. Additionally, in the direction of the beam, cavities can realize a more compact layout.

This paper introduces a design of cavity-based quadrupole moment and energy spread monitor for the Dalian Coherent Light Source (DCLS), an extreme ultra-violet FEL facility with a length of 100 m, and provides simulation results to verify the feasibility of the proposed approach.

THEORETICAL BASIS

While passing through the cavity, the bunch will excite different eigenmodes. The signal amplitude of an eigenmode can be written as

$$V = k_n q \int_{-T}^{T} f(t) \exp(i\omega t)\, dt\,, \tag{1}$$

where q is bunch charge, the final integral is related to the longitudinal distribution of the bunch, and k_n is the loss factor, which is related to the mode type. As shown in Fig. 1, for a rectangular cavity rotated 45° about the axis, its TM220 mode amplitude is proportional to the beam quadrupole moment [5, 6].

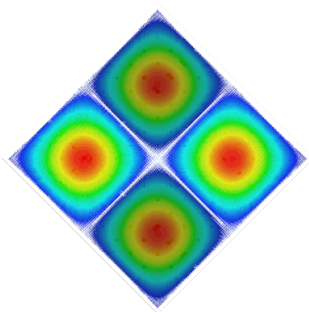


Figure 1: Electric field of TM220 mode in rectangular cavity. Warmer colors represent stronger electric fields.

$$V_{TM220} \propto x^2 - y^2 + \sigma_x^2 - \sigma_y^2\,, \tag{2}$$

where x and y are the beam positions in the two directions. σ_x and σ_y are the beam rms sizes in the two directions. When the bunch length is short and does not change significantly, the quadrupole moment $x^2 - y^2 + \sigma_x^2 - \sigma_y^2$ can be obtained by extracting the charge and the amplitude of the TM220 mode.

Content from this work may be used under the terms of the CC-BY-4.0 licence (© 2023). Any distribution of this work must maintain attribution to the author(s), title of the work, publisher, and DOI

ISBN: 978-3-95450-236-3 ISSN: 2673-5350 doi:10.18429/JACoW-IBIC2023-MOP004

Content from this work may be used under the terms of the CC-BY-4.0 licence (© 2023). Any distribution of this work must maintain attribution to the author(s), title of the work, publisher, and DOI

Assuming that the vertical dispersion, η_y, is zero, the relationship between energy spread and quadrupole moment can be written as

$$\sigma_x^2 - \sigma_y^2 = \beta_x \epsilon_x + (\eta_y \frac{\Delta E}{E})^2 - \beta_y \epsilon_y + g \,, \qquad (3)$$

where β_x and β_y are β functions, η_x is the horizontal dispersion, ϵ_x is the horizontal emittance, and g is the correction factor, which can be determined by calibration. The two directions x and y are interchangeable. Therefore, after excluding the influence of the beam position, the relationship between the TM220 amplitude and the energy spread can be established.

As indicated in Eq. (3), placing the monitor at a position with high value of dispersion function is beneficial to improve the sensitivity and resolution of the quadrupole moment measurement. For a linear accelerator, it is more suitable to place the monitor after the bending magnets.

LAYOUT AND FRAMEWORK

The scheme for measuring beam energy spread using a cavity will be carried out in the undulator section of DCLS. The beam parameters in this section are shown in Table 1.

Table 1: Beam Parameters in the Undulator Section of DCLS

Parameter	Value
Beam energy	300 MeV
Charge	500 pC
Bunch length (rms)	~0.12 mm
Transverse dimension (rms)	~0.1 mm
β function (mean)	6-29 m
Normalized emittance	1–2 mm · mrad

The cavity will be installed after the bending magnet at the end of the undulator section, as shown in Fig. 2. The dispersion at this position is significant, which is advantageous for energy spread measurement. A fluorescent screen is set downstream to get information of beam position and provide online calibration, and the upstream ICT on the bending magnet can synchronously provide absolute measurement of the beam charge. Additionally, an eight-electrode SBPM will be installed for energy spread measurement as a reference, which can also provide information of beam charge and beam position.

The systematic framework is shown in Fig. 3. When the beam passes through the cavity, the signal generated by the excited eigenmodes will be coupled out via feedthroughs. In order to overcome cable attenuation, the signal first enters an amplifier, then passes through long cables to the accelerator tunnel and connects to the analog front end for down conversion. Afterwards, it is fed into the electronics for amplitude extraction and energy spread calculation.

PHYSICAL DESIGN

The TM220 mode of the rectangular cavity can indicate the magnitude of the quadrupole moment. In order to share

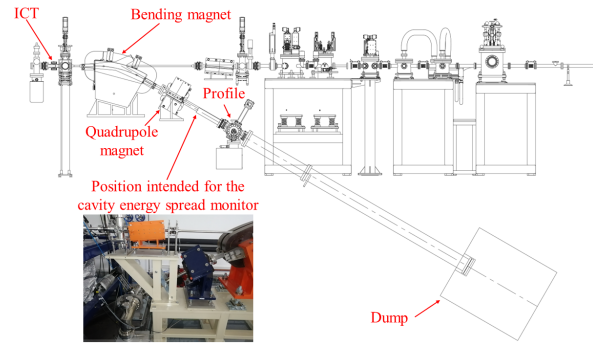


Figure 2: Layout diagram.

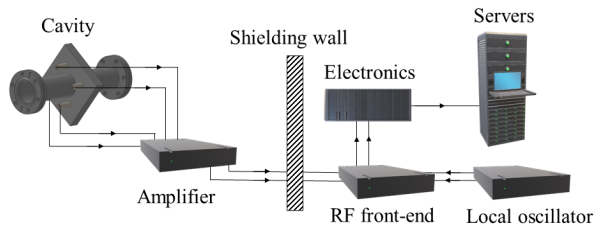


Figure 3: Systematic framework of the cavity quadrupole moment and energy spread monitor.

the analog front end with other cavity monitors on the DCLS, the operating frequency of the TM220 mode is set to be 4.76 GHz.

The relationship between the frequency of the TMmn0 mode and the dimensions of the cavity can be expressed as

$$f_{TM220} = \frac{c}{2}\sqrt{(\frac{m}{a})^2 + (\frac{n}{a})^2} \,, \qquad (4)$$

where c is speed of light in vacuum, and a represents the length of one side of the square cavity. By calculation, we have a = 89.1 mm. In order to reduce the impact on beam, the longitudinal length l of the cavity is set to 10 mm.

The TM220 mode signal is coupled out by feedthroughs. The feedthroughs are set at the position with the strongest electric field of the TM220 mode, and are inserted along the electric field direction for optimal coupling. Four feedthroughs are used to maintain electric field symmetry. The inner conductors of the feedthroughs should not be inserted too deeply to avoid distorting the electric field.

The diameter of the beam pipe at the installation location is 35 mm. The cutoff frequency of it is 5.023 GHz, which ensures that the TM220 mode signal operating at 4.7 GHz does not leak out. The beam pipe will affect the frequencies of all eigenmodes inside the rectangular cavity.

When machining a rectangular cavity, the milling cutter cannot process the edge of the beam direction to 90°, so chamfering must be considered. A square groove is milled on a cubic metal plate to serve as the cavity. Due to the length of the cavity in the z-direction (beam direction) reaching 10 mm, a milling cutter with a blade length of 15 mm and a blade diameter of 6 mm is chosen to enter along the z-

ISBN: 978-3-95450-236-3 ISSN: 2673-5350 doi:10.18429/JACoW-IBIC2023-MOP004

direction for cutting the groove. This will leave chamfers with a radius of 3 mm at the four corners. This also affects the frequencies of the eigenmodes. Therefore, numerical calculations are needed to correct the cavity dimensions obtained from Eq. (4). CST Microwave Studio [7] is used for frequency simulation calculation. The final structure and dimensions of the cavity are determined as shown in Fig. 4 and Table 2.

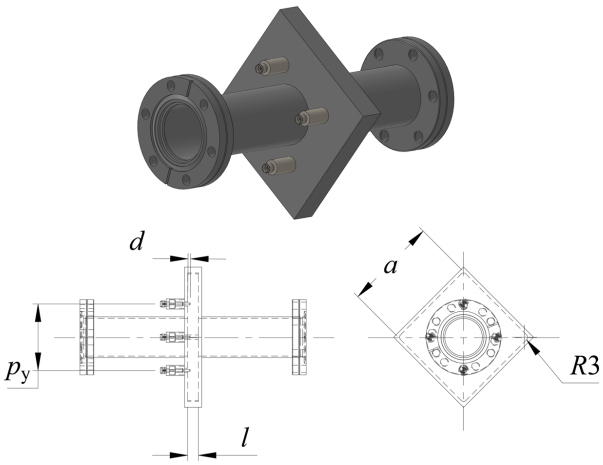


Figure 4: The structure of the rectangular cavity.

Table 2: Optimized Dimensions of the Cavity

Parameter	Value
a	86.2 mm
l	10 mm
p_y	61.8 mm
d	1.4 mm
Chamfer	R3

SIMULATION

The cavity model is established in CST, and virtual beams are loaded for simulation. The beam simulation is divided into two cases. In the first case, the transverse sizes of the beam are zero ($\sigma_x = 0, \sigma_y = 0$), and the beam position is changed. In the second case, the beam is located at the axis ($x = 0, y = 0$), and the transverse sizes are varied. The time-domain and frequency-domain output signals of the cavity are shown in Fig. 5.

The results show that there is a good linear relationship between the amplitude of the TM220 mode and the quadrupole moments. The quadrupole moment sensitivity of the cavity monitor is better than 0.03 mm^2 in the frequency domain. This parameter of the eight-electrode SBPM is generally only on the order of 10^{-3}. The cavity monitor is more likely to achieve better measurement resolution.

The simulation results show that the TM220 mode is successfully excited when the quadrupole moment is present. The variations of quadrupole moments $x^2 - y^2 + \sigma_x^2 - \sigma_y^2$ and the amplitude of TM220 modes obtained through simulation at different beam positions and beam transverse sizes are shown in Fig. 6.

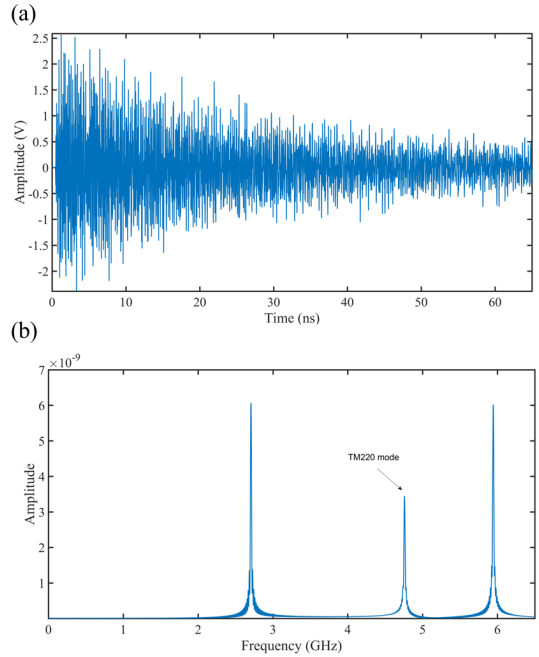


Figure 5: The output signal of the cavity when $x = 10$, $y = 0$, $\sigma_x = 0$, and $\sigma_y = 0$. (a) is the time-domain signal. (b) is the frequency-domain signal.

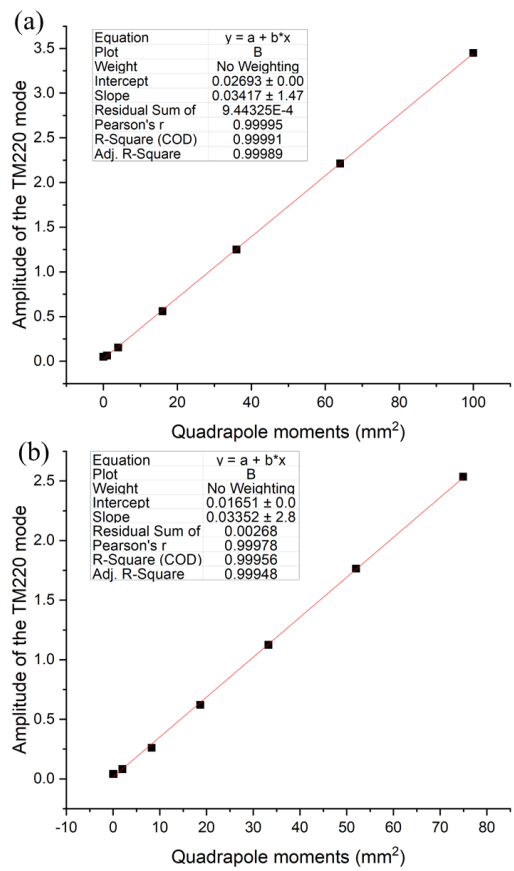


Figure 6: Variation of TM220 mode amplitude with beam quadrupole moment. (a) is x varying from 1 to 10 mm when $\sigma_x = 0, \sigma_y = 0$, and $y = 0$. (b) is σ_y varying from 0.03 to 8.66 mm when $x = 0, y = 0$, and $\sigma_x = 1$ mm.

Content from this work may be used under the terms of the CC-BY-4.0 licence (© 2023). Any distribution of this work must maintain attribution to the author(s), title of the work, publisher, and DOI

ISBN: 978-3-95450-236-3 ISSN: 2673-5350 doi:10.18429/JACoW-IBIC2023-MOP004

SUMMARY

In this paper, the design of the cavity quadrupole moment and energy spread monitor is shown, and the simulation results indicate a good linear relationship between its TM220 mode output signal and the beam quadrupole moment. The beam experiment will be carried out at DCLS soon. This study provides a new approach for nondestructive and high-resolution measurement of beam energy spread.

REFERENCES

[1] M. Satoh, K. Furukawa, and T. Suwada, "Energy-spread-feedback system for the KEKB injector Linac", in *Proc. PAC'05*, Knoxville, TN, USA, May 2005, paper RPAT088, pp. 4212–4214.

[2] T. Suwada, M. Satoh, and K. Furukawa, "Nondestructive beam energy-spread monitor using multi-strip-line electrodes", *Phys. Rev. ST Accel. Beams*, vol. 6, p. 032801, Mar. 2003. doi:10.1103/PhysRevSTAB.6.032801

[3] J. C. Dooling, F. R. Brumwell, L. Donley, G. E. McMichael, and V. F. Stipp, "Beam analysis using the IPNS Linac ESEM", in *Proc. LINAC'04*, Knoxville, Lübeck, Germany, Aug. 2004, paper TUP61, pp. 405–407.

[4] J. Fang, P. Lu, Q. Luo, B. Sun, and X. H. Wang, "Analysis and calculation of beam energy spread monitor for HLS LINAC", in *Proc. IPAC'10*, Kyoto, Japan, May 2010, paper MOPE028, pp. 1029–1031.

[5] D. Whitum and Y. Kolomensky, "Analysis of an asymmetric resonant cavity as a beam monitor", *Rev. Sci. Instrum.*, vol. 70, no. 5, p. 2300, May 1999. doi:10.1103/P10.1063/1.1149756

[6] Q. Luo *et al.*, "New beam diagnostics and eelated study on HLS photo-injector and HLS II", in *Proc. IPAC'14*, Dresden, Germany, Jun. 2014, pp. 3578-3580. doi:10.18429/JACoW-IPAC2014-THPME140

[7] CST, https://www.3ds.com/

Content from this work may be used under the terms of the CC-BY-4.0 licence (© 2023). Any distribution of this work must maintain attribution to the author(s), title of the work, publisher, and DOI

ISBN: 978-3-95450-236-3 ISSN: 2673-5350 doi:10.18429/JACoW-IBIC2023-MOP007

EXPERIMENTAL VERIFICATION OF THE COHERENT DIFRACTION RADIATION MEASUREMENT METHOD FOR LONGITUDINAL ELECTRON BEAM CHARACTERISTICS

R. Panaś*, A. I. Wawrzyniak, NSRC SOLARIS, Kraków, Poland
K. Łasocha, CERN, Geneva, Switzerland
A. Curcio, INFN LNF, Frascati, Italy

Abstract

This paper presents a natural extension of prior theoretical investigations regarding the utilization of coherent diffraction radiation for assessing longitudinal characteristics of electron beams. The study focuses on the measurement results obtained at the SOLARIS synchrotron and their analysis through a theoretical model. The findings are compared with previous estimates of the electron beam's longitudinal profile.

COHERENT DIFFRACTION RADIATION

Electromagnetic radiation is emitted when a beam of charged particles accelerates or changes medium of propagation (abruptly or continuously in terms of the local electromagnetic susceptibility) [1, 2]. If wavelength of the the emitted radiation is comparable or greater than the bunch length, the radiation is said to be "coherent" because the contributions from the distinct particles within the beam interfere constructively, and the bunch radiates as a whole. In the low frequency limit the emitted radiation power is proportional to the square of the bunch intensity, while for intermediate frequency ranges the power decreases with increasing bunch length. For bunch lengths of the picosecond scale, variations in the radiation intensity can be easily monitored by GHz-THz detectors like Schottky diodes [3, 4]. For shorter bunches, far-infrared diagnostics are needed, such as spectrometers [5].

Coherent radiation can be coupled out of the beamlines through suitable transparent windows, eventually transported in air into power detectors. For the diagnostic purposes of the PolFEL project [6], application of the Coherent Diffraction Radiation (CDR) was investigated at SOLARIS [7]. Diffraction radiation is a type of radiation that a bunch of particles emits while passing close to the boundary of two media with different indices of refraction, which allows for non-destructive bunch length measurements [8].

In the experimental setup at SOLARIS, the beam passes through a hollow alluminium disk. The radiation is emitted from localized layers of that surface, imprinting the beam properties into the emitted radiation at the transition plane and enabling diagnostics. The fact that the disk is hollow allows the beam not to be scattered, preserving the emittance even if the particles do not propagate inside it.

The spectral angular distribution of energy emitted backward in the form of diffraction radiation from a perfectly conducting round disk, with an internal and external radius equal to respectively a and b, can be described with the following formula [9, 10]:

$$\frac{d^2I}{d\omega d\Omega} = |F(\omega)|^2 \times \frac{Q^2}{(4\pi^3\epsilon_0 c^5\beta^4\gamma^2)} \times \times \left| \int_a^b d\rho\rho K_1\left(\frac{\omega\rho}{\beta\gamma c}\right) J_1\left(\frac{\omega\rho}{c\sin\theta}\right) e^{\frac{j\omega^2\rho^2}{2c^2}} \right|^2, \quad (1)$$

where Q denotes the bunch charge, ϵ_0 is the vacuum permittivity, c is the velocity of light, β is the ratio of particle velocity to the velocity of light, and γ is the Lorentz factor. The quantity $F(\omega)$ is called the *bunch form factor* and strictly depends on the shape of the electron bunch. The theoretical prediction of the spectral-angular distribution of CDR emitted with the experimental setup at SOLARIS is shown in Fig. 1.

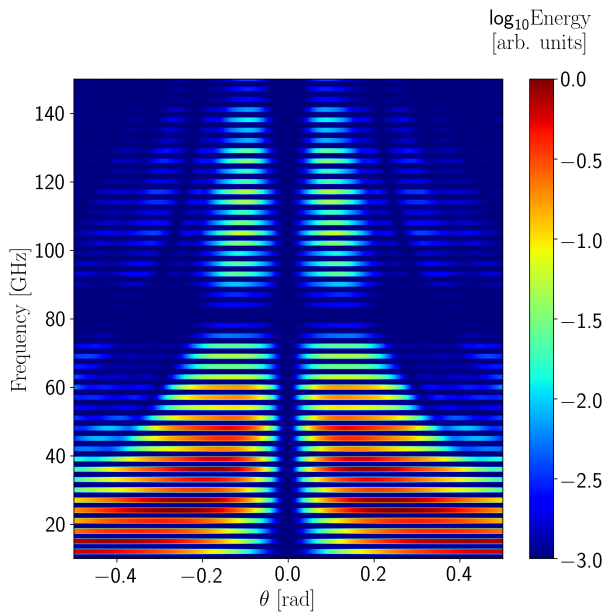


Figure 1: CDR spectral-angular distribution for the SOLARIS injector bunch repetition pattern and beam energy of 550 MeV.

BUNCH LENGTH MEASUREMENT

The diagnostic technique considered for PolFEL is based on the power balance of CDR radiation collected by Schottky

* roman.panas@uj.edu.pl

Content from this work may be used under the terms of the CC-BY-4.0 licence (© 2023). Any distribution of this work must maintain attribution to the author(s), title of the work, publisher, and DOI

ISBN: 978-3-95450-236-3 ISSN: 2673-5350 doi:10.18429/JACoW-IBIC2023-MOP007

Content from this work may be used under the terms of the CC-BY-4.0 licence (© 2023). Any distribution of this work must maintain attribution to the author(s), title of the work, publisher, and DOI

diodes in different ranges of sub- THz radiation. Following Eq. (1), the emitted energy depends on the bunch length through the form factor $F(\omega)$. If the transverse size of the bunch is negligible, one has [11]:

$$F(\omega) = \int_{-\infty}^{\infty} I(t) e^{j\omega t}\, dt, \qquad (2)$$

where $I(t)$ is the normalized dimensionless beam current passing through the disk. Simply speaking, the form factor is the Fourier transform of the beam current. In certain cases, for example when the beam consists of a single Gaussian bunch, an exact analytical formula for the form factor can be given, parametrized by the RMS bunch length. This parameter can be then experimentally retrieved by calculating the ratio of CDR power at two distinct frequencies and comparing it to the theoretical predictions given by Eq. (1). The described technique is not limited to only one type of radiation, and has been previously demonstrated with measurements based on CDR [3] and Coherent Cherenkov Diffraction Radiation [4].

In the SOLARIS linac the beam is bunched, with the 3 GHz bunch repetition rate. The shape of a single bunch differs from the Gaussian and the bunch intensity is modulated proportionally to the 100 MHz sinewave [12, 13]. As result the corresponding form factor also differs from the smooth form factor of a single Gaussian bunch as presented in Fig. 2.

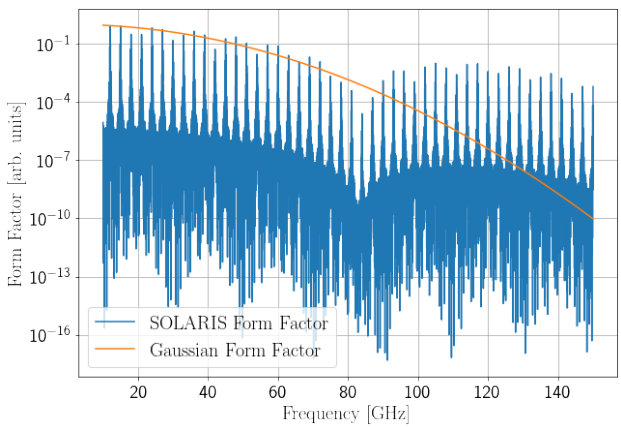


Figure 2: Form factors calculated for SOLARIS injector bunch train and a single Gaussian bunch. In both cases the FWHM bunch length is equal to 12 ps.

Although deriving the information on the bunch length from a narrow frequency band is not possible at SOLARIS, due to the oscillatory character of the form factor, the bunch length might be derived from the cumulative power within the broader frequency bands.

In the previous theoretical study [14] it was determined that the ratio of the powers within 26.5-40 GHz and 33-50 GHz bands allows to discriminate between bunch lengths in the range from 5 to almost 25 ps full width at half maximum (FWHM). Complementary, the power emitted within 50-75 GHz band, while comparing to 33-50 GHz band, can be used to refine an earlier measurement, but cannot serve as a standalone indicator, due to a local extremum it takes for bunch lengths of approximately 16 ps FWHM.

EXPERIMENTAL SETUP AND MEASUREMENTS

The measurement were taken in the end part of the SOLARIS linac, close to the beam dump section. After passing through 0.15 mm thick flange, the electrons move in the air and after 20 cm they reach the experimental setup.

The arrangement for measuring the length of the electron beam profile is visible in Fig. 3. It includes an aluminum radiator with a radius of 2.54 cm and a 5 mm radius hole at its center. Additionally, a golden-coated Ø3" 90° Off-axis parabolic mirror focuses the radiation towards the apertures of three diodes sensitive to different frequency bands are employed as detectors, used alternately.

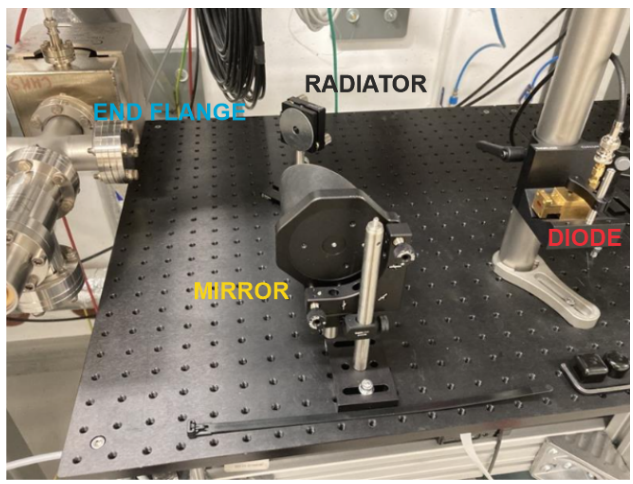


Figure 3: Experimental setup.

Schottky diodes produced by Mi-Wave [15] were used for the experiment, with the frequency band corresponding to the ones discussed in the previous section. An important factor to consider was not only the sensitivity of the diodes, but also their input aperture. A larger aperture allows more radiation to enter the detector and thus for diodes with different apertures, it will change the power balance on the basis of which the longitudinal profile is estimated. The apertures of the diodes differed, therefore it was necessary to normalize the signals with respect to the surface area of the diode aperture.

The diodes were placed in the holder, in the same place. The big difficulty was the fact that it was impossible to adjust the diode position during the beam operation. In the future, this problem will be solved by the installation of remotely controlled platforms on which the diodes will be placed, thanks to which it will also be possible to change the diodes during the measurement without having to pull them out as it is now.

As can be seen in the graph Fig. 4, the signal from the diode in the highest frequency band is at the noise level.

ISBN: 978-3-95450-236-3 ISSN: 2673-5350 doi:10.18429/JACoW-IBIC2023-MOP007

This obviously lowers the accuracy of our measurement and is the most likely cause of the difference from the expected value. For this reason, the ratio of the signals from the diode in the middle and the lowest band was considered the most reliable.

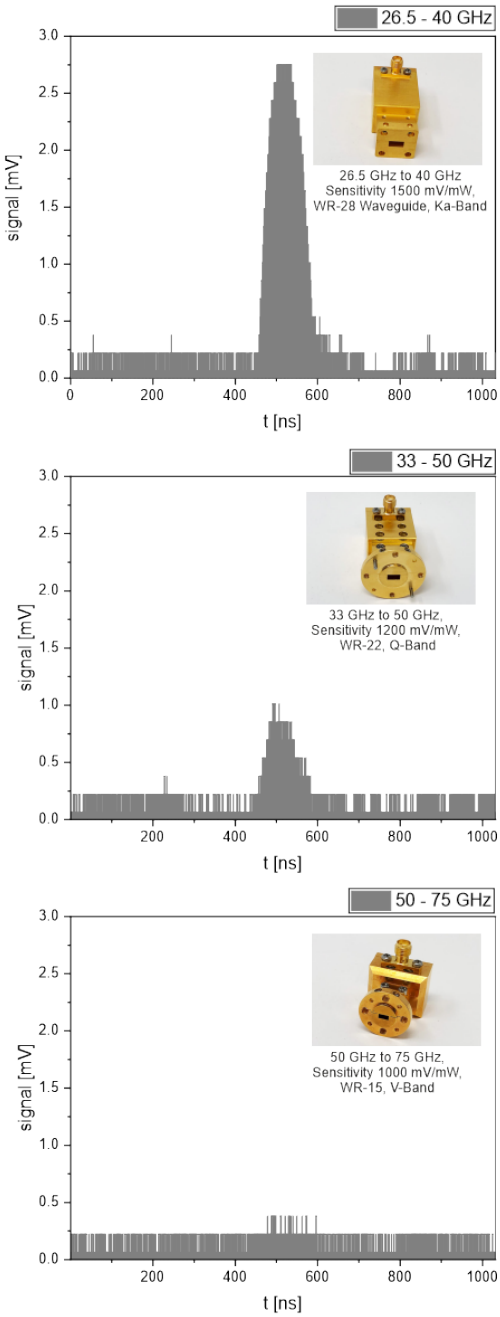


Figure 4: Signals measured by diodes with different bands.

Calculating the ratio of the measured powers, we can compare them with theoretical curves which describe the change in ratio as a function of the bunch length, as presented in Fig. 5. Results from both measurements estimate the FWHM of the longitudinal electron beam profile to be around 20 - 25 ps. In the work [12], the FWHM of the longitudinal electron bunch profile at SOLARIS linac was estimated at 12 ps.

CONCLUSION

In this contribution, progress has been made at SOLARIS towards an experimental test of the CDR-based characterization of the electron beam's longitudinal profile for PolFEL project. Additionally, tools for processing the measured data and calculating the bunch length have been developed and updated. Schottky diodes were acquired and placed in the setup, enabling the first measurements and calculations.

The results obtained from the experiment do not align with the theoretical expectations. The possible cause is a weak signal, which, in the case of a diode in the highest frequency range, made it almost impossible to extract the signal from the noise level.

It is anticipated that by improving the signal strength from the diode in the highest and medium band, the estimated bunch length will decrease and become closer to the one from the previous estimate. In order to increase the signal strength, the system will be re-adjusted using motorized platforms, which could be done online with the present beam. Currently, adjusting the setup with the beam is not feasible. If that proves insufficient, additional horn antennas will be installed on diodes.

The tested system has shown potential, indicating that it can be used as a low-cost alternative to more complex systems like transverse deflecting cavities (TDC) and streak cameras for monitoring the longitudinal beam profile. After appropriate calibration using the methods mentioned above, such a system based on the CDR could monitor the degree of bunch compression after magnetic chicane.

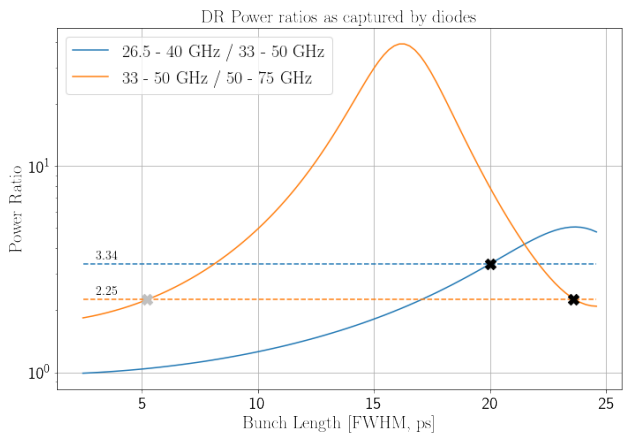


Figure 5: Solid lines: theoretically predicted ratio of CDR power within different bands as a function of the bunch length. Dashed lines: experimentally measured CDR ratios. Black crosses indicate the crossing points and therefore the estimated bunch lengths. Grey cross indicate a crossing point rejected based on the low-medium band ratio.

Content from this work may be used under the terms of the CC-BY-4.0 licence (© 2023). Any distribution of this work must maintain attribution to the author(s), title of the work, publisher, and DOI

ISBN: 978-3-95450-236-3 ISSN: 2673-5350 doi:10.18429/JACoW-IBIC2023-MOP007

REFERENCES

[1] J. D. Jackson, *Classical Electrodynamics*. American Association of Physics Teachers, 1999.

[2] V. L. Ginzburg, "Radiation by uniformly moving sources (Vavilov–Cherenkov effect, transition radiation, and other phenomena)," *Physics-Uspekhi*, vol. 39, no. 10, p. 973, 1996.

[3] A. Curcio *et al.*, "Beam-based sub-THz source at the CERN linac electron accelerator for research facility," *Phys. Rev. Accel. Beams*, vol. 22, p. 020 402, 2 2019. doi:10.1103/PhysRevAccelBeams.22.020402

[4] A. Curcio *et al.*, "Noninvasive bunch length measurements exploiting Cherenkov diffraction radiation," *Phys. Rev. Accel. Beams*, vol. 23, no. 2, p. 022 802, 2020. doi:10.1103/PhysRevAccelBeams.23.022802

[5] T. J. Maxwell *et al.*, "Coherent-Radiation Spectroscopy of Few-Femtosecond Electron Bunches Using a Middle-Infrared Prism Spectrometer," *Phys. Rev. Lett.*, vol. 111, p. 184 801, 18 2013. doi:10.1103/PhysRevLett.111.184801

[6] A. I. Wawrzyniak *et al.*, "Concept of Electron Beam Diagnostics for PolFEL," in *Proc. IPAC'22*, Bangkok, Thailand, 2022, pp. 1055–1058. doi:10.18429/JACoW-IPAC2022-TUPOPT025

[7] A. I. Wawrzyniak, R. Panaś, A. Curcio, M. Knafel, G. Kowalski, and A. Marendziak, "Solaris synchrotron performance and operational status," *Nucl. Instrum. Methods Phys. Res., Sect. B*, vol. 493, pp. 19–27, 2021. doi:10.1016/j.nimb.2021.01.020

[8] A. Potylitsyn, "Transition radiation and diffraction radiation. Similarities and differences," *Nucl. Instrum. Methods Phys. Res., Sect. B*, vol. 145, no. 1, pp. 169–179, 1998. doi:10.1016/S0168-583X(98)00384-X

[9] S. Casalbuoni, B. Schmidt, P. Schmüser, V. Arsov, and S. Wesch, "Ultrabroadband terahertz source and beamline based on coherent transition radiation," *Phys. Rev. ST Accel. Beams*, vol. 12, p. 030 705, 3 2009. doi:10.1103/PhysRevSTAB.12.030705

[10] A. Curcio *et al.*, "Diffractive shadowing of coherent polarization radiation," *Phys. Lett. A*, vol. 391, p. 127 135, 2021. doi:10.1016/j.physleta.2020.127135

[11] O. Grimm, "Principles of longitudinal beam diagnostics with coherent radiation," in *Proc. EPAC'06*, Edinburgh, UK, Jun. 2006.

[12] A. Curcio, R. Panaś, M. Knafel, and A. Wawrzyniak, "Liouville theory for fully analytic studies of longitudinal beam dynamics and bunch profile reconstruction in dispersive lines," *Nucl. Instrum. Methods Phys. Res., Sect. A*, vol. 986, p. 164 755, 2021. doi:10.1016/j.nima.2020.164755

[13] A. Curcio, M. A. Knafel, G. W. Kowalski, R. Panaś, M. Waniczek, and A. I. Wawrzyniak, "Bunch Length Characterizations for the Solaris Injector LINAC," in *Proc. IPAC'21*, Campinas, Brazil, May 2021, pp. 2117–2119. doi:10.18429/JACoW-IPAC2021-TUPAB277

[14] R. Panaś and A. Curcio, "Coherent Difraction Radiation for Longitudinal Electron Beam Characteristics," in *Proc. IBIC'22*, Kraków, Poland, 2022, pp. 291–293. doi:10.18429/JACoW-IBIC2022-TUP28

[15] Milimiter Wave Products Inc., https://www.miwv.com

Content from this work may be used under the terms of the CC-BY-4.0 licence (© 2023). Any distribution of this work must maintain attribution to the author(s), title of the work, publisher, and DOI

ISBN: 978-3-95450-236-3 ISSN: 2673-5350 doi:10.18429/JACoW-IBIC2023-MOP008

CONSIDERATION OF BEAM INSTRUMENTATION FOR SOLARIS LINAC UPGRADE

A. Curcio, INFN LNF, Frascati, Italy
R. Panaś, J. Biernat, M. Ünal, J. Wiechecki, A.I. Wawrzyniak*, NSRC SOLARIS, Kraków, Poland

Abstract

SOLARIS linac currently operates at 540 MeV and is used as an injector to the storage ring, where after the accumulation the energy is ramped up to 1.5 GeV via two active RF cavities. Top-up injection would be of extreme benefits for user operation, therefore a new 1.5 GeV linac is being designed. The idea is to replace the current machine without infrastructural interventions in terms of tunnel expansion. Performed studies demonstrate that the best solution is provided by a Hybrid S-band/C-band LINAC. One of the main goals is to achieve bunch compression below the picosecond level and low-emittance beams for a future short-pulse facility or a Free Electron Laser. Within this presentation the results of performed simulations will be presented together with the concept of different diagnostics as BPMs, current transformers, YAG screens, coherent diffraction radiation monitor distribution.

INTRODUCTION

SOLARIS National Synchrotron Radiation Centre (NSRC) is first light source infrastructure built in Krakow, Poland. Currently it consists of 600 MeV linac with thermionic gun, 1.5 GeV storage ring and 5 operating beamlines serving for the users community. The storage ring operates in the decay mode with 2 injections during the day. An optimal perspective for the future operations at SOLARIS [1] would be the beam injection from the LINAC [2] into the storage ring at full energy, i.e. 1.5 GeV. There are several advantages related to this approach. The most intuitive is the possibility to keep the stored current at a constant level. This would favor the user operation requiring a constant level of brilliance of the synchrotron source and/or of the sources associated to insertion devices. The radiation source, therefore, can operate continuously, avoiding injection downtime and energy ramp. Additionally, from an operational point of view, all the machine settings, which are normally current-depending, could be kept at the same value. Avoiding invasive feedbacks meant to follow the electron current's decay, would allow the establishment of fine feedbacks working around equilibrium conditions for the beam parameters (like emittance, optics and orbit stability). Fine feedbacks could efficiently maintain optimal performances for days.

Furthermore, having a 1.5 GeV LINAC machine would open up a wide range of new possibilities for the facility, solely related to the LINAC as independent module. It's worth specifying that in a top-up injection system the LINAC is permanently serving the storage ring, nevertheless a beam-splitter system might be thought in order to save a fraction of charge for diverse applications, bypassing the transfer line to the ring. It has been already demonstrated the interest of doing electron irradiations with the LINAC [3]. Currently, a diagnostic station placed before the LINAC dump is already under development for tests/experiments on novel concepts of beam diagnostics [4]. A futuristic view of the same area would foresee a Free Electron Laser (FEL). Indeed, such a FEL source would be pulsed on a much shorter scale length than the pulses provided by the storage ring, and it would be designed to cover a different frequency range.

OPTICS DESIGN AND BEAM DYNAMICS

There were several considerations for the new linac design. However due to space constrains in the linac tunnel the decision was made to change the technology from S-band to C-band allowing for higher accelerating gradient. The layout of the new LINAC placed in the existing tunnel is reported in Fig. 1. The schematics of the lattice elements is, instead, reported in Fig. 5. Such schematics will be discussed later on in this paper, specifically regarding the beam instrumentation used for beam diagnostics. The start-to-end simulations studies, from the cathode to the injection point for a Hybrid S-band/C-band LINAC were done by using the ASTRA and elegant [5] codes. The start-to-end simulation has been conducted for several different beam charges [6].

For the case of 100 pC the resulting beam optics in terms of rms beam sizes (Sigma x and y) is reported in Fig. 2. It is possible to notice that the beam size is maintained within the range of a few hundreds microns all along the LINAC, corresponding to a normalized emittance $\varepsilon_{Nx} \simeq \varepsilon_{Ny} \lesssim 5\,\mathrm{mm}\cdot\mathrm{mrad}$. The emittance at the gun is around $1\,\mathrm{mm}\cdot\mathrm{mrad}$ but it reaches such a value in the magnetic compressor due to space charge [6]. The final rms bunch length St is in fact ≃500 fs rms, as depicted in Fig. 3. Such a short bunch length may be used in the future to drive radiation sources or to perform ultra-fast irradiations for different applications.

ERROR STUDIES

Once the start-to-end simulation studies have been finalized, spanning over beam parameters, and beam optics solutions have been found to efficiently transport low-emittance, compressed beams, to the end of the full-energy LINAC, investigation of the errors in the lattice elements has been performed. The goal has been to evaluate if the selected focusing elements and their positioning is suitable for preserving the beam optics even for non-ideal elements, and

* adriana.wawrzyniak@uj.edu.pl

Content from this work may be used under the terms of the CC-BY-4.0 licence (© 2023). Any distribution of this work must maintain attribution to the author(s), title of the work, publisher, and DOI

ISBN: 978-3-95450-236-3 ISSN: 2673-5350 doi:10.18429/JACoW-IBIC2023-MOP008

Content from this work may be used under the terms of the CC-BY-4.0 licence (© 2023). Any distribution of this work must maintain attribution to the author(s), title of the work, publisher, and DOI

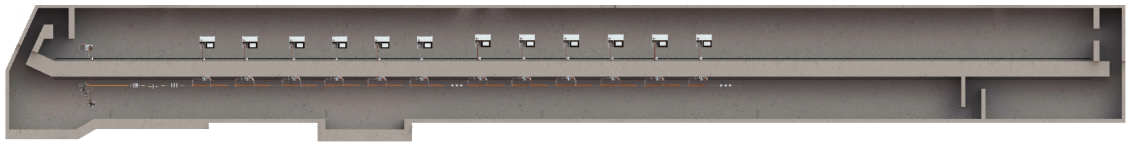


Figure 1: SOLARIS LINAC tunnel: gun on the left, transfer-line on the right.

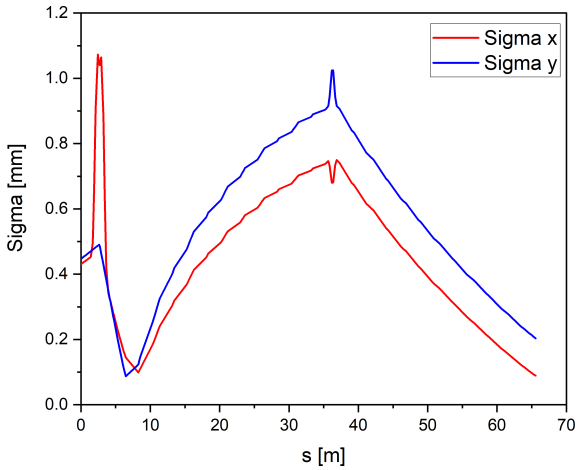


Figure 2: Evolution of the rms beam sizes (horizontal x and vertical y) along the LINAC.

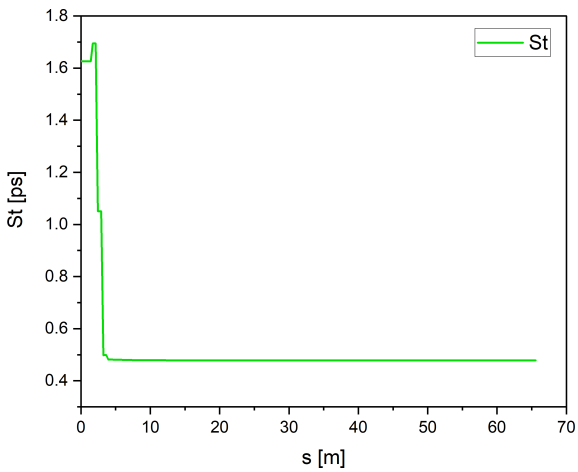


Figure 3: Evolution of the bunch length along the LINAC.

as well to study the beam orbit and how (and where) to correct it in case of spurious offsets along the lattice. The number of correctors has been set to 5 pairs: the first before the magnetic chicane, the second after, two pairs along the C-band LINAC between sections, and finally a pair before the transfer line. Concerning this latter, it includes an extra horizontal corrector for the definition of the horizontal angle of injection, as in the present layout of the SOLARIS injector LINAC. The "global" correction model for elements' alignment has been assumed, in order to minimize the average of error all along the machine, in both planes. For all the selected errors normal distributions have been considered, where the rms error seeds are listed in Table 1. Errors have been considered both for magnetic and RF elements.

Table 1: Rms value for the error distributions (all normal) considered on different elements along the lattice.

Errors and units		Rms error value
Field Amplitude Error	[MV/m]	0.1
Field Phase Error	[deg]	0.1
Cavity/Quad/Solenoid Offset	[mm]	0.1
Cavity/Quad/Solenoid Rotation	[mrad]	0.01
Solenoid Field Error	[mT]	1
Quad Strength Error	[1/m^2]	0.01
Bending Radius Error	[m]	0.001

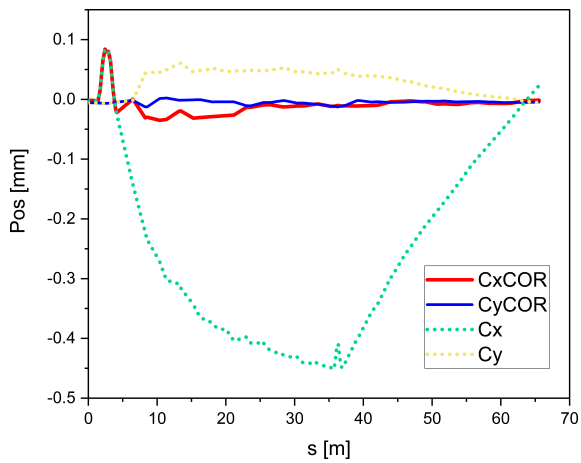


Figure 4: Error studies along linac.

In Fig. 4 the beam centroids are shown with (solid lines) and without (dashed lines) correction, when the errors presented in Table 1 are applied to the lattice configuration. A global correction better than a few tens of microns is reached in the x-plane and a correction on the level of a few microns is reached for the vertical plane y. The difference is due to the fact that the magnetic chicane disperse the beam in the horizontal plane giving an extra kick to the beam to be compensated.

BEAM INSTRUMENTATION

The electron beam diagnostics system should provide information required for the proper accelerator operation, as well as ensure a safe operation. Several types of diagnostic tools to be used to measure the relevant quantities with sufficient precision.

The beam properties are planned to be measured at various places along the SOLARIS LINAC. The diagnostic instruments that are foreseen for this purpose partially will be reused from the existing machine. Currently, for beam

ISBN: 978-3-95450-236-3 ISSN: 2673-5350 doi:10.18429/JACoW-IBIC2023-MOP008



Figure 5: New Elegant lattice including BPMs, correctors and screens.

position and feedback system the stripline BPMs with Libera single pass electronics and correction system is used. For the linac upgarde the additional BPMs and correctors need to be added. The transverse beam size and the beam emittance are within the set of most important parameters for the beam characterisation. Therefore, emittance measurement stations will be available at several positions along the linac. The stations will be equipped with transverse beam size monitors as YAG screens in the distance from the quadrupole magnets. The emittance will be measure with the quadrupole scan. Moreover the YAG screens installed in the disperssive section of bunch compressor and transfer line will allow to determine the energy spread of the bunch. In Fig. 5 we show the latest version of the machine lattice, which includes BPMs, correctors and screens.

Table 2: Description table for the diagnostic flags depicted in Fig. 5.

Flag	Diagnostics
1	BPM 1
2	Screen 1
3	Screen 2
4	BPM 2
5	Screen 3
6	BPM 3
7	BPM 4
8	BPM 5
9	Screen 4
10	BPM 6
11	Screen 5
12	Screen 6
13	BPM 7
14	BPM 8
15	BPM 9
16	Screen 7

In Table 2 we have listed the meaning of the 16 flags found in the Elegant lattice at Fig. 5. The first two BPMs are useful for the knowledge of the beam position at the entrance and exit of the magnetic compressor. The two screens in the compressor are used to measure the beam energy spectrum, to check the alignment and the optics in the magnetic chicane. The third screen is used for quad scan purposes, to measure the beam emittance. The BPMs and screens along the C-band LINAC are used to check and control the beam optics and orbit along the machine. The fifth screen may be also used for quad scan purposes, with the caveat of well-aligning the beam in the C-band that is placed just before it (or switching it off during the measurement). The last two BPMs can give information on the beam angle at the injection.

The last screen yields the final beam profile, matched to enter transfer line. For the bunch length diagnostics some tests are undergoing based on the measurement of Coherent Diffraction Radiation (CDR). Such a method provides information on a limited amount of spectral bands composing the beam spectrum. Therefore, it strictly relies on a model or a direct measurement of the beam spectrum (bunch profile), in order to minimize the error of the measurement. Despite several CDR diagnostic stations may be placed all along the new machine to locally control the bunch length, a direct diagnostic station for the bunch profile (and then spectrum after Fourier transform) may be needed. The current idea is to introduce a S-band RF cavity at the end of the machine, on the straight line after the septum magnet which sends the beam into the transfer line to the ring.

For the current measurement, current transformers will be used distributed all along the machine. One of them may be placed before the magnetic chicane, one after (to measure the possible losses), then one in the middle of the lattice and one at the end after the last focusing doublet.

CONCLUSIONS

We have presented the most updated results for the beam dynamics and the error studies on the newly designed SOLARIS injector LINAC. The Hybrid S-band/C-band technology presented allow for the 1.5 GeV energy LINAC design within SOLARIS tunnel space constrains. This machine will be necessary to implement the top-up injection at the synchrotron facility. Specifically, we have presented the distribution of different beam instrumentation and diagnostics all along the lattice configuration allowing for correction of the beam trajectory with sub-micormeter level and for transversal and longitudinal beam parameters measurements.

ACKNOWLEDGEMENTS

This project is executed under the provision of the Polish Ministry and Higher Education project “Support for research and development with the use of research infrastructure of the National Synchrotron Radiation Centre SOLARIS” under contract nr 1/SOL/2021/2.

REFERENCES

[1] A.I. Wawrzyniak, R. Panaś, A. Curcio, M. Knafel, G. Kowalski, and A. Marendziak, “Solaris synchrotron performance and operational status”, *Nucl. Instrum. Methods Phys., Res. Sect. B*, vol. 493, pp. 19-27, 2021. doi:10.1016/j.nimb.2021.01.020

Content from this work may be used under the terms of the CC-BY-4.0 licence (© 2023). Any distribution of this work must maintain attribution to the author(s), title of the work, publisher, and DOI

ISBN: 978-3-95450-236-3 ISSN: 2673-5350 doi:10.18429/JACoW-IBIC2023-MOP008

[2] A. Curcio, R. Panaś, M. Knafel, and A.I. Wawrzyniak, "Liouville theory for fully analytic studies of longitudinal beam dynamics and bunch profile reconstruction in dispersive lines", *Nucl. Instrum. Methods Phys., Res. Sect. A*, vol. 986, p. 164755, 2021. doi:10.1016/j.nima.2020.164755

[3] A.A. Ahmed, A. Wrońska, A. Magiera, A. Curcio, M. Jaglarz, and A.I. Wawrzyniak, "Study of M99o and long-lived impurities produced in the Mnato (γ, x) reactions using an electron beam", *Radiat. Phys. Chem.*, vol. 177, p. 109095, 2020. doi:0.1016/j.radphyschem.2020.109095

[4] A. Curcio, R. Panaś, M. Knafel, G. Kowalski, M. Waniczek, and A.I. Wawrzyniak, "Bunch Length Characterizations for the Solaris Injector LINAC" in *Proc. IPAC'21*, Campinas, Brazil, May 2021, pp. 2117–2119. doi:10.18429/JACoW-IPAC2021-TUPAB277

[5] M. Borland, "Elegant: A flexible SDDS-compliant code for accelerator simulation", No. LS-287, Argonne National Lab., IL, US, 2000. doi:10.2172/761286

[6] A. Curcio, R. Panaś, A.I. Wawrzyniak, and J. Wiechecki, "Simulation study towards a new injector linac for the SOLARIS synchrotron facility", in *Proc. IPAC'23*, Venice, Italy, May 2023, pp. 1967-1969. doi:10.18429/JACoW-IPAC2023-TUPL109

Content from this work may be used under the terms of the CC-BY-4.0 licence (© 2023). Any distribution of this work must maintain attribution to the author(s), title of the work, publisher, and DOI

ISBN: 978-3-95450-236-3 ISSN: 2673-5350 doi:10.18429/JACoW-IBIC2023-MOP009

A SNAPSHOT OF CERN BEAM INSTRUMENTATION R&D ACTIVITIES

T. Lefevre*, A. Boccardi, S. Jackson, D. Louro Alves, F. Roncarolo,
J. Storey, R. Veness, C. Zamantzas
CERN, Geneva, Switzerland

Abstract

The CERN accelerator complex stands out as unique scientific tool, distinguished by its scale and remarkable diversity. Its capacity to explore a vast range of beam parameters is truly unparalleled, spanning from the minute energies of around a few keV and microampere antiproton beams, decelerated within the CERN antimatter factory, to the 6.8 TeV high-intensity proton beams that race through the Large Hadron Collider (LHC). The Super Proton Synchrotron (SPS) ring plays also a crucial role by slowly extracting protons at 400 GeV. These proton currents are then directed toward various targets, generating all sorts of secondary particle beams. These beams, in turn, become the foundation of a diverse fixed-target research program, enabling scientific exploration across a wide spectrum. Moreover, as CERN looks ahead to future studies involving electron-positron colliders, the development of cutting-edge diagnostics for low emittance and short electron pulses is also underway. This contribution serves as a snapshot, shedding light on the main R&D initiatives currently underway at CERN in the field of beam instrumentation.

INTRODUCTION

The CERN accelerator complex is a dynamic and continually evolving system. Over a decade ago, an ambitious global initiative was launched to enhance the collision capabilities of the Large Hadron Collider (LHC). This initiative aims to achieve higher collision rates and is executed in phases. The initial phase focused on the LHC Injector Upgrade program [1], which successfully generated higher brightness beams within the CERN injector complex. Building on this achievement, the subsequent stage of the high Luminosity LHC upgrade (HL-LHC) [2] is scheduled for implementation from 2026 to 2028. This phase aims to further elevate beam intensities and reduce emittance, introducing novel challenges to beam instrumentation. These instruments must adapt to unprecedented beam densities while maintaining the highest reliability and precision.

Beyond its contributions to the LHC and its physics endeavors, CERN has embarked on a comprehensive consolidation of the fixed target physics program in the 'North Area' of the Super Proton Synchrotron (SPS). This undertaking necessitates a complete overhaul of the instrumentation employed for extracting continuous beams from the SPS. These beams are subsequently directed towards various targets and experimental zones.

Anticipating the completion of the LHC's scientific program, the scientific community's aspirations encompass the exploration of $e^- - e^+$ collisions at up to 380 GeV center of mass energies. While the Compact Linear Collider (CLIC) [3] has been under scrutiny for decades, CERN is currently engaged in assessing the feasibility of the 91-kilometer-long Future Circular Collider (FCC). The FCC would initially focus on lepton collisions [4] and potentially accommodate 100 TeV proton collisions in subsequent phases, using the same infrastructure. Although linear and circular colliders differ in their design and implementation, there are notable similarities in terms of beam properties, beam energy, intensity, transverse and longitudinal sizes, as well as the demand for a high level of radiation tolerance within the tunnel. This suggests the prospect of adapting technologies initially developed for CLIC for use in the FCC-ee.

In this paper, we provide a comprehensive overview of the ongoing R&D endeavors at CERN in the realm of beam instrumentation. This encompasses a spectrum of activities, including the design of innovative electromagnetic pick-ups, the refinement of techniques for measuring transverse profiles of high power density beams, advancements in short longitudinal beam profiling, the optimisation of high dynamic range particle detectors and the latest strides in read-out electronics and digital acquisition systems. By shedding light on these R&D activities, we aim to present the essence of CERN's pursuit of cutting-edge instrumentation techniques.

COMPLEX DESIGN OF ELECTROMAGNETIC PICK-UPS

Within the scope of the HL-LHC program, the demand for large-aperture, high-field quadrupole magnets has surged to compress proton beam sizes during collisions to unprecedentedly minuscule dimensions. This new configuration requires novel cryogenic directional stripline beam position monitors [5], enabling the measurement of counter-propagating beams with a precision surpassing a mere micron. This intricate design encompasses Tungsten alloy inserts, strategically positioned to absorb collision debris and curtail radiation doses to neighboring magnets. Furthermore, these monitors are coated with copper and NEG (Non-Evaporable Getter) coatings, a dual-layer approach that minimizes beam impedance and paves the way for attaining ultra-high vacuum conditions.

Amid recent advancements, beam position monitors (BPMs) with heightened frequency bandwidth have garnered substantial interest. This is not only pertinent to short electron bunches but also to furnish intrabunch monitoring with fast time response for high-intensity proton beams. A range of technologies is presently under exploration, featuring electro-optical (EO) crystals [6] and dielectric pick-ups [7,8].

* thibaut.lefevre@cern.ch

Content from this work may be used under the terms of the CC-BY-4.0 licence (© 2023). Any distribution of this work must maintain attribution to the author(s), title of the work, publisher, and DOI

ISBN: 978-3-95450-236-3 ISSN: 2673-5350 doi:10.18429/JACoW-IBIC2023-MOP009

Content from this work may be used under the terms of the CC-BY-4.0 licence (© 2023). Any distribution of this work must maintain attribution to the author(s), title of the work, publisher, and DOI

EO BPMs promise to replicate the beam's electrical field optically, encompassing a bandwidth spanning from direct current to multi-tens of gigahertz. On the other hand, dielectric pick-ups leverage the phenomenon of charged particles generating coherent Cherenkov diffraction radiation, achieving even greater bandwidth capabilities—on the order of several hundreds of gigahertz in our case. Notably, this technology exhibits potential for extension into the visible wavelength range, offering a well-suited solution for femtosecond-long bunches. The deployment of these innovative technologies is currently under rigorous scrutiny for potential integration into LHC and their performance will be compared to the ones of more traditional high-frequency RF button pick-ups.

MEASURING THE TRANSVERSE PROFILE OF HIGH POWER DENSITY BEAMS

State-of-the-art Interceptive Diagnostics

Optical Transition Radiation (OTR) imaging system a widely adopted tool in linacs and transfer lines, has exhibited great achievement in measuring remarkably small beams, surpassing the realm of a mere micron in spot size [9, 10]. Even if these systems have withstood high charge densities while employing thermally robust material like glassy carbon, OTR imaging systems would get inevitably damaged when encountering beam densities above a certain threshold. In the domain of hadron synchrotron rings, Wire scanners (WS) offer an avenue for swift movement, reaching speeds of up to 20 meters per second [11]. However, they encounter analogous challenges and limitations as carbon wires cannot endure the full beam intensity in numerous machines, such as the SPS and LHC.

In a bid to overcome these hurdles, a pioneering research and development initiative has recently been launched, focusing on low-density materials. Preliminary trials at CERN involved Carbon nanotube wires and screens, although the outcomes have not yet unearthed superior alternatives, the potential they hold is monumental [12]. The existing limitations observed in these tests can be attributed to the material's purity, intertwined with the intricacies of the production process, leaving room for improvement in this aspect. As research continues to unfold, the pursuit of optimal low-density materials for advanced beam instrumentation remains an essential endeavor. By refining these materials and production methods, CERN seeks to break new ground, ushering in a new era of instrumentation capable of withstanding and accurately measuring high-intensity beams in diverse particle physics contexts.

Non-invasive Beam Size Monitoring

Non-invasive instruments hold the potential to address all of these limitations, making them the ultimate solution to the persistent challenges associated with measuring increasingly higher beam intensities.

Monitors utilizing gas ionization or gas fluorescence principles exhibit versatility by operating effectively at low gas pressures. These approaches present an attractive non-invasive solution suitable for high-intensity and relatively low-energy beams. Gas ionization monitors equipped with advanced hybrid pixel detectors equipped have enabled bunch-by-bunch transverse profile measurements with rapid read-out speeds on the order of a few nanoseconds, employing gas pressures ranging from 10^{-7} to 10^{-8} Torr [13]. Gas fluorescence, despite its smaller cross-section compared to ionization, has shown promise by utilizing supersonic gas jets and potentially extended integration times to provide non-intrusive beam imaging capabilities [14]. Ongoing systematic investigations at the CERN accelerator complex are dedicated to comprehensively exploring the performance of both gas ionization and gas-jet fluorescence monitors.

An alternative avenue entails utilizing Optical Diffraction Radiation (ODR) emanating from slits, or Optical Cherenkov Diffraction Radiation (OChDR) emitted within dielectric materials [15]. Methodical studies involving ODR [16] have successfully demonstrated the ability to measure beam sizes as minute as 5 microns in the VUV range. Furthermore, an imaging system employing OChDR, offering enhanced photon yield and simplified detector configuration, exhibited success in previous tests [17]. However, the measured beam sizes were relatively large and prevented a comprehensive assessment of detector resolution and limitations. Both techniques rely on incoherent radiation and are best suited for ultra-relativistic beams with γ values surpassing 10^3 that would be available in future $e^- - e^+$ collider.

For ultra-high energy synchrotrons like the SPS, LHC, 3rd Generation light sources, FCC-ee, and FCC-hh, the emission of synchrotron radiation from bending magnets or undulators emerges as a natural source for beam diagnostics. However, the diffraction limit of the radiation source poses a primary challenge for synchrotron radiation (SR) based transverse beam profile imaging systems, often necessitating operation in the X-ray domain to achieve beam size accuracy at the micron level. To overcome this limitation, alternative methods such as interferometry in the optical [18] and subsequently X-ray range [19] are under investigation.

MEASURING THE LONGITUDINAL PROFILE OF SHORT BUNCHES

Proton bunches coursing through the CERN accelerator complex often span relatively extended durations, typically 1 to 2 nanoseconds (FWHM). However, as bunch charges escalate, the likelihood of encountering instabilities amplifies, intensifying the imperative to meticulously characterize the longitudinal bunch profile with heightened time resolution—on the order of tens of picoseconds. This requirement parallels the upcoming FCC-ee project, where electron and positron bunches of 5 to 30 picoseconds in length are expected to collide.

To tackle this challenge, techniques originally developed for the characterization of short electron bunches in contexts like Free-Electron Lasers or linac colliders have emerged as relevant solutions. Optical monitors employing Streak

ISBN: 978-3-95450-236-3 ISSN: 2673-5350 doi:10.18429/JACoW-IBIC2023-MOP009

cameras were already in use as early as the 1990s. Even today, they remain indispensable tools, offering straightforward operation and furnishing time resolutions within the picosecond realm [20, 21].

Recently, remarkable strides have been achieved through the integration of electro-optical methods. This synergy has enabled the measurement of turn-by-turn (at a few MHz) picosecond-long bunch profiles [22]. These techniques have evolved in a benchmark tool for longitudinal bunch profile monitoring [23], and are considered as good candidate for bunch-by-bunch (66 MHz) longitudinal profile monitors in the context of the FCC-ee project [24].

Meanwhile, instruments focused on capturing the bunch spectrum at elevated frequencies through the emission of coherent radiation [25, 26] present a simpler and cost-effective alternative to optical or electro-optical methodologies. Advanced non-invasive monitors founded on coherent Cherenkov diffraction radiation [27] are presently undergoing design and development, with applications spanning both hadron and lepton accelerators.

DEVELOPING PARTICLE DETECTOR FOR BEAM LOSS MONITORING

Beam loss monitoring (BLM) in the LHC demands measurements with an extraordinarily high dynamic range, spanning approximately 9 orders of magnitude. This is facilitated by ionization chambers [28], working in conjunction with precision electronic systems. Together, they enable measurements reaching down to the picoampere range within integration times of few seconds.

For the observation of rapid beam losses on the nanosecond timescale, Diamond detectors [29] have been strategically positioned at critical locations throughout the accelerator complex, including injection and extraction regions, as well as collimation region. In a continuing evolution, BLMs built on the foundation of Hybrid pixel detector technology developed at CERN are now under development. These novel detectors promise elevated sensitivity, radiation tolerance, and an impressive temporal resolution of 1.2 nanoseconds.

In scenarios demanding extended coverage across substantial distances, such as the FCC-ee or SPS slow-extraction contexts, BLMs that remain insensitive to X-rays while capitalizing on Cherenkov emission are currently under development. These optical monitors leverage radiation-hard optical fibers [30] to fulfill their monitoring roles effectively, showcasing the continuous innovation and adaptation occurring within the field of beam loss monitoring technology.

STATE-OF-THE-ART ELECTRONIC DEVELOPMENT

The CERN Beam Instrumentation group manages an impressive network of approximately 10,000 monitors dispersed throughout the entire accelerator complex. This extensive infrastructure may even expand further (more than double) in the future, especially considering the potential operations of FCC-ee. Managing such extensive systems efficiently has led to a focus on standardization, enabling cost-effective development and streamlined maintenance. Over recent years, the group has developed custom VME-based digital acquisition boards with FMC (FPGA Mezzanine Card) carriers [31]. These boards have played a pivotal role in the upgrades of numerous systems, including SPS BPMs [32], LHC BLMs, luminosity monitors, Wirescanners, and beam current transformers. Impressively, a total of 1,200 of these boards have been produced. The group is currently exploring the optimal form factor for a new DAQ (Data Acquisition) platform.

In the case of large distributed systems like BPMs and BLMs, the electronic acquisition chain typically consists of two parts. The front-end, situated close to the beam line instruments within the machine, acquires data locally and then transmits this information via optical fiber to a back-end system located several kilometers away in non-radioactive galleries or surface buildings. Given the challenging radiation environments within the LHC and SPS, where the electronics must withstand integrated radiation doses of 1 kGy and 10 kGy, respectively, radiation-tolerant to radiation-hard components are crucial. The BI group often employs ASICs and optical transceivers developed by the CERN micro-electronic group for these applications. The FCC-ee tunnel, with its even higher expected radiation levels due to strong synchrotron radiation, necessitates a similar approach for the design of the read-out electronic chain.

With increased beam intensities and a higher number of bunches, the demand for bunch-by-bunch measurements has become pervasive. The group's most recent developments explore the capabilities of RF System-on-Chip (RFSoC) technology, which allows for rapid digitization at multi-gigasamples per second (GSa/s) rates, along with substantial computing performance. Additionally, R&D efforts are underway to investigate ultrafast sampling techniques using electro-optical modulators and time-stretch techniques. These endeavors aim to enable measurements of shorter bunches and shorter bunch spacing.

CONCLUSION

The Beam Instrumentation group at CERN is engaged in an ambitious R&D program. Our goal is to measure lower emittance, higher intensity beams while continually advancing instruments to achieve the highest levels of accuracy and resolution, both in terms of spatial and temporal dimensions. A significant emphasis is placed on the development of non-invasive diagnostic techniques, representing the technology of the future. CERN's forward-looking perspective extends to its long-term future, with a particular focus on high-energy, short electron bunches in the context of $e^- - e^+$ colliders. It's important to note that this contribution does not encompass all of our activities. Our teams are also actively involved in the measurement of very low-intensity beams, which will be covered in a future presentation.

Content from this work may be used under the terms of the CC-BY-4.0 licence (© 2023). Any distribution of this work must maintain attribution to the author(s), title of the work, publisher, and DOI

ISBN: 978-3-95450-236-3 ISSN: 2673-5350 doi:10.18429/JACoW-IBIC2023-MOP009

REFERENCES

[1] J. Abelleira *et al.*, "LHC injector upgrade: Technical design report", Tech. Rep. CERN-ACC-2014-0337, 2014.

[2] M. Zerlauth *et al.*, "The HL-LHC Project Gets Ready for Its Deployment", in *Proc. IPAC'22*, Bangkok, Thailand, Jun. 2022, pp. 50–53. doi:10.18429/JACoW-IPAC2022-MOPOST005

[3] M. Aicheler *et al.*, "A multi-TeV linear collider based on CLIC technology", *CERN Yellow Reports*, CERN-2012-007. doi:10.5170/CERN-2012-007

[4] A. Abada, *et al.*, "FCC-ee: The Lepton Collider, Future Circular Collider Conceptual Design Report Volume 2", *Eur. Phys. J. Special Topics*, vol. 228, no. 2, pp. 261-623, 2019. doi:10.1140/epjst/e2019-900045-4

[5] M. Krupa, D.R. Bett, I. Degl, D. Gudkov, and G. Schneider, "HL-LHC BPM System Development Status", in *Proc. IBIC'22*, Kraków, Poland, Sep. 2022, pp. 408–412. doi:10.18429/JACoW-IBIC2022-WEP12

[6] S.M. Gibson, A. Arteche, T. Lefèvre, and T.E. Levens, "Electro-Optical BPM Development for High Luminosity LHC", in *Proc. IBIC'22*, Kraków, Poland, Sep. 2022, pp. 181–185. doi:10.18429/JACoW-IBIC2022-TU1I1

[7] E. Senes *et al.*, "Dielectric Pick-ups for short bunches", in *Proc. IBIC'23*, Saskatoon, Canada, Sep. 2023, this conference.

[8] C. Pakuza *et al.*, "Electron beam studies on a beam position monitor based on Cherenkov diffraction radiation", presented at the IPAC'23, Venice, Italy, May 2023, paper THPL146, to be published.

[9] B. Bolzon *et al.*, "Very high resolution optical transition radiation imaging system: Comparison between simulation and experiment", *Phys. Rev. ST Accel. Beams*, vol. 18, p. 082803, 2015. doi:10.1103/PhysRevSTAB.18.082803

[10] A. Aryshev *et al.*, "Sub-micron scale transverse electron beam size diagnostics methodology based on the analysis of optical transition radiation source distribution", *J. Instrum.*, vol. 15, p. P01020, 2020. doi:10.1088/1748-0221/15/01/P01020

[11] S. Di Carlo *et al.*, "Assessing the Performance of the New Beam Wire Scanners for the CERN LHC Injectors", in *Proc. IBIC'22*, Kraków, Poland, Sep. 2022, pp. 443–446. doi:10.18429/JACoW-IBIC2022-WEP23

[12] A. Mariet *et al.*, "Simulated Behavior of CNT Wires Irradiated in the HiRadMat Experimental Line at CERN", in *Proc. IBIC'22*, Kraków, Poland, Sep. 2022, pp. 527–531. doi:10.18429/JACoW-IBIC2022-WE3C4

[13] S. Levasseur *et al.*, "Development of a rest gas ionisation profile monitor for the CERN Proton Synchrotron based on a Timepix3 pixel detector", *J. Instrum.*, vol. 12, p. C02050, 2017. doi:10.1088/1748-0221/12/02/C02050

[14] A. Salehilashkajani *et al.*, "A gas curtain beam profile monitor using beam induced fluorescence for high intensity charged particle beams", *Appl. Phys. Lett.*, vol. 120, p. 174101, 2022. doi:10.1063/5.0085491

[15] D.V. Karlovets and A. Potylitsyn, "Universal description for different types of polarization radiation", 2010. doi:10.48550/arXiv.0908.2336

[16] M. Bergamaschi *et al.*, "Noninvasive Micrometer-Scale Particle-Beam Size Measurement Using Optical Diffraction Radiation in the Ultraviolet Wavelength Range", *Phys. Rev. Appl.*, vol.13, p. 014041, 2020. doi:10.1103/PhysRevApplied.13.014041

[17] R. Kieffer *et al.*, "Direct observation of incoherent Cherenkov diffraction radiation in the visible range", *Phys. Rev. Lett.*, vol. 121, p. 054802, 2018. doi:10.1103/PhysRevLett.121.054802

[18] D. Butti, E. Bravin, S.M. Gibson, and G. Trad, "Recent LHC SR Interferometer Simulations and Experimental Results", in *Proc. IBIC'22*, Kraków, Poland, Sep. 2022, pp. 88–91. doi:10.18429/JACoW-IBIC2022-MOP23

[19] M. Siano *et al.*, "Two-dimensional electron beam size measurements with X-ray heterodyne near field speckles", *Phys. Rev. Accel. Beams*, vol. 25, p. 052801, 2022. doi:10.1103/PhysRevAccelBeams.25.05280

[20] C.P. Welsch *et al.*, "Longitudinal beam profile measurements at CTF3 using a streak camera", *J. Instrum.*, vol. 1, p. P09002, 2006. doi:10.1088/1748-0221/1/09/P09002

[21] A.E. Dabrowski *et al.*, "Measuring the bunch frequency multiplication at the 3rd CLIC Test Facility", *J. Instrum.*, vol. 7, p. P01005, 2012. doi:10.1088/1748-0221/7/01/P01005

[22] E. Roussel *et al.*, "Phase Diversity Electro-optic Sampling: A new approach to single-shot terahertz waveform recording", *Light Sci. Appl.*, vol. 11, p. 14, 2022. doi:10.1038/s41377-021-00696-2

[23] R. Pan *et al.*, "Coulomb field strength measurement by electro-optic spectral decoding system at the CALIFES beam line", *Nucl. Instrum. Methods Phys. Res., Sect. A*, vol. 821, pp. 8–12, 2016. doi:10.1016/j.nima.2016.03.043

[24] M. Reissig *et al.*, "Status of a Monitor Design for Single-Shot Electro-Optical Bunch Profile Measurements at FCC-ee", in *Proc. IBIC'22*, Kraków, Poland, Sep. 2022, pp. 455–459. doi:10.18429/JACoW-IBIC2022-WEP26

[25] M. Micheler *et al.*, "Longitudinal beam profile monitor at CTF3 based on Coherent Diffraction Radiation", *J. Phys. Conf. Ser.*, vol. 236, p. 012021, 2010. doi:10.1088/1742-6596/236/1/012021

[26] K. Lekomtsev *et al.*, "Investigation of Coherent Diffraction Radiation from a Dual Target system at CTF3", *J. Phys. Conf. Ser.*, vol. 357, p. 012021, 2012. doi:10.1088/1742-6596/357/1/012021

[27] A. Curcio *et al.*, "Non-invasive beam instrumentation exploiting Coherent Cherenkov Diffraction Radiation", *Phys. Rev. Accel. Beams*, vol. 23, p. 022802, 2020. doi:10.1103/PhysRevAccelBeams.23.022802

[28] M. Saccani, E. Effinger, W. Vigano, and C. Zamantzas, "The Beam Loss Monitoring System after the LHC Long Shutdown 2 at CERN", in *Proc. IBIC'22*, Kraków, Poland, Sep. 2022, pp. 220–224. doi:10.18429/JACoW-IBIC2022-TUP03

[29] E. Calvo Giraldo *et al.*, "The Diamond Beam Loss Monitoring System at CERN LHC and SPS", in *Proc. IBIC'22*, Kraków, Poland, Sep. 2022, pp. 202–206. doi:10.18429/JACoW-IBIC2022-TU2C2

Content from this work may be used under the terms of the CC-BY-4.0 licence (© 2023). Any distribution of this work must maintain attribution to the author(s), title of the work, publisher, and DOI

ISBN: 978-3-95450-236-3 ISSN: 2673-5350 doi:10.18429/JACoW-IBIC2023-MOP009

[30] S. Benítez Berrocal *et al.*, "Beam Loss Localisation with an Optical Beam Loss Monitor in the CLEAR Facility at CERN", in *Proc. IPAC'22*, Bangkok, Thailand, Jun. 2022, pp. 351–354. doi:10.18429/JACoW-IPAC2022-MOPOPT045

[31] A. Boccardi *et al.*, "Ongoing electronic development in the CERN Beam Instrumentation Group: challenges and solutions for the measurement of particle accelerator beam parameters", *J. Instrum.*, vol. 8, p. C03006, 2013. doi:10.1088/1748-0221/8/03/C03006

[32] M. Barros Marin *et al.*, "The Giga Bit Transceiver based Expandable Front-End (GEFE), a new radiation tolerant acquisition system for beam instrumentation", *J. Instrum.*, vol. 11, p. C02062, 2016. doi:10.1088/1748-0221

Content from this work may be used under the terms of the CC-BY-4.0 licence (© 2023). Any distribution of this work must maintain attribution to the author(s), title of the work, publisher, and DOI

ISBN: 978-3-95450-236-3 ISSN: 2673-5350 doi:10.18429/JACoW-IBIC2023-MOP010

DIAGNOSTICS FOR A HIGH EMITTANCE AND HIGH ENERGY SPREAD POSITRON SOURCE

N. Vallis[1]*, F. Marcellini, R. Zennaro, M. Zykova,
P. Craievich, R. Fortunati, R. Ischebeck, E. Ismaili, P. Juranic, G.L. Orlandi, M. Schaer
Paul Scherrer Institute, Villigen, Switzerland
[1]also at EPFL, Lausanne, Switzerland

Abstract

This paper is an overview of a diagnostics setup for highly spread e+e- beams, to be installed at the PSI Positron Production (P^3 or P-cubed) experiment. To be hosted at the SwissFEL facility (PSI, Switzerland) in 2026, P^3 is e+ source demonstrator designed to generate, capture, separate and detect nano-Coulombs of secondary e+ and e- bunches, in spite of their extreme tranverse emittance and energy spread. The experiment will employ an arrangement of broadband pick-ups (BBPs) to detect simultaneously the time structure of secondary e+e- bunches. A spectrometer will follow the BBPs and deflect the e+ and e- onto two unconventional faraday cups that will measure their charge. In addition, the energy spectrum of e+ and e- distribution will be reconstructed through scintillating fibers.

INTRODUCTION

The SwissFEL facility [1] (PSI, Switzerland) will host the PSI Positron Production (P^3 or P-cubed) experiment [2] in 2026, a e+ source demonstrator with potential to improve by an order of magnitude the present state-of-the-art e+ yield. The experiment layout is shown in Fig. 1, featuring a e+ source based on a 6 GeV electron (e-) beam and 17.5 mm-thick (or 5 times the radiation length) amorphous Tungsten target. A capture system will follow the target, consisting of a solenoid system and 2 RF accelerating cavities. The remarkable e+ capture capabilities of P^3 are enabled to great extent by the usage of high temperature superconducting (HTS) solenoid around the target region, as well as a novel standing wave solution for the RF cavities that provides a large iris aperture to maximize e+ capture.

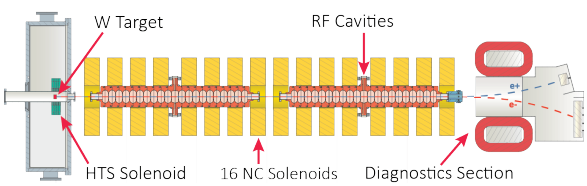


Figure 1: Simplified layout of the P^3 [2].

The experiment diagnostics, whose layout is shown in Fig. 2, will be located directly downstream from the 2^{nd} RF cavity, as illustrated in Fig. 1. This setup will measure the e+e- bunches before and after species separation, equipped with an arrangement of broadband pick-ups (BBPs), 2 Faraday Cups (FCs) and a variety of scintillating detectors. The

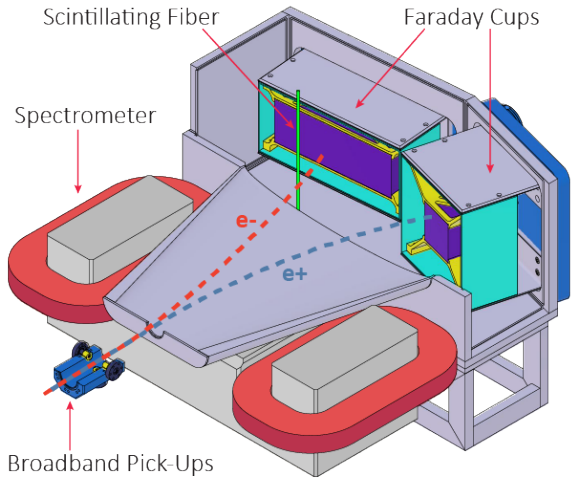


Figure 2: Concept design of the P^3 diagnostics.

BBPs will detect, simultaneously for both particle species, the time structure of the captured e+e- bunches. The FCs and scintillators will be installed in the same vacuum chamber, and will measure the charge and energy spectrum of separate e+ and e- streams. Separation will be provided by a spectrometer, a dipole magnet based on four copper coils and an iron yoke, which will be fed at a maximum current of 340 A in order to reach magnetic fields up to 0.25 T. Additional diagnostics such as the arrangement of screens and cameras are still under discussion.

e+e- Dynamics in P^3

200 pC e- at 6 GeV will impinge upon the 17 mm-thick Tungsten target, yielding a e+e- beam in the multi-MeV and nano-Coulomb range. Table 1 shows the evolution of the e+ bunches along the P^3 capture line. These values clearly indicate that e+ dynamics are are heavily dominated by an extremely high transverse emittance. In the transverse plane, e+ collection relies on the so-called Adiabatic Matching [3,4], a well-known e+ capture technique based on transforming the transverse phase space of newly generated e+ (moderate σ_x and large σ_{px}) into the acceptance of the capture line (large σ_x and moderate σ_{px}). Thus, emittance is not damped but matched and transported up to the diagnostics section. As for the longitudinal beam dynamics, RF fields will generate time structures of many consecutive e+ and e- bunches separated by the S-band $\lambda/2$ (167 ps or 50 mm in the ultrarelativistic regime), with the most particle population concentrated over the first two RF buckets. Two RF working points of interest

* nicolas.vallis@psi.ch

Content from this work may be used under the terms of the CC-BY-4.0 licence (© 2023). Any distribution of this work must maintain attribution to the author(s), title of the work, publisher, and DOI

ISBN: 978-3-95450-236-3 ISSN: 2673-5350 doi:10.18429/JACoW-IBIC2023-MOP010

Table 1: Main parameters of the e+ bunches for RF working points of interest. Simulated with ASTRA [5].

	Φ = (120,-70)	**Φ = (70,-110)**
Q_{e+} [pC]	1246	1155
σ_x, σ_y [mm]	7	
σ_{px}, σ_{py} [MeV/c]	0.5	
ϵ_{norm} [π mm mrad]	≈4000	
σ_t [ps]	≈33	
ΔE_{RMS} [MeV]	100	95

(see Fig. 3) were found in previous optimization studies: Φ = (120,-70), which provides maximum e+ capture and Φ = (70,-110), which will provide maximum energy compression [2]. The quality of measurements must therefore be particularly high for these RF phase configurations.

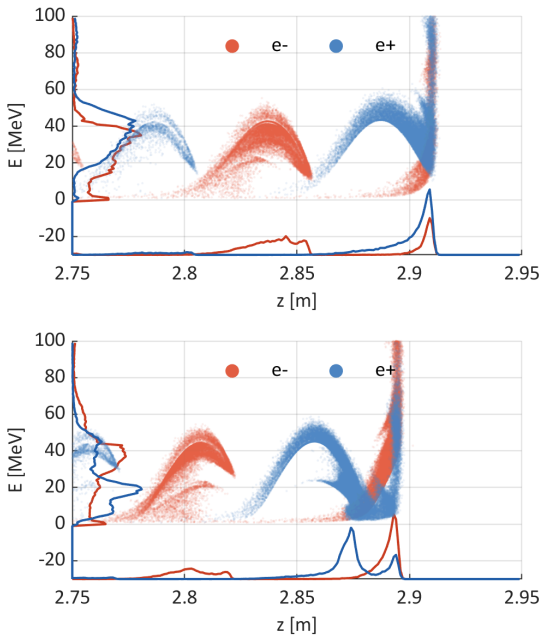


Figure 3: Simulated e+e- distributions near the exit of the 2^{nd} RF cavity (z ≈ 2.8 m) for RF working points of interest: Φ = (120,-70) (top) and Φ = (70,-110) (bottom).

SIMULTANEOUS e+e- DIAGNOSTICS: BROADBAND PICK-UPS

An arrangement of 4 broadband pick-ups (BBPs), shown in Fig. 4, will follow the second RF cavity and detect the wake voltage generated by the captured e+ and e- bunches. This will allow to reconstruct the e+ and e- time structure simultaneously, including measurements of charge, length and separation bunch by bunch. The e+e- time structure will heavily depend on the RF phase, yet the typical distribution will consist of alternating e+ and e- bunches of 33 ps length, and separated by 167 ps, namely half S-band period (see Fig. 3 and Table 1). Therefore, the geometry of the pick-ups was optimized to avoid intrinsic resonances up to frequencies in the range of a few tens of GHz, while providing a relatively high peak voltage. According to a preliminary simulation based on a gaussian approximation of the P^3 bunches (see Fig. 5), the BBPs would detect a ±4.5 V peak voltage signal with very small distortion. Notice that this simulation does not take into account wakefield effects, cable distortion or environment noise.

Two BBP assemblies shown in Fig. 6 have been developed and fabricated, based on broadband feedthroughs of 27 GHz [6] and 65 GHz [7]. The hardware acquisition setup will consist of low attenuation, broad band cables [8] and a high-end oscilloscope of at least 40 GHz pass band and 10 GS/s sampling. Similar solutions based on ultra fast pick-ups are currently used in accelerator facilities such the fast BPMs at the SuperKEKB e+ linac [9, 10] and the Bunch Arrival-Time Monitors at SwissFEL [11].

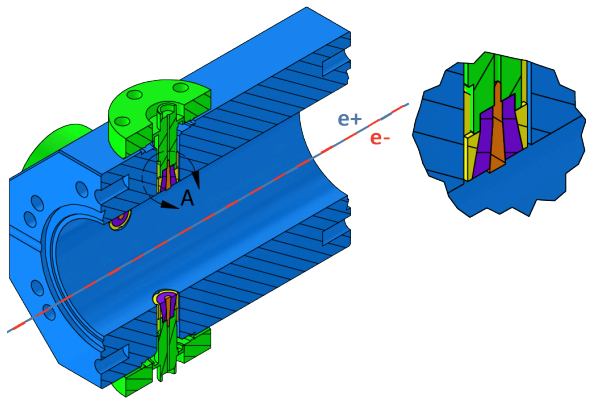


Figure 4: Mechanical design of the 27 GHz BBP assembly.

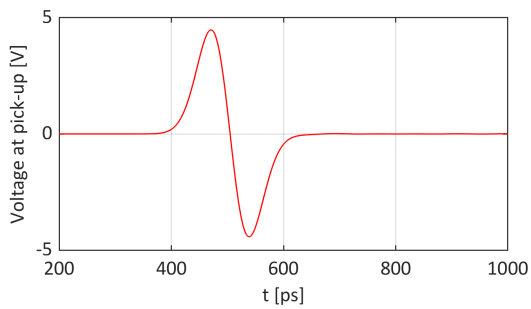


Figure 5: Detected voltage signal by one pick-up using 27 GHz feedthrough arrangement. Signal generated by gaussian bunch of Q_{bunch} = 1 nC and σ_t = 33 ps. Simulated with CST [12].

DIAGNOSTICS AFTER SEPARATION OF e+ AND e-

Faraday Cups

As illustrated in Fig. 2, the spectrometer will deflect the e+ and e- streams onto two faraday Faraday cups (FCs). Due to the extremely large energy (and p_z) spread, the main

Content from this work may be used under the terms of the CC-BY-4.0 licence (© 2023). Any distribution of this work must maintain attribution to the author(s), title of the work, publisher, and DOI

ISBN: 978-3-95450-236-3 ISSN: 2673-5350 doi:10.18429/JACoW-IBIC2023-MOP010

challenge for both FCs is to collect a beam with a high transverse dispersion introduced at the spectrometer, for which each FC will follow a different principle. Note that both e+ and e- could delivered to either FC through a sign inversion of the spectrometer polarity.

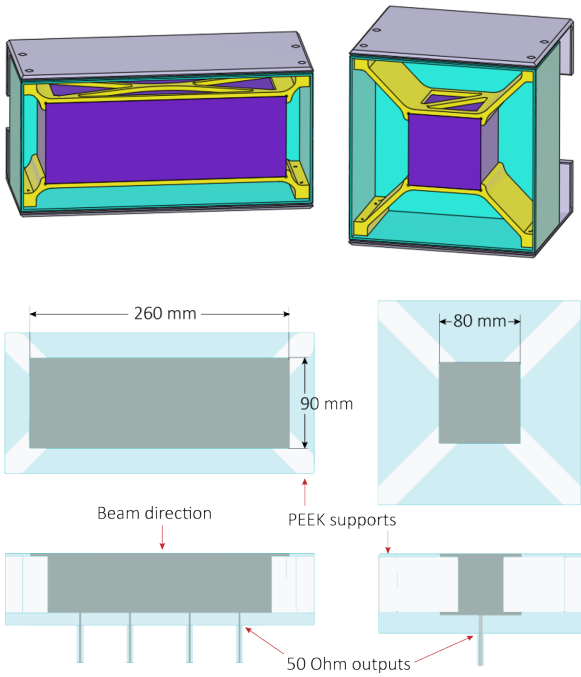


Figure 6: RF (top) and mechanical (bottom) design of 12.5 Ω (left) and 50 Ω (right) FCs, including tungsten blocks, PEEK supports and vacuum space.

The first FC is tuned at 12.5 Ω in pursuit of a large transverse area (260x90 mm), which will maximize the collection of charged particles in a wide energy range of 9-75 MeV. The coaxial impedance, a factor 4 smaller than the 50 Ω standard, can be easily matched to standard circuits through the use of parallel 4 coaxial cables. A second, relatively compact FC (80x80 mm) tuned at 50 Ω will detect charged particles in a larger energy range of 3-90 MeV. Although the smaller transverse size does not allow for single-shot charge measurements in broad energy spectra, the 50 Ω FC will perform energy discriminating measurements by adjusting the spectrometer strength, which determines the energy range of the particles routed towards the FC. A scan of 6 magnetic field values indicated in Table 2 would cover the above mentioned 3-90 MeV range. Figure 7 shows the frequency response of both FC arrangements with four diagonal PEEK supports (as seen in Fig. 6), in both cases above 1 GHz.

Error estimations of the measured e+ charge are shown in Fig. 8 for both FC layouts and all RF phase configurations, showing a reasonably low errors in the vicinity of the RF working point of interest. These error studies are based on ASTRA [5] particle tracking simulations. At Φ = (120,-70), the point for maximum captured e+ charge, the 12.5 Ω and 50 Ω FCs would read -13.6% and -9.4% with respect to the expected 1246 pC. 60 mm-thick W blocks were considered

Table 2: Reference spectrometer strength and measured energy ranges for different channels of FCs. Values based on zero-emittance particles.

	Mag. strength [T]	**E. range** [MeV]
12.5 Ω FC	0.053	9 - 75
50 Ω FC	0.212	50 - 90
	0.120	28 - 50
	0.068	16 - 28
	0.038	9 - 16
	0.021	5 - 9
	0.012	3 - 5

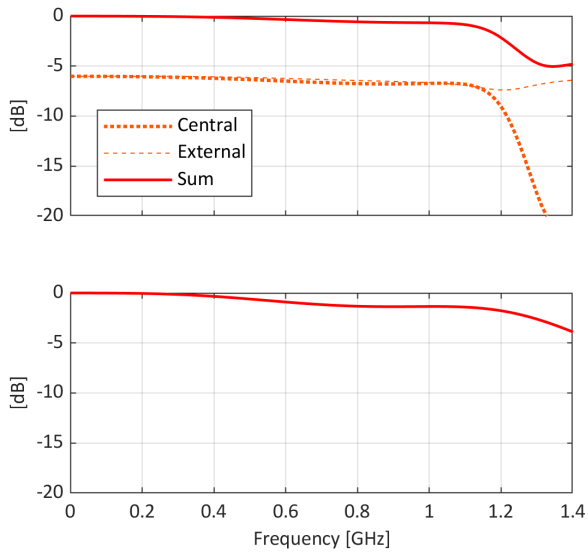


Figure 7: Frequency response of 12.5 Ω (top) and 50 Ω (bottom) FCs. Based on HFSS [13] simulations.

for both FCs in order to maximize charge deposition. Back scattering effects due to the high Tungsten density are disregarded as they are negligible above 10 MeV. On the other hand, poorer charge measurements are expected at lower energies, as particle divergence will have a greater impact in the final transverse position. However, this occurs in regions with relatively small importance for the experiment.

Scintillators in Diagnostics Chamber

Aside from the FCs, the diagnostics chamber will accommodate at least two additional instrumentation setups based on scintillator materials. First, the front face of the FCs will have scintillating screens that will allow cameras mounted outside of the chamber to look at the collected e+ and e- distributoins. These scintillator screens are particularly useful during beam commissioning, as counterpart of the FC signals. However, the large size of the FCs and the transverse emittance of the beam result in a very poor energy resolution, which precludes any usefulness of performing spectral measurements through these devices. The scintillator can either be a coating deposited on the face of the FCs, a screen mounted to the front of the FCs, or a free-standing screen

Content from this work may be used under the terms of the CC-BY-4.0 licence (© 2023). Any distribution of this work must maintain attribution to the author(s), title of the work, publisher, and DOI

ISBN: 978-3-95450-236-3 ISSN: 2673-5350 doi:10.18429/JACoW-IBIC2023-MOP010

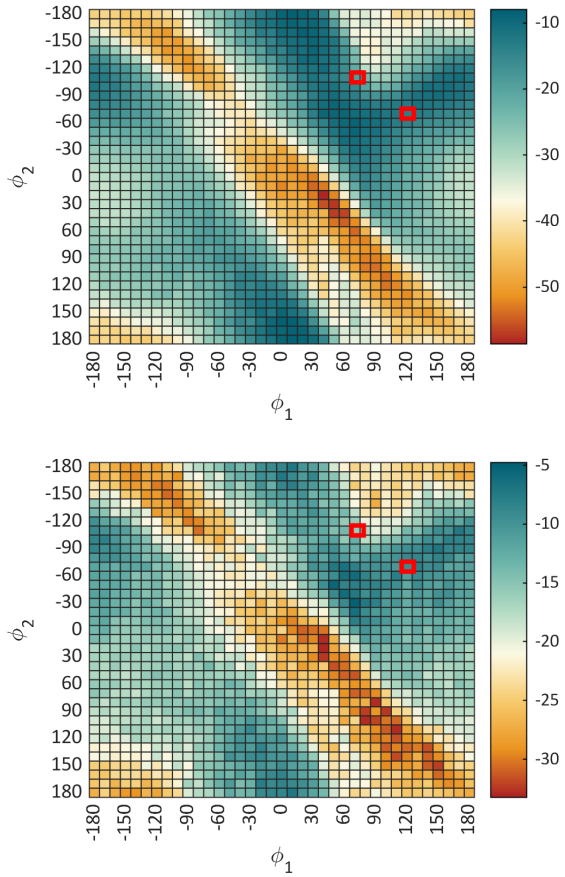


Figure 8: Error (in %) of measured charge by large 12.5 Ω (top) and compact 50 Ω (bottom) FCs over 2D RF phase scan. Estimated through particle tracking simulations with ASTRA [5]. Φ = (120,-70) and Φ = (70,-110) marked in red.

that can be inserted in and out of the chamber. The most likely materials for the screen would be Cr-doped Alumina (Chromox), Biomax, or YAG, which have been used for scintillation in accelerators in the past [14].

An high-resolution spectroscopic setup consisting of at least one pair of scintillator fibers will reconstruct the longitudinal momentum (p_z) spectrum of the e+ and e- distributions. The fibers, vertically oriented, will be hit by a small fraction of the particles corresponding to a narrow division of the energy spectrum. Following the basic principle of beam loss monitors, scintillator fibers will emit a signal proportional to the ionisation energy released by the incident charges. This will allow to scan the dipole field strength over as many points as desired. The baseline location of the first scintillator fiber pair is considered at x = -150 mm and z = 3520 mm (320 mm downstream from the center of the spectrometer). Figure 9 shows a reconstruction of the p_z spectrum for both RF working points of interest, computed through multiple particle tracking simulations. Despite the notoriously good agreements, the reconstruction below does not consider important factors such as scintillator response and signal acquisition. In addition, this spectral detection is supposed to be relative at the moment. Calibration of the fibers is required for absolute charge measurements and is still under investigation.

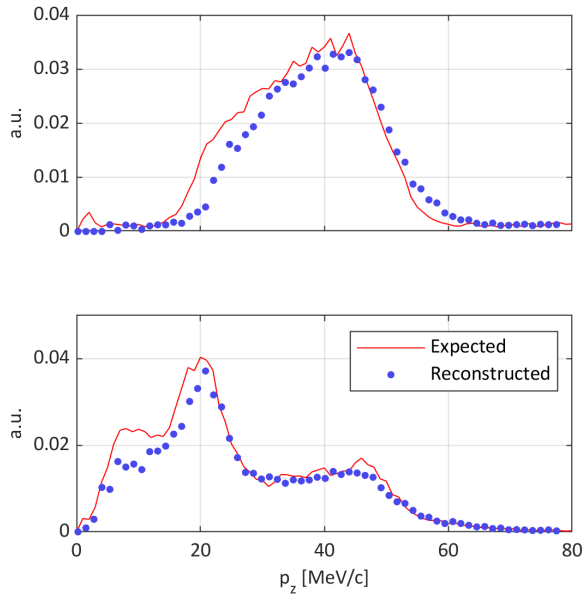


Figure 9: Estimation of p_z reconstruction for Φ = (120,-70) (top) and Φ = (70,-110) (bottom). Computed through through 61 ASTRA simulations ranging dipole field strengths from 0 to 0.3 T and scintillator fibers located at x = -150 mm and z = 3520 mm.

CONCLUSION

This paper introduced the diagnostics for P^3 experiment, consisting of an arrangement of broadband pick-ups (BBPs), 2 types of Faraday cups and a variety of scintillating detectors. The BBPs are currently assembled and under test. Preliminary measurements with ≈10 ps e- bunches are scheduled before the end of 2023. However, despite their design being less advanced,

despite their technical design is still in progress the Faraday cups were studied in greater detail as they will arguably provide the most accurate detection of the captured e+ charge. Thus we performed a preliminary error study based on simulations, envisaging reasonably high quality measurements of the Faraday cups, specially at RF working points of interest.

ACKNOWLEDGEMENT

This work was done under the auspices of the CHART Collaboration (Swiss Accelerator Research and Technology, http://www.chart.ch).

REFERENCES

[1] E. Prat *et al.*, "A compact and cost-effective hard X-ray free-electron laser driven by a high-brightness and low-energy electron beam", *Nat. Photonics*, vol. 14, pp. 748–754, 2020. doi:10.1038/s41566-020-00712-8

Content from this work may be used under the terms of the CC-BY-4.0 licence (© 2023). Any distribution of this work must maintain attribution to the author(s), title of the work, publisher, and DOI

ISBN: 978-3-95450-236-3 ISSN: 2673-5350 doi:10.18429/JACoW-IBIC2023-MOP010

[2] N. Vallis *et al.*, "The P^3 Experiment: a Positron Source Demonstrator for Future Lepton Colliders", 2023. doi:10.48550/arXiv.2308.16803

[3] R. H. Helm, "Adiabatic Approximation for Dynamics of a Particle in the Field of a Tapered Solenoid", SLAC Report No. 4, 1962.

[4] R. Chehab, "Positron Sources", in *Proc. Cern Accelerator School, 3rd general accelerator physics course*, Salamanca, Spain, pp. 105-132, CERN, 1988. doi:10.5170/CERN-1989-005

[5] ASTRA: A Space Charge Tracking Algorithm, https://www.desy.de/~mpyflo/.

[6] 27 GHz SMA Feedthrough for UHV Applications 242-SMAD27G-C16, Allectra GmbH, 2019.

[7] Microwave 1.85 mm (SMA) feedthrough 242-SMAD65G-C16, Allectra GmbH, 2022.

[8] 1.85 mm Male to 3.5 mm Male Cable Assemblies, Pasternack Enterprises, https://www.pasternack.com/1.85mm-male-to-3.5mm-male-cable-assemblies-category.aspx

[9] T. Suwada, M. A. Rehman, and F. Miyahara, "First simultaneous detection of electron and positron bunches at the positron capture section of the SuperKEKB factory", *Sci. Rep.*, vol. 11, p. 12751, 2021. doi:10.1038/s41598-021-91707-0

[10] T. Suwada, "Direct observation of positron capture process at the positron source of the superKEKB B-factory", *Sci. Rep.*, vol. 12, p. 18554, 2022. doi:10.1038/s41598-022-22030-5

[11] V. Arsov *et al.*, "Evaluation of the cone-shaped pickup performance for low charge sub-10 fs arrival-time measurements at free electron laser facilities", *Phys. Rev. Accel. Beams*, vol. 18, p. 012801, 2012. doi:10.1103/PhysRevSTAB.18.012801

[12] CST Studio Suite Electromagnetic Simulation Solvers, https://www.3ds.com/products-services/simulia/products/cst-studio-suite/solvers/

[13] Ansys HFSS, Best-In-Class 3D High Frequency Structure Simulation Software, https://www.ansys.com/products/electronics/ansys-hfss

[14] C. D. Johnson, "The development and use of alumina ceramic fluorescent screens", CERN Report No. CERN-PS-90-42-AR, 1990.

Content from this work may be used under the terms of the CC-BY-4.0 licence (© 2023). Any distribution of this work must maintain attribution to the author(s), title of the work, publisher, and DOI

ISBN: 978-3-95450-236-3 ISSN: 2673-5350 doi:10.18429/JACoW-IBIC2023-MOP011

SAFETY CONSIDERATIONS FOR SHIELD DOOR CONTROL SYSTEMS*

H.A. Watkins†, W. Barkley, C. Hatch, D. Martinez, D. Rai, E. Simakov
Los Alamos National Laboratory, Los Alamos, NM, USA

Abstract

The Accelerator Operations and Technology division is upgrading the control system for a 33-ton shield door that will be used when the Cathodes and RF Interactions in Extremes (CARIE) accelerator begins operations. The door was installed in the 1990's but safety standards such as ISO 13849-1 have since emerged which provide safety requirements and guidance on the principles for the design and integration of safety-related parts of a control system. Applying this standard, a safety controller, safety relays and a light curtain barrier have been added to eliminate injury and exposure of personnel to potential hazards during door operations.

OVERVIEW OF CARIE

Los Alamos National Lab (LANL) is starting construction of a new C-band (5.712 GHz) accelerator test facility for cathode, accelerator, and material science studies. The new facility is called Cathode and RF Interactions in Extremes (CARIE). This accelerator will reside in a radiation protection vault on the Los Alamos Neutron Science Center (LANSCE) mesa. This location will house a cryo-cooled copper RF photoinjector with a high quantum efficiency (QE) cathode and a high gradient accelerator section with beam power up to 20 kW [1].

SHIELD VAULT

CARIE will reside in a 12 by 25-foot interior vault that uses 4-foot-thick magnetite blocks to shield the exterior control and operations areas. The vault was originally designed for use with the Advanced Free Electron Laser (AFEL) project which is no longer in operation. A 33-ton moveable shield door separates the vault from the control room. When closed during CARIE operation, the door protects personnel from neutron and bremsstrahlung radiation, activated air, and ozone. The door is constructed of 12 magnetite concrete blocks welded together on their edges and welded to a reinforced concrete base. The door is mounted on four sets of Hilman rollers and guided by tracks on the floor, the door is opened and closed by a hydraulic piston [2]. The shield vault door will need to open and close multiple times a day to support experimentation within the vault. The original control system was decommissioned and removed in the early 2000's. However, the shield blocks, hydraulic piston and roll track system remain intact (see Fig. 1). Attempts to test the door mechanism and piston were successful and the door is operational from a mechanical perspective. The shield door and existing hydraulic system (see Fig 1).

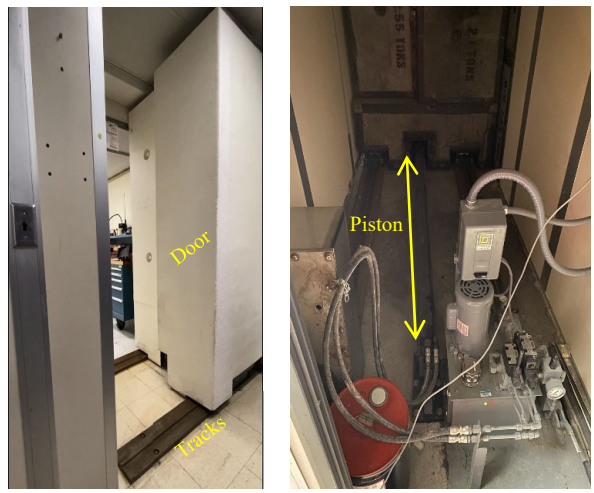


Figure 1: Shield door opening and hydraulic system.

FUNCTIONAL REQUIREMENTS

The purpose of the control system for the shield door is to allow scientists and engineers to easily access the interior vault when CARIE is not in operation and for the door to remain closed when operations commence. The control system requirements are very simple. Open and close buttons mounted exterior to the vault easily meet the functional requirements for operation. Investigation of the mounting points and legacy relay system indicate this is most likely what existed during its operation during the 1990's until decommissioning in early 2000's.

SAFETY REQUIREMENTS

The legacy requirements of safety for the shield door design focused on the radiation shielding that the door provided to the users when the original AFEL was in operation. However, safety of the control system e.g. door operations were not considered or evident in the initial design. ISO 13849-1 is the safety standard that now governs safety requirements for the operation of control systems. This safety standard provides safety requirements and guidance on the principles for the design and integration of safety-related parts of a control system. This standard defines the performance level (PL), which is the discrete level used to specify the ability of safety-related parts of control systems to perform a safety function under foreseeable conditions.

WHAT IS SAFETY? WHAT IS RISK?

Control system engineers must incorporate safety into designs to provide the protective measures needed to insure

* This work was supported by the U.S. Department of Energy through the Los Alamos National Laboratory. Los Alamos National Laboratory is operated by Triad National Security, LLC, for the National Nuclear Security Administration of U.S. Department of Energy (Contract No. 89233218CNA000001).
LA-UR-23-29961
† hwatkins@lanl.gov

Content from this work may be used under the terms of the CC-BY-4.0 licence (© 2023). Any distribution of this work must maintain attribution to the author(s), title of the work, publisher, and DOI

ISBN: 978-3-95450-236-3 ISSN: 2673-5350 doi:10.18429/JACoW-IBIC2023-MOP011

Content from this work may be used under the terms of the CC-BY-4.0 licence (© 2023). Any distribution of this work must maintain attribution to the author(s), title of the work, publisher, and DOI

safe operations. Control system safety can be defined as "freedom of the operator from unacceptable risk." This infers that there is minimal level of risk involved even when a system is considered safe. Risk is then defined as "a combination of the probability of the occurrence of harm and the severity of that harm" [3].

$$\text{Risk} = \text{Severity of harm} \times \text{Probability of the occurrence of harm} \quad (1)$$

RISK ASSESSMENT

Every time we rely upon a control system to reduce risk, we also need to consider the probability that the safety control system itself will fail. If a safety control system fails, it does not provide the risk reduction measure. This is the domain of functional safety and incorporates the PL as its basis to have the control system reliability exceed the needs of the risk reduction measure [4].

Control system engineers should begin with a risk assessment using the flow chart (see Fig. 2) to determine limits, hazards, risk, and the protective measures needed to mitigate exposure to the hazards. This risk assessment was completed for the shield door project and resulted in a design to minimize operator exposure to identified hazards.

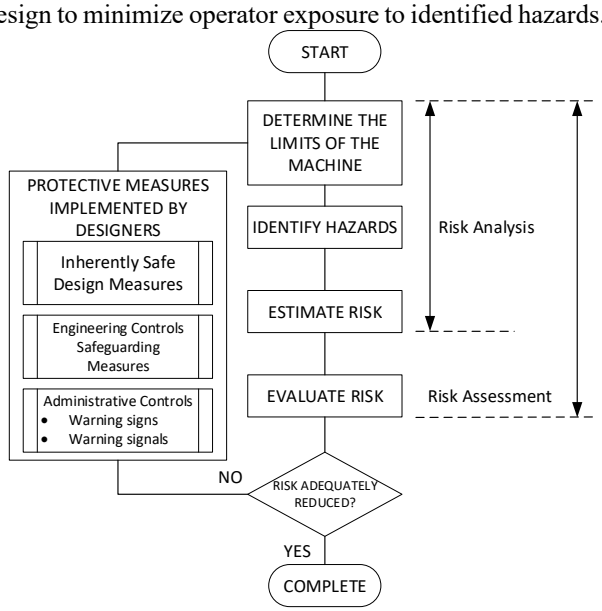


Figure 2: Risk assessment flow chart.

DETERMINE LIMITS

Assessing the operating limits of the machine in question is the first step of the flow chart. The shield door project determined that the limits of the shield door were based on the track structure and the stroke of the hydraulic cylinder. The door being fully opened occurs when the hydraulic cylinder is fully retracted. A leaf style limit switch is placed 1-inch inside of the fully retracted system to allow for an engineering limit. The other limit is full extension of the hydraulic cylinder where the pump is placing 300 psi of fluid pressure through the lines to close the door. The system can reach full closure and the hydraulic cylinder is still able to provide additional stroke of 1-inch. Another engineering limit is added at the door closure to disengage the pump and stop motion. Identifying these limits then allow for moving to the hazard identification step of the flowchart.

INDENTIFY HAZARDS

Mechanical hazards fall into six different categories.

- **Crushing**
- Shearing
- Cutting
- Entanglement
- Drawing-in or **trapping**
- Stabbing or puncture

The shield doors specific mechanical hazard was identified as crushing. The hydraulic piston when in operation can crush the human body and cause serious injury if the hydraulic pump remains engaged and an engineering limit has not been reached.

ESTIMATE RISK

Since a hazard has been identified the next step is to estimate the risk of the crushing hazard of the shield door. The risk estimation chart allows an engineer to determine the degree of risk as a performance level requirement (PLr) given the severity of injury, frequency of exposure to the hazard and the possibility of avoiding the hazard. Figure 3 shows the flow chart with the dashed line estimating risk for the shield door.

S = Severity of Injury
S1: Slight
S2: Serious ←
F = Frequency or exposure to hazard
F1: Seldom to less often ←
F2: Frequent to continuous
P = Possibility of avoiding hazard
P1: Possible under specific conditions ←
P2: Scarcely possible

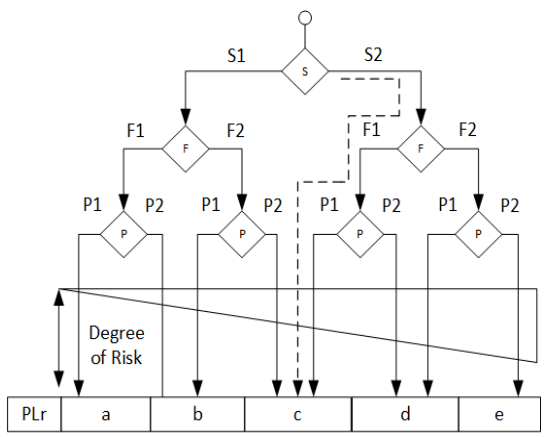


Figure 3: Risk estimation flow chart.

ISBN: 978-3-95450-236-3 ISSN: 2673-5350 doi:10.18429/JACoW-IBIC2023-MOP011

The determination of the required performance level was PLr = PLc. This allows the designer to evaluate the risk and the components needed to mitigate that risk. In the case of the shield door, components that will be selected to mitigate the crushing hazard must meet a minimum rating of PLc to ensure that the component reliability meets or exceeds the risk estimation requirement.

EVALUATE RISK

Now that the hazard and PLr have been identified, it is now possible to implement measures to reduce the exposure to the hazard in the form of protective measures. In the case of the shield door, it is not possible to make it inherently safe which should always be a designer's first evaluation method. The area where the shield door closes allows personnel access when the door is open so safeguarding measures or engineering controls must be implemented to reduce the likelihood of door movement during personnel entry but also provide full operations of the door.

PROTECTIVE MEASURES

Light Barrier

The protective measures chosen to reduce exposure to the crushing hazard of the door during operation was a light barrier system. The light barrier system uses a light array from a transmitter to beam light to a receiver section. When light becomes disrupted the safety programmable logic controller (PLC) senses the disruption and trips the safety relay. The PLC also has test equipment built-in to monitor the health of the light barrier and safety relay to ensure the equipment has not malfunctioned. This system can be mounted at the opening of the shield door to protect personnel trying to enter the vault when the door is in motion.

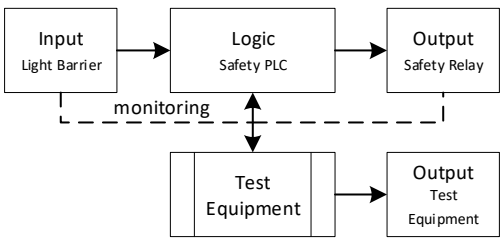


Figure 4: Safety diagram for light barrier.

Figure 4 shows the system as designed where the light barrier interfaces to a safety PLC with a safety relay. The PLC input is then programmed to latch open the output relay when the light barrier is triggered. The safety relay is then added in series to the control relays to disable motion of the door when latched. Latched systems also require a reset input, not pictured, to recover the system to normal operation if a safety event occurs. The test capability built into the safety PLC provides real time functional testing of the light barrier and safety outputs to ensure these systems will function correctly when needed. This improves the performance level rating of the system to PLc.

Status Indicators

Following the risk assessment flow chart and its iterative process it was determined the light barrier works to provide safety when very close to the door threshold however additional risk mitigation would be an administrative control to indicate to users further away that the door was in motion. Administrative controls were added to indicate to users the state of the door. Table 1 indicates the lights and sounds used as administrative controls for this project.

Table 1: Indications for Administrative Controls

Light Indicator	State
Green	Door Open
Orange	Door Closed
Red	Safety Stop
Blink Red	Door In-Motion
Siren	Door In-Motion

Emergency Exit

The important part of iterating through the risk assessment flow chart process is additional hazards may be identified. An additional hazard of trapping was identified during the assessment. The shield door could trap personnel inside if closed, no other exits exist to the vault. Risk estimation shows this is a PLa requirement due to slight risk of injury, seldom frequency and only possible under very specific circumstances. This simplifies the safety diagram where a simple exit override switch can be used interior to the vault and override the close command with an open command.

Emergency Stop

A similar emergency stop button was also provided for situations where operators external to the vault wish to stop all motion or lock out motion. This button did not meet the criteria for a safety requirement and is considered a design feature instead of a safety measure. However, it does provide a single control that allows all motion to be halted and overrides any motion commands of the control system.

PERFORMANCE LEVEL PARAMETER

Before the control system engineer dives into component selection, it's important to understand a manufacture's specification of performance level (PL). The PL must be determined for each safety component of the control system and/or the combination of components that performs a safety function. The following principal aspects are used to establish PL according to ISO 13849-1:

1) Category (Structure) – establishes the required safety function in case of a fault.
2) Diagnostic Coverage – is a measure of the effectiveness of the diagnostics to detect dangerous failures.

Content from this work may be used under the terms of the CC-BY-4.0 licence (© 2023). Any distribution of this work must maintain attribution to the author(s), title of the work, publisher, and DOI

ISBN: 978-3-95450-236-3 ISSN: 2673-5350 doi:10.18429/JACoW-IBIC2023-MOP011

Content from this work may be used under the terms of the CC-BY-4.0 licence (© 2023). Any distribution of this work must maintain attribution to the author(s), title of the work, publisher, and DOI

3) Mean Time to Dangerous Failure (MTTFd) – is the expectation of the safety component to provide failure free functionality.
4) Common Cause Failure – relates to the failure of different components resulting from a single event. [3]

Safety component manufactures will provide the PL ratings of their equipment, but it is the responsibility of the control engineer to implement the correct risk mitigation and testing to ensure those PL ratings meet or exceed the PLr requirements of the system. The PL ratings range alphabetically from a through e and will be called out on a vendor's datasheet as PLa – Ple. PLa would be the minimum level of safety performance and PLe would meet the highest level of safety performance.

COMPONENT SELECTION

Once safety measures have been designed the correct components must be selected to meet both the functional safety requirements and the performance level requirements for reliability. Several manufacturers make safety related equipment. The manufacturers Keyence, IDEC, Phoenix Contact and Schneider were all evaluated for safety related components for this project. Keyence was chosen as the supplier for all safety related components however the other three manufacturers were used for components for the operator control design which resides adjacent to the safety system. Keyence provided the clearest guidance on safety. The manufacturer calls out specifically the PLx ratings of their components, provided on-site engineering support for demonstration and discussed their safety technology in depth.

The Keyence GLR96H was chosen for the light barrier. This barrier has 96 beams and has a protection height of 1.9 m. The beam pitch is 20 mm which is capable of detecting hands, arms or legs. It uses 870 nm infrared LEDs for the light source and supports a detection distance of 15 m. Only 3.5 m distance is required for the door when fully opened. The PL safety rating for this device is PLe (see Fig. 5) which exceeds the PLc requirement determined during risk evaluation [5].

Approved standards	EMC	EMS	IEC61496-1, EN61496-1, UL61496-1
		EMI	EN55011 ClassA, FCC Part15B ClassA, ICES-003 ClassA
	Safety		IEC61496-1, EN61496-1, UL61496-1 (Type 4 ESPE) IEC61496-2, EN61496-2, UL61496-2 (Type 4 AOPD) IEC61508, EN61508 (SIL3), IEC62061, EN62061 (SIL CL3) EN ISO13849-1:2015 (Category 4, PLe) UL508 UL1998

Figure 5: Manufacturer's datasheet.

The Keyence GC-1000R is a safety PLC which also includes built in safety relay outputs. This controller provides the hardware control and safety logic programming necessary to implement the light curtain barrier, latch reset and the emergency stop switch. Included in this safety PLC is the capability to provide test equipment monitoring of the connected devices. This brings the PL safety rating of the controller to a PLe rating which exceeds the original PLc requirement needed to mitigate the crushing risk and the PLa requirement of the trapping risk discovered during risk assessment.

CONCLUSION

Safety considerations for control systems require a risk assessment to ensure that existing or new designs address risk exposure to operators. In the case of the shield door for the CARIE vault two hazards were identified. Engineered safety controls and administrative controls were implemented to reduce the risk of hazard exposure to a minimal level for operators. Los Alamos National Lab has instituted a new focus on disciplined operations. This focus reminds employees to use the safe conduct of research principals to cultivate a questioning attitude about safety and reminds all employees to maintain a healthy respect for what can go wrong. These principles don't just apply to the personnel operating devices such as the shield door but also to the control system engineers who are providing remote control capabilities for these devices.

REFERENCES

[1] E.I. Simakov *et al.,* "Update on the Status of C-Band Research and Facilities at LANL", in *Proc. 5th North American Particle Accel. Conf. (NAPAC'22)*, Albuquerque, New Mexico, USA, August 2022 pp. 855-858. doi:10.18429/JACoW-NAPAC2022-THY

[2] K. Meier, "Engineering Considerations of the Advanced Free Electron Laser Facility", presented at the 13th International Free-Electron Laser Conference, Santa Fe, NM, Aug 1991, paper, unpublished.

[3] *Safety Support Guide Book*, Keyence, Itasca, IL, USA, 2020.

[4] M. Tacchini, *Functional Safety of Machinery, How to Apply ISO13849-1 and IEC 62061*, Poncarale, Brescia, Italy: Wiley, 2023.

[5] GL-RH Data Sheet, Keyence, Itasca, IL, USA Dec 2022.

ISBN: 978-3-95450-236-3 ISSN: 2673-5350 doi:10.18429/JACoW-IBIC2023-MOP013

EXPANSION OF THE MTCA BASED DIRECT SAMPLING LLRF AT MEDAUSTRON FOR HADRON SYNCHROTRON APPLICATIONS

M. Wolf*, M. Cerv, C. Kurfuerst, S. Myalski, M. Repovz, C. Schmitzer
EBG MedAustron GmbH, Wr. Neustadt, Austria
A. Bardorfer, B. Baricevic, P. Leban, P. Paglovec, M. Skabar
Instrumentation Technologies, Solkan, Slovenia

Abstract

The MedAustron Ion Therapy Centre is a synchrotron-based particle therapy facility located in Lower Austria, which delivers proton and carbon ion beams for cancer treatments. Currently the facility treats over 400 patients per year and is expected to double this number in the future. Six years since the start of clinical operation, MedAustron is experiencing end-of-life issues concerning the digital Low Level RF components in the injector and the synchrotron. Replacements for these applications are under development and the chosen hardware is suitable to also update multiple beam diagnostic devices in the facility. Main targets for updates are the Schottky monitors, which were never properly integrated into the MedAustron Control system and the position pickup measurement system, which currently does not support turn by turn measurements. Comparison measurements with other state of the art diagnostic devices are ongoing to demonstrate the capabilities of the generic hardware. Furthermore, these measurements should show the increased usability and diagnostic potential compared to the legacy devices.

INTRODUCTION

MedAustron and Instrumentation Technologies continued to work on a LLRF and beam diagnostic solution to replace all RF applications used at MedAustron and already presented in the last years [1–3]. In the current paper new beam diagnostic usecases in the MedAustron Synchrotron will be shown and measurement results of Schottky detectors and classical Shoebox Pickups will be compared to other off the shelf equipment.

MEASUREMENT SETUP

Position Measurement System

The MedAustron Synchrotron contains multiple beam position monitors in form of Shoebox Pickups. These Pickups are located in different dispersion regions of the Synchrotron and can be used to measure the orbit of the beam circulating in the synchrotron. Head amplifiers are connected to these pickups with short cables to keep the interference and cable influences at a minimum. These head amplifiers generate sum and delta signals out of the pickup plate signals. Afterwards these sum and delta signals are forwarded out of the synchrotron hall and further amplified in distribution amplifiers. The distribution amplifiers generate multiple copies of the pickups signals. Spare outputs of the distribution amplifiers are used to parasitically measure the two horizontal pickups in high and low dispersion regions.

Digital Data Processing of the Position Measurement

The output of the position measurement system is digitized with off the shelf hardware from Vadatech which was presented in Ref. [1]. For the beam position measurement one AMC560 Carrier card and one FMC231 AD/DA converter card is used. The signals produced by the distribution amplifiers are directly sampled and then demodulated to baseband signals using the revolution frequency of the synchrotron. The resulting amplitude of the delta signal is divided by the amplitude of the sum signal, to calculate position information independent of the beam current. The results of this calculation can then be calibrated to represent absolute position data. This calibration will be finalized in the future.

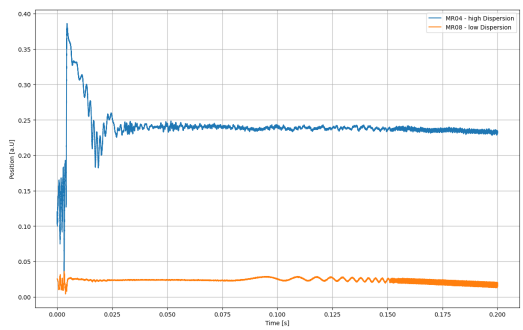


Figure 1: Qualitative position measurement in high and low dispersion regions of the synchrotron.

Schottky Monitors

The Schottky monitors are directly connected to standard low noise amplifiers (FEMTO- HVA-200M-40-F) and afterwards connected to the digitizer hardware outside of the synchrotron hall. In this setup sum and delta signals are calculated after digitizing the signals.

* markus.wolf@medaustron.at

Content from this work may be used under the terms of the CC-BY-4.0 licence (© 2023). Any distribution of this work must maintain attribution to the author(s), title of the work, publisher, and DOI

ISBN: 978-3-95450-236-3 ISSN: 2673-5350 doi:10.18429/JACoW-IBIC2023-MOP013

Content from this work may be used under the terms of the CC-BY-4.0 licence (© 2023). Any distribution of this work must maintain attribution to the author(s), title of the work, publisher, and DOI

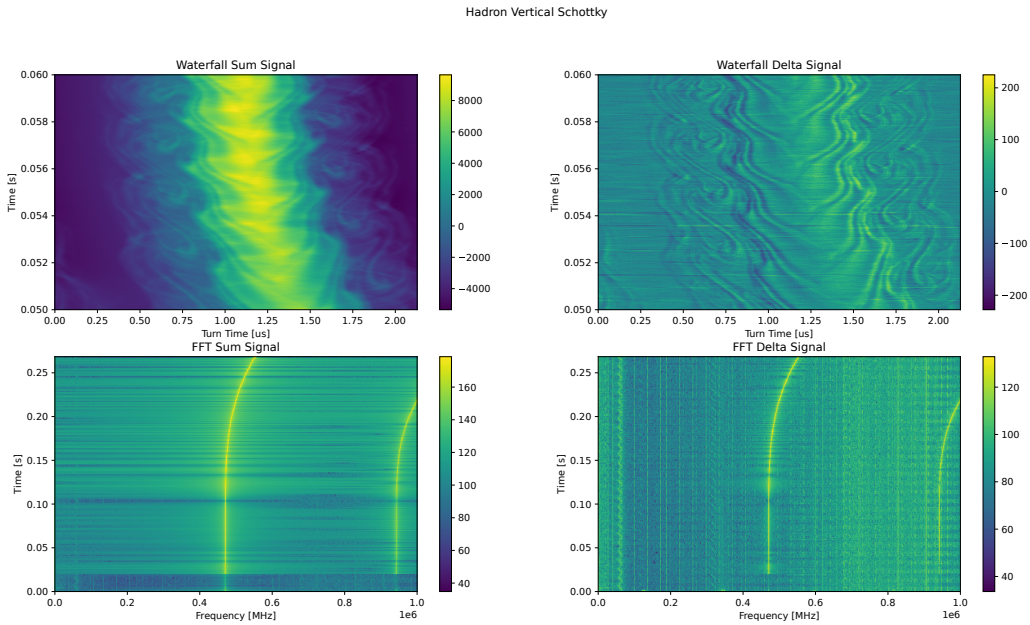


Figure 2: Waterfall diagram and frequency analysis of beam injection with the Libera Hadron.

Digital Data Processing of the Schottky Measurements

The schottky plate data is directly sampled by the µTCA based Vadatech solution and for comparison also by a Libera Hadron. Sum and delta signals are calculated in the digital domain and the results are then plotted in form of waterfall diagrams showing how the particle bunch changes its shape inside the synchrotron. Additionally the data is fed into a FFT algorithm, which should provide information about the revolution frequency, the synchrotron frequency and the beam tune.

MEASUREMENTS

Position Measurement

The position measurement (Fig. 1) shows the injection, adiabatic capture and the start of the acceleration inside the synchrotron. Due to a small mismatch of the Dipole field and the injection energy the beam position drifts a little bit at the beginning. Only after the radial loop is turned on the position stabilizes till the end of the measurement. At the beginning of the acceleration (at 100 ms) field ramping of the magnets is not exactly synchronous to the beam acceleration resulting in a small oscillation seen in the low Dispersion area.

Schottky Measurements

The schottky measurements are done with two different measurement devices and show the beam bunch in a waterfall diagram after capture (MedAustron uses a coasting injection) and before the acceleration starts. Dipole and quadrupole oscillations are clearly visible with both measurement devices. Both of the devices show a good resolution of the beam, which should make a tomography of the beam possible.

The FFT plots show the whole range from the beam injection, the capture and the start of the acceleration. Compared to each other both devices show a good resolution for the sum signals. Differences can only be seen at the Delta plots. There it looks like the Hadron (Fig. 2) exhibits a bit more noise compared to the Vadatech solution (Fig. 3) over almost the whole frequency range shown. Unfortunately none of the two devices can clearly show the beam tune while the beam is captured and without an excitation kick (either by a kicker or transversal RF excitation). Only at the very beginning of the measurement (first 10 ms) a small peak could be seen, which might be the beam tune. Further measurements will be needed to verify if these peaks are really the beam tune and to identify system improvements, which might show the beam tune more clearly.

RESULTS AND OUTLOOK

The chosen new hardware for the MedAustron RF applications continues to improve beam diagnostic capabilities available at the facility. The results show the suitability for the low frequency range needed at MedAustron and the beam resolution and turn by turn measurement bring new diagnostics like a beam tomography within reach. Nonetheless already the shown measurements increase the knowledge about the machine behavior compared to the legacy beam diagnostic devices.

ISBN: 978-3-95450-236-3 ISSN: 2673-5350 doi:10.18429/JACoW-IBIC2023-MOP013

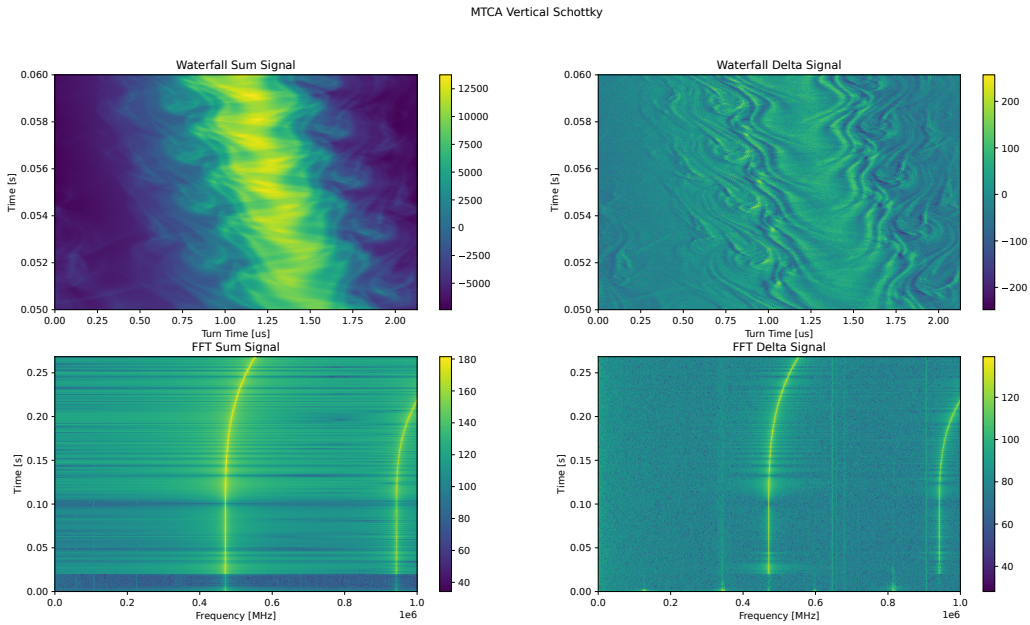


Figure 3: Waterfall diagram and frequency analysis of beam injection with the Vadatech µTCA solution.

REFERENCES

[1] M. Wolf *et al.*, "Development and Integration of a New Low-Level RF System for MedAustron", in *Proc. LINAC'22*, Liverpool, UK, Aug.-Sep. 2022, pp. 764–766. doi:10.18429/JACoW-LINAC2022-THPOPA12

[2] M. Repov *et al.*, "Development of a New Measurement System for Beam Position Pickups in the LINAC and Beam Energy Measurement (Time of Flight) in the MEBT for Medaustron", in *Proc. IBIC'22*, Kraków, Poland, Sep. 2022, pp. 238–240. doi:10.18429/JACoW-IBIC2022-TUP10

[3] M. Wolf *et al.*, "Expansion of the µTCA based direct sampling LLRF at MedAustron for hadron synchrotron applications", presented at the IPAC'23, Venice, Italy, May 2023, paper THPA091, to be published.

Content from this work may be used under the terms of the CC-BY-4.0 licence (© 2023). Any distribution of this work must maintain attribution to the author(s), title of the work, publisher, and DOI

ISBN: 978-3-95450-236-3 ISSN: 2673-5350 doi:10.18429/JACoW-IBIC2023-MOP018

BEAM-DIAGNOSTIC AND T0 SYSTEM FOR THE mCBM AND CBM EXPERIMENTS AT GSI AND FAIR

A. Rost[1*], T. Galatyuk[2,3], V. Kedych[3], M. Kis[2], W. Krüger[3],
J. Pietraszko[2], A. Senger[1], J. Thaufelder[2], F. Ulrich-Pur[2]
[1]FAIR GmbH, Darmstadt, Germany
[2]GSI Helmholtzzentrum für Schwerionenforschung GmbH, Darmstadt, Germany
[3]Institut für Kernphysik, TU Darmstadt, Darmstadt, Germany

Abstract

The Compressed Baryonic Matter (CBM) experiment at the Facility for Antiproton and Ion Research (FAIR) in Darmstadt requires a highly accurate beam monitoring and time-zero (T0) system. This system needs to meet the requirements of the CBM time-of-flight (ToF) measurement system for both proton and heavy ion beams, while also serving as part of the fast beam abort system. To achieve these goals, a detector based on chemical vapor deposition (CVD) diamond technology has been proposed. In addition, new developments using Low Gain Avalanche Detectors (LGADs) are currently under evaluation. This contribution presents the current development status of the beam detector concept for the CBM experiment.

INTRODUCTION

The CBM experiment [1] is a fixed-target, multi-purpose detector that will be used to explore the QCD phase diagram of nuclear matter at high net-baryon densities and moderate temperatures. The experiment will be located at the Facility for Antiproton and Ion Research (FAIR) in Darmstadt, Germany.

The CBM detector will be able to detect hadrons, photons, electrons, and muons in elementary and heavy-ion collisions over the entire energy range provided by the SIS100 heavy-ion synchrotron, from 3 to 11 A GeV for heavy ions and 29 GeV for protons. The measurements will be performed at event rates from 100 kHz up to 10 MHz using free-streaming readout electronics and fast online event reconstruction.

The BMON system consists of a high-speed time-zero (T0) and halo detector. The detector must meet the requirements of the time-of-flight (ToF) measurement system for both proton and heavy-ion beams. Specifically, it must achieve a time precision better than 50 ps (sigma), maintain stable long-term operation even at high interaction rates of 10^7 particles/s, and have a detection efficiency approaching 100%. A summary of the requirements is provided in Table 1.

Table 1: Requirements to the CBM BMON System

Max. beam intensity	10^7 particles/s on sensor
Max. read-out rate	5 MHz per channel
Time precision	50 ps
Position resolution	0.5 mm
Beam spot size on sensor	1 cm (2 sigma)
Sensor thickness	70 µm

THE CBM BEAM MONITORING SYSTEM

The CBM BMON system has been already introduced in [2], it will consist of two detector stations located in front of the CBM target chamber. The T0-station is foreseen to measure the start time of the reaction, while the Halo-station will be used for beam halo monitoring and as a port of a fast beam abort system (BAS). Both detectors will be mounted inside a beam-pipe using commercially available CF 100 vacuum elements, as schematically shown in Fig. 1.

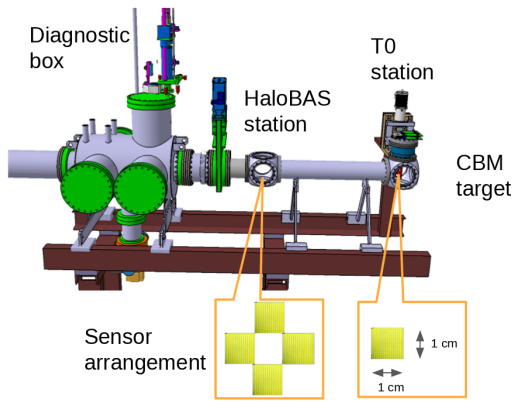


Figure 1: The CBM BMON system consists of two stations for beam halo and T0 measurement. The stations are mounted in standard CF 100 vacuum chambers in front of the CBM target. The T0 station uses a single sensor, while the Halo station uses a mosaic structure of four sensors. The Halo station will also be part of a fast beam abort system (BAS).

The sensor for the T0 station is currently planned to be made using poly-crystal CVD (pcCVD) diamond technology [3]. The sensor will have a thickness of 70 µm and will cover an area of 1×1 cm^2. It will be equipped with a metallization arranged in 16 strips on each side. A detailed description of the sensor and the production and testing of a prototype sensor can be found in [2]. The strip segmentation and orientation, aligned in the x and y-directions, will allow to extract the position information of the beam particles. We are currently also investigating higher segmen-

* a.rost@gsi.de

Content from this work may be used under the terms of the CC-BY-4.0 licence (© 2023). Any distribution of this work must maintain attribution to the author(s), title of the work, publisher, and DOI

ISBN: 978-3-95450-236-3 ISSN: 2673-5350 doi:10.18429/JACoW-IBIC2023-MOP018

tation, i.e. 48x48 strips, for the final CBM T0 sensor. This will increase the rate capability of the sensor.

The halo station is planned to be used as an independent beam monitoring system. The halo detector will consist of a mosaic arrangement of four sensors, each metallized with four strips on both sides. The sensor arrangement is schematically shown in Fig. 1. This arrangement allows to monitor the beam position and its rate during the extraction process. This information will be used to secure sensitive CBM detectors as part of a fast beam-abort system (BAS).

At the moment, we are actively investigating the possibility of using recently developed Low Gain Avalanche Detector (LGAD) technology, especially for proton beams in the CBM experiment. LGAD technology has been shown to be very promising for beam monitoring applications, as it can achieve high time resolution and rate capability [4].

INFLUENCE OF THE T0 DETECTOR ON THE CBM DETECTOR SYSTEM

The influence of the T0 detector on the CBM detector system has been studied using Monte Carlo simulations. The detector was placed at two locations in the simulations: 0.5 m and 2 m in front of the target. A point-like Au beam with an energy of 4 A GeV and a rate of 10^7 ions/s was used. The simulation assumed an Au target with a thickness of 250 µm and 85% of the maximum magnetic field.

In a first study, the widening of the beam due to the diamond material was investigated. The results are shown in Fig. 2. The beam profile is enlarged, but the halo particle rate is not significantly increased. The ratio between the beam spot maximum the beam spot center, at a distance 5 mm from the beam spot maximum, is eight orders of magnitude. This is in agreement with the guidelines of the CBM collaboration.

The additional diamond material in front of the target will also lead to an increased charged particle contamination in the region where the Silicon Tracking System (STS) [5] is located. This is visualized in Fig. 2. However, initial discussions with the CBM STS detector experts suggest that this should not be problematic for its performance.

T0 MANIPULATOR PROTOTYPE

The T0 and halo detectors will be integrated into the CBM beam line in front of the CBM target. The sensors will be mounted inside the vacuum, in standard CF 100 vacuum chambers (see Fig. 3). The feed-through PCBs will be glued into blind flanges.

The T0 detector will be operated for beam intensities of 10^7 particles/s. For higher beam intensities, the T0 detector will need to be removed from the beam axis. We plan to use a step motor in combination with a flexible bellow to allow the remote movement of the sensor from the beam axis. A schematic drawing of a prototype, which is currently being built, is shown in Fig. 3 (right).

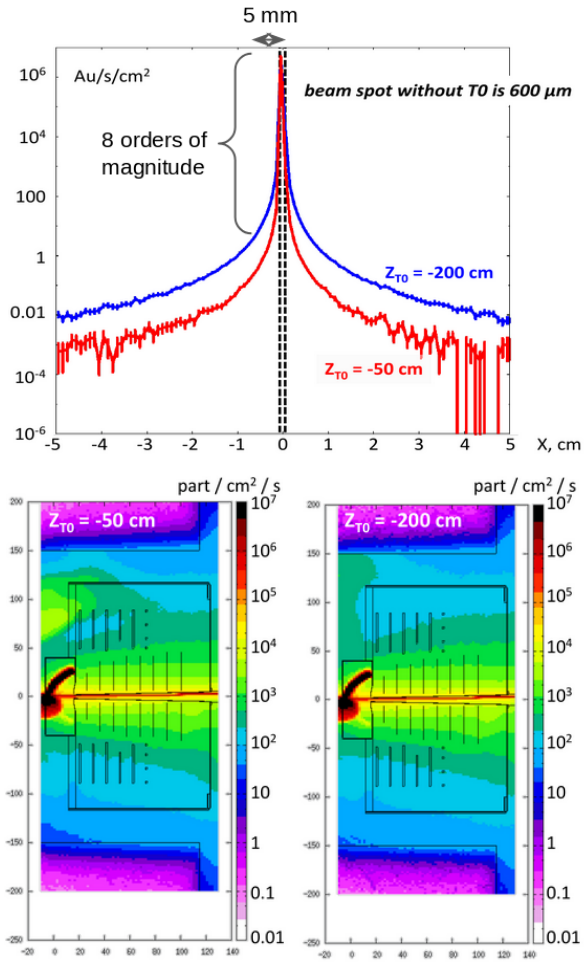


Figure 2: Widening of the beam and charged particle contamination in the STS region for two different T0 positions. **Upper panel:** The widening of the beam due to the diamond material of the T0 detector, which is located 50 cm (red curve) and 200 cm (blue curve) in front of the CBM target. **Lower panel:** The charged particle contamination in the STS region for the two different T0 positions.

SENSOR MOUNT AND FEED-THROUGH PRINTED CIRCUIT BOARD

The T0 sensor will be bonded to a dedicated [6] printed circuit board (PCB) that serves as a sensor holder. A schematic picture of such a PCB is shown in Fig. 4.

To compensate for radiation damage, which will result in a decrease of the signal amplitude, two analog amplification stages are implemented close to the sensor. The sensor PCB will be mounted inside the vacuum chambers. The feed-through PCB (see green part in Fig. 4) will be glued into the flanges of the vacuum chamber.

The T0 detector is designed to operate at beam intensities of up to 10^7 particles/s. Assuming a beam spot diameter of 0.5 cm on the T0 sensor with a metalization of 16 stripes, a rate of 1 MHz per readout channel is expected. The analog signals are discriminated using the PADI ASIC [7] and a

Content from this work may be used under the terms of the CC-BY-4.0 licence (© 2023). Any distribution of this work must maintain attribution to the author(s), title of the work, publisher, and DOI

ISBN: 978-3-95450-236-3 ISSN: 2673-5350 doi:10.18429/JACoW-IBIC2023-MOP018

Content from this work may be used under the terms of the CC-BY-4.0 licence (© 2023). Any distribution of this work must maintain attribution to the author(s), title of the work, publisher, and DOI

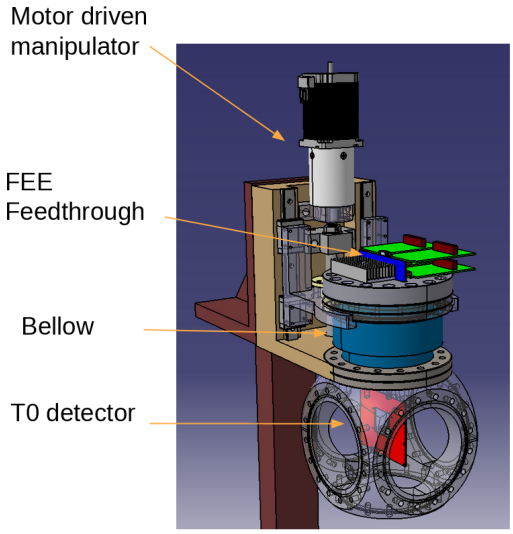


Figure 3: Schematic illustration of the manipulator system for removing the T0 detector from the beam axis.

time-to-digital converter (TDC) is used, the Get4 ASIC [8]. Digital data is then sent to a single Common Readout Interface (CRI) board. A detailed description of the readout system can be found in [2].

SUMMARY AND OUTLOOK

A concept for the CBM BMON detector, consisting of a T0 station and a halo station, has been developed. The T0 station will be used to measure the time of arrival of particles with a precision of 50 ps. It will also be used for beam monitoring purposes and as part of a fast beam abort system.

The system is currently planned to be based on polycrystalline chemical vapor deposition (pcCVD) diamond technology. However, we are also evaluating the recently developed Low Gain Avalanche Detector (LGAD) technology.

The impact of the T0 detector on the performance of the CBM detector system has been studied. It was found that the T0 detector does not negatively influence the performance of the CBM detector system.

A manipulator system has been developed to remove the T0 detector from the beam axis. A demonstrator of the manipulator system is currently in production.

A prototype T0 detector based on pcCVD diamond material has been successfully tested at previous mCBM campaigns. For upcoming campaigns, we plan to further test the T0 detector and evaluate LGAD technology.

ACKNOWLEDGEMENTS

This project has received funding from the European Union's Horizon 2020 research and innovation programme under grant agreement No. 871072. We would like to thank TU Darmstadt and GSI Detector Laboratory for the preparation of the diamond sensors.

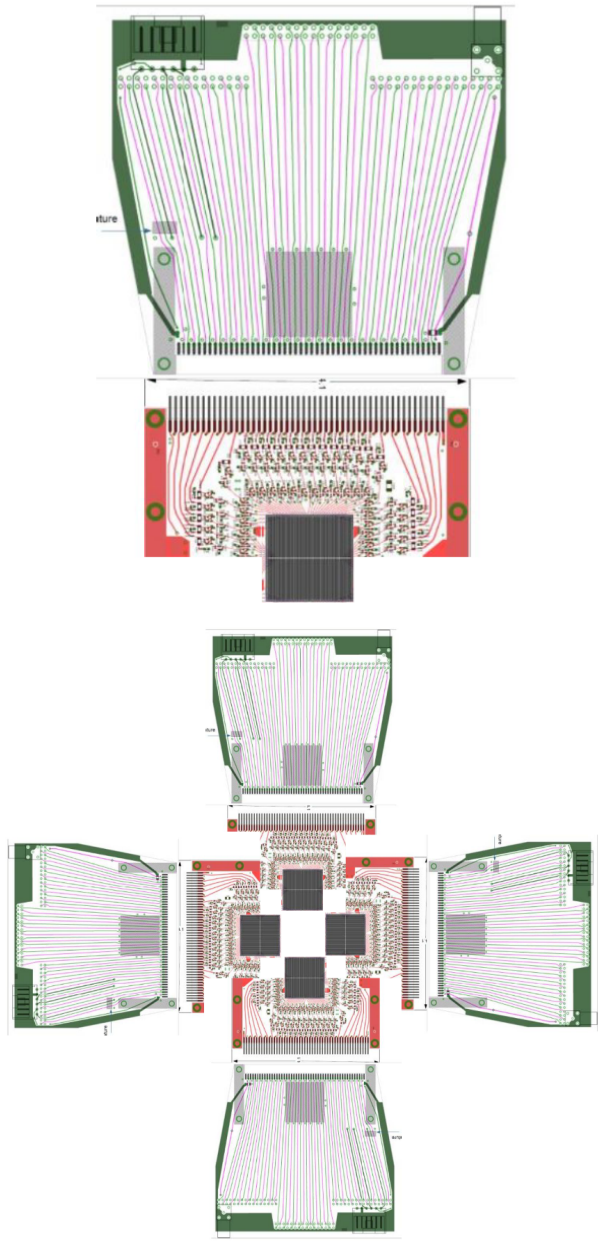


Figure 4: Sensor mount and feed-through PCB. The sensor will be glued into the recess and then bonded to the amplification stage input pads. **Upper panel:** One PCB is needed for the T0 system. **Lower panel:** A mosaic arrangement of four PCBs is used for the halo system.

REFERENCES

[1] P. Senger, "Exploring Cosmic Matter in the Laboratory - The Compressed Baryonic Matter Experiment at FAIR," *Particles*, vol. 2, no. 4, pp. 499–510, 2019. doi:10.3390/particles2040031

[2] A. Rost *et al.*, "Status of Diamond and LGAD Based Beam-Detectors for the mCBM and CBM Experiments at GSI and FAIR", in *Proc. IPAC'22*, Bangkok, Thailand, Jun. 2022, pp. 247–250. doi:10.18429/JACoW-IPAC2022-MOPOPT010

ISBN: 978-3-95450-236-3 ISSN: 2673-5350 doi:10.18429/JACoW-IBIC2023-MOP018

[3] J. Pietraszko, T. Galatyuk, V. Grilj, W. Koenig, S. Spataro, and M. Träger, "Radiation damage in single crystal CVD diamond material investigated with a high current relativistic 197Au beam," *Nucl. Instrum. Meth.*, vol. 763, pp. 1–5, 2014. doi:10.1016/j.nima.2014.06.006

[4] W. Krüger *et al.*, "LGAD technology for HADES, accelerator and medical applications", *Nucl. Instrum. Meth.*, vol. A1039, pp. 167046, 2022. doi:10.1016/j.nima.2022.167046

[5] J. Heuser *et al.*, "Technical Design Report for the CBM Silicon Tracking System (STS)", GSI, Darmstadt, Germany, GSI Report 2013-4, 2013.

[6] J. Pietraszko *et al.* "Low Gain Avalanche Detectors for the HADES reaction time (T0) detector upgrade," *Eur. Phys. J. A*, vol. 56, p. 183, 2020. doi:10.1140/epja/s10050-020-00186-w

[7] M. Ciobanu *et al.*, "PADI, an Ultrafast Preamplifier - Discriminator ASIC for Time-of-Flight Measurements," in *IEEE Transactions on Nuclear Science*, vol. 61, no. 2, pp. 1015–1023, Apr. 2014, doi:10.1109/TNS.2014.2305999

[8] H. Deppe and H. Flemming, "The GSI event-driven TDC with 4 channels GET4," *IEEE Nuclear Science Symposium Conference Record (NSS/MIC)*, pp. 295–298, 2009. doi:10.1109/NSSMIC.2009.5401741

Content from this work may be used under the terms of the CC-BY-4.0 licence (© 2023). Any distribution of this work must maintain attribution to the author(s), title of the work, publisher, and DOI

ISBN: 978-3-95450-236-3 ISSN: 2673-5350 doi:10.18429/JACoW-IBIC2023-MOP019

FIRST TEST WITH MICROTCA BASED CAVITY BPM ELECTRONICS FOR THE EUROPEAN XFEL AND FLASH

B. Lorbeer*, H. T. Duhme, I. Krouptchenkov, T. Lensch, D. Lipka, M. Werner
Deutsches Elektronen-Synchrotron DESY, Germany

Abstract

The European X-ray free-electron laser (E-XFEL) and the FLASH2020+ project for the free electron laser Hamburg (FLASH) at DESY in Hamburg, Germany foresee several machine upgrades in the years to come. At FLASH a whole undulator section in a shutdown starting in summer 2024 and finishing in autumn 2025 is going to be rebuild. Existing button beam position monitors installed in this section of the machine do not deliver sufficient signal strength for future required resolution specification and orbit feedback optimization for machine operation. The resolution limitations will be overcome by replacing the button-based beam position monitors with in-house developed cavity beam position monitors and compact microTCA based radio frequency receiver read-out electronics. The measurement system has been tested and evaluated in a test setup at FLASH.

INTRODUCTION

The two international user facilities European X-ray free-electron (E-XFEL) and the free-electron laser of Hamburg (FLASH) are operated by the Deutsches Elektronen-Synchrotron (DESY) in Hamburg, Germany. Both machines are based on the effect of self-amplified spontaneous emission (SASE) which generates ultra-short photon pulses by cascading several undulators. The photon pulses are based on accelerated electron-bunches which originate from a photo injector driven radio frequency (RF) electron gun. The electron bunches are accelerated in a pulsed superconducting linac at a repetition rate of up to 4.5 MHz. More specifications on the different machine parameters can be found here [1]. The high-resolution transversal beam position measurement of the electron beam along the machines is realized with cavity beam position monitors (CAVBPM). The E-XFEL is already equipped with well performing monitors including read-out electronics [2] from in-kind contribution partners. However, future planned upgrades of the machine [3] with additional CAVBPM will be based on in-house developed read-out electronics. Like the E-XFEL the FLASH facility will be upgraded with approximately 20 monitors within the FLASH2020+ project [4]. A CAVBPM electronics read-out system has been developed in the past few years and is already in operation [5]. These electronics have been modified and enhanced to meet the specifications of the E-XFEL and FLASH where the most demanding requirement is a single bunch resolution of better than 1 um in a charge range from 20 pC up to 1 nC. First tests with these CAVBPMs have been made with a test cavity BPM at FLASH to evaluate the adapted and extended read-out electronics. The charge has been varied over the specified range and the measurement results demonstrate to fulfill the specified resolution.

* bastian.lorbeer@desy.de

CAVITY BEAM POSITION MONITORS AT FLASH AND XFEL

Cavity beam position monitors are composed of a mono-pole and a di-pole resonator from which the electron beam excited modes deliver RF signals from which the charge and the transversal position of the electron beam can be evaluated [6]. The monitors in use at the E-XFEL and in the design procedure for FLASH are also developed in-house [7] and have the characteristics listed in Table 1.

Table 1: Cavity Beam Position Monitor Characteristics E-XFEL and FLASH

Quality	Range
resonance frequency	3.3 GHz
beam pipe diameter	10 – 40.5 mm
mono-pole sensitivity	42.5 – 42.9 Vpk/nC
dipole sensitivity	2.46 – 2.87 Vpk/nC/mm
loaded quality factor	70

ANALOG SIGNAL DYNAMICS

The original developed CAVBPM monitor [8] and corresponding RF front-end electronics [5] have been designed to operate in a charge range from 500 fC up to 100 pC, while the specified charge range in the E-XFEL and at FLASH varies from 20 pC - 1 nC. Due to these different charge ranges and equivalent signal amplitudes modifications in the RF front-end were necessary. For this purpose a typical signal from a mono-pole resonator has been measured at a test cavity at FLASH. The signal is shown in Fig. 1.

Since the signals from the cavity are band-pass filtered in the first place in the RF front-end the signal strength from the band-pass filtered signal has been chosen to determine the necessary front-end dynamics. The derived quantities are summarized in Table 2.

Table 2: Estimation of Expected Signal Powers for the Charge Range From 20 pC–1 nC

Mode/States	Charge	voltage/Vpp	power/dBm
min. charge	20 pC	0.044	–23
max. charge	1 nC	22.25	31

Content from this work may be used under the terms of the CC-BY-4.0 licence (© 2023). Any distribution of this work must maintain attribution to the author(s), title of the work, publisher, and DOI

ISBN: 978-3-95450-236-3 ISSN: 2673-5350 doi:10.18429/JACoW-IBIC2023-MOP019

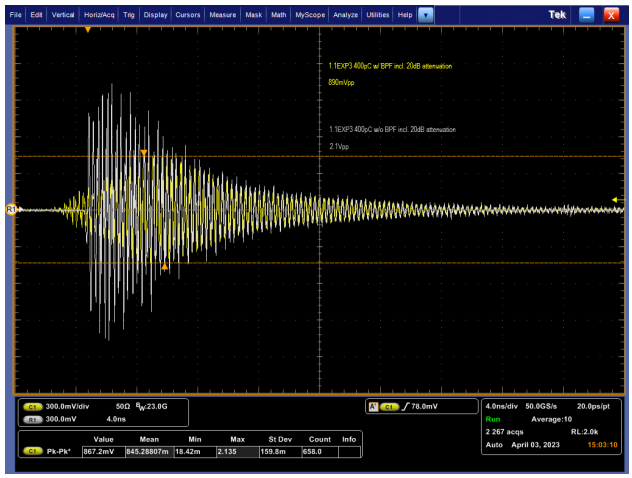


Figure 1: Analog signal from reference resonator and 20 dB additional attenuation measured at 400 pC. White trace: without band-pass filter. Yellow trace: with band-pass filter.

Therefore the mono-pole signal covers a dynamic range of approximately 60 dB with a headroom of 6 dB. A similar estimation for the signal level dynamics of the dipole signal has been made. The front-end receiver dipole channel can accept a minimum signal power of −76 dBm and a maximum of 37.75 dBm exceeding a dynamic range of 100 dB. Special care needs to be taken to avoid an operation of the front-end receiver components beyond the P1dB in amplifiers and demodulator. This is done empirically during commissioning of the electronics. For these first tests the RF front-end receiver introduced in [5] has been modified in the charge channel. The remaining component chain consists of a band-pass filter and a step-attenuator before the RF signal enters the demodulator.

MEASUREMENT SYSTEM SETUP

The measurement principle to estimate the resolution performance of the electronics is based on the idea to separate correlated beam-jitter and un-correlated electronics noise contributions in the measurement. This is done by splitting the signal from one cavity and measure the signal fluctuations in two identical electronics. To obtain a prediction of the position and charge measurement a singular value decomposition (SVD) of two independent measurement channels (either horizontal, vertical, or charge) is applied [9]. The remaining standard deviation of position and charge fluctuations reveals the un-correlated electronics noise from the two systems [1]. Figure 2 shows the connection sheet from the splitters to the modified RF front-end which is housed in a Micro TCA crate.

Data Acquisition

The signals received by the modified RF front-end receiver are digitized on a separate electronics card with six analog

[1] Excluding the losses in the splitter, which promises an improved resolution by at least a factor of $\sqrt{2}$.

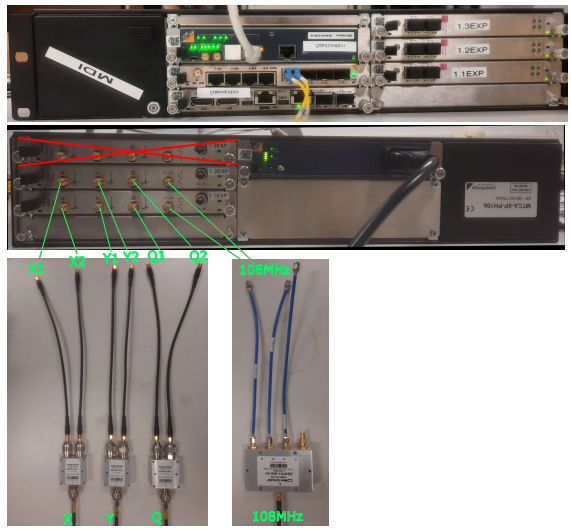


Figure 2: Micro TCA based read-out electronics including CPU, MCH, X2timer, and three digitizer cards. Three power splitters for x,y and q signals from the cavity and an additional splitter for the Master Oscillator reference frequency of 108 MHz.

to digital converters with a 16 bit resolution and a sample rate of 108 MHz. The digitized data is collected in a field programmable gate array (FPGA) and the sampled data is accessed by a hardware (HW) server process in which the final calculation of beam charge and position takes place. To synchronize the local oscillator (LO) phase and obtain phase stable measurements it is necessary to program the phase locked loop (PLL) on the RF front-end receiver from the server panel shown in Fig. 3.

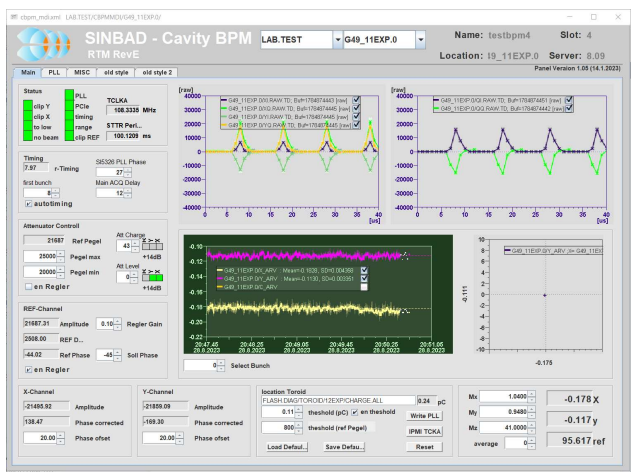


Figure 3: Hardware server with RF front-end interface, raw data read-out and calculated horizontal and vertical position and charge data.

Additional important features of the server are:

- data timing and phasing of intermediate (IF) signals
- a global gain control to adjust signal level depending on charge and x,y-offset

Content from this work may be used under the terms of the CC-BY-4.0 licence (© 2023). Any distribution of this work must maintain attribution to the author(s), title of the work, publisher, and DOI

ISBN: 978-3-95450-236-3 ISSN: 2673-5350 doi:10.18429/JACoW-IBIC2023-MOP019

Content from this work may be used under the terms of the CC-BY-4.0 licence (© 2023). Any distribution of this work must maintain attribution to the author(s), title of the work, publisher, and DOI

- LO reference phase control to stabilize the reference cavity with respect to machine phase and optimize stability and reproducability
- phase offset which need to be adjusted once to find the correct quadrant and sign of di-pole signals phase change
- scaling factors for x, y, and q to adjust calculated values to reasonable physical quantities.

Calibration

The test cavity BPM is mounted on a mover stage with an internal accuracy of 1 µm which can be moved during electron beam operation. Finding the correct scaling factor has been done in an iterative manner by physical movement of the cavity with the help from the mover stage and then comparing the measured value from the electronics. After comparison the scaling factor has been corrected so the measured value matches the physical movement. This has been done over a measurement range of +/- 500 µm. The scaling of the charge values has been done by comparing the readings from a nearby charge measurement monitor and adjusted accordingly to deliver similar results.

MEASUREMENT RESULTS

A synchronous read-out of position and charge data for 220 subsequent bunches has been realized to enable the separation of correlated beam jitter and the un-correlated electronics noise. The result can be shown as a function of the predicted value for the measured charge and position data sets. During the measurement the minimum measured charge has been 19 pC and the maximum was around 307 pC. Figure 4 shows the measured charge versus the predicted charge at 19 pC and Fig. 5 shows the measured x-position versus the predicted x position at a charge of 91 pC.

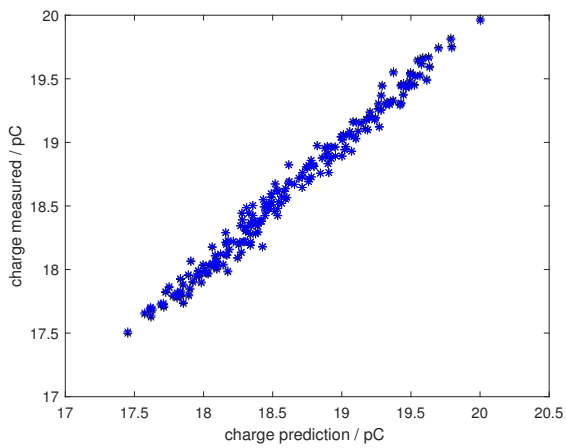


Figure 4: Correlated electronics noise from charge channel front-end receiver. The average charge is avg_q=18.78 pC and the standard deviation of the uncorrelated measurement noise is σ_q = 74 fC.

The following Table 3 shows additional charges where measurement data has been analyzed.

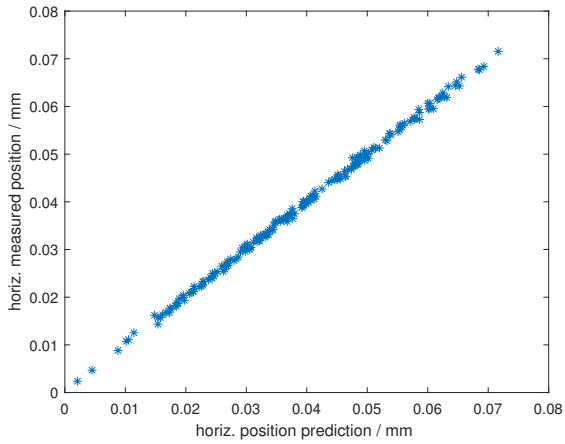


Figure 5: Measured x-position versus the predicted x position. The average charge here is σ_q = 91 pC and the standard deviation of the uncorrelated horizontal jitter is σ_x = 0.542 µm.

Table 3: Calculated resolutions based on measurements at FLASH at different charges. The calculation do not include the factor of $\sqrt{2}$ to compensate for the losses in the splitter.

Charge [pC]	σ_q [fC]	σ_x [µm]	σ_y [µm]
18.78	74	2.637	2.737
91	177	0.542	1.09
153	279	0.795	1.421
307	437	0.412	0.895

SUMMARY AND CONCLUSION

The measurements show that required electron beam position resolution of 1 µm could almost be met for a large charge range neglecting the fact of a reduced signal power of −3 dB in each RF front-end due to the power splitters in the measurement setup. The RF cables from tunnel to rack in this setup is about 50 m long. RF cables in existing cavity BPMs at E-XFEL and for future installations at FLASH2020+ will be more on the order of 30 m which will improve the signal to noise ratio to finally meet the specification goal of 1 µm also at the small charges of 20 pC.

REFERENCES

[1] W. Decking *et al.*, "A MHz-repetition-rate hard X-ray free-electron laser driven by a superconducting linear accelerator", *Nat. Photonics*, vol. 14, pp. 391–397, July 2020.

[2] M. Stadler *et al.*, "Low-Q Cavity BPM Electronics for E-XFEL, FLASH-II and SwissFEL", in *Proc. IBIC'14*, Monterey, CA, USA, Sep. 2014, paper WEPD12, pp. 670–674.

[3] S. Casalbuoni *et al.*, "European XFEL Undulators - Status and Plans", in *Proc. IPAC'22*, Bangkok, Thailand, Jun. 2022, pp. 2737–2740. doi:10.18429/JACoW-IPAC2022-THPOPT061

[4] J. Zemella, J. Roensch-Schulenburg, S. Schreiber, and M. Vogt, "Recommissioning of the FLASH injector and linac", in *Proc.*

ISBN: 978-3-95450-236-3 ISSN: 2673-5350 doi:10.18429/JACoW-IBIC2023-MOP019

IPAC'23, Venice, Italy, May 2023. doi:10.18429/JACoW-IPAC2023-TUPL022

[5] B. Lorbeer *et al.*, "Cavity BPM Electronics for SINBAD at DESY", in *Proc. IBIC'22*, Kraków, Poland, Sep. 2022, pp. 413–415. doi:10.18429/JACoW-IBIC2022-WEP14

[6] R. Lorenz, "Cavity beam position monitors", in *AIP Conf. Proc.*, vol. 451, pp. 53–73, 1998. doi:10.1063/1.57039

[7] D. Lipka *et al.*, "Production of Cavity BPMs for the European XFEL", presented at IBIC'13, Oxford, UK, 2013, FRWMJ5.

[8] D. Lipka, M. Dohlus, M. Marx, S. Vilcins, and M. Werner, "Design of a Cavity Beam Position Monitor for the ARES Accelerator at DESY", in *Proc. IBIC'18*, Shanghai, China, Sep. 2018, pp. 269–272. doi:10.18429/JACoW-IBIC2018-TUPB05

[9] N. Baboi *et al.*, "Resolution Studies at Beam Position Monitors at the FLASH Facility at DESY", in *AIP Conf. Proc.*, vol. 868, pp. 227–237, 2006. doi:10.1063/1.2401409

Content from this work may be used under the terms of the CC-BY-4.0 licence (© 2023). Any distribution of this work must maintain attribution to the author(s), title of the work, publisher, and DOI

ISBN: 978-3-95450-236-3 ISSN: 2673-5350 doi:10.18429/JACoW-IBIC2023-MOP022

REPLACEMENT OF THE SINGLE-PASS BPM SYSTEM WITH MicroTCA.4-BASED VERSATILE ELECTRONICS AT SPring-8

H. Maesaka*, [1], RIKEN SPring-8 Center, Sayo, Hyogo, Japan
H. Dewa, T. Fujita, M. Masaki, N. Hosoda[2], S. Takano[2], JASRI, Sayo, Hyogo, Japan
[1]also at JASRI, Sayo, Hyogo, Japan
[2]also at RIKEN SPring-8 Center, Sayo, Hyogo, Japan

Abstract

We have developed a versatile BPM readout electronics based on the MicroTCA.4 (MTCA.4) platform for the SPring-8 upgrade project, SPring-8-II. The new electronics are comprised of an RF frontend rear transition module (RTM) and a high-speed digitizer advance mezzanine card (AMC) having 10-channel, 16-bit, and 370 MSPS ADC. The field-programmable gate array (FPGA) on the AMC calculates both single-pass (SP) and closed-orbit distortion (COD) beam positions. The current BPM system at SPring-8 consists of approximately twenty SP-dedicated BPMs and more than 250 COD-dedicated ones. In advance of SPring-8-II, so far, we replaced half of the old SP BPM electronics with the new MTCA.4 ones and the rest of the old SP BPM electronics are being renewed this summer. The SP resolution of the new BPM electronics was confirmed to be better than 100 µm for a 0.1 nC single bunch, sufficient for SPring-8-II. The new BPM electronics were applied to regular tuning items, such as the adjustment of kicker magnets for pulsed orbit bumps in the beam injection, and the functionalities were confirmed to be compatible with the old SP BPM system. Thus, the MTCA.4-based BPM electronics are ready for SPring-8-II.

INTRODUCTION

The low-emittance upgrade of the SPring-8 storage ring, SPring-8-II [1] was proposed, and many new accelerator components have been developed. The natural emittance will be squeezed from 2.4 nm rad to 100 pm rad by reducing the beam energy from 8 GeV to 6 GeV and by using a 5-bend achromat lattice (5BA).

A new BPM system for SPring-8-II was also developed. The single-pass (SP) BPM resolution is required to be 100 µm std. for a 0.1 nC injected bunch. The error on the electrical center should be within ±100 µm before the beam-based calibration. The closed-orbit distortion (COD) BPM is demanded to be sufficiently stable within 5 µm peak-to-peak for 1 month. To fulfill these requirements, we studied the following BPM components:

1. Button BPM electrodes made of molybdenum [2].
2. Radiation-tolerant coaxial cables.
3. BPM readout electronics based on MicroTCA.4 (MTCA.4) [3].

Since the new electronics will benefit the operation of the current SPring-8 storage ring, replacement of the BPM electronics was scheduled in advance of the actual upgrade work. The SPring-8 storage ring has 48 cells (44 double-bend cells and 4 long straight ones). There are typically 6 BPMs in each cell and approximately 280 BPMs in total. Before the development of the new MTCA.4-based electronics, the existing BPM system has two types of readout electronics, COD BPM and SP BPM, and typically one BPM out of 12 (6 BPMs × 2 cells) is processed by SP BPM and the other 11 are precessed by COD BPM. Contrary to the old electronics, the new MTCA.4-based electronics have both SP BPM and COD BPM functions. Therefore, both SP BPM and COD BPM can be replaced with the MTCA.4 electronics. Since the SP BPM system is more than 25 years old and hard to maintain, we decided to replace the SP BPM electronics with the MTCA.4 ones in advance of the COD BPM. The COD BPM system will be upgraded to MTCA.4 in the actual SPring-8 upgrade work.

The new electronics were first installed into the current SPring-8 ring to implement the adaptive feed-forward correction (AFC) of the error kick from the fast helicity switching beamline [4] in 2019. Old SP BPMs connected to the four BPM heads connected to the four BPM heads selected for the AFC were replaced with the MTCA.4 at that time. Another ten units of SP BPMs were then upgraded to MTCA.4 in 2021 and the rest of the SP BPM units are being replaced in this summer shutdown period (2023).

We describe the design of the MTCA.4-based BPM electronics and introduce the software for data taking. The basic performance of the SP BPM function is presented and compared with the old SP BPMs.

MTCA.4-BASED ELECTRONICS

A block diagram of the MTCA.4-based electronics is illustrated in Fig. 1. The signal from each BPM electrode is fed into the BPM rear transition module (RTM). The signal is filtered by a band-pass filter at the accelerator frequency of 508.58 MHz and the signal level is adjusted by step attenuators and low-noise RF amplifiers. The signal is then converted to a balanced differential signal by a BALUN since the ADC on the digitizer advanced mezzanine card (AMC) receives a differential balanced signal. The digitizer AMC has 10 ADC channels and hence one board can process signals from two BPMs. The ADC has a 16-bit resolution and a maximum sampling rate of 370 MHz. Since the signal frequency is higher than the Nyquist frequency of the ADC,

* maesaka@spring8.or.jp

Content from this work may be used under the terms of the CC-BY-4.0 licence (© 2023). Any distribution of this work must maintain attribution to the author(s), title of the work, publisher, and DOI

ISBN: 978-3-95450-236-3 ISSN: 2673-5350 doi:10.18429/JACoW-IBIC2023-MOP022

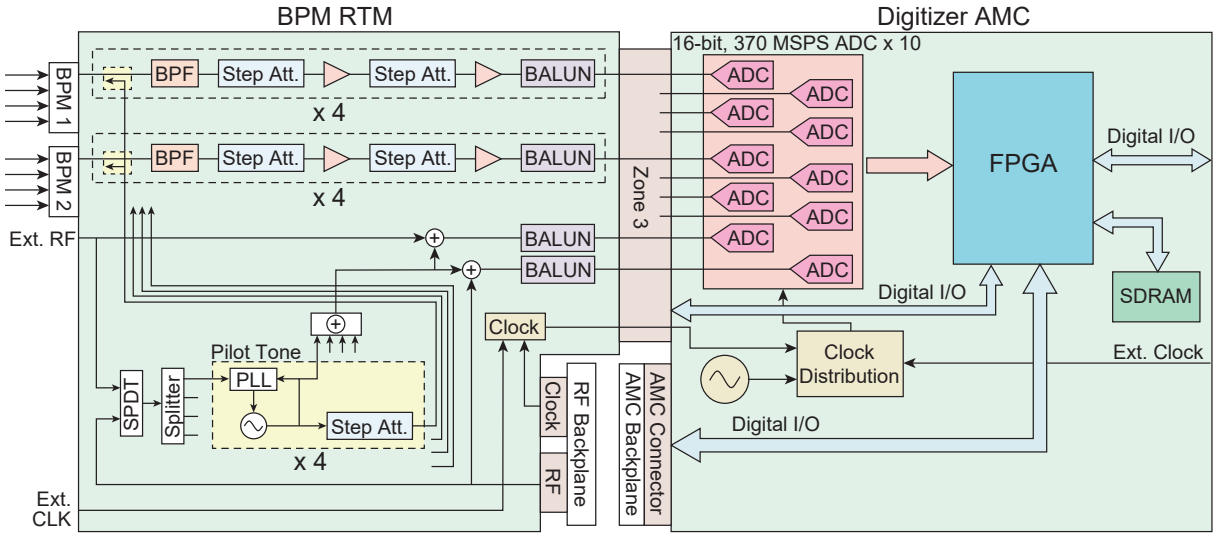


Figure 1: Block diagram of the readout electronics.

the signal is detected by an under-sampling scheme. The actual sampling frequency was set to 363.27 MHz, corresponding to 5/7 of the acceleration frequency. In this case, the waveform taken by the ADC looks like an intermediate frequency (IF) signal having 145.31 MHz. This IF signal is digitally converted to an IQ (In-phase and Quadrature) baseband signal and the amplitude and phase are calculated. The differential over summation (Δ/Σ) of the amplitudes of the four electrodes is calculated, and the beam position is obtained from a polynomial function.

To correct gain drifts etc. of the electronics, the RTM is equipped with a 4-channel pilot tone generator. Each pilot tone generator is connected to each electrode of a BPM.

In the FPGA, both SP BPM and COD BPM are processed in parallel. The SP BPM logic masks the period without any beam signal and integrates input signal power for each turn. The COD-BPM logic decimates the IQ signal to the three data rates, the revolution frequency of 209 kHz (Turn-by-Turn), 10 kHz (Fast Acquisition, FA), and 10 Hz (Slow Acquisition, SA). The Δ/Σ for each signal stream is calculated, and the beam position is computed by a 7th-order polynomial. These data are stored in the RAM on the digitizer AMC and then transferred to the CPU via a PCI-express bus.

The injection timing signal for the SP BPM trigger etc. is distributed by MTCA.4 trigger modules [5] from the SACLA linear accelerator [6]. The trigger module in the BPM system receives the trigger signal from SACLA and transmits the data acquisition trigger to the digitizer AMC via the AMC backplane.

SOFTWARE

The digitizer AMC is controlled by an MTCA.4 CPU module, where the operating system of Ubuntu 16.04 is running. The BPM system is controlled from an operating console by an MQTT messaging system, and the BPM data are taken by the MDAQ framework [7]. All the SA COD BPM data are stored in the event-synchronized database with a data rate of 10 Hz. The other COD BPM data (TbT and FA) and SP BPM data are dumped into data files on request.

Since the SP BPM data needs some timing adjustments before data taking, we developed a graphical user interface (GUI) of SP BPM for convenient data acquisition. A screenshot of the SP BPM GUI is shown in Fig. 2. By using this, we can adjust the revolution trigger timing to the bunch timing from the raw signal amplitude waveforms and then set the injection trigger timing to the first turn of the plot. After the timing adjustment, SP BPM data at an injection trigger can be easily obtained and plotted.

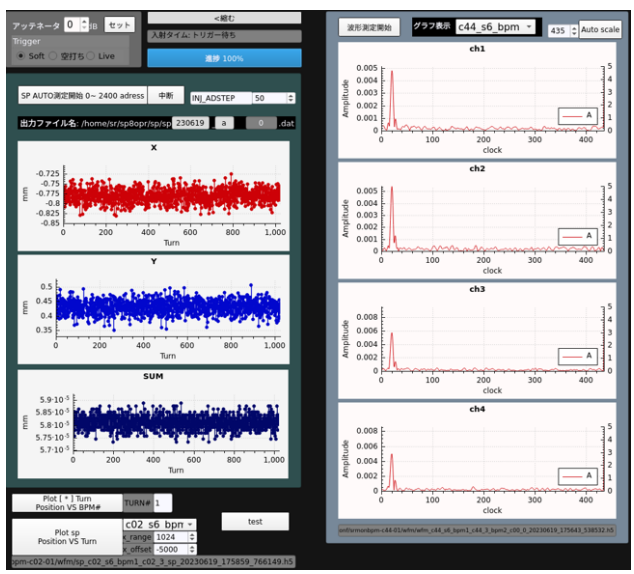


Figure 2: Screenshot of the SP BPM GUI. Horizontal and vertical positions and sum value for each turn are plotted in the left figures, along with some control widgets. The raw signal amplitude waveform for each electrode is shown in the right figures.

Content from this work may be used under the terms of the CC-BY-4.0 licence (© 2023). Any distribution of this work must maintain attribution to the author(s), title of the work, publisher, and DOI

ISBN: 978-3-95450-236-3 ISSN: 2673-5350 doi:10.18429/JACoW-IBIC2023-MOP022

Content from this work may be used under the terms of the CC-BY-4.0 licence (© 2023). Any distribution of this work must maintain attribution to the author(s), title of the work, publisher, and DOI

SP BPM DATA

Injected Beam

An example of SP BPM data from one BPM is plotted in Fig. 3, where a single bunch of approximately 0.2 nC was injected. The sum amplitude is promptly increased at the first turn and almost constant after injection. Since the injected beam is horizontally offset from the beam orbit, a large betatron oscillation was excited in the first few hundred turns. A synchrotron oscillation with a period of about 100 turns is also observed due to a finite horizontal dispersion and errors in energy and timing of the injected bunch. The vertical position data shows small but finite betatron and synchrotron oscillations due to an offset of the beam orbit of the injected bunch and dispersion leakage to the vertical direction. Since the sum signal is calculated by a vector sum of complex amplitude of the four electrodes, the beam arrival phase with respect to the reference RF signal can be also obtained, as shown in the bottom plot of Fig. 3. The synchrotron oscillation is observed in the phase of the sum signal as well, but the oscillation phase is $\pi/2$ shifted from that of the position data. This phase shift is consistent with the time evolution of electrons in the longitudinal phase space.

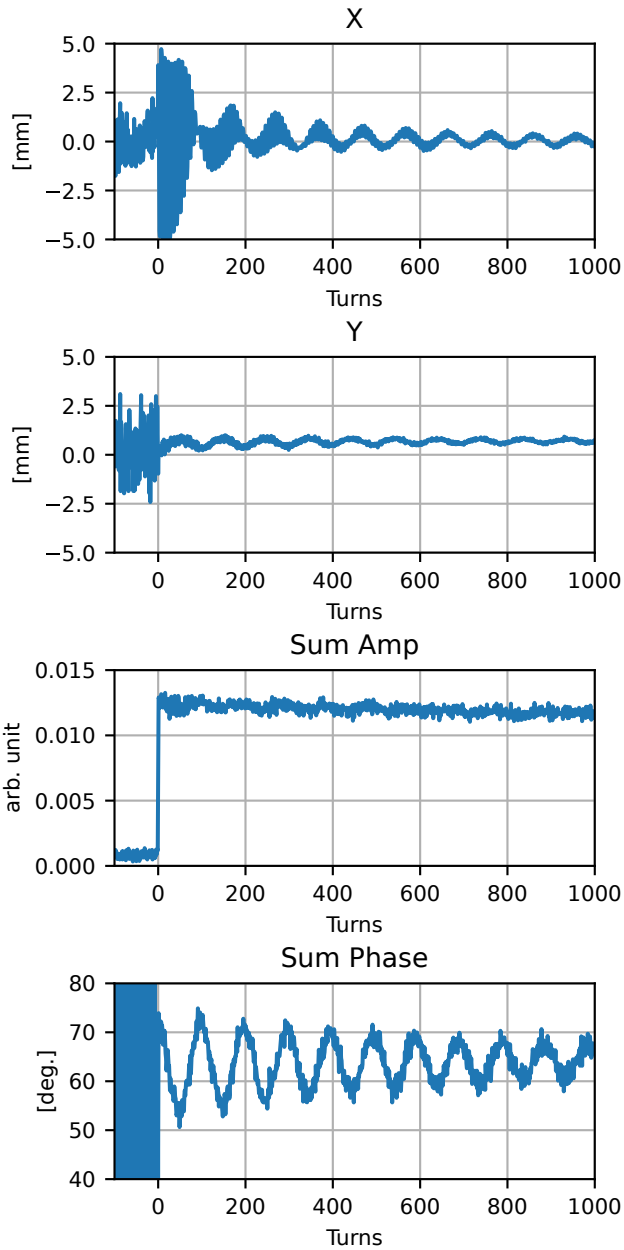


Figure 3: Example of SP BPM data from one BPM at beam injection. Horizontal and vertical beam positions, sum amplitude, and sum phase are shown from top to bottom.

Position Resolution

The position resolution was evaluated by kicking a stored single bunch with kicker magnets to make a pulsed orbit bump for beam injection. The stored current was approximately 0.1 mA, corresponding to 0.5 nC, and the amplitude of the betatron oscillation was approximately 0.4 mm. SP BPM data from 7 BPMs were taken in this measurement. We compared the beam position of one BPM with the prediction from the other 6 BPMs. Figure 4 shows a scatter plot of the horizontal beam position at a specified BPM vs. the prediction from the other BPMs. The standard deviation of the difference between data and prediction for each BPM is thought to be the position resolution. The horizontal position resolution was evaluated to be approximately 17 μm for an electron bunch with 0.5 nC, as plotted in Fig. 5. When the bunch charge is reduced to 1/5 (0.1 nC), the position resolution will be 5 times larger than this value. Even in this situation, the resolution is still below 100 μm and enough for single-pass measurements in SPring-8-II. Since the size of the SPring-8-II vacuum chamber will be smaller than that of

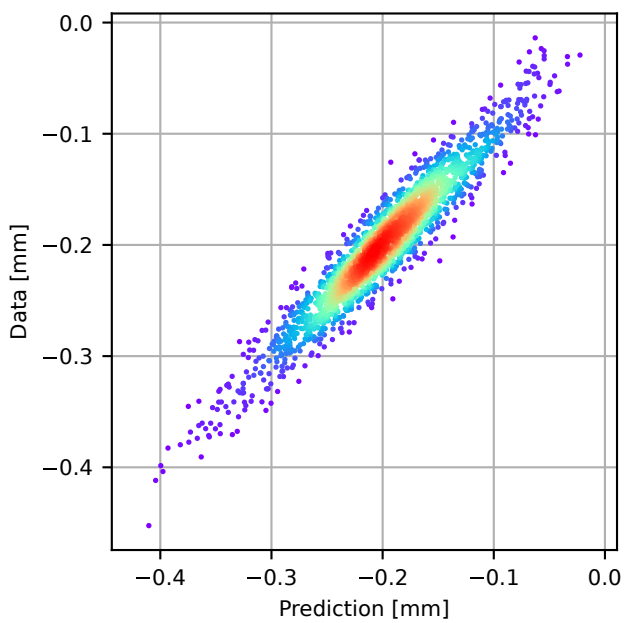


Figure 4: Comparison between the horizontal beam position at a BPM and the prediction from other BPMs.

ISBN: 978-3-95450-236-3 ISSN: 2673-5350 doi:10.18429/JACoW-IBIC2023-MOP022

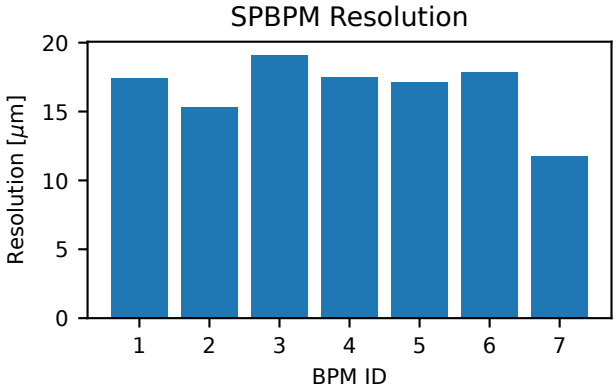


Figure 5: Horizontal SP BPM resolution of 7 BPMs.

the current SPring-8 ring, the SP BPM resolution is expected to be better than this measurement.

Injection Orbit Bump Adjustment

The current SPring-8 storage ring makes a pulsed orbit bump with four dipole kicker magnets for the off-axis beam injection. Since it is important to close the orbit bump as perfectly as possible with matched kicker waveforms so as not to affect the stored beam, adjustment of the dipole kickers is necessary at the beginning of each operation cycle [8]. The kicker magnets used to be adjusted by using the data from the old SP BPM system so that the oscillation of the stored beam is minimized. The same adjustment procedure should work well with the new MTCA.4-based BPM system.

Therefore, we measured the orbit oscillation caused by the kicker magnets with both old and new SP BPM systems to confirm that both data were consistent with each other. The SP BPM data were taken by shifting the kicker magnet timing every 50 RF buckets (98 ns), and the orbit oscillation amplitude due to the residual kick of the kicker magnets for each bunch address was evaluated. Figure 6 shows the RMS of the beam positions at the used SP BPMs as a function of the bunch address. The difference in the oscillation amplitude data between the old and new SP BPMs was small enough (less than 0.1 mm). Consequently, the new MTCA.4 SP BPM system is ready for the tuning of the current SPring-8 storage ring.

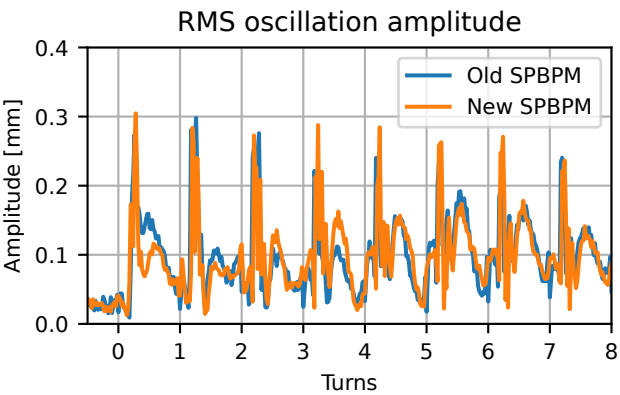


Figure 6: RMS amplitude of the orbit oscillation by the residual kick of the kicker magnets. The blue (orange) line shows the data from the old (new) SP BPM. The horizontal axis shows the bunch timing with respect to the bump pulse timing.

SUMMARY

For the next-generation hard X-ray light source project, SPring-8-II, we developed MTCA.4-based versatile BPM readout electronics. Since the new electronics are applicable to the current SPring-8, we decided to first replace the old SP BPM electronics with the new ones. After finishing the replacement of half of the SP BPM by 2021, we are now upgrading the remaining half this summer. The SP BPM performance of the MTCA.4 electronics were evaluated, and confirmed to be sufficient for both SPring-8 and SPring-8-II. The trajectory of an injected electron beam was appropriately observed. The SP BPM resolution was obtained to be 17 μm for a 0.5 nC single-bunch. The beam oscillation caused by the residual kick of the injection orbit bump was compared between the old and new electronics, and confirmed to be consistent with each other. Thus, the MTCA.4-based BPM electronics are ready for SPring-8-II, and the upgrade work of the BPM system is expected to be smoothly carried out by replacing the readout electronics in advance.

REFERENCES

[1] SPring-8-II Conceptual Design Report, Nov. 2014. http://rsc.riken.jp/pdf/SPring-8-II.pdf

[2] M. Masaki *et al.*, "Design Optimization of Button-type BPM Electrode for the SPring-8 Upgrade", in *Proc. IBIC'16*, Barcelona, Spain, Sep. 2016, pp. 360–363. doi:10.18429/JACoW-IBIC2016-TUPG18

[3] H. Maesaka *et al.*, "Development of MTCA.4-based BPM Electronics for SPring-8 Upgrade", in *Proc. IBIC'19*, Malmö, Sweden, Sep. 2019, pp. 471–474. doi:10.18429/JACoW-IBIC2019-WEBO03

[4] M. Masaki *et al.*, "Adaptive feedforward control of closed orbit distortion caused by fast helicity-switching undulators", *J. Synchrotron Rad.*, vol. 28, pp. 1758–1768, 2021. doi:10.1107/S160057752101047X

[5] H. Maesaka *et al.*, "Development of a Trigger Distribution System Based on MicroTCA.4", in *Proc. IPAC'22*, Bangkok, Thailand, Jun. 2022, pp. 1171–1173. doi:10.18429/JACoW-IPAC2022-TUPOPT067

[6] H. Maesaka *et al.*, "Full Energy On-Demand Beam Injection from SACLA to SPring-8 Storage Ring", in *Proc. IPAC'21*, Campinas, Brazil, May 2021 pp. 4508–4513. doi:10.18429/JACoW-IPAC2021-FRXA01

[7] T. Sugimoto *et al.*, "Status of the control system for fully integrated SACLA/SPring-8 accelerator complex and new 3 GeV light source being constructed at Tohoku, Japan", in *Proc. ICALEPCS'19*, New York, USA, Oct. 2019, pp. 904–908. doi:10.18429/JACoW-ICALEPCS2019-WECPL01

[8] T. Ohshima *et al.*, "Suppression of Stored Beam Oscillation Excited by Beam Injection", in *Proc. EPAC'04*, Lucerne, Switzerland, Jul. 2004, MOPKF047, pp. 414–416.

Content from this work may be used under the terms of the CC-BY-4.0 licence (© 2023). Any distribution of this work must maintain attribution to the author(s), title of the work, publisher, and DOI

ISBN: 978-3-95450-236-3 ISSN: 2673-5350 doi:10.18429/JACoW-IBIC2023-MOP023

THE CONCEPTUAL DESIGN STUDY FOR NEW BPM SIGNAL PROCESSING SYSTEM OF J-PARC MAIN RING (MR)*

K. Satou†, T. Toyama, S. Yamada, J-PARC/KEK, Tokai, Japan

Abstract

The beam position monitor signal processing system, which is a 19-year-old system, has been suffering from gain fluctuation due to contact resistance of the mechanical gain selector and communication disruption caused by an unstable contact of a card edge connector. It also has difficult repairments because some onboard parts have already reached the end of a product-life cycle, and some units have been in an unusable situation. currently, we are on the beam power upgrade campaign to 1.3 MW by increasing the beam bunch current and shortening the main ring operation cycle, and precise beam tunings would require massive waveform data processing and transfer to a storage system than the present system. For this, we have been developing a system based on the 10 GbE optical link. The ADC board, which is under development, performs direct sampling using the third harmonics of accelerating radio frequency. The digital IQ demodulation technique is used to extract the baseband oscillation from the raw data. The obtained raw waveform and closed orbit data are stored in the data storage system. In the presentation, we will report on the progress of development aimed at operation in 2025 and the conceptual design of the new system.

INTRODUCTION

In the J-PARC main ring (MR), 186 beam position monitors (BPMs) have been used to measure beam orbit and beam optic parameters [1, 2]. Its signal processor, BPM circuit (BPMC), designed 19 years ago, has two modes of position measurement:

1) Closed orbit distortion (COD) mode,
2) bunch-by-bunch (BxB) mode.

The first mode is a narrowband measurement that performs a fast Fourier transform on the waveforms digitized with 80 MHz to extract the second harmonic component of the accelerating radio frequency (RF) to obtain the COD. Meanwhile, the second mode is a broadband measurement for measuring bunch waveforms to measure the beam center of each bunch. The position measurement error is approximately 30 and 300 μm for the COD and the BxB modes, respectively [3].

At some BPMC, communication disruption was caused by an unstable contact of a card edge connector. However, this BPMC is too old that some circuit parts have already been discontinued. This makes maintenance work difficult and some BPMCs unusable. If this situation progresses, there is a risk that sooner or later stable MR operation will be hindered.

The BPMC shows the beam position shift due to the change in the contact resistance of a relay. To optimize the input signal level, it has a 20 dB fixed attenuator placed just before the input terminal and a variable attenuator in the BPMC. Depending on the beam condition, the attenuation factor is selected by switching a relay element on the circuit, and its switching frequency is approximately several times per year. The contact surfaces are then exposed to atmospheric gas for a long time because the relay is not strictly shielded. The inspection of the relay surface confirmed that the silicon-based compound was layered. This results in surface contamination and consequently resistance changes. A 0.5 Ω change in contact resistance results in an error of 1.3 mm. Moreover, an error of several millimeters– may occur because of individual differences in relays. This resistance can be reduced by applying a voltage [4]. However, there are large individual differences in this effect, and no clear systematicity has been confirmed so far, therefore, calibration is difficult. To examine the impact of this effect, some consistency check methods between the BPM sensors are now proposed [4, 5].

Moreover, beam tuning above 1 MW is supposed to require high-precision measurement of optics parameters [3]. Thus, it is necessary to process a large amount of highly accurate position data. Improvement of the system is also necessary.

NEW BPM SIGNAL PROCESSOR

We are developing a new signal processor as part of the MR beam power upgrade campaign to 1.3 MW. In the new system, we aim to reduce the position error to 1/3 or less in both modes. To achieve this, we will use the following items:

1. Reduction of the reflection coefficient of the attenuator input terminal,
2. reduction of signal distortion and gain temperature coefficient in the attenuator and ADC,
3. improvement of the vertical resolution of the ADC,
4. improved digital signal processing section.

Figure 1 shows a block diagram of the new system installed in four different buildings. It uses the existing BPM sensors and its signal cables, which are 100-300 m depending on the sensor location. An attenuator unit, ADC card, network interface controller unit (NIC unit), and data storage system have been developed.

The attenuator unit is powered by a nuclear instrumentation module (NIM) standard bin power supply and the ADC card is housed in the same NIM case. The digitized waveform data are delivered over a 10 GbE optical private network and forwarded through the NIC unit to the data storage system. This network uses the user datagram protocol (UDP).

* Work supported by Accelerator and Beamline Research and Technology Development for High-Power Neutrino Beams in the U.S.-Japan Science and Technology Cooperation Program in High Energy Physics.
† email address: kenichirou.satou@j-parc.jp

Content from this work may be used under the terms of the CC-BY-4.0 licence (© 2023). Any distribution of this work must maintain attribution to the author(s), title of the work, publisher, and DOI

ISBN: 978-3-95450-236-3 ISSN: 2673-5350 doi:10.18429/JACoW-IBIC2023-MOP023

The configuration of the attenuator units and the ADC cards will be made through the experimental physics and industrial control system (EPICS), which is a distributed control system on the accelerator control network. The COD and alarm data will also be sent to the control network through the NIC unit. The development of the attenuator unit has already been completed, and we are currently developing the ADC card, NIC unit, and data storage system.

The development of each component will be completed by the end of this fiscal year, and part of the system will be built and tested in the next fiscal year, and mass production will be completed. We plan to start operating the new BPM system by FY2025. This paper provides an overview of the new system and the functions and outlines of each component.

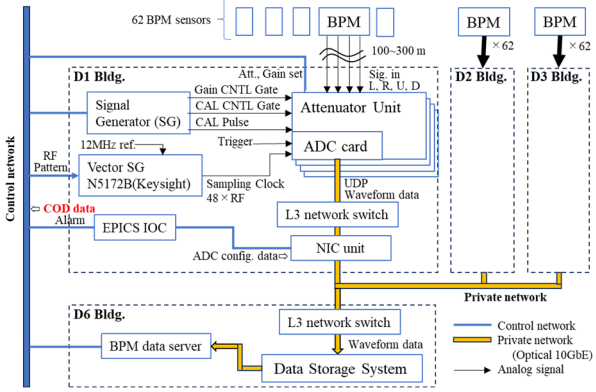


Figure 1: Block diagram of the new BPM system.

COMPONENT DESIGN

In MR, 3 GeV protons are accelerated to 30 GeV in about 1 second. The accelerating frequency of the RF accelerating devices changes from 1.672 to 1.720 MHz, with a harmonic number of 9.

The BPM sensor is a diagonal cut type, and the four signals R, L, U, and D from the right, left, top, and bottom electrodes are transmitted to the BPM signal processing unit via 5D-FB coaxial cables. The sensor capacitance and 50 Ω input impedance form a high-pass filter with a cutoff frequency of approximately 16 MHz, resulting in an output pulse shape of the derivative of the charge bunch as shown in Fig. 2.

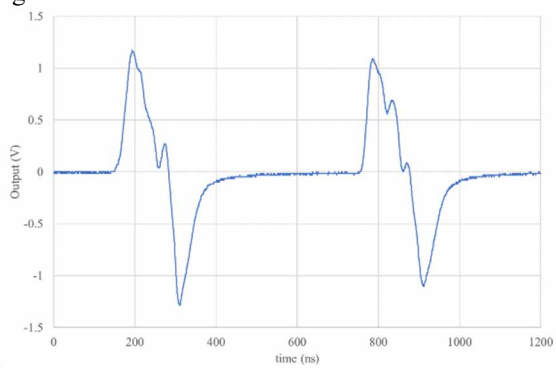


Figure 2: Beam pulse shape of 3 GeV beam.

Attenuator Unit

The new attenuator device has already been developed and is in mass production [6]. Figure 3 shows a block diagram of the new attenuator device.

As the beam bunch shape becomes sharper with acceleration, the signal reaches a maximum voltage of 200 V peak to peak (Vpp) when the beam energy of 30 GeV is reached. To match the input level of an ADC of 2 Vpp, the input signal is attenuated through an RF2033 power divider (−12 dB), a switchable attenuator (−10 dB or 0 dB), a variable gain (G = 1 or 1/2), and an RF transformer (1/2).

The new attenuator uses a reed relay, HFS-1C-05W (manufactured by OKITA Works Co., Ltd.), enclosed in a glass tube filled with nitrogen. It is expected that the contact resistance will be stable for a long time because it is not affected by dust or atmospheric gas because of its sealing. From the Ref. [7], it can be seen that if the reed relay was used within 2E6 times, the contact resistance would be approximately 10 mΩ. This impedance change induces beam position variation of approximately 4 μm. It was implemented using a special socket so that it can be replaced in case the relay exceeds its usage limit or is damaged.

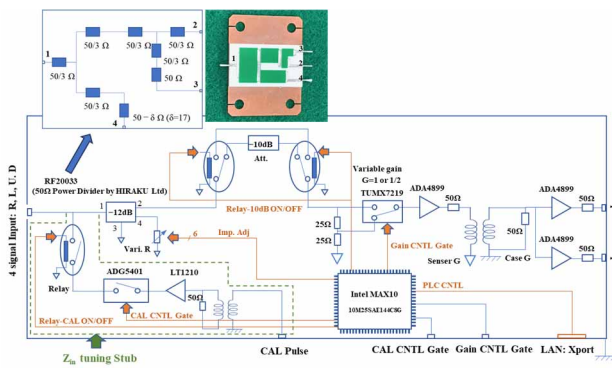


Figure 3: Block diagram of the new attenuator unit.

In the BxB measurements, impedance matching between the signal cable and the attenuator device is important. To achieve fine matching, a circuit to adjust the input impedance was implemented. For adjustment, the power divider RF2033 produced by HIRAKU Ltd. is used (Fig. 3). If a 17 Ω resistor is connected to terminal 4, the input impedance (Z_{in}) and attenuation (Att) seen from the input becomes 50 Ω and 1/4 (−12 dB), respectively.

When 17−δ Ω is connected to this terminal, the impedance seen from the input is given by

$$Z_{in} = 50 - \frac{\delta}{4} - \frac{3}{800}\delta^2. \quad (1)$$

Therefore, Z_{in} can be finely adjusted by the δ with a variable resistor. At the same time, the δ modulates the attenuation to be

$$Att = \frac{3}{8}\frac{400 - 3\delta}{600 - 3\delta}. \quad (2)$$

A high intensity beam can produce up to 200 Vpp at the input terminal of the attenuator unit, so the signal must be attenuated to match the input level of the ADC circuit.

By driving the Z_{in} with any test signal, the gain balance of each channel, cable attenuation, and matching between

Content from this work may be used under the terms of the CC-BY-4.0 licence (© 2023). Any distribution of this work must maintain attribution to the author(s), title of the work, publisher, and DOI

ISBN: 978-3-95450-236-3 ISSN: 2673-5350 doi:10.18429/JACoW-IBIC2023-MOP023

Content from this work may be used under the terms of the CC-BY-4.0 licence (© 2023). Any distribution of this work must maintain attribution to the author(s), title of the work, publisher, and DOI

the cable and Z_{in} can be measured. As shown in Fig. 1, the Z_{in} tuning stab circuit is connected by turning on Relay-CAL. Then, the Z_{in} can be excited with a waveform input from CAL_SIG. The relay is used here because the voltage at Z_{in} is expected to be at a maximum of 200 Vpp for the designed beam power operations.

A burst wave of 5 MHz, its frequency in the main signal band to be processed at the ADC card, is used as a test signal. The wave height of the input wave (first wave) determines the total gain of the attenuator unit and ADC card. The first wave is reflected by the BPM sensor's capacitance (130 pF), and the returned wave is observed as the second wave. The cable attenuation can be estimated from the signal ratio of the second wave to the first wave considering the reflection at the BPM sensor. Before the second wave arrives, it turns off the MOSFET switch ADG5401 by the CAL CNTL GATE to disconnect the impedance of the drive amp from Z_{in}. If the Z_{in} does not match the cable impedance, a part of the second wave will be reflected to the BPM sensor and then observed as the third wave. The reflection coefficient at Z_{in} can be calculated from the third wave, where the third wave height depends on the reflection at Z_{in}, cable attenuation, and reflection at the BPM sensor. Here, at a frequency of approximately 5 MHz, the electrical length is approximately 40 m. Thus, the reflection inside the N-type connector used can be ignored.

Figure 4 shows the test results using a 200 m 3D-FB cable with a Z_{in} of 50 Ω. From the wave heights of the first and second waves, the cable attenuation was estimated to be 32 dB/km at 5 MHz. The actual BPM cable is NH-5D-FB, and its cable attenuation is approximately 1/5. From the third wave, the reflection efficiency at Z_{in} was estimated to be 1.02. In the actual operation, matching is achieved by adjusting Z_{in} so that the wave height of the third wave becomes the minimum value.

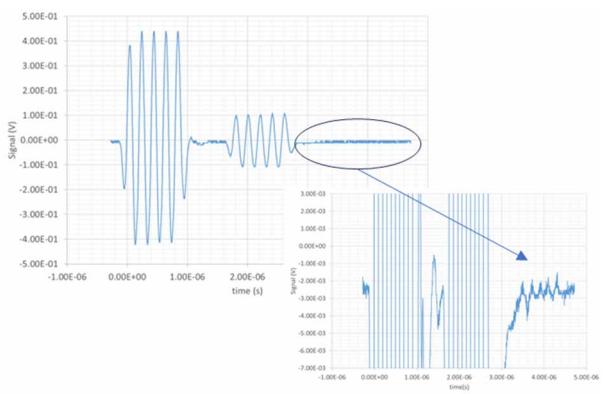


Figure 4: Calibration test signal input at the Z_{in} and multi-reflected waves. The third wave shows impedance mismatching at the input terminal.

In the actual operation, the Relay-CAL is turned off. Therefore, it is necessary that Z_{in} does not change due to the relay operation. The upper part of Fig. 5 shows the difference in S11 with and without the Z_{in} tuning stub circuit. Here, Z_{in} was set to 50 Ω (δ=17). The voltage standing wave ratio (VSWR) at the input terminal was measured in the range of 1 to 10 MHz. In the range of 1 to 5 MHz, they are almost the same within the error. However, in the range of 5 to 10 MHz, the compensation circuit is slightly over-compensated, and a difference of approximately VSWR = 0.002 appears. Currently, the VSWR is within 1.005 in the range of 1 to 10 MHz. The lower part of Fig. 5 shows the Smith chart of Z_{in} at 5 MHz where Z_{in} was shifted by changing δ. As shown in the figure, the impedance moves in the range of 50 ± 1 Ω along the line $\mathrm{Im}(Z_{in}) = 0$. The impedance step is 0.037 Ω, which allows impedance matching down to VSWR < 1.001.

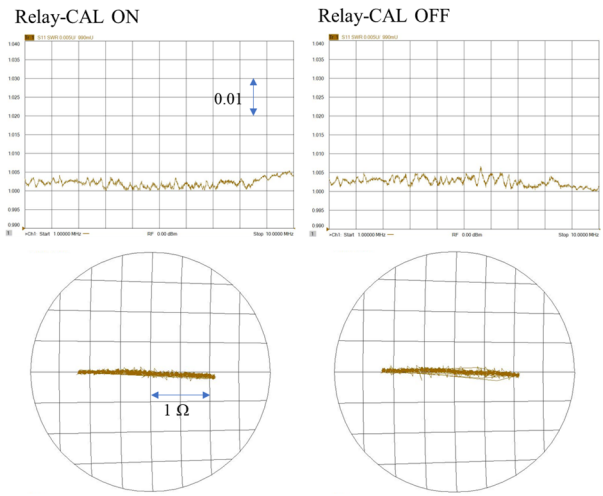


Figure 5: Measurement of impedance matching at the input terminal with and without the Z_{in} tuning stub circuit. The upper part shows VSWR when $Z_{in} = 50\ \Omega$. The lower part shows the footprint in the Smith chart when changing the input impedance.

ADC Card

Figure 6 shows a block diagram of the ADC card under development. The ADC card uses two 16-bit ADCs, LTC2194 from Analog Devices, which perform direct sampling using a 48-multiplied RF clock of approximately 82 MHz. The sampling clock is directly generated using a vector signal generator (SG) N5172B from Keysight based on the RF pattern IQ data and input to the ADC card.

The raw waveform data from the LTC2194 is transmitted and processed using an Arria 10 FPGA from Intel. The timing of each waveform data from a different BPM sensor is synchronized with a delay circuit in the FPGA. To decrease beam signal fluctuations and random noises at each measurement, we average over 1 to N cycles (1 to N MR beam shots) at 1.3 to 5 s MR trigger intervals. For the waveforms processed, filtering with narrowband BPF and IQ demodulation with the third harmonics of the RF is performed to extract a betatron oscillation. Then the I and Q data are processed with LPF, and the amplitude R and a phase θ are calculated. The R data are further processed using LPF, then a sum Σ and a difference δ between the R (U) and L (D) are calculated to obtain horizontal and vertical COD waveform data of approximately 2kSps. When the COD exceeds its preset threshold value, an alarm signal is generated to dump the beams.

ISBN: 978-3-95450-236-3 ISSN: 2673-5350 doi:10.18429/JACoW-IBIC2023-MOP023

Part of the raw waveform data, all waveform data of R, θ, δ, Σ, and the alarm status are stored in DDR4 memory and transferred to the NIC unit by using UDP via a 10 GbE SFP+ optical port.

The processing functions, COD alarm threshold level, and raw data to be saved and transferred are dynamically set by reading the configuration register in the FPGA. The configuration register can be edited through the USB port or from the NIC unit via the SFP+ port.

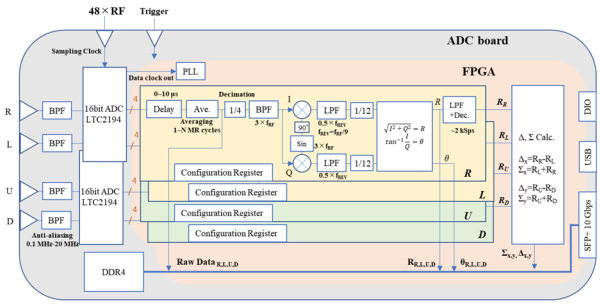


Figure 6: Block diagram of the ADC card.

Network Interface Controller Unit

The NIC unit under development is responsible for communicating with the ADC card though the private optical network, acquiring a set of waveform data from different ADC cards, and sending it to the data storage system. Furthermore, it communicates with an EPICS IOC (Input output controller) via a dedicated API (Application Interface) and delivers the COD data and alarm status onto the control network. The user can write the set value to the configuration register of the ADC card via EPICS records and then read the set value back to the EPICS records.

Data Storage System

The data storage system under development stores a large amount of waveform data sent via UDP from the NIC unit. This system has 16 SATA 16 TB HDD storage and builds RAID5 or 6 with a dedicated hardware RAID card.

In UDP communication, the order in which the data flames transferred from the NIC unit are received is different, and there is no protection against flame data loss. It has the advantage of having less overhead during transfer and can be processed at high speed. The input communication card of the data storage system rearranges the data flames based on the time information in the header information of each flame data and organizes them into a file at each MR cycle. When a flame loss occurs, the user is notified, but no retransmission request is made.

A large amount of waveform data is written in this file, however, the user usually needs only a part of the data, such as the beam oscillation data immediately after beam injection and beam motions when the machine status is changed. It is inefficient to read all data in the file and search for analysis points. Therefore, we consider adopting the HDF5 format as a file system that can extract and read some of the data stored.

CONCLUSION

We are developing a next-generation BPM data processing system to replace the outdated BPMC system, a 19-year-old system since its design. In the new system components, an attenuator unit has been developed and is in mass production. We are currently fine tuning the circuit.

We are now conducting a design study for the ADC card, NIC unit, and data storage system. We plan to complete these developments by JFY2023. Additionally, we plan to build a part of the full system with limited modules in JFY2024, and launch a new system in JFY2025. However, the availability of the FPGA chip, Arria10 270, used in the ADC card is now poor, and there are no prospects for full mass production. Although it appears to be improved in the future, it is necessary to closely examine the FPGA production status.

REFERENCES

[1] K. Satou *et al.*, "Beam Diagnostic System of the Main Ring Synchrotron of J-PARC", in *Proc. HB'08*, Nashville, TN, USA, Aug. 2008, paper WGF11, pp. 472-474.

[2] T. Toyama *et al.*, "Performance and Upgrade of BPMs at the J-PARC MR", in *Proc. IBIC2012*, Tsukuba, Japan, Oct. 2012, paper MOPA26, pp. 107-111.

[3] S. Igarashi *et al.*, "Accelerator design for 1.3-MW beam power operation of the J-PARC Main Ring", *Prog. Theor. Exp. Phys.* vol. 2021, p. 033G01, 2021. doi.org/10.1093/ptep/ptab011

[4] T. Toyama *et al.*, "Recovery and check of the switching relay in the BPMs in the J-PARC MR", presented at the IPAC'23, Venice, Italy, May 2023, paper THPL104, to be published.

[5] T. Asami *et al.*, "High accuracy optics measurement in JPARC MR for 1.3 MW upgrade plan", in *Proceedings of the 19th Annual Meeting of Particle Accelerator Society of Japan*, August 29 – September 1, 2023, Funabashi, Japan.

[6] K. Satou *et al.*, "Development of Signal Attenuator with Low Reflection and Low Distortion for New BPM Signal Acquisition System of J-PARC MR", in *Proceedings of the 19th Annual Meeting of Particle Accelerator Society of Japan*, October 18-21, 2022, Online (Kyushu University), in Japanese.

[7] "OKITA RELAYS CATALOG", OKITA Works Co., Ltd.

Content from this work may be used under the terms of the CC-BY-4.0 licence (© 2023). Any distribution of this work must maintain attribution to the author(s), title of the work, publisher, and DOI

ISBN: 978-3-95450-236-3 ISSN: 2673-5350 doi:10.18429/JACoW-IBIC2023-MOP026

A NOVEL BPM MECHANICAL CENTER CALIBRATION METHOD BASED ON LASER RANGING

Xuhui Tang[1], Yanfeng Sui[1], Jun He, Yaoyao Du, Jianshe Cao, Junhui Yue†
Institute of High Energy Physics, Chinese Academy of Science, Beijing, China
[1] also at University of Chinese Academy of Science, Beijing, China

Abstract

Determining the mechanical center of the beam position monitor (BPM) has been a difficulty for BPM calibration. To solve this problem, a method of positioning the BPM mechanical center based on laser ranging is proposed. This method uses high-precision antenna support as the core locating datum, and high-precision laser ranging sensor (LRS) as the detection tool. By detecting the distances from the LRSs to the antenna support and the distances from the LRSs to the BPM, the mechanical center of the BPM can be indirectly determined. The theoretical system error of this method is within 20 μm, and the experimental results show that the measurement repeatability is 15 μm, This method has low cost and fast speed, which can be used for large-scale calibration.

INTRODUCTION

The BPM system, as the eyes of the particle accelerator, plays an important role in the stability of the beam orbit. About 600 BPMs are produced during the construction of High Energy Photon Source (HEPS) project [1]. Due to processing errors, the mechanical center and electrical center of BPM do not coincide. Therefore, each BPM is demanded to calibrate before use [2]. For the button-type BPM with 45-degree rotation, as shown in Fig. 1, the relationship between position coordinates and electrode signal amplitudes is defined as Eq. (1) [3].

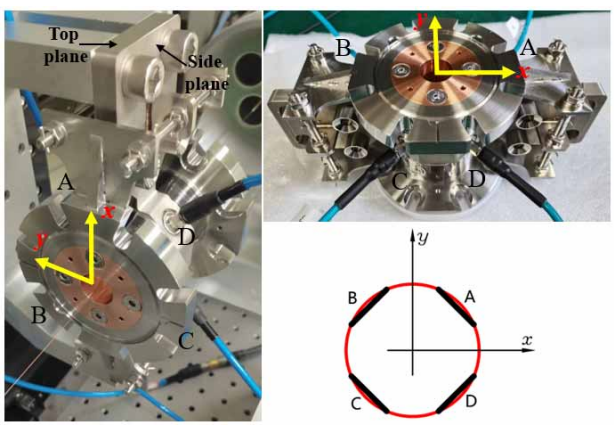


Figure 1: A HEPS BPM and its define of electrode and beam coordinate system.

$$x = K_x \frac{V_a + V_d - V_b - V_c}{V_a + V_b + V_c + V_d} + X_{\text{offset}} = K_x U + X_{\text{offset}} \quad (1)$$

$$y = K_y \frac{V_a + V_b - V_c - V_d}{V_a + V_b + V_c + V_d} + Y_{\text{offset}} = K_y V + Y_{\text{offset}}$$

where K_x, K_y are the BPM sensitivity coefficients, X_{offset}, Y_{offset} are the difference between the BPM electrical center and mechanical center. The process of determining K_x, K_y, X_{offset}, and Y_{offset} is called BPM calibration. A BPM automatic calibration system is shown in Fig. 2 and it is composed of an RF signal source, antenna (Goubau line), precision motion stages and their controller, BPM electronics, and the industrial personal computer [4, 5]. The Goubau line emits transverse electromagnetic (TEM) waves with the excitation of the RF signal source, so as to simulate the electromagnetic field of the charged particle beam in the accelerator to enable BPM calibration [5]. The BPM is driven by the precision motion stages to move in horizontal and vertical directions. The industrial computer saves the real BPM position data recorded by the controller and the calculated BPM position data from the BPM electronics. Then, the sensitivity coefficients and offsets are analyzed by the software algorithm.

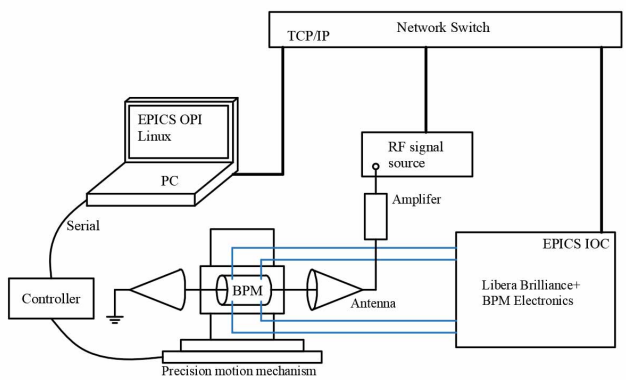


Figure 2: Schematic of BPM automatic calibration system.

In general, it is relatively easy to ascertain the BPM electrical center, as long as the operator observes the four channels of BPM electronics and makes them equal by adjusting the BPM motion stage. To achieve this goal, it is necessary to ensure that the four channels of BPM electronics and the coaxial cables are calibrated. However, finding the mechanical center is extremely difficult, so it is hard to determine X_{offset} and Y_{offset}.

A NEW APPROACH TO DETERMINING BPM MECHANICAL CENTER

The main difficulties in calibrating the mechanical center are as follows: firstly, it is not easy to ensure that the antenna is parallel to the axis of BPM; Secondly, it is almost impossible to directly measure the distance between

Content from this work may be used under the terms of the CC-BY-4.0 licence (© 2023). Any distribution of this work must maintain attribution to the author(s), title of the work, publisher, and DOI

ISBN: 978-3-95450-236-3 ISSN: 2673-5350 doi:10.18429/JACoW-IBIC2023-MOP026

the antenna and the edge of the BPM vacuum chamber; Finally, the high accuracy requirement (tens of micrometers) poses great challenges for manual adjustment. In order to solve the problems above, a high-precision antenna positioning support was designed, and a high-performance laser ranging sensor (span 30±4 mm, resolution 0.5 μm) was introduced as the detection tool for the system self-inspection and seeking BPM mechanical center. The schematic diagram of the positioning system is shown in Fig. 3, where the uppercase letters XYZ represent the geodetic coordinate system (GCS) and lowercase letters *xy* represent the BPM coordinate system. Figure 4 shows the distances that need to be measured to determine the BPM mechanical center, where H and L are the dimensions of BPM, H_s are the dimensions of the antenna support, r is the radius of the antenna, X_s and Y_s are the distances from the LRSs to the antenna support, and X_{bpm} and Y_{bpm} are the distances from the LRSs to BPM. When the antenna is located in the BPM mechanical center, the following relationship is satisfied:

$$Y_s + H_s = Y_{bpm} + \frac{H}{2} + r \tag{2}$$
$$X_s = X_{bpm} + \frac{L}{2} + r$$

Transfer Eq. (2) to Eq. (3). When the position of BPM, namely X_{bpm} and Y_{bpm}, have been adjusted to meet Eq. (3), it can be considered that the mechanical center of BPM has been found.

$$Y_{bpm_M} = Y_s + H_s - \frac{H}{2} - r \tag{3}$$
$$X_{bpm_M} = X_s - \frac{L}{2} - r$$

In Eq. (3), the right side of the equals sign is the parameters of the positioning system. Moreover, only Y_s and X_s are measured values, the rest are all constants. As long as the system state is unchanged, X_{bpm_M} and Y_{bpm_M} are two constants. When the antenna is in the electrical center of BPM, let the distance measured by the two laser sensors be denoted by X_{bpm_E} and Y_{bpm_E}, then the offset between the electrical center and the mechanical center can be calculated as

$$X_{\text{offset}} = -(Y_{bpm_E} - Y_{bpm_M}) \tag{4}$$
$$Y_{\text{offset}} = X_{bpm_E} - X_{bpm_M}$$

The specific calibration operating steps are shown in Table 1.

In Table 1, step 1 is a system self-test, which only needs to be performed once as long as the system state remains unchanged. Step 2 is to make the antenna parallel to the system, and steps 3-4 ensure that the BPM is parallel to the system. Steps 5 and 6 are optional operations. If calibrating from the mechanical center, proceed to step 5. If only measuring offset, perform step 6.

ERROR ANALYSIS

The processing errors of the antenna support and BPM is the main source of system errors. Now assume that the size errors of the support and BPM are ΔH_s and ΔH, so the measured value Y_s in Eq. (3) will turn into $Y_s + \Delta H_s$, and

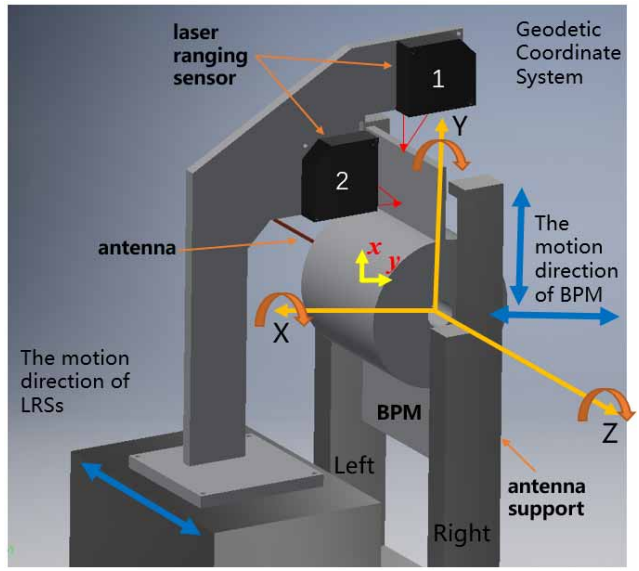


Figure 3: BPM machine center calibration method based on laser ranging.

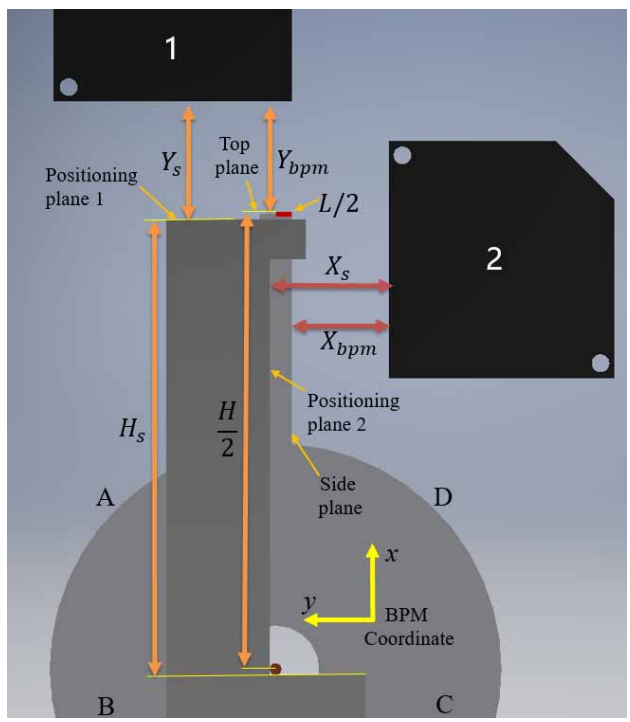


Figure 4: The distances that need to be measured to determine BPM mechanical center.

Y_{bpm_E} will become $Y_{bpm_E} + \Delta H$. Then, the offset in the Y direction is $Y'_{\text{offset}} = Y_{\text{offset}} + \Delta H_s - \Delta H$. Similarly, $Y'_{\text{offset}} = Y_{\text{offset}} + \Delta L - \Delta F$, where ΔL is the size error of the BPM in the X direction, and ΔF is the geometry error of the support's positioning plane. The error model is shown in Fig. 5.

Considering the worst-case scenario, when the error direction of the antenna support is opposite to the BPM, the total systematic errors are the sum of absolute values:

$$\Delta X^s_{\text{offset}} = |\Delta H_s| + |\Delta H| \tag{5}$$
$$\Delta Y^s_{\text{offset}} = |\Delta L| + |\Delta F|$$

Content from this work may be used under the terms of the CC-BY-4.0 licence (© 2023). Any distribution of this work must maintain attribution to the author(s), title of the work, publisher, and DOI

ISBN: 978-3-95450-236-3 ISSN: 2673-5350 doi:10.18429/JACoW-IBIC2023-MOP026

Content from this work may be used under the terms of the CC-BY-4.0 licence (© 2023). Any distribution of this work must maintain attribution to the author(s), title of the work, publisher, and DOI

Table 1: The Steps to Determine the BPM Mechanical Center

Step Number	Operating Items	Operation Purposes
1	Move the LRSs in the Z-direction from the leftmost to the rightmost of the antenna support, and observe whether the data of the two LRSs change	Ensure that the movement direction of the LRSs is parallel to the two positioning planes (shown in Fig. 4) of the antenna support. Then, calculate X_{bpm_M} and Y_{bpm_M} based on Eq. (3).
2	Install BPM. Let the antenna through the BPM vacuum chamber and press it on the positioning planes of the antenna support.	Ensure that the antenna between the two pillars of the support is parallel to the two positioning planes.
3	Move the LRSs in the Z direction, scan the top and sides planes (shown in Fig. 4) of the BPM, and observe whether the readings of the two LRSs change.	Ensure that the axis of the BPM is parallel to the antenna (Eliminating the rotational errors around X-axis and Y-axis)
4	Hold the LRSs at the middle position of the antenna support, move BPM along the Y-axis, and observe whether the reading of the No. 2 LRS changes	Ensure that BPM is placed vertically (Eliminating the rotational error around Z-axis)
5	Adjust the position of BPM so that the distances between BPM and LRSs are equal to X_{bpm_M} and Y_{bpm_M}, which means that the antenna is in the BPM mechanical center at this time.	Align the antenna with the BPM mechanical center, open the automatic calibration software and start the calibration program.
6	Adjust BPM and let the antenna reach its electrical center, read the two LRSs data X_{bpm_E} and Y_{bpm_E}, and calculate offsets according to Eq. (4).	Only measure the electro-mechanical offset

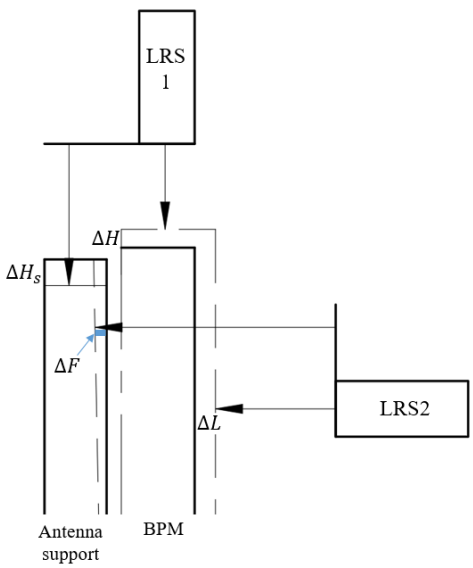


Figure 5: Schematic diagram of system error.

Since the machining error of both antenna and BPM is within 10 μm, the maximum system error is less than 20 μm.

The random error of this method includes the measurement resolution (0.5 μm) of the LRSs, the displacement accuracy (1 μm) of the motion stage, the influence of temperature drift or ground vibration, and the installation repetitive error of the BPM. Among them, the first three are small enough so as to be ignored, while the BPM installation errors will affect the electrical center parameters X_{bpm_E}, Y_{bpm_E}, and the mechanical center parameters X_s, Y_s. which means that installation errors are the main source of random errors.

Installation errors resulting in imperfect parallel within the system that causes rotation errors in in the X, Y, and Z planes of the BPM coordinate system. Theoretically, if steps 3-4 in Table 1 are strictly executed, all installation errors will be eliminated, but the calibration efficiency will be seriously reduced in actual engineering. Therefore, in order to improve calibration efficiency, the BPM installation errors were analyzed without performing steps 3-4, and the results are shown in Table 2. The error generated by rotation around the Z-axis is shown in Fig. 6.

Hence, excluding the errors that can be software eliminated, the measured random errors can be expressed as Eq. (6):

$$\Delta Y^{r}_{\text{offset}} = \Delta X^{rx}_{bpm_E} + \Delta X^{ry}_{bpm_E} + \Delta X^{rz}_{bpm_E} + \Delta X^{rz}_{s} \quad (6)$$
$$\Delta X^{r}_{\text{offset}} = \Delta Y^{rx}_{bpm_E} + \Delta Y^{ry}_{bpm_E} + \Delta Y^{rz}_{bpm_E} + \Delta Y^{rz}_{s}$$

Assuming that $\theta_z = 0.1°$, $l_3 = 4$ mm, $l_4 = 50$ mm, and $H = 210$ mm, the error value $\Delta X^{rz}_s = 7$ μm and $\Delta Y^{rz}_s = 87$ μm will be obtained. Thus, due to the large l_4, slight rotation of the Z axis will cause a large ΔY^{rz}_s, which should be avoided as much as possible. In order to eliminate the installation rotation error, it is necessary to install BPM with a fixed torque wrench.

EXPERIMENT AND DISCUSSION

The physical experimental platform designed according to Fig. 3 is shown in Fig. 7. To improve the calibration efficiency, the two LRSs and precision motion stages are controlled by a computer program. The parameters of the tested BPM are $H = 210$ and $L = 12$. Support parameter $H_s = 182$ and the diameter of the antenna $r = 0.105$. By completing step 1 in Table 1, we can get $X_s = 5.820$, $Y_s = 1.780$, $X_{bpm_M} = -0.287$, and $Y_{bpm_M} = -0.328$. The unit of all above data is mm. Then, install a BPM and

ISBN: 978-3-95450-236-3 ISSN: 2673-5350 doi:10.18429/JACoW-IBIC2023-MOP026

adjust its position until the antenna is located at the electrical center, and measure X_{bpm_E} and Y_{bpm_E}. Repeat the experiment 5 times in three different ways and observe the repeatability accuracy. The experimental data is shown in Table 3.

Table 3 shows that changing only the antenna or BPM results in small random errors, and the repeatability accuracy is within 10 μm. If both of them are changed simultaneously, the repetition precision is approximately 15 μm. The more objects that are changed, the more uncertainties are introduced and the greater the measurement error is obtained. In practical engineering, each calibration requires manual operation of the BPM and antenna at the same time, so the third row in Table 3 is the most realistic. On the basis of three-sigma rule, the range of measurement results is mostly within ±30 μm.

CONCLUSION

In order to quickly, low-cost, and high-precision measure the BPM electro-mechanical offset, a new method using precision antenna support and laser ranging sensor is proposed. The system's mechanical components are designed, and an automatic measurement program was developed. The resolution and maximum absolute error of this method are 15 μm and 20 μm, respectively. Improving the machining accuracy and surface finish of the antenna support, and designing a more reliable antenna pressing mechanism can further improve the calibration accuracy.

ACKNOWLEDGEMENT

This work was funded by the Foundation of Youth Innovation Promotion Association, CAS (Y202005), and the Major achievements cultivation project of major scientific and technological infrastructure, CAS (NE01G74Y2), and the National Natural Science Foundation of China (11805221).

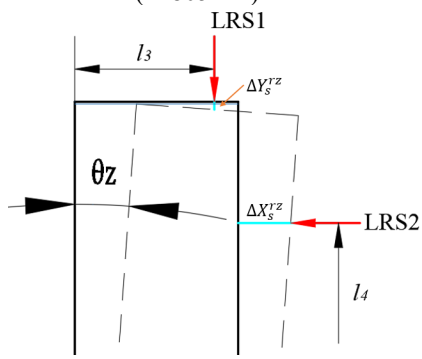


Figure 6: The error model for BPM rotation around Z-axis.

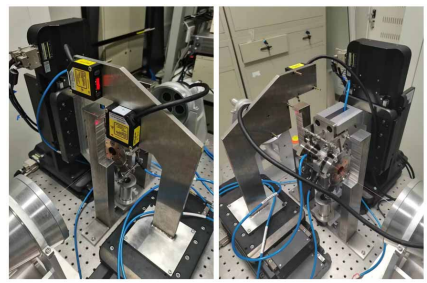


Figure 7: The experimental platform.

Table 3: The Experimental Data (unit: μm)

Measurement operation	σ_{x_offset}	σ_{y_offset}
Repeat installation of the BPM without changing the status of the antenna	3.3	10.2
Repeat installation of the antenna without changing the BPM status	8.1	2.4
Repeat the installation of the antenna and BPM simultaneously	15.4	12.2

Table 2: BPM Installation Errors Analysis

Error Source	Effect on Measurement	Elimination Method
Rotation around X-axis	$\Delta X_{bpm_E}^{rx}$ is difficult to evaluate. $\Delta Y_{bpm_E}^{rx}$ is difficult to evaluate. $\Delta Y_s^{rx} \approx l_1\theta_x$, l_1 is the distance from the laser spot to the X-Y plane. θ_x is the rotational error.	Hardware: Tighten the BPM mounting screws using a fixed torque wrench Software: The LRS1 scans along the Z-axis and the error ΔY_s^{rx} can be eliminated by averaging the measured Y_s at multiple positions.
Rotation around Y-axis	$\Delta X_{bpm_E}^{ry}$ is difficult to evaluate. $\Delta Y_{bpm_E}^{ry}$ is difficult to evaluate. $\Delta X_s^{ry} \approx l_2\theta_y$, l_2 is the distance from the laser spot to the X-Y plane. θ_y is the rotational error.	Hardware: Tighten the BPM mounting screws using a fixed torque wrench Software: The LRS2 scans along the Z-axis and the error ΔX_s^{ry} can be eliminated by averaging the measured X_s at multiple positions.
Rotation around Z-axis	$\Delta X_{bpm_E}^{rz}$ is difficult to evaluate. $\Delta Y_{bpm_E}^{rz}$ is difficult to evaluate. $\Delta Y_s^{rz} \approx l_3\theta_z - H\theta_z^2/2$, l_3 is the distance from the laser spot to the Y-Z plane. θ_z is the rotational error. $\Delta X_s^{rz} \approx l_4\theta_z$, l_4 is the distance from the laser spot to the X-Z plane.	Hardware: Tighten the BPM mounting screws using a fixed torque wrench No feasible software elimination method

Content from this work may be used under the terms of the CC-BY-4.0 licence (© 2023). Any distribution of this work must maintain attribution to the author(s), title of the work, publisher, and DOI

ISBN: 978-3-95450-236-3 ISSN: 2673-5350 doi:10.18429/JACoW-IBIC2023-MOP026

REFERENCES

[1] J. He, Y.F. Sui, Y. Li, *et al*., "Design and fabrication of button-style beam position monitors for the HEPS synchrotron light facility". *Nucl. Sci. Tech.*, vol. 33, p. 141, 2022.

[2] Y. Chung, G. Decker, E. Kahana, *et al.*, "Beam position monitor calibration for the Advanced Photon Source", in *Proc. Int. Particle Accelerator Conference (PAC'93)*, Washington, DC, USA, vol. 3, pp. 2304-2306, 1993.

[3] J.Y. Chen, C.H. Chen, M.S. Chiu, *et al*., "A fast gain calibration algorithm for beam position monitoring", *Nucl. Instrum. Methods Phys. Res., Sect. A,* vol. 932, pp. 56-61, 2019.

[4] X.H. Tang, J. He, J.H. Yue, *et al*., "Development of an automatic calibration system for beam position monitor". *Nucl. Tech.*, vol. 45, p. 020102, 2022.

[5] J. He, Y.F. Sui, Y. Li, *et al*. "Design and optimization of a Goubau line for calibration of BPMs for particle accelerators", *Nucl. Instrum. Methods Phys. Res., Sect. A.,* vol. 1045, p. 167635, 2023.

Content from this work may be used under the terms of the CC-BY-4.0 licence (© 2023). Any distribution of this work must maintain attribution to the author(s), title of the work, publisher, and DOI

ISBN: 978-3-95450-236-3 ISSN: 2673-5350 doi:10.18429/JACoW-IBIC2023-MOP030

DEVELOPMENTS OF 4GSR BPM ELECTRONICS

Si-Won Jang*, Garam Hahn, Jung Yun Huang, Changbum Kim, Dotae Kim, Gyujin Kim, Bokkyun Shin, DongCheol Shin, Donghyun Song
Beam Instrumentation Group, PAL, Pohang, South Korea
Woojin Song, POSTECH, Pohang, South Korea

Abstract

The emittance of the 4th-generation storage ring (4GSR) to be constructed in Cheongju-Ochang, Korea, is expected to be approximately 100 times smaller than the existing 3rd-generation storage ring. With the decrease in emittance, more precise beam stabilization is required. To meet this requirement, the resolution of the beam position monitor (BPM) system also needs to be further improved. We have conducted research and development on the electronics of the BPM system for the 4GSR storage ring. In order to perform fast orbit feedback in the 4GSR storage ring, we need to acquire turn-by-turn beam position data, with a desired beam position resolution of 1 μm. Additionally, prototypes of the bunch-by-bunch monitoring system are being developed for the transverse feedback system and longitudinal feedback system. The internally developed electronics are intended to be modified for future use as monitors for multi-bunch beam energy measurements at the end of the linear accelerator, by adjusting the logic accordingly. In this presentation, we will describe more details of the current status of the development of the beam position monitor electronics for the 4GSR in Korea.

INTRODUCTION

To achieve precise beam orbit stability in the 4th-generation storage ring with an emittance about 100 times smaller than the existing 3rd-generation storage ring [1], a more precise beam position monitor system with higher resolution is required. Figure 1 shows the construction view map of Korea 4GSR. In addition, the design of the 4GSR BPM electronics should be measure and provides Turn by Turn beam position data for Fast Orbit Feedback (FOFB) system with 375 kHz rate, which is a revolution frequency of 4GSR storage ring.



Figure 1: Construction view map of Korea 4GSR.

†siwon@postech.ac.kr

DEVELOPMENT STRATEGY OF 4GSR BPM ELECTRONICS

The strategy for developing 4GSR BPM electronics is as follows: First, we aim to develop BBB (Bunch by Bunch) BPM electronics capable of providing the highest performance for bunch-by-bunch beam position measurements. Subsequently, using this technology as a foundation, we will proceed to develop TbT (Turn by Turn) BPM electronics specifically tailored for the 4GSR storage ring. By integrating the front-end and back-end electronics, we will create Transverse & Longitudinal feedback systems (TFS & LFS), referred to as TFS & LFS BPM electronics.

Following this, we plan to adapt the data processing logic of the BBB electronics into a single-pass logic. This adaptation will enable us to install these electronics along the LTB (Linac. to Booster) beamline in the linear accelerator backend. They will serve as multi-bunch beam energy measurement monitors. The diagram below illustrates the development strategy for 4GSR BPM electronics. Figure 2 shows that the development strategy of 4GSR BPM electronics systems.

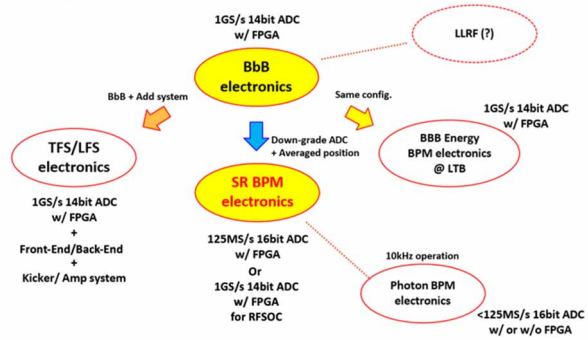


Figure 2: Development strategy of 4GSR BPM electronics.

Development Status of BBB BPM Electronics

The BBB electronics are currently in the prototype development phase [2], and we are undergoing several beam tests to ensure the system's stability. By configuring the desired storage ring parameters and turn counts, we have confirmed the capability of measuring the beam position for all bunches.

Figure 3 shows signal processing logic of BBB electronics. The signal processing procedure of BBB electronics as follows: To obtain a sufficient amount of bunch information, data is collected over several turns. Subsequently, the ADC data from every bunch is rearranged to calculate the beam position information for all bunches in the time domain. However, as previously mentioned, BBB Electronics is also adaptable for use with TbT BPM Electronics.

Content from this work may be used under the terms of the CC-BY-4.0 licence (© 2023). Any distribution of this work must maintain attribution to the author(s), title of the work, publisher, and DOI

ISBN: 978-3-95450-236-3 ISSN: 2673-5350 doi:10.18429/JACoW-IBIC2023-MOP030

Content from this work may be used under the terms of the CC-BY-4.0 licence (© 2023). Any distribution of this work must maintain attribution to the author(s), title of the work, publisher, and DOI

In the case of TbT data, the design ensures that the average beam positions of the bunches are calculated in the time domain for each turn with 375 kHz rate.

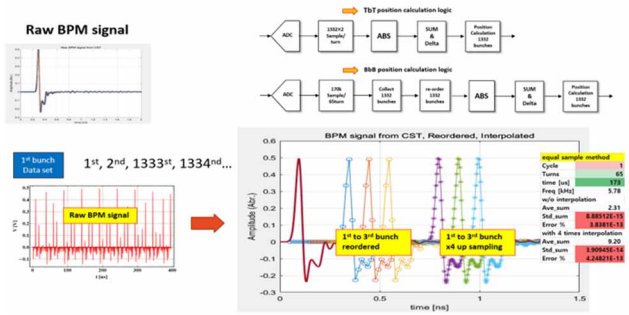


Figure 3: Design and simulation of 4GSR BBB BPM electronics logic.

Figure 4 shows the circuit configuration of the developed prototype BBB electronics. The prototype of BBB Electronics has been designed to synchronize two FMC ADC boards (2 Channel) on a Xilinx evaluation board. It utilizes 1 GS/s ADCs for data acquisition and has successfully measured bunch-by-bunch beam positions with stability during beam tests at the Pohang Accelerator Laboratory's PLS-II (Pohang Light Source-II) storage ring. In the future, to provide even more reliable performance, the entire board is undergoing upgrades. It will also utilize embedded EVR to receive the 500 MHz Master Oscillator RF signal, Machine Clock (MC), and 10 Hz Trigger signal, enabling the utilization of the 4GSR event system.

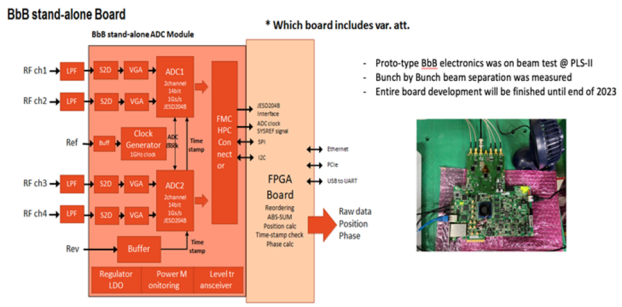


Figure 4: The configuration of BBB BPM electronics.

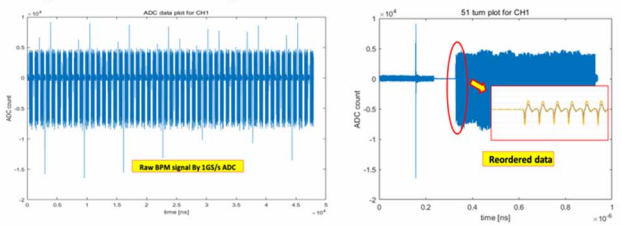


Figure 5: The beam test results of BBB BPM electronics. A signal reconstruction by using BBB signal with 51turn data at PLS-II storage ring.

Figure 5 shows the beam test results of BBB Electronics. After acquiring ADC data for 51 turns at a speed of 1 GS/s, the data was rearranged according to the bunch order, resulting in the acquisition of beam position information for all bunches. While additional data was obtained for sufficient data acquisition and precise signal waveform reconstruction, it is our aim to acquire beam position information for all bunches in a shorter time frame through the design of additional Analog Front-End Electronics, for future application in TFS & LFS.

4GSR SR BPM ELECTRONICS & SYSTEM CONFIGURATION

For the 4GSR Storage Ring (SR), TbT BPM electronics are currently in the process of being developed based on the prototype of the BBB electronics. The timing system for the storage ring utilizes the Event Network to provide Trigger signals and the Machine Clock to the BPM electronics. Additionally, SR BPM electronics employ SFP (Small Form-factor Pluggable) modules to provide X, Y, and Sum information at a speed of 375 kHz for the FOFB controller, Fast Orbit Interlock (FOI) controller, and Fast DAQ server. However, for Slow Acquisition (SA) data required to calculate the closed orbit of the storage ring, it is synchronized with a 10Hz Trigger and transmitted to the EPICS system for beam position information as shown in Fig. 6. Figure 6 shows the I/O port configuration of SR BPM electronics.

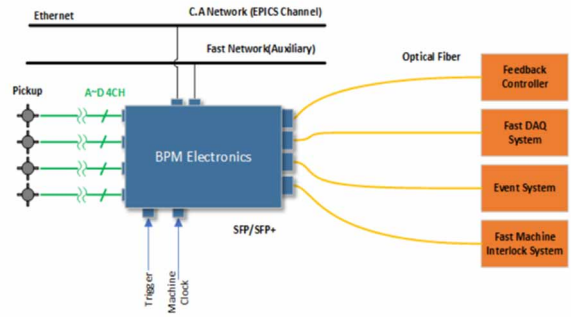


Figure 6: I/O configuration of 4GSR SR BPM electronics.

Figure 7 depict the data flow of SR BPM electronics for TbT data and SA data case, while Fig. 8 illustrates the configuration of BPM cable connections for the storage ring.

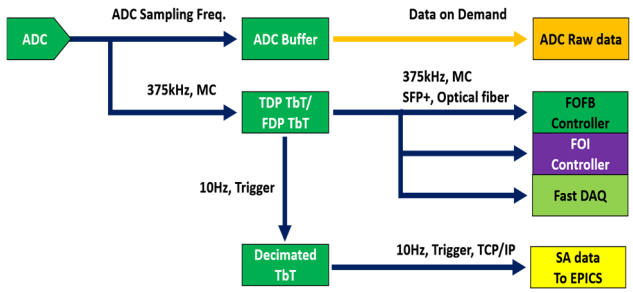


Figure 7: The data flow of 4GSR SR BPM electronics.

The feedback system for 4GSR is structured in two stages, with the first stage being the Slow Orbit Feedback System (SOFB). This system calculates and corrects the closed orbit at a rate of 2 Hz using a total of 288 BPMs and Correctors across the entire storage ring. The corrected closed orbit becomes the new Reference Orbit (Ref. Orbit). Subsequently, the FOFB system operates at each cell, receiving TbT data from BPM electronics at 375 kHz intervals and providing new set point information to the kicker MPS (Magnet Power Supply) every 15.6 khz.

ISBN: 978-3-95450-236-3 ISSN: 2673-5350 doi:10.18429/JACoW-IBIC2023-MOP030

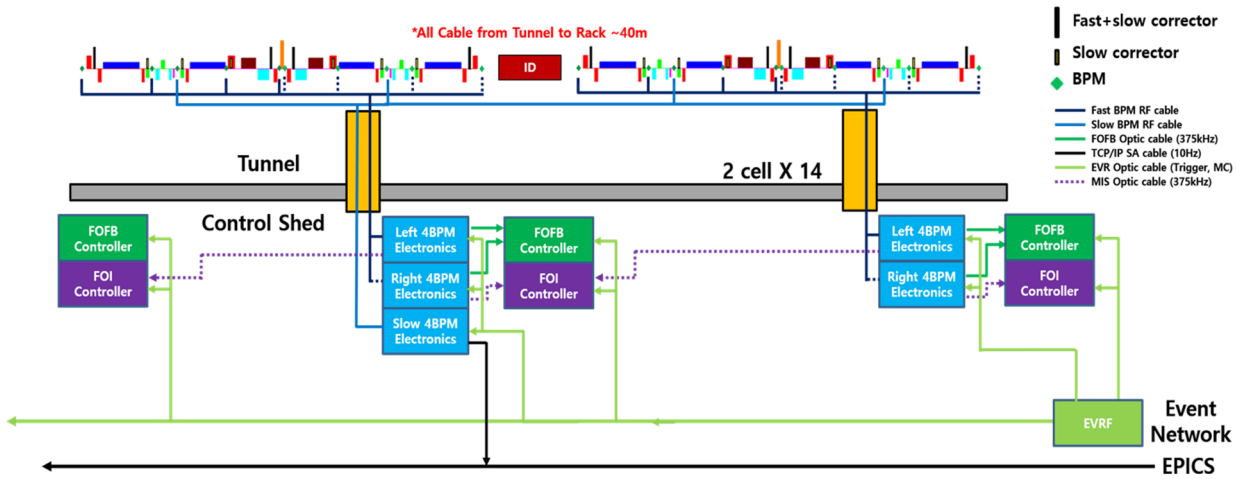


Figure 8: The configuration of BPM RF & timing cable connections for the storage ring.

Ultimately, the FOFB system aims to perform fast orbit feedback at a 10 kHz interval using fast BPMs and fast correctors to achieve a wide suppression bandwidth. While there isn't a master feedback controller for the entire storage ring, the FOFB controller exchanges information between adjacent cells at every turn. As a result, this system swiftly corrects distorted beam orbits in each cell and calculates kick angles for orbit correction based on the overall storage ring's orbit changes. Table 1 describes that the target parameters of the 4GSR feedback system.

Table 1: Specification Goal of 4GSR Beam Stability

Type	Data	Spec.	Conditions
Position Resolution [RMS]	TbT [375 kHz]	1 μm	400 mA 1065 Bunches
	SA [10 Hz]	30 nm	
	TbT [375 kHz]	100 μm	0.1 ~ 1 mA (Commissioning)
	SA [10 Hz]	1 μm	
Beam Current Dependence	-	~1 μm	0.1 mA ~ 400 mA
Absolute Accuracy	-	< 500 μm	Before BBA
		< 5 μm Max.	After BBA
Long-term Stability [RMS]	-	±0.2 μm	Day drift
		1 μm	Week drift

CONCLUSION

The Korean 4GSR project in Ochang is currently under construction with the goal of completion by 2027. The beam position monitor electronics system for 4GSR is in the process of development, and initial beam tests have been conducted by using developed prototype of BBB BPM electronics. Based on this, BPM electronics for the storage ring and feedback systems for both TFS and LFS are also under development. Additionally, preparations are underway for BBB energy measurement BPM electronics, which will be used for multi-batch beam energy measurements at the end of the linear accelerator. The aim is to complete the development of storage ring BPM electronics by the end of 2024. Simultaneously, tests will be conducted at the PLS-II storage ring in collaboration with the ongoing development of the FOFB controller.

ACKNOWLEDGEMENTS

This research was supported by National Research Foundation of Korea (NRF-2021R1I1A1A01060401).

REFERENCES

[1] G.S. Jang et al. “Low emittance lattice design for Korea-4GSR”, *Nucl. Instrum. Methods Phys. Res., Sect. A*, vol. 1034, 2022, p. 166779. doi:10.1016/j.nima.2022.166779

[2] S. W. Jang, “Development of Button BPM Electronics for the Bunch by Bunch Feedback System of 4GSR”, in *Proc. IPAC'22*, Bangkok, Thailand, Jun. 2022, pp. 332-334. doi:10.18429/JACoW-IPAC2022-MOPOPT038

Content from this work may be used under the terms of the CC-BY-4.0 licence (© 2023). Any distribution of this work must maintain attribution to the author(s), title of the work, publisher, and DOI

ISBN: 978-3-95450-236-3 ISSN: 2673-5350 doi:10.18429/JACoW-IBIC2023-MOP031

A STUDY INTO THE LONG-TERM STABILITY OF FRONT END X-RAY BEAM POSITION MONITOR SUPPORT COLUMNS AT DIAMOND LIGHT SOURCE

C. Houghton*, C. Bloomer, L. Bobb, D. Crivelli, H. Patel, J. Melton
Diamond Light Source, Oxfordshire, United Kingdom

Abstract

Sand-filled steel columns are used at Diamond Light Source to support front end X-ray beam position monitors. This approach is chosen due to the relatively large thermal mass of the sand being considered useful to reduce the rate at which expansion and contraction of the column occurred as the storage ring tunnel temperature varied, particularly during machine start-up. With the higher requirements for mechanical stability for the upcoming Diamond-II upgrade, there is now a need to assess and quantify the current system's impact on X-ray beam movement. A study of thermal and mechanical stability has been carried out to quantify the stability performance of the front-end X-ray beam position monitor's columns and the impact that column motion may have on the X-ray beam position measurement. Measurements have been made over a range of different timescales, from 250 Hz up to 2 weeks. The measured stability of the support column is presented, showing that it meets our Diamond-II stability requirements. A comparison of the stability of the column with and without a sand filling is presented.

INTRODUCTION

To monitor and improve the stability of the photon beams, Diamond Light Source utilises X-ray beam position monitors (XBPMs) on most insertion device (ID) front ends. Each XBPM is mounted on a steel support column bolted to the synchrotron floor. Currently, the XBPMs are used as a diagnostics tool, monitoring long-term trends and in some cases for slow (0.2 Hz) beam position feedback [1]. After the Diamond-II upgrade, it is proposed that the front end XBPMs could be included in more critical orbit feedback systems. Therefore the mechanical stability of the XBPMs needs to be assessed. Motion of the steel columns arises from various sources, the largest contribution coming from the vertical thermal expansion of the steel over time, correlated with ambient temperature changes in the tunnel.

Each column is constructed from a hollow square tube with external dimensions of 200 mm x 200 mm and a wall thickness of 10 mm. The manufacturer, FMB Berlin GmbH, specifies that the column is produced using S235JR steel, with a coefficient of linear thermal expansion of $12 \times 10^{-6}\,\mathrm{K}^{-1}$.

The columns are bolted to the concrete floor using four 50 mm long M12 bolts. One of the open questions this work is intended to answer was whether the steel base of the XBPM pressed into the floor by the tension of these four bolts is sufficient to thermally couple the column to the thermal mass of the synchrotron floor slab, or if the column temperature is more correlated with ambient air temperature.

Each column is filled with fine sand intended to improve the thermal stability of the column by increasing its thermal mass. Experimental data was first acquired with the column in its original state, filled with sand. Then, during a machine shutdown, the sand was vacuumed out of the column (approximately 30 kg of dry sand), leaving it hollow, and the experiments were repeated.

EXPERIMENTAL SET-UP

Laser Interferometry

In this experiment a laser-interferometry system[1] was utilised to track variations in the height of the XBPM support column. The setup involved positioning one of the detector heads on the top of the XBPM vessel using a mounting bracket. A plane mirror was positioned on the ground and aligned to the laser beam such that the light is reflected back along the incident path. Figure 1 presents a sketch of this system.

Interferometry, the principle underlying this setup, exploits the wave nature of light. When the laser beam splits and travels different paths – one directly to the detector and the other along the length of the column to the mirror and then to the detector – they recombine, forming an interference pattern. By analysing this pattern, a measurement of the column height variation over time periods of 1 s to days is acquired. For background information on the various principles behind modern interferometry measurements, a useful introduction can be found in [2, 3].

Thermal Monitoring

The temperature of the column, the air, and the concrete floor upon which the column was bolted were measured in order to correlate any variation in column height to the temperature of the column and its surroundings.

A total of five temperature sensors, with a thermal resolution of 0.025 °C, were attached to the support column, on different faces of the column and at different heights. The intent of this was to determine if there were any temperature gradients across the column, or if non-uniformity of the column temperature could lead to bending or twisting of the column as different sides of it expanded or contracted at different rates. One temperature sensor was bolted into a

* claire.houghton@diamond.ac.uk

[1] *Renishaw* RLE10.

Content from this work may be used under the terms of the CC-BY-4.0 licence (© 2023). Any distribution of this work must maintain attribution to the author(s), title of the work, publisher, and DOI

ISBN: 978-3-95450-236-3 ISSN: 2673-5350 doi:10.18429/JACoW-IBIC2023-MOP031

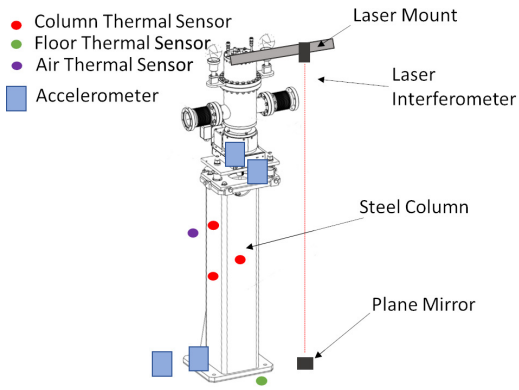


Figure 1: A drawing of the XBPM and its support column, with the locations of the different devices. Piezoelectric seismic accelerometers are shown by blue squares. Circles highlight the locations of the thermal sensors; red for column thermal sensors, purple for air thermal sensors and green for a sensor bolted to the floor. Two thermal sensors which were installed on the back and right side of the column are not shown in the schematic.

25 mm deep hole drilled in the concrete floor at the foot of the XBPM, at an equidistant location between two of the floor bolts of the support column which are separated by 200 mm. This sensor had a low-density packing-foam cover placed over it to insulate it from the ambient air temperature. This way, the sensor measured the long-term temperature stability of the floor slab, without detecting short-term fluctuations in ambient air temperature.

Accelerometers

Piezoelectric seismic accelerometers[2] were used to measure the horizontal and vertical stability of the support column over the frequency range of 10 Hz to 250 Hz with a broadband resolution of 9×10^{-4} m/s^2 rms. Piezoelectric accelerometers use the piezoelectric effect to measure forces induced due to the acceleration of the material. A seismic mass is attached to a sensing piezo-crystal. When under acceleration the seismic mass causes stress on the sensing piezo-crystal which outputs a proportional electrical signal [4]. Four piezoelectric accelerometers were used to measure the support column and the surrounding area, measurements were taken simultaneously. The accelerometers were placed on the floor next to the support column, on the base of the support column, on the top of the support column, and on the stepper motor to which the XBPM vessel is mounted referred to as the XBPM mounting plate, see Fig. 1.

RESULTS

Temperature Stability

Figure 2 shows the variation in the thermal sensor measurements installed on and around the support column over a 50 h period. The air temperature is seen to oscillate by about 0.4 °C peak-to-peak. However, the column has a significantly larger thermal mass, and is to some extent thermally bonded to the concrete floor slab. Thus, the temperature variations of the column are damped relative to the air, and vary over much longer timescales. The column temperature variation is broadly seen to follow the pattern of air temperature variation, albeit low-pass filtered. In addition, the location of the different sensors placed on the column does not make a significant impact on the temperature variation. This suggests that the thermal conductance of the support column is uniform across all faces. This relationship does not change when the sand is removed, see the bottom graph of Fig. 2. This is to be expected, given the thermal conductivity of steel and the timescales over which measurements were made. Over the full 11 day data collection period the standard deviation of the average column temperature was 0.064 °C with sand increasing to 0.071 °C when the sand is removed.

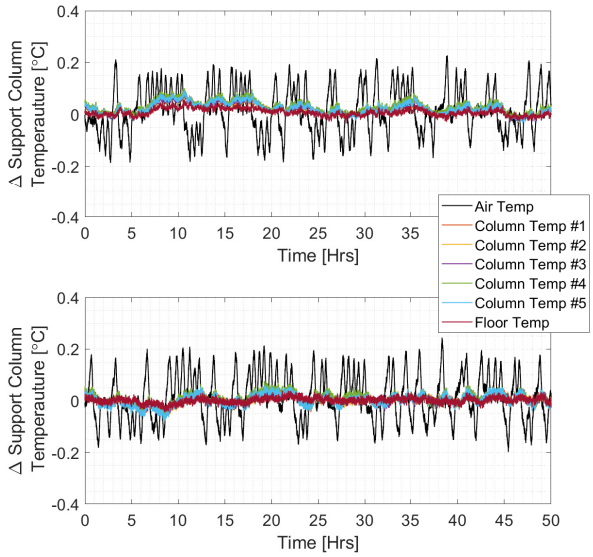


Figure 2: Graph showing the change in air, column and floor temperature over a 50-hour period with sand (Top) and without sand (Bottom).

Short Term Stability

The short-term stability was measured using accelerometers. There are two useful metrics by which the overall stability of the support column and the effect of the internal sand, can be compared: the transmissibility ratio of displacement transmitted through the column, and the power spectral density (PSD) of the motion of the support column.

The transmissibility ratio is the measure of the physical displacement transmitted through a system (i.e. the support column). This was obtained by measuring the motion using the accelerometer mounted at the bottom of the column and comparing the results to the XBPM support column stability using the accelerometer mounted at the top of the column. In the results presented here the ratio was taken from the base plate at the bottom of the support column to the XBPM mounting plate.

Typically, at low frequencies the whole system will move as one body, as all motion is transmitted through the column

[2] *PCB Piezotronics* model 393B31.

Content from this work may be used under the terms of the CC-BY-4.0 licence (© 2023). Any distribution of this work must maintain attribution to the author(s), title of the work, publisher, and DOI

ISBN: 978-3-95450-236-3 ISSN: 2673-5350 doi:10.18429/JACoW-IBIC2023-MOP031

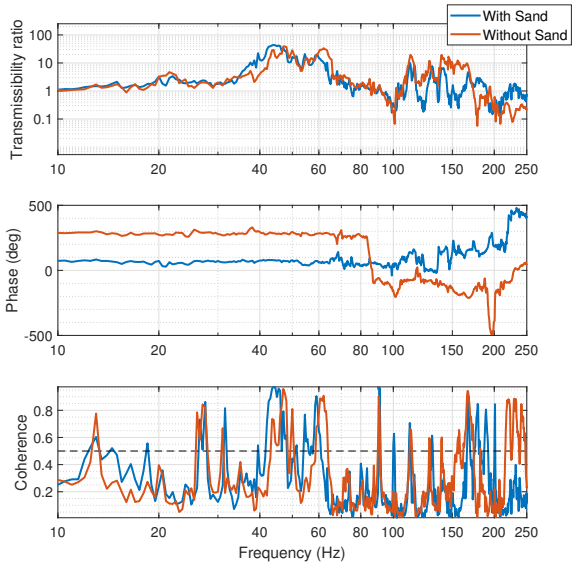


Figure 3: The horizontal transmissibility ratio of the XBPM support column bottom plate to the XBPM mounting plate.

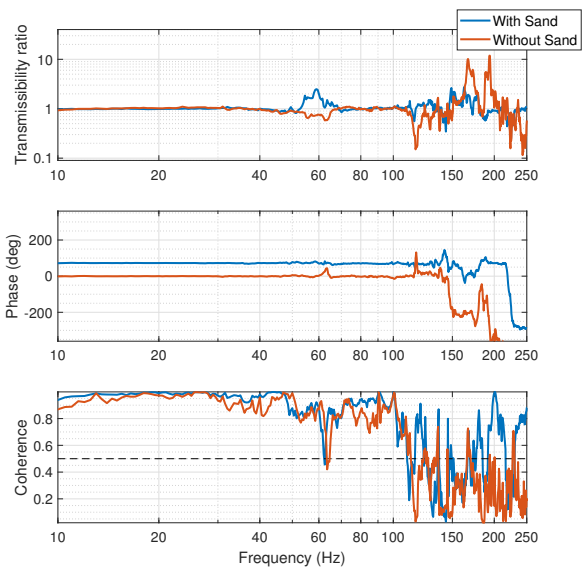


Figure 4: The vertical transmissibility ratio of the XBPM support column bottom plate to the XBPM mounting plate.

(i.e. transmissibility ratio = 1). A transmissibility ratio equal to one means a perfectly rigid system [5]. At higher frequencies the ground motion may no longer be transmitted through the column and is damped (i.e. transmissibility ratio < 1) or ground motion can even be amplified by the column at resonant frequencies (i.e. transmissibility ratio > 1). This enables the amplification, resonances and damping from the column to be seen.

Horizontally, the transmissibility ratio was similar both with and without sand up to ~ 120 Hz, see Fig. 3. There is an amplification of ground motion above 30 Hz in both datasets, with and without sand. The transmissibility ratio without sand shows fewer damping 'troughs' between 140 Hz and 166 Hz suggesting an overall larger amplification in this range of frequencies. There is a relatively large damping trough at 178 Hz in the without sand data which is not present in the column when there is sand. The vibration of the bottom of the column and top of the XBPM mounting plate go out of phase at 84 Hz, likely indicating a resonance of the system. The coherence of the system also has similarities between the two datasets, with slight changes in the peak frequencies. Removing the sand does not make the column more incoherent.

Vertically, the removal of sand has a larger impact on the transmissibility ratio, see Fig. 4. When sand fills the column the transmissibility ratio is close to one across the frequency range, except for a peak at 50 Hz - 70 Hz. New relatively large peaks at 167 Hz and 193 Hz were present once the sand was removed this suggests that the sand works to damp these resonances. Without sand the drop out of phase is shifted from 215 Hz to 144 Hz.

Overall, it is found that there are not significant changes to the short-term stability of the column as a result of the sand. The changes that are present could be explained simply as an effect of small differences in the bolt tightness following the unbolting and re-bolting of securing screws during the sand removal process.

The second metric by which the support column stability can be compared is the power spectral density for the horizontal and vertical motion of the XBPM mounting plate, seen in Fig. 5 and Fig. 6 respectively. The results here are similar to the transmissibility figures, in that they show very similar frequency responses both with and without sand.

Long Term Stability

During a typical week at Diamond Light Source, the electron beam is turned off to allow for machine development and maintenance. During this time the ambient air temperature in the tunnel typically drops as the thermal heating from the accelerator is removed. This temperature drop causes a contraction in the height of the XBPM support column. This can be seen clearly in a relatively large change in the column height in Fig. 7, highlighted by the black dashed line. The beam is returned to users at 9 AM the following day. The maximum change in height of the column during this beam-off period was 6.5 µm for the column with sand and 8.4 µm without sand. The standard deviation of the support column height variation over the 11 day measurement increases from 3.26 µm to 6.3 µm when the sand is removed. This variation is still below the 9.6 µm long-term stability needed for the planned upgrade to Diamond-II.

The correlation between the support column height and the temperature of the column can be seen in Fig. 8. At the start of both datasets the storage ring was not running. For the data set taken with sand, the electron beam was injected up to the user current, 300 mA, within 4 h. However, for the data taken without sand, the current did not reach 300 mA for close to 24 h. Therefore, the time for the column to reach an equilibrium temperature was longer. User current was returned to the machine at ~ 200 h in both runs. The column temperature takes 5 h longer to return to the level prior to the beam dump when it was filled with sand.

Content from this work may be used under the terms of the CC-BY-4.0 licence (© 2023). Any distribution of this work must maintain attribution to the author(s), title of the work, publisher, and DOI

ISBN: 978-3-95450-236-3 ISSN: 2673-5350 doi:10.18429/JACoW-IBIC2023-MOP031

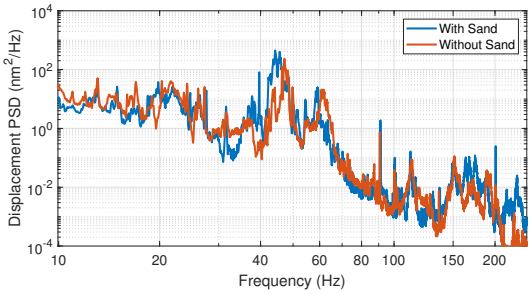


Figure 5: The power spectral density of the horizontal motion taken on the mounting plate of the XBPM.

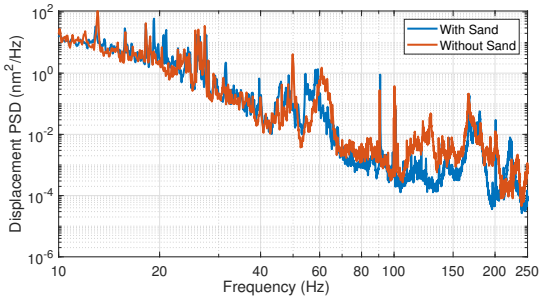


Figure 6: The power spectral density of the vertical motion taken on the mounting plate of the XBPM

Taking into account the expansion of steel, 12×10^{-6} K^{-1}, the column height change is larger than expected given the average column temperature variation. For example, in the top plot of Fig. 8, when the beam is turned off the column temperature drops by ~ 0.1 °C, which should give a change in height of ~ 2.9 µm. The actual measured change in height is around double this. This difference could be due to the XBPM being twisted by neighbouring vacuum vessels also warping or changing as the temperature changes. While the column height is correlated with temperature, it is a complex system that cannot be simplified down to just a steel support column existing in isolation. The column cannot be assumed to be completely vertically rising and falling with the temperature but could be 'bending' due to the tension in the bellows. It is a reasonable assumption that the column itself is not responsible for all the motion that is seen.

CONCLUSION

The mechanical stability of an XBPM support column has been assessed and results show that sand-filled steel columns effectively maintain the required thermal and mechanical stability for supporting front-end X-ray beam position monitors at Diamond Light Source. Through laser interferometry and accelerometer measurements, both short-term and long-term stability were examined, highlighting the negligible impact of sand on high-frequency mechanical stability and its beneficial role in reducing vertical column variations over extended periods. The standard deviation of the column height at a rate of 1 Hz over a period of 11 days was 3.26 µm with sand and increased to 6.3 µm when the sand was removed. These findings verify the stability of the column for the upcoming

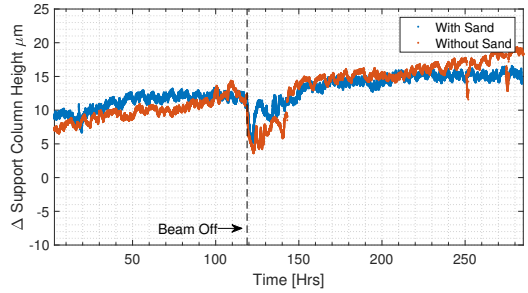


Figure 7: The change in the support column height measured with and without sand filling the column.

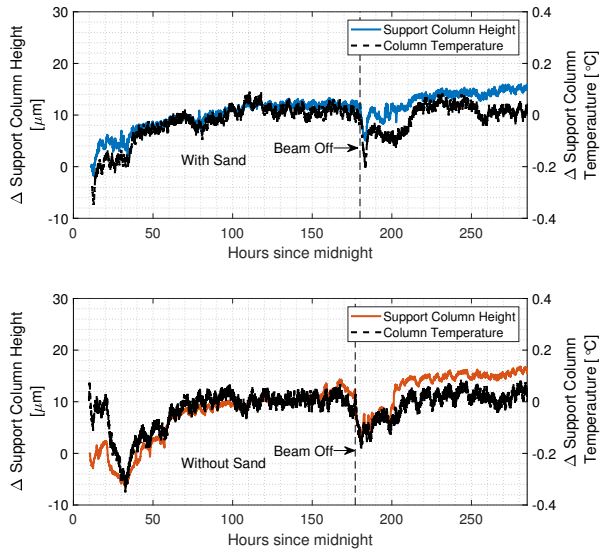


Figure 8: The change in the support column height and the average column temperature measured with (top) and without (bottom) sand filling the column.

Diamond-II upgrade, ensuring accurate and reliable X-ray beam position measurements. Removing the sand improves low-frequency vibrations slightly, but the impact of this is not significant. The current sand-filled steel columns are sufficiently stable to meet the Diamond-II requirements and therefore will remain during the upgrade.

REFERENCES

[1] C. Bloomer, G. Rehm, and C. A. Thomas, "Observation and Improvement of the Long Term Beam Stability using X-ray Beam Position Monitors at DLS", in *Proc. IPAC'10*, Kyoto, Japan, May 2010, paper WEPEB047, pp. 2797–2799.

[2] H. Büchner and G. Jäger, "A novel plane mirror interferometer without using corner cube reflectors", *Meas. Sci. Technol.*, vol 17, pp. 746, 2006. doi:10.1088/0957-0233/17/4/021

[3] S. Yang and Z. Guofeng, "A review on interferometry for geometric measurement", *Meas. Sci. Technol.*, vol. 29, 2018. doi:10.1088/1361-6501/aad732

[4] F. Levinzon, "Ultra-Low-Noise Seismic Accelerometers for Earthquake Prediction and Monitoring", *Earthquakes*, 2017. doi:10.5772/65925

[5] A. Piersol and T. Paez, *Harris' Shock and Vibration Handbook*, McGraw Hill LLC, 2009. ISBN: 0-07-137081-1

Content from this work may be used under the terms of the CC-BY-4.0 licence (© 2023). Any distribution of this work must maintain attribution to the author(s), title of the work, publisher, and DOI

ISBN: 978-3-95450-236-3 ISSN: 2673-5350 doi:10.18429/JACoW-IBIC2023-MOP032

ONE DIMENSIONAL BEAM POSITION MONITOR PROTOTYPE USING INCOHERENT CHERENKOV DIFFRACTION RADIATION

A. Clapp*, Royal Holloway University of London, Egham, UK
also at Diamond Light Source, Didcot, UK
P. Karataev, Royal Holloway University of London, Egham, UK
L. Bobb, G. Cook, Diamond Light Source, Didcot, UK

Abstract

This paper proposes a novel advancement in both the studies of Cherenkov diffraction radiation (ChDR) and beam instrumentation. The proposed beam position monitor (BPM) consists of two identical fused Silica prism radiators, with a fibre collimator attached to each one, which in turn are connected to a photodetector via a series of optical fibres. The setup will be implemented into the booster to storage ring transfer line at Diamond Light Source - an electron light source with 3 GeV beam energy. The prototype proposed aims to test the feasibility of a full BPM utilising ChDR. If proven to be fully realisable, optical rather than capacitive BPM pickups could be more widely distributed. The paper will include the complete design and preliminary results of a one-dimensional BPM, utilising the ChDR effect.

INTRODUCTION

Cherenkov radiation (CR) is the emission of electromagnetic radiation when a charged particle travels through a dielectric medium with a speed greater than that of light in that medium. Observed in 1934 by Cherenkov [1], it has since been expanded upon both theoretically and experimentally. Cherenkov radiation is emitted at a well defined angle denoted the Cherenkov angle θ, given by

$$\cos\theta = \frac{1}{\beta n} \tag{1}$$

where $\beta = v/c$ is the ratio of the charged particle velocity v to the speed of light c, and n is the refractive index of the medium the charged particle particle is travelling through [1]. The emission and directionality of Cherenkov radiation enables this phenomena to be a useful tool in many fields ranging from astrophysics [2] to radiotherapy [3].

The theory of CR has been expanded to account for the situation where the incident relativistic particle is instead travelling close by a medium acting in a manner similar to classical diffraction radiation [4] called Cherenkov Diffraction Radiation [5]. In addition to particle energy and the refractive index of the medium, ChDR is dependent on the impact parameter b which represents the distance between the incident charged particle and the medium. ChDR is produced by a hyper-relativistic particle travelling close to a medium, rather than through it, and given that ChDR is emitted at the well defined Cherenkov angle it is well suited for accelerator diagnostic applications where a non-invasive technique is of paramount importance.

* alec.clapp.2021@live.rhul.ac.uk

The intensity of light emitted increases the closer the particle is to the medium, as such it is necessary to ensure that the incident particle is within the condition

$$b \leq \gamma\lambda \tag{2}$$

where γ refers to the Lorentz factor of the incident particle and λ refers to the wavelength of emitted radiation. The quantity $\gamma\lambda$ refers to the effective electron field radius [6].

For optical wavelengths and an electron beam energy of 3 GeV b is ≤ 3 mm. ChDR has been investigated experimentally and had its applicability to diagnostics examined [7, 8].

BTS TEST STAND

The experiment is located on the Booster To Storage (BTS) transfer line at Diamond Light Source (DLS). The test stand consists of a six-way cross vacuum chamber with a four-dimensional manipulator system which allows for the insertion and removal of experiments. Vertical translation and rotation of the manipulator are automated. It was previously used for another ChDR experiment [9], which tested feasibility of beam position measurements and fundamental ChDR properties.

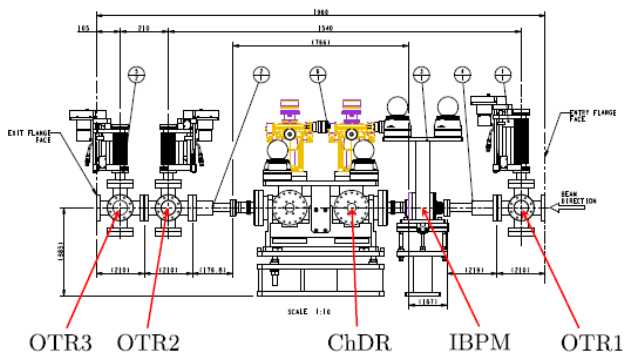


Figure 1: Schematic of BTS test stand.

Figure 1 shows a schematic of the vacuum vessel string on the BTS test stand consisting of three combined Optical Transition Radiation (OTR) and Yttrium Aluminium Garnet (YAG) monitors, and one Inductive Beam Position Monitor (IBPM) developed at CERN [10]. These diagnostic tools are used as references for the beam profile and trajectory through the BTS test stand when taking data with the ChDR BPM. The IBPM provides a reference beam position measurement, which the results from the ChDR BPM are compared against. The first OTR screen is used to measure

Content from this work may be used under the terms of the CC-BY-4.0 licence (© 2023). Any distribution of this work must maintain attribution to the author(s), title of the work, publisher, and DOI

ISBN: 978-3-95450-236-3 ISSN: 2673-5350 doi:10.18429/JACoW-IBIC2023-MOP032

the input beam profile and from this the input beam size into the BTS test stand. OTR2 (see Fig. 1) is used to check alignment of the ChDR BPM assembly with respect to the beam path. Shadowing of the beam profile on this screen indicates that the beam is in contact with the assembly and that correct horizontal/rotational alignment is not achieved. YAG screens have a higher photon yield allowing for beam shadowing to be easier to identify, whereas OTR screens provide better spatial resolution for beam size measurement.

The DLS storage ring has a vacuum rating of 10^{-10} mbar, the BTS transfer line is targeted at Ultra High Vacuum (UHV), therefore the ChDR BPM assembly must also be UHV compatible.

CHDR BPM DESIGN

The 1D ChDR BPM design utilises two pick-ups consisting of identical prisms positioned either side of the electron beam to produce horizontal beam position measurements using ChDR. The intensity of the emitted signal relies on the impact parameter, which from theory displays an exponential decay with increasing impact parameter. For the case of DLS using ChDR emitted at visible wavelengths, the impact parameter should be less than 3 mm. This means that if the beam moves out of this range, the detected signal will be within the noise, providing no useful information on current beam position. Therefore the ChDR BPM pick-ups should have a separation ≤ 3 mm to ensure that simultaneous signals from the two pick-ups can be detected.

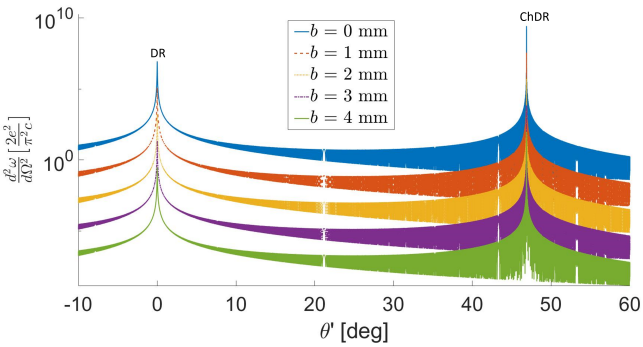


Figure 2: Intensity curve for the fused silica prism, showing the diffraction radiation (DR) peak centered at zero and the ChDR peak centered at the Cherenkov angle.

The ChDR BPM has an adjustable separation to allow for flexibility in measurements. The ChDR output signal intensity was calculated using the single target intensity equation from [11] and is shown in Fig 2. The emitted ChDR signal from one of the pick-ups will be at a maximum when the impact parameter between the electron beam and that pick-up is zero. The minimum separation between two pick-ups should be such that when the electron beam is in the centre of both pick-ups and has an equal impact parameter with both, the emitted ChDR signal is at 1% of the maximum value. This minimum separation was found by creating an

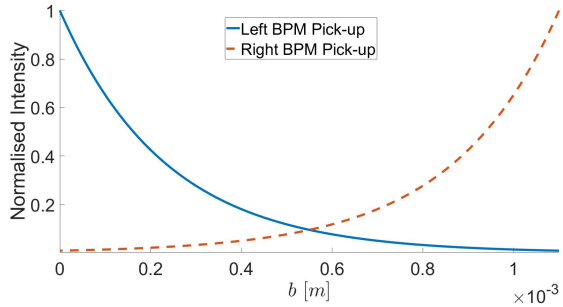


Figure 3: Graph showing the decay of two identical pick-ups either side of a beam with a separation of 1.1 mm.

intensity decay curve, shown in Fig. 3, for the two pick-ups using the results from Fig. 2.

The decay curve in Fig. 3 found that the desired minimum pick-up separation is at 1.1 mm. The separation between the two pick-ups can be increased up to 6.1 mm through the use of spacers. This maximum separation corresponds to an impact parameter of $2\gamma\lambda$ for 500 nm emission or $\gamma\lambda$ for 1000 nm emission.

To couple the ChDR light out from the prisms to optical fibres, collimators are used. To maximise the collected signal, the collimator lenses have been angled such that they are parallel to the output face of the prisms and are positioned by the assembly in close proximity. Figure 4 shows a 3D rendering of the BPM assembly.

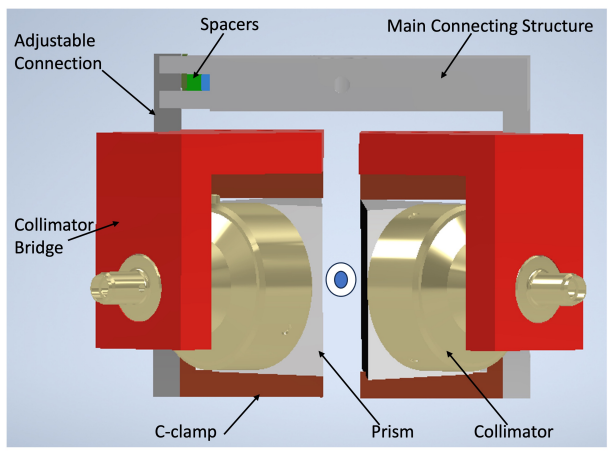


Figure 4: Autodesk inventor 3D rendering of the BPM assembly. Colours are used to differentiate the components: silver is used to denote the prisms; the two collimators are in gold; the C-clamps are in dark orange; collimator bridges are in red; the adjustable connection is in dark grey; the main connecting structure in the light grey and; the spacers in the green and blue.

The assembly itself is made of stainless steel with stainless steel screws. All screw holes are either through or have had a small hole drilled to ensure no cavities are formed to ensure the assembly is UHV compatible. The C-clamps feature a step angled at the Cherenkov angle, this aligns the target to

Content from this work may be used under the terms of the CC-BY-4.0 licence (© 2023). Any distribution of this work must maintain attribution to the author(s), title of the work, publisher, and DOI

ISBN: 978-3-95450-236-3 ISSN: 2673-5350 doi:10.18429/JACoW-IBIC2023-MOP032

ensure the generation face of the prism is flush with clamp and is not angled with respect to the electron beam trajectory.

The main structure is connected to the central actuator, which allows for the assembly to be lowered into the beam path when conducting ChDR experiments. For user beam operation of the storage ring the assembly is retracted beyond the nominal beam pipe diameter to ensure the presence of the assembly does not impact beam injection to the storage ring (see Fig. 5).



Figure 5: 3D rendering of the assembly in its retracted position inside the vacuum chamber from an upstream view.

The generated ChDR light is coupled from UHV compatible fibres inside the vacuum chamber to an external detector via a UHV-to-air fibre feedthrough. The detector is an amplified photodiode with a direct fibre input. The detector has a short rise time of 1 ns and a wide spectral range of 400 – 1000 nm which is ideal for ChDR experiments as it allows for a wide range of experiments to be explored.

PRISM DESIGN

Each ChDR pick-up utilises a prismatic radiator as shown in Fig. 6. The prism is made of UV grade fused Silica. Prisms have been optimised for 500 nm ChDR emission by setting the angle of the output face at 43.2° with respect to the electron beam path, to ensure that light emitted at this wavelength has an outgoing wavefront parallel to this interface. The upstream face is angled at the Cherenkov angle for 500 nm at 46.8° such that all light at this wavelength travels to the output face without encountering any reflections. To reduce signal interference from synchrotron radiation inside the beam pipe, the upstream face and the two triangular faces are coated in a 0.5 µm layer of aluminium.

The vertical size of the target with respect to the electron beam path is 32 mm. To match current theory [11], the vertical size is required to be an order of magnitude larger than the electric field radius $\gamma\lambda$ to ensure that the target appears to be infinitely tall compared to the electric field. This predicts that the intensity decay due to increase in impact parameter, will match that seen in Fig. 3.

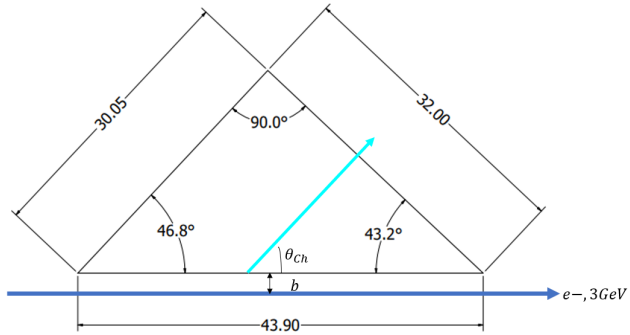


Figure 6: Prismatic Radiator.

CHARACTERISATION OF THE CHDR PICK-UP

To allow for an an accurate measurement of ChDR emission power, all components have been bench tested with a 638 nm laser and a power meter. Starting from the prisms the laser was directed through the the component and then focused into the power meter to accurately measure the power loss through that particular component. Each component was tested individually and the assembly was gradually built up such that the power loss through each section was accurately determined. The two most significant points of power loss were the 0.5 m long UHV fibre and the 2 m long in-air fibre.

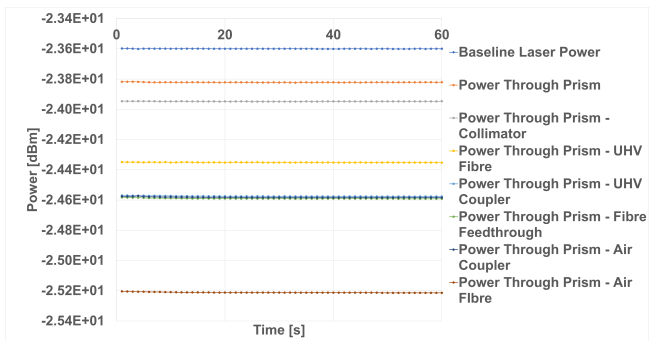


Figure 7: Power loss results of the components inserted into the BTS chamber.

As Fig. 7 shows the overall signal loss through the system is 1.6 dB, which corresponds to a percentage decrease of ~ 30.8%.

PRELIMINARY RESULTS USING ONE CHDR PICK-UP

For initial testing of the assembly, only one pick-up is installed (see Fig. 8). This allows for fundamental measure-

Content from this work may be used under the terms of the CC-BY-4.0 licence (© 2023). Any distribution of this work must maintain attribution to the author(s), title of the work, publisher, and DOI

ISBN: 978-3-95450-236-3 ISSN: 2673-5350 doi:10.18429/JACoW-IBIC2023-MOP032

ments to be undertaken which will then better optimise the insertion of the full two-pick-up BPM. A one pick-up system is far easier to properly align with respect to the electron beam. The initial shifts consisted of finding the correct vertical and rotational positions for the ChDR BPM assembly with respect to the electron beam path.

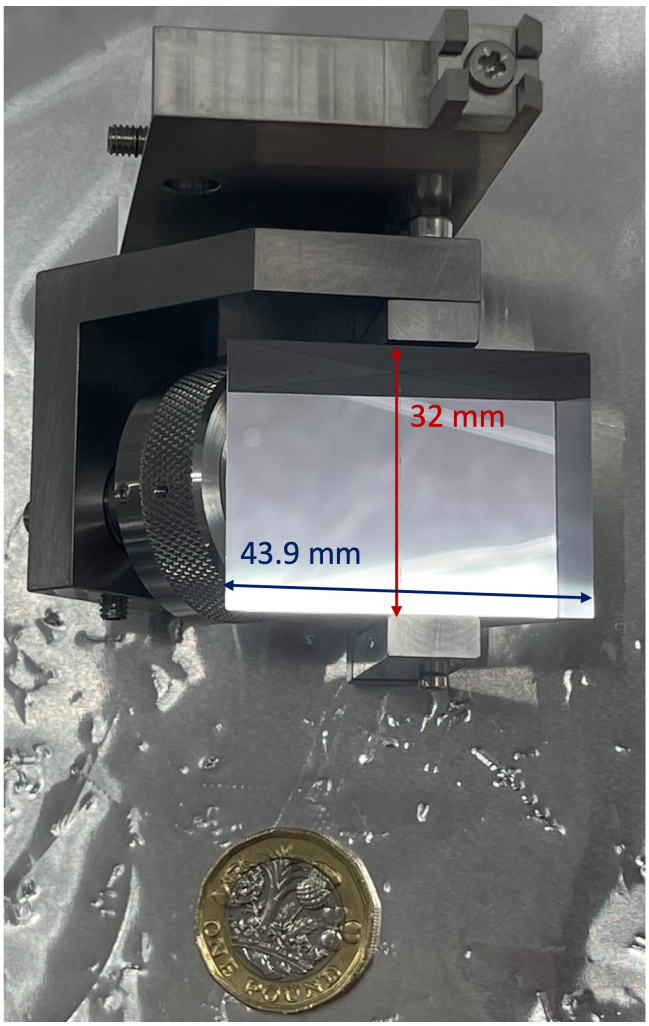


Figure 8: Image of one pick-up ChDR BPM assembly from an angle perpendicular to expected beam path, with a £1 coin for scale.

Initial commissioning of the one pick-up ChDR BPM assembly is underway. Figure 9 shows the beam profile on the YAG screen located at OTR2 (see Fig. 1) shadowed from the ChDR pick-up. This confirms that the beam can be moved sufficiently such that an impact parameter of zero between the electron beam and the ChDR pick-up can be achieved.

Figure 10 shows the output signal given by the interaction between the electron beam and the ChDR pick-up in Fig 9. The shadowing of the electron beam means that the signal from the ChDR detector will be a combination of CR and ChDR. This confirms that radiation emitted at the Cherenkov angle is successfully captured and transmitted through the BPM assembly.

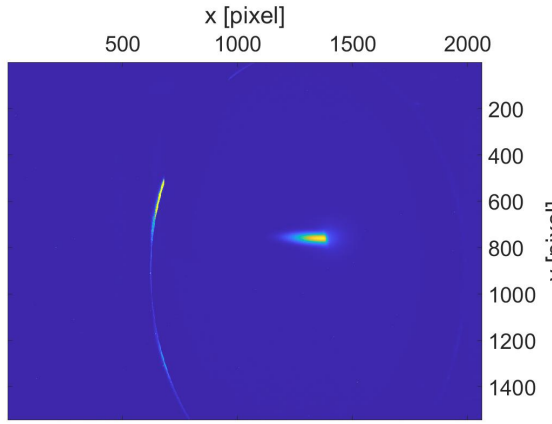


Figure 9: YAG image showing clear shadowing of the beam profile due to ChDR assembly.

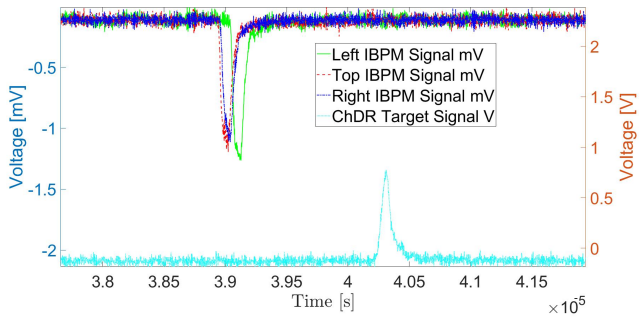


Figure 10: Oscilloscope signal showing the three IBPM signals and the ChDR signal. Voltage divisions of: 50 mV and 0.5 V for the IBPM and ChDR signals respectively.

CONCLUSION

A 1D BPM utilising incoherent ChDR has been designed and characterised in the lab. The assembly has been installed with one pick-up in place on the BTS transfer line at DLS. Initial commissioning tests have been performed and first signals have been detected.

ACKNOWLEDGMENTS

The authors would like to thank the efforts of the engineers from Royal Holloway University of London for creating the stainless-steel assembly and the help of the DLS vacuum group with installing the ChDR assembly into the BTS transfer line.

REFERENCES

[1] P. A. Čerenkov, "Visible Radiation Produced by Electrons Moving in a Medium with Velocities Exceeding that of Light", *Phys. Rev.*, vol. 52, no. 4, pp. 378–379, Aug. 1937. doi:10.1103/physrev.52.378

[2] T. Kajita, "Discovery of atmospheric neutrino oscillations**", *Ann. Phys.*, vol. 528, no. 6, pp. 459–468, May 2016. doi:10.1002/andp.201600086

Content from this work may be used under the terms of the CC-BY-4.0 licence (© 2023). Any distribution of this work must maintain attribution to the author(s), title of the work, publisher, and DOI

ISBN: 978-3-95450-236-3 ISSN: 2673-5350 doi:10.18429/JACoW-IBIC2023-MOP032

[3] D. A. Alexander, A. Nomezine, L. A. Jarvis, D. J. Gladstone, B. W. Pogue, and P. Bruza, "Color Cherenkov imaging of clinical radiation therapy", *Light Sci. Appl.*, vol. 10, no. 1, Nov. 2021. doi:10.1038/s41377-021-00660-0

[4] H. K. Avetissian, G. F. Mkrtchian, M. G. Poghosyan, and K. V. Sedrakian, "Coherent diffraction radiation diagnostics for charged particle beams", *Nucl. Instrum. Methods Phys. Res.*, vol. 528, no. 1–2, pp. 215–219, Aug. 2004. doi:10.1016/j.nima.2004.04.050

[5] A. Savchenko, A. Tiishchenko, and M. Strikhanov, "THz Cherenkov Diffraction Radiation From A Traingular Prism", 11th Int. Symposium (RREPS'15), St Petersburg, Russia, Sept. 2015. https://earchive.tpu.ru/bitstream/11683/22369/1/conference_tpu-2015-C64-C64.pdf#page=110

[6] I. M. Frank, "Coherent Radiation of the Fast Electron in Medium", USSR, 1971. https://www.osti.gov/biblio/4742626

[7] T. Lefevre *et al.*, "Non-invasive Beam Diagnostics with Cherenkov Diffraction Radiation", in *Proc. IPAC'18*, Vancouver, Canada, Apr.-May 2018, pp. 2005–2008. doi:10.18429/JACoW-IPAC2018-WEPAF074

[8] A. Curcio *et al.*, "Noninvasive bunch length measurements exploiting Cherenkov diffraction radiation", *Phys. Rev. Accel. Beams*, vol. 23, no. 2, Feb. 2020. doi:10.1103/physrevaccelbeams.23.022802

[9] D. M. Harryman *et al.*, "First Measurements of Cherenkov-Diffraction Radiation at Diamond Light Source", in *Proc. IBIC'19*, Malmö, Sweden, Sep. 2019, pp. 624–628. doi:10.18429/JACoW-IBIC2019-WEPP037

[10] J. J. G. Garrigos, "Development of the Beam Position Monitors for the Diagnostics of the Test Beam Line in the CTF3 at CERN", PhD Thesis, University of Valencia, 2013.

[11] M. Shevelev and A. S. Konkov, "Peculiarities of the generation of Vavilov-Cherenkov radiation induced by a charged particle moving past a dielectric target", *J. Exp. Theor. Phys.*, vol. 118, no. 4, pp. 501–511, Apr. 2014. doi:10.1134/s1063776114030182

Content from this work may be used under the terms of the CC-BY-4.0 licence (© 2023). Any distribution of this work must maintain attribution to the author(s), title of the work, publisher, and DOI

ISBN: 978-3-95450-236-3 ISSN: 2673-5350 doi:10.18429/JACoW-IBIC2023-MOP033

1L TARGET HARP DIAGNOSTIC DISPLAY TOOL*

A. Walker, E. Kerstiens

Los Alamos National Laboratory, Los Alamos, NM, USA

Abstract

The Los Alamos Neutron Science Center (LANSCE) completed upgrades to its 1L Target Facility, which included installing the new Mark IV target assembly. This added a third tungsten target located upstream of the other two targets. Prior to Mark IV, beam centering on target was achieved by using thermocouples mounted to the quadrants and center of the upper target coolant chamber. It is slightly offset from center of the old upper target and it shadows several of the thermocouples previously used to center beam on target. This required adjustments to the diagnostic tools utilized to monitor position of the H- beam that is being delivered to the 1L target. The original display included the thermocouple readouts and displayed a visual beam profile and position taken from an upstream harp. With some of the thermocouples now being shadowed, an image overlay was added to show where the harp's measured beam position is relative to both the upper and middle targets. This gives the beam operations team an additional level of awareness when it comes to thermocouple temperatures, beam steering, and beam tuning. Details of the display tool and its associated upgrades are presented.

INTRODUCTION

1L HARP Purpose

The purpose of the 1L Target [1] HARP is to provide a profile of beam location as it strikes the target stack. The HARP works in tandem with wire scanners to assist the operations team in beam tuning and loss minimization. The HARP is an extremely valuable tool since the new Mark IV target has been installed. The HARP has a similar program to the wire scanners to show beam position.

1L HARP Diagnostic Display Purpose

The 1L Target HARP Display is an aid to the operations team to provide a graphical representation of beam position. The display aggregates the data from the 1L HARP and utilizes a Gaussian distribution algorithm to provide a "heat map" graphical representation. The display also shows a set of thermocouples that are utilized to further analyze the beam position and intensity.

1L HARP CONSTRUCTION

The 1L Target HARP diagnostic is a set of wires spaced out in the beam line in a grid formation to gather a beam profile. An electrical current is induced in them proportional to beam intensity, which shows the beam profile similar to the wire scanners. The upside to the HARP is it is constantly in the beam line and due to that can be provide constant updates to the beam position. The 1L HARP data can be utilized in a Gaussian fit algorithm to provide a beam position and intensity map. Figure 1 below shows the 1L HARP assembly and wire harness that is part of the 1L Target assembly.



Figure 1: 1L HARP Diagnostic Assembly.

WIRE SCANNERS

1L (Target 1) wire scanner 1, 2, and 3 provides a picture of the beam profile as it is being directed to the target, but don't provide a "live" status of the beam in the event of a tune change. They utilize a single wire inserted in steps in order to get a beam profile. This "live" status is extremely important, and the wire scanners cause significant beam spill making them ineffective for the information needed to visualize. Figure 2 shows a wire scan performed to show beam position in the X and Y axis.

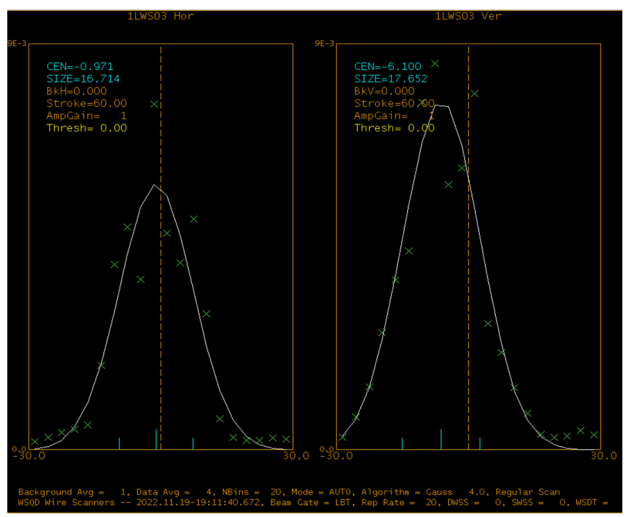


Figure 2: Wire Scanner Diagnostic Tool.

*Work supported by the U.S. Department of Energy, Contract No. DE-AC52-06NA25396

Content from this work may be used under the terms of the CC-BY-4.0 licence (© 2023). Any distribution of this work must maintain attribution to the author(s), title of the work, publisher, and DOI

ISBN: 978-3-95450-236-3 ISSN: 2673-5350 doi:10.18429/JACoW-IBIC2023-MOP033

Content from this work may be used under the terms of the CC-BY-4.0 licence (© 2023). Any distribution of this work must maintain attribution to the author(s), title of the work, publisher, and DOI

NEW MARK IV TARGET

The Mark IV target was installed during the beam outage in 2022. Initial testing and commissioning was performed during the beam run cycle for 2022, and beam on target from 60 to 85 microamps. 2023 expects to see full production beam of 90+ microamps. Installation of the new target required some changes to the diagnostics to better serve the operations team with applicable information. Better analysis of the diagnostics and indications that the operations team needs will continue to be done to further improve the ability to tune the beam on the target.

Target Assembly

Three different target assemblies are utilized to provide neutrons to up to 15 different flight paths for experiments at varying energies. The upper target sits vertically and is housed in tungsten, so getting an accurate picture of the beam profile is key due to thermocouple shadowing and neutron moderation. Below the upper target is the Middle Target which is surrounded by a reflector constructed of beryllium. The lower target also has a liquid hydrogen moderator to further thermalize neutrons being sent to the flight paths. Beam passes down through the top of the assembly and strikes the vertically aligned Upper Target Assembly before passing to the Middle and Lower targets. Figure 3 shows the entire Mark IV Target assembly and its associated components, while Figure 4 (across) shows the upper target assembly portion of the Mark IV Target.

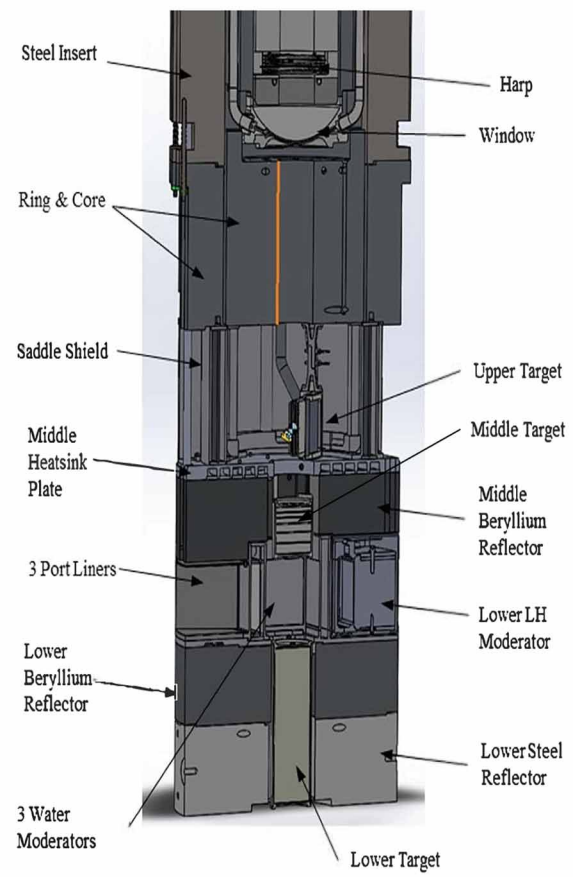


Figure 3: New Mark IV Target.

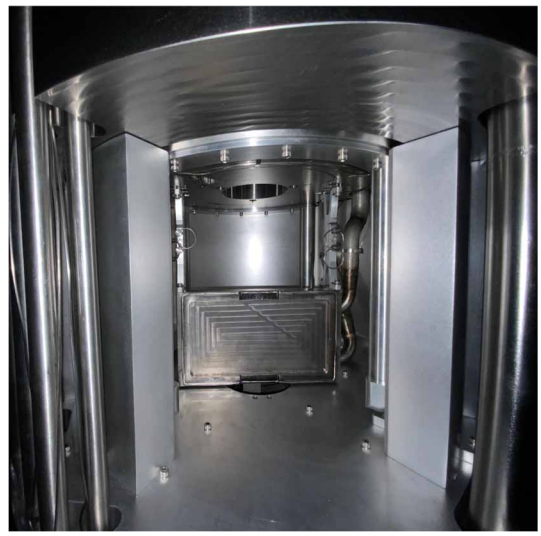


Figure 4: Mark IV Upper Target Assembly.

Thermocouples

Thermocouples are placed in a cross pattern below the upper target assembly to aid operations in determining both the location of the beam striking the target and the intensity of that beam. With the old target assembly there was nothing to "shadow" the thermocouples and potentially hide some of that intensity, so when the Mark IV Target was installed there needed to be some adjustments in order to make operations aware of this beam "shadowing". In the center of the target assembly is the tungsten upper target assembly shadowing the center, half of the lower, and a portion of the upper thermocouple. To the left of the tungsten upper target assembly is water that is shadowing the left, and roughly half of the upper thermocouple. There is no shadowing of the right thermocouple, so reliance solely on thermocouple indications for beam position would be highly unreliable due to three different densities of material covering the different thermocouples.

1L HARP DISPLAY TOOL

The 1L HARP Display Tool is a graphical representation of beam position. It has been in use since 2019 to give the operations team a constantly updating picture of beam position on the 1L Target. It has graphical representations for the thermocouples, vertical upper target assembly, and the water moderator. Thermocouple temperature indications are also shown on the tool to assist operations in beam tuning. Below is a snapshot of the tool without any beam position indication. The pink color is the beam pipe (the circle) and the thermocouples (squares arranged in the cross pattern), the gold color in the upper left in the diagonal shape is the water moderator that is shadowing some thermocouples, and the silver color is the vertical tungsten upper target assembly. Off to the right and the far left is air. Prior to the Mark IV Target installation, there was no need to aid the operations team with this sort of overlay. The HARP tool and wire scanners were sufficient in providing an indication of beam position. However, once the new target was installed, modifications had to be made to ensure

ISBN: 978-3-95450-236-3 ISSN: 2673-5350 doi:10.18429/JACoW-IBIC2023-MOP033

that the correct indications were being utilized due to thermocouple shadowing affecting the temperature indications. Figure 5 is a screenshot of the 1L HARP Display tool without beam on.

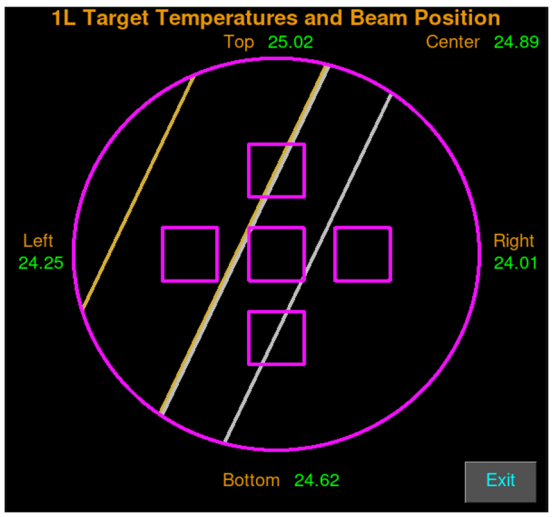


Figure 5: 1L HARP Display Tool (Without Beam).

1L Harp Display Tool (With Beam)

The 1L Harp Display Tool retrieves the HARP data from the EPICS control system and performs a Gaussian fit algorithm to determine the beam position for both the horizontal and vertical positions. This algorithm also determines beam intensity, so a very beneficial indication of both beam location and intensity is provided as an overlay to the thermocouples. This overlay, in addition to the thermocouples and wire scanners is what the operations team utilizes to tune beam as it reaches the 1L Target. The next image is an image with simulated beam position, in order to provide a visual representation of similar to what the operations team would see when tuning. The beam profile would look significantly smaller and would be within the pink circle, but this is a good representation of both the position indication and intensity indications the Gaussian algorithm provides. Figure 6 has simulated beam placed on it to show what the beam position indication looks like.

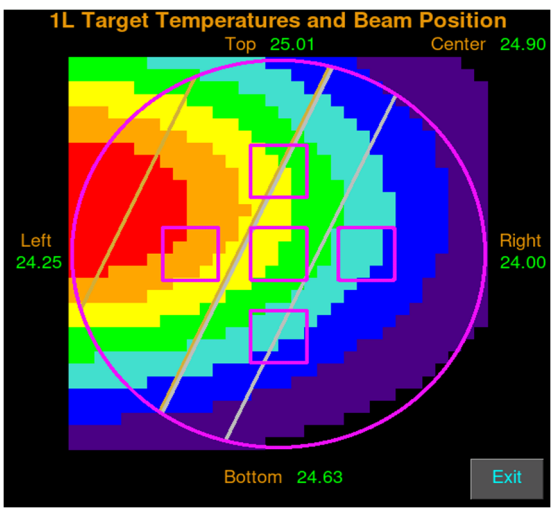


Figure 6: 1L HARP Display Tool (With Simulated Beam).

CHALLENGES

First operation with the new Mark IV Target showed several challenges.

It was unknown how much shadowing the different materials would provide to the various thermocouples. To investigate this, beam was attempted to be centered on each thermocouple to see how each reacted to a given current of beam placed on each. During this evolution, a new problem cropped up that needed to be resolved first.

Steering the beam vertically towards the top thermocouple (the top thermocouple rose in temperature and the bottom lowered) gave the reverse indication with the HARP data and the Gaussian indication (position indication showed the beam moving towards the bottom thermocouple and away from the top thermocouple). This was checked for the horizontal axis and found to respond properly. After utilizing our other diagnostic tools, it was determined that the HARP wires were likely wired backwards. To correct this, a software change was made to reverse the values in the array for the vertical axis. This corrected the position indication issue.

CONCLUSION

Further testing of the thermocouples to determine the extent of shadowing needs to be completed in order to better aid the operations team. Adding the layer of indications for the thermocouples and different moderators has been a benefit to the operations team with their efforts to reliably deliver beam to a newer, smaller beam target.

REFERENCES

[1] E. Kerstiens, *"1L Target, Moderator, Reflector System,"* Reading, Los Alamos National Laboratory, April, 2023.

Content from this work may be used under the terms of the CC-BY-4.0 licence (© 2023). Any distribution of this work must maintain attribution to the author(s), title of the work, publisher, and DOI

ISBN: 978-3-95450-236-3 ISSN: 2673-5350 doi:10.18429/JACoW-IBIC2023-MOP036

A NEW APPROACH FOR CANADIAN LIGHT SOURCE FUTURE ORBIT CORRECTION SYSTEM DRIVEN BY NEURAL NETWORK

S. Saadat* and M. J. Boland[1], Canadian Light Source, Saskatoon, Canada
[1]also at University of Saskatchewan, Saskatoon, Canada

Abstract

The orbit correction system (OCS) of the Canadian Light Source (CLS) comprises of 48 sets of BERGOZ beam position monitors (BPM). Each BPM has the ability to measure the position of the beam in both the *X* and *Y* directions and can record data at a rate of 900 Hz times per second. Inverse Response Matrix (IRM) is utilized to determine the optimal strength of the 48 sets of orbit correctors in both the *X* and *Y* directions, in order to ensure that the beam follows its desired path. The suggestion in this study is to replace the singular value decomposition (SVD) function with a neural network algorithm, which will act as the central processing unit of the orbit correction system. The training model's design includes three hidden layers, and within each layer, there are 96 nodes. The neural network's outputs for regular operations in CLS exhibit a mean square error (MSE) of 10^{-7}. Various difficult scenarios were created to test the OCS at 8.0 mA, using offsets in different sections of the storage ring. However, the new model was able to produce the necessary orbit correctors (OC) signals without any trouble.

INTRODUCTION

The CLS synchrotron light source storage ring consists of twelve sections and operates at a 2.9 GeV energy level. To maintain the stability of the beam position in the storage ring, an Orbit Correction System is utilized to correct any disturbances.

In 2000, the Motorola single-board computer was the initial implementation of a real-time controller [1]. In 2008, the previous system for correcting the orbit was upgraded and replaced by the current OCS [2]. In 2009, CLS developed and tested a new orbit correction system the CLS Matlab application, known as CLSORB, with a high-speed capability [3]. This system offers an adjustable rate range of 20 Hz to 100 Hz.

The OCS at CLS comprises a computer that runs Matlab, along with four Versa Module Eurocards (VMEs). Each VME corresponds to three sections of the storage ring. Additionally, the system also incorporates a Real-Time Executive for Multiprocessor System (RTEMS). The purpose of this advanced system is to ensure that any disturbances caused by electron perturbations are immediately detected and corrected to maintain beam stability and optimal light quality at the beamlines. Hardware and software of the orbit control systems were developed until the RMS deviation of beam motion was reduced to less than one micrometer in both the *X* and *Y* directions. The Accelerator Operations and Development (AOD) team is currently working on upgrading this system, which suggests that there are new developments underway to enhance its functionality and capabilities. This involves improving its efficiency, increasing its accuracy, or adding new features to meet the evolving needs of users. With technological advancements being made every day, it is important to keep upgrading existing systems to stay relevant and efficient in a rapidly changing landscape. The AOD team has embarked on new research to design a Dynamic Orbit Correction System (DOCS) based on Neural Network (NN) algorithm for the orbit correction system. The NN correction system offers advantages over the IRM algorithm, excelling in dynamic adaptability, flexible programming, and computation speed. Unlike the static IRM, the NN system learns from data, making it accurate in changing conditions. Its adaptable nature handles misalignments effectively. The NN's efficient script allows customization and rapid computations, while IRM's matrix recalculations slow it down. The precision and real-time capabilities of this DOCS have been reported [4]. The aim of this research is to improve the accuracy of the neural network model by incorporating deep learning techniques. To achieve this goal, we will conduct experiments and analyze the data to determine the effects of deep learning methods on accuracy.

NEURAL NETWORK

A neural network is a type of machine-learning model inspired by the structure and function of the human brain. It consists of interconnected nodes or neurons that process information to make predictions or decisions [5]. Also, deep learning is a subfield of machine learning that uses neural networks with multiple layers to extract and learn features from data. It is capable of automatically discovering complex patterns and relationships in large datasets [6].

The following sections will briefly discuss the neural network architecture and parameters utilized in the CLS orbit correction system model, and also provide a definition of deep learning loops.

Network Architecture

Designing a neural network architecture requires a significant amount of information about the real system it will be applied to, as the architecture is highly dependent on the specific characteristics and structure of the system. In brief, the CLS orbit correction system is comprised of 96 Bergoz Beam Position Monitors (BPMs) that transmit the beam's position to the IRM at a frequency of 900 measurements per second. The IRM serves as the central processing unit of the OCS, responsible for computing the strength of the Orbit Correctors. Ultimately, the 96 outputs from the IRM

* shervin.saadat@lightsource.ca

Content from this work may be used under the terms of the CC-BY-4.0 licence (© 2023). Any distribution of this work must maintain attribution to the author(s), title of the work, publisher, and DOI

ISBN: 978-3-95450-236-3 ISSN: 2673-5350 doi:10.18429/JACoW-IBIC2023-MOP036

are transmitted to the 96 orbit correctors at a rate of 18 transmissions per second.

In the first step, we designed a neural network algorithm instead of using IRM. For this case, we utilized the TensorFlow-Keras library in Python, which is renowned for its speed and is considered one of the fastest AI modules. The neural network consists of three hidden layers with 96 nodes, and the best activation function was found to be hyperbolic tangent. After a single learning step with 20 epochs, the model achieved a MSE of (3.152×10^{-7}). The Mean Squared Error is a loss function that measures the average squared difference between the predicted values and the actual target values in the training dataset.

Deep Learning Loops

The initial model performed well, and its real-time capabilities were tested on actual data, exhibiting negligible error when the system was in a stable mode. In addition to the aforementioned scenario, there is another situation that should be taken into account, when the beam position changes significantly. In this case, the neural network model must be capable of adapting to these changes in order to provide accurate predictions. Therefore, it is essential to ensure that the model is trained using a diverse set of data that encompasses a wide range of beam positions and conditions. This will enable the model to effectively learn and generalize to new and unseen scenarios, including cases where the beam position changes drastically. In this study, a learning loop was designed to address the issue at hand. The loop begins by loading the initial model, after which a new dataset is evaluated using the model. If the error of the model's output exceeds the expected value, the model is updated with new epochs and activation functions as necessary. Finally, Fig. 1 the accuracy of the updated model is checked, and it replaces the previous model if it performs better.

EXPERIMENTS AND RESULTS

The CLS storage ring is comprised of twelve distinct sections, each of which contains four BPMs and four OCs with both x and y directions. This configuration yields a total of 96 inputs and 96 outputs for the orbit correction system. Figure 2 shows a schematic of BPMs configuration in the storage ring. Ninety-six inputs, which correspond to BPMs, are recorded at a rate of 900 Hz, while the system generates ninety-six outputs, which correspond to OCs, at a rate of 18 Hz.

There are two scenarios that we have assumed for the system. In the first scenario, the system operates in a stable mode, and the learning loop attempts to improve its model accuracy. In the second scenario, the stable mode changes to varying positions, and the learning loop modifies the model to prepare for the future. In this research, we investigated the deep learning capabilities of the DOCS platform. Due to the lack of available real-time data, we collected data from the EPICS at the CLS using a sampling frequency of 900 Hz for BPMs and 18 Hz for OCs. The collected data was saved

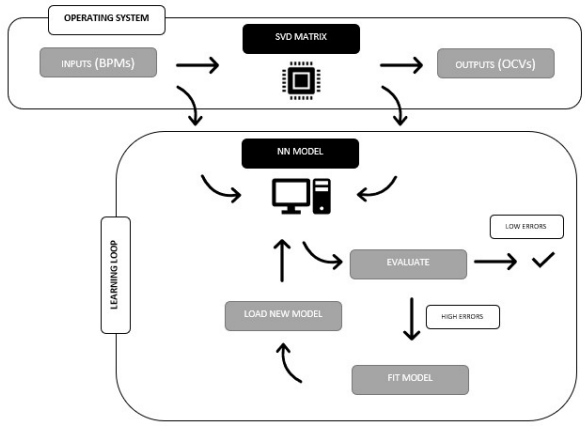


Figure 1: The BPM and OCV datasets from the real system are fed into the learning loops. The NN model uses the BPMs to generate new OCVs, and the error between the predicted and real OCVs is calculated. If the error exceeds the expected threshold, the NN model is updated with the current dataset and replaces the old NN model. This loop is repeated periodically to refine the NN model.

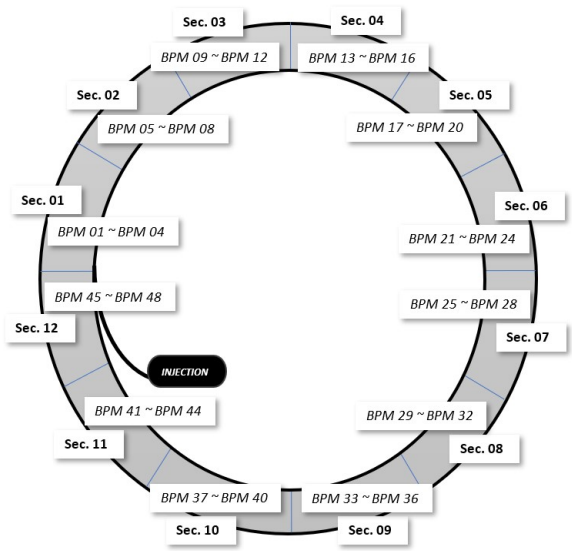


Figure 2: schematic of the CLS (Canadian Light Source) storage ring that comprises twelve sections and 48 BPMs.

in large JSON files, which were then split into smaller files for use in our deep-learning model.

In the first scenario, when the system is functioning normally, we conducted the learning loop four times. During the first phase, we developed the model, while the second to fourth phases involved updating the model. In addition, we introduced a metric called Accumulated Error (AE), which represents the sum of errors across all OCs. The calculation of AE involves taking the absolute difference between the real value of the orbit corrector and the predicted OC, divided by the real data.

Content from this work may be used under the terms of the CC-BY-4.0 licence (© 2023). Any distribution of this work must maintain attribution to the author(s), title of the work, publisher, and DOI

ISBN: 978-3-95450-236-3 ISSN: 2673-5350 doi:10.18429/JACoW-IBIC2023-MOP036

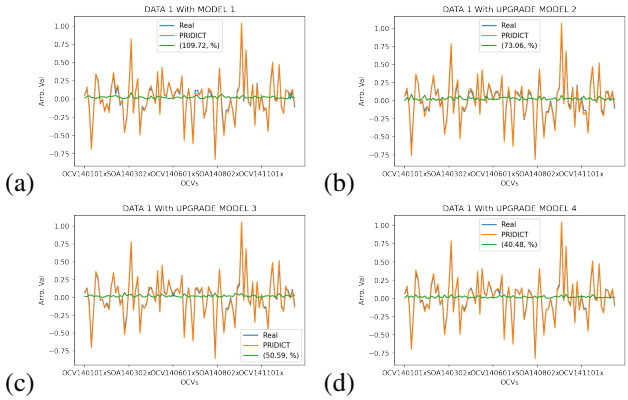


Figure 3: The blue line represents the actual data for 96 OCs obtained through the SVD algorithm. The orange line represents the predicted values for the same OCs obtained through NN models. The green line shows the difference between the actual and predicted values. The green value corresponds to the total error (AE) calculated across all 96 OCs. The horizontal axis shows the 96 orbit correctors. (a) The first model, (b) the first upgrade, (c) the 2nd modification, (d) t6he 3rd upgrade.

Our developed model demonstrates excellent performance, with an AE of 109.72 %. When applied to the 96 OCs, the error rate per OC is estimated to be approximately 1.1 %. Figure 3(a) suggests that the model is robust and reliable in predicting values for the given dataset. We implemented the deep learning loops step by step, beginning with an upgrade without any changes in the epochs and architecture. Remarkably, the AE decreased to 73.06 %, indicating a significant improvement in performance. This corresponds to an error rate of approximately 0.76 % per orbit corrector, which is substantially lower than the previous error rate. Figure 3(b) demonstrates the efficacy of the deep learning approach in improving the accuracy of the model. Continuing with the upgrade, we observed in the Fig. 3(c) a further improvement in the model's performance. The AE decreased to 50.59 %, which equals an error rate of approximately 0.53 % per OC. 4th upgrade, we observed in the Fig. 3(d) again more improvement in the performance. The AE decreased to 40.48 %, or 0.42 % per OC.

In the following scenario, the beam position is expected to undergo a sudden change, presenting a challenging situation for the OCS. We aim to investigate whether this loop can update a model with memorized coefficients, furthermore, we will calculate the error that arises during this process. The objective of this experiment is to evaluate the effectiveness of the updates to the NN model, and to assess whether they result in a decreasing or increasing trend in performance.

At the CLS, a total of four BPMs and four OCs are installed in each section of the storage ring. Each BPM is equipped with both Horizontal (H) and Vertical (V) detectors. Specifically, BPM01–04 are located in section one, and BPM05–08 are installed in section two, and similarly, the BPMs configuration is repeated throughout the remaining sections as shown in Fig. 2.

Table 1: Some of the adjustments made to the reference or offset (µm) were shown to demonstrate the change in BPM values across different sections of the SR. 'H' and 'V' refer to the horizontal and vertical detectors, respectively.

Experiment No.	Section	BPMs	Offset (µm)
1	1	BPM 01 (H)	+1000
		BPM 01 (V)	-1000
2	1	BPM 01 (H)	+500
		BPM 01 (V)	+500
19	ALL	BPM 01-08 (H)	+500
		BPM 01-08 (V)	+500
		BPM 09-16 (H)	-1000
		BPM 09-16 (V)	-1000
		BPM 17-24 (H)	+500
		BPM 17-24 (V)	+500
		BPM 25-32 (H)	-1000
		BPM 25-32 (V)	-1000
		BPM 33-40 (H)	-1000
		BPM 33-40 V)	-1000
		BPM 41-48 (H)	-1000
		BPM 41-48 (V)	-1000
20	ALL	BPM 01-48 (H)	Rand.
		BPM 01-48 (V)	Rand.

In this experiment, the BPM's values in different sections of the SR were changed by adjusting the reference (offset) to create a desired beam position situation (+1 and –1 mm) for the OC system. The system was tested at a beam current of 8.0 mA. Table 1 displays the alterations to the reference (offset) and how they reveal variations in BPM values across distinct SR sections.

The OCS's performance was recorded in the aforementioned scenarios for both BPMs and OCs. This data was subsequently utilized to learn, train, test, and develop DOCS.

In this research, we tested several assumptions and found that the results of all of them were the same. Here, we present one of these results. In the first scenario, the beam is in the position that corresponds to test 1 in the Table 1. The NN model was developed (with 80 epochs and the same architecture) for this situation, and we consider it to be our initial model which has 1.184 % error per OC as shown in Fig. 4(a). The learning loop attempts one upgrade and generates an NN-upgraded model with an error rate of 0.515 % per OC as shown in Fig. 4(b). Following that, a disturbance occurs, and the system transitions into the mode detailed in test 20 of Table 1. The NN model was updated twice during this period, as depicted in Figs. 4(c) and 4(d). The turbulence is controlled, and the perturbation sequence returns to mode 1, the NN model has upgraded twice again shown in Figs. 4(e) and 4(f). Finally, the system experiences a period of instability, during which the perturbation sequence exhibits unpredictable behavior. As a result, the learning loop generates two new updates for the NN model, as shown in Figs. 4(g) and 4(h).

Content from this work may be used under the terms of the CC-BY-4.0 licence (© 2023). Any distribution of this work must maintain attribution to the author(s), title of the work, publisher, and DOI

ISBN: 978-3-95450-236-3 ISSN: 2673-5350 doi:10.18429/JACoW-IBIC2023-MOP036

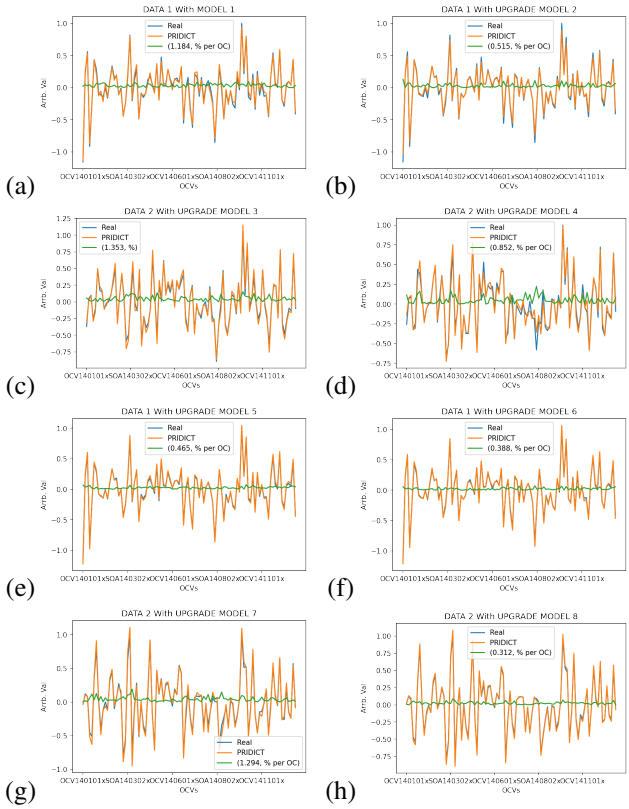


Figure 4: The blue line represents the actual data for 96 OCs obtained through the SVD algorithm. The orange line represents the predicted values for the same OCs obtained through NN models. The green line shows the difference between the actual and predicted values. The green value corresponds to the mean error for each OC. The horizontal axis shows the 96 orbit correctors. (a) The first model, (b) 1st upgrade, (c) 2nd upgrade , (d) 3rd upgrade, (e) 4th upgrade, (f) 5th upgrade, (g) 6th upgrade, (h) 7th upgrade.

The scenario described, demonstrates that updates to the NN model's weight parameters are effective, resulting in a statistically significant decrease in error rates over time.

CONCLUSION

Two conditions of the NN model's effectiveness were investigated, a stable mode and a complex mode. The results for the stable mode demonstrate that error rates decrease over time, from 1.1 % per OC in the first experiment to 0.42 % per OC after four steps. While this result was expected, it provides further confirmation of the effective operation of the deep learning loops in the NN model, which successfully reduce error rates over time in the stable mode condition. The results of the second scenario are less definitive than those of the stable mode upgrade, as shown in Fig. 5. However, they do display a decreasing trend in error rates despite some fluctuations.

Figure 5 shows a decreasing trend in prediction errors for a specific data set (upgrades 1 and 2), but the deep learning model is unable to generalize its performance to new

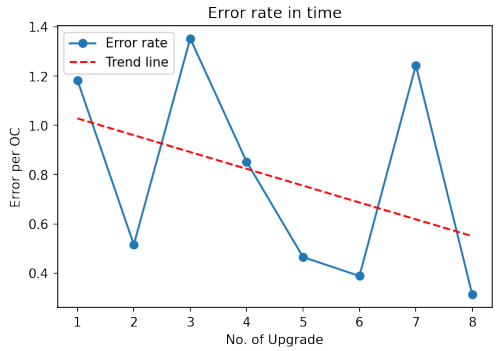


Figure 5: Errors (percentage per OC) are displayed in eight upgraded steps. The blue dots represent the mean errors in each step, the red line shows the trend of the errors.

data sets (upgrade 3) without further training. However, next step training result in reduced errors on new data sets (upgrades 4 and 5). This cycle continues, and the errors decrease smoothly over time. The results demonstrate that the NN model is highly effective, and the Deep Learning loop successfully increasing the model's precision. While the results show promise and suggest that the NN model could be a valuable technology for various applications, it is important to acknowledge the limitations of our study and the need for further research to thoroughly explore its capabilities and potential applications. The current findings, while encouraging, should be viewed with a degree of restraint, and additional studies are warranted to establish the full extent of the NN model's benefits and limitations.

ACKNOWLEDGEMENTS

The authors would like to thank Tonia Batten, Johannes Vogt, Ward Wurtz, Cameron Baribeau, Hamed Shaker, Drew Bertwistle, Mike Bree, and Fredric Le Pimpec, as well as all other AOD members of the CLS operation group.

REFERENCES

[1] L. Dallin, I. Blomqvist, M. de Jong, D. Lowe, and M. Silzer, "The Canadian Light Source", in *Proc. PAC'03*, Portland, OR, USA, May 2003, paper TOPA001.

[2] D. Chabot, "SR1 Orbit Control Design Note", *CLS Document*, 2008.

[3] C.G. Payne and D. Chabot, "Fast Orbit Correction at the Canadian Light Source", in *Proc. PCaPAC'10*, Saskatoon, Canada, Oct. 2010, paper WECOMA02, pp. 9–11.

[4] S. Saadat and M. Boland, "Model of a dynamic orbit correction system based on neural network in CLS", in *Proc. IPAC'23*, Venice, Italy, May 2023, pp. 2862-2865. doi:10.18429/JACoW-IPAC2023-WEPA094

[5] M.T. Hagan, H.B. Demuth, M.H. Beale, and O. De Jesus, *Neural Network Design*, 2002. https://hagan.okstate.edu/NNDesign.pdf

[6] I. Goodfellow, Y. Bengio, and A. Courville, *Deep Learning*, MIT Press, 2016.

Content from this work may be used under the terms of the CC-BY-4.0 licence (© 2023). Any distribution of this work must maintain attribution to the author(s), title of the work, publisher, and DOI

ISBN: 978-3-95450-236-3 ISSN: 2673-5350 doi:10.18429/JACoW-IBIC2023-MOP037

TUNE FEEDBACK AT THE CANADIAN LIGHT SOURCE

W. A. Wurtz*, C. K. Baribeau, A. M. Duffy
Canadian Light Source, Saskatoon, Saskatchewan, Canada

Abstract

In order to maintain good injection efficiency for top-up operation at the Canadian Light Source, we must keep the betatron tunes constant even as changes in insertion device fields cause the tunes to vary. To meet this requirement, we implemented a tune feedback system. We measure the tunes at a rate of 1 Hz using Dimtel bunch-by-bunch systems. The transverse feedback function of the bunch-by-bunch systems provides tune measurements without disturbing the electron beam. We adjust two quadrupole families at a rate of 0.25 Hz to control the horizontal and vertical tunes. In this article we describe the tune feedback system, its development and its performance. The system has proven to be very robust, enabling reliable top-up operation.

INTRODUCTION

The Canadian Light Source (CLS) began operating in top-up mode for user operations in 2021. In top-up mode, charge is injected into the storage ring every few minutes to maintain a constant current with the present target being between 219 and 220 mA. Top-up requires reliable and efficient injection, and the tune feedback application is an important part of our top-up implementation. We developed the tune feedback application in an iterative manner, incorporating feedback from operators and subject matter experts. Through each iteration we identified operational issues, implemented corrections or new features to resolve the issues, tested the new features and their interactions with existing features and deployed the new version. The resulting product can gracefully handle a variety of situations and provides an alarm and diagnostic information for the operators. The algorithm is adjustable for machine studies outside of user mode, or to implement workarounds while we resolve issues with external systems. Overall, the tune feedback application has been successful and top-up operation has been reliable.

TUNE AND INJECTION

For top-up mode, we desire that >90% of the charge injected into the storage ring be captured. We measure the stage 2 injection efficiency using an integrating current transformer (ICT) at the end of the transfer line and the parametric current transformer (PCT) in the storage ring. Because there is some uncertainty in the ICT calibration, we give the stage 2 injection efficiency in arbitrary units (a.u.) with a stage 2 efficiency of 97 a.u. meaning that somewhere between 94 and 100% of the electrons were captured.

We have previously reported on injection efficiency issues caused by a superconducting wiggler, BMIT SCW4 [1], and an elliptically polarizing undulator, SM EPU75 [2]. We show updated injection efficiency tune scans for these devices in Fig. 1. The nominal tunes, represented by a diamond marker, are 10.242 for the horizontal and 4.290 for the vertical. We see that the nominal tunes are on a small island of good injection efficiency, and if the tunes were to shift, the stage 2 efficiency would quickly become unacceptable. Tune shifts are mostly caused by insertion device field changes.

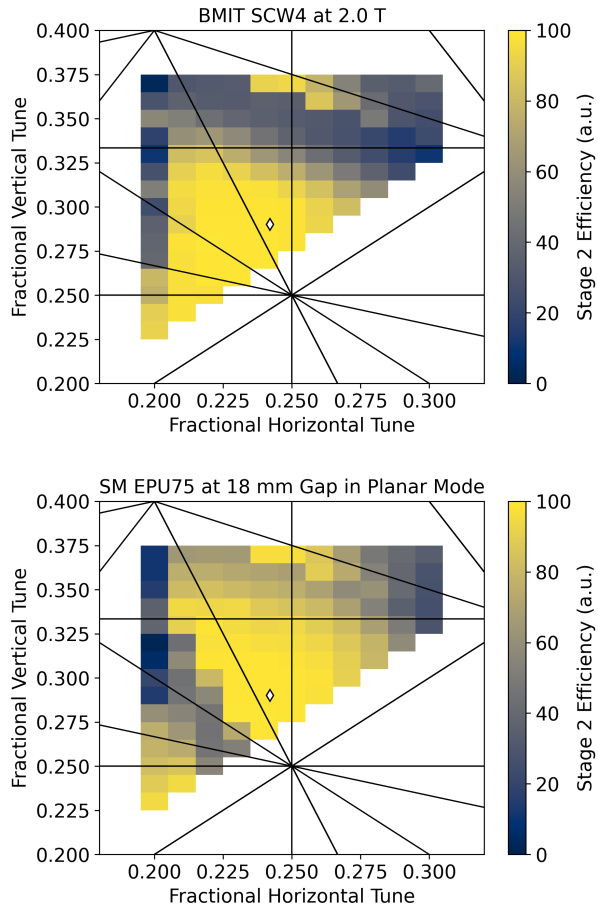


Figure 1: Measurements of injection efficiency as a function of the fractional tunes for two insertion devices with all other insertion devices forced open or turned off. We operated the BMIT SCW4 at approximately half its maximum field in order to avoid quenching the device during the measurement.

We do not measure the integer portions of the tunes during normal operations and obtain the fractional portions by performing a Fourier transform of position data. In this work, if we say that the horizontal tune is 0.242, the integer portion is understood to be 10, and similar for the vertical with an integer portion of 4.

* ward.wurtz@lightsource.ca

Content from this work may be used under the terms of the CC-BY-4.0 licence (© 2023). Any distribution of this work must maintain attribution to the author(s), title of the work, publisher, and DOI

ISBN: 978-3-95450-236-3 ISSN: 2673-5350 doi:10.18429/JACoW-IBIC2023-MOP037

DEVELOPMENT

The tune feedback application began with a simple script written by an accelerator physicist in Python using PyEpics [3]. While it was able to control the tunes during an eight hour machine development shift, it was far from being the robust tool that we needed for reliable operation in user mode.

The script was given to a system analyst and we began developing it into a useful application, taking an approach heavily influenced by flow-based agile [4]. The product vision was for a robust application that would function with essentially 100% uptime and would be easy for the operators to use. For each iteration, we created a backlog of features, ranked them in priority, and implemented them. The CLS machine schedule provides a maintenance shift every week, which allowed us to test our software without beam. If the test was successful, we would then schedule a dedicated shift for online testing with beam. The results from each test informed our revisions to the backlog of features for the next iteration.

As soon as we had a version that was robust enough to survive our attempts to make it fail, we called this version the minimum viable product and began running it in normal operations. We quickly built a new backlog using feedback from our operators and our own observations of how the system functioned in the real environment. We continued to iterate, first quickly, then more slowly until we had a robust application with the features necessary to survive all the cases that it encountered in user and machine studies modes of operations.

The iterative process was essential for this project, and we could not have been successful with a traditional/waterfall approach. With a system as complex and dynamic as a storage ring, there was no way for us to foresee all the features that were needed to make the tune feedback application robust.

THE TUNE FEEDBACK SYSTEM

Figure 2 shows the tune feedback system expert panel. The data and controls displayed on this panel are the result of several development iterations. Grayed fields can only be changed while the tune feedback loop is open.

The CLS storage ring uses Dimtel iGp12 bunch-by-bunch systems [5] for transverse feedback and other bunch-by-bunch applications. When transverse feedback is running, the averaged bunch spectra from these systems contain notches at the tune frequencies due to the negative feedback loop [6, 7]. These notches have proven to be robust measurements of the fractional betatron tunes. The plots 'TFC:2405-101:X:SRAM:SPEC' and 'TFC:2405-102:Y:SRAM:SPEC' in Fig. 2 show example spectral data with notches at the horizontal and vertical tunes, respectively.

We input the CLS injection timing trigger, which has a constant rate of 1 Hz whether we are injecting or not, to the bunch-by-bunch system. The bunch-by-bunch system captures the data to calculate the notched spectra before the trigger. Without this deliberate choice of timing, the injection transient caused when the kickers do trigger would obscure the notches.

There are a variety of circumstances where we require the tune feedback application to cease adjustments to the quadrupoles, such as when the betatron tunes cannot be accurately measured. We have codified these circumstances with a signal status, where the application will only adjust quadrupole settings when the signal status is deemed GOOD. The circumstances that render the signal status anything other than GOOD are configurable in the application's expert panel, however, we permit most settings to be adjusted only when the feedback loop is open.

The notch is always negative in the spectral waveforms and we require that it crosses a threshold, represented by the horizontal lines in the plots. The threshold is determined by calculating the standard deviation of the waveform in a region away from the notch, then multiplying the standard deviation by a user defined number, which is 10.0 in Fig. 2 for both the horizontal and vertical. If the notch does not cross the threshold, which occurs if the stored beam is lost or if the stored current is too low, then the signal is declared LOW and the tune feedback loop will open after a user specified number of attempts, which is set to 3 in Fig. 2.

If a vacuum transient occurred in the storage ring, or if a trigger was misconfigured such that the injection transient appeared in the spectral waveforms, then the waveforms would be positive going, obscuring the notch. To handle this situation we calculate the skewness of the waveforms,

$$g_1 \equiv \frac{m_3}{s^3} \tag{1}$$

where s is the sample standard deviation and

$$m_3 \equiv \frac{1}{N}\sum_{i=1}^{N}(x_i - \bar{x})^3 \tag{2}$$

is the third central moment of the waveform data, x_i with sample mean $\bar{x}$. Skewness is a dimensionless number that is easy to understand intuitively; it tells us whether, and by how much, the distribution is skewed positive or negative.

The application has a user defined maximum skewness threshold, set to 0.0 in Fig. 2 for both horizontal and vertical. If the skewness is above this threshold, the signal is declared BAD and the tune feedback loop will open after a given number of attempted tune measurements, which is set to 15 in Fig. 2.

If the application does not receive fresh data from the bunch-by-bunch system in a given number of seconds, set to 10.0 s in Fig. 2, the signal is declared TIMEOUT and the tune feedback loop will open.

In normal conditions, for the signal to have status GOOD and allow the tune feedback loop to be closed, the notch must be large, the skewness must be negative and the waveforms from the bunch-by-bunch system must be updating.

If we lose the beam in the storage ring, the tune feedback loop opens because the signal goes LOW. It might also be

Content from this work may be used under the terms of the CC-BY-4.0 licence (© 2023). Any distribution of this work must maintain attribution to the author(s), title of the work, publisher, and DOI

ISBN: 978-3-95450-236-3 ISSN: 2673-5350 doi:10.18429/JACoW-IBIC2023-MOP037

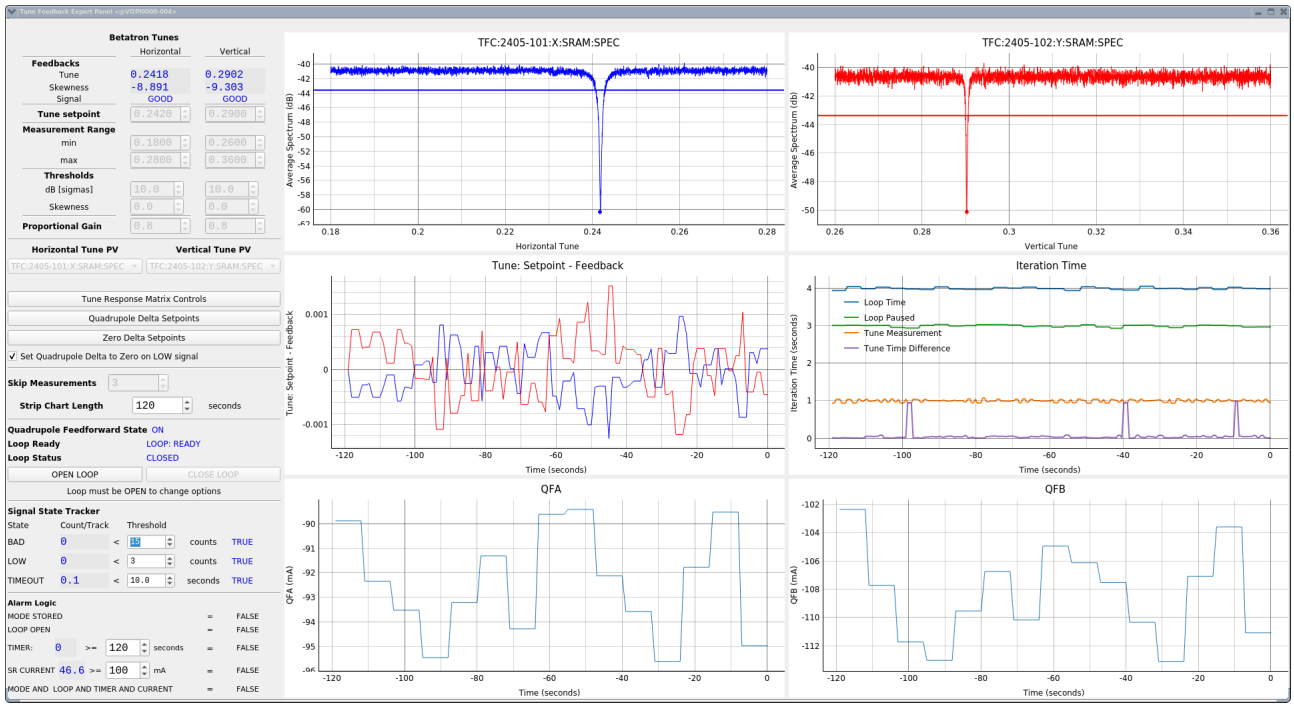


Figure 2: Tune feedback system expert panel.

BAD, but we have specified that LOW will take priority over BAD. After the signal goes LOW, what should the quadrupole set points do? Through testing and experience, we found that we usually want to set the quadrupoles to their default settings, zeroing any offsets that tune feedback has applied. This makes it easier for the operators to perform the recovery injection, when many insertion device gaps are opened. However, for some machine studies activities, we want the opposite behaviour, with the quadrupole values staying unchanged when we intentionally dump the beam. The checkbox 'Set Quadrupole Delta to Zero on LOW signal' on Fig. 2 allows the operator to set the desired behaviour.

For signals that are BAD but not LOW, the tune feedback application does not set the quadrupoles to their default values, and this is a choice based on experience. A BAD signal usually means a vacuum transient is occurring in the storage ring. The desired behaviour is for tune feedback to pause during a short transient, and resume after it passes.

The nominal tune feedback configuration settings are conservative to ensure that the application does not attempt to correct the tunes using questionable data. If there is an issue with the signals from the bunch-by-bunch system, there are many degrees of freedom to adjust in order to keep tune feedback operating. For example, we replaced a failed component external to the bunch-by-bunch system and this caused a slight timing change for an incoming signal. This resulted in notches that were not optimal with some positive going structure and small signals. We were able to adjust the tune feedback application options in order to run with the distorted notches until the bunch-by-bunch system was reoptimized for the shifted timing.

Once we have the tune measurements, we can use two quadrupole families to adjust them. We use the QFA and QFB quadrupole families, which are the two quadrupole families between the ends of the straight sections and the dipoles in the double bend acromats, as shown in Fig. 3. For the CLS storage ring, all of the vertical focusing is done in the dipoles, so there are no vertically focusing quadrupoles. We are able to use two horizontal focusing quadrupoles because the horizontal and vertical betatron functions are very different at these quadrupole locations. The quadrupoles can be adjusted together to control one tune without varying the other.

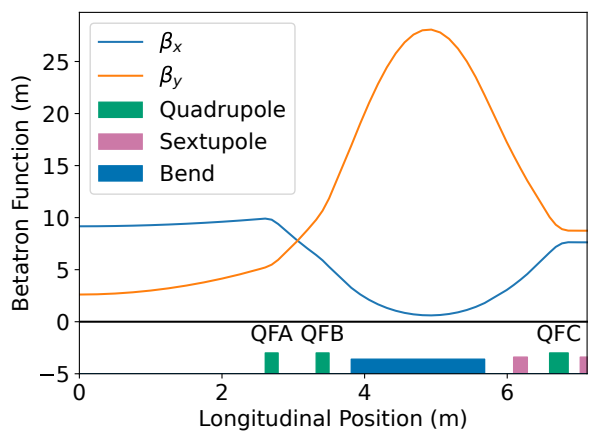


Figure 3: Betatron functions for one half of a double bend acromat cell.

Content from this work may be used under the terms of the CC-BY-4.0 licence (© 2023). Any distribution of this work must maintain attribution to the author(s), title of the work, publisher, and DOI

ISBN: 978-3-95450-236-3 ISSN: 2673-5350 doi:10.18429/JACoW-IBIC2023-MOP037

As we are treating quadrupoles as families, we are performing a global tune correction, not a local correction. The tune feedback application outputs settings to a Quadrupole Feedforward application, which applies offsets to the quadrupole settings without overwriting the nominal settings.

The tune feedback application can measure a 2x2 response matrix by varying the two quadrupole families and measuring the tune shifts. It then inverts the response matrix to determine the necessary change in quadrupole settings to shift the tunes toward the desired setpoints. This is a simple proportional loop and the application includes proportional gains, which are set to 0.8 in Fig. 2. The plot 'Tune: Setpoint - Feedback' in Fig. 2 shows that, as the tunes vary due to noise in magnet power supplies and insertion device motion, the tune feedback application brings the difference toward zero.

The quadrupole power supplies date from the original installation of the storage ring and the design is over 20 years old. They are not intended to be updated quickly and we find that updating them at 0.25 Hz works well. The tune data update at a rate of 1 Hz and the tune feedback application simply skips a number of tune measurements, set to 3 in Fig. 2. The 'Iteration Time' plot in Fig. 2 shows the time to take a tune measurement, the pause when skipping measurements and the total loop time. The 'Tune Time Difference', which should ideally be zero, is not always so; this is a complex timing issue stemming from how we get the information from the bunch-by-bunch system. We chose not to resolve this issue as it would have required substantial investigation time for no practical benefit.

The tune feedback application generates an alarm to tell the operators if the loop is open when it should be closed. The logic developed over several iterations as we worked to suppress nuisance alarms. For modes other than user operations (mode: STORED), tune feedback is not required. If we are delivering low current for beamline conditioning, the signals from the bunch-by-bunch system may not be sufficiently strong, so we don't use tune feedback. After an injection, completing the procedure requires a number of seconds between the operator switching to STORED mode and closing the tune feedback loop; the alarm is suppressed after entering STORED mode for a short time, set to 120 s in Fig. 2. Using this logic, nuisance alarms have been suppressed; if the tune feedback alarm appears in the alarm handler, then there is a real problem. For example, a recent vacuum issue in the storage ring caused a number of tune feedback alarms because the loop was opening when a vacuum transient would cause the signal to be BAD for more than 15 tune measurements. The tune feedback application functioned as designed and the failed vacuum component was identified and replaced.

While the expert panel of Fig. 2 contains many useful features, the operators rarely need to adjust them. Figure 4 shows a very simple GUI, which presents the most important information, allows the operators to turn the systems on and off, and provides access to the expert panel.

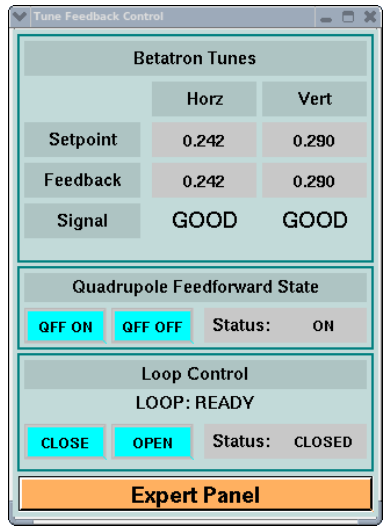


Figure 4: Tune feedback operator controls.

CONCLUSION

When CLS moved from decay mode operation to top-up, we received a very positive response from the user community. With an eclectic mix of insertion devices, the horizontal and vertical tunes will vary as insertion device setpoints are changed. The tune feedback system has been essential for maintaining good injection efficiency in this dynamic environment. The final product is the result of several development iterations and input from many individuals.

ACKNOWLEDGMENTS

We would like to thank D. Teytelman (Dimtel), T. Batten (CLS) and J. Vogt (CLS) for implementing and maintaining the bunch-by-bunch system and teaching us how to use it.

The Canadian Light Source receives funding form the Canadian Foundation for Innovation, the Natural Science and Engineering Research Council of Canada, the University of Saskatchewan, the Canadian Institute for Health Research and the Government of Saskatchewan.

REFERENCES

[1] W. A. Wurtz, L. O. Dallin, and M. J. Sigrist, "Beam Based Measurements with Superconducting Wigglers at the Canadian Light Source with Applications to Nonlinear Beam Dynamics", in *Proc. IPAC'12*, New Orleans, LA, USA, May 2012, paper TUPPP001, pp. 1599–1601.

[2] W. A. Wurtz, C. K. Baribeau, and M. J. Sigrist, "Rectifying unexpected injection issues due to an elliptically polarizing undulator", *Nucl. Instr. and Meth. A*, vol. 1048, p. 168001, 2023. doi:10.1016/j.nima.2022.168001

[3] The PyEpics Collaboration, https://pyepics.github.io/pyepics/index.html

[4] Project Management Institute and Agile Alliance, *Agile Practical Guide*, pp. 24-25, Project Management Institute Inc., 2017.

[5] Dimtel, San Jose, USA. http://www.dimtel.com

Content from this work may be used under the terms of the CC-BY-4.0 licence (© 2023). Any distribution of this work must maintain attribution to the author(s), title of the work, publisher, and DOI

ISBN: 978-3-95450-236-3 ISSN: 2673-5350 doi:10.18429/JACoW-IBIC2023-MOP037

[6] D. Teytelman, *iGp12-285F Signal Processor Technical User Manual*, Rev 2.15, 2019.

[7] D. Teytelman, "Experience with feedback systems in modern synchrotron light sources", presented at the Accelerator Performance and Concepts Workshop, Frankfurt, Dec. 2018. https://indico.gsi.de/event/7510/contributions/33547/attachments/24263/30374/dt_feedback_apec_20181211.pdf

Content from this work may be used under the terms of the CC-BY-4.0 licence (© 2023). Any distribution of this work must maintain attribution to the author(s), title of the work, publisher, and DOI

ISBN: 978-3-95450-236-3 ISSN: 2673-5350 doi:10.18429/JACoW-IBIC2023-MOP038

DEVELOPMENT OF AN ACTIVE BEAM-STABILIZATION SYSTEM FOR ELECTROFISSION EXPERIMENTS AT S-DALINAC*

D. Schneider†, M. Arnold, U. Bonnes, A. Brauch, M. Dutine, R. Grewe,
L. E. Jürgensen, N. Pietralla, F. Schließmann, G. Steinhilber
Technische Universität Darmstadt, Institute for Nuclear Physics, Darmstadt, Germany

Abstract

The r-process fission cycle terminates the natural synthesis of heavy elements in binary neutron-star mergers. Fission processes of transuranium nuclides will be studied in electrofission reactions at the S-DALINAC. Due to the minuscule fissile target, the experimental setup requires an active electron-beam-stabilization system with high accuracy and a beam position resolution in the submillimeter range. In this contribution, requirements and concepts for this system regarding beam diagnostics elements, feedback control and readout electronics are presented. The usage of a beam position monitor cavity and optical transition radiation targets to monitor the required beam parameters will be discussed in detail. Additionally, various measurements performed at the S-DALINAC to assess requirements and limits for the beam-stabilization system will be presented. Finally, the option to use advanced machine learning methods, such as neural networks and agent-based reinforcement learning, will be discussed.

INTRODUCTION

The superconducting Darmstadt linear electron accelerator (S-DALINAC) at the institute for nuclear physics at the Technische Universität Darmstadt is used for scientific research in nuclear spectroscopy and meteorology, nuclear astrophysics and accelerator science [1] and can be operated in energy-recovery modes [2, 3]. The current layout of the S-DALINAC is shown in Fig. 1. Due to its superconducting design the accelerator is able to provide a continuous-wave electron beam at a frequency of 2.997 GHz with a kinetic design energy of up to 130 MeV. The beam quality can be further improved using the scraper systems located in both the low and high energy sections to reach its minimum design energy spread of 10^{-4} with bunch lengths of smaller than 2 ps [4]. The electron beam can be utilized at various experimental setups including the QCLAM magnet spectrometer. Multiple high-resolution (e,e') and (e,e'γ) coincidence experiments have been conducted successfully at the QCLAM [5, 6].

Within the cluster project ELEMENTS a new series of measurements based on electron-induced fission at S-DALINAC is proposed to aim at a better understanding of the natural synthesis of heavy elements in our universe. While the details of the proposed experiment are provided in the following chapter, the requirements for the accelerator facility are challenging due to the miniscule radioactive target of 1 mm, the request of ultra-short bunch lengths in the order of 1 ps and the demand for stable beam conditions for several hundreds of hours of measurement. In particular, the monitoring and control of the beam spot size and position are of importance.

Therefore, a new active beam-stabilization system is being designed for electrofission experiments at the QCLAM spectrometer at the S-DALINAC. This project includes the commissioning of beam diagnostics elements and correction magnets including an in-house developed beam position and phase monitor. Additionally, the electronics layout for signal readout and processing will be designed. The focus is on utilizing existing in-house developed electronics and commercially available solutions. As feedback control algorithm both the performance of traditional PID (Proportional–integral–derivative) controllers and machine learning methods will be assessed. To test and optimize the control mechanism beforehand, the creation of a virtual test environment based on neural networks and beam dynamics simulations are planned.

ELECTROFISSION AT S-DALINAC

In order to investigate fission reactions of actinides and their dependence of the excitation energy of the nucleus, electron-induced fission will be employed at the S-DALINAC. It allows the determination of the excitation energy of the actinide target nucleus. Additionally, higher multipoles can be excited and studied.

A schematic representation of the proposed electrofission setup is shown in Fig. 2. The electron beam will be delivered by S-DALINAC with a beam current of 3 µA, electron energies of the order of 100 MeV and a 3σ beam spot size smaller than 1 mm at the electrofission interaction point. The electrofission target has a diameter of 1 mm and a target thickness of approximately 350 $\mu g/cm^2$. After its interaction with an electron the target nuclei can decay via fission. An accurate description of this process, which is not available up to date, requires the measurement of both fission fragments in coincidence. While e.g. photon-induced fission primarily excites E1 transitions, in electrofission higher multipole orders such as E2 and E3 can be exited. As electron scattering experiments allow the decoupling of excitation energy and momentum transfer, a model-independent multipole decomposition using the electrofission cross section [7]

* Work supported by DFG (GRK2128), BMBF, the state of Hesse within Research Cluster Project ELEMENTS and the LOEWE Research Group Nuclear Photonoics
† dschneider@ikp.tu-darmstadt.de

Content from this work may be used under the terms of the CC-BY-4.0 licence (© 2023). Any distribution of this work must maintain attribution to the author(s), title of the work, publisher, and DOI

ISBN: 978-3-95450-236-3 ISSN: 2673-5350 doi:10.18429/JACoW-IBIC2023-MOP038

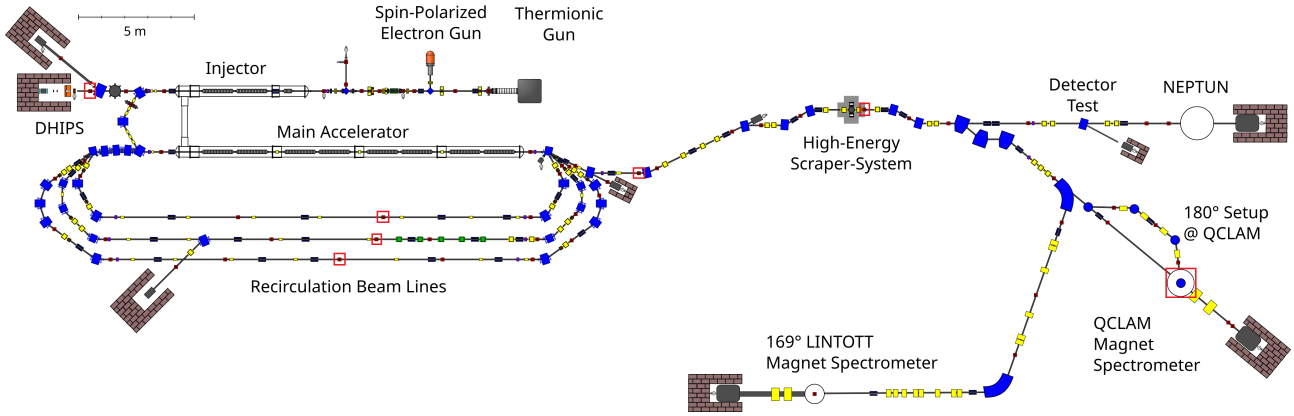


Figure 1: Floorplan of the S-DALINAC. The electrofission experiment as well as the beam stabilization system will be set up at the QCLAM spectrometer. The OTR setups marked in red will be upgraded with fast cameras to allow high-precision beam stability measurements.

$$\frac{d^2\sigma_f}{d\omega\, d\Omega_e} = \sigma_M \sum_{\lambda=0}^{\infty} P_f(E\lambda,\omega)|F(E\lambda,q,\omega)|\frac{dB}{d\omega}(E\lambda,\omega)$$

is possible. Here, ω is the excitation energy, Ω_e the solid angle of the spectrometer, σ_M the Mott cross section, λ the multipole order, P_f the fission probability, F the form factor and B the strength function. Due to its relatively low cross section, measurement periods in the order of several hundreds of hours are planned.

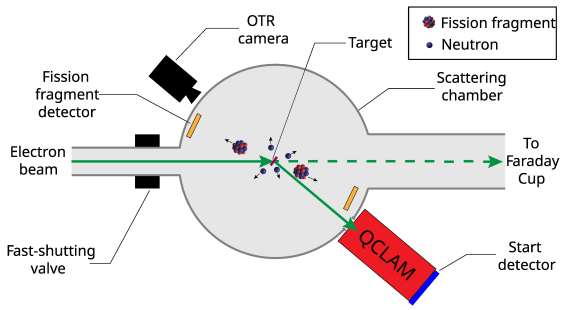


Figure 2: Schematic overview of the electrofission setup design. After interacting with an electron the target nucleus decays via fission. Both fission fragments are detected in coincidence with double sided silicon strip detectors.

DESIGN OF THE BEAM STABILIZATION SYSTEM

The proposed electrofission experiment demands a high control and stability of beam parameters over a large measurement period. As the long-term stability of the beam position and size has not been studied at the S-DALINAC, several existing OTR (optical transition radiation) screen stations (see Fig. 1) are upgraded by ultra-fast cameras that can reach 300-600 fps (frames per second). Within the upcoming beamtime the beam stability and frequency of distortions, and therefore the required frequency of the beam stabilization system, is examined. The desired position resolution and mean stability of the stabilization system is aimed to be smaller than 500 µm. The design layout of the active beam stabilization system is outlined in Fig. 3.

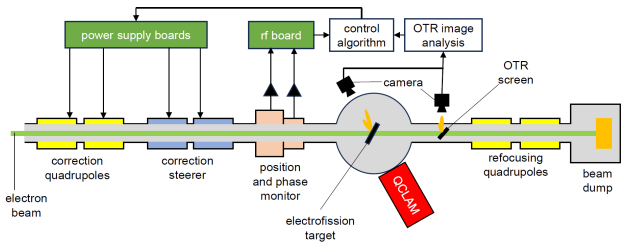


Figure 3: Sketch of the beam stabilisation system. OTR light emitted by both the electrofission target and OTR target is evaluated to determine the beam profile. Additionally, a non-destructive beam position measurement is deducted with a resonator cavity. The signal will be processed by the control algorithm to adjust the correction magnet currents.

Beam Diagnostics

To receive a transverse center beam position signal for beam spots of smaller than 500 µm two methods are proposed and pursued in parallel. As preferred method the observation of OTR directly emitted at the electrofission target is proposed. Transition radiation is emitted when a relativistic charged particle crosses the boundary between two media with different permittivity as the electric field has to rearrange at the boundary [8]. The radiated power for an electron with Lorentz factor $\gamma \gg 1$ can be described by [9]

$$W_o(\theta) = \frac{e^2}{4\pi^3\epsilon_0 c}\frac{\beta^2\sin^2\theta}{(1-\beta^2\cos^2\theta)^2}$$

with $W_o = d^2W/d\omega d\Omega$ the spectral energy distribution and $\beta = v/c$ the electron velocity. Additionally, the total transmitted intensity is proportional to γ and the plasma frequency of the target material. The emitted OTR light can be observed with a fast camera. The analysis of the target image gives access to the beam profile parameters right at

Content from this work may be used under the terms of the CC-BY-4.0 licence (© 2023). Any distribution of this work must maintain attribution to the author(s), title of the work, publisher, and DOI

ISBN: 978-3-95450-236-3 ISSN: 2673-5350 doi:10.18429/JACoW-IBIC2023-MOP038

the electrofission interaction point. Here, the resolution and frequency of the transverse beam profile signal is only dependent on the OTR intensity and camera resolution and frame rate as the OTR is emitted instantaneously and no broadening effects occur. A beam position resolution of $\ll$ 100 µm at a frequency of 35 Hz has been measured at OTR setups at the S-DALINAC [10]. The observation of OTR at the target material has been used before to improve the experimental analysis at the QCLAM [11].

Depending on the target material and the QCLAM interaction chamber geometry it cannot be guarantied that OTR at the electrofission target is accessible. Therefore, an alternative method is pursued in parallel. The beam will be monitored non-destructively with an in-house developed cavity beam position monitor shortly before the interaction chamber [12]. As the cavity beam position monitor is currently decommissioned, a first test of its performance has been conducted (see Fig. 4). With the existing electronics beam positions with an increment of 1 mm could be resolved at a beam current of 500 nA. In order to derive the beam position at the interaction point, an OTR screen will be installed behind the electrofission target and the emitted OTR light will be evaluated as in option 1. A position resolution of 100 µm of the cavity beam position monitor has been shown for beam currents of 1 µA [12]. The resulting position resolution at the interaction point will be examined within the commissioning phase.

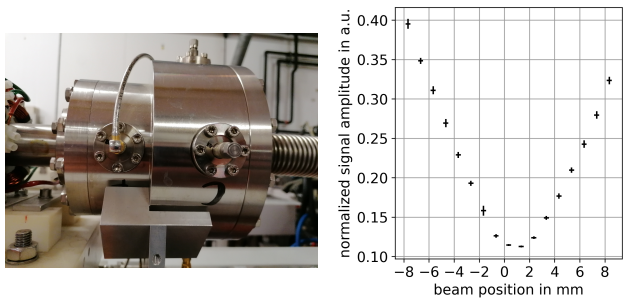


Figure 4: Left: Image of an in-house developed cavity beam position monitor for non-destructive phase and beam position measurements. Right: Test of a decommissioned cavity beam position monitor with existing readout electronics at a beam current of 500 nA. Beam positions with an increment of 1 mm can be resolved.

Readout Electronics

The choice of readout electronics depends strongly on the required repetition rate of the beam stabilization system. The OTR cameras will be chosen to have the maximum resolution for the given system repetition rate.

For the cavity beam position monitor, the extracted signal power is $P \propto x^2 I^2$ where x is the transverse beam shift and I is the beam intensity. To be sensitive to $x < 1$ mm for beam currents of 100 nA to 2 µA while protecting the following electronics of large P induced by $x \gg 1$ mm in the beam tuning process, the existing amplification electronics will be substituted with state-of-the-art low-noise amplifiers and an adjustable attenuation. For the signal processing of the amplified 2.997 GHz signal, in-house developed rf boards are available. They consist of an IQ (In-phase and quadrature) demodulator, an amplitude detector and a FPGA (Field Programmable Gate Array). The transverse center beam position is calculated directly from the IQ vector on the FPGA.

The power control boards of the correction steerers are in-house developed power supplies with an input signal processing of up to 7 Hz. If a faster signal processing is required, new power control boards have to be acquired. The hardware implementing the control algorithm depends on the control cycle repetition rate. The EPICS-based control system (Experimental Physics and Industrial Control System) allows scanning frequencies of up to 10 Hz [13, 14]. For higher frequencies FPGA boards with implemented control algorithm configurations can be used.

Feedback Control

A first test of a feedback control using a Python-based PID controller with EPICS interface has been conducted. A steerer has been used to manipulate the beam position while a second correction steerer was controlled to stabilize the beam to a fixed position on a downstream beryllium oxide screen. Both steerer magnets were operated with a frequency of 5 Hz. The horizontal center beam position was calculated by Gaussian fits on the vertically projected image profile. As shown in Fig. 5 the correction steerer was able to stabilize the beam within a 2σ-interval of 0.84 mm. Yet, beryllium oxide has broadening effects and the strong distortion of the beam most likely does not model the noise of the S-DALINAC electron beam sufficiently. A beam stabilization test measurement using an OTR target is scheduled for the upcoming beamtime where a higher beam stability is expected.

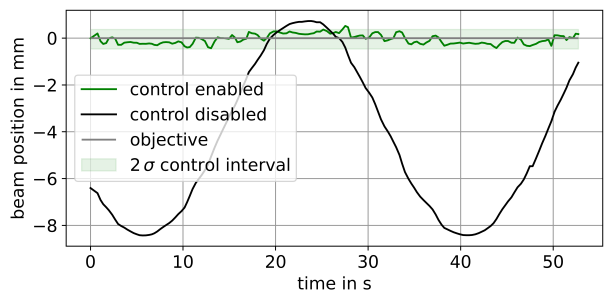


Figure 5: First test of a beam stabilization with a PID controller and implemented fast target analysis algorithm. Despite the strong simulated distortion, the correction magnet was able to keep the center beam position within a 2σ-interval of 0.84 mm.

As surrogate models of accelerator subsystems have been proven useful in analyzing and refining the underlying system, it is planned to create such a system based on both

Content from this work may be used under the terms of the CC-BY-4.0 licence (© 2023). Any distribution of this work must maintain attribution to the author(s), title of the work, publisher, and DOI

ISBN: 978-3-95450-236-3 ISSN: 2673-5350 doi:10.18429/JACoW-IBIC2023-MOP038

simulations and machine learning techniques like neural networks or polynomial chaos [15]. The constructed surrogate models will serve as training and testing environments for different control algorithms, such as PID controllers and supervised learning agents.

CONCLUSION

The S-DALINAC is well suited to provide a high-quality electron beam for the upcoming electrofission experiments. Yet, due to its challenging requirements including a beam spot size of 1 mm and a position stability of 500 µm, an active beam stabilization system is essential for the success of the electrofission project. Multiple OTR setups are currently being upgraded to allow a systematic investigation of the beam stability within the upcoming beamtime. The presented design of the stabilization utilizes existing in-house knowledge while remaining flexible to match the electrofission setup requirements.

REFERENCES

[1] N. Pietralla, "The Institute of Nuclear Physics at the TU Darmstadt", *Nucl. Phys. News*, vol. 28, no. 2, pp. 4–11, 2018. doi:10.1080/10619127.2018.1463013

[2] M. Arnold *et al.*, "First operation of the superconducting Darmstadt linear electron accelerator as an energy recovery linac", *Phys. Rev. Accel. Beams*, vol. 23, p. 020101, 2020. doi:10.1103/PhysRevAccelBeams.23.020101

[3] F. Schliessmann *et al.*, "Realization of a multi-turn energy recovery accelerator", Nat. Phys., vol. 19, pp. 597–602, 2023. doi:10.1038/s41567-022-01856-w

[4] F. Hug, "Erhöhung der Energieschärfe des Elektronenstrahls am S-DALINAC durch nicht-isochrones Rezirkulieren", Ph.D. thesis, Technische Universität Darmstadt, Darmstadt, Germany, 2013. https://tuprints.ulb.tu-darmstadt.de/id/eprint/3469

[5] G. Steinhilber, "The electron-gamma coincidence set-up at the S-DALINAC" , Ph.D. thesis, Technische Universität Darmstadt, Darmstadt, Germany, 2023. doi:10.26083/tuprints-00022993

[6] C. Lüttge *et al.*, "Large-aperture system for high-resolution electron scattering", *Nucl. Instrum. Methods Phys. Res., Sect. A*, vol. 366, no. 2-3, pp. 325–331, 1995. doi:10.1016/0168-9002(95)00497-1

[7] F. Zamani-Noor and D. S. Onley, "Virtual photon theory in electrofission", *Phys. Rev. C*, vol. 33, no. 4, pp. 1354–1366, 1986. doi:10.1103/PhysRevC.33.1354

[8] V. L. Ginzburg and I. M. Frank, "Radiation of a uniformly moving electron crossing a boundary between two media", *JETP*, vol. 16, p. 15, 1946.

[9] V. L. Ginzburg and V. N. Tsytovich, "Several problems of the theory of transition radiation and transition scattering", *Phys. Rep.*, vol. 49, pp. 1-89, 1979.

[10] J. Pforr, "Strahldynamik und -diagnose am Energierückgewinnenden S-DALINAC", Ph.D. thesis, Technische Universität Darmstadt, Darmstadt, Germany, 2020.

[11] M. Singer, "Entwicklung und Inbetriebnahme eines neuen Datenaufnahmesystems am QCLAM-Spektrometer", Ph.D. thesis, Technische Universität Darmstadt, Darmstadt, Germany, 2020. doi:10.25534/tuprints-00011636

[12] S. Döbert, "Nichtlineare Zeitreihenanalyse der Feldamplitude der supraleitenden Beschleunigungsstrukturen und Aufbau eines HF-Monitorsystems zur zerstörungsfreien Strahldiagnose am S-DALINAC", Ph.D. thesis, Technische Universität Darmstadt, Darmstadt, Germany, 1999.

[13] M. Konrad, "Development and Commissioning of a Digital RF Control System for the S-DALINAC and Migration of the Accelerator Control System to an EPICS Based System", Ph.D. thesis, Technische Universität Darmstadt, Darmstadt, Germany, 2013.

[14] EPICS – Experimental Physics and Industrial Control System, https://epics.anl.gov/

[15] D. Schneider, "Sensitivitätsanalyse der Strahlführungselemente des S-DALINAC unter Anwendung von Polynom-Chaos", master thesis, Technische Universität Darmstadt, Darmstadt, Germany, 2021.

Content from this work may be used under the terms of the CC-BY-4.0 licence (© 2023). Any distribution of this work must maintain attribution to the author(s), title of the work, publisher, and DOI

ISBN: 978-3-95450-236-3 ISSN: 2673-5350 doi:10.18429/JACoW-IBIC2023-MOP039

TRANSVERSE MULTI-BUNCH FEEDBACK DETECTOR ELECTRONICS USING DIRECT SAMPLING ANALOG-TO-DIGITAL CONVERTERS FOR THE SYNCHROTRON RADIATION SOURCE PETRA IV

S. Jablonski*, H.-T. Duhme, U. Mavrič, S. Pfeiffer, H. Schlarb
Deutsches Elektronen-Synchrotron, Hamburg, Germany

Abstract

PETRA IV, a new fourth generation synchrotron radiation source planned at DESY, will require a transverse multi-bunch feedback (T-MBFB) system to damp transverse instabilities and keep the beam emittance low. The critical part of the T-MBFB is a detector that must measure bunch-by-bunch, i.e. every 2 ns, position variations with the resolution not worse than 1 µm for the beam dynamic range of ±1 mm. In this paper, we present the conceptual design of the T-MBFB detector from the beam position pickups to the direct sampling ADCs. We analyze noise sources limiting the detector resolution and present measurement results based on the evaluation modules.

INTRODUCTION

PETRA IV will operate in two modes, i.e. the brightness and timing mode. The requirements for the T-MBFB are summarized in Table 1. Due to short bunch spacing of 2 ns and low bunch charge of 0.4 nC in the brightness mode, it is more challenging to fulfill the resolution requirement of 1 µm in this mode than in the timing mode. Therefore, all performance calculations in this paper are done for the brightness mode. It is expected that in the timing mode the results are similar or better.

T-MBFB DETECTOR SCHEME

Figure 1 presents a simplified block diagram of the vertical T-MBFB detector electronics. The horizontal detector differs only in the connection of the stripline electrodes to the combiners in such a way that the detector is sensitive to horizontal bunch variations. Hence, it will not be discuss further in the text.

The stripline BPM is composed of four electrodes equally distributed around the beam pipe, i.e. every 90°, with a characteristic impedance Z_o of 50 Ω. For the vertical beam position measurement, electrical pulses from the upper and lower pick-ups are combined together, creating signals V_{AB} and V_{CD}, respectively. The signals are doubled in the pulse multiplier, and further, they are subtracted from each other in the bunch offset compensation. The difference signal ΔV is fed to the front-end electronics (DRTM-MBFB-FE) and the digitizer (DAMC-DS5014RT), which are implemented in the MicroTCA.4 form factor. The above mentioned hardware is described in more detail in the following sections.

* szymon.jablonski@desy.de

Table 1: PETRA IV design parameters in the brightness (**B**) and timing (**T**) mode and the requirements for the T-MBFB.

Design Parameter	Value
Energy E	6 GeV
Revolution freq. f_{rev}	130.12 kHz
Emittance ϵ_x/ϵ_y	< 20/4 pm rad (**B**) < 50/10 pm rad (**T**)
Total current I	200 mA (**B**), 80 mA (**T**)
Number of bunches	max. 3840 (**B**), 80 (**T**)
Bunch charge q_b	~0.4 nC (**B**), ~7.7 nC (**T**)
Bunch spacing T_{rep}	2 or 4 ns (**B**), 96 ns (**T**)
Bunch length σ_t	~45 ps (**B**), ~64 ps (**T**)
Betatron freq. f_x/f_y	23.4 kHz, 35.2 kHz
T-MBFB det. bandwidth	750 − 1250 MHz
Max. bunch offset r_{dc}	±1 mm (from vacuum chamber center)
Max. betatron osc. amplitude r_{ac}	±1 mm
T-MBFB det. resolution	< 1 µm (SNR> 60 dB)
T-MBFB damping time	< 40 turns (for r_{ac} < 200 µm)

MODEL OF THE PICKUPS AND ANALOG ELECTRONICS

Electron Bunch in the Vacuum Chamber Center

The frequency-domain transfer impedance of a stripline cylindrical electrode can be modelled as [1]:

$$Z(\omega) = j\frac{\alpha}{2\pi} Z_o \exp\left[-j\omega\left(\frac{L}{c_0}+\Delta t\right)\right]\frac{\sin(\omega\Delta t)}{\omega\Delta t}\sin\left(\omega\frac{L}{c_0}\right), \quad (1)$$

where c_0 is the speed of light in vacuum, L is the length of the electrode, R is the radius of the vacuum chamber, α is the electrode width in rad (geometric coverage factor), Δt is a time delay given by $\Delta t = R\alpha/c_0$. Assuming the electron bunch traveling in the middle of the vacuum chamber is a point charge in the transverse direction and has a Gaussian shape in the longitudinal direction with the rms bunch length of σ_t, the stripline coupler output voltage is

$$V(\omega) = Z(\omega) q_b \exp\left[\frac{-(\omega\sigma_t)^2}{2}\right], \quad (2)$$

where q_b is the bunch charge.

Figure 2 presents amplitude spectrum at the stripline coupler output for the brightness mode (3840 bunches, rep. rate

Content from this work may be used under the terms of the CC-BY-4.0 licence (© 2023). Any distribution of this work must maintain attribution to the author(s), title of the work, publisher, and DOI

ISBN: 978-3-95450-236-3 ISSN: 2673-5350 doi:10.18429/JACoW-IBIC2023-MOP039

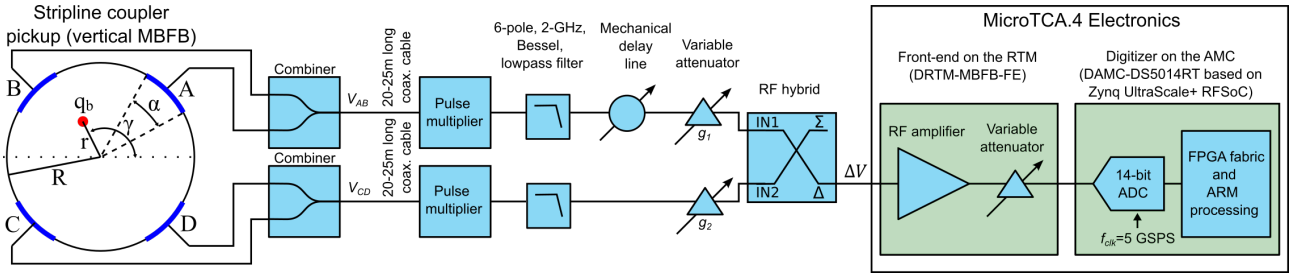


Figure 1: Simplified block diagram of the vertical T-MBFB detector electronics.

of 2 ns, q_b=0.4 nC, σ_t=45 ps) and for different electrode lengths L of 150 mm and 75 mm. The electrode length determines the optimal operating frequency of the receiver, which is around 500 MHz and 1 GHz, respectively. These frequencies correspond to the first and second harmonic of the multi-bunch spectrum with the bunch repetition rate of 2 ns. The vacuum chamber radius R is 17 mm and the electrode width α is 0.6 rad. The transfer function roll-off for the 150 mm-electrode is steeper and the magnitude decrease equals about 3 dB for the fastest multi-bunch mode at ±250 MHz. Hence, we decided to use the shorter 75 mm-electrode, for which the magnitude decrease is only 1 dB.

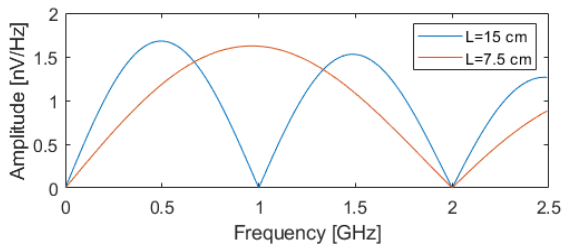


Figure 2: Amplitude spectrum at the stripline coupler output for the brightness mode (3840 bunches, rep. rate of 2 ns, q_b=0.4 nC, σ_t=45 ps) and for different electrode lengths L of 150 mm and 75 mm.

Instead of cylindrical electrodes, flat electrodes were selected as they are easier to be manufactured. However, the geometrical coverage factor is slightly different for both designs. Electromagnetic simulations [2] shown that the flat electrodes have lower sensitivity by a coefficient β of about 0.89, which will be further used to scale the signal amplitude.

Bunch Offset from the Vacuum Chamber Center

With different machine configurations, the electron bunch can be shifted by r from the centre of the vacuum chamber and rotated with respect to the electrode axis by an angle of γ (see Fig. 1). The output voltage $V(\omega)$ for different bunch positions is scaled by a coefficient $s(r,\gamma)$ given by [3]

$$s(r,\gamma) = 1 + \frac{4}{\alpha}\sum_{n=1}^{\infty}\frac{1}{n}\left(\frac{r}{R}\right)^n \cos(n\gamma)\sin\left(\frac{n\alpha}{2}\right). \quad (3)$$

Finally, the output voltage at each electrode is

$$V_x(\omega, r, \gamma_x) = \beta V(\omega) s(r,\gamma), \quad (4)$$

where the subscript x defines the electrode A, B, C or D. The electrode angles equal $\gamma_A = \gamma - \pi/4$, $\gamma_B = \gamma - 3\pi/4$, $\gamma_C = \gamma - 5\pi/4$, $\gamma_D = \gamma - 7\pi/4$. To make the detector sensitive only to vertical bunch oscillations, the upper and the lower electrode outputs must be combined together. The summed signals, using only the first order component of Eq. (3) (this simplification makes an estimation failure lower than 6 % for small $r \leq 1$ mm), are given by

$$\begin{aligned} V_{AB}(\omega, r) &= V_A(\omega, r, \gamma_A) + V_B(\omega, r, \gamma_B) \\ &= \beta V(\omega)\left[2 + \frac{4\sqrt{2}}{\alpha}\left(\frac{r}{R}\right)\sin\left(\frac{\alpha}{2}\right)\right], \end{aligned} \quad (5)$$

$$\begin{aligned} V_{CD}(\omega, r) &= V_C(\omega, r, \gamma_C) + V_D(\omega, r, \gamma_D) \\ &= \beta V(\omega)\left[2 - \frac{4\sqrt{2}}{\alpha}\left(\frac{r}{R}\right)\sin\left(\frac{\alpha}{2}\right)\right] \end{aligned} \quad (6)$$

for γ in the range of $[0, \pi]$. Bunch offset from the vacuum chamber center r includes information about the vertical constant orbit shift r_{dc} and the vertical betatron oscillation amplitude r_{ac}, i.e. $r = r_{dc} + r_{ac}$.

Bunch Offset Compensation

For high detector resolution, the full-scale input range of an ADC should be used to sample only the betatron oscillation signal (amplitude modulation), which is about 22 dB weaker as the "carrier" signal. The carrier is suppressed by more than 30 dB by subtracting both signals V_{AB} and V_{CD} using an RF hybrid as shown in Fig. 1. Before subtraction, both signals are conditioned using variable attenuators g_1 and g_2 to get the same carrier amplitude. They are also filtered with a 6-pole, lowpass, 2 GHz bandwidth, Bessel filter having a transfer function $F(\omega)$. Due to linear phase response of the filter, it does not produce any ringing overlapping the next bunch. Assuming all electrical components are lossless, the vertical betatron oscillation voltage at the output of the bunch offset compensation equals

$$\begin{aligned} \Delta V(\omega) &= g_1 V_{AB}(\omega, r) - g_2 V_{CD}(\omega, r) \\ &= (g_1 + g_2)\,\beta V(\omega) F(\omega)\left[\frac{4\sqrt{2}}{\alpha}\left(\frac{r_{ac}}{R}\right)\sin\left(\frac{\alpha}{2}\right)\right]. \end{aligned} \quad (7)$$

Content from this work may be used under the terms of the CC-BY-4.0 licence (© 2023). Any distribution of this work must maintain attribution to the author(s), title of the work, publisher, and DOI

ISBN: 978-3-95450-236-3 ISSN: 2673-5350 doi:10.18429/JACoW-IBIC2023-MOP039

SNR of the Analog Electronics

Integrating $\Delta V(\omega)$ within the MBFB detection range from 750 MHz to 1250 MHz for the maximum betatron oscillation amplitude of $r_{ac} = 1$ mm gives rms voltage of 0.25 V. Referring this voltage to thermal noise of 50 Ω load resistor gives SNR of 85 dB. However, the electrical components and 25-m long coaxial cables connecting the pickups and the detector electronics introduce insertion loss that degrades the SNR. The estimated loss is about 15 dB that reduces the SNR of the analog electronics to 70 dB, which is still 10 dB more than required for the T-MBFB. However, the resolution limiting component is the digitizer, which is discussed in the following section.

DIRECT SAMPLING DIGITIZER

Direct Sampling vs. Down-Conversion

MBFB systems are mainly based on two detection schemes, i.e. the direct sampling scheme as shown in Fig. 1 or the down-conversion scheme, which additionally involves an analog mixer in front of a digitizer to shift the detection band to baseband. In the past, the down-conversion scheme was preferred as ADCs did not have enough bandwidth for direct sampling of wideband RF pulses. In recent years, the ADC technology has moved forward - not only the input bandwidth and sampling rate have increased, but also ADC front-ends became better in terms of noise.

Noise floor of the down-conversion scheme is usually 3 dB lower than the direct sampling scheme (if using the same ADC for both cases). However, the direct sampling has a few advantages over the down-conversion:

- The down-conversion requires a more complex hardware including the local oscillator (LO).
- The baseband detectors are more susceptible to electromagnetic interference (EMI), e.g. due to switched-mode power supplies.
- Up-conversion of 1/f noise of the ADC front-end is reduced in the direct sampling suppressed carrier detector [4] (carrier suppression is implemented in the bunch offset compensation module). In contrary, the baseband detector resolution degrades due to 1/f noise of the ADC.
- Designing of the front-end electronics with flat magnitude and linear phase is more difficult for the baseband detector ([23.4 kHz, 250 MHz] spans over 4.03 decades) than for the direct sampling detector ([750 MHz, 1250 MHz] spans only over 0.22 decades). Moreover, the DC coupling of the baseband detector requires additional electronics for the common-mode voltage adjustment.

Zynq UltraScale+ RFSoC

Taking into account the pros and cons of both detector schemes, the direct sampling has been selected using the Zynq UltraScale+ RFSoC ADC. It has 14-bit resolution, sampling rate of 5 GSPS and an input bandwidth of 6 GHz. This module includes also FPGA and processing system that allows for flexible data processing like I/Q digital down-conversion, calculation of the bunch-by-bunch oscillation amplitudes and the transverse MBFB implementation.

Digitizer Noise and Interleaving Spurs

The betatron oscillation signal converted to digital can be written as [5]

$$\Delta V_k = [n_k + \Delta V(kT_s - x_k)](1 - r_k) + n_q, \qquad (8)$$

where k is the sample number, T_s is the sampling period, n_k is the additive noise of the ADC input stage, x_k is the combined timing jitter caused by aperture jitter (time fluctuations in the ADC sample and hold) and by clock timing jitter, r_k is the voltage reference noise, n_q is the quantization noise (white, uniformly distributed with zero-mean). Noise sources n_k, x_k, r_k and n_q are independent random processes.

Timing jitter x_k has a negligible impact for the amplitude measurements. Quantization noise PSD can be estimated by

$$S_{n_q}(f) = -20\log(2^m) - 10\log(f_s/2) \approx -178[\mathrm{dBFS/Hz}], \quad (9)$$

where m is the number of bits (14) and of f_s is the sampling rate (5 GSPS), which is also a negligibly small number. The voltage reference noise r_k is usually considerably lower than the input stage additive amplitude noise [5], which was measured to be −155 dBc/Hz at 1 GHz. The integrated amplitude noise within the detector range gives the SNR of 67 dB. However, the single pulse, corresponding to one bunch, occupies about a half of the possible measurement 2-ns time window that reduces the SNR by about 3 dB down to 64 dB — this is shown in more detail in the next section.

Each of the ADCs in the Zynq UltraScale+ RFSoC is built on multiple sub-ADCs in an interleaving architecture. The interleaving process requires that a calibration algorithm to be carried out, described in detail in Ref. [6]. Because of the suppressed-carrier operation of the T-MBFB, the ADCs can only be calibrated in the machine start-up. Later the calibration coefficients are frozen. The long-term behaviour of the ADCs needs be studied in detail, but we do not expect any detrimental effects, because the system is located in a temperature stabilized environment.

Even if the calibration procedure is carrier out, there are some residual interleaving spurs. Since the gain and time skew spurs depend on the input signal level, they are very low for no-carrier operation. The DC offset spurs at $nf_s/8$ ($n = 1 \ldots 8$) are below 80 dB and the sampling frequency f_s is so selected that the spurs do not overlap with the coupled-bunch oscillation modes.

SNR Improvement - ADC Parallelization and Pulse Multiplication

The basic detector structure provides the detector SNR of 64 dB, which is a 4-dB safety margin to the requirements. However, the SNR can be further improved by two hardware extensions, i.e. ADC parallelization and pulse multiplication.

Content from this work may be used under the terms of the CC-BY-4.0 licence (© 2023). Any distribution of this work must maintain attribution to the author(s), title of the work, publisher, and DOI

ISBN: 978-3-95450-236-3 ISSN: 2673-5350 doi:10.18429/JACoW-IBIC2023-MOP039

Content from this work may be used under the terms of the CC-BY-4.0 licence (© 2023). Any distribution of this work must maintain attribution to the author(s), title of the work, publisher, and DOI

The single RFSoC module includes eight ADCs. Four ADCs can be used for the T-MBFB detector and the rest are planned to be used for different diagnostics like the measurement of bunch-by-bunch phase or absolute bunch position in the vacuum chamber. The noise floor improvement factor is a square root of the number of parallel ADC channels, which is 6 dB for four ADCs. The parallelization not only improves the detector resolution, but it also provides redundancy in case of hardware failures.

The pulse multiplier improves the resolution by 3 dB, which was presented in our previous publication [7].

DIGITIZER PERFORMANCE EVALUATION AT PETRA III

The digitizer performance was evaluated at PETRA III using the sum signal from four stripline electrodes. The sum signal amplitude depends only on the bunch charge, it does not change with the transverse bunch oscillations. Since, the bunch charge is relatively stable (life time is about 1.5 h, the short-term pulse amplitude variations are dominated by residual amplitude noise of the ADC. Figure 3 presents the pulse signal converted to digital with the sampling clock of about 5 GSPS generated by the RFSoC internal PLL and synchronized to the machine main oscillator. In the digital domain, the RF pulse is IQ down-converted to baseband, lowpass filtered and decimated by 10. Using IQ values, the bunch-by-bunch and turn-by-turn amplitudes are calculated. In the next step, the SNR is computed for each bunch in the bunch train based on 132 revolutions, the SNR values are presented in Fig. 4. The averaged SNR equals 66 dB, which is only 1 dB worse than was estimated for 2-ns long pulse using the laboratory setup. In the future PETRA IV, the single pulse will be twice shorter (as written in the previous sections), therefore the SNR will decrease down to 63 dB.

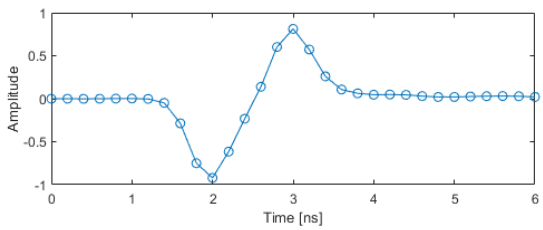


Figure 3: Digitized bunch pulse at PETRA III with the sampling rate of 5 GSPS.

CONCLUSION

In this paper, we presented the structure of the T-MBFB detector for PETRA IV. The detector resolution, specified by SNR, was analyzed separately for the analog electronics and the digitizer. The analog electronics was analytically modelled to have SNR better than 70 dB. The digitizer was experimentally tested both in the laboratory conditions and at PETRA III. The analysis shows that the dominant noise source is the digitizer front-end noise, which limits the detector resolution to 63 dB for the PETRA IV system. This

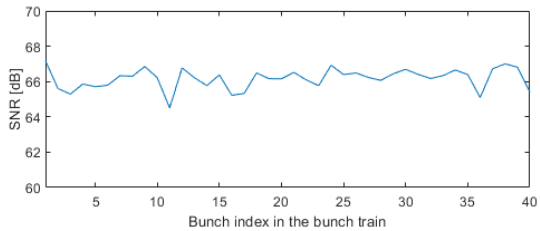


Figure 4: SNR of the RFSoC based T-MBFB detector evaluated at PETRA III in the timing mode with 40 bunches.

fulfills the project requirements, however, if needed in the future, the SNR can be improved by the ADC parallelization and pulse multiplication to more than 70 dB.

REFERENCES

[1] M. Wendt, "BPM Systems: A brief Introduction to Beam Position Monitoring", 2020. doi:10.48550/arXiv.2005.14081

[2] S. Strokov, "Stripline monitor simulation. S-parameters, Signal strength and quality", Internal Report, Aug. 2022.

[3] R. E. Shafer, "Beam position monitoring", in *AIP Conf. Proc.*, vol. 212, pp. 26–58, 1990. doi:10.1063/1.39710

[4] E. Rubiola and V. Giordano, "Advanced interferometric phase and amplitude noise measurements", in *Rev. Sci. Instrum.*, vol. 73, no. 6, pp. 2445–2457, Jun. 2002. doi:10.1063/1.1480458

[5] A. C. Cárdenas-Olaya, E. Rubiola, *et al.*, "Noise characterization of analog to digital converters for amplitude and phase noise measurements", in *Rev. Sci. Instrum.*, vol. 88, no. 6, pp. 065108, Jun. 2017. doi:10.1063/1.4984948

[6] Zynq UltraScale+ RFSoC RF Data Converter v2.6 Gen 1/2/3/DFE LogiCORE IP Product Guide (PG269), https://docs.xilinx.com/r/en-US/pg269-rf-data-converter/RF-ADC-Calibration-Mechanism

[7] S. Jabłoński *et al.*, "Conceptual Design of the Transverse Multi-Bunch Feedback for the Synchrotron Radiation Source PETRA IV", in *Proc. IBIC'22*, Kraków, Poland, Sep. 2022, pp. 488–491. doi:10.18429/JACoW-IBIC2022-WEP36

ISBN: 978-3-95450-236-3 ISSN: 2673-5350 doi:10.18429/JACoW-IBIC2023-MOP041

MODIFIED FAST ORBIT FEEDBACK CONTROLLER FOR DISTURBANCE ATTENUATION IN LONG STRAIGHTS FOR DIAMOND-II *

S. Banerjee[1,†], I. Kempf[1,2], M. Abbott[1], L. Bobb[1],
[1] Diamond Light Source, Didcot, United Kingdom
[2] University of Oxford, Oxford, United Kingdom

Abstract

At Diamond Light Source, the fast orbit feedback (FOFB) uses one array of correctors and the controller is designed using the internal model control (IMC) structure. The Diamond-II upgrade will introduce an additional array of fast correctors and a new controller that is designed using the generalised modal decomposition, increasing the overall closed-loop bandwidth from 140 Hz to 1 kHz. Although simulation results have shown that the resulting beam displacement is within specification in all straights, they have also shown that the performance on long straights is limited, particularly in the vertical plane. In this paper, the controller is tuned in order to increase the FOFB performance in long straights by introducing a mode-by-mode regularisation parameter. The performance of the controller beyond 1 kHz is assessed using new disturbance data and a new measurement noise model, showing that the Diamond-II performance criteria are met, even in the presence of measurement noise.

INTRODUCTION

At Diamond Light Source (Diamond), the fast orbit feedback (FOFB) attenuates disturbances in the storage ring and reduces the root-mean square deviation of the electron beam to ≤10 % of the beam size up to 140 Hz in both planes. The FOFB uses 173 beam position monitors (BPMs) and 172 identical corrector magnets, and the control algorithm is based on the internal model control (IMC) structure, which is naturally amenable to systems with large time delays. The controller is designed using the modal decomposition, which decouples the multi-input multi-output (MIMO) systems into sets of single-input single-output systems using the singular value decomposition (SVD) of the orbit response matrix (ORM) [1].

Due to advances in detector speed and resolution at Diamond-II [2], the beam stability requirements are raised to 3 % of the beam size up to 1 kHz, such as shown in Table 1. The increased closed-loop bandwidth in turn requires to introduce an additional corrector type. The FOFB at Diamond-II will use 252 slow correctors with a bandwidth of ∼ 200 Hz and 144 fast correctors with a bandwidth of ∼ 8 kHz. To accommodate the fast correctors, the Diamond FOFB controller has been extended and adapted to the Diamond-II configuration [3]. Analogous to Diamond, the MIMO system is decoupled into sets of two-input single-output (TISO) and SISO systems using the generalised singular value decomposition (GSVD), which is a two-matrix factorisation technique [4]. The decoupled systems are then embedded in the IMC structure and the controllers designed using mid-ranging control [5]. In addition, a tunable regularisation matrix is included in the feedback loop to avoid large control inputs and increase the robustness of the controller.

Table 1: Beam Size, Relative and Absolute Orbit Stability Requirements at Standard Straight Source Points [2].

Parameter	Diamond	Diamond-II
Beam size H/V	123 µm/3.5 µm	30 µm/4 µm
Rel. stability	10 % up to 100 Hz	3 % up to 1 kHz
Abs. stability H/V	12 µm/0.35 µm	0.9 µm/0.12 µm

H: horizontal, V: vertical, BW: bandwidth

As part of the Diamond-II design, the performance of the new control algorithm has been assessed using estimates of the Diamond-II disturbance [6]. Although this has shown that the Diamond-II controller meets the beam stability requirements, it has also shown that the performance for primary BPMs on the long straights of the new multi-bend achromat (MBA) lattice is worse than on the standard straights and mid straights. To reduce this performance difference, this paper extends the approach presented in [3] by introducing mode-based weights for the regularisation matrix, increasing the control effort for primary BPMs on long straights. The performance of the FOFB is then reassessed, considering both disturbance and a new measurement noise model.

DISTURBANCE

The Diamond-II disturbance data presented in Ref. [6] has been extended from 1 kHz to 2.44 kHz. The data includes power spectral density (PSD) estimates of ground and girder vibrations, RF and power supply noise, and is scaled using the local beta function to obtain the disturbance profile at each BPM, such as shown in Fig. 1 for the upstream primary BPM of the first standard straight, which is comparable to primary BPMs in other straight.

Note that the PSDs from Fig. 1 lack phase information, which complicates the analysis of the MIMO system. Since the ORMs are ill-conditioned, most of the measured disturbance is concentrated in the modes associated with large singular values of the ORMs. However, this is not reflected in the PSDs from Fig. 1, and therefore impacts the performance estimation of the MIMO system.

* Work supported by Diamond Light Source
† Corresponding author: shohan.banerjee@diamond.ac.uk.

Content from this work may be used under the terms of the CC-BY-4.0 licence (© 2023). Any distribution of this work must maintain attribution to the author(s), title of the work, publisher, and DOI

ISBN: 978-3-95450-236-3 ISSN: 2673-5350 doi:10.18429/JACoW-IBIC2023-MOP041

Content from this work may be used under the terms of the CC-BY-4.0 licence (© 2023). Any distribution of this work must maintain attribution to the author(s), title of the work, publisher, and DOI

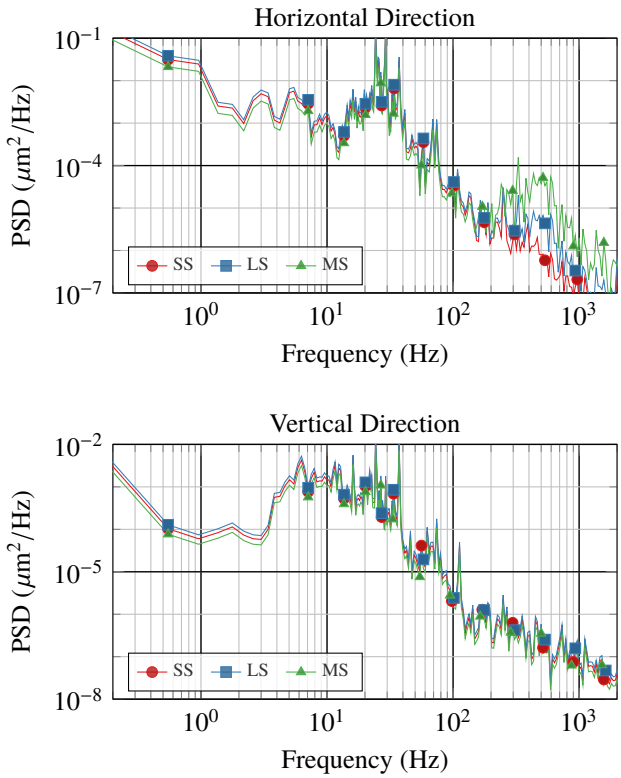


Figure 1: Estimated power spectral densitiy (PSD) of the uncorrected horizontal and vertical disturbance for Diamond-II at primary BPMs on long straights (LS), standard straights (SS), and mid straights (MS). The values are averaged over upstream and downstream BPMs.

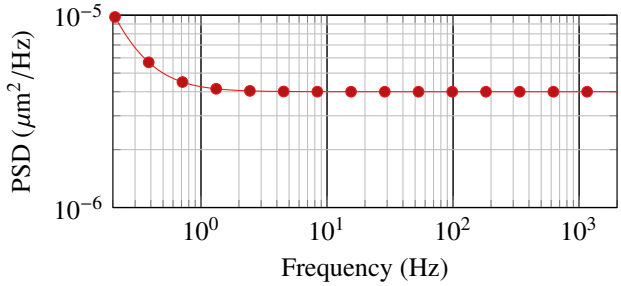


Figure 2: Power spectral densitiy (PSD) obtained from the Diamond-II measurement noise model.

MEASUREMENT NOISE

The FOFB at Diamond-II will also use new BPMs [7], and this reassessment includes a new measurement noise model. The PSD of the measurement noise is assumed to be $N(\omega) := \alpha^2/\omega^2 + \beta^2$, where $\alpha := 0.5\,\mathrm{nm}/\sqrt{\mathrm{Hz}}$ and $\beta := 2\,\mathrm{nm}/\sqrt{\mathrm{Hz}}$ are chosen based on the BPM specifications for Diamond-II. Figure 2 shows the resulting PSD, which is used for both horizontal and vertical directions. Comparing with Fig. 1, the PSD of the measurement noise is several orders of magnitude lower than the PSD of the disturbance for frequencies below 100 Hz, of similar magnitude between 100 Hz and 1 kHz, and represents a significant contribution from 1 kHz on.

CONTROLLER

The electron beam dynamics at Diamond-II are

$$y(s) = R_\mathrm{s} g_\mathrm{s}(s) u_\mathrm{s}(s) + R_\mathrm{f} g_\mathrm{f}(s) u_\mathrm{f}(s) + d(s), \qquad (1)$$

where the s is the Laplace variable and the subscripts s and f refer to slow and fast. The vectors $y(s)$, $u_{(\cdot)}(s)$ and $d(s)$ represent the beam position, the corrector inputs, and the disturbances, respectively, and the matrices $R_\mathrm{s} \in \mathbb{R}^{n_y \times n_\mathrm{s}}$ and $R_\mathrm{f} \in \mathbb{R}^{n_y \times n_\mathrm{f}}$ with $n_y = n_\mathrm{s} = 252$ and $n_\mathrm{f} = 144$ the ORMs for the slow and fast correctors, which are obtained from selecting the corresponding columns of a larger ORM $R \in \mathbb{R}^{n_y \times (n_\mathrm{s}+n_\mathrm{f})}$. The scalar transfer functions $g_\mathrm{s}(s)$ and $g_\mathrm{f}(s)$ model the temporal dynamics of the correctors, and include the frequency responses of the DAC, ADC, signal processing filters, power supplies, magnets, and copper vessel for slow correctors and stainless steel and copper vessel for fast correctors.

The IMC structure used for Diamond-II is shown in Fig. 3, where $P(s) := [R_\mathrm{s} g_\mathrm{s}(s)\ R_\mathrm{f} g_\mathrm{f}(s)]$ is the plant, $\bar{P}(s) := [\bar{R}_\mathrm{s} \bar{g}_\mathrm{s}(s)\ \bar{R}_\mathrm{f} \bar{g}_\mathrm{f}(s)]$ the plant model, $Q(s) := \mathrm{diag}(Q_\mathrm{s}(s), Q_\mathrm{f}(s))$ the IMC filter, $u(s) := [u_\mathrm{s}(s)^\mathrm{T}\ u_\mathrm{f}(s)^\mathrm{T}]^\mathrm{T}$, and $n(s)$ is the measurement noise. Note that $n(s)$ affects $y(s)$ when the control loop is closed, i.e. when $us(s)$ and $uf(s)$ in Eq. (1) are replaced with a control law that uses the measured position $y(s) + n(s)$.

The IMC filters invert the plant and are defined as $Q_{(\cdot)}(s) := P^\dagger_{(\cdot)}(s) T_{(\cdot)}(s)$, $(\cdot) = \{\mathrm{s}, \mathrm{f}\}$, where it is assumed that $\bar{P}(s) = P(s)$ and $T_{(\cdot)}(s)$ are tunable transfer functions designed in the companion paper [8]. The matrix $\Upsilon \in \mathbb{R}^{(n_\mathrm{s}+n_\mathrm{f}) \times n_y}$ is used to accommodate systems with fewer slow than fast correctors, and the matrix $\Gamma \in \mathbb{R}^{n_y \times n_y}$ is the regularisation matrix that is defined as

$$\begin{aligned} \Gamma &:= (RR^\mathrm{T} + \mu I)^{-1} RR^\mathrm{T} \\ &= U\,\mathrm{diag}\left(\frac{\sigma_1^2}{\sigma_1^2 + \mu}, \ldots, \frac{\sigma_{n_y}^2}{\sigma_{n_y}^2 + \mu} \right) U^\mathrm{T} \end{aligned} \qquad (2)$$

where $\mu \geq 0.1$ the regularisation parameter and the SVD $R = U\Sigma V^\mathrm{T}$ was substituted for R. Given $T_{(\cdot)}(s)$, the choice of μ influences both closed-loop bandwidth and corrector demand. A large value of μ ($\mu \gg \sigma_{n_y}$) reduces both closed-loop bandwidth and corrector demand, but a small value of μ can yield large corrector inputs and even an unstable closed-loop [9]. The choice $\mu = 0.1$ results in a maximum fast corrector demand of 276 mA, which is below the limit of 920 mA [2].

MODE-BY-MODE REGULARISATION

As for Diamond, the Diamond-II ORMs are ill-conditioned, i.e. the ratio of largest to smallest singular value is large. Because the IMC filters invert the plant, the corrector inputs are proportional to $R^\dagger_{(\cdot)}$, producing large corrector inputs for disturbances in the direction of standard singular vectors associated with small singular values of $R^\dagger_{(\cdot)}$. While the regularisation matrix Γ is used to reduce the

ISBN: 978-3-95450-236-3 ISSN: 2673-5350 doi:10.18429/JACoW-IBIC2023-MOP041

Table 2: Targets and expected IBMs up to 1 kHz for Diamond-II at primary BPMs on long straights (LS), mid straights (MS), and standard straights (SS). The values are averaged over upstream and downstream BPMs.

	Noise	μ_i	Horizontal IBM (µm)			Vertical IBM (µm)		
			LS	MS	SS	LS	MS	SS
Target			1.20	0.90	0.97	0.23	0.14	0.18
FOFB OFF	No		0.68	0.46	0.61	0.25	0.20	0.21
Upper bound from Eq. (6)	No	0.1	0.48	0.23	0.35	0.25	0.09	0.12
Simulation	No	0.1	0.17	0.06	0.08	0.17	0.05	0.07
Upper bound from Eq. (6)	No	$f(\theta_i)$	0.48	0.23	0.35	0.26	0.09	0.12
Simulation	No	$f(\theta_i)$	0.17	0.06	0.08	0.17	0.05	0.07
FOFB OFF	Yes		0.69	0.47	0.61	0.26	0.21	0.22
Upper bound from Eq. (6)	Yes	0.1	0.50	0.26	0.38	0.26	0.12	0.14
Simulation	Yes	0.1	0.18	0.08	0.09	0.18	0.07	0.09
Upper bound from Eq. (6)	Yes	$f(\theta_i)$	0.50	0.26	0.38	0.26	0.12	0.15
Simulation	Yes	$f(\theta_i)$	0.18	0.08	0.09	0.18	0.07	0.09

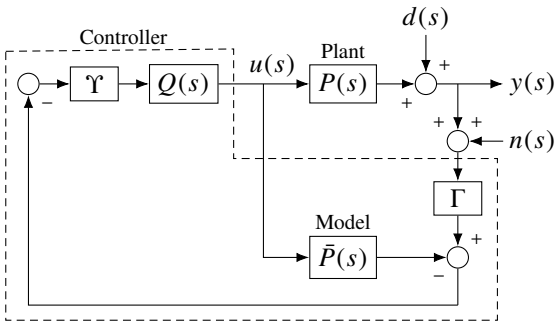


Figure 3: IMC structure with corrector setpoints $u(s)$, disturbances $d(s)$, beam positions $y(s)$, and measurement noise $n(s)$.

corrector inputs, it also reduces the overall bandwidth and therefore the performance at primary BPMs. To improve the performance at primary BPMs, Γ from Eq. (2) is redefined as

$$\Gamma := U \operatorname{diag}\left(\frac{\sigma_1^2}{\sigma_1^2+\mu_1}, \ldots, \frac{\sigma_{n_y}^2}{\sigma_{n_y}^2+\mu_{n_y}}\right) U^{\mathrm{T}}, \tag{3}$$

where $\mu_1, \ldots, \mu_{n_y} \geq 0$ are mode-based regularisation parameters. The mode-based regularisation parameters are defined as $\mu_i = f(\theta_i)$ with

$$\mu_i := \frac{\mu_{\max} - \mu_{\min}}{\theta_{\max} - \theta_{\min}} (\theta_i - \theta_{\min}) + \mu_{\min}, \tag{4}$$

where $\mu_{\min} := 0.01 \leq \mu_i \leq \mu_{\max} := 0.1$, $\theta_{\min} := \min_i \theta_i$, $\theta_{\max} := \max_i \theta_i$, and

$$\theta_i := \operatorname{acos}\left(|w^{\mathrm{T}} U_i| / \|w\|_2\right). \tag{5}$$

The variable θ_i describes the acute angle between U_i, the ith left singular vector of R, and a vector $w \in \mathbb{R}^{n_y}$ with ones at indices of interest and zeroes otherwise. For example, to prioritise primary BPMs, w can be assigned ones at indices corresponding to primary BPMs, lowering the value of μ_i for modes that form a small angle with w and hence increasing the controller gain for these modes. For the following analysis, all primary BPMs are prioritised using Eq. (4), and these results are compared against a regularisation matrix with $\mu_i = 0.1$ for all modes.

In general, large controller gains will result in a high closed-loop bandwidth, whereas small controller gains will result in a low closed-loop bandwidth. Although the regularisation matrix limits the corrector setpoints, it also reduces the bandwidth for modes associated with small singular values, and therefore the overall controller performance. However, if most of the disturbance is concentrated in modes associated with large singular values, the regularisation matrix does not significantly impact the controller performance, such as it is the case for Diamond. Note that this is not the case for the disturbance data from Fig. 1, which lacks phase information.

RESULTS AND DISCUSSION

Because the PSDs from Fig. 1 lack phase information, the performance of the controller is estimated using two different methods. First, assuming that the measurement noise PSD $N_i(\omega)$ and the disturbance PSD $D_i(\omega)$ are uncorrelated, the PSD $Y_i(\omega)$ of BPM i can be upper-bounded by

$$Y_i(\omega) \leq Y_i(\omega)|_D + Y_i(\omega)|_N, \tag{6}$$

where

$$Y_i(\omega)|_D := \left(\sum_{k=1}^{n_y} |S_{ik}(\mathrm{j}\omega)| \sqrt{D_k(\omega)}\right)^2$$

$$Y_i(\omega)|_N := \left(\sum_{k=1}^{n_y} |I - S_{ik}(\mathrm{j}\omega)| \sqrt{N_k(\omega)}\right)^2$$

and $S_{ik}(\mathrm{j}\omega)$ refers to element on row i and column k of the sensitivity, i.e. the transfer functions from disturbance and

Content from this work may be used under the terms of the CC-BY-4.0 licence (© 2023). Any distribution of this work must maintain attribution to the author(s), title of the work, publisher, and DOI

ISBN: 978-3-95450-236-3 ISSN: 2673-5350 doi:10.18429/JACoW-IBIC2023-MOP041

Content from this work may be used under the terms of the CC-BY-4.0 licence (© 2023). Any distribution of this work must maintain attribution to the author(s), title of the work, publisher, and DOI

noise to the output, which is defined as

$$S(s) := I - P(s)Q(s)\Upsilon(I + (\Gamma - I)P(s)Q(s)\Upsilon)^{-1}\Gamma. \quad (7)$$

Second, the PSDs from Fig. 1 can be used to sample a time series for each BPM by adding a random phase, and the time series can be used in simulations. Although the resulting performance does not represent a strict upper bound, the results can be interpreted as a worst-case scenario. Because the Diamond-II disturbance does not reflect the characteristic distribution in modal space, the regularisation matrix significantly reduces the overall performance.

The integrated beam motions (IBMs) up to 1 kHz obtained from the upper bound using Eq. (6) and the simulations for $\mu_i = f(\theta_i)$ and $\mu_i = 0.1$ are summarised in Table 2, which also shows the corresponding beam stability target. The first part of the table shows the performance without noise, so that FOFB OFF corresponds to the IBM of the disturbance. For both choices of μ_i, the simulation yields significantly better results than the upper bound from Eq. (6). Except for the long straights in the vertical direction, the upper bound is below target, suggesting that the Diamond-II stability specifications are met. Although the primary BPMs are prioritised, the choice $\mu_i = f(\theta_i)$ does not improve the performance, but increases the upper bound from Eq. (6), and leaves the simulation results unchanged. On one hand, this is related to the lack of phase information for the disturbance data from Fig. 1. On the other, these results suggest that decreasing μ_i below $\mu_{\max}$ does not significantly affect the regularisation gains from Eq. (3) and the closed-loop bandwidth, i.e. both $\mu_{\max}$ and $\mu_{\min}$ in Eq. (4) would need to be lowered further to yield a performance increase on primary BPMs. However, this would also increase the corrector demand above the Diamond-II limit of 920 mA.

The second half of Table 2 shows the performance in the presence of measurement noise, so that FOFB OFF corresponds to the IBM obtained after adding $D(\omega)$ and $N(\omega)$. Compared to the case without noise, the IBM for FOFB OFF is ~ 0.01 µm larger. As for the case without noise, the simulations yield significantly better results than the upper bound from Eq. (6), and the different choices of μ_i do not impact the performance. Except for the long straights that are 0.03 µm above target in the vertical direction, the upper bounds from Eq. (6) is within target.

CONCLUSION

With the aim of improving the FOFB performance at primary BPMs, a new regularisation matrix was defined using mode-by-mode regularisation parameters. The regularisation parameters were reduced for those modes that impact the primary BPMs most. The performance of the resulting controller was evaluated using a conservative upper bound and in simulations, and compared against a controller that uses a constant regularisation parameter. Two scenarios were considered, one with measurement noise and disturbance, and one with disturbance only. The measurement noise was modelled based on the specifications for the new Diamond-II electron BPMs.

The simulation results have shown that the Diamond-II specifications are met on all straights for both scenarios, whereas with the upper bound, the IBM on long straights is 0.03 µm above target. For both simulations and upper bounds, the new mode-by-mode regularisation matrix has not led to any performance improvements. It remains unclear why, but it is suspected that the lack of phase information for the Diamond-II disturbance data impacts the regularisation and the resulting performance.

On-going work at Diamond is reassessing the slow and fast corrector demand using the new disturbance data and the new measurement model. In addition, the fast corrector models will be updated once they are prototyped.

Future research could analyse the impact of the regularisation matrix in more detail, e.g. by considering a robust performance criteria in modal space and or by modifying the controller dynamics in generalised modal space. In addition, the results could be reassessed using disturbance data that reflects the characteristic modal distribution.

REFERENCES

[1] S. Gayadeen and S. R. Duncan, "Design of an electron beam stabilisation controller for a synchrotron," *Contr. Eng. Pract.*, vol. 26, pp. 201–210, May 2014. doi:10.1016/j.conengprac.2014.01.012

[2] M. G. Abbott *et al.*, "Diamond-II technical design report," Diamond Light Source, Tech. Rep., Aug. 2022. https://www.diamond.ac.uk/Home/News/LatestNews/2022/14-10-22.html

[3] I. Kempf, P. J. Goulart, and S. Duncan, "Control of Two-Array Cross-Directional Systems using the Generalised Singular Value Decomposition," *arXiv*, doi:10.48550/arXiv.2308.08631

[4] G. H. Golub and C. F. Van Loan, *Matrix Computations*, 4th ed. The Johns Hopkins Univ. Press, 2013.

[5] S. Gayadeen and W. Heath, "An internal model control approach to mid-ranging control," in *Proc. IFAC Symp. Adv. Contr. Chem. Process*, Jul. 2009, pp. 542–547.

[6] I. P. S. Martin *et al.*, "Orbit Stability Studies for the Diamond-II Storage Ring," in *Proc. Int. Part. Accel. Conf. (IPAC'22)*, Bangkok, Thailand, Jul. 2022, pp. 2602–2605. doi:10.18429/JACoW-IPAC2022-THPOPT017

[7] L. T. Stant *et al.*, "Diamond-II Electron Beam Position Monitor Development," in *Proc. IBIC'22*, Kraków, Poland, Dec. 2022, pp. 168–172. doi:10.18429/JACoW-IBIC2022-MO3C2

[8] I. Kempf, M. Abbott, L. Bobb, G. B. Christian, G. Rehm, and S. Duncan, "Fast Orbit Feedback for Diamond-II," presented at IBIC'22, Saskatoon, Canada, this conference.

[9] S. Gayadeen, S. R. Duncan, and G. Rehm, "Optimal control of perturbed static systems for synchrotron electron beam stabilisation," *IFAC PapersOnLine*, vol. 50, no. 1, pp. 9967–9972, 2017, 20th IFAC World Congress.

ISBN: 978-3-95450-236-3 ISSN: 2673-5350 doi:10.18429/JACoW-IBIC2023-MOP043

USING LAG COMPENSATOR IN ORBIT FEEDBACK*

Igor Pinayev†, Brookhaven National Laboratory, Upton, NY, USA

Abstract

Growing demand on the beam orbit stability requires higher loop gain within the operational bandwidth. Increasing the gain leads to the increase of the unity gain frequency and creates problems with systems stability due to the additional phase shifts caused by the trims (power supplies, eddy currents in vacuum chambers, etc.) and filtering of beam position data. Conventionally employed systems have 20 dB/decade slope near the unity gain providing 90° phase shift which is sufficient for stability. Utilizing one or more lag compensators allows to increase the gain at low frequencies while keeping phase margin acceptable. The paper provides more details on the proposed solution as well as simulations of how the transients will be modified.

INTRODUCTION

Rejection of the disturbance in the linear system feedback is proportional to the gain of the open loop. If the open loop gain is described by a transfer function G(s) the suppression of the disturbance is given by formula:

$$P(s) = \frac{1}{1+G(s)} \quad (1)$$

Increase of the slope to 40 dB/decade by adding additional pole into the signal chain increases the phase shift to 180° and makes system unstable. Increase of the implemented gain is limited by the requirement of the system stability. The phase shift caused by different elements of orbit feedback (trims with power supplies [1], eddy currents in vacuum chamber [1], filters implemented in the beam position monitors [2], latency in the signal propagation chain [3]) can turn negative feedback into positive one and make system unstable. Typically, the transfer function of the orbit feedback system is described by few poles. The lowest frequency pole is user defined and might be at zero frequency if integrator is utilized. The second pole is defined by hardware and is the main limiting factor in the system bandwidth. Therefore, at high frequencies the loop gain is inversely proportional to the frequency

$$|G(f)| \cong \frac{f_c}{f} \quad (2)$$

where f_c is crossover frequency where gain is unity. Since the slope of the Bode plot is usually fixed (-20 dB/decade for single pole), increase in suppression of the high-frequency disturbances requires increase of the crossover frequency.

LAG COMPENASTOR

Usage of lag compensation provides higher low-frequency gain [4]. The transfer function of lag compensator is

$$D(s) = \alpha \frac{Ts+1}{\alpha Ts+1},\ \alpha > 1 \quad (3)$$

where α is the ratio between zero/pole breakpoint frequencies and T is time constant. At DC the lag compensator provides additional gain α > 1. But it also creates negative phase shift. For α=10 phase shift is almost 60° and can create a long ringing response or even cause instability. This drawback can be overcome by using more compensators with different time constants. This will increase the slope of the Bode diagram above 20 dB/decade but keep phase margin acceptable as it can be seen in Fig. 1.

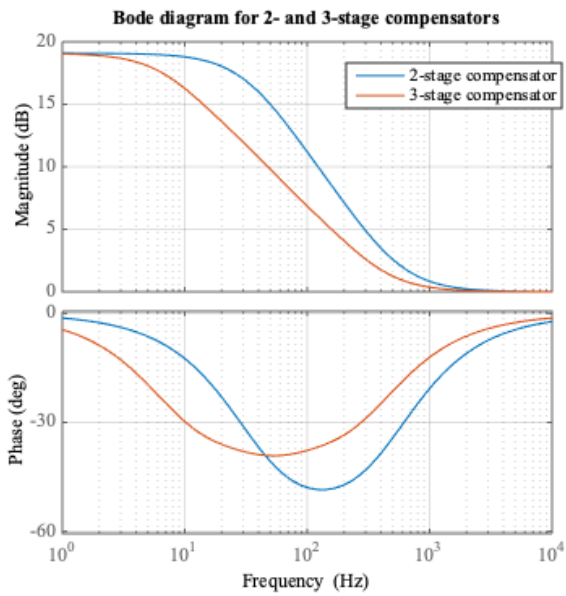


Figure 1: Bode plot of the open loop with two and three lag compensators. Total gain increase is the same but maximal phase shift different for three-stage it is 40° and for two-stage it is 50°.

IMPLEMENTATION IN ORBIT FEEDBACK

Figure 2 shows implementation of stages lag compensator the single input – single output (SISO) system with integrator in error amplifier and single pole at 800 Hz. Three stages providing 20 dB gain at DC were used. Figure 3 shows noise suppression and phase of the residuals.

* Work supported by Brookhaven Science Associates, LLC under Contract No. DE-SC0012704 with the U.S. Department of Energy
† pinayev@bn.gov

Content from this work may be used under the terms of the CC-BY-4.0 licence (© 2023). Any distribution of this work must maintain attribution to the author(s), title of the work, publisher, and DOI

ISBN: 978-3-95450-236-3 ISSN: 2673-5350 doi:10.18429/JACoW-IBIC2023-MOP043

Content from this work may be used under the terms of the CC-BY-4.0 licence (© 2023). Any distribution of this work must maintain attribution to the author(s), title of the work, publisher, and DOI

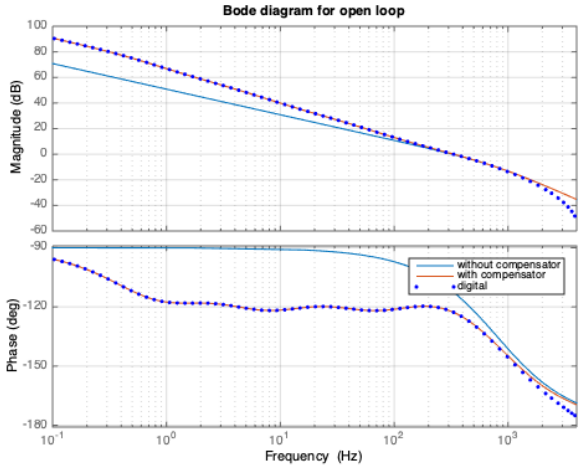


Figure 2: Example of the open loop gain with integrator and a pole at 800 Hz. Additional gain at low frequencies is about 20 dB, the phase margin is about 60° with and without compensator. Dots correspond to the digital system with 10 kHz sampling rate.

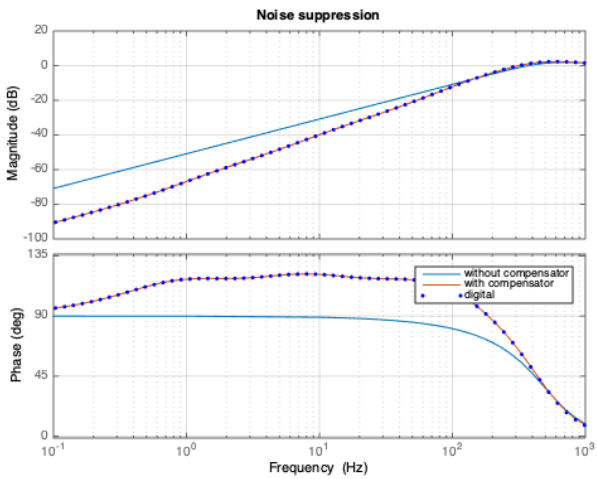


Figure 3: Noise suppression plot for closed loop.

While the stability of the system does not change much with introduction of the lag compensator the transient response changes noticeably. Figure 4 shows that the overshoot increases from 2% to 16 % for system with lag compensator and longer tail appears.

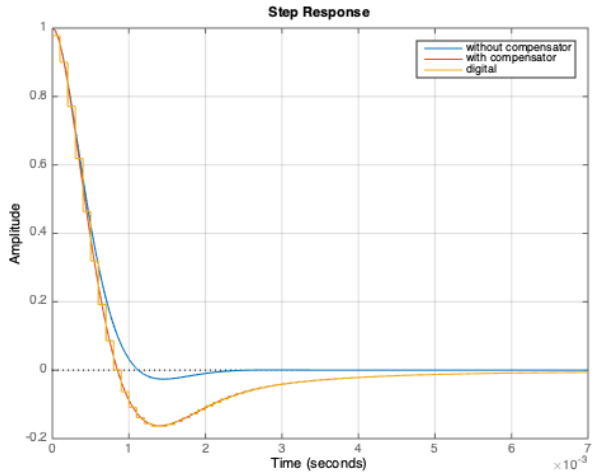


Figure 4: Transient response to the disturbance of the feedback system.

CONCLUSION

Implementation of the lag compensator allows to increase the suppression of the low-frequency disturbances without increase of the feedback bandwidth. Such solution does not change system stability but affect slightly transient dynamics.

REFERENCES

[1] N. Hubert, L. Cassinari, J.-C. Denard, A. Nadji, L. S. N. Nadolski, and D. Pedeau, "Design of a Fast Orbit Feedback for SOLEIL", in *Proc. DIPAC'05*, Lyon, France, Jun. 2005, paper POT019.

[2] E. Plouviez, "Optimizing the BPM processor filter for the fast orbit correction", presented in 6th DEELS Workshop, ESRF, Jun. 2019.

[3] D. Bulfone, R. De Monte, V. Forchi, G. Gaio, and M. Lonza, "Design of a Fast Global Orbit Feedback System for the ELETTRA Storage Ring", in Proc. ICALEPCS'05, Geneva, Switzerland, Oct. 2005, paper P3_011.

[4] G.F. Franklin, J.D. Powell, and A. Emami-Naeini, *Feedback Control of Dynamic Systems*, Upper Saddle River, NJ, USA: Pearson Prentice Hall, 2006.

ISBN: 978-3-95450-236-3 ISSN: 2673-5350 doi:10.18429/JACoW-IBIC2023-MOP044

"INSTANTANEOUS" LIFETIME MEASUREMENT IN STORAGE RING WITH TOP-UP INJECTION*

Igor Pinayev†, Brookhaven National Laboratory, Upton, NY, USA

Abstract

Top-up operation becomes routine in the light sources. The goal of the top-up operation is to keep the current of the circulating beam stable to avoid variations of the heat load on the beamline optics. It is also considered for the electron-ion collider to maintain the polarization of the electron beam. Frequent re-injection makes measurement of the beam lifetime very difficult if possible. Since, only part of the bunch train is refreshed during the injection cycle then the distribution of the bunch charges in the train has a characteristic saw-tooth distribution. The slope of saw tooth is defined by the lifetime and filling frequency and can be used for the measurements. The data for processing can be obtained either from fast current transformer or from the raw ADC signal from beam position monitor. In this paper we present the theoretical considerations as well as experimental data from NSLS-II storage ring.

TOP-UP OPERATION OF THE NSLS-II

To satisfy requirements of the beam stability NSLS-II storage ring operates with top-up. Presently, around 1200 buckets out of 1320 are filled. The stored current is 400 mA, and lifetime is around 12 hours as shown in Fig. 1. Each 200 seconds approximately 100 bunches are injected into the ring to maintain current level [1, 2]. Therefore, top-up cycle takes 40 minutes. In the electron-ion collider being built at Brookhaven National Laboratory the refill is expected each two seconds making conventional lifetime measurement harder.

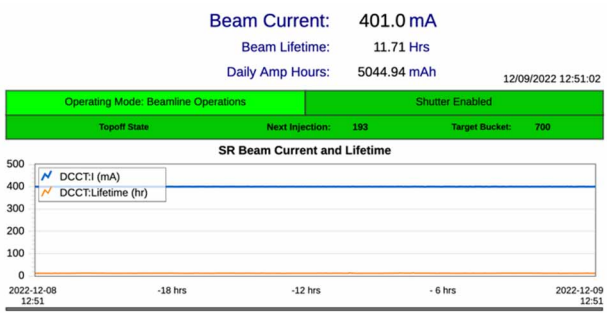


Figure 1: Screenshot of NSLS-II status showing stored beam current and beam lifetime of 11.7 hours from the DCCT data between injections.

NSLS-II BEAM POSITION MONITORS

NSLS-II BPMs are processing 500 MHz signal induced by the circulating beam. The parameters of the bandpass filters define the rising and falling of the induced train as well as ringing down as one can see the in Fig. 2. After amplification the signal is sampled with analog-to-digital converter [3]. The ADC sampling rate is chosen so that there are 310 readings per turn. The clock is phased locked to the RF frequency. The down sampling results in the 500 MHz signal being converted into the 80 periods per turn. There is possibility to extract buffer of 100000 consecutive ADC readings per channel (more than 322 turns) for the offline analysis.

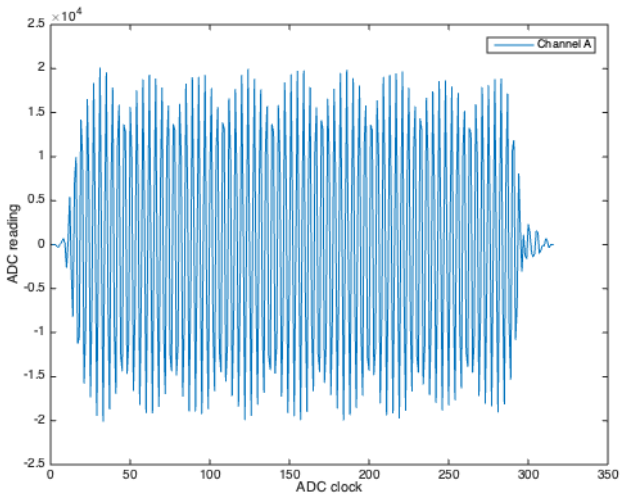


Figure 2: Raw ADC signal from NSLS-II beam position monitor. The visible modulation is due to the limited sampling rate (just below four readings per period).

To evaluate the signal level evolution along the train the sliding window was used. The user defined number of data samples around the current ADC clock were used to perform sine wave fit and the amplitude of the wave was used as signal strength. The 310 samples were padded with zeros on both sides for these calculations. The result is shown in Figs. 3 and 4. The sliding fit was using 11 points to smear the modulation caused by artefacts in the NSLS-II injection complex. The step down is clearly visible near ADC clock 236. The amplitude of the step as well as average amplitude can be used for the evaluation of the beam lifetime (in assumption that injection is stable in time) from the period of the top-up:

$$\tau_{lifetime} = T_{top-up} \frac{\langle amplitude \rangle}{step} \quad (1)$$

The step was calculated as difference between two linear fits on the left and on the right sides shown in Fig. 4. The modulation of the intensity is caused by modulation of charge trains in the NSLS-II injection system.

* Work supported by Brookhaven Science Associates, LLC under Contract No. DE-SC0012704 with the U.S. Department of Energy
† pinayev@bn.gov

Content from this work may be used under the terms of the CC-BY-4.0 licence (© 2023). Any distribution of this work must maintain attribution to the author(s), title of the work, publisher, and DOI

ISBN: 978-3-95450-236-3 ISSN: 2673-5350 doi:10.18429/JACoW-IBIC2023-MOP044

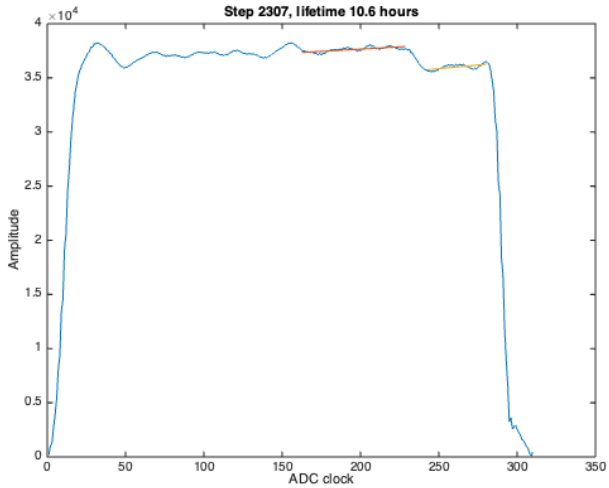


Figure 3: Amplitude of the BPM signal along the bunch train. Two red lines shows linear fit of the latest filled (left) and earliest filled (right) parts of the train. The estimated lifetime is 10.6 hours.

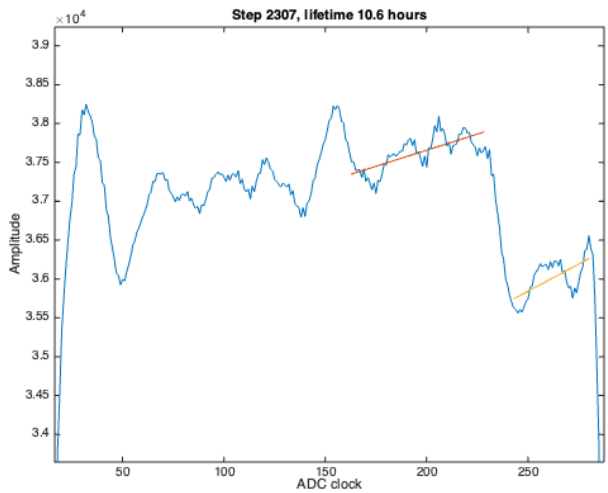


Figure 4: Zoomed in view on the step in the fill pattern.

As it was mentioned before the top-up operation causes the saw-tooth modulation of the bunch charge since the time from the injection into each bunch varies with its position in the train. Slope in the fill pattern can be used for lifetime measurements as well as it is shown in Fig. 5. The slope is measured as growth rate of the amplitude per ADC clock, time "span" is virtual fill time difference between the first bunch and the last bunch in the sequence (it is not actual time since the train of 100 bunches is injected). The modulation of the fill pattern can affect the accuracy of the measurement as well as stability of the injection system. For example, if all data between ADC samples 20 and 230 is used the calculated lifetime will grow to 18 hours, most likely due to the excessive charge injection into the region 50-150 ADC clocks.

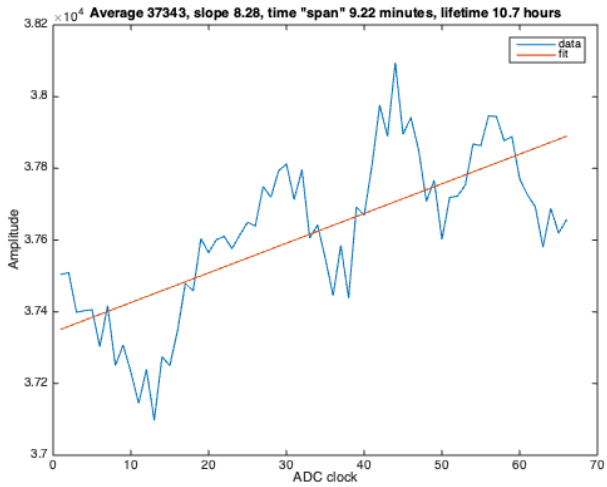


Figure 5: Lifetime measurement from the slop of the amplitude. The region selected is just before the step down.

CONCLUSION

Preliminary analysis of the BPM data from NSLS-II showed feasibility of using raw BPM data for an "instantaneous" measurement of the lifetime. The measurement accuracy can be adversely affected by modulation of injected beam amplitude as well as drifts in the delivered charge.

ACKNOWLEDGEMENTS

Author would like to thank Victor Smaluk from NSLS-II for collecting and providing BPM data.

REFERENCES

[1] R. Fliller, A.A. Derbenev, T. Shaftan, G-M. Wang, "Top Off Algorithm Development and Commissioning at NSLS-II," in *Proc. 7th Int. Particle Accelerator Conf. (IPAC'16),* Busan, Korea, May 2017, pp. 2988-2990. doi:10.18429/JACoW-IPAC2016-WEPOW060

[2] R. P. Fliller, A.A. Derbenev, V. Smaluk, X. Yang, "Top Off of NSLS-II with Inefficient Injector," *in Proc. 9th Int. Particle Accelerator Conf. (IPAC'18)*, Vancouver, Canada, May 2018, pp. 1327-1329. doi:10.18429/JACoW-IPAC2018-TUPMF036

[3] K. Vetter, J. Mead, B. Podobedov, Y. Tian, W. Cheng, "The BNL EBPM Electronics, High Performance for Next Generation Storage Rings," in *Proc. of North American Particle Accelerator Conf. (NAPAC2016),* Chicago, IL, USA, October 2016, pp. 1-5. doi:10.18429/JACoW-NAPAC2016-MOA2IO02

Content from this work may be used under the terms of the CC-BY-4.0 licence (© 2023). Any distribution of this work must maintain attribution to the author(s), title of the work, publisher, and DOI

ISBN: 978-3-95450-236-3 ISSN: 2673-5350 doi:10.18429/JACoW-IBIC2023-MOP045

ROBUST EMITTANCE MEASUREMENTS*

I. Pinayev†, Brookhaven National Laboratory, Upton, NY, USA

Abstract

The quadrupole scan is commonly used for measurement of beam emittance. The found dependence of the beam size vs. quadrupole strength is fitted with parabola, which coefficients are used for emittance calculations. The measurement errors can cause substantial variations in the emittance value. Sometimes the fitted parabola has negative minimum value, making impossible emittance calculation. We propose more robust data processing modifying the quadrupole scan procedure using or weighted fit for parabola. The experimental results are presented.

INTRODUCTION

Emittance serves as measure of the transverse phase space occupied by the beam as well as a measure of beam quality in many applications. By definition [1] emittance is

$$\varepsilon_x^2 = \sigma_x^2\sigma_{x'}^2 - \sigma_{xx'}^2 \quad (1)$$

where σ_x^2 and $\sigma_{x'}^2$ are variances, and $\sigma_{xx'}$ is covariance of beam distribution.

Commonly used technique is scanning of a focusing element such as a quadrupole or a solenoid and measuring dependence of the transverse beam size on a profile monitor [2, 3]. The obtained data are fit with a parabola which coefficients are used for calculating emittance. In some cases, even slight changes in the data can cause substantial variation of the emittance value. This is due to that we are subtracting two large numbers. Example of such measurement is shown in Fig. 1.

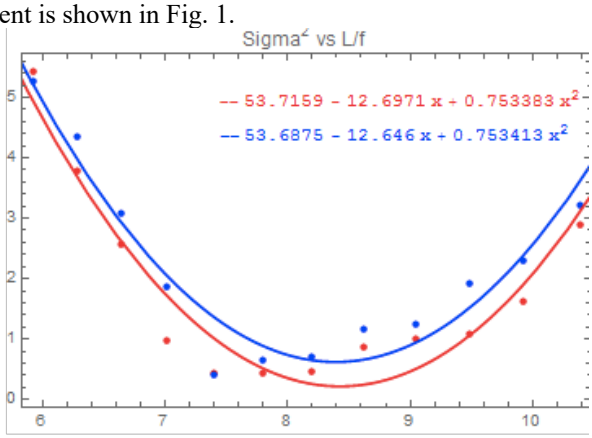


Figure 1: The horizontal axis shows ratio of distance from the solenoid center to the profile monitor and solenoid's focal length. Vertical axis shows the square of the r.m.s. beam size in mm^2.

The maximal difference between the parabolic fit coefficients is 0.2%. Distance from the solenoid to the profile monitor is 3.63 m. Emittance for the blue curve is 0.19 mm mrad, and for the red curve it is 0.11 mm mrad, difference is factor of 2.

Moreover, due to the statistical variations the value of the fitted parabola minimum can be less than zero making the data set unusable for obtaining value of the emittance.

MODIFICATION OF SCAN

We are going to modify the procedure to avoid such subtracting. We can present beam angular distribution as sum of correlated and uncorrelated parts, so that for each particle $x' = \alpha x + \tilde{x}'$, where α is correlation factor and $\tilde{x}'$ is uncorrelated angular spread. Correlation factor can be found from the covariance:

$$\alpha = \sigma_{xx'}/\sigma_x^2 \quad (2)$$

Beam emittance can be found from Eq. (1)

$$\varepsilon_x^2 = \sigma_{x0}^2\sigma_{\tilde{x}'0}^2 \quad (3)$$

where σ_{x0}^2 is r.m.s beam size at focusing element, and $\sigma_{\tilde{x}'0}^2$ is uncorrelated angular spread.

After passing through a focusing element with focal length F and drift with length L the beam size at the observation point can be found

$$\sigma_x^2 = \left(1-\frac{L}{F}\right)^2\sigma_{x0}^2 + 2\alpha L\left(1-\frac{L}{F}\right)\sigma_{x0}^2 + L^2(\alpha^2\sigma_{x0}^2 + \sigma_{\tilde{x}'0}^2) \quad (4)$$

The minimum size is observed when $1 - L/F = -\alpha L$ and minimal size is:

$$\sigma_{xmin}^2 = L^2\sigma_{\tilde{x}'0}^2 \quad (5)$$

So, from $1 - L/F_{min}$ corresponding to the minimal beam size one can find the first order correlation factor α between transverse positions and angles of the particles in the bunch, and the uncorrelated angular spread can be calculated using the minimal beam size.

Now we need to find beam size at focusing element to calculate beam emittance. For this purpose, we can measure the beam size when focusing element is off ($1/F = 0$):

$$\sigma_x^2 = \sigma_{x0}^2 + 2\alpha L\sigma_{x0}^2 + \alpha^2L^2\sigma_{x0}^2 + \sigma_{xmin}^2 \quad (6)$$

and

$$\sigma_{x0}^2 = \frac{\sigma_x^2-\sigma_{xmin}^2}{(1+\alpha L)^2} = \frac{\sigma_x^2-\sigma_{xmin}^2}{(L/F_{min})^2} \quad (7)$$

Emittance can be found using formula below:

$$\varepsilon^2 = \frac{\sigma_x^2-\sigma_{xmin}^2}{(L/F_{min})^2}\frac{\sigma_{xmin}^2}{L^2} \quad (8)$$

If the beam is converging to the minimal size with focusing element off or close to such condition, then there can be significant error in determination of the beam size at the

* Work supported by Brookhaven Science Associates, LLC under Contract No. DE-SC0012704 with the U.S. Department of Energy
† pinayev@bnl.gov

Content from this work may be used under the terms of the CC-BY-4.0 licence (© 2023). Any distribution of this work must maintain attribution to the author(s), title of the work, publisher, and DOI

ISBN: 978-3-95450-236-3 ISSN: 2673-5350 doi:10.18429/JACoW-IBIC2023-MOP045

Content from this work may be used under the terms of the CC-BY-4.0 licence (© 2023). Any distribution of this work must maintain attribution to the author(s), title of the work, publisher, and DOI

focusing element. In this case we can use the setting of the focusing element providing for substantially different beam size and use the formula below for calculation of the beam size

$$\sigma_{xo}^2 = \frac{\sigma_x^2 - \sigma_{xmin}^2}{(1-L/F)^2 + 2\alpha L(1-L/F) + L^2\alpha^2} \quad (9)$$

If we set $1/F = \alpha$ (passing through the focusing element removes linear correlation) and measured beam size will be

$$\sigma_x^2 = \sigma_{x0}^2 + L^2\sigma_{x'0}^2 \quad (10)$$

Because the beam is converging ($\alpha = -1/L$), this will require defocusing element which cannot be realized with solenoids. But we can set focusing so that waist will be achieved in the middle between focusing element and the profile monitor ($1/F = \alpha + 2/L$). In this case beam size at profile monitor will be close to beam size in the focusing element and Eq. (10) can be used as well.

WEIGHTED FIT

Another approach for solving the problem is to utilize the weighted fit. In most cases well-known formulas or standard functions for the polynomial fit are used. Such approach implies that errors in the measurement of beam size are independent of beam size and are constant. The following error function is used for fit evaluation:

$$\chi^2 = \Sigma\left(\sigma_{meas}^2 - \sigma_{fit}^2\right)^2 \quad (11)$$

It is possible to measure few data points at the fixed focusing element setting to find the variation of the measured beam size.

$$\chi^2 = \Sigma\frac{\left(\sigma_{meas}^2 - \sigma_{fit}^2\right)^2}{\sigma_{error}^2} \quad (12)$$

Implementing multiple measurements at each setting of focusing element slows down the process. If we assume that relative error in the beam size measurement is relative constant, then we can modify the error function in the following way:

$$\chi^2 = \Sigma\left(1 - \frac{\sigma_{fit}^2}{\sigma_{meas}^2}\right)^2 \quad (13)$$

Figure 2 shows the fitting curves for the same set of experimental data points with regur and weighted fits.

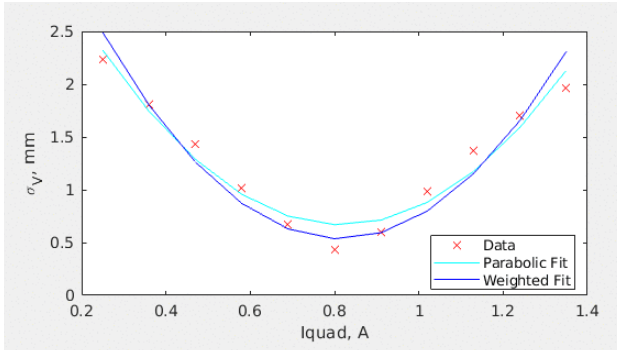


Figure 2: Experimental data of quadrupole scan with regular fit (light blue) and weighted fit (dark blue).

CONCLUSIONS

Two methods are proposed and experimentally tested for increasing robustness of the emittance measurements.

REFERENCES

[1] S.Y. Lee, "Transverse Motion", in *Accelerator Physics*, World Scientific, pp. 53-55, 1999.

[2] M.G. Minty and F. Zimmermann, "Transverse Beam Emittance Measurement and Control", in *Measurement and Control of Charged Particle Beams*, Springer, pp. 101-104, 2003.

[3] M.C. Ross, N. Phinney, G. Quickfall, J.C. Sheppard, H. Shoaee, "Automated Emittance Measurement in the SLC", in *Proc. PAC'87*, Washington, DC, USA, pp. 725-728.

ISBN: 978-3-95450-236-3 ISSN: 2673-5350 doi:10.18429/JACoW-IBIC2023-MOP046

MEASUREMENT OF SLICE EMITTANCE WITH DEFLECTING CAVITY AND SLIT*

I. Pinayev†, Brookhaven National Laboratory, Upton, NY, U.S.A.

Abstract

In this paper we describe the system for the of measurement slice emittance utilizing transverse deflecting cavity and slit. The image of the beam passing through the slit is used to measure slice intensity and uncorrelated angular divergence. Beam size at slit location is measured by scan of the beam across the slit with calibrated trim. The angular kick by the trim is taken into the account during calculations. Data processing and the experimental results are presented.

INTRODUCTION

Coherent Electron Cooling experiment carried out at RHIC [1] requires small slice emittance of 15 MeV electron beam with high peak current.

Many applications require knowledge of the local properties of the beam distribution. These properties include slice emittance and/or slice energy spread. In most cases the emittance is measured by a quadrupole scan when beam is streaked with transverse deflecting cavity [2, 3]. For a low-energy beam with high peak current the measurements are affected by space charge forces. If beam is not centered with quadrupole, then it will be steered during the scan what can mix different slices.

To overcome these difficulties slit scan be used [4]. The slit is moved across the beam and image is observed on a downstream profile monitor. The angular distribution is estimated from the spatial distribution observed on the screen, and the transverse beam size at the location of the slit is found from the dependence of image intensity from slit position. In our experiment we utilize a fixed slit, and we are scanning the beam with help of calibrated trim.

EXPERIMENTAL SET UP

Beam parameters are measured in the dedicated beamline shown in Fig. 1 [5].

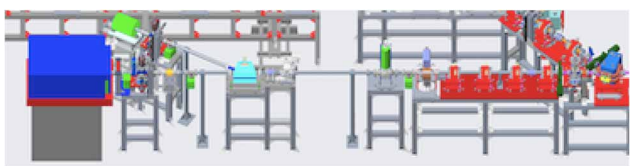


Figure 1: Layout of the diagnostics line. There are four quadrupoles to adjust the beam optics for measurement, followed by a transverse deflecting cavity. Beam can be observed on three profile monitors.

The beam is matched with four quadrupoles. The transverse deflecting cavity tuned to 1.3 MHz provides vertical streak of the beam [6]. Beam can be observed with three profile monitors. The first profile monitor is placed before the 45-degree dipole and used for measurement of the longitudinal profile of the beam. This screen is also used for slice emittance measurement using quadrupole scan. Second profile monitor is placed before the high-power dump and is preceded by a vertical slit. This combination is used for slice emittance measurement described in this paper. The third profile monitor is placed after the 45-degree dipole and is used for measurement of the energy slew and slice energy spread.

The scan of the beam across the slit is performed with two calibrated horizontal trims. The first trim changes position of the beam on the slit and the second trim is restoring initial beam angle (it has the same kick of opposite sign) thus performing parallel scan of the beam over the slit.

Beamlet intensity w_i is estimated from the image brightness inside of the region of interest (ROI). The beamlet angle α_i is found from its center of gravity on the profile monitor and uncorrelated divergence $\sigma_{x'i}$ from the beamlet width. The measured beam size is corrected for the final resolution of the system defined by point spread function of the optical system and slit width. The result of the scan is shown in Fig. 2.

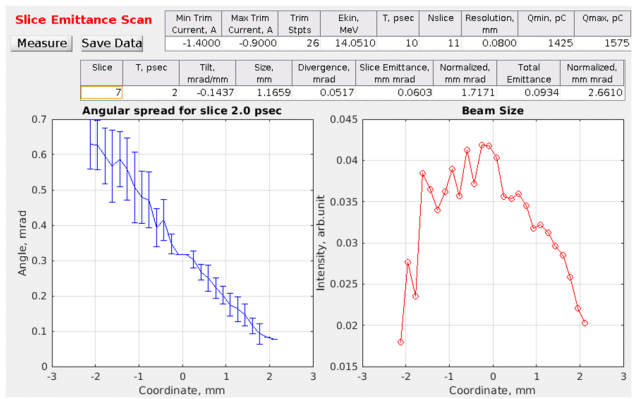


Figure 2: The result of scan of the beam parameters. On the left side one can see phase space plot for the slice at 2 ps from the beam center. Negative sign of the correlated angular spread indicates the beam convergence. R.m.s. beam size is calculated from the right plot, the uncorrelated angular divergence from the left plot. Both values are used for calculation of the slice emittance.

The slice emittance is calculated using conventional formula:

$$\varepsilon_{slice}^2 = \langle x^2 \rangle \langle x'^2 \rangle - \langle xx' \rangle^2 \quad (1)$$

* Work supported by Brookhaven Science Associates, LLC under Contract No. DE-SC0012704 with the U.S. Department of Energy
† pinayev@bnl.gov

Content from this work may be used under the terms of the CC-BY-4.0 licence (© 2023). Any distribution of this work must maintain attribution to the author(s), title of the work, publisher, and DOI

ISBN: 978-3-95450-236-3 ISSN: 2673-5350 doi:10.18429/JACoW-IBIC2023-MOP046

The average values for position and angle are supposed to be equal to zero. The displacement of the beam by trim is Δ_i and beamlet r.m.s. size is:

$$\langle x^2 \rangle = \sum \Delta_i^2 w_i / \sum w_i \quad (2)$$

and beam divergence is:

$$\langle x'^2 \rangle = \sum (\alpha_i^2 + \sigma_{x'i}^2) w_i / \sum w_i \quad (3)$$

Similar, the correlation term is found:

$$\langle xx' \rangle = \sum \Delta_i \alpha_i w_i / \sum w_i \quad (4)$$

The slice is defined by region of interest on the profile monitor. The location of the ROI is fixed during the measurement and temporal scan is done by changing the phase of deflecting cavity. Such approach does not require knowledge of the cavity voltage and calibration of deflecting angle. The calibration, however, is used for setting the vertical size of ROI.

The emittance of the whole bunch is calculated from the slices data. The weight of each slice is sum of the beamlet intensities. The position and angle of each slice is weighted average. Uncorrelated angular divergence is used from the slice data. Emittance calculation is based on Eqs. (1-4). The emittance of the whole beam is displayed upon completion of the last slice measurement as shown in Fig. 3.

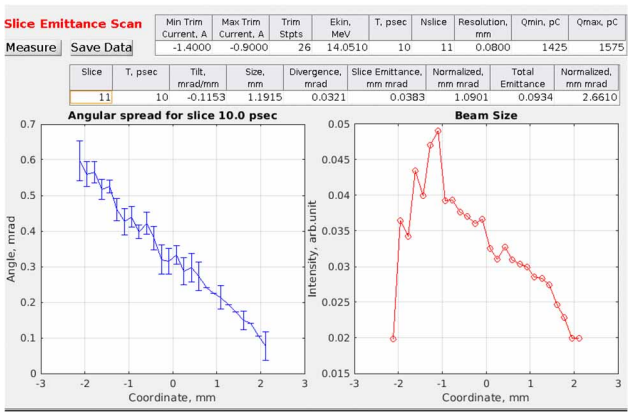


Figure 3: The snapshot of the last slice emittance measurement with displayed emittance of the whole beam.

CONCLUSION

We have developed and applied the slice emittance measurement system utilizing fixed slit and deflecting cavity. The system allows to obtain slice parameters such as size, uncorrelated angular spread, and correlated divergence. The parameters for whole beam are calculated from the slices' data. The system is regularly used for CeC accelerator operation and tuning.

REFERENCES

[1] I. Pinayev *et al.*, "Performance of CeC PoP Accelerator," in *Proc. 10th Int. Particle Accelerator Conf. (IPAC'19)*, Melbourne, Australia, May 2019, pp. 559-561. doi:10.18429/JACoW-IPAC2019-MOPMP050

[2] M. Roehrs, C. Gerth, M. Huening, H. Schlarb, "Slice Emittance Measurements at FLASH", in *Proc. 10th European Particle Accelerator Conf. (EPAC'06),* Edinburgh, Scotland, UK, June 2006, pp. 77-79.

[3] J. Rudolph, M. Abo-Bakr, T. Kamps, J. Teichert, "Slice Emittance Measurement at ALBE/SRF Injector", in *Proc. DIPAC'11*, Hamburg, Germany, May 2011, pp. 416-418.

[4] R. Niemczyk *et al.*, "Slit-based Slice Emittance Measurements Optimization at PITZ", in *Proc. IBIC'19*, Malmo, Sweden, Sep. 2019, pp. 318-321. doi:10.18429/JACoW-IBIC2019-TUPP013

[5] T.A. Miller *et al.*, "Overview of Beam Instrumentation and Commissioning Results from the Coherent Electron Cooling Experiment at BNL", in *Proc. IBIC'18*, Shanghai, China, Sep. 2018, pp. 43-47. doi:10.18429/JACoW-IBIC2018-MOPA09

[6] S.A. Belomestnykh, V.D. Shemelelin, K.W. Smolenski, V. Veshcherevich, "Deflecting Cavity for Beam Diagnostics in ERL Injector", in *Proc. 22nd Particle Accelerator Conf. (PAC'07)*. Albuquerque, New Mexico, USA, Aug. 2007, pp. 2331-2333.

Content from this work may be used under the terms of the CC-BY-4.0 licence (© 2023). Any distribution of this work must maintain attribution to the author(s), title of the work, publisher, and DOI

ISBN: 978-3-95450-236-3 ISSN: 2673-5350 doi:10.18429/JACoW-IBIC2023-TU1I01

BEAM INSTRUMENTATION CHALLENGES FOR HIGH-ENERGY AND LOW-EMITTANCE BEAM AT SuperKEKB

G. Mitsuka*, KEK, 1-1 Oho, Tsukuba, Ibaraki, Japan

Abstract

The SuperKEKB electron–positron collider, which started the commissioning in February 2016, is a luminosity frontier machine for the search for new physics. In this presentation, we review the main challenges we face for the high-energy and low-emittance beam at SuperKEKB, fast and low-noise beam-orbit feedback system, X-ray beam-profile monitors for measurements for the beam size of 10 µm, novel diamond mirrors with extremely high thermalconductivity for extracting synchrotron radiation, and various type's beam loss diagnostics for the identification orpossibly early detection of sudden beam losses. This presentation includes future directions of the R&D—X-rayinterferometry for micron-level beam size measurements and fast optics measurements with the gated turn-by-turn BPMs—towards next-generation light source facilities and high-energy colliders.

OVERVIEW OF SuperKEKB

SuperKEKB is a positron–electron collider with a nanobeam scheme [1], which currently achieves the world's highest luminosity for producing B meson pairs. SuperKEKB consists of a 4 GeV positron ring (LER) and a 7 GeV electron ring (HER) [2]. The nanobeam scheme allows the vertical beta function at the interaction point to be much smaller than the bunch length. The vertical beta function and the beam size at the interaction point are the smallest in the world among colliders. The machine operation started in March 2018 with a test run to verify a nano-beam scheme, and then the physics run began in March 2019. The vertical beta function at the interaction point, β_y^*, has been squeezed down to 1.0 mm during 2019. We tested for further squeezing in β_y^* down to 0.8 mm for approximately one week in 2020 and 2022. Adopting a crab-waist scheme for both rings since the 2020 spring run has increased the luminosity. The crab-waist ratio is 80 % and 40 % in LER and HER, respectively. The crab-waist scheme at SuperKEKB is combined with the local chromaticity correction in the interaction region. We achieved a peak luminosity of $4.65 \times 10^{34}\,\mathrm{cm^{-2}s^{-1}}$ with $\beta_y^* = 1.0$ mm in the physics run and the highest luminosity of $4.71 \times 10^{34}\,\mathrm{cm^{-2}s^{-1}}$ without data acquisition by the Belle-II detector. The machine parameters that accomplished the peak luminosity and those for the target luminosity in 2028 are presented in Table 1.

As of September 2023, we are in a long shutdown to upgrade the Belle-II detector and SuperKEKB. SuperKEKB is scheduled to resume operations in December 2023.

* gaku.mitsuka@kek.jp

Table 1: SuperKEKB Machine Parameters Achieved on 8 June 2022 and Expected in 2028

Parameters		8 June 2022 LER	8 June 2022 HER	2028 LER	2028 HER
I	[A]	1.321	1.099	2.75	2.20
n_b		2249		2345	
I_b	[mA]	0.587	0.489	1.17	0.938
β_x^*	[mm]	80.0	60.0		
β_y^*	[mm]	1.0	1.0	0.6	0.6
ξ_y		0.0407	0.0279	0.0604	0.0431
ε_y	[pm]	31.7		21	
Σ_y^*	[µm]	0.252		0.160	
σ_z	[mm]	5.69	6.02	7.23	7.05
Crab-waist ratio	[%]	80	40		
L	$[\mathrm{cm^{-2}s^{-1}}]$	4.65×10^{34}		2.4×10^{35}	

BEAM PROFILE MONITORS

The realization of a low-emittance beam is essential for high luminosity in SuperKEKB. Accordingly, accurately measuring small beam sizes and short bunch lengths is entrusted to beam diagnostic systems.

SuperKEKB operates synchrotron radiation monitors in the X-ray and visible light regions to measure the beam profile, say, beam size and bunch length. Here, we report the recent updates of the X-ray beam size monitors and visible-light beam profile monitors.

X-ray Beam Size Monitors

The X-ray beam size monitor (XRM) is dedicated to measuring the electron and positron vertical beam size using X-ray synchrotron radiation and will be capable of single-shot (single bunch, single turn) measurements [3]. The XRMs are installed one to each main ring. Since the fast silicon-strip detectors and the fast readout systems developed under the US-Japan collaboration were not in time, we have measured the vertical beam sizes by analyzing the X-ray-induced images projected on the scintillator screens. X-rays produced by the bending magnet pass through the coded aperture optical mask about 10 m downstream and enter a detector box 30 m further downstream, where the scintillator screen and CMOS camera are housed.

The beam study results, which commenced in May–July 2018, suggest the point spread function $\sigma_s = 6.6$ µm, consistent with the simulation-estimated spatial resolution of the imaging system and scattering in the beamline. The overall performances of XRMs in LER and HER are accurate and satisfy the measurement accuracy presently required by SuperKEKB.

Content from this work may be used under the terms of the CC-BY-4.0 licence (© 2023). Any distribution of this work must maintain attribution to the author(s), title of the work, publisher, and DOI

ISBN: 978-3-95450-236-3 ISSN: 2673-5350 doi:10.18429/JACoW-IBIC2023-TU1I01

Content from this work may be used under the terms of the CC-BY-4.0 licence (© 2023). Any distribution of this work must maintain attribution to the author(s), title of the work, publisher, and DOI

As shown in Table 1, we will further squeeze the vertical β function to 0.6 mm, and the design beam size at the zero current is 7 µm. Since the current XRM would be insufficient to meet this more demanding requirement, we started upgrading the XRM to a spatial coherence-based interferometer. Figure 1 shows an overview of the X-ray interferometer. The interferometer uses the double slit with a spacing of 30 µm instead of a coded aperture optical mask. Accordingly, the measurement method changes from geometrical to wave optics. The width of both slits is 15 µm. The synchrotron radiation generated at the emission point (bending magnet) passes through the double slit located about 10 m downstream from the emission point. Then, it enters the detector box 30 m further downstream.

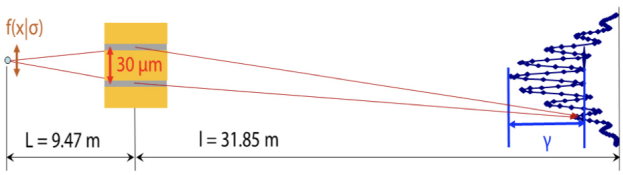


Figure 1: Schematic view of the X-ray interferometer at SuperKEKB.

Figure 2 (a) shows the simulated interference fringes with a beam size of 10 µm and X-ray energies of 9 keV and 15 keV. Figure 2 (b) shows the interference fringes first measured in March 2022, but nothing is actually visible. When we performed the beam test, the beam size was 25 µm, which was too large to measure interference fringes (prior to changing to the double slit, we performed measurements using the normal XRM with coded aperture). After the SuperKEKB electron ring resumes operation in January 2024, we will temporarily switch to the test beam optics to achieve a beam size of 10 µm and try the beam test again. The following two points are future challenges for the X-ray interferometer: 1) Limit the X-ray wavelength. As shown in Fig. 2 (a), a broad X-ray wavelength range causes interference fringes to overlap, leading to a loss of measurement accuracy. The most affordable Cu foil filter or a noble gas filter, such as Kr gas, can pass the X-ray around 10 keV. 2) Introduction of an X-ray reflection mirror. In order to completely superimpose the X-rays passing through the double slits each other, a total reflection mirror, not yet installed, is necessary.

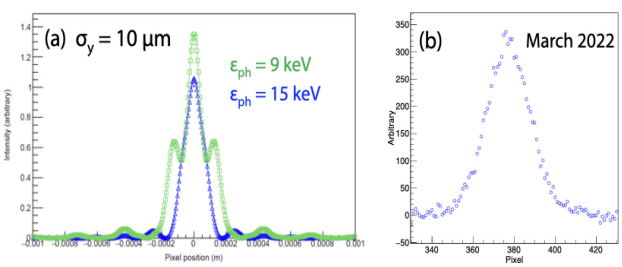


Figure 2: (a) Simulated interference fringes with a beam size of 10 µm and X-ray energies of 9 keV and 15 keV. (b) Measured interference fringes with a beam size of 25 µm.

Beam Halo Monitors

The most significant background events to the Belle-II detector consist of 1) scattering of the beam by residual gas in the beam pipe and 2) Touschek scattering, which is the scattering of electrons or positrons within the bunch. Both of these scattering events create a cloud-like halo around the central core of the beam, which comes to a background event for the Belle II detector. The beam halo also induces radioactivation of other accelerator components. Since the beam halo will be a significant problem, especially in high-current operation toward increasing luminosity, direct measurement and understanding of the beam halo is necessary.

We developed the coronagraph for measurements of beam halo in 2020-2021 [4]. The coronagraph consists of three stages of optical systems: objective, re-diffraction, and relay systems. An objective system with a long focal length was required as we would use the coronagraph 60 m downstream of the synchrotron radiation emission point. Because of the dimension of the diamond extraction mirror (20 mm (W) × 23 mm (H)) installed at 23.6 m downstream of the emission point, the entrance pupil of the objective system was accordingly limited. Aiming to achieve enough resolution in these constraints, we designed a reflective telephoto system based on the Gregorian telescope for the objective system. The focal length was 7028 mm, and the front principal plane was at the diamond extraction mirror. The re-diffraction and relay systems were designed based on a Kepler-type telescope. As a result of initial testing in 2022 using the SuperKEKB electron and positron beams, the performance of the objective system had a diffraction-limited quality, and we achieved a contrast of six orders of magnitude.

Shown in the left panel of Fig. 3 is a result taken in LER on 2022 March at the average bunch current 0.61 mA. Although patterns of the beam halos in LER irregularly change in each shot, the beam halo in LER is radially available away from the beam core and seems more substantial than that in HER. The result in HER in the right panel of Fig. 3 was taken at a comparable bunch current 0.55 mA as in LER. This tendency may originate in a difference in the beam collision scheme; we made the LER measurements in beam-beam collisions, but no beam-beam collision occurred during the HER measurements. Note that the beam-induced background to the Belle-II detector is known to be more abundant in LER than in HER.

Synchrotron Radiation Extraction Mirror Renovation

The polycrystalline diamond-based synchrotron radiation extraction mirror enables precise measurement of beam profiles using visible light, including beam halo measurements. For correctly measuring the beam profiles, thermal deformation of extraction mirrors must be minimized as low as possible and thus has been one of the significant issues in synchrotron radiation monitors.

ISBN: 978-3-95450-236-3 ISSN: 2673-5350 doi:10.18429/JACoW-IBIC2023-TU1I01

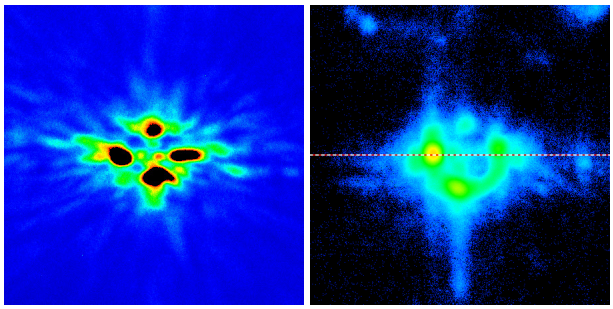


Figure 3: Measurements for beam halos in LER (left) and HER (right).

We developed platinum-coated diamond mirrors in 2019 to obtain better initial flatness and suppress thermal deformation [5]. The diamond mirrors were made with an optical-quality polycrystalline-diamond substrate with thermal conductivity 1800 W/(mK) and had a size of 20 mm (W) × 31 mm (H) × 1.2 mm (D). In optical testing with a laser interferometer performed before installation into the SuperKEKB ring, we confirmed the surface flatness better than $\lambda/5$ (λ is a reference wavelength 632.8 nm, see Fig. 4.) The diamond mirrors were installed in electron and positron rings in the 2020 summer and 2021 summer, respectively. Though irradiation for a year at the beam current greater than 1 A, we observed surface flatness better than $\lambda/4$ at the beam current ranging from 50 mA to 1 A. Figure 5 indicates the surface flatness at 45 mA (left) and 1049 mA (right), measured by a Hartmann test using a square array screen. We conclude that the extraction mirror has no beam current-dependent deformation below 1 A.

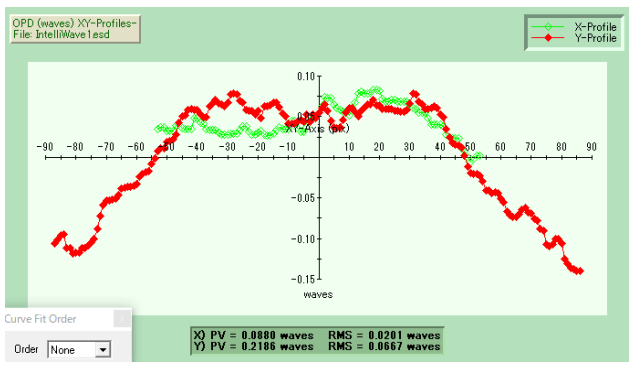


Figure 4: Measurement for the surface flatness of the extraction mirror with a laser interferometer.

BEAM POSITION MONITORS

SuperKEKB needs to squeeze vertical beam sizes at the interaction point down to 50 nm and minimize betatron coupling (X-Y coupling) and dispersion function, causing an increase in beam size. Additionally, betatron function measurements and their corrections are essential since a disturbance of the betatron function leads to a dynamic aperture reduction and vertical emittance growth.

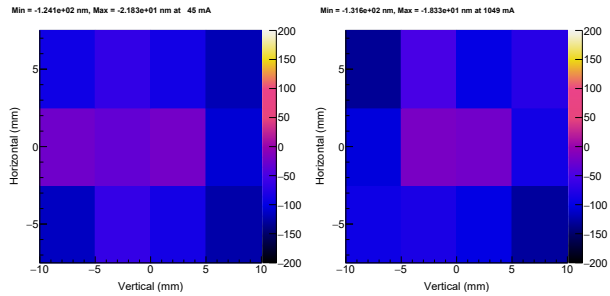


Figure 5: The surface flatness measured by a Hartmann test using a square array screen at 45 mA (left) and 1049 mA (right).

At SuperKEKB, we usually measure X-Y coupling and vertical dispersion by closed orbit analysis for a beam artificially excited by steering magnets. The two types of narrowband detectors are utilized for closed orbit analysis, 508 MHz and 1 GHz, depending on the cutoff frequency of the chamber. The 1 GHz narrowband detectors have been used since the KEKB accelerator, the predecessor of SuperKEKB. The 508 MHz narrowband detectors are newly installed in LER to deal with lower cutoff frequency. The beam optics measurements and their correction using the narrowband detectors need a few tens of minutes.

Gated Turn-by-Turn Monitors

For fast measurements for beam optics, including X-Y coupling during beam-beam collisions, we utilize the injection kickers or the transverse feedback kickers to excite a specific non-colliding bunch while leaving colliding bunches unaffected. Electrode signals from beam position monitors (BPMs) for only a non-colliding bunch are specially processed by the gated turn-by-turn beam position monitors (GTBTs) [6]. The narrowband detector, taking 4 s per measurement, has a positioning resolution of 2 μm, considerably better than the GTBTs, having several tens of μm resolution.

A GTBT detector has four-channel BPM inputs. Incoming BPM electrode signals first go to a fast RF gating switch [7] that accepts signals from only a non-colliding bunch (pilot bunch) and rejects signals from others. Insertion loss owing to the RF gating is 4 dB and the isolation is 80 dB, both of which fully meet our requests. Rejected BPM signals return to four-channel BPM outputs connecting to an external 508 MHz narrow-band detector circuit in charge of a closed orbit analysis. Accepted pilot bunch signals are processed in a GTBT through 508 MHz bandpass filters, low-noise amplifiers (total gain 40 dB), log-ratio amplifier (ADL5513), peak hold circuit, and are finally analog-digital converted by a 14-bit ADC (ADS850). The Xilinx/AMD FPGA controls a timing signal to synchronize these processes. Table 2 shows the GTBT specifications.

In Gen1, analog components from the RF switch to the log-ratio amplifier were mounted on a digital circuit board with an FPGA, causing digital noise to the analog circuit. On the contrary, in Gen2, the above analog components are modularized and housed in an aluminum box to separate

Content from this work may be used under the terms of the CC-BY-4.0 licence (© 2023). Any distribution of this work must maintain attribution to the author(s), title of the work, publisher, and DOI

ISBN: 978-3-95450-236-3 ISSN: 2673-5350 doi:10.18429/JACoW-IBIC2023-TU1I01

Content from this work may be used under the terms of the CC-BY-4.0 licence (© 2023). Any distribution of this work must maintain attribution to the author(s), title of the work, publisher, and DOI

them from the digital board. The update in the analog circuit in Gen 2 significantly reduced the noise floor and increased the dynamic range by 5 dB.

Table 2: Gated Turn-by-Turn Monitor Specifications

Parameters	Gen1	Gen2
FPGA	Spartan-6	Zynq
Low-noise amp.	HMC616	PGA-103+
Log amp.	ADL5513	ADL5513
ADC	ADS850	ADS850
Linearlity	> −75 dBm	> −80 dBm
Number of monitors	140	2

BEAM-ORBIT FEEDBACK SYSTEM

Beam-orbit Feedback at the Interaction Point

In collider accelerators, beam orbit variation causes a lateral distance between the two beam axes at the interaction point, reducing luminosity. When the quadrupole magnet near the interaction point vibrates, the beam undergoes a dipole kick, and the closed orbit changes, resulting in a shift of the closed orbit equivalent to the magnitude of the magnet variation.

The displacement of the quadrupole magnet has been simulated and measured, resulting in the primary oscillation of several 10 Hz, and the distance between the beams at the interaction point is about 20 nm. We have developed a feedback system to compensate for the orbit variation at the interaction point of several 10 Hz.

Figure 6 shows a schematic diagram of the beam-orbit feedback system. There are four BPMs, two on the left side and two on the right side of each ring, across the interaction point at a distance of about 0.5 m from the interaction point. A total of eight steering magnets placed at HER control the vertical orbit at the interaction point. The button electrode is made with a rod with a diameter of 1.8 mm to reduce the beam power received by the electrodes. We use Alumina for the vacuum seal and rod support. The body and rod are made of titanium and brazed to a Cu-Ni flange. The power at the detection frequency of 509 MHz is −4.3 dBm. The signal level at the entrance of the signal processing circuit, including cable loss, is −17.5 dBm and −13.3 dBm on the left and right sides, respectively. In the signal processing circuit, the 509 MHz component of the beam signal is analog down-converted to the intermediate frequency of 16.9 MHz. The analog to digital converted signal is further down-converted to the baseband frequency by a digital down converter, and a digital filter finally limits bandwidth. The feedback controller receives four BPMs' position information from the filter board via the high-speed serial data transfer. The Xilinx/AMD Vertex-5 FPGA calculates the kick angle of the steering magnets required for beam orbit feedback.

The steering power controller inputs the steering magnet's kick angle from the upstream feedback controller, converts it to an analog signal by a 16-bit DAC, and outputs it to the magnet power supply. There are two inputs to the steering power controller; one is the kick angle for fast feedback sent from the feedback controller at a rate of 32 kHz via optical fiber. The other is a kick angle with an update rate of about 1 Hz sent via EPICS channel access, which is used to set the slow vertical feedback, horizontal dithering feedback, and horizontal and vertical DC bump orbits [8].

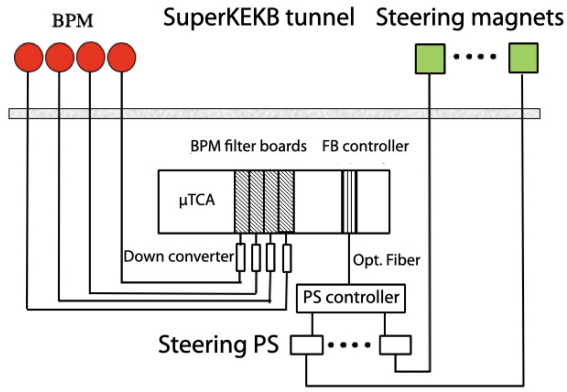


Figure 6: Schematic diagram of the beam-orbit feedback system.

Bunch-by-bunch Feedback System

Many bunches must be stored in the SuperKEKB ring with a 4 ns separation toward a target luminosity. In such a condition in the storage ring, the beams' electromagnetic fields interact with the vacuum components and the ions and electron clouds in the vacuum chamber, resulting in beam instability. A bunch-by-bunch feedback system was developed to observe and suppress unwanted beam instability. See Ref. [9] for details of the system.

CHALLENGES TO SUDDEN BEAM LOSS EVENTS

Currently, the biggest obstacle to increasing the beam current in SuperKEKB is the sudden beam loss, which is a sudden beam abort that results in the loss of about half of the beam charge within 2–3 turns. For more details on the sudden beam loss, refer to Ref. [10].

Although we have not clarified the mechanism of sudden beam loss, the discharge phenomenon is one of the most likely scenarios. According to this scenario, metallic dust in the beam pipe or vacuum chamber is plasmaized by the electromagnetic field caused by the beam. An intensely grown plasma generates an electric field like an arc discharge at a certain moment, and the discharge suddenly kicks a part of the bunch train. The kicked bunch loses most of the bunch charge at the collimator, which has the narrowest aperture in the ring.

Bunch Oscillation Recorder

The bunch oscillation recorder measures the variation in the position of the kicked bunch. See Ref. [11] for a detailed description of the bunch oscillation recorder. Figure 7 shows an example of a bunch oscillation recorder measurement,

ISBN: 978-3-95450-236-3 ISSN: 2673-5350 doi:10.18429/JACoW-IBIC2023-TU1I01

where the bunch position has fluctuated rapidly in horizontal and vertical directions since three turns before the beam aborts.

We currently have only one bunch oscillation recorder in each ring, so it is impossible to determine where the vibration started in the ring. It is also impossible to determine whether the betatron phase advance accidentally obscured the oscillations or whether the amplitude of the oscillations was indeed small. To solve these problems, we started developing a new bunch oscillation recorder to be utilized in addition to the existing bunch oscillation recorders. One plan is a simple bunch oscillation recorder [11], which uses analog hybrid circuits to process the signals from the button electrodes and digitally sample them using an oscilloscope.

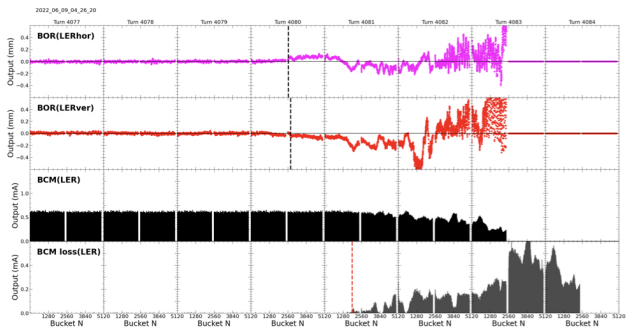


Figure 7: Sudden beam loss event measured with the bunch oscillation recorder (courtesy of M. Aversano, Nagoya University).

RFSoC-based Bunch Oscillation Recorder

Another idea is the bunch oscillation recorder using the Xilinx/AMD RF System on Chip (RFSoC), which contains an 8-channel 12-bit ADC/DAC, FPGA, and Arm processor in a single chip. This structure has the advantages of easy handling without the need to design and implement communication lines between the ADC/DAC and FPGA and high-speed sampling to obtain bunch-by-bunch information. The structure of the RFSoC-based bunch oscillation recorder shown in Fig. 8 is as follows. First, a bandpass filter (center frequency of 0.5 – 2.0 GHz) placed upstream limits the bandwidth. Next, a low-noise amplifier amplifies the signal to compensate for the loss caused by the insertion of the bandpass filter. The signal is then digitally down-converted to baseband in RFSoC and decimated at 509 MHz. Finally, the FPGA and the Arm processor convert the digital signal to horizontal and vertical positions. The ring buffer memory is saved after receiving the abort trigger signal and waiting for a few turns.

We have started the first phase of development of the above detector using RFSoC evaluation board ZCU111. As of September 2023, the following two tests are underway: 1) Loop back the pseudo-signal created by RF-DAC to RF-ADC to test the implementation of digital down-conversion. 2) Create a pseudo-signal using a 125 MHz step recovery diode and select the bandwidth with a 2 GHz comm-type bandpass filter. A mezzanine card with a balun, surface-mounted bandpass filter, and low-noise amplifier will be made soon. A novel RFSoC bunch oscillation recorder will be put into commissioning as soon as possible after the SuperKEKB operation resumes in December 2023.

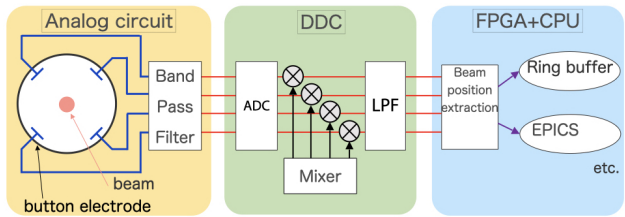


Figure 8: Schematic diagram of the RFSoC-based bunch oscillation recorder.

REFERENCES

[1] T. Abe *et al.*, "Technical Design Report of SuperKEKB", https://kds.kek.jp/indico/event/15914/

[2] Y. Ohnishi, "Recent progress of SuperKEKB project and future prospect", in *Proc. IPAC'23*, Venice, Italy, May 2023, pp. 1321-1324. doi:10.18429/JACOW-IPAC2023-TUOGB1

[3] E. Mulyani *et al.*, "First measurements of the vertical beam size with an X-ray beam size monitor in SuperKEKB rings", *Nucl. Instrum. Methods. Phys. Res., Sect. A*, vol. 919, pp. 1–15. doi:10.1016/j.nima.2018.11.116

[4] G. Mitsuka, H. Ikeda, and T.M. Mitsuhashi, "Design and Construction of Optical System of the Coronagraph for Beam Halo Observation in the SuperKEKB", in *Proc. IPAC'22*, Bangkok, Thailand, Jun. 2022, pp. 769–771. doi:10.18429/JACoW-IPAC2022-TUOXGD1

[5] G. Mitsuka, H. Ikeda, and T.M. Mitsuhashi, "Renovation of the SR Beam Profile Monitors with Novel Polycrystalline Diamond Mirrors at the SuperKEKB Accelerator", in *Proc. IPAC'22*, Bangkok, Thailand, Jun. 2022, pp. 313–315. doi:10.18429/JACoW-IPAC2022-MOPOPT031

[6] M. Tobiyama, H. Fukuma, H. Ishii, and K. Mori, "Development of Gated Turn-by-Turn Position Monitor System for the Optics Measurement During Collision of SuperKEKB", in *Proc. IBIC2013*, Oxford, UK, Sep. 2013, paper MOPF32, pp. 295–298.

[7] T. Naito *et al.*, "Beam Oscillation Monitor for the Multi-bunch Beam", in *Proc. IPAC2013*, Shanghai, China, May. 2013, paper MOPME018, pp. 506–508.

[8] Y. Funakoshi *et al.*, "Orbit feedback system for maintaining an optimum beam collision", *Phys. Rev. ST Accel. Beams*, vol. 10, p. 101001, 2007. doi:10.1103/PhysRevSTAB.10.101001

[9] M. Tobiyama *et al.*, "Bunch by bunch feedback systems for SuperKEKB rings", in *Proc. PASJ'16* Chiba, Aug. 2016, paper TUOM06.

[10] H. Ikeda, "Observation of sudden beam loss in SuperKEKB", in *Proc. IPAC'23*, Venice, Italy, May 2023, pp. 698-701. doi:10.18429/JACOW-IPAC2023-MOPL072

[11] M. Tobiyama, H. Ikeda, and G. Mitsuka, "Development of Bunch Position Monitors to Observe Sudden Beam Loss of SuperKEKB Rings", presented at IBIC'23, Saskatoon, Canada, Sep. 2023, paper TUP002, this conference.

Content from this work may be used under the terms of the CC-BY-4.0 licence (© 2023). Any distribution of this work must maintain attribution to the author(s), title of the work, publisher, and DOI

ISBN: 978-3-95450-236-3 ISSN: 2673-5350 doi:10.18429/JACoW-IBIC2023-TU1I02

BEAM INSTRUMENTATION PERFORMANCE DURING COMMISSIONING OF THE ESS NORMAL CONDUCTING LINAC

I. Dolenc Kittelmann*, R. Baron, E. Bergman, E. Donegani, V. Grishin, H. Hassanzadegan, H. Kocevar, N. Milas, R. Miyamoto, M. Mohammednezhad, F. Nilen, D. Noll, K. Rosengren, T. Shea, R. Tarkeshian, C. Thomas
European Spallation Source ERIC, Lund, Sweden

Abstract

Once constructed, the European Spallation Source (ESS) will be a 5 MW pulsed neutron source based on a 2 GeV proton linac delivering 2.86 ms long pulses at a 14 Hz repetition rate. This paper focuses on the beam instrumentation performance during the recent linac beam commissioning up to drift tube linac (DTL) tank 4 with 74 MeV output energy. Instrumentation and measurement results will be presented for beam parameters such as current, position, energy, emittance and beam loss.

INTRODUCTION

The European Spallation Source (ESS) is a neutron-based research facility, currently under construction and designed to deliver the world's brightest neutron beams [1, 2]. The neutron production will be based on the bombardment of a tungsten target with a proton beam generated by a pulsed linac. The linac will accelerate and transport the protons towards the target through a normal-conducting (NCL) and superconducting (SCL) linac (Fig. 1) resulting in a beam with a peak current of 62.5 mA, 2.86 ms pulse length, 14 Hz repetition rate, and energy of 2 GeV once the linac design average power of 5 MW is reached.

For a high-power machine like the ESS linac, one of the biggest challenges during its commissioning and operations is to minimize beam losses and protect its components by adequately adjusting the electromagnetic elements and achieving ideal beam parameters. A comprehensive set of proton beam instrumentation has been developed to provide detailed beam property measurements throughout the linac and thus to support achieving the required beam parameters. The set comprises instruments for beam characterisation along the linac to provide beam profile, position, energy, current and loss measurements [3].

The ESS linac commissioning is performed in phases. Each commissioning phase is focused on the linac parts up to the selected beam destination. In parallel, the linac installation downstream of the end-destination continues. Three commissioning phases have been completed successfully with low power beam and end-destinations in LEBT (2018-2019) [4, 5], in MEBT (2021-2022) [6] and at the end of DTL1 reaching 21 MeV (2022) [7–9]. From April to July 2023, the commissioning has advanced to the fourth phase, reaching the end of the DTL4 tank with an output energy of 74 MeV. Towards the end of 2024, the beam commissioning will continue to the Dump, while the first beam on target is planned to be achieved at the end of 2025 followed by the start of the user program in 2026.

This paper focuses on ESS beam instrumentation deployed for the DTL4 commissioning phase and highlights their key features and contributions during this phase.

BEAM INSTRUMENTATION FOR THE NCL COMMISSIONING

The ESS beam instrumentation is being deployed in a staged approach. Systems that are critical for meeting commissioning goals proceed through a formal verification process beginning with unit testing in the laboratory followed by integrated system testing, and finally, formal testing with beam to achieve operational status. Figure 1 summarises the instrumentation systems installed for the DTL4 commissioning run. The Faraday Cups (FCs), Beam Current Monitor (BCM), and Beam Position Monitor (BPM) have all gone through the aforementioned formal verification workflow. In addition, several other systems, at an intermediate stage of their development were deployed for diagnostic beam studies to gain early operational experience. The Wire Scanners (WSs) [10], Emittance Measurement Unit (EMU) [7] and two types of Beam Loss Monitors (BLMs) were deployed at this level. Beam studies with the neutron-sensitive BLM (nBLM) and horizontal EMU station offered valuable data for system development as well as beam characterisation and the results are presented here together with results with the FCs, BPM and BCM systems. In addition, some limited beam studies were performed with WSs, the vertical EMU station and the Ionisation Chamber based BLM [11] system. Results from these systems will be covered in future publications.

Faraday Cups

Three Faraday cups were operational during the DTL4 commissioning. Once inserted, each FC is a beam end-destination and measures the transported beam current at the destination. The FC locations were in the LEBT [5, 12], in the MEBT [12, 13] and in a dedicated shielding at the (foreseen) position of DTL5 [12, 14] tank. All FCs are water-cooled and rely on a pneumatic actuator to move in or out of the beamline.

The LEBT FC is designed to withstand full power at the ion source exit, namely 75 keV proton beam pulses with up to 100 mA current, 6 ms pulse length at 14 Hz repetition rate. However, MEBT and DTL4 FC can cope with only

* Irena.DolencKittelmann@ess.eu

Content from this work may be used under the terms of the CC-BY-4.0 licence (© 2023). Any distribution of this work must maintain attribution to the author(s), title of the work, publisher, and DOI

ISBN: 978-3-95450-236-3 ISSN: 2673-5350 doi:10.18429/JACoW-IBIC2023-TU1I02

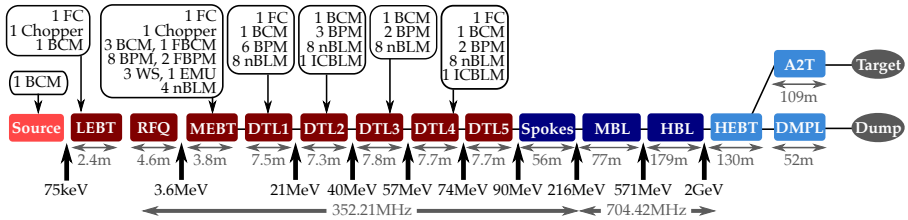


Figure 1: ESS linac: the normal-conducting linac (NCL, in red) is composed of an ion source, Radio Frequency Quadrupole (RFQ), Drift Tube Linac (DTL) with five tanks, Low Energy (LEBT) and Medium Energy Beam Transport (MEBT) sections. Spoke, Medium Beta (MBL) and High Beta (HBL) Linac constitute the Superconducting Linac (SCL, in dark blue). Beam transport and delivery to Target and tuning Dump consist of High Energy Beam Transport (HEBT) line, Accelerator-to-Target (A2T) line and the dump line (DMPL). Beam instrumentation and choppers used in the 2023 commissioning run are indicated.

reduced beam power. The MEBT FC supported commissioning activities with 3.6 MeV beam and current up to nominal 62.5 mA with up to 5 µs or 50 µs pulse length at 14 Hz or 1 Hz repetition rate, respectively. When the destination was the DTL4 FC, the beam parameters envelop was set to allow commissioning studies with low (up to 6 mA) beam current up to 50 µs pulse length and up to 14 Hz repetition rate or high beam current (up to 62.5 mA) up to either 5 µs or 50 µs pulse length and 1 Hz or 0.2 Hz repetition rate, respectively. Restrictions were set on the allowed energy range at the DTL4 FC location (i.e. required acceleration in consecutive tanks) depending on particular sets of beam parameter limits.

At the end of the commissioning and after four weeks of radioactive decay, the residual dose rate of approximately 1 mSv/h in the vicinity of the DTL4 FC allowed the removal the DTL4 FC to leave space for installing the DTL5 tank. During the next commissioning phase and the years to come of operation of the ESS accelerator, there will be four FCs permanently installed in the NCL: one in the LEBT, one in the MEBT, one in the DTL2 intertank and one in the DTL4 intertank.

Beam Current Monitors

Nine Beam Current Monitors were successfully used during the DTL4 beam commissioning phase [15]. Most of these sensors are custom-designed by Bergoz to meet the ESS requirements, including the beam pipe dimensions, magnetic shielding and protection for the BCM ceramic.

The analogue signal from each BCM sensor is first buffered and amplified in a wall-mount Front End (FE) unit and then filtered and further processed in a custom-designed Back End (BE) in the BCM rack. The signal is then converted to digital and FPGA processed to provide the required beam monitoring and machine protection functions.

The BCMs allowed beam current measurement with 0.1 mA accuracy and with a noise level lower than 50 µA peak-to-peak and bandwidth of 1 MHz. The measurements included pulse profile, average beam current over a region of interest (ROI) and pulse charge with each BCM. These measurements also aided the machine operators in identifying electrons from the cavities due to multipacting and RF/vacuum breakdowns (Fig. 2) as well as the (expected) scattered beam from the MEBT chopper dump (Fig. 3). Given that the BCM is located directly after the MEBT chopper dump while the other beam measurement devices, such as the BPMs and the FCs, are located further downstream, the scattered beam could only be measured by this BCM due to the geometrical constraints.

The BCM system further provided a precise measurement of the width, repetition rate and arrival time of the beam trigger for consistency checks, thus avoiding unexpected beams due to human errors and/or timing system-related issues.

A post-mortem ring buffer was implemented in the BCM firmware to capture BCM data upon a beam trip. It proved to be a very effective tool for trip analysis and improvements in beam availability. Furthermore, differential interlocks with several BCM pairs were verified with beam and used for beam loss measurement and machine protection.

A BCM channel with a modified beam trigger was successfully tested and verified for 1-hour average beam current measurements with accuracy better than 1 µA.

Figure 2 shows a low current beam pulse measured by seven BCMs from the LEBT to the DTL tank4. Figure 3 shows an example of the pulse width reduction and scattered beam, both caused by the MEBT chopper.

A complete suite of protection functions was used to detect whether, among others, the amplitude, width and repetition rate of the beam pulse were outside the allowed limits and ensure their consistency with the selected beam mode. It included several thresholds that were configured by the BCM firmware based on the selected beam mode and destination. The thresholds were chosen to be consistent with the predefined sets of envelopes. However, some adjustments were made in the configuration of the protection functions based on a beam damage assessment. These were mainly to address beam availability issues due to RF breakdowns and other disturbances originating from the cavities [15].

Beam Position and Phase Monitors

Beam position and phase monitors have been extensively used in this commissioning to characterise the proton beam properties. Beam studies including trajectory correction,

Content from this work may be used under the terms of the CC-BY-4.0 licence (© 2023). Any distribution of this work must maintain attribution to the author(s), title of the work, publisher, and DOI

ISBN: 978-3-95450-236-3 ISSN: 2673-5350 doi:10.18429/JACoW-IBIC2023-TU1I02

Content from this work may be used under the terms of the CC-BY-4.0 licence (© 2023). Any distribution of this work must maintain attribution to the author(s), title of the work, publisher, and DOI

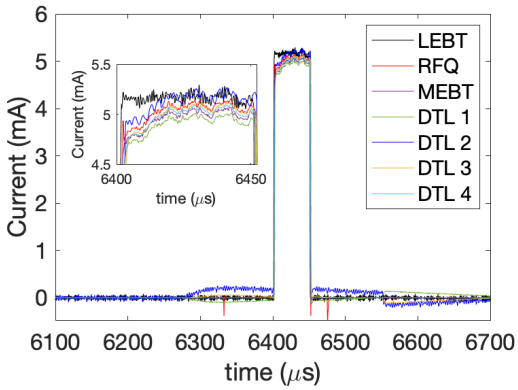


Figure 2: ESS beam pulse as measured with the LEBT, RFQ, MEBT, DTL1 and DTL4 BCMs. The negative spikes on the RFQ BCM readout (red) are due to multipacting, and the small changes in the baseline level with the DTL2 BCM (blue) are due to the field emission from the cavities.

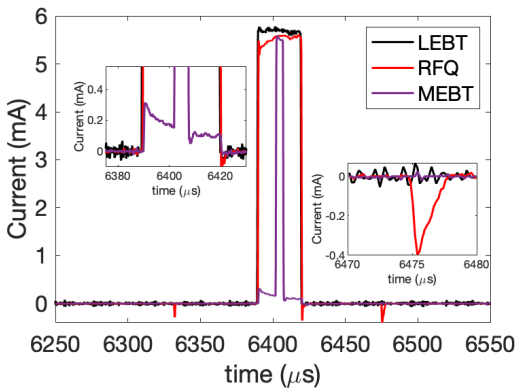


Figure 3: Beam pulses from the LEBT (black), RFQ (red) and MEBT BCM located in the middle of MEBT after the chopper dump (violet). The none-zero floor of MEBT BCM waveform is due to the scattered beam from the MEBT chopper dump.

RF phase scans, longitudinal pulse shape tuning and beam timing characterisation, have been performed based on the data provided by the 21 BPMs in operation during the DTL4 commissioning phase.

The ESS BPM system has several FPGA-based processing channels delivering data in EPICS Process Variables. Data streams for individual antenna's raw data, at approximately 20 MHz bandwidth and 88 MSa/s are available, as well as near-IQ waveforms for positions, magnitudes and beam phase measurements. Typical waveforms for positions and phases are measured at a rate of approximately 5.8 MHz with a bandwidth around 2 MHz [16]. Scalars for averaged data are also calculated at a rate of 1 value per beam pulse in a ROI determined by timing events. BPM waveforms have proven crucial in understanding and adjusting the parameters of the machine to optimize uniformity in pulse characteristics within a pulse and timing characterisations of the beam.

The RF system in NCL operates at 352.21 MHz while the BPMs were designed to operate at the 704.4 MHz second harmonic in order to minimise the interference across the systems. The RF processing chain of the BPM signals and data have been standardized for all the BPMs.

Eight MEBT BPMs were designed based on matched stripline sensors [17] and installed in the machine.

Thirteen DTL BPMs were designed based on shorted stripline sensors and commissioned in DTL tanks 1, 2, 3 and 4. Interference between BPMs and RF system was more strongly observed in the DTL1, but has been addressed during the commissioning. In some locations inside the DTL tanks, where the drift tubes are close to the RF ports, the RF system couples strongly to the second harmonic, which then leaks to the BPM sensors near the RF ports interfering with the beam signal excited on the BPM striplines. Additional RF high-pass filters were introduced on the BPM inputs to filter the first harmonic that couples into the BPM striplines.

Reported BPM measurements during a typical phase scan are presented in Fig. 4. During the phase scan, the set-point of the RF cavity phase under test is plotted together with the phase of the signals measured by BPMs. The measured amplitude of the BPM signals also changes as a function of the cavity RF phase set-point since the bunch length varies with the cavity RF phase and is also presented in the same plot.

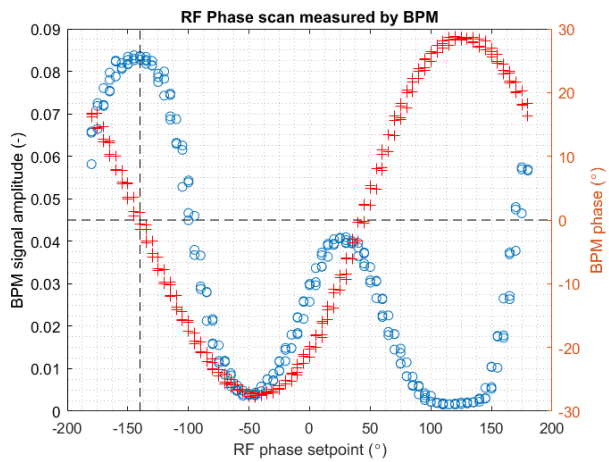


Figure 4: Typical phase scan measurements performed by a downstream MEBT BPM during a phase scan. BPM amplitude and BPM phase are shown on the plot as a function of the RF phase of MEBT buncher 1.

Beam studies slots during the DTL4 commissioning run were assigned to long-term stability measurements of the beam characteristics, and the BPM phase and amplitude measurements are reported in Fig. 5.

Emittance Measurement Unit

The MEBT EMU is a slit-grid type with a grid located 368 mm downstream of a slit with 100 µm aperture. The grid consists of 24 tungsten wires of 35 µm diameter mounted with a pitch of 0.5 mm. Signals are generated by secondary

ISBN: 978-3-95450-236-3 ISSN: 2673-5350 doi:10.18429/JACoW-IBIC2023-TU1I02

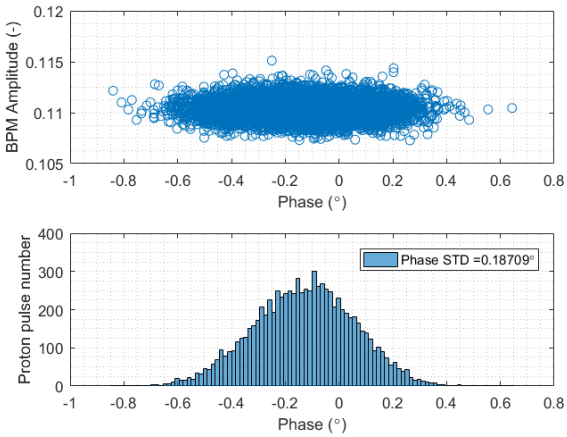


Figure 5: Stability measurements of the beam phase and amplitude recorded with one of the BPMs in MEBT over 4 hours of operation with a 6 mA and 5 µs beam.

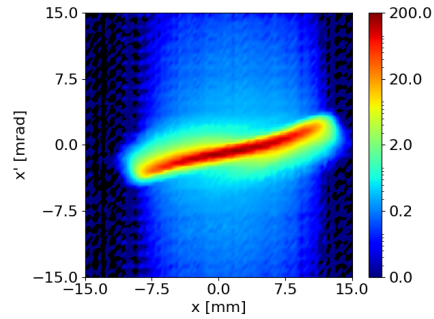


Figure 6: Emittance figure after baseline subtraction with 1 kV bias voltage applied.

electron emission and acquired by configurable gain stages followed by 5 MSa/s digitisers. The grid PCB is surrounded by bias plates that can be biased up to ±1.2 kV to control the electric field experienced by the electrons. The tungsten wires mounted on the bias plates enhance the field created by the plates.

The instrument commissioning activities focused on signal quality investigations and some initial beam studies. Measurements without bias show significant negative signals from secondary electrons picked up on wires adjacent to those exposed to the beam. When biased sufficiently (>500 V), these negative signals are suppressed. At the same time, due to the effective emission of secondary electrons, the positive signal on the exposed wires is enhanced by approximately a factor of 4.

Figure 6 shows an example of a scanning result in the horizontal plane with 167 µm resolution, taking multiple acquisitions of the grid signals with the grid position shifted by 0/3, 1/3 and 2/3 of the wire pitch to improve angular resolution. The signal is integrated over the final 15 µs of the 30 µs long beam used for measurement. The first 15 µs shows varying emittance, likely from space charge compensation in the LEBT. The background extending across the entire range of measured x' is a suspected result of beam scattering from the slit aperture. It was found to follow a Gaussian function and can be subtracted. A preliminary analysis shows an RMS emittance consistent with the beam physics model.

Beam Loss Monitors

Two types of BLM systems differing in detector technology have been conceived at ESS. The nBLM [18] is based on 82 neutron detectors primarily covering the lower energy part of the ESS linac. Conversely, the ICBLM [11] consists of 266 ionisation chambers [19], located predominantly in the high energy parts of the ESS linac.

The ESS nBLM system is based on neutron-sensitive Micromegas devices, specially designed for the lower energy part of the ESS linac [20]. Two types of nBLM detectors with complementary functionality have been developed. Fast detectors (nBLM-F) are designed to detect fast losses in accidental scenarios when high particle fluxes are expected. On the other hand, slow detectors (nBLM-S) primarily aim to monitor losses with low particle fluxes. The nBLM system is designed to discriminate beam loss–induced fast neutrons from the background (RF-induced photons, background slow neutrons) on an event-by-event basis. It is achieved by continuous real-time FPGA-based data processing of digitised raw signal sampled at 250 MHz from each nBLM detector, resulting in fully processed data streams for monitoring and machine protection purposes. Additionally, detailed data at various stages of data processing are being buffered and can be retrieved on demand.

During the previous two commissioning phases, the nBLM system underwent initial deployment and first studies with ESS beam. In 2023, the system installation advanced to take part in studies during the DTL4 commissioning run with 36 nBLM detectors covering MEBT and the first four DTL tanks. Detailed data holding information about interesting events (neutron, noise or background events) and monitoring data have been continuously recorded for two weeks. Furthermore, several dedicated experiments with stable beam conditions were performed where a selected set of beam parameters was kept unchanged for ≈30 min. All data taken during this commissioning period is currently being analysed offline in order to study the system response, explore the background and noise environment and develop a procedure for setting the system configuration. An example of extracted information is shown in Fig. 7 representing a distribution of neutron events over time in machine cycle recorded with one of the nBLM-F detectors. The plot demonstrates a 50 µs and 5 µs beam pulse starting at ~6.5 ms. Figure 8 summarises preliminary results on the number of neutron events (single neutron or pile-up) per beam pulse recorded with nBLM detectors during a set of time periods with different beam currents and pulse lengths. For the fast detectors the observed peaks at end of DTL3 and DTL4 are found to be consistent with the observations from activation surveys. The peak at the end of DTL1 could be qualitatively explained with the simulation results [21] indicating that

Content from this work may be used under the terms of the CC-BY-4.0 licence (© 2023). Any distribution of this work must maintain attribution to the author(s), title of the work, publisher, and DOI

ISBN: 978-3-95450-236-3 ISSN: 2673-5350 doi:10.18429/JACoW-IBIC2023-TU1I02

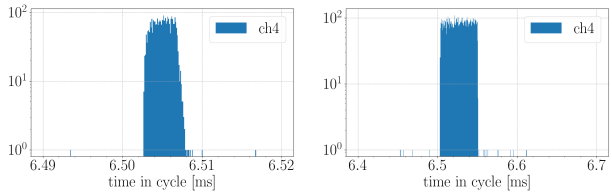


Figure 7: Distribution of neutron events over time in cycle recorded with one of the nBLM-F detectors during a ~2 hour and ~2.5 hour time window with a 5 µs (left) and 50 µs (right) long beam pulse, respectively.

majority of particles outside of the DTL1 acceptance are expected to be lost at this location. Note that, for slow detectors, the event rate differs from the actual neutron rate due to pile-up. Further analysis is ongoing in order to account for that.

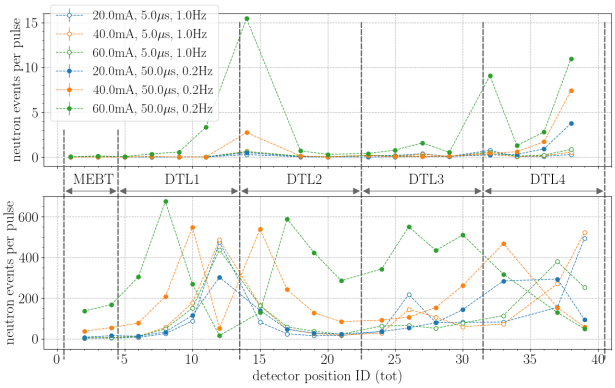


Figure 8: Preliminary results of number of neutron events recorded with fast (top) and slow (bottom) nBLM detectors for different beam parameters.

Bunch-by-bunch Characterization

The Fast BPM (FBPM) and Fast BCM (FBCM) systems provide high bandwidth and high sampling rate measurements for bunch-by-bunch characterisation of the beam. The FBCM, with 700 MHz bandwidth is based on a Bergoz Fast Current Transformer and a 20 GSa/s acquisition system. The Fast BPM is based on two regular stripline BPMs, positioned 30.1 cm apart, with separate 20 GSa/s acquisition systems each incorporating 3 GHz analog front-end electronics. Propagation delays between the FBPM channels are matched to ±50 ps resulting in an energy measurement accuracy of ±20 keV with a precision of ±100 keV [7]. The FBCM and FBPM were both used to verify LEBT and MEBT chopper rise and fall times and for precise timing alignment of the two choppers.

When a protection function identifies unacceptable beam conditions, the Fast Beam Interlock System (FBIS) [22] utilizes several actuators to inhibit beam production. These actuators include the LEBT and MEBT choppers that dump the beam that is already propagating through the front end of the linac. Under controlled test conditions, the FBPM system characterised the reaction time of the complete interlock chain. For this test, a fault was instigated by lowering the maximum current threshold in the MEBT BCM system located just after the MEBT chopper. The full interlock chain consists of the BCM system, signal transmission, FBIS processing, signal transmission to the choppers and the chopper systems themselves. When the MEBT chopper was used, the measured reaction time was approximately 2.3 µs (Fig. 9) and when only the LEBT chopper was used, the measured reaction time was approximately 3.2 µs. The reaction time difference between the two cases is due to the beam propagation time between the LEBT chopper and MEBT chopper.

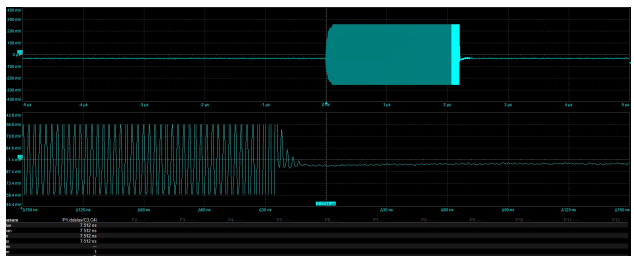


Figure 9: Full chain interlock reaction time measured by the fast BPM with both LEBT and MEBT chopper included in the systems for inhibiting beam production.

CONCLUDING REMARKS

The primary role of the NCL at this phase of the ESS project is to provide an appropriate beam for the commissioning of the remaining accelerator. As evidenced in the preceding sections, the NCL beam instrumentation systems supported the NCL commissioning and are ready to support the upcoming campaigns: 1. initial commissioning of the entire SCL and the beam transport line to the linac Dump and 2. first beam on target by transporting beam through the dogleg and A2T beam delivery system.

In parallel with the NCL commissioning activities, the diagnostics team continued to install SCL and transport line instrumentation. Downstream of DTL4, the instrumentation suite will include an additional 10 BCMs, 77 BPMs, 46 nBLMs, 262 ICBLMs, 5 pairs of Ionisation Profile Monitors [23], 9 pairs of WSs in SCL and A2T, 3 pairs of Fast Wire scanners in the HEBT, 3 Imaging systems [24, 25] and 4 Aperture Monitors [26].

ACKNOWLEDGEMENTS

The authors wish to thank to all past and present colleagues from ESS and external institutes who contributed to the ESS linac project. In particular, we appreciate the critical support received during the design, development, manufacturing, installation and testing of the BI systems.

Content from this work may be used under the terms of the CC-BY-4.0 licence (© 2023). Any distribution of this work must maintain attribution to the author(s), title of the work, publisher, and DOI

ISBN: 978-3-95450-236-3 ISSN: 2673-5350 doi:10.18429/JACoW-IBIC2023-TU1I02

REFERENCES

[1] S. Peggs *et al.*, "ESS technical design report," ESS ERIC, Tech. Rep. ESS-DOC-274, 2013. http://eval.esss.lu.se/cgi-bin/public/DocDB/ShowDocument?docid=274

[2] R. Garoby *et al.*, "The European Spallation Source design," *Phys. Scr.*, vol. 93, no. 1, p. 014 001, 2018. doi:10.1088/1402-4896/aa9bff

[3] T. Shea *et al.*, "Overview and Status of Diagnostics for the ESS Project," in *Proc. of International Beam Instrumentation Conference (IBIC'17)*, Grand Rapids, MI, USA, 2018, paper MO2AB2, pp. 8–15. doi:10.18429/JACoW-IBIC2017-MO2AB2

[4] C. Derrez *et al.*, "Initial Performance of the Beam Instrumentation for the ESS IS & LEBT," in *Proc. 10th International Particle Accelerator Conference (IPAC'19)*, Melbourne, Australia, 2019, paper WEPGW076, pp. 2650–2653. doi:10.18429/JACoW-IPAC2019-WEPGW076

[5] N. Milas *et al.*, "Commissioning of the ESS Front End," in *Proc. HB'21*, Batavia, IL, USA, 2022, paper THDC2, pp. 225–230. doi:10.18429/JACoW-HB2021-THDC2

[6] N. Milas *et al.*, "Beam Tuning Studies in the ESS MEBT," in *Proc. 11th Int. Beam Instrum. Conf. (IBIC'22)*, Kraków, Poland, 2022, paper MO2C2, pp. 6–10. doi:10.18429/JACoW-IBIC2022-MO2C2

[7] T. Shea *et al.*, "Beam Instrumentation Performance During Commissioning of the ESS RFQ, MEBT and DTL," in *Proc. 11th Int. Beam Instrum. Conf. (IBIC'22)*, Kraków, Poland, 2022, paper MOP07, pp. 32–36. doi:10.18429/JACoW-IBIC2022-MOP07

[8] R. Miyamoto *et al.*, "Beam Commissioning of Normal Conducting Part and Status of ESS Project," in *Proc. 31st International Linear Accelerator Conference (LINAC'22)*, Liverpool, UK, 2022, paper MO1PA02, pp. 18–24. doi:10.18429/JACoW-LINAC2022-MO1PA02

[9] D. C. Plostinar *et al.*, "Status of the Normal Conducting Linac at the European Spallation Source," in *Proc. IPAC'22*, Bangkok, Thailand, 2022, paper WEPOTK001, pp. 2019–2022. doi:10.18429/JACoW-IPAC2022-WEPOTK001

[10] C. Derrez *et al.*, "Wire Scanner Systems at the European Spallation Source (ESS): Tests and First Beam Commissioning Results," in *Proc. 31st International Linear Accelerator Conference (LINAC'22)*, Liverpool, UK, 2022, paper TUPOJO13, pp. 372–375. doi:10.18429/JACoW-LINAC2022-TUPOJO13

[11] I. D. Kittelmann *et al.*, "Ionisation Chamber Based Beam Loss Monitoring System for the ESS Linac," in *Proc. 8th International Beam Instrumentation Conference (IBIC'19)*, Malmö, Sweden, 2019, paper MOPP023, pp. 136–140. doi:10.18429/JACoW-IBIC2019-MOPP023

[12] E. Donegani, I. Bustinduy, C. Derrez, T. Grandsaert, A. R. Páramo, and T. Shea, "Status of the Faraday Cups for the ESS linac," in *Proc. IBIC'19*, Malmö, Sweden, 2019, paper MOPP044, pp. 205–208. doi:10.18429/JACoW-IBIC2019-MOPP044

[13] A. R. Páramo *et al.*, "Design of the ESS MEBT Faraday Cup," in *Proc. IBIC'19*, Malmö, Sweden, 2019, paper MOPP014, pp. 106–110. doi:10.18429/JACoW-IBIC2019-MOPP014

[14] E. L. B. Cheymol, "Conceptual Design of the ESS DTL Faraday Cup," in *Proc. LINAC 2014*, Geneva, Switzerland, paper MOPP037, pp. 140–142.

[15] H. Hassanzadegan *et al.*, ""BCM System Optimization for ESS Beam Commissioning through the DTL Tank4"," in *Proc. 12th Int. Beam Instrum. Conf. (IBIC'23)*, Saskatoon, Saskatchewan, Canada, 2023, this conference, paper TUP038.

[16] R. Baron *et al.*, "ESS Beam Position and Phase Monitor System," in *Proc. IBIC'19*, Malmö, Sweden, 2019, pp. 543–547. doi:10.18429/JACoW-IBIC2019-WEPP015

[17] S. Varnasseri *et al.*, "Design and fabrication of stripline bpm for the ess mebt," *NIMA*, vol. 987, p. 164 835, 2021. doi:10.1016/j.nima.2020.164835

[18] I. Dolenc Kittelmann *et al.*, "Neutron sensitive beam loss monitoring system for the european spallation source linac," *Phys. Rev. Accel. Beams*, vol. 25, no. 2, p. 022 802, 2022. doi:10.1103/PhysRevAccelBeams.25.022802

[19] I. D. Kittelmann and V. Grishin, "Detector response studies of the ESS Ionization Chamber," in *Proc. 12th Int. Beam Instrum. Conf. (IBIC'23)*, Saskatoon, Saskatchewan, Canada, 2023, paper TUP004, this conference.

[20] L. Segui *et al.*, "Detector design and performance tests of the ess-neutron beam loss monitor detectors," *JINST*, vol. 18, no. 01, P01013, 2023. doi:10.1088/1748-0221/18/01/P01013

[21] Y. Levinsen *et al.*, "Beam Dynamics Challenges in the ESS Linac," in *Proc. of ICFA Advanced Beam Dynamics Workshop on High-Intensity and High-Brightness Hadron Beams (HB'16)*, Malmö, Sweden, 2016, paper TUAM3Y01, pp. 315–318. doi:10.18429/JACoW-HB2016-TUAM3Y01

[22] S. Gabourin *et al.*, "The ESS Fast Beam Interlock System: First Experience of Operating With Proton Beam," in *Proc. LINAC'22*, Liverpool, UK, 2022, paper MOPORI17, pp. 265–267. doi:10.18429/JACoW-LINAC2022-MOPORI17

[23] J.Marroncle *et al.*, "Non-Invasive Profiles for the cold linac part of the ESS accelerator," in *Proc. 12th Int. Beam Instrum. Conf. (IBIC'23)*, Saskatoon, Saskatchewan, 2023, paper TUPD36, this conference.

[24] C. A. Thomas *et al.*, "Preliminary Measurement on Potential Luminescent Coating Material for the ESS Target Imaging Systems," in *Proc. IBIC'16*, Barcelona, Spain, Sep. 2016, paper TUPG82, pp. 559–562. doi:10.18429/JACoW-IBIC2016-TUPG82

[25] E. Adli *et al.*, "Progress of the ESS Proton Beam Imaging Systems," in *Proc. LINAC'22*, Liverpool, UK, 2022, paper TUPOJO20, pp. 394–397. doi:10.18429/JACoW-LINAC2022-TUPOJO20

[26] C. Thomas *et al.*, "J-PARC Test of ESS Beam on Target Diagnostics Prototypes Aperture Monitor and GRID," in *Proc. IBIC'19*, Malmö, Sweden, 2019, paper TUPP032, pp. 387–391. doi:10.18429/JACoW-IBIC2019-TUPP032

Content from this work may be used under the terms of the CC-BY-4.0 licence (© 2023). Any distribution of this work must maintain attribution to the author(s), title of the work, publisher, and DOI

ISBN: 978-3-95450-236-3 ISSN: 2673-5350 doi:10.18429/JACoW-IBIC2023-TU1C03

AN EXPERIMENTAL SETUP FOR PIXE ANALYSIS IN A MEDICAL CYCLOTRON AT TENMAK-NUKEN

G. Turemen*, S. Bulut, U. Kaya, D. Porsuk, N. O. Serin, E. Yeltepe
TENMAK-NUKEN, Ankara, Türkiye

Abstract

A 30 MeV cyclotron is operated at TENMAK-NUKEN for producing medical radioisotopes with three beamlines and a fourth beamline is dedicated for research purposes. The minimum energy of extracted proton beam from cyclotron is 15 MeV. There is no facility in Türkiye for applying ion beam analysis techniques (IBA) currently. These techniques generally require 1-5 MeV proton beam energy. An energy degrader system was designed and installed on the R&D beamline for this purpose. The degrader system is capable of decreasing the energy down to 1 MeV with pA to µA current levels. A high vacuum irradiation chamber is designed and installed at the end of the beamline. The chamber has ports to install several types of detectors for different IBA techniques. This work includes the description of the setup and preliminary PIXE measurements.

INTRODUCTION

Cyclotrons are compact particle accelerator systems used for scientific research, medical and industrial applications. Turkish Energy, Nuclear and Minerals Research Agency (former Turkish Atomic Energy Authority) acquired a 30 MeV energy proton cyclotron with associated systems dedicated to the production of medical radioisotopes and scientific research purposes in 2011. The accelerator facility (TENMAK-PAF) has three beamlines for production of medical isotopes and another beamline for scientific research purposes. The research vault comprises a five-port electromagnet which can deflect the proton beam up to an angle of ∓40° with respect to the beam axis. The minimum beam energy and current provided by the cyclotron is 15 MeV and 0.1 µA respectively. This constraint on energy and current excludes certain applications. One of these applications is ion beam analysis (IBA) which finds use in a wide range of disciplines such as chemistry, biology, solid state physics, materials science, archaeology, anthropology etc. Non-destructive IBA techniques in general and certain irradiation requests from internal/external researchers require relatively low particle energies and low beam currents, i.e. 1-5 MeV energy with pA-nA current levels. A way to decrease the energy and the current is to let the beam pass through a thin foil during which the particles interact with the foil medium causing a decrease in energy and current. In this work, development and tests of the irradiation system and preliminary studies with PIXE method are described.

* gorkem.turemen@tenmak.gov.tr

IRRADIATION SETUP

Low-energy and low-current irradiations for the required absorbed doses demand additional effort and equipment in medical cyclotrons due to the design priorities for this type of accelerators. Therefore an energy degrader system is developed to decrease the energy of the cyclotron extracted beam. The cyclotron's original beam current measurement system is capable of measuring the current down to 0.1 µA which is convenient for radioisotope production purposes but not suitable for material irradiations and non-destructive analysis. Thus, a beam current measurement system is designed to measure the beam current down to tens of pA levels. Also, an irradiation chamber, an energy degrader system and various collimators were manufactured to irradiate assorted types of samples while controlling the beam energy, size and position (see [1] for details). The irradiation system requires additional conditions for shielding, positioning of the particle/radiation detectors and data acquisition systems to perform non-destructive analysis (Fig. 1). The secondary gamma and neutron radiation generated from the energy degraders is the primary concern due to increased background radiation in X-ray and gamma analysis. A water-cooled degrader system is installed in the cyclotron room, just after the extraction of the beam, to decrease the radiation background in the R&D room.

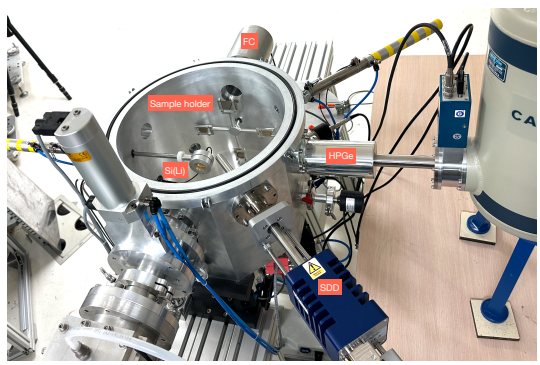


Figure 1: Irradiation system and detector placement.

Energy Degrader System

A water-cooled degrader (Fig. 2) system degrades the beam energy down to 3 MeV from 15.6 MeV using three stacked pyrolytic graphite foils with a total thickness of 1.3 mm. The foil stack is sandwiched between copper blocks and aluminum flanges for adequate cooling and collimation. The cooling system of the degrader assembly utilizes deionized water from the cyclotron cooling loop with a flow of

Content from this work may be used under the terms of the CC-BY-4.0 licence (© 2023). Any distribution of this work must maintain attribution to the author(s), title of the work, publisher, and DOI

ISBN: 978-3-95450-236-3 ISSN: 2673-5350 doi:10.18429/JACoW-IBIC2023-TU1C03

6 L/min. The water circulates in welded copper tube and the system is tested up to 350 W beam power with inconsiderable temperature increase. The collimators are manufactured from aluminum to avoid persisting induced radioactivity. A safety interlock in the PLC software is put into effect to avoid overheating of the degrader with a PT100 sensor.

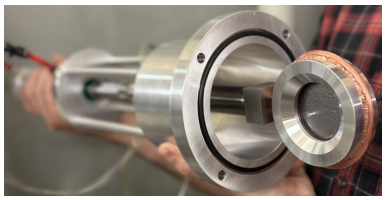


Figure 2: Water-cooled energy degrader.

Irradiation Chamber

An in-vacuum irradiation chamber is installed at the end of the R&D beamline. The chamber has openings for various devices to measure the beam profile, current, energy and detectors to detect secondary particles and prompt radiation. A port has a pneumatic cylinder which moves a 40 mm laser marked alumina beam screen in front of the beam at 45° to the beam direction. A port with a glass window allows the observation of the beam profile on the screen and on the samples. The other ports are reserved for radiation detectors for other ion beam applications. The chamber has a four-arm motorized carousel sample holder to irradiate different samples in a single run. A Faraday cup (FC) is installed at the far end of the chamber to measure and monitor the beam current. The beam from the 5-port magnet enters the chamber through a conical collimator and a replaceable circular aluminum collimator along the beam axis. The former has four isolated electrical connections to monitor the beam position and size. The vacuum is maintained at around $1x10^{-6}$ mbars with a two-stage pump system.

Radiation Detection System

A Si(Li) detector (RT-500-5-E/T-M/B, Mirion Technologies) is used for measuring the beam energy and energy spread. This detector has 5 mm thickness, a resolution of 30 keV at 5.5 MeV energy and is capable of measuring beam energies up to 30 MeV. The energy calibration of this detector is done in vacuum with a planar source of mixed alpha emitters (Americium-241, Plutonium-239, Uranium-234/238). A pneumatic cylinder moves the Si(Li) detector in front of the beam perpendicular to the beam axis. A vacuum operable silicon drift detector (SDD-EDS, Rayspec) for PIXE analysis is installed at an angle of 45 degrees with the beam axis. This detector has a thickness of 8 µm and a resolution of 133 eV at 5.9 keV. These specifications are convenient for distinguishing X-rays of different elements up to 20 keV energy with sufficient counting efficiency.

BEAM SHAPING AND MEASUREMENTS

IBA techniques require low energy and low current ion beams compared to a beam from a medical cyclotron. The extracted beam from the cyclotron has a minimum energy of 15 MeV and minimum measurable current of 0.1 µA. A degrader system is used to lower the beam energy down to the energies required for IBA techniques. The beam diffused by the carbon foil is refocused with the quadrupole doublets and shaped with collimators. The beam energy is degraded to 3.7 MeV with an energy spread of 0.97 MeV FWHM (measured with Si(Li) detector) for an incoming beam energy of 15.9 MeV. Monte Carlo [2] simulations and actual measurement results of the energy and the spread of the beam after the degrader system is shown in Fig.3. The measured peak shape is close to the simulation results except for a lower FWHM. The reason for higher FWHM in the simulations may be not taking into account the two quadrupole doublets in the code.

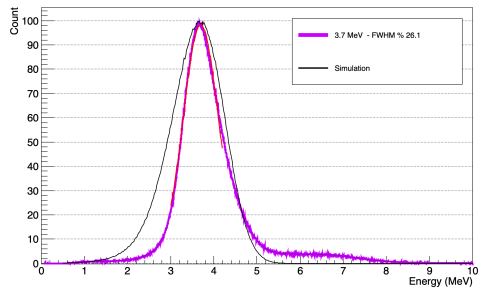


Figure 3: Si(Li) measurement and FLUKA simulation.

The following measurements were made for two different settings in the experiments: In the first case, beam shaping collimator aperture at the entrance of the irradiation chamber is 1 mm. The recofused beam is measured as 235 pA in the irradiation chamber Faraday cup for a beam current of 10 µA at the cyclotron stripper. In the second case, for a collimator aperture of 10 mm, the beam current is measured as 7 nA in the irradiation chamber Faraday cup for a beam current of 4 µA at the cyclotron stripper. This corresponds to a 0.002% and 0.175% current reduction for 1 mm and 10 mm final collimator aperture, respectively. The current stability at pA levels is shown in Fig.4. It is possible to lower the current down to 5 pA level with the ∓2.5 pA uncertainty by optimizing the ion source parameters and applying data manipulation methods such as noise filtering. The stability of the current is important for charge integration which directly affects the uncertainty analysis, especially for non-conducting samples in IBA techniques.

The beam size is measured as 11.4 mm on the alumina screen with a 10 mm collimator. Homogeneity of the beam is measured as 90% for 8 mm beam size using image processing techniques (Fig.5). This homogeneity ensures irradiating the samples as evenly as possible thus allowing bulk PIXE analysis of inhomogeneous samples with higher accuracy.

Content from this work may be used under the terms of the CC-BY-4.0 licence (© 2023). Any distribution of this work must maintain attribution to the author(s), title of the work, publisher, and DOI

ISBN: 978-3-95450-236-3 ISSN: 2673-5350 doi:10.18429/JACoW-IBIC2023-TU1C03

Content from this work may be used under the terms of the CC-BY-4.0 licence (© 2023). Any distribution of this work must maintain attribution to the author(s), title of the work, publisher, and DOI

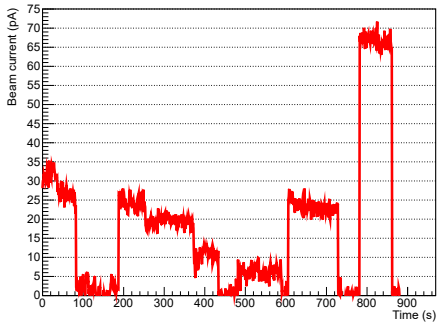


Figure 4: Current stability.

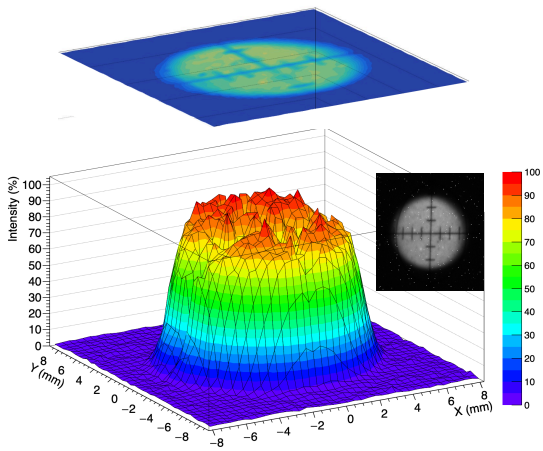


Figure 5: Beam homogeneity measurement.

PRELIMINARY PIXE ANALYSES

Several preliminary experiments are done with the non-destructive analysis system constructed in TENMAK PAF R&D irradiation vault. GUPIXWIN [3] software is used in the analyses. This software offers several PIXE analysis modes. One of these methods, analysis with H value, uses a certified reference material to calculate a value which is expected to remain almost constant for a well-defined geometry, surface roughness and sample composition for the X-ray energies of interest (1-20 keV). The instrumental value, H incorporates detector solid angle and calibration factor of charge integration [4]. It also includes corrections for geometry, detector crystal thickness and any imprecise data used in the software [5]. The H value method is selected in the experiments as the initial choice of analysis technique due to ease of use, less dependence on energy resolution and time consuming precise geometric parameter measurements of the setup required for standardless analysis. The reference concentration values of the element(s) in the standard foil is used to calculate the H value of the analysis setup.

The angle between the sample surface normal and the detector normal is approximately 10°. The X-ray spectra are acquired with a digital analyser (CAEN). 99.99% gold with a thickness of 50 µm is irradiated to determine the H value and its variation with X-ray energy by a proton beam

Table 1: Comparison of XRF and PIXE Analyses of the Standard Mix Foil

Element	XRF(%)	Unc.(∓)	PIXE(%)	Unc.(∓)
Copper	56.17	N.A	56.16	0.22
Nickel	41.66	N.A	41.95	0.17
Manganese	1.29	N.A	1.23	0.008
Iron	0.68	N.A	0.57	0.005

with an energy of 3.2 MeV and an average current of 7 nA for 155 seconds. The H value calculated with the irradiated gold standard foil is 0.000489. This H value is used for the analysis of 99.99% copper and mix standard foil (composition: 55% Cu, 45% Ni, thickness: 100 µm) irradiated under the same experimental conditions. The elemental composition is measured as 100% for copper foil and the analysis results of the mix standard foil are given in Table 1. PIXE spectrum of the mix standard foil is shown in Fig. 6. The analysis results indicate negligible dependence of the H value on X-ray energy in the spectral region of interest. The elemental concentrations of the mix sample is compatible with measurements done with a portable XRF spectrometer (no uncertainties are reported with this detector). The software reports the counting statistics uncertainty and peak fitting uncertainty for the PIXE analysis. The reported uncertainty values in Table 1 is the combined uncertainty of these two components. The major component of the combined uncertainty is due to the peak fitting process. Reducing the background in the setup and setting the peak fitting parameters more precisely are expected to decrease the uncertainty and the limit of detection considerably.

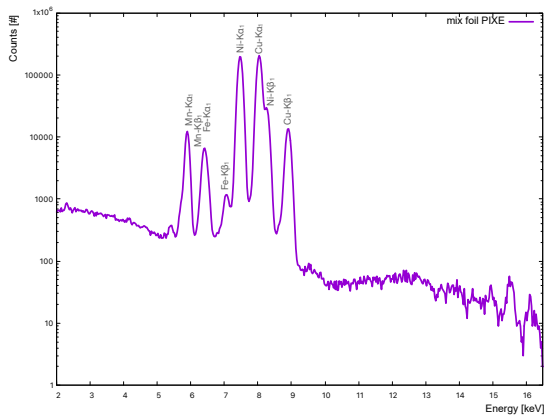


Figure 6: PIXE spectrum of the mix standard foil.

As for real life samples, the setup is used to determine the elemental content of 1 TL (Turkish Lira) metal coins. Coins minted on different dates are placed in the experimental chamber with a mix standard foil. This foil is used to determine the H value. Table 2 shows a comparison of PIXE and portable XRF analysis results. We believe that the main reason for the differences is the changes in the sample position due to the holder mechanism in the PIXE test system

ISBN: 978-3-95450-236-3 ISSN: 2673-5350 doi:10.18429/JACoW-IBIC2023-TU1C03

Table 2: Comparison of XRF and PIXE Analysis Results of 1 TL Metal Coins

Element	1 TL(2009)		1 TL(2015)		1 TL(2022)	
	PIXE	XRF	PIXE	XRF	PIXE	XRF
	%		%		%	
Copper	73.2	71.78	71.22	70.56	76.70	72.63
Nickel	14.37	15.63	14.78	16.34	15.02	15.96
Zinc	9.12	9.53	8.74	9.13	8.57	8.50
Manganese	0.14	0.13	0.33	0.262	0.15	0.12
Iron	0.17	0.17	0.46	0.44	0.07	0.05

and the background X-rays produced by scattered protons inside the chamber. Therefore, several improvements are planned in this direction such as using a collimator around the detector, an absorber on the detector endcap and voltage suppressors around the sample for stray electrons and coating the chamber walls.

CONCLUSION AND OUTLOOK

A non-destructive analysis setup at TENMAK-PAF medical cyclotron facility is designed and assembled in the R&D vault. This setup is consists of a number of additional beam shaping equipment and measurement systems required by IBA methods. PIXE method is applied for the first time in Türkiye and the preliminary results are satisfactory. Detectors for IBA techniques such as PIGE (HPGe) and RBS (PIPS) detectors are installed and measurements are ongoing. Further modifications are needed to improve the accuracy of the measurements through the use of electron suppressors, adjusting the measurement geometry (i.e. moving the sample closer to the detector), shielding and/or collimating the detectors. Future plans also include moving the setup to the 40° port (rightmost port of the 5-port magnet) and utilizing a water-cooled slit to achieve a better energy resolution. These changes will have a positive impact on the reliability of the measurements in the application of complementary ion beam analysis methods.

ACKNOWLEDGMENTS

This study is funded by TENMAK with a project No. A2.H1.P9. We would like to thank Dr. Yakup Kalaycı for doing the XRF measurements.

REFERENCES

[1] A. N. Yuksel, G. Turemen, S. Bulut, N. O. Serin, O. Yavas, "Design of beam instrumentation for in-vacuum materials irradiation and testing in a 30 MeV medical cyclotron", *Nucl. Instrum. Methods Phys. Res., Sect. A*, vol. 977, pp. 164290, 2020. doi:10.1016/j.nima.2020.164290

[2] A. Ferrari, "FLUKA Code-2011.2x.6: A multi-particle transport code", CERN-2005-10, INFN/TC05/11, SLAC-R-773, 2005.

[3] M.I. Govil, "Proton Induced X-ray Emission–A tool for non-destructive trace element analysis", *Current Science*, vol. 80, no. 12, pp. 1542–1549, 2001.

[4] J. A. Maxwell, W. J. Teesdale and J. L. Campbell, "The Guelph PIXE software package II", *Nucl. Instrum. Methods Phys. Res., Sect. B*, vol. 95, no. 3, pp. 407-–421, 1995. doi:10.1016/0168-583x(94)00540-0

[5] A. Shariff, K. Blow, M. Elfman, P. Kristiansson, K. Malmqvist, and J. Pallon, "Calibration of a new chamber using gupix software package for pixe analysis", *Nucl. Instrum. Methods Phys. Res., Sect. B*, vol. 189, no. 1, pp. 131-137, 2002. doi:10.1016/S0168-583X(01)01018-7

Content from this work may be used under the terms of the CC-BY-4.0 licence (© 2023). Any distribution of this work must maintain attribution to the author(s), title of the work, publisher, and DOI

ISBN: 978-3-95450-236-3 ISSN: 2673-5350 doi:10.18429/JACoW-IBIC2023-TU2I02

FIRST DIRECT MEASUREMENT OF ELECTRON AND POSITRON BUNCH CHARACTERISTICS DURING POSITRON CAPTURE PROCESS AT THE POSITRON SOURCE OF THE SuperKEKB B-FACTORY

T. Suwada*, High Energy Accelerator Research Organization (KEK),
also at SOKENDAI (The Graduate University for Advanced Studies), Tsukuba, Japan

Abstract

Electron (e^-) and positron (e^+) bunch characteristics were directly measured for the first time using wideband beam monitors (WBMs) and a detection system at the e^+ source of the SuperKEKB B-factory. Both secondarily generated e^- and e^+ bunches after the e^+-production target were clearly identified during their dynamical capture process at locations of the WBMs under a two-bunch acceleration scheme. Not only the longitudinal but also transverse bunch characteristics, the time intervals between the e^- and e^+ bunches, bunch lengths, transverse bunch positions, and bunch charges were simultaneously and separately measured for each bunch as a function of the capture phase to investigate their dynamical capture process. The results show that quite symmetric dynamical behaviors for both the bunch characteristics were observed. The new WBMs open up a new window for direct measurements of both bunches during their dynamical capture process.

INTRODUCTION

High-intensity e^+ sources are indispensable and challenging in high-energy e^+e^- colliders to achieve the high luminosity required for high-energy physics experiments. In general, conventional e^+ sources [1] comprise a e^+-production target and a e^+ capture section subsequently located. Positrons are produced by impinging high-energy primary e^- beams with high intensity to a target of a high-Z material through a e^+e^- pair-production process in an electromagnetic cascade shower. The total amount of produced positrons is principally dominated by two main factors. One is the primary e^- beam power, the product of the e^- beam intensity and energy, and the other is the target characteristics of material and thickness. The resulting transverse emittances of positrons secondarily generated from the target are very large owing to the large momentum and angular spreads through an electromagnetic cascade shower process and multiple scattering in the target.

Only some parts of the positrons ejected forward are immediately captured in the e^+ capture section, in which they are focused in the transverse plane with strong axial magnetic fields, and they are captured in radio-frequency (RF) buckets of multiple accelerating structures (ACCs) in the longitudinal direction. Note that in the e^+ capture section, not only positrons but also secondarily generated electrons with approximately equivalent amounts of bunch charges simultaneously emerge from the target through this process. They are immediately and simultaneously captured in the subsequent capture section. While the e^- bunch is stopped by a beam stopper after passing the capture section, the e^+ bunch is separated from the e^- bunch and it is further accelerated by subsequent accelerating structures. After the capture section, the e^+ intensity can be measured using a beam position monitor (BPM) (or a beam intensity monitor).

An essential role of the e^+ capture section is to increase the e^+ capture efficiency as much as possible. The capture efficiency is generally simulated and optimized on the basis of beam dynamics in multidimensional transverse and longitudinal parameter spaces, which are related to electromagnetic fields of accelerating structures and magnetic fields in the capture section. Moreover, the transverse parameters of primary electrons, namely, transverse positions, injection angles, and impinging radii at the target, are also those in multidimensional parameter spaces. It is generally difficult to fully optimize the capture efficiency only by simulations. The optimization procedure should also be experimentally investigated to optimize it in multidimensional parameter spaces under realistic operation conditions.

An objective function to be optimized is only the e^+ intensity obtained after passing the e^+ capture section because no instrumentation devices are installed in it. It is generally difficult to determine not the local optimum but the global optimum in terms of the e^+ intensity with one objective function in multidimensional parameter spaces. This is because it is difficult to separately measure the e^+ and e^- bunches in the capture section by a conventional technique.

It is challenging to simultaneously and separately measure the e^+ and e^- bunch characteristics to directly verify complicated beam dynamics in the capture section and to optimize the e^+ intensity under the realistic operation condition. This is the main reason why the WBMs and detection system were developed at the e^+ source of the SuperKEKB B-factory.

HISTORICAL BACKGROUND

The purpose of introducing WBMs is to simultaneously and separately measure not only longitudinal but also transverse bunch characteristics for both e^- and e^+ bunches in the capture section. Here, I mention the background for introducing WBMs in 2018, in which preliminary investigations were started. One of the preconditions for installing any monitor in the capture section is the use of simple electromagnetic detection monitors because no advanced optical devices can be applied owing to limited installation spaces.

* tsuyoshi.suwada@kek.jp

Content from this work may be used under the terms of the CC-BY-4.0 licence (© 2023). Any distribution of this work must maintain attribution to the author(s), title of the work, publisher, and DOI

ISBN: 978-3-95450-236-3 ISSN: 2673-5350 doi:10.18429/JACoW-IBIC2023-TU2I02

Two accelerators projects with a conventional e^+ source were developed previously. One is the SLAC linear collider (SLC) at SLAC National Accelerator Laboratory, where the commissioning of the e^+ source began in early September of 1986 [2]. The other is the advanced photon source (APS) with a e^+ storage ring at Argonne National Laboratory (ANL), where the linac commissioning began in early October of 1993 [3].

To the best of my knowledge, in 2018, there was a detection technique [2] in the time domain developed by the SLC group and another detection technique [4] in the frequency domain developed by the ANL group. A conventional button-type monitor was installed to measure both e^- and e^+ bunch intensities in the capture section of the SLC e^+ source. This monitor directly detected the signal waveforms of both bunches in the time domain immediately after the high-gradient capture section. It was difficult to separately measure them owing to both the limited frequency bandwidth and sampling frequency at that time.

On the other hand, conventional stripline-type beam position monitors were installed to measure the transverse beam positions of e^+ bunches in the capture section of the APS e^+ source. This was a e^+ source without any e^+e^- separator owing to limited installation spaces; therefore, some specific detection techniques were consequently required since it was difficult to simultaneously detect both bunches. A heterodyne technique was applied to their detection circuit using an *RF* acceleration frequency (2856 MHz). The 2856 MHz component of the detected signal with a pulse width of 30 ns was filtered, amplified, and down-converted to 70 MHz with a bandwidth of 5 MHz. The output pulses from a logarithmic amplifier were captured in track-and-hold circuits, then digitized by AD converters. Thus, since the detection circuit was based on a technique in the frequency domain, it was difficult to separately detect both bunches under mixed bunch conditions.

It is clear that if a detection technique in the time domain is chosen, several difficult issues are encountered and should be solved, that is, how to considerably reduce (or correct with high accuracy) any high-frequency signal losses in the detection circuit and transmission lines. On the other hand, if a technique in the frequency domain is chosen, we cannot separately measure any bunch characteristics. I recognized in 2019 that for this issue, a de-embedding technique [5] was critical in the detection technique in the time domain, although it was challenging.

The de-embedding technique is a mathematical procedure that removes any effects of unwanted portions of a structure, which are embedded in the measured data by subtracting their contribution. Any *RF* and microwave networks are characterized using scattering parameters (S-parameters), which are easily measured with a vector network analyzer (VNA). By applying S-parameters to any signal detection circuit and transmission lines defined as the device under test (DUT), the amplitude losses and phase distortions between the input and output of the DUT can be corrected on the basis of the de-embedding technique without adding any devices.

By way of example, I tried to measure amplitude losses and phase distortions for one of the actually applied coaxial cables, which were measured with a high-performance oscilloscope equipped with the de-embedding technique by supplying a short test pulse with a width of 30 ps at FWHM. The results showed that the output pulse was properly corrected in the time domain and it was well reproduced on the oscilloscope display in real time with nearly the same pulse height and width in comparison with the original input pulse. This was the reason why I was convinced and chose the detection technique in the time domain with the embedding technique for WBMs.

SUPERKEKB e^+ SOURCE

The SuperKEKB (SKEKB) e^+ source is one of the conventional e^+ sources and its schematic is shown in Fig. 1. Other designs have already been described in detail elsewhere [6]. Here, only an additional explanation is given. Two conventional BPMs (SP15-15 and SP16-15) and two WBMs (SP15-25 and SP16-25) were newly installed along with three horizontal and one vertical steering magnets (STX and STY, respectively) in the capture section during the summer shutdown in 2020. These steering magnets are required to correct not only the transverse orbits of the e^+ bunch due to the off-axis bombardment to the target but also any misalignments of the magnet system generating axial magnetic fields in the capture section.

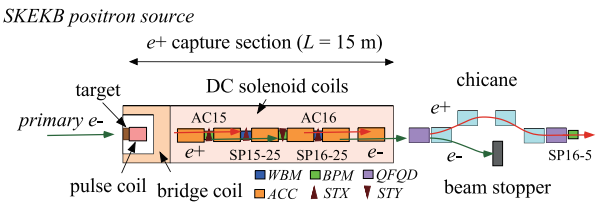


Figure 1: Schematic of the SKEKB e^+ source; QFQD: quadrupole focusing (QF) and quadrupole defocusing (QD) magnetic systems.

SP15-15 (SP15-25) is located 2.7 m (5.3 m) behind the target, and SP16-15 (SP16-25) is located 7.9 m (10.5 m) behind it. Conventional BPMs were installed to measure the transverse positions and intensity of the injection e^- bunch with conventional detection electronics. On the other hand, the WBMs with a bandwidth of ~10 GHz were used to simultaneously measure the transverse and longitudinal characteristics of both the e^- and e^+ bunches.

SIGNAL DETECTION SYSTEM

A photograph of the new beam monitor and its detection system for the two WBMs are shown in Figs. 2 (*a*) and (*b*), respectively. The total length of the monitor including two bellows and quick-release flange couplings (NW40, standard KF flange) at both ends is 431 mm, and the inner diameter is 38 mm. The inner surface of the front bellows is covered

Content from this work may be used under the terms of the CC-BY-4.0 licence (© 2023). Any distribution of this work must maintain attribution to the author(s), title of the work, publisher, and DOI

ISBN: 978-3-95450-236-3 ISSN: 2673-5350 doi:10.18429/JACoW-IBIC2023-TU2I02

Content from this work may be used under the terms of the CC-BY-4.0 licence (© 2023). Any distribution of this work must maintain attribution to the author(s), title of the work, publisher, and DOI

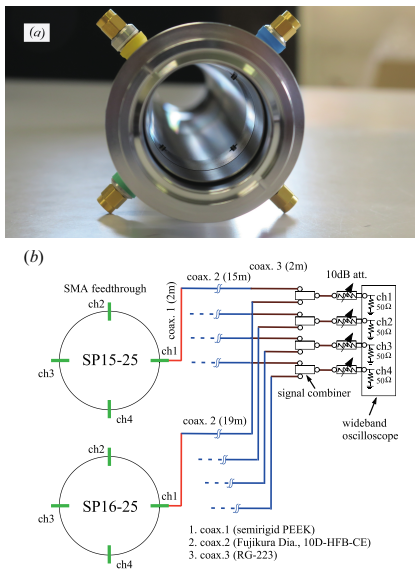


Figure 2: (a) Photograph of the WBM and (b) the detection system for the two WBMs.

with a cylindrical pipe to remove any irregularity and suppress any wakefield effects caused at the monitor front as much as possible. The pickups of the monitor are made of SMA-type vacuum feedthroughs composed of a central conductor pin made of Kovar and a dielectric substance made of ceramic. The four pickups, two horizontal and two vertical, are mounted on the upstream side of the monitor with $\pi/2$ rotational symmetry. The tips of the center pins protrude for a length of 1 mm toward the monitor center from the inner surface of the monitor.

Two sets of four signals detected with high-frequency pickups from each WBM are sent to four *RF* combiners (Marki Microwave, PD-0R618, BW0.6–18 GHz) with coaxial cables, where the eight signals are combined. A set of the combined four signals is directly sent to a wideband real-time oscilloscope (Keysight Technologies, Infiniium V DSOV134A, BW13 GHz, 40 GSa/s). The *RF* combiners are independently connected to four input channels of the oscilloscope with a fixed coaxial attenuator of 10 dB in front of each input channel, which is terminated with an internal 50-Ω terminator.

The original signal waveforms detected in the time domain are transformed to the frequency domain by applying a standard fast-Fourier transformation (FFT), and they are corrected by using the loss data on the basis of the de-embedding technique in the frequency domain. The losses for the transmission cables and *RF* combiners were measured with a VNA in advance. The corrected signal waveforms in the frequency domain were transformed to the time domain by applying an inverse FFT using a software-based Bessel filter with fourth-order roll-off at the cutoff frequency of 9.1 GHz. The corrected signal waveforms in the time domain are pulse-by-pulse displayed on the oscilloscope without any significant latency.

SIGNAL WAVEFORM ANALYSIS

The pickup signal of the WBMs is a bipolar differential signal induced by a single-bunched beam, whereas it is corrected in the frequency domain on the basis of the de-embedding technique. The typical signal waveforms detected at SP15-25 in the nominal operation are shown in Fig. 3. Figure 3(a) (Fig. 3(c)) shows the differential signal

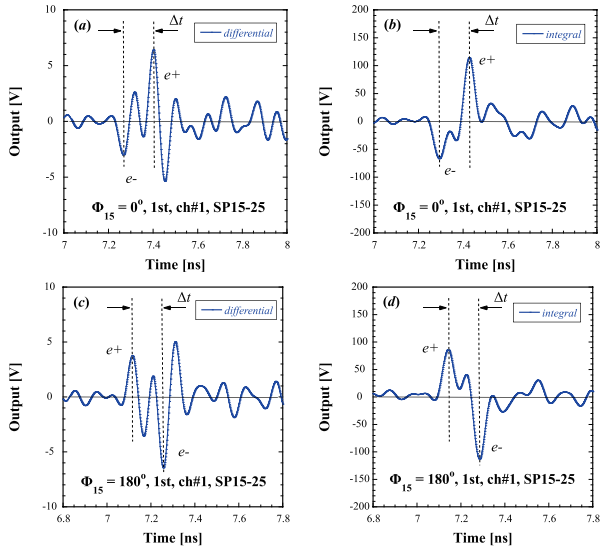


Figure 3: Typical signal waveforms (ch#1) in the nominal operation detected at SP15-25. (a) Differential waveform at $\Phi_{15} = 0^{o}$, (b) its integrated waveform, (c) differential waveform at $\Phi_{15} = 180^{o}$, and (d) its integrated waveform.

waveform of SP15-25 at $\Phi_{15} = 0^{o}$ ($\Phi_{15} = 180^{o}$) under the nominal (180° phase shifted) operation condition after the frequency correction, where Φ_{15} indicates the capture phase of AC15. Figure 3(b) (Fig. 3(d)) shows the corresponding integrated signal waveform. It is found that the signal polarity $(-, +)$ $((+, -))$ corresponds to the e^- and e^+ (e^+ and e^-) bunch signals in the time sequence, that is, the e^- (e^+) bunch precedes the e^+ (e^-) bunch in the time domain at the corresponding capture phase.

Note that the amplitude of the signal baseline before the bunch at SP15-25 is due to the intrinsic noise floor of the oscilloscope. On the other hand, the baseline level after the bunch is due to wakefields generated from upstream accelerating structures. The time interval Δt between the bunch signals can be defined by that between their peak positions from Figs. 3(b) and (d) (or Figs. 3(a) and (c)).

The bunch characteristics can be analyzed on the basis of the results of the waveform analyses. The bunch length can be defined by analyzing the pulse width in root mean square (rms) for the integrated waveform. The bunch charge can be analyzed by calculating the area properly defined in the time region of the pulsed signal. The transverse positions of the bunch can be analyzed by using the four pulsed areas obtained from four pickups on the basis of a conventional beam position analysis procedure.

ISBN: 978-3-95450-236-3 ISSN: 2673-5350 doi:10.18429/JACoW-IBIC2023-TU2I02

Thus, in terms of the e^- and e^+ bunch characteristics, the time interval, bunch lengths, transverse bunch positions, and bunch charges can be simultaneously and separately measured with WBMs. The detailed analysis and calibration procedures have already been described elsewhere [7,8] (see also references therein for an extended list).

MEASUREMENT RESULTS

Characteristic Analyses

Figure 4 shows the variations in the time interval (Δt) between the e^- and e^+ bunches at SP15-25 and SP16-25 as a function of Φ_{15} with a step phase of 10°, for which the phase Φ_{16} of AC16 was concurrently changed by the same step phase. Note that the phases $\Phi_{15} = 0°$ and $\Phi_{16} = 0°$ are defined under the nominal operation condition. It can be seen

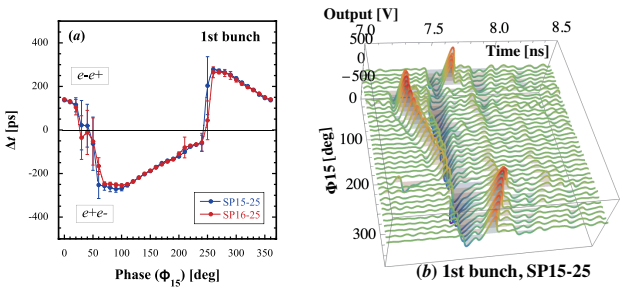


Figure 4: (*a*) Variations in Δt between the e^- and e^+ bunches as a function of Φ_{15} at SP15-25 and SP16-25. The solid curves drawn through data points are a guide to the eye. (*b*) 3D plots for the e^- and e^+ bunches at SP15-25 as a function of the phase Φ_{15} and time. The reference time is given by the arrival time of the e^- bunch.

that there are two intersections at $\Delta t = 0$ in the variations at $\Phi_{15} \simeq 50°$ and $\Phi_{15} \simeq 250°$. The results show that the line-order switch for the e^- and e^+ bunches due to their dynamical phase-slip process in the axial direction was observed as functions of the capture phase. The e^+ (e^-) bunch precedes the e^- (e^+) bunch in the phase region of $\Phi_{15} \simeq 50°$-$250°$ ($\Phi_{15} \simeq 0°$-$50°$ and $\Phi_{15} \simeq 250°$-$360°$), which corresponds to $\Delta t < 0$ ($\Delta t > 0$). This means that the e^+ and e^- bunches are in the accelerating and decelerating (decelerating and accelerating) phase regions for AC15, respectively. It can be understood that the e^+ (e^-) bunch is in the decelerating (accelerating) region under the nominal operation condition.

Figure 5 shows the variations in the transverse position displacements for the e^- and e^+ bunches at SP15-25 and SP16-25 including all the data points. Figure 5(*a*) (Fig. 5(*b*)) shows the variations for the accelerated and decelerated e^- (e^+) bunches.

It can be found that there are almost no characteristic differences in the transverse positions depending on the capture phase, even at the capture phase under the nominal operation condition and those giving the maximum charge. It is interesting that the cluster for each bunch rotates in the transverse plane owing to their cyclotron motion in the longitudinal direction between SP15-25 and SP16-25.

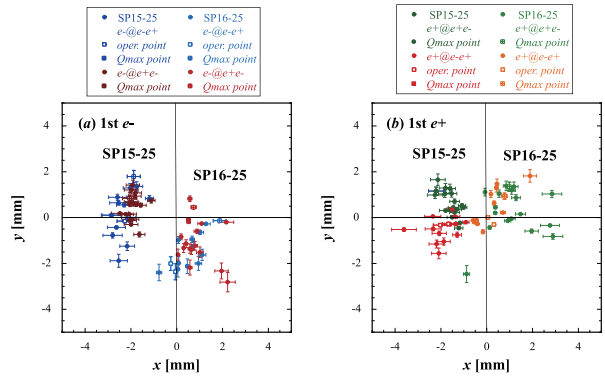


Figure 5: Variations in the transverse position displacements for the accelerated and decelerated (*a*) e^- and (*b*) e^+ bunches at SP15-25 and SP16-25 including all the data points.

Figure 6 shows the variations in the charges for the e^- and e^+ bunches at SP15-25 and SP16-25 as a function of the capture phase. Figure 6(*a*) (Fig. 6(*b*)) shows those for the e^- and e^+ bunches at SP15-25 (SP16-25). The results show

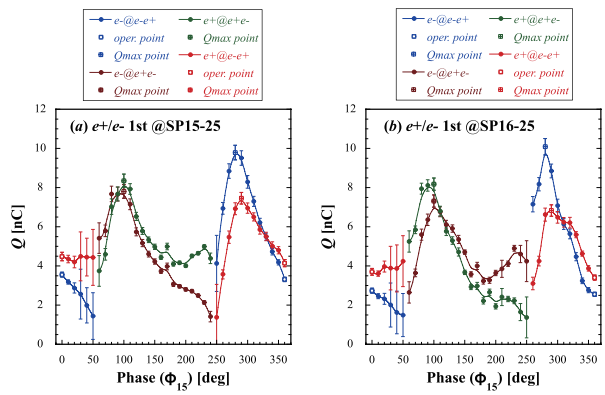


Figure 6: Variations in the bunch charges for the e^- and e^+ bunches at (*a*) SP15-25 and (*b*) SP16-25 as a function of the capture phase. The solid lines are only a guide to the eye.

that quite symmetric behaviors in terms of the variations in the charges for both the bunches are observed except for the charge excess for the e^- bunch due to the Compton effect. It can be seen that there are two capture phases in the accelerated and decelerated regions giving the maximum charge at which the capture phases for the e^- bunch agree with those for the e^+ bunch with high accuracy. It is important to point out that the charge excess at the capture phase in the accelerated region is ~20% (~10%) relative to that in the decelerated region for the e^- (e^+) bunch at SP15-25. On the other hand, the charge excess is ~27% (~17%) for the e^- (e^+) bunch at SP16-25. The results show that the accelerated bunch may be of great advantage to the decelerated bunch from the viewpoint of the bunch charge excess in the capture section.

Content from this work may be used under the terms of the CC-BY-4.0 licence (© 2023). Any distribution of this work must maintain attribution to the author(s), title of the work, publisher, and DOI

ISBN: 978-3-95450-236-3 ISSN: 2673-5350 doi:10.18429/JACoW-IBIC2023-TU2I02

Content from this work may be used under the terms of the CC-BY-4.0 licence (© 2023). Any distribution of this work must maintain attribution to the author(s), title of the work, publisher, and DOI

Characteristic Correlation Analyses

Δt and charges in the accelerated and decelerated e^- and e^+ bunches were simultaneously and separately measured at SP15-25 and SP16-25 including all the data points. Figure 7 shows the variations in the correlations in terms of Δt and bunch charges for the accelerated and decelerated e^- (or e^+) bunches at SP16-25 to those at SP15-25 including all the data points. Note that Δt analyzed for the e^- and e^+ bunches are the same according to their definition. Figure 7(a) shows the variations in the correlations for the accelerated and decelerated e^- bunches, and Fig. 7(b) shows those for the accelerated and decelerated e^+ bunches. It can be found

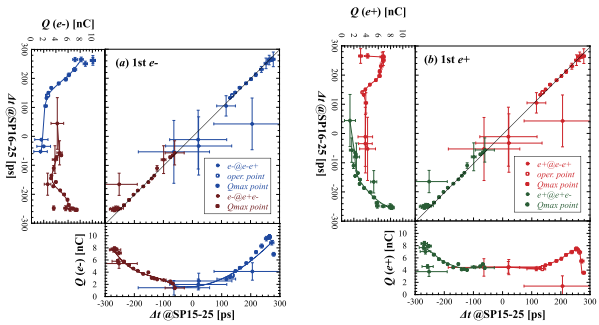


Figure 7: Variations in the correlations between Δt and charges in the accelerated and decelerated (a) e^- and (b) e^+ bunches at SP15-25 and SP16-25 including all the data points. The solid lines are only a guide to the eye.

that all the data points form a straight line tilted by 45° to the horizontal axis in the accelerated and decelerated e^- and e^+ bunches. The results again show that the phase-slip process occurs during the passage of both the bunches in AC15 and it is fixed at AC16. They also show that Δt giving the maximum charge is obtained at the nearly largest time intervals, in other words, at which the phase slip is induced to a maximum degree in AC15. The Δt values at the maximum charge are -268 ± 11 ps and 264 ± 9 ps on average for the decelerated and accelerated e^- bunches, respectively. On the other hand, the Δt values are -268 ± 11 ps and 253 ± 7 ps on average for the accelerated and decelerated e^+ bunches, respectively.

Figure 8 shows the variations in the correlations in terms of the bunch lengths and charges for the e^- and e^+ bunches at SP15-25 and SP16-25 including all the data points. Figure 8(a) (Fig. 8(b)) shows the variations for the accelerated and decelerated e^- (e^+) bunches. It is found that the data points in the correlations are on a polynomial curved line rather than on a straight line tilted by 45° to the horizontal axis in both the accelerated e^- and e^+ bunches. The result shows that although any phase-slip process halts during the passage of both the bunches in AC15, the bunch lengthening (or shortening) is generated owing to particle displacement in the bunch in the longitudinal direction in accordance with the longitudinal dynamics depending on the capture phases.

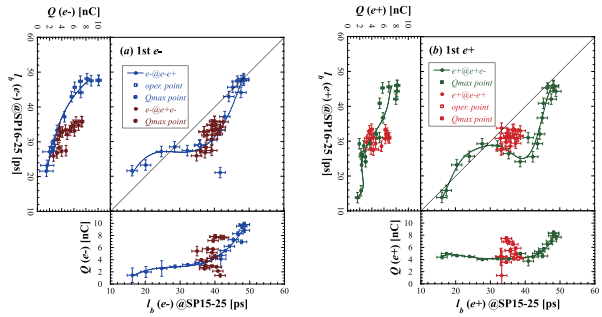


Figure 8: Variations in the correlations between the bunch lengths and charges for the accelerated and decelerated (a) e^- bunches and (b) e^+ bunches at SP15-25 and SP16-25 including all the data points. The solid lines are only a guide to the eye.

CONCLUSION

Direct simultaneous measurements of the secondarily generated e^- and e^+ bunch characteristics in the longitudinal and transverse directions were successfully performed for the first time with the WBMs and detection system under a two-bunch acceleration scheme at the e^+ capture section of the SuperKEKB B-factory. Such wideband detection techniques can be applied to conventional e^+ sources and also advanced e^+ sources in future accelerator projects. The obtained results may also improve simulations in any e^+ capture section, and thus, the e^+ intensity can be systematically and fully optimized by applying this technique along with detailed simulations in multidimensional parameter spaces towards high-intensity e^+ sources.

REFERENCES

[1] I. Chaikovska *et al.*, "Positron sources: from conventional to advanced accelerator concepts-based colliders", *J. Instrum.*, vol. 17, no. 5, pp. P05015, 2022. doi:10.1088/1748-0221/17/05/P05015

[2] J. Clendenin *et al.*, "SLC Positron Source Startup", in *Proc. LINAC'88*, Williamsburg, VA, USA, Oct. 1988, paper TH3–17, pp. 568–570.

[3] N. Galayda, "The Advanced Photon Source", in *Proc. PAC'95*, Dallas, TX, USA, May 1995, paper MAD02, pp. 4–8.

[4] R. Fuja and Y. Chung, "The APS linac beam position monitors and electronics", *AIP Conference Proceedings*, vol. 281, pp. 248–255, 1992. doi:10.1063/1.44344

[5] Keysight Technologies, Inc., Keysight Application Note 5980-2784EN.

[6] T. Kamitani *et al.*, "SuperKEKB Positron Source Construction Status", in *Proc. IPAC'14*, Dresden, Germany, Jun. 2014, pp. 579–581. doi:10.18429/JACoW-IPAC2014-MOPRI004

[7] T. Suwada *et al.*, "First simultaneous detection of electron and positron bunches at the positron capture section of the SuperKEKB factory", *Sci. Rep.*, vol. 11, pp. 12751, 2021. doi:10.1038/s41598-021-91707-0

[8] T. Suwada, "First direct measurement of electron and positron bunch characteristics at the positron source of the SuperKEKB B-factory", *AIP Advances*, vol. 13, pp. 045021, 2023. doi:10.1063/5.0145776

ISBN: 978-3-95450-236-3 ISSN: 2673-5350 doi:10.18429/JACoW-IBIC2023-TU2C03

SUB-20 fs SYNCHRONIZATION BETWEEN MODE-LOCKED LASER AND RADIO-FREQUENCY SIGNAL *

J.G. Wang[1], B.W. Wu[2,3], B. Liu[1,†]
[1] Shanghai Advanced Research Institute, Chinese Academy of Science, Shanghai, China
[2]Shanghai Institute of Applied Physics, Chinese Academy of Sciences, Shanghai, China
[3]University of Chinese Academy of Sciences, Beijing, China

Abstract

The femtosecond synchronization and distribution system of the Shanghai soft X-ray free-electron laser facility (SXFEL) and Shanghai high repetition rate XFEL and extreme light facility (SHINE) are based on the optical pulse trains generated by passively mode-locked lasers. The passively mode-locked laser has ultralow noise in the high offset frequency (<5 fs, [1 kHz- 1 MHz]). In this paper, we report precise synchronization of the low-noise passively mode-locked laser to the radio frequency (RF) master oscillator. RF-based phase-locked loop scheme, the absolute jitter of the phase-locked passively mode-locked laser is less than 20 fs integrated from 10 Hz up to 1 MHz.

INTRODUCTION

Large-scale femtosecond stability has become an urgent requirement in modern free-electron lasers (FELs) facilities. At SXFEL [1] and for the SHINE, a pulsed optical synchronization has been used. The central component of the pulsed optical synchronization is the low-noise mode-locked laser which operates at telecommunication wavelength(~1550 nm). The use of low noise mode-locked laser as the optical master oscillator has become an excellent way to achieve an effectively synchronized network by distributing the optical master oscillator output to the individual end stations by length stabilized and dispersion compensated fiber links. The fiber links are based on a balanced optical cross-correlation method [2-4].

The optical synchronized network composed of fiber links distribute high-purity pulsed reference signals to three different types of end stations along the complete FEL facility to achieve femtosecond synchronization.

The bunch arrival time monitor based on the electro-optical modulator (EOM) scheme [5] is used to measure the arrival time of electron bunch with femtosecond accuracy at some special positions along the accelerator and undulator.

The remote lasers synchronization using two-color balanced optical cross-correlation [6, 7] is used to synchronize remote lasers, such as the photocathode lasers in the injector, the seed lasers near the undulator, and the pump-probe lasers in the experiment stations, to the output of fiber links

The laser-RF synchronization using a balanced optical· microwave phase detector enables timing detection between the output fiber link and radio frequency signal zero-crossing for stable RF signal re-generation which is needed in the SRF cavities and beam-diagnostic devices.

Being the heart of the optical synchronized network, the low-noise performance of the optical master oscillator is of tremendous importance. Due to the inherent characteristic of the optical master oscillator, the cavity length is easily affected by environmental fluctuations. The optical master oscillator is stabilized by the phase-locked loop against the radio frequency master oscillator to ensure long-term stability.

RF-BASED OPTICAL MASTER OSCILLATOR SYNCHRONIZATION

A common microwave phase-locking technique is used for synchronization between the optical master oscillator and RF master oscillator.

Figure 1 describes the RF-based experimental setup of synchronization between the optical master oscillator and RF master oscillator. For this test setup a commercial mode-locked laser from Menhir Photonics, which operates at 238-MHz repetition rate with 1558-nm center wavelength and 170-fs pulse duration, was used as the optical master oscillator. The RF reference signal at 1428-MHz is supplied by a 1428-MHz RF master oscillator (Rohde & Schwarz).

In order to achieve phase detection for synchronization purposes, it is necessary to convert pulsed optical signals into electrical signals. The photodetector generates electrical signals with high spectral purity harmonics of the laser repetition rate. A power splitter is used to split the electrical signal from the photodetector into two parts. A sixth harmonic of the photodetected electronic spectrum is filtered out using an RF bandpass filter and a low noise amplifier in combination with an RF phase detector. Meanwhile, another frequency comb with the same repetition rate as the optical master oscillator is filtered out using another bandpass filter and a low noise amplifier in combination with an RF phase frequency detector. The fundamental frequency is used for coarse tuning for the setting phase point. The sixth harmonic frequency is used for fine-tuning for precise synchronization. The lock on the higher harmonic improves the performance. The phase error signal between the RF reference signal from the RF master oscillator and optical master oscillator signal is fed to the digital controller. Once the phase-locked loop (PLL) was established using the RF-based laser-to-RF synchronization setup, a traditional method of measuring the timing jitter of the optical master oscillator was used. The scheme has been widely adopted by the current state-of-the-art signal source analyzers (SSAs). The phase noise of the obtained RF signal from the optical master oscillator is converted to ampli-

* This work is supported by the National Natural Science Foundation of China (12105348 and 12275341)
† bo.liu@sari.ac.cn

Content from this work may be used under the terms of the CC-BY-4.0 licence (© 2023). Any distribution of this work must maintain attribution to the author(s), title of the work, publisher, and DOI

ISBN: 978-3-95450-236-3 ISSN: 2673-5350 doi:10.18429/JACoW-IBIC2023-TU2C03

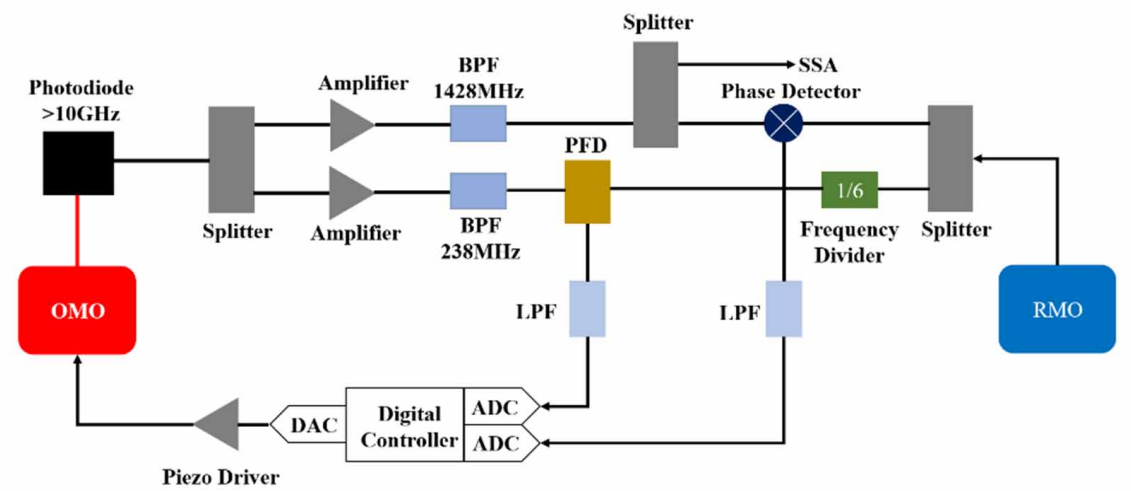


Figure 1: A block diagram of the RF-based synchronization between optical mater oscillator and RF master oscillator. Abbreviations: OMO: optical master oscillator; RMO: RF master oscillator; BPF: bandpass filter; PFD: phase frequency detector; ADC: Analogue to Digital Converter; DAC: Digital to Analogue Converter; SSA: signal source analyzer.

tude change by phase detection with a lower noise local oscillator.

MEASUREMENT RESULT

As mentioned before, in order to obtain the test results, we have built an experimental setup. Simultaneously, we measured the phase noise of the RF master oscillator and the optical master oscillator using a signal source analyzer APPH20G from Anapico.

The measurement of the RF master oscillator took place in the femtosecond synchronization laboratory in the SXFEL. The measurement of the optical master oscillator needs a part of the experimental setup. The pulsed optical signals from the optical master oscillator are coupled to the fiber-coupled photodetector, and the converted RF signals are divided into two by the power splitter. One of them is further boosted by the high gain low noise amplifier and transmitted to a custom bandpass filter.

The phase noise of the RMO (in Fig. 2), the free-running OMO (in Fig. 3), and the synchronized OMO (in Fig. 4) were measured using a signal source analyzer, respectively.

In the bandwidth from 10 Hz up to 1 MHz the integrated RMS jitter for the RF master oscillator is 8.0 fs.

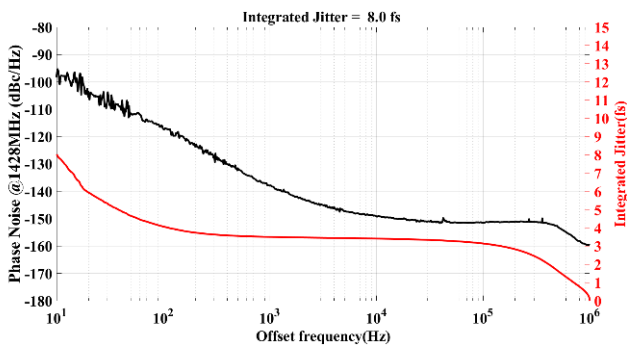


Figure 2: Phase noise measurement result of the RF master oscillator and its integrated timing jitter for the frequency range [10 Hz, 1 MHz].

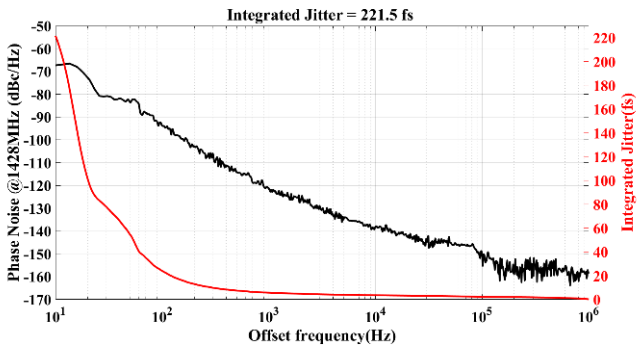


Figure 3: Phase noise measurement result of the free-running optical master oscillator and its integrated timing jitter for the frequency range [10 Hz, 1 MHz].

In the bandwidth from 10 Hz up to 1 MHz the integrated RMS jitter for the free-running optical master oscillator is 221.5 fs.

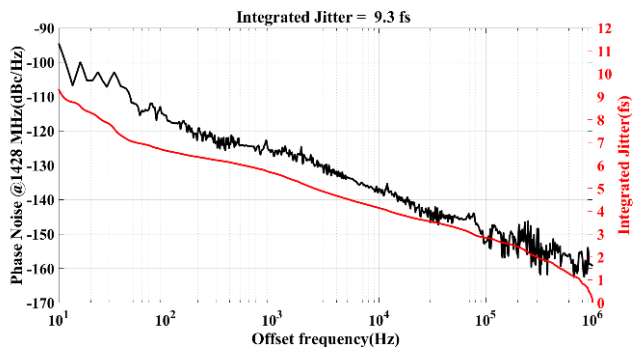


Figure 4: Phase noise measurement result of the synchronized optical master oscillator and its integrated timing jitter for the frequency range [10 Hz, 1 MHz].

In the bandwidth from 10 Hz up to 1 MHz the integrated RMS jitter for the synchronized optical master oscillator is 9.3 fs.

Content from this work may be used under the terms of the CC-BY-4.0 licence (© 2023). Any distribution of this work must maintain attribution to the author(s), title of the work, publisher, and DOI

ISBN: 978-3-95450-236-3 ISSN: 2673-5350 doi:10.18429/JACoW-IBIC2023-TU2C03

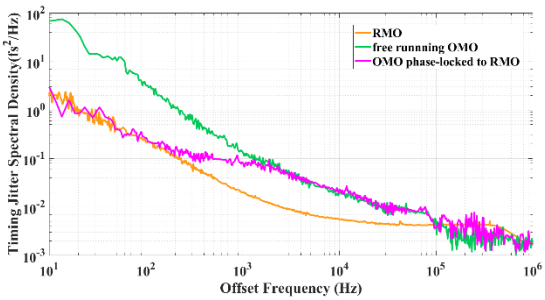


Figure 5: Timing jitter spectral density of the RF master oscillator, the free-running optical master oscillator, and the phase-locked optical master oscillator.

Figure 5 summarizes the phase noise measurement results. Curves RMO and free-running OMO are the absolute phase noise of the RF master oscillator and the optical master oscillator, respectively. By locking the optical master oscillator to the RF master oscillator with ~2 kHz PLL bandwidth, we can achieve a better absolute phase noise in optical pulse trains by combining the phase noise of the RF master oscillator (inside the locking bandwidth) and the optical master oscillator (outside of the locking bandwidth).

In Fig. 5, it can be seen that the spectral density of free-running OMO from 1-kHz to 100-kHz offset frequency is higher than the RMO. This is limited by the fundamental noise sources such as thermal noise and shot noise. Actually, the optical master oscillator displays ultralow noise performance at high offset frequency [8, 9].

OUTLOOK

Due to the low sensitivity of the RF-based synchronization, residual phase noise and long-term stability have not yet been carried out. Furthermore, there are several particular problems related to the RF-based microwave phase-locking technique, which involves the use of a photodetector, low-noise amplifier, and bandpass filter. In addition to the fundamental noise sources mentioned, the RF-based technique also has several issues. Typical sensitivity of the RF phase detectors on the order of a few μV/fs. Relative amplitude fluctuations of optical pulse trains lead to phase noise (AM-to-PM effects) [10-13].

In order to achieve high sensitivity and long-term stability, a balanced optical microwave phase detector (BOMPD) scheme based on a 3X3 coupler is being studied and tested.

In the future, the RF-based synchronization will introduce an out-of-loop measurement setup based on the BOMPD to achieve a more comprehensive stability evaluation.

CONCLUSION

In this paper, we have presented the use of an RF-based phase-locking technique to achieve sub-20 fs synchronization accuracy between mode-locked laser and RF master oscillator. The RMS timing jitter of the RF-locked optical pulse train is 9.3 fs when integrating from 10 Hz to 1 MHz offset frequency. As expected, inside the locking bandwidth (~1 kHz), the absolute phase noise of the optical master oscillator follows that of the RF master oscillator, and the phase noise outside the locking bandwidth follows the absolute phase noise of the extracted RF signal from the optical master oscillator. Due to the noise floor of the measurement setup, the actual phase noise at high offset frequency is smaller.

ACKNOWLEDGMENTS

This work is supported by the National Natural Science Foundation of China (12105348 and 12275341).

REFERENCES

[1] Z.T. Zhao *et al.,* “Shanghai soft X-ray Free-Electron Laser facility”, *Chinese Journal of Lasers*, vol. 46, p. 0100004, 2019.

[2] J. Kim *et al.,* "Long-term femtosecond timing link stabilization using a single-crystal balanced cross correlator", *Opt. Lett.,* vol. 32, no. 9, pp. 1044-1046, 2007.

[3] J. Kim, J. A. Cox, J. Chen, and F. X. Kärtner, "Drift-free femtosecond timing synchronization of remote optical and microwave sources," *Nature Photon.*, vol. 2, no. 12, pp. 733-736, 2008.

[4] S. Schulz *et al.,* "Femtosecond all-optical synchronization of an X-ray free-electron laser," *Nat. Commun.*, vol. 6, no. 5938, 2015.

[5] F. Löhl *et al.*, "Electron bunch timing with femtosecond precision in a superconducting free-electron laser", *Phys. Rev. Lett.,* vol. 104, no. 144801, 2010.

[6] K. Şafak, M. Xin, Q. Zhang, S. Chia, O.D. Mücke, and F.X. Kärtner, “Jitter analysis of timing-distribution and remote-laser synchronization systems”, *Opt. Express* 24, no. 19, pp. 21752–21766, 2016.

[7] H. Li, L.-J. Chen, H.P.H. Cheng, J.E. May, S. Smith, K. Muehlig, A. Uttamadoss, J.C. Frisch, A.R. Fry, F.X. Kärtner, and P.H. Bucksbaum, “Remote two-color optical-to-optical synchronization between two passively mode-locked lasers”, *Opt. Lett.* 39, no. 18, p. 5325, 2014.

[8] K. Şafak, M. Xin, P. T. Callahan, M. Y. Peng, and F. X. Kärtner, “All fiber-coupled, long-term stable timing distribution for free-electron lasers with few-femtosecond jitter”, *Structural Dynamics*, vol. 2, p. 041715, 2015.

[9] M. Y. Peng *et al.*, “Long-term Stable, Large-scale, Optical Timing Distribution Systems With Sub-femtosecond Timing Stability”, in *Proc. FEL'13*, New York, NY, USA, Aug. 2013, paper TUOANO02, pp. 156-159.

[10] E. Ivanov, S. Diddams, and L. Hollberg, “Study of the Excess Noise Associated with Demodulation of Ultra-Short Infrared Pulses*”, IEEE Transactions on Ultrasonics, Ferroelectrics, and Frequency Control*, vol. 52, pp. 1068–1074, 2005.

[11] J. Taylor *et al.,* “Characterization of power-to-phase conversion in high-speed P-I-N photodiodes”, *IEEE Photon. J.,* vol. 3, pp. 140-51, 2011.

[12] W. Zang *et al.*, “Amplitude to phase conversion of InGaAs pin photo-diodes for femtosecond lasers microwave signal generation”, *Appl. Phys. B*, vol. 6, pp. 301-8, 2011.

[13] D.H. Phung *et al.,* “Phase measurement of a microwave optical modulation: characterization and reduction of amplitude-to-phase conversion in 1.5 μm high bandwidth photodiodes”, *J. Lightwave Technol.* vol. 32, pp. 3759-67, 2014.

Content from this work may be used under the terms of the CC-BY-4.0 licence (© 2023). Any distribution of this work must maintain attribution to the author(s), title of the work, publisher, and DOI

ISBN: 978-3-95450-236-3 ISSN: 2673-5350 doi:10.18429/JACoW-IBIC2023-TU3I01

COMMISSIONING OF THE LCLS-II MACHINE PROTECTION SYSTEM FOR MHz CW BEAMS*

J. A. Mock†, A. S. Fisher, R. T. Herbst, P. Krejcik, L. Sapozhnikov
SLAC National Accelerator Laboratory, Menlo Park, United States

Abstract

Beam power at the LCLS-II linac and FEL can be as high as several hundered kW with CW beam rates up to 1 MHz. The new MPS has a latency of less than 100 µs to prevent damage when a fault or beam loss is detected. The MPS architecture encompasses the multiple FEL beamlines served by the SC linac and can mitigate a fault in one beamline without impacting the beam rate in a neighboring beamline. The MPS receives inputs from various devices including loss monitors and charge monitors as well as magnet power supplies and BPMs to pre-emptively turn of the beam if a fault condition is detected. Link nodes distributed around the facility gather the input data and stream it back to a central processor that signals other link nodes connected to beam rate control devices. The system design and some experience during initial commissioning are discussed.

INTRODUCTION

The Linear Accelerator Facility at the SLAC National Accelerator Laboratory (SLAC) has seen a significant upgrade to the Linac Coherent Light Source (LCLS) facility with the installation of LCLS-II. This new accelerator and undulator complex was designed to increase capacity at SLAC for photon science using the free electron lasers. A high level diagram of the new facility is shown in Figure 1.

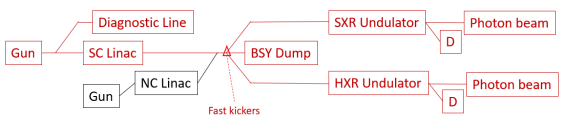


Figure 1: A high level map of the new LCLS-II facility (red), alongside the old NC linac. The new LCLS-II MPS has mitigation devices to inhibit beam or reduce beam rate at either the gun or the fast kickers, to each of the destinations shown.

Because it uses superconducting RF cavities, the LCLS-II accelerator is capable of delivering electrons with a minimum bunch spacing of 1 µs and maximum electron energy of 4 GeV, leading to a maximum overall beam power of 120 kW. An upgrade is also in progress to raise the energy to 8 GeV which will further double this power. The high rate and high power potential of these beams requires safety systems capable of reacting to beam events such that operations remain safe. The personnel protection and beam containment systems (PPS and BCS) are safety systems designed to protect people from radiation-based hazards, and the Machine Protection System (MPS) is designed to protect the accelerator from damaging itself. The MPS is not a credited safety system, so it is designed to be more agile to allow a variety of operating conditions while still protecting the accelerator.

SYSTEM REQUIREMENTS

The scope of the MPS is confined exclusively to shutting off the electron beam when a fault condition occurs that can potentially damage beam line hardware. Other systems that protect high power devices such as power supplies, RF power sources, vacuum systems, or cryogenic systems are handled separately as equipment protection.

Response Time

A key driving parameter of the MPS is the maximum allowable time interval in which the beam must be shut off before damage can occur. The MPS requirement for the original LCLS dictated that the electron beam be shut off within one beam pulse at the full repetition rate of 120 Hz. This is not possible in LCLS-II where the minimum bunch spacing is only 1 µs and propagation delay for a signal in a cable from one end of the accelerator to the other can be as long as 20 µs, not including additional processing delays incurred from electronics. The MPS baseline beam shutoff time, defined as the time between detection of fault and suppression of the electron beam, is required to not exceed 100 µs to avoid catastrophic damage to the beam line, though in principle the MPS physics requirement is as low as reasonable achievable. Not every fault condition requires the fast shutoff time of 100 µs. For example, a slow change in some state, such as a temperature rising, allows ample time for the control system to warn of the impending change. Therefore, MPS responses to prompt events such as beam loss mitigate within the fast response window, and other, slower events and more complicated logic process within a 360 Hz window, equal to the processing time of the legacy LCLS-I MPS.

As shown in Figure 1, the LCLS-II accelerator can deliver to some combination of an injector diagnostic line, one of two undulator beamlines, or through the linac to a high power dump in the SLAC Beam Switchyard (BSY). The default destination for the electron beam is this high power dump. Pulsed kicker magnets are used to kick the beam into one of the other beamlines, which means if the pulser does not kick, the beam will need to travel to the BSY beam dump. Therefore, the MPS uses this high power dump as its primary mitigation device for downstream faults. It grants

* SLAC is supported by the U.S. Department of Energy, Office of Science, under contract DE-AC02-76SF00515
† jmock@slac.stanford.edu

Content from this work may be used under the terms of the CC-BY-4.0 licence (© 2023). Any distribution of this work must maintain attribution to the author(s), title of the work, publisher, and DOI

ISBN: 978-3-95450-236-3 ISSN: 2673-5350 doi:10.18429/JACoW-IBIC2023-TU3I01

and revokes permits to the various kicker magnets in order to control beam power or completely inhibit beam to the other destinations. Additionally, the MPS can inhibit the beam within the entire facility by mitigating at the electron gun (through an interaction with the drive laser of the phot-injector). The mitigation device for each destination can be treated independently and all can operate at the response times listed above.

The LCLS-II accelerator can operate side-by-side with the old normal conducting (NC) linac which has a separate MPS operating independently, so that faults in one system do not interact with the other beam.

During the LCLS-II commissioning phase, overall beam power will be limited. The maximum repetition rate through the superconducting linac is 93 kHz, and the maximum repetition rate through the undulator complex is 1 kHz. This limitation allows the MPS to grow into its role as the system comes online and is better understood on the scale of the facility. During this phase, the MPS must shut off the beam in the linac within the 100 µs window at the gun, but in the undulator complex the system can respond as slowly as 1 ms and still inhibit the beam before the next bunch would enter those beamlines.

Inputs

The MPS takes inputs from many types of beamline devices which it uses to determine the state of the accelerator. Types of inputs are:

- Obstructions. Objects like vacuum valves or diagnostic screens can impede the path of the electrons. If these objects are struck, they can be damaged. Depending on the type, an obstruction will cause the beam to be rate limited or shut off. Obstructions all have at least one physical limit switch associated with the OUT position that is an input to the MPS. If the obstruction is not in the OUT position, the beam is shut off to preemptively avoid damage to the component. Some obstructions, such as profile monitor screens, allow beam when they are IN, and those devices have IN switches in MPS as well. When the device gets to its IN position, the MPS fault clears and beam can be allowed again, typically at a lower repetition rate with lower power.
- Beam Loss Monitors [1–3]. MPS brings in beam loss measurements from three types of beam loss monitors. First, a series of optical fibers run the length of the accelerator, divided into approximately 200 m segments. These fibers interact with beam loss to produce light which is detected and integrated into a measure of the beam loss within a zone. Second, point beam loss monitors are placed at strategic locations such as collimators to measure beam loss from that point. These two types of beam loss monitor are shared between the BCS and MPS systems. Finally, MPS has a fast beam loss monitor installed at every undulator. These are detectors that detect Cherenkov light produced by the interaction of beam loss with the material. Each of these beam loss inputs has an adjustable threshold, beyond which the beam will be tripped.
- Destination Dipole and Chicane Bend Magnets. The MPS ensures the beam makes it to one of the beam dumps. Independent MPS magnet current monitors are used to ensure certain bend magnets are at appropriate levels so the beam can safely traverse the beam pipe. The MPS magnet current tolerance bands are set automatically and derived from the expected beam energy.
- Bunch Charge Monitors (BCMs). Toroid detectors are placed at strategic locations in the accelerator complex to measure beam charge to the various destinations. The MPS uses these data to determine that the beam is being delivered to the proper destination. Additionally, the MPS verifies that the maximum beam power is not being violated nor is charge being lost along the linac.
- Beam Position Monitors (BPMs). The measured X and Y values from each BPM are used by MPS to verify the electron orbit is within an acceptable envelope. This is used to preemptively prevent beam loss in the event of large orbit excursions. Additionally, the measured charge at each BPM can be used as a secondary measure of the beam charge at any location in the same way as a beam charge monitor. The timing pattern for triggering the BPM acquisition carries meta data with the expected bunch charge on each pulse allowing a fast comparator to trip the beam if the measured charge is not within a specified tolerance of the expected charge [4].
- General Digital Inputs. The MPS is designed to read in any signal that can be turned into a present / absent electrical signal. This allows maximum flexibility for what can be interlocked with the system. As an aside, faults from the photon systems (MPS for the photon beamlines) are handled as generic digital inputs. Due to the changing nature of photon systems needed to accommodate many different users, the photon groups maintain a more flexible MPS system and uses digital inputs to send data to the electron systems to mitigate rate or inhibit the photon beam. The photon beam transport lines do not have any fat shut-off means, so it is necessary to suppress the electron beam with the MPS to protect sensitive photon systems needing a fast reponse.

SYSTEM DESIGN

The MPS is comprised of a collection of distributed devices known colloquially as Link Nodes that collect and process data and send them off to a central processor referred to as the central node. The central node collects these data and compares them against a pre-programmed logic table to determine the overall state of the accelerator. The output of this calculation is then distributed to other link nodes that grant or revoke permits to mitigation devices to allow beam to certain destinations. The link nodes and cen-

Content from this work may be used under the terms of the CC-BY-4.0 licence (© 2023). Any distribution of this work must maintain attribution to the author(s), title of the work, publisher, and DOI

ISBN: 978-3-95450-236-3 ISSN: 2673-5350 doi:10.18429/JACoW-IBIC2023-TU3I01

Content from this work may be used under the terms of the CC-BY-4.0 licence (© 2023). Any distribution of this work must maintain attribution to the author(s), title of the work, publisher, and DOI

tral nodes process their data and send out new messages with each 1 µs clock cycle from the LCLS-II timing system. The link nodes connect to the central node via a dedicated, low-latency communication network with a bandwidth of 5 Gbps. The central node is capable of receiving and processing data from 12 of these links. The MPS network is unidirectional - the link nodes send messages when the timing system trigger is present. To conserve bandwidth and avoid many km-long fiber runs, the link nodes are arranged into a daisy chain whereby one link node feeds its information to the next until no more than half of the available bandwidth is consumed. A diagram of the MPS network is shown in Figure 2.

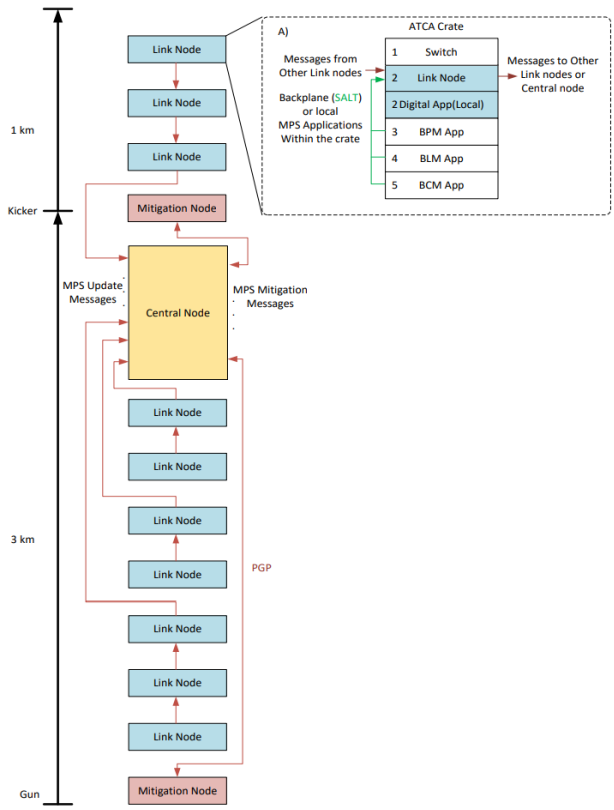


Figure 2: The low-latency MPS communication network.

Because the MPS operates at the full 1 MHz repetition rate of LCLS-II, the core functionality of the link nodes and central node is achieved within an FPGA. The MPS is built upon the SLAC Common Platform, a generalized facility for beam instrumentation based on the ATCA shelf format [5]. The various beamline diagnostics such as BPMs, BCMs, and BLMs also use this platform. The insert in Figure 2 shows a typical ATCA crate installation at SLAC. Each crate includes a network switch in slot 1, a link node in slot 2, and application payloads in the other slots. A computer with local 10 Gbps network is connected to the crate switch to provide a mechanism for asynchronous data transfer from the FPGAs to the control system [6]. The application payloads all contain an MPS firmware block which handles applying thresholds to analog data, converting the analog signals into digital bits to be sent to the central node. The full complement of logic is distributed across the entire system to preserve bandwidth to ensure future expand-ability. The LCLS-II project saw the installation of approximately 100 link nodes (ATCA crates) and 500 discrete applications (slots within the crate).

Central Node

The central node is built on the same SLAC common platform ATCA-based architecture as the link nodes and other accelerator diagnostic systems. The high-level central node architecture is shown in Figure 3. The central node

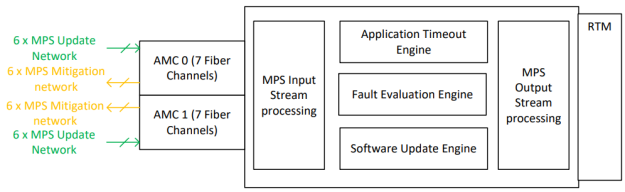


Figure 3: The high-level central node architecture.

is responsible for receiving data from 12 input streams and process them to determine the overall permit state of the accelerator. After the input stream processing, three different fault processing engines are run.

- Application Timeout Engine. This engine is responsible for ensuring that every application in the system sends a unique message on each clock cycle. The allowed latency of this engine is 7 µs, and if it takes longer than that to receive a unique message, the application timeout engine will issue a timeout fault and revoke the permits from all destinations since it does not know which destinations are possibly affected by the missing data.
- Fault Evaluation Engine. This engine is responsible for evaluating the fast faults against the pre-programmed firmware rules tables. Beam loss monitors, BPMs, BCMs, and in principle any fault with a single input (OK / Not OK) is evaluated as a fast fault. The input data are evaluated against the fast fault rules table by this engine every accelerator clock cycle.
- Software Update Engine. Faults that have inputs that change slowly (for example temperature) or more complicated logic tables (for example, a screen with an IN and OUT position) are evaluated as slow faults by a software algorithm. The central node streams synchronous input data via the software update engine from the FPGA to a process running on the attached computer at the slow 360 Hz update rate. The software algorithm receives these input data and evaluates the more complicated logic tables to compute a software permit set. This permit set is sent back to the firmware to be included in the final permit calculation.
- Timing System Verification. The MPS uses the timing system to impose rate limits, and it must verify the timing system is doing as asked. The timing pattern is read in by the central node so the beam rate and charge

ISBN: 978-3-95450-236-3 ISSN: 2673-5350 doi:10.18429/JACoW-IBIC2023-TU3I01

expected at each destination can be computed to verify all is as expected. If information in the timing stream is found to be out of compliance with what the MPS has dictated, the MPS will revoke all permits from all destinations.

The permits computed by these engines are all combined to form the final permit state for each destination. The final permit per destination is defined as the lower allowed state from each of these. These permits are broadcast back out to certain link nodes which are also connected to mitigation devices as well as the timing system. The shutoff mechanisms are discussed in the next section.

Shutoff Mechanism

The MPS has two mitigation paths. It can inhibit the electron beam completely with its own, independent mechanisms or it can impose a power (rate) limit by requesting the timing system reduce the beam rate to a particular destination. The MPS treats the timing system as an untrusted partner - the MPS requests a rate from the timing system and then verifies the timing system has delivered. This rate reduction mechanism allows the MPS to be proactive in some situations. For example, all Beam Position monitors (BPMs) are input devices to the MPS. The BPMs measure the position and bunch charge of the beam within the beam pipe and feed this data to the MPS at the full 1 MHz rate. If the MPS detects that the beam orbit (trajectory) or bunch charge is deviating outside its pre-determined tolerance band, the MPS can first impose a rate reduction so the accelerator operators can correct the deviation and resume high power operation. If the orbit deviation is not corrected or gets worse, the MPS will completely inhibit the beam before damage were to occur. The same mechanism can be applied for beam loss - power can be reduced when beam loss is detected, allowing operators to address the issue before the complete shutoff of the beam.

Each beamline destination shown in Figure 1 has a mitigation device that receives permits from the MPS via one of the link nodes. Pulsed kicker magnets direct beam from the main linac line into the hard X-ray and soft X-ray beamlines as well as the injector diagnostic beamline. The pulsed power supplies are triggered by the LCLS-II timing system, so rate MPS rate reduction is achieved by adjusting the trigger patterns driving these magnets. In the event that rate reduction is not good enough, an operational permit from MPS to the pulsed kicker power supply is revoked, effectively shutting off the magnet. The main linac mitigation is governed by the laser at the photo-injector. Rate reduction is achieved by adjusting the laser triggering timing pattern, and full shut off of the beam is achieved when the MPS revokes a permit and shuts off the laser completely. In this way, the MPS uses the timing system to mitigate power but does not rely on the timing system if the beam must be completely shut off. Each mitigation device has a direct permit from the MPS that can be revoked if needed.

Central Node Concentrator

In principle, the MPS can function as a distributed set of link nodes sending data to a single central node located near the center of the linear accelerator facility which can then issue permits based on one overarching calculation. The full extent of the SLAC linear accelerator facility is longer that 4 km, and the fast beam shutoff time would be dominated by signal propagation if the MPS were constructed with this scheme. To reduce the propagation latency, the central node duties were split from one node into three. This design is shown in Figure 4. Each central node is independent and

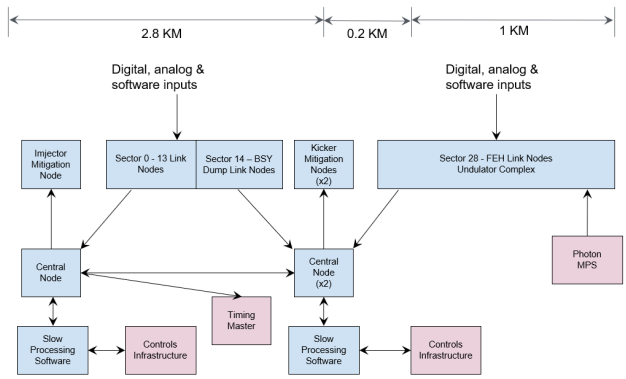


Figure 4: The overall design of the LCLS-II MPS system.

contains its own set of inputs and rules tables. After computing the final permits from the fast and slow fault engines, the final permit states are exchanged between all central nodes, keeping them synchronized with each other. Two central nodes - one near the gun and one near the undulator kicker magnets - handle the superconducting linac and the beam transport line through the high-power dump in the beam switchyard. The third central node, also located near the undulator kicker magnets, handles inputs pertaining to the undulator complex including the undulator transport line between the kicker magnets and undulators.

Software

The software supporting the MPS central node and link node is built upon the EPICS toolkit. An EPICS IOC connects to and provides synchronous and asynchronous control and readout of the firmware and software algorithms contained within each node. EPICS channel access and PV access are used to exchange status data from each node to the control system for operations. The high level software architecture is shown in Figure 5. The central node publishes its fault history to a MongoDB database which can be queried by control room tools so operations can reconstruct faults to determine why beam may have tripped off. The timing system operates Beam Synchronous Acquisition (BSA) data buffers for every fast diagnostic on the machine. When an MPS fault occurs the circular BSA buffers are frozen and contain the last 60 seconds of data from the accelerator before the trip. This allows operators to delve into the root

Content from this work may be used under the terms of the CC-BY-4.0 licence (© 2023). Any distribution of this work must maintain attribution to the author(s), title of the work, publisher, and DOI

ISBN: 978-3-95450-236-3 ISSN: 2673-5350 doi:10.18429/JACoW-IBIC2023-TU3I01

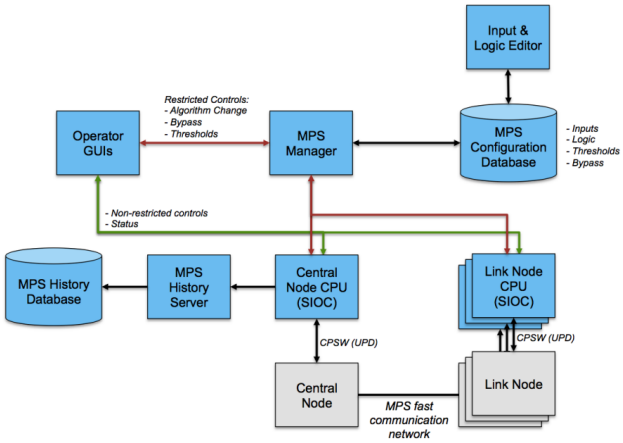


Figure 5: The MPS software architecture.

cause of difficult-to-diagnose machine trips by correlating orbits, energy, losses etc. leading up to the trip.

The overall MPS configuration is stored in a sqlite database. Python scripts are used to insert and extract data into this database. The extraction process produces all necessary EPICS database support as well as the logic tables that are eventually published into the central node firmware rules. Additionally, input and logic reports are generated as output from this configuration database. In this way, the configuration database is a single source of truth for the MPS configuration.

The control room tools provided include software diagnostic screens that show status information about each link node and the central node. Additional screens show status of inter-link node communication status, network bandwidth, and message latency. Information about input status are provided at the link node and central node levels. All of these data are provided as individual EPICS variables and stored in the EPICS archive appliance. The output of the logic tables and permits are shown in a GUI with searchable interface and ability to query the history as well as live faults. To minimize interruptions to the software stack in the central node that computes the slow logic, fewer EPICS variable pertaining to the output of the logic are published in lieu of the logic GUI querying the configuration database with a single PV per fault to reconstruct the status.

OPERATIONAL EXPERIENCE

The MPS was installed and checked out over a multi-year period and was completed before the LCLS-II commissioning activities began. Thus, it was a tool in use for commissioning activities. Before major activities began to each beamline, the fast MPS shutoff times were measured. These are shown in Table 1. The times shown represent a measurement of the time from detection of fault to the loss of the laser or kicker pulse. The kicker shutoff time is slower than the laser shutoff time, and has not yet reached the 100 µs fast shutoff requirement. The measured maximum time of 110 µs is still faster than the beam minimum beam spacing of 1 ms in use for commissioning. Further investigation will be undertaken to understand and correct this slower-than-desirable signal before high power operation commences.

Table 1: Measured Shutoff Times

Destination (device)	Commissioning required shutoff	Measured shutoff
Linac (laser)	100 µs	20 µs
Diagnostic (kicker)	10 ms	1 ms
Hard X-ray (kicker)	1 ms	70 µs
Soft X-ray (kicker)	1 ms	110 µs

The superconducting linac commissioning demonstrated 93 kHz beam rate operation. During this demonstration, the MPS relied on BPM orbit interlocks and BLM interlocks to ensure all the beam reached the high power dump in the beam switch yard. The MPS did its job to stay out of the way of operations unless intervention was necessary at which point the control room tools provide information about what the problems are.

The undulator complex commissioning utilized the undulator beam loss monitors to verify clean trajectory through the undulators. Electron bunches were sent one at a time through the undulator, with analysis of each bunch trajectory happening before the next bunch was sent. On the soft x ray undulator beamline, the MPS beam loss monitors showed that the first shot attempted was lost at the first girder. After trajectory tuning, the undulator beam loss monitors showed the second electron bunch traversed cleanly through the undulators with minimal beam loss measured.

CONCLUSIONS

The LCLS-II MPS has been designed to be as logically simple as possible to maintain robust and stable operation while still providing a flexible platform that can conform to the needs of the facility. The system has been fully installed and commissioned. It is currently in use to support commissioning activities and provides protection of beamline components from damage by the accelerator itself. As the facility advances and accelerator power levels increase, the system will evolve to meet these needs as necessary.

REFERENCES

[1] A. S. Fisher, R. C. Field, and L. Y. Nicolas, "Evaluating Beam-Loss Detectors for LCLS-2", in *Proc. IBIC'16*, Barcelona, Spain, Sep. 2016, pp. 678–681. doi:10.18429/JACoW-IBIC2016-WEPG23

[2] A. S. Fisher *et al.*, "Commissioning Beam-Loss Monitors for the Superconducting Upgrade to LCLS", in *Proc. IBIC'22*,

Content from this work may be used under the terms of the CC-BY-4.0 licence (© 2023). Any distribution of this work must maintain attribution to the author(s), title of the work, publisher, and DOI

ISBN: 978-3-95450-236-3 ISSN: 2673-5350 doi:10.18429/JACoW-IBIC2023-TU3I01

Kraków, Poland, Sep. 2022, pp. 207–210. doi:10.18429/JACoW-IBIC2022-TU2C3

[3] A.S. Fisher *et al.*, "Commissioning the Beam-Loss Monitoring System of the LCLS Superconducting Linac", in *Proc. IBIC'23*, Saskatoon, Canada, Sep. 2023, this conference.

[4] C. Bianchini Mattison *et al.*, "LCLS-II Timing System and synchronous bunch data acquisition", in *Proc. IBIC'23*, Saskatoon, Canada, Sep. 2023, this conference.

[5] J.C. Frisch *et al.*, "A FPGA Based Common Platform for LCLS2 Beam Diagnostics and Controls", in *Proc. IBIC'16*, Barcelona, Spain, Sep. 2016, pp. 651–654. doi:10.18429/JACoW-IBIC2016-WEPG15

[6] J.A. Vásquez, J.M. D'Ewart, K.H. Kim, T. Straumann, and E. Williams, "YCPSWASYN: EPICS Driver for FPGA Register Access and Asynchronous Messaging", in *Proc. ICALEPCS'17*, Barcelona, Spain, Oct. 2017, pp. 1707–1709. doi:10.18429/JACoW-ICALEPCS2017-THPHA138

Content from this work may be used under the terms of the CC-BY-4.0 licence (© 2023). Any distribution of this work must maintain attribution to the author(s), title of the work, publisher, and DOI

ISBN: 978-3-95450-236-3 ISSN: 2673-5350 doi:10.18429/JACoW-IBIC2023-TU3C02

FPGA ARCHITECTURES FOR DISTRIBUTED ML SYSTEMS FOR REAL-TIME BEAM LOSS DE-BLENDING

M.A. Ibrahim*, M.R. Austin, J.M. Arnold, J.R. Berlioz, P. Hanlet,
K.J. Hazelwood, J. Mitrevski, V.P. Nagaslaev, D.J. Nicklaus, G. Pradhan, A.L. Saewert,
B.A. Schupbach, K. Seiya, R.M. Thurman-Keup, N.V. Tran, A. Narayanan[1]
Fermi National Accelerator Laboratory†, Batavia, IL USA
J.YC. Hu, C. Xu, J. Jiang, H. Liu, S. Memik, R. Shi, A.M. Shuping, M. Thieme
Northwestern University‡, Evanston, IL USA
[1]also at Northern Illinois University, DeKalb, IL USA

Abstract

The Accelerator Real-time Edge AI for Distributed Systems (READS) project's goal is to create a Artificial Intelligence (AI) system for real-time beam loss de-blending within the accelerator enclosure, which houses two accelerators: the Main Injector (MI) and the Recycler Ring (RR).

In periods of joint operation, when both machines contain high intensity beam, radioactive beam losses from MI and RR overlap on the enclosure's beam loss monitoring Beam Loss Monitor (BLM) system, making it difficult to attribute those losses to a single machine. Incorrect diagnoses result in unnecessary downtime that incurs both financial and experimental cost. The ML system will automatically disentangle each machine's contributions to those measured losses, while not disrupting the existing operations-critical functions of the BLM system.

This paper will focus on the evolution of the architectures, which provided the high-frequency, low-latency collection of synchronized data streams to make real-time inferences. The ML models, used for learning both local and global machine signatures and producing high quality inferences based on raw BLM loss measurements, will only be discussed at a high-level.

INTRODUCTION

Accelerator Complex

After the Collider Physics program [1] ended in 2011, RR was re-purposed as a proton stacker for Main Injector, delivering 8-120 GeV beam to multiple experiments and facilities. The RR is directly installed above MI, such that their beam lines' centers are physically separated by only about 120 cm. As a result, when high intensity beams are in both machines simultaneously, understanding beam losses becomes a significant concern during normal operation of the accelerator complex (Fig. 1).

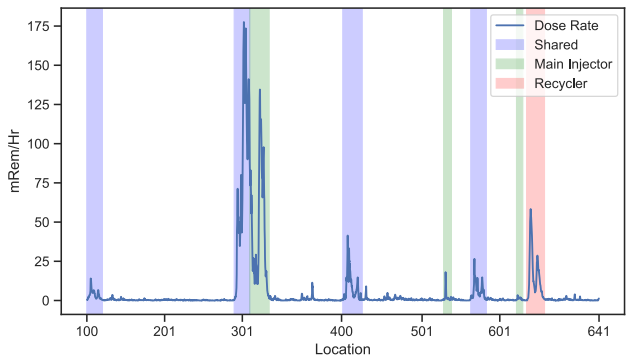


Figure 1: Plot of localized beam losses based on tunnel residual dose rates.

Beam Loss Monitoring

Real-time localized beam losses for both the MI and RR are monitored by over 250 argon gas ionization chamber-type BLM detectors. These signals are received, processed, and instrumented within a Versa Module Eurocard (VME)-based architecture, forming a distributed network of 7 VME "front-end nodes" around the 2.2 mile complex. Together, they capture and report spatially-identifiable and time-correlated integrated beam loss measurements on all BLM detectors within the enclosure for display and analysis [2].

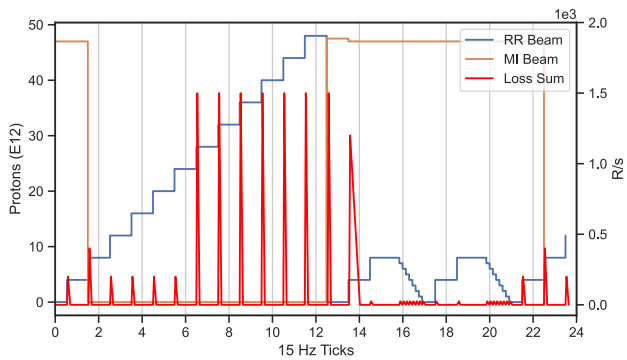


Figure 2: Example to overlay beam events and expected losses during a machine cycle.

Although the origin of radioactive losses measured on any operational BLM can be difficult to attribute to a single machine, experts can often manually decipher and attribute losses to either MI or RR, based on timing, machine state, and physical location within the ring (Fig. 2).

* Equal contribution
† Operated by Fermi Research Alliance, LLC under Contract No.De-AC02-07CH11359 with the United States Department of Energy. Additional funding provided by Grant Award No. LAB 20-2261
‡ Performed at Northwestern with support from the Departments of Computer Science and Electrical and Computer Engineering

Content from this work may be used under the terms of the CC-BY-4.0 licence (© 2023). Any distribution of this work must maintain attribution to the author(s), title of the work, publisher, and DOI

ISBN: 978-3-95450-236-3 ISSN: 2673-5350 doi:10.18429/JACoW-IBIC2023-TU3C02

READS DISTRIBUTED NETWORK

The current BLM VME nodes were not designed to simultaneously output all BLM measurements to ACNET [3], at their VME digitizers' maximum polling frequency of 320 Hz. Instead, through the ACNET Data Pool Managers (DPM), the time resolution of the integrated loss measurements is relatively course (33 Hz, max).

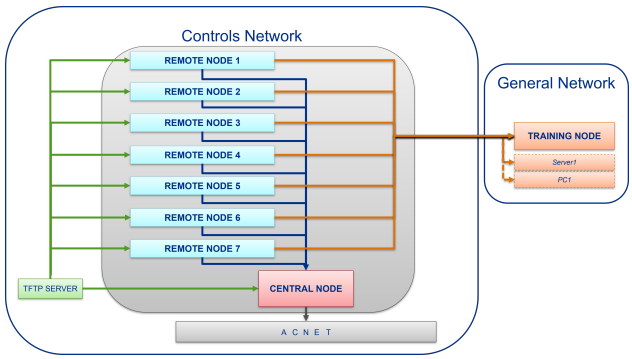


Figure 3: Block diagram of READS distributed network.

Consequently, READS Distributed Network (Fig. 3) provides a separate data path, which does not disturb normal operations of the BLM system. The main components of this network are Remote Data Aquisition (DAQ) Nodes, Central Deblending Node, and Training Nodes.

CLIENT-SERVER MODEL

The Distributed Data Communications Protocol (DDCP) (Fig. 4) is a lightweight User Datagram Protocol (UDP) application layer protocol, used within the READS network to establish client-server relationships between the Remote DAQ Nodes and ML-related nodes (i.e. the Training Node and Central Deblending Node).

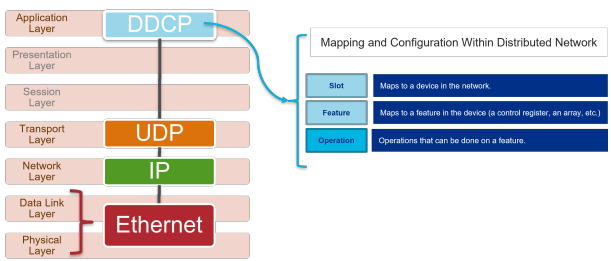


Figure 4: Block diagram of DDCP Ethernet stack.

DAQ nodes act as DDCP servers while ML-related nodes act as DDCP clients. While DDCP had been previously used to read and write parameters between operational nodes of other systems, development was needed to implement a streaming service. This feature pushes data from the server to the client automatically after just one client request. Furthermore, each server can connect to multiple clients; clients can connect to multiple servers. Optimizations were also needed to preserve configuration compliance across the READS network, ensuring packets can be efficiently aggregated and correctly correlated.

REMOTE DAQ NODE

Uniquely registered within the Controls Network, a *VME Reader Card* is integrated into each BLM VME node and serves as a Remote DAQ Node within the READS network. Utilizing a *Critical Link MitySOM-5CSX* System On Module (SOM) (Fig. 5), it passively monitors the VME backplane as well as generates data streams of User Datagram Protocol (UDP) packets with a customized application layer [4].

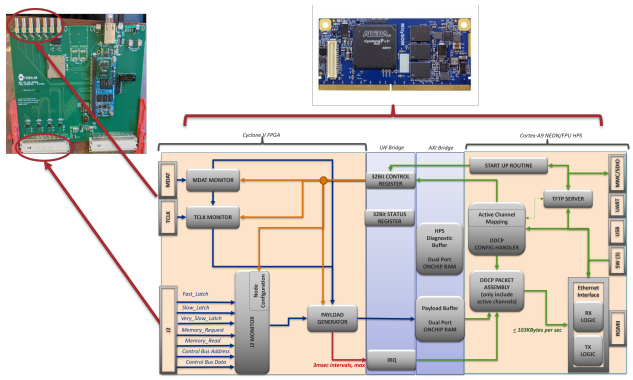


Figure 5: Block diagram of SOC architecture of Remote DAQ Node.

The SOM hosts an *Altera Cyclone V* System On Chip (SOC), which is a highly-integrated infrastructure of both a Field Programmable Gate Array (FPGA) and dual-core *ARM Cortex-A9* Hard Processor Subsystem (HPS). The architecture of the Remote DAQ Node was implemented and optimized to provide consistent Ethernet performance to support the multiple clients, DDCP data streams, and remote troubleshooting.

The FPGA is responsible for the receiving integrated sums from the BLMs as well as encoded signals from the global event system and frame links, in order to generate each packet's payload. Each packet's data payload include epoch second, millisecond time-stamping, event-based counters, decoded global clock events, machine readings and state information for proper synchronization and correlation (Fig. 6). Also, the streams are aligned, with respect to a single, asynchronous global clock event, which regularly occurs at 5 sec intervals. Assembly of the READ data packets, and serialized transmission of packets into data streams, and management of other Ethernet communication falls to the HPS. Other supported services are Trivial File Transfer Protocol (TFTP) for remote programming and booting, Kerberized Secure Shell Protocol (SSH) for expert accessibility, and ping for verifying proper network registration.

TRAINING NODES

The Training Node is a designated server on the general network, that receives and archives data streamed from the Remote DAQ Nodes into a storage device. Functionally, the server mimics the DPM but provides for faster data collection rates at 333 Hz. These Training Data Sets are then used offline to develop, train, and optimize an U-Net-based ML model, which was prototyped using Sample Data Sets

Content from this work may be used under the terms of the CC-BY-4.0 licence (© 2023). Any distribution of this work must maintain attribution to the author(s), title of the work, publisher, and DOI

ISBN: 978-3-95450-236-3 ISSN: 2673-5350 doi:10.18429/JACoW-IBIC2023-TU3C02

Content from this work may be used under the terms of the CC-BY-4.0 licence (© 2023). Any distribution of this work must maintain attribution to the author(s), title of the work, publisher, and DOI

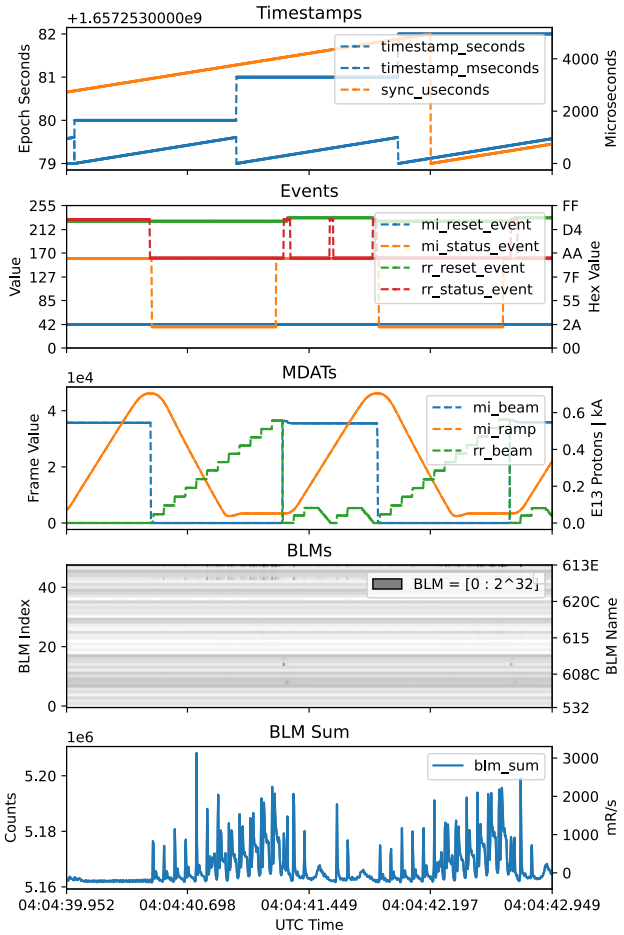


Figure 6: Display of data collected and streamed from a Remote DAQ Node.

collected at 33 Hz from the existing BLM System via the ACNET DPM [5]. Training data sets capture measurements collected during normal operation but also during special study times. During such times, the beam event timeline is manipulated to purposefully keep events for RR and MI from overlapping, thus only having beam in one machine at a time. Moreover, to ensure that a broad range of loss conditions are captured, moderate beam losses were also generated at all locations in both machines using various miss-configurations of the machines. This allowed for verification of the model on data that is possible but not generated during normal operations.

CENTRAL DE-BLENDING NODE

A Central De-blending Node ingests streamed packets from the Remote DAQ nodes to output inferences, which attributes the origin of the loss at each BLM location [6]. The Central Node uses a *REFLEX CES Achilles Arria10SoC SOM*, which is a mezzanine card that mounts onto a carrier board in a rack-wide chassis [7]. As in the Remote DAQ Node, this SOM also provides an embedded systems environment with both a FPGA and a dual-core *ARM Cortex-A9* HPS (Fig. 7). However, the Central Node hosts an *Altera Arria 10* SOC.

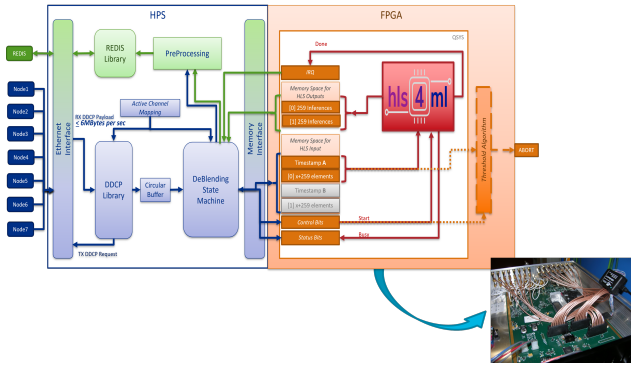


Figure 7: Block diagram of SOC architecture of Central Deblending Node.

The FPGA implements an embedded inference engine based on the trained model. Optimizations at the algorithm level, high-level synthesis level, and communication protocol level improved the overall node's speed, power consumption, and resource usage.

Packets, containing the engine's required inputs, are received, deserialized, correlated in time, and queued for input by the HPS. The engine outputs real-time inferences back to the HPS. These inferences are in percentages, attributing the likelihood of the integrated beam loss at each BLM to either the MI or RR. Then, the HPS provides these results to control system for display within the Main Control Room. Development in the HPS focused on minimizing the latency and optimizing the consistency of the arbitration of state machines handling Ethernet interface and lightweight bridge interfaces.

ML Model Implementation

A workflow was developed to integrate open-source tools, which have been successfully used to implement neural networks on *Xilinx* chips, with *Intel* FPGA compilation and build tools (Fig. 8). *HLS4ML* was used to translate the original U-Net model, written in *Keras*, to High Level Synthesis (HLS) for the Intel HLS compiler.

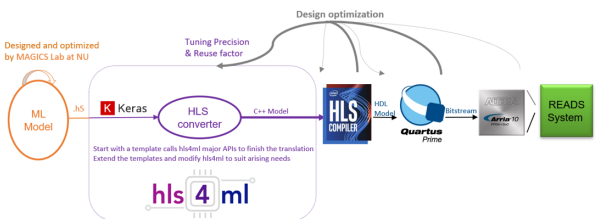


Figure 8: Block diagram of Keras to HLS4ML workflow.

Beam studies have confirmed that the ML model works well for ring-wide loss attribution, but not for narrower localized losses. The implemented neural network had a maximum latency of 1.74 ms and average latency of 1.2 ms meeting the required specification. Transfers between HPS and FPGA were about 200 µs.

Control System Interface

The resulting inferences need to be accessible to Main Control Room operators and experts thru existing tools used

ISBN: 978-3-95450-236-3 ISSN: 2673-5350 doi:10.18429/JACoW-IBIC2023-TU3C02

to tune and diagnose the accelerators. In order to do so, the Central Node establishes a connection to a *RE mote DI ctionary S erver* (REDIS) server, which acts a versatile data structure server that can be used as a database, cache, streaming engine, and message broker to ACNET. In this manner, arrayed ACNET devices for the inferences are updated in real time and are available for fast time plotting via a READS *JAVA* Open Access Client (OAC). The fully deployed system satisfies the 3 ms latency requirement for the complete data signal path through the READS network (Fig. 9).

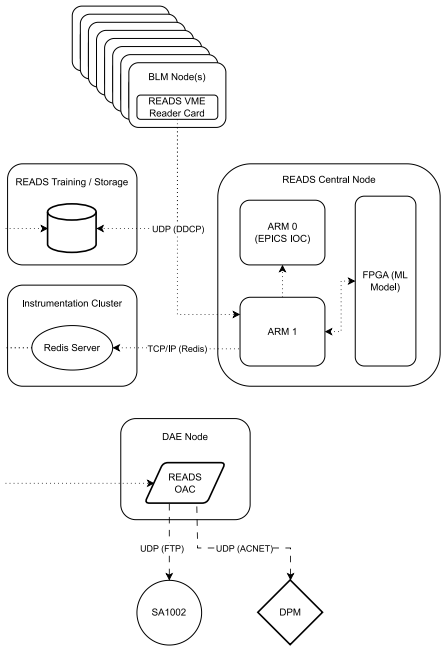


Figure 9: Dath Path to and from READS network to ACNET Control System.

CONCLUSION

READS successfully implemented and deployed the first operational FPGA-based edge-AI system in the Fermilab accelerator complex. Distributed remote nodes create and stream BLM readings from around the accelerator complex to perform near real-time inferences at a centralized node, which feed ACNET devices available to operators. Also, dedicated beam studies confirmed that ML model implementation agrees with the offline predictions from the Keras model. As a result, operators have a new tool to attribute percentages of beam loss, from each BLM, in MI and RR (Fig. 10). The system is expected to reduce pulse inefficiencies during tuning as well as unnecessary downtime due to tripping off the incorrect machine.

ACKNOWLEDGMENTS

This work was produced by Fermi Research Alliance, LLC under Contract No. DE-AC02-07CH11359 with the U.S. Department of Energy, Office of Science, Office of High Energy Physics. Publisher acknowledges the U.S. Government license to provide public access under the DOE Public Access Plan [8]. Additional funding provided by Grant Award No. LAB 20-2261 [9].

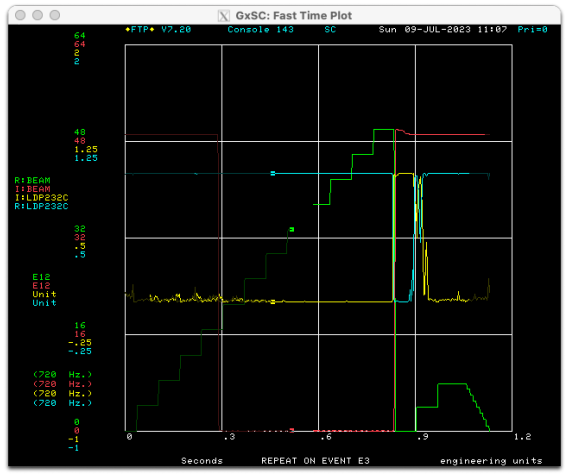


Figure 10: Real-time ML inferences on Fast Time Plot display - I:LDP232C and R:LDP232C are the loss percentage attribution for 232C BLM.

REFERENCES

[1] G. Jackson, "The Fermilab Recycler Ring Technical Design Report. Revision 1.2," Nov. 1996. doi:10.2172/16029

[2] A. Baumbaugh *et al.*, "The upgraded data acquisition system for beam loss monitoring at the fermilab tevatron and main injector," *Journal of Instrumentation*, vol. 6, no. 11, Nov. 2011. doi:10.1088/1748-0221/6/11/T11006

[3] J. F. Patrick, "The Fermilab Accelerator Control System," in *Proc. ICAP'06*, Chamonix, Switzerland, Oct. 2006, pp. 246–249. https://jacow.org/icap06/papers/WEA2IS03.pdf

[4] J. Berlioz *et al.*, "Synchronous High-Frequency Distributed Readout for Edge Processing at the Fermilab Main Injector and Recycler," in *Proc. NAPAC'22*, Albuquerque, NM, USA, Nov. 2022, pp. 79–82. doi:10.18429/JACoW-NAPAC2022-MOPA15

[5] K. Hazelwood *et al.*, "Real-Time Edge AI for Distributed Systems (READS): Progress on Beam Loss De-Blending for the Fermilab Main Injector and Recycler," in *Proc. IPAC'21*, Campinas, SP, Brazil, Aug. 2021, paper MOPAB288, pp. 912–915. doi:10.18429/JACoW-IPAC2021-MOPAB288

[6] M. Thieme *et al.*, "Semantic Regression for Disentangling Beam Losses in the Fermilab Main Injector and Recycler," in *Proc. NAPAC'22*, Albuquerque, NM, USA, Nov. 2022, pp. 79–82. doi:10.18429/JACoW-NAPAC2022-MOPA15

[7] M. Ibrahim *et al.*, "Preliminary Design of Mu2E Spill Regulation System (SRS)," in *Proc. IBIC'19*, Malmö, Sweden, Nov. 2019, pp. 177–180. doi:10.18429/JACoW-IBIC2019-MOPP033

[8] *DOE Public Access Plan*. https://www.energy.gov/doe-public-access-plan

[9] Department of Energy, Office of Science. "Data, Artificial Intelligence, and Machine Learning at DOE Scientific User Facilities, DOE National Laboratory Program Announcement Number: LAB 20-2261." (2020), https://science.osti.gov/-/media/grants/pdf/lab-announcements/2020/LAB_20-2261.pdf

Content from this work may be used under the terms of the CC-BY-4.0 licence (© 2023). Any distribution of this work must maintain attribution to the author(s), title of the work, publisher, and DOI

ISBN: 978-3-95450-236-3 ISSN: 2673-5350 doi:10.18429/JACoW-IBIC2023-TU3C03

COLLIMATOR SCAN BASED BEAM HALO MEASUREMENTS IN LHC AND HL-LHC*

P. Hermes†, M. Giovannozzi, C. E. Montanari[1], S. Morales Vigo[2,3], M. Rakic[4], S. Redaelli, B. Salvachua, CERN, Geneva, Switzerland, [1]also at University of Manchester, UK
[2]also at Cockcroft Inst. Accel. Sci. Tech., Warrington, Cheshire, UK,
[3]also at University of Liverpool, UK, [4]also at EPFL, Lausanne, Switzerland

Abstract

Measurements in the CERN Large Hadron Collider (LHC) have indicated that the population of the transverse beam halos is greater than that of a Gaussian distribution. With the upcoming High-Luminosity project (HL-LHC), the stored beam energy in the beam halo could become large enough to threaten the integrity of the collimation system. Given the unprecedented stored beam energies of about 400 MJ, currently achieved at the LHC, and roughly 700 MJ planned at the HL-LHC, conventional measurements are difficult. Considerable efforts in the ongoing LHC Run 3 are dedicated to characterising experimentally the transverse beam halos, and its diffusion properties, after the LHC Injector Upgrade (LIU) in preparation for HL-LHC operation. Halo and diffusion measurements are currently based on collimator scans, where robust collimators are inserted in steps into the circulating beam halo. In this contribution, we present techniques for halo characterisation employed in LHC and compare results obtained from such measurements in LHC Run 2 and the ongoing LHC Run 3. We present plans for measurements in the remainder of LHC Run 3 and describe the expected challenges for halo characterization in HL-LHC.

INTRODUCTION

The Large Hadron Collider (LHC) at CERN is a 27 km long circular collider for protons and heavy ions [1]. LHC design beam intensities are so high that even small amounts of beam loss can generate beam dumps, triggered by the interlock system, magnet quenches, or even damage to machine equipment. To preserve the integrity of the machine hardware and avert potential hazards arising from uncontrolled beam losses, the LHC is equipped with a multi-stage collimation system, predominantly located in the betatron collimation insertion region IR7 [1, 2]. Additional details on the collimation system are provided in the following section.

While methods of active and non-destructive monitoring of beam halos are currently under study [3], the current state-of-the-art method for studying the beam halo is scraping with the LHC collimators. In LHC Run 1 (2009–2013) and Run 2 (2015–2018) measurements, up to 5% of the total stored beam energy was found at transverse amplitudes greater than 3 σ_N [4] in a given transverse plane (we refer to this subset of beam particles as *halo* in the following). σ_N denotes the nominal beam size using the LHC's nominal normalised emittance of 3.5 µm rad. Measured emittances were typically smaller than this conservative value. With the upcoming High Luminosity upgrade (HL-LHC) [5], stored beam energies in the order of 700 MJ are expected to be reached. The scaling to different beam parameters for the higher-brightness HL-LHC beams is complex. Assuming, for example, that similar fractions of the total stored beam energies were located in the beam halo, the stored beam energy above 3 σ_N would yield 35 MJ. This is enough to damage the LHC collimators in case of sudden orbit shifts, for example, in case of crab-cavity failure [6]. Therefore, measures are needed to mitigate this peril.

Hollow electron lenses (HEL) [7] for active halo removal are considered to be deployed in HL-LHC, but cannot be manufactured in time for Run 4 operation. Understanding the formation and population of the halo in LHC Run 3, the final run before HL-LHC installation, is therefore a critical task. The main goals of these activities are reviewing the expected risk from the halo population in HL-LHC, exploring alternative mitigation strategies, and defining requirements for monitoring the halo in HL-LHC.

In this article, we review the technique used for halo quantification in the LHC and discuss data recorded in LHC Run 2 to compare against measurements performed in Run 3. We will then outline the merits of additional measurements planned for in LHC Run 3 and close the article with an outlook on the challenges of halo quantification for HL-LHC.

COLLIMATOR SCANS FOR HALO MEASUREMENTS

LHC collimators are equipped with one or two movable jaws of a robust material used to scatter and/or absorb beam particles. Different collimator types are used, following a defined hierarchy [8]. Primary collimators (TCP) are the only LHC components designed to be directly exposed to the main beam. They are built with two 60 cm long jaws made of a low-density material [9]. This assures robustness against high loads of particle fluxes while providing scattering toward larger amplitudes, where the particles can be intercepted by the secondary collimators and their shower absorbers. Each jaw can be moved independently by two stepper motors, with a step size of 5 µm [10].

Each collimator is equipped with a beam loss monitor (BLM) [11] downstream, as illustrated in Fig. 1. BLMs are ionisation chambers, measuring local secondary particle showers created when particles leave the beam vacuum and interact with surrounding matter. More than 3000 BLMs

* Work supported by the HL-LHC project.
† pascal.hermes@cern.ch

Content from this work may be used under the terms of the CC-BY-4.0 licence (© 2023). Any distribution of this work must maintain attribution to the author(s), title of the work, publisher, and DOI

ISBN: 978-3-95450-236-3 ISSN: 2673-5350 doi:10.18429/JACoW-IBIC2023-TU3C03

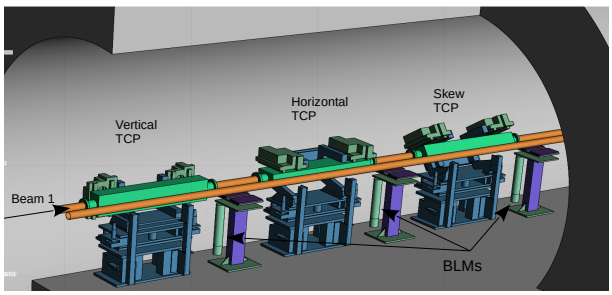


Figure 1: 3D model of LHC Beam 1 primary collimators (TCPs) in the LHC tunnel. The BLMs downstream of each collimator are clearly visible. Image source: Ref. [12].

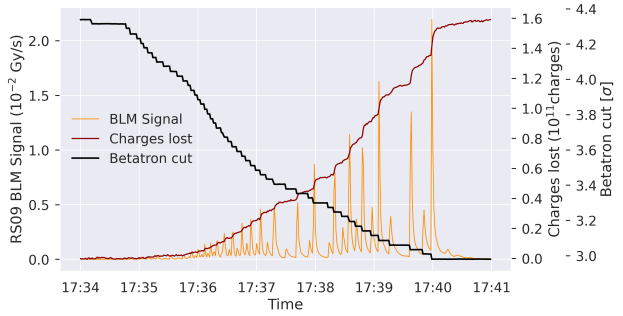


Figure 2: Data recorded during a vertical scraping of LHC Beam 2 (B2V). The black line shows the betatron cut applied. The red line reflects the cumulative amount of charges lost, measured with the BCTDC (initial total beam intensity of 2.38×10^{13} charges). The orange line represents the BLM signal at the collimator with 1.3 s integration time.

are installed in the LHC, allowing for global monitoring of particle losses over twelve different integration times from 40 µs to 84 s [11]. They are part of the LHC beam interlock system: a beam dump is triggered if signals recorded in the LHC BLMs exceed predefined thresholds [13]. Furthermore, diamond-BLMs (dBLMs) are installed downstream of the primary collimators, providing a time resolution in the ns range to identify bunch-by-bunch losses [14].

Halo Measurement Technique

Halo measurements are based on beam scraping with the collimator jaws by moving one or both TCP jaws towards the beam centre in steps, thus reducing the applied betatron cut in the horizontal (H) or vertical (V) plane. This is done after a beam-based alignment of the jaws to ensure that the centre of the beam at the collimator is accurately known [15]. The precise knowledge of the collimator jaw positions allows computing the cut in beam σ_N units. The starting point of the scan is typically the nominal collimator position of 5 σ_N for LHC Run 2 and Run 3 at top energy. All collimators, except the TCP, remain in their nominal positions. Halo measurements are usually performed with the highest stored beam energies, which is representative of nominal high-intensity physics operation as effects such as impedance, Landau octupoles, beam-beam, *e*-cloud, etc. are nominal. The highest stored beam energy during a measurement in 2022 was roughly 200 MJ.

Consider Fig. 2, where measured data is shown for a measurement performed in 2022. The collimator betatron cut is shown as a black line. The individual collimator steps of 5 µm step size are clearly visible. The loss of beam particles is visible as spiking in the collimator BLM signal (orange line) when the jaw is moved. The red line shows the number of particles lost since the beginning of the scraping, measured with the direct current LHC Beam Current Transformer (BCTDC) [16]. In the example shown, roughly 1.6×10^{11} charges were lost during the scraping to a betatron cut of 3 σ_N, roughly 0.7 % of the initial beam intensity.

Considering each collimator step, a clear change of the BCT signal is not measurable for the small loss amounts when scraping at large betatron amplitudes. With the noise level and sensitivity of the BCTDC, a clear intensity drop is visible if it exceeds a value of the order of 10^9 charges. A similar boundary is observed for the total intensity derived from the bunch-by-bunch measurement with the fast BCT (BCTFR) [16].

The BLM signal shows clear spikes already at larger betatron amplitudes with lower halo densities. The BLMs can therefore be used to identify smaller amounts of lost particles, thanks to their higher sensitivity and a large dynamic range of more than 10^8 (10 pA–1 mA). For the BLMs at the primary collimators, beam losses of the order of 5×10^4 charges to 5×10^{12} charges could be detected.

BCT-based Post Processing

Based on the change in beam intensity recorded with BCTFR or BCTDC at each collimator step, the cumulative halo content can be derived. The total fraction of the beam intensity stored above a given amplitude is directly deduced from the fraction of the initial intensity lost until a given betatron cut is reached. The limited sensitivity for small loss amounts discussed before imposes a lower limit for the halo that can still be quantified. This is visible in the comparison of the reconstructed halo population using the BCTDC and the BLM system (see next section) shown in Fig. 3. We used the minimum and maximum of the BCTDC signal, while a given collimator setting was applied, to quantify the uncertainty.

Using the BCTFR signal, it is possible to disentangle the lost intensity for each circulating bunch. Analyses of the latter unveiled considerable differences in the bunch-by-bunch halo population. It is also noteworthy that the BCTFR signal is logged for longitudinally confined beam particles, while the BCTDC signal also records de-bunched beam intensity.

BLM-based Post Processing

A calibration model can be applied to a subset of BLM signals, measured in Gy/s, to estimate the number of charges lost per collimator step [17]. This allows us to benefit from their larger dynamic range, which is especially useful in

Content from this work may be used under the terms of the CC-BY-4.0 licence (© 2023). Any distribution of this work must maintain attribution to the author(s), title of the work, publisher, and DOI

ISBN: 978-3-95450-236-3 ISSN: 2673-5350 doi:10.18429/JACoW-IBIC2023-TU3C03

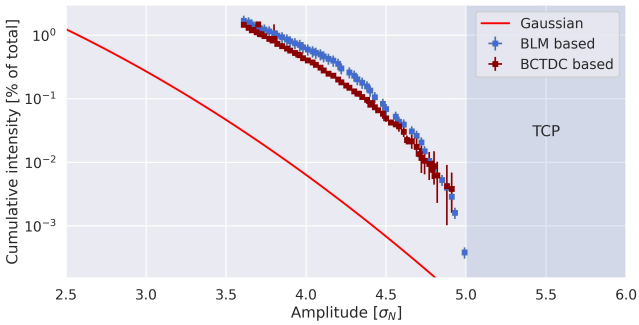


Figure 3: Example of halo population vs. amplitude, derived from a halo scraping measurement in 2022. The halo population derived from BCTDC data is marked in red, from BLM data in blue. The Gaussian is given for reference and refers to the nominal emittance of 3.5 µm rad.

regions with low particle densities. The calibration is based on the response of the BLM signal to beam losses in the different TCPs, measured during collimation qualification loss maps [18]. These are machine-protection validation tests during which well-defined beam loss scenarios are reproduced independently by exciting the beams horizontally or vertically with white noise. The response of the BLM signal to each beam loss scenario is then calculated as the accumulated BLM signal divided by the total lost intensity measured by the BCT.

The BLMs with high and similar signal responses to the loss scenarios involving one of the beams and low signal responses for the other beam are selected and a combined signal response to beam impacts on the TCPs is calculated. The lost charges are then calculated by multiplying this signal response by the sum of the selected BLMs signals. The uncertainty in the measurements is given by considering the noise in the BCTs and BLMs signals both during the loss maps and the beam scraping periods. This calibration is especially useful to disentangle beam losses due to luminosity burn-off and from collimation cleaning.

The blue graph in Fig. 3 shows the relative fraction of total beam intensity lost throughout a scraping to 3 σ_N, estimated based on the BLM calibration obtained in 2022.

Conclusions

The BLM- and BCT-based analysis deliver similar results for the halo population. For large amplitudes, with low beam densities, the intensity drop is below the noise level and the BCT measurement is not usable. Thus, especially when measurements at larger betatron amplitudes are carried out, the BLM-based analysis becomes the method of choice.

MEASUREMENT RESULTS

LHC Run 2

The measurements carried out in LHC Run 2 are described in detail in Ref. [4]. Here, we review the main findings in Ref. [4] and provide additional information for the measurement in which the highest halo population was found (fill 6194).

Eleven measurements were carried out, two of which with nominal optics, and the rest with so-called ATS optics [19]. All measurements, except one, were performed with colliding beams at the smallest β^* applied (in LHC IP1 and IP5) in the given year: 40 cm in 2016 (nominal optics) and 2017 (ATS), and 25 cm in 2018 (ATS). One measurement was performed with separated beams, in the "flat-top" stage of the 2018 LHC cycle with β^* =1 m.

A summary of the maximum lost beam intensity K for a subset of the measurements, taken from Ref. [4], is shown in Fig. 4. It is based on a simple BLM calibration, using only one BLM. A clear pattern across the measurements cannot be identified, and a direct comparison is not possible due to the different minimum betatron cut P_{min} (in nominal beam size) reached in the different measurements. Also, the beam emittances were different in each fill.

A maximum value of K of almost 5 % of the total stored beam energy is reached in the B2V plane for an amplitude greater than 3.1 σ_N in fill 6194. Two more planes (B1H/B1V) show a population greater than 4 %. However, this fill was exceptional in different ways: the bunch intensities were of 1.3×10^{11} particles per bunch (ppb), compared to 1.15×10^{11} ppb in the other measurements. The emittances measured with the wire scans [20] at injection were highest during fill 6194: between 2.6 µm rad and 2.8 µm rad, compared to 1.7 µm rad to 2.5 µm rad for all other measurements (we assumed a 20 % emittance increase during the energy ramp [21]). The larger beam size in this fill partially explains the higher halo population. The scraping was done in an environment of strong non-linearities: The octupoles were operated at their maximum currents of 570 A, compared only with 340 A to 400 A in the other fills. The combination of the high halo population observed could be explained by a non-linear deformation of the phase space. The collimator position measured in linear beam σ_N would then reflect a different, smaller, betatron cut than expected.

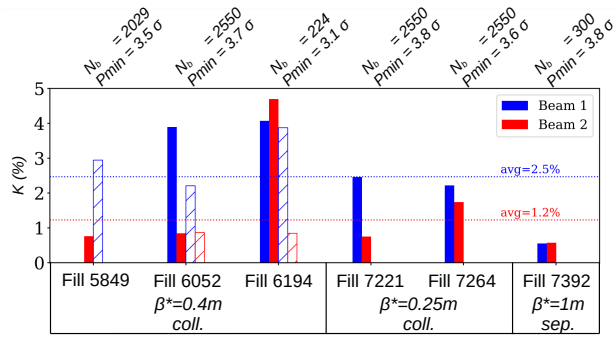


Figure 4: Halo content, K, for selected Run 2 measurements. N_b refers to the number of bunches, P_{min} to the minimum betatron cut achieved with the primary collimator. Hatched/solid bars: H/V plane. All measurements were done with ATS optics. Figure adapted from Ref. [4].

Content from this work may be used under the terms of the CC-BY-4.0 licence (© 2023). Any distribution of this work must maintain attribution to the author(s), title of the work, publisher, and DOI

ISBN: 978-3-95450-236-3 ISSN: 2673-5350 doi:10.18429/JACoW-IBIC2023-TU3C03

It is foreseen to study this hypothesis further in dedicated particle-tracking simulations including beam-beam effects.

For Fill 7392, the measurement after the energy ramp and before colliding the beams shows a comparably low halo population of less than 0.5 %. We interpret this finding as an indication that the relevant halo formation process could be induced by collisions.

LHC Run 3

Three halo population measurements were performed in 2022 after several hours of collisions in regular physics fills, at the end of the luminosity levelling [22] with $\beta^* = 30$ cm. After each scraping a dedicated sequence of collimator settings was applied to measure non-linear diffusion coefficients [23]. The first two measurements were made with the primary purpose of gathering data for BLM calibration, for which it was necessary to separate the colliding beams. The last scraping was fully dedicated to halo quantification and diffusion studies, and the beams were kept in collision.

The halo contents derived from the measurements are summarised in Fig. 5. The halo content observed is below those measured in Run 2. The maximum is reached with 1.3 % of the total stored beam intensity above 3.5 σ_N in the B1H plane during fill 8387 with a bunch intensity of 1.44×10^{11} p. Note that the beams injected into the LHC in Run 3 were produced after full deployment of the LIU project with an improved brilliance compared to Run 2. In this fill, emittances of up to 2 µm rad were measured.

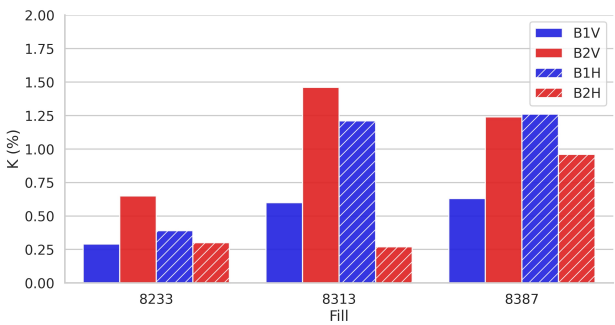


Figure 5: Fraction of beam intensity lost per scraping, K, for selected Run 3 measurements. Hatched/solid bars: H/V plane. Note the different scale compared to Fig. 4.

PLANS FOR THE REMAINDER OF RUN 3

The formation and magnitude of the beam halo are not well understood. We intend to carry out a series of measurements for the remainder of LHC Run 3 to gain a more tangible understanding of the halo population throughout the LHC cycle, with beam properties as closely as possible to the HL-LHC parameters. Measurements in the final stage of luminosity levelling will be repeated with bunch intensities approaching the Run 4 intensities of at least 1.7×10^{11} ppb [24].

Measurements at the injection stage are planned to understand the correlation of the LHC halo population to scrapings in the CERN Super Proton Synchrotron (SPS), the LHC's injector. The insights will help determine the potential of reducing the halo content at injection. These measurements are planned to be enhanced by wire-scan measurements with different gains of the shower detector to create sensitivity to the lower signal at the halo.

All measurements carried out so far were made by serial scraping of the horizontal and vertical planes with the same beam. This could introduce a bias for the plane that is scraped secondly. We intend to study this at injection energy by scraping one bunch train in plane H and injecting another bunch train without dumping the previous one to scrape both in the V plane. The latter shall then be combined with a subsequent energy ramp of the two scraped trains and one unaltered train. This will allow to identify the halo repopulation during the ramp and quantify the halo population after the energy ramp, before bringing the beams into collision.

OUTLOOK TOWARDS HL-LHC

As introduced before, the beam halo could pose a serious threat to HL-LHC operational safety and/or efficiency. Scraping measurements will remain an important method also in the HL-LHC era. However, having means of active and non-destructive halo monitoring for interlocking becomes crucial. The requirement of being nondisruptive to the circulating beam led to the consideration of synchrotron radiation as a sensible carrier of information. A synchrotron light-based coronagraph [3] was designed for the LHC and testing of the device is ongoing during LHC Run 3. This device must be capable of accurately identifying halo populations at amplitudes between 3.6 σ_N and 8.5 σ_N, to cover all relevant operational scenarios [24]. Note that for HL-LHC, σ_N corresponds to a reference normalised transverse emittance of 2.5 µm rad. An interlock strategy could be based on the integrated stored beam energy within a given distance from the TCPs, in two dimensions. Sudden orbit shifts of up to 2 σ_N should be tolerated. Therefore, a beam dump should be triggered if the halo content within $N_P - 2\,\sigma_N$ exceeds a certain threshold, where N_P is the half-gap of the primary collimator. Possible means of active halo depletion without HELs are currently under study.

CONCLUSION

The large population of transverse beam halos could pose a serious threat to HL-LHC. We discussed the technique of collimator scans to quantify transverse beam halos in the LHC, based either on BCT measurements or calibrated BLM signals. Both provide similar results, but the BLM method is also sensitive to lower loss levels and is the only method available for large amplitudes with low beam intensities. The Run 2 and Run 3 scraping data show a large variability of the recorded halo populations that is not fully understood. More measurements during LHC Run 3 are needed to understand the halo population and formation in HL-LHC. Halo monitoring and interlocking strategies in HL-LHC must be developed to ensure machine safety at any time.

Content from this work may be used under the terms of the CC-BY-4.0 licence (© 2023). Any distribution of this work must maintain attribution to the author(s), title of the work, publisher, and DOI

ISBN: 978-3-95450-236-3 ISSN: 2673-5350 doi:10.18429/JACoW-IBIC2023-TU3C03

REFERENCES

[1] O. S. Brüning *et al.*, "LHC Design Report," Tech. Rep., 2004. doi:10.5170/CERN-2004-003-V-1

[2] R. Bruce *et al.*, "Simulations and measurements of beam loss patterns at the CERN Large Hadron Collider," *Phys. Rev. ST Accel. Beams*, vol. 17, no. 8, p. 081 004, 2014. doi:10.1103/PhysRevSTAB.17.081004

[3] A. Goldblatt, E. Bravin, F. Roncarolo, G. Trad, and T. M. Mitsuhashi, "Design and Performance of Coronagraph for Beam Halo Measurements in the LHC," in *Proc. IBIC'16*, Barcelona, Spain, Sep. 2016, pp. 253–256. doi:10.18429/JACoW-IBIC2016-MOPG74

[4] A. Gorzawski *et al.*, "Probing LHC halo dynamics using collimator loss rates at 6.5 TeV," *Phys. Rev. ST Accel. Beams*, vol. 23, p. 044 802, 2020.

[5] O. Aberle *et al.*, *High-Luminosity Large Hadron Collider (HL-LHC): Technical Design Report*. CERN, Geneva, Switzerland, 2020. doi:10.23731/CYRM-2020-0010

[6] A. Santamaria Garcia, "Experiment and Machine Protection from Fast Losses caused by Crab Cavities in the High Luminosity LHC," Doctoral Thesis, 2018. doi:10.5075/epfl-thesis-8533

[7] S. Redaelli *et al.*, "Hollow electron lenses for beam collimation at the High-Luminosity Large Hadron Collider (HL-LHC)," *J. Instrum.*, vol. 16, no. 03, P03042, 2021. doi:10.1088/1748-0221/16/03/p03042

[8] R. Bruce, R. Assmann, L. Lari, and S. Redaelli, "Collimator hierarchy limits: assumptions and impact on machine protection and performance," *MPP Workshop March 2013, Annecy, France*, 2013.

[9] C. Accettura *et al.*, "Overview of material choices for HL-LHC collimators," presented at IPAC'23, Venice, Italy, May 2023, paper WEPA148.

[10] S. Redaelli, R. W. Assmann, R. Losito, and A. Masi, "Final Implementation and Performance of the LHC Collimator Control System," in *Proc. PAC'09*, Vancouver, Canada, May 2009, pp. 4788–4790.

[11] B. Dehning *et al.*, "The LHC Beam Loss Measurement System," 2007, LHC-PROJECT-Report-1025, CERN-LHC-PROJECT-Report-1025.

[12] E. Skordis *et al.*, *Updates on FLUKA simulations of the 4 TeV quench test*, Presentation in the LHC Collimation Working Group 181, 2014.

[13] B. Puccio, A. Castañeda, M. Kwiatkowski, I. Romera, and B. Todd, "The CERN Beam Interlock System: Principle and Operational Experience," in *Proc. IPAC'10*, Kyoto, Japan, May 2010, pp. 2866–2868.

[14] E. C. Giraldo *et al.*, "The Diamond Beam Loss Monitoring System at CERN LHC and SPS," in *Proc. IBIC'22*, Kraków, Poland, 2022, pp. 202–206. doi:10.18429/JACoW-IBIC2022-TU2C2

[15] G. Valentino *et al.*, "Comparison of LHC Collimator Beam-Based Alignment Centers to BPM-Interpolated Centers," in *Proc. IPAC'12*, New Orleans, LA, USA, May 2012, pp. 2062–2064.

[16] D. Belohrad, L. K. Jensen, O. R. Jones, M. Ludwig, and J. J. Savioz, "The LHC Fast BCT system: A comparison of Design Parameters with Initial Performance," CERN, Tech. Rep., 2010, CERN-BE-2010-010.

[17] S. M. Vigo *et al.*, "Beam lifetime monitoring using beam loss monitors during LHC Run 3," presented at IPAC'23, Venice, Italy, May 2023, paper THPL086.

[18] V. Moens, R. Bruce, S. Redaelli, B. Salvachua, and G. Valentino, "Comparison of LHC Beam Loss Maps using the Transverse Damper Blow up and Tune Resonance Crossing Methods," in *Proc. IPAC'13*, Shanghai, China, May 2013, pp. 1008–1010.

[19] S. Fartoukh, "Achromatic telescopic squeezing scheme and application to the LHC and its luminosity upgrade," *Phys. Rev. ST Accel. Beams*, vol. 16, no. 11, p. 111 002, 2013. doi:10.1103/PhysRevSTAB.16.111002

[20] J. Bosser and C. Bovet, "Wire Scanners For LHC," CERN, Tech. Rep., 1997, LHC-Project-Note-108.

[21] S. Papadopoulou *et al.*, "Monitoring and Modelling of the LHC Emittance and Luminosity Evolution in 2018," in *Proc. IPAC'19*, Melbourne, Australia, May 2019, pp. 3212–3215. doi:10.18429/JACoW-IPAC2019-WEPTS046

[22] S. Fartoukh *et al.*, "LHC Configuration and Operational Scenario for Run 3," CERN, Tech. Rep., 2021, CERN-ACC-2021-0007.

[23] C. E. Montanari, A. Bazzani, M. Giovannozzi, P. Hermes, and S. Redaelli, "Recent measurements and analyses of the beam-halo dynamics at the CERN LHC using collimator scans," presented at IPAC'23, Venice, Italy, May 2023, paper WEPA022.

[24] R. Tomas Garcia *et al.*, "HL-LHC Run 4 proton operational scenario," CERN, Tech. Rep., 2022, CERN-ACC-2022-0001.

Content from this work may be used under the terms of the CC-BY-4.0 licence (© 2023). Any distribution of this work must maintain attribution to the author(s), title of the work, publisher, and DOI

ISBN: 978-3-95450-236-3 ISSN: 2673-5350 doi:10.18429/JACoW-IBIC2023-TU3I04

COMPARISON OF DIFFERENT BUNCH CHARGE MONITORS USED AT THE ARES ACCELERATOR AT DESY

T. Lensch*, D. Lipka, R. Neumann, M.Werner
Deutsches Elektronen-Synchrotron DESY, Germany

Abstract

The SINBAD (Short and INnovative Bunches and Accelerators at DESY) facility, also called ARES (Accelerator Research Experiment at SINBAD), is a conventional S-band linear RF accelerator allowing the production of low charge ultra-short electron bunches within a range of currently 0.01 pC to 250 pC. The R&D accelerator also hosts various experiments. Especially for the medical eFLASH experiment an absolute, non-destructive charge measurement is needed. Therefore different types of monitors are installed along the 45 m long machine: A new Faraday Cup design had been simulated and realized. Further two resonant cavities (Dark Current monitors) and two Beam Charge Transfomers (Toroids) are installed. Both, Dark Current Monitors and Toroids are calibrated independently with laboratory setups. At the end of the accelerator a Bergoz Turbo-ICT is installed. This paper will give an overview of the current installations of charge monitors at ARES and compare their measured linearity and resolution.

INTRODUCTION

The SINBAD facility (Short and INnovative Bunches and Accelerators at DESY) hosts various experiments in the field of production of ultra-short electron bunches and novel high gradient acceleration techniques. ARES (Accelerator Research Experiment at SINBAD), is a conventional, 45 m long S-band linear RF accelerator allowing the production ultra-short electron bunches (fs to sub-fs) with high stability. The machine is operated with a repetition rate of 10 Hz with a charge range of 0.01 pC up to 250 pC. ARES is used for applications related to accelerator R&D in the field of advanced and compact longitudinal diagnostics and accelerating structures development, test of new accelerator components, machine learning and others. In the field of medical application studies an experiment has been set up to perform studies on cancer irradiation techniques with electron beams. For this experiment an absolute, non-destructive charge measurement is essential [1] .

As ARES is also related to Accelerator R&D several dedicated charge monitors had been installed: one Faraday Cup and a Dark Current Monitor (DaMon) at the gun section, one DaMon and two Beam Charge Transformers (Toroid) along the machine and one Bergoz Turbo-ICT [2] in-vacuum at the end of the beam line. An additional Bergoz in-air ICT [3] is installed 30 cm next to the T-ICT outside the beamline.

* timmy.lensch@desy.de

CHARGE MONITORS AT ARES

Faraday Cup

Simulations of at DESY existing Faraday Cup geometries showed 4 % to 22 % of primary and secondary charged particles escaping from the cup. This does not fulfill the ARES demand for an absolute charge measurement at the Gun. Due to this, a new Faraday Cup geometry had been simulated for an energy of 5 MeV. This geometry of a copper cup with an inner diameter of 15 mm, inner depth of 24 mm and an Aluminum plate inlay shows only 0.6 % of charged particles escaping from the Faraday Cup in the simulation. Also different beam configurations (pencil beam, out of center, angled beam) had been taken into account. None of them showed more than 1 % loss of charged particles [4]. Figure 1 shows the final design of the simulated Faraday Cup for ARES prior vacuum installation.

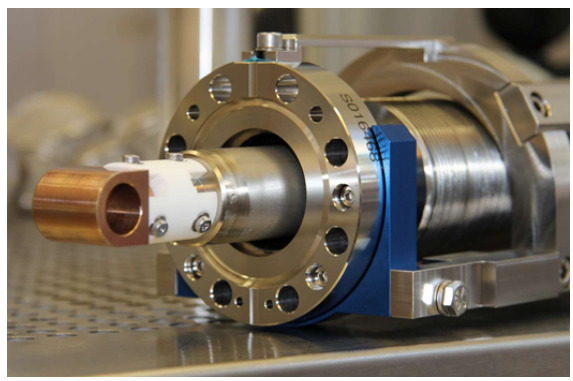


Figure 1: New Faraday Cup mounted with ceramic spacer on a mover rod.

The signal from the Faraday Cup is connected to an MicroTCA system [5] via a 15 MHz low pass and a pre amplifier. A Struck SIS8300-L2D [6] ADC board samples the pulse with 125 MS/s. The charge is reconstructed using a *pulse form fit* with three samples as described in Ref. [7]. For calibration of the electronics and cables an electrical pulse which corresponds to 1 nC is fed into the front end box input. An appropriate scaling factor is set in the software.

Beam Charge Transformers (Toroids)

Different types of in-house developed charge monitors based on transformers (Toroids) had been used at DESY machines since the 1980s. Beginning in 2010 an optimization of existing Toroids for the E-XFEL and FLASH accelerator had been started. These new monitors are based on one or two ferrite cores with four pickup coils, each consisting of a single winding. These four coils are combined outside the Toroid housing. The read out procedure is the same as with

Content from this work may be used under the terms of the CC-BY-4.0 licence (© 2023). Any distribution of this work must maintain attribution to the author(s), title of the work, publisher, and DOI

ISBN: 978-3-95450-236-3 ISSN: 2673-5350 doi:10.18429/JACoW-IBIC2023-TU3I04

Content from this work may be used under the terms of the CC-BY-4.0 licence (© 2023). Any distribution of this work must maintain attribution to the author(s), title of the work, publisher, and DOI

the Faraday Cup. Details of the optimization details can be found in Ref. [8]. An additional calibration coil is used to fed an electrical pulse which corresponds to 1 nC to the Toroid core(s). An appropriate scaling factor is configured in software to match the calibration pulse. Figure 2 shows a Toroid Beam Charge Monitor installed in ARES.

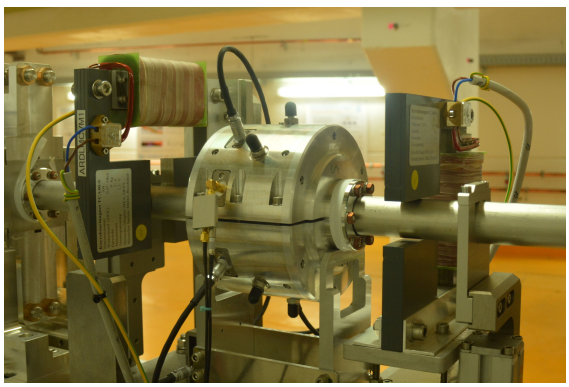


Figure 2: Toroid installed in the ARES accelerator. The diameter of the beam pipe is 34 mm, the length of the Toroid (flange to flange) is 150 mm.

Dark Current Monitors

The Dark Current Monitor (DaMon) was invented to measure dark current of accelerators with 1.3 GHz acceleration freqeuncy. The monitor consists of a stainless steel resonator with TM010 mode at 1.3 GHz with a loaded quality factor about 200. This results in a bandwidth of about 6 MHz and a decay time of 50 ns. The cavity is connected to a RF front end electronic (RFFE) which implements two channels. One is a dark current channel *DC* with a local oscillator, down conversion and a logarithmic detector. The second channel is for measuring charge, *Q* with a logarithmic detector only. For a 3 GHz accelerator like ARES, both channels, *DC* and *Q*, are used for charge measurement to increase the dynamic range. For calibration an Arbitrary Waveform Generator (AWG), which feeds a signal to the DaMon RFFE, is used. Details of the system and the calibration can be found in Ref. [9].

Bergoz Turbo ICT

At the very end of the beam line a Bergoz Turbo-ICT (T-ICT) is installed in vacuum. Together with the BCM-RF-E electronic the T-ICT is operated with a 10 Hz timing trigger in the Sample&Hold mode. After the T-ICT conversion has finished a trigger is given to a Keithley DMM7510 High Resolution Digital Volt Meter (DVM) which is read out over Ethernet [10]. A look up table, implemented in software with data from Bergoz' calibration to further improve the result. The measurement range given by Bergoz is 50 fC to 300 pC, the noise is 10 fCrms or 1% of bunch charge.

Bergoz ICT

For test purposes a Bergoz in-air ICT is installed direct after the end of the beamline, 30 cm after the T-ICT. A detailed description of the ICT principle can be found in Ref. [11]. The in-air ICT is read with an 12 bit oscilloscope, which is also doing averaging, integrating and scaling the 70 ns long pulse to get a value in pC. Figure 3 shows both, T-ICT in vacuum and the neighboured in-air ICT.

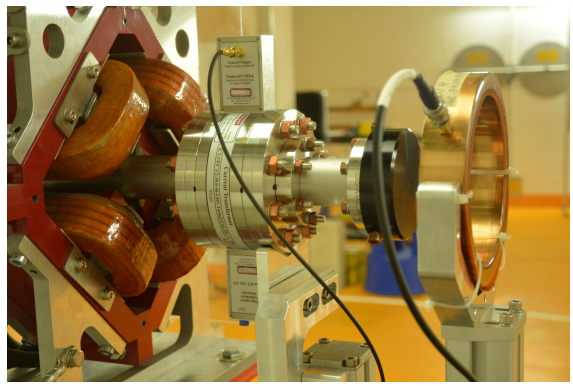


Figure 3: T-ICT (left) installed in vacuum, output window of the beam line (black cover in the middle) and the in-air ICT (copper colored toroidial shape on the right). The electrons are used for in-air experiments direct downstream the in-air ICT.

The ICT installation is improvised yet. Later the setup might be moved easily to other DESY machines which allows the installation in-air (*take-away-charge-reference*).

MEASUREMENTS

For the linearity and resolution measurements the ARES accelerator was setup with 100 % beam transport down to the T-ICT and the in-air ICT at (45 m). In total 14 different charges in the range from 0.1 pC to 153 pC at a bunch repetition rate of 10 Hz had been carried out. For each charge 500 values of each monitor had been taken synchronously. As the Faraday Cup measures destructive, its data had been taken independently (move FC in, take 500 values, move FC out, take 500 values for the other monitors, move FC in, change charge, ...). The DaMon *DC* channels are limited to less than 20 pC. Therefore a sweep from 0.1 pC to 13 pC had been carried out. The DaMon *Q* channels, the Toroids and the T-ICT had been measured with a sweep of 1 pC to 153 pC.

Linearity

The upper plots of the Figs. 4 to 8 show the monitor charge as a function of the Faraday Cup, the lower plots show the ratio of the monitor to Faraday Cup as a function of the Faraday Cup charge. The error bars shown are the standard deviation caused by beam charge variation.

Figure 8 shows the linearity fit slope, fit offset and the in-air ICT charges relative to the Faraday Cup. As this setup is improvised yet, this measurement should not be taken as a face value yet.

Resolution using Standard Deviation (rms)

A reference charge was defined by using all existing charge information (except the device under test), including also the

ISBN: 978-3-95450-236-3 ISSN: 2673-5350 doi:10.18429/JACoW-IBIC2023-TU3I04

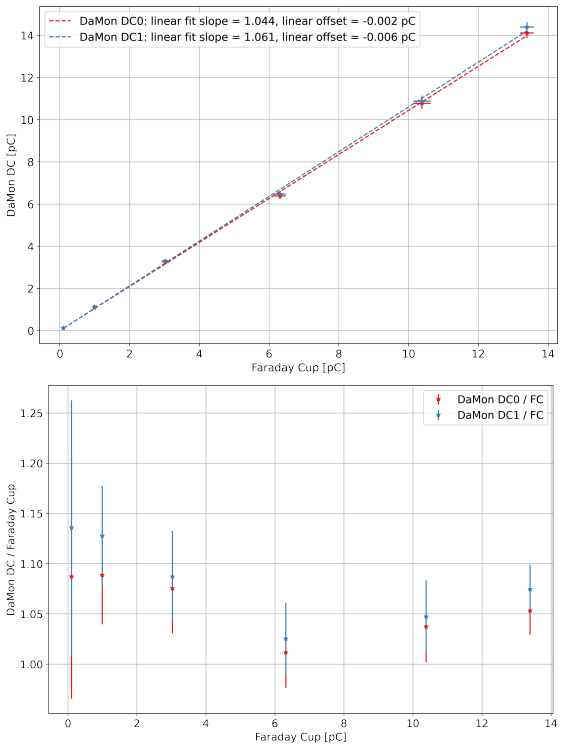


Figure 4: Linearity of the DaMon *DC* channel.

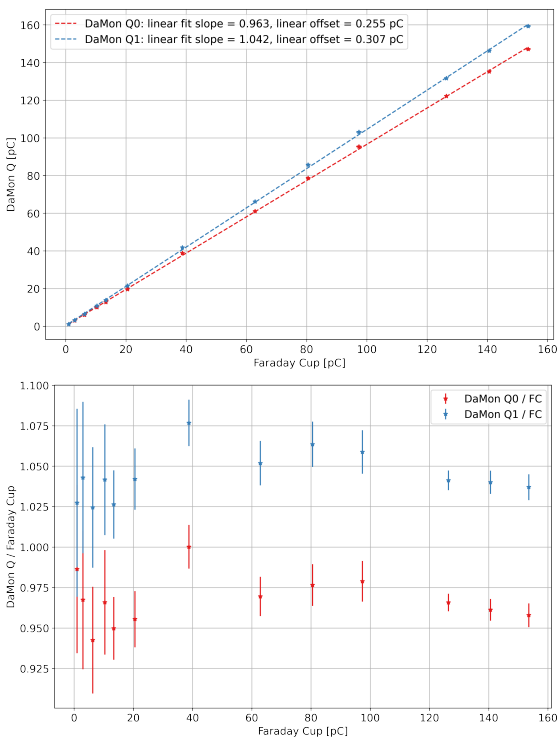


Figure 5: Linearity of the DaMon *Q* channel.

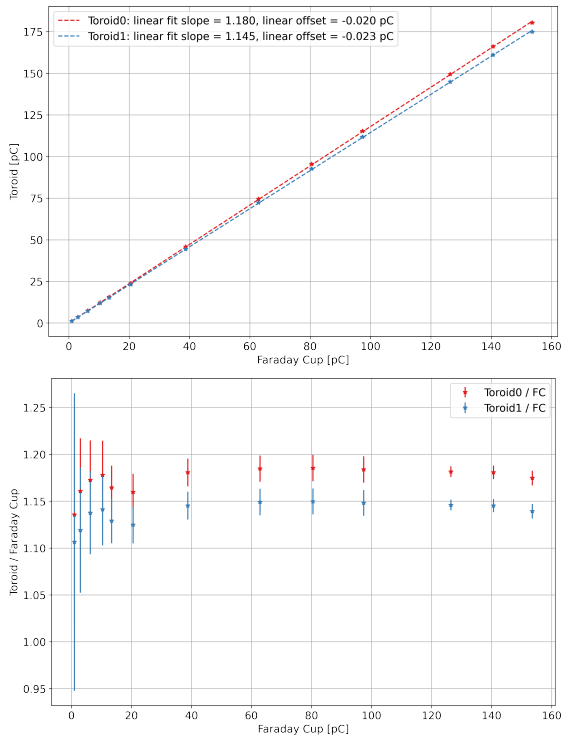


Figure 6: Linearity of the Toroids.

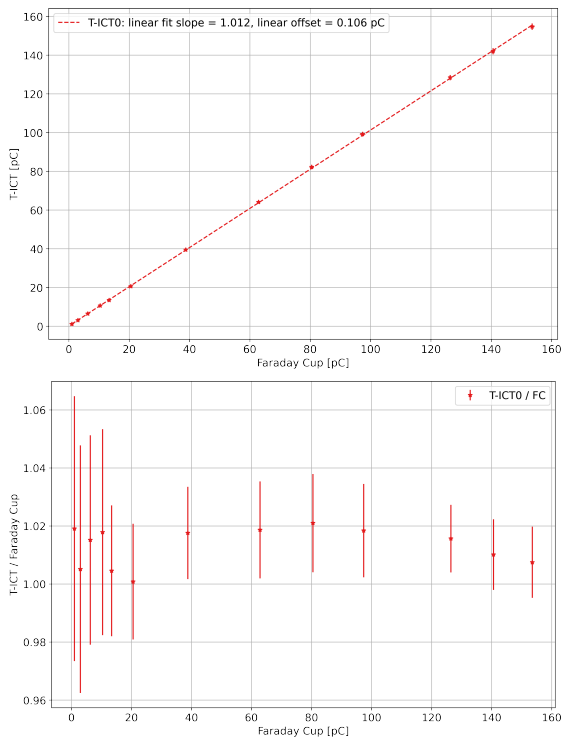


Figure 7: Linearity of the T-ICT.

existing Cavity BPMs. This reduced the statistical variation of the charge determination and it was used to determine the resolution of the monitor under test. This procedure is machine optics independent. A detailed description of this calculation can be found in Ref. [12]. To get better results, also charges measured by seven Cavity BPMs had been included. These devices can measure charge as well, but are not calibrated independent [13]. The resolution had been calculated for the DaMon channels *DC* and *Q*, the Toroids and the T-ICT. Figures 9 and 10 show the resolutions.

Content from this work may be used under the terms of the CC-BY-4.0 licence (© 2023). Any distribution of this work must maintain attribution to the author(s), title of the work, publisher, and DOI

ISBN: 978-3-95450-236-3 ISSN: 2673-5350 doi:10.18429/JACoW-IBIC2023-TU3I04

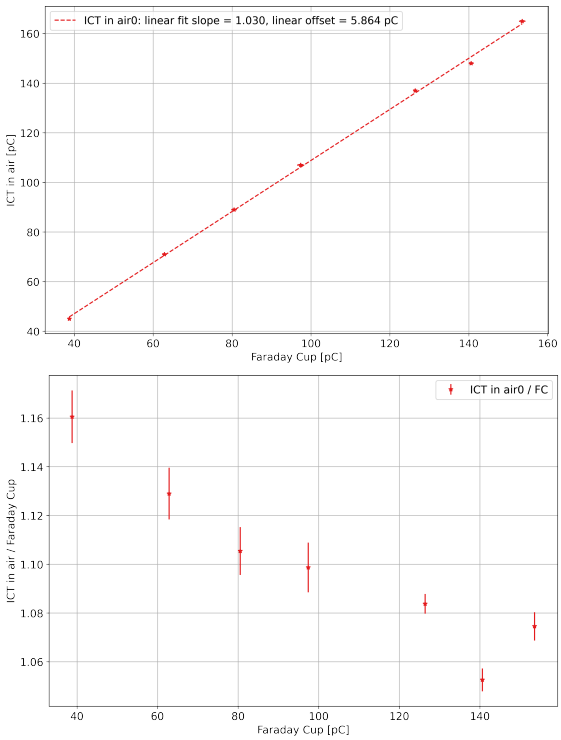


Figure 8: Top: measured charge of the in air ICT as a function of Faraday Cup charge; below the ratio of the in-air ICT to Faraday Cup charge as a function of Faraday Cup charge. Both in the range of 30 pC to 153 pC.

As the in-air ICT could not be measured synchronous to the other monitors, the resolution could not be determined.

Results

Table 1 shows the linearity and resolution measured at ARES.

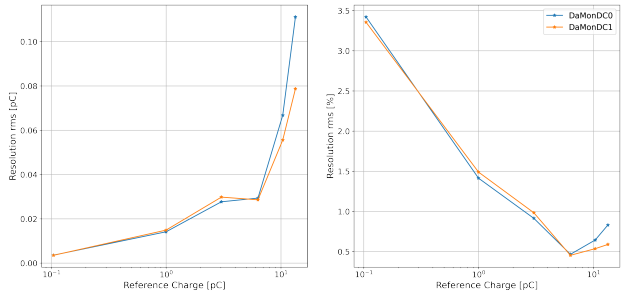


Figure 9: Absolute and relative resolution of the DaMon *DC* channels in the range of 0.1 pC to 13 pC.

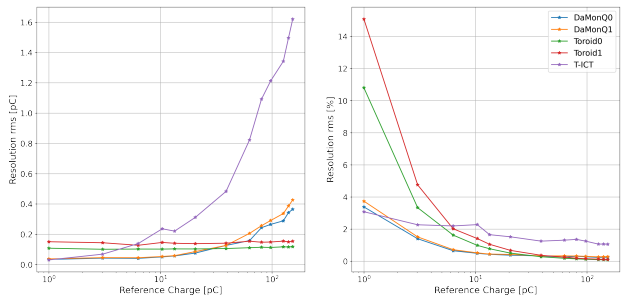


Figure 10: Absolute and relative resolution of DaMon *Q* channels, Toroids and T-ICT, each in the range of 1 pC to 153 pC.

The DaMon *DC* channels are limited to a maximum charge of about 20 pC. For a range from 0.1 pC to 13 pC the DaMon *DC* channels show reasonable linearity results. The resolution measured up to about 6 pC is the best of all charge monitors compared during this measurements.

For the charge range from 1 pC to 153 pC both, the DaMon *Q* channels and the T-ICT show reasonable results of linearity with a linear fit slope of almost 1 and an offset of close to 0 pC.

Table 1: Resolution results for all monitors. Upper values are the upstream monitor.

	DaMon DC	**DaMon Q**	**Toroid**	**T-ICT**
Charge Range	0.1 pC - 13 pC	1 pC - 153 pC	0.1 pC - 13 pC	0.1 pC - 13 pC
Linear fit Slope				
Monitor 1	1.04	0.96	1.18	1.01
Monitor 2	1.06	1.04	1.15	—
Linear fit Offset				
Monitor 1	-0.002 pC	0.26 pC	-0.02 pC	0.11 pC
Monitor 2	-0.006 pC	0.31 pC	-0.02 pC	—
Resolution	(@0.1 pC - @13 pC)	(@1 pC - @153 pC)	(@1 pC - @153 pC)	(@1 pC - @153 pC)
Monitor 1	4 fC - 111 fC 3.4% - 0.83%	34 fC - 366 fC 3.4% - 0.2%	108 fC - 119 fC 10.8% - 0.1%	31 fC - 1621 fC 3.1% - 1.1%
Monitor 2	3.7 fC - 90 fC 3.36% - 0.59%	37 fC -427 fC 3.7% - 0.23%	151 fC - 154 fC 15.1% - 0.1%	— —
Use for	Resolution <6 pC	Resolution >6 pC – 60 pC	Resolution >60 pC	Absolute charge

Content from this work may be used under the terms of the CC-BY-4.0 licence (© 2023). Any distribution of this work must maintain attribution to the author(s), title of the work, publisher, and DOI

ISBN: 978-3-95450-236-3 ISSN: 2673-5350 doi:10.18429/JACoW-IBIC2023-TU3I04

The Toroids show a linear fit slope of 18 respectively 15% higher compared to the Faraday Cup but also an offset of nearly 0 pC. Nevertheless, the relative plot in Fig. 2 shows good linear accordance to the Faraday Cup, so that a correction can easily be applied. Depending on the charge range, different areas of resolution could be determined in our setup. The DaMon *Q* channels show the best resolution between 6 pC – 60 pC, the Toroids for charges greater than 60 pC. As the upstream Toroid in ARES has a dual core installation the resolution is better (10.8%) than the downstream Toroid (15.8%), which only has a single core installed. For higher charges both Toroids converge to a resolution of 100 fC. The T-ICT's resolution might suffer from the installation in ARES: the cable between the T-ICT in the beamline and the Bergoz electronics outside had to be extended by about 30 m. The cable damping had been compensated, but environmental noise is captured anyway. However, the monitor is suitable for absolute measurements out of the box.

CONCLUSION AND OUTLOOK

Three DESY in-house developed monitors had been presented briefly. These monitors had been compared to each other and to two commercial available monitors (ICT and T-ICT) from Bergoz. Taking the new Faraday Cup as a (destructive) reference at the Gun Section it could be shown that the in-house developed (non destructive) Toroids and the DaMons are very linear compared to the Faraday Cup. Additionally the Bergoz T-ICT at the end of the beam line shows a very good linearity as well. Also the resolution of all (non destructive) monitors could be calculated. All this monitors can be read out with the required repetition rate of 10 Hz. In the future we would like to improve the calibration scheme of the Toroids. The in-air ICT can be moved and be used as a kind of *take-away-charge-reference* to easy cross-check charge measurements in other DESY accelerators.

ACKNOWLEDGEMENTS

We would like to thank for development, installation and commissioning of the charge monitors and all related work: Maike Pelzer, Jürgen Kruse, Christian Wiebers, Norbert Wentowski, Zlatan Pisarov, Klaus Knaack, Artem Novokshonov, Jörg Neugebauer, Sergey Strokov, Bastian Lorbeer, Hans-Thomas Duhme, Igor Krouptchenkov and Jorgen Lund-Nielsen† from the Diagnostics group. For their patience during our time consuming measurements and iterations we would thank also the ARES operation team: Florian Burkhart, Willi Kuropka, Hannes Dinter, Frank Mayet, Max Kellermeier and Sonja Jaster-Merz.

REFERENCES

[1] F. Burkart, R.W. Aßmann, H. Dinter, S. Jaster-Merz, W. Kuropka, F. Mayet, and *et al.*, "The ARES Linac at DESY", in *Proc. LINAC'22*, Liverpool, UK, Aug.-Sep. 2022, pp. 691–694. doi:10.18429/JACoW-LINAC2022-THPOJO01

[2] https://www.bergoz.com/products/turbo-ict/

[3] https://www.bergoz.com/products/ict/

[4] Sergey Strokov, private communication

[5] https://www.picmg.org/openstandards/microtca

[6] https://www.struck.de/sis8300-12.html

[7] M. Werner *et al.*, "A Toroid Based Bunch Charge Monitor System with Machine Protection Features for FLASH and XFEL", in *Proc. IBIC'14*, Monterey, CA, USA, 2014, pp. 521–524.

[8] M. Werner *et al.*, "Sensitivity Optimization of the Standard Beam Current Monitors for XFEL and FLASH II", in *Proc. DIPAC'11*, Hamburg, Germany, 2011, pp. 197–199.

[9] D. Lipka *et al.*, "Charge Measurement with Resonators at ARES", presented at IBIC'23, Saskatoon, CA, September 2023, paper TUP037, this conference.

[10] https://www.tek.com/de/products/keithley/digital-multimeter/dmm7510#

[11] K. B. Unser, "Measuring bunch intensity, beam loss and bunch lifetime in LEP", Report CERN-SL-90-27-BI", 1990, https://cds.cern.ch/record/209858

[12] N. Baboi *et al.*, "Resolution Studies at Beam Position Monitors at the FLASH Facility at DESY", in *Proc. BIW'06*, Batavia, IL, USA, May 2006, *AIP Conf. Proc.*, vol. 868, pp. 227–237. doi:10.1063/1.2401409

[13] B. Lorbeer *et al.*, "Cavity BPM Electronics for SINBAD at DESY", in *Proc. IBIC'22*, Kraków, Poland, Sep. 2022, pp. 413–415. doi:10.18429/JACoW-IBIC2022-WEP14

Content from this work may be used under the terms of the CC-BY-4.0 licence (© 2023). Any distribution of this work must maintain attribution to the author(s), title of the work, publisher, and DOI

ISBN: 978-3-95450-236-3 ISSN: 2673-5350 doi:10.18429/JACoW-IBIC2023-TU3C05

LOW INTENSITY BEAM CURRENT MEASUREMENT OF THE ASSOCIATED PROTON BEAM LINE AT CSNS

R.Y. Qiu, W.L. Huang, F. Li, L. Zeng, Muhammad Abdul Rehman, M.Y. Liu, Q.R. Liu, R.J. Yang, T. Yang, Z.H. Xu, Z.X. Tan
Institute of High Energy Physics, Chinese Academy of Sciences, Beijing, China
Spallation Neutron Source Science Center, Dongguan, China

Abstract

The Associated Proton beam Experiment Platform (APEP) beamline is the first proton irradiation facility to use naturally-stripped protons which come from H- beams interacting with the residual gas in the linac beampipe at CSNS. The stripped beam current, which is in the order of 0.1% of the original H- beam and approximately 10 microamperes, should be measured precisely to provide the proton number for irradiation experiments. Therefore, a low-intensity beam current measurement system was developed with considerations to eliminate the external interferences. An anti-interference design is adopted in this system with an elaboration of probes, cables and electronic low-noise technology to minimize the impact of environmental noise and interferences. This improves the signal-to-noise ratio and enables a more precise measurement of the microampere-level pulsed beam current. The system was installed and tested during the summer maintenance in 2021 and 2022. It shows a good agreement with the measurement of the Faraday cup.

INTRODUCTION

The linear accelerator of China Spallation Neutron Source (CSNS) consists of a negative hydrogen ion source, a 3 MeV radio frequency quadrupole accelerator (RFQ), and a 4-tank drift tube linear accelerator (DTL) [1]. The negative hydrogen ion beam is accelerated to 80 MeV and then injected into the Rapid Cycling Synchrotron (RCS) by charge-exchange stripping. The proton beam is then accelerated to 1.6 GeV and finally extracted to bombard the tungsten target for neutron production with a repetition rate of 25 Hz [3]. In the linac of CSNS, a portion of H- beam interacts with the residual gas. As a result, in the beampipe there are three types of particles with different charge states: H^- (~15 mA, 100~500 μs), hydrogen atom (H^0), and proton (H^+). The associated proton beam current is about 0.1% of the original H^- beam. Therefore, the APEP beam line is established from the bending magnet at the end of linac. The number of protons in the beam is a crucial parameter for irradiation experiments.

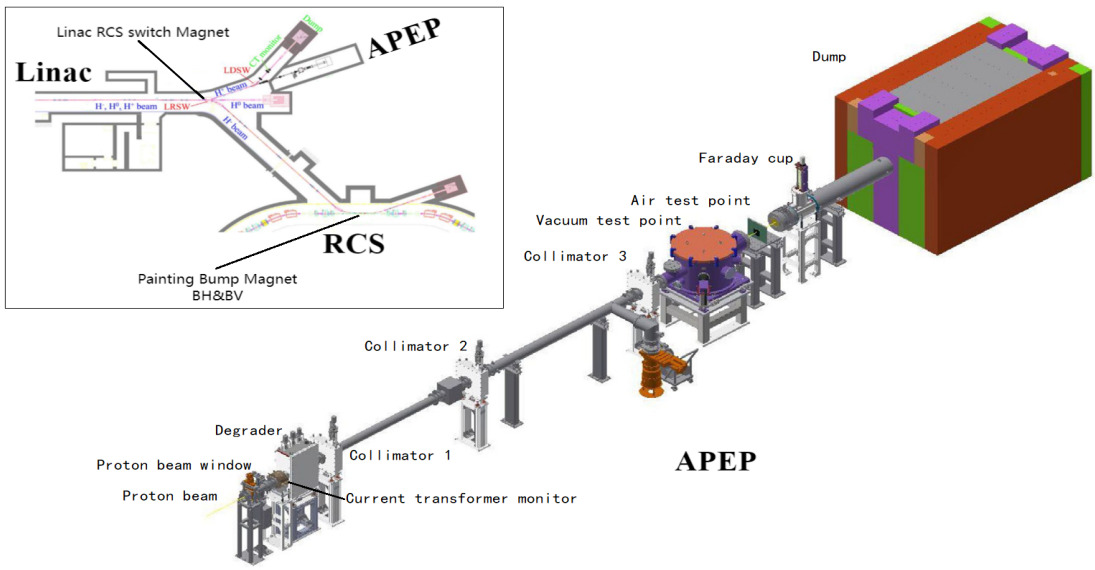


Figure 1: Layout of the APEP beam line. [2].

Figure 1 shows the layout diagram of the APEP area. There are three devices used for measuring beam intensity. The first one is the current transformer measurement system located at the entrance of APEP. In order to precisely measure this microampere-level beam intensity, a low-intensity beam current measurement system was developed in 2021. It achieved stable measurements by addressing external interferences in September 2022.The second device, located behind collimator3, is the beam intensity measurement system based on the secondary electron emission method. The third device is the Faraday cup beam intensity measurement device located in front of the DUMP. The two devices behind are currently undergoing debugging.

Content from this work may be used under the terms of the CC-BY-4.0 licence (© 2023). Any distribution of this work must maintain attribution to the author(s), title of the work, publisher, and DOI

ISBN: 978-3-95450-236-3 ISSN: 2673-5350 doi:10.18429/JACoW-IBIC2023-TU3C05

This article primarily focuses on the design of the micro-ampere-level beam intensity measurement system for the beam current transformer.

Table 1: Parameters of the Associated Proton Beam

Parameter	Value
Proton Beam Energy	80 MeV
Repetition Frequency	25 Hz
Number of Particles	~5.0*10^{10} ppp@100 kW
Macro Bunch Length	100 μs ~ 500 μs
Proton Beam Intensity	20 μA@400 μs,100 kW

SYSTEM DESIGN

Design of Beam Current Detector

Before developing a current transformer, several soft magnetic alloy materials were tested and compared. Finally, an iron-based soft magnetic alloy core was selected due to its high magnetic permeability (μ_r), low coercivity (H_c), high saturation magnetic induction (B_s) and low cost. In the design of the transformer, it is necessary to consider that the droop of the 500 μs macro pulse signal should be less than 1% within the pulse width, that is, $\tau_{droop} > 0.05$ s or $f_{low\text{-}cutoff} = 7$ Hz. According to the measured noise level of the experiment, the turns of the secondary coil N_s was selected as 50. An additional coil of 1 turn was wound for the online calibration. Since the inner diameter of the vacuum pipeline is Φ110 mm, a soft magnetic core of Fe-based nanocrystalline alloy (nominal relative magnetic permeability $\mu_r \approx 90000$@10 Hz) with an inner diameter $D_i = 130$ mm, outer diameter $D_o = 160$ mm and longitudinal length $h = 25$ mm was selected for winding the current transformer. The equivalent inductance L_s of the sensor was calculated according to Eq. (1) as 0.175 H. It was measured by an LCR meter (HIOKI IM3536) to be 0.176 H@10 Hz, which is close to the theoretical calculation.

$$L_s = N_S{}^2 \frac{\mu_0 \mu_r f_{fill}}{2\pi} h \ln \frac{D_o}{D_i} \quad (1)$$

Here in Eq. (1): $\mu_0 = 4\pi \times 10^{-7}$ H/s is the vacuum magnetic permeability and $f_{fill} = 0.75$ is the filling factor of the ribbons forming the soft magnetic core. The input impedance of electronics r = 2.5 Ω, leads to the droop time constant of the pulse signal $\tau_{droop} = L_s/r = 0.062 > 0.05$ s, which meets the design requirements.

As shown in Fig. 1,the APEP current transformer is installed at the downstream of a bending magnet, which is used to guide the associated proton beam to the L-Dump or the APEP beam line. The stray magnetic field may cause the current transformer of APEP-CT to be magnetically saturated and fail to accurately measure the beam current strength of associated protons, so it is necessary to design a magnetic shield semi-surrounding the outside of the current transformer, as the inner shielding shown in Fig. 2. Considering the environmental stray magnetic field, a double-layered DT4 magnetic shield is designed according to Eq. (2). In this formula, $p=b^2/a^2$, where a and b are respectively the outer diameter and inner diameter of the cylindrical magnetic shield layer, and μ_r is the relevant permeability of magnetic material [4]. The magnetic shielding efficiency of a double-layered DT4 shield is calculated as a product of that of each layer with a radial thickness of 1 mm, that is, 37.8×38.7=1463, which is better than that of a single layer permalloy shield (S of which is 1220) with a radial thickness of 2.0 mm and a same outer diameter of Φ162 mm. The comparison of different magnetic shield is showed in Table 2. What's more, the material of DT4 is easy to process and costs much less. It can be seen that compared with a single-layer permalloy shield, this scheme has low cost and can meet the requirements of current transformers for magnetic shielding effect.

$$S = \frac{4\mu_r p}{(\mu_r^2+1)(p-1)+2\mu_r(p+1)} \quad (2)$$

Table 2: Calculation of Different Magnetic Shields as the Inner Shielding of APEP-CT

Layer Material	b mm	a mm	p	μ_r	S
DT4	162.0	160.0	1.0252	6000	37.8
DT4	158.0	156.0	1.0258	6000	38.7
Permalloy	162.0	158.0	1.0513	106	1220

A fully-enclosing outer shield of the APEP-CT sensor acts as a low-impedance path of the wall current and an RF shielding [5].

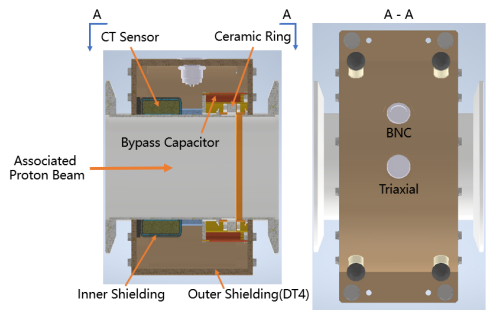


Figure 2: APEP CT sensor and magnetic shields.

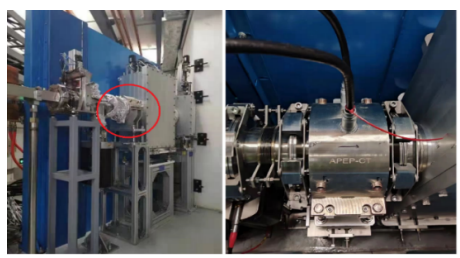


Figure 3: Proton beam intensity detector installed at the APEP tunnel.

Design of Electronic Circuit

As a current transformer, when the sensor detects the proton beam current, the induced output signal is a very weak current (here N_s=50). In the design of electronics, we use a transimpedance amplifier as the first-stage IV conversion chip. For instance, a 10 μA beam current passes through the sensor core with the 50-turn secondary coil, the input current of the electronics will be 200 nA. The input

Content from this work may be used under the terms of the CC-BY-4.0 licence (© 2023). Any distribution of this work must maintain attribution to the author(s), title of the work, publisher, and DOI

ISBN: 978-3-95450-236-3 ISSN: 2673-5350 doi:10.18429/JACoW-IBIC2023-TU3C05

Content from this work may be used under the terms of the CC-BY-4.0 licence (© 2023). Any distribution of this work must maintain attribution to the author(s), title of the work, publisher, and DOI

and feedback resistances of the electronics are r = 2.5 Ω and R_f = 10 kΩ * 20 separately. When selecting a low-noise operational amplifier, the input bias current I_b cannot be ignored. The bandwidth of the electronics should be designed to minimize high frequency noise introduction while meeting the rise time requirement. The circuit diagram is shown in Fig. 4. The electronic baseline is automatically adjusted by a technique of baseline dynamic feedback [6].

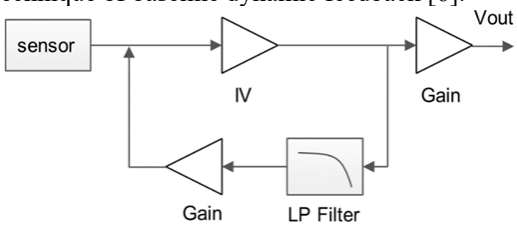


Figure 4: Diagram of CT electronics.

Experiments on Cable Selection and Shielding

We tested two kinds of cables to transport the signal from the sensor output to the electronics input. A comparison was made among the noise measurements of four-core cables (two-core twisted pair with braided outer shield) and triaxial cables under different grounding methods with the same sensor and electronics. It showed that the best signal-to-noise ratio was obtained when the triaxial cables were grounded at both ends. After the multi-point grounding test, it was found that outermost layer of triaxial cable was grounded to the vacuum pipeline at the sensor end, and the electronic end was grounded to cabinet ground to achieve the best effect, as shown in Fig. 5.

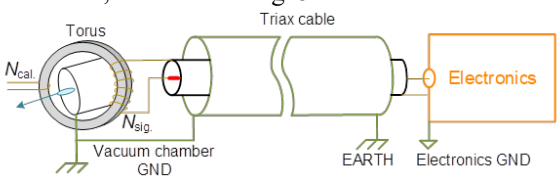


Figure 5: Diagram of the triax cable grounding to minimize noises.

SYSTEM CALIBRATION AND TESTING

System Calibration

We used a high precision pulsed current source Keithley 6221 to generate a current of square wave with a 500 μs pulse width in a range of 2~10 μA, which passed through the calibration coil of the APEP-CT sensor to simulate the beam current. The induced current in the secondary coil is input to the electronics via a 25 m triaxial cable and the electronics output voltage is measured by an oscilloscope or JYTEK DAQ for the data acquisition and waveform display. The calibration formula is obtained by a linear fitting of the electronic output amplitude with the simulated input beam current intensity. Through this formula, the undertest beam intensity can be calculated along with the background de-noising at a homo-metric beam-off zone during operation. Thereby we realized a precise low intensity measurement of the associated pulsed proton beam. After the system commissioning, the rise time of the electronics achieved < 10 μs, the droop time is < 1%/ms, and the relevant error of the calibration data is within 1% FS, as shown in Figs. 6 and 7. The parameters of this low intensity measurement system meet the design requirements.

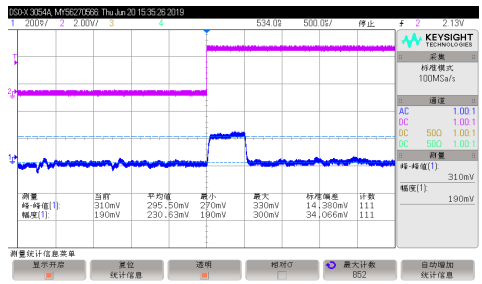


Figure 6: The blue signal is the electronics output with 1 μA calibrated input current.

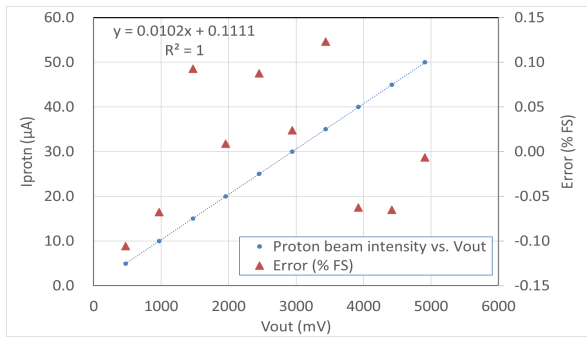


Figure 7: CT Electronics calibration data.

Troubleshooting and Experimentation for Interference Investigation

The low beam intensity measurement system was installed in the APEP tunnel during the summer maintenance in 2021. In the following accelerator operation, we performed several beam tests with this system, which needs guiding the beam to the APEP beamline. It performed abnormal due to significant interferences. The interference was large and stable, characterized by a fixed frequency relating to the beam current. A Faraday cup at the end of the APEP beam line detects the same interference signal, but with a relatively smaller impact, shown in Fig. 8.

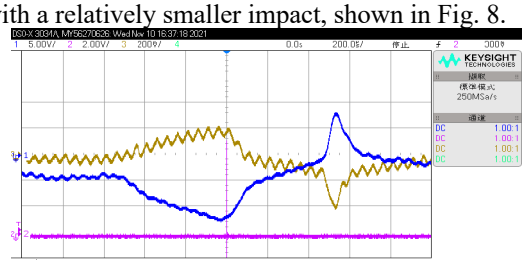


Figure 8: Measurement of the APEP-CT and Faraday cup electronic output waveforms. Blue trace is the signal of Faraday Cup. Yellow trace is that of APEP-CT. Purple trace is the timing trigger signal.

We made a thorough examination of the CT interference sources along the APEP beamline and RCS. The magnetic elements such as Linac RCS Switch Magnet, Painting Bump Magnet at the RCS injection zone, and Extraction Magnets at the extraction zone were sequentially shut

ISBN: 978-3-95450-236-3 ISSN: 2673-5350 doi:10.18429/JACoW-IBIC2023-TU3C05

down. The position of the magnet is shown in Fig. 1. The BH (Horizontal painting bump magnets) and BV (vertical painting bump magnets) are used for the horizontal and vertical painting respectively in the phase space of the injected beam. The main contribution of interference is from BH, followed by BV, which has a high similarity to the current curve of the power supply during the beam injection in the phase space painting mode. The correlation indicated that the interference was transmitted from the orbit bumper to the APEP-CT sensor along the accelerator vacuum pipe. The distance is about 55 meters. While other interference effects to the APEP-CT are small enough to be ignored.

Due to the consistent shape and amplitude of the interference signal, the DAQ system is triggered by the Timing system, allowing it to collect the interference signal once without a beam and save it as the background interference signal. Subsequently, for each subsequent signal collection with a beam, the interference signal is subtracted in order to restore the beam signal.

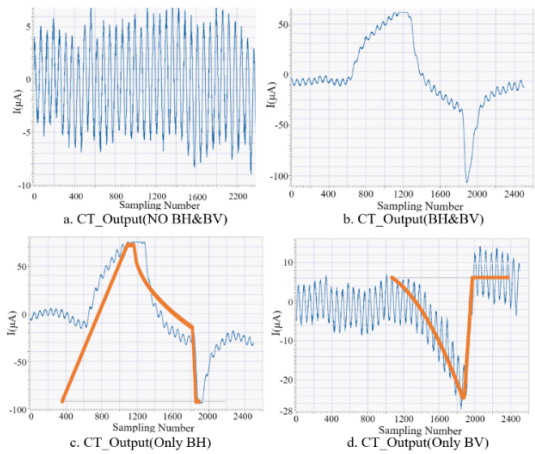


Figure 9: Output of APEP-CT electronics under different accelerator operation conditions. Pic (a) without BH and BV magnets operation. Pic (b) with the BH & BV magnet enabled. Pic (c) with only the BH magnet enabled. Pic (d) with only the BV magnet enabled.

To keep the interferences and high harmonics of the beam out of the sensor cavity, a bypass capacitor was designed (as shown in Fig. 2), and installed during the summer maintenance in 2022. The design principle of the bypass capacitor is described in Ref. [7]. The wall current splits in two: the high frequencies pass through the capacitance of the ceramic gap, which cancel the high frequency part of the beam "seen" by the sensor, and the low frequencies follow the wall current bypass, therefore do not pass through the sensor hole. Here, we built a capacitor over the ceramic gap with layers of copper foil separated by a layer of 100 μm-thick Kapton foil. The cavity impedance was dominated by the nanocrystalline core, which is measured to be 63.8 Ω@1 kHz and will be much bigger in higher frequencies. The bypass capacitance is designed as 5 nF, allowing the main part (<50 kHz) of the beam passing through the sensor hole. To obtain the desired capacitance value, the overlapping area is obtained by [8]:

$$S = {C\,d}/{\varepsilon_r \varepsilon_0} \qquad (3)$$

where: C is the capacitance [F],

$S = 1.61\times10^{-2}$ is the overlapping area [m^2],

$d = 1\times10^{-4}$ is the dielectric thickness [m],

ε_r is the relative dielectric constant, 3.5 for Kapton polyimid,

ε_0 is the dielectric constant 8.86 x 10^{-1}.



Figure 10: A bypass capacitor over the ceramic gap was built in the APEP-CT sensor.

Test Results

After the bypass capacitor was installed in the APEP-CT sensor, we successfully measured the associated proton beam in low intensity, shown in Fig.11. It was observed that the interference from the BH and BV magnets diminished significantly, and in fact, became barely noticeable. The signal-to-noise ratio of the beam signal was improved, and the amplitude of the pulsed associated proton beam intensity is clearly measured as 16.8 μA. The blue waveform represents the signal from the APEP-CT system, while the red waveform represents the current intensity signal measured by the Faraday cup after the beam passes through the energy degrader.

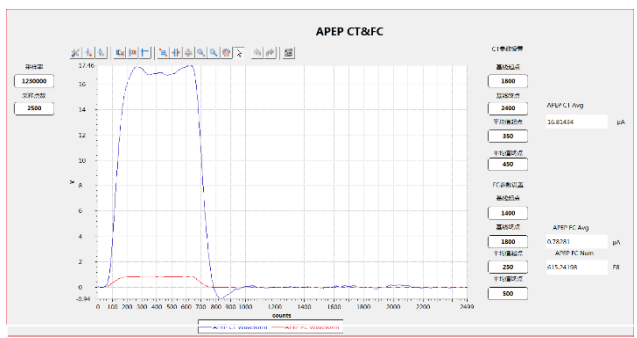


Figure 11: Output of the electronics of the APEP-CT and Faraday cup.

CONCLUSIONS

In the beam line of the Associated Proton beam Experiment Platform at CSNS, the proton beam intensity is a crucial parameter for irradiation experiments. The APEP-CT system achieves a signal-to-noise ratio improvement and meets the design specification for microampere-level current intensity measurement by implementing methods such as, the bypass capacitance design, the cable shielding and grounding methods, a low-noise electronic with the correct LP-filter design, and background noise subtraction algorithms in DAQ.

Content from this work may be used under the terms of the CC-BY-4.0 licence (© 2023). Any distribution of this work must maintain attribution to the author(s), title of the work, publisher, and DOI

ISBN: 978-3-95450-236-3 ISSN: 2673-5350 doi:10.18429/JACoW-IBIC2023-TU3C05

REFERENCES

[1] S. Wang, Y. An, S. Fang *et al.*, "An overview of design for CSNS/RCS and beam transport," *Sci. China Phys. Mech. Astron,* vol. 54, no. 2, pp. 239–244, 2011. doi:10.1007/s11433-011-4564-x

[2] Yingyi Liu, Hantao Jing *et al.*, "Physical design of the APEP beam line at CSNS," *Nuclear Insrum. Methods Phys. Res. Sect. A,* vol. 1042, article id. 167431, 2022. doi:10.1016/j.nima.2022.167431

[3] S. Y. Xu, "Beam Commissioning Experience of CSNS/RCS", in *Proc. IPAC'19,* Melbourne, Australia, May 2019, pp. 1012-1014. doi:10.18429/JACoW-IPAC2019-MOPTS068

[4] G. Feng and Z. He, "Calculation and simulation of geomagnetic field shielding effectiveness of projectile body" [in Chinese], *Acta Metrologica Sin*., vol. 31, pp. 141-144, 2010. doi:10.3969/j.issn.1000-1158.2010.02.11

[5] Bergoz Instrumentation, *AC Current Transformer User's Manual*, Rev. 5.4, 2021.

[6] Q. Zhou and Z. Wang, "A DC-servo baseline restorer and its implementation in biomedical instrumentation", in *Proc. SPIE'06*, vol. 6040, pp. 320-325, 2005. doi:org/10.1117/12.664226

[7] W.L. Huang *et al.*, "A Dual Functional Current Monitor for Stripping Efficiency Measurement in CSNS", in *Proc. IBIC'19,* Malmö, Sweden, Sep. 2019, pp. 96-99. doi:10.18429/JACoW-IBIC2019-MOPP011

[8] Bergoz Instrumentation, *New Parametric Current Transformer User's Manual*, Rev. 1.1, 2014.

Content from this work may be used under the terms of the CC-BY-4.0 licence (© 2023). Any distribution of this work must maintain attribution to the author(s), title of the work, publisher, and DOI

ISBN: 978-3-95450-236-3 ISSN: 2673-5350 doi:10.18429/JACoW-IBIC2023-TUP002

DEVELOPMENT OF BUNCH POSITION MONITORS TO OBSERVE SUDDEN BEAM LOSS OF SuperKEKB RINGS

Makoto Tobiyama, Hitomi Ikeda, Gaku Mitsuka
KEK Accelerator Laboratory, 1-1 Oho, Tsukuba, Japan
also Department of Accelerator Science, SOKENDAI, Tsukuba, Japan

Abstract

In the SuperKEKB rings, we have encountered extremely fast beam losses occurring primarily within one to two turns in some parts of the bunch train. Such sudden beam loss induced severe failure in the vertical collimator heads, quenches on the superconducting final quadrupoles, and damage on the Belle II detector in some cases. It is essential to investigate the cause and take countermeasures. This paper presents the phenomena clarified by the bunch current and position monitor of the bunch feedback system. The upgrade plan for the existing monitor, and recently developed simple monitors installed in the suspected area is also introduced.

INTRODUCTION

The SuperKEKB collider consists of 7 GeV electrons (HER) and 4 GeV positron (LER) rings with the circumference of 3 km. To achieve much higher luminosity than previous KEKB collider, the nanobeam collision method was adopted with low emittance and low x-y coupling. Up to 2022b runs, new world record of highest luminosity of $4.7 \times 10^{34}\mathrm{cm}^{2}\mathrm{s}^{-1}$has been achieved with lower beam current than KEKB, with β_y*=1 mm which is much shorter than the natural bunch length of ~6 mm [1]. The beam currents were 1.3 A for LER and 1.1 A for HER with the stored number of bunches of 2249, which corresponds to almost 2 RF bucket filling pattern. The next target of the luminosity after the long shutdown 1 (LS1) form Jun 2022 to Dec 2023 is to increase the luminosity more than $10^{35}\mathrm{cm}^{-2}\mathrm{s}^{-1}$ as soon as possible. During luminosity runs, we have encountered many so-called sudden beam loss (SBL) events on both ring which losses some part of bunch train within one or two turns when we have exceeded the bunch current of some threshold value (~0.65 mA for LER) [2]. The SBL usually damages the head of vertical beam collimators (and other accelerator components), quenches the final focusing superconducting magnets (QCSs), and causes huge backgrounds to Belle-II detector. Since the luminosity will be proportional to the bunch current product, those limitations on the bunch current are a big obstacle to achieve target luminosity. To understand the cause of SBL, and to take countermeasure to it, it is essential to monitor the beam behavior just before the SBL event, such as the bunch-by-bunch position and currents, the fastest beam loss points along the ring, vacuum burst if exist, etc.

We have used the bunch oscillation recorders (BORs) and bunch current monitors (BCMs) as the by-products of the bunch feedback systems installed in the ring to observe the SBL. Though the BORs and BCMs can separate the bunch information with the minimum bunch space of 2 ns, they have large limitations on such very quick event because of the location of the monitor is only one position per ring: it is impossible to estimate the cause point.

We have developed the simplified, low-cost BOR to place it in the suspicious point to observe the rough bunch oscillations and intensities. We are also trying to collect more detailed data by effectively using the existing system. The main parameters of the SuperKEKB rings on 2022b is shown in Table 1.

Table 1: Main Parameters of SuperKEKB in 2022b Runs

	HER	LER
Energy (GeV)	7	4
Circumference (m)	3016	
Maximum beam current (mA)	1099	1321
Max. bunch current (mA)	1	1.5
Natural bunch length (mm)	5	6
RF frequency (MHz)	508.886	
Harmonic number	5120	
Synchrotron Tune	0.028	0.024
Momentum compaction	0.00045	0.00032
L. damping time (ms)	29	23
Natural Emittance (nm)	4.6	3.2
Peak luminosity ($\mathrm{cm}^{-2}\mathrm{s}^{-1}$)	$4.7\mathrm{x}10^{34}$	
Bunch current monitor	1	1
Bunch oscillation monitors	3	3

SUDDEN BEAM LOSS

Monitors to Measure the Sudden Beam Loss

We have post-mortem monitor system to measure the bunch positions (x, y and longitudinal) and bunch intensity just before the beam abort event (BORs and BCM). As we use the same bunch position / intensity detector for the bunch feedback systems that down convert the $4 \times f_{RF}$=2 GHz components of the bunch signal, the outputs are proportional to both the bunch intensity and the bunch position distortion. The 18k10 digitizing board mainly consists of a fast 8-bit ADC (MAX108), a Spartan6 (XC6SLX45) daughter card with the form for a SO-DIMM card (Mars MX1) and VME-IF CPLDs [3]. They are mounted on a double width, 6U VME card. As we use the

Content from this work may be used under the terms of the CC-BY-4.0 licence (© 2023). Any distribution of this work must maintain attribution to the author(s), title of the work, publisher, and DOI

ISBN: 978-3-95450-236-3 ISSN: 2673-5350 doi:10.18429/JACoW-IBIC2023-TUP002

Content from this work may be used under the terms of the CC-BY-4.0 licence (© 2023). Any distribution of this work must maintain attribution to the author(s), title of the work, publisher, and DOI

same RF signal (=509 MHz) as the ring to drive the ADC, the recorded information is completely synchronized to that from the bunch in the ring. During normal operation, those BORs and BCM are triggered by the quick intensity drop of DCCT such as beam abort event and record 4k turns before the trigger. The button electrodes for bunch feedback are placed in the Fuji straight section where almost no dispersion remains.

We have two sets of Libera Briiliance+ position detector per ring to also measure the post-mortem information in tern-by-turn mode, with roughly 90° of betatron phase advance at OHO straight section also with dispersion free. In LER, we also have another Libera Brilliance+ installed in the arc section with larger horizontal dispersion.

The beam loss monitor system is used to trigger the beam abort to protect the Belle II detectors and accelerator hardware. Ion chambers (ICs), PIN-photodiodes, and optical fiber systems are used as the beam loss monitoring sensors; most of the PINs are placed to the collimators of each ring to identify the ring where beam loss has occurred. ICs, on the other hand, are installed thought the tunnel and cover a larger space. Location of collimators are shown in Fig. 1. Normally it needs about 5-30 μs to abort the beam after the beam abort request.

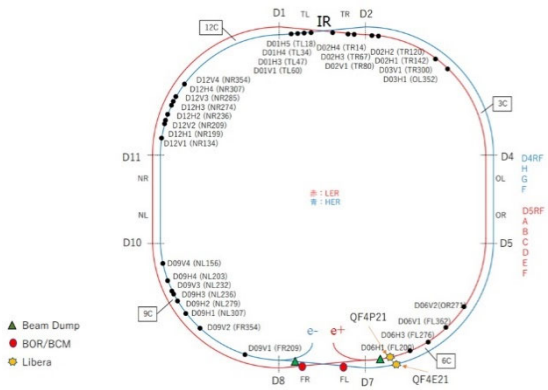


Figure 1: Location of the beam collimators of SuperKEKB ring.

Example of Sudden Beam Loss (SBL) Event

Figure 2 shows an example of the bunch current change for HER and LER, where the first row show the bunch current and the second row show the difference in bunch current from the previous turn 6-7 turns before the beam abort; this corresponds to the loss of the bunch current from the previous turn [3]. Part of the bunch train suddenly disappears just before the abort. Such beam losses had occurred in both HER and LER but SBLs in LER were much damaged the head of collimators, caused QCS quenches and damaged the inner-most detector of Belle-II. In the SBL of Fig. 2, the first and largest beam loss was recorded in the PIN diode around D6V1 vertical collimator but other PINs of collimators downstream of D6V1, optical fiber loss monitor around OHO straight section and Belle-II detector showed fast and significant beam loss [4].

Bunch oscillation from BORs have been measured simultaneously with the bunch current, the orbit can be estimated from the data. An example of the orbit behavior is shown in Fig. 3. Just before the beam loss begins, the orbit has slightly changed but the amount of change was small, on the order of 0.1 mm at the FB monitor. Even after the beam loss, the change in orbit was the order of 1 mm which might not be easy to explain the bunch loss with the excursion outside physical limit by the collimator.

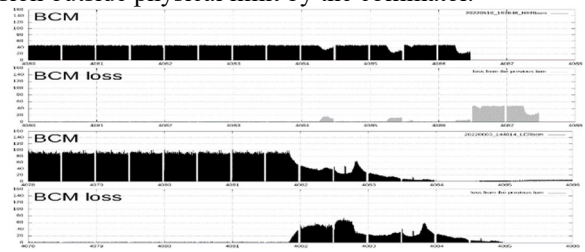


Figure 2: An example of the bunch current change of HER (upper) and LER (lower).

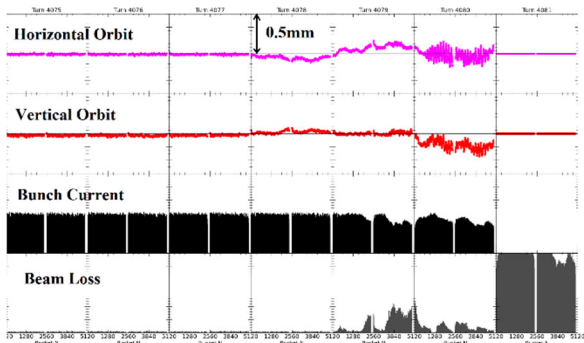


Figure 3: An example of bunch orbit variation and beam loss of LER.

We have also checked the post-mortem record (roughly 1 s before the abort) of the Libera using turn-by-turn mode. No significant orbit change was found in OHO and arc data. The beam size fluctuations just before SBL has been measured using an X-ray beam size monitor (XRM) with an ultrahigh speed CMOS camera to take 1 μs gate data at the revolution frequency of 99 kHz. Up to now no sign of a significant change in vertical beam size before the SBL has been observed. Vacuum pressure bursts have been observed all over the place and rarely repeat in the same section except at the collimators. Though some part of such vacuum burst might be the result of beam loss rather than the cause of the SBL, the collimator section, especially with damaged heads are still suspicious.

The known features of the SBL in LER are summarized as follows:

1. Some parts of the bunch train were lost in one or two turns without growth of oscillation: completely different from the normal coupled-bunch instabilities.
2. There appears to be a bunch current threshold (~0.65 mA/bunch) for the occurrence of SBL. The correlation with the total beam current appears to be rather weaker.
3. Beam loss mainly starts around D6V1 collimator where the effective vertical gap was the narrowest in the ring. There exist some SBL events which started D2V1 collimator when we occasionally operated the

ISBN: 978-3-95450-236-3 ISSN: 2673-5350 doi:10.18429/JACoW-IBIC2023-TUP002

vertical gap of D6V1 larger due to the damaged heads of the collimator.

4. The BOR data have shown no significant beam excursion just before the SBL. It is strongly suspected that there was a strong kicking source between the Fuji-straight section and D6 arc section where first beam loss occurred.

Identifying the components where the beam is suddenly kicked is essential to understanding and taking countermeasure to the SBL.

UPGRADE PLAN FOR THE EXISTING BUNCH POSITION MONITORS

Since the BORs can record the position data in one location of the ring, it is essentially impossible to simultaneously determine the position and the beam divergence at that time. It is desirable to add the bunch position data with different betatron phase simultaneously.

In our transverse (horizontal and vertical) bunch feedback system, we have constructed two independent feedback loops in both HER and LER, with the betatron phase advance roughly 60 to 90 degrees at the monitor locations. The iGp12 digital filters [5] has two data acquisition functions; one with external SRAM of 12MB, which corresponds about 2.4 k turn of position data, and the other is the block memory (BRAM) in a FPGA. As the SRAM data is normally used to monitor the status of the feedback during operation, especially to check whether the feedback loop is clearly resistive or not, and also to perform the transient-domain measurements to estimate the unstable modes of coupled-bunch instabilities, it is not good idea to stop the automatic data acquisition and wait for the beam loss trigger. On the other hand, though the size of the block RAM is short, about 96 turns of data, it should work to get the real phase space information in the case of SBL. The EPICS software sequencer has been developed to monitor the second hardware trigger of iGp12s which is the same beam loss timing as the BOR trigger and transfer the BRAM data to the NAS. After the restart of the ring operation, the calibration data will be taken to get the fine conversion factor to the position.

SIMPLIFIED BUNCH OSCILLATION/INTENSITY MONITOR

To find the source point of the sudden beam kick, it is needed to spread the BOR like monitor before and after the suspicious components in the ring. Since the cutoff frequency of the vacuum chamber in the arc section is much lower (about 0.9 GHz) than that of bunch feedback section of Fuji straight section (about 2.8 GHz), we will not be able to use the same RF circuit of BOR as the bunch position detector. Moreover, the existing BOR system is too expensive and too complicated in setup at new location. During the operation of 2022b, we have tried to construct simplified bunch oscillation / intensity monitor system based using inexpensive 4-ch 2.5 GSPS digital oscilloscope of analog bandwidth of 1 GHz and connect it the existing BPM just before the D6V1 collimator. Figure 4 shows the block diagram of the system.

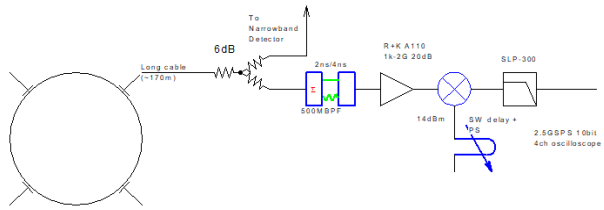


Figure 4: Block diagram of simplified BOR at 2022b.

We have split the existing BPM signal into two ways using 6 dB power splitters. 2-tap cable-type comb filters of 508 MHz were used to enhance f_{RF} component of the beam. Though the bunch signal separation less than 4 ns will be impossible due to the lower frequency detection, still the bunch position information could give us enough information on the source of the kick. The signal was down converted with the same RF signal and after the 300 MHz Bessel-type low pass filter (LPF), the detected signal was recorded by the digital oscilloscope. To rebuild the horizontal and vertical bunch position and intensity, off-line calculation process using 4-ch data has been prepared.

Unfortunately, this system did not work as expected. At first, as the isolation of double-balanced mixer and RF amplifier was not enough (about 70 dB), leaked LO signal had disturbed the narrowband detector. Moreover, we could not reconstruct the position data even with the known large bunch oscillation at the wrong injection time. On the other hand, the bunch intensity was almost successfully reconstructed.

We speculate that the reason for the poor reconstruction is the insufficient resolution (<10bit) of the oscilloscope. By employing RF hybrid circuit to subtract the analog signal before the oscilloscope, the position signal should have much better S/N.

We have developed the 509 MHz analog hybrid circuit which solve the signals of diagonal BPM, as shown in Fig. 5. The output of the hybrid will be directly sampled by the oscilloscope without analog down conversion. After data transfer to server CPU, the numerical I/Q detection will be done with off-line mode.

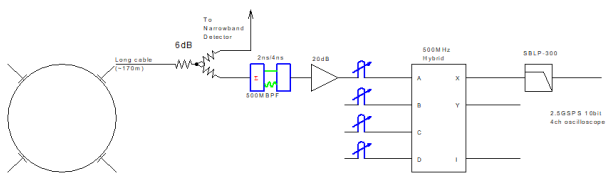


Figure 5: Simplified BOR with 508 MHz Hybrid.

The RF characteristics of the Hybrid has been tested using the network analyzer and the simulated BPM signal using the step recovery diode with 508 MHz comb filter. Figure 6 shows an example of measured S-parameter (A to sum port) and the time domain response (A to (A+B)-(C+D) port and C to (A+B)-(C+D) port). Excellent frequency and time response has been confirmed. Phase balances between the channels have also been checked and

Content from this work may be used under the terms of the CC-BY-4.0 licence (© 2023). Any distribution of this work must maintain attribution to the author(s), title of the work, publisher, and DOI

ISBN: 978-3-95450-236-3 ISSN: 2673-5350 doi:10.18429/JACoW-IBIC2023-TUP002

confirmed less than 3 degrees in the frequency range less than 1.2 GHz.

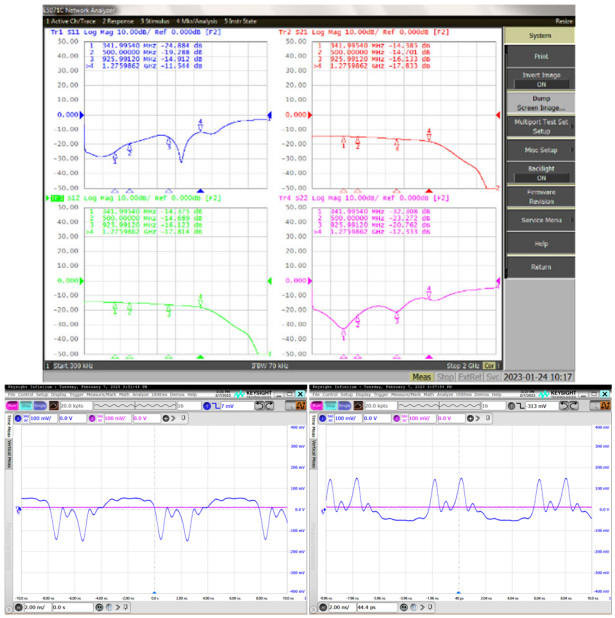


Figure 6: An example of frequency response (upper, A to sum port) and the time domain response (lower left, A to X, lower left A to Y).

The sampling rate of the oscilloscope will be reduced to 2.5 GSPS with the 4-ch operation mode. We have checked the response of the oscilloscope in the realistic configuration by changing the frequency and kind of low pass filter also using SRD signal. Figure 7 shows and example of the detected signal after Bessel type (933 MHz) LPF with 5 GSPS and 2.5 GSPS. In this case, it is impossible to reproduce the signal intensity with the 2.5 GSPS due to largely missing signal.

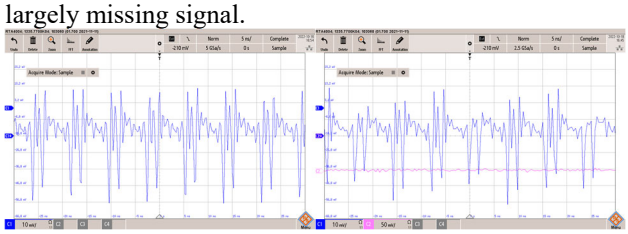


Figure 7: Example of the detected signal with 5 GSPS(left) and 2.5 GSPS(right).

To get equal response with the 2.5 GSPS mode, we will need to insert LPF with much lower cutoff frequency, say, less than 300 MHz. This also cause the signal separation between the bunches much challenging. Figure 8 shows an example of the signal with 300 MHz Bessel LPF, after numerical I/Q detection and digital LPF.

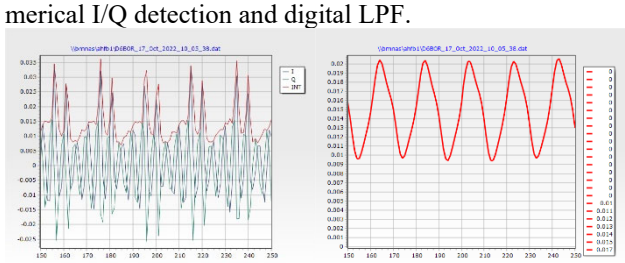


Figure 8: An example of the results of off-line analysis.

Another simple way to overcome this difficulty is, to prepare better oscilloscope which could sample all 4 channels with the sampling rate of 5 GSPS. We have obtained another new oscilloscope for the purpose and will use with much relaxed conditions for the LPFs. Currently, we are planning to install two system in LER, one on the same place as 2022b: upstream of the D6V1 collimator, and the other at the upstream of newly installed vertical collimator, D5V1 which will be configured to be the most effective collimator to cut beam halo.

The EPICS device support using socket connection, and the EPICS sequencer to transfer the data from the oscilloscope to the NAS has been ready and will be tested after the restart of the beam commissioning of LER on Dec, 2023.

SUMMARY

To investigate the cause of the sudden beam loss observed in SuperKEKB rings, we are preparing several kinds of post-mortem bunch position monitors which record the behavior of individual bunch positions and intensities over several turns just before the SBL event. For the rough bunch position and intensity detection around the suspected location in the ring, simplified bunch oscillation recorder based on the hybrid circuit and the digital oscilloscope. The required parameter on the cutoff frequency of the LPF and digital filter are also checked and are ready to test with the real beam.

The authors would like to express their sincere appreciation to the MDI colleagues who constructed and provided the ultra-fast loss monitor with fine timing base. They thank the commissioning group of SuperKEKB for their help and suggestions in the operation and machine development. This work is partly supported by the US-Japan collaboration in High Energy Physics (R&D for SuperKEKB and the next generation high luminosity colliders).

REFERENCES

[1] Y. Ohnishi, “Recent progress of SuperKEKB project and future prospect”, presented at the IPAC'23, Venice, Italy, May 2023, paper TUOGB1, to be published.

[2] H. Ikeda *et al.*, “Observation of sudden beam loss in SuperKEKB”, presented at the IPAC'23, Venice, Italy, May 2023, paper MOPL072, to be published.

[3] M. Tobiyama, “Improvement of Data Transfer Speed of Large Memory Monitors”, in *Proc. IBIC'14*, Monterey, CA, USA, Sep. 2014, paper WEPD05, pp. 642-646.

[4] Y. Liu *et al.*, “Study of beam loss of SuperKEKB based on new loss monitor system for Belle II”, presented in JPS2022, Okayama, Japan, 2022.

[5] https://www.dimtel.com/products/igp12

Content from this work may be used under the terms of the CC-BY-4.0 licence (© 2023). Any distribution of this work must maintain attribution to the author(s), title of the work, publisher, and DOI

ISBN: 978-3-95450-236-3 ISSN: 2673-5350 doi:10.18429/JACoW-IBIC2023-TUP004

DETECTOR RESPONSE STUDIES OF THE ESS IONIZATION CHAMBER

V. Grishin*, I. Dolenc Kittelmann, ESS ERIC, Lund, Sweden
E. Effinger, A.T. Lernevall, W. Vigano, C. Zamantzas, CERN, Geneva, Switzerland
P. Boutachkov, GSI, Darmstadt, Germany

Abstract

The European Spallation Source (ESS), currently under construction in Lund, Sweden, will be a pulsed neutron source based on a proton linac. The ESS linac is designed to deliver a 2 GeV beam with a peak current of 62.5 mA at 14 Hz to a rotating tungsten target for neutron production. One of the most critical elements for protection of an accelerator is a Beam Loss Monitoring (BLM) system. The system is designed to protect the accelerator from beam-induced damage and unnecessary activation of the components.

The main ESS BLM system is based on ionization chamber (IC) detectors. The detector was originally designed for the LHC at CERN resulting in production of 4250 monitors in 2004-2008 (IC-2004). In 2014-2017 a new production of 830 detectors (IC-2016) with a modified design was carried out to replenish spares for LHC and make a new series for ESS and GSI. This contribution focuses on the results from a measurement campaigns performed at the HiRadMat (High-Radiation to Materials) facility at CERN, where response of IC-2016 detectors has been studied. The results may be of interest to other facilities that are using existing or plan to use new generation of IC monitors as BLM detectors.

INTRODUCTION

The European Spallation Source (ESS) is a science facility [1, 2], which is currently being built in Lund, Sweden and will provide neutron beams for neutron-based research. The neutron production will be based on bombardment of a tungsten target with a proton beam of 5 MW average power. A linear accelerator (linac) will accelerate protons up to 2 GeV and transport them towards the target, through a sequence of a normal conducting (NC) and superconducting (SC) accelerating structures (Fig. 1). In 2023 the beam commissioning of Normal Conducting Linac (NCL) has successfully advanced up to including fourth DTL tank.

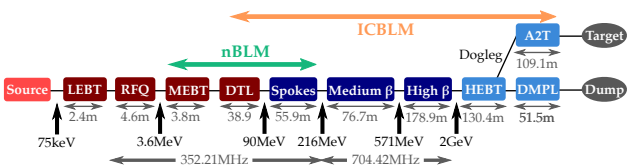


Figure 1: Layout of the ESS linac and BLM system coverage. Red colour represents the NC and blue the SC parts of the linac.

Beam Loss Monitoring (BLM) systems play an important role in machine commissioning, tuning, and operation. By measuring secondary particle rates close to the beam line, these systems provide information about beam loss levels along the machine. The BLM systems are designed to protect the machine from beam-induced damage by detecting unacceptably high beam losses and promptly triggering a request to the Beam Interlock System to stop the beam production. Two types of BLM systems differing in detector technology have been conceived at ESS. The neutron sensitive BLM (nBLM) system [3] is based on 82 neutron detectors primarily covering the lower energy part of the ESS linac. Conversely, the Ionisation Chamber-based BLM (ICBLM) system [4] consists of 266 ionisation chambers (ICs) located almost exclusively along the SC part of the linac.

The ESS ICBLM system is based on parallel plate gas Ionisation Chambers (ICs) originally developed by CERN for LHC (IC-2004) [5] and manufactured and tested in 2004-2008 at the Institute for High Energy Physics (IHEP) in Protvino. IC-2004 type detectors were selected as the ICBLM detectors due to their fast response, no gain variation (with possible exception around the target region) and large dynamic range of 10^8 (pA–mA). In addition to this, they require little maintenance. New production line (IC-2016) [6] was set up in 2014-2017 for ESS, CERN and GSI needs.

When introducing a new detector, it is important to validate its response versus corresponding simulations. In order to validate and fully characterise the new chambers their response in terms of drift time, calibration and saturation was studied at the HiRadMat (High-Radiation to Materials) facility at CERN. The facility offfers the opportunity to perform these unique tests due to several reasons, namely, possibility of beam parameters in wide desired range, available beam diagnostics, availability of cables with required grounding, last but not least, having HiRadMat experts around for fast feedback during the test. BLM experiments have been performed at HiRadMat since 2012, starting with experiments BLM19 and BLM2. Currently, the BLM55 experiment is dedicated to focus on three studies:

- Comparison of the IC production lines IC-2004 and IC-2016.
- Comparison of two types of Little Ionization Chambers (LICs), namely, LHC type (LIC-sem) and new LIC with IC ceramics (LIC-ic).
- Testing of the new Proportional Chambers (PCs).

DETECTOR DESIGNS UNDER TESTS

The IC detector active zone consists of 61 parallel electrodes with a 5.75 mm distance between the electrodes in

* Viatcheslav.Grishin@ess.eu

Content from this work may be used under the terms of the CC-BY-4.0 licence (© 2023). Any distribution of this work must maintain attribution to the author(s), title of the work, publisher, and DOI

ISBN: 978-3-95450-236-3 ISSN: 2673-5350 doi:10.18429/JACoW-IBIC2023-TUP004

Content from this work may be used under the terms of the CC-BY-4.0 licence (© 2023). Any distribution of this work must maintain attribution to the author(s), title of the work, publisher, and DOI

IC-2004 detectors. The gap between electrodes in IC-2016 detectors, was reduced to 5.71 mm for every second electrode while keeping the same spacer length. The electrodes are made of a 0.5 mm and 0.54 mm thick aluminium in case of IC-2004 and IC-2016 detectors, respectively. The gap between electrodes is built to reduce the drift path and recombination probability of the ions and electrons, in order to achieve the desired linearity.

Little Ionization Chambers (LICs) were designed by Protvino and CERN to reduce the sensitivity with respect to the IC-2004 detectors. The reduction of active volume decreases the drift charge production resulting in lower sensitivity. It is interesting to compare the two types of LICs, namely the LHC type (LIC-sem), where Secondary Emission Monitors (SEM) insulators were used and the new LICs with IC ceramic disk (LIC-ic). The original LIC design was found to exhibit additional signal not related to the incoming particle showers. Thus, the ceramic insulator was replaced with the IC ceramic disk under the assumption that this would cure the non-uniformities close to the ceramic resulting in additional signal. Moreover, LIC was designed to reduce the sensitivity by a factor of 20-30 compared to the IC-2004 detectors, however, a factor of ~12 was reached for LIC-sem. The difference can be attributed to the difference in ceramic plates between LIC-ic and LIC-sem.

The new detector prototype, Proportional Chamber (PC), has the same outside geometry as IC-2004 detectors and was designed to achieve higher gain compared to the IC-2004 detectors, namely ~10–100 higher, depending on the applied bias voltage. Six new PC prototypes filled with different gas mixture and different central wire diameter have been manufactured. One of these PCs has been tested at HRM together with the ICs. This PC is filled with Ar+CO_2 gas mixture and has a central wire with 25 µm diameter.

BLM55 HIRADMAT SETUP

HiRadMat is a user facility at CERN, designed to provide high-intensity short-pulse 440 GeV/c proton or 173.5 GeV/n ^{208}Pb beams to a dedicated target area [7]. The unique capability of HiRadMat is to test the dynamic effects of short beam pulses on material samples or full scale accelerator components like beam loss monitors, collimators or beam dumps as well as particle detectors.

The BLM detectors are placed on a mechanical support at 3.2 m downstream from the start of the dump (Fig. 2). A FLUKA based simulation of expected particle fields around the dump has been performed (Fig. 3)[1]. The simulation indicates that at 3.2 m–3.3 m downstream from the start of the dump and at height ~80 cm the absorbed dose is approximately uniform and homogeneous in beam direction. Moreover, the doses are expected within the statistical error to be approximately independent of the vertical position at the detector locations.

The BLM detectors are connected from the area of HiRadMat dump to the Control Room in BA7 (Fig. 4). Due to low signal current the detector cables are connected through one patch panel and not grounded (Fig. 5). Data acquisition was performed with an oscilloscope (Tektronix, MSO 5) with a sampling rate of 6.25 GHz, where 1-6 waveforms per beam intensity (protons per bunch) were recorded for offline analysis.

RESULTS FROM 2022 SETUP

IC Results

Four IC detectors, two from IC-2004 production and two from IC-2016 production, were placed in a mixed row-column positions with respect to the dump (Fig. 6). The data was collected at several beam intensities ranging from 1 to 288 bunches per pulse.

Figure 7 shows the extracted charge as a function of beam intensity where charge was calculated over 80 µs time window from the signal start. The figure demonstrates a linear response and no saturation at high fluxes for all four IC detectors under test. According to the aforementioned simulation, the dose is expected to be uniform at all four detector locations. The measured signal response is consistent with simulation predictions for 3 detectors (two from IC-2004 and one from IC-2016) with variations ~15%, indicating that the differences in this case are dominated by the detectors location. However, there is a larger discrepancy for one of the IC-2016 detector, namely ~35%, which is assumed to be due to detector location and/or potentially larger variations in detector sensitivity.

Nitrogen filed ICs, are expected to have charge drift times of ~300 ns [8] and 84 µs [9] for electrons and ions, respectively. However, the measured signal was observed to exhibit longer ion drift times with the signal shape closer to what is expected for a coaxial instead of planer geometry in the region where ion drift is expected to dominate (Figs. 8 and 9). The observations could be explained by electronic attachment (electron reaction with neutral molecules) and/or more than one gas component contributing to the positive charge drift.



Figure 2: BLM detector setup at HiRadMat test.

[1] Courtesy of J. Hunt and L. Esposito, CERN

ISBN: 978-3-95450-236-3 ISSN: 2673-5350 doi:10.18429/JACoW-IBIC2023-TUP004

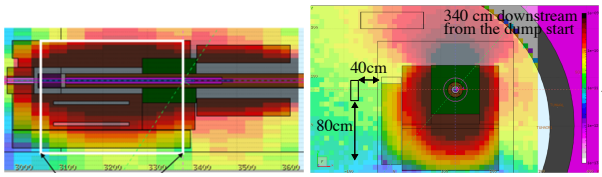


Figure 3: Simulated dose map (288 bunches) around the BLM detector locations (black square) at HiRadMat dump.



Figure 4: Data acquisition in Control Room BA7.



Figure 5: Cable connections in the tunnel.

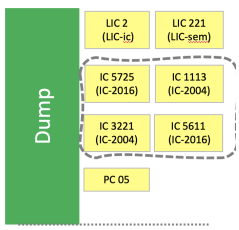


Figure 6: IC locations (marked with gray dashed line).

LIC Results

The two LIC detectors, LIC-sem (LHC type with SEM insulators) and the new LIC-ic (with ceramic disk as in IC), were tested in parallel with IC detectors. The IC to LIC ratio of measured integrated charge in 80 µs was observed to be as expected around 20 for LIC-ic and 12 for LIC-sem (Fig. 11) at higher intensities. Larger discrepancies at lower intensities are due to lower LIC sensitivity. The ratio values were extracted by comparing the charge measured with each LIC to the average value of the charge measured by the two IC detectors placed just below the LICs (Fig. 10, left).

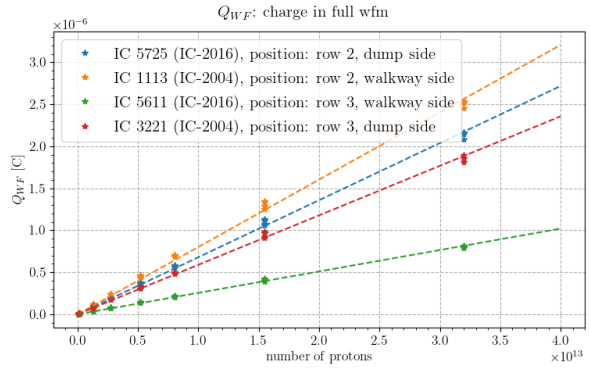


Figure 7: Charge collected with IC detectors versus beam intensity.

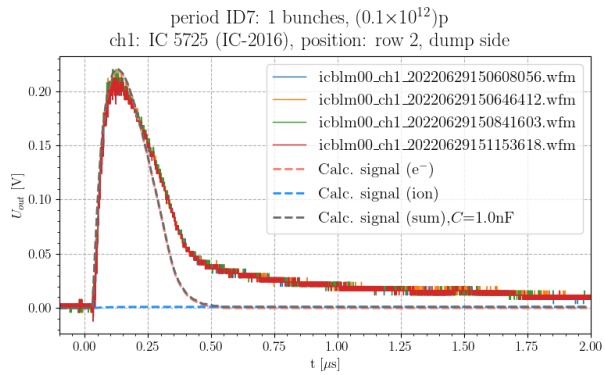


Figure 8: Measured and calculated IC signal for beam intensity of 1 bunch per pulse.

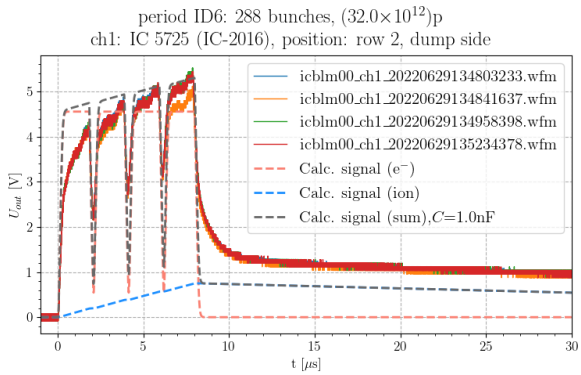


Figure 9: Measured and calculated IC signal for beam intensity of 288 bunches (4 trains of 72 bunches) per pulse.

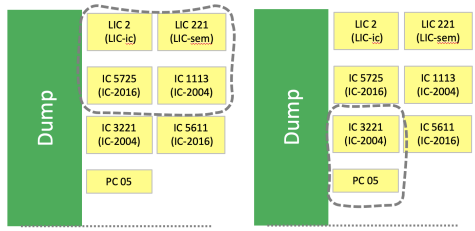


Figure 10: IC and LIC (left) and IC and PC (right) detectors used to for calculation of charge rations in Figs. 11 and 12, respectively.

Content from this work may be used under the terms of the CC-BY-4.0 licence (© 2023). Any distribution of this work must maintain attribution to the author(s), title of the work, publisher, and DOI

ISBN: 978-3-95450-236-3 ISSN: 2673-5350 doi:10.18429/JACoW-IBIC2023-TUP004

Content from this work may be used under the terms of the CC-BY-4.0 licence (© 2023). Any distribution of this work must maintain attribution to the author(s), title of the work, publisher, and DOI

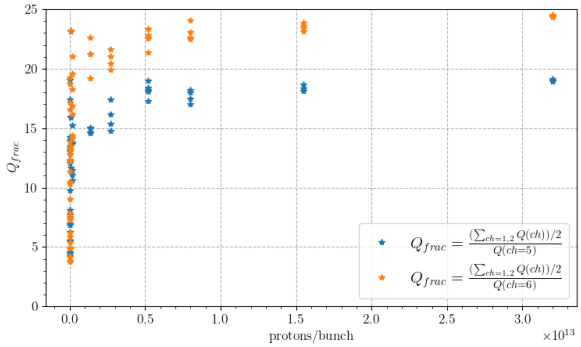


Figure 11: Measured IC/LIC charge ration versus beam intensity. Blue points corresponds to LIC-sem and orange points to LIC-ic.

PC Results

The experimental prototypes of the PCs with different gases and central wires have been designed by Protvino to achieve ~10–100 higher gain compared to IC-2004 detectors. A voltage scan has been performed for one of the PCs at two different beam intensities. Figure 12 shows the extracted ratio of charge collected by PC and charge collected by IC placed directly above the PC (Fig. 10, right). The charge was calculated as an integral over a 80 µs time window from the signal start. The observed ratio is around 6–10 at 1.8 kV. The differences are potentially due to the detector positions with PC positioned rather low where higher variations in doses can be expected.

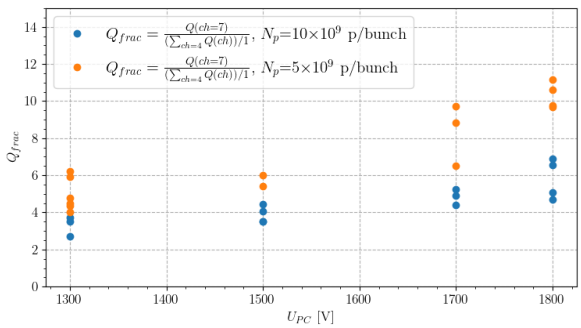


Figure 12: Measured PC/IC charge ratio as a function of bias voltage for two intensities.

CONCLUSION

2022 IC results indicate similar performance of IC-2004 and IC-2016 detectors. However, detector-to-detector performance variations are potentially larger for IC-2016 monitors compared to the IC-2004 monitors. In order to resolve this question, further study has been performed in 2023 with IC data taking during two beam time runs in July and August 2023 at HiRadMat. The analysis of this data is currently on-going.

For LICs the results show the ration IC/LIC to be as expected around 20 for LIC-ic and 12 for LIC-sem at higher beam intensities while larger discrepancies were observed at lower intensities. The ration PC/IC was found to be around 6–10 at 1.8 kV. Nevertheless, LIC-ic and PCs require more time and further efforts to test, design, simulate and issue a new prototype production line.

ACKNOWLEDGEMENTS

The authors wish to express their gratitude to R. Baron, C. Derrez and T. Shea, who provided support at ESS. The authors would also like to gratefully acknowledge the help of the HiRadMat team, P. Simon, N. Charitonidis and A. Goillot for their support during the experiment at HiRadMat and making the experiment possible. Additionally, the authors thank to J. Hunt and L. Esposito from CERN for the dose simulations and to A. Larionov, A. Koshelev, M. Sleptsov from IHEP for their collaboration. This project has been receiving funding from the European Union's Horizon 2020 Research and Innovation program under Grand Agreement No. 730871 with TA Project Identifier: ARIES-CERN-HiTadMat-2020-01. In 2023 this project has received funding from the Horizon Europe EC funded EURO-LABS project under Grant Agreement No. 101057511 with Project Identifier EURO-LABS-2023-HRMT55-1/2.

REFERENCES

[1] R. Garoby *et al.*, "The European Spallation Source design," *Phys. Scr.*, vol. 93, no. 1, p. 014 001, 2018. doi:10.1088/1402-4896/aa9bff

[2] S. Peggs *et al.*, "ESS technical design report," ESS ERIC, Tech. Rep. ESS-DOC-274, 2013. http://eval.esss.lu.se/cgi-bin/public/DocDB/ShowDocument?docid=274

[3] I. Dolenc Kittelmann *et al.*, "Neutron sensitive beam loss monitoring system for the european spallation source linac," *Phys. Rev. Accel. Beams*, vol. 25, no. 2, p. 022 802, 2022. doi:10.1103/PhysRevAccelBeams.25.022802

[4] I. D. Kittelmann *et al.*, "Ionisation Chamber Based Beam Loss Monitoring System for the ESS Linac," in *Proc. IBIC'19*, Malmö, Sweden, Sep. 2019, pp. 136–140. doi:10.18429/JACoW-IBIC2019-MOPP023

[5] E. B. Holzer *et al.*, "Development, Production and Testing of 4500 Beam Loss Monitors," in *Proc. EPAC'08*, Genoa, Italy, Jun. 2008, pp. 1134–1136. https://jacow.org/e08/papers/TUPC037.pdf

[6] V. Grishin, B. Dehning, A. V. Koshelev, A. Larionov, V. S. Seleznev, and M. Sleptsov, "Ionization Chambers as Beam Loss Monitors for ESS Linear Accelerator," in *Proc. IBIC'17*, Grand Rapids, MI, USA, Aug. 2017, pp. 454–457. doi:10.18429/JACoW-IBIC2017-WEPWC03

[7] F. J. Harden *et al.*, "Hiradmat: A facility beyond the realms of materials testing," *J. Phys. Conf. Ser.*, vol. 1350, no. 1, p. 012 162, 2019. doi:10.1088/1742-6596/1350/1/012162

[8] A. Peisert and F. Sauli, *Drift and diffusion of electrons in gases: a compilation (with an introduction to the use of computing programs)*. CERN, 1984. doi:10.5170/CERN-1984-008

[9] H. Ellis, R. Pai, E. McDaniel, E. Mason, and L. Viehland, "Transport properties of gaseous ions over a wide energy range," *At. Data Nucl. Data Tables*, vol. 17, no. 3, pp. 177–210, 1976. doi:10.1016/0092-640X(76)90001-2

ISBN: 978-3-95450-236-3 ISSN: 2673-5350 doi:10.18429/JACoW-IBIC2023-TUP005

COMMISSIONING THE BEAM-LOSS MONITORING SYSTEM OF THE LCLS SUPERCONDUCTING LINAC*

Alan S. Fisher†, Namrata Balakrishnan, Garth Brown, Edward Chin, William G. Cobau, John E. Dusatko, Bryce T. Jacobson, Sung Kwon, Jeremy Mock, Jino Park, Jeremy Pigula, Evan Rodriguez, Jacob Rudolph, Daniel Sanchez, Leonid Sapozhnikov, James J. Welch
SLAC National Accelerator Laboratory, Menlo Park, California, USA

Abstract

A 4-GeV superconducting linac has been added to the LCLS x-ray FEL facility at SLAC. Its 120-kW, 1-MHz beam requires new beam-loss monitors (BLMs) for radiation protection, machine protection, and diagnostics. Long radiation-hard optical fibres span the full 4 km from the electron gun of the SC linac to the final beam dump. Diamond detectors at anticipated loss points and other points of concern provide local protection. Detector signals are continuously integrated with a 500-ms time constant and compared to a loss threshold. If crossed, the beam is halted within 0.1 ms. Commissioning began in March 2022 with the 100-MeV injector and with RF processing of the cryomodules. At IBIC 2022 last September, we presented commissioning results from the injector BLMs. In October, the beam accelerated through the full linac, passed through the bypass transport line above the LCLS copper linac, and stopped at an intermediate dump. In August it continued through the soft x-ray undulator and achieved first lasing. Here we present BLM commissioning at energies up to 4 GeV and rates up to 100 kHz. We discuss measurements and software using the fast diagnostic-waveform output to localize beam losses and to detect wire-scanner signals.

INTRODUCTION

Over the past few years, SLAC removed the first km of the 3-km copper normal-conducting (NC) copper linac and replaced it with a superconducting (SC) linac with 35 12-m-long cryomodules operating at f_{RF} = 1.3 GHz and two third-harmonic cryomodules. Each has 8 RF cavities and operates at a temperature of 2°K. All have been installed in the first 700 m of the tunnel. The SC linac, driven with continuous-wave (CW) RF power, produces 4-GeV bunches with variable spacing at rates up to 1 MHz (f_{RF}/1400). The 750-keV electron gun is also driven by CW RF, but at 186 MHz (f_{RF}/7) and followed by a 1.3-GHz buncher. A planned high-energy (HE) upgrade in the remaining 300 m will later double the energy. Before this doubling, the beam power at full rate and at a maximum bunch charge of 300 pC will reach 120 kW. At this time, the full linac has been commissioned to 3.5 GeV and first lasing has been achieved in the soft x-ray (SXR) undulator at 1 kHz.

The risk of damaging beam loss led to the development of a new protection system, including long optical fibres (long beam-loss monitors, LBLMs) that cover the full 4 km from gun to dump in sections of up to 200 m, and diamond detectors (point beam-loss monitors, PBLMs) that protect small sections or devices such as collimators [1].

At the previous IBIC, in September 2022, only the injector region, the first 50 m through the first cryomodule (80 to 100 MeV), had been commissioned. We reported then [2] on the initial performance of the LBLMs and the one PBLM in this low-energy region. Over the past year, the full beam-loss system has been tested. We now can provide a more complete look at its performance.

LONG BEAM-LOSS MONITORS

Integrated Beam-Loss Signals

Radiation-hard quartz optical fibres (FBP600660710 from Polymicro) run parallel to the beam (z direction, west to east), in lengths of up to 200 m. Beam losses generate showers that pass through the beampipe and fibre, emitting Cherenkov light that travels to the ends of the fibre. At the downstream end, the light is measured by a photomultiplier tube (PMT) outside the tunnel, in a rack-mounted chassis.

The beam can pulse at a steady 1 Hz to 1 MHz, in single shots, or with variable spacings. Consequently, protection is based not on shot-by-shot loss but from the total loss in 500 ms, integrated by an *RC* circuit. This signal is amplified and compared on the board to the Beam Containment System (BCS) threshold. BCS can stop the beam, the RF cavities and, if necessary, the electron gun. It is analogue, simple, and robust, without awareness of beam rate or the beamline causing the loss. The same integrated signal is buffered and sent to the Machine Protection System (MPS) [3], where it is digitised and compared to a second level below the BCS threshold, to trip the beam first. It is aware of timing and beamline selection. It acts by blocking the photocathode laser or by halting downstream kickers that direct the beam. If dark current causes persistent losses, MPS escalates to BCS, which can halt the gun RF.

The SC linac regions L0B through L3B (here "B" distinguishes these from the LCLS NC linac, in the third km) are separated by warm regions for collimation and bunch compression. Each region is spanned by two fibres, linked for redundant protection in two BCS "chains", also called "A" and "B". Linac A-chain fibres are on the north wall at beam height and 90 cm horizontally from the beam. B fibres are on the ceiling and to the south, at a 3-m distance. The different views give the pair similar but not identical responses. Because the thick cryomodule walls require extra gain, fibres span warm or cold regions, but not both. PMT gains for B fibres are somewhat higher to compensate for greater distance. Fibre mounting in transport lines is different; some have only an A fibre.

* SLAC is supported by the U.S. Department of Energy, Office of Science, under contract DE-AC02-76SF00515.
† afisher@slac.stanford.edu

Content from this work may be used under the terms of the CC-BY-4.0 licence (© 2023). Any distribution of this work must maintain attribution to the author(s), title of the work, publisher, and DOI

ISBN: 978-3-95450-236-3 ISSN: 2673-5350 doi:10.18429/JACoW-IBIC2023-TUP005

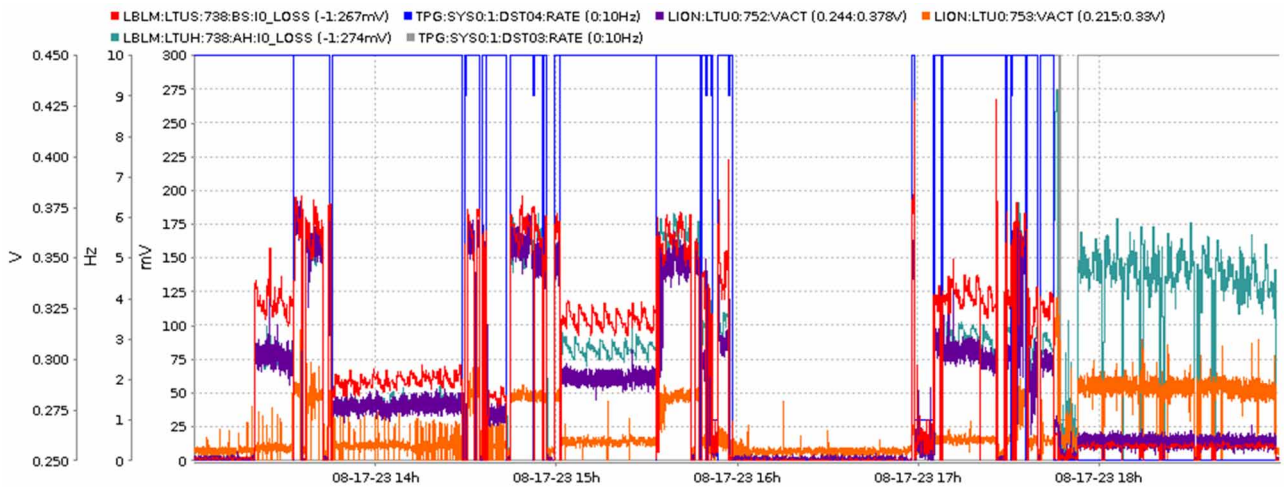


Figure 1: Comparison of LBLM and LION signals in the LTU as 10-Hz beam was switched from the soft x-ray (SXR, north side) beamline to the hard x-ray (HXR, south) line. Blue: Rate to SXR. Grey: Rate to HXR. Red: LBLM on SXR side. Green: LBLM on HXR side. Purple: LION on SXR side. Orange: LION on HXR side. Both LBLMs and LIONs responded to the switch and gave similar signals, but the LIONs appear noisier.

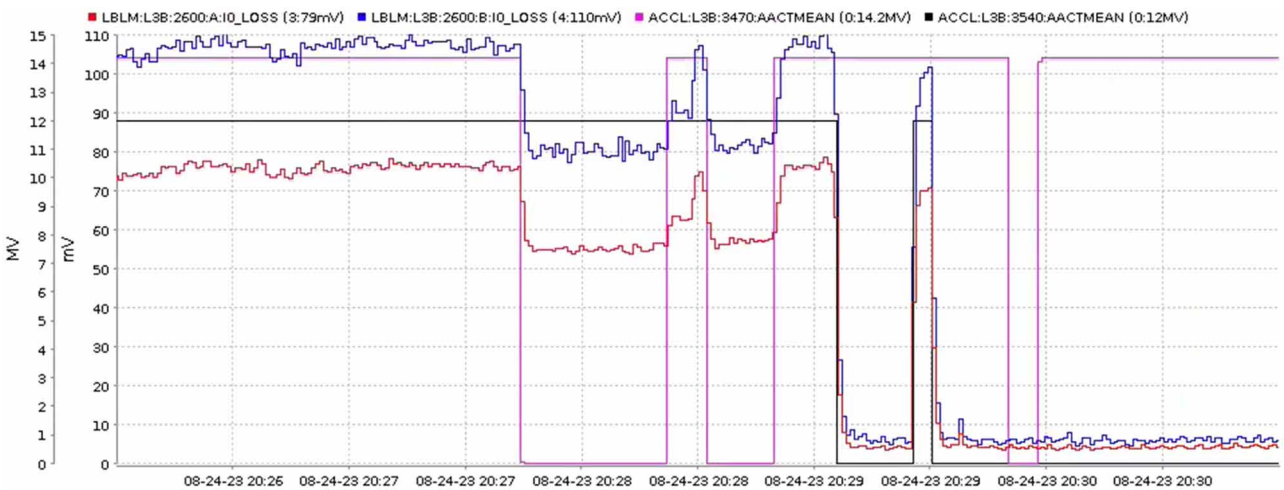


Figure 2: LBLM signals from cryomodule field emission. Two fibres span the downstream half of L3B, on the wall (red) and ceiling (blue). Both signals suddenly jumped up, and MPS tripped the photocurrent. The gun dark current was low. Cryomodules along this region were cycled off and on, one at a time. Losses dropped somewhat with module 34 cavity 7 (CM34-7, magenta) but went nearly to zero when CM35-4 (black) was shut off.

Previously long coaxial ionization chambers (LIONs) protected regions of NC beamlines. Modelling showed that these are not suited to the SC beam: at high loss rates the space charge of slowly moving ions can screen the internal bias field, suppressing the response [1]. Figure 1 compares two fibres and two LIONS in the linac-to-undulator (LTU) transport tunnel. It shows one of each type near the beamline leading to the hard x-ray undulator (south side of the tunnel) and another pair near the soft x-ray (north) side. As a 10-Hz beam was sent first into the soft and then into the hard line, the signal strengths shifted accordingly. The LIONs and fibres responded similarly at this low rate, but the LIONs were somewhat noisier.

Dark Current and Field Emission

Losses of dark current emitted by the CW electron gun exceed photocurrent losses through the first short linac (L0B) and the first collimation region (COL0). Also, since dark current and photocurrent gain the same energy, some dark current travels the length of the accelerator and produces losses far downstream. LBLMs integrate both loss sources to provide overall protection.

Field emission from a cryomodule cavity is another loss source unrelated to photocurrent from the gun. In Fig. 2, the A and B fibres spanning the second half of L3B detected a sudden increase in loss that followed the RF amplitude of cryomodule 35 cavity 4 (CM35-4). Losses disappeared when this cavity was shut off. There was also some sensitivity to CM34-7. The observations suggest that electrons emitted at a site in CM35-4 accelerated upstream (the direction depends on the site and emission phase) into CM34, where they were lost. Indeed, a subsequent radiation survey found a hot spot at CM34. The fibre detected this loss signal through the thick cryomodule wall.

Content from this work may be used under the terms of the CC-BY-4.0 licence (© 2023). Any distribution of this work must maintain attribution to the author(s), title of the work, publisher, and DOI

ISBN: 978-3-95450-236-3 ISSN: 2673-5350 doi:10.18429/JACoW-IBIC2023-TUP005

Diagnostic Waveforms

The 500-ms *RC* integrator sends the low-frequency component of the PMT signal through an op amp to BCS and MPS. The high frequencies, after a buffer and an external amplifier with adjustable gain, provide a fast diagnostic waveform showing the arrival time of a Cherenkov loss pulse at the PMT. The z coordinate of this loss can be found using a known loss point and the propagation speed (1.5 c).

A wire scanner passing through the beam adds loss peaks downstream. Shot-by-shot numerical integration over these peaks gives the charge scattered by the wire. This is acquired synchronously with the encoder for the wire position to measure beam profiles.

A graphical user interface (GUI) using the Python Display Manager shows the diagnostic waveform, to aid in localizing losses and in setting the integration gate for wire scans. The GUI can plot the waveform of the selected LBLM against time or z, adjust the amplifier's gain, zoom in on a region of interest in the million-point record, highlight the gate interval, and add crosshairs to mark features. The user can pause the running display and, with a buffer of the ten most recent waveforms, toggle back in time, save the buffer, or load a previously saved buffer.

Problems

Commissioning has uncovered various problems.

Gain The gains of all PMTs are set to deliver equal response. Small adjustments of each bias voltage balance the tube-to-tube variation in gain and compensate for the distance to the different fibre locations. We performed initial calibrations (discussed below) to check the attenuation in the thick steel housing of cryomodules for the associated fibres. Conversely, because the 2-km bypass beamline over the NC linacs (FACET-II and LCLS) has a thin stainless-steel beampipe and few magnets to attenuate showers, fibre signals there were quite strong and could saturate the digitiser. We then changed the selectable gain of the op amp following the integrator, raising the gain for cryomodule fibres from 6 to 69 and lowering the gain for the bypass from 6 to 1. In regions that require a low radiation limit—the LTU (in a ground-level bunker) and the Undulator Hall—the gains are set to 20 rather than 6. Calibrations now show that the sensitivities are well balanced.

PMT Failures Since fibre attenuation, both inherent and radiation-induced, increases inversely with wavelength, the LBLMs use red-sensitive cooled PMTs, the Hamamatsu H7422P-40 [1]. These have sensitive GaAsP photocathodes and a low limit of 2 μA on the time-average anode current. Their delicacy may be responsible for a few premature failures that do not appear to be related to this current limit. We have asked Hamamatsu to investigate the failures. This model has since been replaced by the H16722P-40. It may be more robust, with a limit of 40 μA and somewhat higher gain. We have ordered several.

Self-Check The upstream end of each fibre has an LED used for a continuous self-check. Very weak light from the LED is modulated at 0.8 Hz (75 periods of the 60-Hz power line). A lock-in amplifier implemented in a digital signal processor (DSP) selectively detects this frequency in the PMT signal [1]. We have encountered two problems.

A built-in Peltier cooler lets the PMT operate at 0°C, but only if the exterior of the module remains below 35°C. On a hot summer afternoon, the interior of our racks routinely reaches 45 to 50°C. We added a secondary Peltier cooler to our LBLM chassis that limits the PMT housing to 30°C. However, we did not consider that LED emission decreases with temperature, following $\exp(-K\Delta T)$ [4] for a rise ΔT. The coefficient K is 0.00952/°C for the GaP and InAlGaP diodes we use for our different self-check wavelengths [5]. Emission drops by 68% over a temperature range from 10 to 50°C. This shows up as both a diurnal and seasonal variation in the detected self-check amplitude. We are now investigating compensation using a resistor with a negative temperature coefficient in the constant-current loop driving the LED. The emission drop may be reduced to 7%.

Also, sharp spikes in beam loss cause bipolar jumps in the detected self-check. Calculations show that the wide bandwidth of a loss spike passes a jump decaying with the filter's slow (~1 minute) time constant. Superposed on the peak are oscillations at 0.8 Hz damping with the *RC* time constant. A longer digital filter should reduce the effect.

POINT BEAM-LOSS MONITORS

Integrated Loss Signals

PBLMs use a 4-mm-square chip of single-crystal diamond that is 0.5 mm thick (Cividec type B1HV). A beam-loss shower passing through the chip creates electron-hole pairs that are drawn to electrodes plated on opposite faces and biased with a 250-V difference [1]. We have found that only single crystals bring the signal immediately to zero when losses stop [1]. Charge is trapped at the crystal boundaries of polycrystalline material, significantly delaying both the rise and especially the fall of the signal.

Like the LBLMs, PBLM electronics integrate signals with a 500-ms *RC* time constant. Again, MPS should trip first, and BCS only at a higher threshold. Many of the PBLMs for both BCS and MPS hang from the ceiling midway between beamlines of the LTU, to protect both, and cover a region extending about 20 m upstream.

Other PBLMs are mounted at halo collimators and trip only MPS. At this stage of commissioning, scraping in collimators provides most of our PBLM data. In Fig. 3, the $+y$ (vertical) jaw of an LTU collimator was fully open while the $-y$ jaw was scanned across the beam. The charge gradually dropped at the next beam-position monitor (BPM) downstream. The PBLM signal rose as the charge fell.

Figure 4 shows a collimator 2.2 km from the gun, after a dogleg. The photocurrent beam was off, but dark current from the gun reached this spot and heated the collimator jaws, which had insufficient cooling. Shortly before the temperature rise, the PBLM signal jumped up, reaching the saturation level of the digitiser (650 mV). One jaw was opened, and a solenoid at the gun was then refocused to reduce the dark current downstream. The PBLM signal fell abruptly, and the temperature began decreasing.

Content from this work may be used under the terms of the CC-BY-4.0 licence (© 2023). Any distribution of this work must maintain attribution to the author(s), title of the work, publisher, and DOI

ISBN: 978-3-95450-236-3 ISSN: 2673-5350 doi:10.18429/JACoW-IBIC2023-TUP005

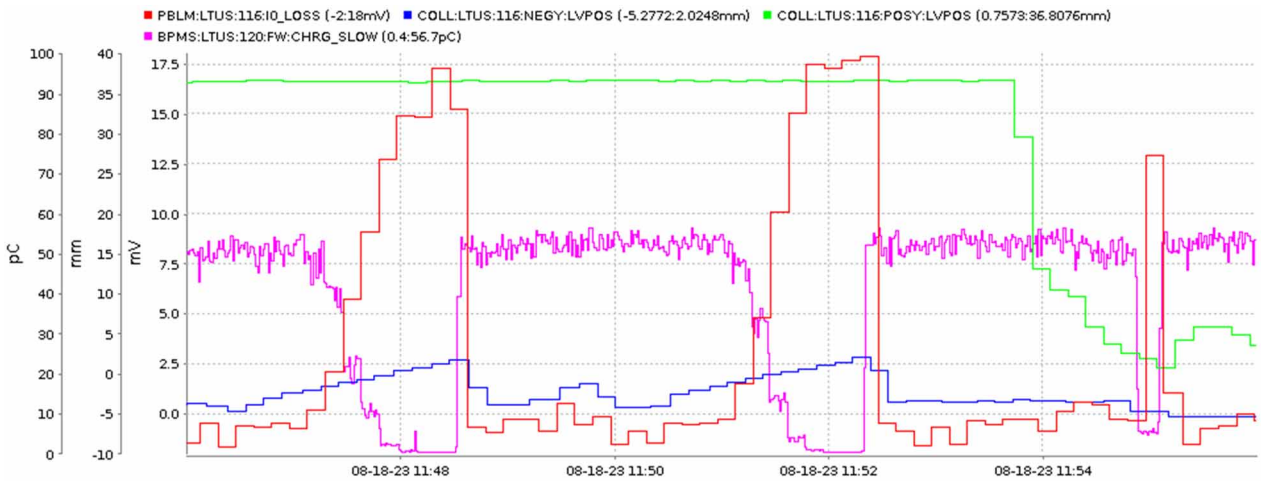


Figure 3: The positive (+y, green) jaw of an LTU vertical collimator was fully open as the negative (−y, blue) jaw scanned across the beam. The bunch charge (magenta) transmitted to the next BPM dropped as the PBLM signal (red) rose.

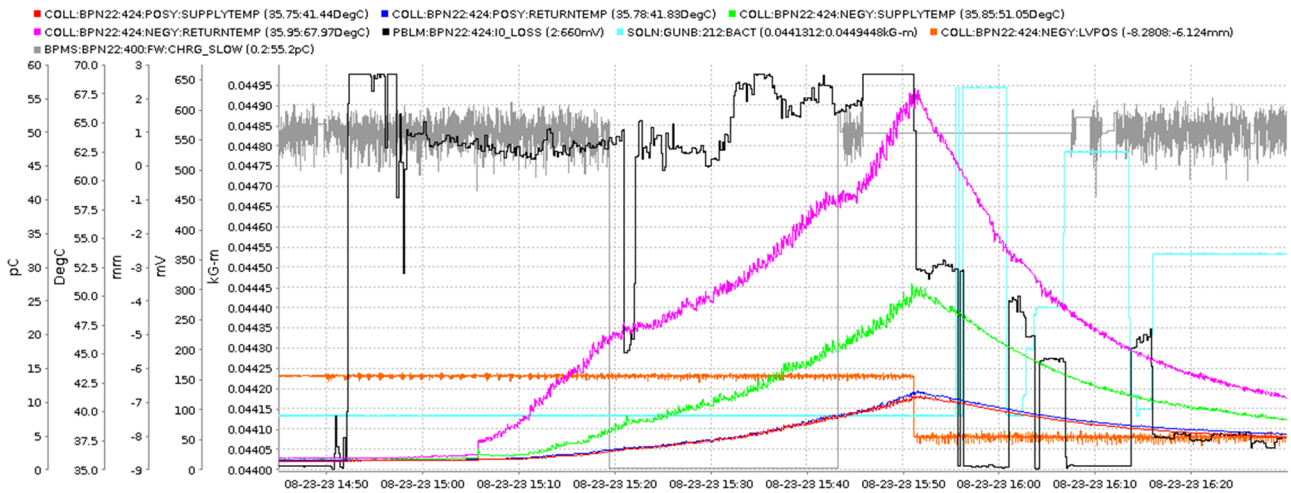


Figure 4: The PBLM signal (black) at a collimator 2.2 km from the gun rose abruptly. Jaw temperatures climbed soon after and continued rising with the photocurrent (grey) off. The loss signal was lowered first by opening the −y jaw (orange) by 1.8 mm and then by lowering dark current with a solenoid at the gun (cyan). The temperatures began to drop.

CALIBRATION

Relating lost beam energy to loss signals is complex, due to the interplay of local shielding, varied beam direction, radiation distribution, and loss location along the accelerator. We get the signal distribution by varying each steering magnet over its full range, one at a time, to cover every beam-loss location and trajectory. To avoid damage, bunches are fired not at a continuous rate but in short bursts of 1 to 100, separated by up to 2 ms. The longer bursts are needed at the low-energy end of the linac to lose enough beam energy. The burst energy is kept well below any known damage thresholds for instantaneous heating. Only one burst per beam-loss trajectory is needed.

We define the sensitivity of a BLM as ratio of the strongest signal (mV) to the lost beam energy (J). The signal-size histogram helps set thresholds, based on the fraction of events we wish to trip on and the energy-loss limit for each region. A setting near full sensitivity would fail to trip on significant loss events, but a low choice would trip frequently on noise.

REFERENCES

[1] A.S. Fisher *et al.*, "Beam-loss detection for the high-rate superconducting upgrade to the SLAC Linac Coherent Light Source", *Phys. Rev. Accelerators and Beams,* vol. 23, p. 082802, 2020. doi: 10.1103/PhysRevAccelBeams.23.082802

[2] A. S. Fisher *et al.*, "Commissioning Beam-Loss Monitors for the Superconducting Upgrade to LCLS", in *Proc. IBIC'22*, Kraków, Poland, Sep. 2022, pp. 207-210. doi:10.18429/JACoW-IBIC2022-TU2C3

[3] J.A. Mock *et al.*, "Commissioning of the LCLS-II Machine-Protection System for MHz CW beams", presented at IBIC 2023, Saskatoon, SK, Canada, Sep. 2023, paper TU3I01.

[4] S.C. Bera *et al.*, "Temperature Behaviour and Compensation of Light-Emitting Diode", IEEE Photonics Tech. Lett. vol. 17, pp. 2286-2288, 2005. doi: 10.1109/LPT.2005.858154

[5] https://tachyonlight.com/analysis-of-the-influence-of-temperature-on-led

Content from this work may be used under the terms of the CC-BY-4.0 licence (© 2023). Any distribution of this work must maintain attribution to the author(s), title of the work, publisher, and DOI

ISBN: 978-3-95450-236-3 ISSN: 2673-5350 doi:10.18429/JACoW-IBIC2023-TUP006

SIMULATION AND SHOT-BY-SHOT MONITORING OF LINAC BEAM HALO*

Alan S. Fisher†, Mei Bai, Thomas Frosio, Alessandro Ratti, John Smedley, Juhao Wu
SLAC National Accelerator Laboratory, Menlo Park, California, USA
Isar Mostafanezhad and Ben Rotter, Nalu Scientific, Honolulu, Hawaii, USA

Abstract

FELs require a reproducible distribution of the bunch core at the undulator entrance for robust and reliable lasing. However, various mechanisms drive particles from the core to form a beam halo, which can scrape the beampipe of the undulator and damage its magnets. Collimators can trim the halo, but at the 1-MHz repetition rate of SLAC's LCLS-II superconducting linac, the collimator jaws can be activated and damaged. The Machine Protection System (MPS) can detect excessive radiation and halt the beam, but repeated MPS trips lead to significant downtime. Halo control begins by studying its structure, formation, and evolution, using a sensitive halo monitor. To that end, we are developing a pixellated diamond sensor. Diamond offers a dynamic range of up to 7 orders of magnitude, extending from the edge of the core to the faint halo expected at greater distances. Nalu Scientific has developed fast electronics for high-rate shot-by-shot readout. Initial tests are starting with a prototype 16-pixel sensor at the beam dump of SLAC's FACET-II test facility. The tests and simulations will guide more elaborate sensor designs.

INTRODUCTION

Generating a beam with the desired particle distribution in the core of each bunch and maintaining this distribution as the beam travels is a critical requirement for accelerators. However, various mechanisms drive particles from the core into a beam halo. At x-ray free-electron laser (XFEL) facilities, the shape of the bunch core at the entrance of the undulator is crucial for lasing. Reproducibility of this shape is necessary for robust and reliable performance. If a halo surrounds the core, it could scrape on the undulator beampipe, generating a radiation shower that damages the undulator's permanent magnets. Our numerical simulation of LCLS-II with a start-to-end electron beam-dynamics model finds that collective effects will cause an electron beam—4 GeV, repeating at 300 kHz, 180 pC, plus both dark current and halo electrons—to scrape 1 to 10 W at the undulator entrance. Collimators are commonly used to trim the halo, but at the 1-MHz repetition rate of LCLS-II, the resulting radiation could activate and damage the collimator jaws, making this approach problematic. Moreover, the Machine Protection System (MPS) detects excessive radiation and halts the beam, but repeated MPS trips creates significant downtime for users.

Advanced techniques to detect and mitigate halo are necessary. Non-destructive characterization of the halo distribution is crucial for understanding in detail the mechanisms behind its formation and for identifying countermeasures. We are developing pixellated diamond sensors surrounding the beam core, to monitor halo noninvasively ("parasitically"), shot by shot, with high spatial and temporal resolution. Diamond offers several orders of magnitude of dynamic range, allowing measurements from the edge of the core to the faint halo expected at greater distances. Below we describe an initial test using a diamond chip with 16 pixels, by the beam dump of FACET-II [1], the test-beam facility at SLAC. Fast electronics built by Nalu Scientific [2] provide shot-by-shot pixel readout.

* SLAC is supported by the U.S. Department of Energy, Office of Science, under contract DE-AC02-76SF00515.
† afisher@slac.stanford.edu

PIXELLATED DIAMOND DETECTORS

Diamond Sensors

The diamond sensor used in this monitor is based on more than a decade of experience using diamond as an x-ray beam diagnostic [3-5]. In effect, these devices form a solid-state ionization chamber: a photon or electron excites an energetic electron within the material, which then loses energy via electron-electron scattering, producing one electron-hole pair for each 13.3 eV [6] of deposited energy. The FACET electron beam is near the minimum of the dE/dx curve, with an expected collisional energy loss of 35 keV/electron for a 50-μm-thick diamond. With the current electronics, we anticipate being sensitive to 10 electrons per pixel.

These devices have demonstrated a linear dynamic range spanning 11 orders of magnitude with photons [3, 4], due to the lack of recombination in the bulk, and are very radiation tolerant. We anticipate at least 7 orders of magnitude when used with electrons. The device can be read in pulsed or current mode. The goal is to resolve the halo in space—by dividing the chip's surface into pixels using lithographic patterning of the electrodes—and in time—by using pulse-mode readout for shot-by-shot data. In addition to its radiation hardness, diamond is an attractive medium for halo monitoring because its low Z makes it significantly less sensitive than other semiconductors to bremsstrahlung photons, which create background for direct halo detection.

Figure 1 shows the relatively simple patterned diamond in the FACET-II test. The chip is a square single crystal, 4 mm on each side and 50 μm-thick. Four parallel electrode strips, each platinum with a width of 750 μm and a thickness of 25 nm, cross one face with a 1-mm period. The second face has four similar strips, but orthogonal to those on the first. Their intersections form a 4×4 grid of pixels. Figure 2 shows a microscope photograph of the diamond.

Future detectors are envisioned with many more pixels, spread over several chips. Each detector will surround the

Content from this work may be used under the terms of the CC-BY-4.0 licence (© 2023). Any distribution of this work must maintain attribution to the author(s), title of the work, publisher, and DOI

ISBN: 978-3-95450-236-3 ISSN: 2673-5350 doi:10.18429/JACoW-IBIC2023-TUP006

bunch core while remaining outside the beam stay-clear radius, to measure the halo noninvasively. A close approach to this radius will require a mechanical adjustment of the size of the central hole.

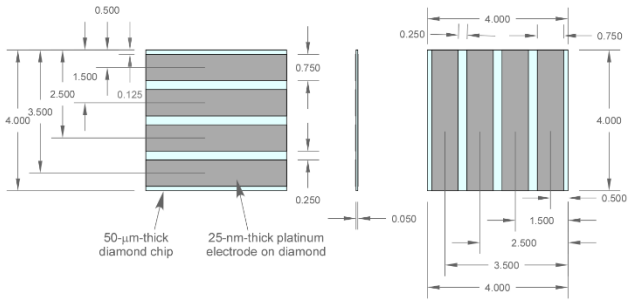


Figure 1: Pattern (in mm) of the platinum electrodes on both faces of the diamond chip.

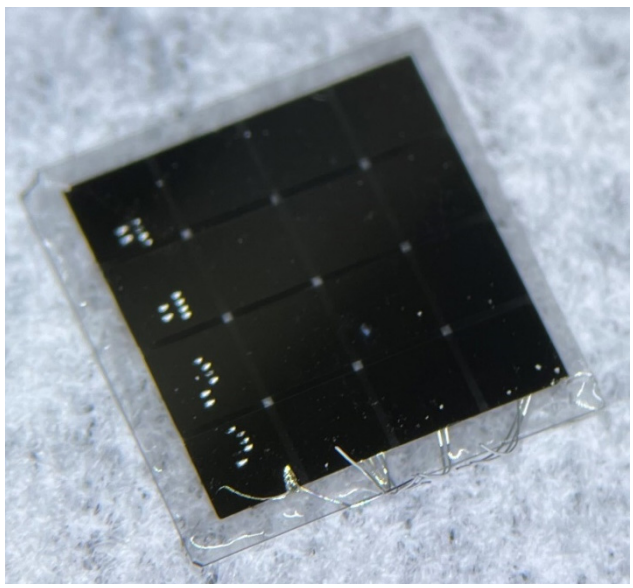


Figure 2: A microscope photo of the diamond. The diamond is clear. The electrodes, which appear black, on the upper surface run parallel to the lower edge. Those on the lower face can be seen through the gaps in the upper electrodes. Old wires from a previous bonding to the circuit board hang from the lower edge.

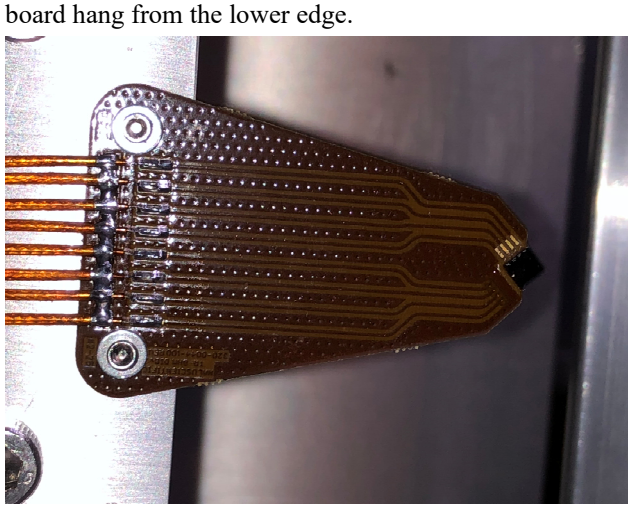


Figure 3: The diamond detector of Fig. 2, mounted on the printed circuit for fan-out to the 8 coaxial cables.

Shot-by-Shot Pixel Readout

The device tested at FACET-II evolved from the readout designed for a Time-Resolved Beam-Halo Monitor (TR-BHM) developed by Nalu Scientific in collaboration with another of the authors (J. Smedley).

The eight strips are wire bonded to a small printed-circuit board (Fig. 3) supporting the chip and fans out to eight coaxial cables running to a nearby amplifier box. Each channel is AC-coupled to the amplifier and DC coupled to a bias voltage. The DC supply is typically set to 30 V. The amplifier outputs are digitised in a separate module further from the beamline and transported over ethernet to a computer outside the tunnel. We use Nalu Scientific's AARDVARC digitiser hardware [2] along with Nalu's *Naluscope* software for viewing and control.

Normally the strips on one side are grounded (for example, the horizontal strips, which correspond to the y coordinate) and those on the other are biased (vertical, giving the x coordinate). In a low-density halo, only one pixel may receive charge. This pixel is identified by the horizonal and vertical strips that receive nonzero signals. With a higher density, the bias is applied to only one strip of the four. Then the x coordinate is determined by the bias and the y profile comes from reading the charge on the grounded face. The bias is moved from strip to strip over four shots, giving the full pixel distribution. For an $N{\times}N$ grid, this method is a trade-off: N shots rather than one, but $2N$ cables and channels rather than N^2. The advantage is less significant for our simple chip than for future devices.

HALO TEST AT FACET-II

FACET-II [1] is SLAC's test facility for advanced accelerator research, primarily studies of plasma-wakefield acceleration. The vertical bend at the beam dump serves as a spectrometer for the resulting wide changes in beam energy from an initial energy of typically 10 GeV. Electrons exit the beamline vacuum through a flange with a 5-mm-thick aluminium window and pass through more than 2 m of air while going over a diagnostics table and bending downward into the dump. This arrangement is convenient for a proof-of-principle test. It provides a first look at halo without the need for in-vacuum motion of the diamond sensor. After a long downtime, FACET-II is now being tuned, starting at the injector. The beam should be sent to the dump around the time of this conference. We anticipate beginning parasitic measurements shortly afterward.

The detector is mounted 185 cm from the window, at beam height and on a 50-mm horizontal translation stage. At one end of the travel, the beam core is roughly centred on the chip. We will begin with it fully retracted away from the beam. Then the signals from the chip will give an indication of the noise background, from the pulsed RF power and from the beam itself. This noise floor sets one end of the measurement's dynamic range. The beam can be stopped on a collimator just upstream to see the ambient electronic noise. The additional noise when the beam next goes to the dump will give the background due to the beam.

Content from this work may be used under the terms of the CC-BY-4.0 licence (© 2023). Any distribution of this work must maintain attribution to the author(s), title of the work, publisher, and DOI

ISBN: 978-3-95450-236-3 ISSN: 2673-5350 doi:10.18429/JACoW-IBIC2023-TUP006

We will then translate the diamond slowly toward the beam while monitoring the signals. An increase should be seen once the beam enters the halo. This movement can be continued until the beam is approaches within perhaps 2σ of the centre (where σ is the RMS beam size). The dump bend can scan the halo vertically to vary the signals as the dipole shifts beam above and below the detector. Small controlled horizontal moves can be made with a horizontal corrector. (With no readback other than a video image of the position, the translation stage is imprecise for horizontal scanning.) The signals must be carefully watched near the core to avoid saturation. Damage to the simple FR4 circuit board is a concern if too much beam scatters from the diamond; a more expensive ceramic board will be needed in the next in-vacuum test (discussed below). The dynamic range extends at least between the highest level that seems safe and the noise floor.

Additional tests are needed to validate the halo measurement, since halo has an uncertain distribution that can extend to several times σ from the beam centre. The detector should appropriately register changes in the bunch size as the spectrometer quadrupoles change the focus. A suitable phase advance can image the collimator about 50 m upstream of the dump onto the detector. As the jaws are opened or closed, the moving image of the jaws should cut into the halo.

SIMULATION OF DIAMOND RESPONSE

We conducted a simulation to find the spread of the bunch after travel through the window and the air path, and the resulting charge deposition in the diamond. This study used a GEANT4 [7] model replicating the real geometry of the pixellated diamond detector (Fig. 4). The model integrates the intricate arrangement of strips and the diamond itself. Essential parameters such as particle position, direction, and energy entering the FACET-II exit flange are obtained from the ELEGANT beam-dynamics code [8]. Figure 5 (a) shows the transverse distribution at the exit window. The x and y projections, in Figs. 5(b) and (c) respectively, demonstrate that both distributions have long tails of halo electrons. The much lower density of the tails calls for a detector with a wide dynamic range, to record electrons in both the core and halo. The parameters are given to the GEANT4 simulation, which includes the exit window, the 185-cm air path to the diamond, and the detector itself.

Our simulation applies two distinct scoring approaches. The first is based on transfer functions provided by Cividec [9], a manufacturer of diamond detectors. These provide the interaction probabilities of various particle types within the diamond and the resulting charge generated, as a function of particle energy. The data accounts only for electrons, photons, protons, and neutrons. In the second scoring method, GEANT4 directly computes the energy deposition within the diamond, and an electron-hole pair is created for every 13.3 eV deposited [6].

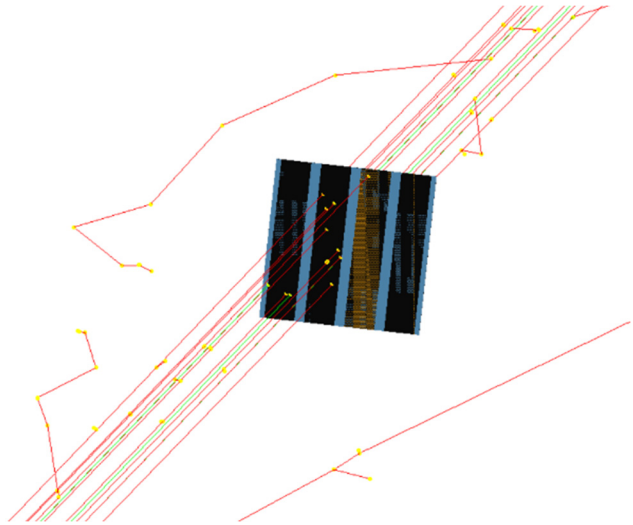


Figure 4: A GEANT4 simulation in which 10 primary 10-GeV electrons pass through the air path and the diamond detector. Electrons are shown in red and photons in green.

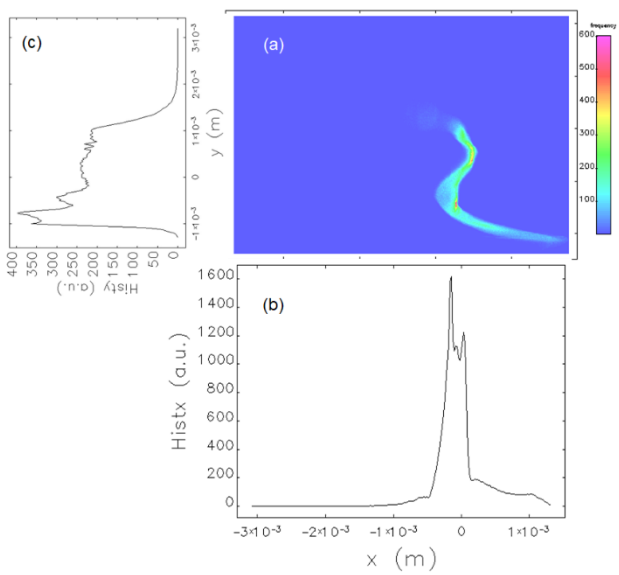


Figure 5: (a) Simulated transverse distribution of the electron bunch at the exit window, with projections along the (b) x and (c) y coordinates.

We find that these two methods agree both qualitatively and quantitatively. The spatial distribution of the diamond signals aligns well, while relative differences of 20% to 60% (Fig. 6) are observed between the two approaches. To ascertain whether these discrepancies are due to secondary particles beyond electrons, photons neutrons, and protons, we simulated the energy deposited by alpha particles, deuterons, pions, and ions produced by interactions with air. We find a negligible contribution from these secondaries to the total energy deposition within the diamond, less than 0.015%, with 0.01% originating from alpha particles. This correspondence suggests that the simulation captures the diamond detector's response, which we will benchmark with our upcoming measurements.

Content from this work may be used under the terms of the CC-BY-4.0 licence (© 2023). Any distribution of this work must maintain attribution to the author(s), title of the work, publisher, and DOI

ISBN: 978-3-95450-236-3 ISSN: 2673-5350 doi:10.18429/JACoW-IBIC2023-TUP006



Figure 6: Comparison of the GEANT4 simulation results for FACET-II using the two scoring methods, in fC per primary electron. Left: Cividec transfer functions. Centre: Energy deposition from GEANT4. Right: Relative difference.

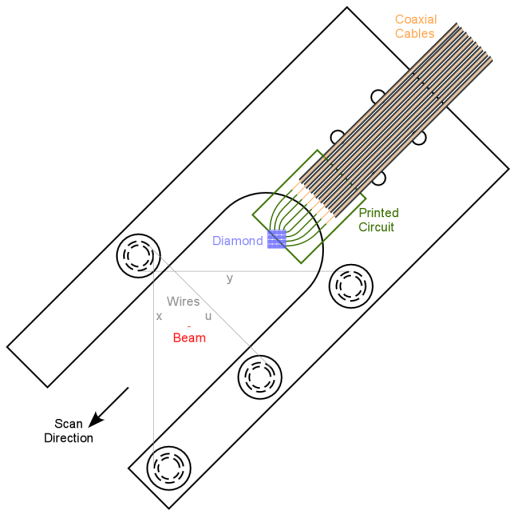


Figure 7: Sketch of a modified wire-scanner "harp".

FUTURE WORK

FACET-II Measurement in Vacuum

As we begin the in-air measurements at the FACET-II beam dump, we are designing the next phase, a test in vacuum. To translate the detector from outside the beam into the halo, we will modify a surplus wire scanner. Minor changes to the "wire card" or "harp" that holds the wires will allow mounting the diamond on the moving stage (Fig. 7). The signals from the 8 strips will be connected through the vacuum in coaxial cables to a feedthrough flange for processing by Nalu's electronics outside. The wire scanner allows us to measure the profile of the bunch core and the coordinates of it centroid relative to the diamond's pixels. As the wire scanner moves the diamond through the halo, we will be able to map the halo over a region much larger than the size of the chip.

Halo Evolution

Effective halo mitigation must be guided by a better understanding of halo formation by interpreting measurements with simulations. These are also needed to guide the design of more advanced sensors, so that their extent and resolution can match the halo distribution at various locations along the FACET-II or LCLS-II beamlines. The complexities underlying beam halo are not yet well modelled and involve high-order nonlinear beam dynamics.

We plan to develop start-to-end particle-in-cell (PIC) numerical simulations of halo formation and evolution along the accelerator as extensions of various existing codes. Several well-benchmarked numerical simulation codes—including ASTRA, GPT, Elegant, Lucretia, and IMPACT—have been used successfully in designing and operating LCLS, LCLS-II, FACET and FACET-II, from electron-bunch generation through acceleration and bunch compression. These codes are well suited to form the basis for a model of beam halo.

However, due to the large extent of the beam's distribution in 6-dimensional phase space, a high-order map for beam dynamics must be carefully implemented to model the generation and evolution of beam halo in the injector, accelerator, and bunch compressors. In particular, the core beam's collective effects can drive the halo to execute betatron motion at large amplitude and with potentially significant chromatic effects. In the compressors, the model must incorporate 3-dimensional coherent synchrotron radiation (CSR) [10] to properly study transverse effects.

Understanding the formation and evolution of halo along the accelerator, through both measurement and simulation, will ultimately provide techniques for mitigating halo at its sources. These developments should prove valuable for LCLS and other XFELs.

REFERENCES

[1] FACET-II Conceptual Design Report, SLAC, 2015.

[2] L. Macchiarulo *et al.*, "Design improvements and first results for the revision 3 of AARDVARC Waveform Sampling System on Chip", in *Proc. IEEE NSS-MIC 2020*, Boston, MA, USA (virtual), November 2020. doi:10.1109/NSS/MIC42677.2020.9507950

[3] J. Bohon, E. Muller, J. Smedley, "Development of diamond-based X-ray detection for high-flux beamline diagnostics", *J. Synchrotron* Radiat., vol. 17, pp. 711-718, 2010. doi:10.1107/S0909049510031420

[4] E. Muller *et al.*, "Transmission-mode diamond white-beam position monitor at NSLS", *J. Synchrotron Radiat.*,vol. 19, pp. 381-387, 2012. doi:10.1107/S0909049512005043

[5] T Zhou *et al.*, "Pixelated transmission-mode diamond X-ray detector", *J. Synchrotron Radiat.*, vol. 22, pp. 1396-1402, 2015. doi:10.1107/S1600577515014824

[6] J. Keister and J. Smedley, "Single Crystal Diamond Photodiode for Soft x-ray Radiometry", *Nucl. Instrum.Methods A*, vol. 606, 774-779, 2009. doi:10.1016/j.nima.2009.04.044

[7] S. Agostinelli *et al.*, "GEANT4–a simulation toolkit", *Nucl. Instrum.Methods A*, vol. 506, pp. 250-303, 2003. doi:10.1016/S0168-9002(03)01368-8

[8] M. Borland, "ELEGANT: A Flexible SDDS-Compliant Code for Accelerator Simulation", Advanced Photon Source LS-287, September 2000.

[9] E. Griesmayer, personal communication. https://cividec.at

[10] Y. Cai and Y. Ding, "Three-dimensional Effects of Coherent Synchrotron Radiation by Electrons in a Bunch Compressor", Phys. Rev. Accel. Beams, vol. 23, p. 014402, 2020. doi:10.1103/PhysRevAccelBeams.23.014402

Content from this work may be used under the terms of the CC-BY-4.0 licence (© 2023). Any distribution of this work must maintain attribution to the author(s), title of the work, publisher, and DOI

ISBN: 978-3-95450-236-3 ISSN: 2673-5350 doi:10.18429/JACoW-IBIC2023-TUP007

USE OF THE ISAC-II FLIGHT TIME MONITORS TOWARD AUTOMATED TUNING

S. Kiy*, P. Jung, T. Planche, O. Shelbaya, V. Verzilov, TRIUMF, Vancouver, BC, Canada

Abstract

A time-of-flight measurement system has been in use at ISAC-II since 2006 for the phasing of cavities and accurate ion beam velocity measurements across the nuclear chart. This system is heavily relied upon as the primary energy-time domain diagnostic downstream of the ISAC-II linac. Ongoing High Level Applications (HLA) development at TRIUMF has enabled the use of methods that are being applied to these measurements - both for processing and automation of data acquisition. An update will be provided on operational experience with the system over the past 10 years including its recent re-calibration and error analysis. A brief summary of the current HLA framework will be given, including a database for beam measurements and the ability to carry out sequential measurement processes. Finally, the way in which these developments enable beam-based calibration of cavity parameters and a shift to model-based tuning methods is discussed.

INTRODUCTION

The present configuration of the ISAC-II linac was installed in two phases, in 2006 [1] and 2010 [2]. Each phase consists of 20 superconducting quarter wave resonators designed to provide a total effective voltage of 40 MV for the full linac. Phase-I houses two cavity types ($\beta = 0.057$ and $\beta = 0.071$) and consists of 5 cryomodules, while phase-II has a single cavity design ($\beta = 0.110$) and consists of 3 cryomodules. Each of the eight cryomodules houses a single superconducting solenoid which provides transverse focusing to the beam. The primary diagnostic devices for measurements of beam velocity and phasing of cavities are three flight time monitors (FTMs) downstream of the ISAC-II linac. The FTMs were originally installed in 2006 [3] and later upgraded in 2011 [4] to have allow their positions to be adjustable with respect to the ion beam.

Shown in Fig. 1, these diagnostics are composed of a 50 µm wire aligned along the axis of a grounded cylinder, with a negative bias of ~2 kV applied to the wire. The full cylinder is actuated at 45 degrees from horizontal into the beam, and the ions induce emission of secondary electrons from the wire. These secondary electrons move away in the electric field and are detected by a micro channel plate (MCP) detector with a time resolution of better than 100 ps.

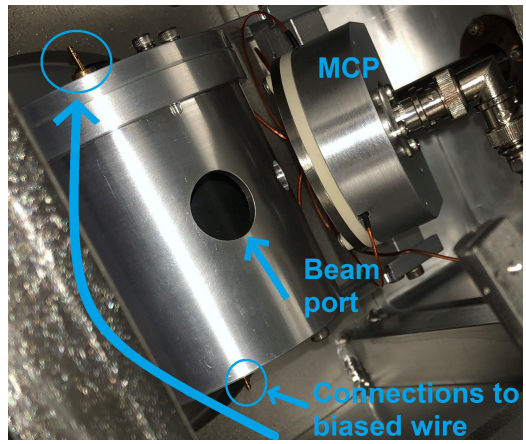


Figure 1: ISAC-II Flight Time Monitor Canister showing beam port and MCP.

OPERATIONAL EXPERIENCE

Maintenance

The FTMs have been regularly used since they were last upgraded in 2011. During this time they have been regularly used both for time of flight (TOF) measurements for calculating the beam velocity, as well as for setting cavity phases during setup to experiments (phase-TOF scans). The latter technique can be a fairly time consuming way to set cavity phases, and with ISAC-II typically serving between 5 and 10 experiments per calendar year, the FTMs can often end up being used for a total of 100 hours or more per year.

These monitors have proven to be very reliable over the past 12 years. The only major repairs required over this time has been the replacement of two of the three MCPs in 2016, and the replacement of the tungsten wires due to increased signs of field emission which can cause damage the MCPs.

Calibration

A calibration laser was installed in 2011 to measure and correct for small discrepancies of delays in cables of the three separate monitors [4]. While it was initially envisioned routinely re-check the calibration, the process was only repeated just recently during the first half of 2023. The same procedure described in Ref. [4] was carried out to measure the arrival time of the laser at each of the three monitors, with the resulting TOF spectrum shown in Fig. 2. Shown below in Table 1, the recent calibration indeed showed small changes in the timing offsets relative to the typical flight times between the monitors.

The change in calibrations in Table 1 is attributable to 2016 maintenance of the system, during which monitors were removed and MCPs replaced. Plotting the relative

* spencerkiy@triumf.ca

Content from this work may be used under the terms of the CC-BY-4.0 licence (© 2023). Any distribution of this work must maintain attribution to the author(s), title of the work, publisher, and DOI

ISBN: 978-3-95450-236-3 ISSN: 2673-5350 doi:10.18429/JACoW-IBIC2023-TUP007

Content from this work may be used under the terms of the CC-BY-4.0 licence (© 2023). Any distribution of this work must maintain attribution to the author(s), title of the work, publisher, and DOI

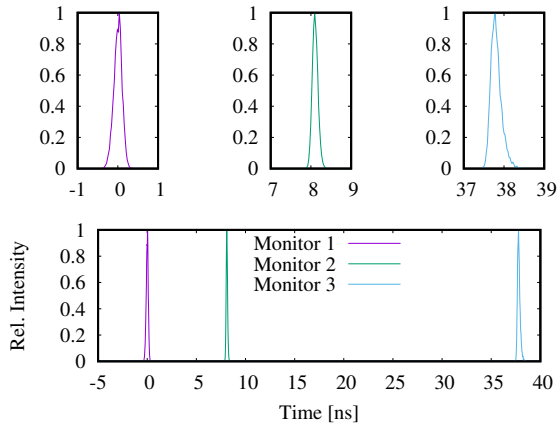


Figure 2: Time-of-flight measurement of the calibration laser.

Table 1: Summary of changes in FTM offsets, measured with respect to the first monitor.

FTM	Change [ns]
2	-0.7
3	+0.04

difference of velocities calculated between different pairs of monitors (V_{12}, V_{23}, V_{13}) supports this, as it shows a step function in the difference at the same date the work was done.

Low Intensity Measurements

Since 2020, the FTMs are now in regular use to measure low intensity radioactive beams prior to delivery to experiments. An example of the TOF measurement for a ^{20}Mg beam in 2023 is shown in Fig. 3.

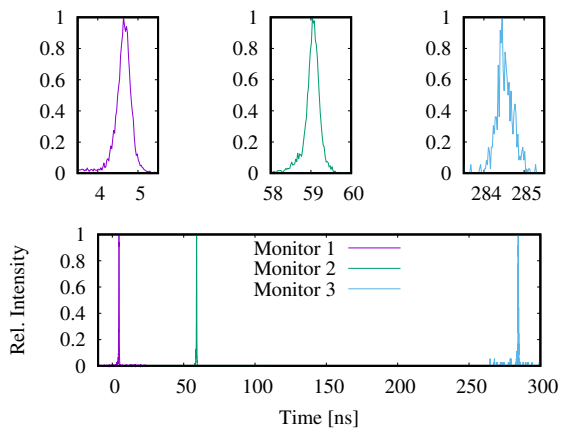


Figure 3: Time-of-flight measurement of a beam of $^{20}Mg^{6+}$ at an intensity of 9×10^3 /s.

These monitors have in principle been capable of measuring intensities down to as low as 10^4 ions/s since their initial installation in 2006. However in practice this was not done regularly until 2020. The new method for low intensity TOF measurements is:

1. Establish a tune with a stable beam at the desired energy.
2. Carefully document the necessary positions of the FTMs for the established tune.
3. Scale the tune and switch to the radioactive beam.
4. Set MCP bias to its maximum allowable voltage and restore FTM positions to their established values.
5. Collect for extended periods of time (up to 30 minutes).

Using this method, the energy of radioactive beams of ^{11}Li at 8×10^3 /s, ^{59}Cu at 5×10^3 /s, and ^{20}Mg at 9×10^3 /s have been successfully measured so far.

UNCERTAINTIES AFFECTING FTM MEASUREMENTS

During the recent 2023 laser calibration, data was also collected to further investigate the uncertainties involved in the FTM measurements. Previous data collected in 2022 [5] for repeat measurements of a beam of $^{20}Ne^{4+}$ showed non-negligible deviations in calculated beam centroids at the three monitors. This deviation increased when the transverse positions of the monitors were moved and there was a clear correlation observed between FTM position and beam centroid for all three monitors as shown in Fig. 4.

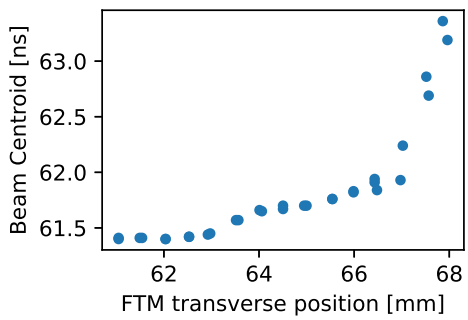


Figure 4: Correlation between transverse position of FTM with measured beam centroid for a $^{20}Ne^{4+}$ beam.

As it can be difficult to assess whether the changes in centroid were due to drifts and correlations in the beam, some repeat measurements were carried out with the calibration laser for comparison to $^{20}Ne^{4+}$ data from 2022. The resulting deviations in beam centroids at the three different monitors are shown in Tables 2 (for $^{20}Ne^{4+}$) and 3 (for calibration laser).

Table 2 shows a significant increase in deviation when the FTM positions are varied vs fixed. This is apparent for both cases of the ISAC-II linac off, and ISAC-II linac on (bunching cavity and 37 SC quarter-wave cavities on). In contrast to this, the measurements with the laser show a much smaller

ISBN: 978-3-95450-236-3 ISSN: 2673-5350 doi:10.18429/JACoW-IBIC2023-TUP007

Table 2: Standard deviation of repeat measurements of the time centroid of the $^{20}Ne^{4+}$ beam at each of the three FTMs under various conditions in 2022 (reproduced from Ref. [5]).

Measurement	σ_1 [ps]	σ_2 [ps]	σ_3 [ps]
Linac off, static FTMs	300	300	400
Linac off, moving FTMs	700	700	800
Linac on, static FTMs	20	30	70
Linac on, moving FTMs	70	170	90

Table 3: Standard deviation of repeat measurements of the time centroid of the calibration laser at each of the three FTMs under various conditions in 2023. The conditions of the laser are identical in each of the three cases.

Measurement	σ_1 [ps]	σ_2 [ps]	σ_3 [ps]
Static, over 2.5 hrs	6	0	5
Static, over 8.3 hrs	27	5	17
Moving, over 1.7 hrs	16	4	9

deviation. Although there does appear to be an increase in deviation if the monitor positions are varied, the effect is much smaller than for the beam-based measurements.

Based on this, the conclusion is that, due to the small amount of beam that the 50 µm wire of the FTMs intersects, it is likely measuring a real difference in the arrival time of different slices of beam as it is moved. There is a known chromatic bend in the upstream ISAC-I section that contributes to (x, E) coupling [6], which later due to the solenoids in ISAC-II is mixed with the y dimension. Further to this, the quarter-wave resonators in use at ISAC-II are known to have a phase dependent vertical steering effect [7], that while minimized may also be contributing to couplings between the transverse and longitudinal coordinates.

AUTOMATIC DATA COLLECTION

Automation

A High Level Application (HLA) task force was implemented at TRIUMF [8] in 2017 to try and automate various tasks where possible and to utilize real-time physics simulations to expedite machine configuration changes as well as improve reliability. This has led to the development of sequential measurements [9], which consist of a series of commands that are managed by the HLA server and sent to EPICS [10]. This allows for automated measurements that previously required highly repetitive manual changes and saving of data either by operators or beam physicists. One example of a task that this expedites are standard phase-energy scans of the ISAC-II quarter wave resonators either for calibration of cavity amplitudes, or for identifying the correct accelerating phase during setup to an experiment.

Beam Database

Also described in Ref. [9], a beam database (beamDB) has been developed which allows for a more structured and searchable way to catalog measurements of an ion beam at TRIUMF. Historically, built-in tools from EPICS and EDM (Extensible Display Manager) have been used to dump data from an EDM screen to a user-defined filename on a fileshare server. Intensity measurements were saved solely as HTML tables within an electronic logbook. This approach made it difficult for others to find past measurements, to identify which optics settings were in use for a measurement, or even to know the beam in use for a given measurement. In contrast to this, the implemented beamDB pairs the sequential measurement process with a way to save data, collecting multiple related diagnostic measurements together in a fixed format together with the entire machine state for each measurement. In reference to operation of the ISAC-II linac, this beamDB allows for saving of TOF profiles continuously throughout a phase-energy scan.

Future Work

The central part of the HLA framework is an internal web API for accessing EPICS. This web API handles multiple functions including: authentication, writing to EPICS, maintaining process variable (PV) monitors with EPICS, long-running sequential measurements, and read/write access to the beam database. An upgrade to the web API is underway that will modularize the code, separating many of the functions into different services that can be maintained and re-deployed independently. Along with this will be the addition of a new service to allow for optimization of EPICS PVs, that can then be run within a sequential measurement. This will be a significant improvement to the use of the ISAC-II FTMs, as it will allow the count rates on the FTMs to be maximized via optimization of their positions before each set of profiles is saved (Fig. 5).

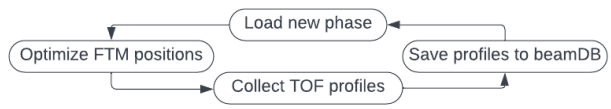


Figure 5: Sequential measurement process for collecting calibration data for ISAC-II cavities.

MODEL BASED PHASING OF ISAC-II LINAC

A recently completed MSc thesis [5] has utilized the FTMs and other work summarized in this paper to begin implementing model based phasing of the ISAC-II linac. This involved two main parts - the first was to collect phase-energy calibration data for each of the 40 cavities in the ISAC-II linac. From this, the scaling between the control system amplitude and the physical field of a cavity could be calculated, as well as the phase offsets of all cavities. These

Content from this work may be used under the terms of the CC-BY-4.0 licence (© 2023). Any distribution of this work must maintain attribution to the author(s), title of the work, publisher, and DOI

ISBN: 978-3-95450-236-3 ISSN: 2673-5350 doi:10.18429/JACoW-IBIC2023-TUP007

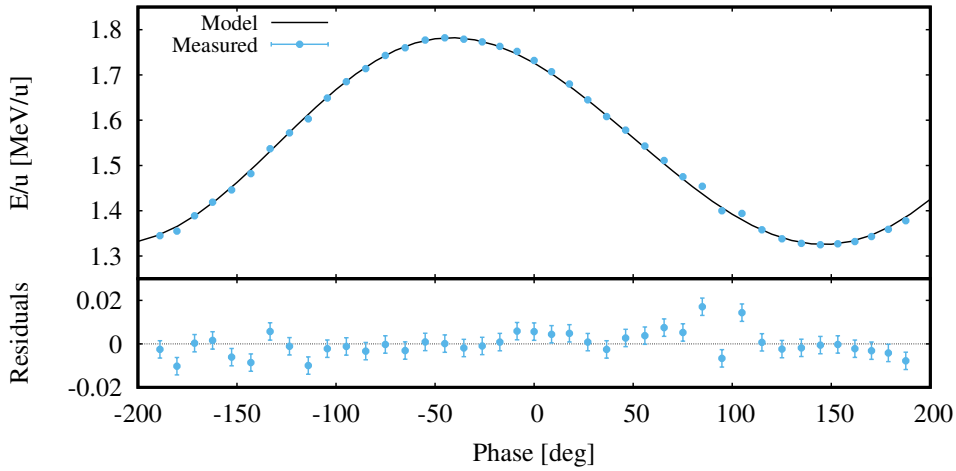


Figure 6: Energy-phase scan and resulting model fit for first linac cavity.

are then input into a model of the machine in an envelope code, TRANSOPTR [11]. This model was then used for the second part of this project, verification of the new approach - using the model to predict the necessary phases for given beam properties (mass, charge, input energy, and requested output energy).

The phase-energy calibration data during this work (and historically in general) has been difficult to collect due to the relative positioning of the FTMs with respect to the 40 linac cavities. The 40 cavities are spaced over approximately 18.6 metres, with the three FTMs at distances of 2.74, 4.93, and 13.99 metres downstream of the last cavity. There are no longitudinal diagnostics within the linac, and as a result the beam must be transported by up to 32.6 metres (in the case of the first cavity) between the cavity being adjusted and the last FTM. Further to this, the relative energy gain is quite significant at the start of the linac, with the first cavity increasing the beam energy by between 10 and 30%. For the first half of the linac, especially the first few cavities, this means that as the phase is changed, the necessary settings for the solenoids for transport are changing significantly due to energy alone, on top of which the RF focusing effect is changing by a non-negligible amount. The Facility for Rare Isotope Beams (FRIB), has implemented automated calibration of the linac model and instant phase setting [12] that has a number of similarities to the approach used at ISAC-II. However by contrast, FRIB has a BPM after each cryomodule, and a diagnostics-per-cavity number that is much higher than ISAC-II.

Recently, semi-automated phase-energy scans have been successfully tested, using the model to calculate necessary changes to optics as the phase is scanned, and automatically saving data before moving to the next phase. The only manual adjustments still in use were occasional optimization of the FTM positions and steering through the linac. This allows for much more detailed scans, such as that shown in Fig. 6, which in turn improve the accuracy of the model. The data shown in Fig. 6 took approximately one hour to collect compared to a manual scan for the same cavity a year early which took over four hours. The two calibrations taken one year apart using different ion beams and amplitude setpoints agreed to within 2%.

CONCLUSION

The flight time monitors in ISAC-II have been reliable diagnostics over the past 17 years for both measurement of the beam velocity as well as phasing of cavities. Recent calibrations have been done to ensure their continued accuracy, and various other improvements summarized here have contributed to their use in automated tuning tools. The ISAC-II flight time monitors are now being used to collect detailed phase-energy scans which are automated and saved to a beam database. The resulting calibrations from these detailed scans are expected to continue increasing the accuracy of the ISAC-II model and hence the model-based tuning techniques which rely on it.

REFERENCES

[1] R.E. Laxdal, "Commissioning and Early Experiments with ISAC II", in *Proc. PAC'07*, Albuquerque, NM, USA, Jun. 2007, paper THXAB01, pp. 2593–2597. https://jacow.org/p07/papers/THXAB01.pdf

[2] M. Marchetto, "Commissioning of the 20MV Superconducting Linac Upgrade at TRIUMF", in *Proc. PAC'11*, New York, NY, USA, Mar.-Apr. 2011, paper FROBN4, pp. 2570–2574. https://jacow.org/PAC2011/papers/FROBN4.pdf

[3] V.A. Verzilov, R.E. Laxdal, M. Marchetto, and W.R. Rawnsley, "Time Domain Diagnostics for the ISAC-II Superconducting Heavy Ion Linac", in *Proc. DIPAC'07*, Venice, Italy, May 2007, paper WEPB07, pp. 247–249. https://jacow.org/d07/papers/WEPB07.pdf

[4] V.A. Verzilov, J. Lassen, R.E. Laxdal, and M. Marchetto, "Upgrade of the ISAC Time-of-flight System", in *Proc. IPAC'11*, San Sebastian, Spain, Sep. 2011, paper TUPC065, pp. 1147–1149. https://jacow.org/IPAC2011/papers/TUPC065.pdf

Content from this work may be used under the terms of the CC-BY-4.0 licence (© 2023). Any distribution of this work must maintain attribution to the author(s), title of the work, publisher, and DOI

ISBN: 978-3-95450-236-3 ISSN: 2673-5350 doi:10.18429/JACoW-IBIC2023-TUP007

[5] S. Kiy, "Automated Optimization of the ISAC-II Heavy Ion Linac," TRIUMF, University of Victoria, Tech. Rep. TRI-BN-23-15, 2023, https://dspace.library.uvic.ca/bitstream/handle/1828/14955/Kiy_Spencer_MSc_2023.pdf.

[6] O. Shelbaya, "Model Coupled Accelerator Tuning (PhD thesis)," TRIUMF, UVic Dept. of Physics & Astronomy, Tech. Rep. TRI-BN-23-04, 2023, https://dspace.library.uvic.ca/handle/1828/14804.

[7] A. Facco and V. Zvyagintsev, "Beam steering in superconducting quarter-wave resonators: An analytical approach," *Phys. Rev. ST Accel. Beams*, vol. 14, p. 070101, Jul 2011. doi:10.1103/PhysRevSTAB.14.070101

[8] C. B. Barquest *et al.*, "Web-Based Control Room Applications at TRIUMF", in *Proc. IPAC'18*, Vancouver, Canada, Apr.-May 2018, pp. 4832–4835. doi:10.18429/JACoW-IPAC2018-THPML078

[9] S. Kiy *et al.*, "Beam Tuning Automation Activities at TRIUMF," in *Proc. HIAT'22*, Darmstadt, Germany, Jun.-Jul. 2022, pp. 52–56. doi:10.18429/JACoW-HIAT2022-TU2C4

[10] L. R. Dalesio, A. Kozubal, and M. Kraimer, "Epics architecture," Los Alamos National Lab., NM (United States), Tech. Rep., 1991.

[11] R. A. Baartman, "Fast Envelope Tracking for Space Charge Dominated Injectors", in *Proc. LINAC'16*, East Lansing, MI, USA, Sep. 2016, pp. 1017–1021. doi:10.18429/JACoW-LINAC2016-FR1A01

[12] A. S. Plastun and P. N. Ostroumov, "Instant Phase Setting in a Large Superconducting Linac," in *Proc. NAPAC'22*, Albuquerque, NM, USA, Aug. 2022, paper THZD1, pp. 885–890. doi:10.18429/JACoW-NAPAC2022-THZD1

Content from this work may be used under the terms of the CC-BY-4.0 licence (© 2023). Any distribution of this work must maintain attribution to the author(s), title of the work, publisher, and DOI

ISBN: 978-3-95450-236-3 ISSN: 2673-5350 doi:10.18429/JACoW-IBIC2023-TUP009

BUNCH LENGTH MEASUREMENT SYSTEM DOWNSTREAM THE INJECTOR OF THE S-DALINAC*

A. Brauch†, M. Arnold, M. Dutine, J. Enders, R. Grewe, L. E. Jürgensen,
N. Pietralla, F. Schliessmann, D. Schneider
Technische Universität Darmstadt, Dept. of Physics, Institute for Nuclear Physics,
Schlossgartenstr. 9, Darmstadt, Germany

Abstract

The S-DALINAC is a thrice recirculating electron accelerator with a continuous-wave beam at a frequency of 2.9972(1) GHz. Short bunches are crucial to enable tuning of the machine for operation as an energy-recovery linear accelerator. Currently, measurements of the bunch length are accomplished by using the radio-frequency zero-crossing method. Since this method is time consuming, a new setup for these measurements using a streak camera is developed. Optical transition radiation emitted from an aluminum-coated Kapton screen is used to map the bunch length information to a light pulse which enables an accurate measurement compared to a scintillating screen. The light pulse can then be evaluated with the streak camera. This contribution will present the current status of the measurement setup as well as its design and properties.

INTRODUCTION

The superconducting Darmstadt electron linear accelerator S-DALINAC was originally established as a twice-recirculating accelerator in 1991 operating at a radio frequency of 2.9972(1) GHz. An upgrade of the machine adding a third recirculation beamline in 2015/16 was performed. This beamline also features an adjustment system for the path length of the electrons in the second recirculation beamline with a range of 10 cm which is identical to the wavelength of the operation frequency (see Fig. 1). It is possible to recover the energy of this beam by passing the main accelerator a second time if this system is set to an 180° phase shift and the beam passing the main accelerator for the first time is led to the respective beamline. This operation mode called 1×ERL (1× Energy-Recovery Linear accelerator) was achieved in 2017 for the first time at the S-DALINAC [1]. Four years later a 2×ERL mode was demonstrated by accelerating and decelerating the beam twice [2]. More than 87 % of the beam energy were recovered in this mode. The efficiency was observed to decrease with the increase of the initial current at the electron gun. The effect is partly caused by the greater bunch length in high current operation. Therefore, the minimization of this parameter is important for reaching higher currents and efficiencies in ERL operation. This requires a setup for measuring the bunch length.

BUNCH LENGTH MEASUREMENTS DOWNSTREAM THE INJECTOR

The current method for bunch length measurements is based on the radio-frequency zero-crossing method [3]. An RF (radio-frequency) cavity is used to impose a momentum chirp on a bunch.

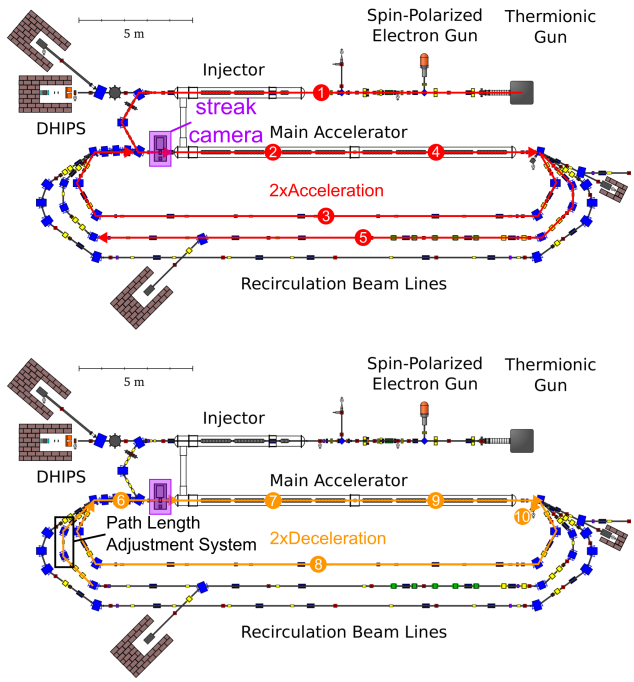


Figure 1: The layout of S-DALINAC including the beam path for operation in 2×ERL mode (following [2]). The top image shows the acceleration in this mode. After passing the injector in (1) the beam is led to its main acceleration in (2). Following the first recirculation beamline (3) the beam is accelerated a second time in the main accelerator (4). The beam then enters the second recirculation beamline (5). The bottom image shows the deceleration of the beam in 2×ERL mode. Because of the path length adjustment system the beam receives a phase shift of 180° in (6). The first deceleration takes place in (7) and the beam is again led through the first recirculation beamline in (8). The second deceleration stage (9) reduces the beam energy to the energy that was originally provided by the injector linac. At this energy, the beam is dumped (10). The intended bunch length measurement setup location for commissioning is also shown in purple.

* Work supported by the State of Hesse within the Cluster Project ELEMENTS (Project ID 500/10.006) and by DFG (GRK 2128 AccelencE).
† abrauch@ikp.tu-darmstadt.de

Content from this work may be used under the terms of the CC-BY-4.0 licence (© 2023). Any distribution of this work must maintain attribution to the author(s), title of the work, publisher, and DOI

ISBN: 978-3-95450-236-3 ISSN: 2673-5350 doi:10.18429/JACoW-IBIC2023-TUP009

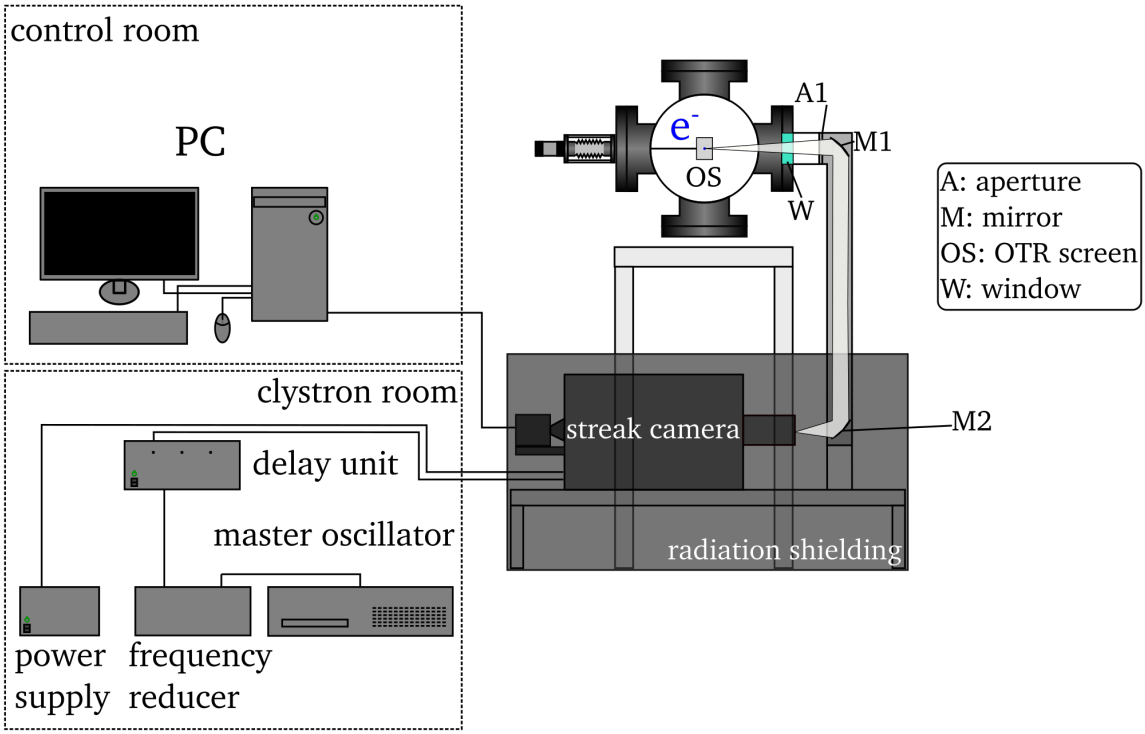


Figure 2: Current setup for measuring bunch lengths via OTR screens and a streak camera. The emitted light pulses from the screen are transported and focused via two off-axis parabolic mirrors on the entrance slit in front of the camera. All electrical devices for the streak camera will be stored in rooms that are protected from radiation.

After a dispersive section the transverse beam profile of this bunch is measured with a scintillating screen. Because of the dispersive section the size of the beam on the target is connected to the induced momentum chirp which again is dependent on the bunch length. Using this method to evaluate the bunch length has some significant drawbacks:

- The initial transverse beam size and the scintillating screen itself cause the measurement to be an upper estimate of the bunch length only.
- The measurement is only valid at the position of the used RF cavity and must be extrapolated otherwise.
- It is impossible to determine the bunch length value when all RF cavities are operated in intended operation, that is, when all RF cavities are operated at their design values.

These issues make it impossible to monitor the bunch length parameter in ERL operation properly. Therefore, a new setup for bunch length measurements downstream the injector has been developed. All components are currently in the procurement phase. Figure 2 shows a sketch of measuring bunch lengths with this new setup. An optical transition radiation (OTR) screen is used to create light pulses with the same length as the electron bunches. These pulses are transported via optical elements to a streak camera which then measures the length of these pulses. Next to the streak camera the setup requires an OTR screen, an electrical reference signal, a radiation shielding and optical elements. Details of the shielding will be determined from upcoming measurements. The electrical reference signal will be produced by the master oscillator.

The main goal with this setup is to provide an accurate and robust method for measuring the bunch length just before the main accelerator with a time resolution of better than 1 ps. This is required for specific machine settings and ERL operation. However, smaller values of the bunch length are favorable to further improve ERL operation [2]. In non-ERL operation the bunch length is 2 ps and will be monitored with this setup as well [4]. In the following section the contributions to the total time resolution of the setup will be discussed and estimates for the main contributions from the optical setup in front of the streak camera and the electrical reference signal will be investigated.

TIME RESOLUTION OF THE NEW BUNCH LENGTH MEASUREMENT SETUP

Several uncertainties contribute to the total time resolution R_t of the streak camera setup. Assuming no correlations between these contributions, the total resolution can be approximated by:

$$R_t = \sqrt{R_{ttd}^2 + R_{slit}^2 + R_{jitter}^2 + R_{rest}^2}. \quad (1)$$

Here, R_{ttd} is the contribution from the transit time dispersion of the photoelectrons and the electrical deflector inside the streak camera. This is the lower limit to the resolution of streak cameras and can be estimated to be $\approx$ 100 fs for commercial devices [5]. This limit is assumed to be valid

Content from this work may be used under the terms of the CC-BY-4.0 licence (© 2023). Any distribution of this work must maintain attribution to the author(s), title of the work, publisher, and DOI

ISBN: 978-3-95450-236-3 ISSN: 2673-5350 doi:10.18429/JACoW-IBIC2023-TUP009

Content from this work may be used under the terms of the CC-BY-4.0 licence (© 2023). Any distribution of this work must maintain attribution to the author(s), title of the work, publisher, and DOI

for the procured streak camera C10910 from Hamamatsu Photonics.

The beam profile of the light pulses reduces the resolution of the streak camera. It can be controlled with a slit in front of the device so that its contribution to the total resolution is R_{slit}. However, it is better to reduce the spatial intensity profile of the light pulse prior to entering the slit in the first place. This allows for more photons to be collected for the measurement and increases its accuracy. The optics in front of the streak camera and their impact on the resolution will be shown in the following section.

The electrical reference signal used to synchronize the streak camera with the S-DALINAC will be supplied by the master oscillator of the machine. Its phase noise creates a time jitter R_{jitter} that reduces the resolution of the setup. A measurement of this value at the location of the setup and its influence on the resolution is discussed below.

Finally, R_{rest} contains all contribution from minor sources to the total resolution. These are e.g. dispersion in the optics of the camera, misalignment of the orientation of the OTR screen and fluctuations of the beam. Although this value is assumed to be negligible, it can be estimated by measuring the total resolution and subtracting the other three contributions from it.

It follows that for achieving a total time resolution of at least 1 ps the condition below must be true:

$$\sqrt{R_{\mathrm{slit}}^2 + R_{\mathrm{jitter}}^2 + R_{\mathrm{rest}}^2} < 995\,\mathrm{fs}. \tag{2}$$

OPTICS OF THE NEW BUNCH LENGTH MEASUREMENT SETUP

A preliminary design assumed an optical system with a telescope and periscope in front of the streak camera [6]. The former reduced the beam profile of the light pulses and collimated them while the latter prevented a direct line of sight to the streak camera from the OTR screen. At the same time the streak camera could be located close to the floor of the accelerator hall which additionally protects the camera from radiation. Still, a radiation shielding around the streak camera was required to prevent gamma rays and neutrons from damaging the camera sensor at the end of the device.

After further simulations with the software OSLO (Optics Software for Layout and Optimization) [7] the optics were changed. Two main conditions must be met by the setup to be used in front of the streak camera:

- The light pulse created by the OTR screen has a large opening angle (14.6° in the lowest energy scenario). Collimating the light for transportation and focusing on the slit of the streak camera is required as soon as possible behind the screen window.
- The light pulse must be focused as small as possible through the input slit in front of the streak camera.

These conditions led to the current setup shown in Fig. 3. The refractive telescope was replaced by a mirror design because its focus on the streak camera slit was larger than with the purely reflective setup. At the same time the reflective setup can focus all wavelengths of the incident light and improve the accuracy of the bunch length measurement setup. The input optics of the streak camera include an achromatic relay lens which allows to make use of the independence from the wavelength. However, the input optics may be removed entirely. The alignment of the two off-axis parabolic mirrors in Fig. 3 was chosen so that aberrations caused by off-axis light beams could be counteracted [8]. At the focal point the spot size radius r of the on-axis light beams is 1.36 µm while the spot size radius of the off-axis light beams is 1.37 µm.

The contribution of the optical setup to the total resolution can be estimated with the acquired results. The screen at the end of the camera has a diameter d of 18 mm [9]. The slowest time the camera needs to streak over the screen in one cycle, T, is 100 ps. The contribution from the optical setup R_{slit} can be calculated following [10]

$$R_{\mathrm{slit}} = \frac{T}{d} r, \tag{3}$$

resulting in a contribution to the time resolution of approx. 8 fs with the slowest streak speed. Further analysis of the setup in regards to tolerances in the components will be conducted before the necessary components are procured.

TIME JITTER FROM THE MASTER OSCILLATOR

The signal of an RF oscillator contains random fluctuations in phase. These are dependent on the offset frequency of the supplied carrier signal. An electrical device like the streak camera accepts a passband from the RF oscillator that contains these random fluctuations. This leads to a time jitter (or phase jitter) in the device which degrades the resolution of the measurement. A measurement of the time jitter from

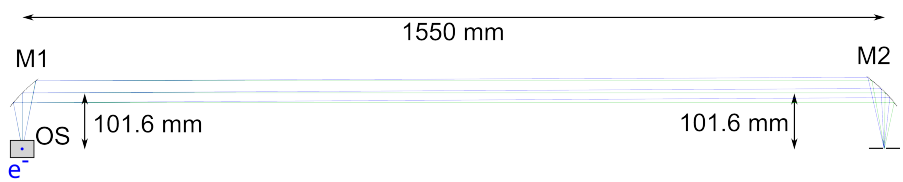


Figure 3: Sketch of the current optics setup in front of the streak camera. The rays shown are drawn by OSLO [7] and visualize the on-axis beams (green) and off-axis beams (blue). The latter are at a distance of 0.5 mm from the center of the electron spot on the target which is to be expected at the setup. Both mirrors are the same off-axis parabolic mirror with a focal length of 101.6 mm.

ISBN: 978-3-95450-236-3 ISSN: 2673-5350 doi:10.18429/JACoW-IBIC2023-TUP009

the 2.9972(1) GHz master oscillator of the S-DALINAC at the commissioning location close to the main accelerator entrance was performed with a spectrum analyzer (Rohde & Schwarz FSV). A graph of the results from 120 min of measurements is shown in Fig. 4. The time jitter caused by the master oscillator is computed using the integration of the measured phase noise A following [11]

$$R_{\text{jitter}} = \frac{10^{A/20}}{\sqrt{2}\pi f_0}. \quad (4)$$

Hereby, f_0 is the frequency of the master oscillator. Boundaries must be set for the integration. The upper integration limit is 200 kHz and is set by the passband of the streak camera. The lower limit is 100 Hz and was chosen because of anomalous behavior close to the carrier frequency. This is most likely caused by the phase noise of the reference oscillator inside the spectrum analyzer. A proper measurement method for phase noise close to the carrier frequency will be needed since this area has the most significant contribution to the time jitter. An average of 0.403(6) ps for R_{jitter} was calculated from the 120 min of measurements. While this value is still lower than the required total time resolution it is larger than the contribution from the optical setup. It is also a lower limit to the expected time jitter since the phase noise close to the carrier frequency could not be measured. This may increase the time jitter to a value over 1 ps. A new master oscillator with lower phase noise was procured. The time jitter of this device is yet to be measured and is expected to be smaller.

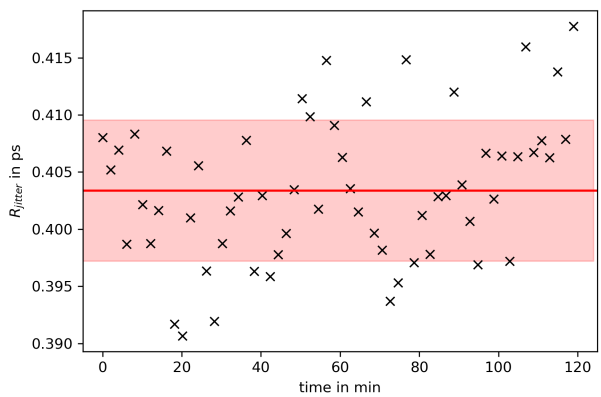


Figure 4: Measurements of R_{jitter} at 2.9972(1) GHz with a duration of 120 min. The phase noise for each measurement was integrated from 100 Hz to 200 kHz. The error band displays the standard deviation of the extracted average from all measurements.

CONCLUSION

A new setup for evaluating the bunch length behind the injector of the S-DALINAC is procured to improve 2×ERL operation by minimizing the bunch length. The optical setup in front of the streak camera and master oscillator of the S-DALINAC will have an impact on the total time resolution of the bunch length measurement. The optical setup was revised and will not significantly degrade the targeted resolution of 1 ps. Contributions from the master oscillator's time jitter have been estimated to amount to about 400 fs; however, future measurements close to the carrier frequency will need to demonstrate that the required resolution of better than 1 ps can be reached. A new master oscillator was procured and is expected to perform better than the current device [12].

REFERENCES

[1] M. Arnold *et al.*, "First operation of the superconducting darmstadt linear electron accelerator as an energy recovery linac," *Phys. Rev. Accel. Beams*, vol. 23, no. 2, p. 020 101, Feb. 2020. doi:10.1103/PhysRevAccelBeams.23.020101

[2] F. Schliessmann *et al.*, "Realization of a multi-turn energy recovery accelerator," *Nat. Phys.*, vol. 19, no. 4, pp. 597–602, Apr. 2023. doi:10.1038/s41567-022-01856-w

[3] D. X. Wang, G. A. Krafft, and C. K. Sinclair, "Measurement of femtosecond electron bunches using a rf zero-phasing method," *Phys. Rev. E*, vol. 57, no. 2, pp. 2283–2286, Feb. 1998. doi:10.1103/PhysRevE.57.2283

[4] F. Hug, "Erhöhung der Energieschärfe des Elektronenstrahls am S-DALINAC durch nicht-isochrones Rezirkulieren," Ph.D. dissertation, Technische Universität Darmstadt, Darmstadt, Germany, 2013.

[5] P. A. Jaanimagi, "Breaking the 100-fs barrier with a streak camera," in *Fourth-Generation X-Ray Sources and Ultrafast X-Ray Detectors*, International Society for Optics and Photonics, vol. 5194, 2004, pp. 171–182. doi:10.1117/12.512747

[6] A. Brauch, M. Arnold, J. Enders, L. E. Jürgensen, N. Pietralla, and S. Weih, "Bunch Length Measurement Systems at S-DALINAC," in *Proc. IBIC'22*, Kraków, Poland, Dec. 2022, pp. 96–99. doi:10.18429/JACoW-IBIC2022-MOP26

[7] Lambda Research Corporation, "OSLO - optics software for layout and optimization," EDU Version 2023. https://lambdares.com/

[8] C. Brückner, G. Notni, and A. Tünnermann, "Optimal arrangement of 90° off-axis parabolic mirrors in THz setups," *Optik*, vol. 121, no. 1, pp. 113–119, 2010. doi:10.1016/j.ijleo.2008.05.024

[9] Hamamatsu Photonics K.K., "Universal streak camera C10910 Instruction Manual," May 2018.

[10] M. M. Shakya and Z. Chang, "Achieving 280fs resolution with a streak camera by reducing the deflection dispersion," *Appl. Phys. Lett.*, vol. 87, no. 4, p. 041 103, Jul. 2005. doi:10.1063/1.2001732

[11] W. Kester, "Converting oscillator phase noise to time jitter," *Tutorial MT-008, Analog Devices*, 2009.

[12] Rohde & Schwarz, "R&S SGS100A SGMA RF Source - Specifications," Jan. 2019.

Content from this work may be used under the terms of the CC-BY-4.0 licence (© 2023). Any distribution of this work must maintain attribution to the author(s), title of the work, publisher, and DOI

ISBN: 978-3-95450-236-3 ISSN: 2673-5350 doi:10.18429/JACoW-IBIC2023-TUP010

INTERMEDIATE FREQUENCY CIRCUIT COMPONENTS FOR INTEGRATION OF ON-CHIP AMPLIFIER WITH THz DETECTORS

R. Yadav [1,*], S. Preu, Terahertz Devices and Systems, TU Darmstadt, Darmstadt, Germany
A. Penirschke, High Frequency Tech., Mittelhessen Univ. of Appl. Sci., Friedberg (Hesse), Germany
[1]also at High Frequency Tech., Mittelhessen Univ. of Appl. Sci., Friedberg (Hesse), Germany

Abstract

The demand for THz detectors for beam diagnosis and alignment at THz generating accelerator facilities increases continuously especially for room temperature applications. The Zero-Bias Schottky Diode (ZBSD) and field effect transistor (TeraFET) based Terahertz (THz) detectors are well suited for both, signal power detection at DC as well as Pulse shape diagnostics by down-conversion at intermediate frequencies (IF). The limited signal strength due to the roll-off factor of the low pass filter characteristic of the detectors at higher THz frequencies requires wide-band amplifiers to enhance the IF signal from a few µW to nW well above the noise floor of the subsequent post detection electronics. Using external amplifiers would enhance the signal losses even further due to additional connectors and rf-cable losses and degrade the signal to noise ratio (SNR). In order to maximize the SNR, we propose to have an on-chip amplifier integrated in the detectors intermediate frequency (IF) circuit in the same housing. In this work, we present the design and parametric analysis of components for transition to an IF circuit, which will be integrated in the ZBSD and TeraFET on chip with amplifier. A rigorous design analysis has been done to find the optimal parameters for wide-band operation in order to enhance the detector's resolution to capture pulses in the pico-second range with the help of fast post detection electronics.

INTRODUCTION

Research and development of materials and components in the Terahertz (THz) domain has been done rigorously since last couple of decades in order to explore this part of electromagnetic spectrum [1–3]. Due its excellent characteristics, the THz domain has numerous applications such as in imaging, spectroscopy, quality control, security, medical industry, astronomy, communications, energy and matter research, beam diagnostics and alignment at accelerator facilities, etc. [3]. The increasing demand for using this frequency spectrum has led the scientists to develop THz sources and detectors in this operable range. Room-temperature THz detectors developed in Refs. [4–6] are proved to be a cutting-edge technology for detector applications in THz domain. The detector itself is composed of both active and passive part. The active part consists of a semiconductor device such as Field Effect Transistors (TeraFET), Zero-Bias Schottky Diode (ZBSD), etc. The passive part is composed of all passive components which are used for connecting active to RF connector and later on post-detection electronics. The TeraFET or ZBSD rectifies the THz signal coupled through a silicon lens and is further down-converted from THz to millimeter frequency range [1]. The received signal is typically feed to the post detection electronics by using the intermediate frequency circuit (IF). For the detection of pico-second range pulses, it is necessary to increase the IF bandwidth components in the IF circuit as well as impedance matched circuitry to harness the full potential of the detectors [7]. Considering the important requirement for the optimization of the detector IF circuitry, in this paper we present the transition and ultra-broadband planar power divider (UBPPD) components which will be used for integrating the amplifier on-chip together with active devices in a same housing. The transition structures and UBPPD are investigated using 3D electromagnetic field simulation software (CST).

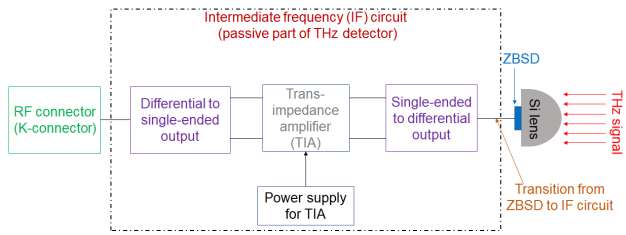


Figure 1: Block diagram of the THz detector.

TRANSMISSION LINES AS TRANSITION STRUCTURES

The block diagram of THz detector circuit is shown in Fig. 1. The blocks inside the dotted box represents the intermediate frequency (IF) circuit. The THz signal incident on the silicon lens is coupled to Zero-Bias Schottky Diode (ZBSD), which is mounted on the back side of the silicon lens (depicted as blue colour in Fig. 1.). A planar power divider along with a broadband phase shifter will be used to convert the rectified signal from single-ended to the differential input of the Trans-impedance amplifier (TIA). The output of the IF circuit is fetched to the read-out electronics via an RF connector (K-connector in this case as our target is to optimize detector initially until 40 GHz).

Figure 2 shows the transmission lines from TeraFET or ZBSD to the IF circuit. The dimensions of these structures are calculated according to Refs. [8, 9]. Four different types of transmission lines such as coupled micro-strip lines (Fig. 2 (a)), co-planar wave-guide with only signal on top (Fig. 2 (b)), co-planar wave-guide (Fig. 2 (c)) and micro-strip line (Fig. 2 (d)) is investigated. All transmission line structures are simulated on a thin-film substrate with a thickness

* rahul.yadav@iem.thm.de

Content from this work may be used under the terms of the CC-BY-4.0 licence (© 2023). Any distribution of this work must maintain attribution to the author(s), title of the work, publisher, and DOI

ISBN: 978-3-95450-236-3 ISSN: 2673-5350 doi:10.18429/JACoW-IBIC2023-TUP010

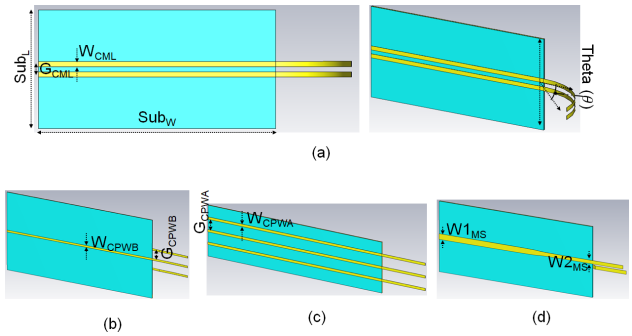


Figure 2: Investigated transition structures from active device (ZBSD) to IF circuit (a) Microstrip coupled lines, (b) Co-planar wave guide (CPW) as signal on top, (c) Co-planar wave guide (CPW) as all three ground-signal-ground on top and (d) Micro-strip line.

of 4.5 µm and a dielectric constant of $|\varepsilon|$ of 2.8. Table 1 shows the abbreviations meaning and dimensions of the structures shown in Fig. 2.

Table 1: Dimensions of the Transition Structures

Abbreviation	Full form	Dimension [mm]
G_{CML}	Gap between co-planar micro-strip lines	0.011
$GCPW_A$	Gap for CPW type A	0.050
$GCPW_B$	Gap for CPW type B	0.012
Sub_H	Substrate height	0.0045
Sub_L	Substrate length	0.25
Sub_W	Substrate width	1
W_{CML}	Width of co-planar micro-strip line	0.011
W_{CPWA}	Width of CPW A	0.012
W_{CPWB}	Width of CPW B	0.012
$W1_{MS}$	Width of micro-strip line	0.020
$W2_{MS}$	Width of micro-strip line tapered	0.012

The flexibility of having more degree of freedom while having transition from ZBSD or TeraFET to IF circuit gives an upper limit for the orientation of the other components. Therefore to understand the effect of bending (θ) the transition structures, we studied this effect on coupled micro-strip lines as shown in Fig. 3. The return loss (RL) is given as [8]:

$$RL(dB) = -20 \cdot log|\Gamma| \,, \tag{1}$$

where $|\Gamma|$ is voltage reflection coefficient. The transmission coefficient (T) and insertion loss (IL) is given by [8]:

$$T = 1 + \Gamma \tag{2}$$

$$IL(dB) = -20 \cdot log|T| \,. \tag{3}$$

Theta (θ) is varied from 0 to 90°. Figure3 (a) shows the transmission variation versus frequency. It is observed that at lower frequencies (below 10 GHz) the variation of (θ) doesn't have a significant effect, however between 30 to 40 GHz, ($\theta = 0°$) have less transmission as compared to the other variable (θ). While observing the phase (Fig. 3 (b)), it varies linearly along the frequency for coupled micro-strip line.

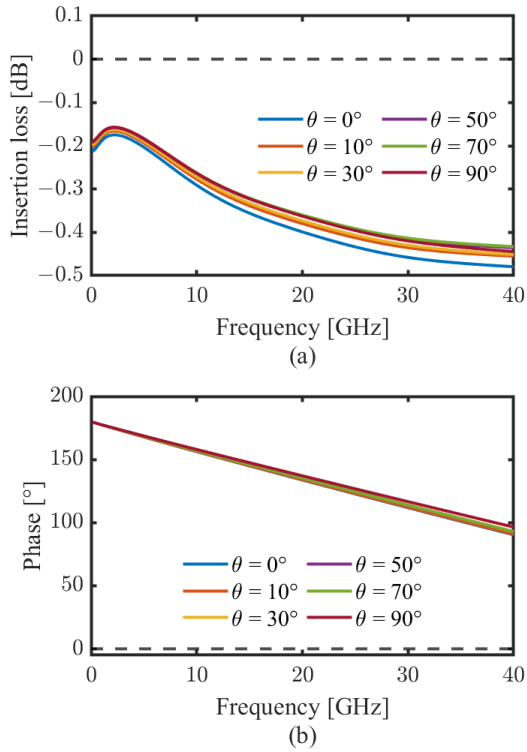


Figure 3: Study of varying θ on performance of coupled micro-strip line (a) Insertion loss over the frequency and (b) Variation of phase over the frequency.

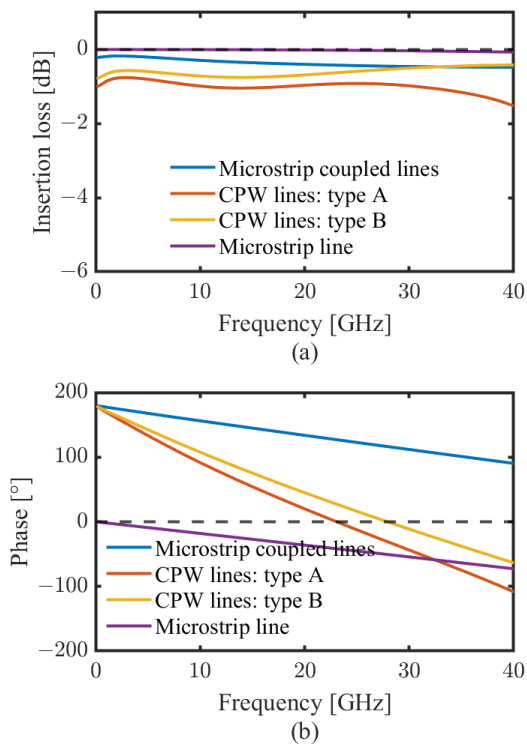


Figure 4: Comparison of different types of transition for a bending angle θ is 0°.

Content from this work may be used under the terms of the CC-BY-4.0 licence (© 2023). Any distribution of this work must maintain attribution to the author(s), title of the work, publisher, and DOI

ISBN: 978-3-95450-236-3 ISSN: 2673-5350 doi:10.18429/JACoW-IBIC2023-TUP010

Content from this work may be used under the terms of the CC-BY-4.0 licence (© 2023). Any distribution of this work must maintain attribution to the author(s), title of the work, publisher, and DOI

Figure 4 shows the comparison of all four transition structures. The CPW based structures A and B have −1 dB IL over the whole frequency range (Fig. 4 (a)) but having a zero-phase crossing at ~25 GHz (Fig. 4 (b)). For micro-strip and coupled micro-strip lines no zero-phase crossing is observed and at the same time IL is −0.5 dB. The results propose that micro-strip lines are the optimum solution as a transition structures in this specific case.

ULTRA-BROADBAND PLANAR POWER DIVIDER (UBPPD)

A power divider sub-divides the power either equally or unequally [8, 10, 11]. For the development of compact THz detectors we need an ultra-broadband planar power divider (UBPPD) in order to divide the power equally in two arms (represented by block single-ended to differential output in Fig. 1), which will be further phase shifted by using a 180° phase shifter.

Figure 5 shows the investigated ultra-broadband planar power divider (UBPPD). The capacitively or inductively loaded concept of transmission line has been used (Fig. 5 (a)) here to reduce the circuit size and increase bandwidth. This lead to increase of capacitance or inductance per unit length, which ultimately lead to slower wave propagation because of decrease in phase velocity. Figure5 (b) shows the sketch of two sections of UBPPD.

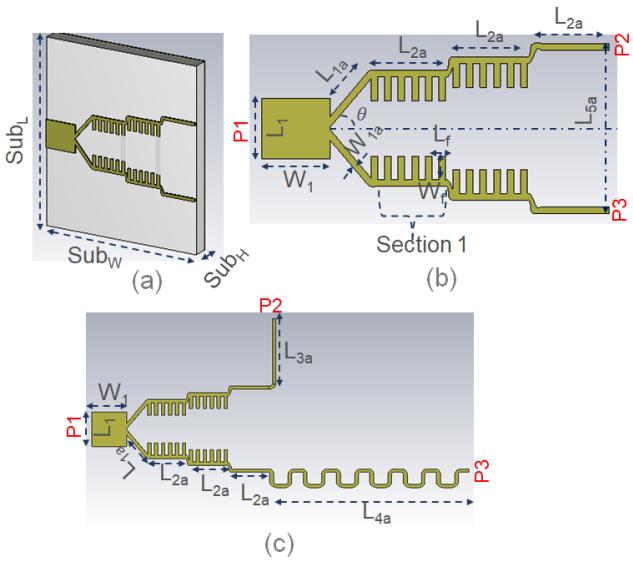


Figure 5: Ultra-broadband planar power divider (UBPPD) (a) Block diagram of UBPPD with substrate RO4350B LoPro, (b) Sketch of two section UBPPD and (c) Sketch of UBPPD with phase delay and shift transmission lines.

All the abbreviations in the Fig. 5 are show in Table 2 with there respective values used for investigation. The structure was investigated on RO4350B LoPro.

The angle between the two arms (θ) plays an important role in UBPPD performance. Fig. 6 (a) shows the effect of varying the θ on UBPPD performance. Clearly $\theta = 55°$ is have better $|S_{11}|$ results compared two $\theta = 35°$ and $\theta = 45°$.

Table 2: Dimensions of UBPPD Structure

Abbreviation	Full form	Dimension [mm]
L_f	Length of the finger	0.05
L_1	Length signal coupling pad	0.45
L_{1a}	Length of transition arm	0.44
L_{2a}	Length of single section	0.57
L_{3a}	Length of power divided arm for phase shifter	0.95
L_{4a}	Length of power divided arm for phase shifter with meander line	2.9
L_{5a}	Distance between two out ports P2 and P3	1.26
Sub_H	Substrate height	0.25
Sub_L	Substrate length	3
Sub_W	Substrate width	2.5
W_f	Width of a finger	0.18
W_1	Width of signal coupling pad	0.50
W_{1a}	Width of transition arm	0.060

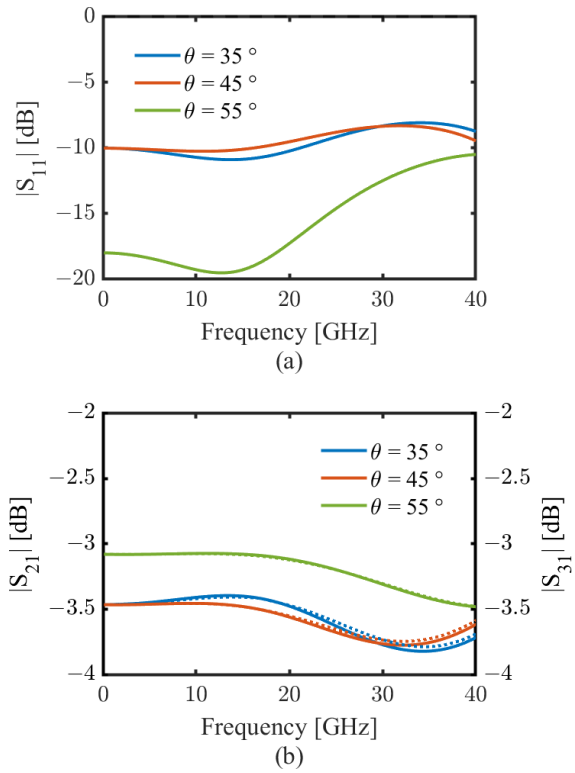


Figure 6: (a) Effect of varying (θ) on $|S_{11}|$ and (b) Effect of varying (θ) on $|S_{21}|$ and $|S_{31}|$.

Ideal power divider should have $|S_{21}| = |S_{31}|$ and as shown in Fig. 6 (b), the UBPPD have $|S_{21}| \approx |S_{31}|$ and quite stable over the whole frequency range. These varying (θ) investigation was performed for two section UBPPD (Fig. 5 (b)).

The proposed UBPPD was investigated for different sections (each section is 0.57 mm long). Figure 7 shows the performance of 3 different UBPPD having 2, 4 and 6 sections.

ISBN: 978-3-95450-236-3 ISSN: 2673-5350 doi:10.18429/JACoW-IBIC2023-TUP010

More sections in UBPPD means having a larger transmission line, which changes the electrical length of the signal and ultimately results in degrading the performance of the component. Amplitude unbalance is calculated by $|S_{31}| - |S_{21}|$ and the phase unbalance is calculated as $deg(S_{31}) - deg(S_{21})$. Figure 7 (a) shows the amplitude unbalance for 2, 4 and 6 section UBPPD. The 2 section structure have ±0.005 dB of unbalance and its comparatively stable over frequency, while for 4 section it is ±0.01 dB and ±0.02 dB for 6 sections UBPPD. Similar trend is observed for phase unbalance as well Fig. 7 (b). Therefore, its better to have 2 sections UBPPD for the IF circuit.

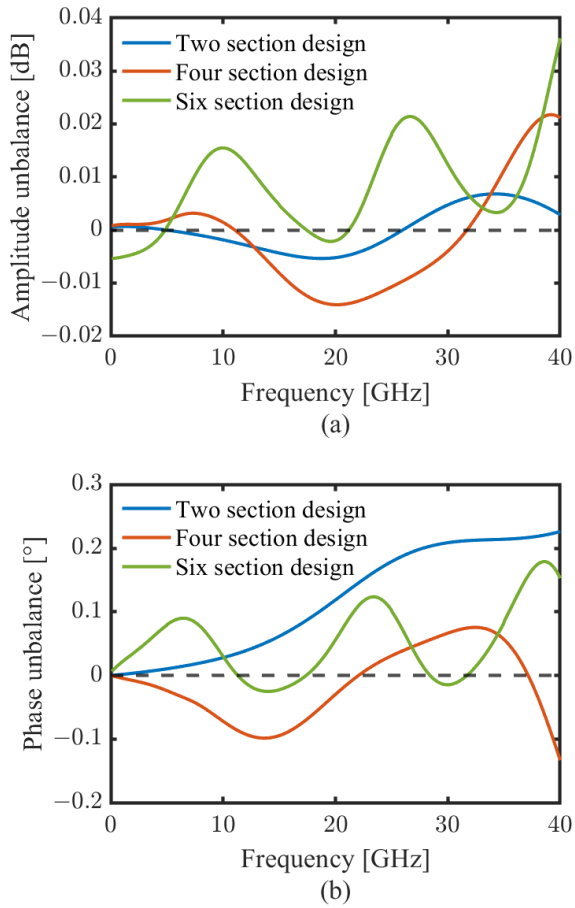


Figure 7: (a) Amplitude unbalance comparison for different sections and (b) Phase unbalance comparison for different sections.

As a pre-liminary study on using the phase shifter with UBPPD we investigated on meander shaped structures as shown in Fig. 5 (c). The meander shaped quarter-wavelength structure is used for the phase shifting as meander shaped structures leads to periodic variation of propagating signal and slow it down as the phase velocity decreases along it. The $|S_{11}|$ parameters are well below -10 dB until 40 GHz (Fig. 8 (a)) while the $|S_{21}|$ and $|S_{31}|$ have slightly bigger amplitude unbalance of ±2 dB (Fig. 8 (b)) and the phase unbalance is also significant along with flip at 15 GHz and 25 GHz as shown in Fig. 8 (c).

CONCLUSION

The transition from THz detecting device such as TeraFET and ZBSD to IF electronics is a crucial part for the overall detector optimization. The parameter study on the variation of bending the transition structures exhibits significant impact on the propagating signal. From four different investigated structures, we found that the micro-strip line may be the best option for a transition structures. The UBPPD is crucial to divide the power equally in two arms which will than be phase shifted by using a planar phase shifter (the investigation on broadband planar rogers substrate based 180° phase shifter is still under progress) and finally feed to the broadband amplifier. The investigated two section UBPPD is the optimal solution (considering rogers substrates) for the broadband phase shifter and will be fabricated by using photo-lithography process and clean room technologies.

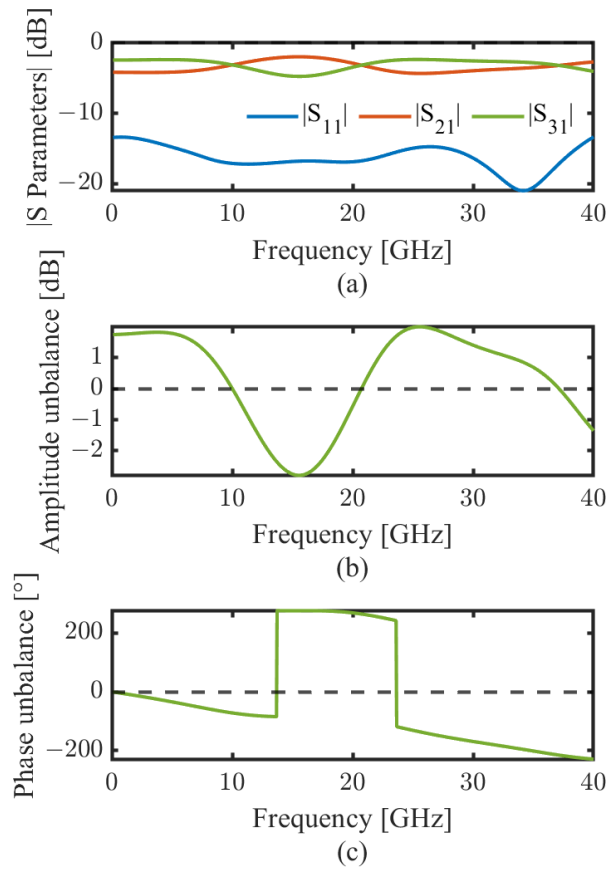


Figure 8: Two section UBPDD with meander phase shifter (a) S-parameters, (b) Amplitude unbalance and (c) Phase unbalance.

ACKNOWLEDGEMENT

This work is supported by the German Federal Ministry of Education and Research (BMBF) under contract no. 05K22RO1 at Mittelhessen University of Applied Sciences, Friedberg (Hesse), Germany. We are thankful for the cooperation with TU Darmstadt, Darmstadt, Germany and other cooperative partners under this BMBF project.

Content from this work may be used under the terms of the CC-BY-4.0 licence (© 2023). Any distribution of this work must maintain attribution to the author(s), title of the work, publisher, and DOI

ISBN: 978-3-95450-236-3 ISSN: 2673-5350 doi:10.18429/JACoW-IBIC2023-TUP010

REFERENCES

[1] G. Carpintero, E. Garcia-Munoz, H. Hartnagel, S. Preu, and A. Raisanen, *"Semiconductor Terahertz Technology: Devices and Systems at Room Temperature Operation"*, John Wiley & Sons, 2015. doi:10.1002/9781118920411.

[2] E.J. Jaeschke, S. Khan, J.R. Schneider, and J.B. Hastings, *"Synchrotron Light Sources and Free-Electron Lasers: Accelerator Physics, Instrumentation and Science Applications"*, 2nd Edition, Cham: Springer International Publishing, 2020. doi:10.1007/978-3-030-23201-6.

[3] *Handbook of Terahertz Technologies: Devices and Applications*, H.J. Song and T. Nagatsuma Eds. New York, NY, USA: Jenny Stanford Publishing, 2015. doi:10.1201/b18381.

[4] R. Yadav, F. Ludwig, F.R. Faridi, J.M. Klopf, H.G. Roskos, S. Preu, and A. Penirschke, "State-of-the-Art Room Temperature Operable Zero-Bias Schottky Diode-Based Terahertz Detector Up to 5.56 THz", *Sensors*, vol. 23, no. 7, p. 3469. doi:10.3390/s23073469.

[5] S. Regensburger, S. Winnerl, J.M. Klopf, H. Lu, A.C. Gossard, and S. Preu, "Picosecond-Scale Terahertz Pulse Characterization With Field-Effect Transistors", *IEEE Trans. Terahertz Sci. Technol.*, vol. 9, no. 3, pp. 262-271, May 2019. doi:10.1109/TTHZ.2019.2903630

[6] A. Penirschke, M. Soboryntskyy, S. Preu, M. Mittendorff, S. Winnerl, M. Hoefle, O. Cojocari, and R. Jakoby, "Compact quasi-optical Schottky detector with fast voltage response", in Proc. *2014 39th International Conference on Infrared, Millimeter, and Terahertz waves (IRMMW-THz)*, Tucson, AZ, USA, 2014, pp. 1-2. doi:10.1109/IRMMW-THz.2014.6956027.

[7] R. Yadav, A. Penirschke, and S. Preu, "Comparative Study of Broadband Room Temperature THz Detectors for High and Intermediate Frequency Response", in *Proc. IPAC'22*, Bangkok, Thailand, Jun. 2022, pp. 257-259. doi:10.18429/JACoW-IPAC2022-MOPOPT013

[8] D.M. Pozar, *Microwave Engineering*, John Wiley & Sons, Inc., Hoboken, 2011.

[9] R.W. Klopfenstein, "A Transmission Line Taper of Improved Design", in *Proc. IRE*, vol. 44, no. 1, pp. 31-35, Jan. 1956. doi:10.1109/JRPROC.1956.274847

[10] B. Deutschmann and A. F. Jacob, "Compact Ultra-Broadband Power Dividers with Integrated Resistors", in *48th Eur. Microwave Conf. (EuMC)*, Madrid, Spain, 2018, pp. 620-623. doi:10.23919/EuMC.2018.8541600

[11] E.J. Wilkinson, "An N-way Power Divider", *IRE Trans. on Microwave Theory Tech.*, vol. 8, p. 116-118, Jan. 1960. doi:10.1109/TMTT.1960.1124668

Content from this work may be used under the terms of the CC-BY-4.0 licence (© 2023). Any distribution of this work must maintain attribution to the author(s), title of the work, publisher, and DOI

ISBN: 978-3-95450-236-3 ISSN: 2673-5350 doi:10.18429/JACoW-IBIC2023-TUP011

GEOMETRY STUDY OF AN RF-WINDOW FOR A GHz TRANSITION RADIATION MONITOR FOR LONGITUDINAL BUNCH SHAPE MEASUREMENTS

S. Klaproth*[1], A. Penirschke, Technische Hochschule Mittelhessen, Friedberg, Germany
R. Singh, GSI Helmholtzzentrum für Schwerionenforschung, Darmstadt, Germany
H. De Gersem, Technische Universität Darmstadt, Darmstadt, Germany
[1]also at Technische Universität Darmstadt, Darmstadt, Germany

Abstract

GHz Transition Radiation Monitors (GTRs) can be used to measure longitudinal beam profiles even for low β beams. In contrast to traditional methods e.g., Fast Faraday Cups (FFCs) and Feschenko monitors, GTRs are a non-destructive measurement method and are able to resolve bunch-by-bunch longitudinal profiles at the same time. It is planned to measure the transition radiation outside the beam line through a custom-design RF window within a frequency range up to 8 GHz using broadband antenna structures. The material and the shape of the RF-window is crucial in order to minimize the fraction of the transition radiation that is not propagating in the direction of the antenna. In this contribution, we show a study of different geometries to suppress reflections generated at the transition to the RF-window. For higher permittivity the reflections becomes stronger, simultaneously reducing the measured signal strength at the position of the antenna. Secondly the RF-window's material must be UHV compatible and should be durable.

INTRODUCTION

The longitudinal bunch shape is important for conditioning and verifying the beam dynamics of LINACs. In the case of the GSI UNILAC, the bunch velocities β typically range from 0.05 to 0.15. For these slow bunches, the self-field widens significantly alongside the beam axis, rendering direct measurement of the longitudinal bunch shape inherently ambiguous [1]. This applies to devices such as phase probes and other pick-ups. Therefore, more common tools for longitudinal bunch shape measurements of low-beta beams are FFCs and Feschenko monitors.

FFCs measure the profile by collecting the bunch charge in a 50 Ω optimized cup. Typically, the beam's self-fields are shielded to suppress signal widening caused by early arriving fields on the collector. This enables FFCs to detect the bunch shape with high precision on a bunch-by-bunch basis. Additional considerations must be taken on the emission of secondaries during the design phase and later on while interpreting the measured signals. Nevertheless, the destructive measurement makes a further usage of the beam impossible [2–4].

Feschenko monitors, on the other hand, measure the average bunch shape. The beam passes by a thin wire generating secondary electrons. The longitudinal structure of the beam is coherently transformed to the transversal distribution of these secondaries using an RF-deflector [2, 5]. The interaction of the beam and the wire is minimal, allowing the bunches to remain suitable for further acceleration.

A new candidate for bunch shape measurements is the GTR. This type of device is still under investigation, but has the potential to combine the advantages of both FFCs and Feschenko monitors, enabling bunch-by-bunch measurements without beam destruction. The GTR comprises three major components: a metal target plate with an aperture to generate transition radiation while the beam passes through, an RF-window for decoupling the transition radiation from the inner beam line to the outside simultaneously maintaining the vacuum, and an antenna/coupler structure to observe the radiation as seen in Fig. 1. This promising concept has

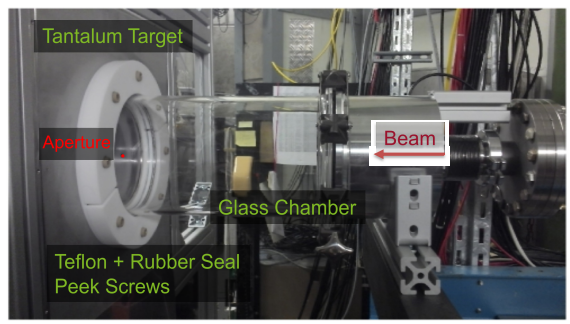


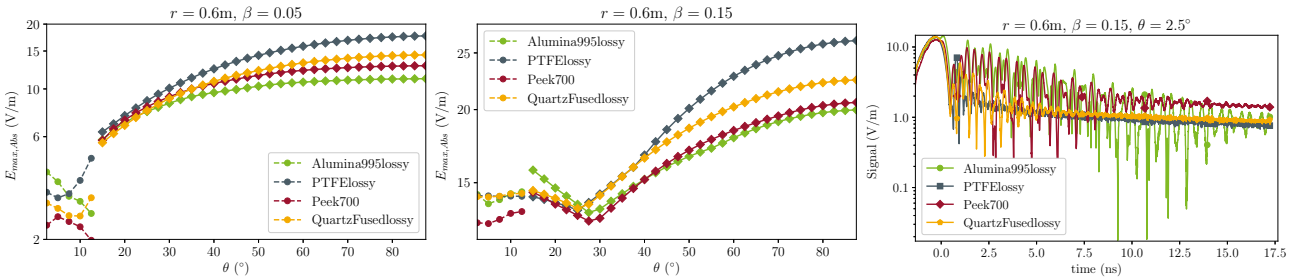
Figure 1: Experimental Setup of the proof-of-concept measurements [6].

been tested successfully at GSI [6]. Consequently, further investigations were made to optimize the RF window in the current setup. Simulations were carried out using different possible materials for the RF window, both ideal [7] and realistic [8], to examine their influence on the expected transition radiation signal. Thereby, a cylindrical RF-window with a wall thickness of 10 mm analog to the proof-of-concept measurement has been used. In Fig. 2a,b, we illustrate the expected maximum peak field (E_{max}) for two different typical β values at GSI UNILAC. It becomes evident, that a low relative permittivity ϵ_r is advantageous for maximizing the expected signal amplitude. The antenna should be positioned at an angle θ at least above 40°. As a rule of thumb for high β beams, $\theta = \frac{1}{\gamma}$ provides a good approximation for the angle at which the transition radiation peak power is emitted [10]. In case of GSI UNILAC this corresponds to approximately 55° to 60°. But actually at these low β values the maximum intensity rises continuously towards

* Stephan.Klaproth@iem.thm.de

Content from this work may be used under the terms of the CC-BY-4.0 licence (© 2023). Any distribution of this work must maintain attribution to the author(s), title of the work, publisher, and DOI

ISBN: 978-3-95450-236-3 ISSN: 2673-5350 doi:10.18429/JACoW-IBIC2023-TUP011



(a) (b) (c)

Figure 2: The maximum amplitude of the transition radiation peak $E_{\max}$ at 0.6 m distance for (a) $\beta = 0.05$ and (b) $\beta = 0.15$ and (c) the reflections after the transition radiation passed for different realistic materials [9]. A circle marker identifies an observation position inside and a diamond outside the vacuum chamber.

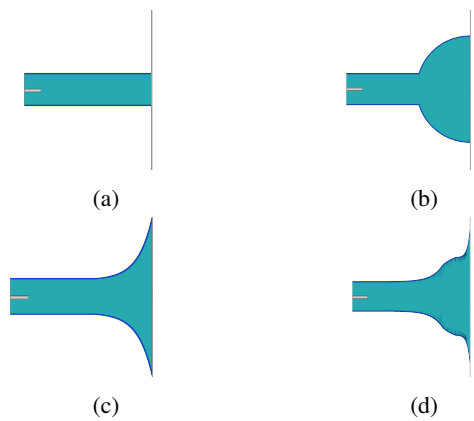
the target as shown in Fig. 2a and 2b. It can be noticed that only the necessary geometric distance of the antenna to the target gives an upper bound to the positioning angle θ.

$$\vec{E} = \frac{q \cdot \beta}{2\pi\epsilon_0 c_0 |\vec{R}|} \frac{\sin\theta\,\delta\left(|\vec{R}|c_0^{-1} - t\right)}{1 - \beta^2\cos^2\theta} (\hat{e}_x \cos\theta + \hat{e}_z \sin\theta)\,. \quad (1)$$

The electrical field of transition radiation for a single charge in the far-field may be calculated using Eq. (1) [11]. It shows that signal strength increases linearly with higher β values. Therefore, the optimal position for the antenna should be chosen with respect to the lowest expected β case to achieve the best overall performance of the GTR. The performance also depends on the suppression of reflections. Consequently, the spacing between the bunches defines a time gap within which reflections shall relax to prevent interference with the measured signal of the following bunch. The UNILAC operates at 36 MHz to 108 MHz, corresponding to a spacing of 27.78 ns to 9.26 ns between two consecutive bunches. In Fig. 2c we illustrate the signal within the vacuum chamber at $|\vec{R}| = 0.6$ m and $\theta = 2.5°$ at a velocity $\beta = 0.15$. The simulation time has been adjusted so that zero aligns with the transition radiation peak to be measured, followed by its reflections. While the reflections fade away for all materials within 27.78 ns for all materials, the faster operation mode of 108 MHz may encounter interference between the transition radiation of the following bunch and the reflections of the current one, depending on the RF-window material used. A well-chosen material can minimize this interaction. For instance, the reflection amplitude and relaxation time of quartz-glass perform similarly well compared to PTFE, while Peek and Alumina suffer significantly from slowly decaying reflections within the vacuum chamber. For the quartz-glass RF-window the expected total relaxation time is about 7.5 ns, which is shorter than the time gap of the fast operation mode of the UNILAC. So we do not expect severe impacts on the following measured bunch shape due to reflections of the previous transition radiation. The impact of the transition radiation on the following bunch itself is also expected to be negligible, with electric fields of about 100 V m^{-1} compared to the self-fields of the bunch, typically in the range of tens to hundreds of kV m^{-1}. Both low ϵ_r materials would be sufficient in terms of their electrical properties. But the material class PTFE is typically used only inside a vacuum chamber or for low vacuum applications, as it may not be vacuum-tight against hydrogen and other light particles [12, 13]. Therefore, we focus in our geometry study on the quartz-glass material only. During this geometry study of the RF-window our aim is to increase the amplitude of the measured signal outside the vacuum chamber while reducing the amplitude and relaxation time of the reflections inside the beam line to further minimize their impact on the measurements.

SIMULATIONS

Several shapes were evaluated using the CST® PIC-solver [9]. The first shape is a cylindrical design, which was also used in the material analysis, and it includes a larger variant with a 0.5 m inner radius (Fig. 3a). The second shape is a spherical geometry with an inner radius of 0.5 m (Fig. 3b). The highest transmission through the window is expected when the transition radiation impinges orthogonally on the window surface.



(a) (b) (c) (d)

Figure 3: The shapes studied: (a) cylindrical, (b) spherical, (c) exponential horn, (d) combination of spherical and exponential horn design.

The third shape is an exponential horn (Fig. 3c) with a mouth of 0.5 m. This shape is intended to disperse the transition radiation as much as possible to create only low amplitude reflections. The last shape is a combination of

Content from this work may be used under the terms of the CC-BY-4.0 licence (© 2023). Any distribution of this work must maintain attribution to the author(s), title of the work, publisher, and DOI

ISBN: 978-3-95450-236-3 ISSN: 2673-5350 doi:10.18429/JACoW-IBIC2023-TUP011

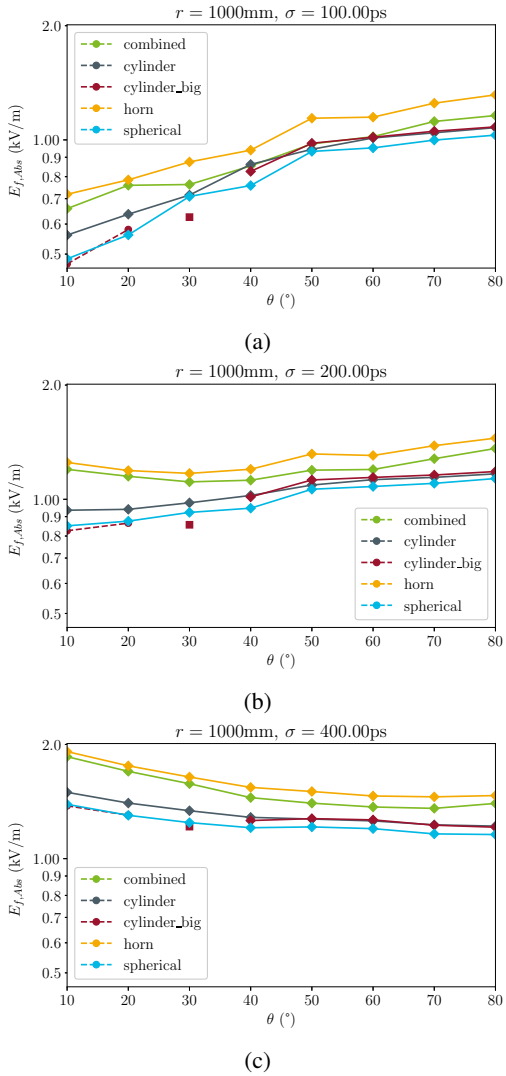


Figure 4: Maximum signal strength of the transition radiation $E_{\max}$ at 1 m distance for different geometries and bunch lengths: (a) $\sigma_b = 100$ ps, (b) $\sigma_b = 200$ ps, (c) $\sigma_b = 400$ ps. A circle marker identifies an observation position inside and a diamond outside of the vacuum chamber and a square identifies an observer within the chamber walls.

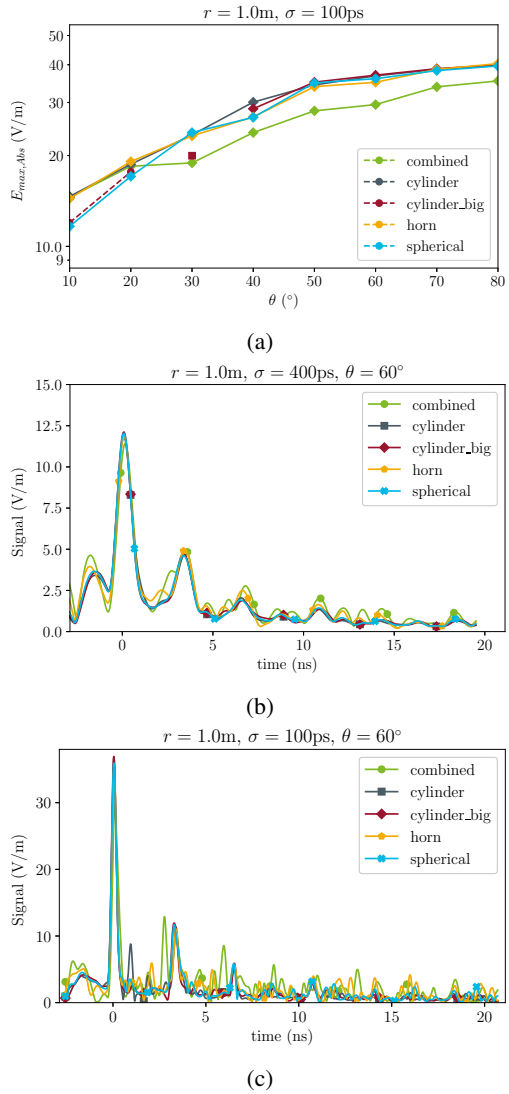


Figure 5: Signal of the transition radiation inside the RF-window in (a) at $|\vec{R}| = 0.4$ m and $\theta = 0°$ for a $\sigma_b = 400$ ps bunch and outside at $|\vec{R}| = 1$ m and $\theta = 60°$ for (b) $\sigma_b = 400$ ps and (c) $\sigma_b = 100$ ps bunch.

exponential horn and spherical shape (Fig. 3d). The spherical part spans between 50° to 70° with an inner radius of 0.4 m and is enclosed by two exponential horn sections. In all cases the wall thickness is kept to 10 mm using fused-quartz-glass as RF-window material simulating 10^{10} single charged particles in a Gaussian shaped bunch.

In Fig. 4 the maximum intensity of the transition radiation is plotted against the observation angle θ at a distance of $|\vec{R}| = 1$ m for $\beta = 0.15$ across all geometries, considering three different bunch lengths. Clearly the combined shape performs subpar compared to all other geometries. The maximum intensity increases with θ for both shorter bunches (Fig. 4a, 4b), as well as for the $\sigma_b = 400$ ps case till $\theta = 60°$. Beyond this angle the maximum intensity of the transition radiation stagnates for longer bunches. The exponential horn geometry shows a slightly lower maximum amplitude compared to the cylindrical and spherical shapes, but the difference is negligible. Notably, the maximum intensity scales linearly with the bunch charge density [11], as expected. All simulations have been performed with the same total charge, resulting in a halving of the bunch charge density between bunch lengths of $\sigma_b = 100$ ps to 200 ps. Consequently, the maximum intensity also decreases by half, from approximately 40 V m^{-1} to 20 V m^{-1}, and quartered from about 40 V m^{-1} to 10 V m^{-1} for $\sigma_b = 100$ ps to 400 ps. In Fig. 5a we show the signal of the transition radiation and reflections along the beam axis at a distance of $|\vec{R}| = 0.4$ m from the target for a σ_b=400 ps bunch. For the first 6 ns, the spherical geometry has a higher amplitude than the horn-shaped RF-window. Afterward, the reflections become even smaller in amplitude. In the case of the small cylindrical shape, the signal appears to have a low reflectivity. However, this is due to the overlap between the first reflection

Content from this work may be used under the terms of the CC-BY-4.0 licence (© 2023). Any distribution of this work must maintain attribution to the author(s), title of the work, publisher, and DOI

ISBN: 978-3-95450-236-3 ISSN: 2673-5350 doi:10.18429/JACoW-IBIC2023-TUP011

Content from this work may be used under the terms of the CC-BY-4.0 licence (© 2023). Any distribution of this work must maintain attribution to the author(s), title of the work, publisher, and DOI

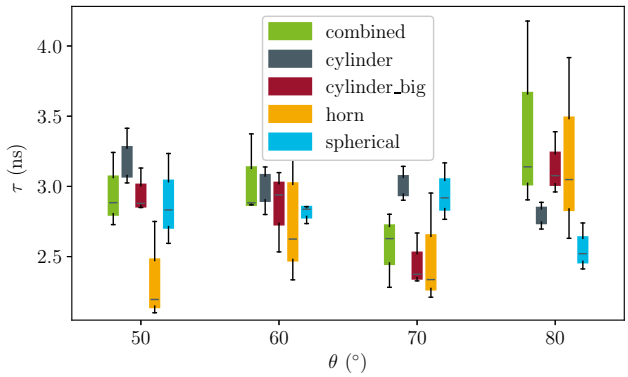
and the actual transition radiation signal. As a result, the transition radiation signal broadens, and the maximum amplitude shifts. This first reflection becomes visible in the big cylindrical shape case around 4 ns. Here, the longer travel distance of the reflection leads to the delayed signal and therefore the reflection is separated from the transition radiation. The widening of the transition radiation signal also occurs for the horn-shaped geometry, with a small kink visible after 1.9 ns. This kink is caused by reflections at the outer part of the horn mouth, where the gap between the target and RF-window is small. These early reflections overlap with the transition radiation, ultimately leading to a widening. The primary peak of the reflected transition radiation inside the RF-window can be reduced by up to 12 % comparing the highest amplitude of the spherical and the lowest of horn shape. The transition radiation peak of the following bunch will interact with the remaining reflections at 9.26 ns, which represents a minimum. So, we do not expect significant interference effects between the reflected signals of consecutive bunches. To further confirm this, additional multi-bunch simulations are required. In Fig. 5b,c the signal outside the RF-window is shown at $\theta = 60°$ in $|\vec{R}| = 1$ m distance at $\beta = 0.15$ for two bunch widths of $\sigma_b = 400$ ps and 100 ps. The aim outside the RF-window is to maximize the transition radiation signal. With the exception of the combined shape, all geometries exhibit nearly the same amplitude. This is particularly pronounced in the $\sigma_b = 100$ ps case, where the amplitude is approximately 25 % smaller than the others. In Fig. 5c, the first reflection of the small cylindrical geometry becomes visible approximately 1 ns after the main peak. This reflection overlaps in the $\sigma_b = 400$ ps case leading to the widening of the signal as discussed already earlier. Additionally, the early reflection of the horn shape can be seen between 1 ns to 3 ns, resulting in the kink for longer bunches. The best separation between the signal and reflections is achieved with the spherical and the larger cylindrical geometries. In terms of relaxation time τ we perform an exponential fit

$$s(t) = s_0 \exp^{\frac{-t}{\tau}} + C, \quad (2)$$

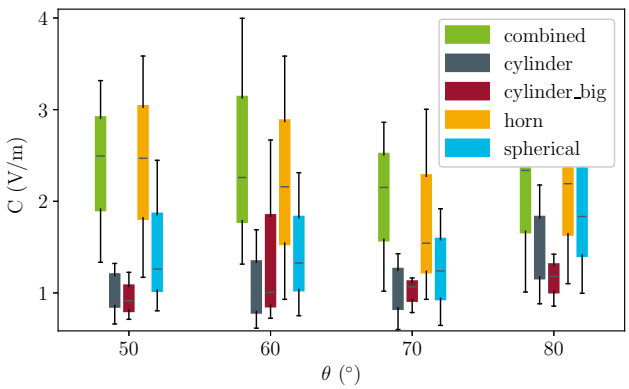
with s_0 the maximum amplitude of the primary transition radiation peak and the increased noise floor offset C. The results of the fit are shown in in Fig. 6. The horn-geometry's decay time τ is the smallest on average with 2.7 ns, but the increased noise floor C is one of the worst together with the combined shape up to 2 V m^{-1} higher than the other geometries. All other shapes have a decay time τ of about 3 ± 0.3 ns with a small advantage for the spherical and the larger cylindrical shape. The smallest increased noise floor C of about 1.1 ± 0.1 V m^{-1} is achieved with the big cylindrical shape, followed closely by the spherical geometry 1.4 ± 0.3 V m^{-1}.

CONCLUSION

In this paper, we have demonstrated that the permittivity of the RF-window has a significant impact on the reflections of the transition radiation in a GTR. Additionally, we showed that the shape of the window does not have a major effect on the measurable intensity of the transition radiation outside the RF-window. Inside the RF-window, the horn geometry can reduce the amplitude by up to 12 % at the cost of a slightly widened signal. The lowest decay time τ and increased noise floor C are achieved with the bigger cylindrical and the spherical designs. The advantage of the alternative geometries are the ability to separate the transition radiation from the reflections, with the horn geometry offering some improvement and the spherical shape performing best in this regard. We plan to equip a GTR with a spherical shaped RF-window to test its influence in a new measurement campaign also adding antennas with higher bandwidth up to 8 GHz bandwidth. Furthermore, simulations of multiple bunches will be performed to compare with measurements with respect to the overlapping of reflections and the desired transition radiation peaks.



(a)



(b)

Figure 6: (a) Decay constant τ and (b) offset C of the exponential decay fit averaged over σ_b (100, 200, 400 ps) for each angle θ.

ACKNOWLEDGEMENTS

This work is supported by the German Federal Ministry of Education and Research (BMBF) under contract no. 05P21RORB2. Joint Project 05P2021 - R&D Accelerator (DIAGNOSE).

ISBN: 978-3-95450-236-3 ISSN: 2673-5350 doi:10.18429/JACoW-IBIC2023-TUP011

REFERENCES

[1] P. Forck, P. Kowina, and D. Liakin, "Beam Position Monitors," *Synchrotron Radiation News*, vol. 1, no. 3, 2008. https://www.researchgate.net/publication/236630408_Beam_Position_Monitors

[2] R. Singh *et al.*, "Comparison of Feschenko BSM and Fast Faraday Cup with Low Energy Ion Beams," in *Proc. IBIC'21*, Pohang, Rep. of Korea, Oct. 2021, pp. 407–411. doi:10.18429/JACoW-IBIC2021-WEPP16

[3] R. Singh, P. Forck, S. Klaproth, T. Reichert, A. Reiter, and G. O. Rodrigues, "Simulation and Measurements of the Fast Faraday Cups at GSI UNILAC," in *Proc. IBIC'22*, Kraków, Poland, Dec. 2022, pp. 286–290. doi:10.18429/JACoW-IBIC2022-TUP25

[4] K. Mal, S. Kumar, G. Rodrigues, and R. Singh, "Study and improvements of a radially coupled coaxial Fast Faraday cup design toward lower intensity beams," *AIP Advances*, vol. 12, no. 12, p. 125 223, Dec. 2022. doi:10.1063/5.0131890

[5] A. Feschenko, "Methods and instrumentation for bunch shape measurements," in *Proc. PAC'01*, Chicago, IL, USA, vol. 1, 2001, pp. 517–521. https://jacow.org/p01/PAPERS/ROAB002.PDF

[6] R. Singh, T. Reichert, and B. Walasek-Hoehne, "Optical transition radiation based transverse beam diagnostics for nonrelativistic ion beams," *Phys. Rev. Accel. Beams*, vol. 25, no. 7, p. 072 801, Jul. 2022. doi:10.1103/PhysRevAccelBeams.25.072801

[7] S. Klaproth, H. D. Gersem, A. Penirschke, T. Reichert, and R. Singh, "Advancing to a GHz Transition Radiation Monitor for Longitudinal Charge Distribution Measurements," in *Proc. IPAC'22*, Bangkok, Thailand, Jul. 2022, pp. 267–270. doi:10.18429/JACoW-IPAC2022-MOPOPT018

[8] S. Klaproth, H. D. Gersem, and A. Penirschke, "Analysis of Real Materials for the RF Window of a GHz Transition Radiation Monitor," DPG-Frühjahrstagung SMUK23 - AKBP 17.5, Mar. 2023.

[9] *CST Studio Suit 2023™ SP5*. https://www.3ds.com/products-services/simulia/products/cst-studio-suite/

[10] L. C. L. Yuan, C. L. Wang, H. Uto, and S. Prünster, "Formation-Zone Effect in Transition Radiation Due to Ultrarelativistic Particles," *Phys. Rev. Lett.*, vol. 25, no. 21, pp. 1513–1515, Nov. 1970. doi:10.1103/PhysRevLett.25.1513

[11] R. Singh, "Longitudinal Beam Diagnostics R&D at GSI-UNILAC," in *Proc. HIAT'22*, Darmstadt, Germany, Aug. 2022, paper TH2I2, pp. 144–149. doi:10.18429/JACoW-HIAT2022-TH2I2

[12] B. Sebők, M. Schülke, F. Réti, and G. Kiss, "Diffusivity, permeability and solubility of H2, Ar, N2, and CO2 in poly(tetrafluoroethylene) between room temperature and 180°C," *Polymer Testing*, vol. 49, pp. 66–72, 2016. doi:10.1016/j.polymertesting.2015.10.016

[13] G. Lee, *Materials for ultra-high vacuum*, UNT Digital Library - online, Aug. 1989. https://digital.library.unt.edu/ark:/67531/metadc1185924/

Content from this work may be used under the terms of the CC-BY-4.0 licence (© 2023). Any distribution of this work must maintain attribution to the author(s), title of the work, publisher, and DOI

ISBN: 978-3-95450-236-3 ISSN: 2673-5350 doi:10.18429/JACoW-IBIC2023-TUP012

FIRST MEASUREMENTS OF AN ELECTRO-OPTICAL BUNCH ARRIVAL-TIME MONITOR PROTOTYPE WITH PCB-BASED PICKUPS FOR ELBE

B. E. J. Scheible[1]*, A. Penirschke, Technische Hochschule Mittelhessen, Germany
M. K. Czwalinna, N. T. A. Nazer, H. Schlarb, S. Vilcins-Czvitkovits
Deutsches Elektronen-Synchrotron DESY, Germany
M. Freitag, M. Kuntzsch, Helmholtz-Zentrum Dresden Rossendorf HZDR, Germany
W. Ackermann, H. De Gersem, Technische Universität Darmstadt, Germany
[1]also at Technische Universität Darmstadt, Germany

Abstract

A vacuum-sealed prototype of an electro-optical bunch-arrival-time monitor has been commissioned in 2023. It consists of a pickup structure and a low-π-voltage ultra-wideband traveling-wave electro-optical modulator. The stainless-steel body of the pickup structure is partially produced by additive manufacturing and includes four pickups as well as an integrated combination network on a printed circuit board. This novel design aims to enable single-shot bunch-arrival-time measurements for electron beams in free-electron lasers with single-digit fs precision for low bunch charges down to 1 pC. The theoretical jitter-charge-product has been estimated by simulation and modeling to be in the order of 9 fs pC. The new prototype is tailored for validation experiments at the ELBE accelerator beamline. In this contribution first measurement results are presented.

INTRODUCTION

For synchronizing many subsystems and for stabilizing the arrival time of electron bunches an all-optical approach is used in several large free-electron-laser (FEL) facilities [1], where the arrival time is particularly critical for applications like pump-probe experiments [2]. The system requires a master laser oscillator phase-locked to the main RF oscillator, which emits picosecond laser pulses as timing reference [1, 3]. Furthermore, an actively stabilized distribution system must be established to transfer these pulses along the facility with minimal drift [1]. The electro-optical (EO) bunch arrival-time monitor (BAM) [1] is one of various end-stations in the all-optical synchronization system.

EO-BAM Operating Principle

In contrast to cavity-based BAM in radio-frequency (RF) synchronization [4], where the electron bunch excites a rather slowly decaying resonance, the EO-BAM detects an evanescent bipolar voltage signal [1]. The voltage is induced by the co-moving electric field of a bunch as the surface currents are disturbed by the pickup. The transient voltage leads to a current, which is transmitted via coaxial cables to a Mach-Zehnder-type electro-optical modulator (EOM) [1]. Usually the signals of two or more angular distributed pickups are combined to compensate for orbit variations [5]. The voltage signal serves as input for the EOM, where the intensity of the reference laser pulse is modulated accordingly [1]. The EOM bias voltage is set to a value such that the laser pulse amplitude is reduced to 50 % of the maximum value in order to make use of the bipolar pickup signal. By adjustable delay lines the system is tuned to perfect timing, so that the reference pulse and the zero crossing (ZC) of the voltage signal coincide at nominal bunch arrival time without additional modulation [6]. Early or late bunches result in a positive or negative signal, which causes an intensity modulation [1]. The laser-intensity modulation is processed by dedicated receiver electronics [3, 6]. A calibration curve is used to deduce the arrival time for every electron bunch [3, 6].

For future applications it is desirable to reach lower bunch charges, while at the same time the demands for synchronization accuracy rise as well. The current BAMs are equipped with 40 GHz cone-shaped pickups designed for bunch charges down to 20 pC [5], which achieve an overall resolution of 3.5 fs with 250 pC nominal bunch charge in the synchronization system of the European XFEL [7]. For low charges the signal strength and therefore also the BAM sensitivity decreases rapidly.

EO-BAM Upgrade

To pave the way for 1 pC operation of the European XFEL, an upgrade of the arrival-time diagnostics is mandatory. To reach the goal of maintaining a resolution below 10 fs even at this low-charge operation, an upgrade of the main BAM components is necessary. First the RF part, comprising of the pickup structure and the signal transmission, and second, the EOM must be redesigned. The bandwidth of both components should be increased up to 100 GHz and the length of the transmission line has to be reduced [8].

The EOM's half-wave voltage V_π needs to be lowered in order to reach a high modulation with the low expected signal strength. To reduce cable losses especially at high frequencies, the EOM will be placed closer to the beamline and thus the radiation hardness has been examined. In a future upgrade it might even be integrated in the RF structure.

For the pickup system, it was proposed to have pickups and combination network integrated on a printed circuit board (PCB) [8, 9]. This idea was first combined with rod-shaped

* bernhard.scheible@iem.thm.de

Content from this work may be used under the terms of the CC-BY-4.0 licence (© 2023). Any distribution of this work must maintain attribution to the author(s), title of the work, publisher, and DOI

ISBN: 978-3-95450-236-3 ISSN: 2673-5350 doi:10.18429/JACoW-IBIC2023-TUP012

pickups mounted on top of this PCB (rPCB) to maximize the effective pickup surface and reduce the wake loss while minimizing the distance between pickup and beam [10]. The reported slew rate at ZC was 171.6 mV ps^{-1} pC^{-1}, exceeding the project goal by 14 % [10]. For the construction of a first vacuum-sealed prototype, it was decided to use a planar version of the rod-shaped pickups, for simplified manufacturing with a slight improvement of the signal [11].

The potential resolution of the upgraded BAM was estimated using the simulation results of rPCB pickups, the measured response of a new EOM prototype and typical noise contribution. With the assumptions made in [12] a jitter-charge product of about 9 fs pC is expected, which reaches the project goal.

PROTOTYPE DESIGN

The first vacuum-sealed prototype of an EO-BAM based on planar pickups with integrated combination network, shown in Fig. 1, has been tailored for tests at the ELBE accelerator in the Helmholtz-Zentrum Dresden Rossendorf (HZDR). Vacuum compatibility of the prototype was realized in close cooperation with DESY and HZDR. It is connected with a DN40 ConFlat (CF) flange to an inner beamline diameter of 36 mm, while the minimal clearing between the pickups is 10 mm. The feedthrough module can be attached to the side with a DN25 CF flange. A sliding contact is used for the connection between the feedthroughs inner conductor and the end of the two stage combination network, which is integrated on a substrate. The V-type RF connector is limited to a bandwidth from DC to 65 GHz according to the manufacturer's specification.

The layout of the PCB was chosen similar to the PCB presented in [11] and shown in Fig. 1, but adapted for the mechanical and electrical material properties. As substrate a Rogers TMM® 10i laminate with dielectric constant Dk of 9.8 ± 0.245, a thickness of 380 µm and 35 µm of copper cladding was chosen [13]. The short-term vacuum compatibility has been tested at HZDR in a single batch of four different 20×40 mm substrate samples at once. The baseline pressure in the test chamber was 3×10^{-9} mbar. Due to the raw samples the pressure did not drop below 2×10^{-7} mbar. After the samples were baked at up to 105 °C for a total of almost three days, the pressure dropped to 7×10^{-9} mbar. The baseline could presumably be reached after some time, so that the test is considered successful.

The position of the PCB relative to the feedthrough is a critical dimension. The PCB rests on a ledge in the body and fits into a notch cut into a bulge at the feedthrough-module's surface to ensure that a good electrical contact is provided between inner conductor and trace, as well as between the ground plate and the outer conductor. On the opposite side two dowel pins jam the PCB in position, because a tilt out of the transverse axis was also identified as a critical defect in the tolerance analysis [11].

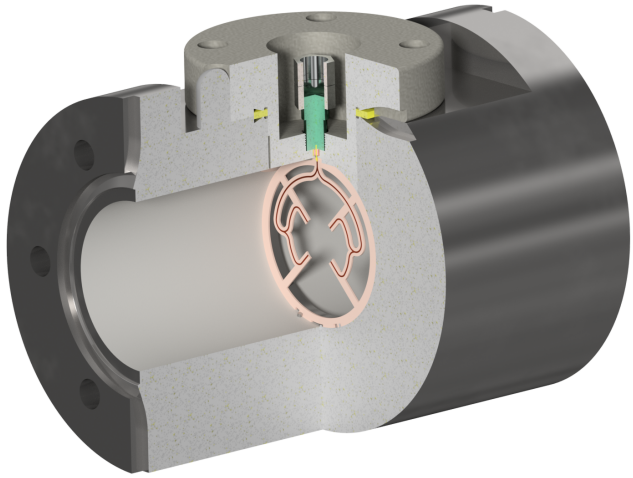


Figure 1: Rendering of the PCB-based BAM prototype.

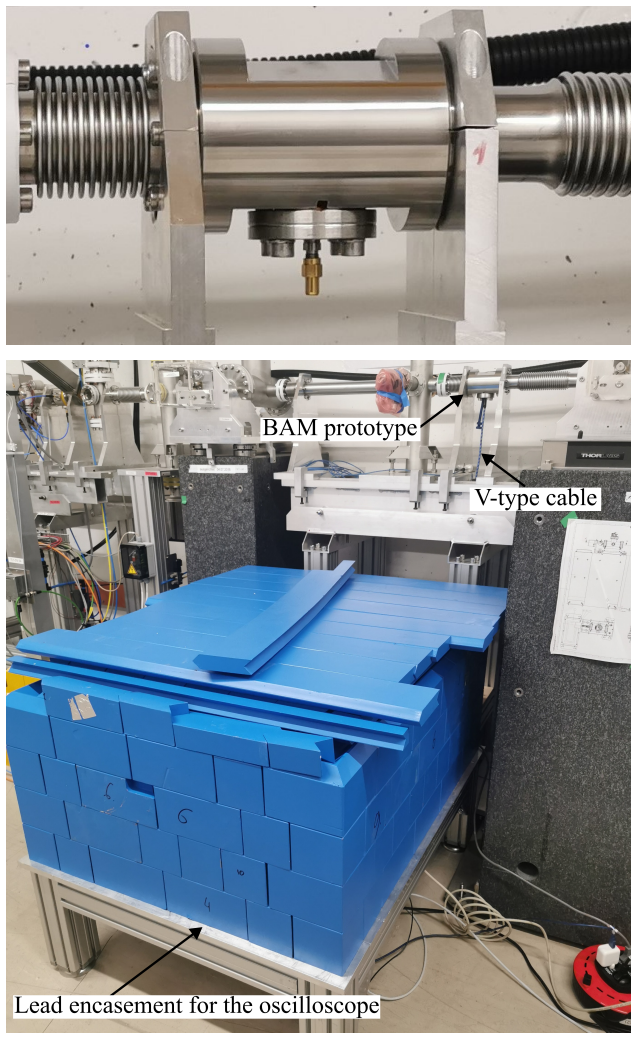


Figure 2: Close-up of the prototype installed between two bellows in the THz beamline of ELBE (top) and measurement setup in the beamline cave, before installing additional fans and α-radiation absorber (bottom).

Content from this work may be used under the terms of the CC-BY-4.0 licence (© 2023). Any distribution of this work must maintain attribution to the author(s), title of the work, publisher, and DOI

ISBN: 978-3-95450-236-3 ISSN: 2673-5350 doi:10.18429/JACoW-IBIC2023-TUP012

RF MEASUREMENT AT ELBE

In the course of a dedicated machine development shift at ELBE, two 2-day shifts were allocated for RF measurements with the novel EO-PCB-BAM prototype. A third shift is scheduled for December 2023, to measure the performance of the system with EOM.

Measurement Setup

Figure 2 (top) shows a close-up to the prototype between two bellows in the ELBE THz beamline. Off measurement time, the output was terminated with 50 Ω as shown in the picture. For measuring the RF signal, a two-port real-time oscilloscope, the Keysight UXR1102A, with maximum bandwidth of 110 GHz was used. To protect the oscilloscope against radiation, it has been encased in the custom lead crate shown in Fig. 2 (bottom), which was afterwards covered in an absorber to moderate the α-radiation stemming from the beam dump. The oscilloscope was remotely operated from the control room during measurements. Due to the distance between the oscilloscope and the BAM, two coaxial v-cable had to be used. A 121.9 mm Huber+Suhner SUCOFLEX® 570S and a 20.3 mm Rosenberger 70W-08S1-08S1-00203 extended by a v-female-female connector.

Measurement Results

Figure 3 shows an exemplary result of the first measurement shift. The full bandwidth of the Keysight UXR1102A oscilloscope was utilized in this case, with a brick-wall filter with roll-off at 113 GHz. The charge measurement was unreliable in this charge regime, but with a cathode current of (1.4 ± 0.2) µA and a repetition rate of 0.41 MHz in CW-mode, the mean bunch charge at the source is approximately 3.45 pC. Since a strong fluctuation was observed during the measurement, the segmented mode was used to save a batch of 1024 pulses for averaging.

The decisive slew rate is (99.27 ± 10.62) mV ps^{-1} in this measurement. The error is expected to be mainly a consequence of charge fluctuations, thus the average slew rate should match the average charge with significantly lower uncertainty. The peak-to-peak voltage and rise time are (1.52 ± 0.11) V respectively (24.52 ± 1.09) ps.

Discussion

The measurements were carried out using a combined transmission line length of more than 1.4 m with high attenuation above 11 dB at 67 GHz. For the final EOM-integrated BAM it is planned to omit the external cable completely. Furthermore, the simulated signal was also taken directly at the feedthrough port. The scattering parameters of the assembly of the two cables and the v-female-female connector, shown in Fig. 4, have been measured for de-embedding.

The transmission line is modeled with a two-port network as shown in Fig. 5. The outgoing signal at port 2 in a two-port network is defined as

$$V_2^- = |S_{21}|\, V_1^+ + |S_{22}|\, V_2^+ \,, \qquad (1)$$

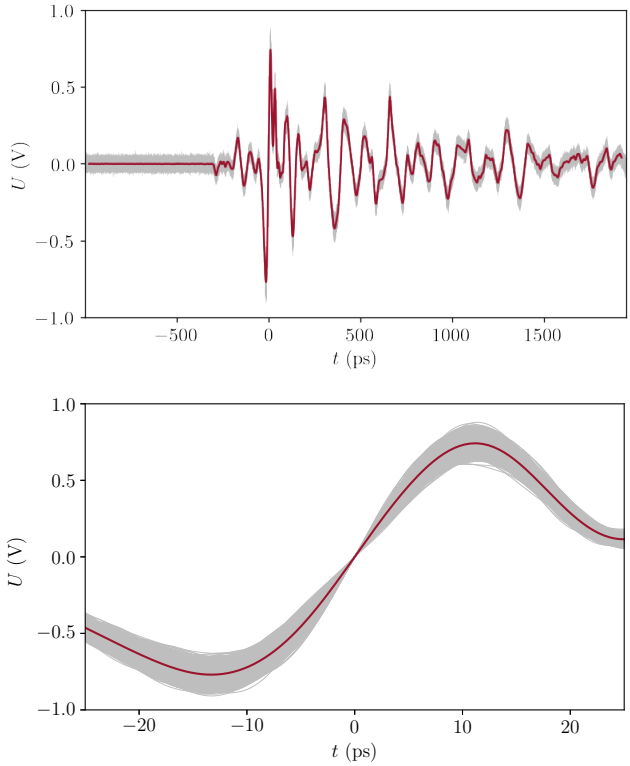


Figure 3: Measurement #34 (2023-07-27) with a total bunch charge of approximately 3.45 pC. A set of 1024 pulses is plotted in gray and the average signal in red. The top figure includes about 2 ns of ringing and the bottom is zoomed to the main pulse.

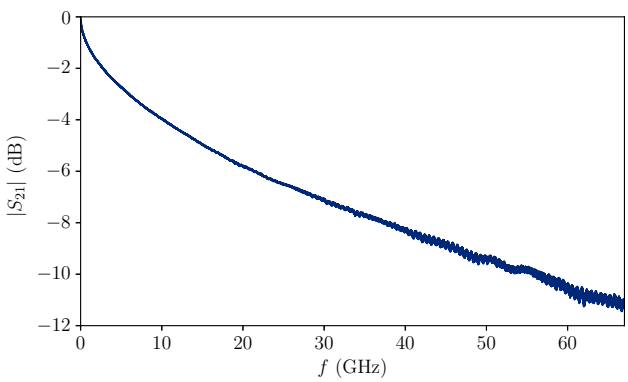


Figure 4: Scattering parameter of the 20.3 mm Rosenberger and 121.9 mm Huber+Suhner cables with the connector as used in the measurements.

where + denotes the incident and − the reflected wave [14]. In these measurements it will be assumed that no wave will be reflected in the oscilloscope, leading to $V_2^+ \approx 0$. With $S_{21} \neq 0$ in the whole signal spectrum, it is possible to get the simplified input signal by

$$V_1^+ = \frac{V_2^-}{|S_{21}|} \qquad (2)$$

in frequency domain. The measured time-domain signal must be transformed by fast Fourier transform before this

Content from this work may be used under the terms of the CC-BY-4.0 licence (© 2023). Any distribution of this work must maintain attribution to the author(s), title of the work, publisher, and DOI

ISBN: 978-3-95450-236-3 ISSN: 2673-5350 doi:10.18429/JACoW-IBIC2023-TUP012

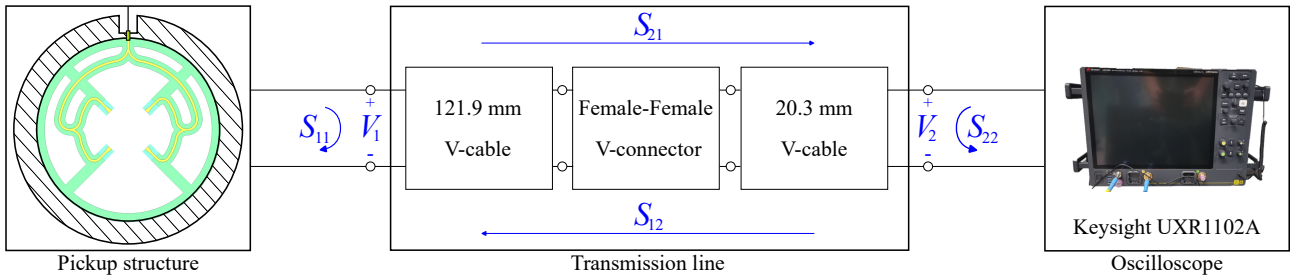


Figure 5: Block diagram of the electrical setup with scattering parameter for de-embedding.

step. With inverse fast Fourier transform, the de-embedded time-domain signal is retrieved afterwards.

After de-embedding the whole RF transmission line, the slew rate at main zero-crossing is $(275.71 \pm 34.64)\,\mathrm{mV\,ps^{-1}}$ with a peak-to-peak voltage and rise time of $(4.16 \pm 0.31)\,\mathrm{V}$ respectively $(24.08 \pm 1.34)\,\mathrm{ps}$. Supposing a linear dependency on the bunch charge [15, 16], the measured slew rate is normalized to $79.9\,\mathrm{mV\,ps^{-1}\,pC^{-1}}$ and just above half of the project goal. This could potentially allow for the desired BAM resolution down to 2 pC.

Figure 6 shows the simulated signal compared to the mean of 1024 measured pulses after de-embedding. For the simulation the bunch-charge was set to 3.5 pC for comparable results. The measured and the simulated signals coincide very well in the vicinity of the bunch and deviate otherwise. The slew rate is even lower, at $235.50\,\mathrm{mV\,ps^{-1}}$, which is significantly worse than in the previously proposed design with a thin glass substrate. This indicates that the TMM® 10i substrate is not optimal.

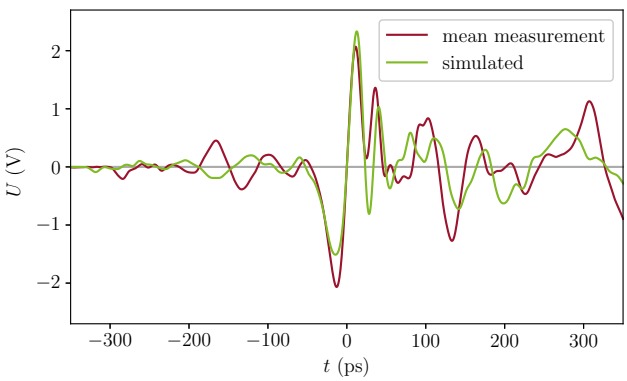


Figure 6: Comparison of the simulated signal and the average measured signal given in Fig. 3 after simplified de-embedding.

CONCLUSION AND OUTLOOK

The first prototype led to promising results and showed that a PCB-based BAM with planar implementation of rod-shaped pickups is viable. It must be emphasized that the prototype was not built to exploit its full potential. In particular, the use of a thinner fused-silica substrate should provide for further improvements. This is also advisable, since the current substrate might suffer radiation damage in long-term use due to its hydrocarbon content. After disassembling, the BAM must also be analyzed for defects caused by beam incidence and radiation.

Although the first prototype could not reach the project goal in accordance with simulations using the same materials, it already exceeds the performance reported for the current pickups [15, 17]. Since not all relevant data was reported with the results, the comparison must be treated with caution and ideally a comparative study should follow for a robust validation.

In summary, the preliminary review suggests that the novel design approach is operational and provides a significant improvement. By simulation it is likely that a different substrate will considerably improve the signal. Furthermore, the principle is expected to be transferable to other applications. If the in-depth analysis confirms the positive result and the measurements with an EOM, planned for December 2023, are successful, an improved prototype will be built. If possible, a W-type connector should be used, to extend the bandwidth limit to more than 100 GHz. In addition, it is reasonable to explore different PCB topologies in a non-vacuum structure, in a test chamber or with a free-space beam. Finally, it is foreseen to build a new BAM for FLASH and for the European XFEL.

ACKNOWLEDGEMENTS

Work supported by the German Federal Ministry of Education and Research (BMBF) under contracts No. 05K19RO1 and No. 05K22RO2.

We would like to thank *Keysight* for their generous offer, to provide the UXR1102A oscilloscope for these measurements, as well as Dr. Thomas Kirchner from Keysight, for his technical support. We would also like to thank the *Helmholtz-Zentrum Dresden Rossendorf* (HZDR) for granting us beam time and all the staff involved in installing the BAM or working in the control room during measurements. Finally, we would also like to thank *Neue Technologien GmbH & Co. KG* (NTG) for the close cooperation during construction of the prototype and the opportunity to carry out the final assembly on their premises.

Content from this work may be used under the terms of the CC-BY-4.0 licence (© 2023). Any distribution of this work must maintain attribution to the author(s), title of the work, publisher, and DOI

ISBN: 978-3-95450-236-3 ISSN: 2673-5350 doi:10.18429/JACoW-IBIC2023-TUP012

REFERENCES

[1] F. Löhl *et al.*, "Electron bunch timing with femtosecond precision in a superconducting free-electron laser", *Phys. Rev. Lett.*, vol. 104, no. 14, pp. 144801, Apr. 2010. doi:10.1103/PhysRevLett.104.144801

[2] E. A. Seddon *et al.*, "Short-wavelength free-electron laser sources and science: a review", *Rep. Prog. Phys. Phys. Soc. (GB)*, vol. 80, no. 11, pp. 115901, 2017. doi:10.1088/1361-6633/aa7cca

[3] M. Viti *et al.*, "Recent upgrades of the bunch arrival time monitors at FLASH and European XFEL", in *Proc. IPAC'17*, Copenhagen, Denmark, May 2017, pp. 695–698. doi:10.18429/JACoW-IPAC2017-MOPIK072

[4] M. Hansli *et al.*, "A beam arrival time cavity for REGAE at DESY", in *Proc. IPAC'14*, Dresden, Germany, Jun. 2014, pp. 1820–1822. doi:10.18429/JACoW-IPAC2014-TUPRI104

[5] A. Angelovski *et al.*, "High bandwidth pickup design for bunch arrival-time monitors for free-electron laser", *Phys. Rev. Spec. Top. Accel Beams*, vol. 15, no. 11, pp. 112803, 2012. doi:10.1103/PhysRevSTAB.15.112803

[6] K. P. Przygoda *et al.*, "MicroTCA.4 based optical frontend readout electronics and its applications", in *Proc. IBIC'16*, Barcelona, Spain, Sep. 2016, pp. 67–70. doi:10.18429/JACoW-IBIC2016-MOPG13

[7] M. K. Czwalinna *et al.*, "Beam arrival stability at the European XFEL", in *Proc. IPAC'21*, Campinas, Brazil, May 2021, pp. 3714–3719. doi:10.18429/JACoW-IPAC2021-THXB02

[8] A. Penirschke, W. Ackermann, M. K. Czwalinna, M. Kuntzsch, and H. Schlarb, "Concept of a novel high-bandwidth arrival time monitor for very low charges as a part of the all-optical synchronization system at ELBE", in *Proc. IBIC'19*, Malmö, Sweden, Sep. 2019, pp. 560–563. doi:10.18429/JACoW-IBIC2019-WEPP019

[9] B. E. J. Scheible, W. Ackermann, M. K. Czwalinna, H. De Gersem, A. Penirschke, and H. Schlarb, "Evaluation of a novel pickup concept for ultra-low charged short bunches in X-ray free-electron lasers", in *Proc. IBIC'20*, Santos, Brazil, Sep. 2020, pp. 145–149. doi:10.18429/JACoW-IBIC2020-WEPP21

[10] B. E. J. Scheible *et al.*, "Bunch arrival-time measurement with rod-shaped pickups on a printed circuit board for X-ray free-electron lasers", in *Proc. IBIC'21*, Pohang, Korea, Sep. 2021, pp. 417–420. doi:10.18429/JACoW-IBIC2021-WEPP19

[11] B. E. J. Scheible, A. Penirschke, H. De Gersem, H. Schlarb, M. K. Czwalinna, and W. Ackermann, "Tolerance analysis of a bunch arrival-time monitor design with rod-shaped pickups on a printed circuit board for the European XFEL and FELBE", presented at the IPAC'23, Venice, Italy, May 2023, paper THPL190, to be published.

[12] A. Kuzmin *et al.*, "Modeling and experimental evaluation of a bunch arrival-time monitor with rod-shaped pickups and a low-pi-voltage ultra-wideband traveling wave electro-optic modulator for X-ray free-electron lasers", in *Proc. IBIC'22*, Krakow, Poland, Sep. 2023, pp. 447–450. doi:10.18429/JACoW-IBIC2022-WEP24

[13] Rogers Corporation, https://www.rogerscorp.com/advanced-electronics-solutions/tmm-laminates/tmm-10i-laminates/.

[14] David M. Pozar, *Microwave Engineering*, John Wiley & Sons, 2011.

[15] A. Angelovski *et al.*, "Evaluation of the cone-shaped pickup performance for low charge sub-10 fs arrival-time measurements at free electron laser facilities", *Phys. Rev. Spec. Top. Accel Beams*, vol. 18, no. 1, pp. 012801, 2015. doi:10.1103/PhysRevSTAB.18.012801

[16] B. E. J. Scheible *et al.*, "Pickup development for short low-charge bunches in x-ray free-electron lasers", *Phys. Rev. Accel. Beams*, vol. 24, no. 7, pp. 072803, Jul. 2021. doi:10.1103/PhysRevAccelBeams.24.072803

[17] A. Kuhl, "Entwicklung und Realisierung eines 40 GHz Ankunftszeitmonitors für Elektronenpakete für FLASH und den European XFEL", Ph.D. Thesis, Technische Universität Darmstadt, Darmstadt, Germany, 2015.

Content from this work may be used under the terms of the CC-BY-4.0 licence (© 2023). Any distribution of this work must maintain attribution to the author(s), title of the work, publisher, and DOI

ISBN: 978-3-95450-236-3 ISSN: 2673-5350 doi:10.18429/JACoW-IBIC2023-TUP014

DESIGN AND TEST OF A PROTOTYPE 324 MHz RF DEFLECTOR IN THE BUNCH SHAPE MONITOR FOR CSNS-II LINAC UPGRADE*

W.L. Huang†,1, X.Y. Liu, Y.F. Sui, X.J. Nie
Institute of High Energy Physics, CAS, Beijing, China
Q.R. Liu, M.Y. Liu, University of Chinese Academy of Sciences, Beijing, China
[1]also at China Spallation Neutron Source, Dongguan, China

Abstract

During the upgrade of linac in CSNS-II, the beam injection energy will increase from 80.1 MeV to 300 MeV and the beam power from 100 kW to 500 kW. A combined layout of superconducting spoke cavities and elliptical cavities is adopted to accelerate H- beam to 300 MeV. Due to a ~10 ps short bunch width at the exit of the spoke SC section, the longitudinal beam density distribution will be measured by bunch shape monitors using low energy secondary emission electrons. As the most important part of a bunch shape monitor, a prototype 324 MHz RF deflector is designed and tuned on the basis of a quasi-symmetric lambda/2 325 MHz coaxial resonator, which was fabricated for the C-ADS proton accelerator project. Preliminary parameters of the bunch shape monitor are presented. Simulation of the RF deflector and test results in the laboratory are described and analysed.

INTRODUCTION

China Spallation Neutron Source (CSNS) is the first pulsed neutron source built in China [1]. It consists of an 80 MeV H- linac, a 1.6 GeV proton rapid cycling synchrotron (RCS), two beam transport lines and a target station. We achieved the design goal of phase I with protons bombarding the target at a beam power of 100 kW in Feb. 2022, and now begins the upgrade project to 500 kW. During the linac upgrade, the DTL section will be followed by a section of 324 MHz double-spoke superconducting cavities and a section of 648 MHz elliptical superconducting cavities [2], as shown in Fig. 1. The proton beam will be accelerated to 300 MeV at the exit of the 8th cryomodule in the second SC section.

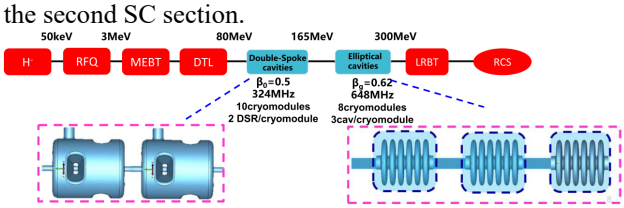


Figure 1: Superconducting cavities in CSNS-II [2].

Longitudinal bunch density distribution in ion linac is one of the main characteristics of accelerated beam. Bunch shape information is extremely important for medium energy accelerators consisting as a rule of two main parts with different rf frequencies. Results of bunch shape measurement after accelerating tank may be used to set rf phase and amplitude. What's more, longitudinal bunch density may be used to calculate energy spectrum and longitudinal beam emittance [3-6]. In the CSNS-II linac upgrade plan, two bunch shape monitors will be installed. The transverse and longitudinal beam parameters at the BSM installation point are listed in Table 1.

Table 1: Micro Bunch Parameters in the Linac of CSNS-II

Micro Bunch	Spoke 1	ELL7
Energy (MeV)	86.97	300.1
RF Freq. (MHz)	324	648
Φrms(°)	2.77	1.05
X_{rms}(mm)	2.27	2.38
Y_{rms}(mm)	4.1	2.28
Z_{rms}(mm)	2.86	1.75

Due to the ultrahigh bandwidth requirement and long cable attenuation, the normal phase detectors, such as fast current transformers and wall current monitors, are not suitable to measure the bunch shape in ion linacs. The technique of a coherent transformation of a temporal bunch structure into a spatial charge distribution of secondary electrons through RF-modulation was initially implemented by R. Witkover for BNL linac [7]. An energy (longitudinal) RF-modulation of low energy secondary electrons was used. In the Feschenko type Bunch Shape Monitor (BSM), developed in INR RAS, a transverse RF-scanning is used [8]. Thus a similar BSM is adopted in the linac upgrade project of CSNS-II, as shown in Fig. 2.

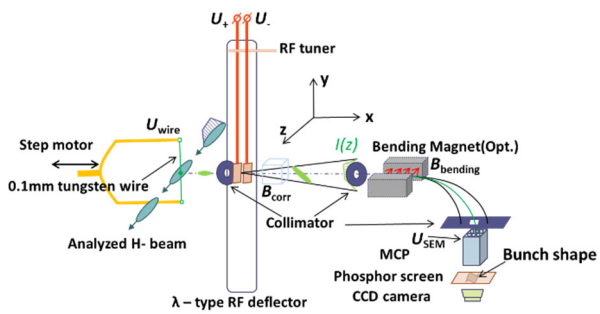


Figure 2: Configuration of bunch shape monitors in CSNS-II.

As the most important part of a bunch shape monitor, a prototype 325 MHz RF deflector was fabricated for the longitudinal bunch shape measurement in C-ADS. Due to the limitation of installing space, it was assumed to be tested at the CSNS linac. This paper will illustrate its design parameters and test results in the laboratory.

* Work supported by Natural Science Foundation of Guangdong Province, 2021A1515010269, National Natural Science Foundation, 11475204
† huangwei@ihep.ac.cn

Content from this work may be used under the terms of the CC-BY-4.0 licence (© 2023). Any distribution of this work must maintain attribution to the author(s), title of the work, publisher, and DOI

ISBN: 978-3-95450-236-3 ISSN: 2673-5350 doi:10.18429/JACoW-IBIC2023-TUP014

Content from this work may be used under the terms of the CC-BY-4.0 licence (© 2023). Any distribution of this work must maintain attribution to the author(s), title of the work, publisher, and DOI

RF DEFLECTOR DESIGN

The prototype 325 MHz RF deflector is a quasi-symmetric coaxial λ/2 standing wave resonator. It is mainly composed of a resonating cavity, two deflecting plates, two RF ports, two HV ends, two bellows and ceramic supports, as shown in Fig. 3.

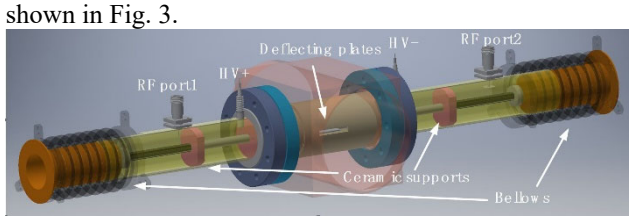


Figure 3: Structure of the C-ADS 325 MHz RF deflector.

CST Simulations

The prototype RF deflector was simulated in MW studio of CST to get a proper resonant frequency f_0 and to optimize the s-parameters. The geometry parameters are listed in Fig. 4. By changing the gaps between the tuner ends of the inner core and the cavity ends moved via bellows, that is, (L_tune_in, L_tune_out) within (5~20 mm), the resonant frequency was calculated in the CST eigenmode solver.

Finally, the combination of (L_tune_in, L_tune_out) were swept and verified to get the f_0 of the RF deflector and a tuning range of ±5 MHz, as shown in Fig. 5 a) and b). The S21 is lower than -30 dB at 325 MHz.

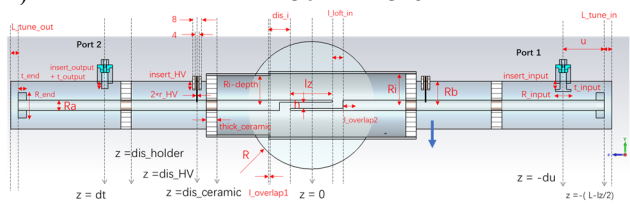


Figure 4: Geometry parameters of the prototype RF deflector.

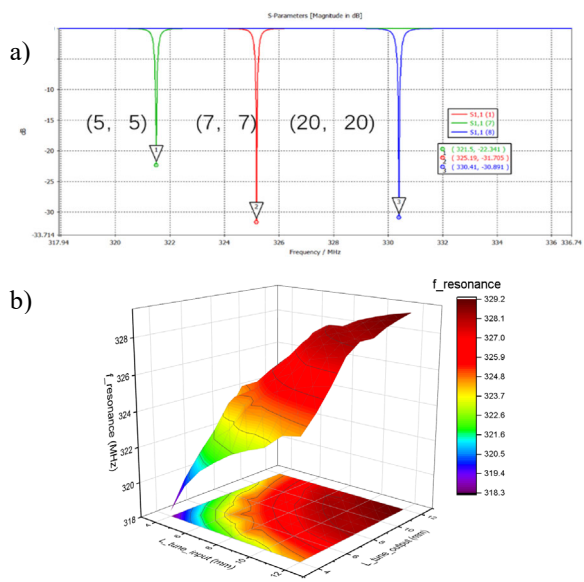


Figure 5: S21 calculation in CST by changing the combination of (L_tune_in, L_tune_out) to get the tuning range.

According to Fig. 5 b), we modified the (L_tune_in, L_tune_out) as (6.2, 6.2) for the RF deflector, and had a resonant frequency of 324 MHz, the same as the RF frequency of DTLs in CSNS. Fig. 6 a) and b) show the electric field distribution in the RF deflector at the resonant frequency of 324 MHz and the calculation of S-parameters. It indicated that this prototype RF deflector could be used to deflect the secondary emission electrons from a wire scanner bombarded by ion beam, and works at 324 MHz, synchronizing to the RF frequency of DTL and SC sections.

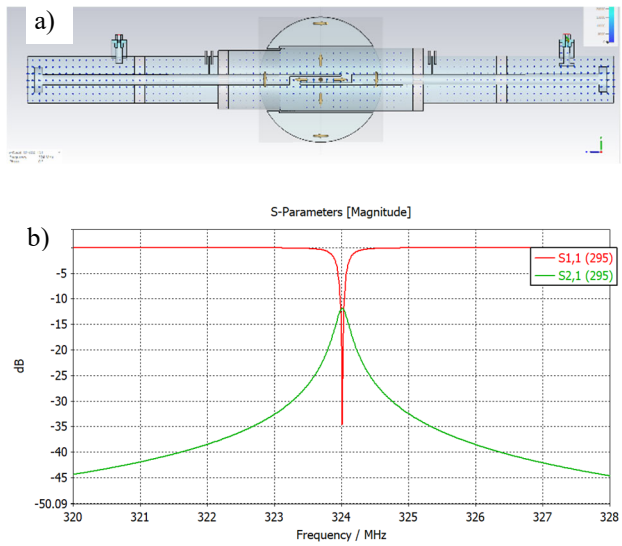


Figure 6: E-field distribution in the prototype RF deflector at 324 MHz and the S-parameters.

MEASUREMENTS IN LAB

The prototype RF deflector was fabricated at a domestic manufacturer. Figure 7 gives the two parts before assembly. It's a pity that there was no locating pin in the initial design, which brought the difficult of alignment during assembly.

The s-parameters were measured via a Keysight E5061B network analyser, shown in Fig. 8. The S11@324 MHz is only -8 dB, which is much bigger than the simulation result and means more power should be fed in to establish an RF field for deflecting the secondary electrons. A mechanical optimization in the second version of RF deflector design is undergoing.

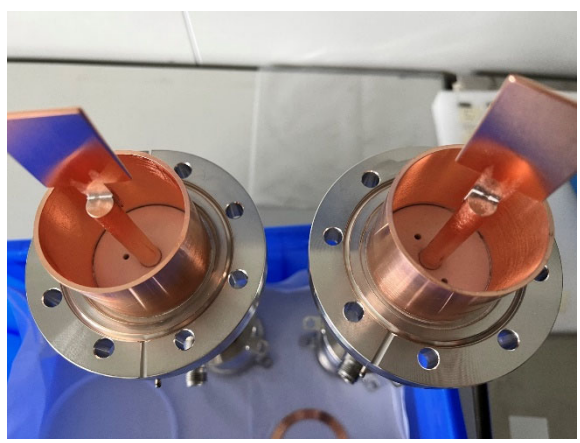


Figure 7: Two parts of the prototype RF deflector.

ISBN: 978-3-95450-236-3 ISSN: 2673-5350 doi:10.18429/JACoW-IBIC2023-TUP014

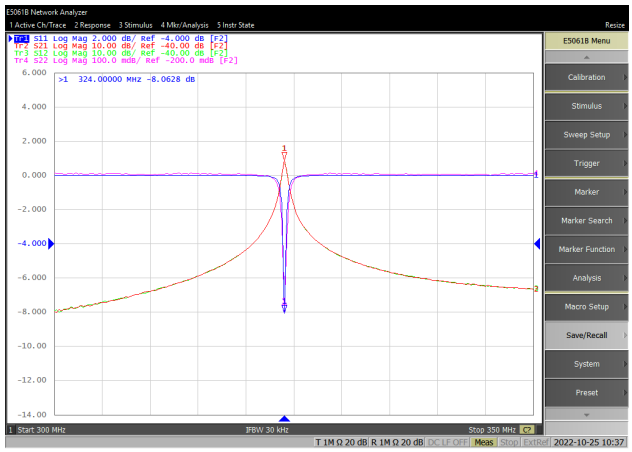
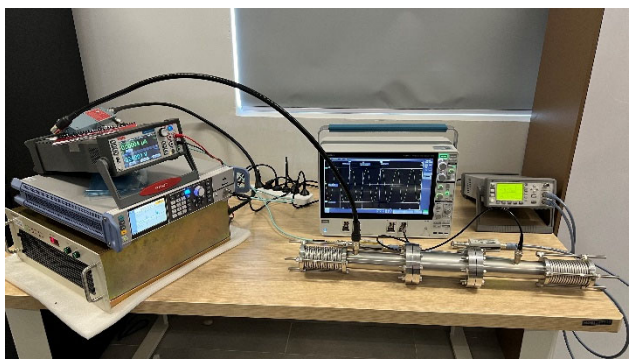


Figure 8: S-parameters of the prototype RF deflector measured by Keysight E5061B.

Figure 9 shows the high power test to the deflector with a 1 kW power amplifier, which is excited by an R&S SMA100B RF signal source. The resonator worked well and there is no waveform distortion observed.


Figure 9: Tested by a 324 MHz power amplifier (Pmax=1 kW).

A test bench with a Kimball electron gun will be established at the end of this year. Then the secondary electron beam path in the deflector could be verified by tuning the amplitude and the phase of the RF field, and the high voltages on the plates.

CONCLUSION

A prototype of RF deflector was design as a 325 MHz λ/2 quasi-symmetric resonator for C-ADS project. It is also suitable to work at 324 MHz by adjusting the gap between the bellow end and the core end. The S21 parameter got unsatisfactory due to the difficulty of alignment.

ACKNOWLEDGEMENTS

The authors are grateful to Ms. Yuan Jingchun, Mr. Li Rong for the good discussion of this work.

REFERENCES

[1] H.-S. Chen, and X.-L. Wang, “China's first pulsed neutron source”, *Nat. Mater.*, vol. 15, pp. 689-691, 2016. doi:10.1038/nmat4655

[2] J. Peng, “CSNS-II Superconducting Linac Design”, presented at the LINAC'22, Liverpool, UK, Aug.-Sep. 2022, paper FR1AA02, unpublished.

[3] A.V. Feschenko and P. N. Ostroumov, “Bunch Shape Measuring Technique and its Application for an Ion Linac Tuning”, in *Proc. LINAC'86,* Stanford, CA, USA, Jun. 1986, paper WE3-30, pp. 323-327.

[4] A. Feschenko, “Technique and Instrumentation For Bunch Shape Measurements”, in *Proc. RuPAC'12*, Saint Petersburg, Russia, Sep. 2012, paper FRXOR01, pp. 181-185.

[5] A. V. Feschenko, “Bunch Shape Monitors Using Low Energy Secondary Electron Emission”, *AIP Conf. Proc.*, vol. 281, p. 185, 1992. doi:10.1007/978-1-4020-5724-3_43

[6] Y.V. Bylinsky, A.V. Feschenko, and P.N. Ostroumov, “Longitudinal emittance measurement of the 100 MeV proton beam”, in *Proc. PAC'91,* San Framcisco, CA, USA, 1991, pp. 3062-3063, vol. 5, 1991. https://jacow.org/p91/PDF/PAC1991_3062.PDF

[7] R.L. Witkover, “A non-destructive bunch length monitor for a proton linear accelator”, *Nucl. Instrum. Methods Phys. Res., Sect. A*, vol. 137, pp. 203-211, 1976. doi:10.1016/0029-554X(76)90330-X

[8] A.V. Feschenko and P.N. Ostroumov, “Bunch shape measurements at the INR Linac”, in *Proc. Workshop Adv. Beam Instrum.*, pp. 236-245, 1991. doi:10.1109/PAC.1993.309344

Content from this work may be used under the terms of the CC-BY-4.0 licence (© 2023). Any distribution of this work must maintain attribution to the author(s), title of the work, publisher, and DOI

ISBN: 978-3-95450-236-3 ISSN: 2673-5350 doi:10.18429/JACoW-IBIC2023-TUP021

DEVELOPMENT OF THE RF PHASE SHIFTER WITH FEMTOSECOND TIME DELAY RESOLUTION FOR THE PAL-XFEL LASER SYSTEM*

D.C. Shin†, G.J. Kim, H. -S. Kang, G. Mun, C.-K. Min
Pohang Accelerator Laboratory, Pohang, South Korea

Abstract

We introduce the RF Phase Shifter (RPS) developed in the Pohang Accelerator Laboratory X-ray Free-Electron Laser (PAL-XFEL) to control the timing of optical laser system. This equipment is designed to finely adjust the timing of laser pulses with femtosecond scale by manipulating the phase of the RF reference using a couple of Direct Digital Synthesizer (DDS) devices. Furthermore, it is designed with low phase noise and low phase drift features in order to minimize the impact on the system in an open-loop operation.

Currently these units are installed at the Injection site, Hard X-ray and Soft X-ray Beamline. They are implemented for the feedback control of the photocathode gun phase at the Injector and for the use in pump-probe experiments at the Beamlines. This paper describes the design, fabrication, and experimental results of the RPS, as well as its usage status at PAL-XFEL.

INTRODUCTION

Optical Laser systems have been established in the Injector and Beamlines at PAL-XFEL for generating a highly stable electron beam and ultrafast X-ray sciences.

Time delay is a critical function in laser systems. In the Injector section of PAL-XFEL, laser time delay is utilized to compensate for drift of the electron beam. In the Beamline, it is employed to control the time delay of the pump laser in pump-probe experiments. The time delay of lasers can typically be adjusted by altering the physical length of the laser path using mirrors and delay stages. The PAL-XFEL laser system has employed this method since its early operational stages [1].

However, the approach involving delay stages can lead to degradation in laser quality due to vibration and shift in laser focus. Additionally, the difficulty in adjusting the time delay at pulse-to-pulse speed (60 Hz) results in the waste of the probe laser in pump-probe experiments.

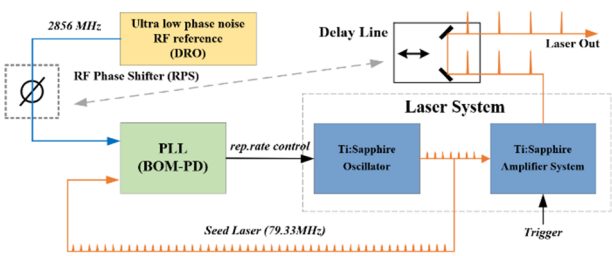


Figure 1: RPS and delay stage in the injector laser.

To address these aspects, we believed that a digital time delay control device would be more effective than mechanical time delay methods. As shown in Fig. 1, we considered installing an RF phase shifter between the REF and PLL to modify the phase. By adjusting the phase in this manner, we expected that a corresponding time delay proportional to the phase change would naturally occur during the Lock Tracking process of the PLL. Additionally, we fabricated a prototype device and confirmed its operation to be as expected.

We manufactured and installed a total of six devices in both the Injector laser and Beamline laser systems. In the following section, we will introduce the fabrication process and outcomes of the RF Phase Shifter.

DESIGN OF THE RPS

Key Specifications

Considering the requirements from the laser team and the limitations of electronic devices, we have defined the specifications as follows:

- Phase Control Resolution: 0.0055 degrees
- Control Range: $(-2^{\wedge 30} \sim 2^{\wedge 30}) \times$resolution
- Linearity (0~360 degrees): ≤ ±0.05 degrees
- Update Rate: ≥ 10 kHz
- Stability degrees/day: ≤ 0.1 degrees
- Phase Noise: ≤ -150 dBc@100 kHz~1 MHz

Determination of Phase Shifting Methods

We explored various phase shifting methods to develop a unit that satisfies the specifications at a reasonable cost. Initially, we considered Digital/Voltage Controlled Phase Shifter components due to their affordability and straightforward control mechanisms. However, after reviewing the datasheets, we determined that they would not meet the required resolution and linearity specifications [2, 3].

The vector modulation approach allows for high resolution implementation, but due to hardware issues such as phase unbalance in Hybrid and Combiner, as well as I/Q DC offset, the linearity of the output phase deteriorates. Therefore, meticulous calibration efforts are required to meet the linearity specifications. However, even with such calibration, we had determined that achieving the less than ±0.05 degrees linearity is very challenging [4].

Next, we examined the DDS device. The DDS enables precise frequency/phase control and fast response characteristics by converting digital values obtained through the 'Phase Accumulator' and 'Amplitude/Sine Converter' into RF signals via the DAC (Digital-to-Analog Converter) [5].

* Work supported by Ministry of Science and ICT of Korea
† dcshin@postech.ac.kr

Content from this work may be used under the terms of the CC-BY-4.0 licence (© 2023). Any distribution of this work must maintain attribution to the author(s), title of the work, publisher, and DOI

ISBN: 978-3-95450-236-3 ISSN: 2673-5350 doi:10.18429/JACoW-IBIC2023-TUP021

Figure 2 shows the block diagram of the AD9914 DDS that we applied. The AD9914 has a 16-bit phase offset value, providing a phase resolution of approximately 0.0056 degrees (360/2^16). Although the DAC's resolution is limited to 12 bits, the phase truncation process that maintains the higher bits ensures that all 16 bits of phase information are preserved [5].

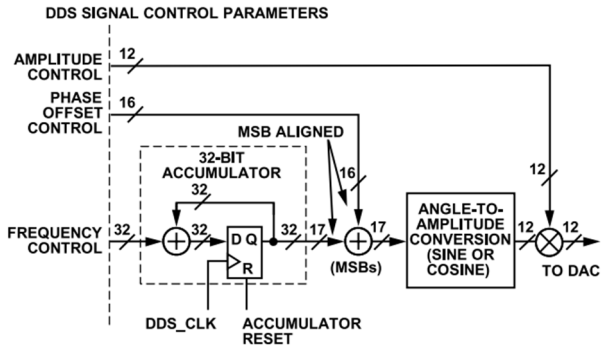


Figure 2: AD9914 block diagram [6].

Frequency Plan of the System

When performing frequency up-conversion and down-conversion, the phase of the output signal generally mirrors the changes in the phase of the input signal. Therefore, we had planned to utilize the DDS output as an Intermediate Frequency (IF) signal and feed it into the mixer in the process of converting the RF 2856 MHz REF input frequency. Then we can control the output phase by manipulating the phase of this DDS signal.

The design concept is shown in Fig. 3.

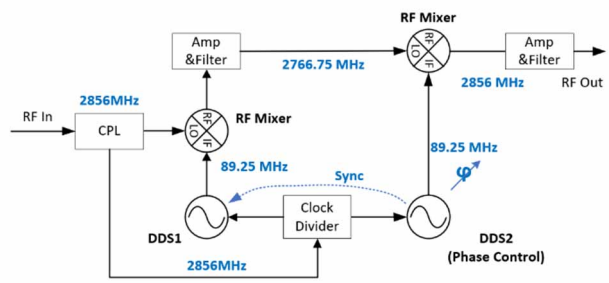


Figure 3: RPS frequency plan.

On the other hand, in order to minimize the generation of spurious signals during the conversion process, we initially set the DDS output frequency to a few hundred MHz. However, based on the information from the datasheet of AD9914, we confirmed that higher output frequencies lead to deteriorated residual phase noise performance [6]. Therefore, we made a trade-off between spurious reduction and phase noise performance. Consequently, we determined the DDS output frequency to be 89.25 MHz.

FABRICATION OF THE RPS

The following block diagram shows the internal structure of the fabricated unit.

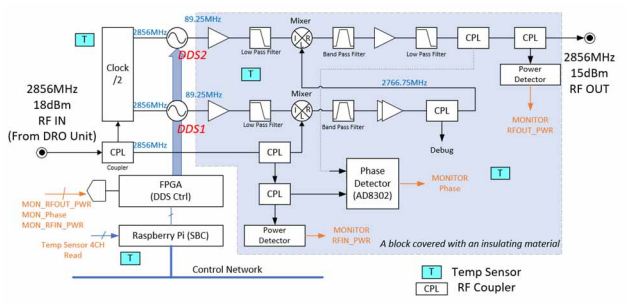


Figure 4: RPS block diagram.

The Power of the input REF signal is sufficiently large to drive the mixer, so it is directly routed to the mixer's LO port after passing through the coupler without an additional amplifier. The output from the coupler serves as the master clock for the DDS, and an ADCLK925 1:2 clock buffer is employed to supply the signal to two DDS chip.

The frequency of the down-converted signal at the first mixer is 2766.75 MHz, and this signal is then passed through a filter and amplifier before being fed into the LO port of the second mixer. The IF signal produced by the second DDS and the 2766.75 MHz signal are mixed together at the up-conversion mixer and it generates an RF signal at 2856 MHz. The phase control in this process is achieved by adjusting the phase offset value of the DDS dedicated to up-conversion. An FPGA was utilized for DDS timing control, and a Raspberry Pi, acting as a Single Board Computer, was employed for EPICS IOC processing.

In Fig. 4, the blue region represents the temperature-controlled area. To minimize drift caused by external temperature variations, this area is surrounded by thick insulation material, and external chiller along with specially designed heat dissipation plates are used to control the temperature. For precise temperature monitoring, temperature sensors are placed at four locations within the unit. Additionally, power detectors and phase detectors are mounted inside the RF modules for continuous monitoring of input/output power and phase. Figure 5 shows the fabricated unit.

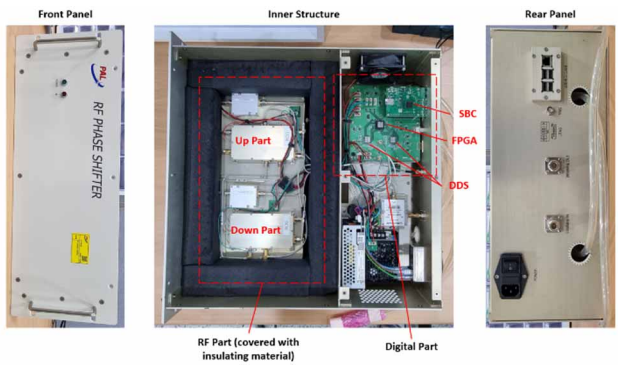


Figure 5: The fabricated unit.

The control board containing the DDSs was exposed to room temperature due to the longer wavelength of the IF band, which results in reduced sensitivity to temperature changes.

Meanwhile, the RF circuitry is placed in an area with temperature control. It is tightly integrated within a metal

Content from this work may be used under the terms of the CC-BY-4.0 licence (© 2023). Any distribution of this work must maintain attribution to the author(s), title of the work, publisher, and DOI

ISBN: 978-3-95450-236-3 ISSN: 2673-5350 doi:10.18429/JACoW-IBIC2023-TUP021

Content from this work may be used under the terms of the CC-BY-4.0 licence (© 2023). Any distribution of this work must maintain attribution to the author(s), title of the work, publisher, and DOI

housing which is further affixed to a metal heat dissipation plate, enhancing thermal conductivity between the heat dissipation plate and the RF circuitry. Furthermore, as the cooling fluid flows through the heat dissipation plate from the chiller, heat exchange takes place. Therefore, to ensure a high level of temperature stability, it is important for the insulation performance to be excellent, and the temperature of the cooling fluid should remain consistent.

PERFORMANCE AND USAGE

Performance

Phase Noise Figure 6 displays the measurement results of the input and output phase noise characteristics of the RPS, displaying that the desired phase noise performance of 150 dBc or lower is achieved in the target frequency range exceeding 100 kHz.

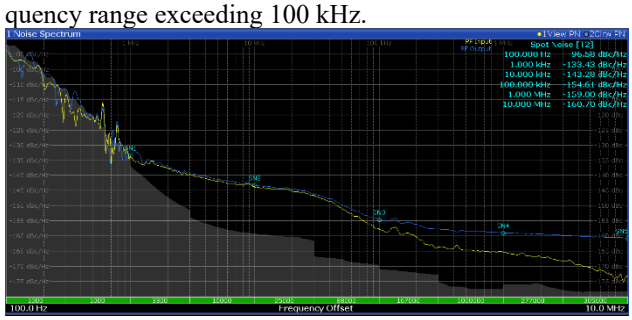


Figure 6: Phase noise, yellow: REF, blue: RPS output.

Long Term Stability The measurement of long-term stability utilized the Phase Detector from i-tech Corp., as well as the LLRF deployed at PAL-XFEL.

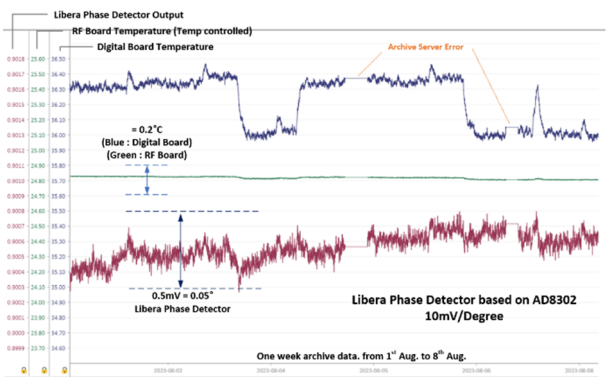


Figure 7: Long-term stability by i-tech phase detector.

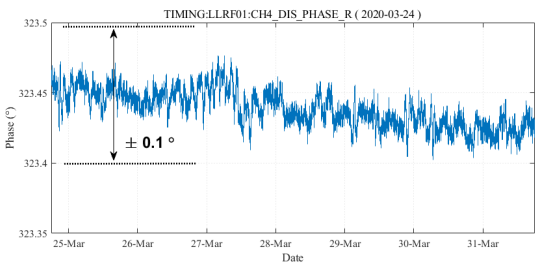


Figure 8: Long-term stability by LLRF.

As shown in Figs. 7 and 8, both sets of results demonstrated a stability of 0.1 degrees per week. To minimize errors, the output voltage of the Phase Detector was set to 0.9 V. This device features an output characteristic of 10 mV per degree [7].

Resolution and Linearity To demonstrate the resolution performance of the RPS, we incrementally increased the phase of the RPS by 0.0055 degrees using LLRF for testing. Figure 9 shows the results, clearly indicating increments of 0.0055 degrees. For reference, the phase measurement performance of LLRF is rms 0.01 degrees.

Figure 10 shows the results of the linearity measurements for the RPS. The RPS phase was incremented in 10 degrees steps from 0 to 350 degrees, and the phase measurements obtained through LLRF are displayed on the left vertical axis, with the relative error indicated on the right vertical axis. It can be observed that the relative error remains within ±0.05 degrees.

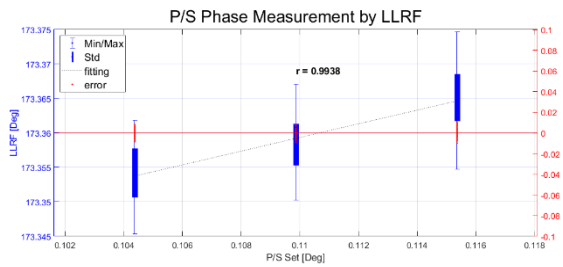


Figure 9: RPS resolution (0.0055 degrees/step).

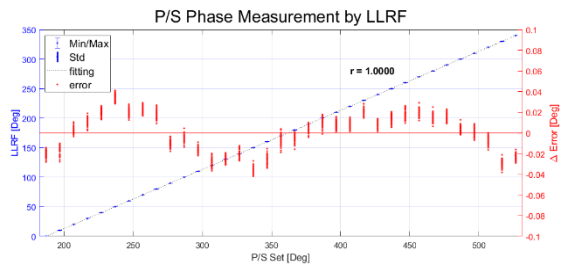


Figure 10: RPS linearity (10 degrees/step).

Usage of PAL-XFEL

PFS units have been installed in the Hard/Soft X-ray Beamline laser room and the Injector laser room. The installation images are shown in Fig. 11.

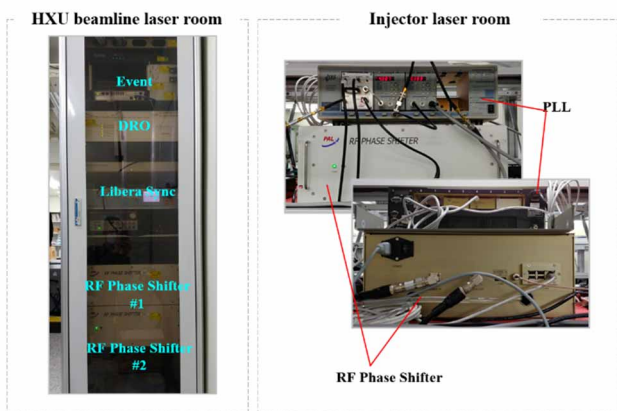


Figure 11: RPSs in the beamline and injector.

In the Injector laser, the RPS is utilized to correct phase drift between laser and electron beam. As depicted in Fig. 12, the RPS adjusts the laser delay time by reading the

ISBN: 978-3-95450-236-3 ISSN: 2673-5350 doi:10.18429/JACoW-IBIC2023-TUP021

position value of the BPM located downstream of the Gun and making adjustments based on the error.

In the beamline, the RPS is currently used partially for pump-probe experiments. It appears that many users still prefer the time delay control method using the conventional motion stage. However, we plan to actively explain the advantages of the device to users in order to increase opportunities for its usage.

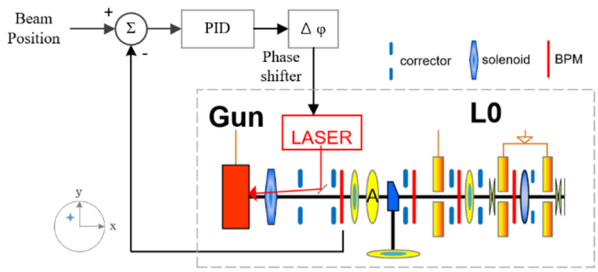


Figure 12: Feedback using RPS in the injector.

SUMMARY

We have developed a cost-effective phase controller with a manufacturing cost of less than $10,000, and through experiments, we have confirmed its satisfactory performance. As mentioned earlier, this unit is currently operated as a Gun laser feedback system for PAL-XFEL, and we anticipate its gradual expansion for pump-probe experiments in the beamline.

REFERENCES

[1] M. Kim, C.K. Min, and I. Eom, "Laser systems for time-resolved experiments at the Pohang accelerator Laboratory X-ray Free-Electron Laser beamlines", *J. Synchrotron Rad.*, vol. 26, pp. 868-873, 2019. doi: 10.1107/S1600577519003515

[2] Analog Device, "HMC647ALP6E Digital Phase Shifter Datasheet", https://www.analog.com

[3] Mini-Circuits, "JSPHS-1000 Voltage Controlled Phase Shifter Datasheet", https://minicircuits.com

[4] P. Tosovsky, D. Valuch, "Improvement of RF Vector Modulator Performance by Feed-forward Based Calibration", *Radioengineering,* vol. 19, no. 4, pp. 627-632, 2010.

[5] Analog Device, "A Technical Tutorial on Digital Signal Synthesis", https://www.analog.com

[6] Analog Device, "AD9914 Direct Digital Synthesizer Datasheet", https://www.analog.com

[7] Instrumentation Technologies, "Libera Phase Detector User Manual", https://www.i-tech.si

Content from this work may be used under the terms of the CC-BY-4.0 licence (© 2023). Any distribution of this work must maintain attribution to the author(s), title of the work, publisher, and DOI

ISBN: 978-3-95450-236-3 ISSN: 2673-5350 doi:10.18429/JACoW-IBIC2023-TUP022

CHARACTERISATION OF CHERENKOV DIFFRACTION RADIATION USING ELECTRO-OPTICAL METHODS

A. Schlögelhofer[1,*], T. Lefèvre, S. Mazzoni, E. Senes, CERN, Geneva, Switzerland
L. Duvillaret, KAPTEOS, Saint-Helene-du-Lac, France
[1] also at TU Wien, Vienna, Austria

Abstract

The properties of Cherenkov diffraction radiation (ChDR) have been studied extensively during the recent years to be exploited for non-invasive beam diagnostic devices for short bunches. The dependence of charge and the influence of the bunch form factor on the coherent part of the radiated spectrum have been demonstrated and studied in the past. However, the actual field strength of coherent ChDR as well as its study in time domain need further investigation. In this contribution we are using electro-optical techniques to investigate and quantify these parameters. The electro-optical read-out brings the advantage of high bandwidth acquisition and insensitivity to electromagnetic interference, whereas at the same time a large fraction of the acquisition setup can be installed and operated outside of the radiation controlled areas. We will present experimental results from the CLEAR facility at CERN as well as simulations of the peak field of the temporal profile of beam-generated ChDR pulses.

INTRODUCTION

Cherenkov diffraction radiation (ChDR) describes the radiation produced at the surface of a dielectric by the electric field of a relativistic charged particle passing by in the vicinity of the dielectric. This mechanism is illustrated in Fig. 1, where the ChDR is emitted at the well-defined Cherenkov angle $cos(\theta_{Ch}) = 1/(n_1\beta)$ with n_1 denoting the refractive index of the dielectric medium and $\beta = v/c$ the normalized velocity of the charged particle. The produced ChDR can be analysed to measure critical properties of a beam of charged particles, e.g. its length or position [1]. While previous work focused on studying the qualitative behaviour of ChDR and measuring the frequency spectrum to reconstruct beam properties [2–4], this contribution shows the measurement of the electric field strength generated by coherent ChDR in terms of absolute numbers by sampling its temporal profile.

METHODOLOGY

An electro-optical probe (eo-probe) [5] was used to obtain a real-time high bandwidth measurement insensitive to electromagnetic interference.

Working Principle of the Eo-Probe

The eo-probe is fully dielectric and, amongst other optical elements, contains a sensing crystal made out of BSO ($Bi_{12}SiO_{20}$). It utilizes the Pockels effect, which describes the linear change of the refractive index of a medium exposed to an external electric field. This induced refractive index change introduces a birefringence in the BSO crystal. A continuous-wave sensing laser of known polarization is sent through the crystal. During exposure to an external electric field, the BSO crystal alters the polarization state of the sensing laser. The modulated laser light passes through polarizers, and its changed polarization state is then analyzed with fast photodiodes. Using this principle, the eo-probe measures the electric field vector up to field strengths of MV/m.

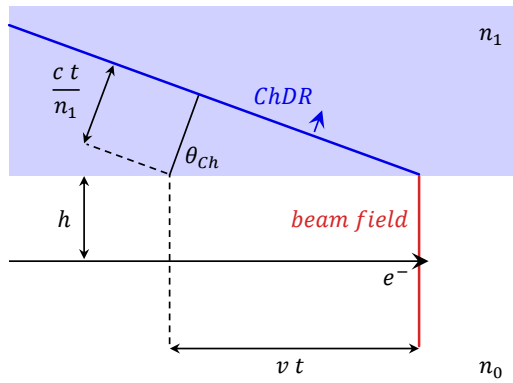


Figure 1: Schematic of the ChDR principle in a dielectric medium ($n_1 \approx 3$). The Cherenkov condition $n_1 \cdot v/c > 1$ must be satisfied to produce ChDR.

The eo-probe (with a bandwidth ≤ 10 GHz) was placed in the accelerator hall. All the other parts of the detection system were placed outside the radiation-controlled area. The sensing laser was transported to the probe via 20-metre-long optical fibres. The signal was measured with a high-bandwidth oscilloscope (10 GHz, 256 GSa/s, 10-bit) and then corrected for the change of insertion loss during the measurement as well as converted according to the antenna factor of the probe to obtain an absolute electric field measurement. As the electric field strength scales linearly with the bunch charge, the bunch charge was also independently recorded. All the data presented in this contribution are normalized to a bunch charge of 300 pC.

CALIBRATION

To calibrate the system's response, a first measurement campaign was performed on the direct beam field of an electron bunch propagating in air.

The bandwidth of the data acquisition system is limited to 10 GHz. Therefore, as electron bunches at the CLEAR

* andreas.schloegelhofer@cern.ch

Content from this work may be used under the terms of the CC-BY-4.0 licence (© 2023). Any distribution of this work must maintain attribution to the author(s), title of the work, publisher, and DOI

ISBN: 978-3-95450-236-3 ISSN: 2673-5350 doi:10.18429/JACoW-IBIC2023-TUP022

facility [6] typically are only a few ps long, the bandwidth is insufficient to measure the entire power spectrum of the electron bunches. The direct beam field of an electron bunch was measured to calibrate the data acquisition system for short bunches. The calibration setup is illustrated in Fig. 2. This measurement was compared to the analytical formula describing the peak electric field strength obtained from the direct beam field of a particle bunch [7]:

$$E_{analytic} = \frac{e}{2\sqrt{2}\pi^{3/2} c \epsilon_0} \frac{N}{\sigma} \frac{1}{r} \tag{1}$$

where e denotes the elementary charge, c is the speed of light in vacuum, and ϵ_0 is the vacuum permittivity (it is assumed $\epsilon_0 = \epsilon_{air}$ in this frequency range). The transverse distance from the beam is denoted r (cf. Fig. 2). The number of particles in the bunch N and the bunch length σ must be adapted to the experimental conditions. For a charge of 300 pC and a bunch length of 5 ps (1 σ), Eq. (1) yields $E_{analytic} = 1435.2 / r$ [V/m] for the peak electric field.

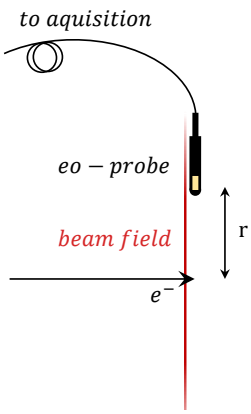


Figure 2: Schematic of the measurement of the direct beam field using an eo-probe. For the calibration measurement, the distance r between the beam and eo-probe was varied over a distance of ≈ 100 mm.

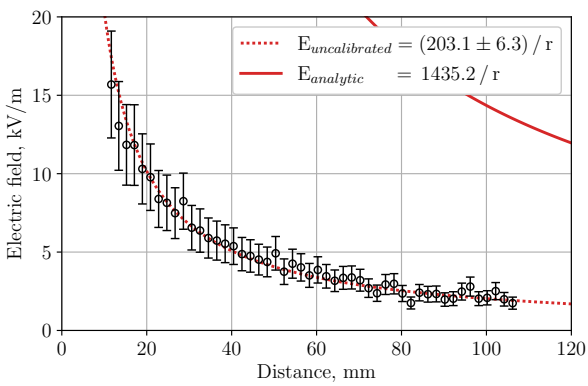


Figure 3: Uncalibrated peak electric field strength of the beam field as a function of the distance (dashed line) to be compared to the analytical expectation (solid line).

Figure 3 shows the measured peak electric field strength as a function of the distance from the beam. The measured value of 203.1 ± 6.3 V is smaller by a factor 7.1 ± 0.2 than the analytical value of 1435.2 V. This discrepancy is expected due to the bandwidth limitation of the acquisition system itself as well as the timing jitter between the trigger signal and the electron beam. Both these effects lead to a lower signal amplitude being measured and the resulting discrepancy is discussed in detail below.

Bandwidth Limitation

The bandwidth of the acquisition system was limited to an upper frequency of 10 GHz for all the presented measurements. As the electron bunches are only a few ps long, a significant part of the high-frequency spectrum is not measured accordingly. This behaviour is shown in Fig. 4 and accounts for a factor ≈ 4.0 for a bunch length of 5 ps (1 σ) and an upper-frequency limitation of 10 GHz.

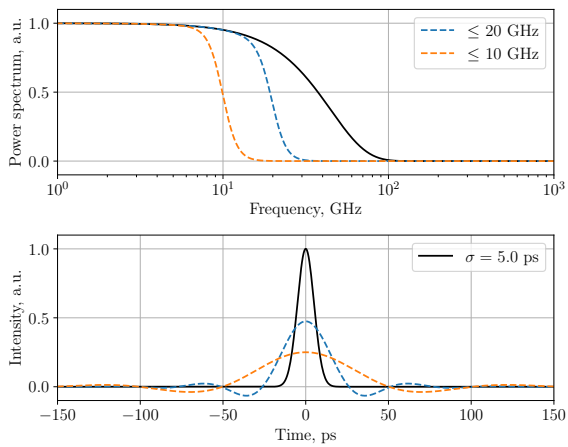


Figure 4: Power spectrum and time profile of bandwidth limited acquisition (dashed lines) compared to full bandwidth (solid line).

Timing Jitter

Single shot traces were analyzed to get a rough estimate of the reduction of the peak signal due to the timing jitter present. For the data point closest to the beam (r = 11.7 mm), 600 single-shot traces were acquired. The average of the maximum of each single trace divided by the maximum of the averaged traces yields a factor 2.1, which is also illustrated in Fig. 5.

Together with the bandwidth limitation, this rough estimation yields a total scaling factor of 8.4, which needs to be compared to the obtained factor of 7.1 from the calibration measurement. Using this simple approach, we would overestimate the results by ≈ 18%. However, it shows that the obtained factor of 7.1 from the calibration is justified.

Content from this work may be used under the terms of the CC-BY-4.0 licence (© 2023). Any distribution of this work must maintain attribution to the author(s), title of the work, publisher, and DOI

ISBN: 978-3-95450-236-3 ISSN: 2673-5350 doi:10.18429/JACoW-IBIC2023-TUP022

Content from this work may be used under the terms of the CC-BY-4.0 licence (© 2023). Any distribution of this work must maintain attribution to the author(s), title of the work, publisher, and DOI

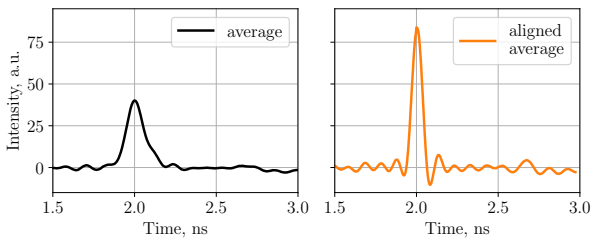


Figure 5: Traces from the closest data point r = 11.7 mm. Left: Average of all traces. Right: Average of traces aligned in time to the maximum of each trace.

MEASUREMENT OF THE COHERENT CHDR FIELD

Using the same eo-probe and acquisition setup as for the calibration measurement, the electric field strength of ChDR emitted from a dielectric radiator was measured. A schematic of the installation is shown in Fig. 6. The experiment was installed in air, therefore $n_0 \approx 1$. The radiator was made out of Alumina (97.6% Al_2O_3) with a relative permittivity of $\epsilon_r \approx 9.0$ (1.0 – 8.5 GHz, 25°C) [8]. The radiator had a cylindrical geometry with a diameter of 36 mm and a central axis length of 47.6 mm. It was inserted into a metal body at its Cherenkov angle $\theta_{Ch} = 70.55°$ and machined to be flush with the chamber aperture (∅ 80 mm). The centre of the chamber aperture was aligned at the corresponding beam position using a reference laser. During the measurements, the whole setup was moved transversely with a motorized linear stage to vary the impact parameter h from 10 - 50 mm. The eo-probe was positioned 10 mm away from the radiator surface on the central axis of the radiator.

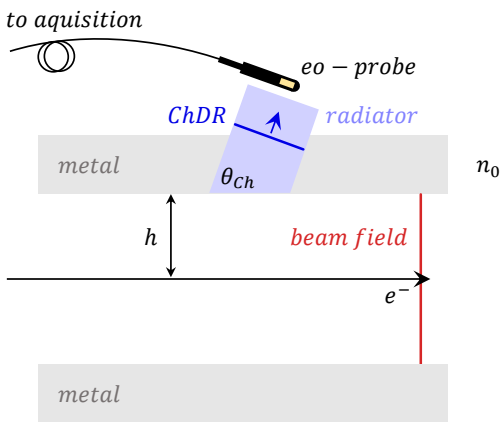


Figure 6: Schematic of the ChDR measurement setup. The impact parameter h was varied during the measurement by moving the setup with respect to the electron beam.

The measurement results are shown in Fig. 7. The peak electric field 10 mm from the exit surface of the radiator is shown as a function of the impact parameter h. The absolute values after calibration are shown in blue. Error bars indicate the standard deviation of each measurement. The experimental data was fitted for a $1/h$ decay. The orange markers stem from a CST simulation [9] considering the experimental setup in a 3D layout. The peak electric field was sampled at 10 mm from the exit surface of the radiator. Table 1 gives an overview of the simulation parameters.

Table 1: CST Simulation Parameters

Solver		Wakefield
Bandwidth		100 GHz
Cells / wavelength		10
Bunch charge		300 pC
Bunch length	σ	5 ps
Lorentz factor	γ	392.4
Impact parameter	h	10-50 mm
Relative permittivity (Al_2O_3)	ϵ_r	9.0

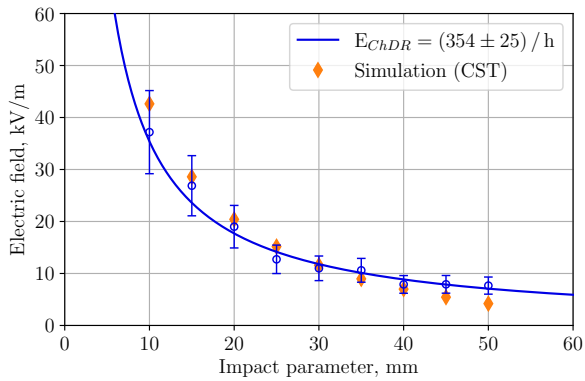


Figure 7: Calibrated peak electric field strength of coherent ChDR as a function of the impact parameter. Absolute values after calibration are shown in blue, error bars indicate the standard deviation of each measurement.

DISCUSSION AND CONCLUSION

The measurement of the absolute electric field strength of ChDR showed that for a short electron bunch (5 ps (1 σ), 300 pC, 200 MeV) the peak electric field is in the order of 10 kV/m for an alumina radiator. It decreases proportionally to the inverse distance between the particle beam and the radiator surface. It also was shown that the numerical simulations performed with CST agree with the experimental findings regarding absolute numbers of the peak electric field. This qualifies numerical simulations to predict coherent ChDR for different beam parameters and radiator geometries. The knowledge of the absolute value of the electric field generated by coherent ChDR enables the targeted development of dielectric diagnostic devices like bunch length monitors and beam position monitors.

ISBN: 978-3-95450-236-3 ISSN: 2673-5350 doi:10.18429/JACoW-IBIC2023-TUP022

ACKNOWLEDGEMENTS

This work was supported by the European Union's Horizon 2020 Research and Innovation Programme under grant no. 951754 (FCCIS).

REFERENCES

[1] T. Lefèvre *et al.*, "Cherenkov diffraction radiation as a tool for beam diagnostics", in *Proc. 8th Int. Beam Instrum. Conf. (IBIC'19)*, Malmö, Sweden, Sep. 2019, pp. 660-664. doi:10.18429/JACoW-IBIC2019-THA001

[2] E. Senes *et al.*, "Beam position detection of a short electron bunch in presence of a longer and more intense proton bunch for the AWAKE experiment", in *Proc. 10th Int. Beam Instrum. Conf. (IBIC'21)*, Pohang, Korea, Sep. 2021, pp. 75-79. doi:10.18429/JACoW-IBIC2021-MOPP17

[3] C. Pakuza *et al.*, "Electron beam studies on a beam position monitor based on Cherenkov diffraction radiation", presented at the 14th Int. Particle Accelerator Conf. (IPAC'23), Venice, Italy, May 2023, paper THPL146, to be published.

[4] A. Curcio *et al.*, "Beam-based sub-THz source at the CERN linac electron accelerator for research facility", *Physical Review Accelerators and Beams*, vol. 22, Feb. 2019. doi:10.1103/PhysRevAccelBeams.22.020402

[5] KAPTEOS, Electric Field Probe EL5, https://en.kapteos.com/eoprobe-datasheet

[6] D. Gamba *et al.*, "The CLEAR user facility at CERN", *Nucl. Instrum. Methods Phys. Res., Sect. A*, vol. 909, 2018. doi:10.1016/j.nima.2017.11.080

[7] M. Ferrario, M. Migliorati and L. Palumbo, "Space charge effects", in *Proc. of the CAS-CERN Accelerator School: Advanced Accelerator Physics*, Trondheim, Norway, Aug. 2013, pp. 331-356. doi:10.5170/CERN-2014-009.331

[8] AL 300 (Mac-A976W), Morgan Advanced Materials https://www.morgantechnicalceramics.com/media/4810/al300.pdf

[9] Dassault Systèmes Simulia Corp., CST Studio Suite 2022 https://www.3ds.com/products-services/simulia/products/cst-studio-suite

Content from this work may be used under the terms of the CC-BY-4.0 licence (© 2023). Any distribution of this work must maintain attribution to the author(s), title of the work, publisher, and DOI

ISBN: 978-3-95450-236-3 ISSN: 2673-5350 doi:10.18429/JACoW-IBIC2023-TUP023

APPLICATION OF A CAMERA ARRAY FOR THE UPGRADE OF THE AWAKE SPECTROMETER

Eugenio Senes* [1], F. Pannell [2], D.A. Cooke [2], S. Mazzoni [1], M. Turner [1], M. Wing [2], G. Zevi Della Porta [1,3]
[1] CERN, Geneva, Switzerland
[2] University College London, London, United Kingdom
[3] Max Planck Institute for Physics, Munich, Germany

Abstract

The first run of the AWAKE experiment successfully demonstrated the acceleration of an electron beam in the plasma wakefields of a relativistic proton beam. The planned second run will focus on the control of the emittance of accelerated electrons, requiring an upgrade of the existing spectrometer. Preliminary measurements showed that this might be achieved by improving the resolution of the scintillator and with a new design of the optical system. This contribution discusses the application of a digital camera array in close proximity of the spectrometer scintillator, to enable the accelerated electron beam emittance measurement.

INTRODUCTION

In the AWAKE experiment, a 19 MeV electron bunch gets accelerated in the wakefield of a rubidium plasma [1]. The plasma wake is driven by a 400 GeV proton bunch produced in the CERN Super Proton Synchrotron.

In order to measure the characteristics of the accelerated electron beam, a magnetic spectrometer was installed downstream of the plasma cell. The development of the magnetic spectrometer is reported in [2–4].

The core functions of the electron spectrometer are to measure on the accelerated electron beam:

1. The beam peak energy and energy profile
2. The beam charge
3. The beam emittance

In AWAKE Run 1 the resolution proved to be too limited to measure the beam emittance; a study was launched to improve the spectrometer system for AWAKE Run 2. This paper discusses possible technical implementations to improve the spectrometer resolution, focusing on a high resolution optical system. Possible modifications of the spectrometer magnetic lattice to transport the accelerated beam will be discussed elsewhere, and go beyond the scope of this work.

SPECTROMETER DESIGN

Beamline Components

The magnetic components of the spectrometer have not changed since AWAKE Run 1 [5, 6]. The electron and proton beams exit the plasma, pass through a quadrupole doublet and then through a dipole magnet. A dipole field up to 1.5 T separates the electron and proton beams, introducing a spatial dependence for the electron beam energy in the range 30 MeV-8.5 GeV. After the dipole, the accelerated electrons traverse a 2 mm thick vacuum window, and impact on a 1 m-long plastic scintillator. The scintillator currently in use is a 0.5 mm thick DRZ-High, a terbium-doped, gadolinium oxysulfide (Gd_2O_2S:Tb) screen produced by Mitsubishi Chemical. The particle transport through the spectrometer was simulated and validated through measurements with partially stripped ions [7, 8]. A layout of the spectrometer system is shown in Fig. 1.

Optical System

Information on the electron beam structure is reconstructed from the emitted light pattern produced by the scintillator. An accurate imaging of the scintillator emission is essential for a correct measurement of the electron beam parameters.

During AWAKE Run 1, the scintillation light was propagated through a 17 m-long optical line, to reach an intensified camera in a dedicated dark room outside the high radiation area [9, 10]. The camera is equipped with a 400 mm photographic lens, in order to resolve the whole scintillator. Although this system worked, the optical resolution proved to be too limited for emittance measurements.

Recent developments in the CMOS camera infrastructure for AWAKE allowed for placing cameras inside the experimental hall. A camera array was installed within 1.5 m of the scintillator, to record its light. This system is described in detail later on.

Beam Charge Measurement

In order to measure the total accelerated charge, the scintillator light yeld is calibrated against a known electron charge. In the past, the calibration was performed by installing the scintillator and the camera in the CLEAR test accelerator [11], and using electron beams with known charge. To allow for the in-situ calibration, a commercial Integrating Current Transformer (ICT) from Bergoz [12] was installed in the beamline upstream of the dipole. The charge signal is detected with custom electronics within a range of 750 pC.

* eugenio.senes@cern.ch

Content from this work may be used under the terms of the CC-BY-4.0 licence (© 2023). Any distribution of this work must maintain attribution to the author(s), title of the work, publisher, and DOI

ISBN: 978-3-95450-236-3 ISSN: 2673-5350 doi:10.18429/JACoW-IBIC2023-TUP023

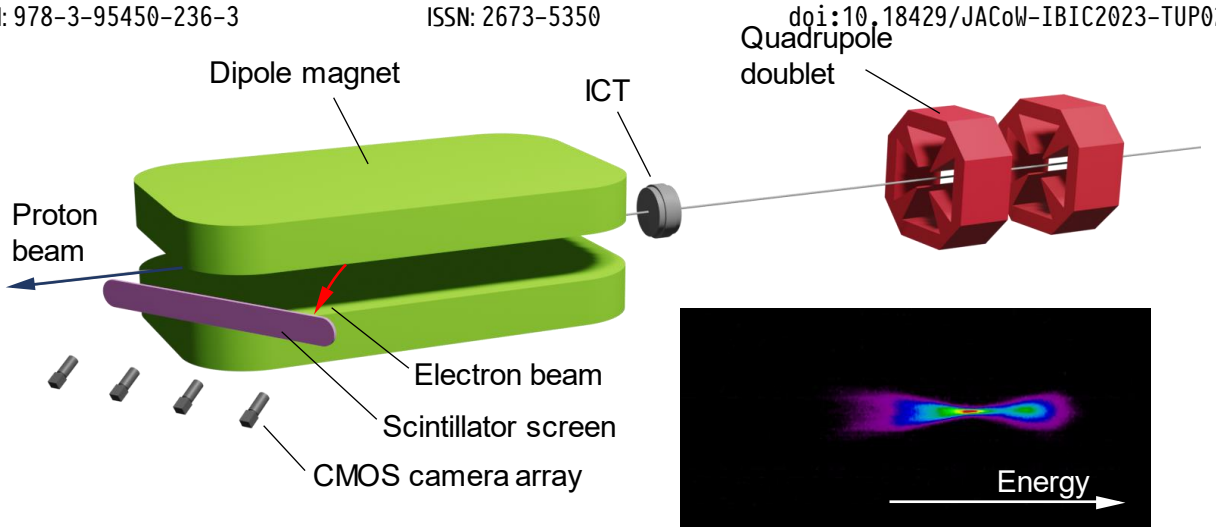


Figure 1: Layout of the spectrometer system in AWAKE. The inset shows a sample image of an accelerated beam from one of the cameras in the array.

DIGITAL CAMERA SYSTEM

Digital Camera Array

A general description of the digital camera infrastructure for AWAKE was given in Ref. [13]. The measurements shown in this work are performed with Basler acA1920-40gm cameras. The camera specifications are shown in Table 1. These devices showed a good resistance to modest radiation environments, and are remotely powered, allowing for reboot to recover from single event upset failures. The cameras are hardware triggered with a 750 µs delay, to capture the decay of the scintillation light. As the light emission is peaked at 545 nm, each camera is equipped with a 525 ± 46 nm bandpass filter to reduce the background.

A resolution in the order of 100 µm can be reached with sufficient camera magnification. This is a tradeoff between the distance to the scintillator and the objective focal length. The limitation, arising from high magnification, is that each camera can image only a part of the spectrometer. A camera array is set up to allow the imaging of a larger area of the spectrometer. The larger spectrometer image is then reconstructed by combining the camera images. The recomposition algorithm is described later on. The camera array is placed within 1.5 m from the scintillator, with an angle of 30° below the beam plane. This allows both for removing the cameras from the beam plane, where the radiation is higher, and for leaving free space in the optical line towards the intensified camera.

The selected camera lenses are Fujinon HF75HA1S with a focal length of 75 mm and an aperture of f/2.8. The camera array was placed at 110 cm from the scintillator, that is the minimum focusing distance of the lenses. The setup was reproduced in the lab, where USAF1951 targets were used to measure the point spread function (PSF) and hence infer the resolution. Additionally, a different camera model (Basler acA2040-35gm) was tested, featuring smaller pixel size and smaller sensor format. Both cameras showed that the resolution is dominated by the pixel size of the camera, and that optical resolutions as low as 77 and 48 µm are reachable at 110 cm distance, respectively. The camera parameters and resolutions are reported in Table 1. These tests showed that high resolution can be achieved at the expense of the field of view. To resolve the full 1 m-long scintillator, the array would require 7 and 11 cameras, respectively. Additionally, the use of sensors with smaller pixel size allows for increasing the distance to the scintillator, reducing the radiation damage.

Table 1: Comparison of parameters for the tested cameras. The top half shows camera specifications. The bottom half shows the measured resolution with 75 mm lens at 110 cm distance from the target.

Model		acA1920-40gm	acA2040-35gm
Resolution	[px]	1920 × 1200	2048 × 1536
Pixel size	[µm]	5.86 × 5.86	3.45 × 3.45
Sensor format		1/1.2"	1/1.8"
Lens		HF75HA1S - 75 mm f/2.8	
Magnification		0.076	
Field of view	[cm]	14.9	9.5
Pixel object size	[µm]	77	45
PSF σ	[µm]	77	48

Camera Calibration

Camera calibration is an essential part of understanding the three-dimensional aspects of objects from two-dimensional images. Extracting metric information from the 2D images acquired by the AWAKE spectrometer camera array forms the basis of the accelerated electron bunch analysis.

The mapping of a 3D point **X** in the real-world, to a 2D pixel coordinate, **x**, can be described via Eq. (1):

Content from this work may be used under the terms of the CC-BY-4.0 licence (© 2023). Any distribution of this work must maintain attribution to the author(s), title of the work, publisher, and DOI

ISBN: 978-3-95450-236-3 ISSN: 2673-5350 doi:10.18429/JACoW-IBIC2023-TUP023

Content from this work may be used under the terms of the CC-BY-4.0 licence (© 2023). Any distribution of this work must maintain attribution to the author(s), title of the work, publisher, and DOI

$$\mathbf{x} = \mathbf{PX} \quad (1)$$

where **P** is the projection matrix – a combination of the intrinsic camera calibration parameters and extrinsic camera parameters of position and orientation.

The process of camera calibration in this work employs Zhang's method, where the camera observes a planar pattern at different translations, rotations and tilts [14]. This technique offers a simplified, easily reproducible calibration procedure compared to the multiple, orthogonal planes used in 3D reference object-based calibration methods.

The procedure begins by mounting a pattern of known structure and size, in this case a chessboard, on a flat surface. The camera is fixed and the chessboard is imaged at different orientations. The OpenCV-Python [15] library is used and, for every image, a coordinate system is defined in which the chessboard forms the XY plane; all points lying on the chessboard have Z = 0. With this approach, the mapping between coordinate systems is simplified as the last column of the rotation matrix within **P** can be eliminated.

The corners of the chessboard pattern are located as key points through a function based on the Harris corner detection algorithm [16]. With each point representing an equation in the coordinate mapping system, the camera calibration parameters are obtained from the homography of real-world points to image points. Figure 2 shows the chessboard calibration target repeatedly imaged through one camera on the spectrometer array, with the corners successfully identified.

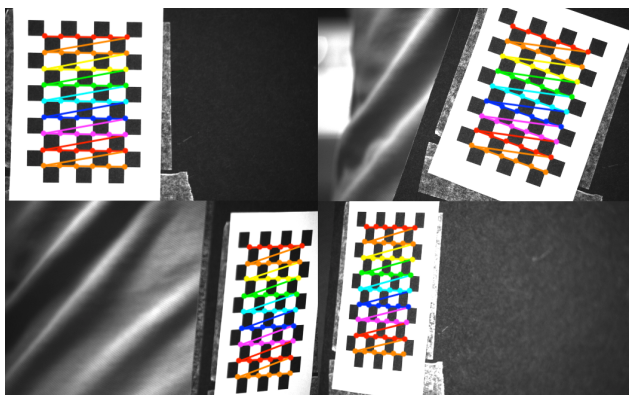


Figure 2: Chessboard calibration pattern captured at different positions and orientations. The corners are located with OpenCV.

Lens distortion effects, such as the ones illustrated in Fig. 3, arise from the lens optical design. The calculation of the camera matrix, distortion coefficients, translation and rotation vectors in the camera calibration procedure allows for the compensation of this effect.

Perspective Correction

As described earlier, the camera array views the spectrometer scintillator screen from an angle of 30° below the beam plane. Whilst it has practical advantages, this setup introduces a perspective distortion to the acquired images. By looking up at the screen, a foreshortening effect is created, where shapes higher up in the image appear condensed compared to shapes of the same size at the bottom.

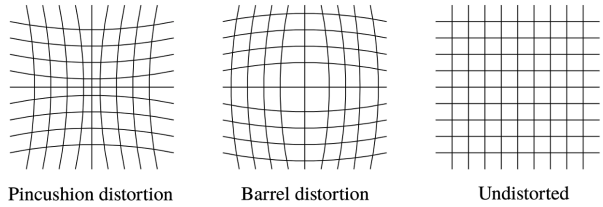


Figure 3: Examples of radial lens distortion, where light rays deviate from rectilinear projection.

Figure 4 demonstrates this effect. The left figure shows an uncorrected USAF1951 resolution target viewed through a spectrometer camera. The right figure is the same image but corrected for the perspective distortion. In addition to the rectified scaling offered by the perspective correction, as evidenced by the lengthened bars and increased target height, the image is rotated to create a 'head on' view of the target. The perspective correction was achieved by mapping the coordinates of the target corners in the unprocessed image to the corresponding corners in a scale, technical drawing of the same target.

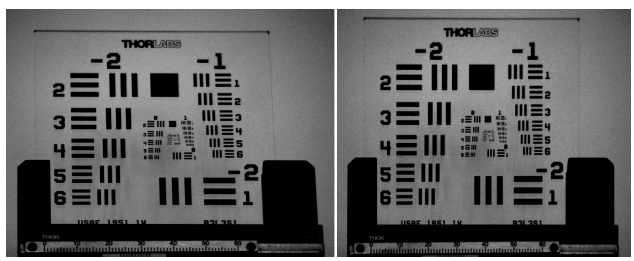


Figure 4: USAF1951 resolution target as seen from an unprocessed spectrometer image 30° below the beam plane (left) and a perspective corrected image to view 'head on' (right).

Emittance measurements with the camera array involve extracting the transverse size of the electron beam waist. Without perspective correction, the measured beam size will differ from reality, impacting the validity of emittance results. It is therefore essential to apply the appropriate perspective correction prior to analysis.

To correct the scintillator screen for perspective distortion, a screen target with commensurate dimensions with the scintillator is temporarily placed across the screen and imaged by all cameras in the array. Similarly to the resolution target perspective correction, key coordinates from the acquired images are mapped to the equivalent features in a technical drawing of the screen target. This can be seen in Fig. 5, where corrected images are sampled up to the same size of the drawing.

ISBN: 978-3-95450-236-3 ISSN: 2673-5350 doi:10.18429/JACoW-IBIC2023-TUP023

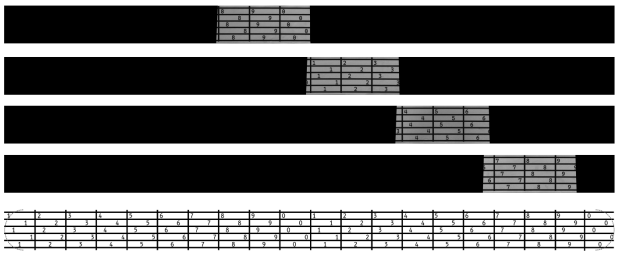


Figure 5: Perspective corrected images of the sub region within the field of view for each camera, with a technical drawing of the spectrometer screen target (bottom).

Image Recombination

By matching the size of the sub region images from each camera to the reference target, the images can be easily combined to create a single image of the target, representing the field of view of the entire camera array.

The four sub region images are overlaid by mapping them in-turn onto the reference target. Empty pixels are discarded, and any regions of overlap are accounted for by taking the average intensity value of the shared pixels.

Figure 6 shows the initial recombination result from overlaying two neighbouring camera images with this method. Whilst the geometric features of the target are successfully matched, it is clear this recombination suffers from vignetting effects.

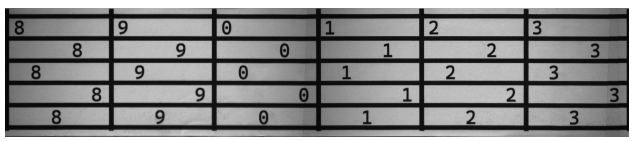


Figure 6: Two adjacent sub regions of the screen target overlaid for image recombination. Due to vignetting, the distinct images and seams are apparent.

By imaging an approximately uniform light source through one of the array cameras and the 75 mm lens, a calibration image is obtained, essentially creating a vignetting map. By dividing the screen target images by the normalised vignetting map, the variations in brightness across the target images are compensated.

Figure 7 is the result of complete image recombination of the four spectrometer cameras, correcting for vignetting, lens and perspective distortion.



Figure 7: All four spectrometer camera images combined into a single image of the screen target.

The leading advantage to this image recombination technique is the lack of constraint around overlap between cameras in the array. If images were combined via an image stitching method, this would require a sufficient overlap between neighbouring cameras, ensuring an adequate number of common descriptors could be identified. This constraint reduces the maximum field of view achievable compared to recombination by image overlaying for a camera array of a given size.

Resolution

It is worth noting that the lens distortion and perspective corrections performed in this work change the underlying pixel grid of the images, and are therefore interpolations. For this reason, it is important to assess the resolution both prior to and after these corrections. The reference image is sampled upwards, creating a reference with substantially more pixels than the images from the camera array. This reduces any loss of information during the perspective correction from the original image grid to the reference.

The image resolution is measured by imaging a resolution target and calculating the Modulation Transfer Function (MTF). In the case of the resolution targets in Fig. 4, the 0.5 MTF value before correction is ~3.9 line pairs per mm. After distortion and perspective correcting the image, the 0.5 MTF value is calculated as ~3.8 line pairs per mm. This shows a negligible change in the overall resolution due to image processing. It therefore remains advantageous to correct for the lens and perspective distortions prior to emittance analysis.

CONCLUSIONS

The AWAKE experiment continues studying the plasma acceleration of electrons in a wakefield generated by a proton bunch. To allow the measurement of the accelerated electron beam, improvements in the spectrometer system are required. This work discusses the improvements of the spectrometer optical system, with the aim of high-resolution imaging of the 1 m-long scintillator. The use of a camera array is proposed, and the hardware selection is presented. The image processing algorithm to recombine the single camera images into the full scintillator image is described, as well as the impact on the overall resolution of the process.

ACKNOWLEDGEMENTS

The authors would like to thank Mr. Itaru Sakamoto and the Mitsubishi Chemical Corp. for kindly providing the test scintillator samples. The authors would like to acknowledge the SPS and AWAKE operation teams, M. Gasior and T. Levens for the ICT support and S. Burger for the stimulating discussions.

REFERENCES

[1] E. Adli *et al.*, "Acceleration of electrons in the plasma wakefield of a proton bunch," *Nature*, vol. 561, no. 7723, pp. 363–367, 2018. doi:10.1038/s41586-018-0485-4

[2] L. C. Deacon *et al.*, "Development of a Spectrometer for Proton Driven Plasma Wakefield Accelerated Electrons at AWAKE," in *Proc. IPAC'15*, Richmond, VA, USA, May 2015, pp. 2601–2604. doi:10.18429/JACoW-IPAC2015-WEPWA045

Content from this work may be used under the terms of the CC-BY-4.0 licence (© 2023). Any distribution of this work must maintain attribution to the author(s), title of the work, publisher, and DOI

ISBN: 978-3-95450-236-3 ISSN: 2673-5350 doi:10.18429/JACoW-IBIC2023-TUP023

Content from this work may be used under the terms of the CC-BY-4.0 licence (© 2023). Any distribution of this work must maintain attribution to the author(s), title of the work, publisher, and DOI

[3] L. C. Deacon *et al.*, "A Spectrometer for Proton Driven Plasma Accelerated Electrons at AWAKE - Recent Developments," in *Proc. IPAC'16*, Busan, Korea, May 2016, pp. 2605–2608. doi:10.18429/JACoW-IPAC2016-WEPMY024

[4] F. Keeble *et al.*, "The AWAKE Electron Spectrometer," in *Proc. IPAC'18*, Vancouver, Canada, Apr.-May 2018, pp. 4947–4950. doi:10.18429/JACoW-IPAC2018-THPML118

[5] J. Bauche *et al.*, "A magnetic spectrometer to measure electron bunches accelerated at AWAKE," *Nucl. Instrum. Methods Phys. Res., Sect. A*, vol. 940, pp. 103–108, 2019. doi:10.1016/j.nima.2019.05.067

[6] F. Keeble, "Measurement of the electron energy distribution at awake," Ph.D. dissertation, University College London, 2019.

[7] D. A. Cooke *et al.*, "Measurement and application of electron stripping of ultrarelativistic $^{208}Pb^{81+}$," *Nucl. Instrum. Methods Phys. Res., Sect. A*, vol. 988, p. 164 902, 2021. doi:10.1016/j.nima.2020.164902

[8] D. A. Cooke *et al.*, "Calibration of the AWAKE Electron Spectrometer with Electrons Derived from a Partially Stripped Ion Beam," in *Proc. IPAC'19*, Melbourne, Australia, May 2019, pp. 2694–2696. doi:10.18429/JACoW-IPAC2019-WEPGW089

[9] S. Mazzoni *et al.*, "Beam Instrumentation Developments for the Advanced Proton Driven Plasma Wakefield Acceleration Experiment at CERN," in *Proc. IPAC'17*, Copenhagen, Denmark, May 2017, pp. 404–407. doi:10.18429/JACoW-IPAC2017-MOPAB119

[10] I. Gorgisyan *et al.*, "Commissioning of Beam Instrumentation at the CERN AWAKE Facility After Integration of the Electron Beam Line," in *Proc. IPAC'18*, Vancouver, Canada, Apr.-May 2018, pp. 1993–1996. doi:10.18429/JACoW-IPAC2018-WEPAF070

[11] D. Gamba *et al.*, "The CLEAR user facility at CERN," *Nucl. Instrum. Methods Phys. Res., Sect. A*, vol. 909, pp. 480–483, 2018, 3rd European Advanced Accelerator Concepts workshop (EAAC2017). doi:10.1016/j.nima.2017.11.080

[12] Bergoz Instrumentation. https://www.bergoz.com/

[13] E. Senes *et al.*, "Recent AWAKE Diagnostics Development and Operational Results," no. 13, pp. 343–346, 2022. doi:10.18429/JACoW-IPAC2022-MOPOPT042

[14] Z. Zhang, "A flexible new technique for camera calibration," *IEEE Trans. Pattern Anal. Mach. Intell.*, vol. 22, no. 11, pp. 1330–1334, 2000. doi:10.1109/34.888718

[15] G. Bradski, "The openCV library," *Dr. Dobb's Journal: Software Tools for the Professional Programmer*, vol. 25, no. 11, pp. 120–123, 2000.

[16] P. Ram and S. Padmavathi, "Analysis of harris corner detection for color images," in *2016 International Conference on Signal Processing, Communication, Power and Embedded System (SCOPES)*, 2016, pp. 405–410. doi:10.1109/SCOPES.2016.7955862

ISBN: 978-3-95450-236-3 ISSN: 2673-5350 doi:10.18429/JACoW-IBIC2023-TUP026

BUNCH COMPRESSOR MONITORS FOR THE CHARACTERIZATION OF THE ELECTRON BUNCH LENGTH IN A LINAC-DRIVEN FEL

G. L. Orlandi*
Paul Scherrer Institut, Villigen, Switzerland

Abstract

The lasing performance of a Free Electron Laser (FEL) strongly relies on a precise characterization of the electron bunch length and on the control and stabilization of the bunch compression settings of the machine under normal user operations. In a FEL driver linac, the so-called Bunch Compressor Monitors (BCMs) normally ensure the non-invasive monitoring of the electron bunch length. BCMs, being sensitive to the temporal coherent threshold of the radiation energy emitted by the electron beam crossing the last dipole of a magnetic chicane or a holed diffraction screen just downstream, can provide a bunch length dependent signal resulting from the integration of the detected radiation pulse energy over the acceptance frequency band of the detector. Thanks to the non-invasiveness, BCMs are primary diagnostics in a FEL to stabilize the bunch compression by feeding back the RF settings of the accelerating structure. In this contribution, we present a formal method to determine an absolute measurement of the electron bunch length from the analysis of a BCM signal.

INTRODUCTION

The lasing performance of a linac driven x-ray Free Electron Laser (FEL) strongly depends on the beam quality and capability to preserve it all along the entire acceleration and compression stages of the electron beam. Electron beams with a small emittance and a smooth longitudinal profile are typically generated in a FEL by photocathode guns. In order to counteract the effects of beam emittance dilution due space charge at the early stage of the acceleration, relatively long bunch lengths are generated at the cathode. Hence the necessity to longitudinally compress the electron bunch-length at higher energy stages of the acceleration. Besides a characterization and optimization of the beam emittance, the machine set up for FEL users' operations requires an optimization of the compression scheme by means of precise measurements of the electron bunch length that represents the upper limit for the laser pulse duration. In a linac driven FEL, absolute and precise measurements of the electron bunch length are normally carried out by means of rf Transverse Deflecting Structures (TDSs). The rf field resonating in a TDS structure induces a chirp of the transverse momentum of the electrons in the bunch vs the electron arrival time. The imaging and the analysis of the spatial trace produced by the electron beam impinging on a downstream view-screen permits to estimate the electron bunch length provided that a calibration of the image centroid vs TDS phase is known [1–5]. Main drawback of a TDS based measurement of the electron bunch length is the fully beam invasiveness as well as possible machine protection issues due to beam losses. After the initial machine set-up, the monitoring of the electron bunch-length during FEL users' operations is normally ensured by Bunch Compressor Monitors (BCMs) [6–13] also called Bunch Length Monitors. In a linac-driven FEL, a BCM is normally designed to detect the synchrotron radiation (SR) emitted by the electron beam while crossing the fourth dipole of a magnetic chicane or the diffraction radiation produced by the electron beam passing through a holed diffraction screen placed just downstream of the magnetic chicane. The wavelength acceptance of a BCM detector is designed to match with the temporal coherent enhancement of the radiation spectral energy emitted by the electron beam at the given compression stage. BCMs in a linac-driven FEL such as, for instance, SwissFEL [14, 15] are typically designed not to perform a spectral reconstruction of the detected radiation energy distribution by means of a spectrometer. Main goal of a BCM is to provide - in a real-time - a bunch-length dependent signal to the machine compression feedback rather than an off-line reconstruction of the absolute value of the electron bunch length from a cumbersome analysis of a spectrogram. In most of the cases, the BCM output signal is hence the result of the integration of the detected radiation energy over the full acceptance wavelength band of the detector. The bunch-length dependent output signal of a BCM can be so fruitfully exploited for a fully non-invasive and shot-sequential monitoring of the electron beam during a FEL users' session and for a stabilization of the bunch compression by means of a feedback loop of the rf parameters (field phase and amplitude) of the accelerating structures.

In the present work, we will present a formal method of analysis of the BCM signals that permits an absolute determination of the electron bunch length. The implementation of the aforementioned formal method will be presented for two different scenarios: the simple case of a BCM equipped with a single detector; the more advanced case of a BCM equipped with two detectors with a different wavelength band of acceptance which are simultaneously illuminated by the same light pulse emitted by the electron beam thanks to a beam splitter and a suitable optics. In the case of a BCM with a single detector, the presented method permits to track the relative variation of the electron bunch length with respect to a reference value - either the mean value over a sequence of data acquisition or the shot-sequential value - as a function of the corresponding statistical fluctuations of the measured relative variations of the beam charge and BCM signal. In the case of a BCM equipped with two independent detectors having a different acceptance wavelength

* gianluca.orlandi@psi.ch

Content from this work may be used under the terms of the CC-BY-4.0 licence (© 2023). Any distribution of this work must maintain attribution to the author(s), title of the work, publisher, and DOI

ISBN: 978-3-95450-236-3 ISSN: 2673-5350 doi:10.18429/JACoW-IBIC2023-TUP026

band, the proposed method permits an absolute determination of the electron bunch length from a suitable analysis of the relative statistical fluctuations of the signals of the two BCM detectors and of the charge signal readout. For a complete overview of the mathematical derivation of the method and of the numerical simulations of the expected performances, the reader is addressed to the pre-print [16]. In the present proceedings, the relevant aspects of the formal derivation of the method will be outlined as well as the beneficial applications to the beam diagnostics of a linac-driven FEL.

THE EXPERIMENTAL SET-UP

In order to insert into a realistic framework the analysis method of the BCM output signals for the absolute determination of the electron bunch length, we will refer to the case of SwissFEL where three BCMs are presently in operation.

SwissFEL is a x-ray linac-driven Free Electron Laser (FEL) facility [14, 15] in operation since 2019 at Paul Scherrer Institut (www.psi.ch). Driven by a S-band injector and a C-band booster covering the beam energy range 2.1 – 5.8 GeV, SwissFEL is designed to provide tunable and coherent light pulses in the wavelength region 7 – 0.7 and 0.7 – 0.1 nm in two distinct machine branches: the hard x-ray beam line ARAMIS and the soft x-ray beam line ATHOS. An S-band photocathode simultaneously illuminated by two UV lasers emits - at a repetition rate of 100 Hz - electron bunches with a duration of about 3 ps (rms) according to a 28 ns long two-bunch macrostructure. Before being split apart in two distinct machine brunches, the two bunches of the electron macrostructure experiences a longitudinal compression in two magnetic chicanes [10, 11, 17–20]. In the first magnetic chicane (BC1), the compression is operated by means of an off-crest rf acceleration of the beam in the S-band injector and a X-band linearization of the beam energy chirp. After the first magnetic chicane, a suitable off-crest setting of the rf phases of the Linac-1 of the booster provides the further energy chirping to the electron beam before entering the second magnetic chicane (BC2). For the two nominal operation modes of SwissFEL (200 and 10 pC), a longitudinal compression of the electron beam by a factor 150 and 300 up to 20 and 3 fs (rms) can be achieved, respectively. After each compression stage, the electron bunch length and the horizontal slice emittance can be characterized by means of two rf Transverse-Deflecting-Structures (TDS): a S-band and a C-band structure, respectively. Recently an after-burning X-band TDS - the so called POLARIX [21] - is in operation just downstream of the ATHOS undulator beam line. For the 10 pC operation mode, a further bunch compression up to the sub-fs level can be operated in the magnetic chicane (ECOL) of the ARAMIS energy collimator. The two main magnetic chicanes (BC1 and BC2) of SwissFEL as well as the magnetic chicane of the ARAMIS energy collimator (ECOL) are equipped with BCMs. Both the BC1-BCM and ECOL-BCM collect the Edge-SR emitted by the electron beam while crossing the front edge of the fourth dipole of the magnetic chicane; for the BC2-BCM a diffraction radiation screen placed just downstream of the second magnetic chicane constitutes the radiation source. The BC1-BCM, being designed for monitoring electron bunches in the range 220 – 290 fs (rms), is equipped with two independent Schottky diodes which are sensitive up to more than 2 THz. The two Schottky diodes are simultaneously illuminated by the same radiation pulse which two beam splitter in cascade split off into two optical paths. Two different THz high-pass filters with a low frequency cut-off of 0.3 and 0.6 THz (so-called "thick grid" type) define the low frequency limits of the radiation spectral energy collected by the two detectors of the BC1-BCM. The BC2-BCM detector is a Mercury-Cadmium-Telluride (MCT) covering the wavelength range 2 – 12 μm to monitor 3 – 25 fs (rms) bunch-lengths. In the ECOL-BC1 a calcium fluoride (CaF_2) beam splitter permits to illuminate simultaneously a pyrodetector and an optical fiber spectrometer covering the wavelength bands 0.9 – 4.0 and 0.9 – 2.5 μm, respectively.

THE METHOD

The formal expression of the temporal coherent component of the spectral distribution of the radiation energy emitted per unit of angular frequency $\omega = 2\pi\nu$ by a bunch of N electrons while crossing the dipolar field of the bending magnet of a chicane or the hole of a diffraction radiation screen reads:

$$\frac{dI^{Ne}(\omega)}{d\omega} \simeq N(N-1)F(\omega)\frac{dI^{e}(\omega)}{d\omega} \simeq N^2F(\omega)\frac{dI^{e}(\omega)}{d\omega}, \quad (1)$$

where $\frac{dI^e(\omega)}{d\omega}$ is the radiation energy spectrum of the single particle and $F(\omega)$ is the longitudinal form factor (FF) of the electron beam [22, 23]. In the formula above, we implicitly assume that the integration over the acceptance solid angle of the detector has been performed as well as that beam transverse size effects on the FF can be neglected because of the highly collimation features of the electron beam as normally occurring in a linac-driven FEL. The FF is defined as the square module of the Fourier transform of the density distribution of the N electron coordinates along the longitudinal direction. For a Gaussian beam with a length σ, it reads:

$$F(\omega) = \left|\int_{-\infty}^{+\infty} e^{j\omega z/c}\rho_z(z)dz\right|^2 = e^{-(\frac{\omega\sigma}{c})^2}. \quad (2)$$

The method of analysis of the BCM signal we are going to introduce is based on a formalism that expresses the shot-sequential relative variation of the BCM ouput signal - for instance, with respect to the mean value over a sequence of BCM signal acquisitions under a steady state regime of the machine - as a function of the corresponding relative variations of the electron bunch length σ and of the beam charge N. Because of the formal dependence on the shot-to-shot relative variations of bunch-dependent quantities (σ and N), the proposed method - as clearer hereinafter - is weakly dependent on bunch-independent features such as the spectral

Content from this work may be used under the terms of the CC-BY-4.0 licence (© 2023). Any distribution of this work must maintain attribution to the author(s), title of the work, publisher, and DOI

ISBN: 978-3-95450-236-3 ISSN: 2673-5350 doi:10.18429/JACoW-IBIC2023-TUP026

distribution of the single particle spectrum that, for a given wavelength band of the BCM, does not change from a rf shot to another. Consequently, for the further formal developments, we will refer to the normalized expression of Eq. (1) with respect to the single particle spectrum $\frac{dI^e(\omega)}{d\omega}$. Such a normalization procedure of Eq. (1) appears even more reasonable and feasible considering that, in many experimental contexts, the single particle radiation energy spectrum is weakly dependent or even independent of the angular frequency in the given wavelength band of acceptance of the BCM detector. For instance, this is the case of the single particle spectrum of the Edge-SR in the long wavelength regime [24, 25] which can be reasonably applied to two of the three BCMs of SwissFEL.

Upon normalizing Eq. (1) with respect to the single particle spectrum $\frac{dI^e(\omega)}{d\omega}$ and performing the integration of the two sides of the resulting "normalized" expression of Eq. (1) with respect to the frequency band of acceptance of the BCM detector $\Delta\omega = (\omega_{max} - \omega_{min})$, the "normalized" output signal of the BCM reads

$$I = \int_{\omega_{min}}^{\omega_{max}} d\omega \left(\frac{dI^{Ne}(\omega)}{d\omega} / \frac{dI^e(\omega)}{d\omega} \right). \tag{3}$$

Finally, upon applying the natural logarithm to the two sides of Eq. (3)

$$\ln(I) = 2\ln(N) + \ln(\int_{\omega_{min}}^{\omega_{max}} d\omega F(\omega)), \tag{4}$$

the shot-sequential relative variation of the BCM signal $\frac{\Delta I}{I} = \frac{I^* - I}{I}$ due to the corresponding differential relative variations of the bunch charge $\frac{\Delta N}{N} = \frac{N^* - N}{N}$ and of the form factor $\frac{\Delta F}{F} = \frac{F^* - F}{F}$ - the latter one due to a relative fluctuation of the bunch length $\frac{\Delta\sigma}{\sigma} = \frac{\sigma^* - \sigma}{\sigma}$ - reads

$$\frac{\Delta I}{I} = 2\frac{\Delta N}{N} + \frac{\int_{\omega_{min}}^{\omega_{max}} d\omega [F^*(\omega) - F(\omega)]}{\int_{\omega_{min}}^{\omega_{max}} d\omega F(\omega)}. \tag{5}$$

In previous equation, according to a Taylor series expansion at the first order in $\frac{\Delta\sigma}{\sigma}$, the FF variation in the integrand of Eq. (5) can be explicitly expressed as [26]

$$F^*(\omega) - F(\omega) = e^{-(\frac{\omega\sigma}{c})^2(1+\frac{\Delta\sigma}{\sigma})^2} - e^{-(\frac{\omega\sigma}{c})^2} \simeq$$
$$\simeq -2\frac{\Delta\sigma}{\sigma}\left(\frac{\omega\sigma}{c}\right)^2 e^{-(\frac{\omega\sigma}{c})^2} = -2\frac{\Delta\sigma}{\sigma}\left(\frac{\omega\sigma}{c}\right)^2 F(\omega). \tag{6}$$

Upon replacing in the integrand of Eq. (5) the above Taylor series approximation of the FF difference and explicitly calculating the integral over the frequency band of acceptance of the detector $\Delta\omega = (\omega_{max} - \omega_{min})$, the shot-sequential relative variation of the BCM signal can be expressed as a function of the related beam-synchronous relative variations of the bunch charge and length by means of the following equation:

$$\frac{\Delta I}{I} = 2\frac{\Delta N}{N} + \frac{\Delta\sigma}{\sigma} G(\sigma, \Delta\omega), \tag{7}$$

where

$$G(\sigma, \Delta\omega) = \left\{ \frac{2\sigma}{\sqrt{\pi}c} \frac{\left[e^{-(\frac{\omega\sigma}{c})^2}\omega\right]_{\omega_{min}}^{\omega_{max}}}{\left[erf(\omega\sigma/c)\right]_{\omega_{min}}^{\omega_{max}}} - 1 \right\} \tag{8}$$

with $erf(x)$ indicating the error function [27]. More information on the above obtained results in [16]. The relative variations of the physical quantities indicated in Eqs. (7) and (8) can be intended either as the shot-sequential evolution from a given machine shot to the subsequent one or, under conditions of steady state machine operations, as the relative statistical fluctuations of such quantities with respect to the corresponding mean values over a beam-synchronous sequence of acquired data. According to the formula in Eqs. (7) and (8), the shot-sequential relative variation of the electron bunch length $\frac{\Delta\sigma}{\sigma}$ can be tracked as a function of the corresponding relative variations of the measured BCM output signal $\frac{\Delta I}{I}$ and of the bunch charge $\frac{\Delta N}{N}$ provided that a calibration of the BCM signal can be performed with an absolute measurement of the bunch length σ, for instance, by means of a Transverse Deflecting Strucure (TDS) [1–5].

In the particular case of a BCM equipped with two independent detectors simultaneously collecting in two different frequency bands $\Delta\omega_i = (\omega_{max}^i - \omega_{min}^i)$ - with $i = 1, 2$ - the coherent radiation light pulse split off by a beam splitter into two distinct optical paths, the formula in Eqs. (7) and (8) applied to each of the two detector signals $\left(\frac{\Delta I}{I}\right)_i$ - with $i = 1, 2$ - allows for an absolute determination of the electron bunch length σ by means of the following equation:

$$\left[\left(\frac{\Delta I}{I}\right)_2 - 2\frac{\Delta N}{N}\right] = \frac{G(\sigma, (\Delta\omega)_2)}{[G(\sigma, (\Delta\omega)_2) - G(\sigma, (\Delta\omega)_1)]} \times$$
$$\times \left[\left(\frac{\Delta I}{I}\right)_2 - \left(\frac{\Delta I}{I}\right)_1\right]. \tag{9}$$

For more details on the formal derivation of the Eq. (9) and how this formula can be practically handled to determine the absolute value of the electron bunch length σ from the analysis of the beam-synchronously acquired sequences of a two-detector BCM signals I_i - with $i = 1, 2$ - and of the beam charge readouts N, the reader is addressed to [16]. In this bibliographic reference, the complete derivation of the formal results is supported by numerical simulations for a benchmark of the predictions of the obtained formulae.

CONCLUSIONS AND OUTLOOK

A fully non-invasive monitoring of the bunch length in a linac-driven Free Electron Laser (FEL) is normally performed by a Bunch Compressor Monitor. The BCM input signal is the radiation emitted by the electron beam when experiencing a longitudinal compression, i.e., while crossing the last bending dipole of a magnetic chicane or the holed screen of a diffraction radiator placed just downstream of it. The BCM sensitivity to the electron bunch length is as higher as better is the matching of the acceptance wavelength band of the detector with the threshold of the temporal coherent

Content from this work may be used under the terms of the CC-BY-4.0 licence (© 2023). Any distribution of this work must maintain attribution to the author(s), title of the work, publisher, and DOI

ISBN: 978-3-95450-236-3 ISSN: 2673-5350 doi:10.18429/JACoW-IBIC2023-TUP026

Content from this work may be used under the terms of the CC-BY-4.0 licence (© 2023). Any distribution of this work must maintain attribution to the author(s), title of the work, publisher, and DOI

enhancement of the radiation spectral energy emitted by the electron beam. Most of the BCMs in operation in a FEL are equipped not with a spectrometer for the off-line reconstruction of the temporal coherent enhancement of the radiation energy spectrum but with a broad band detector providing a real-time output signal that is the result of the full integration of the collected radiation energy over the wavelength band of acceptance of the detector itself. Therefore, the output signal of a BCM does not provide an absolute estimate of the electron bunch length but a charge and bunch-length dependent signal. Nevertheless, thanks to the non-invasiveness, the BCM output signal can be fruitful exploited to stabilize the bunch compression in a linac by feeding back phases and amplitudes of the rf accelerating structures. With reference to the formal results and numerical simulations reported in [16], in this conference proceedings we presented a mathematical method that permits to decouple in the BCM output signal the independent contribution of the bunch length and charge. In the case of a BCM equipped with a single detector, under conditions of a steady state machine operations and provided that the BCM signal has been previously calibrated by means of an absolute measurement of the bunch length, the proposed method permits to track the shot-sequential relative variation of the electron bunch length as a function of the corresponding beam-synchronously acquired relative variations of the BCM output signal and of the charge signal. Moreover, in the case of a BCM equipped with two independent detectors with different wavelength bands of acceptance, which are simultaneously illuminated by the same radiation pulse split off into two distinct optical paths by a beam splitter, the proposed method permits an absolute determination of the electron bunch length by means of a suitable analysis of the two-detector BCM signals and of the charge signal. Perspectives and potentialities of the proposed mathematical method of analysis of the BCM signal appear clear. Thanks to the proposed method, the compression feedback loop of the linac can be fed with a post-processed BCM signal that is not a simply bunch-dependent signal but is itself an absolute measurement of the electron bunch length. Moreover, in CW superconducting linac-driven FEL, where the non-invasiveness is a mandatory feature for most of the electron beam diagnostics, the implementation of the proposed method allows for a fully non-invasive, shot-sequential and absolute determination of the electron bunch-length.

REFERENCES

[1] P. Emma, J. Frisch, and P. Krejcik, "A Transverse RF Deflecting Structure for Bunch Length and Phase Space Diagnostics", SLAC, Stanford, USA, Rep. LCLS-TN-00-12, 2000.

[2] P. Krejcik, R. Akre, L. Bentson, and P. Emma, "A Transverse RF Deflecting Structure for Bunch Length and Phase Space Diagnostics", in *Proc. PAC'01*, Chicago, IL, USA, Jun. 2001, paper WPAH116, pp. 2353–2355.

[3] D. Alesini *et al.*, "RF deflector design and measurements for the longitudinal and transverse phase space characterization at SPARC", *Nucl. Instrum. Methods Phys. Res., Sect. A*, vol. 568, pp. 488-502, Dec. 2006.

[4] M. Röhrs *et al.*, "Time-resolved electron beam phase space tomography at a soft x-ray free-electron laser", *Phys. Rev. ST Accel. Beams*, vol. 12, p. 050704, May 2009. doi:10.1103/PhysRevSTAB.12.050704

[5] P. Craievich, R. Ischebeck, F. Loehl, G. L. Orlandi, and E. Prat, "Transverse Deflecting Structures for Bunch Length and Slice Emittance Measurements on SwissFEL", in *Proc. FEL'13*, New York, NY, USA, Aug. 2013, paper TUPSO14, pp. 236–241.

[6] O. Grimm, S. Casalbuoni, L. Fröhlich, O. Peters, and J. Rossbach, "The Synchrotron Radiation Beamline at TTF2", in *Proc. EPAC'04*, Lucerne, Switzerland, Jul. 2004, paper THPLT046, pp. 2586–2588.

[7] J. Wu, P. Emma, and Z. Huang, "Coherent Synchrotron Radiation as a Diagnostic Tool for the LCLS Longitudinal Feedback System", in *Proc. PAC'05*, Knoxville, TN, USA, May 2005, paper TOAC005, pp. 428–435.

[8] J. Wu and P. Emma, "Linac Coherent Light Source (LCLS) Bunch-Length Monitor Using Coherent Radiation", in *Proc. LINAC'06*, Knoxville, TN, USA, Aug. 2006, paper TUP015, pp. 277–239.

[9] H. Loos, T. Borden, P. Emma, J. C. Frisch, and J. Wu, "Relative Bunch Length Monitor for the Linac Coherent Light Source (LCLS) using Coherent Edge Radiation", in *Proc. PAC'07*, Albuquerque, NM, USA, Jun. 2007, paper FRPMS071, pp. 4189–4191.

[10] F. Frei *et al.*, "Development of Electron Bunch Compression Monitors for SwissFEL", in *Proc. IBIC'13*, Oxford, UK, Sep. 2013, paper WEPC36, pp. 769–771.

[11] F. Frei and R. Ischebeck, "Electron Bunch Compression Monitors for Short Bunches - Commissioning Results from SwissFEL", in *Proc. IBIC'19*, Malmö, Sweden, Sep. 2019, pp. 578–581. doi:10.18429/JACoW-IBIC2019-WEPP026

[12] N. M. Lockmann, C. Gerth, B. Schmidt, and S. Wesch, "Non-invasive THz spectroscopy for bunch current profile reconstructions at MHz repetition rates", in *Phys. Rev. Accel. Beams*, vol. 23, 2020. doi:10.1103/PhysRevAccelBeams.23.112801

[13] C. Gerth and N. M. Lockmann, "Bunch Compression Monitor Based on Coherent Diffraction Radiation at European XFEL and FLASH", in *Proc. IBIC'21*, Pohang, Korea, Sep. 2021, pp. 400–403. doi:10.18429/JACoW-IBIC2021-WEPP14

[14] "SwissFEL Conceptual Design Report", PSI, Villgen, Switzerland, Rep. PSI Bericht Nr. 10-04, Apr. 2012.

[15] T. Schietinger *et al.*, "Commissioning experience and beam physics measurements at the SwissFEL Injector Test Facility", in *Phys. Rev. Accel. Beams*, vol. 19, 2016. doi:10.1103/PhysRevAccelBeams.19.100702

[16] G.L. Orlandi, "Absolute and non-invasive determination of the electron bunch length in a Free Electron Laser using a Bunch Compressor Monitor", 2023. doi:10.48550/arXiv.2305.17042 doi:10.21203/rs.3.rs-3228455/v1

[17] G. L. Orlandi *et al.*, "Bunch-Compressor Transverse Profile Monitors of the SwissFEL Injector Test Facility", in *Proc. IBIC'12*, Tsukuba, Japan, Oct. 2012, paper MOPB82, pp. 271–275.

ISBN: 978-3-95450-236-3 ISSN: 2673-5350 doi:10.18429/JACoW-IBIC2023-TUP026

[18] G. L. Orlandi *et al.*, "Characterization of Compressed Bunches in the SwissFEL Injector Test Facility", in *Proc. IBIC'13*, Oxford, UK, Sep. 2013, paper TUPF08, pp. 515–518.

[19] B. Keil *et al.*, "Status of The SwissFEL BPM System", in *Proc. IBIC'15*, Melbourne, Australia, Sep. 2015, pp. 497–501. doi:10.18429/JACoW-IBIC2015-TUPB065

[20] G. L. Orlandi, R. Xue, *et al.*, "Bunch length and energy measurements in the bunch compressor of a free-electron laser", in *Phys. Rev. Accel. Beams*, vol. 22, 2019. doi:10.1103/PhysRevAccelBeams.22.072803

[21] E. Prat, A. Malyzhenkov, and P. Craievich, "Sub-femtosecond time-resolved measurements of electron bunches with a C-band radio-frequency deflector in x-ray free-electron lasers", in *Rev. Sci. Instrum.*, vol. 94, 2023. doi:10.1063/5.0144876

[22] J. S. Nodvick and D. S. Saxon, "Suppression of Coherent Radiation by Electrons in a Synchrotron", *Phys. Rev.*, vol. 96, pp. 180–184, 1954. doi:10.1103/PhysRev.96.180

[23] C. J. Hirschmugl, M. Sagurton, and G. P. Williams, "Multiparticle coherence calculations for synchrotron-radiation emission", *Phys. Rev. A*, vol. 44, pp. 1316–1320, 1991. doi:10.1103/PhysRevA.44.1316

[24] R.A. Bosch, "Edge radiation in an electron storage ring", *Il Nuovo Cimento D*, vol. 20, pp. 483–493, 1998. doi:10.1007/BF03185543

[25] R. A. Bosch, "Extraction of edge radiation within a straight section of Aladdin", *Rev. Sci. Instrum.*, vol. 73, pp. 1423–1426, 2002. doi:10.1063/1.1435813

[26] G.L. Orlandi, "Misura della lunghezza del pacchetto di elettroni dell'acceleratore lineare superconduttivo TTF (tesla test facility) con la radiazione di transizione e di diffrazione", Tesi di dottorato XII ciclo, TDR 2000 000337, Biblioteca Nazionale Centrale di Firenze, 2000. https://opac.bncf.firenze.sbn.it/bncf-prod/resource?uri=TSI0000337&v=l&dcnr=0

[27] I.S. Gradshteyn and I.M. Ryzhik, *Table of Integrals, Series, and Products*, Ed. 5, A. Jeffrey Editor, Academic Press, 1994.

Content from this work may be used under the terms of the CC-BY-4.0 licence (© 2023). Any distribution of this work must maintain attribution to the author(s), title of the work, publisher, and DOI

ISBN: 978-3-95450-236-3 ISSN: 2673-5350 doi:10.18429/JACoW-IBIC2023-TUP027

MICROBUNCHING OF THERMIONIC CATHODE RF GUN BEAMS IN THE ADVANCED PHOTON SOURCE S-BAND LINAC *

J. Dooling†, A. Brill, N. Kuklev, I. Lobach, A. Lumpkin, N. Sereno, Y. Sun
Argonne National Laboratory, Lemont, IL, USA

Abstract

We report on measurements of beams from thermionic cathode (TC) rf guns in the Advanced Photon Source S-Band Linac. These measurements include the macropulse out of both new and existing TC guns as well as the observation of microbunching within the micropulses of these beams. A gun chopper limits the macropulse FWHM duration to the 10 ns range. Our objectives were to analyse the new TC gun and investigate microbunching within a TC-rf-gun-generated beam. Our diagnostics elucidated longitudinal beam structures from the ns to the fs time scales. Coherent transition radiation (CTR) interferometers responding to far-infrared wavelengths were employed after each compression stage to provide the autocorrelations of the sub-ps micropulse durations. The first compression stage is an alpha magnet and the second a chicane. A CCD camera was used to image the beam via optical transition radiation from an Al screen at the end of the linac and also employed to measure coherent optical transition radiation (COTR) in the visible range. The COTR diagnostic observations, implying microbunching on a fs time scale, are presented and compared with a longitudinal space-charge impedance model.

INTRODUCTION

The injection system of the Advanced Photon Source (APS) has relied on thermionic cathode (TC) rf guns as electron-beam sources since 2001 [1]. This will continue to be the case for the APS Upgrade with the multi-bend achromatic magnet lattice installation in the 6 GeV storage ring currently in progress [2]. There are two such S-Band TC rf guns installed in the linac so that one is a "hot" spare. We report the basic testing of the beams from new generation TC rf guns manufactured by RadiaBeam Technologies (RBT) [3] in terms of the ≈10 ns long macropulse composed of micropulses with an S-Band repetition frequency (2856 MHz). We obtained basic macropulse data for a newly installed RBT gun to comparison with one of a set of three TC rf guns purchased from AET Associates (AET) in 2001. The AET guns have been the primary electron source for the APS since that time.

Our interest was to measure the charge of each micropulse within the macropulse structure from the chopper-gated [4], TC-rf gun [5–7]. The extraction of charge from the TC rf gun involves high-power rf applied to the cathode; thus, the extracted charge comes in a series of micropulses. With the macropulse temporal distribution, we can then determine the charge per micropulse. Only the AET gun was employed for the bunch compression experiment discussed below.

In the APS linac, the micropulse duration after the alpha magnet is sub-ps. After further compression in the chicane, longitudinal space charge (LSC) induced microbunching within the micropulses generates coherent optical transition radiation (COTR) when striking the downstream intercepting Al screen. The COTR (visible wavelengths, fs temporal scale) was transported out of the tunnel to a CCD camera, and the images were recorded. We present a comparison of the observed COTR enhancements with the predictions of a LSC-impedance model.

EXPERIMENTAL DESCRIPTION

A schematic of the linac with components relevant for the present discussion is presented in Fig. 1. Compression is provided by the alpha magnet at the end of the gun beam line and the L3 chicane after the first four accelerating structures in L2. Coherent Transition Radiation far-infrared (CTR FIR) interferometers, positioned in the L2 section (L2:CTR) and after the chicance (L3:CTR), provide longitudinal pulse length data [8]. Average current is monitored immediately after the gun and macropulse charge is measured after the alpha magnet in the linac beamline. Optical transition radiation (OTR) and COTR are generated by an Al screen (S5:OTR, as shown in Fig. 1) when struck by the electron beam. An optical transport line guides the light to a camera system outside of the tunnel.

A block diagram of the macropulse duration measurement is presented in Fig. 2. Raw beam signals from the four button pickups are input to 20 dB directional couplers (Mini-Circuits ZGDC20-33HP+). The coupled signals ("c") are combined to form the sum output (Mini-Circuits ZN4PD-642W-S+) which is fed into one channel of a fast oscilloscope with 50 Ω input impedance. The main, uncoupled signals continue on to the analog conditioning electronics associated with the rest of the S-band linac BPMs [9–11]. Because of capacitive coupling, the DC component of the macropulse is not present. Alternatively, the summing unit can be bypassed to provide coupled input to the oscilloscope from all four of the BPM channels. Four channel input allows for observation of beam position within the macropulse. The BPM rf signals are digitally undersampled by the oscilloscope's analog-to-digital converter following the discussion in Ref. [12].

A new 1.5-cell, TC rf gun developed by RBT was installed at the RG1 location in the linac during the December 2022-January 2023 APS maintenance period. We wished to measure the macropulse waveform of this gun to compare with that of the operating TC gun. Further tests with the RBT

* Work supported by the U.S. D.O.E., Office of Science, Office of Basic Energy Sciences, under contract number DE-AC02- 06CH11357.
† dooling@aps.anl.gov

Content from this work may be used under the terms of the CC-BY-4.0 licence (© 2023). Any distribution of this work must maintain attribution to the author(s), title of the work, publisher, and DOI

ISBN: 978-3-95450-236-3 ISSN: 2673-5350 doi:10.18429/JACoW-IBIC2023-TUP027

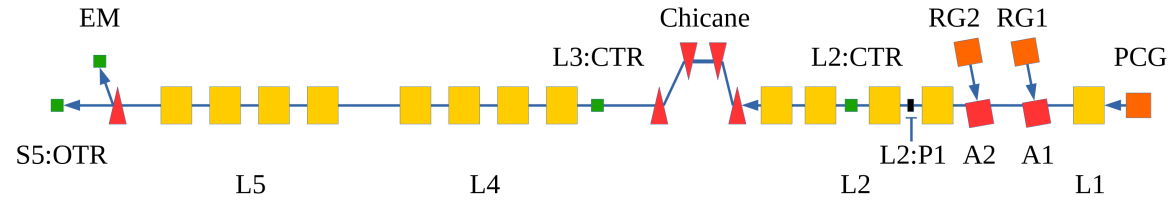


Figure 1: Linac schematic. The main accelerating sections are designated LX where X=1,2,4, and 5. Sections 2, 4, and 5 each have four 3-m SLEDed S-band accelerating structures. A1 and A2 are the alpha magnets associated with two TC rf gun beamlines RG1 and RG2. L2:P1 represents the BPM location for the macropulse measurements. L*:CM are current/charge monitors, ES is a spectrometer, triangles represent dipole magnets, and OTR images are collected at the S5:OTR station.

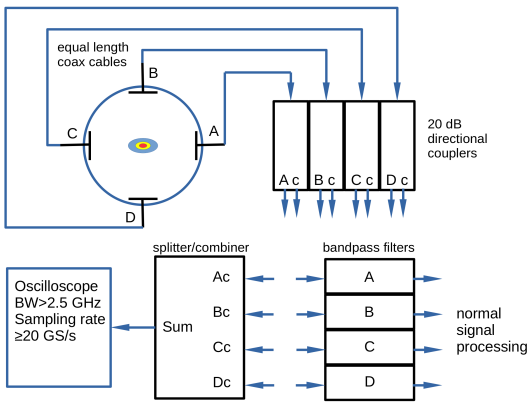


Figure 2: Macropulse measurement schematic.

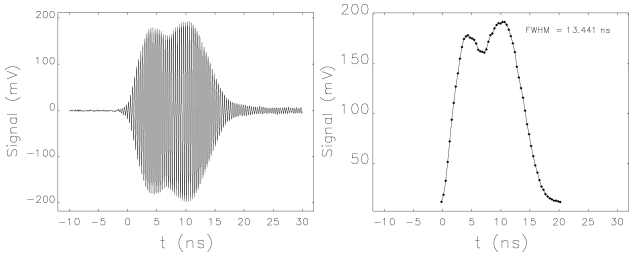


Figure 3: Left: Raw macropulse signal from the AET RG2 gun. Right: Peak detect envelope of the same signal.

gun will be conducted once accelerator operations resume in Fall 2023. Only the AET gun, installed in the RG2 location, was used in the bunch compression experiment discussed below.

MACROPULSE WAVEFORMS

An example of a raw macropulse waveform from one of the AET guns is plotted in Fig. 3, left. Figure 3, right shows the same signal after peak-detection processing to yield the envelope. This AET gun is located in the RG2 station; this is the gun beamline closest to the entrance of the linac known as the L2 section. A sampling rate, f_s of 20 GS/s provides 7 samples per fundamental rf period (350 ps) and yields a relatively smooth envelope after peak detection.

Macropulse data acquired for one of the new RadiaBeam guns is presented in Fig. 4. In this case, the gun is located in the RG1 station, approximately 3 m further from the L2

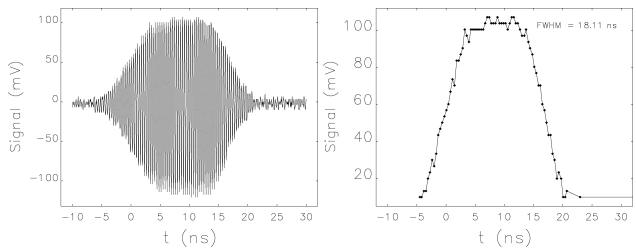


Figure 4: Left: Raw macropulse signal from the RG1 RadiaBeam gun. Right: Peak detect envelope of the same signal.

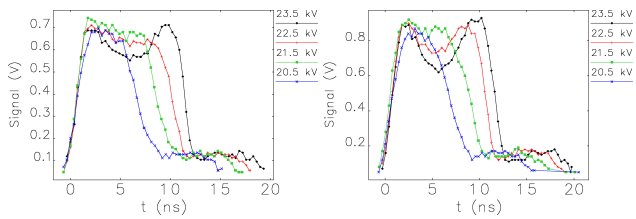


Figure 5: Macropulse envelope waveforms from the RG2 AET gun with varying chopper voltages for 190 mA (left) and 300 mA (right).

linac section than the RG2 gun. Transmission losses RG1 are typically higher than for RG2. Each station has its own chopper system; in the case of RG1 the chopper pulse is longer than that for RG2.

The macropulse waveforms were also observed as the chopper voltage as well as the average gun output current were varied. Waveforms at four chopper voltages are presented in Fig. 5 left and right for gun currents of 190 and 300 mA, respectively. Cathode heater power was varied to change the average gun current for the waveforms presented in Fig. 5. At higher voltages, we observed a double peak in the macropulse envelope. In this case, the beam is swept past the slit on the rising edge of the voltage pulse and again on the falling edge. Gun chopper voltage is the method used to control the charge per macropulse in the linac while the gun cathode heater power is typically maintained at a constant value. Macropulse duration varies from approximately 7 to 11 ns for both current levels as the chopper is raised from 20.5 to 23.5 kV. Current and charge data collected from current monitors in the linac during these measurements are presented in Table 1.

Content from this work may be used under the terms of the CC-BY-4.0 licence (© 2023). Any distribution of this work must maintain attribution to the author(s), title of the work, publisher, and DOI

ISBN: 978-3-95450-236-3 ISSN: 2673-5350 doi:10.18429/JACoW-IBIC2023-TUP027

Table 1: RG2 Current and Charge Measurements

Chopper voltage (kV)	190 mA I_{CM} (mA)	190 mA Q_{CM2} (nC)	300 mA I_{CM} (mA)	300 mA Q_{CM2} (nC)
20.5	191	0.85	303	1.04
21.5	189	1.07	302	1.37
22.5	191	1.26	303	1.56
23.5	191	1.37	300	1.64

MICROPULSES AND MICROBUNCHING

The gun output current after the alpha magnet is modeled as a train of charge delta functions where each charge pulse is separated from its neighbor by one rf period. The current waveform may be expressed as,

$$I_g(t) = A(t)\delta\left(t - t_s - \frac{2\pi n}{\omega_{rf}}\right), \quad (1)$$

where $A(t)$ is the time-varying amplitude of the macropulse, t_s is time slip or jitter, δ is the delta function, and ω_{rf} is the radian frequency of RG2 rf drive power. The total charge is then determined integrating Eq. (1) over time,

$$Q = \int I_g(t)dt = \sum_n A\,(t_n) \quad (2)$$

where $t_n = t_s + 2\pi n/\omega_{rf}$. Respective calibration factors for the AET RG2 gun operating at currents of 190 mA and 300 mA are 56.33 ±0.97 pC/V and 55.36 ±1.49 pC/V; the maximum charge per micropulse at these currents are 39.99 ±0.88 pC and 49.88 ±1.66 pC.

For bunch compression studies, we are interested in the micropulse peak current. Compression studies were conducted with the RG2 AET TC gun beam. Two coherent transition radiation (CTR) interferometers are installed in the APS linac [8, 13]; one in the L2 section (L2CTR) between the second and third accelerating structures (AS), and another following the chicane in L3 (L3CTR), see Fig. 1. The four AS of L2 may be phased to chirp the pulses prior to the chicane to facilitate bunch compression. The beam energy after the L2 section was 150 MeV. The L2CTR sees the effect of the alpha magnet compression, whereas L3CTR observes compression provided by the chicane. Autocorrelations of the CTR signals at these two locations are presented in Fig. 6. Assuming a Gaussian profile for the compressed bunch, the rms bunch duration can be approximated as $\sqrt{2}\sigma_z/c$. For the autocorrelation scans shown in Fig. 6 this yields 300 fs and 130 fs from L2CTR and L3CTR, respectively. We assumed that the micropulse length is approximately constant over the macropulse duration. Using the FWHM duration, 50 pC results in a current of 170 A after the L3CTR. This current level is consistent with predictions made in Ref. [5].

During bunch-compression studies, gun output current was increased to 650 mA. Phasing the L2 AS to maximize compression, COTR was observed on the S5:OTR monitor, at an energy of 375 MeV [14]. Examples of OTR and

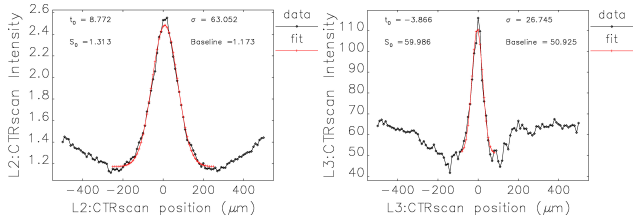


Figure 6: Autocorrelations of the coherent transition radiation signals from the L2CTR (left) and L3CTR (right) along with Gaussian fits to the central peak. RG2 (AET) source.

COTR emission are presented in Fig. 7. Emission intensity contour and profile data with L2 rf phased away from maximum compression are shown in the top row; the bottom row presents enhanced emission (COTR) at the maximum compression phase. The macropulse beam charge was monitored at L5:CM during data acquisition and was stable to less than 3 percent for both compressed and uncompressed measurements. The COTR/OTR intensity ratio is about 6.5 at the most enhanced spatial location. The two COTR-enhanced locations in the lower image (maximum compression) are approximately σ_x=380 μm by σ_y=50 μm in size. Compressed micropulse peak current was approximately 200 A.

Examining the effect of longitudinal space-charge (LSC) impedance, we plot in Fig. 8 Eq. (26) from Ref. [15] for R_{56} = 65 mm. With an rms energy spread of 2 keV, a gain of 5.7 is obtained at 800 nm. Signal intensity is proportional to the product of the COTR gain and the sensitivity of the CCD sensor integrated over the wavelength range of interest (400-1000 nm). Picking a COTR gain value in the red end of the range is meant to represent a rough estimate of the enhancement ratio. The gain is in reasonable agreement with the enhancement factor determined for the data plotted in Fig. 7. This is the first time a comparison has been done of empirical COTR gain from a TC rf gun source with an LSC impedance model.

Previous simulations of the LSC instability showed that microbunching in the visible wavelength regime can be supported if the slice energy spread of the microbunched portion of the beam is approximately 2-4 keV [16]. Using a PC rf gun source, an LCLS-I experiment generated COTR gain consistent with a slice energy spread of 3 keV. In the context of Ratner's LSC model, a 2 keV slice energy spread would be indicated to explain the observed COTR gain for the microbunched portion of the TC rf gun beam. This value is much smaller than the measured ensemble energy spread.

Broadband visible regime COTR enhancements have also recently been reported in laser-plasma-wakefield-accelerated beams [17–19], but this is a different microbunching mechanism. In this case, intense fields from a 100-TW-class drive laser interacting with the plasma electrons lead to microbunching.

SUMMARY

We described a method to measure the macropulse waveform of the APS TC rf guns. This method requires an oscillo-

Content from this work may be used under the terms of the CC-BY-4.0 licence (© 2023). Any distribution of this work must maintain attribution to the author(s), title of the work, publisher, and DOI

ISBN: 978-3-95450-236-3 ISSN: 2673-5350 doi:10.18429/JACoW-IBIC2023-TUP027

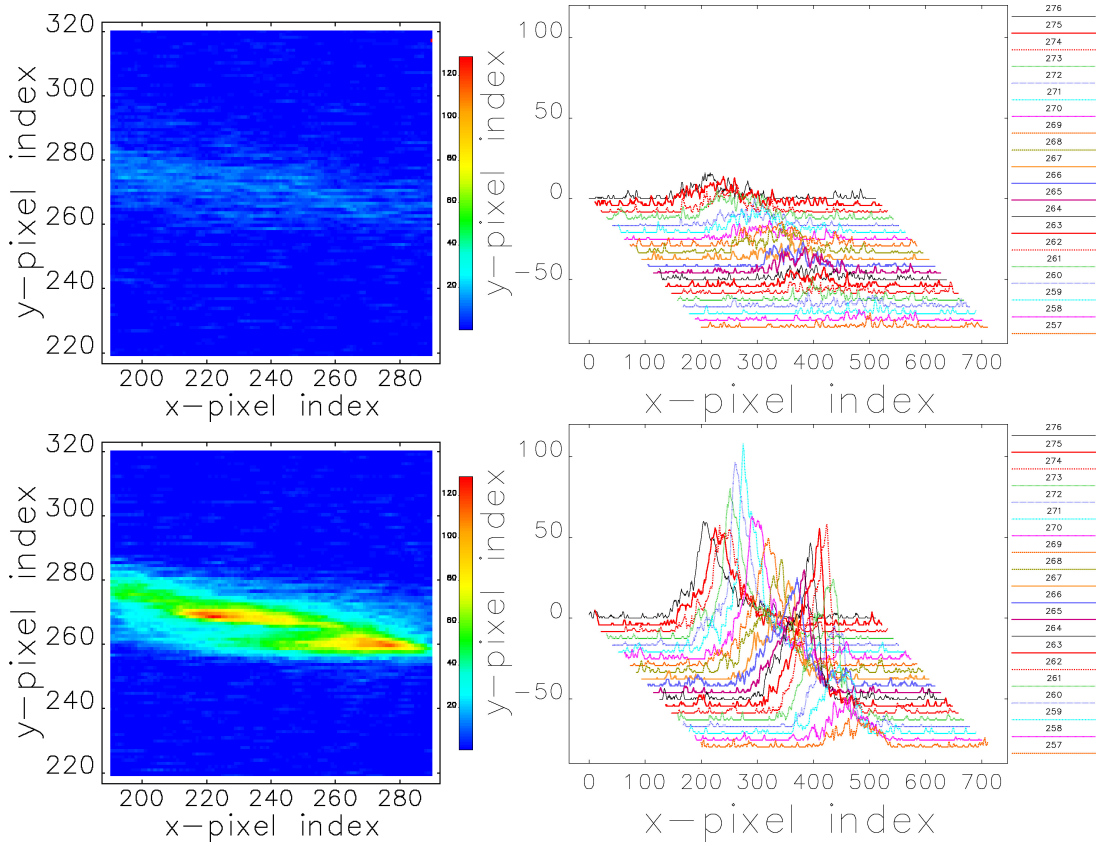


Figure 7: Top: Intensity contour plot (left) and line profiles (right) away from peak compression. Bottom: Intensity contour plot and line profiles near peak compression.

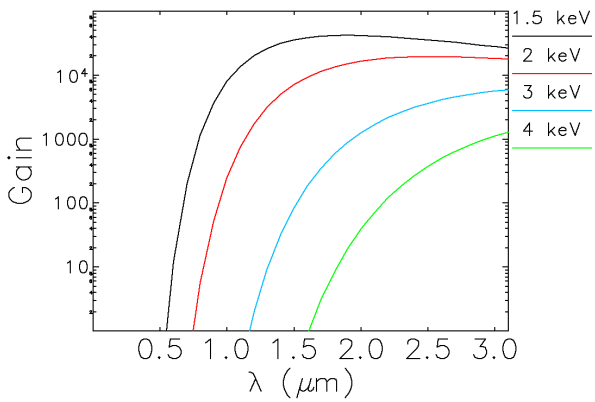


Figure 8: Microbunching gain as a function of wavelength for R_{56} = 65 mm with rms energy spread as a parameter.

scope with bandwidth and sampling rate sufficient to monitor the fundamental frequency of the rf applied to extract beam from the gun; in the present case, this requires a bandwidth > 2.5 GHz and sampling rate > 20 GS/s for 2865 MHz S-band rf. Measurement of the macropulse envelope allows for calibration of the microbunch charge and thereby calculation of peak currents after bunch compression. AET and RadiaBeam TC guns were tested and, accounting for differences in the chopper systems, behaved in a similar manner. Other methods employing diodes could be explored to eliminate the cost of an oscilloscope [20].

Additionally, we have inferred the presence of LSC-induced microbunching at visible wavelengths via the COTR mechanism from TC rf gun beams. After two stages of compression and with further acceleration to 375 MeV, an enhancement factor of 6.5 was observed in OTR near maximum compression. The enhanced emission is attributed to the generation of COTR from microbunching in the TC rf gun-generated micropulses. Analytical models indicate that a slice energy spread of only a few keV is needed for microbunching (COTR gain) at visible wavelengths where the CCD camera is sensitive. The importance of slice energy spread as it applies to a TC-rf gun-generated beam is analogous to what was reported for PC gun [16] and LPWA [17] beams. Further investigations including spectral measurements of the microbunching phenomena are warranted.

ACKNOWLEDGEMENTS

Thanks to R. Soliday and H. Shang for assistance with analysis scripts, of APS ANL.

REFERENCES

[1] K. J. Beczek, J. W. Lewellen, A. Nassiri, and E. Tanabe, “A Rationalized Approach to Thermionic RF Gun Design,”

Content from this work may be used under the terms of the CC-BY-4.0 licence (© 2023). Any distribution of this work must maintain attribution to the author(s), title of the work, publisher, and DOI

ISBN: 978-3-95450-236-3 ISSN: 2673-5350 doi:10.18429/JACoW-IBIC2023-TUP027

in *Proc. PAC'01*, Chicago, IL, USA, Jun. 2001. https://jacow.org/p01/papers/WPAH052.pdf

[2] "Advanced Photon Source Upgrade Project Final Design Report," Advanced Photon Source, Argonne National Laboratory, Tech. Rep., 2019. https://publications.anl.gov/anlpubs/2019/07/153666.pdf

[3] S. V. Kutsaev *et al.*, "A New Thermionic RF Electron Gun for Synchrotron Light Sources," in *Proc. NAPAC'16*, Chicago, IL, USA, Oct. 2016, pp. 453–456. doi:10.18429/JACoW-NAPAC2016-TUB3CO04

[4] Y. W. Kang *et al.*, "Beam Chopper for the Low-Energy Undulator Test Line (LEUTL) in the APS," in *Proc. PAC'97*, Vancouver, Canada, May 1997, pp. 2699–2701.

[5] M. Borland, "A High-Brightness Thermionic Microwave Electron Gun," Available as SLAC Report 402, Ph.D. dissertation, Stanford University, 1991. https://www.slac.stanford.edu/pubs/slacreports/reports03/slac-r-402a.pdf

[6] M. Borland, "An Improved Thermionic Microwave Gun and Emittance-Preserving Transport Line," in *Proc. PAC'93*, Washington D.C., USA, Mar. 1993, pp. 3015–3018.

[7] J. W. Lewellen *et al.*, "Operation of the APS RF Gun," in *Proc. LINAC'98*, Chicago, IL, USA, Aug. 1998, pp. 863–865. https://jacow.org/l98/papers/TH4042.pdf

[8] A. H. Lumpkin, W. J. Berg, M. Borland, J. W. Lewellen, and N. S. Sereno, "Initial CTR-Based Bunch Length Measurements of Linac Beams Following the APS Bunch Compressor," in *Proc. FEL'03*, Tsukuba, Japan Sept. 2003, pp. 2420–2422. https://jacow.org/p03/PAPERS/WPPB005.pdf

[9] A. E. Grelick, "RF and Beam Diagnostic Instrumentation at the Advanced Proton Source (APS) Linear Accelerator," in *Proc. LINAC'96*, Geneva, Switzerland, Aug. 1996, pp. 851–853. https://jacow.org/l96/papers/THP75.pdf

[10] R. Lill, O. Singh, and N. Arnold, "New Beam Position Monitor System Design for the APS Injector," *AIP Conference Proceedings*, vol. 648, no. 1, pp. 401–408, 2002. doi:10.1063/1.1524426

[11] N. S. Sereno, M. Borland, and R. Lill, "Automated correction of phase errors in the advanced photon source linac," *Phys. Rev. ST Accel. Beams*, vol. 11, no. 7, p. 072 801, 2008. doi:10.1103/PhysRevSTAB.11.072801

[12] M. Wendt, "Direct (Under)Sampling vs Analog Downconversion for BPM Electronics," in *Proc. IBIC'14*, Monterey, CA, USA, Sep. 2014, pp. 486–494. https://jacow.org/IBIC2014/papers/WEIYB1.pdf

[13] A. Lumpkin, B. Yang, W. Berg, J. Lewellen, N. Sereno, and U. Happek, "Electron beam bunch length characterizations using incoherent and coherent transition radiation on the APS SASE FEL project," *Nucl. Instrum. Methods Phys. Res., Sect. A*, vol. 445, pp. 356–361, 2000.

[14] A. H. Lumpkin, "Beam Diagnostics for Coherent Optical Radiation Induced by the Microbunching Instability," in *Proc. FEL'13*, New York, NY, USA, Aug. 2013, pp. 169–172. https://jacow.org/FEL2013/papers/TUOBNO01.pdf

[15] E. Saldin, E. Schneidmiller, and M. Yurkov, "Klystron instability of a relativistic electron beam in a bunch compressor," *Nucl. Instrum. Methods Phys. Res., Sect. A*, vol. 490, pp. 1–8, 2002.

[16] D. F. Ratner, A. Chao, and Z. Huang, "Three-dimensional Analysis of Longitudinal Space Charge Microbunching Starting from Shot Noise," in *Proc. FEL'08*, Gyeongju, Korea, Aug. 2008, pp. 338–341. https://jacow.org/FEL2008/papers/TUPPH041.pdf

[17] C. Lin *et al.*, "Long-Range Persistence of Femtosecond Modulations on Laser-Plasma-Accelerated Electron Beams," *Phys. Rev. Lett.*, vol. 108, p. 094 801, 2012.

[18] A. H. Lumpkin *et al.*, "Coherent Optical Signatures of Electron Microbunching in Laser-Driven Plasma Accelerators," *Phys. Rev. Lett.*, vol. 125, p. 014 801, 2020. doi:10.1103/PhysRevLett.125.014801

[19] M. LaBerge *et al.*, "Coherent 3D Microstructure of Laser-Wakefield-Accelerated Electron Bunches," in *Proc. FEL'22*, 2022. doi:10.18429/JACoW-FEL2022-THAI2

[20] M. Gasior, "First Results from the LHC Schottky Monitor Operated with Direct Diode Detection," in *Proc. BIW'12*, Newport News, VA, USA, Apr. 2012, pp. 222–224. https://jacow.org/%20BIW2012/papers/TUPG044.pdf

Content from this work may be used under the terms of the CC-BY-4.0 licence (© 2023). Any distribution of this work must maintain attribution to the author(s), title of the work, publisher, and DOI

ISBN: 978-3-95450-236-3 ISSN: 2673-5350 doi:10.18429/JACoW-IBIC2023-TUP028

COLLIMATOR IRRADIATION STUDIES AT THE ADVANCED PHOTON SOURCE*

J. Dooling†, W. Berg, M. Borland, J. Calvey, L. Emery, A. Grannan, K. Harkay, Y. Lee, R. Lindberg, G. Navrotski, V. Sajaev, N. Sereno, J. Stevens, Y. Sun, K. P. Wootton
Argonne National Laboratory, Lemont, Illinois, USA
N. Cook, RadiaSoft LLC, Boulder, Colorado, USA
D. Lee, S. Riedel, University of California, Santa Cruz, Santa Cruz, California, USA

Abstract

We present results from a recent collimator irradiation experiment conducted in the Advanced Photon Source (APS) storage ring. This experiment is the third in a series of studies to examine the effects of high-intensity electron beams on potential collimator material for the APS-Upgrade (APS-U). The intent here is to determine if a fan-out kicker can sufficiently reduce e-beam power density to protect horizontal collimators planned for installation in the APS-U storage-ring. The fan-out kicker (FOK) spreads the bunched-beam vertically allowing it to grow in transverse dimensions prior to striking the collimator. In the present experiment, one of the two collimator test pieces is fabricated from oxygen-free copper; and the other is from 6061-T6 aluminum. As in past studies, diagnostics include turn-by-turn BPMs, a diagnostic image system, fast beam loss monitors, a pin-hole camera, and a current monitor. Post-irradiation analyses employ microscopy and metallurgy. To avoid confusion from multiple strikes, only three beam aborts are carried out on each of the collimator pieces; two with the FOK on and the other with it off. Observed hydrodynamic behavior will be compared with coupled codes.

INTRODUCTION

Previous whole-beam-loss experiments carried out in 2019 and 2020 in the Advanced Photon Source (APS) storage ring (SR) studied effects in aluminum and titanium collimator test pieces [1–3]. No steps were taken to mitigate damage caused by the high intensity electron beam during these earlier studies. In the present experiment, a vertically-deflecting fan-out kicker (FOK) was employed to spread the beam bunch train transversely on both aluminum and copper targets. The action of the FOK spreads both the bunch train as well as individual bunches; in the latter case, by forcing them into regions of non-linear focusing.

Unlike earlier collimator experiments, where studies were carried out at the beginning of a user run, this study took place during the final Machine Studies period at the end of APS SR operations. The collimator test pieces were installed for the entire final run and thus were well conditioned for the experiment.

* Work supported by the U.S. D.O.E.,Office of Science, Office of Basic Energy Sciences, under contract number DE-AC02- 06CH11357.
† dooling@anl.gov

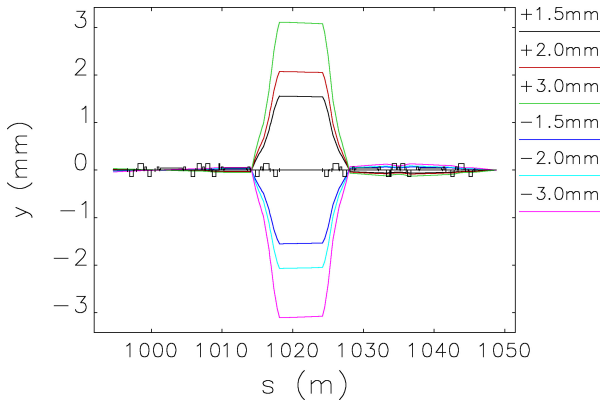


Figure 1: Vertical bumps in the Sector 37 region modeled with `elegant`.

Table 1: Beam Abort Case List Parameters

Case No.	Vertical Offset (mm)	Mat'l	FOK Voltage (kV)	Vertical Defl. Angle y' (μrad)
0	+1.5	Cu	2	245.0
1	-1.5	Al	2	245.0
2	-2.0	Al	1	122.5
3	+3.0	Cu	0	0
4	-3.0	Al	0	0
5	+2.0	Cu	3	367.5

EXPERIMENTAL DESCRIPTION

As in previous experiments, the collimator test piece targets were placed in the Sector 37 (S37) straight section approximately 2 m downstream of the fourth S37 rf cavity. Vertical orbit bumps in the S37 region used to separate the strike regions on the targets were simulated with `elegant` [4, 5] and shown in Fig. 1. With positive y-bumps, the beam strikes copper and with negative bumps, the beam intercepts aluminum.

Six separate whole-beam aborts with 200 mA, 6 GeV beam were employed to strike the collimator test pieces; three on the copper and three on the aluminum. The six cases are summarized in Table 1.

Content from this work may be used under the terms of the CC-BY-4.0 licence (© 2023). Any distribution of this work must maintain attribution to the author(s), title of the work, publisher, and DOI

ISBN: 978-3-95450-236-3 ISSN: 2673-5350 doi:10.18429/JACoW-IBIC2023-TUP028

Content from this work may be used under the terms of the CC-BY-4.0 licence (© 2023). Any distribution of this work must maintain attribution to the author(s), title of the work, publisher, and DOI

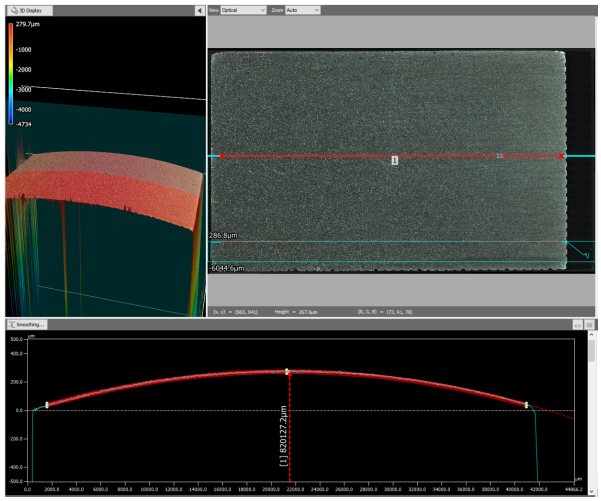


Figure 2: Surface images and profile obtained with a Keyence VR3200 microscope for the Al test piece.

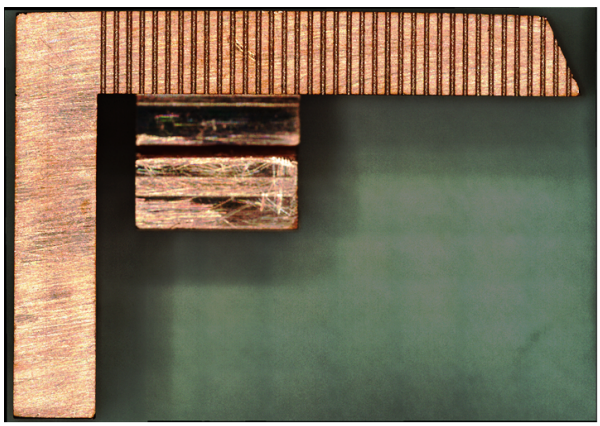


Figure 3: Copper test piece showing 1-mm-spaced rulings on the gap side.

MEASUREMENTS

Pre-Studies

Surface analysis was performed on each of the test pieces. An 80 cm radius was machined into each of the pieces beam-facing surfaces; this relatively large radius resulted in a 0.28 mm peak height above the chord connecting the upstream and downstream ends as shown in Fig. 2 for the aluminum piece. These images were recorded using a Keyence VR3200 microscope. The peak or apex is where we expect the beam to strike first during a loss event. The full length of the chord from the upstream to downstream edges of the beam-facing collimator surface is 41 mm.

For fiducialization and wakefield studies, 1 mm-spaced rulings were machined on the side of the copper piece facing the gap, see Fig. 3. Rulings were also added to the aluminum piece, but not on the gap side. The rulings depths were nominally specified as 0.127 mm (5 mils); for every fifth ruling, the depth was specified as 0.254 mm or 10 mils.

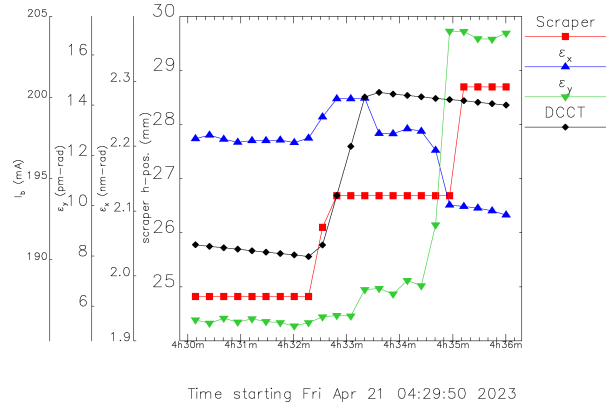


Figure 4: Case 0 horizontal and vertical emittances as the collimators are positioned for the dump. Scraper refers to the horizontal position of the collimator apex; at h-pos = 30.85 mm, the apex is nominally at chamber centerline.

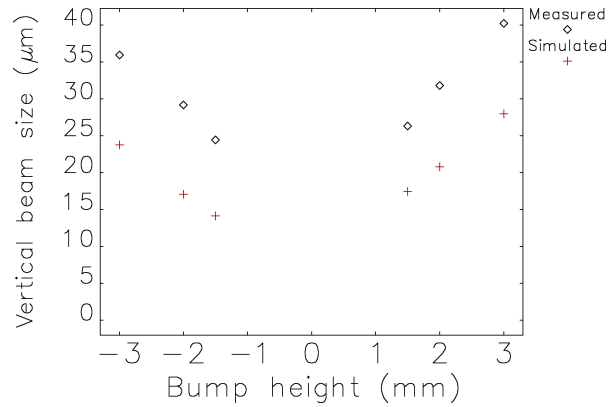


Figure 5: Predicted and measured vertical beam sizes.

Studies

A total of six whole-beam dumps were conducted. All six loss events were carried out with stored beam current of 200 mA and a 972-bunch fill pattern. The whole-beam loss events are initiated by muting the rf drive once the collimator test pieces were in place.

Pinhole Camera The S35 pinhole camera is an important diagnostic providing horizontal and vertical beam sizes which in turn provide beam emittances when combined with machine lattice functions. Sextupole magnets within the bump were inadvertently left powered during the beam abort study which led to an planned increase in vertical emittance. An example of the growth in vertical emittance is shown for case 0 in Fig. 4 as the collimators are moved toward the horizontal parking position for beam dumps. The plot ends with the beam dump. The apex of the collimators are nominally placed 2 mm from the beam centerline prior to initiating a beam abort corresponding to h-pos=28.85 cm. Predicted and measured vertical sizes for the six cases presented here are plotted in Fig. 5.

ISBN: 978-3-95450-236-3 ISSN: 2673-5350 doi:10.18429/JACoW-IBIC2023-TUP028

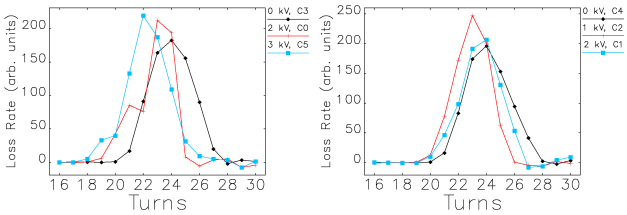


Figure 6: Measured loss rates in the copper (left) and aluminum collimator test pieces.

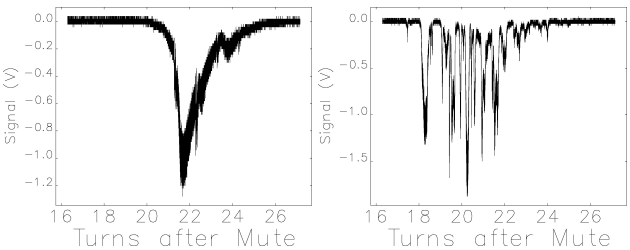


Figure 7: Fast fiber optic beam loss signals in S6 for Cases 3 (FOK=0 kV, left) and 5 (FOK=3 kV).

Turn-by-Turn BPMs Differentiated sum signals from the turn-by-turn (TBT) BPMs provide the loss rate during the whole-beam loss events. Measured loss rates from the TBT BPMs are plotted in Fig. 6. Based on `elegant` simulations for APS-U, FOK voltages should be kept less than 3 kV.

Fast Fiber Optic Beam Loss Monitors Fast fiber-optic beam loss monitors (FOBLM) provide intra-turn loss information. With a rise-time of approximately 2 ns, the FOBLM is not fast enough to resolve the losses from individual bunches in a 972-bunch fill pattern (1296 buckets at 352 MHz, with 3 of 4 buckets filled), the diagnostic can observe time-averaged behavior. In Fig. 7 losses in S6 are shown for Cases 3 and 5 (FOK=0 and 3 kV). Large variations in the loss signal is seen for the 3 kV case. These large fluctuations are not desirable and can lead to losses outside the collimator regions.

Diagnostic Imaging System Immediately following the whole-beam-loss study an image was acquired of the upstream end of the collimator surfaces. The image shown in Fig. 8 shows the effects of the six strikes listed in Table 1.

Post Studies

Gamma Spectroscopy Radiation monitors indicated the copper test piece to be activated. Gamma spectroscopy found approximately 135 pCi of cobalt-57. Gamma spec measurements were conducted over an integration time of 1 hour on July 27, 2023 roughly 3 months after irradiation. No activation was indicated in the aluminum piece.

Photography Photographs of the collimator beam-facing surfaces are presented in Fig. 9. The orientation of the two images is similar to the arrangement of the collimator

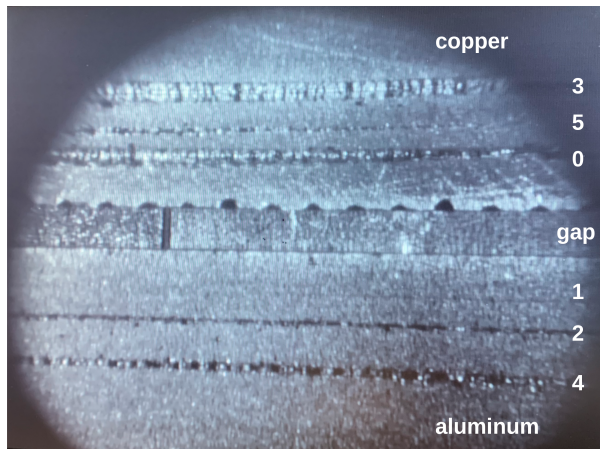


Figure 8: Image of the upstream end of the collimator surfaces after whole-beam strikes. Numbering refers to the Cases list in Table 1.

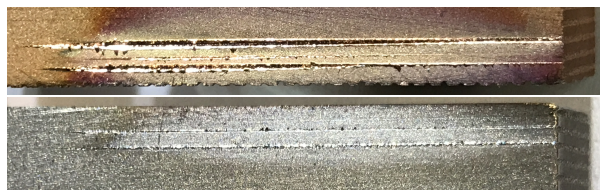


Figure 9: Photographs of strike regions in copper (top) and aluminum. Beam was moving from right to left.

test pieces when mounted during the experiment. In Fig. 9 the full length of the damaged region (3.3 cm) is shown; whereas in Fig. 8, the image covers only the upstream region of the mounted pieces with a 11 mm field of view.

Metallurgy Though we do not yet have access to the test pieces used for the April 2023 study, metallurgical analysis has been performed on the aluminum pieces irradiated during the January 2020 experiment [1]. After cutting and polishing to 0.05 µm, the color tinting chemical etchant "Weck's Reagent" was used by immersion for 30 seconds to highlight micro-segregation of different phases in aluminum, especially to differentiate the melted, heat affected and unaffected base metal properties of the irradiated regions. An example of this analysis is shown in Fig. 10. Under polarized lighting, the melt regions generally have a green tint highlighting turbulent mixing present during the rapid melting and solidification process. The orange color highlights unaffected aluminum alloy base metal. Close inspection shows a heat affected but non-melted zone between the two regions. (Grey/black areas are encapsulating plastic used to preserve surface features.) The double beam-strike image shows metal ejection and re-solidification onto open surfaces.

Content from this work may be used under the terms of the CC-BY-4.0 licence (© 2023). Any distribution of this work must maintain attribution to the author(s), title of the work, publisher, and DOI

ISBN: 978-3-95450-236-3 ISSN: 2673-5350 doi:10.18429/JACoW-IBIC2023-TUP028

Content from this work may be used under the terms of the CC-BY-4.0 licence (© 2023). Any distribution of this work must maintain attribution to the author(s), title of the work, publisher, and DOI

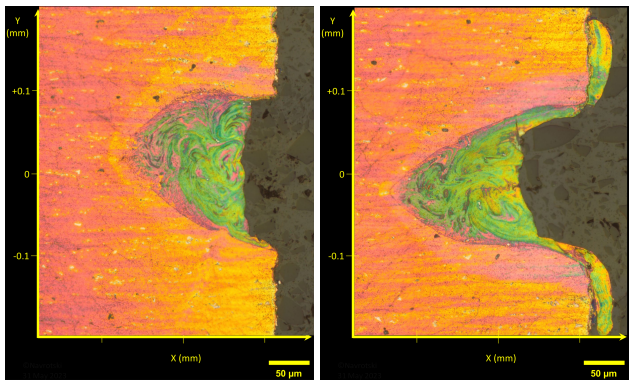


Figure 10: Metallurgical analysis of irradiated aluminum test piece cross sections from January 2020. Single strike at 200 mA (left) and double strikes at 200 mA (right). The images are from separate y-position strike locations.

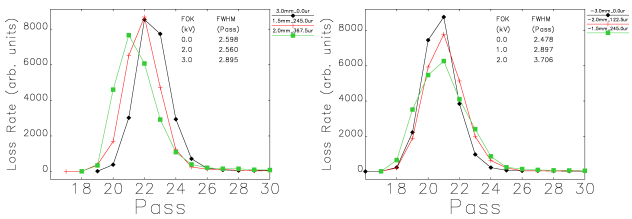


Figure 11: Simulated loss rates in the copper (cases 3, 0, 5; left) and aluminum (cases 4, 2, 1) collimator test pieces. Refer to Table 1 for case numbers.

SIMULATIONS

Dose Distributions with `elegant` and MARS

Plots of `elegant`-derived loss rates for strikes on aluminum and copper test pieces are presented in Fig. 11. These temporal profiles can be compared with the measured loss rates shown in Fig. 6. We observe that the loss duration appears to increase with FOK voltage for the simulated loss rates; this trend is not evident in the measured TBT data.

The x-integrated `elegant`-generated transverse loss distributions (all Passes) are presented in Fig. 12 for strikes on aluminum with FOK voltage settings of 0, 1, and 2 kV. These and the other four distributions will be used as input for MARS [6] to generate temporal dose distributions with a time increment of 1 turn or pass (3.68 µs) [7]. The dose distributions are in turn used as input to the hydrodynamics code, FLASH [8]. Figure 12 shows significant spreading of the loss with 2 kV on the FOK relative to the 0 voltage case.

Simulating Liquid Phase with FLASH

Simulations of damage to collimator materials done with the FLASH hydrodynamics code [8] have thus far not included any modeling of a "liquid phase". Instead, the collimator material in each cell is treated as a solid and is not evolved by FLASH until the electron temperature, T_{ele}, in that cell exceeds a threshold temperature, T_{thresh} = 4115 K for Al, and 4252.5 K for Cu).

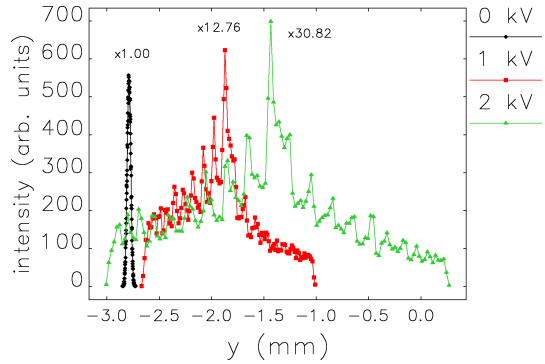


Figure 12: Simulated x-integrated y-loss intensity distributions on aluminum based on measured emittance for FOK voltages of 0, 1, and 2 kV. Using 0 kV as the reference, the amplitudes of the 1 and 2 kV profiles are increased by factors of 12.76 and 30.82 indicating the reduction of intensity the FOK provides.

We plan to begin modeling the liquid phase, first for copper and then for aluminum. The first step will be to replace the constant thermal conductivity model for solid phase copper (which is currently being used) with a more accurate model in the temperature range $0K < T_{ele} \leq T_{melt,Cu}$ where $T_{melt,Cu} \approx 1358$ K is the melting point of copper [9]. Then a new phase transition from solid to liquid will be added at $T_{ele} = T_{melt,Cu}$. This first implementation will focus be on more accurately modeling the density [10], thermal conductivity [11], and specific heat of liquid copper in the temperature range of $T_{melt,Cu} \leq T_{ele} \leq T_{thresh}$. The phase transition to plasma will still occur at T_{thresh} = 4252.5 K

In preliminary simulations, adding a liquid phase has helped avoid nonphysical "islands" of solid copper that are not connected to the main collimator material. It also allows the vaporized copper to re-liquefy from the plasma phase, a feature not previously implemented. Eventually we hope to be able to evolve the state of the liquid phase collimator material using the hydrodynamics capabilities of FLASH.

SUMMARY

A third whole-beam-abort experiment was conducted to study whether a vertical FOK could be utilized to protect the horizontal collimators planned for the APS-U SR. Tests were carried out on both aluminum and copper targets. In the case of aluminum, a FOK voltage of 2 kV was sufficient to protect the target; however, for copper even a 3 kV kick was not enough to prevent damage. For both targets, damage was reduced as FOK voltage was increased. The data collected will provide useful information for benchmarking our coupled-code simulation effort modeling the effects of whole-beam loss events in fourth generation light sources.

ACKNOWLEDGMENTS

Thanks to R. Soliday and H. Shang for assistance with analysis scripts, of APS ANL. Thanks also to Health Physics personnel M. Henry and J. Edwards.

ISBN: 978-3-95450-236-3 ISSN: 2673-5350 doi:10.18429/JACoW-IBIC2023-TUP028

REFERENCES

[1] J. Dooling *et al.*, "Collimator irradiation studies in the argonne advanced photon source at energy densities expected in next-generation storage ring light sources," *Phys. Rev. Accel. Beams*, vol. 25, no. 4, p. 043 001, 2022. doi:10.1103/PhysRevAccelBeams.25.043001

[2] J. C. Dooling *et al.*, "Diagnostics for Collimator Irradiation Studies in the Advanced Photon Source Storage Ring," in *Proc. IBIC'20*, Santos, Brazil, Sep. 2020, pp. 26–33. doi:10.18429/JACoW-IBIC2020-TUAO02

[3] J. C. Dooling *et al.*, "Studies of Beam Dumps in Candidate Horizontal Collimator Materials for the Advanced Photon Source Upgrade Storage Ring," in *Proc. NAPAC'19*, Lansing, MI, USA, Sep. 2019, pp. 128–131. doi:10.18429/JACoW-NAPAC2019-MOPLM14

[4] M. Borland, "elegant: A Flexible SDDS-Compliant Code for Accelerator Simulation," Advanced Photon Source, Tech. Rep. LS-287, 2000. doi:10.2172/761286

[5] Y. Wang and M. Borland, "Implementation and Performance of Parallelized Elegant," in *Proc. PAC'07*, Albuquerque, NM, USA, Jun. 2007, pp. 3444–3446. doi:10.1109/PAC.2007.4440453

[6] N. V. Mokhov, "The Mars Code System User's Guide," Fermilab, FN 628, 1995. doi:10.2172/1987276

[7] J. C. Dooling *et al.*, "Hydrodynamic and Beam Dynamic Simulations of Ultra-Low Emittance Whole Beam Dumps in the Advanced Photon Source Storage Ring," in *Proc. NAPAC'22*, Albuquerque, NM, USA, 2022, pp. 390–393. doi:10.18429/JACoW-NAPAC2022-TUPA21

[8] B. Fryxell *et al.*, "FLASH: An adaptive mesh hydrodynamics code for modeling astrophysical thermonuclear flashes," *Astrophys. J. Suppl. Ser.*, vol. 131, no. 1, p. 273, 2000. doi:10.1086/317361

[9] J. G. Hust and A. B. Lankford, "Thermal Conductivity of Aluminum, Copper, Iron, and Tungsten for Temperatures from 1 K to the melting point," National Institute of Standards and Technology, U.S. Department of Commerce, Boulder, Colorado, Tech. Rep. NBSIR 84-3007, 1984, pp. 4–15. https://www.govinfo.gov/content/pkg/GOVPUB-C13-5dca61206b094d8b3a54099ebcff1baa/pdf/GOVPUB-C13-5dca61206b094d8b3a54099ebcff1baa.pdf

[10] J. A. Cahill and A. D. Kirshenbaum, "The density of liquid copper from its melting point (1356 K to 2500 K and an estimate of its critical constants1,2," *J. Phys. Chem.*, vol. 66, no. 6, pp. 1080–1082, 1962. doi:10.1021/j100812a027

[11] M. Assael, A. Chatzimichailidis, K. Antoniadis, W. Wakeham, M. Huber, and H. Fukuyama, "Reference correlations for the thermal conductivity of copper, gallium, indium, iron, lead, nickel and tin," *High Temp.-High Pressures*, no. 46, 2017.

Content from this work may be used under the terms of the CC-BY-4.0 licence (© 2023). Any distribution of this work must maintain attribution to the author(s), title of the work, publisher, and DOI

ISBN: 978-3-95450-236-3 ISSN: 2673-5350 doi:10.18429/JACoW-IBIC2023-TUP029

A HYBRID APPROACH TO UPGRADE HARDWARE FOR THE PROTON STORAGE RING FAST KICKER

T. Ramakrishnan, J. Duran, H. Watkins
Los Alamos National Laboratory, Los Alamos, USA

Abstract

The Los Alamos Neutron Science Center (LANSCE) Proton Storage Ring (PSR) needs precise timing to ensure successful extraction of the bunched protons. The current control system's hardware is obsolete and unmaintainable. The task was to replace the 1980's era CAMAC control and timing system for the PSR extraction kickers. This included a system which halts charging of the kickers after a duration without firing to prevent equipment damage. A hybrid approach was taken to integrate a Berkeley Nucleonics Corporation (BNC) pulse generator that was controlled by a soft input/output controller (IOC) and National Instrument (NI) compact Reconfigurable Input/Output (cRIO) IOC. This allowed for flexibility and modularity of the software and hardware development. This approach built the framework to streamline robust deployment of hybrid systems and develop a solution for upgrades of other LANSCE kickers.

INTRODUCTION

Proton Storage Ring

The LANSCE proton storage ring (PSR) [1], Fig. 1, is used to collect and bunch protons. The alignment and frequency of the protons are changed continuously to keep them inside the ring for multiple cycles which are then ejected to the Lujan Mark IV target [2] to produce neutrons which are used in several experiments.

Fast Kicker Purpose & Controls Upgrade

The storage fast kicker (SRFK) [3] system consists of a DC power supply, a Blumelein [4] that acts as a capacitor, and two plates (SRFK71 and SRFK81) as well as a control system that directs and monitors certain functionality. The fast kicker system is responsible for extracting the bunched protons from the PSR and sending them down the beam line towards the neutron producing target.

The control system that was upgraded used an obsolete, 1980's, CAMAC form factor. It is worth mentioning that it had no safety mechanisms in place for over charging the fast kicker Blumlein which is holding the charge that is being provided in a pulsed fashion by a DC power supply. The newly deployed and functionality advanced control system utilizes a hybrid approach by using two commercial of the shelf systems (a) BNC 577 pulse generator [5] for generating delayed pulses and (b) cRIO [6] for reading back the status of an RF switch and keeps track of charging pulses to the Blumlein. The hybrid approach also extends to the controls software implementing (a) soft IOC to control the BNC 577 and (b) NI cRIO based IOC that has a field programable gate architecture (FPGA) [7] backplane interacting with the modules for high-speed data acquisition.

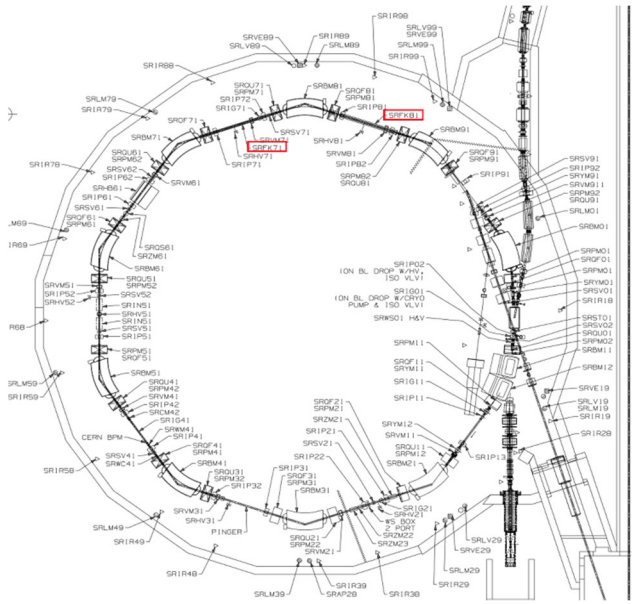


Figure 1: LANSCE Proton Storage Ring with magnet locations.

PSR TIMING STRUCTURE

LANSCE has a distributed Master Timer system [8] which provides timing gates to different systems across the accelerator facility. A subset of these gates is for the PSR operating at a nominal 20 Hz rep rate. The ones of interest for the kickers are Extraction Kicker Charge Gate (EKCG), Storage Ring Extraction Window (SREW), and Extraction Kicker Long Fire (EKLF).

The beam pulse structure is known as Long Bunch Enable Gate (LBEG). Within each LBEG pulse, there are ~2000 pulses mini pulses whose period is designed to be equal to the time for 800 MeV beam to circulate in the PSR at a rate of 2.8 MHz. The mini pulse is high/present for 270 ns and low/absent for 90 ns. This creates a gap in the beam which allows for the bunched protons to be extracted without interacting with incoming beam.

The EKLF gate is responsible for firing the kickers and extracting the beam. Two conditions must be met to extract, first the SREW much be high and second the EKLF pulse is synchronized with 2.8 MHz reference. These ensure the incoming and outgoing beams will not interact.

* This work was supported by the U.S. Department of Energy through the Los Alamos National Laboratory. Los Alamos National Laboratory is operated by Triad National Security, LLC, for the National Nuclear Security Administration of U.S. Department of Energy (Contract No. 89233218CNA000001). † tyagir@lanl.gov, LA-UR-23-30144

Content from this work may be used under the terms of the CC-BY-4.0 licence (© 2023). Any distribution of this work must maintain attribution to the author(s), title of the work, publisher, and DOI

ISBN: 978-3-95450-236-3 ISSN: 2673-5350 doi:10.18429/JACoW-IBIC2023-TUP029

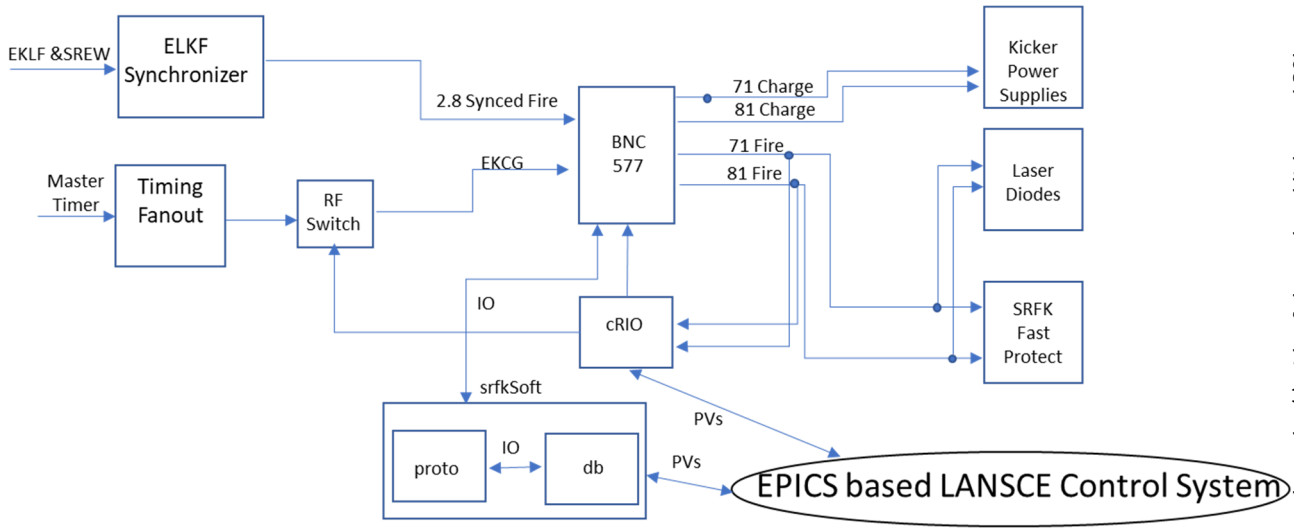


Figure 2: Software and hardware architecture for SRFK upgrade.

HARDWARE ARCHITECTURE

In the following we describe the hybrid hardware architecture in more detail. The complete hardware architecture is presented in Fig. 2, where it details the two major hardware controls the BNC 577 configuration shown in Table 1, and the NI cRIO which interact with the timing, power supply, synchronizer, switch, diodes, and fast protect system. The BNC pulse generator, Fig. 3, that the user can set pulse widths and delays for generating the pulses used to time the kicker. The delay and charging of the kickers are dependent on the length of the Blumlein cables which vary kicker to kicker. The LANSCE Master Timer system gates that the entering and exiting beam does not interact. When the BNC receives a timing gate, EKCG or ELKF, it triggers and delays an output pulse to the kickers. The Fast Protect system ensures that there is always a successful discharge of kickers which in turn eliminates radiation spill by shutting off the beam if it is not extracted from the PSR.

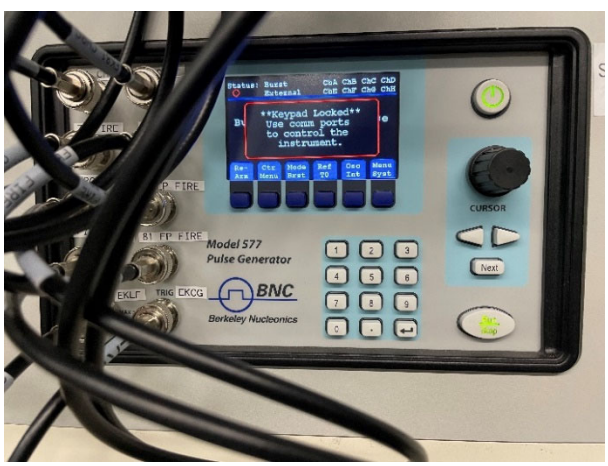


Figure 3: BNC pulse generator.



Figure 4: 8 card NI cRIO.

Table 1: BNC Specifications

Feature	Description
Channels	4 or 8 ind. channel outputs
Resolution	250 ps
Accuracy	1 ns + .0001 x setpoint
RMS Jitter	< 50 ps (channel to channel)
Voltage	5 V for TTL; 45 V for Adjustable
Pulse Width	10 ns – 1000 s
Memory	12 Storage Slots

Table 2: NI cRIO 9038 Specifications

Feature	Description
NI 9425	Binary Inputs
NI 9401	Counters
NI 9205	Analog Input with delays
NI 9262	Pulse Generation
NI 9485	Binary Outputs
NI 9485	Binary Outputs
NI 9485	Binary Outputs
NI 9264	Analog Outputs

Content from this work may be used under the terms of the CC-BY-4.0 licence (© 2023). Any distribution of this work must maintain attribution to the author(s), title of the work, publisher, and DOI

ISBN: 978-3-95450-236-3 ISSN: 2673-5350 doi:10.18429/JACoW-IBIC2023-TUP029

Content from this work may be used under the terms of the CC-BY-4.0 licence (© 2023). Any distribution of this work must maintain attribution to the author(s), title of the work, publisher, and DOI

The 8 card NI cRIO, Fig. 2, handles readbacks and tracks counts with a delay using the NI 9401-counter card, NI 9205 analog input card that is triggered after a 7500 µs delay, NI 9485 binary command card, and NI 9264 analog command cards, all the NI cRIO module configurations are shown in Table 2. The delay is based on the charge gate and is needed to ensure that the readback voltage is sampled at the peak of the charge ramp. The counters ensure that the number of charge and fire pulses are the same. If there are more charge pulses than fire pulses, the NI 9485 is closed which flips an RF switch to prevent further charge timing pulses from reaching the BNC. This is how we ensure that the fast kickers are not over charged. The NI 9264 is used to change the setpoint voltage of the kickers.

SOFTWARE ARCHITECURE

The complete software architecture for the LANSCE control system (LCS) is presented in Fig. 2 interacting with the hardware. At LANSCE we use the Experimental Physics and Industrial Control System (EPICS) architecture [9]. EPICS is a set of open-source software tools, libraries, and applications developed collaboratively and used worldwide to create distributed soft real-time control systems for scientific instruments such as particle accelerator, telescopes, and other large scientific experiments. It gives access to various levels of functionality for IOCs using process variables (PVs) which can have multiple user defined attributes that are available to other users who would like to access the system. Users can set/change values and are able to get readbacks using PVs which are ascribed to control a feature of a specific equipment. The PVs are housed inside the database located inside an IOC which allow the users of LCS to access the PVs across the site on consoles that are connected to LCS.

The BNC pulse generator has a serialized communication protocol using a MOXA [10] serial to ethernet adapter. The serial commands are interpreted by a stream-protocol file which associates the commands to the process variables (PV). The stream-protocol is designed to handle asynchronous data using EPICS. The input/output PVs configured in the stream-protocol is then associated with a database file that sets attributes to the PVs such as description, units, etc. Databases are important for EPICS to function because they are necessary to define PVs and can be generated either manually or programmatically through a template. In this project we handle calculation inside the database using calc and calcout record types. The PVs handle multiple types of input and output data, in this project we used analog output, analog input, binary output, and binary input.

The PVs for the BNC 577 were handled via stream-protocol and were housed in a virtual soft IOC called srfkSoft, Fig. 3. Soft IOCs are created as virtual instances of an IOC rather than a physical controller such as a NI cRIO. This can be housed in remote servers which allows the developers to access it remotely from all consoles on the LCS. Soft IOCs have been instrumental in reducing the number of physical sites to house hardware and provides a clear and robust approach to setting up disparate pieces of hardware using a single type of IOC flavor.

The NI cRIO software involves an object-oriented programming (OOP) FPGA code written in LabVIEW that generates a bit file. This bit file is used by a C++ device support code that assigns the data received from the device asynchronously to the EPICS PVs. We then use EPICS templates to define the attributes of the PVs in the database. The IOC in this case is the physical NI cRIO that is deployed on to the field. This approach differs from the soft IOC case because we require high speed data from the NI cRIO FPGA for controlling some of the devices that require faster responses. Hence, it is beneficial to have the IOC integrated with the cRIO system.

HYBRID APPROACH

The hybrid approach that was undertaken for this project focused on establishing versatility for system design by having two simple approaches to hardware and software architectures that were both integrated in the larger LCS framework. The ability to create PVs using soft IOCs on virtual machines for the BNC 577 pulse generator and physical IOCs using NI cRIO's FPGA backplane. This effort flows well with our long term LANSCE modernization [11] project that is focused on reducing the number of disparate control systems to a more unified approach. We used this homogenous approach principle to incorporate a soft IOC to handle the stream device input/output control PVs and use an existing deployed cRIO to handle the readbacks, counters, and set time delays for the pulses.

A hybrid approach by incorporating stream device protocol for BNC pulse generator accompanied by a soft IOC and an industrial input output (IIO) using cRIO with a self-contained IOC helped us easily upgrade the legacy CAMAC system that was used to control the SRFKs for over a decade. The flexibility this approach offers without introducing additional complexity to providing solutions will be useful moving forward with upgrading control systems at LANSCE and at other accelerator facilities that rely on the EPICS architecture.

CONCLUSION

The results have shown that the new hybrid system consisting of the BNC 577 pulse generator and cRIO is functionally equivalent to the CAMAC system it is replacing. Further we now have better control of the counters to time the kicker more accurately than in the past, which protects the equipment from being over charged. All these improvements will be beneficial as our organization is transitioning LANSCE away from its legacy hardware.

ACKNOWLEDGEMENTS

We would like to thank Scott Baily for creating the IIO LabVIEW template and helping with the 9205 card's time-delay as well as 9401 counter code troubleshooting which were instrumental in giving new capabilities to the storage ring fast kicker that it has never had previously.

ISBN: 978-3-95450-236-3 ISSN: 2673-5350 doi:10.18429/JACoW-IBIC2023-TUP029

REFERENCES

[1] L.M. Earley, G.P. Lawrence, and J.M. Potter, "Rapidly tuned buncher structure for the Los Alamos proton storage ring (PSR)", *IEEE Transactions on Nuclear Science*, 30(4), pp. 3511-3513, 1983.

[2] M. Mocko and G. Muhrer, "Fourth-generation spallation neutron target-moderator-reflector-shield assembly at the Manuel Lujan Jr. neutron scattering center", *Nucl. Instrum. Methods Phys. Res., Sect. A*, vol. 704, pp. 27-35, 2013.

[3] J.F. Power, B. Blind, and A.J. Jason, "The Los Alamos proton storage ring fast-extraction kicker system", *IEEE Trans. Nucl. Sci.*, vol. 32(5), pp. 3021-3023, 1985.

[4] J. Tang, "Rapid cycling synchrotrons and accumulator rings for high-intensity hadron beams", *Rev. Accel. Sci. Technol.*, vol. 6, pp. 143-169, 2013.

[5] M.A. Mustafa, D. Shekhtman, and N.J. Parziale, "Single-Laser Krypton Tagging Velocimetry (KTV) Investigation of Air and N2 Boundary-Layer Flows Over a Hollow Cylinder in the Stevens Shock Tube", *AIAA Scitech 2019 Forum*, p. 1820, 2019.

[6] D. Baros, "Upgrading the Data Acquisition and Control System of the LANSCE LINAC", in *Proc. PAC'11*, New York, NY, USA, Mar.-Apr. 2011, paper MOP256, pp. 588-590.

[7] M. Pieck *et al.*, "LANSCE Control System Upgrade Status and Challenges", in *Proc. ICALEPCS'15*, Melbourne, Australia, Oct. 2015, pp. 464-467. doi:10.18429/JACoW-ICALEPCS2015-MOPGF161

[8] R. Merl, R. Clanton, E. Bjorklund, S. Baily, and F. Shelley, "The LANSCE Timing Reference Generator (No. LA-UR-13-26955)", Los Alamos National Lab. (LANL), Los Alamos, NM, USA, 2013.

[9] M. Pieck, C.D. Hatch, J.O. Hill, H.A. Watkins, and E.E. Westbrook, LANSCE Control System's 50th Anniversary, 2022.

[10] L.G. Foggetta, B. Buonomo, and P. Valente, "Evolution of Diagnostics and Services of the DANE Beam Test Facility", in *Proc. IPAC'15*, Richmond, VA, USA, May 2015, pp. 904-906. doi:10.18429/JACoW-IPAC2015-MOPHA049

[11] E. Bjorklund and S.A. Baily, "Tailoring the Hardware to Your Control System", in *Proc. ICALEPCS'11*, Grenoble, France, Oct. 2011, paper THAAUST01, pp. 1171-1173.

Content from this work may be used under the terms of the CC-BY-4.0 licence (© 2023). Any distribution of this work must maintain attribution to the author(s), title of the work, publisher, and DOI

ISBN: 978-3-95450-236-3 ISSN: 2673-5350 doi:10.18429/JACoW-IBIC2023-TUP031

BEAM TEST OF A HARMONIC KICKER CAVITY*

M. W. Bruker†, J. Grames, J. Guo, J. Musson, S. A. Overstreet, G. T. Park, T. Plawski, M. Poelker, R. Rimmer, H. Wang, C. Wilson, S. Zhang
Thomas Jefferson National Accelerator Facility, Newport News, VA, USA
M. Pablo, B. Roberts, D. Speirs, Electrodynamic, Albuquerque, NM, USA

Abstract

A harmonically resonant kicker cavity designed for beam exchange in a circulator cooler was built and successfully tested at the Upgraded Injector Test Facility (UITF) at Jefferson Lab. This type of cavity is being considered for the injection scheme of the Rapid Cycling Synchrotron at the Electron-Ion Collider, where the spacing of neighboring bunches demands very short kicks. Operating with five transversely deflecting modes simultaneously that resonate at 86.6 MHz and consecutive odd harmonics thereof, the prototype cavity selectively deflects 1 of 11 electron bunches while leaving the others unperturbed. An RF driver was developed to synthesize phase- and amplitude-controlled harmonic signals and combine them to drive the cavity while also separating the modes from a field-probe antenna for RF feedback and dynamic tuning. Beam deflection was measured by sweeping the cavity phase; the deflection waveform agrees with expectations, having sub-nanosecond rise and fall times. No emittance increase is observed. Harmonically resonant cavities like the one described provide a new capability for injection and extraction at circulators and rings.

INTRODUCTION

In circulating accelerators, the minimum bunch spacing needed to accommodate the rise/fall time of a kicker can limit the design options for the bunch train. Originally developed for the Circulating Cooler Ring, a hypothetical ring with 11 revolutions driven by an energy-recovery linac that was intended to be part of the Jefferson Lab Electron-Ion Collider [1], the harmonic kicker cavity offers a new option for applications where every nth bunch must be deflected [2]. One such application is the injection into the Rapid Cycling Synchrotron at the Electron-Ion Collider [3], where one out of four consecutive bunches is injected at a time; here, the bunch spacing is 1.6 ns, and each set of four bunches is followed by a gap of 12 µs, encouraging the use of a pulsed device but out of reach for a stripline due to the short bunch spacing.

A harmonic kicker is a transversely deflecting cavity that can be excited at multiple harmonic frequencies at the same time, allowing one to Fourier-synthesize any deflection waveform containing only these frequencies; the high Q of the modes compared to a stripline makes the drive power manageable, while pulsed drive is still possible if the gap between sets of bunches is sufficiently long. Figure 1 shows a model of the prototype reduced to the most important parts.

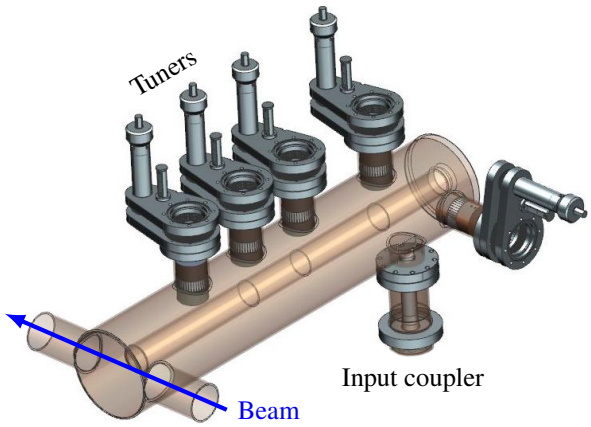


Figure 1: CAD model of a 5-mode harmonic kicker cavity. Five stub tuners are needed to tune all modes. The RF signal is coupled in through a single port; another port serves as the field probe (not shown here).

An example waveform providing a kick to 1 out of 11 bunches is shown in Fig. 2. The usefulness of this type of waveform is not characterized by its absolute flatness outside of the main peak but by the locations of its zero crossings or minor peaks, depending on design. While conceptually flexible, the mode structure of such cavities must be chosen according to the bunch timing of the intended application.

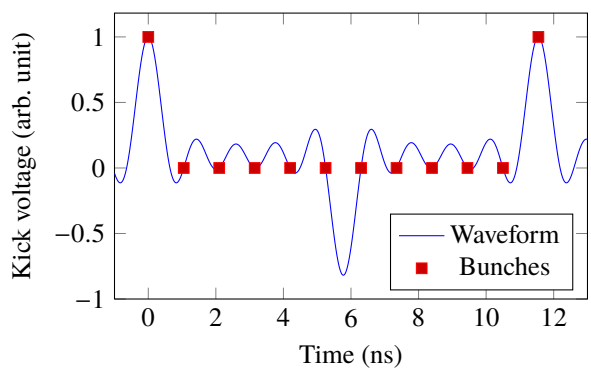


Figure 2: Kick action only on bunches at a bunch frequency equal to the fundamental of the kick waveform, f_{HK} = 86.6 MHz; in this example, all 11 buckets are filled at a bunch frequency of $11 f_{HK}$ = 952.6 MHz.

Compared to placing multiple cavities with different resonant frequencies in series, combining the modes in one cavity has the upside of providing all the deflection in the

* Work supported by the U.S. Department of Energy, Office of Science, Office of Nuclear Physics under contract DE-AC05-06OR23177. Multi-Harmonic driver development has been supported by DOE's NP SBIR program (DE-SC0020566).
† bruker@jlab.org

Content from this work may be used under the terms of the CC-BY-4.0 licence (© 2023). Any distribution of this work must maintain attribution to the author(s), title of the work, publisher, and DOI

ISBN: 978-3-95450-236-3 ISSN: 2673-5350 doi:10.18429/JACoW-IBIC2023-TUP031

same location, thereby avoiding bunch displacement due to the extra drift between cavities; however, note that only odd harmonics can readily be produced in a single cavity of this type.

Drawing from a diverse collaboration for fabrication [4], tuning [5], and drive-circuit design, we produced working prototypes of the cavity and the drive circuit and performed a beam test to verify the basic aspects of the cavity performance. The following sections describe the methods and results.

HARMONIC ARBITRARY WAVEFORM GENERATOR

The cavity is controlled by a specially designed drive circuit called the Harmonic Arbitrary Waveform Generator (HAWG). A synthesized RF source phase-locked to the master oscillator of the accelerator is used to generate an 86.6 MHz harmonic comb. The desired harmonic signals are divided from the harmonic comb onto individual channels using a harmonic combiner and divider [6]. Once isolated, each harmonic signal is phase- and amplitude-controlled using I/Q modulator ICs, amplified, and recombined to the cavity's drive antenna using a second harmonic combiner. While the cavity is designed for an input power of multiple kW, the present version of the HAWG provides 100 W per channel. With this power, the cavity produces its nominal deflection of ~ 4 mrad at 6.5 MeV/c.

Signals from the coupling antenna of the cavity are directed to a third harmonic divider where the harmonic signals are separated to individual I/Q demodulator ICs, allowing for both RF feedback and stub-tuner control for each mode.

BEAM GENERATION AND SYNCHRONIZATION

The beam test of the cavity was performed at Jefferson Lab's Upgraded Injector Test Facility (UITF). Designed to be accessible and reconfigurable with relatively little logistical effort, this accelerator delivers short (<1 ps) electron bunches at up to 8 MeV with an average current of 100 nA (limited only by radiation shielding). The beam is generated by a laser-driven DC photogun at 200 keV, ballistically bunched, and accelerated to the final energy by a compact, superconducting booster [7]. All RF elements run at $f_0 = 1497$ MHz; the signal pulsing the laser determines the bunch timing. In principle, the machine supports bunches at any subharmonic of f_0; also, configurable low-frequency (50–200 Hz) macropulses gating the drive laser can be set up regardless of bunch timing.

The frequencies useful for this experiment are determined by the cavity design. The cavity fundamental $f_{HK} \approx 86.6$ MHz is related to the machine base frequency f_0 by

$$\frac{f_{HK}}{f_0} = \frac{7}{121}.$$

The highest frequency that is a subharmonic of both f_{HK} and f_0 is $f_0/121 \approx 12.4$ MHz, making this frequency ideal for placing all bunches on the same cavity phase, whereas its 11th harmonic, $f_0/11 \approx 136.1$ MHz, could be used to probe all 11 phases of interest at the same time. The simplest way to measure the deflecting action of the kicker cavity is to send bunches at $f_0/121$; this way, all bunches are deflected the same, avoiding the complication of temporally selective detection downstream. The angle of deflection can then be measured as a function of relative phase by shifting the cavity waveform in time.

The frequencies needed for all RF systems (normally including the laser) come from the main RF synchronization chassis of the machine, which contains multiple independent phase-locked loops (PLLs) operating from a common 10 MHz reference. Because the $f_0/121$ signal needed for this experiment was not readily available from the laser PLL, we instead used a commercial frequency generator (CG635 by Stanford Research) synchronized to the same 10 MHz reference. Due to the nature of the frequency ratio, there is no way to produce the exact frequency with this generator, but with 16 digits of frequency resolution, the phase drift due to frequency mismatch is $< 0.1°$ per day.

Another CG635 set to the same frequency supplied the reference signal for the PLLs in the HAWG that generate all frequencies for the harmonic cavity, allowing for independent phase control of the HAWG with a single knob.

Apart from phase-synchronous RF drive of all components, an additional complication was the necessity for pulsed operation of the HAWG. While the device is designed for CW operation in principle, the duty cycle was limited to 10 % for this experiment as a precaution. In order to prevent bunches from being delivered with the cavity off, we operated the laser in macropulse mode with a pulse width of 400 µs and a delay of 100 µs with respect to the 50–200 Hz trigger signal, and gated the HAWG with a stretched copy of this trigger signal so that it would turn on sooner than the beam and turn off later, giving the cavity time to ring in. The timing is shown schematically in Fig. 3.

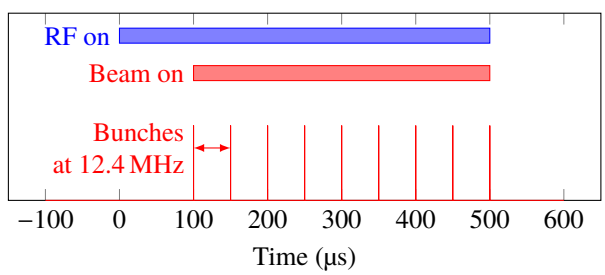


Figure 3: Macropulse timing for clean beam delivery while the cavity is on. Bunch spacing exaggerated for visual clarity.

The macropulse beam mode increases the bunch charge for the same average current, improving the signal-to-background ratio of the BPMs, which is too low for them to be sensitive in CW mode because of the average-current limitation of the UITF. On the other hand, because the

Content from this work may be used under the terms of the CC-BY-4.0 licence (© 2023). Any distribution of this work must maintain attribution to the author(s), title of the work, publisher, and DOI

ISBN: 978-3-95450-236-3 ISSN: 2673-5350 doi:10.18429/JACoW-IBIC2023-TUP031

Content from this work may be used under the terms of the CC-BY-4.0 licence (© 2023). Any distribution of this work must maintain attribution to the author(s), title of the work, publisher, and DOI

macropulses are generated electro-optically with a finite contrast ratio of ≈ 250, very low macropulse duty cycles such as those needed for viewscreen-safe operation result in a high relative level of CW background during the nominally-off time window, obscuring the desired image on viewscreens after the kicker. This issue is not significant for other diagnostics because they can be used at higher beam duty cycles; also, the BPM data acquisition is gated to the macropulse signal and therefore insensitive to CW background.

BEAM-LINE SETUP

For this experiment, we chose a beam momentum of 6.5 MeV/c for deflection angles ≤ 4 mrad at full HAWG output power. The deflection was detected by a pair of BPMs located downstream of the cavity. With the cavity off, the beam orbit was set up to be as flat as possible throughout this section and geometrically centered in the cavity. A pair of quadrupole magnets combined with a wire scanner located at the downstream end of the beam line was used to measure the transverse phase space; because the bunch frequency was chosen to place all bunches at the same kicker phase, the deflection from the kicker could be steered out with a pair of correctors, restoring the orbit through the emittance-measurement section. Figure 4 shows a schematic layout, while Fig. 5 shows a photo of the cavity installed in the UITF beam line.

RESULTS

Deflection Waveform

Due to time constraints, the beam test was performed without automatic stub-tuner control and RF feedback. However, after iterative matrix-based tuning of all modes and with temperature-regulated water flowing through the inner conductor of the cavity, we found that the frequency stability of all modes was well within the bandwidth. The limited RF duty cycle helped keep detuning due to RF heating to a minimum.

As a first test, we drove the cavity at half power per channel one mode at a time, the other amplifiers off, and scanned the HAWG reference phase to measure the deflection waveform at each frequency. The angle of deflection for each phase follows from the position signals of two subsequent BPMs located downstream of the cavity. Figure 6 shows an example of this measurement performed at the ninth harmonic, demonstrating the single-mode deflection is a clean sine wave.

Having tested each mode individually, we powered all modes at the same time, measured the superposition waveform, and adjusted the phase and amplitude setpoints of the modes to give equal phases and amplitudes in the deflection waveform as determined by a fit of

$$f(\phi) = f_0 + \sum_{k=1}^{5} A_k \cos\left[(2k-1)\phi - \phi_k\right] \qquad (1)$$

with $\phi = 7\phi_{\mathrm{ref}}$. With all A_k equal and all $\phi_k = 0$, this would give the desired waveform shown in Fig. 2.

Table 1: Fit Parameters for Waveform in Fig. 7

k	A_k (mrad)	ϕ_k
1	0.47	1°
2	0.46	2°
3	0.46	4°
4	0.43	4°
5	0.38	−16°

The waveform so obtained is shown in Fig. 7, its parameters listed in Table 1. While the waveform visually resembles the target, the numbers show a discrepancy in the highest mode. The dominant limitation preventing an accurate and reproducible synthesis of the target waveform is the lack of both tuning feedback and RF feedback in the present setup, causing the phases to wander. In practice, this is exacerbated by each phase being slightly interdependent with the corresponding amplitude due to imperfections of the RF elements in the HAWG, especially in the highest mode.

The adjustability of the modes turned out to be further limited by multipacting, which could be observed as a vacuum response and intermittent jumps in the cavity field for

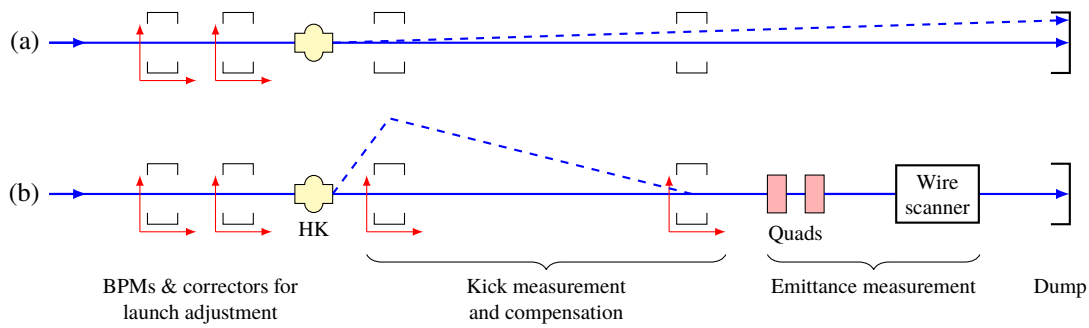


Figure 4: Conceptual sketch of the beam line for the kicker test. Part (a) shows the essential components of the setup for measuring only the deflection, while part (b) includes a kick correction with two steerers to restore the orbit for consistent quad scans. The dashed line represents the beam orbit with the kicker turned on; it is exaggerated for clarity in the bottom figure.

ISBN: 978-3-95450-236-3 ISSN: 2673-5350 doi:10.18429/JACoW-IBIC2023-TUP031

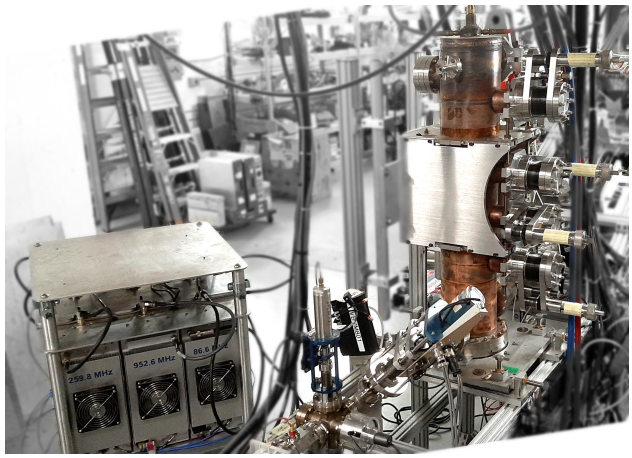


Figure 5: Harmonic kicker installed in the UITF beam line with the HAWG next to it.

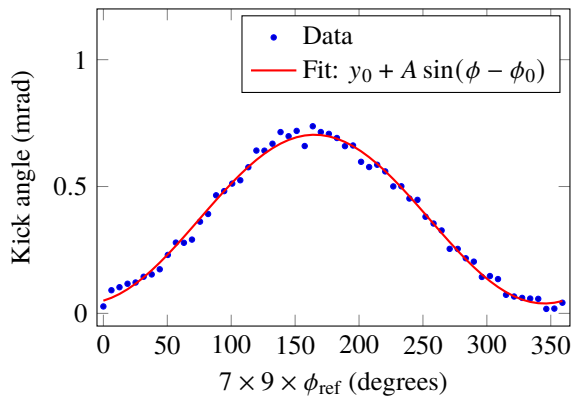


Figure 6: Deflection waveform with only the 9th harmonic (779.4 MHz) being driven at nominally 50 % output power. The phase ϕ_{ref} being scanned is that of the 12.4 MHz reference and is scaled up accordingly for clarity. The beam angle is not explicitly corrected to give zero with the cavity off. $y_0 = 0.372(3)$ mrad, $\phi_0 = 75.1(7)°$, $A = 0.333(4)$ mrad.

several different combinations of RF parameters. While our attempts to process out the multipacting between beam shifts were unsuccessful, it is not expected to be present at higher levels of drive power as needed for the beam momenta of practical applications.

Transverse Phase Space

As is the case for all deflecting cavities, the time-dependent deflecting field of the harmonic kicker will transform the spread of arrival times—i.e., the bunch length—into a spread of transverse angles, deteriorating the 2-d emittance if the bunch length is significant compared to the temporal slope of the field around the central bunch phase. Multipole components of the field will further affect the transverse phase space if the transverse beam size is significant. As a sanity check to verify that neither effect is visible with the default bunch length of the UITF and an optics setup that ensures $\sigma_{x,y} \ll 1$ mm, we performed quad scans at the end of the line at different cavity phases, correcting for

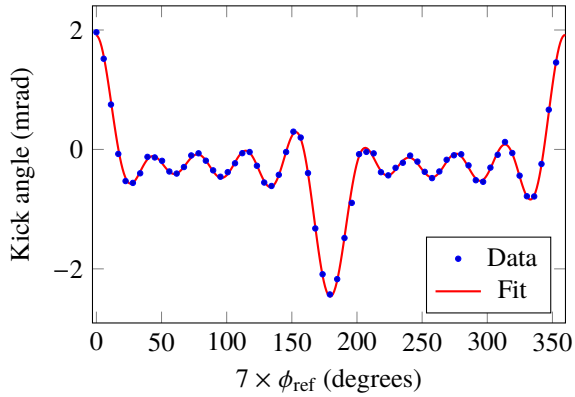


Figure 7: Deflection waveform with all five modes powered and optimized.

the deflection with steering coils. The results are listed in Table 2, showing no measurable impact on transverse phase space regardless of kicker phase; the point at 0° is at peak deflection, whereas that at 15.4° is at maximum negative slope.

Table 2: Downstream Twiss Parameters in the Deflecting Plane of the Kicker

$7\phi_{\mathrm{ref}}$	α	β (m)	ϵ (nm)
off	-9.9	21.4	26.3
0°	-9.6	19.9	26.7
15.4°	-9.5	20.0	24.4

CONCLUSION

We successfully operated the harmonic kicker with all five modes and performed a beam-based measurement and optimization of the deflection waveform, finding no unexpected issues other than multipacting. We expect the technical limitations of the drive circuit to be fully resolved by ongoing development efforts, making harmonic kicker cavities a viable option for future accelerator designs.

REFERENCES

[1] S. Benson *et al.*, "Development of a Bunched Beam Electron Cooler Based on ERL and Circulator Ring Technology for the Jefferson Lab Electron-Ion Collider," in *Proc. of Workshop on Beam Cooling and Related Topics (COOL'17)*, Bonn, Germany, 2018, pp. 72–76. doi:10.18429/JACoW-COOL2017-WEM12

[2] G. T. Park, J. Guo, R. A. Rimmer, H. Wang, and S. Wang, "Beam exchange of a circulator cooler ring with an ultrafast harmonic kicker," *Phys. Rev. Accel. Beams*, vol. 24, no. 6, p. 061 002, 2021. doi:10.1103/PhysRevAccelBeams.24.061002

[3] F. Willeke and J. Beebe-Wang, "Electron ion collider conceptual design report 2021," 2021. doi:10.2172/1765663

Content from this work may be used under the terms of the CC-BY-4.0 licence (© 2023). Any distribution of this work must maintain attribution to the author(s), title of the work, publisher, and DOI

ISBN: 978-3-95450-236-3 ISSN: 2673-5350 doi:10.18429/JACoW-IBIC2023-TUP031

[4] S. Overstreet *et al.*, "Manufacturing the Harmonic Kicker Cavity Prototype for the Electron-Ion Collider," in *Proc. NA-PAC'22*, Albuquerque, NM, USA, 2022, pp. 601–603. doi:10.18429/JACoW-NAPAC2022-WEZD6

[5] Y. Huang, H. Wang, R. A. Rimmer, S. Wang, and J. Guo, "Multiple harmonic frequencies resonant cavity design and half-scale prototype measurements for a fast kicker," *Phys. Rev. Accel. Beams*, vol. 19, no. 12, p. 122 001, 2016. doi:10.1103/PhysRevAccelBeams.19.122001

[6] B. F. Roberts, *Harmonic Combiner and Divider*, US patent 11 303 005, 2022.

[7] M. Bruker *et al.*, "Operational Experience of the New Booster Cryomodule at the Upgraded Injector Test Facility," in *Proc. NAPAC'22*, Albuquerque, NM, USA, 2022, pp. 640–643. doi:10.18429/JACoW-NAPAC2022-WEPA12

Content from this work may be used under the terms of the CC-BY-4.0 licence (© 2023). Any distribution of this work must maintain attribution to the author(s), title of the work, publisher, and DOI

ISBN: 978-3-95450-236-3 ISSN: 2673-5350 doi:10.18429/JACoW-IBIC2023-TUP034

AXIAL CRYOGENIC CURRENT COMPARATOR (CCC) FOR FAIR

L. Crescimbeni†[1], F. Schmid[1], Friedrich-Schiller-University Jena, Jena, Germany
D. M. Haider, A. Reiter, M. Schwickert, T. Sieber
GSI Helmholtz Centre for Heavy Ion Research, Darmstadt, Germany
M. Schmelz, R. Stolz[3], V. Zakosarenko[4], Leibniz IPHT, Jena, Germany
T. Stoehlker[1,2], V. Tympel[1], Helmholtz Institute Jena, Jena, Germany
[1]also at GSI Helmholtz Centre for Heavy Ion Research, Darmstadt, Germany
[2]also at Institute for Optics and Quantum Electronics, Jena, Germany
[3]also at Technical University Ilmenau, Ilmenau, Germany
[4]also at supracon AG, Jena, Germany

Abstract

The Cryogenic Current Comparator (CCC) is a superconducting device based on an ultrasensitive SQUID (superconductive quantum interference device) magnetometer (fT range). Measuring the beam azimuthal magnetic field, it provides a calibrated non-destructive measurement of beam current with a resolution of 10 nA or better, independent from ion species and without tedious calibrations procedure. The non-interceptive absolute intensity measurement of weak ion beams (< 1 µA) is essential in heavy ion storage rings and in transfer lines at FAIR. With standard diagnostics, this measurement is challenging for bunched beams and virtually impossible for coasting beams. To improve the performance of the CCC detector several upgrades are under study and development: One is the investigation of a new type of CCC using an alternative magnetic shield geometry. The so-called "axial" geometry will allow for much higher magnetic shielding factor, an increased pick-up area, and a reduced low frequencies noise component. Further improvements and optimizations of the detector will be presented. The CCC will be tested on the beamline at the end of 2023 allowing to define the best possible version for FAIR.

INTRODUCTION

After proof of principle with an earlier CCC version [1], the first prototype of CCC for GSI and FAIR is the FAIR-Nb-CCC-xD (Fig. 1) that is part of the family of CCC-XD that has been developed for the use with the beamline dimensions at FAIR HEBT (Ø 150 mm).

The CCC is installed in a beam-line cryostat [2] equipped with a helium reliquifier¶ that provides stable operating conditions.

The CCC has been tested in CRYRING@ESR [3] confirming the viability of the detector and its current resolution in the order of nA. The test in CRYRING@ESR has shown some limitation of the system like the limited slew rate and the low magnetic shielding. The CCC prototype is built out of niobium, causing high costs and several mechanical difficulties in the construction process (for example the needing of electron beam wielding). Other than this, the FAIR-Nb-CCC-xD is equipped with a high permeability core, that produces low frequencies noise (due to trapped magnetic field) and introduces the need of a low pass circuit to avoid resonances, reducing the maximum bandwidth of the system.

To improve these aspects of the detector a new version of the CCC, with an axial geometry, has been developed.

NEW AXIAL CORELESS CCC

A new type of CCC, developed together with IPHT Jena, will be built out of lead with an axial shield geometry and without a high permeability core (Fig. 1).

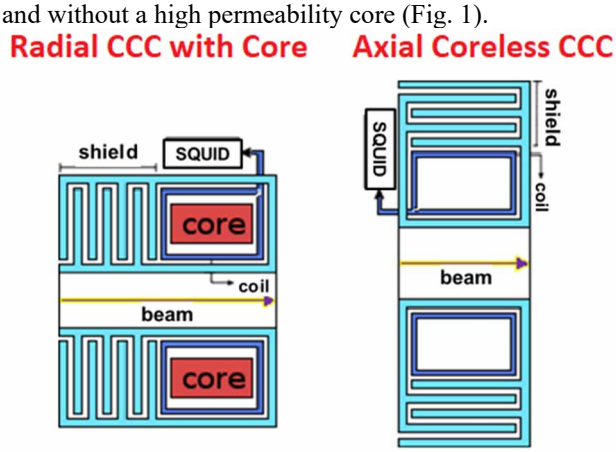


Figure 1: Left: Radial Geometry, like the FAIR-Nb-CCC-xD, with high permeability core. Right: Axial geometry coreless CCC, made of lead, the pickup coil is filled only with non magnetic foam for structural support.

The axial CCC is expected to be less sensitive to external perturbations, in particular very low-frequency noise (<1 Hz), caused by magnetic field caught inside the core material [4], and less sensitive to mechanical perturbation.

The new coreless lead CCC will have a much higher screening factor due to the axial magnetic shield composed of 10 layers of lead sheet [5]. The simulation shows a theoretical screening factor higher than 200 dB, reducing the effect of a magnetic perturbation in the order of 10 µT

*Work supported by AVA – Accelerators Validating Antimatter the EU H2020 Marie-Curie Action No. 721559 and by the BMBF under contract No 05P21SJRB1.
†l.crescimbeni@gsi.de
¶Model PT415 from Cryomech Inc, Syracuse, NY, USA

Content from this work may be used under the terms of the CC-BY-4.0 licence (© 2023). Any distribution of this work must maintain attribution to the author(s), title of the work, publisher, and DOI

ISBN: 978-3-95450-236-3 ISSN: 2673-5350 doi:10.18429/JACoW-IBIC2023-TUP034

Content from this work may be used under the terms of the CC-BY-4.0 licence (© 2023). Any distribution of this work must maintain attribution to the author(s), title of the work, publisher, and DOI

(amplitude similar to the dipole ramp perturbation observed with the CCC at CRYRING@ESR) to a level below detection threshold of the detector.

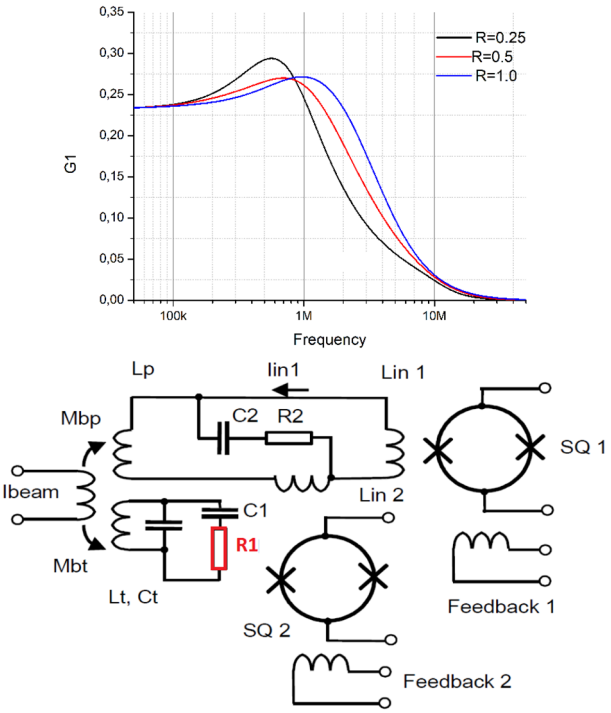


Figure 2: Simulations of the transfer function for CN4 SQUID and schematic of the two parallel squid system. Upper: CN4 squid transfer function. Lower: Circuit Schematic, can be seen the two squids and their feedback system, the damping circuit has been added to avoid resonance peaks in the frequency of interest. The chosen value for the resistance is 0.5 Ohm, to provide the smoothest gain without decreasing the bandwidth.

The improved screening factor, together with the expected lower sensitivity to low-frequency perturbation should increase the sensitivity of the detector in the accelerator environment. This new CCC will be equipped with a parallel SQUID system (Fig. 2), a sensitive SQUID with a lower bandwidth (type CN4, Leibniz IPHT/supracon AG) and a higher bandwidth SQUID with lower sensitivity (type CN2, same provider).

The parallel use of two SQUIDs refers to the introduced cascade principle [6]. The two parallel SQUID system, thanks to the higher bandwidth, will allow to sensibly improve the slew rate of the detector without introducing additional filtering elements, so without decreasing the resolution due to additional thermal noise, (as it was done for the FAIR-Nb-CCC-xD in CRYRING [3]).

PROTOTYPE CONSTRUCTION

The first prototype of the axial coreless CCC has been built in collaboration with IPHT Jena (Fig. 3).

The first part that has been built were the 10 layers meander structure, composing the magnetic shielding. The external meander is built out of a 1 mm pb sheet, placed on the inside of a 250 mm radius fiberglass cylinder to provide structural integrity. The internal structure of 9 meanders are instead built out of 0.25 mm thick Pb-Sl sheet, overlapped with thin electric-insulation layers. The meander structure is then connected to the upper and lower surface of the CCC, built out of 1.5 mm Pb sheets.

At the end of the meander structure the pickup-coil has been built up, in this process two coils of 0.25 mm thickness Pb-Sl sheet are wrapped around a structure composed of XPS Polystyrene foam to provide the required stabilization.

The meanders and the pickup coil are then enclosed in a fiberglass cylinder of 320 mm to provide rigidity to the system and protect it from deformation due to handling during test and installation. The structure is then completed with a last layer of 1 mm Pb sheet that connects the upper and the lower extremity of the CCC.

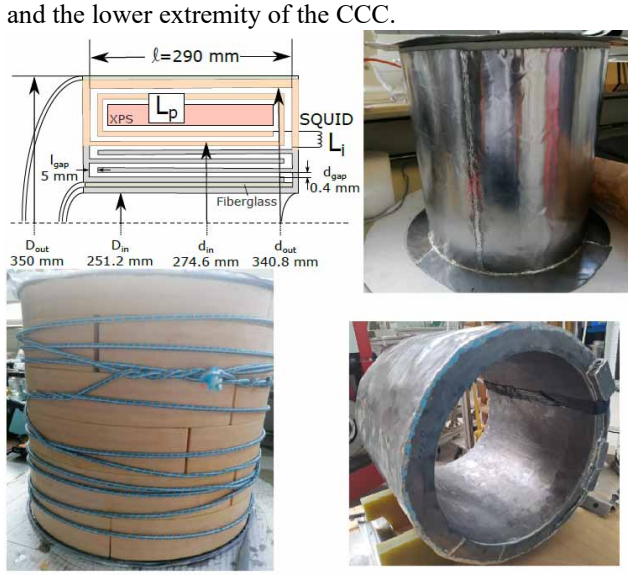


Figure 3: Construction steps of axial CCC. Up left: Scheme of axial CCC. Up right: First meander of the meander structure, the fiberglass cylinder can be seen on the upper part. Down Left: XPS support structure for the pickup coils during assembly. Down Right: Axial lead CCC completed, on the upper corner it's also possible to see the squid box.

The Pickup coil is finally connected through two Pb strips to the squid box installed on top of the CCC. The Pb box in which the SQUIDs are enclosed is necessary to shield them from external magnetic fields.

All the soldering has been performed with Pb-Sn material, to make sure that also the soldering connection are superconductive, and the insulant is kept in place by cryo-glue.

FIRST TEST OF AXIAL CORELESS CCC

The Axial CCC has first been tested in the laboratory at FSU Jena (Fig. 4). This test has allowed us to measure the performance of the detector in a controlled environment. The following measurement steps have been performed to stepwise characterize the properties of the axial CCC:

ISBN: 978-3-95450-236-3 ISSN: 2673-5350 doi:10.18429/JACoW-IBIC2023-TUP034



Figure 4: Left: FSU Jena Laboratory with wide-neck cryostat. Right: Axial coreless CCC during installation, the squid box and the cabling is also visible on the top of the CCC. The white windings on the cryostat are the Helmholtz coils for the magnetic shield test. The CCC is at rest in the bottom part of the cryostat.

Current resolution: Using the calibration line of the cryostat it was possible to estimate the current resolution of the system, around 10 nA (Fig. 5).

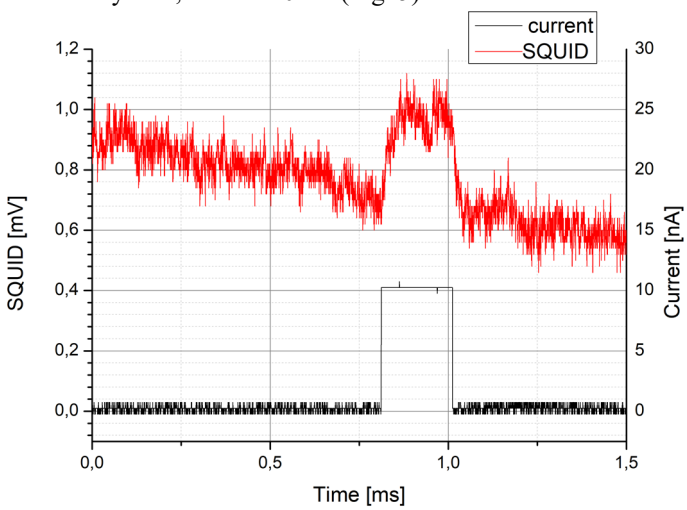


Figure 5: Current resolution of CN4 squid: The black waveform is the rectangular waveform used as input, the red waveform is the squid signal. Maximum current resolution is around 10 nA, lower signal can't be distinguished over the noise floor.

There are two main reason for this low current resolution compared to classical CCC [1 nA]:

- Less coupling of the pickup to the magnetic field of the beam due to the lack of the high permeability core
- Higher noise component at higher frequencies, the noise floor measured with the axial CCC (around 5-10 nA) is unexpectedly more than ten times higher than the noise floor measured in the lab with radial core CCCs, because of low-pass filtering, which is not present in the axial CCC. The low-pass filter is required to avoid resonances, due to the high magnetic permeability core inductance, that together with the capacity of the magnetic shield meander structure behave as an LC circuit. In the coreless CCC the inductance of the pickup coil is much lower, so the low-pass filter is not needed. The resonance frequency of the system is much higher than the maximum bandwidth of the used squids.

Slew Rate: A first estimation of the slew rate has been performed in the cryostat in Jena, estimating the value at around 4 μA/μS, a strong improvement from the 0.16 μA/μS of the FAIR-nB-CCC-xD [3]. It will be possible to reach higher slew rates with further optimization of the hardware (like squid cabling) or of the squid circuit. This will allow to use the CCC for monitoring a higher spectrum of signals without decreasing the current resolution.

Magnetic Shielding: The FSU cryostat is equipped with a pair of Helmholtz coils (Fig. 4) to provide a magnetic field up to 1 mT. The previous test of the FAIR-Nb-CCC-xD has shown a quite high sensitivity to external magnetic field. In CRYRING@ESR the dipole field (~100 μT) produced a signal from the SQUID in the order of 10 nA. For the axial CCC we were not able to detect any squid response to the external magnetic field of 1 mT. Only using a waveform generator to drive the Helmholtz coil we were able to distinguish a small response in the frequency spectrum of the noise, estimating a SQUID signal lower than 0.1 nA. This result doesn't allow to calculate the exact screening factor of the axial CCC or even to verify a theoretical value of ~200 dB (which is anyway not feasible), but it is good enough to confirm that the new shield geometry strongly improves the magnetic screening factor, effectively removing external magnetic fields from the CCC signal.

TEST OF AXIAL CCC IN THE BEAM-LINE CRYOSTAT AT GSI

We proceeded to install the axial CCC in the beam-line cryostat in GSI (Fig. 6). Even if the test in the well shielded laboratory Jena was successful, the high noise component we found there has arisen some worries, which unfortunately found confirmation in the test.

The sensitive squid has shown a very unstable V-ϕ characteristic (Fig. 7), obtained by applying a well defined signal to a coil wound around the SQUID or to the calibration line. This produces a 'calibration' field that is used to obtain the modulation of the squid (in Volt) as a function of the applied field (ϕ).

The working point of the squid in the Flux Looked Loop (FLL) mode is set where the characteristic curve crosses the zero voltage line. To have a stable working point that allows to use the squid in the FLL mode, which is essential for the data acquisition, the characteristic curve

Content from this work may be used under the terms of the CC-BY-4.0 licence (© 2023). Any distribution of this work must maintain attribution to the author(s), title of the work, publisher, and DOI

ISBN: 978-3-95450-236-3 ISSN: 2673-5350 doi:10.18429/JACoW-IBIC2023-TUP034

should cross the zero line in a definite point. If the characteristic curve is not stable due to excessive noise, like at our measurement shown in Fig. 6, it is impossible to define a stable working point for the squid.

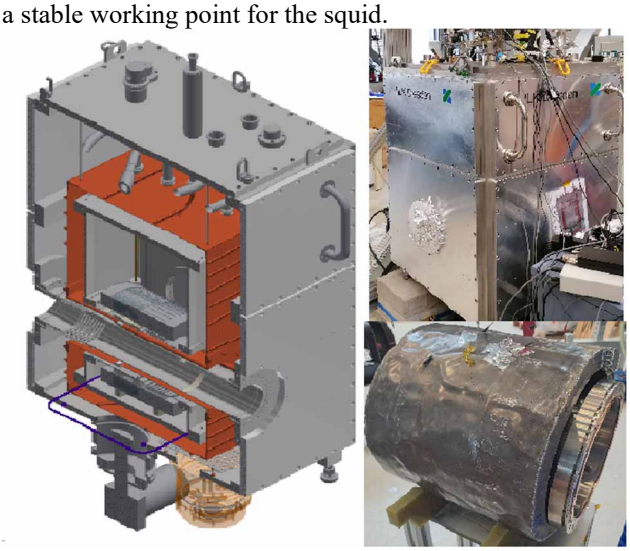


Figure 6: GSI setup, left: cryostat scheme, upper right: cryostat vacuum vessel, lower right: picture of the CCC during installation. The CCC is installed over the He-container tube, the thermal shield tube and finally the UHV tube of the beamline.

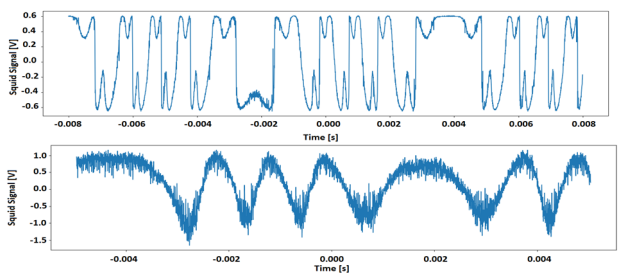


Figure 7: Upper: Squid characteristics in the laboratory in Jena. Lower: Squid characteristic at GSI cryostat. It's possible to see how the characteristic has a deformed shape in respect to the optimal one measured in Jena, moreover the noise has in some points almost half of the full amplitude of the characteristic curve. With a noise component so high the characteristic is very unstable and it's not possible to find a stable working point

The test at GSI has shown that the axial coreless CCC is currently not a valid detector for installation in the beamline cryostat. The absence of a stable working point makes it impossible to perform beam measurement with the CCC.

It was only possible to use the low sensitivity SQUID, that can work independently of the FLL mode, to collect information on the noise (estimated to be higher than 1 µA, around 50 times higher than the noise floor of the classical radial CCC with core). Further investigations will mainly use the low sensitivity SQUID to get a better understanding how the noise couples that strongly to axial coreless CCC and also why the noise is much higher than expected.

CONCLUSION AND NEXT STEPS

The test of the axial coreless CCC has highlighted the issues of the prototype, in particular the low coupling with the beam field due to the lack of the core that together with the high noise floor level, especially at higher frequencies, make the prototype not able to work in the accelerator environment. The test at FSU Jena laboratory has, however, confirmed the validity of the axial magnetic shielding and the effectiveness of the squid cascade system to improve the slew-rate of the detector.

Even if it is confirmed that the axial coreless CCC will not be the solution for FAIR, we are able to use the information achieved on the effectiveness of the axial geometry and the squid cascade system to develop a new prototype of CCC of axial geometry, the Double Core axial CCC, inspired on the design of the CCC Sm (Smart & small) [7].

At the end of 2023 the FAIR-nB-CCC-xD will be tested on the beam line at GSI, allowing us to perform a final test of the cryostat and of the detector on the transfer lines, as they will be used in FAIR. In the first half of 2024 we will test the first prototype of the double core axial CCC in the laboratory, followed by a beamline test in summer 2024.

REFERENCES

[1] A. Peters *et al.,* "A Cryogenic Current Comparator for the absolute Measurement of nA Beams", *AIP Conf. Proc. 451*, pp.163-180, 1998.

[2] D. M. Haider *et al.*, "Versatile Beamline Cryostat for the Cryogenic Current Comparator (CCC) for FAIR", in *Proc. IBIC'19*, Malmö, Sweden, Sep. 2019, pp. 78-81. doi:10.18429/JACoW-IBIC2019-MOPP007

[3] L. Crescimbeni *et al.*, "The Cryogenic Current Comparator at CRYRING@ESR", in *Proc. IBIC'22*, Kraków, Poland, Sep. 2022, pp. 300-303. doi:10.18429/JACoW-IBIC2022-TUP31

[4] V. Zakosarenko *et al.*, "Coreless SQUID-based cryogenic current comparator for non-destructive intensity diagnostics of charged particle beams", *Supercond. Sci. Technol.,* vol. 32, p. 014002, 2018. doi:10.1088/1361-6668/aaf206

[5] H. De Gersem, N. Marsic *et al.,* "Finite-element simulation of the performance of a superconducting meander structure shielding for a cryogenic current comparator*", Nucl. Instrum. Methods Phys. Res. Sect. A,* vol. 840, pp. 77–86, 2016. doi:10.1016/j.nima.2016.10.003

[6] T. Schönau and M. Schmelz, *et al.,* "SQUID-based setup for the absolute measurement of the Earth's magnetic field", *Supercond. Sci. Technol.,* vol. 26, number 3, p. 035013, 2013. doi:10.1088/0953-2048/26/3/035013

[7] V. Tympel *et al.*, "Creation of the First High-Inductance Sensor of the New CCC-Sm Series", in *Proc. IBIC'22*, Kraków, Poland, Sep. 2022, pp. 469-472. doi:10.18429/JACoW-IBIC2022-WEP30

Content from this work may be used under the terms of the CC-BY-4.0 licence (© 2023). Any distribution of this work must maintain attribution to the author(s), title of the work, publisher, and DOI

ISBN: 978-3-95450-236-3 ISSN: 2673-5350 doi:10.18429/JACoW-IBIC2023-TUP035

MULTI-TILE ZINC-OXIDE-BASED RADIATION-HARD FAST SCINTILLATION COUNTER FOR RELATIVISTIC HEAVY-ION BEAM DIAGNOSTICS: PROTOTYPE DESIGN AND TEST*†

M. Saifulin[1,‡], P. Boutachkov, C. Trautmann[1], B. Walasek-Höhne
GSI Helmholtz Center for Heavy Ion Research, Darmstadt, Germany
P. Rodnyi, I. Venevtsev, Peter the Great Polytechnic University, St. Petersburg, Russia
E. Gorokhova, JSC S.I. Vavilov State Optical Institute, St. Petersburg, Russia
[1]also at Technical University Darmstadt, Darmstadt, Germany

Abstract

This contribution summarizes the design and performance test of a prototype radiation-hard fast scintillation detector based on the indium-doped zinc oxide ceramic scintillator, ZnO(In). The prototype detector has been developed for use as a beam diagnostics tool for high-energy beam lines of the SIS18 synchrotron at the GSI Helmholtz Center for Heavy Ion Research GmbH. The new detector consists of multiple ZnO(In) scintillating ceramics tiles stacked on the front and back sides of a borosilicate light guide. The performance of the detector was tested in comparison to a standard plastic scintillation detector with 300 MeV/u energy ^{40}Ar, ^{197}Au, ^{208}Pb, and ^{238}U ion beams.

The investigated prototype exhibits 100% counting efficiency and radiation hardness of a few orders of magnitude higher than the standard plastic scintillation counter. Therefore, it provides an improved beam diagnostics tool for relativistic heavy-ion beam measurements.

INTRODUCTION

The heavy-ion accelerator facility at the GSI Helmholtz Center for Heavy Ion Research (Darmstadt, Germany) and other similar ion-beam facilities worldwide provide energetic heavy-ion beams for a wide range of research purposes, including fundamental nuclear and particle physics, atomic and plasma physics, material sciences, radiation biology, and cancer therapy research.

Various diagnostics systems are used to measure heavy-ion beam parameters to ensure the safety and reliability of the accelerator facility operation, as well as to optimize the beam delivery to the experimental locations. For example, this includes beam position, profile, intensity, energy, and emittance measurements.

The information provided by the beam diagnostics tools is used by the operating team for the online feedback controls of the accelerator and beam transfer lines. This helps to maintain the desired quality and stability of the beam. The beam diagnostics systems are also used by experimental users directly for the characterization and calibration of the experimental setups, which require precise knowledge of the incoming beam parameters.

In particular, at the high-energy beam transfer lines (HEST) of the GSI facility, the intensity of heavy-ion beams slowly extracted from the SIS18 synchrotron is measured using three different detector types (particle detector combination, PDC): scintillation counter (SC), ionization chamber (IC) and secondary electron monitor (SEM). Each detector type is used to cover a specific range of beam intensity [1].

Plastic scintillation counters based on BC-400 (Saint Gobain), or EJ-212 (Eljen Technology) scintillators are currently used as a part of the HEST ion beam intensity diagnostics, covering counting rates in the range up to 1×10^6 ions/s. The heavy-ion beams induce a large amount of radiation damage when passing through the plastic scintillator. This leads to frequent detector services where plastic scintillators are exchanged, which is highly undesirable from an operational point of view.

In this work, we investigated an alternative to the plastic scintillation counter, that could provide less frequent detector maintenance through the use of a more radiation-hard scintillator. We developed a new detector prototype based on indium-doped zinc oxide (ZnO(In)) ceramic scintillator. We report on the new prototype design and performance, which was evaluated experimentally through in-beam tests and simulations using the OpenGATE [2].

ZINC OXIDE CERAMIC SCINTILLATOR

Zinc oxide (ZnO) is a well-known inorganic compound used in various applications [3–5]. In particular, it has been used for the detection of X-rays and α-particles [6–9].

ZnO exhibits two luminescence bands when excited by light or ionizing radiation: (1) emission in the ultraviolet (UV) spectral range (~390 nm) with a short scintillation decay time (<1 ns), and (2) emission in a broad-band with a maximum around 550 nm wavelength (green luminescence) with a longer decay time (>1 µs). The green luminescence is unsuitable for fast-counting applications. Therefore, it is avoided either by annealing in a reducing environment or doping with a group 3A element impurities, such as Al, Ga, or In [3, 10, 11].

In-doped and Ga-doped ZnO ceramics prepared by uniaxial hot pressing in vacuum have been investigated as promising scintillators for fast heavy ion counting appli-

* The results presented in this contribution are based on the work performed before the 24th of February 2022.
† DLR funded this work within the ERA.Net RUS Plus Project RUS_ST2017-051.
‡ m.saifulin@gsi.de (corresponding author)

Content from this work may be used under the terms of the CC-BY-4.0 licence (© 2023). Any distribution of this work must maintain attribution to the author(s), title of the work, publisher, and DOI

ISBN: 978-3-95450-236-3 ISSN: 2673-5350 doi:10.18429/JACoW-IBIC2023-TUP035

Content from this work may be used under the terms of the CC-BY-4.0 licence (© 2023). Any distribution of this work must maintain attribution to the author(s), title of the work, publisher, and DOI

cations [12–15]. They exhibit orders of magnitude higher radiation hardness than plastic scintillators, and thus can provide longer exploitation time before scintillator replacement is required. Furthermore, narrow signals with the pulse width below 1 ns can be obtained, when ZnO(In) scintillation is registered with a fast photomultiplier tube. This resolves pile-up limitations for the micro-spill structure measurements [13].

The fast scintillation component in ZnO is located close to its self-absorption edge. Thus, the detection of fast scintillation photons through a few millimeters thick ZnO is not efficient. This peculiarity and difference compared to standard plastic scintillators have been considered in the new ZnO-based prototype detector design.

PROTOTYPE DETECTOR DETAILS

Prototype Detector's Parts

The detector consists of three main components: the active volume, the light guide, and the photosensor, as shown in Fig. 1.

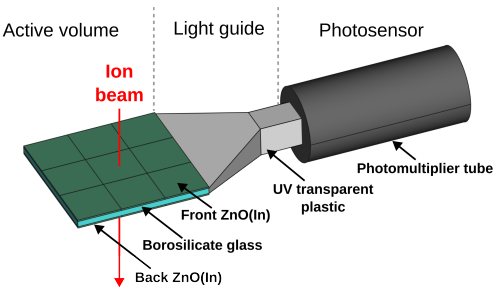


Figure 1: Schematic view of the multi-tile ZnO-based scintillation counter prototype.

The active volume is the central part of the detector that directly interacts with the incident ion beam. It consists of square-shaped scintillator tiles made of ZnO(In), stacked on both the front and back sides of a borosilicate glass plate. When the ion beam passes through the active volume, it deposits part of its energy in the scintillator and borosilicate glass layers, leading to the emission of scintillation light.

The scintillation mainly comes from ZnO(In) layers, as they efficiently convert the deposited energy into light photons. Due to self-absorption, the scintillation photons mainly go out from the material through the surfaces where ions enter and exit the scintillating tile. The borosilicate glass, which is transparent to scintillation photons from ZnO(In), acts as a light guide, assisting in collecting scintillation light from the ZnO(In) surfaces. This arrangement enables the extraction of scintillation photons from the active volume.

An additional light guide made of UV-transparent plastic is used to match the shapes of the borosilicate glass and photosensor. Optical silicon (Momentive, RTV-615) improves light coupling between the plastic light guide and both borosilicate glass output and photosensor input.

The photosensor, responsible for converting scintillation light into an electrical output signal, consists of a photomultiplier tube (PMT, Hamamatsu R6427).

The active volume and the light guide are fixed on a 3D-printed holding structure and wrapped with Teflon to improve light collection and black tape to avoid penetration of any external light.

In the design of the new ZnO-based scintillation counter, only the active volume component is replaced, while the plastic light guide and photomultiplier tube remain unchanged compared to the standard plastic scintillation counter for GSI beam diagnostics. This design approach ensures the proven performance and compatibility with existing plastic scintillation counter components, while introducing the enhanced scintillation properties of ZnO(In) in the active volume.

Materials of the Active Volume

The 0.046 at.% In^{3+} doped ZnO ceramic scintillators have been produced at the Joint Stock Company "Research and Production Corporation S.I. Vavilova" (St. Petersburg, Russia) using the uni-axial hot pressing in vacuum. The obtained ZnO(In) ceramics were polished and cut into $15 \times 15 \times 0.5\,mm^3$ square tiles.

The borosilicate radiation-hard glass (material catalog name BK7G18) was purchased from SCHOTT (Germany) and cut into the $50 \times 50 \times 2\,mm^3$ rectangular shape. The material surfaces had a root-mean-square roughness of 2–4 µm.

The ZnO(In) ceramic tiles and BK7G18 plate are fixed together using a Kapton tape as shown in Fig. 2.

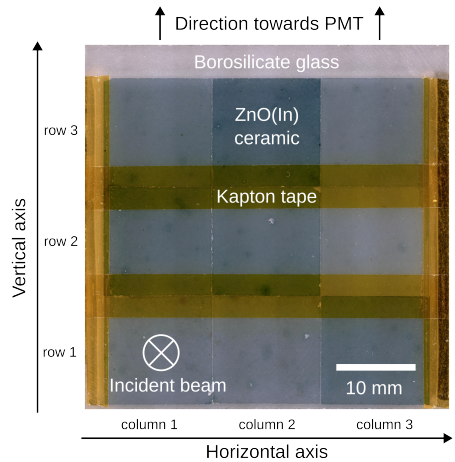


Figure 2: Photograph of the prototype detector's active area. The white crossed circle shows the incident beam direction and the beam spot size in scale with the active area.

EXPERIMENTAL PERFORMANCE TEST

To evaluate the performance of the prototype detector, a series of tests were conducted at GSI using ion beams extracted from the SIS18 accelerator. The experimental parameters are summarized in Table 1.

The ^{40}Ar, ^{197}Au, ^{208}Pb, and ^{238}U ions had an initial energy of 300 MeV/u. Before reaching the entrance of the proto-

ISBN: 978-3-95450-236-3 ISSN: 2673-5350 doi:10.18429/JACoW-IBIC2023-TUP035

Table 1: Experimental Beam Parameters and Photomultiplier Gains Used for the Tests of the Prototype Detector

Ion	Energy, MeV/u	Energy loss, MeV	PMT gain
^{40}Ar	300 [a]	231.85 [c]	2.20×10^6
	297.14 [b]	516.89 [d]	(1300 V)
		240.39 [e]	
^{197}Au	300 [a]	4654.27 [c]	1.15×10^5
	288.62 [b]	10900 [d]	(850 V)
		5499.17 [e]	
^{208}Pb	300 [a]	5006.94 [c]	1.15×10^5
	288.41 [b]	11800 [d]	(850 V)
		5932.97 [e]	
^{238}U	300 [a]	6272.86 [c]	1.15×10^5
	287.32 [b]	14900 [d]	(850 V)
		7586.86 [e]	

[a] SIS18 extraction energy, [b] Energy at the prototype detector entrance, [c] front ZnO(In), [d] borosilicate glass, [e] back ZnO(In)

type detector, the ion beams underwent energy loss. This loss occurs as the beam exits the vacuum chamber through a 100 µm thick stainless-steel window and travels a 40 cm distance through air. To accurately determine the incident beam energies and quantify the energy losses within the detector's active volume layers, the ATIMA code was employed [16]. For the energy loss calculations, we used 5.5 g/cm^3 ZnO(In) and 2.58 g/cm^3 BK7G18 material density.

The ion beam was collimated to a circular spot with a diameter of 5 mm before interacting with the prototype detector. The prototype detector was mounted on a stage capable of horizontal and vertical movement, enabling exposure of different regions of the active volume to the ion beam.

A standard plastic scintillation counter was placed behind the prototype and used as the reference detector.

Output signals from both the prototype and reference detectors were digitized and read out with a high-speed oscilloscope (Tektronix MSO58) with a bandwidth of 2 GHz. The reference detector provided a trigger for the oscilloscope read-out. The counting efficiency of the prototype detector relative to the reference detector was estimated by counting the number of prototype detector signals higher than 50 mV.

The PMT gain of the prototype detector was adjusted so that the maximum amplitude of the signal is of the order of 1 V.

RESULTS AND DISCUSSION

Contribution of Borosilicate Glass Signal

By scanning the incident ion beam near the edge of the prototype's active volume, we collected signals corresponding to ions passing through: (1) only borosilicate glass plate, (2) borosilicate glass with one layer of ZnO(In), and (3) borosilicate glass with two layers of ZnO(In).

As shown in Fig. 3, the scintillation light yield of the borosilicate glass (BSG) is lower compared to the ZnO(In)

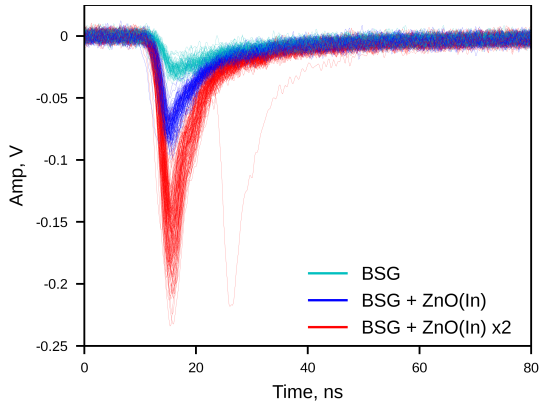


Figure 3: Signals of the prototype detector exposed to 300 MeV/u Au ion beam at the edge of the active volume.

scintillator. In the case of Au ion irradiation, the signal amplitude from the borosilicate glass layer is around 30 mV, while the signal amplitude from borosilicate glass with one layer of ZnO(In) is almost 3 times larger. The signal from the borosilicate glass with two layers of ZnO(In) scintillator is roughly 5 times larger than the signal from the borosilicate glass.

Despite the lower energy loss in ZnO(In) compared to borosilicate glass (see Table 1), ZnO(In) scintillation light represents the main part of the output signal amplitude, indicating that it is a brighter scintillator than the BK7G18.

For all three investigated regions, the registered output signals have a rise time of 2.5 ns. This rise time is related to the response of the PMT and has nothing to do with the scintillation material and beam position in the active area.

The use of borosilicate glass provides a solution to overcome the challenge related to the self-absorption of ZnO(In). It provides efficient extraction of scintillation light out from the active volume and, at the same time, it has a negligible contribution to the prototype's output signal.

Prototype Detector Signals Across Active Volume

Figure 4 shows the prototype output signals registered when different ion beams hit the active volume at different locations. We collected 10000 output signals corresponding to individual ions passing through the center of each ZnO(In) scintillating tile located at various horizontal and vertical positions (various columns and rows), as is shown in Fig. 2.

Depending on the beam position, there is no difference in the signals registered along the horizontal axis (fixed row, various columns). In contrary to that, there is a significant change in the output signal amplitude along the vertical axis (fixed column, different rows). The signal amplitude dependency along the vertical axis has a similar trend for all the investigated ion species.

It should be noted that the plastic light guide and PMT are placed along the vertical axis. The higher amplitude signals are registered when the beam hits the active volume closer to the PMT (row 3 in Fig. 4).

Content from this work may be used under the terms of the CC-BY-4.0 licence (© 2023). Any distribution of this work must maintain attribution to the author(s), title of the work, publisher, and DOI

ISBN: 978-3-95450-236-3 ISSN: 2673-5350 doi:10.18429/JACoW-IBIC2023-TUP035

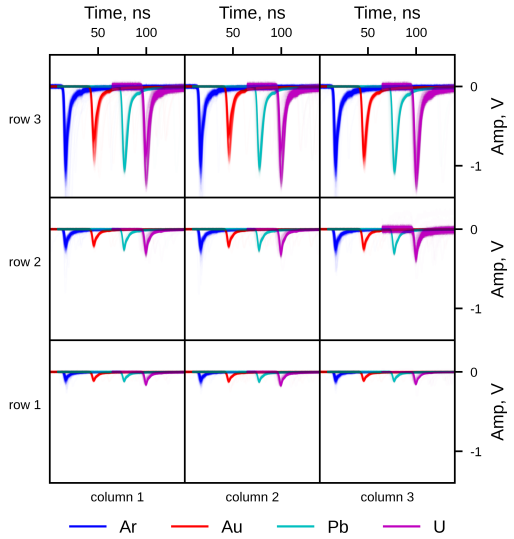


Figure 4: Output signals obtained for various ion beams hitting the prototype detector at different horizontal and vertical positions. Signals of different ion species are shifted on the x-axis for better visibility and comparison. Each subplot corresponds to the center of the scintillating tile in the corresponding column and row, as shown in Fig. 2.

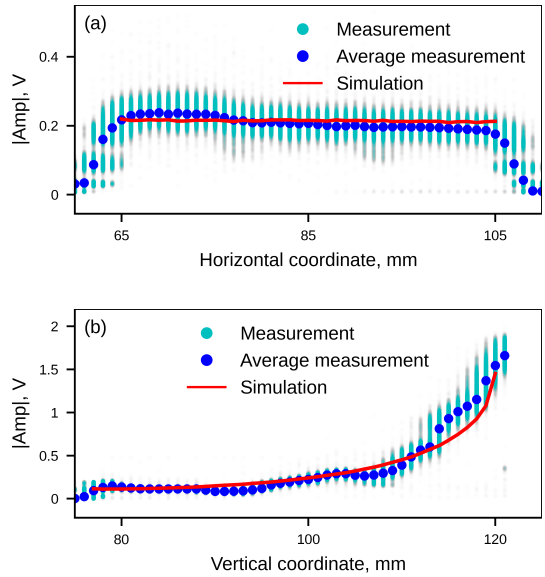


Figure 5: The signal amplitude changes for the 300 MeV/u Au beam incident at various positions on the active volume. Figures (a) and (b) correspond to beam scans along the horizontal and vertical axis, respectively.

Light Propagation Simulation

The propagation of the scintillation light from ZnO(In) through BK7G18 glass was simulated using the OpenGATE [2]. As a result of the simulation, it was found that the ZnO(In) scintillation photons transmission through the BK7G18 glass varies from 2 to 9% depending on the vertical axis coordinate. Figure 5 shows a comparison of the experimentally measured signal amplitude and the simulation result, confirming that the prototype signal amplitude variation is consistent with the ZnO(In) scintillation light transmission through the BK7G18 glass.

Further borosilicate glass plate optimizations (geometry and surface quality) together with OpenGATE simulations are required to find the optimal shape and surface quality of the borosilicate glass to suppress the changes in the output signal amplitude along the vertical axis of the active volume.

Prototype Detector Counting Efficiency

The counting efficiency has been estimated as a ratio of the number of ions counted by the prototype divided by the number of ions counted by the reference detector. Despite the signal amplitude variation in the vertical axis, the prototype detector exhibits 100% counting efficiency relative to the plastic scintillator for all the investigated ion species.

SUMMARY

We developed a new radiation-hard fast scintillation detector prototype based on ZnO(In) transparent scintillation ceramics to be used for relativistic heavy-ion beam intensity diagnostics.

The developed prototype showed 100% counting efficiency relative to the standard plastic scintillation counter when tested with Ar, Au, Pb, and U heavy-ion beams at 300 MeV/u energy. By considering the few orders of magnitude higher radiation hardness of ZnO(In) than plastic scintillator, the new prototype provides an improved beam diagnostics tool.

We observed a spatial dependency of the prototype output signal amplitudes registered when the ion beam hits different positions on the active volume. We showed that this dependency is related to the ZnO(In) scintillation light transmission through the borosilicate glass. The experimentally observed signal amplitude change is in agreement with the light transmission through the borosilicate glass simulated by OpenGATE.

The borosilicate glass, used as a part of the active volume, exhibited scintillation light yield much lower than ZnO(In). Thus, it makes a negligible contribution to the prototype detector output signal and serves mainly as the light guide.

In the current prototype version, we used a rectangular-shaped borosilicate light guide. Further investigations of more complex shapes of the light guide are needed to eliminate the spatial dependency of the output signal.

REFERENCES

[1] P. Forck, P. Heeg, and A. Peters, "Intensity measurement of high-energy heavy ions at the GSI facility," in *AIP Conf. Proc.*, American Institute of Physics, vol. 390, 1997, pp. 422–429. doi:10.1063/1.52298

[2] S. Jan *et al.*, "GATE: A simulation toolkit for PET and SPECT," *Phys. Med. Biol.*, vol. 49, no. 19, p. 4543, 2004. doi:10.1088/0031-9155/49/19/007

Content from this work may be used under the terms of the CC-BY-4.0 licence (© 2023). Any distribution of this work must maintain attribution to the author(s), title of the work, publisher, and DOI

ISBN: 978-3-95450-236-3 ISSN: 2673-5350 doi:10.18429/JACoW-IBIC2023-TUP035

[3] Ü. Özgür *et al.*, "A comprehensive review of ZnO materials and devices," *J. Appl. Phys.*, vol. 98, no. 4, pp. 1–103, 2005. doi:10.1063/1.1992666

[4] C. Klingshirn *et al.*, "65 years of ZnO research–old and very recent results," *Phys. Status Solidi B*, vol. 247, no. 6, pp. 1424–1447, 2010. doi:10.1002/pssb.200983195

[5] R. Sahani and A. Dixit, "A comprehensive review on zinc oxide bulk and nano-structured materials for ionizing radiation detection and measurement applications," *Mater. Sci. Semicond. Process.*, vol. 151, p. 107 040, 2022. doi:10.1016/j.mssp.2022.107040

[6] Q. Zhang *et al.*, "An ultrafast X-ray scintillating detector made of ZnO(Ga)," *J. Instrum.*, vol. 12, no. 12, P12033, 2017. doi:10.1088/1748-0221/12/12/P12033

[7] J. S. Neal, L. A. Boatner, N. Giles, L. Halliburton, S. Derenzo, and E. Bourret-Courchesne, "Comparative investigation of the performance of ZnO-based scintillators for use as α-particle detectors," *Nucl. Instrum. Methods Phys. Res., Sect. A*, vol. 568, no. 2, pp. 803–809, 2006. doi:10.1016/j.nima.2006.09.041

[8] J. S. Neal *et al.*, "Investigation of ZnO-based polycrystalline ceramic scintillators for use as α-particle detectors," *IEEE Trans. Nucl. Sci.*, vol. 56, no. 3, pp. 892–898, 2009. doi:10.1109/TNS.2008.2004702

[9] R. Sahani, C. Kumari, A. Pandya, and A. Dixit, "Efficient alpha radiation detector using low temperature hydrothermally grown ZnO:Ga nanorod scintillator," *Sci. Rep.*, vol. 9, no. 1, pp. 1–9, 2019. doi:10.1038/s41598-019-47732-1

[10] E. Gorokhova *et al.*, "Development and study of ZnO:In optical scintillation ceramic," *J. Opt. Technol.*, vol. 82, no. 12, pp. 837–842, 2015. doi:10.1364/JOT.82.000837

[11] E. Gorokhova *et al.*, "Structural, optical, and luminescence properties of ZnO:Ga optical scintillation ceramic," *J. Opt. Technol.*, vol. 85, no. 11, pp. 729–737, 2018. doi:10.1364/JOT.85.000729

[12] P. Boutachkov *et al.*, "Radiation hardness investigation of Zinc oxide fast scintillators with relativistic heavy ion beams.," in *Proc. IBIC'19*, Malmö, Sweden, Sep. 2019, pp. 71–73. doi:10.18429/JACoW-IBIC2019-MOPP005

[13] P. Boutachkov *et al.*, "Novel Fast Radiation-Hard Scintillation Detectors for Ion Beam Diagnostics," in *Proc. IBIC'22*, Kraków, Poland, 2022, pp. 515–518. doi:10.18429/JACoW-IBIC2022-WE3I1

[14] M. Saifulin *et al.*, "ZnO(In) Scintillation Light Spectra Investigation for Heavy Ion Detector Application," in *Proc. IBIC'22*, Kraków, Poland, 2022, pp. 294–295. doi:10.18429/JACoW-IBIC2022-TUP29

[15] M. Saifulin *et al.*, "Ionoluminescence and optical transmission investigation of ZnO(In) fast ceramic scintillator irradiated with swift heavy ions," *J. Appl. Phys.*, vol. 132, no. 19, p. 195 901, 2022. doi:10.1063/5.0110205

[16] H. Geissel, H. Weick, C. Scheidenberger, R. Bimbot, and D. Gardes, "Experimental studies of heavy-ion slowing down in matter," *Nucl. Instrum. Methods Phys. Res., Sect. B*, vol. 195, no. 1-2, pp. 3–54, 2002. doi:10.1016/S0168-583X(02)01311-3

Content from this work may be used under the terms of the CC-BY-4.0 licence (© 2023). Any distribution of this work must maintain attribution to the author(s), title of the work, publisher, and DOI

ISBN: 978-3-95450-236-3 ISSN: 2673-5350 doi:10.18429/JACoW-IBIC2023-TUP036

CRYOGENIC CURRENT COMPARATORS (CCC) AS LOW INTENSITY DIAGNOSTICS FOR ION BEAMS*

T. Sieber†, D. M. Haider, M. Schwickert, GSI, Darmstadt, Germany
L. Crescimbeni[1], F. Schmidl, Friedrich-Schiller-University Jena, Jena, Germany
M. Schmelz, R. Stolz[3], V. Zakosarenko[4], Leibniz IPHT, Jena, Germany
T. Stoehlker[1,2], V. Tympel, Helmholtz Institute Jena, Jena, Germany
N. Marsic
TEMF, Institute for Theory of Electromagnetic Fields, Technical University, Darmstadt, Germany
J. Tan, CERN European Organization for Nuclear Research, Geneva, Switzerland
[1]also at GSI Helmholtz Centre for Heavy Ion Research, Darmstadt, Germany
[2]also at Institute for Optics and Quantum Electronics, Jena, Germany
[3]also at Technical University Ilmenau, Ilmenau, Germany
[4]also at supracon AG, Jena, Germany

Abstract

The Cryogenic Current Comparator (CCC) is a SQUID based superconducting device for intensity measurement. It was firstly proposed as a beam diagnostics instrument in the mid ´90s at GSI. After prove of principle the CCC was introduced into other facilities, showing great potential for high resolution measurements as well as raising considerable mechanical and cryogenics challenges and costs.

In the course of planning for FAIR the CCC has been revitalized. Systematic investigations started - also involving now commercially available SQUID systems - which led to improvements of detector and cryostat. The developments resulted in nA spill measurements at GSI (2014) followed by the installation of a CCC in CERN Antiproton Decelerator (AD), which has become a key instrument.

Since then optimization of the device is ongoing, with respect to various operating conditions, system robustness, current resolution and last but not least system costs. Alternative CCC versions with improved magnetic shielding have been developed as well as ‚Dual Core' versions for background noise reduction. We give an overview of CCC optimization and development steps, with focus on applications at GSI and FAIR.

INTRODUCTION

The Cryogenic Current Comparator measures the beam intensity via the beam azimuthal magnetic field, which is for nA currents in the fT range. The device consists of a superconducting shielding, which provides an attenuation of non-azimuthal external fields in the range -70 dB to -140 dB, depending on the shield geometry (see below). The shielding guides the superconducting Meissner-Current (compensation current for the beam magnetic field) to the internal pickup loop, which allows for DC measurements as a matter of principle. The pickup loop is basically a one-winding coil around a high permeability ring core, acting as a flux concentrator. The latter is used in the 'classical' CCC shown in Fig. 1 to ensure efficient coupling of the beam magnetic field to the SQUID circuit. The arrangement can be regarded as a transformer with the particle beam being the primary winding and the pickup coil the secondary winding. The signal from the pickup coil is fed (via a matching transformer for impedance matching) to a DC SQUID (Superconducting Quantum Interference Device) magnetometer, which is operated in a compensation circuit, using a so called Flux Locked Loop (FLL) electronics [1]. Figure 1 shows the currently used arrangement, originally developed at the PTB (Physikalisch-Technische Bundesanstalt) [2] and adapted to the accelerator application at GSI [3].

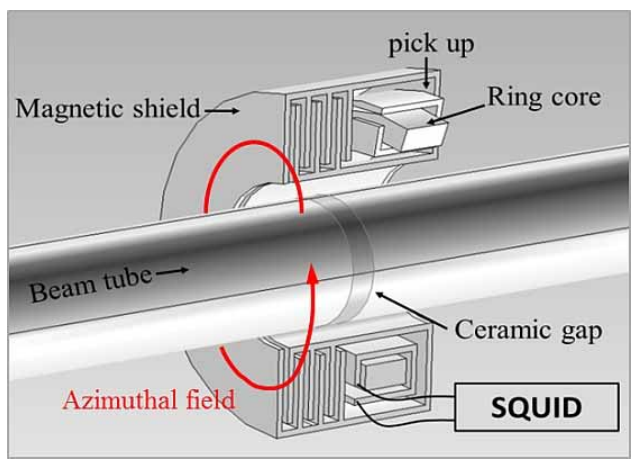


Figure 1: Classical CCC, shielding geometry with radial meanders and high permeability ring core.

Recent developments at IPHT Jena have shown that it is possible to build a CCC without toroidal core, using a shielding with axial meander geometry [4], consequently the device is called coreless or axial CCC (see Fig. 2). This

* supported by BMBF under contracts 05P18RDRB1 and 05P18SJRB1
†T.Sieber@gsi.de

Content from this work may be used under the terms of the CC-BY-4.0 licence (© 2023). Any distribution of this work must maintain attribution to the author(s), title of the work, publisher, and DOI

ISBN: 978-3-95450-236-3 ISSN: 2673-5350 doi:10.18429/JACoW-IBIC2023-TUP036

new shielding/pickup design promised a number of advantages, like reduced magnetic noise and baseline drift (both mainly caused by the toroidal core), significantly reduced costs and weight due to inherent better mechanical stability (which allows for lead as shielding material). Furthermore, the axial structure offers an easy manufacturing and most of all a significantly increased shielding efficiency.

In addition to the two mentioned CCC varieties, a third CCC type is currently under investigation, which combines the axial meander geometry with a doubled classical toroidal core pickup [5]. This version, called the double core CCC or DCCC, is an attempt to combine and improve the positive features, which have been identified at the different CCC systems so far. Figure 2 shows the three CCC types schematically.

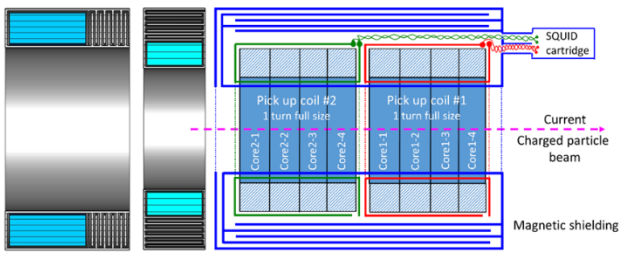


Figure 2: Magnetic shieldings with radial (left) and axial (middle) meanders. The ring-core of the radial CCC is indicated in blue, the detector volume of the axial CCC in turquois. Right: Schematic sectional view of the DCCC with axial meanders and two independent, fourfold segmented (due to material width limitations) toroidal cores.

CLASSICAL (RADAL) CCC

The classical CCC, as it is shown in Fig. 1, has been operated successfully in accelerator beamlines at GSI [6], and CERN [7], measuring currents <10 nA at bandwidths 2-10 kHz. For FAIR, significantly larger detector dimensions are required, therefore a so called CCC-XD (eXtended Dimensions, with inner/outer diameter: 250 mm/350 mm) has been designed and extensively tested in the laboratory [8] and in CRYRING [9]. Although shielding efficiency is anti-proportional to shielding inner diameter, the CCC-XD reached - due to careful shielding design, toroid material choice [10] and sophisticated SQUID electronics and controls [11] - a performance similar or better than its predecessors. The magnetic shielding provides (like for the CERN/AD CCC with inner/outer diameter: 185 mm/280 mm) an attenuation of external fields of -70 dB. It is made from Niobium, which is - regarding its mechanical properties - considered the best choice for CCCs at large dimensions. The much smaller GSI CCC prototype [3] (inner/outer diameter: 147 mm/260 mm) was built from Lead.

The CCC-XD, in combination with its specially designed cryostat [12], was originally considered to be the first of series for five planned CCC systems at FAIR. Nonetheless, already during its construction and assembly, investigations on the coreless axial CCC (see below) started in parallel, with the goal to eliminate unwanted effects (low frequency Barkhausen noise, temperature dependent offset drift, microphony) related to the toroidal core. Moreover, a more efficient magnetic shielding seemed desirable because of the disturbing influence of nearby dipole and quadrupole magnets (see Fig. 3). Despite these drawbacks, the prototype of the CCC-XD was operated successfully in CRYRING@ESR, showing with appropriate filtering of dipole and cryostat effects (see Fig. 3) a current resolution <10 nA at 10 kHz bandwidth. Slew rate problems at higher currents and fast rise-times could be solved by damping the SQUID circuit with an inductive load. Figure 4 shows such a 'high current' measurement in CRYRING with CCC in comparison to standard diagnostics, IPM and DCCT (Bergoz PCT).

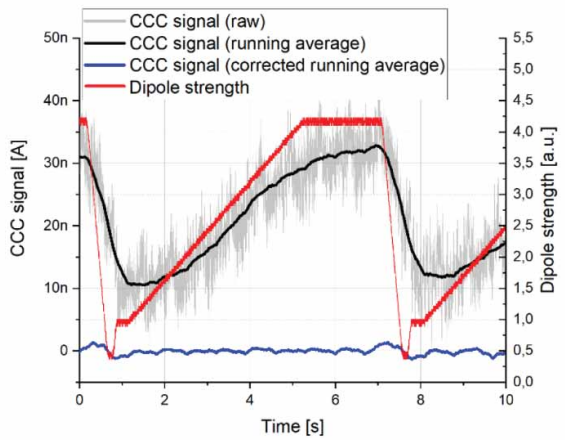


Figure 3: Effect of dipole ramp in CRYRING on CCC-XD measurement. Since the dipole ramp is deterministic it can be subtracted with an appropriate transfer function. The 1.4 Hz pertubation from the cryostat pulse tube cooler, visible on the raw signal, was eliminated by a software bandblock filter (1-3 Hz) [9].

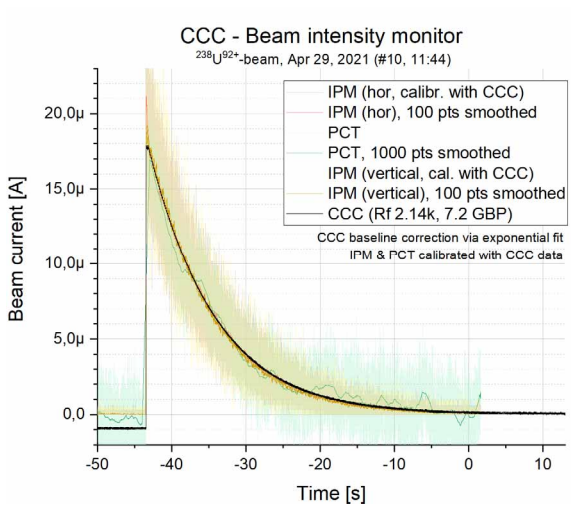


Figure 4: CCC current measurement compared to IPM and PCT in CRYRING. Rf = Feedback resistor value, GBP = Gain Bandwidth Product of the SQUID electronics [9].

Content from this work may be used under the terms of the CC-BY-4.0 licence (© 2023). Any distribution of this work must maintain attribution to the author(s), title of the work, publisher, and DOI

ISBN: 978-3-95450-236-3 ISSN: 2673-5350 doi:10.18429/JACoW-IBIC2023-TUP036

Content from this work may be used under the terms of the CC-BY-4.0 licence (© 2023). Any distribution of this work must maintain attribution to the author(s), title of the work, publisher, and DOI

Independent from parallel and future steps of CCC development, it could be demonstrated in CRYRING that the classical CCC system is appropriate for nA current measurement at slow extracted beams in transfer lines and low intensity exotic ion beams in the storage rings at FAIR. Room for optimization was identified in the requirement of filtering external (periodic) disturbances, the necessary slew rate damping (which reduces current resolution) as well as in the high costs of the system, mainly because of the Niobium shielding.

AXIAL CCC DESIGN

As a solution for some of the above mentioned problems a coreless CCC with axial meander geometry has been proposed by IPHT Jena. In this design the SQUID is directly connected to the inner part of the shielding, which becomes therefore pickup coil and shielding at the same time. Figure 5 shows on the left hand side a cross section of the shielding torus.

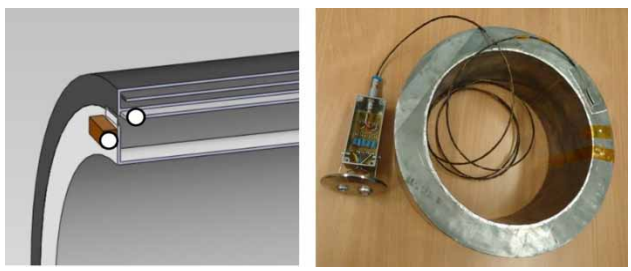


Figure 5: Alternative shielding geometry with axial meanders (left), the SQUID, housed in the little brown box, is connected between the two marked dots. Right: prototype of the Axial CCC made from Lead with attached SQUID electronics.

Compared to the classical CCC, the production of the axial version is much simpler, due to the possibility of wrapping lead sheets around a GFK carrier (compared to electron beam welding of the Niobium meanders). The costs for the shielding/pickup are therefore significantly reduced (to ~1/10). Another big advantage of this design is the improved magnetic shielding. From the analytical model in Ref. [2] as well as from FE simulations [13] it was shown that the shielding efficiency depends basically on the path length of the meanders. Since each of the axial meanders has the full length of the detector, a comparatively small number of meanders is sufficient to provide a much higher damping than with the classical shielding. Realistic values are -140 dB instead of classical -70 dB, the high attenuation factor could be verified in laboratory tests and can to large extent solve the problem of interference from nearby magnetic elements.

Since the high permeability ring core is omitted, the coupling of the axial pickup to the beam is much weaker than in the classical setup. The pickup inductance now depends completely on the detector volume (Fig. 5, left, volume below the meanders) and is in the order of nH, compared to µH with toroidal core. This has on the one hand the advantage of matching the pickup to the SQUID inductance (~10 nH) without necessity of a matching transformer (which might introduce its own thermal noise and slew rate problems), on the other hand, the signal from the beam magnetic field is much weaker (by a factor ~100) and parasitic inductance (e.g. connection cables) play a bigger role. The basic question during axial CCC development was, if the lower signal strength would be compensated by the improved noise properties and SQUID coupling, resulting in an improved SNR. First evidence that this trade off might not work out was the detection of an unexpected high intrinsic noise in the range between 1 Hz and 1 kHz measured on the axial CCC prototype during laboratory tests. Figure 6 shows for comparison a noise spectrum from the CCC-XD (blue) compared to the axial CCC (black). The expected positive effect from the missing core is not evident, even at very low frequencies <1 Hz. Also in the critical region for microphonic effects (~10-100 Hz) the noise of the axial CCC is an order of magnitude higher.

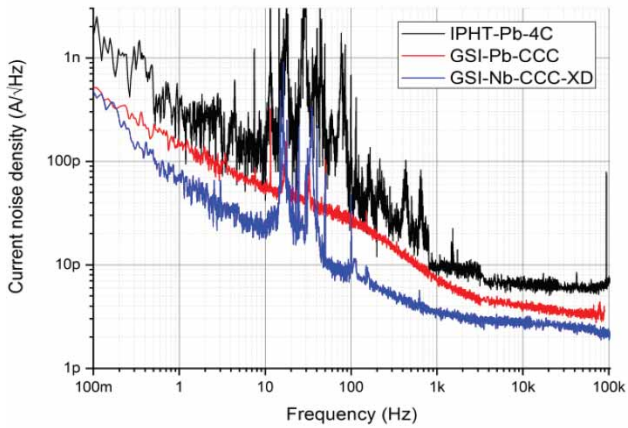


Figure 6: Noise spectra measured at the FAIR CCC-XD (blue), the GSI prototype from [3] (red) and one of the first prototypes of the axial CCC, shown in Fig. 5.

This result is still analyzed and under discussion, damping properties of the matching transformer and the toroidal core might play a bigger role than expected. Also, the exact reproduction of this measurement is quite difficult. Nonetheless, from recent laboratory tests it also seems that the axial pickup is extremely sensitive to rf-disturbances, a kind of influence that can (partially) be shielded in the laboratory, but not in the accelerator environment, since it propagates along the beamtube, through the detector.

A detailed report from development work and latest test measurements can be found in Ref. [14]. The application of the axial detector at FAIR seems at the moment questionable and has to be further investigated. In any case we consider the cost reduction due to axial meander production from Lead and the superior magnetic shielding properties as extremely valuable results from axial CCC development.

DUAL CORE CCC (DCCC)

The DCCC was originally designed to eliminate the low frequency disturbances from magnetization jumps, which have been observed in the Nanoperm© toroidal cores. Since

ISBN: 978-3-95450-236-3 ISSN: 2673-5350 doi:10.18429/JACoW-IBIC2023-TUP036

these jumps occur randomly in each core, they can easily be subtracted from the beam current signal (seen by both pickups/cores simultaneously), which leads to an improved SNR.

Since the CCC-XD for FAIR had so far the best noise behaviour and current resolution, the components chosen for the pickup and SQUID system of the DCCC were identical to the CCC-XD. To combine all advantages our CCC systems have shown so far and to facilitate the production (and reduce costs) the magnetic shielding was designed as an axial type, built from lead, which resulted in a setup like shown in Fig. 2, right. Figure 7 shows a completed prototype of the DCCC with 300 mm outer diameter and closed axial shielding.



Figure 7: DCCC prototype, built from lead with diameter 300 mm and length 600 mm. Left: Pickup coils #1 and #2 mounted to the inner cylinder of the shielding (covered with tape). Right: DCCC completed and closed, with the outer meander shielding and the SQUID housing.

The DCCC has been extensively tested to investigate the influence of different geometries and magnetic core materials on the current noise density and in particular on resonant behaviour and eigenmodes of the system, which have strong influence on the current resolution as well as on operation stability [15]. Additional use of mu-metal shielding was tested as well as different ways of connecting the pickup coils (e.g. in series and parallel).

During this process it could be shown that inversely connected SQUIDS will suppress the influence of high frequency noise by adding the SQUID signals either analogue by differential amplifier or digitized via software differentiation. In total the optimization of the CCC LC circuit (L: pickup inductance, C: meander capacitance) together with the elimination of Barkhausen and rf noise lead to a strongly reduced noise floor. Figure 8 shows the noise density spectra of the DCCC compared to an advanced axial CCC prototype. Obviously the DCCC noise density is much lower due to the possibility of noise subtraction by dual core.

Independent from properties of a special CCC type, it could be shown during the same measurement campaign that further noise reduction can be achieved if the system is operated at superfluid Helium temperature (2.1 K), to avoid the disturbances from He boil off.

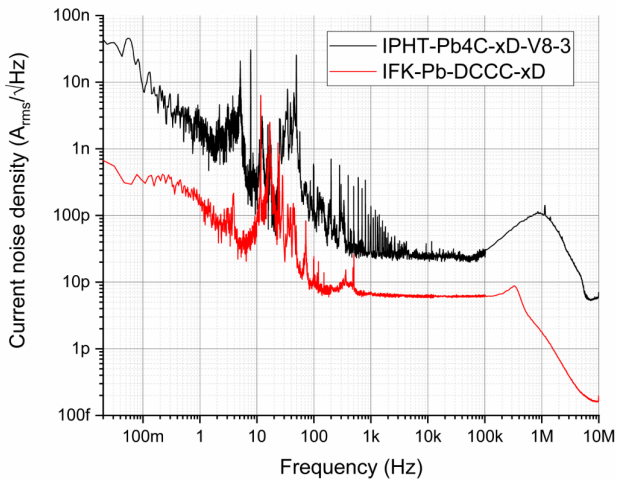


Figure 8: Comparison of current noise from an advanced axial CCC prototype (black) and a dual core CCC (red) at XD-dimensions (outer diameter: 350 mm).

SUMMARY AND OUTLOOK

Two CCC detectors, based on the classical PTB design, made from Niobium, are in standard operation at CERN AD or have shown solid performance in CRYRING at GSI/FAIR. We conclude that our CCC system, the combination of cryostat and classical CCC detector, is appropriate to serve as a basis for nA current diagnostics in FAIR and other machines. In parallel an alternative axial shielding/pickup design has been developed to avoid unfavorable properties of the classical CCC. This axial CCC has recently been tested in the laboratories at Jena and in the beamline cryostat at GSI, it was found to provide a significant improvement concerning magnetic shielding efficiency as well as production effort, materials and costs. However, regarding the current measurement respectively the CCC functionality in general the axial CCC is still suffering from too high sensitivity to background noise and has to be further investigated. As a third variety a dual CCC has been designed to combine the advantages of the two earlier versions. In addition to a high pickup efficiency and superior magnetic shielding properties the usage of two pickups and SQUIDs in parallel provides excellent noise spectra. Beam experiments with the DCCC are planned for 2024.

REFERENCES

[1] F. Kurian, “Cryogenic Current Comparators for precise Ion Beam Current Measurements”, PhD thesis, University of Frankfurt, Germany, 2015.

[2] K. Grohmann, H. D. Hahlbohm, D. Hechtfischer, and H. Lübbig, “Field attenuation as the underlying principle of cryocurrent comparators 2. Ring cavity elements”, *Cryogenics*, vol. 16, no. 10, pp. 601–605, 1976.

[3] A. Peters *et al.*, “A Cryogenic Current Comparator for the absolute Measurement of nA Beams”, *AIP Conf. Proc. 451* pp.163-180, 1998.

Content from this work may be used under the terms of the CC-BY-4.0 licence (© 2023). Any distribution of this work must maintain attribution to the author(s), title of the work, publisher, and DOI

ISBN: 978-3-95450-236-3 ISSN: 2673-5350 doi:10.18429/JACoW-IBIC2023-TUP036

Content from this work may be used under the terms of the CC-BY-4.0 licence (© 2023). Any distribution of this work must maintain attribution to the author(s), title of the work, publisher, and DOI

[4] V. Zakosarenko *et al.,* "Coreless SQUID-based cryogenic current comparator for non-destructive intensity diagnostics of charged particle beams", *Supercond. Sci. Technol.,* vol. 32, Dec. 2018, p. 014002. doi: 10.1088/1361-6668/aaf206

[5] V. Tympel *et al.*, "Creation of the First High-Inductance Sensor of the New CCC-Sm Series", in *Proc. IBIC'22*, Kraków, Poland, Sep. 2022, pp. 469-472. doi:10.18429/JACoW-IBIC2022-WEP30

[6] T. Sieber *et al.*, "Optimization Studies for an Advanced Cryogenic Current Comparator (CCC) System for FAIR", in *Proc. IBIC'16*, Barcelona, Spain, Sep. 2016, pp. 715-718. doi:10.18429/JACoW-IBIC2016-WEPG40

[7] M. F. Fernandes *et al.*, "Operation of a Cryogenic Current Comparator with Nanoampere Resolution for Continuous Beam Intensity Measurements in the Antiproton Decelerator at CERN", in *Proc. IPAC'18*, Vancouver, Canada, Apr.-May 2018, pp. 4741-4744. doi:10.18429/JACoW-IPAC2018-THPML044

[8] V. Tympel *et al.*, "Cryogenic Current Comparators for 150 mm Beamline Diameter", in *Proc. IBIC'17*, Grand Rapids, MI, USA, Aug. 2017, pp. 431-434. doi:10.18429/JACoW-IBIC2017-WEPCF07

[9] D. M. Haider *et al.*, "Commissioning of the Cryogenic Current Comparator (CCC) at CRYRING", in *Proc. IBIC'21*, Pohang, Korea, Sep. 2021, pp. 349-352. doi:10.18429/JACoW-IBIC2021-WEOB02

[10] R. Geithner *et al.*, "An Improved Cryogenic Current Comparator for FAIR", in *Proc. IPAC'12*, New Orleans, LA, USA, May 2012, paper MOPPR020, pp. 822-824.

[11] http://www.magnicon.com/squid-electronics

[12] D. M. Haider *et al*., "Versatile Beamline Cryostat for the Cryogenic Current Comparator (CCC) for FAIR", in *Proc. IBIC'19*, Malmö, Sweden, Sep. 2019, pp. 78-81. doi:10.18429/JACoW-IBIC2019-MOPP007

[13] N. Marsic, H. De Gersem, W.F.O. Mueller, F. Kurian, M. Schwickert, and T. Sieber, "Analytical and Numerical Performance Analysis of a Cryogenic Current Comparator", in *Proc. IPAC'17*, Copenhagen, Denmark, May 2017, pp. 160-162. doi:10.18429/JACoW-IPAC2017-MOPAB037

[14] L. Crescimbeni *et al.,* "Axial Cryogenic Current Comparator (CCC) for FAIR", presented at IBIC'23, Saskatoon, Canada, September 2023, paper TUP034, this conference.

[15] Max Stapelfeld, "Experimentelle Untersuchungen zum System design von Kryogenen Stromkomparatoren", PhD thesis Friedrich Schiller University Jena, Germany, 2022.

ISBN: 978-3-95450-236-3 ISSN: 2673-5350 doi:10.18429/JACoW-IBIC2023-TUP037

CHARGE MEASUREMENT WITH RESONATORS AT ARES

T. Lensch, D. Lipka*, R. Neumann, M. Werner
Deutsches Elektronen-Synchrotron DESY, Notkestr. 85, Hamburg, Germany

Abstract

The ARES facility (Accelerator Research Experiment at SINBAD) is an accelerator to produce low charge ultrashort electron bunches within a range of currently 0.5 pC to 200 pC. Especially for eFLASH experiments at ARES an absolute, non-destructive charge measurement is required. To measure an absolute charge of individual bunches different types of monitors are installed. A destructive Faraday Cup is used as reference charge measurement device. To measure the charge non-destructively 2 Toroids, 1 Turbo-ICT and 2 cavity monitors are installed. The latter system consists of the cavity, front-end electronics with logarithmic detectors and µTCA ADCs. The laboratory calibration of the cavity system is performed by using an arbitrary waveform generator which generate the same waveform like the cavity with beam. This results in a non-linear look-up table used to calculate the ADC amplitude in charge values independent of beam-based calibration. The measured charges from the cavity monitors agree very well within few percent in comparison with the Faraday Cup results.

MOTIVATION

The beam charge determination is one of the most important properties to be measured in all accelerators. For this several monitor systems are developed and installed at every accelerator, but the absolute value of charge is always in discussion. At the Accelerator Research Experiment at SINBAD (ARES) [1–6] we installed different types of charge monitor systems: 2 Toroids, 1 Turbo-ICT and 2 cavity monitors. The charge value results are compared with a Faraday cup who serves as a reference system with good agreement to the other monitors; the expected charge loss of the Faraday Cup due to lost particles is simulated and smaller than 0.6 % [7]. The cavity monitor system consists of a resonator where the first monopole mode at 1.3 GHz carries with the amplitude the charge information. This monitor system is firstly developed to detect the dark current from accelerators with the same accelerator frequency where the single dark current bunches generate superimposed fields within the resonator [8]; for this reason the system is called Dark current Monitor (DaMon). It was found that this resonating system is able to measure very low values of bunch charges. Therefore, the DaMon system is installed at several accelerators at DESY [9–12] to measure the bunch charge from several fC up to few nC. The calibration of the amplitude to the charge from a resonator to get the absolute charge is the issue of this contribution.

* dirk.lipka@desy.de

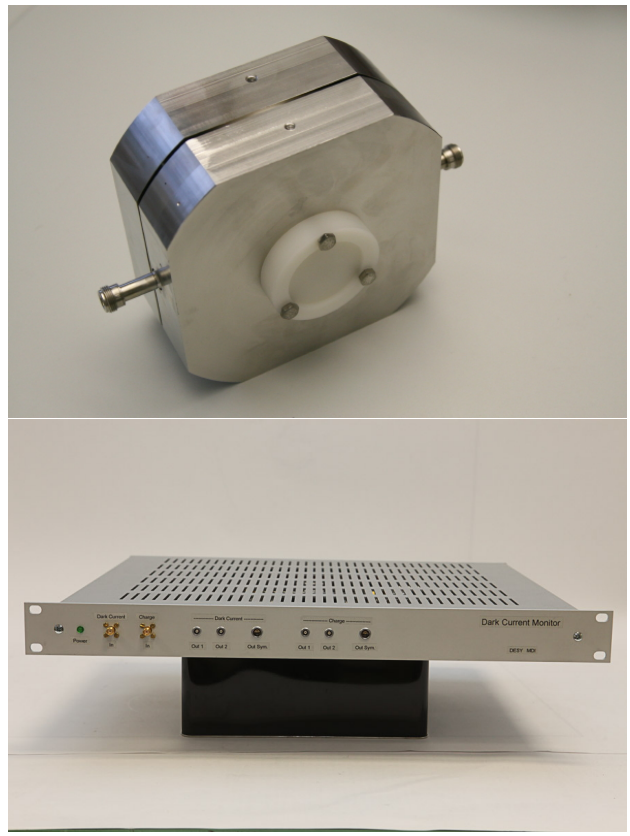


Figure 1: Picture of the resonator and the electronics box with front panel.

SETUP

The DaMon system consists of the resonator integrated into the beamline, a front-end electronics (see an example in Figure 1) and ADCs. One resonator has two identical outputs to ensure symmetry in the resonator, which are connected with low loss coaxial cables to the front-end electronics. Both inputs are processed differently in the electronics. The charge channel (Q) is in most applications attenuated to be able to provide higher charges with band pass filters, logarithmic detectors (for high dynamic range) and followed by gain and offset adjustments to adapt to the 16 bit ADC. The dark current channel (DC) has in addition a down converter in the logarithmic detector with free oscillating reference signal to provide higher sensitivity. This channel was foreseen to superimpose the dark current bunches with acceleration frequency 1.3 GHz but for other accelerators this channel is used for bunch charge measurement too. Therefore, the DC channel provides higher sensitivity and can be used for lower charge values compared to the Q channel.

Content from this work may be used under the terms of the CC-BY-4.0 licence (© 2023). Any distribution of this work must maintain attribution to the author(s), title of the work, publisher, and DOI

ISBN: 978-3-95450-236-3 ISSN: 2673-5350 doi:10.18429/JACoW-IBIC2023-TUP037

CALIBRATION PROCEDURE

The sensitivity of the resonator (or amplitude of the oscillating voltage as a function of the charge) is calculated with the resonance frequency f, the connection impedance Z, the external quality factor Q_{ext} and the shunt impedance $\left(\frac{R}{Q}\right)$ to be $S = \pi f \sqrt{\frac{Z}{Q_{ext}}\left(\frac{R}{Q}\right)}$ [13]. Here f and Q_{ext} are measured for each resonator; the shunt impedance is used from simulation results but should only negligible vary for each resonator. The charge can be calculated with the measured amplitude U to be $Q = U/S$. Up to the electronics the amplitude is reduced due to the attenuation of the cables, therefore each cable attenuation is measured at the resonance frequency 1.3 GHz. The electronics processes the signals differently at each channel, described in the setup chapter. To calibrate the electronics in the laboratory a signal at the resonance frequency with different amplitudes are generated and the output are monitored. For the dark current channel a continuous wave (CW) was applied which was sufficient for this kind of measurement. Since the DaMon system was developed for the dark current measurement the same CW signal was applied for the Q channel. But this CW signal enters different sections of the logarithmic detectors compared to a pulsed signal. Therefore, a pulsed signal should be more suitable for the calibration for the charge. Especially when the DC channel is used to measure the bunch charge since the down conversion is different in comparison of a damped signal. The pulsed signal (damped signal) is generated with an arbitrary waveform generator, see Figure 2. The generated signal corresponds in frequency and decay time with those expected from the resonator. The amplitude is varied to get a table of the electronics response function. In Figure 2 the output of the electronics is visible with an oscilloscope for one amplitude. The final calibration is realized with the installed electronics in the rack room with connected 16 bit ADC.

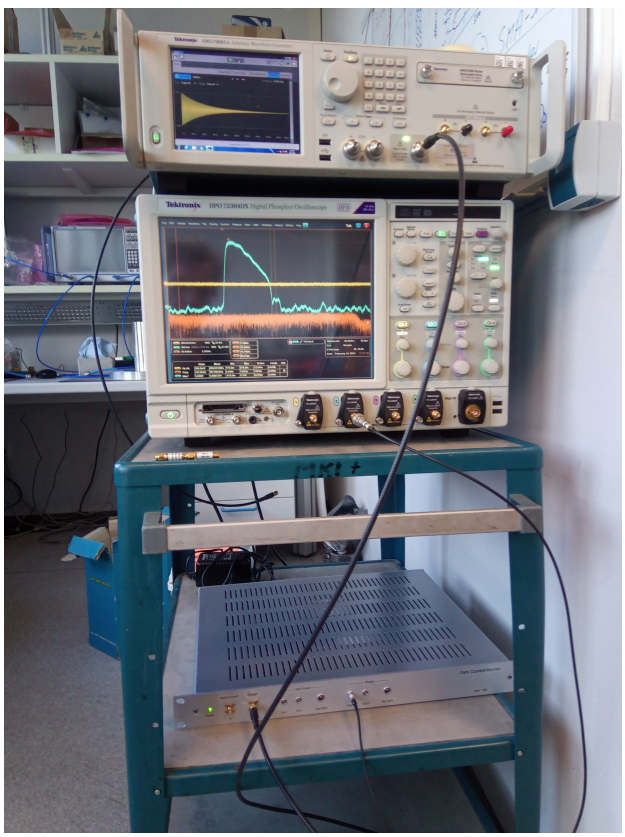


Figure 2: Calibration setup in the laboratory.

The resulting electronics responds is shown in Figure 3 for the Q and DC channel. The CW signal measurements agree to each other but for a pulsed signal a difference is visible for higher amplitudes. The number of measurement points for the old CW was increased to check that charge non-linearities are not caused due to interpolations from the electronics responds. For the overall calibration the pulsed signals are used to generate a look-up table for each channel including the information about each resonator sensitivity, cable attenuation and ADC conversion to voltage. Between each point in the table the values are interpolated to calculate from the measured ADC amplitude back to the charge.

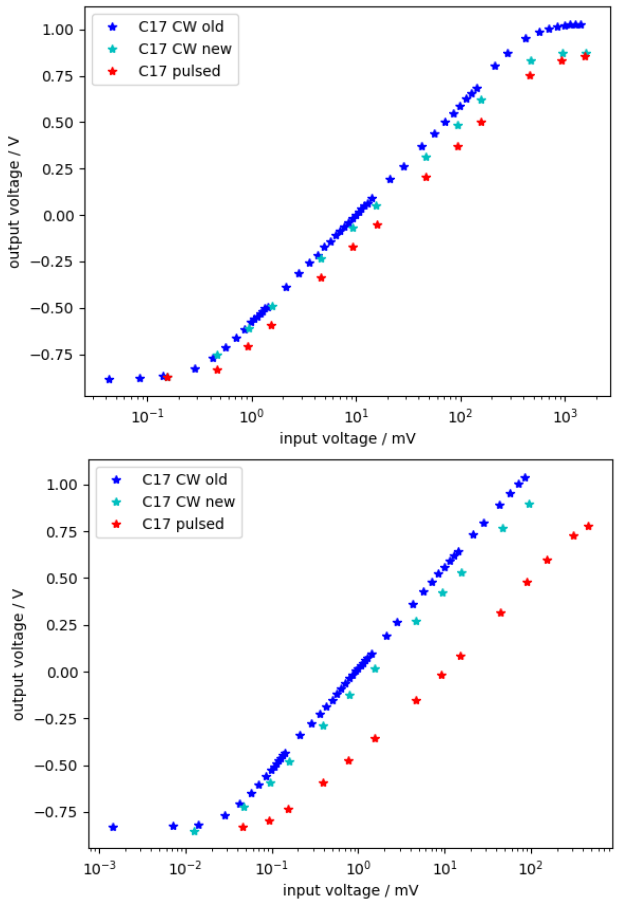


Figure 3: Response function for Q channel on top and for the DC channel below for electronics serial C17 installed at ARES. Each channel has three measurements: dark blue with CW signal in the laboratory, bright blue for CW signal and 16 bit ADC and red for pulsed signal.

Content from this work may be used under the terms of the CC-BY-4.0 licence (© 2023). Any distribution of this work must maintain attribution to the author(s), title of the work, publisher, and DOI

ISBN: 978-3-95450-236-3 ISSN: 2673-5350 doi:10.18429/JACoW-IBIC2023-TUP037

BEAM CHARGE MEASUREMENT RESULTS

In Figure 4 the measurement of the first DaMon system at ARES for the Q channel and a charge range up to 210 pC is shown. The Q channel is attenuated with 20 dB before the signal enters the electronics to provide a charge range up to 1 nC. The values are compared with the Faraday Cup

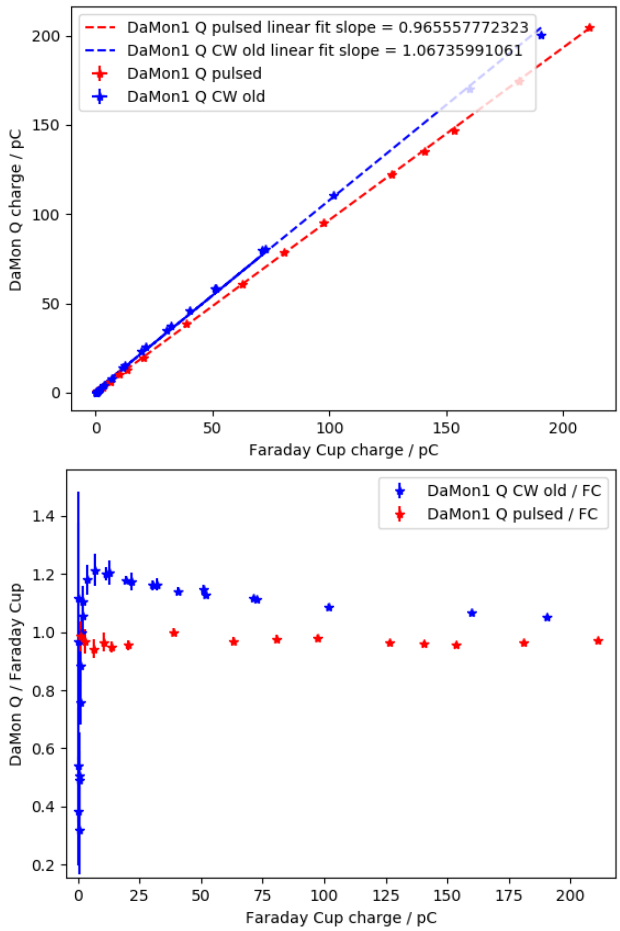


Figure 4: Top: measured charge of the resonator Q channel as a function of Faraday Cup charge; below the ratio of Q channel to Faraday Cup charge as a function of Faraday Cup charge. Error bars are standard deviation caused by beam charge variation.

charges. The absolute values on top are fitted with a polynomial 1. order. The slope shows the factor between DaMon Q channel and Faraday Cup results: with CW calibration a disagreement of 6.7 % is shown, with the pulsed signal the disagreement is reduced to −3.4 %. The lower diagram shows the ratio between Q channel and Faraday Cup charges as a function of Faraday Cup charge. For charges above 100 pC the values are linear, therefore for accelerators operating above this value the DaMon Q channel shows the same as the Faraday Cup, below this charge the CW calibration shows non-linearities. This non-linearity is reduced to ±3 % with the pulsed signal calibration.

Figure 5 shows the charge measurement results with the DC channel in comparison with the Faraday Cup; here the charge range is only up to 15 pC because for higher charges the electronics is in saturation. Therefore, this channel is intended for small charges. The absolute values are fitted

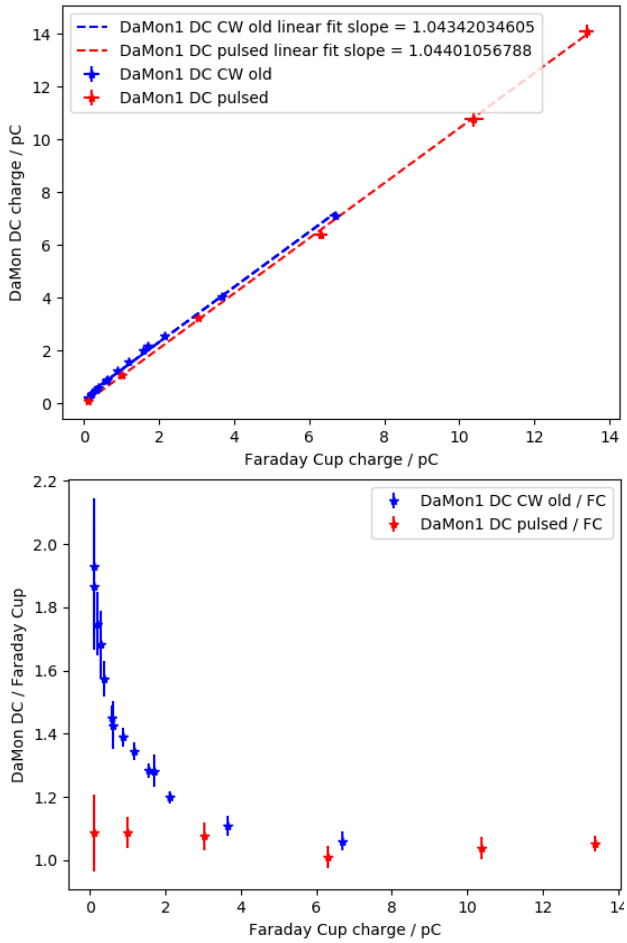


Figure 5: Top: measured charge of the resonator DC channel as a function of Faraday Cup charge; below the ratio of DC channel to Faraday Cup charge as a function of Faraday Cup charge. Error bars are standard deviation caused by beam charge variation.

too and show almost the same slope; the CW values were defined only up to 10 pC. In the lower diagram the ratios are shown and a strong non-linearity is visible for the CW calibration with an overestimation of the charge by a factor of almost 2. With the pulsed signal calibration the variation from a linearity is reduced to be only ±5 %. Still slightly higher charge is measured with the DC channel which could be corrected beam based.

SUMMARY AND OUTLOOK

Charge measurement with resonators must be calibrated carefully. A beam independent laboratory calibration was developed and the results were compared with a Faraday cup. A calibration with CW pulses show non-linearities for low charges. A laboratory calibration with the same signal as it

Content from this work may be used under the terms of the CC-BY-4.0 licence (© 2023). Any distribution of this work must maintain attribution to the author(s), title of the work, publisher, and DOI

ISBN: 978-3-95450-236-3 ISSN: 2673-5350 doi:10.18429/JACoW-IBIC2023-TUP037

is expected from the resonator improves the non-linearity and absolute charge values. The laboratory calibrations will be improved due to automatic variation of the amplitude of the signal generator and readout from the ADC. In addition, a new electronics board is in development as a rear transition module for μTCA crates with larger dynamic range due to two additional amplifiers for different amplitudes for each channel.

REFERENCES

[1] U. Dorda *et al.*, "The Dedicated Accelerator R&D Facility Sinbad at DESY", in *Proc. IPAC'17*, Copenhagen, Denmark, May 2017, pp. 869–872. doi:10.18429/JACoW-IPAC2017-MOPVA012

[2] B. Marchetti *et al.*, "Status Update of the SINBAD-ARES Linac Under Construction at DESY", in *Proc. IPAC'17*, Copenhagen, Denmark, May 2017, pp. 1412–1414. doi:10.18429/JACoW-IPAC2017-TUPAB040

[3] E. Panofski *et al.*, "Status Report of the SINBAD-ARES RF Photoinjector and LINAC Commissioning", in *Proc. IPAC'19*, Melbourne, Australia, May 2019, pp. 906–909. doi:10.18429/JACoW-IPAC2019-MOPTS026

[4] F. Burkart *et al.*, "The Experimental Area at the ARES LINAC", in *Proc. IPAC'19*, Melbourne, Australia, May 2019, pp. 867–870. doi:10.18429/JACoW-IPAC2019-MOPTS014

[5] B. Marchetti*et al.* "SINBAD-ARES - A Photo-Injector for external Injection Experiments in novel Accelerators at DESY", *J. Phys. Conf. Ser.*, vol. 1596, no. 1, p. 012036, 2020. doi:10.1088/1742-6596/1596/1/012036

[6] E. Panofski *et al.* "Commissioning Results and Electron Beam Characterization with the S-Band Photoinjector at SINBAD-ARES", *Instruments*, vol. 5, no.3, p. 28, 2021. doi:10.3390/instruments5030028

[7] T. Lensch *et al.*, "Comparison of different bunch charge monitors used at the ARES accelerator at DESY", in *Proc. IBIC'23*, Saskatoon, Canada, Sept 2023, paper TU3I04, this conference.

[8] D. Lipka, W. Kleen, J. Lund-Nielsen, D. Noelle, S. Vilcins, and V. Vogel, "Dark Current Monitor for the European XFEL", in *Proc. DIPAC'11*, Hamburg, Germany, May 2011, paper WEOC03, pp. 572–574.

[9] D. Noelle *et al.*, "Commissioning of the European XFEL", in *Proc. LINAC'18*, Beijing, China, Sep. 2018, pp. 994–999. doi:10.18429/JACoW-LINAC2018-FR2A02

[10] T. Plath, J. Roensch-Schulenburg, J. Rossbach, H. Schlarb, S. Schreiber, and B. Steffen, "Commissioning and Diagnostics Development for the New Short-Pulse Injector Laser at FLASH", in *Proc. IBIC'13*, Oxford, UK, Sep. 2013, paper TUPC03, pp. 353–356.

[11] D. Lipka, J. Lund-Nielsen, and M. Seebach, "Resonator for Charge Measurement at REGAE", in *Proc. IBIC'13*, Oxford, UK, Sep. 2013, paper WEPF25, pp. 872–875.

[12] S. Jalas *et al.*, "Bayesian Optimization of a Laser-Plasma Accelerator", *Phys. Rev. Lett.*, vol. 126, no.10, p. 104801, 2021. doi:10.1103/PhysRevLett.126.104801

[13] D. Lipka, M. Dohlus, M. Marx, S. Vilcins, and M. Werner, "Design of a Cavity Beam Position Monitor for the ARES Accelerator at DESY", in *Proc. IBIC'18*, Shanghai, China, Sep. 2018, pp. 269–272. doi:10.18429/JACoW-IBIC2018-TUPB05

Content from this work may be used under the terms of the CC-BY-4.0 licence (© 2023). Any distribution of this work must maintain attribution to the author(s), title of the work, publisher, and DOI

ISBN: 978-3-95450-236-3 ISSN: 2673-5350 doi:10.18429/JACoW-IBIC2023-TUP038

BCM SYSTEM OPTIMIZATION FOR ESS BEAM COMMISSIONING THROUGH THE DTL TANK 4

H. Hassanzadegan, R. A. Baron, S. Gabourin, H. Kocevar, M. Mohammednezhad, J. Murari, S. Pavinato, K. Rosengren, T. Shea, R. Zeng, European Spallation Source ERIC, Lund, Sweden
K. Czuba, P. K. Jatczak, Warsaw University of Technology, Warsaw, Poland

Abstract

The ESS BCM system is not only used for beam measurement but it also plays an important role for machine protection particularly in the normal-conducting part of the linac. During the previous beam commissionings to the MEBT and DTL1 FCs and before the cavities were fully conditioned, RF breakdowns and other types of discharges in the cavities had a major impact on beam availability due to the Fast machine protection functions of the BCM. Following an investigation on the root cause of the beam trips, the configuration of the machine protection functions was modified to improve beam availability in the more recent beam commissioning to the DTL4 FC. In addition to this, some optimizations were made in the BCM system to improve beam measurement, and a few more functions were added based on new requirements. This paper reports on these improvements and the results obtained during the beam commissioning through the DTL4.

INTRODUCTION

The ESS Beam Current Monitor (BCM) system includes in total nineteen AC Current Transformers (ACCTs) and one Fast Current Transformer (FCT) which are all from Bergoz. Ten of these ACCTs are installed in the normal conducting part of the linac that extends from the Ion Source (ISrc) to the Drift Tube Linac (DTL) tank 5. These sensors overall allow beam measurement at the interface between a section and the following one, and after the temporary beam dumps in the Low Energy Beam Transport (LEBT) and Medium Energy Beam Transport (MEBT) sections. The other nine ACCTs will be installed in the Linac Warm Units (LWUs) in between the cryomodules in the Medium Beta Linac (MBL), High Beta Linac (HBL), High Energy Beam Transport (HEBT) and in the Accelerator To Target (A2T) and Dump Line (DmpL) sections.

The analogue signal form each ACCT is buffered and amplified by a wall-mount Front End (FE) module from Bergoz, and then filtered and further processed in a custom designed Back End (BE) unit in the BCM rack. The signal is then converted to digital and FPGA processed by a Struck SIS8300-KU board in a mTCA crate. The digital signal processing includes baseline restoration, droop compensation, digital filtering, post mortem data buffering as well as a complete suite of machine protection functions that are tailored to meet the ESS beam and machine requirements. Part of these functions are used to measure the amplitude, width and repetition frequency of the beam pulse and send a beam abort request to the Fast Beam Interlock System (FBIS) within 1 μs if the measured values exceed their thresholds. The BCM firmware configures the machine protection functions including the levels and activation/deactivation of the thresholds based on a beam mode and a beam destination ID that are distributed over the ESS network before starting with beam. Time windows for the expected beam pulses from the ISrc and LEBT/MEBT choppers are generated by the BCM firmware using some events which are distributed by the ESS Timing System (TS) over an optical fibre network at well-defined times before the arrival of each pulse. These time windows are then used for measuring the beam properties including average beam current over a region of interest and pulse length/charge. The BCM firmware also checks the exact timing of the TS events for any inconsistency with the selected beam mode due to possible bugs in the timing tables, human errors etc. This feature has proven to be very useful to avoid potential damages due to ex. a wrong trigger length/frequency resulting in excessive beam power on a temporary beam dump. Other protection functions include differential beam interlocks with several BCM pairs, errant beam detection and BCM internal checks [1].

Each ACCT includes a calibration winding that is used not only to calibrate the sensor but also to test and verify the system with a test pulse from a waveform generator before starting with beam. A Wetest script is used to sweep the pulse amplitude, width and frequency in multiple steps from a minimum to a maximum, and in each step the full signal chain from the sensor up to the EPICS Process Variables (PVs) including all the protection functions are automatically tested and verified.

BEAM COMMISSIONINGS THROUGH THE LEBT, MEBT AND DTL TANK 1

With the start of the beam commissioning through the LEBT (Sep. 2018) and MEBT (Nov. 2021) [2], a large number of beam trips were initiated by the BCM system and in particular the errant beam interlock. An investigation then showed that part of the trips was due to Electro Magnetic Interference (EMI) issues caused by the safety relay (i.e. ground relay), High Voltage Power Supply (HVPS) and the high power contactors of the ISrc. The issue was then resolved by improving the groundings of both the ISrc cage and the electronics racks, reinforcing the shielding and grounding of the ISrc/LEBT BCM FEs, additional EMI filters, surge protectors, analogue filters on the HVPS current/voltage readouts and digital processing in the BCM FPGA. The tests also showed that a broken insulator around a LEBT repeller ring resulted in some sparks and these occasionally caused some large spikes on the LEBT BCM readout thus adding to the beam trips. The

Content from this work may be used under the terms of the CC-BY-4.0 licence (© 2023). Any distribution of this work must maintain attribution to the author(s), title of the work, publisher, and DOI

ISBN: 978-3-95450-236-3 ISSN: 2673-5350 doi:10.18429/JACoW-IBIC2023-TUP038

Content from this work may be used under the terms of the CC-BY-4.0 licence (© 2023). Any distribution of this work must maintain attribution to the author(s), title of the work, publisher, and DOI

repeller was then repaired through a LEBT intervention and that fixed the issue with the sparks, but an uncareful reassembly of the LEBT components then resulted in some broken connectors as well as a short circuit through the LEBT BCM sensor by a thermocouple cable, and these rendered this BCM temporarily non-operational. The broken connectors were then replaced and the short-circuit was removed through another LEBT intervention. With the start of the beam commissioning through the DTL tank 1 (June 2022), a large number of spikes showed up on the DTL1 BCM readout and these had a major impact on beam availability. In order to better analyse the beam trips, a Post Mortem (PM) function was then added to the BCM firmware. This includes a configurable ring buffer that keeps the most recent BCM data with a sample rate of 88 MSPS from all the channels, and freezes the buffer contents as soon as the Beam Permit is changed to NOK. For the spike analysis, the buffer size was set to 1.1 GB that is equivalent to 1 s of BCM data (i.e. 400 ms before plus 600 ms after a beam trip). The PM data analysis then showed a correlation between the spikes and the DTL RF/vacuum levels, but the root causes of the spikes were understood and the issue was resolved only after the start of the following beam commissioning through the DTL tank 4.

BEAM COMMISSIONING THROUGH THE DTL TANK 4

In April 2023 with the start of the DTL tanks 1-4 RF conditioning activities, spikes were frequently observed with the DTL BCMs and in particular tank 2, but fewer spikes were observed in the tank 1 compared to the previous beam run in June 2022. A thorough investigation on the root cause of the spikes then showed the followings:

1. The inner surface of the DTL tanks emits electrons when it is subject to the RF pulse. These electrons travel a short distance after they exit from both the beam entrance and the beam exit ports of the tanks. Part of the electrons reach the BCM sensors which are installed in between each two tanks and that results in a small spike of max 0.2 mA on the BCM readout.
2. Two small spikes of typically -0.3 mA are observed on the Radio Frequency Quadrupole (RFQ) BCM readout at the rising and falling edges of the RF pulse due to multipacting.
3. The rising edge of the ISrc beam pulse results in a small spike of +0.6 mA approximately on the LEBT BCM readout.
4. RF breakdowns and other types of discharges in the cavities result in large spikes on the DTL BCM readouts. These spikes can easily hit the machine protection thresholds and cause beam trips by the BCM and the RF Local Protection System (LPS).
5. RF and vacuum breakdowns in the MEBT buncher 3 cavity can cause spikes with an amplitude of a few tens of mA on the MEBT BCM 2. The spikes start showing up when the buncher 3 voltage goes above ~130 kV.
6. An RF breakdown in a DTL tank induces a current in the BCM calibration windings. In the ISrc to DTL tank 2 sections, calibration windings of seven BCM sensors are connected in series, and the induced current can cause beam trips by the LEBT, RFQ and MEBT BCMs as well even if the protection functions of the DTL BCMs are disabled.

The investigation confirmed that most of the spikes listed above are directly linked to RF and vacuum, and they become less frequent with cavity conditioning. The spikes of type 1-3 are overall very small and do not cause an issue. Figure 1 shows a beam pulse with an amplitude of 4.5 mA and width of 50 μs that is measured by all the BCMs from the LEBT to the DTL tank 4. The differences in the pulse amplitude (beam loss), the small spikes on the RFQ BCM readout (multipacting) and the baseline variations due to the secondary particles from the DTL1-3 are visible in the plot.

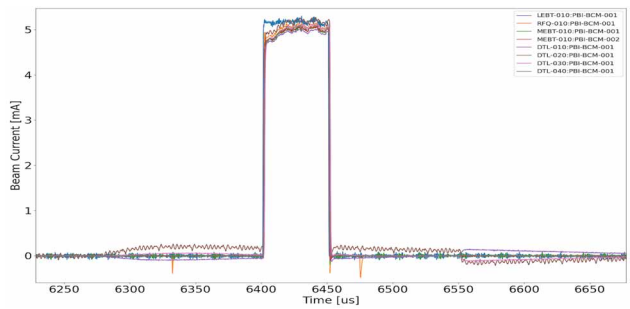


Figure 1: A low current beam pulse that is measured by eight BCMs from the LEBT to the DTL tank 4.

In order to improve the beam availability due to the spike types 4-5, following an assessment by a Beam Damage Team (BDT), the interlocks on the beam amplitude and errant beams in the DTL section were replaced by Medium-speed differential thresholds on beam losses. This however did not compromise the errant beam interlock function because any errant beam would still be detected by the Fast thresholds of another four BCMs located upstream of the DTL BCMs.

Figure 2 shows the BCM PM data including a large spike (i.e. RF breakdown) on the DTL2 BCM readout causing signal saturation with this channel as well as some ringing on the other channels (item 6 in the spikes summary).

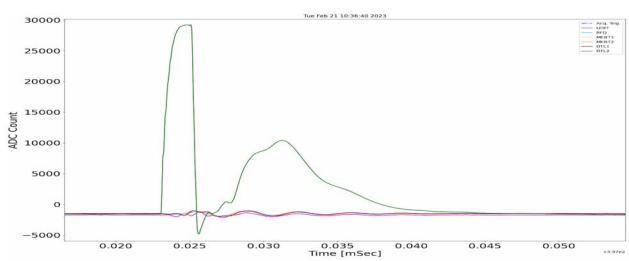


Figure 2: A large spike on the DTL2 BCM readout causing some ringing on the other BCM channels.

ISBN: 978-3-95450-236-3 ISSN: 2673-5350 doi:10.18429/JACoW-IBIC2023-TUP038

Given that the BCM signal drifts with temperature are extremely small, this issue was easily resolved by disconnecting the BCM calibration cables after the system was calibrated and the in-situ tests were completed before starting with beam.

The combination of the above-mentioned action items fully resolved the beam availability issue with the BCM.

DIFF BCM INTERLOCKS

Differential BCM interlocks are mainly used to measure beam losses between a BCM pair and stop the beam if the losses exceed a threshold. The BCM firmware allows using three types of differential interlocks, being: Fast, Medium-speed and Slow for each pair. The Fast and Medium-speed thresholds are set on the differential current and they can include a configurable moving average filter as well. The Slow threshold is however set on the cumulative charge per cycle and it gets reset shortly before the arrival of the next pulse.

Figure 3 shows the absolute and differential beam currents from a differential pair with the RFQ BCM and MEBT BCM 1. The difference in the pulse lengths (20 µs vs. 5 µs) is due to the MEBT chopper, and the 0.1 mA step before the MEBT BCM 1 pulse is the scattered beam from the MEBT chopper dump. For the beam commissioning to the DTL tank 4, the Fast and Slow differential interlocks were disabled, but the Medium-speed one was enabled with several BCM pairs. The width of the moving averager was set to 55 µs (LEBT-RFQ BCM pair) and 6 µs (three pairs between the consecutive DTL tanks from 1 to 4) to make the differential interlocks less sensitive to the spikes from the RF breakdowns, but sensitive enough to beam losses that have the potential to cause a damage. This proved to be an effective method to avoid unwanted beam trips particularly at the start of the beam commissioning and before the cavities were fully conditioned.

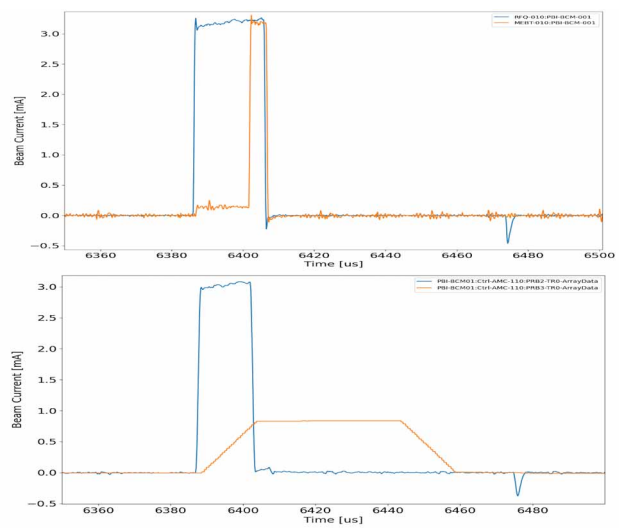


Figure 3a: RFQ BCM (blue) and MEBT BCM 1 (orange) readouts. Figure 3b: Fast (blue) and Medium-speed (orange) differential currents for the above pair; the amplitude of the Medium-speed signal is 70% lower than the Fast one due to the moving averager.

OTHER IMPROVEMENTS

Fast BCM

The Fast BCM (i.e. FCT) is installed towards the MEBT end and it is mainly used for verifying the 10 ns rising/falling edges of the beam pulse from the MEBT chopper. The analogue signal from the FCT is measured by a fast oscilloscope with a sample rate of up to 20 GSPS and an overall measurement bandwidth of 700 MHz. Figure 4 shows a screenshot of the FCT signal. The falling edge of the beam pulse and the beam bunches and their frequency spectrum up to the second harmonic (i.e. 2*352 MHz) can be seen in the screenshot.

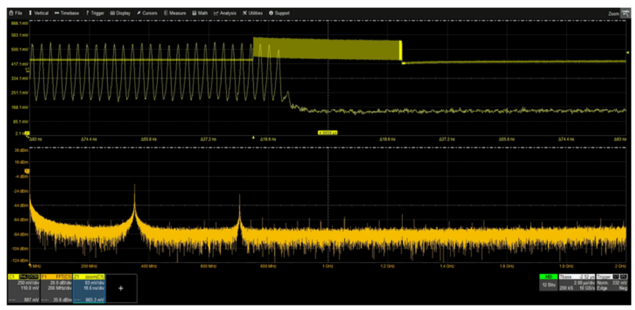


Figure 4: The falling edge of the beam pulse from the MEBT chopper as measured by the Fast BCM.

One Hour Average Beam Current Measurement with sub-µA Accuracy

During the beam commissioning to the DTL, a temporary shield wall was used to isolate the DTL tank 4 from the downstream sections. This allowed to run the beam to the DTL4 FC and in parallel continue with the installation work in the superconducting part of the linac. Under these conditions, personnel safety regulations set a limit of 1 µA average beam current over a rolling period of one hour to ensure the workers would not receive a radiation dose rate higher than 3 µS/h. The limit was imposed in the first hand by only allowing certain beam modes, but the BCM system was also used to ensure the actual beam current would not exceed the 1 µA limit. Given that the required accuracy needed to be by ~4 orders of magnitude better than that the regular BCM accuracy (i.e. +/- 0.8 mA), this measurement could only be successfully done after the following issues were resolved:

- Any DC offset due to measurement errors needed to be precisely removed from the BCM readout. This particularly applies to the baseline restoration function.
- The LEBT/MEBT choppers with a reduced electrode voltage result in some leakage beam which can potentially get accelerated by the RF in the following sections and contribute to the radiation dose. The regular BCM channels however may not always measure leakage beams because of the chosen triggers for the baseline restoration function. In order to fix this issue, a copy of the MEBT BCM 2 signal was used for the sub-µA beam measurement but its trigger was

Content from this work may be used under the terms of the CC-BY-4.0 licence (© 2023). Any distribution of this work must maintain attribution to the author(s), title of the work, publisher, and DOI

ISBN: 978-3-95450-236-3 ISSN: 2673-5350 doi:10.18429/JACoW-IBIC2023-TUP038

Content from this work may be used under the terms of the CC-BY-4.0 licence (© 2023). Any distribution of this work must maintain attribution to the author(s), title of the work, publisher, and DOI

configured differently so that it would not be blind to potential leakage beams.

- An earlier study shows that below 85% of the nominal RFQ voltage, the beam will be lost either in the RFQ or in the downstream sections [3]. Then, this particular BCM channel was configured to only measure the beam within the time window of the RF pulse, and this significantly improved the measurement accuracy comparted to a continuous measurement.

Figure 5 shows a 20-hour history of the charge per pulse as well as the 1-hour average beam current including any leakage beams within the RF pulse window. The peak value is 0.27 μA which is equivalent to 27% of the "budget". The tests showed that the BCM can indeed measure the average beam current with an accuracy significantly better than 1 μA provided that the triggers are all correct.

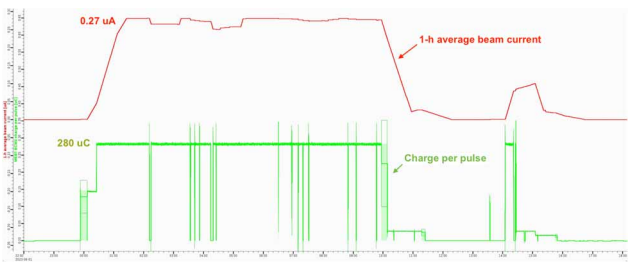


Figure 5: 20-hour history of the charge per pulse as measured by the MEBT BCM 2 (green) and the 1-hour average beam current with sub-μA measurement accuracy (red).

LVDS to RS-485 / Optical Converter

The existing BCM-FBIS interface uses four Low Voltage Differential Signalling (LVDS) channels, being three discrete and one customized serial data link. The discrete channels are used for the Beam Permit, BCM Ready and Beam Presence signals. The serial data is Manchester encoded and used for sending the same information as the discrete channels (for redundancy purposes) as well as some more information including beam mode/destination IDs, life-sign counter, beam exist flags etc. with an update rate of 100 kHz. Although this interface has so far worked without a major issue, concerns over its reliability with long cables in noisy environments triggered the development of some new electronics in collaboration with the Warsaw University of Technology (WUT) with the aim of making the interface more robust. The new electronics consist of a transmitter Printed Circuit Board (PCB) for data aggregation and LVDS conversion to RS-485/optical as well as a receiver PCB for optical signal conversion to RS-485. The transmitter comes in two form factors being: 1) mTCA Advanced Mezzanine Card (AMC) with two channels, and 2) Rack-mount unit with up to four channels. The two form factors are planned respectively for the BCM and the Beam Position Monitor (BPM) systems. Figure 6 shows the first prototype of the transmitter AMC that was successfully tested at ESS in April 2023 together with a receiver unit and the BCM/FBIS electronics.

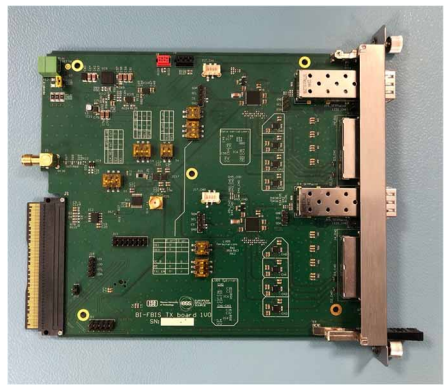


Figure 6: Photo of the new LVDS to RS-485/optical converter AMC (Courtesy of Pawel. K. Jatczak - WUT).

SUMMARY AND OUTLOOK

During the ESS beam commissioning through the DTL tank 4, nine BCM channels were successfully used for beam measurement, machine protection and timing synchronizations. At the start of the commissioning, the beam availability was impacted by a large number of beam trips due to spikes on the BCM readouts. An investigation then showed that the spikes were partly due to EMI and other types of external disturbances, and partly due to RF / vacuum breakdowns particularly in the DTL section. The issue was then resolved by addressing the EMI issues and reconfiguring part of the BCM protection functions to make them less sensitive to the spikes but sensitive enough to beam losses that pose a damage potential. During the same commissioning run, a Fast BCM, a Medium-speed differential interlock and a special BCM channel with sub-μA measurement accuracy were successfully tested and verified with beam as well. It is planned to continue with the BCM activities in 2023-2024 by installing in total ten new BCMs in the DTL tank 5 and the superconducting part of the linac as well as three BCMs in a new ISrc-LEBT Test Stand that is under construction. It is also planned to make the BCM-FBIS interface more robust by deploying a newly developed RS-485/optical interface module. The other parts of the system including the electronics, FPGA firmware, software and the operator interfaces have already become mature following a few rounds of improvements, hence no major changes are planned in the near future.

REFERENCES

[1] H. Hassanzadegan *et al.*, "Machine Protection Features of the ESS Beam Current Monitor System", in *Proc. IPAC'18*, Vancouver, Canada, Apr.-May 2018, pp. 2058-2060. doi:10.18429/JACoW-IPAC2018-WEPAF088

[2] R. Miyamoto *et al.*, "Beam Commissioning of Normal Conducting Part and Status of ESS Project", in *Proc. LINAC'22*, Liverpool, UK, Aug.-Sep. 2022, pp. 18-24. doi:10.18429/JACoW-LINAC2022-MO1PA02

[3] E. Sargsyan, "ESS RFQ Error Study", May 2014, ESS Internal Report.

ISBN: 978-3-95450-236-3 ISSN: 2673-5350 doi:10.18429/JACoW-IBIC2023-TUP041

APS UPGRADE RADIATION SAFETY BEAM CURRENT INTERLOCK*

R. Keane†, K. Harkay, N. Sereno, Argonne National Laboratory, Lemont, IL, USA
A. Caracappa, C. Danneil, K. Ha, J. Mead, D. Padrazo
Brookhaven National Laboratory, Upton, NY, USA

Abstract

The Advanced Photon Source upgrade (APS-U) replaces the APS storage ring with a new Multi-Bend Acromat (MBA) storage ring utilizing on-axis swap-out injection requiring up to 20 nC charge per injected electron bunch, more than a three-fold increase from the original ring. Enforcement of radiation safety limits for the new storage ring will be accomplished by a new beam charge monitor interlock that acquires the accumulated beam charge in the Booster-to-Storage ring (BTS) transfer line and disables injection when the charge limit over a pre-set time period is exceeded. The new interlock is based on the existing APS Beam Shut-Off Current Monitor (BESOCM) that has been in operation in the APS injector for many years and incorporates significant improvements over the existing system. New features include use of direct digitization and FPGA processing, extensive remote monitoring capabilities, expanded self-test and fail-safe functions, and the ability to adjust settings and monitor status remotely via EPICS. The new device integrates a test pulse (self-check) feature that verifies the integrity of the integrating beam current transformer (ICT) and cable system used to detect the beam signal. This paper describes the new BTS interlock (BESOCM) design and presents results of bench test and in-machine evaluation of the prototype and production units.

INTRODUCTION

The existing APS BESOCM system limits the amount of accelerated charge in the APS Linac over a 1 minute accumulation period in order to enforce radiation safety requirements. If the limit is exceeded, the BESOCM disables the beam by inhibiting several necessary systems. The BESOCM continually tests itself by creating a single test pulse of ~2.5 nC after every beam trigger and sending the pulse through a test winding in the current transformer in the beam line, and has some addition fail-safes that monitor the trigger and integration gate [1,2].

The new BTS BESOCM will function similarly to the legacy system, but with far more adjustments and self-test functions, and will include robust remote monitoring capabilities.

APS ACIS System

The APS Access Control and Interlock System (ACIS) includes both personnel protection and radiation safety interlocks that act to disable accelerated and/or stored beam for a variety of abnormal conditions. The system uses dual redundant chains denoted A and B, and relies on fault tolerant hardware such as relay contacts and PLCs. The BTS BESOCM electronics chassis contains two redundant sets of electronics that interface to the ACIS system via safety rated relays.

APS Radiation Safety and FPGA Development

APS radiation safety requirements are stated in APS safety assessment documents and specify the risks and consequences of off-normal beam loss events [3]. Since the BTS BESOCM is a layer of protection added as part of the MBA upgrade, the FPGA firmware development process followed a graded approach based on the low specified risk, i.e., identical hardware was used in both chains A & B with separate firmware developers for each chain. Each developer worked independently to implement the FPGA functions as defined in the BESOCM engineering specification document. Independent code reviews were also performed on each FPGA code design.

BTS BESOCM SYSTEM DESIGN

Figure 1 shows a block diagram of the BESOCM system. The electron beam bunch charge is sensed by an Integrating Current Transformer (ICT) in the BTS beam line. The ICT has two independent identical test windings that allow beam to be simulated by passing a test pulse through the winding. One test winding is always in use during BESOCM operation, to provide the self-test pulse to the ICT. The second winding is used only during validation or testing. The ICT connects to the BESOCM electronics chassis, located outside the beam tunnel, via three coax cables.

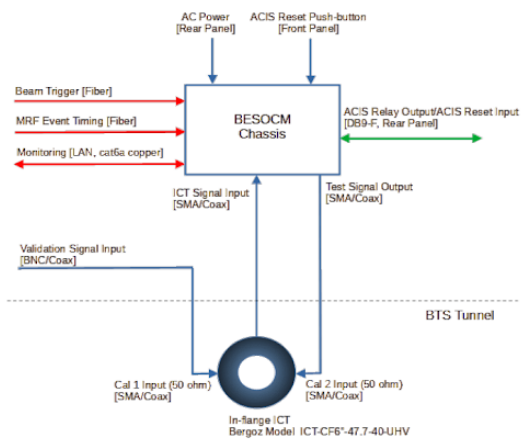


Figure 1: BESOCM system block diagram.

* Work supported by the U.S. Department of Energy, Office of Science, under Contract No. DE-AC02-06CH11357
† keane@anl.gov

Content from this work may be used under the terms of the CC-BY-4.0 licence (© 2023). Any distribution of this work must maintain attribution to the author(s), title of the work, publisher, and DOI

ISBN: 978-3-95450-236-3 ISSN: 2673-5350 doi:10.18429/JACoW-IBIC2023-TUP041

Content from this work may be used under the terms of the CC-BY-4.0 licence (© 2023). Any distribution of this work must maintain attribution to the author(s), title of the work, publisher, and DOI

The BESOCM performs the following measurements on each electron bunch, and will trip ACIS if any are outside preset limits:

- Accumulated beam charge
- Single beam bunch charge
- Beam timing

Correct beam timing is determined by comparing the arrival time of a detected bunch to the expected window based on the timing of the external trigger.

For each of three test pulses, the following checks are performed, and if the result is outside preset limits, a fault is generated:

- Pulse charge (integration)
- Pulse amplitude (peak)
- FWHM
- Baseline

In addition to beam and test pulse generated faults, the BESOCM has several system fail-safes faults (see Table 1).

Table 1: Fault Conditions

Fault #	Condition
1	Beam Pulse High
2	Beam Accumulator High
3	Beam Baseline Integrity
4	Test Pulse 1 Fail
5	Test Pulse 2 Fail
6	Test Pulse 3 Fail
7	CRC Bad
8	Charge Outside Window
9	Power Bad
10	ADC Saturation
11	Keylock in Program
12	Force Trip
13	ACIS Reset Hold-off
14	No Clock
15	reserved
16	No Trigger

Any fault will trip the ACIS relay to the unsafe state and latch until reset. The reset can only be accomplished manually, either by pressing the front panel reset button or via a remote reset signal input on the ACIS DB9 connector (see Fig. 1). The BESOCM front panel provides an LED indicator for each of the faults listed in Table 1. An EPICS PV is also available for each fault for remote monitoring.

Integrating Current Transformer (ICT)

The ICT is located in the BTS beam line (see Fig. 1). It outputs a gaussian-like pulse in response to a beam bunch passing through it; the area under this pulse is proportional to the bunch charge. The ICT is designed to output a pulse of at least ~20 ns width, even for very short beam pulses, resulting in a signal bandwidth below a few tens of MHz. Therefore, direct digitization of the ICT signal is achievable with reasonable sample rates. We used a 200 Msps, 16-bit ADC for the BESOCM design (LTC2107). The ICT is available from the manufacture with an optional test winding. We requested a custom ICT design with two test windings to allow for validations to be performed without impacting the self-test function.

As in our existing BESOCM system, a single ICT is used for both chains; each chain independently analyses the self-test pulses to provide redundancy. In response to our request, the ICT manufacturer (Bergoz) performed failure testing of ICTs by creating various failure conditions and recording the effects on the ICT response. The results demonstrate that the BESOCM self-test pulse function will detect ICT failures such as windings shorted or open, internal component failures, etc. This testing provided additional justification for using a single common ICT for both chains [4].

BESOCM CHASSIS DESIGN

The BESOCM chassis (see Figs. 2 and 3) contains several circuit boards:

- FPGA Processing Boards (A & B)
- Test Pulse Generator Board
- ICT Buffer and Fan-out Board
- ACIS Interface (Relay) Board
- Power Supply Distribution Board

A brief description of each board is given below.



Figure 2: BESOCM chassis, front view.

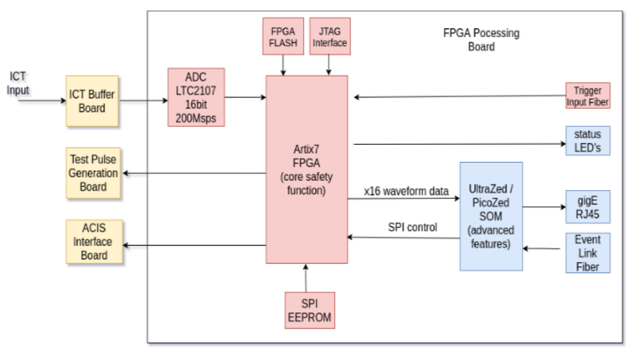


Figure 3: BESOCM chassis components block diagram. The components inside the border are duplicated for each of the two chains.

FPGA Processing Board

The FPGA processing board includes the Artix 7 FPGA, the ADC that digitizes the ICT signal, ACIS latch circuit,

ISBN: 978-3-95450-236-3 ISSN: 2673-5350 doi:10.18429/JACoW-IBIC2023-TUP041

watchdog ICs that monitor timing signals and power, and connectors to mount the PicoZed SOM modules. The board provides I/O connections for the PicoZed LAN, USB-serial and MRF event receiver external connectors on the front panel.

Test Pulse Generator Board

The test pulse generator board schematic is shown in Fig. 4. The circuit generates up to four different test pulses that are sent to the test winding of the ICT via a coax cable to simulate beam pulses of varying charge. The pulse is selected using a fast analog switch controlled by the FPGA. The charge level of each pulse is set by a fast MOSFET along with an attenuation network and DC block. For each pulse, the FPGA provides two timing signals that control the delay and width of the pulse. The pulse width adjustment allows control over the resulting pulse charge. The MOSFET produces a small but significant transient pulse; the adjustable delay allows the test pulse to be positioned such that it combines with the switch transient, effectively eliminating it as an issue [5].

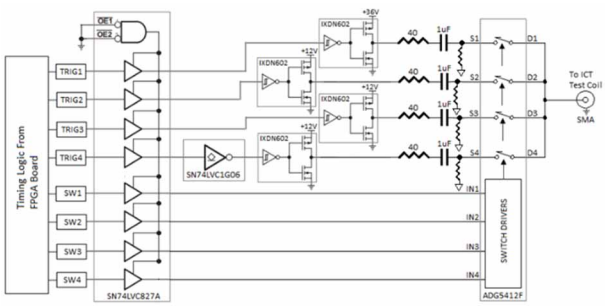


Figure 4: Test pulse generator circuit.

The BESOCM is configured to use three test pulses in sequence that cover the operating range of the ADC.

ACIS Interface Board

The ACIS interface board has two safety-rated relays that provide the interface to the ACIS system chains A & B via a DB9 connector on the BESOCM rear panel. This board also includes a reset relay with an externally driven coil that resets the fault latches in the same manner as the front panel reset switch, allowing operators to reset faults remotely from the control room.

SYSTEM SETTINGS AND MONITORING

EPICS IOC

The PicoZed SOM daughter boards run Ubuntu Linux. Each board implements an embedded EPICS IOC that provides process variable (PVs) for all settings and readbacks, including waveforms.

CSS GUI Screens

Extensive Control System Studio (CSS) engineering screens were developed by the BNL team. The screens allow monitoring of the BESOCM in real time and include digitized waveforms of the beam ICT output and the three test pulses along with test parameter measurement results on the waveforms. Plots of the accumulator and beam history for the previous hour are displayed, along with live and latched fault status. Power supply voltage and current, and board temperatures are also displayed. Separate screens for the beam pulse, and each test pulse, with more detailed analysis are available, along with a post-mortem screen that saves BESOCM data at the time of the last fault (see Fig. 5).

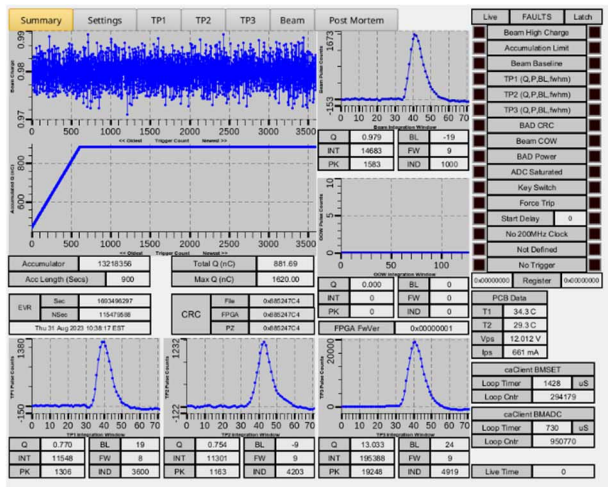


Figure 5: Engineering Summary screen; tabs provide access to other screens with more detailed information.

Changing System Settings

The BESOCM stores the system settings in a flash EEPROM on the FPGA main board, along with a CRC hash. Upon power up, the settings and CRC are transferred to FPGA memory. During operation the BESOCM continuously re-calculates the CRC on every 1 Hz trigger to ensure the integrity of the settings data.

The EPICS IOC provides PVs for all the settable parameters, such as accumulation time, beam limits, test pulse limits and timing, beam charge calibration, etc. As all these settings are critical to the BESOCM function, strict control over any changes to the settings is required. Therefore, we implemented a hardware enable using a key switch on the front panel that enables or disables writing to the EEPROM. When the BESOCM is in its normal operating mode, the key switch is in the "run" position which prevents any data transfer into the EEPROM. When the key switch is set to "program" writing to the EEPROM is enabled and an ACIS trip state is always asserted. This prevents beam from being transferred through the BTS line. APS administrative controls require the BESOCM to be re-validated after any switch to "program".

The CSS Settings screen is shown in Fig. 6. The screen is divided into three sets of equivalent PVs. The top set is the editor; the middle set displays the contents of the settings file; the bottom set displays the FPGA values. The buttons on the right control the transfer of settings from the editor to the FPGA via the settings file and flash EEPROM. Changes can only occur when the front panel keylock is set to "program". The editor section allows

Content from this work may be used under the terms of the CC-BY-4.0 licence (© 2023). Any distribution of this work must maintain attribution to the author(s), title of the work, publisher, and DOI

ISBN: 978-3-95450-236-3 ISSN: 2673-5350 doi:10.18429/JACoW-IBIC2023-TUP041

settings to be written to and read from the settings file. The settings file is used to temporarily store the settings; in normal operation only the FPGA values are relevant. Any discrepancy in the value of a setting between the three sections is highlighted in red (not shown). The red boxes on the right indicate the key switch is in "run" mode.



Figure 6: The Settings screen.

EVALUATION AND TESTING

Three production units have been delivered to APS from BNL. Each unit has been tested and evaluated in the lab with simulated beam without issues. One unit was installed in the BTS during the final APS run and performed as expected. Once the upgraded BTS beam line is operational, we plan to do extensive statistical analysis with real beam to determine the best settings for the various fault limits with different beam charge, timing, etc., with the goal of ensuring maximum fail-safe function and minimal interruption to operations from spurious trips.

VALIDATION

APS requires annual re-validation of safety systems. We are currently developing a new validation procedure for the BTS BESOCM that will test and validate each of the beam and self-test fault functions. The extensive EPICS PVs will aid in automating the new validation procedure.

CONCLUSION

In preliminary testing and evaluation, the BTS BESOCM has operated reliably and is a significant advancement over the existing BESOCM system. We are preparing to install it in the upgraded BTS line and expect it to be fully operational when the upgraded BTS line is commissioned.

ACKNOWLEDGMENTS

The authors would like to acknowledge Glenn Decker, Ken Belcher, Joe Lenner, Bob Hettel, Dan Paskvan and Andrew Johnson for their help and support.

REFERENCES

[1] X. Wang *et al.*, "High Beam Current Shut-off Systems in the APS Linac and Low Energy Transfer Line," in *Proc BIW'94*, Vancouver, Canada, vol. 333. pp. 274-285, 1995. doi.org/10.1063/1.48051

[2] A. Pietryla *et al.*, "Design of the Beam Shut-off Current Monitor Upgrade for the Advanced Photon Source," in *Proc. BIW'00,* Cambridge, USA, vol. 546, pp. 527-534, 2000. doi.org/10.1063/1.1342626

[3] K.C. Harkay et al., "Radiation Safety Considerations For The APS Upgrade Injector", in *Proc. IPAC'21,* Campinas, Brazil, May 2021, pp. 445-448. doi:10.18429/JACoW-IPAC2021-MOPAB123

[4] N. Sereno *et al.*, "Justification for use of a single ICT for the APS-U BTS BESOCM," ANL/APS, Lemont, IL, Technical Report DIAG-TN-2021-033, 2021.

[5] A. Caracappa *et al.*, "Method to Remove Test Pulse Switch Transients and Long-Term Bench Testing for the BTS BESOCM Electronics," ANL/APS, Lemont, IL, Technical Report DIAG-TN-2022-045, 2022.

Content from this work may be used under the terms of the CC-BY-4.0 licence (© 2023). Any distribution of this work must maintain attribution to the author(s), title of the work, publisher, and DOI

ISBN: 978-3-95450-236-3 ISSN: 2673-5350 doi:10.18429/JACoW-IBIC2023-TUP042

NANO-AMP BEAM CURRENT DIAGNOSTIC FOR LINAC-TO-ESA (LESA) BEAMLINE*

S.T. Littleton†, A.S. Fisher, T. Raubenheimer, SLAC, Stanford, CA, USA
C. Huang, Evergreen Valley High School, San Jose, CA, USA

Abstract

The LESA beamline is designed to transport dark current from the LCLS-II and LCLS-II-HE superconducting linacs to the End Station A for various fixed target experiments. The primary experiment is expected to be the Light Dark Matter eXperiment (LDMX) which required beam currents of a few pA. The operation of the beam line must be parasitic to the LCLS-II / LCLS-II-HE FEL operation. The dark current in the LCLS-II is expected to be at the nA-level which will be below the resolution of most of the LCLS-II diagnostics (it will be degraded before the experiments as necessary). This paper will describe a possible non-destructive diagnostic using synchrotron radiation that could be applied at multiple locations along the LCLS-II and the LESA beamline.

INTRODUCTION

The SLAC Linac to End Station A (LESA) beamline is a staged concept to provide a near-CW beam at 186 MHz and sub-harmonics thereof to the SLAC End Station A (ESA) for experiments in particle physics requiring pA to 25 nA electron beams with multi-GeV electron energy [1]. This capability is achieved parasitically by extracting unused bunches from the LCLS-II/LCLS-II-HE superconducting RF (SRF) linac [2, 3].

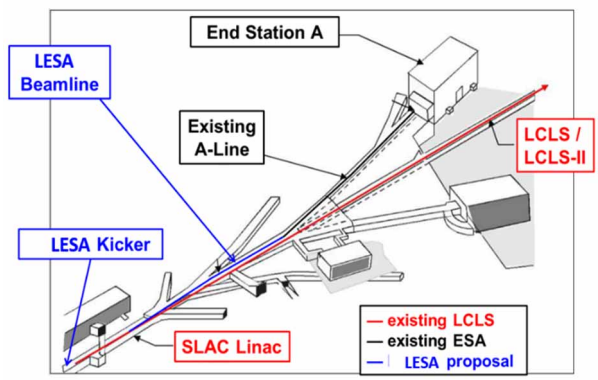


Figure 1: Schematic of LESA beamline starting in SLAC linac and connecting to the A-line.

The LESA beamline begins in Sector 28 of the SLAC linac and continues into the Beam Switchyard, where it connects with the A-line as illustrated in Fig. 1. The beamline consists of (1) a long-pulse kicker and septum magnet to divert low-current bunches off the LCLS-II dump line, (2) a 250m long transfer line from the kicker in Sector 29 to the existing A-line, delivering beam to End Station A, (3) minor improvements in the existing End Station A infrastructure, and (4) an optional laser oscillator that augments the dark current with a well-defined, low-current beam at 46 MHz repetition rate within a ~500 ns macropulse between LCLS-II/LCLS-II-HE primary bunches as illustrated in Fig. 2.

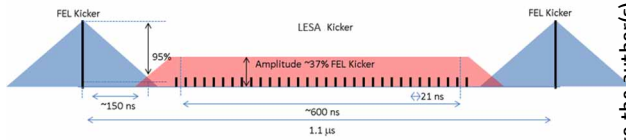


Figure 2: LCLS-II pulse structure showing primary pulses with 10^8 e- and LESA bunches from the gun with 30 e- per bunch. The LESA beam will control the bunch population with an additional seed laser and/or a spoiler/collimation system to deliver final current in the pA to µA range.

Table 1: LESA Electron Beam Parameters for an Ultra-Low-Current Beam (Baseline) and a Possible Upgrade

Experiment Parameters	**Ultra-low-current**	**Low-current (upgrade)**
Energy	4.0 GeV (upgrade to 8.0 GeV in 2027)	4.0 GeV (upgrade to 8.0 GeV in 2027)
Bunch spacing	5.4 – 65 ns	5.4 ns
Bunch charge	0.04 – 10,000 e^-	70,000 e^- (10 fC)
Macro pulse beam current	0.1 – 25 nA	2 µA
Duty cycle	55% (600 ns out of 1.1 µs)	55% (600 ns out of 1.1 µs)
Norm. emittance (rms)	~100 µm; <1000 µm	~1 µm
Bunch energy spread	<1%	<1%
IP spot size w/ rastering	4 cm x 4 cm	<250 µm including jitter
Electrons per year	10^{15} e- / year	10^{19} e- / year

LESA is being constructed in two stages: the first stage, S30XL, is nearly complete and will demonstrate the dark current extraction from the SRF linac while the 2nd stage, on which construction is just starting, will transport the extracted current to ESA. S30XL will be commissioned in late 2023 while the full LESA beamline is planned to be complete at the end of 2024.

* Work supported in part by DOE contract DE-AC02-76-SF00515.
† seantl@stanford.edu.

Content from this work may be used under the terms of the CC-BY-4.0 licence (© 2023). Any distribution of this work must maintain attribution to the author(s), title of the work, publisher, and DOI

ISBN: 978-3-95450-236-3 ISSN: 2673-5350 doi:10.18429/JACoW-IBIC2023-TUP042

Content from this work may be used under the terms of the CC-BY-4.0 licence (© 2023). Any distribution of this work must maintain attribution to the author(s), title of the work, publisher, and DOI

The presently envisioned program for LESA comprises dark sector physics, electron-nuclear scattering measurements for the neutrino program, and a test beam program [4]. Beam parameters are listed in Table 1.

One of the many challenges for the LESA beamline is to quantify the very low current beam in a parasitic manner. The expectation is that the incoming dark current will be at the level of a few nA; if necessary, this will be attenuated before the End Station using a spoiler in the A-line. Ongoing measurements at LCLS-II indicate this level of dark current at the end of the SRF linac [5].

S30XL SYNCHROTRON RADIATION

This paper will address one possible concept for a non-destructive diagnostic using synchrotron radiation and a sensitive x-ray detector that could be applied at multiple locations along the LCLS-II and the LESA/S30XL beamline. The goal is to routinely measure 100 nA to 10 pA beams at the beginning of the LESA/S30XL beamline non-destructively so that we can tune the SRF linac and set the scattering foil correctly.

The LESA/S30XL beamline is illustrated schematically in Fig. 3. As shown, the S30XL kicker and septum extract dark current from the SRF Dump beamline and transport it across the CuRF linac before it is deflected to be parallel to the other beamlines and put into a low-power dump. LESA will transport this into the A-line and ESA.

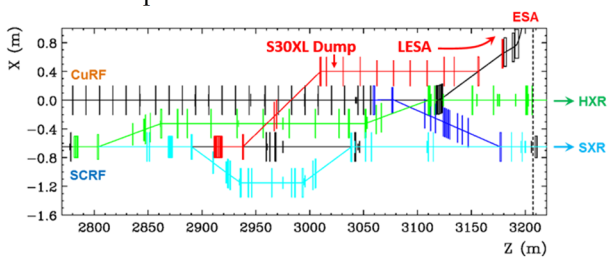


Figure 3: Schematic of the LESA/S30XL beamline (red) along with the SCRF beamline to the HXR FEL (green) and the SCRF beamline to the SXR FEL (blue).

The last dipole in the S30XL line before the Dump is a 1-meter bend and will deflect the beam by 19.1 mrad. The magnetic field is 2.5486 kG at 4 GeV and twice that at 8 GeV. The instantaneous radiated power and the photon critical wavelength are given by the equations:

$$P_\gamma = \frac{cC_\gamma}{2\pi}\frac{E^4}{\rho^2} \qquad E_c[keV] = 2.22\frac{E^3[\mathrm{GeV}]}{\rho[\mathrm{m}]},$$

where E is the electron energy, ρ is the bending radius, and C_γ = 8.85e-5 [m/GeV^3]. With a beamline of 4 GeV and a bending radius of 52.4 meters, the instantaneous radiated power is 3.94 x 10^8 keV/s. The critical photon energy is 2.71 keV at 4 GeV and 21.68 keV at 8 GeV and the number of photons emitted per second for a photon of energy u can be determined using the equation [6]:

$$n(u) = \frac{P_\gamma}{u_c^2} F\left(\frac{u}{u_c}\right),$$

where u_c is the photon critical energy, E_c, and $F(u/u_c)$ is a function that can be written as:

$$F(\xi) = \frac{9\sqrt{3}}{8\pi}\int_\xi^\infty K_{\frac{5}{3}}(\xi')d\xi',$$

where K is a modified Bessel function. These photons will be swept in angle as the electron traverses the dipole and will have a vertical angle that scales as 1/γ but depends on the photon energy.

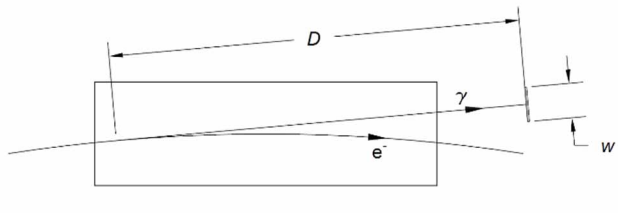


Figure 4: In the diagnostic under consideration, bending magnet radiation is intercepted by a sensitive detector.

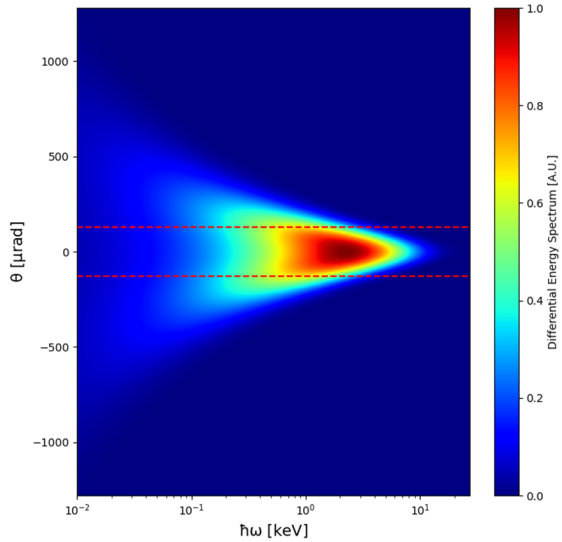


Figure 5: Differential spectrum of the radiation emitted by 4 GeV electrons passing through the bend.

INTERCEPTED SPECTRUM

The spectrum intercepted by a detector of height h and width w a distance D from the location where the radiation is emitted, as shown in Fig. 4, will differ from the full spectrum emitted by the electrons, since some low-energy photons will be radiated at vertical angles greater than $\theta_{max} = h/2D$. To find the intercepted spectrum, we must begin with the full differential spectrum [7], shown in Fig. 5.

$$\frac{d^2I}{d\omega\, d\Omega} = \frac{e^2}{12\pi\varepsilon_0 c}\left(\frac{\omega\rho}{c}\right)^2\left(\frac{1}{\gamma^2}+\theta^2\right)^2 G(\zeta),$$

where

$$G(\zeta) = K_{2/3}^2(\zeta) + \frac{\theta^2}{1/\gamma^2+\theta^2}K_{1/3}^2(\zeta)$$

and

$$\zeta = \frac{\omega\rho}{c}\left(\frac{1}{\gamma^2}+\theta^2\right)^{3/2}.$$

ISBN: 978-3-95450-236-3 ISSN: 2673-5350 doi:10.18429/JACoW-IBIC2023-TUP042

Integrating over vertical angles θ between $-h/2D$ and $h/2D$, we find that the spectrum intercepted by a 4.5 mm x 4.5 mm detector at various distances is modified as shown in Fig. 6.

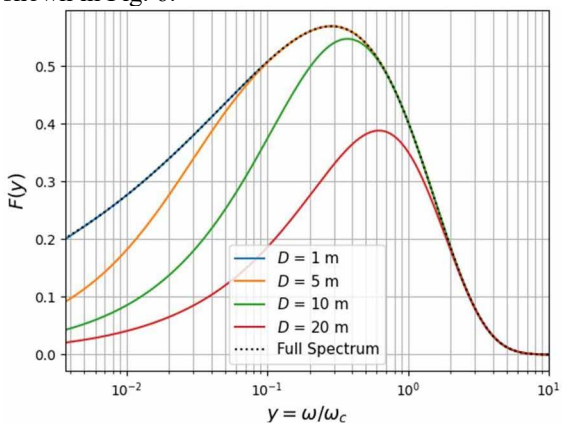


Figure 6: The energy spectrum of the photons intercepted by a 4.5 mm x 4.5 mm detector at various distances from the point where the radiation is emitted.

DETECTOR RESPONSE

We have modeled the response of a 500 µm-thick Cividec B1 CVD diamond detector to the incident synchrotron radiation spectrum, based on data provided by Cividec [8] regarding the mean charge produced in the detector as a function of incident photon energy. Using an eighth-order polynomial fit to the Cividec data, with the constraint that the response goes to zero near the ionization energy of carbon, we multiplied the intercepted photon spectrum by the charge response curve, as shown in Fig. 7. We then integrated over photon energies to estimate the total charge Q produced in the detector per beam electron for detector distances of 1, 2, 5, 10, and 20 m, for both the 4 GeV beam and the 8 GeV LCLS-II-HE beam. The results are shown in Table 2.

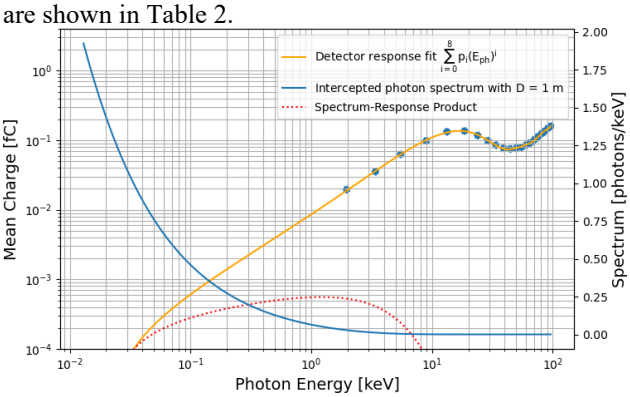


Figure 7: A side-by-side comparison of the photon spectrum and the diamond detector response curve on a log-log plot. The seemingly large region with no response data is a negligible part of the integral.

At 186 MHz, a 10 nA dark current beam would contain roughly 336 electrons per bunch. For $D = 1$ m, the corresponding detector charge would be 1 fC/bunch for the 4 GeV beam or 10 fC/bunch for the 8 GeV beam. When coupled with a Cividec C6 fast charge amplifier [9], with a gain of 5.4 mV/fC, such a signal may provide useful bunch-by-bunch data, though further amplification may be required locally to prevent noise from contaminating the signal on its way out of the tunnel.

Table 2: Expected Charge Produced by the Cividec Diamond Detector Per Electron in the LESA Beamline

D [m]	Q [fC/e$^-$] (4 GeV beam)	Q [fC/e$^-$] (8 GeV beam)
1	3.1×10^{-3}	3.0×10^{-2}
2	1.5×10^{-3}	1.5×10^{-2}
5	6.1×10^{-4}	6.0×10^{-3}
10	3.0×10^{-4}	3.0×10^{-3}
20	1.3×10^{-4}	1.4×10^{-3}

CONCLUSION

We have investigated the feasibility of using synchrotron radiation emitted by dark current in LCLS-II and LESA to measure the associated nA-level currents. The detector we modeled, a Cividec B1 CVD diamond detector, shows promise as a potential detector for currents at the higher end of the anticipated range of the dark current. To measure lower currents, especially at the pA level, we will explore alternative detectors, such as low-gain avalanche diodes (LGADs) and CCD arrays. The measurement may also be sensitive to the radiation background in the accelerator tunnel. Further studies are needed to characterize the background in the proposed detector location and explore collimation and shielding strategies.

REFERENCES

[1] T. Markiewicz *et al.*, "The SLAC Linac to ESA (LESA) Beamline for Dark Sector Searches and Test Beams", *arXiv*. doi:10.48550/arXiv.2205.13215

[2] T. Raubenheimer, ed., LCLS-II Final Design Report, internal SLAC document, 2015.

[3] T. Raubenheimer, ed., LCLS-II-HE Conceptual Design Report, LCLSII-HE-1.1- DR-0001 and SLAC-R-1098, Mar. 2018.

[4] A description of LESA and its science program can be found in SLAC-R-1147. The LESA beamline has been known as DASEL, S30XL, and YABBL.

[5] Y. Ding, private communication, 2023.

[6] M. Sands, "The physics of Electron Storage Rings", SLAC-121, 1971.

[7] J.D. Jackson, *Classical Electrodynamics*. Wiley. (1998).

[8] Cividec Instrumentation, "Particle interaction with diamond", internal working paper for Alan Fisher of SLAC, 2017.

[9] Cividec Instrumentation, Electronics Application Note.

Content from this work may be used under the terms of the CC-BY-4.0 licence (© 2023). Any distribution of this work must maintain attribution to the author(s), title of the work, publisher, and DOI

ISBN: 978-3-95450-236-3 ISSN: 2673-5350 doi:10.18429/JACoW-IBIC2023-TUP044

THE DIGITAL SIGNAL PROCESSING CHAIN OF THE CERN LIU BWS

D. Belohrad*, J. Emery, J. C. Felipe,
A. Goldblatt, A. Guerrero, M. M. Nieto, F. Roncarolo
European Organisation for the Nuclear Research (CERN), Geneva, Switzerland

Abstract

Between 2019 and 2023, as part of the LHC Injectors Upgrade (LIU), a major renovation of the CERN wire scanners (BWSs) was performed. The main driving force was to prepare the wire scanners for the High-Luminosity LHC (HL-LHC), during which the instantaneous luminosity is expected to double, to around $5 \times 10^{34}\text{cm}^{-2}\text{s}^{-1}$. In 2021 seventeen LIU BWSs were installed in the CERN PS complex and the Super Proton Synchrotron (SPS). Additionally, two BWSs were installed in the LHC, at the end of 2022, to be ready for the 2023 LHC run. The contribution aims to describe in detail the technical implementation of the data acquisition chain (DAQ) and digital signal processing of the photomultipliers of the newly installed BWSs. Particular attention is given to the design of the analogue front-end, signal conversion, and data processing chain — providing data for the profile reconstruction. The synchronisation of the incoming digitised signal with the machine timing is also addressed, as it differs significantly between the PS complex and the LHC and SPS. Finally, the limitations of the system are discussed.

INTRODUCTION

The BWS functional and engineering specifications, as well as commissioning and first operational results, were already documented in the last few years [1–3]. This paper is intended to complement the information about the LIU BWS project with the details about the new DAQ design, development, and implementation.

The previous BWS DAQ, completed in the early 2000s, was based on in-house developed digital acquisition board (DAB), equipped with two individual bunch measurement systems (IBMSs) [4, 5]. They were general-purpose platforms targeting various LHC and SPS instrumentation.

The IBMSs included an analogue integrator ASICs, able to deliver bunch-per-bunch information, e.g. of the secondary particle shower used to reconstruct beam profiles with BWSs. These were converted into digital data streams using 40 MSPS 14-bits ADCs, and then processed by the DAB's FPGA.

As discussed more in detail later in the paper, a new DAQ generation was designed and implemented, as part of the LIU BWS project. The DAQ is based on a modern FPGA VME FMC Carrier [6], equipped with a fast FMC ADC, which allows the bunch-per-bunch signals reconstruction via digital integration.

* david.belohrad@cern.ch

DAQ CHALLENGES AND SOLUTIONS

The LIU BWSs installed in the entire CERN accelerator complex use the same DAQ. This makes maintenance and spares management easier, but implies challenges in the DAQ gate-ware design to adapt to the different accelerators beam parameters. In order to set up the systems, diagnose problems and function during normal operation, the DAQ has to produce bunch-per-bunch integrals together with raw data acquired by the ADC.

The differences between the Proton Synchrotron Complex (CPS) and SPS installations are formalized as follows.

In the CPS the beam can be represented as:

- *bunch pattern* in the Proton Synchrotron (PS), and
- *continuous flow of bunches*, as e.g. in the Proton Synchrotron Booster (PSB), (Fig. 1).

In the CPS the bunches are separated into their respective turns by *Turn tag*s. The turn tag is a revolution period signal delivered by the accelerator RF subsystem. The number of bunches in the turn is supplied by SW as a *harmonic number* (H). Knowing the total number of samples in turn (S_{tot}) and H we determine the *integrating window* for each bunch. The bunch-per-bunch integrals $S_{bunch,turn}$ are calculated as the sum of samples over the integrating windows.

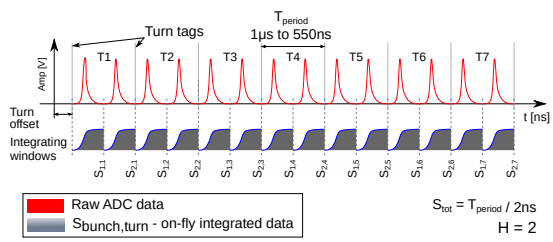


Figure 1: Example of an ideal PSB data acquisition, assuming there are two bunches and the wire passes through a transverse portion of the beam with a constant number of particles during the 7 turns displayed.

In the SPS the integrating windows are not artificially created from the harmonic number. They are identified by the bunch tags delivered together with turn tags via the beam synchronous timing (BST) [7]. The bunch-per-bunch integrals are calculated as the sum of samples between two consecutive bunch tags.

In both cases, a major challenge lies in tracking the tags, since their period changes during the acceleration cycle. In the worst case of the CERN PSB the period changes from 1 µs at injection to ≈ 550 ns at extraction. Another difficulty is to find a correct phase relation between the tags delivered to DAQ and the bunches in the sampled data. The tags

Content from this work may be used under the terms of the CC-BY-4.0 licence (© 2023). Any distribution of this work must maintain attribution to the author(s), title of the work, publisher, and DOI

ISBN: 978-3-95450-236-3 ISSN: 2673-5350 doi:10.18429/JACoW-IBIC2023-TUP044

have to fit to 'no-beam' in the data to minimise cross-talk between consecutive bunch slot integrals. Assuming the bunch spacing (used for the bunch tags) is well known, the phasing relies on the *Turn offset* shown in Fig. 1. Both the turn offset and the number of ADC samples per bunch must be set before starting the ADC data processing. The DAQ trigger (occurring once per scan) is not synchronised with the machines' timing (defining the turn clocks) and RF settings (defining the first bunch position in the turn and the bunch spacing). Therefore, the turn offset and the bunch tags setting cannot rely on previous acquisition sets. In addition, as the acquisition starts when the wire does not yet intercept the beam, the first turn signal cannot be used either for setting on the fly the phasing. Therefore, the DAQ features two processing modes that are implemented in the same way for the CPS and SPS systems:

1. **Capture**: The ADC samples are tagged by turn and bunch marks and written into volatile memory, together with S_{tot} per turn.
2. **Integration**: The volatile memory is read back to calculate the bunch integrals.

The raw data from up to 64 scans can be captured and stored in the volatile memory. It is used to estimate the correct turn offset, perform the digital integration and reconstruct the beam profile from any of the ADC channels, as many times as needed.

DAQ IMPLEMENTATION

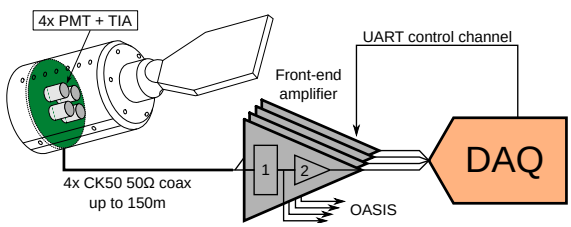


Figure 2: BWS data acquisition chain.

The acquisition chain of a BWS is illustrated in Fig. 2. The secondary particle shower, produced when the BWS wire interacts with the beam, is intercepted by a scintillator coupled to 4 separate photo multipliers (PMTs) (Hamamatsu R9880U). They share the same HV power supply and are read-out in parallel. In order to enhance the detection dynamic range at a constant PMT voltage, optical density filters of different attenuation are installed between the scintillator and the 4 PMTs. For each machine and its beam types, a common PMT voltage is defined such, that at least one of the ADC channels is not saturated and provides enough signal to noise ratio (SNR).

Signal Conditioning

To maximise the SNR of the measurement, the PMTs signals are amplified directly at the source. Current-feedback *trans-impedance amplifier*s (TIAs) with a gain of 500 mV/mA and output impedance of 50 Ω convert the PMT current-source signals to voltage. Four coaxial cables bring the analogue signals to the surface *front-end amplifier* (FEA) that provides a two-stage amplification and filtering to the DAQ input. In the first stage, the signals pass through 260 MHz non-reflective low pass filters, are buffered and sent in parallel to the CERN OASIS monitoring system [8], and to the second FEA gain stage. The gain setting for the second stage, switchable between 0 dB and 10 dB, is common for all four channels. Each second gain stage is also equipped with adjustable bipolar offset used to minimise the DC baseline shifts. Antialiasing filters, with a cut-off frequency of approximately 250 MHz, are used to remove high-frequency content. The offset and gain of the FEA can be set remotely via SW through the *UART control channel*.

The analogue bandwidth of both amplifiers exceeds the system functional specification of 100 MHz. The overall bandwidth limitation comes from the coaxial cables used (type CERN CK50, ≈ 6 dB/100 m at 400 MHz). In some BWS installations, the coaxial cable lengths exceed 150 m. This causes the analogue signal pile-up at the DAQ inputs such, that the individual bunches cannot be clearly separated. Such a *cross-talk* has to be minimised by the digital signal processing.

Analogue to Digital Converter

The DAQ for the CERN LIU BWSs is composed of a new generation VME FMC Carrier (VFC) [6] developed at CERN, hosting an ADC FMC, with specifications shown in Table 1.

Table 1: BWS ADC Specifications. ENOB and SFDR Compliance is Required in the Bandwidth of 70 — 250 MHz

Property	Value
Number of channels	4
Sampling rate	≥ 500 MSPS
Digital interface	JESD204B
Form factor	FMC, VFC compatible
Analogue input coupling	AC, DC
ENOB	≥ 9.5
SFDR	≥ 70 dBc

In 2019, it was not possible to find FMCs of this type off-the-shelf, so CERN conducted a market survey to procure a prototype and then a series of 60 pieces. The tender was won by IAM Electronics GmbH. In October 2020, there were thirty 4-channel 14-bits 500 MSPS FMC ADC modules available at CERN. The design was released under the CERN Open Hardware Licence [9].

The block schematic of the module is shown in Fig. 3. The analogue input consists of four DC-coupled single-ended to differential amplifiers (LMH5401), followed by passive 900 MHz LC filters. Those define the analogue input bandwidth of the sampling system. The analogue signals from

Content from this work may be used under the terms of the CC-BY-4.0 licence (© 2023). Any distribution of this work must maintain attribution to the author(s), title of the work, publisher, and DOI

ISBN: 978-3-95450-236-3 ISSN: 2673-5350 doi:10.18429/JACoW-IBIC2023-TUP044

Content from this work may be used under the terms of the CC-BY-4.0 licence (© 2023). Any distribution of this work must maintain attribution to the author(s), title of the work, publisher, and DOI

each channel are fed into a single 500 MSPS 4-channel ADC from Texas Instruments. The converted digital data are streamed through high-speed serial lines to the FPGA using the JESD204B protocol [10]. The JESD204B synchronisation signals are generated by the FPGA gate-ware (shown in orange in Fig. 3).

The fast ADC sampling rate and high-speed serial transmission require ultra-clean clock with sub-picosecond jitter. Such clock is delivered by jitter-attenuating PLL from Silicon Labs. An external 48 MHz crystal is used in the loop-back of the internal PLL oscillator to define the base frequency. The PLL outputs provide not only 500 MHz reference for the ADC, but also the 1.016 MHz SYSREF for the JESD204B, and a 500 MHz clock for the FPGA transceiver block (shown in green in Fig. 3). To reduce even further the SFDR, the installed DC/DC converters synchronise their switching to SYSREF.

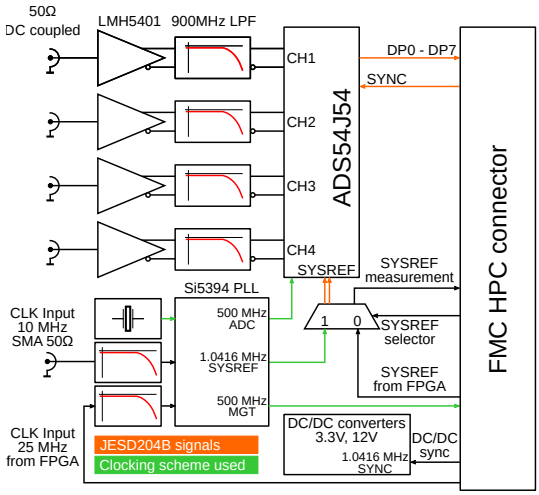


Figure 3: Simplified block schematic of the 4-channel 14-bits 500 MSPS FMC ADC module from IAM Electronics GmbH.

Firmware Implementation

The VFC is a VME64x carrier chosen to house the FMC ADC. The carrier was developed and produced specifically for the CERN Beam Instrumentation group to serve as a common development platform. It is equipped with a single FMC high-pin count slot, two 8 Gbit DDR SDRAMs, and a 115k-cell Intel ArriaV GX FPGA. The board can receive the SPS and LHC BST either through an optical interface or through the P0 VME connector when installed in a LHC type VME crate. The DAQ raw data signal processing is entirely implemented in the VFC FPGA. The processing chain is shown in Fig. 4.

The ADC data stream is received through eight 5 Gbit transceiver lanes (HSSI). As the transceivers are *not* located on the same side of the FPGA, the JESD204B subsystem has to be instantiated manually — by generating two physical interfaces (PHYs), using two different clock sources, joined by a JESD204B MAC. This creates a mesochronous clock network in which the (unknown) phase between the clocks is defined by physical routing and does not represent a problem.

The JESD204B IP core delivers data as a stream of 256-bit frames. The frame clock frequency is 125 MHz, so a data frame is received every 8 ns. Each frame contains 4 samples of 4 channels. The ADC samples, which are 14 bits, are left-aligned in 16-bit bit vectors. The two least significant bits (LSBs) of each sample are set to zero.

In capture mode, the channel samples are tagged to identify where bunches and turns start within the data stream. For each channel, the corresponding sample's LSB within a frame is set when tags are intercepted in the timing signal. For this to work properly, the SPS timing signal has to be *reconstructed* in the 500 MHz ADC clock domain. In the original 160 MHz BST clock domain, the turn tags always come in phase with bunch tags. Thus, the turn tag automatically identifies the start of the bunch as well. Due to a meta-stability caused by the clock domain crossing, the tags can be — in the ADC clock domain — mutually delayed by a single clock cycle, in any order. The turn tag has to be re-aligned in the ADC clock domain to the closest bunch tag received.

Two DDR SDRAM IP cores, clocked at 533 MHz, communicate with SDRAMs. This clock speed was chosen as a compromise between achieving maximum transfer speeds and minimising failures to close the timing of the FPGA. For such configuration, the SDRAM connecting interface is clocked at 125 MHz. Sharing the same clock speeds between the JESD204B and DDR controllers for storing the tagged samples into the SDRAMs would be advantageous. Unfortunately, the VFC SDRAMs do not provide enough transfer bandwidth, as it is significantly lowered by SDRAM refresh cycles. The only possibility to write the tagged data into the SDRAMs is to reduce their amount and provide an elastic buffer to cover the dead time. This means storing only 11 bits out of 14 of each sample, plus one control bit. By capturing 4 channels at the same time, we can encode the bunch and turn marks into control bits of 2 different channels, and use the other 2 remaining channels to serially encode S_{tot}. The 12-bit datagrams are packed into two 128-bit data streams by the *data packing* block shown in Fig. 4. Packed data is sent to elastic buffers to be scheduled for writing into the SDRAMs. The size of the elastic buffers was designed to cover a 20 ms acquisition window, using 40 % of the available internal FPGA memory. Capture can be triggered by both SW and hardware (HW). In the real environment, the trigger comes through the HW from the BWS resolver [11]. The rising and falling edges of the trigger signal determine the start and stop of a single acquisition. Up to 64 consecutive acquisitions can be stored in the SDRAM, and the *index memory* identifies their start and end addresses. During the capture, the amplitudes of all 4 channels in the digitised signals are inspected. The amplitudes are sorted into 8 levels, and the maximum per-channel levels reached are encoded together with the addresses into the 64-bit index memory record. The SW can efficiently decide on the best channel to use for the profile generation by analysing this information.

ISBN: 978-3-95450-236-3 ISSN: 2673-5350 doi:10.18429/JACoW-IBIC2023-TUP044

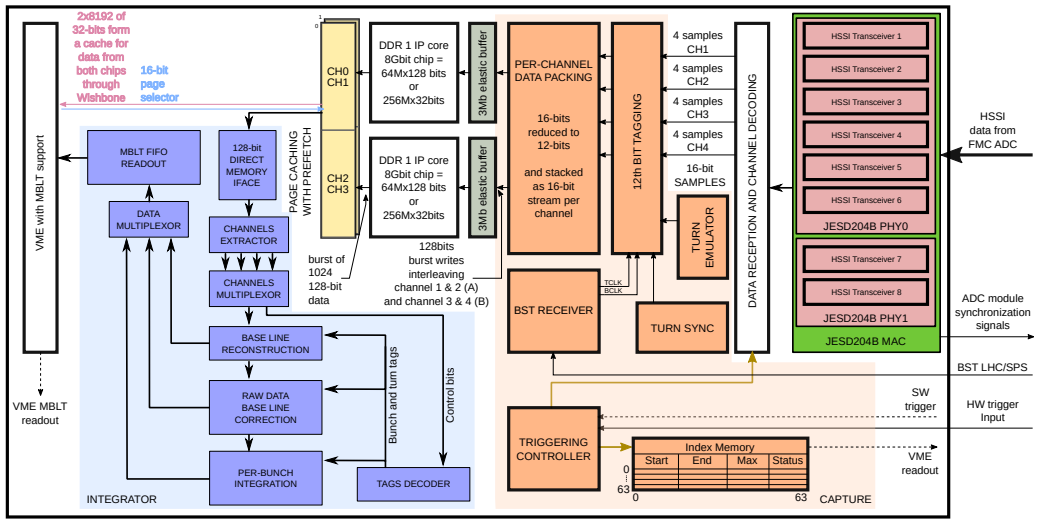


Figure 4: FPGA design block schematic.

In the integrating mode, either raw ADC or per-bunch integrated data can be obtained. The signal processing is applied to the data *previously captured, and stored into the SDRAMs*. Raw data serve mainly to identify the turn offset. The integrated data are used to reconstruct the profile.

Once a chunk of raw data is read, the offset is determined by searching for the delay between the bunch tags and the bunch apexes. This information — together with the SDRAM address start and the best channel to use — is written by the SW into the integrator. By starting the integrator, the *direct memory interface* (DMI) (Fig. 4) pre-fetches and continuously delivers the pages of the captured data from the SDRAMs. The *channels extractor* unpacks the 128-bit data back into 4 separate channels and their respective control bits. The *tags decoder* reconstructs from the samples' control bits the tags and S_{tot}. In case of CPS BWSs the bunch tags are generated *on-the-fly*. The tags are used in successive blocks to manipulate the raw data. Only one raw data channel at a time can be selected for further processing. Figure 5 shows an example of the raw and integrated data, as well as the tags, of the uncorrected acquisition.

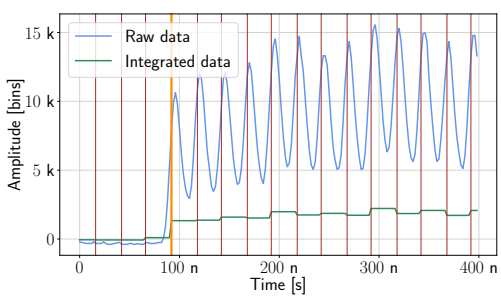


Figure 5: Raw and uncorrected PS acquisition on `PR.BWS.65H`, LHC cycle with 48 bunches (H=84), no baseline correction.

The bunch tags together with the selected raw data are used to regenerate the baseline of the signal. The baseline data stream is constructed by sampling raw data at two consecutive tags, and generating the linear approximation between them. Such a stream is subtracted from the original data to suppress the baseline and therefore minimise the signal pile-up. The *Per-Bunch Integrator* sums all the corrected data between two consecutive bunch tags. A VME A32D64 multiplexed block transfer (MBLT) is used to deliver the data to the CPU, achieving the transfer speed of ≈ 30 MBytes/s.

A card register allows for the disabling of baseline restoration and integration. This can be helpful, for example, for reading raw ADC data through the MBLT mechanism. Additionally, each processing block can be individually connected to the VME interface to inspect intermediate signal processing products.

CONCLUSION

The article presents the DAQ for the BWSs installed in the entire CERN accelerator complex. Since January 2021, more than **150 thousands scans** were performed and the DAQ is fully commissioned for the operation in the CPS and SPS. The commissioning of the DAQ for the LHC BWSs is expected in 2024.

Using VFC in combination with FMC ADC from IAM Electronics represents a trade-off between fully exploiting the technical capabilities of the ADC module, and the possibility to use an in-house common platform for development. While the presented solution fully complies with the required BWS specifications, it can be limiting for other CERN beam instrumentation systems, where 4-channel raw data need to be stored into the VFC DDR SDRAMs.

REFERENCES

[1] J. Emery *et al.*, "Commissioning of the LHC injectors BWS upgrade," in *Proc. IBIC'22*, Pohang, Korea, Sep. 2021, pp. 239–243. doi:10.18429/JACoW-IBIC2021-TUPP18

Content from this work may be used under the terms of the CC-BY-4.0 licence (© 2023). Any distribution of this work must maintain attribution to the author(s), title of the work, publisher, and DOI

ISBN: 978-3-95450-236-3 ISSN: 2673-5350 doi:10.18429/JACoW-IBIC2023-TUP044

[2] A. Guerrero, D. Belohrad, J. Emery, S. Jackson and F. Roncarolo, "Modular software architecture for the new CERN injector wire-scanners", in *Proc. ICALEPCS'21*, Shanghai, China, Oct. 2021, pp. 487-491. doi:10.18429/JACoW-ICALEPCS2021-TUPV037

[3] S. Di Carlo *et al.*, "Commissioning of the LHC injectors upgrade fast wire scanners and first experimental results", *Nucl. Instrum. Methods Phys. Res.*, vol. 1053, p. 168328, 2023. doi:10.1016/j.nima.2023.168328

[4] E. Calvo *et al.*, "The LHC orbit and trajectory system", in *Proc. 6th European Workshop on Beam Diagnostics and Instrumentation for Particle Accelerators (DIPAC'03)*, Mainz, Germany, May 2003, pp. 187–191.

[5] A. Guerrero, H. Jakob, R. Jones, and J. J. Savioz, "The SPS individual bunch measurement system", in *Proc. 5th European Workshop on Diagnostics and Beam Instrumenation (DIPAC'01)* Grenoble, France, May 2001.

[6] A. Boccardi, "Ongoing electronic development in the CERN Beam Instrumentation Group: challenges and solutions for the measurement of particle accelerator beam parameters", *J. Instrum.* vol. 8, Mar. 2013. doi:10.1088/1748-0221/8/03/C03006

[7] J.J. Savioz, "BOBR: The beam synchronous timing receiver interface for the beam observations", Technical Specification, CERN, Geneva, Switzerland, Rep. LHC-BI-ES-XXXX.XX rev 1.0 Draft, http://www.cern.ch/TTC/BOBRspec.pdf

[8] S. Deghaye, D. Jacquet, I. Kozsar, and J. Serrano, "Oasis: A new system to acquire and display the analogue signals for LHC", in *Proc. ICALEPCS'03*, Gyeongju, Korea, Oct. 2003.

[9] Open Hardware Repository, "FMC ADC 500M 14b 4CHA", https://ohwr.org/project/fmc-adc-500m14b4cha

[10] Texas Instruments, "JESD204B Overview", https://www.ti.com/lit/pdf/slap161

[11] J. Emery and F. Roncarolo, "CERN LIU beam wire scanner behavioural interface between hardware-firmware-software", Engineering Specification, CERN, Geneva, Switzerland, Rep. EDMS:2665438, https://edms.cern.ch/document/2665438

Content from this work may be used under the terms of the CC-BY-4.0 licence (© 2023). Any distribution of this work must maintain attribution to the author(s), title of the work, publisher, and DOI

ISBN: 978-3-95450-236-3 ISSN: 2673-5350 doi:10.18429/JACoW-IBIC2023-TUP045

REAL TIME MOMENTUM SPREAD MEASUREMENT OF THE CERN ANTIPROTON DECELERATOR BEAM

P. Freyermuth*, B. Dupuy, D. Gamba, CERN, Geneva, Switzerland

Abstract

Constant optimisation and diagnostics of the cooling processes in the CERN antiproton decelerator (AD) relies on a de-bunched beam momentum spread real time measurement. This article will describe the renovation of the acquisition chain of the longitudinal Schottky diagnostics in the AD, using standard CERN hardware and software to maximize reliability, ease maintenance, and meet the requirements for standard operational tools. The whole chain, from the pick-up to the operation software applications will be described with emphasis on the implementation of the data processing running on the front-end computer. Limitations will also be discussed and outlook for further development given.

THE AD LONGITUDINAL PICK-UP

The AD longitudinal pick-up (LPU) consists of two specially designed ultra-low noise ferrite-loaded beam current transformers and amplifiers [1]. They are optimized respectively for high (0.25 – 30 MHz) and low (0.02 – 3 MHz) frequency ranges.

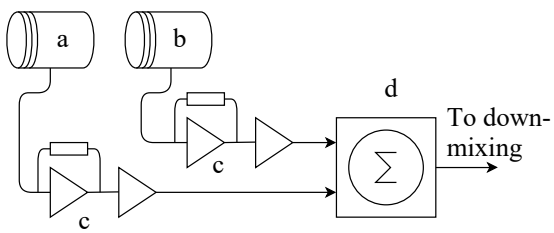


Figure 1: LPU transformers (a & b), amplifiers (c) and summing unit (d).

The output signals of the two transformers are filtered and added together by a summing unit to obtain a flat frequency response over the 0.02-30 MHz bandwidth (Fig. 1). This system is used since the AD went operational in 2001.

SIGNAL DOWN-MIXING

The longitudinal Schottky spectrum of a de-bunched beam consists of bands of frequencies (Schottky bands), located around harmonics (n) of the average revolution frequency. The momentum spread distribution can be derived from these Schottky bands. The power spectral density of these bands decreases with n, but the width of these bands increases by a factor n (Eq. 1) [2].

$$\Delta f = n\, f_0\, \eta\, \frac{\Delta p}{p} \quad , \tag{1}$$

where Δf is the width of the Schottky band, n is the harmonic number, f_0 is average revolution frequency, η is the slip factor given by the synchrotron parameters and Δp/p is the momentum spread.

The band selection, therefore, of the harmonic, is a balance between signal-to-noise ratio, frequency resolution, and LPU and acquisition bandwidth.

To accommodate the different revolution frequencies of the AD cooling plateaus, the signal from the LPU is mixed with a signal generated from a harmonic of the revolution frequency minus 50 kHz (Table 1).

Table 1: Down Mixing Frequencies

Plateau momentum [MeV/c]	Revolution frequency [kHz]	Harmonic	Mixing frequency [kHz]
3574	1589.411	2	3128.822
2000	1487.722	2	2925.445
300	500.465	8	3953.721
100	174.155	8	1343.240

The mixing unit includes filters for image frequency rejection. The result is a transposition of the signal to a fixed centre frequency of 50 kHz, enabling fixed parameters for different cooling plateau energies and modest analogue-to-digital converter (ADC) hardware specifications.

An additional 32 dB amplifier is also placed before the mixer (Fig. 2), pulling the signal strength into the range of the ADC sensitivity.

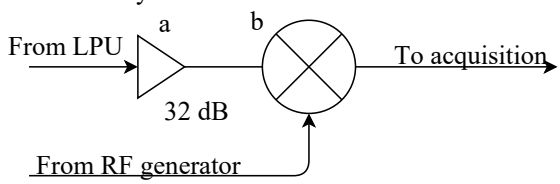


Figure 2: Simplified schematic of the signal down-mixing with a low-noise amplifier (a) and the mixing and filtering unit (b).

* pierre.freyermuth@cern.ch

Content from this work may be used under the terms of the CC-BY-4.0 licence (© 2023). Any distribution of this work must maintain attribution to the author(s), title of the work, publisher, and DOI

ISBN: 978-3-95450-236-3 ISSN: 2673-5350 doi:10.18429/JACoW-IBIC2023-TUP045

Content from this work may be used under the terms of the CC-BY-4.0 licence (© 2023). Any distribution of this work must maintain attribution to the author(s), title of the work, publisher, and DOI

SIGNAL ACQUISITION

The signal acquisition was previously performed by a now obsolete National Instrument ADC module. It has been replaced by a CERN Open Analogue Signal Information System (OASIS) [3].

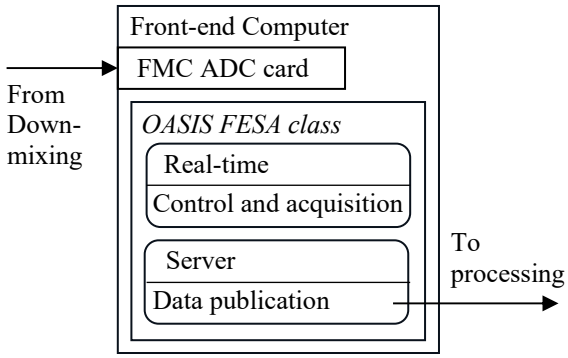


Figure 3: Overview of the acquisition system.

It consists of a 4 channel 100 million samples per second (Msps) 14-bit ADC card embedded on a FPGA Mezzanine Card format (FMC). The ADC card is operated in a Front-End Computer (FEC) by the OASIS system. OASIS is using the CERN Front-End Software Application (FESA) framework [4], enabling clients to subscribe remotely to the digitalized signal data (Fig. 3).

A typical acquisition setting is a sampling rate of 3 Msps during a 100 ms segment, for a total of 3E5 samples per segment. The acquisition segment is repeated and published continuously at 5 Hz. The voltage range is set to the maximum sensitivity at +/- 50 mV.

PROCESSING

The computation of the Schottky spectrum is performed by compiled C++ code running on the same FEC as the acquisition, using the FESA Framework (Fig. 4).

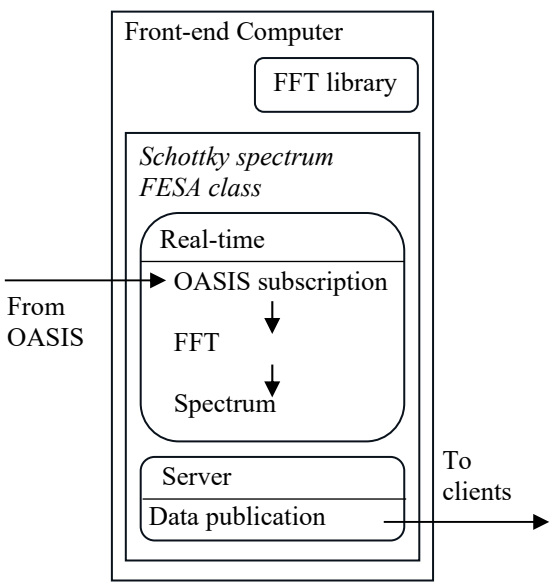


Figure 4: Overview of the signal data processing.

The real time layer of the FESA class is subscribed to the OASIS device and receives the raw data. The optimised library FFTW [5] is used for the fast Fourier transform (FFT) of each acquired segments.

The power spectrum is computed, and only a frequency range centred around 50 kHz is stored. The typical frequency range corresponding to the AD momentum spread capabilities is 48 – 52 kHz. It allows a data reduction down to 500 points per spectrum, easing the data transfer and storage.

The server layer of the FESA class takes care of the publishing of computed data to the subscribed clients.

The FEC is fitted with an Intel Core i5 CPU and can run two instances of the FESA class, producing and publishing Schottky spectra at 5 Hz per device.

Additionally, another FESA class generates snapshots of a Schottky spectrum, only updated at key moments along the AD deceleration cycle (Fig. 5).

AD OPERATION

The main goal of the renovation of the acquisition and processing chain was to be able to get a visual representation of the momentum envelop along all the AD cooling plateaus. (Fig. 5).

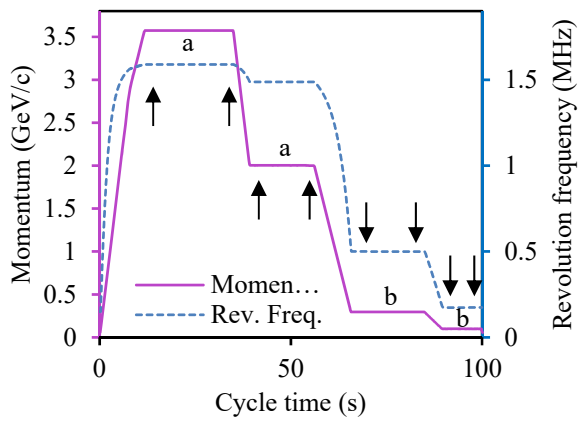


Figure 5: The two stochastic (a) and the two electron (b) cooling plateaus of the AD deceleration cycle, and the key moments indicated by black arrows.

Such real time publication of the longitudinal Schottky spectrum enables live animation in multiple applications used daily in operation. Live data availability is particularly relevant for a slow cycling machine, giving the operators the opportunity to apply corrections before the start of the next cycle, reducing setting-up and diagnostic time.

The Operation Application

A java application has been developed for the operators, available on control rooms computers (Fig. 6). Schottky spectra are displayed in a three-dimensions chart. The time axis is kept horizontal to be synchronised with other two dimensions time charts. The power spectrum value is colour coded, and the vertical axis represents the frequency.

ISBN: 978-3-95450-236-3 ISSN: 2673-5350 doi:10.18429/JACoW-IBIC2023-TUP045

The AD magnetic field and circulating intensity chart is synchronized with the time horizontal axis and displayed at the bottom. The actual spectrum is displayed on the right and synchronized with the vertical frequency axis. All the charts are animated with the real time publishing of the data at a rate of 5 Hz.

This application is daily used by the operators for diagnostic and fine tuning. The resulting picture is easily memorised by operators, and any drift or shape changes can be spotted efficiently in one look. It is also a useful asset for time consuming setup and adjustment, such as the tuning of the stochastic cooling, where the representation of the evolution of the beam momentum envelop along the cooling process is instrumental.

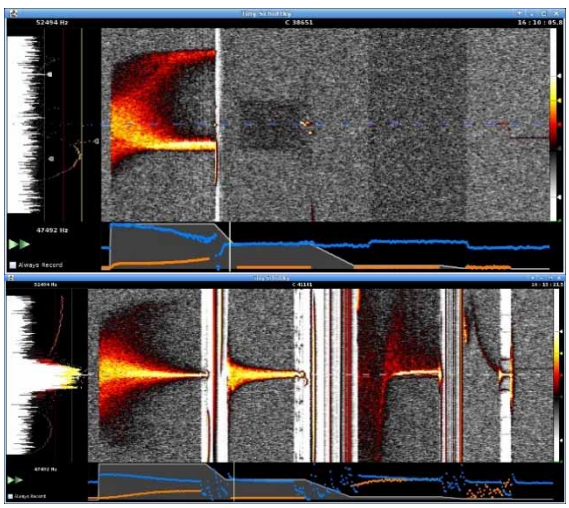


Figure 6: Real time longitudinal Schottky spectrum showing a de-tuned stochastic cooling system during AD start-up (top) and a nominal AD operation cycle (bottom).

Long Term Logging

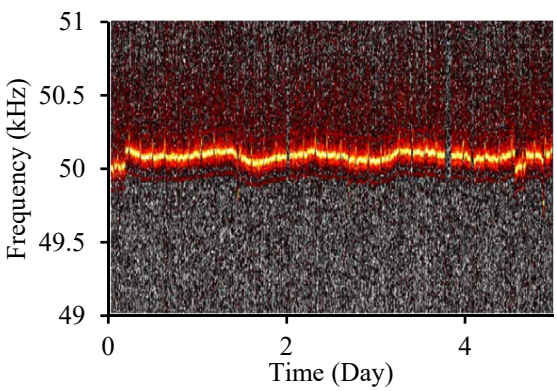


Figure 7: Example of historical data of the longitudinal Schottky spectrum at the end of the 300 MeV/C cooling plateau, over 5 days.

Schottky spectra at the start and the end of each of the four cooling plateaus (Fig. 5) are recorded for every AD cycle using NXCALS, the CERN logging infrastructure [6]. It allows machine stability analysis over several days and observation of any drifts of the cooling systems (Fig. 7).

Averaging

The full cycle length Schottky spectrum recording of each AD cycles are also saved as an image. By averaging images of several cycles during a stable operation period, one can enhance the details of the envelop of the longitudinal cooling processes performance (Fig. 8).

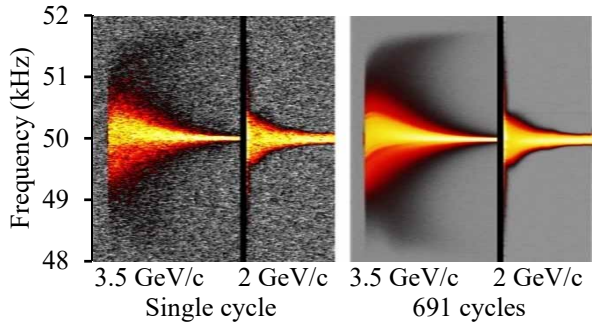


Figure 8: A single Schottky recording of the stochastic cooling plateaus (left) and the average of 691 recordings (right).

The Anti-Proton Production Status Screen

Displayed on large screens in control rooms and published worldwide via a CERN webpage [7], the status screen (also called “fix-display”) of the AD now integrates the real time animated Schottky spectrum. This addition enables better, and faster diagnostics of the AD cooling processes for a prompt action from the operation team.

LIMITATIONS

Due to hardware limitations, the generated signal derived from the revolution frequency, used for the down mixing process, works only for stable energy plateaus. In addition, the dynamic of the signal for bunched beam is too high for the acquisition chain. This prevents the system to give any valid measurements during ramps.

The LPU rather weak signal during the 300 MeV/c and 100 MeV/c low energy plateaus is also a known limitation of the system. Consequently, less details of the momentum envelop during the electron cooling processes are visible.

CONCLUSION AND OUTLOOK

The AD longitudinal Schottky measurement for operation has been renovated and successfully deployed with standard CERN hardware and software. It is used for day-to-day operation, and it is a key asset for setup and diagnostics.

Further improvements are under studies, like the computation of the actual momentum spread in percent instead of the signal frequency.

A feasibility study to deploy a similar system for the ELENA machine, where the beam energy is even lower, is ongoing.

Content from this work may be used under the terms of the CC-BY-4.0 licence (© 2023). Any distribution of this work must maintain attribution to the author(s), title of the work, publisher, and DOI

ISBN: 978-3-95450-236-3 ISSN: 2673-5350 doi:10.18429/JACoW-IBIC2023-TUP045

ACKNOWLEDGEMENTS

We would like to thank the CERN OASIS, RF and OP-AD team for their installation work, support and advises. In particular B. Ninet, D. Lampridis, M.E. Angoletta, A. Findlay, G. Tranquille, and L. Ponce.

REFERENCES

[1] C. Gonzalez and F. Pedersen, "An ultra-low noise ac beam transformer for deceleration and diagnostics of low intensity beams.", *Particle Accelerator Conference, New York, USA,* 29 March - 2 April, 1999, pp. 474-476. doi: 10.1109/PAC.1999.795736

[2] D. Boussard, "Schottky noise and beam transfer function diagnostics 1995 ed.", in *CAS - CERN Accelerator School: 5th Advanced Accelerator Physics Course*, pp.749-782. doi: 10.5170/CERN-1995-006.749

[3] What is OASIS?, https://be-dep-css.web.cern.ch/oasis

[4] What is FESA?, https://be-dep-css.web.cern.ch/fesa

[5] FFTW, https://www.fftw.org

[6] J.P. Wozniak and C. Roderick, "NXCALS - Architecture and Challenges of the Next CERN Accelerator Logging Service", in *Proc. ICALEPCS'19*, New York, NY, USA, Oct. 2019, pp. 1465-1469. doi:10.18429/JACoW-ICALEPCS2019-WEPHA163

[7] AD-ELENA, https://op-webtools.web.cern.ch/Vistar/vistars.php?usr=ADE

Content from this work may be used under the terms of the CC-BY-4.0 licence (© 2023). Any distribution of this work must maintain attribution to the author(s), title of the work, publisher, and DOI

ISBN: 978-3-95450-236-3 ISSN: 2673-5350 doi:10.18429/JACoW-IBIC2023-TUP046

STATUS OF THE RFSoC-BASED SIGNAL PROCESSING FOR MULTI-BUNCH AND FILLING-PATTERN FEEDBACKS IN THE SLS2.0

P. Baeta, B. Keil, G. Marinkovic, Paul-Scherrer-Institut (PSI), Villigen, Switzerland

Abstract

Having effectively evaluated the RF System-On-Chip (RFSoC) as a suitable technology for the SLS2.0 Filling Pattern Feedback (FPFB) and Multi-bunch Feedback (MBFB), our current focus lies in realizing and expanding the required real-time Digital Signal Processing (DSP) algorithms on an RFSoC evaluation board. This contribution outlines the present status of our feedback systems, including recent outcomes derived from testing prototypes both in the laboratory and with beam signals at the storage ring.

INTRODUCTION

The Swiss Light Source (SLS), a 3rd generation synchrotron light source at Paul Scherrer Institute (PSI), will be upgraded by a cutting-edge storage ring magnet lattice with reverse bends. The new machine, the SLS2.0, will provide a much lower emittance and higher beam energy, ultimately increasing the hard X-ray brightness and making the SLS competitive with other newer facilities [1]. Moreover, upgrading the SLS includes modernizing aging systems, such as the multi-bunch feedback (MBFB) and the filling pattern feedback (FPFB). After we assessed the suitability of RF System-On-Chip (RFSoC) for implementing the MBFB and FPFB of SLS 2.0 [2], we proceeded with deploying the feedback systems on the ZCU111 evaluation board from Xilinx/AMD, which features an RFSoC [3]. In the hardware section of this paper, we present an overview of the set-up installed at the SLS for testing the new MBFB and FPFB designs, which includes an RF-front-end (RFFE) prototype and the RFSoC-based digital back-end. The subsequent Firmware and Software section covers a real-time implementation of bunch-charge and arrival-time measurement for the FPFB, along with DSP firmware upgrades in the MBFB design. Lastly, we report prototype results from testing RFSoC-based systems in the laboratory and at the SLS storage ring, utilizing RF beam position monitor (BPM) signals.

HARDWARE

Figures 1(a) and 1(b) depict a block diagram of the hardware set-up at the SLS storage ring for prototyping our RFSoC-based solution of the FPFB and MBFB systems. The signals from four capacitive electrodes of an SLS beam position monitor (BPM) are connected to an RF hybrid network, yielding the sum signal (S), proportional to the bunch charge, and the difference signals (X and Y), proportional to the bunch charge and the horizontal and vertical bunch position offsets. The RFFE module consists of digital step attenuators (DSAs) and RF amplifiers for conditioning the position signals S, X, and Y. Figure 1(a) presents the signal conditioning path for each of the three MBFB planes. The RFFE prototype has a bandwidth of approx. 1000 MHz, online user-controllable gain/attenuation adjustments, and on/off switching capabilities for each analog signal conditioning path. The previous MBFB at SLS1.0 used a commercial RFFE that down-converted BPM signals from 1.25-1.5 GHz to the baseband. The new RFFE represents a transition toward direct sampling of S, X, and Y signals. The digital back-end in Figure 1(b) comprises the ZCU111 evaluation board and two interface boards. The ZCU111 is the core of the feedback systems, performing the data acquisition and processing. The Xilinx/AMD FMC-XM500 card breaks out the nets of the RFSoC data converters of the ZCU111. The ADCs acquire the conditioned signals S, X, and Y from the RFFE. The ZCU111 can control the RFFE signal gain and power with a second adapter board. In the context of the MBFB, the DACs generate the correction signals, closing the feedback loop. The correction signals undergo amplification, including upconversion to 1.5 GHz in the longitudinal plane, before driving the MBFB kickers. As for the FPFB, embedded real-time software processes the sum signal (S), calculating bunch charge. This process concludes by providing injection control information across successive top-up cycles, as needed, to close the filling pattern feedback loop.

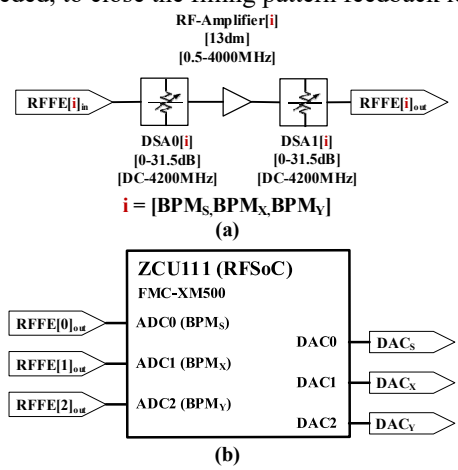


Figure 1: Block diagram of the FPFB and MBFB hardware set-up. (a) RF Front-end (RFFE) module for conditioning position signals from the SLS beam position monitor (BPM). (b) The Digital back-end module incorporates the ZCU111 evaluation board for data acquisition, processing, and communication with the SLS control system.

FIRMWARE AND SOFTWARE

Figures 2 and 3 illustrate the firmware block diagrams for the FPFB and MBFB systems implemented on the RFSoC platform. The Xilinx RF Data Converter is the core IP of the design. This IP configures the ADCs and DACs of the RFSoC and establishes the AXI stream data interface

Content from this work may be used under the terms of the CC-BY-4.0 licence (© 2023). Any distribution of this work must maintain attribution to the author(s), title of the work, publisher, and DOI

ISBN: 978-3-95450-236-3 ISSN: 2673-5350 doi:10.18429/JACoW-IBIC2023-TUP046

Content from this work may be used under the terms of the CC-BY-4.0 licence (© 2023). Any distribution of this work must maintain attribution to the author(s), title of the work, publisher, and DOI

of each converter with the programmable logic (PL) [3]. The EPICS IOC, operating on one of the two ARM CPU of the RFSoC processing system (PS), handles the configuration and data transfer between the feedback and SLS control systems via an Ethernet interface. The PS and PL interfaces include AXI bus and PL to PS interrupts. The I2C bus controls the on-board PLLs, which define the clock frequency of the RFSoC converters. The reference clock of the design is received from the master generator for the SLS storage ring high-power RF systems (f_{RF} =~500 MHz). For the MBFB system, all data converters run in multi-tile synchronization (MTS) mode, guaranteeing temporal sample alignment among ADCs and DACs and reproducible latency from ADC to DAC after a power cycle. The PL clock and data converter clocks in the MBFB firmware design are synchronized to the external reference clock and, thus, to the electron beam revolution frequency. In the FPFB design, the ADCs and PL operate in different clock domains, realizing an interleaving scheme to increase the effective ADC sample rate.

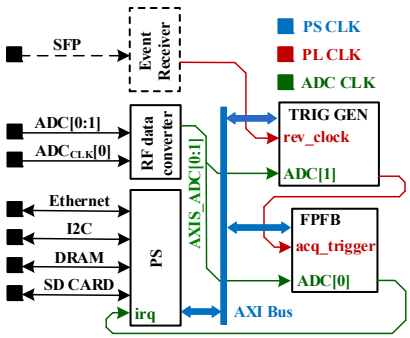


Figure 2: Firmware block diagram of the RFSoC-based FPFB system.

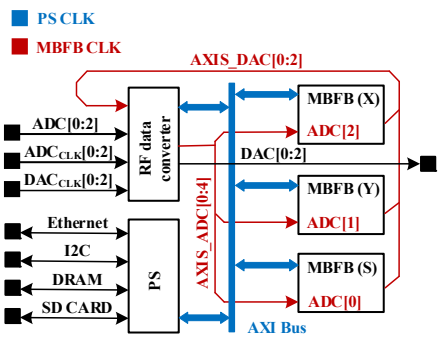


Figure 3: Firmware block diagram of the RFSoC-based MBFB.

Filling Pattern Feedback (FPFB) Systems

There are substantial changes in the firmware/software implementation compared to the design presented in Ref. [2]. The current FPFB firmware consists of a data-acquisition block that records the input data stream of the ADC0 running at a sampling frequency, f_S. The harmonic number of the SLS ring is 480, and the SLS machine reference clock, f_{RF}, is approximately 500 MHz. For $f_S = 8 \times f_{RF}$, the number of samples per bunch is 8, and per turn is $N = 8 \times 480$. To increase the effective sampling rate of the ADC0 by a factor of M, f_S is set such that a fractional number of samples per turn is acquired, and the data of M turns is interleaved.

$$f_s = \frac{f_{RF} \times 8 \times (M \times N - 1)}{(N \times M)} \quad (1)$$

In our prototype system, the interleave factor M is 16, resulting in an effective sampling rate of ~ 64 Gs/s.The ADC0 samples the sum signal, S, which contains the bunch charge and arrival-time information. The trigger generator IP controls the data acquisition, providing a periodic trigger, $acq_trigger$, with a period of ~ 960 ns (480 bunches, or one beam turn) and synchronized with the machine revolution clock. The $acq_trigger$ is the reference for bunch indexing. The data corresponding to bunch zero is the first eight samples after the rising edge of $acq_trigger$, and bunch 479 is the last eight samples before the acquisition of a new turn. After acquiring the sum signal, S, over 16 turns, the ADC0 data stream is stored in a BRAM in PL, and the data-acquisition block generates an interrupt request, irq, to the Zynq UltraScale+ MPSoC Processing System (PS) [3]. The PS is connected to the memory block in the PL via the AXI bus and the Xilinx AXI BRAM controller IP. The real-time software for the FPFB, implemented in C, runs on the RPU0 CPU of the PS. The interrupt request, irq, starts the interrupt handler function. First, the raw data of the 16 turns is read from the BRAM and interleaved, resulting in one interleaved turn. The data of the interleaved turn is split into 480 bunch windows of 2 ns (or 128 samples).

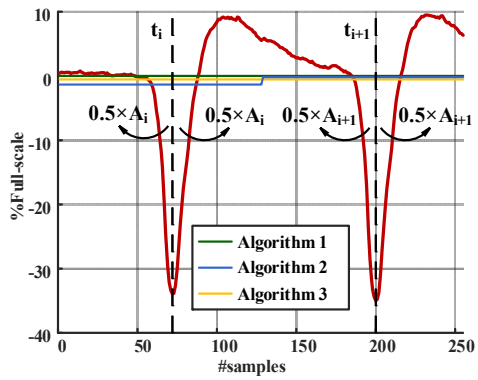


Figure 4: Sum signal, S, for two bunch windows of 2 ns, illustrating bunch pulses of the bunch train. The area A_i between the negative pulse (red curve) and the baseline (blue, yellow, and green curves) is used to estimate the charge of the bunch b_i. The Time t_i, which splits A_i in two equal parts, is an estimate for the arrival time of b_i.

Figure 4 shows the sum signal, S, for two bunch windows. For each bunch window, A_i, is the area between the negative pulse, the red curve, and the baseline. We considered three different algorithms for baseline calculation. The first algorithm, the green curve, defines the baseline as zero. In the second algorithm, the baseline is the average of the sum signal, S, over a single bunch window. In the third algorithm, the baseline is the average value of the sum signal, S, over the interval of $k_{bunch_windows}$ bunch windows defined by the user, aiming to reduce the effects of

ISBN: 978-3-95450-236-3 ISSN: 2673-5350 doi:10.18429/JACoW-IBIC2023-TUP046

baseline fluctuations on the ADC recordings. The charge of a bunch b_i , with index i , is the calculated area A_i times a common factor k_{charge} which translates area, A_i, into bunch charge in Coulombs. The bunch arrival time of b_i is the time t_i, which splits the area, A_i, equally by two. After calculating the bunch charge and arrival time, the RPU0 leaves the interrupt service routine, re-arming the data-acquisition block. The measurement is repeated at the next rising edge of the $acq_trigger$. The filling pattern information and configuration parameters of the FPFB can be accessed via EPICS channels. The electron bunches are sorted by charge with the information the system provides, and a list with sorted bunch indices is ready for control the injections of the next top-up cycle. The execution time of the interrupt sub-routine within the real-time software, encompassing the bunch-charge and bunch arrival measurements, alongside the statistics of the measurements (moving average and root mean square error), averages approximately 93 milliseconds. This implementation successfully satisfies the requirements of the FPFB, given that top-up injections occur at intervals of 320 milliseconds.

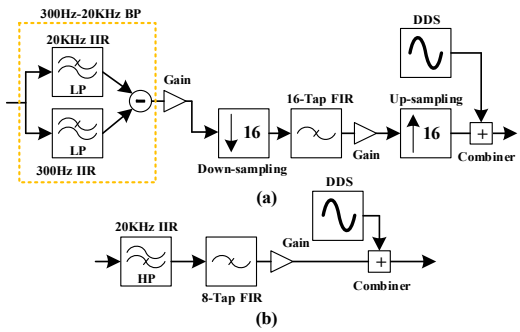


Figure 5: Block diagram of the MBFB firmware. (a) Longitudinal and (b) transverse planes.

Multi-bunch Feedback (MBFB) Systems

In alignment with the firmware design presented in Ref. [2], the interface between ADCs and PL in the latest MBFB firmware operates at f_{RF} (~500 MHz), streaming eight samples in parallel $f_s = 8 \times f_{\mathrm{RF}}$ (~4 Gs/s). In the subsequent processing stage, the input data stream is decimated by a factor of eight. The user selects, via EPICS channels, which of the eight samples, P_i, of the position signal is subjected to processing. Since the bunch window containing the bunch-pulse has 2 ns or eight samples, the P_i selection is such that the sample is close to the pulse peak, facilitating direct sampling. Figures 5(a) and 5(b) show the digital signal processing paths for the longitudinal and transverse planes of the MBFB, respectively. The digital filters (DF) process the selected position data P_i of each bunch i, generating the correction signals C_i. The coefficients and gain of the digital filters are reconfigurable via EPICS to inhibit coherent bunch oscillations. Furthermore, the latency of the DSP paths is adjustable in steps of 2 ns (bunch length), and in the output stage, the user can fine-tune with 250 ps resolution when applying the bunch correction signal C_i to precisely kick the bunch i. In addition to the basic MBFB features, the new firmware design features a multi-bunch excitation framework, which uses a DDS IP core to excite a single or set of bunches, presently with a fixed frequency. We foresee a bunch excitation mode featuring a frequency sweep or phase noise within a predefined frequency range for the next firmware upgrade. The excitation will allow the incorporation of advanced diagnostics tools, such as excitation-damping measurements, betatron and synchrotron tune measures, and automated tuning.

STATUS AND RESULTS

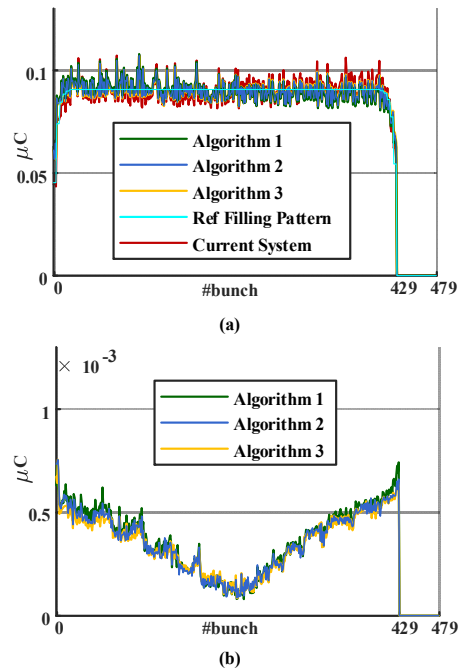


Figure 6: (a) Bunch charge measurement and (b) RMS noise of the measurements with different algorithms.

Filling Pattern Feedback (FPFB) Systems

Figure 6(a) shows the measurement results of the bunch charge obtained at the SLS storage ring using the current FPFB system and with the RFSoC-based system. Figure 6(b) compares the root mean square error (RMSE) of the different algorithms for bunch-charge measurement realized on the RFSoC-based FPFB. Algorithm 3 has slightly better performance. The baseline of Algorithm 3 is set as the average value of the sum signal, S, for eight bunch windows. Figure 7(a) shows the bunch arrival-time measurement results with the RFSoC-based system for the three baseline algorithms. Figure 7(b) compares the root mean square error (RMSE) in the bunch-arrival time measurement for each algorithm, where Algorithm 3 has the lowest RMSE. After successfully implementing the bunch-arrival time and bunch charge measurement in real-time software, the next step is to accelerate the algorithms in PL such that the MBFB can use the bunch-arrival time to correct longitudinal bunch oscillations.

Multi-bunch Feedback (MBFB) Systems

The present firmware version of the RFSoC-based MBFB has been designed to be functionally equivalent to the existing SLS MBFB based on 8-bit VMEbus ADC and DAC

Content from this work may be used under the terms of the CC-BY-4.0 licence (© 2023). Any distribution of this work must maintain attribution to the author(s), title of the work, publisher, and DOI

ISBN: 978-3-95450-236-3 ISSN: 2673-5350 doi:10.18429/JACoW-IBIC2023-TUP046

Content from this work may be used under the terms of the CC-BY-4.0 licence (© 2023). Any distribution of this work must maintain attribution to the author(s), title of the work, publisher, and DOI

boards. The MBFB functionality was tested in the laboratory by comparing the open loop response of the VME-based MBFB hardware versus the RFSoC MBFB system for the same input signal and configuration parameters (digital filter coefficients and gains). Moreover, the digital delay control of the DSP processing path was adjusted such that the responses of both systems were aligned in time. Figure 8 shows the open-loop response of the horizontal plane for both systems. The higher ADC resolution of the prototype MBFB system results in lower noise in the correction signal C_i (DAC response). The MBFB prototype system and the RFFE prototype have been tested with beam signals at the SLS. Figure 9 compares the output signal from the existing commercial RFFE and the RFFE prototype for the storage ring filled with a single bunch. The results show that for a single bunch, the signal-to-noise ratio of the correction signal allows the replacement of the present analog downconverter RF front-end (RFFE) for direct sampling of the BPM signals. However, further improvements to the new RFFE and signal processing are foreseen. We plan to use delay lines and interleave multiple ADC channels to increase the effective sampling rate of the current ADC running at 4 Gs/s, facilitating the direct sampling (sample the pulse peak) in a more realistic filling pattern scenarios of the storage ring, where phase slippage of the bunches are present as shown in Figure 7(b).

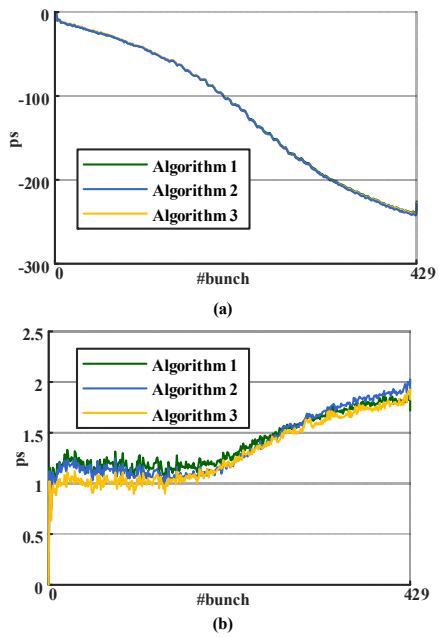


Figure 7: (a) Bunch arrival-time measurement and (b) RMS noise of the measurements with different algorithms.

CONCLUSION AND OUTLOOK

We have implemented the MBFB and FPFB real-time DSP algorithms on an RFSoC platform (ZCU111). The FPFB low-level software, utilized for bunch-charge and arrival-time measurements, meets the time constraints, as the execution time of the algorithms is shorter than the top-up cycles. Among the tested algorithms, Algorithm 3 exhibits a smaller RMS noise by reducing the effects of the baseline fluctuations in the ADC recordings of the sum signal. Next, we foresee the acceleration of the method in firmware such that the bunch-arrival time information can be used for the longitudinal MFFB. Regarding the MBFB, we have conducted a functional verification of the firmware by comparing the hardware response of the VME-based and RFSoC-based MBFB. Our next steps include testing the MBFB feedback closed-loop in SLS and SLS 2.0 and integrating advanced diagnostic tools such as excitation-damping measurements, tune measurements, and automatic parameter tuning. Finally, tests with the new RFFE motivate us to investigate a digital solution (ADC/DAC interleaving) for sampling the BPM signals and driving kicker amplifiers directly with simplified analog pre/post-conditioning, eliminating up/down conversion.

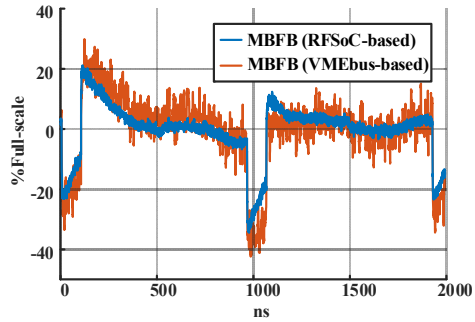


Figure 8: Comparison of the open-loop response (horizontal plane) between the RFSOC and the VMEbus-based MBFB system.

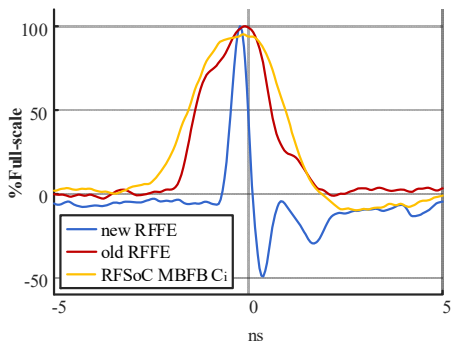


Figure 9: Comparison of the existing RFFE output signal (red) and the RFFE prototype (blue) for the storage ring filled with a single bunch. The yellow curve is the feedback response (horizontal plane) from the RFSoC MBFB.

REFERENCES

[1] A. Streun, "SLS 2.0, the Upgrade of the Swiss Light Source", in *Proc. IPAC'22*, Bangkok, Thailand, Jun. 2022, pp. 925-928. doi:10.18429/JACoW-IPAC2022-TUPOST032

[2] P. H. Baeta Neves Diniz Santos, B. Keil, and G. Marinkovic, "RF System-on-Chip for Multi-Bunch and Filling-Pattern Feedbacks", in *Proc. IBIC'22*, Kraków, Poland, Sep. 2022, pp. 379-382. doi:10.18429/JACoW-IBIC2022-WE2C4

[3] Xilinx, https://www.xilinx.com/products/boards-and-kits/zcu111.html

ISBN: 978-3-95450-236-3 ISSN: 2673-5350 doi:10.18429/JACoW-IBIC2023-WE1C03

THz ANTENNA-COUPLED ZERO-BIAS SCHOTTKY DIODE DETECTORS FOR PARTICLE ACCELERATORS

R. Yadav[1,*], S. Preu, Terahertz Devices and Systems, TU Darmstadt, Darmstadt, Germany
A. Penirschke, High Frequency Tech., Mittelhessen Univ. of Applied Sciences, Friedberg, Germany
J. Michael Klopf, M. Kuntzsch, Helmholtz-Zentrum Dresden-Rossendorf, Dresden, Germany
[1]also at High Frequency Tech., Mittelhessen Univ. of Applied Sciences, Friedberg, Germany

Abstract

Semiconductor-based broadband room-temperature Terahertz (THz) detectors are well suitable for beam diagnosis and alignment at accelerator facilities due to easy handling, compact size, no requirement of cooling, direct detection and robustness. Zero-Bias Schottky Diode (ZBSD) based THz detectors are highly sensitive and extremely fast, enabling the detection of picosecond scale THz pulses. This contribution gives an overview of direct THz detector technologies and applications. The ZBSD detector developed by our group has undergone several tests with table-top THz sources and also characterized with the free-electron laser (FEL) at HZDR Dresden, Germany up to 5.56 THz. In order to understand the rectification mechanism at higher THz frequencies, detector modelling and optimization is essential for a given application. We show parametric analysis of a antenna-coupled ZBSD detector by using 3D electromagnetic field simulation software (CST). The results will be used for optimization and fabrication of next generation ZBSD detectors, which are planned to be commissioned at THz generating FEL accelerator facilities in near future.

INTRODUCTION

The electromagnetic spectrum from 0.1 to 10 THz was commonly known as terahertz (THz) gap until recently as rigorous research and development have led to develop sources, detectors and components which help to bridge the THz gap [1]. Among available tabletop THz sources, accelerator based sources such as free electron lasers (FEL), synchrotrons and linear particle accelerators generate coherent as well as non-coherent THz signals [2]. THz signals can be used for various applications such as spectroscopy, study of matters, medical imaging, etc. [3]. THz detectors plays a crucial role in order to harness the full power of THz signals in various applications. These detectors can be classified into several categories based on their working principles (such as thermal detectors, electrical detectors etc. [1]), operating ranges (frequency of coverage for example narrow or broadband [1]) and operating conditions (room temperature or cryogenic conditions [1, 4–8]). There has been a rigorous work for the development of Schottky diode for THz applications [7, 9–11].

Zero-Bias Schottky Diode (ZBSD) based THz detectors are an end product of combination of ZBSD, antenna, planar electronic components and post detection electronics. Therefore, the overall performance of the ZBSD detector is dependent on all these components. In order to optimize the ZBSD THz detectors, in this paper we focus on the investigation of planar antennas for antenna-coupled ZBSD detector, which is planned to be primarily commissioned at ELBE facility in Helmholtz Zentrum Dresden-Rossendorf (HZDR), Germany and other facilities too.

* rahul.yadav@iem.thm.de

SIGNAL RECTIFICATION IN ZBSD

For conventional Schottky diodes, the external bias V modifies the Schottky barrier height, which led the electrons to cross the barrier and ultimately led to set the operating point of Schottky diode by reducing differential resistance (R_{diff}) [11, 12]. In case of ZBSD, the material is engineered in such a way that at $V = 0$ sufficient electrons are able to cross the barrier, yet with sufficient non-linearity of the IV characteristics to cause rectification. The ZBSD used for the detector development in our group are fabricated on Indium Gallium Arsenide (InGaAs) substrate which have electron affinity of 4.5 eV. Due to the proprietary reason by ACST GmbH, the in-depth information of Schottky diode itself is out of context of this paper. The ZBSD used here feature a quasi-vertical structure for Schottky and ohmic contact [9], rather than either having only planar or only vertical structure [11].

The signal rectification takes place at the Schottky contact of ZBSD, which can be understand by using Taylor series [13] as follows: The incident (monochromatic) Terahertz wave is transformed to a bias by the antenna as

$$U_0(t) = U_0 \cos(\omega t) \tag{1}$$

where $U_0(t)$ is the signal with amplitude U_0 and angular THz frequency ω. By using the Taylor series expansion of the exponential diode characteristic up-to second order, the diode current I_0 becomes

$$I_0(t) = A_1 U_0 \cos(\omega t) + A_2 U_0^2 \cos^2(\omega t) + ... \tag{2}$$

$$= A_1 U_0 \cos(\omega t) + \frac{1}{2} A_2 U_0^2 + \frac{1}{2} A_2 U_0 cos(2\omega t) \tag{3}$$

where the second term in Eq. (3) is the DC term. The first and second terms are derived from diode characteristics [11]:

$$A_1 = \frac{1}{R_{diff}} \tag{4}$$

$$A_2 = \frac{1}{2 \cdot R_{diff} \cdot \eta \cdot U_T} \tag{5}$$

Content from this work may be used under the terms of the CC-BY-4.0 licence (© 2023). Any distribution of this work must maintain attribution to the author(s), title of the work, publisher, and DOI

ISBN: 978-3-95450-236-3 ISSN: 2673-5350 doi:10.18429/JACoW-IBIC2023-WE1C03

Content from this work may be used under the terms of the CC-BY-4.0 licence (© 2023). Any distribution of this work must maintain attribution to the author(s), title of the work, publisher, and DOI

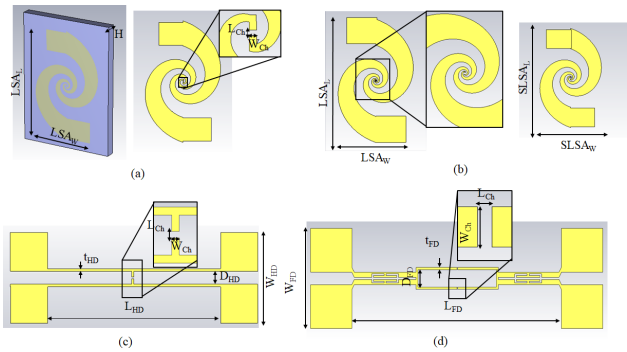


Figure 1: Sketch of the antennas investigated for ZBSD THz detectors (inset shows the central part where ZBSD is coupled) (a) left: antenna with substrate view, right: 1.5 turns log spiral antenna, (b) left: 2.5 turns log-spiral antenna, right: 1.5 turns smaller-log spiral antenna, (c) H-dipole antenna and (d) Folded dipole antenna. Note: antennas are excited using discrete port in CST between two electrodes in channel $L_{Ch} \times W_{Ch}$, where practically ZBSD is located.

where in Eq. (5), η is diode ideality factor and U_T is semiconductor (InGaAs) thermal voltage. As the second order term contains a rectified component $I_D C = A_2 U_0^2$, A_2 is directly proportional to the responsivity of the ZBSD.

ANTENNA-COUPLED ZBSD DETECTOR

The antenna plays a crucial role in the performance of the detector because it couples the incident THz radiation to the ZBSD, where it gets rectified. Planar antennas are used in this work to couple the ZBSD for detector development. The selection of the antenna depends on the desired application and required bandwidth. Table 1 shows different types of antennas which are used for the development of ZBSD THz detector.

Table 1: Investigated Antenna for ZBSD THz Detector

S.No	Antenna type	Abbreviation
1	Log-spiral	LSA
2	Small log-spiral	SLSA
3	H-dipole	HD
4	Folded dipole	FD

The LSA and SLSA are self-complimentary, frequency-independent antennas, which means theoretically they have no limitation on operational bandwidth. However, practically the upper bandwidth limitation is defined by the innermost arm radius and lower frequency by outermost arm radius [14] as shown in Fig. 1 (a) and (b).

We also investigated antenna types that are frequently applied in Terahertz photomixers, such as the H-dipole (HD) antenna (Fig. 1 (c)). In this type of antenna, either the central bar (high frequencies) the arm structure (low frequencies) radiates as the wave propagates along it. These type of antennas are considered as broadband antennas. In order to increase the detector sensitivity in narrow-band operation, investigations on performance of folded dipole (FD) antennas were also performed (Fig. 1 (d)).The dimensions of the investigated antennas are mentioned in Table 2.

Table 2: Dimensions of the Structures

Abbreviation	Full form	Dimension [µm]
LSA_L	Log-spiral antenna length	1174.25
LSA_W	Log-spiral antenna width	557.60
H	Substrate height	4.5
L_{Ch}	Channel length	2.4, 3, 6, 8
W_{Ch}	Channel width	2.4, 10
$SLSA_L$	Small log-spiral antenna length	413.14
$SLSA_W$	Small log-spiral antenna width	200.90
L_{HD}	H-dipole antenna length	700
W_{HD}	H-dipole antenna width	350
D_{HD}	H-dipole antenna arm distance	50
t_{HD}	H-dipole antenna arm thickness	10
W_{FD}	Folded-dipole antenna width	458
L_{FD}	Folded-dipole antenna length	1020
D_{FD}	Folded-dipole antenna arm distance	80
t_{FD}	Folded-dipole antenna arm thickness	10

The ZBSD will be fabricated on an Indium Gallium Arsenide (InGaAs) substrate which is equivalent to the area mentioned by $L_{Ch} \times W_{Ch}$ in the Fig. 1. The ZBSD will be integrated with the antenna, which will be fabricated on the film-thin substrate of 4.5 µm thickness and dielectric constant of $|\varepsilon_r| = 2.8$.

RESULTS AND DISCUSSION

The dielectric constant of the material on which antenna-coupled ZBSD is fabricated plays an important role in the performance of the detector. According to babinet's principle [14], the radiation impedance (Z_A) of self-complimentary antenna (LSA and SLSA) is inversely proportional to its effective refractive index (n_{eff}) and thus to its dielectric constant as

$$Z_A = \frac{Z_0}{2 \cdot n_{eff}} \tag{6}$$

$$Z_A = \frac{Z_0}{\sqrt{2 \cdot (\varepsilon_1 + \varepsilon_2)}} \tag{7}$$

where, Z_0 is the wave impedance in free space (377 Ω), ε_1 is dielectric constant of free space (1) and ε_2 is dielectric constant of thin-film substrate (2.8). Considering the respective values of ZBSD fabrication material, unloaded radiation resistance is Z_A=137 Ω. Figure 2, shows the effect of $|\varepsilon_r|$ variation on the performance of LSA antenna with 10×8 µm^2 channel when exciting the antenna from the center (where ZBSD is located), which directly relates to the ZBSD detector performance as well. The $|S_{11}|$ (scattering parameters in the channel $L_{Ch} \times W_{Ch}$ where practically ZBSD is located) shows standing waves for almost all $|\varepsilon_r|$ until 0.6 THz due to the inductive part of the antenna being dominant (Fig. 2(d)), while above 0.6 THz the imaginary part of radiation impedance becomes capacitive which leads

ISBN: 978-3-95450-236-3 ISSN: 2673-5350 doi:10.18429/JACoW-IBIC2023-WE1C03

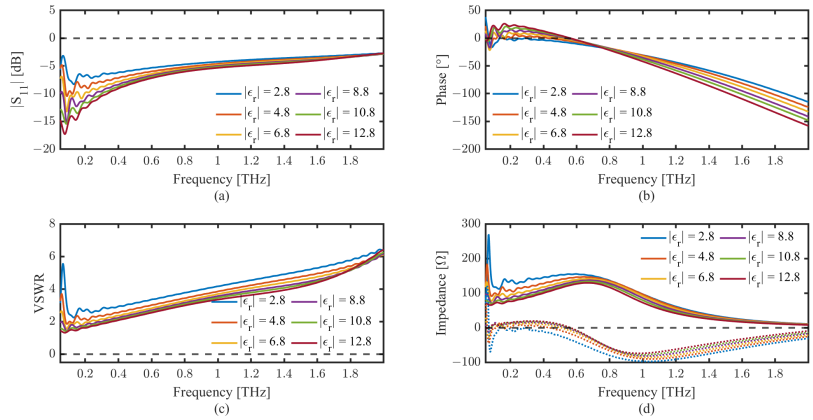


Figure 2: Effect of variable $|\varepsilon_r|$ on LSA antenna with 10×8 µm^2 channel with ZBSD having $C_j = 1$ fF and $R_{diff} = 5$ kΩ, (a) $|S_{11}|$, (b) Phase response, (c) VSWR response and (d) Impedance, solid lines represent real part and dotted lines represent imaginary part.

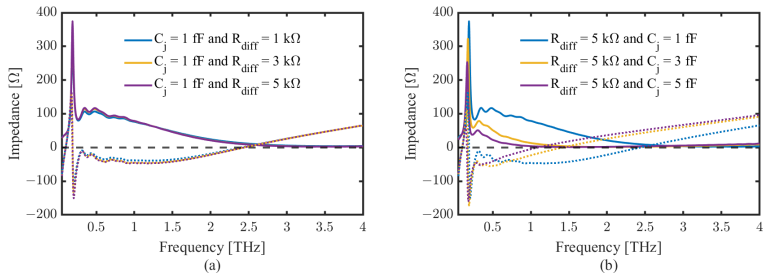


Figure 3: (a) Total device impedance for constant $C_j = 1$ fF and variable R_{diff}, (b) Total device impedance for variable C_j and constant $R_{diff} = 5$ kΩ with SLSA antenna with 2.4×2.4 µm^2 channel. Dotted lines: imaginary part, solid lines: real part of impedance, on substrate of 4.5 µm thickness and dielectric constant of $|\varepsilon_r| = 2.8$.

to sign flip of phase (Fig. 2(b)). The voltage standing wave ratio (VSWR) is almost below 3 up to 0.8 THz and then increases gradually to 6 at 2 THz (Fig. 2(b)), which means as frequency increases the capacitive part of the radiation impedance become significantly important.

The junction capacitance (C_j) and differential resistance (R_{diff}) are the important parameters of ZBSD which effect the antenna performance as a function of frequency. Fig. 3(a) shows the variation of R_{diff} while keeping the $C_j = 1$ fF constant. The variation in differential resistance does not affect the radiation impedance of the detector. As the frequency increases, the capacitive part of impedance become inductive after 2.5 THz. This is because the wavelength is reaching towards the same dimension of the central electrodes (where the ZBSD is coupled). When in the case of R_{diff} is kept constant at 5 kΩ and C_j is variable (Fig. 3(b)), the radiation impedance of the antenna is changed significantly. The lower the junction capacitance C_j is, the higher is the real part of radiation impedance and longer the frequency range over which the imaginary part stays capacitive before becoming inductive. This proves that it is important to have lower C_j to have better responsivity of the device at higher THz frequency. Therefore, we selected to consider $C_j = 1$ fF and $R_{diff} = 5$ kΩ for remaining studies in this work.

Figure 4 shows the radiation impedance versus frequency response from 0.05 to 4 THz (except LSA 2.4×2.4 µm^2 which is from 0.05 to 2 THz only) with variable channel dimensions of 10×3 µm^2, 10×6 µm^2 and 2.4×2.4 µm^2 for all the four types of antennas considered for investigation in this study. LSA with channel dimension of 10×3 µm^2 and 10×6 µm^2 have real Z_A of 133 Ω at lower frequencies (0.05 THz), which further decreases to 50 Ω at 1 THz (Fig. 4 (a)). The smaller channel dimension of 2.4×2.4 µm^2 have real Z_A of 268 Ω at 0.069 THz and decreases to approximately 100 Ω at 1 THz. This shows the better device response with smaller channel dimensions for LSA type devices. The smaller log-spiral devices (SLSA) are 2.84 times smaller in length compared to LSA devices. The SLSA devices in Fig. 4 (b) shows the resonance behaviour around 0.1 THz for all the three channel dimensions, which afterwards drop of real (Z_A) to 78 Ω for 2.4×2.4 µm^2 channel and almost 50 Ω for both 10×3 µm^2 and 10×6 µm^2 channel. While the real part is almost similar for 10×3 µm^2 and 10×6 µm^2 (as observed in Fig. 4 (a) and (b)), the imag (Z_A) shows the smaller channel length have slightly prolonged capacitive behaviour. The H-dipole antenna has resonances at 0.16, 0.38 and 0.61 THz as shown in Fig. 4 (c) for all studied channel dimensions. The HD with 2.4×2.4 µm^2 have real (Z_A) of 2.3 kΩ compared to approx 1.9 kΩ for both 10×3 µm^2 and 10×6 µm^2 channel at 0.16 THz. The folded dipole antenna (FD) is a narrow band resonant having the resonance peak at 0.2 THz as shown in Fig. 4 (d). This type of antenna can be used to boost up the device responsivity at particular frequency for a very specific frequency selective application.

Content from this work may be used under the terms of the CC-BY-4.0 licence (© 2023). Any distribution of this work must maintain attribution to the author(s), title of the work, publisher, and DOI

ISBN: 978-3-95450-236-3 ISSN: 2673-5350 doi:10.18429/JACoW-IBIC2023-WE1C03

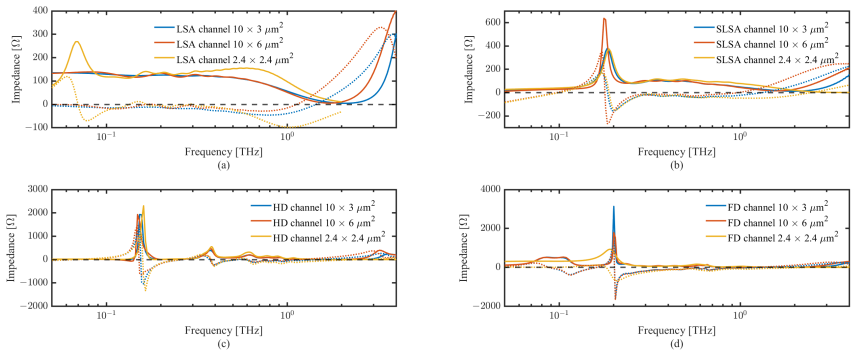


Figure 4: Antenna radiation impedance versus frequency response for variable channel dimensions of (a) 1.5 turn log-spiral antenna, (b) 1.5 turn small log-spiral antenna, (c) H-dipole antenna and (d) folded-dipole antenna from 0.05 to 4 THz. Dotted lines: imaginary part, solid lines: real part of radiation impedance, on substrate of 4.5 µm thickness and dielectric constant of $|\varepsilon_r| = 2.8$.

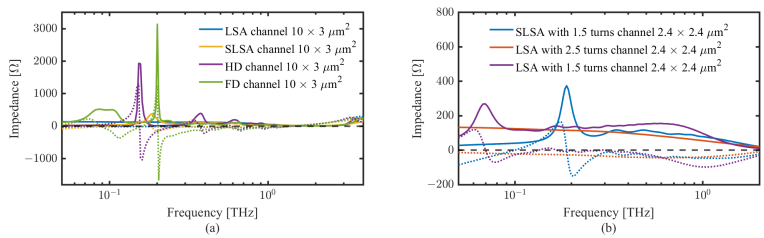


Figure 5: (a) Comparison of radiation impedance of all the four investigated antennas with channel dimension of 10×3 µm^2 from 0.05 to 4 THz and (b) comparison of log-spiral antennas with channel dimension of 2.4×2.4 µm^2 from 0.05 to 2 THz. Dotted lines: imaginary part, solid lines: real part of radiation impedance, on substrate of 4.5 µm thickness and dielectric constant of $|\varepsilon_r| = 2.8$.

Figure 5 (a) compares the impedance response for all four types of antennas with channel dimension of 10×3 µm^2 (this channel dimension is used for comparison because a device with smaller channel length has comparatively better response). Clearly the HD and FD devices are the best option for frequency selective improvement due to their resonant behaviour at specific frequencies. The LSA and SLSA devices are the best choice for broadband applications, however with frequency their responsivity decreases [7]. As shown in Fig. 6, the device reponsivity decreases as f^{-6} towards higher THz frequencies. On comparing the LSA and SLSA antennas impedance for 2.4×2.4 µm^2 channel dimension, it is observed that both antennas have resonant peaks at 0.07 and 0.2 THz, respectively. The response for LSA is higher than SLSA at lower frequencies as expected, but above approx. 1 THz, the response of SLSA is slightly better as shown in Fig. 5 (b). The antenna with 2.5 turns features non-resonant behaviour and response decreases gradually over frequency. It does not have any prominent inductive component.

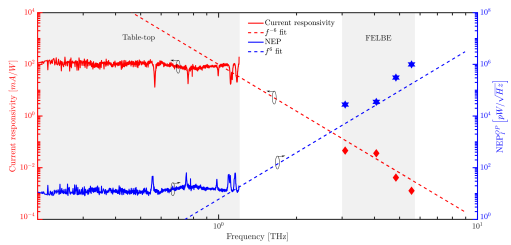


Figure 6: Responsivity of the log-spiral antenna-coupled broadband THz detector [7].

CONCLUSION

In this paper, we investigated the importance of antenna selection and design based on the desired operational bandwidth. At higher THz frequency, typical antenna sizes are much bigger compared to the THz wavelength incident on the detector, therefore only the central electrodes play a crucial role. We investigated and showed the importance of channel dimension in antenna design in this paper. The proper selection of C_j and R_{diff} is important for the better device response. The selection of the antenna type is often a trade-off between its responsivity and operational bandwidth. Short channel dimensions (here 10×3 µm^2 and 2.4×2.4 µm^2) are best choices for future device fabrication. The antenna studies presented here provide the expected performance of the optimized ZBSD detectors to be fabricated in the near future under this project.

ACKNOWLEDGEMENT

This work is supported by the German Federal Ministry of Education and Research (BMBF) under contract no. 05K22RO1 at Mittelhessen University of Applied Sciences, Friedberg (Hesse), Germany. Parts of this research were carried out at ELBE at the Helmholtz-Zentrum Dresden - Rossendorf e.V.

Content from this work may be used under the terms of the CC-BY-4.0 licence (© 2023). Any distribution of this work must maintain attribution to the author(s), title of the work, publisher, and DOI

ISBN: 978-3-95450-236-3 ISSN: 2673-5350 doi:10.18429/JACoW-IBIC2023-WE1C03

REFERENCES

[1] G. Carpintero, E. Garcia-Munoz, H. Hartnagel, S. Preu, and A. Raisanen, *Semiconductor terahertz technology: devices and systems at room temperature operation*, John Wiley & Sons, 2015. doi:10.1002/9781118920411

[2] E.J. Jaeschke, S. Khan, J.R. Schneider, and J.B. Hastings, *Synchrotron light sources and free-electron lasers: Accelerator physics, instrumentation and science applications*, 2nd Edition, Cham: Springer International Publishing, 2020. doi:10.1007/978-3-030-23201-6

[3] H.J. Song and T. Nagatsuma, *Handbook of terahertz technologies: devices and applications*, CRC press, 2015. doi:10.1201/b18381.

[4] S. Preu, M. Mittendorff, S. Winnerl, O. Cojocari, and A. Penirschke, "THz Autocorrelators for ps Pulse Characterization Based on Schottky Diodes and Rectifying Field-Effect Transistors", *IEEE Trans. Terahertz Sci. Technol.*, vol. 5, no. 6, pp. 922-929, Nov. 2015. doi:10.1109/TTHZ.2015.2482943

[5] S. Regensburger, S. Winnerl, J.M. Klopf, H. Lu, A.C. Gossard, and S. Preu, "Picosecond-Scale Terahertz Pulse Characterization With Field-Effect Transistors", *IEEE Trans. Terahertz Sci. Technol.*, vol. 9, no. 3, pp. 262-271, May 2019. doi:10.1109/TTHZ.2019.2903630

[6] A. Penirschke *et al.*, "Compact quasi-optical Schottky detector with fast voltage response", in *Proc. 39th IRMMW-THz*, 2014, pp. 1-2. doi:10.1109/IRMMW-THz.2014.6956027

[7] R. Yadav *et al.*, "State-of-the-Art Room Temperature Operable Zero-Bias Schottky Diode-Based Terahertz Detector Up to 5.56 THz", *Sensors*, vol. 23, no. 7, p. 3469. doi:10.3390/s23073469

[8] J.L. Hesler and T.W. Crowe, "Responsivity and noise measurements of zero-bias Schottky diode detectors", in *Proc. ISSTT*, 2007, pp. 89-92. https://api.semanticscholar.org/CorpusID:9361326

[9] O. Cojocari, C. Sydlo, H.-L. Hartnagel, S. Biber, J. Schur, and L.-P. Schmidt, "Schottky–structures for THz-application based on quasi-vertical design-concept", in *Proc. 16th Int. Symp. Space THz Technol.*, pp. 490–495, May 2005. https://api.semanticscholar.org/CorpusID:108540009

[10] I. Mehdi, J.V. Siles, C. Lee, and E. Schlecht, "THz Diode Technology: Status, Prospects, and Applications", in *Proc. IEEE'17*, vol. 105, no. 6, pp. 990-1007, Jun. 2017. doi:10.1109/JPROC.2017.2650235

[11] M. Hoefle, "Concepts and Design of Zero-bias Schottky Detectors for Millimetre Wave Applications", PhD thesis, TU Darmstadt, Germany, Shaker Verlag, 2015. doi:10.2370/9783844039405

[12] A.Y.C. Yu, "The metal-semiconductor contact: an old device with a new future", *IEEE Spectr.*, vol. 7, no. 3, pp. 83–89, Mar. 1970. doi:10.1109/MSPEC.1970.5213256

[13] D.M. Pozar, *Microwave Engineering*, John Wiley & Sons, 2011. ISBN:978-0-470-63155-3

[14] C.A. Balanis, *Antenna theory: analysis and design*, John Wiley & Sons, 2016. doi:10.1002/9780470294154

Content from this work may be used under the terms of the CC-BY-4.0 licence (© 2023). Any distribution of this work must maintain attribution to the author(s), title of the work, publisher, and DOI

ISBN: 978-3-95450-236-3 ISSN: 2673-5350 doi:10.18429/JACoW-IBIC2023-WE2C02

SOFTWARE DEFINED RADIO BASED FEEDBACK SYSTEM FOR TRANSVERSE BEAM EXCITATION*

P. J. Niedermayer**, R. Geißler, R. Singh
GSI Helmholtzzentrum für Schwerionenforschung, Darmstadt, Germany

Abstract

Controlling stored beams in particle accelerators requires specially designed RF signals, such as needed for spill control via transverse excitation. The software-defined radio (SDR) technology is adopted as a low cost, yet highly flexible setup to generate such signals in the kHz to MHz regime. A feedback system is build using a combination of digital signal processing with GNU Radio and RF Network-on-Chip (RFNoC) on a Universal Software Radio Peripheral (USRP). The system enables digitization of signals from particle detectors and direct tuning of the produced RF waveforms via a feedback controller – implemented on a single device. To allow for triggered operation and to reduce the loop delay to a few ms, custom OOT and RFNoC blocks have been implemented. This contribution reports on the implementation and first test results with beam of the developed spill control system.

INTRODUCTION

Radio Frequency Knock Out (RF-KO) extraction [1] is a standard method used to extract stored particle beams from synchrotrons through transverse excitation, providing spills of particles for experiments and medical therapy. It uses a beam optics near a third order resonance driven by sextupole fields [2]. The non-linear amplitude and phase detuning effects create a separatrix in phase space [3]. Transverse electromagnetic RF fields are applied to increase the betatron amplitude of particles in a controlled manner. This process, referred to as excitation, drives the particles into the separatrix. As a result, the motion becomes unbound, and the particles can be extracted at a septum.

The excitation system consists of an RF signal generator, RF amplifiers, and a *stripline kicker* inside which the RF fields act on the beam. Here, the signal generator is the central element by which the extraction process, and thus the spill, can be controlled.

The primary goal is to maintain a constant spill rate, that is, to extract an equal number of particles per unit time. To reach this goal, two complementary strategies exist: On timescales above about 50 ms, the signal amplitude is controlled by a complex function or a feedback system based on measured spill rates [4]. On smaller timescales not accessible by the feedback system, the signal waveform is optimized to reduce statistical fluctuations [5].

SOFTWARE-DEFINED RADIOS

Software-defined radio (SDR) is an RF transceiver technology where signal processing is implemented in software on computer processors (CPUs) and/or field-programmable gate arrays (FPGAs). It is widely used in radio communication systems, but has potential applications in many fields. An SDR typically consists of a frontend with ADCs and DACs, and a backend performing the digital signal processing (DSP). Here, a Universal Software Radio Peripheral (USRP) is used as off-the-shelf frontend to generate the RF signals. For implementation of the DSP chain, the open source framework GNU Radio [6] is used in combination with the RF Network-on-Chip (RFNoC) technology [7], which enable a flexible, graphical design of signal processing flow graphs by combining predefined and custom blocks. With SDRs being adopted by an increasing number of users in the accelerator community [8–10], collaboration and sharing of algorithms between institutes is easily possible [11].

IMPLEMENTATION

The excitation, feedback and spill control system builds on the development of a beam excitation system with applications in beam diagnostics [12]. The device does not only generate the excitation signals required for RF-KO extraction, but also processes the signals of a spill detector monitoring the extraction process. A feedback controller adjusts the excitation signal amplitude in order to maintain a constant spill rate on the detector. Statistical fluctuations on timescales below about 50 ms down to 10 µs – which are not accessible by spill feedback systems – are reduced by an automatic optimization of the used excitation signal waveforms. The implementation and realization of the system is described in detail in Refs. [11, 13].

COMMISSIONING

The spill control and feedback system was commissioned at the Cooler Synchrotron (COSY) accelerator in Jülich. For spill detection, a Low Gain Avalanche Detector (LGAD) developed by Ref. [14] for the High Acceptance Di-Electron Spectrometer (HADES) was used, which was being tested by the HADES LGAD group at COSY at the time.

Figure 1 shows a 20 s spill recorded with the developed system. Excitation with a constant signal level shows – as expected for this kind of slow extraction – a significant drift of the achieved spill rate over the course of the extraction. The feedback system, if switched on, is able to adjust the excitation level such as to maintain a constant spill rate on the detector. More details are available in Refs. [11, 13].

* This project has received funding from the European Union's Horizon 2020 Research and Innovation programme under GA No 101004730.
**p.niedermayer@gsi.de

Content from this work may be used under the terms of the CC-BY-4.0 licence (© 2023). Any distribution of this work must maintain attribution to the author(s), title of the work, publisher, and DOI

ISBN: 978-3-95450-236-3 ISSN: 2673-5350 doi:10.18429/JACoW-IBIC2023-WE2C02

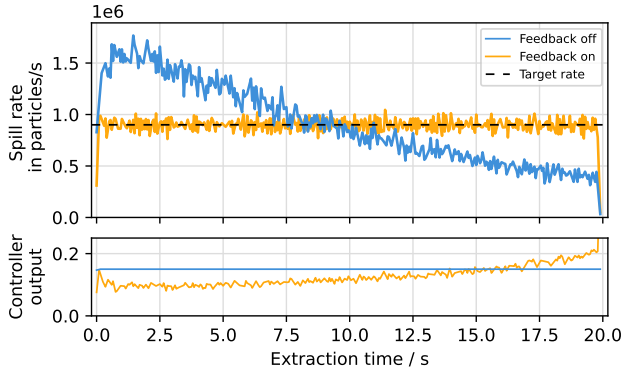


Figure 1: Measured spill rate and controller output with and without active feedback. Plot resolution: 50 ms.

ACKNOWLEDGEMENTS

The authors would like to express our gratitude to the whole team of the COSY accelerator in Jülich for their support during the preparation and execution of the beamtime. We are very thankful to Jerzy Pietraszko and the HADES LGAD group for providing us with an excellent detector signal. Bastian Bloessl and Eike Feldmeier are thanked for their support with GNU Radio and advice on SDRs. Finally, we acknowledge support by the beam instrumentation department of GSI.

REFERENCES

[1] K. Hiramoto and M. Nishi, "Resonant beam extraction scheme with constant separatrix", *Nucl. Instrum. Methods Phys. Res., Sect. A*, vol. 322, no. 2, pp. 154–160, 1992. doi:10.1016/0168-9002(92)90023-W

[2] M. Benedikt *et al.*, "Proton-Ion Medical Machine Study (PIMMS): Part I", CERN/PS 99-010 (DI), 1999. https://cds.cern.ch/record/385378

[3] Y. Kobayashi and H. Takahashi, "Improvement of the Emittance in the Resonant Beam Ejection", in *Proc. HEACC'67*, Cambridge, MA, USA, 1967, pp. 347–351.

[4] C. Schömers, E. Feldmeier, J. Naumann, R. Panse, A. Peters, and T. Haberer, "The intensity feedback system at Heidelberg Ion-Beam Therapy Centre", *Nucl. Instrum. Methods Phys. Res., Sect. A*, vol. 795, pp. 92–99, 2015. doi:10.1016/j.nima.2015.05.054

[5] P. J. Niedermayer, R. Singh, G. Franchetti, E. C. Cortés García, E. Feldmeier, and T. Haberer, "Investigation of micro spill in RF KO extraction using tailored excitation signals", in *Proc. IPAC'23*, Venice, Italy, 2023, pp. 2398–2401. doi:10.18429/JACoW-IPAC2023-TUPM094

[6] GNU Radio project, *GNU Radio*, version 3.10, 2007. https://www.gnuradio.org

[7] M. Braun, J. Pendlum, and M. Ettus, "RFNoC: RF Network-on-Chip", in *Proc. GRCon16*, Boulder, CO, USA, 2016. https://pubs.gnuradio.org/index.php/grcon/article/view/3

[8] E. Feldmeier *et al.*, "Upgrade of the Slow Extraction System of the Heidelberg Ion-Beam Therapy Centre's Synchrotron", in *Proc. IPAC'22*, Bangkok, Thailand, 2022, pp. 2509–2512. doi:10.18429/JACOW-IPAC2022-THPOST029

[9] R. Steinhagen *et al.*, "GNU Radio 4.0 for real-time signal-processing and feedback applications at FAIR", in *Proc. IPAC'23*, Venice, Italy, 2023, pp. 4637–4640. doi:10.18429/jacow-ipac2023-thpl099

[10] F. Kuehteubl *et al.*, "Investigating alternative extraction methods at MedAustron", in *Proc. IPAC'23*, Venice, Italy, May 2023. doi:10.18429/JACoW-IPAC2023-TUPM091

[11] S. Radio Beam Exciter. https://git.gsi.de/p.niedermayer/exciter

[12] P. Niedermayer and R. Singh, "Novel Beam Excitation System Based on Software-Defined Radio", in *Proc. IBIC'22*, Kraków, Poland, 2022, pp. 133–136. doi:10.18429/JACOW-IBIC2022-MOP36

[13] P. J. Niedermayer, R. Singh, and R. Geißler, "Software-Defined Radio Based Feedback System for Beam Spill Control in Particle Accelerators", in *Proc. GRCon23*, 2023, unpublished.

[14] J. Pietraszko *et al.*, "Low Gain Avalanche Detectors for the HADES reaction time (T_0) detector upgrade", *Eur. Phys. J. A*, vol. 56, no. 7, p. 183, 2020. doi:10.1140/epja/s10050-020-00186-w

Content from this work may be used under the terms of the CC-BY-4.0 licence (© 2023). Any distribution of this work must maintain attribution to the author(s), title of the work, publisher, and DOI

ISBN: 978-3-95450-236-3 ISSN: 2673-5350 doi:10.18429/JACoW-IBIC2023-WE2C03

BEAM INSTRUMENTATION HARDWARE ARCHITECTURE FOR UPGRADES AT THE BNL COLLIDER-ACCELERATOR COMPLEX AND THE FUTURE ELECTRON ION COLLIDER*

R. Michnoff†, C. Degen, L. DeSanto, D. Gassner, S. Hafeez, R. Hulsart, J. Jamilkowski, J. Mead, K. Mernick, G. Narayan, P. Oddo, M. Paniccia, J. Pomaro, A. Pramberger, J. Renta, F. Severino
Brookhaven National Laboratory, Upton, NY, USA

Abstract

Many beam instrumentation systems at Brookhaven National Laboratory's Collider-Accelerator complex are over 20 years old and in need of upgrading due to obsolete components, old technology and the desire to provide improved performance and enhanced capabilities. In addition, many new beam instrumentation systems will be developed for the future Electron Ion Collider (EIC) that will be housed in the existing Relativistic Heavy Ion Collider (RHIC) tunnel. A new BNL designed custom hardware architecture is planned for both upgrades in the existing facility and new systems for the EIC. A general-purpose carrier board based on the Xilinx Zynq Ultrascale+ System-on-Chip (SoC) will interface with a family of application specific daughter cards to satisfy the requirements for each system. This paper will present the general architecture that is planned, as well as details for some of the application specific daughter cards that will be developed.

EXISTING FACILITY HARDWARE

When RHIC was commissioned in 2000, the majority of instrumentation systems were based on the VME platform. While this has worked very well over the years, options for system upgrades and new systems for the EIC have been carefully considered [1].

A custom-designed Beam Position Monitor (BPM) module (named V301) was developed in 2015 that uses the VME form factor but does not include a VME bus interface [2]. Each module instead includes a direct Ethernet communication interface for higher level control and general data transfer. The V301 is based on the Xilinx Zynq gate array. Four 400 MSPS ADC converters are provided for measurement of BPM pickup signals and onboard filter options are included to process electrons or ions with various bunch repetition rates. The on-board Zynq ARM processor runs Linux with embedded software for processing and communication to higher level systems. Beam synchronous clocks are received by a single board in the chassis and distributed via unused P2 pins to all of the V301 modules. One major benefit of this system is that up to 15 V301 boards can be housed in a single VME chassis, and module replacement is very simple when necessary.

Another VME form factor module (named V340) based on the Zynq Ultrascale+ SoC was also recently developed. This module includes a high pin count FMC connector to enable using both custom and 3rd party FMC modules. The V340 is planned to be used for current transformer data acquisition and processing, as well as other applications.

In 2009 the RHIC RF group developed a Xilinx Virtex-5 based carrier board with custom daughter cards specific for RF applications [3]. This system is housed in a custom developed 3U chassis and runs the VxWorks real-time operating system directly on the Virtex 5 gate array.

OVERVIEW OF THE EIC

The EIC is scheduled to be fully commissioned with beam in 2034 and consists of the following major subsystems as shown in Fig. 1:

- Existing Hadron injector systems
- Hadron Storage Ring (HSR)
- Electron Pre-Injector (Polarized electron source and Linac)
- Rapid Cycling Synchrotron (electron accelerator) (RCS)
- Electron Storage Ring (ESR)

The existing Collider-Accelerator complex injector systems - Tandem, Electron Beam Ion Source (EBIS), Linac with polarized proton source, booster and Alternating Gradient Synchrotron (AGS) - will continue to be used for injection into the new HSR. Therefore, the existing systems need to be maintained and/or upgraded to support the EIC operation. The HSR will reuse significant portions of the existing Relativistic Heavy Ion Collider (RHIC) machine which is scheduled to complete its final beam run in 2025. The electron pre-injector, RCS and ESR will be completely new machines.

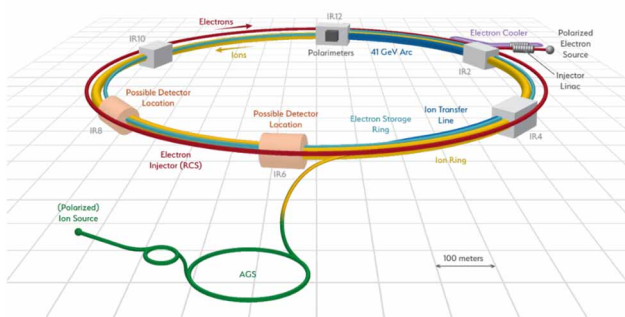


Figure 1: Layout of EIC.

Figure 2 lists the new instrumentation systems planned to be developed for the EIC machine. Note that this list does not include systems that are planned to be upgraded for the existing hadron injector systems.

* Work supported by Brookhaven Science Associates, LLC under Contract No. DE-SC0012704 with the U.S. Department of Energy
† michnoff@bnl.gov

Content from this work may be used under the terms of the CC-BY-4.0 licence (© 2023). Any distribution of this work must maintain attribution to the author(s), title of the work, publisher, and DOI

ISBN: 978-3-95450-236-3 ISSN: 2673-5350 doi:10.18429/JACoW-IBIC2023-WE2C03

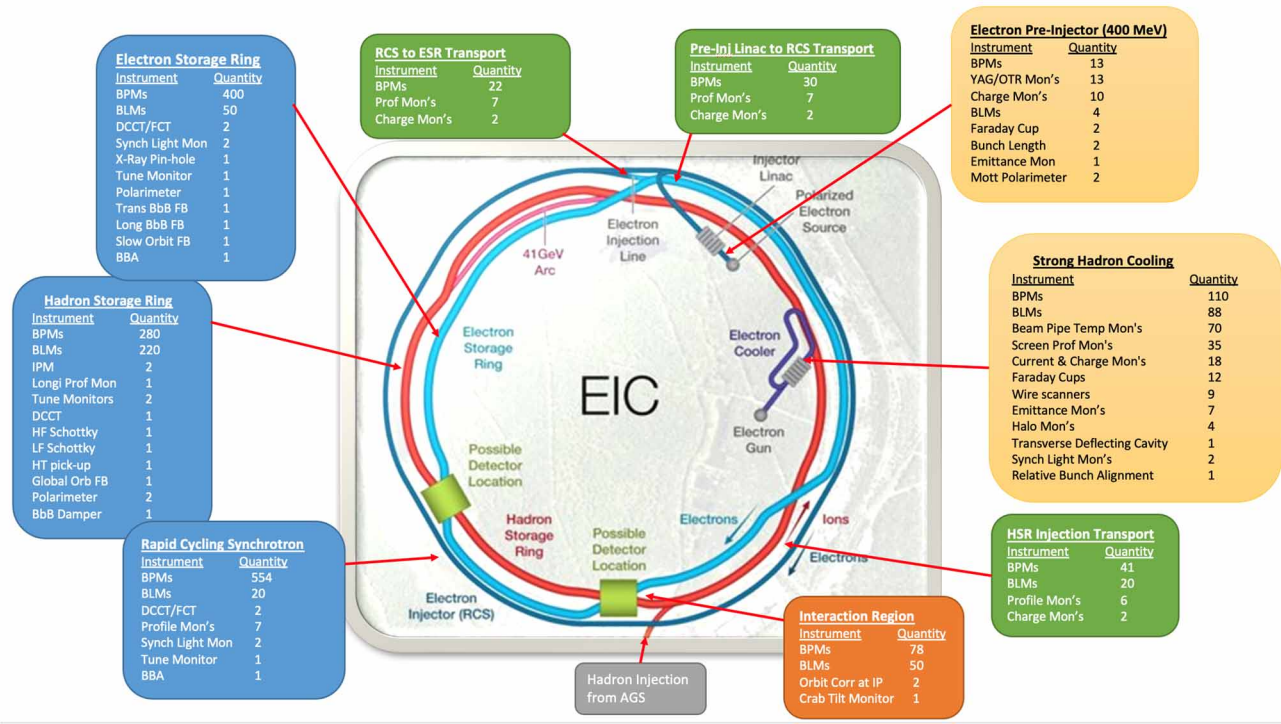


Figure 2: EIC instrumentation list for each subsystem, excluding the existing hadron injector machines.

OVERVIEW OF COMMON PLATFORM

The knowledge gained from the RF developed Virtex-5 based system, the Instrumentation System V301 Zynq-based BPM module and the V340 Ultrascale+ based module has been instrumental in the evolution to the new Xilinx Zynq Ultrascale+ SoC based carrier module that will accommodate 2 daughter cards via custom-defined pinouts on high-speed connectors. A mockup of the system is provided in Fig. 3.



Figure 3: Mockup of common platform chassis with carrier module and one of two daughter cards installed.

Carrier Module

A block diagram of the common platform carrier module is provided in Fig. 4. The external dimensions of the module are 15.5" wide by 10" deep, with a 3" x 6" cut-out for the power supply module.

The major features include:

- Xilinx Zynq Ultrascale+ SoC
- 4 GB DDR4 memory
- 4 120-pin connectors to support 2 daughter sites
- 8 SFP modules with crosspoint switch for configurable routing to on-board Ultrascale+ or daughter sites
- Dual RJ-45 Ethernet ports
- RJ-45 connector for RS-232 serial console port
- 16 Digital I/O LEMO connectors, 4 inputs, 4 outputs, 8 bidirectional
- External clock input passed to the daughter sites
- System clock input with PLL for generating beam synchronous clocks

Daughter Cards

A suite of daughter cards is in the process of being developed to support controls, RF, beam instrumentation and other applications.

Each daughter card will include a gate array for local control and for communication and data transfer to/from the carrier module. A memory mapped interface will be implemented between the carrier and daughter modules using AXI (Advanced eXtensible Interface) buses bridged by a Xilinx AXI Chip2Chip core over a Xilinx Aurora serial link. For large buffers of data, dedicated DDR memory may be provided on the daughter card and transferred to higher level workstations either by the carrier module after transferring the data from the daughter card to the carrier module memory or directly through a dedicated Ethernet connection on the daughter card.

The daughter cards slide into the front of the chassis with rails to guide the board to the carrier module connectors.

Content from this work may be used under the terms of the CC-BY-4.0 licence (© 2023). Any distribution of this work must maintain attribution to the author(s), title of the work, publisher, and DOI

ISBN: 978-3-95450-236-3 ISSN: 2673-5350 doi:10.18429/JACoW-IBIC2023-WE2C03

Content from this work may be used under the terms of the CC-BY-4.0 licence (© 2023). Any distribution of this work must maintain attribution to the author(s), title of the work, publisher, and DOI

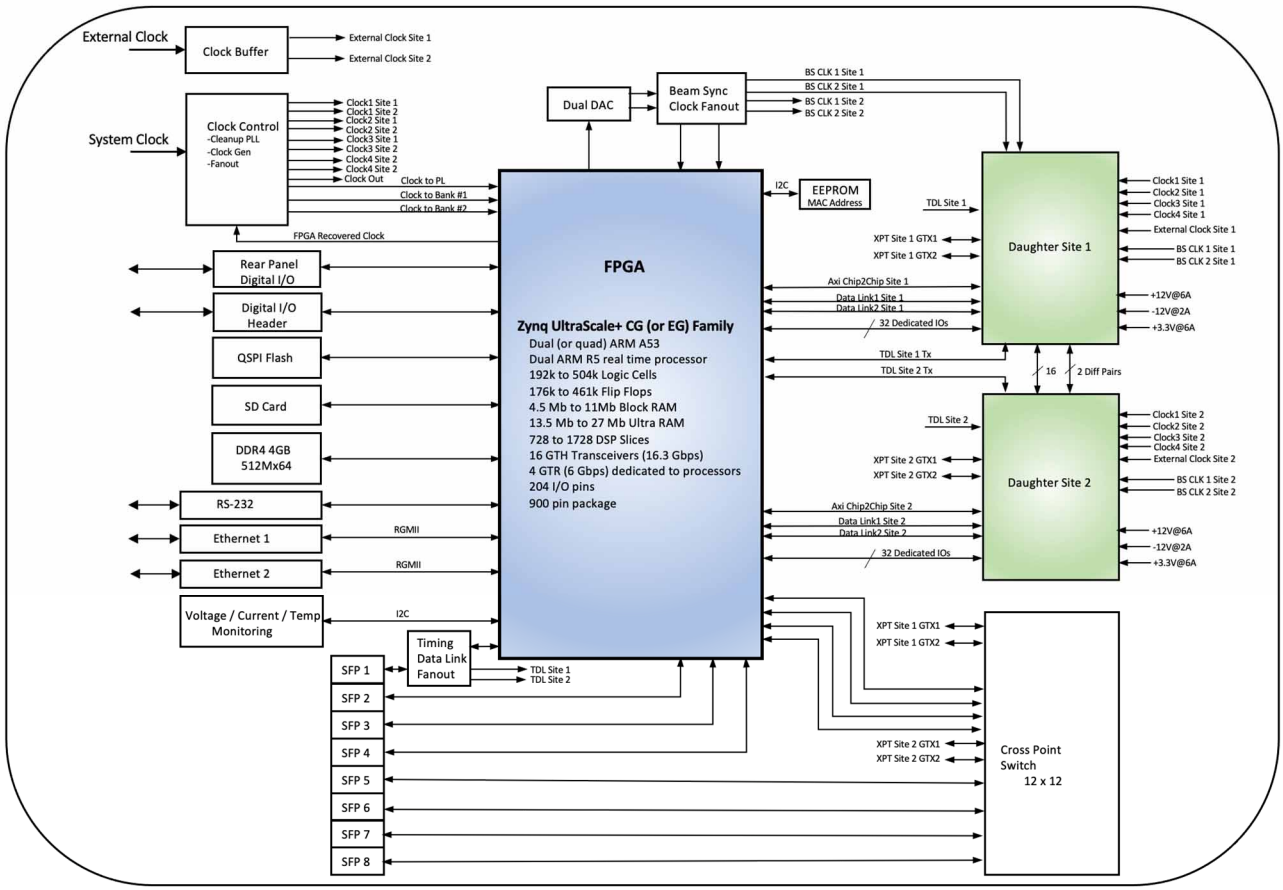


Figure 4: Block diagram of common platform carrier board.

The carrier module will provide +3.3 V@8 A, +12 V@6 A and -12 V@2 A to each daughter card. Two Samtec ERM8-060-01-L-D-EM2 connectors on each daughter card will be used for communication between the carrier module and the daughter card.

Signal Conditioner Modules

Some daughter cards will be designed to accommodate a signal conditioner module that can include buffers, filters, etc. for application specific needs. The signal conditioner module can also be used to provide application specific connector needs. For example, the multi-wire profile monitor system will likely use multi-pin connectors while the loss monitor system might use BNC connectors. Providing this capability within a simple signal conditioner module prevents the need to design several similar ADC daughter cards.

Power Supply

A dedicated power supply for each common platform chassis will be provided. The exact details for this power supply are still being developed.

Chassis

Each common platform chassis will include one power supply, one carrier module and up to 2 daughter cards. The chassis will be 19" rack mountable and will typically be 2U in height. Some assemblies may require a larger height to accommodate the necessary panel space for connectors. For example, a 32-channel ADC daughter card with 32 BNC connectors, as planned for the beam loss monitor system, will require a height of more than 2U.

Cooling

As shown in Fig. 3, several small fans are planned to be used to provide cooling across the carrier module and daughter cards.

SYSTEMS TO BE SUPPORTED

The beam instrumentation systems that are planned to be supported by the common platform hardware include the following:

- Beam position monitor systems (BPM)
- Beam Loss monitor systems (BLM)
- Multiwire beam profile systems
- Beam current and charge monitoring systems
- Ionization Profile Monitor systems (IPM)
- Tune measurement systems
- Transverse injection damper systems
- And more

ISBN: 978-3-95450-236-3 ISSN: 2673-5350 doi:10.18429/JACoW-IBIC2023-WE2C03

The following sections provide preliminary system architecture details related to how the primary instrumentation systems will be supported using the common platform hardware.

Beam Position Monitors

A block diagram of the BPM daughter card is shown in Fig. 5. The EIC BPM system requirements require different filters and different data acquisition modes for each of the major subsystems. A common filter footprint will be designed to accommodate the different filter requirements using one common printed circuit board (PCB).

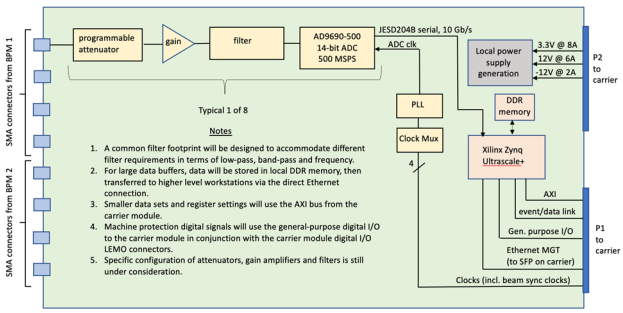


Figure 5: Block diagram of BPM daughter card.

The AD9690-500, 500 MSPS, 14-bit ADC is presently being considered for the BPM system, but further evaluation is required before making a final decision. This ADC uses the high speed JESD204B serial link (10 Gbit/s) for data transfer to the Ultrascale+ SoC.

The direct Ethernet connection to the Xilinx Zynq Ultrascale+ SoC will provide options for data to be sent directly to higher level workstations, bypassing the FPGA on the carrier module. Running Linux or other operating system directly on the on-board SoC is also an option, which would allow an EPICS IOC or RHIC Controls ADO to reside on the daughter card.

Tune Measurement and Transverse Injection Damper Systems

The tune measurement and transverse injection dampers systems will use the BPM daughter card, but with custom firmware to synchronize beam kicks and measurements.

The present plan is to provide beam kicks to a stripline via high voltage Behlke switches or similar.

Multiwire Profiles, Beam Loss Monitors, and Ionization Profile Monitor Systems

A general purpose 32-channel, 16-bit 5 MSPS analog input daughter card is presently being developed to accommodate a variety of system needs, including multiwire beam profiles, BLM and IPM systems (Fig. 6).

Each system will include custom firmware for the specific application, as well as a custom designed signal conditioner module to provide the specific front-end filter and external connector needs.

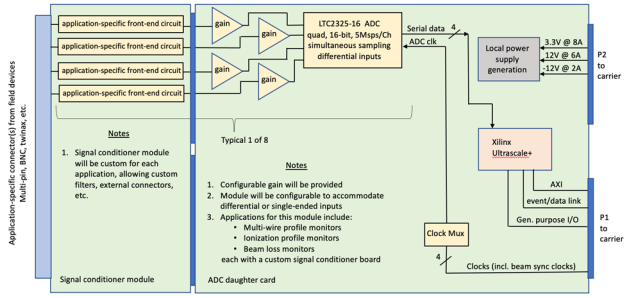


Figure 6: Block diagram of 32-chan 5 MSPS daughter card.

Beam Current and Charge Monitor Systems

For DC beam current measurements, DC Current Transformers (DCCT) and Faraday Cups will use a high-precision Analog Input/Output daughter card (Fig. 7). The daughter card will include low noise high bit count ADC and DAC components. The DAC output will generate a remotely configurable current source for the calibration of the DCCTs and other current transformers. This daughter card is still in the early design phase, and the specific ADC and DAC still need to be selected.

For bunch charge measurements (Wall Current Monitors (WCM), Integrating Beam Current Transformers (ICT), and Fast Current Transformers (FCT), etc.) another custom daughter card similar to the BPM module will be developed, but with DC coupled inputs and 1 GSPS or faster ADCs. This module is also in the very early design phase.

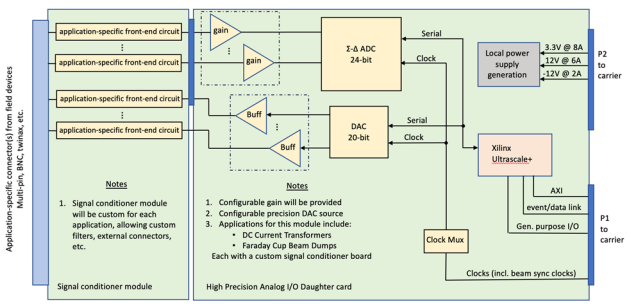


Figure 7: Block diagram of precision ADC/DAC daughter card.

REFERENCES

[1] R. J. Michnoff *et al.*, "Preliminary Design of a Real-Time Hardware Architecture for eRHIC", in *Proc. ICALEPCS'15*, Melbourne, Australia, Oct. 2015, pp. 1099-1102. doi:10.18429/JACoW-ICALEPCS2015-THHB2001

[2] R. L. Hulsart, P. Cerniglia, N. M. Day, R. J. Michnoff, and Z. Sorrell, "A Versatile BPM Signal Processing System Based on the Xilinx Zynq SoC", in *Proc. IBIC'16*, Barcelona, Spain, Sep. 2016, pp. 646-649. doi:10.18429/JACoW-IBIC2016-WEPG12

[3] T. Hayes and K. S. Smith, "A Hardware Overview of the RHIC LLRF Platform", in *Proc. PAC'11*, New York, NY, USA, Mar.-Apr. 2011, paper MOP283, pp. 645-647.

Content from this work may be used under the terms of the CC-BY-4.0 licence (© 2023). Any distribution of this work must maintain attribution to the author(s), title of the work, publisher, and DOI

ISBN: 978-3-95450-236-3 ISSN: 2673-5350 doi:10.18429/JACoW-IBIC2023-WE3I01

GAS JET BASED FLUORESCENCE PROFILE MONITOR FOR LOW ENERGY ELECTRONS AND HIGH ENERGY PROTONS AT LHC

O. Sedlacek*[1], O. Stringer, C. Welsch, A. Webber-Date, H. Zhang
University of Liverpool and Cockcroft Institute, Daresbury, Warrington, UK
M. Ady, A. R. Churchman, S. Mazzoni, A. Rossi, M. Sameed, G. Schneider,
C. C. Sequeiro, K. Sidorowski, R. Veness, CERN, Geneva, Switzerland
P. Forck, S. Udrea, GSI, Darmstadt, Germany
[1] also at CERN, Geneva, Switzerland

Abstract

The ever-developing accelerator capabilities of increasing beam intensity, e.g. for High Luminosity LHC (HL-LHC), demand novel non-invasive beam diagnostics. As a part of the HL-LHC project a Beam Gas Curtain monitor (BGC), a gas jet-based fluorescence transverse profile monitor, is being developed. The BGC uses a supersonic gas jet sheet that traverses the beam at 45° and visualizes a two-dimensional beam-induced fluorescent image. The principle of observing photons created by fluorescence makes the monitor insensitive to present electric or magnetic fields. Therefore, the monitor is well suited for high-intensity beams such as low-energy electron beam of Hollow Electron Lens (HEL), and HL-LHC proton beam, either as a profile or an overlap monitor. This talk will focus on the first gas jet measured transverse profile of the 7 keV hollow electron beam. The measurements were carried out at the Electron Beam Test Stand at CERN testing up to 5 A beam for HEL. A comparison with Optical Transition Radiation measurements shows consistency with the BGC results. The BGC installation of January 2023 at LHC is shown, including past results from distributed gas fluorescence tests.

INTRODUCTION

The High Luminosity upgrade of the LHC (HL-LHC) aims at extending its operability by a decade by increasing its instantaneous luminosity by a factor of five beyond its present design value [1]. The main feature of HL-LHC is the upgrade of the focusing triplets to allow for a smaller β^* in the interaction region, combined with compact superconducting radio frequency crab cavities for bunch rotation. For these systems to operate safely, a Hollow Electron Lens (HEL) is being studied to improve the cleaning performance of the collimation system. Optimal performance of the HEL requires a means to measure the relative position of the hollow, low-energy electron beam with respect to the LHC proton beam in a non-invasive way. It is in this context, a collaboration between CERN, University of Liverpool and GSI was established to design and produce a Beam Gas Curtain (BGC) as an overlap monitor for the HEL [2–7]. The strategy for commissioning the BGC consists of a parallel validation of its performance in both the Electron Beam Test Stand (EBTS) [8] and the LHC during the present run 3. In this contribution, we report on the recent progress of the BGC at the EBTS and present the configuration of the ongoing LHC installation.

* Ondrej.Sedlacek@cern.ch

BGC INSTRUMENT

Principle of Detection

The BGC working principle is outlined in Fig. 1. The monitor is based on a flat, supersonic gas jet referred to as a "curtain", which perpendicularly crosses the beams' path with the flat edge at 45° with respect to the horizontal plane (see Fig. 1). The beams excite the gas atoms or molecule through collisions. Subsequent radiative deexcitation leads to photon emission (fluorescence). The fluorescence footprint on the gas curtain thus directly relates to the particle beams' 2D transverse particle distributions, allowing for the observation of the beams' 2D transverse profiles in a non-invasive way.

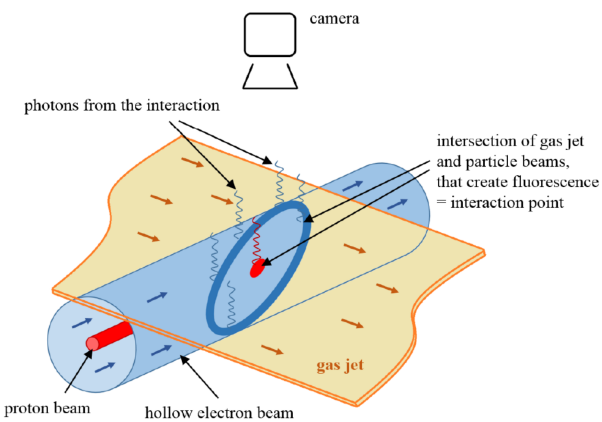


Figure 1: Working principle of the BGC.

Working Gas

Neon, nitrogen, and argon have been selected as working gases for the BGC, each presenting advantages and disadvantages that affect the monitor's performance. Their fluorescence processes are described in Eqs. (1)–(3):

$$Ne + p/e^- \rightarrow (Ne)^* + p/e^- \rightarrow Ne + \gamma + p/e^- \quad (1)$$

$$N_2 + p/e^- \rightarrow (N_2^+)^* + e^- + p/e^- \rightarrow N_2^+ + \gamma + e^- + p/e^- \quad (2)$$

$$Ar + p/e^- \rightarrow (Ar^+)^* + e^- + p/e^- \rightarrow Ar^+ + \gamma + e^- + p/e^- \quad (3)$$

Content from this work may be used under the terms of the CC-BY-4.0 licence (© 2023). Any distribution of this work must maintain attribution to the author(s), title of the work, publisher, and DOI

ISBN: 978-3-95450-236-3 ISSN: 2673-5350 doi:10.18429/JACoW-IBIC2023-WE3I01

Neon gas curtains have the highest density. However, neon has the lowest (expected) cross-sections and light yields. At the same time, the relevant transition takes place within the neutral atom, see Eq. (1) at 585.4 nm [9, 10]. Therefore, it is not affected by the beam's space charge during the atom's fluorescence lifetime[1] of 16 ns. Additionally, neon and argon are a noble gases and, as such, they don't saturate the Non-Evaporable Getter (NEG) coating often present at LHC [10].

Nitrogen gas jets have the highest light yields. Its strongest fluorescence line is expected at a wavelength of 391.4 nm. It is a transition within the molecular ion N_2^+ with a lifetime[1] of 60 ns and, therefore, the beam's space charge will interact with the excited gas molecules and distort the observed distribution. The result of a simulation of the distortion caused by one nominal LHC bunch is shown in Fig. 2. The distortion increases the rms width of the observed distribution from 350 µm to 490 µm. In the case of a bunch train the distortion reaches 570 µm. For more simulations of space-charge distortions see [11].

Argon gas has two fluorescence peaks close to each other at 454.5 nm and 476.5 nm. Using a wider optical filter to capture both peaks allows for a total light yield that is between nitrogen and neon at the expense of a higher background. The transitions are ionic and therefore subject to space-charge induced distortion but thanks to the short lifetime[1] of 6 ns and larger atomic mass compared to nitrogen the distortion is minimal.

For more information on the comparison of different working gasses using a Gaussian electron beam see [3].

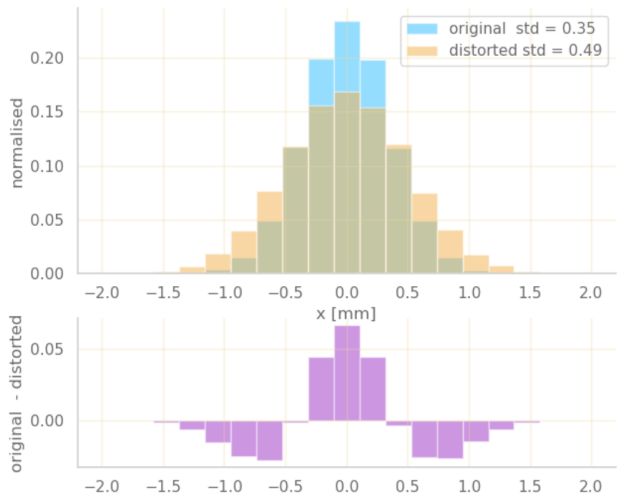


Figure 2: Space charge effect on observed horizontal distribution of one nominal LHC bunch for a thin nitrogen curtain.

BGC Description

The supersonic gas curtain is created by letting the gas to expand into vacuum through a small nozzle and (partly) propagate through a set of skimmers that ensure a low transverse temperature within the jet thus obtained. The third skimmer is rectangular giving the jet its final curtain shape. The gas is in a molecular flow regime, allowing the jet to retain its rectangular cross-section throughout the path across the beam pipe. After crossing the particle beams the jet is pumped out in a dump chamber, which is separated from the interaction chamber by a fourth skimmer to limit back-scattering of gas molecules and therefore minimise the pressure in the interaction chamber.

Part of the photons created by fluorescence get focused by a 40 mm dia., 160 mm focal length apochromatic lens triplet onto a band-pass filter and are finally detected by an intensified camera. The optical band-pass filter limits photons to the wavelengths of interest, e.g. 585 ± 10 nm in the case of Ne. The intensified camera employs double-stage Micro Channel Plate (MCP) amplification allowing for single photon detection.

The observed fluorescent light yield N_γ is given by:

$$N_\gamma = Z \cdot \sigma \cdot \frac{I \cdot \Delta t}{e} \cdot n \cdot d \frac{\Omega}{4\pi} \cdot T \cdot T_f \cdot \eta_{\mathrm{pc}} \cdot \eta_{\mathrm{MCP}}, \quad (4)$$

where σ is the fluorescence cross-section, I the beam current, Δt the integration time, Z the charge state of the passing particle, e the elementary charge, n the curtain's gas density, d the curtain's effective thickness, Ω the acceptance solid angle of the optical system, T the transmittance of the optical system including flange window, T_f the transmittance of the optical filter, η_{pc} the quantum efficiency of a photocathode, and η_{MCP} the efficiency of a the MCP.

Profile Broadening Due to Curtain Thickness

The thickness of the gas jet curtain causes a broadening of the observed vertical beam profile, since fluorescence is produced in the whole volume of the curtain crossed by the beam. Assuming rotational symmetry for the beam and curtain homogeneity in the horizontal plane, the effect can be modelled in 2D. In the case of the BGC the observed profile $I(y)$ is then [10]:

$$I(y) = \int_{-d/2}^{d/2} \rho(\xi)\phi(y - \frac{2}{\sqrt{2}}\xi)d\xi, \quad (5)$$

where ρ is the gas curtain density, ϕ the beam flux, d the gas curtain thickness, ξ the integration coordinate across the curtain's thickness, and y the coordinate along the camera's detector, which in 2D is represented by a line.

Figure 3 shows simulations of profile broadening for a Gaussian beam of rms width σ_{beam} due to a uniform gas curtain. For a curtain thickness $d = \sigma_{\mathrm{beam}}$ and $d = 2 \cdot \sigma_{\mathrm{beam}}$, the observed σ is $\approx 1.08 \cdot \sigma_{\mathrm{beam}}$ and $1.37 \cdot \sigma_{\mathrm{beam}}$, respectively. In the case of the BGC at LHC, the skimmer thickness is $d = 2.7\sigma_{\mathrm{beam}}$, causing a broadening of the vertical distribution of 61 %, as expected. This is acceptable due to the fact that the BGC was conceived as an overlap monitor for the HEL at LHC, where the centroid rather than the profile of the transverse distribution is to be determined. In order to accurately reconstruct the vertical profile, the thickness

[1] Average time between excitation and emission of relevant photon.

Content from this work may be used under the terms of the CC-BY-4.0 licence (© 2023). Any distribution of this work must maintain attribution to the author(s), title of the work, publisher, and DOI

ISBN: 978-3-95450-236-3 ISSN: 2673-5350 doi:10.18429/JACoW-IBIC2023-WE3I01

Content from this work may be used under the terms of the CC-BY-4.0 licence (© 2023). Any distribution of this work must maintain attribution to the author(s), title of the work, publisher, and DOI

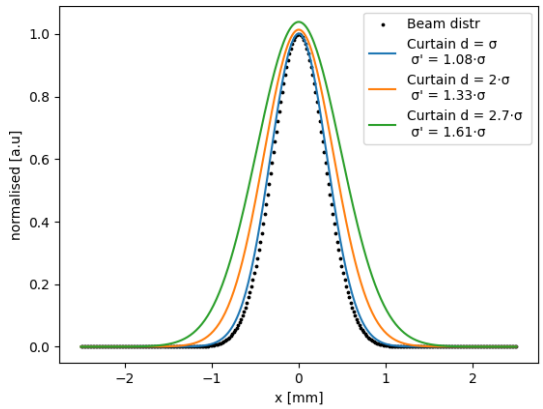


Figure 3: 2D estimations of a vertical beam profile broadening due to finite gas curtain thickness. The beam distribution was chosen to be Gaussian with $\sigma = 0.3$ mm. The gas distribution was homogeneous within thickness d.

of the skimmer should be minimised and the broadening accurately modelled for a realistic gas curtain profile.

For more detailed information see [10] and for simulations of hollow beam profile broadening see [11].

GAS CURTAIN MEASUREMENTS

During the initial testing of the BGC in the lab at Cockcroft Institute, the interaction chamber was replaced with a special chamber containing a movable pressure gauge as shown in Fig. 4. An ion gauge is enclosed within a small chamber with a 1 mm pinhole in the direction of the gas jet. This experimental setup allows for gas density measurements within the portion of the gas jet that interacts with the beam. For more details see [12, 13].

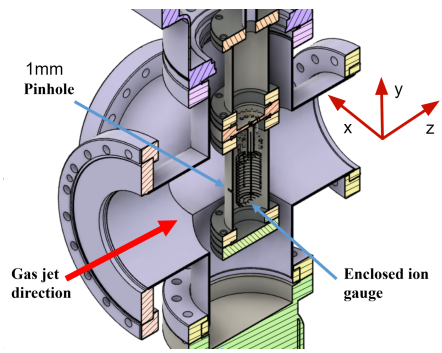


Figure 4: Movable pressure gauge 3D model showing the enclosed ion gauge which is then attached to a stepper motor for each direction. The gas density is sampled through a 1 mm pinhole [12].

The measured transverse density profiles of N_2 and Ne gas jets as obtained with a 0.7 mm thick 3rd skimmer are shown in Fig. 5 plots a) and b), respectively. Both distributions exhibit a good density uniformity. The effective curtain lengths are 12.5 ± 0.5 nm for N_2 and 12.7 ± 0.6 nm for Ne. There are no obvious differences between the shapes of the two profiles, both their lengths and thicknesses agree within measurement errors. As mentioned earlier, the maximum density is larger in the case of Ne, which is due to the difference in the number of degrees of freedom between Ne atoms and N_2 molecules.

Figure 5 plot c) shows the density profile of a nitrogen curtain obtained with a 0.7 mm thick 3rd skimmer. Using the smaller skimmer reduces the maximum density by ≈25 % as well as its effective length down to 10.7 ± 0.7 nm. This, combined with a reduced profile thickness, FWHM of 11.7 ± 0.02 nm, will reduce the fluorescence light yield. However, as experimentally observed at the EBTS, the smaller skimmer leads to a lower background pressure of $8.63 \cdot 10^{-8}$ mbar with respect to the one of $2.04 \cdot 10^{-7}$ mbar due to the larger one. This compensates the lower signal. In addition, a lower thickness also reduces profile broadening, as pointed out in the previous section.

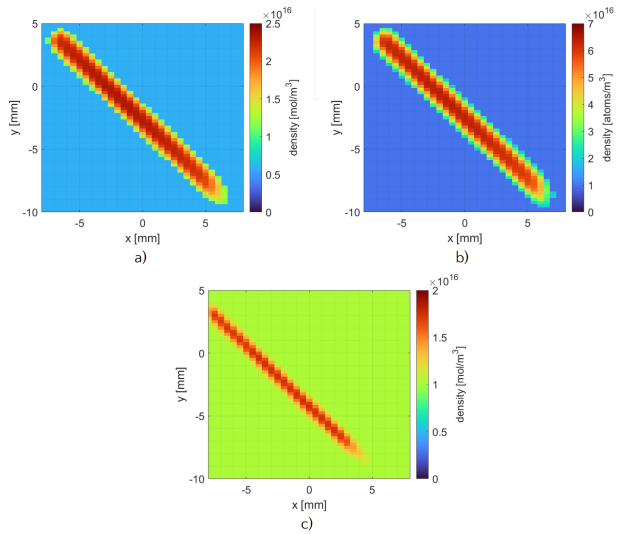


Figure 5: Gas curtain density measurements using a movable pressure gauge. Each pixel corresponds to a position of the movable pressure gauge. a) N_2 curtain using 0.7×9 mm 3rd skimmer. b) Ne curtain using 0.7×9 mm 3rd skimmer. c) N_2 curtain using 0.3×9 mm 3rd skimmer.

EXPERIMENTS WITH HOLLOW ELECTRON BEAMS

The EBTS currently serves as a test stand for the HEL. The BGC was installed at the EBTS to validate its ability to measure a 7 keV hollow electron beam with up to 5 A peak current. The electron beam is magnetized by immersion in a magnetic field and then guided further in a solenoid field. The outer and inner radius of the electron beam can be varied by changing the magnetic field strengths.

Figure 6 shows BGC measurements of the hollow electron beam's transverse profile with different gases. The electron beam was pulsed with a peak intensity of 1.5 A, a 25 µs pulse duration and a 10 Hz repetition rate. Nitrogen, neon and argon were used as working gases and the effective integration time was equivalent to 2 s of a DC beam. The

ISBN: 978-3-95450-236-3 ISSN: 2673-5350 doi:10.18429/JACoW-IBIC2023-WE3I01

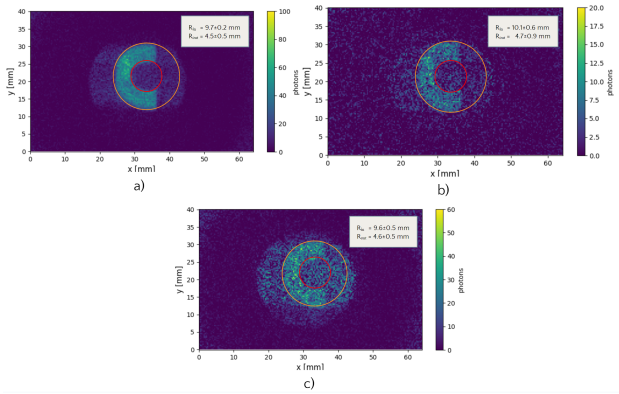


Figure 6: Beam gas curtain measurements of hollow electron beam transverse profile. Nitrogen a), neon b), and argon c) were used as a working gas.

e-beam radii determined with each gas agree within the measurement errors. As expected, the light yield of the nitrogen curtain was the highest, leading to the best image quality. Neon curtains show the lowest light yield, while the higher one of argon curtains is accompanied by a stronger background. This is due to the wider bandwidth of the optical filter used for Ar to allow for integration over several spectral peaks.

The size of the beam was larger than that of the curtain, therefore the distribution could be measured only partially. This allowed for the measurement of the effective curtain size. The 3rd skimmer used for this measurements was 0.3×9 mm and the measured curtain effective length, 12.1 ± 0.3 nm, was larger than expected from measurements with the movable pressure gauge shown in Fig. 5 c). However, it was observed that the exact width of the curtain slightly changes from one alignment of the nozzle and skimmers to another which could explain the 1.4 mm difference.

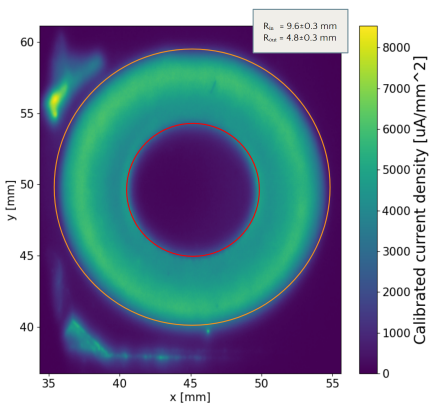


Figure 7: Transverse profile of a 7 keV, 1.1 A peak intensity hollow electron beam as measured with an OTR screen. The profile was averaged over 100 beam pulses of 25 µs duration each.

To benchmark the profiles measured by the BGC, an optical transition radiation (OTR) screen was installed in its place. Glassy carbon was the material of choice to sustain the high charge density. The OTR signal was observed with a single-stage intensified camera. Figure 7 shows a transverse beam profile of a 7 keV, 1.1 A peak intensity pulsed hollow electron beam, featuring 25 µs long pulses. The integration time was equivalent to 2.5 ms of DC electron beam. The observed distribution is rather smooth with a higher current density towards the outer edge of the profile. The measured beam size agrees with the BGC measurements. However, due to a technical fault within one of the power supplies, the magnetic field around the electron gun was 25 % lower than in the case of the EBTS measurements resulting in a smaller transverse profile. This might be explained a slight, but visible, ellipsoid shape of the observed distribution which might be a measurement arte. For more OTR measurements of hollow electron beams taken during another experimental campaign see [14].

EXPERIMENTS WITH LHC PROTON BEAMS

In 2022, BGC collaboration installed and operated an experiment at the LHC where Ne was injected in the beam pipe. Figure 8 a) shows the installation. The preliminary results and details of the installation were presented in Ref. [15]. In 2023, the gas jet was installed at the same position, completing the installation of the BGC at the LHC, as shown in Fig. 8 b).

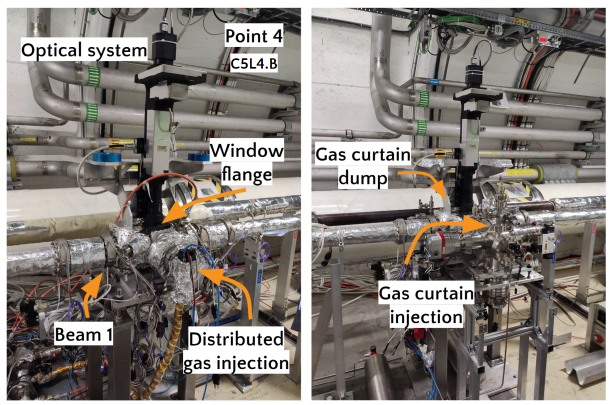


Figure 8: a) Distributed neon fluorescence experiment installation at LHC Point 4. b) Beam Gas curtain installation at LHC Point 4.

Distributed Gas

In the distributed gas experiment, a local pressure bump of several meters in length was created in one of the LHC's beam pipes by injecting neon until a peak pressure of $2.2 \cdot 10^{-8}$ mbar (Ne corrected) was reached. The fluorescence photons were captured by an optical system consisting of an apochromatic lens triplet, a band-pass filter at 585 ± 10 nm and a double-stage MCP intensified camera for single photon detection.

Content from this work may be used under the terms of the CC-BY-4.0 licence (© 2023). Any distribution of this work must maintain attribution to the author(s), title of the work, publisher, and DOI

ISBN: 978-3-95450-236-3 ISSN: 2673-5350 doi:10.18429/JACoW-IBIC2023-WE3I01

Content from this work may be used under the terms of the CC-BY-4.0 licence (© 2023). Any distribution of this work must maintain attribution to the author(s), title of the work, publisher, and DOI

Figure 9 shows a result from the fluorescence campaign. This is a measurement of a full LHC beam with $1.5 \cdot 10^{14}$ protons and an integration time of 430 s. The expected cross-section was estimated to be $4.7 \cdot 10^{-22}$ cm^2 in accordance with [10].

Table 1: The optical system parameters of the BGC and distributed gas experiment. The quantum efficiency of the photocathode corresponds to the sensitivity around wavelengths of 585 nm. Units for optical acceptance are 4π Sr.

Parameter	Value
Optical acceptance	$1.43 \cdot 10^{-3}$
QE of Photocathode	0.09
MCP efficiency	0.75
Transmittance of filter	0.80
Trans. of opt. system	0.85

Based on this expected cross-section and datasheet parameters of the optical system efficiencies, as summarised in Table 1, the expected light yield was 2.5x higher than observed. This is rather good agreement with respect to the fact that only data points at very low energies were available for the extrapolation of the expected cross-section. Several sanity checks were performed to ensure the validity of the signal. The signal rose with the integration time roughly linearly. Turning off the gas injection caused the signal peak to vanish as expected. Lastly, varying the position of the optical system distance along its optical axis did show that the beam is in focus.

The gas injection was validated also against increased beam losses or any other effect on the beam. No visible additional losses above the noise were observed by the LHC operators, deeming the gas injection transparent for the beam.

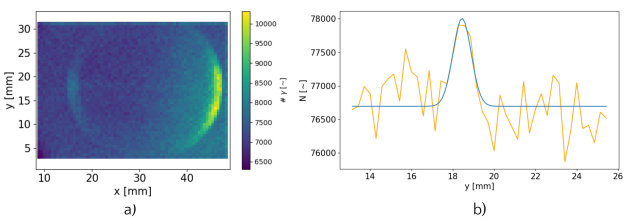


Figure 9: Ne fluorescence measurements at LHC with distributed gas. a) Observed 2D distribution showing the LHC beam horizontally across the field of view and a bright ring of synchrotron radiation. b) The horizontal profile of the LHC beam [15].

BGC at LHC

At the beginning of 2023, the full BGC was installed at the LHC, replacing the distributed gas injection with a neon gas curtain injection and dump chamber.

Testing the gas curtain at LHC increased the background pressure up to roughly $4 \cdot 10^{-8}$ mbar. This is an acceptable local background pressure level for the LHC. The monitor operation with gas curtain injection was validated and deemed acceptable for a safe operation of the LHC. The validation was done during beam injection, energy ramp from 450 GeV to 6.8 TeV and finally collisions, i.e. for the whole standard LHC fill.

The measured neon gas curtain density is equivalent to a pressure of $3.31 \cdot 10^{-6}$ mbar at room temperature. This constitutes an increase of the local gas density by a factor of 150.5. The smaller 0.3×9 mm 3rd skimmer was installed to limit the gas load onto the LHC vacuum and improve the background pressure. This choice, in comparison to the larger 0.7×9 mm 3rd skimmer, reduces the gas jet thickness by a factor of ≈2, and the curtain density by ≈25 %, but also it's broadening effect. The gas curtain installation allowed for minimally invasive 2D distribution measurements with a significant integration time decrease. The first results are currently being analysed.

CONCLUSIONS

This paper presents the BGC, a two-dimensional profile monitor utilizing the fluorescence of a supersonic, curtain shaped gas jet. The curtain density profile was measured for neon and nitrogen as well as for two sizes of the 3rd skimmer. The densities show good transverse uniformity. On the EBTS, the transverse profile of the hollow electron beam was measured using nitrogen, neon, and argon gas curtains. The measured beam radii for each gas are in agreement. Furthermore, a hollow electron profile measurement using the OTR method was shown. Fluorescence induced by 6.8 TeV proton beam at LHC was measured during distributed gas experiments. The results show a faint signal of the beam. The BGC was installed at the LHC for two-dimensional profile observations of the LHC beam. The first measurements show a significantly increased signal-to-noise ratio compared to previous fluorescence experiments at the LHC. The monitor was validated with the LHC beam and deemed safe for LHC operation. The BGC is now in operation at the LHC for characterisation with ultra-high energy proton and lead beams.

ACKNOWLEDGMENTS

This work was supported by STFC under grant agreement ST/P006752/1 and is a part of the HL-LHC project.

REFERENCES

[1] A. Giorgio *et al.*, "High luminosity large hadron collider HL-LHC", *arXiv*, 2017. doi:10.48550/arXiv.1705.08830

[2] S. Udrea *et al.*, "Development of a Fluorescence Based Gas Sheet Profile Monitor for Use With Electron Lenses: Optical System Design and Preparatory Experiments", in *Proc. IBIC'17*, Grand Rapids, MI, USA, Aug. 2017, pp. 359–363. doi:10.18429/JACoW-IBIC2017-WEPCC08

[3] A. Salehilashkajani *et al.*, "A gas curtain beam profile monitor using beam induced fluorescence for high intensity charged particle beams", *Appl. Phys. Lett.*, vol. 120, no. 17, 2022. doi:10.1063/5.0085491

ISBN: 978-3-95450-236-3 ISSN: 2673-5350 doi:10.18429/JACoW-IBIC2023-WE3I01

[4] A. Salehilashkajani *et al.*, "Commissioning of the Prototype for a New Gas Curtain Beam Profile Monitor Using Beam Induced Fluorescence for HL-LHC", in *Proc. IPAC'19*, Melbourne, Australia, May 2019, pp. 2709–2712. doi:10.18429/JACoW-IPAC2019-WEPGW093

[5] V. Tzoganis and C.P. Welsch, "A non-invasive beam profile monitor for charged particle beams", *Appl. Phys. Lett.*, vol. 104, no. 20, p. 204104, 2014. doi:10.1063/1.4879285

[6] H.D. Zhang *et al.*, "A Supersonic Gas-Jet Based Beam Induced Fluorescence Prototype Monitor for Transverse Profile Determination", in *Proc. IPAC'17*, Copenhagen, Denmark, May 2017, pp. 458–461. doi:10.18429/JACoW-IPAC2017-MOPAB139

[7] H.D. Zhang *et al.*, "A Supersonic Gas Jet-Based Beam Profile Monitor Using Fluorescence for HL-LHC", in *Proc. IPAC'18*, Vancouver, Canada, Apr.-May 2018, pp. 1891–1894. doi:10.18429/JACoW-IPAC2018-WEPAF034

[8] A. Rossi *et al.*, "DC and Pulsed Electron Beam Test Facility at CERN", in *Proc. IPAC'23*, Venice, Italy, May 2023, pp. 1953–1956. doi:10.18429/JACOW-IPAC2023-TUPL104

[9] R. Hampf, J. Wieser, and A. Ulrich, "Light emission processes in the context of optical beam profile monitors", in *Eur. Phys. J.*, vol. 77, no. 51, 2023. doi:10.1140/epjd/s10053-023-00624-6

[10] S. Udrea and P. Forck, "Milestone1.1, 1.2, and 1.6 report", GSI, Darmstadt, Germany, 2018, Report No. CERN-EDMS-2333411 and CERN-EDMS-2333413.

[11] O. Sedlacek *et al.*, "Simulations of Space-Charge and Guiding Fields Effects on the Performance of Gas Jet Profile Monitoring", in *Proc. IPAC'21*, Campinas, Brazil, May 2021, pp. 898-901. doi:10.18429/JACoW-IPAC2021-MOPAB283

[12] H.D. Zhang, A. Salehilashkajani, O. Sedlacek, and C.P. Welsch "Characterization of a supersonic gas jet for charged particle beam profile monitor", *arXiv*, 2022. doi:10.48550/arXiv.2205.05386

[13] H.D. Zhang *et al.*, "Imaging a high-power hollow electron beam non-invasively with a gas-jet-based beam profile monitor", in *Proc. IPAC'23*, Venice, Italy, May 2023, pp. 4529-4532. doi:10.18429/JACoW-IPAC2023-THPL066

[14] O. Sedlacek, M. Sameed, *et al.*, "Optical Transition Radiation Measurements of a High Intensity Low Energy Hollow Electron Beam on Electron Beam Test Facility", in *Proc. IPAC'23*, Venice, Italy, May 2023, pp. 3905-3908. doi:10.18429/JACoW-IPAC2023-THPA002

[15] O. Sedlacek *et al.*, "HL-LHC Beam Gas Fluorescence Studies for Transverse Profile Measurement", in *Proc. IBIC'22*, Kraków, Poland, September 2022, pp. 261–264. doi:10.18429/JACoW-IBIC2022-TUP17

Content from this work may be used under the terms of the CC-BY-4.0 licence (© 2023). Any distribution of this work must maintain attribution to the author(s), title of the work, publisher, and DOI

ISBN: 978-3-95450-236-3 ISSN: 2673-5350 doi:10.18429/JACoW-IBIC2023-WE3C02

DEVELOPMENT OF A PRECISE 4D EMITTANCE METER USING DIFFERENTIAL SLIT IMAGE PROCESSING

Bokkyun Shin†, Chang-Kyu Sung, Garam Hahn, Pohang Accelerator Laboratory, Pohang, Korea
Moses Chung, Ulsan National Institute of Science and Technology, Ulsan, Korea

Abstract

We have developed a highly precise 4D emittance meter for X-Y coupled beams with 4D phase- space (x-x', y-y', x-y', y-x') which utilizes an L-shaped slit and employs novel analysis techniques. Our approach involves two types of slit-screen image processing to generate pepper-pot-like images with great accuracy. One which we call the "differential slit" method, was developed by our group. This approach involves combining two slit-screen images, one at position x and the other at position x + the size of the slit, to create a differential slit image. The other method we use is the "virtual pepper-pot (VPP)" method, which combines x-slit and y-slit images to produce a hole (x, y) image. By combining that hole images, we are able to take extra x-y' and y-x' phase-space. The "differential slit" method is crucial for accurately measuring emittance. Through simulations with 0.1 mm slit width using Geant4, the emittance uncertainties for a 5 nm rad and 0.2 mm size electron beam were 5% and 250% with and without the "differential slit", respectively. In this presentation, we provide a description of the methodology, the design of slit, and the results of the 4D emittance measurements.

INTRODUCTION

In the accelerator the accurate measurement of 4D emittance, the phase space parameters (xx', yy', xy', yx') is important optimizing x-y coupled particle beam properties. This measurement has been accomplished through two primary methods: the pepper-pot and dual slit scanning techniques. However, each of these methods comes with its own set of limitations, such as resolution and time-consuming.

The recently developed 4D emittance measurement is so-called "the Virtual Pepper Pot (VPP)" method, which is image processing to generate a pepper-pot-like image using x and y axis slit scan data [1].

However, it is important to note that both the dual slit scanning and VPP methods have uncertainties related to the width of the slits. To further enhance the capabilities of the VPP method, this paper proposes an additional improvement: the "Differential Slit" method. This method employs image processing is utilized to generate virtual narrower slit images by the positions of the slit at x and x + slit width. This approach aims to minimize the uncertainties associated with slit size, enhancing the accuracy of emittance measurements.

We describe the method of "differential slit" image processing with VPP method and show precision efficiency using the simulation.

† bkshin@postech.ac.kr

SLIT DESIGN

The development and application of an L-type slit scanner, which moves to scan X and Y-axis images in a single-axis movement. This slit-scanner design is intended for electron beam testing at PAL-eLABs (or PAL-ITF) [2]. PAL-eLABs utilizes RF photo-cathode guns to generate electron beams with energy up to 70 MeV.

Beam profile imaging is achieved by capturing images through the slit and subsequently viewing them on scintillation screens and/or Optical Transition Radiation (OTR) detectors. These screens and detectors are positioned at distances of 3.5 meters away from the slit.

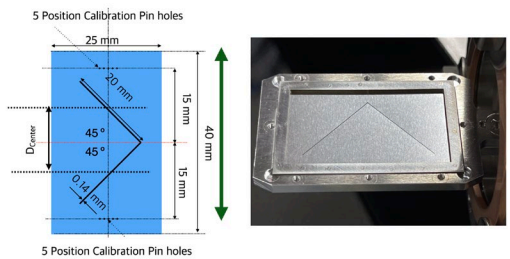


Figure 1: Slit design and manufactured slit scanner.

Two critical aspects of the slit design have been considered: the slit width size and the thickness of the slit plate including its material. Figure 1 shows slit design and manufactured prototype slit. The distance between the X and Y slit centers (D_{center}) is determined considering 15 mm by the beam size to prevent overlapping X and Y slit image in a shot. A thickness and material of slit plate 50 μm stainless steel has been selected to minimize background from 70 MeV beam scattering with plate and slit punching by etching. And 5 pin holes at bottom and top of slit to get in-site position calibration. The prototype slit was succeeded manufacture with 140 μm slit width and 100 μm diameter calibration pinhole.

SIMULATION

The simulation data is generated using the Geant4 [3] and image analyzer OpenCV [4]. Electron interaction with slit and screen are simulated by Geant4. And from energy deposition in the screen to image data by Open CV. The beam condition is used PAL-eLABs [2], 70 MeV and emittance ~10 nm rad and beam is artificially rotate for 4D emittance for the 4D phase space study. And Beam Profile screen using the YAG ($Y_3Al_5O_{12}$) is located 3.5 meters away from a slit. The slit is moved every 20 μm from fully open which is equivalent as 10 Hz beam repetition rate with continuously moving a velocity of 0.2 mm/s. The images vertical resolution is 12 bit which is common resolution of CMOS camera, and they are stored in a scaled 16-bit video format.

Content from this work may be used under the terms of the CC-BY-4.0 licence (© 2023). Any distribution of this work must maintain attribution to the author(s), title of the work, publisher, and DOI

ISBN: 978-3-95450-236-3 ISSN: 2673-5350 doi:10.18429/JACoW-IBIC2023-WE3C02

In simulation setup, background noise sources are a critical consideration. two primary sources of background noise are identified: beam scattered by the slit plate and camera sensor noise. beam scattered noise is produce using the Geant4. The noise with 50 μm stainless steel with 3.5 m way screen does not significantly affect by analysis. It is uniformly distributed in the screen and its signal-to-noise ratio (SNR) is smaller than 1/1000. The camera noise was randomly generated in simulation, which is approximately 5% of the camera sensor cavity.

ANALYSIS

Analysis involves four steps: position calibration, the differential slit image process, VPP image process [1], and phase space reconstruction.

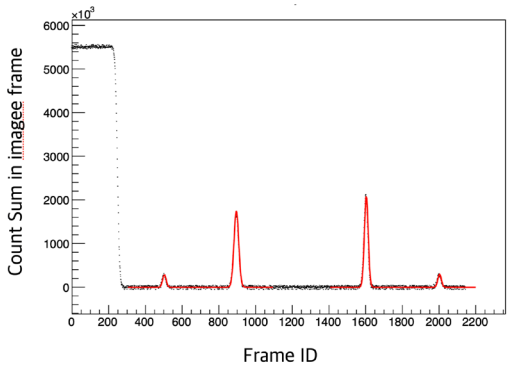


Figure 2: Frame ID vs Sum of count in sensor, left high mesa is signal when slit is opened and four peaks represent calibration pin holes and slits.

In this initial step, position calibration is performed by correlating frame numbers with the sums of signals in the captured images. Figure 2 shows the relationship between frame number and the sum of the signal in the image. In Fig. 2, the highest mesa corresponds to when the slit is fully opened. And the first and last peaks obtained from this calibration process are linked to the position calibration pinhole, enabling the determination of the slit's speed and the matching of frame IDs with positions.

The second step, the **Differential Slit** method is introduced as an innovative approach in this research to enhance precision in data analysis. This method involves the use of two images captured at different slit positions. Specifically, images are selected based on the condition slit position difference is smaller than slit moving step. For this study i^{th} frame and $i+7^{th}$ frame is chosen for differential slit image. The image processing is then performed using the minimum pixel pick up using the two images. An example of a differential slit image is show in Fig. 4. Figure 4 a) shows beam particle distribution and slit position green and blue box, and b) and c) are the image on the screen at 3.5 meter away from slit. Figure 3 d) displays the result of the differential slit image obtained by selecting the minimum pixel count, in contrast to images b) and c).

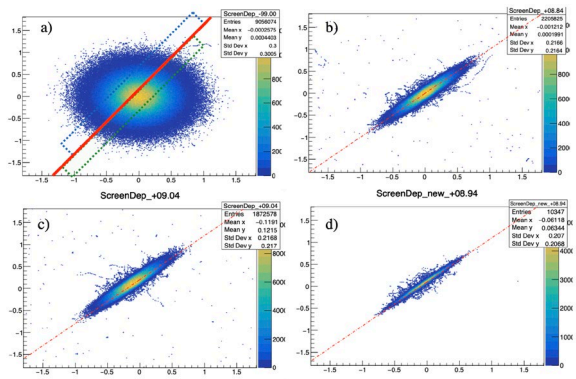


Figure 3: Differential Slit mage processing: a) beam profile at screen and slit position; b), c) screen image by the green and blue dot boxes; d) differential slit image using minimum pixel pick up using the image b) and c).

The VPP Method is employed as the third step in the analysis process. The image processing steps here are similar to those of the Differential Slit Method, utilizing min (cx, cy), where 'c' represents photon counts in the pixel, and 'x' and 'y' denote positions in the x and y axes. Figure 5 describes process of VPP method. It is also using the minimum pixel count selecting. Using the VPP method in combination with the differential slit images yields images that resemble those obtained from a pinhole, enhancing the quality of data.

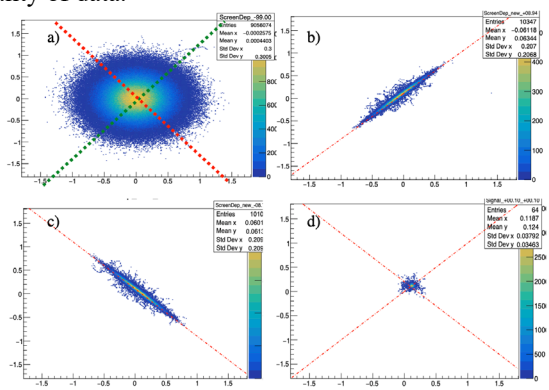


Figure 4: VPP image processing: a) beam profile at screen and slit position; b), c) differential image by the green and blue dot lines; d) pin hole image from the VPP image process using b) and c).

In the final step, phase space reconstruction is carried out which is shows in Fig. 5. This involves using the x and y pinhole images obtained from the previous steps. Phase space was reconstructed. And through 2D-Gaussian fitting, emittance and Twiss parameters are analyzed in the Fig. 5 red ellipse.

RESULT

As a result of these analysis steps, the entire process takes approximately 10 seconds using GPU processing. Table 1 shows the input and reconstructed parameters of each phase-space. In the result, emittance uncertainties from input are less than 10%. But without the difference slit method, the result of emittance uncertainty higher

Content from this work may be used under the terms of the CC-BY-4.0 licence (© 2023). Any distribution of this work must maintain attribution to the author(s), title of the work, publisher, and DOI

ISBN: 978-3-95450-236-3 ISSN: 2673-5350 doi:10.18429/JACoW-IBIC2023-WE3C02

than 250%. Overall, these four steps enable a comprehensive and precise analysis of the experimental data, providing valuable insights into the behaviour of the system under study.

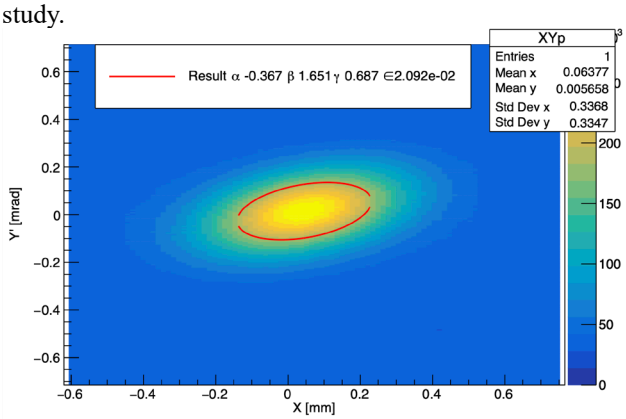


Figure 5: Phase reconstruction and emittance and Twiss parameter analysed by 2D Gaussian fitting.

Table 1: The Result of Input and Reconstructed

Phase Space	α	β	ε
X-X' in	4.467	4.390	7.449
X-X' out	3.871	4.549	7.650
X-Y' in	-0.379	1.377	23.73
X-Y' out	-0.367	1.651	21.24
X-X' in	-0.479	0.826	23.87
X-X' out	-0.467	1.000	22.16
X-Y' in	1.914	2.161	9.137
X-Y' out	1.821	2.496	8.932

EXPERIMENT PLAN

The experiment plan the slit-based analysis method at PAL-eLABs is shown below.

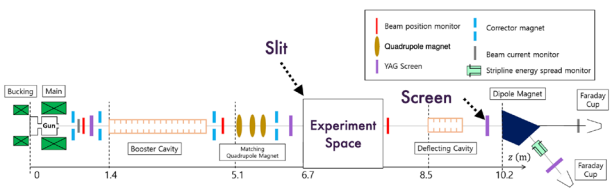


Figure 6: PAL-eLABs lattice layout.

Figure 6 shows the lattice of the PAL-eLABs. The slit will be installed experiment space and the screen will be used at before Dipole Magnet. The x-y coupling beam for 4D emittance such as rotation beam is tuning by bucking coil or skew quadrupole magnet after the accelerator. After the successful measurement. The slit will be applying in Korea-4GSR LINAC to measure x-y coupling.

SUMMARY

The VPP method with L type slit is a significant advancement of measurement time efficiency compared to traditional dual slit scan method. And the differential slit method introduced in this paper represents an additional step forward in improving measurement precision. Only applying one step of analysis without any instrument improves uncertainty from slit width. In this simulation study using 100 μm slit width of 50 μm stainless steel with this method, the uncertainty is dramatically improved from 250% to 10% which is small step but great achievement. Consequently, this method is becoming a crucial technique in any slit-screen experiment.

ACKNOWLEDGEMENTS

This research was supported in part by the Korean Government MSIT (Multipurpose Synchrotron Radiation Construction Project) (RS-2022-00155836) and UNIST CHEA by the National Research Foundation of Korea (Grants No. NRF-2016R1A5A1013277 and No. RS-2022-00154676).

REFERENCES

[1] G.Z. Georgiev and M. Krasilnikov, "Virtual Pepper-Pot Technique for 4D Phase Space Measurements", in *Proc. IBIC'19*, Malmö, Sweden, Sep. 2019, pp. 586-590. doi:10.18429/JACoW-IBIC2019-WEPP029

[2] S.J. Park *et al.*, "Construction of Injector Test Facility (ITF) for the PAL XFEL", in *Proc. IPAC'13,* Shanghai, China, May 2013, paper WEPWA043, pp. 2220-2222.

[3] S. Agostinelli *et al.*, "Geant4-a simulation toolkit", *Nucl. Instrum. Methods Phys. Res., Sect. A,* vol. 506, no. 3, July 2003, pp. 250-303, 2003. doi:10.1016/S0168-9002(03)01368-8

[4] OpenCV, https://opencv.org

Content from this work may be used under the terms of the CC-BY-4.0 licence (© 2023). Any distribution of this work must maintain attribution to the author(s), title of the work, publisher, and DOI

ISBN: 978-3-95450-236-3 ISSN: 2673-5350 doi:10.18429/JACoW-IBIC2023-WE3C03

RADIATION HARD BEAM PROFILE MONITORS FOR THE NORTH EXPERIMENTAL BEAMLINES CERN

E. Buchanan*, J. Cenede, S. Deschamps, W. Devachelle,
A. Frassier, J. Kearney, R. G. Larsen, I. O. Ruiz
CERN, Geneva, Switzerland

Abstract

A new radiation hard profile monitor is being researched and developed for the North Area Beamlines at CERN. The monitor must have a spatial resolution of 1 mm or less, an active area of 20 x 20 cm, a low material budget (0.3%) and be operational in a beam that has a rate of ~2×10^{11} p/s in the full energy range of 0.5 – 450 GeV/c. The current focus is the study of different detection mediums: silica optical fibres (Cherenkov radiation) and glass capillaries filled with liquid scintillator. Prototypes of the different fibre candidates have been tested at different beam facilities at CERN: the M2 beamline and IRRAD. The key properties tested are the light yield and radiation tolerance.

INTRODUCTION

Since the late 1970s, Multi Wire Proportional Chambers, Delay Wire Chambers and Filament Scintillators have been used in the North Area Beamlines to provide the profile and positions of the beams [1]. However, the performance of these detectors is now degrading due to aging effects and there are limitations on the maximum intensity at which they can operate. As part of an upgrade to the beamlines, starting from 2027, the majority of these detectors will be replaced [2]. For the low intensity beamlines (~ 10^8 particles per spill), a scintillating fibre detector called the eXperimental Beam Profile Fibre monitor (XBPF) will be installed [3]. The XBPF consists of a single array of 192 plastic scintillating fibres (SCSF-78) from Kuraray with a square cross-section and 1 mm thickness. Each fibre is individually read-out using si-pm's. A photograph of an XBPF is shown in Fig. 1. For the high intensity beamlines (~ 10^{11} particles per spill), the XBPF is not expected to have sufficient radiation tolerance, therefore a new radiation hard profile monitor is currently being researched and developed. Ideally the new detector will have a similar silhouette to the XBPF, but the active medium will be replaced with a material that has a higher radiation tolerance. This article describes the different detection mediums that are being studied and presents recent beam test results.

DETECTOR REQUIREMENTS

The new radiation hard profile monitor has the following requirements:

- active area of 20 cm × 20 cm,
- a low as possible material budget (~0.3% X_0),

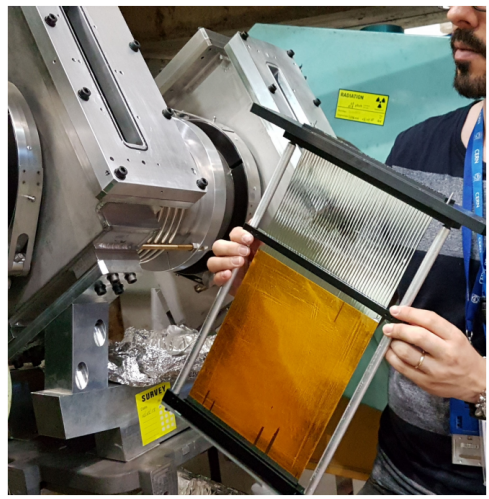


Figure 1: The XBPF detector.

- a spatial resolution of 1 mm,
- measure particle rates from ~ 10^4 to ~ 10^{11} in the full energy range of 0.5 – 450 GeV/c,
- operational up to 2 MGy, equivalent to a minimum of 8 years of operation, and
- operational in vacuum (10^{-3} mbar) and in air.

ACTIVE MEDIUMS

Two different active materials are currently being studied: silica optical fibres and silica capillary fibres filled with liquid scintillator.

Silica Optical Fibres

Silica optical fibres are widely used in the telecommunications industry. They consist of a central silica core surrounded by a cladding layer which has a lower refractive index, enabling the transmission of light via total internal reflection. A well-known phenomenon is the production of Cherenkov light in silica fibres when charged particles pass through them [4]. Often for data transmission in high radiation environments, for example high energy physics experiments, this is an unwanted source of background. However, for some applications, this phenomenon can be exploited as a signal, such as Beam Loss Monitors [5].

The Cherenkov light peaks in the UV wavelengths and is emitted in a cone relative to the impinging particles direction. The angle depends on the refractive index of the

* emma.buchanan@cern.ch

Content from this work may be used under the terms of the CC-BY-4.0 licence (© 2023). Any distribution of this work must maintain attribution to the author(s), title of the work, publisher, and DOI

ISBN: 978-3-95450-236-3 ISSN: 2673-5350 doi:10.18429/JACoW-IBIC2023-WE3C03

material and the velocity of the charged particle, which is expected to be ~ 40° in silica for relativistic particles [6]. Silica quartz is known to be more radiation hard compared to plastics [7]. There are, however, two consequences of irradiation damage that will effect the performance: radiation induced attenuation which decreases light transmission and a change in the refractive index [7].

For fibre testing, multimode optical fibre's were purchased from Thorlabs with two different diameters, 600 µm and 1000 µm. These fibres where cut to 20 cm lengths using a ruby fibre scribe. Additionally, quartz glass rods of 1000 µm, and length 20 cm were purchased from Hilgenberg GmbH. These rods have no cladding and therefore have a higher refractive index gradient with respect to air, hopefully increasing the trapping efficiency of the light.

Capillary Fibres

Capillary fibres are small tubes of quartz glass with a hollow core. They propagate light via total internal reflection if you fill them with a material with a higher refractive index than glass. One option is to fill them with liquid scintillator. Traversing charge particles will produce scintillation light which will then be propagated towards the end of the fibre. Liquid scintillators are intrinsically more radiation hard than plastic scintillators. From literature, it was found that the light yield of liquid scintillator EJ-309[1] decreases 25% per 0.5 MGy compared to a 30% decrease per 10 kGy for plastic scintillators [3, 8]. Also from literature, liquid scintillator BC-599-13, was found to have no change in light transmission up to 1 MGy [9]. Radiation damage will occur in the quartz glass capillary but as long as the refractive index remains lower than the liquid scintillator, light should still propagate.

Two different glass capillaries were purchased from Hilgenberg GmbH, both with length 20 cm and an outer diameter of 1000 µm. One fibre type had a inner diameter of 580 µm and the other, 800 µm. A larger inner diameter will give a larger light yield but are more breakable. The capillaries were filled with liquid scintillator EJ-309 from Eljen Technology. The refractive index of the scintillator is 1.57 and the wavelength of maximum emission is 424 nm. The liquid was contained in the fibre by gluing both ends using NOA61 UV cure optical adhesive [10]. A photograph of a liquid filled capillary is shown in Fig. 2.



Figure 2: A liquid filled capillary when exposed to UV torch.

BEAM TESTS

Different fibre tests have been performed at two different beam facilities at CERN: The M2 beamline and IRRAD.

[1] EJ309 liquid base containing 16% of the fluorescent dye DSB1

The M2 Prototype

The M2 beamline is part of the North Experimental Area CERN. Currently the M2 beamline can provide high-energy and high-intensity hadron beams, at a momentum of 280 GeV/c and a maximum rate of 10^8 particles per spill. The line can also provide muons and electrons [1]. A prototype device has been installed 69 m from the target.

A photograph of the M2 prototype is shown in Fig. 3. The prototype is made up of three different fibre sections with 64 fibres each of: 1000 µm optical fibres, EJ-309 filled capillary fibres with inner diameter 580 µm, and 600 µm silica optical fibres. They are readout individually by the si-pms on the XBPF readout board. The prototype can be rotated around the *y*-*z* axis and is mounted on a linear motor along the *y*-axis. A blackbox is placed over the prototype during operations.

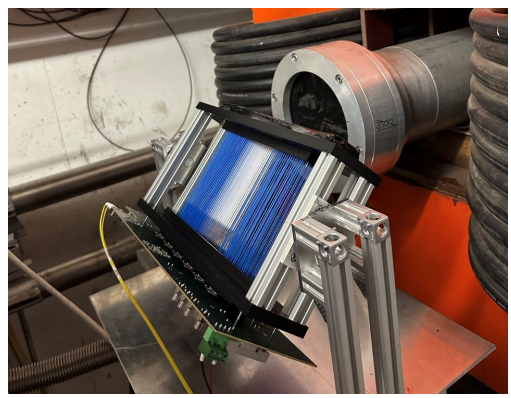


Figure 3: The M2 prototype rotated at 45°.

IRRAD Tests

IRRAD is a proton irradiation facility at CERN. IRRAD provides a slowly extracted primary proton beam of momentum 24 GeV/c delivered in spills with a maximum intensity of 5×10^{11} particles per spill over a duration of ~ 400 ms [11].

A quartz silica rod and a EJ-309 filled capillary (inner diameter of 800 µm) were installed at IRRAD to test their light yield and light transmission while being irradiated up to 2.85 MGy. The rod and fibre were each attached to a 30 m 1000 µm silica optical fibre (glued using NOA61), known as a transport fibre, to transmit the light from the irradiation area to a CMOS camera in the barracks. Two 12 V halogen bulbs where programmed to flash in between spills of the beam to check the light transmission. A photograph of the IRRAD setup is shown in Fig. 4. A blackbox is placed over the setup during operations. The exposure of the camera was set to 500 ms to ensure the full particle spill was captured and optical filters were placed over the end of transport fibres to stop camera saturation.

Content from this work may be used under the terms of the CC-BY-4.0 licence (© 2023). Any distribution of this work must maintain attribution to the author(s), title of the work, publisher, and DOI

ISBN: 978-3-95450-236-3 ISSN: 2673-5350 doi:10.18429/JACoW-IBIC2023-WE3C03

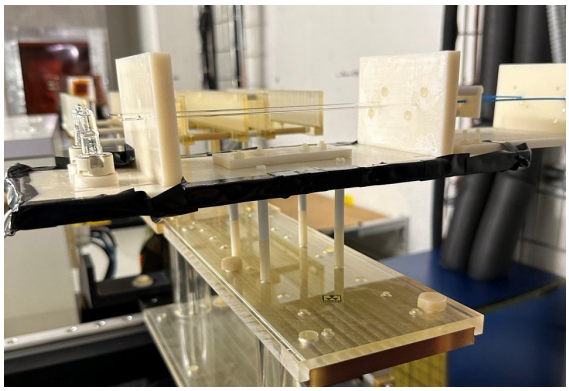


Figure 4: A quartz rod and EJ-309 capilary fibre installed at IRRAD. Two halogen bulbs are seen on the left and the transport fibres are seen on the right (blue cladding).

RESULTS

The M2 Prototype

The M2 prototype was tested with a mixed hadron beam with a momentum of 190 GeV/c and a rate of ~ 3×10^5 particles per spill. A nearby scintillation paddle was used to trigger the detector and reduce noise. Example profiles are shown in Fig. 5, measured when the prototype was placed 45° relative to the beam. Insufficient signal was measured in the silica fibres when the prototype was perpendicular to the beam. A higher signal was measured in the capillaries compared to the silica optical fibres (30% compared to the 1000 µm silica fibre), as expected. A 76% lower signal was measured in the 600 µm compared to the 1000 µm. The reduced signal when comparing the 600 µm and the 1000 µm silica fibres is not linear, this could be accounted for by the inconsistent cutting techniques that may result in varied light losses. A summary of the beam profile σ and average efficiencies are shown in Table 1.

Table 1: M2 Prototype Results Summary

Fibre type	Profile σ	Efficiency %
1000 µm	3.50 ± -0.03	46.4
EJ-309 Capillary	3.92 ± 0.04	64.8
600 µm	3.57 ± 0.01	15.1

IRRAD Tests

The IRRAD setup, as shown in Fig. 4, was installed for one week. The average rate was 5×10^{11} particles per spill and there were limited periods of no beam. The max dose reached was 2.85 MGy in an area of 10×10 mm^2. An example image taken by the camera when the bulbs were flashing is shown in Fig. 6. The integral of each light spot was calculated and plotted for each spill as a function of the timestamp for when the bulb was flashed and when the beam was traversing. The light transmission and the light yield for the quartz rod are shown in Figs. 7 and 8 respectively.

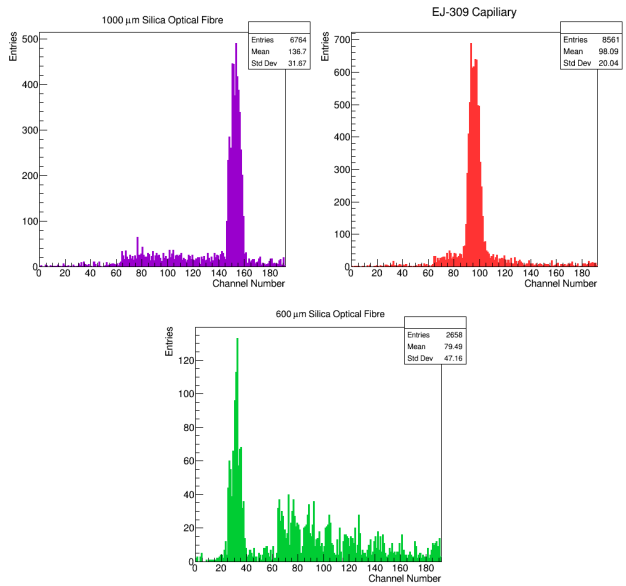


Figure 5: Beam profile measuring using 1000 µm silica fibres (top left), EJ-309 capillaries (top right), 600 µm silica fibres (bottom).

Both the light transmission and light yield decrease exponentially with a 66% drop in transmission and a 95% drop in light yield. The bulb emits a wide spectrum of wavelengths, whereas Cherenkov light peaks in the UV. The lower light yield may be due to increased absorption in the UV wavelengths. Increased light transmission is seen during short periods over the week which correlate to periods of no beam. This increase is due to annealing. The light transmission and the light yield for the EJ-309 capillary are shown in Figs. 9 and 10 respectively. The light transmission only fluctuated 3%, suggesting a negligible difference in light transmission, as reported in literature [9]. The light yield decreased 50%. These results suggest that the radiation tolerance of the EJ-309 capillary is higher compared to the quartz rod.

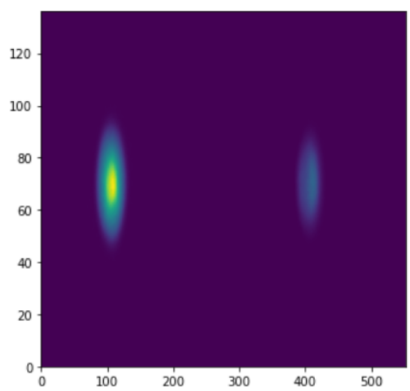


Figure 6: An example image from the CMOS camera when the bulbs are flashing. The light from the quartz rod is seen on the left and the capillary is shown on the right.

Content from this work may be used under the terms of the CC-BY-4.0 licence (© 2023). Any distribution of this work must maintain attribution to the author(s), title of the work, publisher, and DOI

ISBN: 978-3-95450-236-3 ISSN: 2673-5350 doi:10.18429/JACoW-IBIC2023-WE3C03

Content from this work may be used under the terms of the CC-BY-4.0 licence (© 2023). Any distribution of this work must maintain attribution to the author(s), title of the work, publisher, and DOI

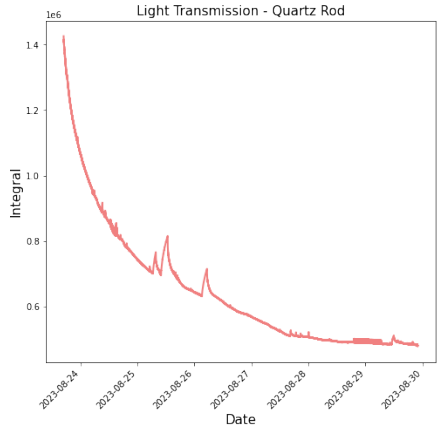


Figure 7: Light transmission of the quartz rod.

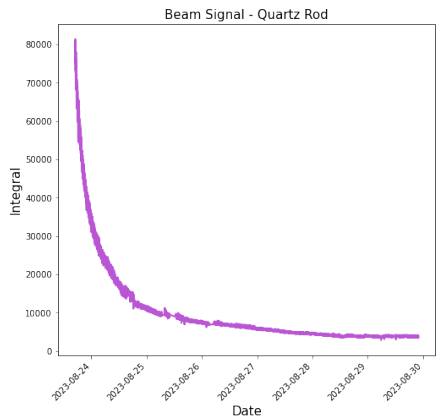


Figure 8: Light yield of the quartz rod.

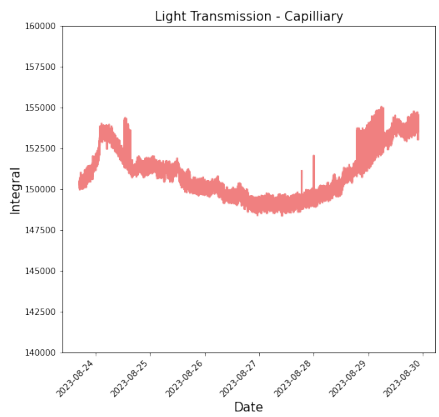


Figure 9: Light transmission of the EJ-309 capillary.

CONCLUSION

The beam profile monitors currently installed in the North Area Beamlines need to be replaced and upgraded. A scintillating fibre detector, called the XBPF will be installed in the lower intensity beamlines (~ 10^8 particles per spill). These devices do not have the required radiation tolerance for the higher intensity beamlines (~ 10^{11} particles per spill), therefore a new radiation hard profile monitor is required.

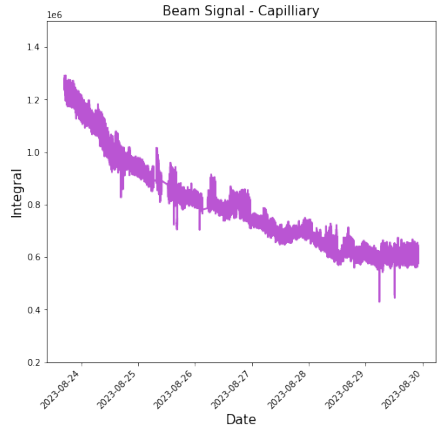


Figure 10: Light yield of the EJ-309 capillary.

Silica optical fibres and liquid scintillator filled capillary fibres were tested as options for a new active material replacing the scintillation fibres. From tests performed at the M2 beamline CERN and IRRAD, it was found that liquid filled capillaries have a higher radiation tolerance, in terms of both light transmission and light yield compared to silica quartz rods. This R&D effort is still ongoing. The M2 prototype needs to be tested at higher particle rates to check that sipms do not reach saturation. Additionally, a new fibre type will be tested: hollow core optical fibres [12] filled with a scintillation gas will be qualified later this year.

REFERENCES

[1] D. Banerjee *et al.,* "The North Experimental Area at the CERN Super Proton Synchrotron", CERN, Geneva, Switzerland. CERN-ACC-NOTE-2021-0015, Jul. 2021. https://cds.cern.ch/record/2774716

[2] "Medium-Term Plan for the period 2023-2027 and Draft Budget of the Organization for the sixty-ninth financial year 2023", CERN, Geneva, Switzerland. CERN/SPC/1182/Rev., Sept. 2022. https://cds.cern.ch/record/2838413

[3] I. Ortega Ruitz *et al.,* "The XBPF, a new multipurpose scintillating fibre monitor for the measurement of secondary beams at CERN", *Nucl. Instrum. Methods Phys. Res., Sect. A*, vol. 951, p. 162996, Jan. 2020. doi:10.1016/j.nima.2019.162996

[4] S. Girard *et al.,* "Overview of radiation induced point defects in silica-based optical fibers", *Rev. Phys.*, vol. 4, 2019. doi:10.1016/j.revip.2019.100032

[5] S. Benítez Berrocal *et al.,* "Beam loss localisation with an optical beam loss monitor in the CLEAR facility at CERN", in *Proc. 13th Int. Particle Accelerator Conf. (IPAC'22)*, Bangkok, Thailand, Jun. 2022, pp. 351-354. doi:10.18429/JACoW-IPAC2022-MOPOPT045

[6] A. S. Beddar *et al.,* "Cerevkov light generated in optical fibres and other light pipes irradiated by electron beams", *Phys. Med. Biol.*, vol. 37, p. 925, Jul. 2000. doi:10.1088/0031-9155/37/4/007

[7] V. Hagopian, "Radiation damage of quartz fibers", *Nucl. Phys. B Proc. Suppl.*, vol. 78, no. 1, pp. 635-638, 1999. doi:10.1016/S0920-5632(99)00616-7

ISBN: 978-3-95450-236-3 ISSN: 2673-5350 doi:10.18429/JACoW-IBIC2023-WE3C03

[8] R. Ruchti *et al.* "Thick-wall, liquid-filled quartz capillaries for scintillation and wavelength shifting applications", in *38th Int. Conf. on High Energy Physics - Poster Session (ICHEP'16)*, Chicago, USA, Aug. 2016. doi:10.22323/1.282.0935

[9] M. Gui *et al.,* "Radiation damage effects on liquid scintillating fibers", *Radiat. Phys. Chem.*, vol. 41, no. 1, pp. 237-242, 1993. doi:10.1016/0969-806X(93)90061-X

[10] M. Montecchi and Q. Ingram, "Study of some optical glues for the Compact Muon Solenoid at the large hadron collider of CERN", *Nucl. Instrum. Methods Phys. Res., Sect. A*, vol. 465, no. 2, pp. 329–345, 2001. doi:10.1016/S0168-9002(01)00678-7

[11] B. Gkotse *et al.*, "IRRAD: The New 24 GeV/c Proton Irradiation Facility at CERN", in *Proc. 12th Int. Topical Meeting on Nuclear Applications of Accelerators (AccApp'15)* Washington D.C., USA, Nov. 2015. https://inspirehep.net/literature/1688990

[12] H. Sakr *et al.,* "Hollow core optical fibres with comparable attenuation to silica fibres between 600 and 1100 nm", *Nat. Commun.* vol. 11, Nov. 2020. doi:10.1038/s41467-020-19910-7

Content from this work may be used under the terms of the CC-BY-4.0 licence (© 2023). Any distribution of this work must maintain attribution to the author(s), title of the work, publisher, and DOI

ISBN: 978-3-95450-236-3 ISSN: 2673-5350 doi:10.18429/JACoW-IBIC2023-WEP001

NON-INVASIVE PROFILERS FOR THE COLD PART OF ESS ACCELERATOR

J. Marroncle, P. Abbon, F. Belloni, F. Bénédetti*, B. Bolzon, N. Chauvin, D. Chirpaz-Cerbat, M. Combet, M. Desmons, Y. Gauthier, T. Hamelin, C. Lahonde, P. Legou, O. Leseigneur, Y. Mariette, JP Mols, V. Nadot, M. Oublaid, G. Perreu, F. Popieul, B. Pottin, Y. Sauce, L. Scola, F. Senée, J. Schwindling, G. Tauzin, O. Tuske, S. Tzvetkov, CEA-Saclay, Gif-sur-Yvette, France
I. Dolenc Kittelmann, A. Gevorgyan, H. Kocevar, R. Tarkeshian, C. Thomas, ESS Lund, Sweden

Abstract

Several Non-invasive Profile Monitors are being installed along the accelerator to support the commissioning, tuning and operation of the powerful proton based ESS linear accelerator. In the low energy parts of the ESS linac (3.6 MeV to 90 MeV), the residual gas pressure is high enough to measure the transverse beam profile by using fluorescence induced by the beam on the gas molecules. However, in the ESS linac sections above 90 MeV, protons are accelerated by superconductive cavities working at cryogenic temperatures and high vacuum. Therefore, the signal based on the fluorescence process is too weak, while ionization can counteract this drawback.

We have provided five IPM (Ionization Profile Monitors) pairs for energies ranging from 100 to 600 MeV. The design of such monitors is challenging due to weak signal (as a result of high proton energy and low pressure $<10^{-9}$ mbar), tight space constraints inside the vacuum chamber, space charge effect, ISO-5 cleanliness requirement, and electrode polarization at ±15 kV.

This publication will detail the development we followed to fulfil the ESS requirements.

INTRODUCTION

The European Spallation Source (ESS) [1], presently under construction at Lund (Sweden), will consist of a 537 m long linear proton accelerator delivering a 2 GeV proton beam with a 5 MW power to a tungsten target, equipped with a highly optimized neutron moderator capable of providing a bi-spectral (thermal and cold) neutron beam to 42 beam ports, 22 of which are followed by a flight path leading to faraway measuring stations.

A perfect knowledge of the proton beam is critical for maximizing the number of protons on target and minimizing beam losses. Transverse beam profile monitors are therefore essential to support the tuning of the beam for good operation of the facility, both during its commissioning and in everyday operation.

Due to the high beam power, all beam profilers to be used at nominal operating conditions will be non-invasive type. In the frame of the in-kind contribution agreement signed with ESS, CEA has delivered to the European Spallation Source five Non-invasive Profile Monitors (NPMs) to be installed in the Cold Linac section: one in the Spoke section, 3 in the β-medium section, and one in the β-high section. These transverse beam profile monitors will cover proton energies ranging between 90 MeV and 600 MeV and are conceived to deliver one profile/pulse at a residual gas pressure of 10^{-9} mbar with an uncertainty on the beam width of less than 10% of its dimension (see Refs. [2] and [3] for a profiler detailed overview).

At such high proton energies and low residual gas pressure, the NPMs located on the superconductive beam line are based on the ionization of the residual gas. In the warm sections, transverse beam profiles are measured by using the fluorescence of the gas molecules induced by the beam.

ESS IPM DESCRIPTION

Two parts can be considered for describing an IPM (Fig. 1): the inner, situated inside the vacuum chamber, and the outer part. The beam traverses the cage approximately at its center.

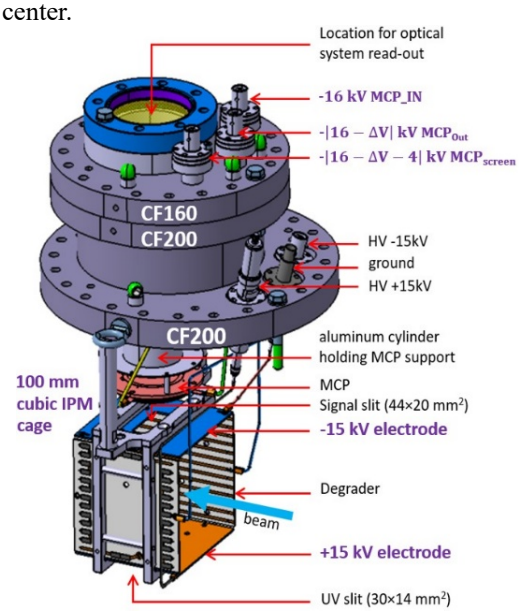


Figure 1: An ESS IPM.

Then, the ions and electrons, by-products of beam-residual gas interactions, drift under the influence of the electric field applied between both electrodes through a slit for ions before collection onto an MCP (Micro-Channel Plate). The MCP is equipped with a phosphorescent screen, allowing electric signal conversion to an optical one. To enhance the electric field uniformity, degraders positioned perpendicular to the electrodes are designed.

* Presently at LIPAc Rokkasho

Content from this work may be used under the terms of the CC-BY-4.0 licence (© 2023). Any distribution of this work must maintain attribution to the author(s), title of the work, publisher, and DOI

ISBN: 978-3-95450-236-3 ISSN: 2673-5350 doi:10.18429/JACoW-IBIC2023-WEP001

On the outer part, the read-out is done with an optical system consisting of a lens and a CMOS camera. The HV connectors are used for the MCP and the cage polarization, linked with copper wires (1 mm). The control of the camera daq and the HV system is fully implemented in EPICS.

FEASIBILITY STUDY

When the project was initiated in mid-2016, several challenges were encountered that necessitated preliminary studies to assess the feasibility of such IPMs. These challenges can be summarized as follows:

- Ionization signal strength.
- Limited space inside the vacuum chamber.
- The space charge effect.
- Background particles that may hide or distort the profile, but were not inquired.
- ISO-5 cleanliness.

The following sections will be devoted to these topics.

Ionization Signal Strength

The nominal beam conditions for IPMs are low pressure, likely below 10^{-9} mbar, with a residual gas composition of H_2 (79%), CO (10%), CO_2 (10%) and N_2 (1% in mass), 62.5 mA beam intensity, and a beam width $\sigma_{X,Y}$ = 2 mm. During beam commissioning, the intensity may decrease to 1 mA, which will require an excess of read-out sensitivity.

Bethe's relation ([4] original) gives the mean energy losses by a charged particle per unit of media length; thus, knowing the average energy for producing ion/e pairs, we deduced their numbers in Table 1.

Table 1: e/ion Pairs Produced at Various Beam Energies

E (MeV)	97	280	628
e/ion (pairs/cm)	$1.0\ 10^5$	$4.9\ 10^4$	$3.4\ 10^4$

The electrode slit allowing the ions to pass toward the MCP is 2 cm large.

IPM Vacuum Chamber

The vacuum chamber, hosting a pair of Wire Scanners and a pair of IPMs, appears quite crowded, as illustrated in Fig. 2. The CF200 flanges (yellow) highlight their overlap. To address this issue, an adjustment is made by shifting the center of the IPM-X cage by 36 mm relative to the flange, enabling its insertion into the chamber.

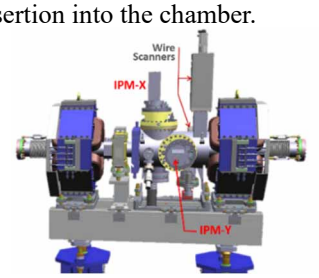


Figure 2: The Linear Warm Unit (LWU) comprises a vacuum chamber that includes 2 IPMs and 2 Wire Scanners.

In such a constrained space, two 100 mm cubic IPM cages, along with conductive discs, are securely attached to the chamber, perpendicular to the beam direction, and located 33 mm upstream and downstream from both IPM edges. The diameter of the hole in each disc is 100 mm, similar to that of the beam pipe. The purpose of these components is to ensure and improve the uniformity of the electric field inside the cage by grounding them as much as possible. In Fig. 3, a simulation conducted using COMSOL software [5] shows the original Gaussian profile achieved by a perfect field (green) and the reconstructed profile obtained by tracking (blue) ions into a realistic electric field taking into account the discs, which are in good agreement.

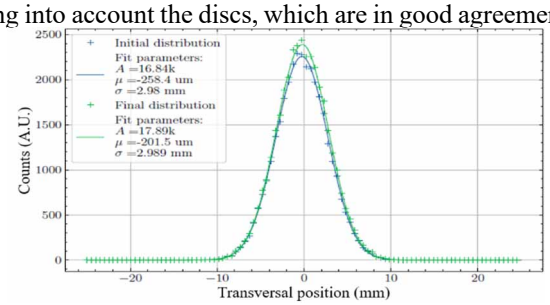


Figure 3: Gaussian profiles reconstructed by tracking for the original (green) and for the realistic profile (blue).

Space Charge Effect

One of the ESS requirements is to measure the beam width with a maximum total error in the RMS beam extension of less than ±10%. This becomes difficult to achieve in ESS conditions due to the space charge effect on the beam profile measurement.

The effects of space charge are twofold: they affect the charged particle beam and any other charge in its proximity. Our focus is on the later.

A charge generated at rest between two parallel plates kept at different voltages drifts towards the electrodes travelling parallel to the electric field lines. In an ideal case of a perfectly uniform electric field, the point where the charge meets the electrode will simply be the projection of its initial position on the electrode. In IPMs, charges are created via gas ionization, and the beam profile is reconstructed this way. However, the presence of a charged particle beam, necessary to create ionization charges, induces an electromagnetic field that modifies the trajectories of the electrons and the ionized gas molecules and thus introduces a shift between the point where they should have ideally met the electrode and the point where they reach it. The measured beam profile, therefore, will differ from the real one by an amount that depends on the beam intensity, the beam size, the beam energy, and the strength of the electric field applied between the electrodes.

Therefore, a simulation code was developed at CEA Saclay [6]. The momenta distributions for electrons are calculated using Garfield++ [7] while for ions the assumption $\overrightarrow{p_{ion}} = -\overrightarrow{p_e}$ was applied.

Calculations presented in Fig. 4 are performed for both ionization by-products, electrons and ions, versus the injected beam size into an IPM with a 300 kV/m electric field.

We observe that at ESS, the precision is consistently exceeds the required level for electrons. For ions, even at 90 MeV and a beam size larger than 2 mm, $|\Delta_X|$ is below

Content from this work may be used under the terms of the CC-BY-4.0 licence (© 2023). Any distribution of this work must maintain attribution to the author(s), title of the work, publisher, and DOI

ISBN: 978-3-95450-236-3 ISSN: 2673-5350 doi:10.18429/JACoW-IBIC2023-WEP001

5%. The influence of the beam pulse diminish at higher energies due to pulse particle velocities, which reduce their impact on the scattered particles. As a result, IPMs must meet the requirements for beam width measurement, which can be achieved by establishing a high electric field inside their cages, around 300 kV/m.

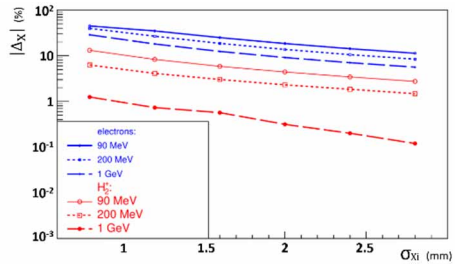


Figure 4: Space charge effect on the measured profiles for electrons and H_2^+ ions versus injected beam size. The IPM electric field is 300 kV/m.

ISO-5 Cleanliness

Due to their proximity to the superconductive cavities, IPMs must be delivered at ESS with a high cleanliness level, namely ISO-5, to prevent dust contamination and limit field emission. This implies that their designs must integrate compliant materials and that the test bench must be installed inside a laminar air flux.

The deployed logistics are pretty heavy, as listed below:

- Washing and rinsing all components in an ultrasonic bath,
- Transporting them in a basin filled with dezionized water to an ISO-7 clean room to prevent dust deposition,
- Moving them into an ISO-5 room for drying. Once completed, the integration of an IPM pair can start. An ionization gun with pure nitrogen gas is used for detaching particles, and a particle counter is used to check the ISO-5 level. All elements were mounted except the MCP and their copper wire connections.
- Finally, both IPMs are inserted into their vacuum chambers and wrapped inside a double ISO-5 plastic bag.
- The 5 IPM pairs follow these procedures and are stored in a laboratory.
- Then, we started integrating one pair, followed by another, into the test bench inside a laminar air flux. Baking is necessary as soon as the MCP comes in contact with air. Several mounting, dismounting are necessary due to the narrow space devoted to IPMs, which are finally characterized.
- The IPM survey and insertion inside its vacuum chamber are performed in a laboratory to pump and ensure that the IPM can travel in a static vacuum.

Feasibility Conclusion

The identified challenges have been largely addressed, with only a few minor difficulties encountered. Following a thorough review, the design of prototypes started. In the subsequent sections, we present some results from the prototype testing using a 3 MeV proton beam at the IPHI accelerator located at CEA Saclay [8].

PROTOTYPE TESTS AT IPHI

Three types of IPM were designed: A) equipped with an MCP featuring a phosphorescent screen and an optical read-out (lens + CMOS); B) incorporating conductive strips engraved on an electrode with the read-out of the strip current; C) similar to B) but with the addition of a simple MCP set before the strip plate for amplifying the strip current.

The optimal MCP can be polarized in asymmetric mode, one grounded electrode and the other at the HV, or in symmetric mode, meaning electrode polarization at ±HV.

We also have solid scintillators for comparison. All these instruments were inserted into a large vacuum chamber, moved in 2018 to IPHI, delivering a proton beam at 3 MeV working between 0.7 mA to 40 mA in pulse mode (0.1 to 1 ms) at 1 Hz during our tests.

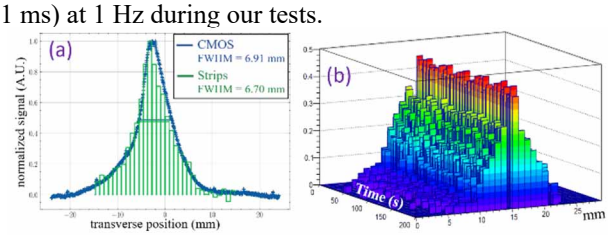


Figure 5: Strip and CMOS profile comparison (a). Profile measured for every pulse with MCP amplifying current (b).

First conclusion: A more sensitive integration-electronic for sampling the strip current is needed. However, it works very well when the physical signal is amplified by a simple MCP, which is quite similar to the optical read-out profile, as shown in Fig. 5a.

Second conclusion: We have opted for the optical read-out system due to the potential issues arising from the connections inside the beam pipe associated with the strip option, which may be challenging to resolve. Additionally, the strip option necessitates the use of an MCP, introducing a second fragile element in the system.

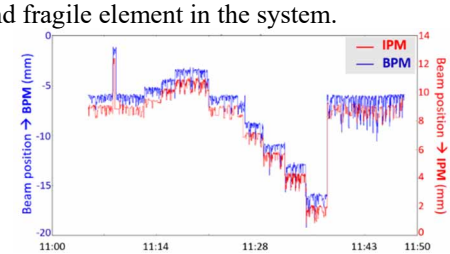


Figure 6: Correlations between IPM and BPM.

Figure 5b shows the ability to measure the beam profile for every pulse using the IPM equipped with an MCP amplifier of the strip currents, similar to the optical IPM.

During the experiment, we noticed a “slow” shift of the beam profile, which came back swiftly to the same position after a while. Initially, some electronic charge loading and discharging were suspected. However, a strong correlation between IPM and beam position monitor (BPM) favoured an objective observation of beam position shift, as shown

Content from this work may be used under the terms of the CC-BY-4.0 licence (© 2023). Any distribution of this work must maintain attribution to the author(s), title of the work, publisher, and DOI

ISBN: 978-3-95450-236-3 ISSN: 2673-5350 doi:10.18429/JACoW-IBIC2023-WEP001

in Fig. 6, with a small disagreement due to monitor calibrations.

A few other interesting results were obtained, such as:

- Beam width convergence, refers to the electric field threshold above which the beam width stays constant. The optical IPM achieved this at around 100 kV/m for a 10 mA beam intensity and 125 kV/m at 30 mA.
- The beam size variation was studied with an IPM when the perpendicular electric field of a second IPM was varied from 0 to 200 kV/m. The beam size increases by less than 75 µm. The same study, but for the beam position, shows a displacement of around 0.4 mm. For both studies, there was no correction of the beam deviation induced by the upstream IPM in the downstream one.
- The uniformity of the electric field was assessed in the center of the IPM by sweeping the beam inside the cage. Results are consistent with expectations. To illustrate, a thin conductive 100 µm weft mesh was placed above the slit to enhance the electric field. In Fig. 7, a CMOS image captures the fine grid weft, confirming the uniformity of the electric field.

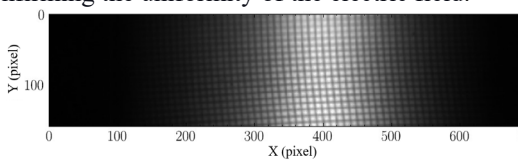


Figure 7: Beam signal observed through the mesh.

The main conclusion of this test is the extrapolation of IPHI data to ESS experimental conditions. For doing this, we requested a stable low beam intensity of 0.7 mA by 50 µs pulses (1 Hz) with 4 10^{-8} mbar residual gas pressure. Taking all these conditions, the cross-section ratios and the gas composition, results in a signal higher at 97 MeV and at 1.6 GeV, but 0.9 times lower at 2 GeV compared to ESS. Thus, we decided to modify the optical IPM mainly by:

- Taking a double MCP with a P43 phosphorescent screen for increasing the gain and their lifetimes
- Polarizing the IPM in symmetrical mode, -15 kV and +15 kV which improves the electric field uniformity
- Modifying the mechanics to give easier access to the MCP (weakest element) and having the same pieces for X and Y thanks to a rotating trick.

The final IPM versions take into account these remarks.

IPM INTEGRATION AND TEST

The first phase of ISO-5 integration is time consuming, mainly due to achieving ISO-5 standards with Macor materials. During the second phase of integration finalization and HV tests, several issues arose, with the most notable ones including:

- Correctly crawling the connection cables into the narrow chamber to set them at reasonable distances from grounded items. Several short circuits were induced, implying the need to break the vacuum, fix wire position, and bake necessitating at least one week.
- For minimizing matter, MCPs are screwed on 3 pillars, which must be tightened by fingers, but this was not mentioned by the provider. Therefore, a few of them were broken, particularly after baking. Finally, the solution was found by releasing slacks at screw level (Fig. 8). A small spring was added on each screw (Fig. 8(b)) to give longitudinal slack, while screws were filed on the top thread part for releasing transversal slack (Fig. 8(c)).

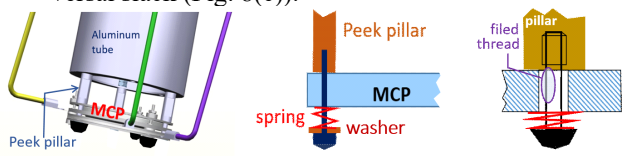


Figure 8: MCP fixed on 3 pillars (a), spring for longitudinal slack (b), filed thread for transverse slack (c).

To check the MCP gain, we used a UV lamp, which is fixed on the opposite side of the IPM vacuum chamber. UV photons have to cross a quartz viewport, and a small slit centred in the +15 kV electrode, the second slit (-15 kV) before reaching the MCP. Such a result is shown in Fig. 9.

Our acceptance criteria was IPM is validated when it is able to sustain ±15 kV with a $\Delta MCP_{In\text{-}Out} \gtrsim 1.3$ kV for more than 24 hours. This means that MCP is polarized at -16 kV for In, -14.7 kV for Out, and -10.7 kV for the Screen.

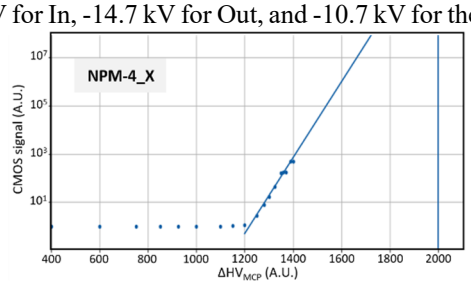


Figure 9: MCP gain measured with a UV lamp.

To complete the IPM processing, it is surveyed with a 3D Faro arm before being inserted into a vacuum chamber. Then, it is pumped once again at around 10^{-7} mbar, ready to be sent to ESS Lund under static vacuum. Finally, the 10 IPMs were delivered in pairs, the latest in August 2023.

CONCLUSION

The processes involved in the design, assembly, testing, and validation of the 10 IPMs for the cold section of the ESS accelerator have been succinctly described.

The challenge of operating the IPMs in a symmetric polarization mode at ±15 kV was encountered. The read-outs of the IPMs are facilitated by a CMOS camera utilizing an MCP equipped with a phosphorescent screen. One of the most demanding requirements was the achievement of ISO-5 cleanliness quality, which necessitated a significant logistical effort complicated by the limited space within the vacuum chamber.

All IPMs have been delivered to ESS Lund and are currently undergoing testing or installation stages.

The authors wanted to thank Stéphane Berry, Pierre Bosland and Catherine Madec, who kindly taught, advised and helped us achieve ISO-5.

Content from this work may be used under the terms of the CC-BY-4.0 licence (© 2023). Any distribution of this work must maintain attribution to the author(s), title of the work, publisher, and DOI

ISBN: 978-3-95450-236-3 ISSN: 2673-5350 doi:10.18429/JACoW-IBIC2023-WEP001

REFERENCES

[1] R. Garoby *et al.,* "The European Spallation Source Design", *Phys. Scr.*, vol. 93, no. 12, p. 014001, 2018. doi:10.1088/1402-4896/aa9bff

[2] F. Bénédetti, "Design of non-invasive profile monitors for the ESS proton beam", Ph.D. thesis, Phys. IRFU/DEDIP, CEA Paris Saclay, France, 2019. [IRFU-19-22-T]

[3] F. Bénédetti *et al.,* "Design and Development of Ionization Profile Monitors for the Cryogenic sections of the ESS Linac", in *Proc. ANIMA 2019*, Portoroz, Slovenia, June 2019. doi:10.1051/epjconf/202022501009

[4] H. Bethe, "Zur Theorie des Durchgangs scheneller Korpuskularstrahlen durch Materie", in Annalen der Physik, vol. 397, no. 3, pp. 325-400, 1930. doi:10.1103/PhysRevLett.114.050511

[5] COMSOL, Inc, COMSOL Multiphysics 5.3a Reference Manuel, 2019. https://www.comsol.com/

[6] F. Belloni *et al.*, "Space Charge Effects Studies for the ESS Cold Linac Beam Profiler", in *Proc. IBIC'18*, Shanghai, China, Sep. 2018, pp. 371-374. doi:10.18429/JACoW-IBIC2018-WEOC04

[7] K. Baraka, S. Biagi, A. Folkestad, J. Renner, H. Schindler, N. Shiell, I. Smirnov, R. Veenhof, and K. Zenker, "Garfield++ simulation of tracking detectors", http://garfieldpp.web.cern.ch/garfieldpp

[8] R. Gobin *et al.,* "High Intensity Beam Production at CEA/Saclay For The IPHI Project", in Proc. ECRIS'16, Busan, Korea, Aug.-Sep. 2016, pp. 83-85. doi:10.18429/JACoW-ECRIS2016-WEPP01

Content from this work may be used under the terms of the CC-BY-4.0 licence (© 2023). Any distribution of this work must maintain attribution to the author(s), title of the work, publisher, and DOI

ISBN: 978-3-95450-236-3 ISSN: 2673-5350 doi:10.18429/JACoW-IBIC2023-WEP002

STUDY OF VISIBLE SYNCHROTRON RADIATION MONITOR ON SOLEIL BOOSTER

A. Moutardier*, G.Cauchon, M. Chevrot, Z. Fan, N. Hubert, S. Kubsky, M. Labat, M. Thomasset
Synchrotron SOLEIL, Gif-Sur-Yvette, France

Abstract

In the scope of SOLEIL II, the booster must also be upgraded to reduce from 130 to 5 nm · rad the emittance of the beam delivered to the ring. Control of the emittance in the booster will become crucial to ensure the nominal performance of the storage ring injection. The SOLEIL I booster is already equipped with a Visible Synchrotron Radiation Monitor (MRSV). This equipment, made of an extraction mirror and a simple optical system, was originally planned to be used only for beam presence verification but has not been used routinely for operation since the commissioning in 2005. The control and acquisition systems had to be refreshed to be usable again and allow the beam size measurement along the booster energy ramp. The extraction mirror was replaced due to unexpected degradation leading to a second spot appearing on the camera. This paper traces back the MRSV upgrades from understanding the cause of mirror degradation until mirror replacement and the first proper beam visualisation, achieved at the beginning of 2023.

INTRODUCTION

Fourth-generation synchrotron light sources are presently emerging all around the world. Those machines target ultra-low emittances, below hundred of pm.rad, enabling the delivery of photon beams with unprecedented brilliance.

In this context, the French synchrotron light source SOLEIL is planning an upgrade for the late 2020s, referred to as SOLEIL-II. The targeted emittance in the storage ring is 88 pm · rad in the horizontal plane and 35 pm · rad in the vertical plane. To reach such a low emittance, all SOLEIL's accelerators will have to be upgraded, i.e. the storage ring but also the linac and the booster. The requirements on the booster beam quality will be significantly increased, and an emittance measurement along the energy ramp in the booster will be mandatory.

This emittance measurement could be done using a Visible Synchrotron Radiation Monitor (MRSV). In order to confirm this strategy, preliminary tests are ongoing on the present SOLEIL booster, using the MRSV system installed, but barely used, since 2006.

This paper traces back the issues encountered with this diagnostic and presents the solutions considered to achieve an emittance measurement along SOLEIL's booster ramp.

* alexandre.moutardier@synchrotron-soleil.fr

MRSV DESIGN

An MRSV is an electron beam diagnostic which enables to image the synchrotron radiation emitted inside a dipole at its source point. It usually simply consists of an extraction mirror, to collect and deflect the synchrotron radiation out of the accelerator vacuum chamber, an imaging system and a camera. SOLEIL's booster MRSV setup is shown in Fig. 1. The extraction mirror is a simple Pyrex glass, silver-coated, flat mirror, mounted at 45° to deflect the synchrotron radiation in the vertical plane. The imaging system consists of three lenses allowing it to reach a magnification of 0.24. The camera is a CCD camera (Model acA1920-50gm from Basler [1]). A UHV viewport of fused silica between the extraction mirror and the first lens ensures the transition from vacuum to air.

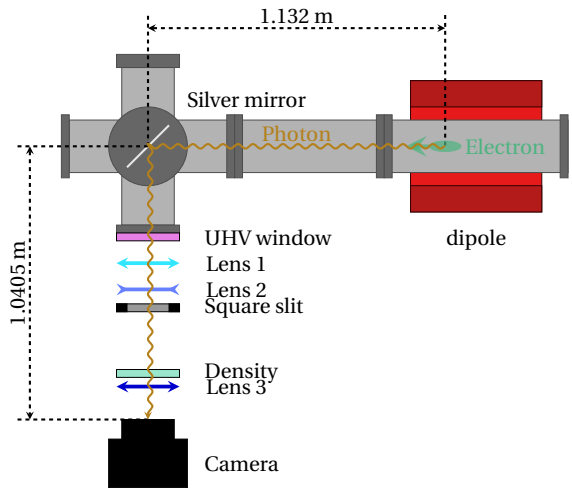


Figure 1: Experimental setup of the MRSV implemented on the booster of SOLEIL.

On many synchrotrons, MRSVs are simply used to check beam presence and its rough stability. But MRSVs can also be used to measure the electron beam size inside the source dipole [2]. In this case, the Point-Spread-Function (PSF) must be accurately considered because dipoles create a longitudinally extended source point. The PSF corresponds to the light distribution of one electron (or zero emittance and energy spread beam) in the image plane which can not be resumed to an infinitesimal point. The light distribution of the real beam (finite emittance and energy spread) results from the convolution of this PSF with the electron beam distribution at the source point magnified by the imaging system. Both the PSF and the light distribution from the whole beam in the image plane can be accurately simulated using SRW [3] as shown in Fig. 2.

Content from this work may be used under the terms of the CC-BY-4.0 licence (© 2023). Any distribution of this work must maintain attribution to the author(s), title of the work, publisher, and DOI

ISBN: 978-3-95450-236-3 ISSN: 2673-5350 doi:10.18429/JACoW-IBIC2023-WEP002

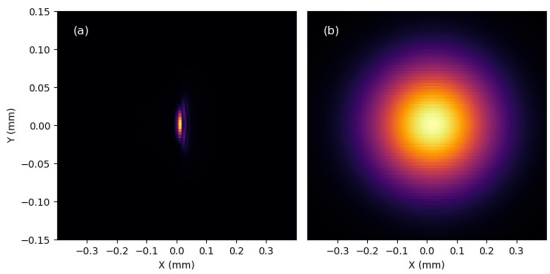


Figure 2: Simulation of the synchrotron radiation in the image plane of the booster's MRSV. (a) Single electron case, i.e. PSF, (b) Finite emittance case. Simulation with SRW at the end of the booster ramp using a beam of 2.75 GeV, 8 nC, 130 nm · rad horizontal emittance and 4.5 nm · rad vertical emittance.

Once deconvoluted from the simulated PSF, the image measured on the MRSV camera can provide the electron beam size in the image plane, allowing retrieval of the electron beam size at the source point, and finally, assuming that optics functions are known, the electron beam emittance.

MRSV ISSUE

Double Beam Observation

A few months after the commissioning of SOLEIL in 2006, the booster's MRSV monitor started to exhibit two spots, as shown in Fig. 3 (b), instead of the single one as expected from Fig. 2. However, since this MRSV was only used for beam presence verification and no major failure at ring injection was noticed, this anomaly was not thoroughly addressed, and the double spot remained for more than a decade.

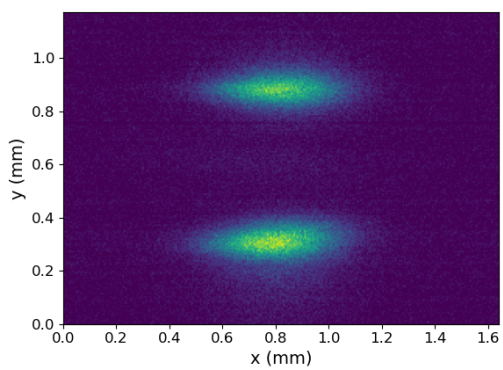


Figure 3: Image of SOLEIL's booster MRSV recorded at the end of 2022, i.e. while the double spot issue was still unsolved.

But in the scope of SOLEIL-II, since a similar system could become a key diagnostic for the booster and downstream storage ring operation, it was decided a year ago to tackle this issue.

A first series of machine studies enabled to exclude the possibility of beam instability, two orbits, or even orbit shifting, confirming that the diagnostic itself was malfunctioning. Then, the position of each component of the MRSV was carefully checked and compared with the theoretical design.

Extraction Mirror Degradation

Eventually, the guilty was found to be the extraction mirror. The inspection of this mirror through the UHV window without breaking the booster vacuum is not easy. However, it seemed that a black strip was covering part of the mirror. Following this observation, new SRW simulations were attempted, including the presence of an obstacle equivalent to the black strip that had been observed. But such an obstacle on the mirror only led to some diffraction features in the image plane, not to two spots. We therefore simply decided to replace the mirror with a new one, though exactly of the same type and geometry.

In January 2023, the extraction mirror has been dismounted. As suspected, the mirror was strongly damaged, as shown in Fig. 4, with the presence of a thick dark strip all across the mirror (at the location of the synchrotron radiation fan) and a clear iridescence besides the dark strip. The dark strip is attributed to carbon deposition. This hypothesis has been confirmed by placing the mirror for ten minutes in an O_2 plasma chamber [4] to remove all visible black traces. Iridescence is a well-known phenomenon which could be easily attributed to a strong heat-up.

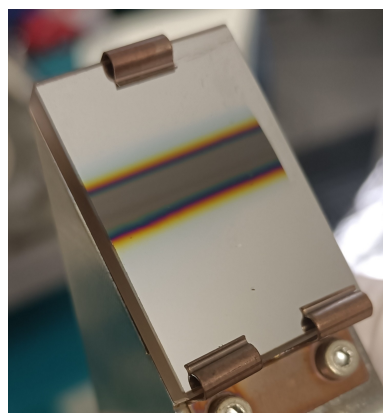


Figure 4: Picture of the booster's MRSV extraction mirror, after nearly 18 years of operation.

Once cleaned, the mirror surface was scanned using a white light interferometer (WLI [5]) at SOLEIL's surface Laboratory. This technique enabled to map the 3D surface of the mirror. As shown in Fig. 5, it clearly appeared that the mirror presented a groove, exhibiting a 5 µm deep valley all along the synchrotron radiation fan location. In addition, the upper and lower parts of the mirror, with respect to the horizontal/synchrotron radiation fan axis, were found to be tilted by an angle of roughly 1 mrad. Lastly, some drops could also be noticed, attributed to a local melting of the silver coating. The main result of this measurement is the observation of an angle between the mirror's lower and upper

Content from this work may be used under the terms of the CC-BY-4.0 licence (© 2023). Any distribution of this work must maintain attribution to the author(s), title of the work, publisher, and DOI

ISBN: 978-3-95450-236-3 ISSN: 2673-5350 doi:10.18429/JACoW-IBIC2023-WEP002

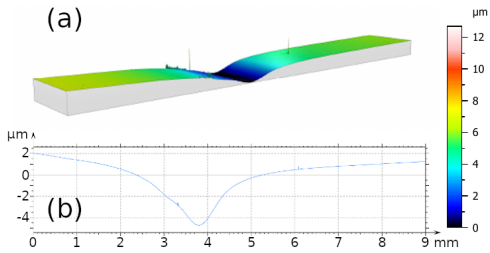


Figure 5: Results of the laser interferometry performed on the extraction mirror of the booster's MRSV after 18 years of operation. (a) 3D map of the mirror surface. (b) Mirror surface height along the vertical axis, i.e. line profile along the top image.

parts. Indeed, such an angle can induce a different pointing for the upper and lower parts of the synchrotron radiation fan (the middle part not being reflected due to the dark strip) towards the image plane, which could easily explain the double spot previously observed.

MRSV Issue Solving

Those observations indicate clearly that the synchrotron radiation has strongly damaged the extraction mirror. Due to a lack of time for a new design, a similar extraction mirror has been immediately mounted to replace the damaged one. During the following beam time at low injection rate, a nice single spot very close to the prediction was observable (Fig. 6 (a)). A survey of the MRSV image reveals that only a few weeks of operation lead to visible deformation of the MRSV spot (Fig. 6 (b)), hence a very quick degradation of the new mirror.

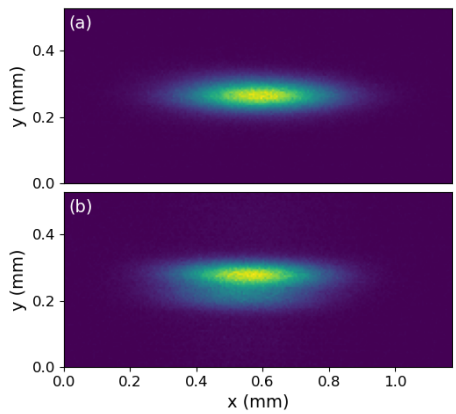


Figure 6: Image of SOLEIL's booster MRSV recorded (a) just after, (b) two weeks after, the replacement of the old extraction mirror (March 2023).

NEXT STEPS

Dark strip, iridescence and melted silver drops on the mirror were intuitively linked to an over-heat of the extraction mirror. But in the scope of SOLEIL-II, a reliable correlation between those observations and numerical thermal simulations must be established.

First, an estimation of the average power deposited on the mirror has been made relying on SRW simulations and assuming the booster to be running at 3 Hz in the higher charge mode (8 nC). The 2D average power density distribution was computed in the plane of the extraction mirror. The total average power was estimated to be ≈ 6 W, and the average power density to be ≈ 0.26 W/mm^2. The thermo-mechanical behaviour of the extraction mirror has been simulated using the synchrotron radiation 2D power density map and a 3D modelling of both the extraction mirror and its environment in the Ansys software [6]. According to this work, the mirror surface temperature at equilibrium could reach 500°C, as shown in Fig. 7 (a). Without silver coating, this temperature could even heat up to 1000°C. Hence any defect in the mirror coating could easily lead to a local melting of the silver (silver fusion point: 961.8°C).

The reason for such high temperatures is the poor thermal conductivity of Pyrex glass ($\approx 1.2\,\mathrm{W\,m^{-1}\,K^{-1}}$). The heat load from the synchrotron radiation is locally stored by the mirror instead of dissipating within the whole mirror substrate and then through the mirror holder, finally leading to serious damage. To increase the lifetime of our extraction mirror, a first simple solution will be to change the mirror substrate material from Pyrex glass to Copper, offering a much higher thermal conductivity ($\approx 400\,\mathrm{W\,m^{-1}\,K^{-1}}$). The performances in terms of final temperature expected using such a mirror are presented in Fig. 7 (b). Thanks to a more efficient heat diffusion inside the mirror and towards its support, the final equilibrium temperature could drop down to 200°C.

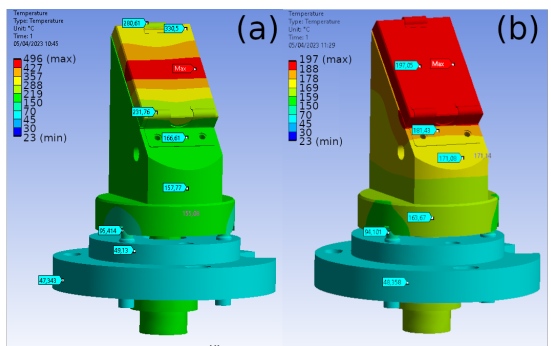


Figure 7: Surface temperature of the extraction mirror and its support simulated with Ansys using a mirror made of (a) Pyrex, i.e. actual mirror, (b) Copper, both silver coated.

Following these encouraging results, a new mirror (Copper substrate with UV-enhanced Aluminium coating) has been ordered. It has been mounted during last summer breakdown and commissioned on the 1st of September 2023. As expected, resulting image is a beam spot with similar intensity as Fig. 6 (a) in the same conditions. A regular survey is scheduled to check the presence of spot deformation (characteristic of mirror degradation) but with lower operating temperature, no degradation of the surface is expected in the

Content from this work may be used under the terms of the CC-BY-4.0 licence (© 2023). Any distribution of this work must maintain attribution to the author(s), title of the work, publisher, and DOI

ISBN: 978-3-95450-236-3 ISSN: 2673-5350 doi:10.18429/JACoW-IBIC2023-WEP002

future. Beam size measurement is now possible along the RF booster ramp and will hopefully be available for daily operation in the coming months.

CONCLUSION

We presented our first steps towards a future reliable beam size/emittance measurement along SOLEIL's booster energy ramp. After nearly twenty years of operation, we understood that the extraction mirror of our MRSV diagnostic was suffering a high heat load, not compatible with beam size measurement. We now expect to be able to achieve a reliable emittance measurement by the end of the year. All this work will be especially useful in the frame of the SOLEIL-II booster and associated diagnostics design.

ACKNOWLEDGEMENTS

Also thanks to S. Morand, M.-A. Tordeux (SOLEIL).

REFERENCES

[1] acA1920-50gm Basler ace GigE camera, https://docs.baslerweb.com/aca1920-50gm

[2] Å. Andersson *et al.*, "Determination of a small vertical electron beam profile and emittance at the Swiss Light Source", *Nucl. Instrum. Methods Phys. Res., Sect. A*, vol. 591, 2008, pp. 437–446. doi:10.1016/j.nima.2008.02.095

[3] O. Chubar and P. Elleaume, "Accurate and Efficient Computation of Synchrotron Radiation in the Near Field Region", in *Proc. EPAC'98*, Stockholm, Sweden, Jun. 1998, paper THP01G, pp. 1177–1179.

[4] *DIENER Pico*, Diener Plasma GmbH & Co. KG, Ebhausen, Germany, https://pdf.directindustry.com/pdf/diener-electronic-gmbh-co-kg/pico/50802-157239.html

[5] *firebolt*, (GBS) mbH, Ilmenau, Germany, https://www.gbs-ilmenau.de/index.php/en/pages-2/370-123-35

[6] *Academic Research Mechanical*, Ansys, https://www.ansys.com/products/structures/ansys-mechanical

Content from this work may be used under the terms of the CC-BY-4.0 licence (© 2023). Any distribution of this work must maintain attribution to the author(s), title of the work, publisher, and DOI

ISBN: 978-3-95450-236-3 ISSN: 2673-5350 doi:10.18429/JACoW-IBIC2023-WEP005

EFFECT OF INCOHERENT DEPTH OF FIELD FOR BEAM HALO MEASUREMENT WITH THE CORONAGRAPH IN SuperKEKB

T. Mitsuhashi†, H. Ikeda and G. Mitsuka, KEK

Abstract

In the case of beam profile measurement by imaging system, observed apparent beam profile will change by the incoherent depth of field. This apparent change of beam profile, especially extra beam tail in one side has certain influence for beam halo measurement using the coronagraph, because it has a large dynamic range of 6-digit contrast. Since the magnitude of asymmetric tail is depending on bending radius, this effect is larger in large high energy physics machine which has a long bending radius. This effect is studied with geometrical optics and coronagraph measurement of beam halo in the SuperKEKB. As a conclusion, the IDF effect has significant effect in the beam halo observation with coronagraph at SuperKEKB.

INTRODUCTION

For the measurement of beam image, the incoherent depth of field (IDF) due to horizontal instantaneous opening of the Synchrotron Radiation will apparently modify the horizontal profile of beam image in asymmetric manner. We have presented this IDF effect for horizontal beam size measurement with interferometry in IBIC2017 [1]. In the interferometry, The IDF effect deduces spatial coherence in horizontal direction, and correction is necessary for the horizontal beam size measurement with interferometry [1]. The IDF effect has not only reducing the spatial coherence, but also modify the apparent horizontal beam profile with asymmetric manner. As a result, observed beam image with focusing system will be deformed. Especially, tis asymmetric deformation of beam profile can introduce extra asymmetric distribution in beam tail (or halo) which is existing surrounding of beam core. We studied this effect using the geometrical optics in the case of beam halo measurement with coronagraph in the SuperKEKB. And compare the measurement result s of beam halo with the coronagraph [2].

EFFECT OF INCOHERENT DEPTH OF FILED FOR APPARENT DEFORMATION OF BEAM PROFILE

In the horizontal plane, the profile of beam is modified apparently by IDF with the instantaneous opening of the SR in the horizontal plane as shown in Fig. 1.

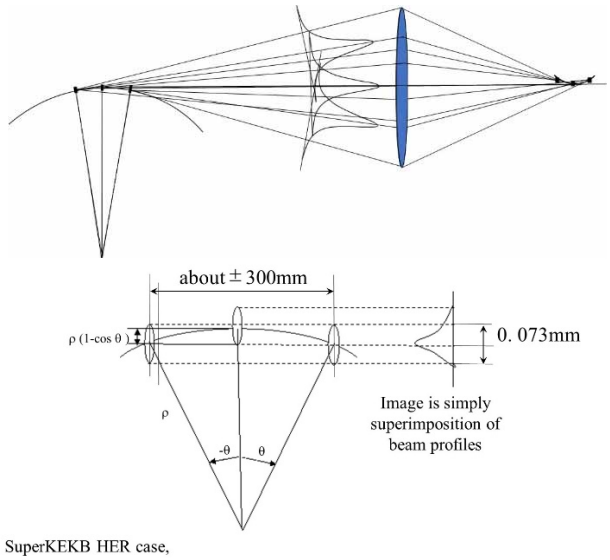


Figure 1: Apparent beam profile with the IDOF effect by the instantaneous opening of the SR in the horizontal plane in the SuperKEKB HER case.

In the geometrical Optics, the intensity distribution in the entrance aperture has no effect for imaging as shown in Fig. 2. Also, due to small emittance of the source beam, opening angle and source size is very smaller than opening of SR in the visible light region, this effect will be negligible small for IODF.

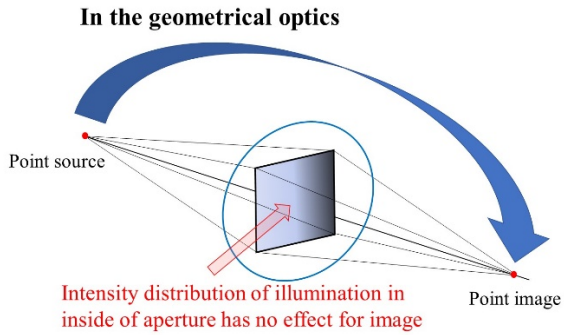


Figure 2: Point to point transfer of source point into imaging point in the geometrical optics.

Denote the total intensity of SR inside of the entrance aperture in horizontal plane by I(θ) as a function of horizontal observation angle θ, the apparent beam shape $\sigma_a(x)$ is given by,

$$\sigma_a(x) = \int \mathrm{I}(\theta) \cdot \frac{exp\left[\frac{-[\mathrm{x} - \rho\{1 - cos(\theta)\}]^2}{2\sigma^2}\right]}{\sigma \cdot \sqrt{2\pi}} \mathrm{d}\theta \quad , \qquad (1)$$

where the original beam profile is assumed to be a Gaussian distribution.

For the discussion of horizontal IODF, we need knowledge of instantaneous intensity distribution of SR in horizontal plane to evaluate I(θ).

†email address: toshiyuki.mitsuhashi@kek.jp

Content from this work may be used under the terms of the CC-BY-4.0 licence (© 2023). Any distribution of this work must maintain attribution to the author(s), title of the work, publisher, and DOI

ISBN: 978-3-95450-236-3 ISSN: 2673-5350 doi:10.18429/JACoW-IBIC2023-WEP005

Content from this work may be used under the terms of the CC-BY-4.0 licence (© 2023). Any distribution of this work must maintain attribution to the author(s), title of the work, publisher, and DOI

The SR from circular trajectory is written by Schwinger in 1945 [3, 4]. He only gave his theory for the case of horizontal observation angle ξ=0.

For the case in the horizontal observation angle $\xi \neq 0$, is discussed by one of author [1]. The intensity radiated per unit frequency interval per unit solid angle is given by

$$\frac{d^2I}{d\omega d\Omega} = \frac{e^2}{3\pi^2 c}\left(\frac{\omega\rho}{c}\right)^2\left(\frac{1}{\gamma^2}+\psi^2+\xi^2\right)^2\left[K_{2/3}^2(\zeta) + \frac{\psi^2}{\frac{1}{\gamma^2}+\psi^2+\xi^2}K_{1/3}^2(\zeta)\right], \quad (2)$$

where,

$$\zeta = \frac{\omega\rho}{3c}\left(\frac{1}{\gamma^2}+\psi^2+\xi^2\right)^{\frac{3}{2}} \quad (3)$$

The result given by Eq. (2) indicates both of vertical intensity distribution and horizontal instantaneous intensity distribution have same angular dependence. This result is same as in the result from qualitative discussion in K.J. Kim [5]. The total intensity of SR in entrance aperture is given by integrating instantaneous intensity distribution in inside of the aperture. The horizontal total intensity inside the aperture is given by integrating the Eq. (2) in horizontal direction inside the entrance aperture,

$$I(\theta) = \int \frac{e^2}{3\pi^2 c}\left(\frac{\omega\rho}{c}\right)^2\left(\frac{1}{\gamma^2}+(\psi+\theta)^2\right)^2\left[K_{\frac{2}{3}}^2(\zeta) + \frac{\psi^2}{\frac{1}{\gamma^2}+\psi^2}K_{1/3}^2(\zeta)\right]d\psi \quad , \quad (4)$$

where,

$$\zeta = \frac{\rho}{3c}\left(\frac{1}{\gamma^2}+\psi^2\right)$$

SIMULATION OF HORIZONTAL BEAM PROFILE WITH IOD EFFECT

A simulation of horizontal beam profile using the Eq. (1) is performed for Super KEKB HER and LER.
The parameter of source bend and horizontal beam size of the HER and LER are summarized in Table 1.

Table 1: Parameter of Bending Source

	HER	LER
Beanding radius	580.0 m	177.4 m
Beam Energy	7 GeV	4 GeV
Horizontal beam size	226 μm	177 μm

The result of beam profile with and without IDF effect in linear scale and log scale for HER an LER is shown in Figs. 3 and 4 respectively.

As shown in Fig. 3 (a), a slight asymmetry is seen in horizontal beam profile due to a long bending radius in HER. R=580 m in HER. This asymmetry in profile is clearer in log plot as shown in Fig. 3 (b).

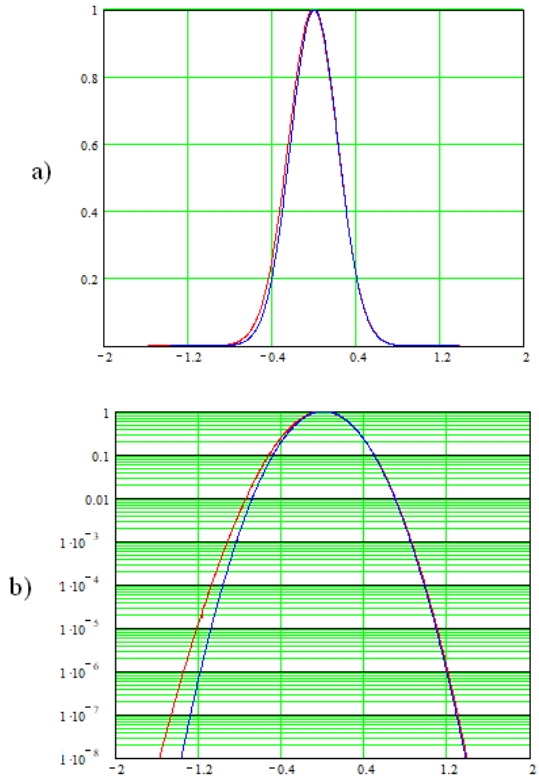


Figure 3: Simulation result of horizontal beam profile image for HER. (a)leaner scale, (b) log scale. Red line: beam profile image with IDF, blue line without IDF.

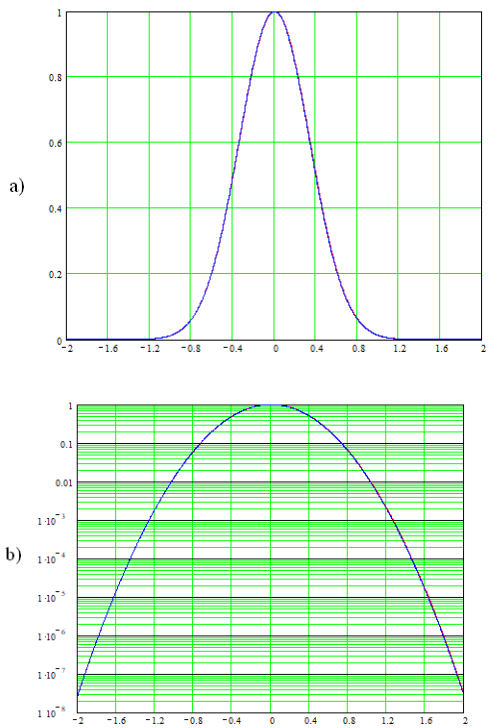


Figure 4: Simulation result of beam profile image for LER. (a): leaner scale, (b): log scale. Red line: beam profile image with IDF, blue line without IDF, but both curvatures are almost same and overlapped in each other.

ISBN: 978-3-95450-236-3 ISSN: 2673-5350 doi:10.18429/JACoW-IBIC2023-WEP005

On the other hand, due to rather short bending radius (177.4 m in LER), the same result for LER has almost no asymmetry in beam profile as shown in Fig. 4. From Fig 4, the effect of IDF in LER is very small and beam profiles with IDF and without IDF is almost same.

As a result, beam profile change in the outside aria from 5 σ of the beam size will be very small, and no significant effect of IDF for beam halo observation in 6-digit in the SuperKEKB with the coronagraph. We expect some beam halo will exist in this aria.

OBSERVATION OF BEAM CORE AND HALO WITH CORONAGRAPH

The effect of IODF for beam core image and beam halo image are observed experimentally using the coronagraph [4] for both of HEL and LER in the SuperKEKB. The result of observed beam profile on the direct focal plane of objective system of coronagraph at HER is shown in Fig. 5. A plot of horizontal profile of distribution is also shown in Fig. 5. From this figure, a slight asymmetry in horizontal distribution of beam core image is observed. On other hand, profile of beam tail is very symmetry in this observation result. Since this extent of asymmetry in the image is sometimes appear due to residual aberration of objective system, but the wavefront error in coronagraph system including the extraction polycrystal-diamond mirror is smaller than λ/5 [6], so beam image in Fig. 5 is diffraction limited one. The extent of horizontal profile of beam image in HER with this observation result is good agreement with the simulation result in Fig. 3 (a). The outside aria from 5 σ of the beam size seems having no significant IODF effect.

The beam halo is observed with the coronagraph in 6-digit contrast. The result of halo observation in HER is shown in Fig. 6 [2]. An intensity distribution along the horizontal plane is also shown in this figure. The beam core image and opaque square image for blocking the glare of beam core are superimposed in this figure for reference.

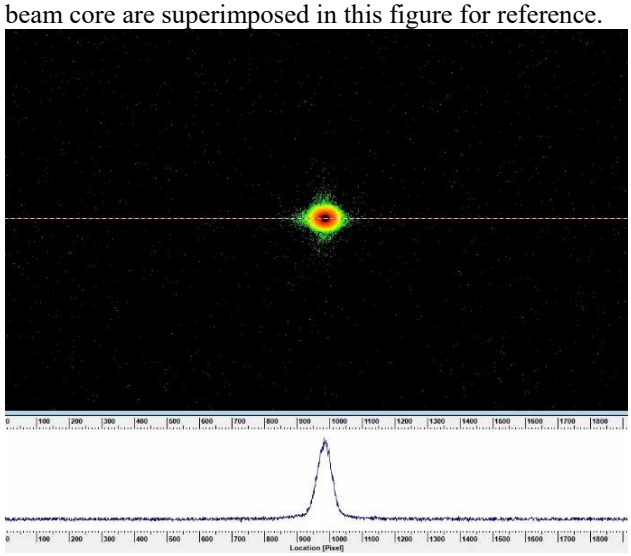


Figure 5: Result of observed beam core profile in HER. Upper: beam core image, lower horizontal profile of the image.

The intensity of beam halo (note this intensity is not peak intensity in Fig. 6) is 2 x 10^{-6} to the peak intensity of the beam core. We observed no significant effect of IDF in horizontal halo profile.

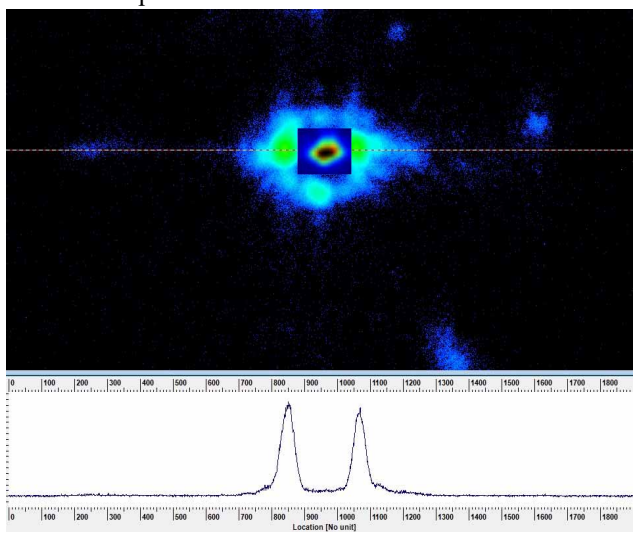


Figure 6: Result of beam halo observation with the coronagraph in 6-digit contrast in HER. Upper: beam halo image, lower: horizontal profile of the halo image.

The result of halo observation in LER is shown in Fig. 7. An intensity distribution along the horizontal plane is also shown in this figure. As same manner, in Fig. 6, the beam core image and opaque square image for blocking the glare of beam core are superimposed in this figure for reference. Different from HER, an interesting beam halo is observed in LER. As same as in HER, we observed no significant effect of IDF in horizontal halo.

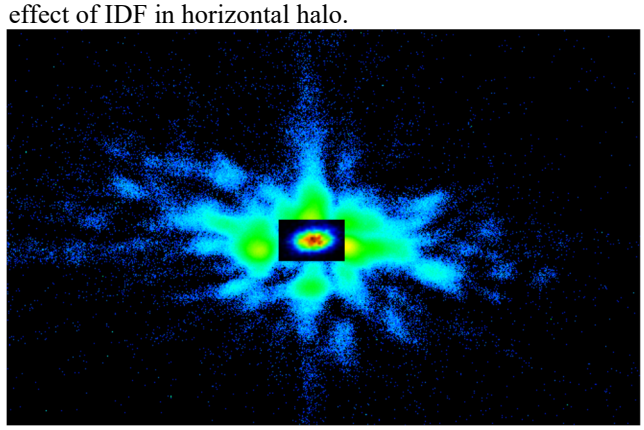


Figure 7: Result of beam halo observation with the coronagraph in 6-digit contrast in LER.

CONCLUSION

The effect of IDF for beam core image and beam halo image by using the coronagraph are studied with geometrical optics and experimentally observation for both of HEL and LER in the SuperKEKB. From the observation result, we detect no significant effect of IDF in horizontal halo profile of both of HER and LER. We can conclude IDF effect is enough smaller in the halo observation with the coronagraph in SuperKEKB.

Content from this work may be used under the terms of the CC-BY-4.0 licence (© 2023). Any distribution of this work must maintain attribution to the author(s), title of the work, publisher, and DOI

ISBN: 978-3-95450-236-3 ISSN: 2673-5350 doi:10.18429/JACoW-IBIC2023-WEP005

REFERENCES

[1] T.M. Mitsuhashi, M. J. Boland, and W. J. Corbett, "Horizontal Opening of the Synchrotron Radiation and Effect of Incoherent Depth of Field for Horizontal Beam Size Measurement", in *Proc. IBIC'17*, Grand Rapids, MI, USA, Aug. 2017, pp. 364-368. doi:10.18429/JACoW-IBIC2017-WEPCC09

[2] G. Mitsuka, H. Ikeda, and T. M. Mitsuhashi, "Design and Construction of Optical System of the Coronagraph for Beam Halo Observation in the SuperKEKB", in *Proc. IPAC'22*, Bangkok, Thailand, Jun. 2022, pp. 769-771. doi:10.18429/JACoW-IPAC2022-TUOXGD1

[3] J. Schwinger "On Radiation by Electron in a Betatron" in *A Quantum Legacy: Seminal paper of J. Schwinger,* B.G. Englert, Ed., Singapore, World Scientific, 2000, pp. 307-331.

[4] J. Schwinger "On the Classical Radiation of Accelerated Electrons", *Phys. Rev*. vol. 75, p.1912, 1949. doi.org/10.1103/PhysRev.75.1912

[5] K.J. Kim, "Characteristics of Synchrotron Radiation", in AIP conference proceedings 184, p. 364, 1989.

[6] G. Mitsuka, H. Ikeda, and T. M. Mitsuhashi, "Renovation of the SR Beam Profile Monitors with Novel Polycrystalline Diamond Mirrors at the SuperKEKB Accelerator", in *Proc. IPAC'22*, Bangkok, Thailand, Jun. 2022, pp. 313-315. doi:10.18429/JACoW-IPAC2022-MOPOPT031

Content from this work may be used under the terms of the CC-BY-4.0 licence (© 2023). Any distribution of this work must maintain attribution to the author(s), title of the work, publisher, and DOI

ISBN: 978-3-95450-236-3 ISSN: 2673-5350 doi:10.18429/JACoW-IBIC2023-WEP006

DEVELOPMENT OF PEPPER-POT EMITTANCE MONITOR FOR HIGH-INTENSITY ION BEAM ACCELERATED BY RIKEN AVF CYCLOTRON

Y. Kotaka*, K. Kamakura, H.Yamaguchi, N. Imai, Y. Sakemi
Center for Nuclear Study, University of Tokyo, Wako, Japan
J. Ohnishi, Riken Nishina Center, Wako, Japan
K. Hatanaka†, Research Center for Nuclear Physics, Osaka University, Ibaraki, Japan

Abstract

At the Center for Nuclear Study of the University of Tokyo, the measurement of Electric Dipole Moment of Francium (Fr) is underway with the world highest precision. Fr is generated by nuclear fusion reaction by irradiating gold with oxygen ion beam accelerated by RIKEN AVF Cyclotron. The required beam intensity is 18 eμA or more. However, the average beam transport efficiency drops to be around 66% as the beam intensity exceeds 10 eμA. To solve the problem, a pepper-pot emittance monitor (PEM) for high-intensity beams has been developed. Referencing the PEM used for the injection beams of AVF Cyclotron, we have developed three additional items. The first is reducing the radiation damage to a camera, which is placed away from the beamline. The distance between the camera and PEM is 2.2 m, and the average image position accuracy of 0.15 mm is achieved. The second is the angular accuracy suitable for the accelerated beam. The required angular accuracy is estimated to be less than 0.3 mrad. A beam test for the first and second items is planned. The third is a beam shutter system to prevent PEM from heating due to beam. The measurement time by the system reaches 0.27 seconds now.

INTRODUCTION

At the Center for Nuclear Study of the University of Tokyo (CNS), the measurement of Electric Dipole Moment (EDM) of Francium (Fr) is underway with the world highest precision [1]. Fr is generated by nuclear fusion reaction by irradiating the gold target of EDM experiment device (EDM target) with $^{18}O^{6+}$ ion beam of 7 MeV/u accelerated by RIKEN AVF Cyclotron. Our goal is transporting $^{18}O^{6+}$ ion beam of more than 18 eμA (400 W), without loss and converging beam to be 1 mm of standard deviation (SD) of the beam distribution on the EDM target shown in Fig. 1.

CNS performs experiments in the three courses of C12 for EDM, CRIB [2], and E7B for students of the University of Tokyo in the E7 experiment room of RIKEN Nishina Center shown in Fig. 1. Figure 2 shows the beam transport efficiencies from AVF Cyclotron to C12, CRIB, and E7B as a function of beam intensities. As beam intensities are larger than 10 eμA, the average beam transport efficiency is 0.66. The stronger beam intensity tends to lower the beam transport efficiency. Figure 3 shows beam emittances measured by 2D emittance monitor (EM_C01) shown in Fig. 1 tend to expand as beam intensities increase. We think beam transport efficiencies decrease as beam emittances expand as a function of beam intensities. However, we cannot measure a high intensity beam emittance because the cooling ability of EM_C01 is suitable for less than 130 W beam power [3].

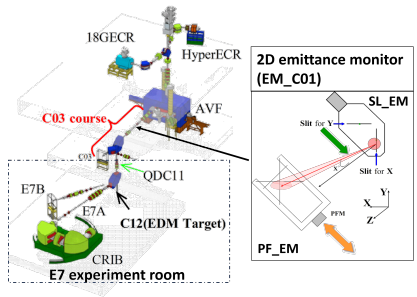


Figure 1: AVF Cyclotron and beamlines to the experiment devices. EM_C01 is shown in the right.

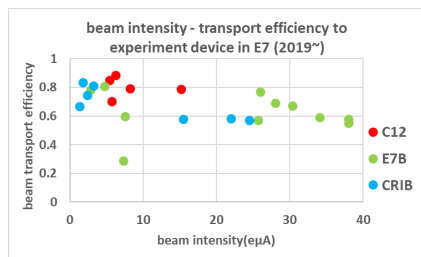


Figure 2: The relationship between beam intensity and transport efficiency to C12(red), E7B(green), and CRIB(blue)

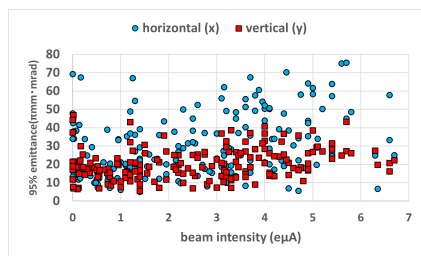


Figure 3: The relationship between beam intensity and 95% horizontal (blue) and vertical (red) beam emittance.

To solve the problem, a pepper-pot emittance monitor (PEM) [4, 5] for high-intensity beams has been developed.

* kotaka@cns.s.u-tokyo.ac.jp
† Deceased.

Content from this work may be used under the terms of the CC-BY-4.0 licence (© 2023). Any distribution of this work must maintain attribution to the author(s), title of the work, publisher, and DOI

ISBN: 978-3-95450-236-3 ISSN: 2673-5350 doi:10.18429/JACoW-IBIC2023-WEP006

Content from this work may be used under the terms of the CC-BY-4.0 licence (© 2023). Any distribution of this work must maintain attribution to the author(s), title of the work, publisher, and DOI

Referencing the PEM for the injection beams of AVF Cyclotron [6], we have developed three additional items which are reducing the radiation damage to a camera, improving angular accuracy suitable for the accelerated beam, and a beam shutter system to avoid heating PEM due to beam.

REDUCING RADIATION DAMAGE

Figure 4 shows our developed PEM. The mask is 1 mm thick copper plate having holes set at the same interval according to a grid system. The beam image passing through each hole and glowing on the fluorescent plate, which is tilted 45 degrees against beam axis, is taken with digital camera through the window. We get the relationship between the beam intensity passing through each hole and the beam position on the fluorescent plate from the image.

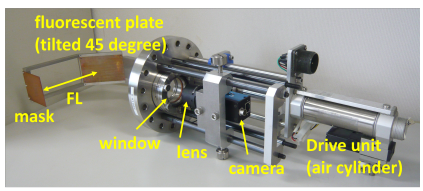


Figure 4: The image of the developed PEM.

The radiation damage of camera due to beam is unavoidable. To reduce the radiation damage, we think setting a camera away from the beam line and surrounding it with shielding material. Moreover, we select an inexpensive camera outputting NTSC signals (720×480 pixels) in view of frequent replacing a damaged camera. This time, we explain the camera optic system. The diameter of the window to see the fluorescent plate is 48 mm to install PEM on the flange of ICF152. The effective area (50×50 mm^2) of the fluorescent plate must be viewed. With only tele lens, we cannot view the entire area of the fluorescent plate as shown on the left view in Fig. 5. By inserting an intermediate lens between the tele lens and the fluorescent plate, we can view the entire area [3]. We use an achromatic lens with a focal length of 200 mm as an intermediate lens to suppress image distortion. Under these conditions, the image of the fluorescent plate is shown on the right view in Fig. 5. The distance between the camera and PEM can be extended to 2.2 m.

We estimate the position accuracy of this image. We marked the lines to make grid points on the fluorescent plate. After the projective transform coefficients between the bitmap coordinates of the grid points and the designed plane coordinates of correspondent grid points are determined, all the bitmap points of the image are transformed to designed plane coordinates. The relationships between the displacement of the transformed grid positions with respect to the correspondent designed positions on plane coordinates and the designed positions on plane coordinates are shown in Fig. 6 . The SDs of the displacements was 0.16 and 0.14 mm in the horizontal (left view) and vertical (right view) direction, respectively.

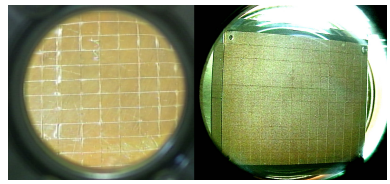


Figure 5: The images taken by camera with tele lens from 2.2 m away. The left view is without intermediate lens and the right view is with intermediate lens.

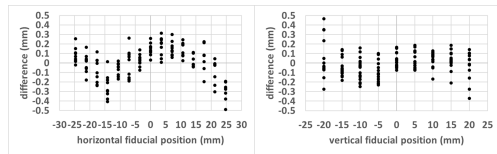


Figure 6: The relationship between the displacement of transformed positions with respect to designed positions.

ESTIMATING REQUIRED ACCURACY

The required measurement accuracies for PEM will be estimaed to calculate beam trajectories by applying the measured beam emittances as initial values because they depend on the beam emittances of AVF Cyclotron.

EM_C01 is located 3550 mm from AVF Cyclotron shown in Fig. 7. The measuring way of EM_C01 is moving the slit with the width of 0.1 mm set at intervals of $1/\sqrt{2}$ mm and measuring the beam position distribution passing through the slit by the beam profile monitor (BPM) set 320 mm behind the slit. The BPM measures the beam position distribution in one dimension by sweeping wire with the diameter of 0.1 mm perpendicular to the beam direction. The slit and BPM of EM_C01 are named SL_EM and PF_EM, respectively. The beam angle is calculated by using the displacement of the beam positions measured by BPM with respect to the position of slit. However, we cannot measure true beam emittances because of unsolved measurement errors. Therefore, we estimate the true emittance in another way.

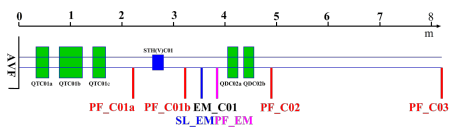


Figure 7: The schematic view of beam transport line to C03.

We can solve the σ matrix with three measurements of BPMs theoretically. We have five BPMs which are PF_C01a, PF_C01b, PF_EM, PF_C02, and PF_C03 shown in Fig. 7. However, we must note the beam distribution of the AVF Cyclotron beam is not a normal distribution and is left-right asymmetric. As the typical SD of the beam distribution of PF_C03 is around 1 mm, the bounds of solutions of the equation can be limited. Therefore, we select the measured beam distributions of PF_C03, PF_C02, and PF_EM irradiated with $^{19}F^{7+}$ beam of energy 6.68 MeV/u and intensity 5 eμA shown in Fig. 8. Horizontal and vertical directions

ISBN: 978-3-95450-236-3 ISSN: 2673-5350 doi:10.18429/JACoW-IBIC2023-WEP006

perpendicular to beam direction are denoted as x and y (mm), respectively. The angles of x and y are denoted as x' and y' (mrad), respectively. The SD of x, x', y, and y' distributions are denoted as SDx, SDx', SDy, and SDy', respectively. The (SDx, SDy) of PF_C03, PF_C02, and PF_EM are (1.6, 1.3), (5.6, 4.8), and (7.1, 2.8), respectively. The equations of σ matrix are shown in Eq. (1) and Eq. (2).

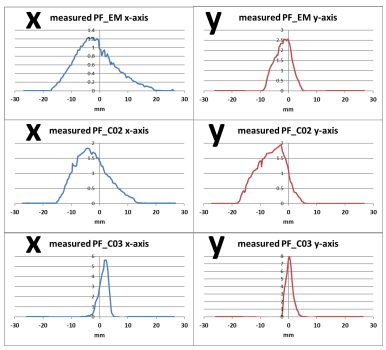


Figure 8: The three measured beam distributions. The top is PF_EM. The middle is PF_C02. The bottom is PF_C03.

$$\begin{pmatrix} \sigma_{11}(C02) \\ \sigma_{21}(C02) \\ \sigma_{22}(C02) \end{pmatrix} = \begin{pmatrix} m_{11} & m_{12} & m_{13} \\ m_{21} & m_{22} & m_{23} \\ m_{31} & m_{32} & m_{33} \end{pmatrix} \begin{pmatrix} \sigma_{11}(EM) \\ \sigma_{21}(EM) \\ \sigma_{22}(EM) \end{pmatrix} \quad (1)$$

$$\begin{pmatrix} \sigma_{11}(C03) \\ \sigma_{21}(C03) \\ \sigma_{22}(C03) \end{pmatrix} = \begin{pmatrix} 1 & 2L & L^2 \\ 0 & 1 & L \\ 0 & 0 & 1 \end{pmatrix} \begin{pmatrix} \sigma_{11}(C02) \\ \sigma_{21}(C02) \\ \sigma_{22}(C02) \end{pmatrix} \quad (2)$$

Where σ_{11}, σ_{22}, and σ_{21} are SDx^2, SDx'^{2}, and the covariance of x and x'. The m_{ij} in the Eq. (1) is matrix element from PF_EM to PF_C02 including doublet quadrupole magnet. Equation (2) is the matrix for drift length of L from PF_C02 to PF_C03. The unknown six values which are σ_{21} and σ_{22} of three BPMs can be solved as the number of equation is six. For the σ matrix of y, Eq. (1) and Eq. (2) can be solved by changing the subscript 2 to 4 and 1 to 3.

As σ_{22} of PF_C02 and PF_C03 obtained by solving Eq. (1) and Eq. (2) were negative, they are not solutions. Presuming the SDx of PF_EM to be 8.0 mm changing from 7.1 mm, the solutions shown in Table 1 are obtained. Equation (3) is the σ matrix at the EM_C01 calculated with Table 1. We consider the effect of replacing 7.1 by 8.0 mm of SDx of PF_EM is small because the beam distribution is left-right asymmetric, and the full width is about 40 mm. Besides, a coupling between x and y is not considered.

Table 1: Solved σ Matrix from Three BPMs Presuming SDx of PF_EM to Be 8.0 mm

	σ_{11}	σ_{21}	σ_{22}	σ_{33}	σ_{43}	σ_{44}
PF_EM	64.0	67.46	71.20	7.84	1.47	0.56
PF_C02	31.36	-8.45	2.48	23.04	-5.87	1.59
PF_C03	2.56	-0.33	2.48	1.69	-0.65	1.59

$$\begin{pmatrix} \sigma_{11} & \sigma_{12} & \sigma_{13} & \sigma_{14} \\ \sigma_{21} & \sigma_{22} & \sigma_{23} & \sigma_{24} \\ \sigma_{31} & \sigma_{32} & \sigma_{33} & \sigma_{34} \\ \sigma_{41} & \sigma_{42} & \sigma_{43} & \sigma_{44} \end{pmatrix} = \begin{pmatrix} 28.1 & 44.6 & 0 & 0 \\ 44.6 & 72.0 & 0 & 0 \\ 0 & 0 & 7.9 & 1.3 \\ 0 & 0 & 1.3 & 0.6 \end{pmatrix} \quad (3)$$

Using Eq. (3) presumed to be true, we estimate the error in the beam distribution at the EDM target due to the EM_C01 measurement error. Our purpose is to make a beam transport system having the beam distribution with SD of 1 mm on the EDM target. Defining the beam direction as z axis (mm), Fig. 9 is the envelope from EM_C01 (z = 0) to EDM target (z = 8120) calculated by TRANSPRT [7] applying Eq. (3) as initial values. The views of lower and upper half are envelopes of x and y, respectively. The red box indicates the quadrupole magnet, and the blue box indicates the bending magnet. Though the last quadrupole magnet is currently doublet, a triplet quadrupole magnet is virtually used to converge beam at the EDM target. The momentum dispersion (dp/p) is 0.006 as an average value. The dp/p is variable by the beam condition of AVF Cyclotron.

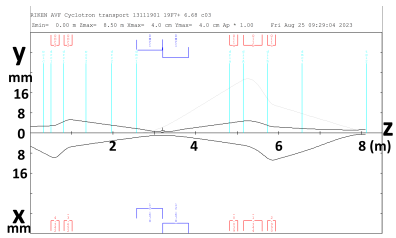


Figure 9: The beam envelopes applying Eq. (3) as initial values by TRANSPORT for σ_{11} and σ_{33} to be around 1 mm at the EDM Target.

Next, we will explain the process flow to see the beam size at EDM target as a function of angular error as following. We generated 500000 particles as random numbers following 4-variables normal distribution having the element of Eq. (3). The 4-variables correspond to (x, x', y, y') of a particle. We select the particles passing slits at z = 0 with a width of 0.1 mm set at intervals of $1/\sqrt{2}$ mm in the (x, y) plane and transport them to z = 320 behind the slits. At z = 320, we generate the random numbers following normal distribution having SD as a position error, and add the random numbers as an error to the (x, y) of the transported particles. The angles of particles are recomputed by using the displacement of the (x, y) of transported particles given error at z = 320 with respect to the (x, y) of the setting position of slits at z = 0. For every particle at z = 0, we replace the original (x, y) by the designed (x, y) of the setting position of the slits and replace the original (x', y') by the recomputed (x', y'). Using the replaced (x, x', y, y') of particles, we calculate σ matrix including angular error. Inputting the σ matrix to TRANSPORT, we calculate SDx and SDy at the EDM target keeping magnet parameters. Figure 10 shows the relationship between the SDx and SDy at the EDM target and the angular error. We found angular accuracy of PEM needs to be less than 0.3 mrad.

Content from this work may be used under the terms of the CC-BY-4.0 licence (© 2023). Any distribution of this work must maintain attribution to the author(s), title of the work, publisher, and DOI

ISBN: 978-3-95450-236-3 ISSN: 2673-5350 doi:10.18429/JACoW-IBIC2023-WEP006

Content from this work may be used under the terms of the CC-BY-4.0 licence (© 2023). Any distribution of this work must maintain attribution to the author(s), title of the work, publisher, and DOI

By the above-mentioned error simulation method, we have possibility to divide error components from the beam emittance presumed to be true. Therefore, we plan to identify the measurement errors of PEM by beam test. As we require low beam emittance, no correlation between x and y, and three BPMs in a beam line, we decided to test in Micro Analysis Laboratory, Tandem accelerator (MALT), The University of Tokyo [8]. The PEM installation with tele lens camera optics was complete. This beamline has two BPMs at 735 mm upstream and 2070 mm downstream from the PEM. Moreover, as the PEM becomes BPM with the average position error of 0.15 mm, we have three BPMs.

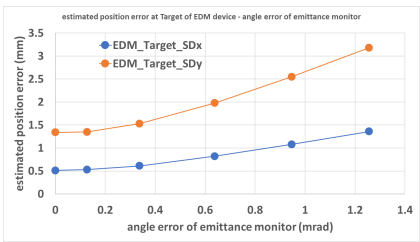


Figure 10: The relationship between angular errors (mrad) of an emittance monitor and the calculated SD of beam position distribution at the EDM Target.

BEAM SHUTTER SYSTEM

The beam shutter system is developed to shorten the measurement time to avoid heating PEM due to beam irradiation of 400 W or more. The beam stops by applying a high voltage to the electrode set in the beam line just behind an ion source and bending the beam sideways. High voltage power supply (Hamamatsu Photonics C9619) with a voltage of -2 kV and a rise time of 0.15 seconds is used. Figure 11 shows the schematic diagram of beam shutter system.

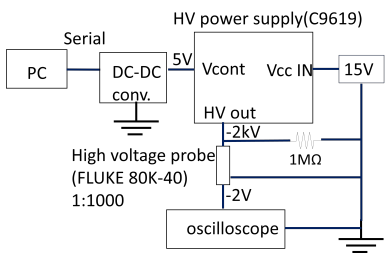


Figure 11: The schematic diagram of beam shutter system.

The measurement flow consists of (1) beam stop (HV ON), (2) PEM insertion, (3) beam irradiation (HV OFF), (4) beam image capture (5) beam stop (HV ON), and (6) PEM evacuation. Time reduction is required between (3) and (5). We measure the time change of this flow by seeing the output of high voltage power supply through an oscilloscope. Though the output high voltage is -2 kV, it is dropped to -2 V by a high voltage probe (FLUKE 80K-40) to input it to oscilloscope. Figure 12 shows the oscilloscope view while measuring and we achieved 0.27 seconds from (3) to (5).

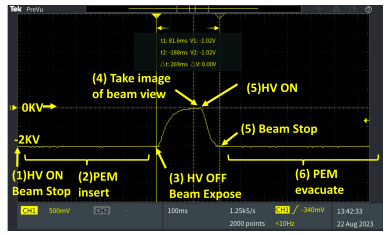


Figure 12: The measured chopping time by oscilloscope.

CONCLUSION

Improving camera optical system to cover the entire area of the fluorescent plate extends the distance between the camera and the PEM up to 2.2 m while the average position error of the fluorescent plate is 0.15 mm. The angular accuracy of the PEM required to calculate the beam trajectory to the EDM target is 0.3 mrad. To investigate the measurement errors, we installed PEM in MALT. We achieved the measuring time of 0.27 seconds by a beam shutter system to avoid heating PEM due to beam irradiation.

ACKNOWLEDGEMENTS

We would like to thank S. Shimoura, M. Kase, and A. Goto for great support.

This work was supported by JSPS KAKENHI Grant Number JP20K12481.

REFERENCES

[1] Y. Sakemi *et al.*, "Fundamental physics with cold radioactive atoms", *AIP Conf. Proc.*, vol. 2319, no. 1, pp. 080020, 2021. doi:10.1063/5.0037134

[2] Y. Yanagisawa *et al.*, "Low-energy radioisotope beam separator CRIB", *Nucl. Instrum. Methods Phys. Res., Sect. A*, vol. 539, no. 1, pp. 74–83, 2005. doi:10.1016/j.nima.2004.09.041

[3] Y. Kotaka *et al.*, "Current status of developing 4D emittance monitor for ion beams accelerated by RIKEN AVF Cyclotron", in *Proc. 18th Annual Meeting of PASJ*, pp. 873-877, 2021.

[4] T. Hoffmann *et al.*, "Emittance measurements of high current heavy ion beams using a single shot pepperpot system", *AIP Conf. Proc.*, vol. 546, pp. 432–439, 2000. doi:10.1063/1.1342615

[5] L. E. Collins and P. T. Stroud, "Extraction of high current ion beams with low divergence", *Nucl. Instrum. Methods*, vol. 26, pp. 157-166, 1964. doi:10.1016/0029-554X(64)90067-9

[6] Y. Kotaka *et al.*, "Development of the Calculation Method of Injection Beam Trajectory of RIKEN AVF Cyclotron with 4D Emittance Measured by the Developed Pepper-Pot Emittance Monitor", in *Proc. IBIC'19*, Malmö, Sweden, Sep. 2019, pp. 351–354. doi:10.18429/JACoW-IBIC2019-TUPP022

[7] D. C. Carey, K. L. Brown and F. Rothacker, "Third-Order TRANSPORT with MAD Input A Computer Program for Designing Charged Particle Beam Transport Systems", FERMILAB-Pub-98/310, 1998.

[8] Micro Analysis Laboratory, Tandem accelerator website, The University of Tokyo, https://malt.um.u-tokyo.ac.jp/.

ISBN: 978-3-95450-236-3 ISSN: 2673-5350 doi:10.18429/JACoW-IBIC2023-WEP007

BEAM PROFILE MEASUREMENT USING HELIUM GAS LIGHT EMISSION AND BEPM FOR SUPERHEAVY ELEMENT SEARCH EXPERIMENT

T. Watanabe*, T. Adachi, P. Brionnet, O. Kamigaito,
K. Morimoto, T. Nishi, A. Uchiyama, RIKEN, Wako, Japan
A. Kamoshida, National Instruments Japan Corporation, Tokyo, Japan
K. Kaneko, R. Koyama, SHI Accelerator Service Ltd., Wako, Japan

Abstract

The newly constructed superconducting linear accelerator (SRILAC) is now in operation with the aim of discovering new superheavy elements and advancing the production of medical radiation isotopes. Because it is crucial to extend the durability of the expensive Cm target for as long as possible, these experiments require the accelerated V beam to be sufficiently widened. To this end, a helium gas light emission monitor (HeLM) has been introduced to measure the beam profile. Because He gas flows within the target chamber, by capturing the light emitted from He gas with a CCD camera, the beam profile can be obtained nondestructively and continuously. These measurements are handled through programming in LabVIEW, with analyzed data integrated into an EPICS control system. A method to estimate the beam envelope has been recently developed by leveraging the measured quadrupole moments with beam energy position monitors (BEPMs), and incorporating calculations of the transfer matrix. The synergistic use of HeLM and BEPM plays a useful role in accurately controlling the beam size at the Cm target.

INTRODUCTION

To upgrade the RIKEN Heavy-ion Linac (RILAC), the Superconducting RILAC (SRILAC) has been constructed, and successful commissioning has been completed [1]. These accelerators are being operated to advance research into even heavier synthetic elements [2]; build on the discovery of element 113, Nihonium [3]; and enhance the production capability of the short-lived radioisotope ^{211}At, which is anticipated to have applications in cancer therapy [4]. Over the past three years, the V beam, accelerated by both the RILAC and SRILAC, has been irradiated onto the Cm target for superheavy elements research.

BEAM PROFILE MEASUREMENT USING He GAS LIGHT EMISSION

RILAC, SRILAC, and GARIS Ⅲ

A schematic drawing of the RILAC, SRILAC, GARIS Ⅲ, and production apparatus for medical RIs is shown in Fig. 1. The V beam, accelerated by both RILAC and SRILAC, is irradiated onto the Cm targets inside a target chamber. To prevent the Cm targets from melting due to the beam irradiation, several thin Cm targets are mounted on a 30-cm radius wheel, which rotates at 2000 rpm. GARIS Ⅲ separates the superheavy elements from the unwanted particles, achieving high background noise reduction, by using dipole and quadrupole magnets. Furthermore, helium gas is introduced so that the electron charges of the superheavy elements converge to a certain value. Even if superheavy elements with different charges are ejected from the target, because the charges of superheavy elements become equal while they are passing through the helium gas, it is possible to collect the desired superheavy elements.

Target Chamber and HeLM for GARIS Ⅲ

To protect the Cm target, it is essential to extend its durability for as long as possible. Therefore, the accelerated V beam must not only hit the Cm target but also be adequately widened. A schematic drawing of the beam line with a differential pumping system and the target chamber for GARIS Ⅲ is shown in Fig. 2. Baffle electrodes are installed at the top, bottom, left, and right to detect the edge of the beam, and a carbon slit is installed in front of the target to cut the edge of the beam. CCD cameras monitor how the beam irradiates the target through view ports located upstream and downstream of the target. In Fig. 2, the beam comes from the left side, hits the Cm targets, and then proceeds to GARIS Ⅲ. Since He gas flows within the target chamber,

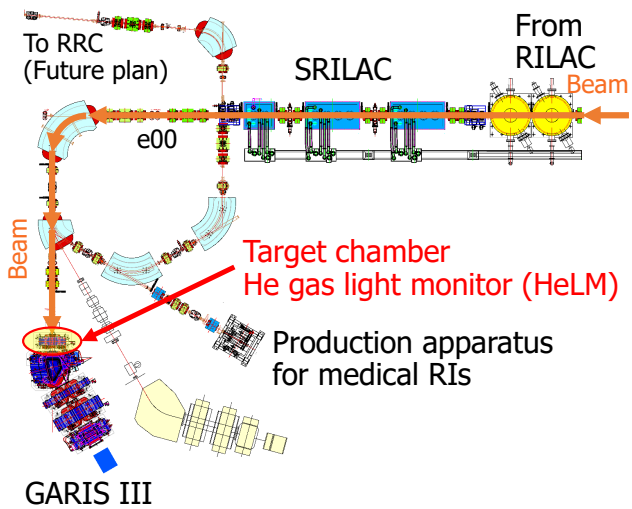


Figure 1: Schematic drawing of the RILAC, SRILAC, GARIS Ⅲ, and production apparatus for medical RIs.

* wtamaki@riken.jp

Content from this work may be used under the terms of the CC-BY-4.0 licence (© 2023). Any distribution of this work must maintain attribution to the author(s), title of the work, publisher, and DOI

ISBN: 978-3-95450-236-3 ISSN: 2673-5350 doi:10.18429/JACoW-IBIC2023-WEP007

Content from this work may be used under the terms of the CC-BY-4.0 licence (© 2023). Any distribution of this work must maintain attribution to the author(s), title of the work, publisher, and DOI

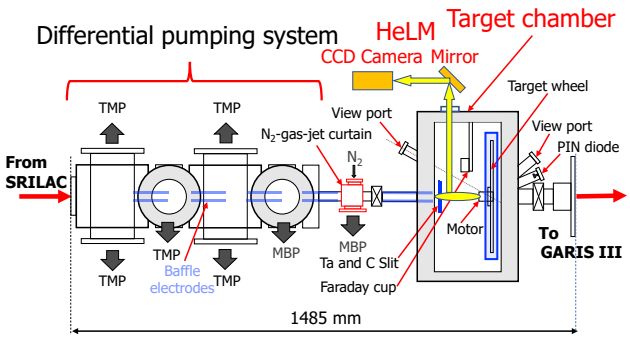


Figure 2: Schematic drawing of the beam line with the differential pumping system and target chamber for GARIS Ⅲ.

its electrons are excited through collisions with the beam, and the light is emitted when the electrons return to their ground state during the de-excitation process. By capturing the emitted light with a CCD camera, the beam profile can be obtained nondestructively and continuously.

A picture of the target chamber and the He gas light monitor is shown in Fig. 3. Hereafter, the He gas light monitor is referred to as "HeLM". To detect the light emitted from helium gas, a light window is located at the top of the target chamber. Since the target chamber is in an extremely high radiation environment, the light-receiving elements for the CCD camera gradually deteriorate as the experiment progresses. The CCD camera used for the HeLM is a small commercial monitor camera that employs CMOS elements. To minimize deterioration, the emitted light is reflected by a mirror located near the light window, and the reflected light is received by the CCD camera, which is set far from the target. However, even with this system, radiation damage cannot be completely avoided, and the CCD camera needs to be replaced approximately every two months. The detachable lens is reused after the CCD camera is replaced. The image signal obtained with the CCD camera is sent to a video server through an analog cable, and the digitized image data are transmitted to a HeLM controller via Ethernet. The specifications of the lens, CCD camera and video server are provided in Table 1.

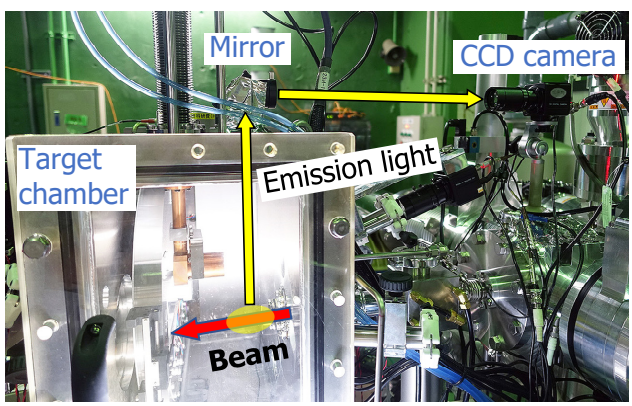


Figure 3: Photograph of the target chamber and HeLM. The emitted light is reflected by a mirror located near the light window and the reflected light is received by the CCD camera.

Table 1: Specifications of the Lens, CCD Camera, and Video Server

	Lens for CCD camera
CCTV* Lens	For 1/3 or 1/4 inch sensor
Focus	Focal length 6-60 mm (variable)
Iris	Manual F1.6
	CCD camera
Sensor	Sony307 1/3 inch CMOS
Video resolution	Pal/NTSC 1920 × 1080
Electrical shutter	1/50 ~1/10,000 s
	Video server
Model No.	AXIS Q7404
Chanel number	4
Video compression	H.264 MPEG-4 Part 10/AVC Motion JPEG
Resolution	720 × 480 ~176 × 120
Frame rate	30 frames/s
Processor	ARTPEC-3 × 4
Memory	Main 128MB × 4, Flash 128MB × 4
CCTV*	Closed Circuit Television

Programming for Image Acquisition and Analysis with LabVIEW and Web API

To analyze the beam profile, the HeLM controller obtains image data from the video server using a Web API (Application Programming Interface). The program to access the video server and save the acquired data is implemented with the Web API and the C++ OpenCV library. To achieve near real-time performance, one image frame is acquired every 200 ms.

The image data acquisition and analysis program is built using LabVIEW. LabVIEW includes a "Vision Development Module" designed for developing image processing applications to automate visual inspection tasks in industrial and other fields. This module contains "NI Vision Assistant" software, which allows developers to create application software interactively, confirming the results step by step. After confirming that the application software was working correctly, it was converted to a VI (Virtual Instrument) and integrated into the main HeLM program. The program could be completed in a short period of time using the NI Vision Assistant.

The front panels of the aforementioned application software and the analyzed results of the emitted He gas light are shown in Fig. 4. Since the details of the target are confidential, the length is expressed in pixel dimensions. The upper and lower front panels can be switched using a tab selection button. In the upper front panel, the measured results and setting selections are displayed as follows: (a) The result of integrating the brightness in the direction of travel of the beam and the result of a Gaussian fit, (b) An image of He gas emission, (c) The value of a Gaussian fit 1σ and the deviation from the center, and (d) The setting panel for the

ISBN: 978-3-95450-236-3 ISSN: 2673-5350 doi:10.18429/JACoW-IBIC2023-WEP007

fitting region, which can be selected manually or through direct numerical input.

The result of the integrated luminance along the beam direction represents the transverse beam profile, and the Gaussian fitted 1σ is defined as the beam width. In the lower panel, the history of the Gaussian fitted 1σ is recorded at the following scales: 1 minute (top), 1 hour (middle), and 1 day (bottom), as shown in Fig. 4(e). If the experimental user sets the maximum and minimum thresholds for the beam width 1σ, and the beam width exceeds those thresholds, the HeLM controller can automatically send a warning email to the user.

At the RI Beam Factory (RIBF) at the Nishina Center for Accelerator-Based Science, the distributed control environment system known as EPICS (Experimental Physics and Industrial Control System) has been implemented to operate and manage accelerators and large-scale experimental apparatuses. EPICS facilitates communication between servers and clients using the communication protocol known as Channel Access (CA). Here, the Input Output Controller (IOC) is a pivotal software component within EPICS that connects the controlled devices to the CA communication network and offers so-called Process Variable (PV) data. The analyzed data obtained by the HeLM monitor are stored in the PVs. However, due to security considerations, the HeLM controller is linked to the general LAN, which is isolated from the dedicated EPICS LAN. Consequently, data from both networks are relayed through a proxy server using the HTTP client method.

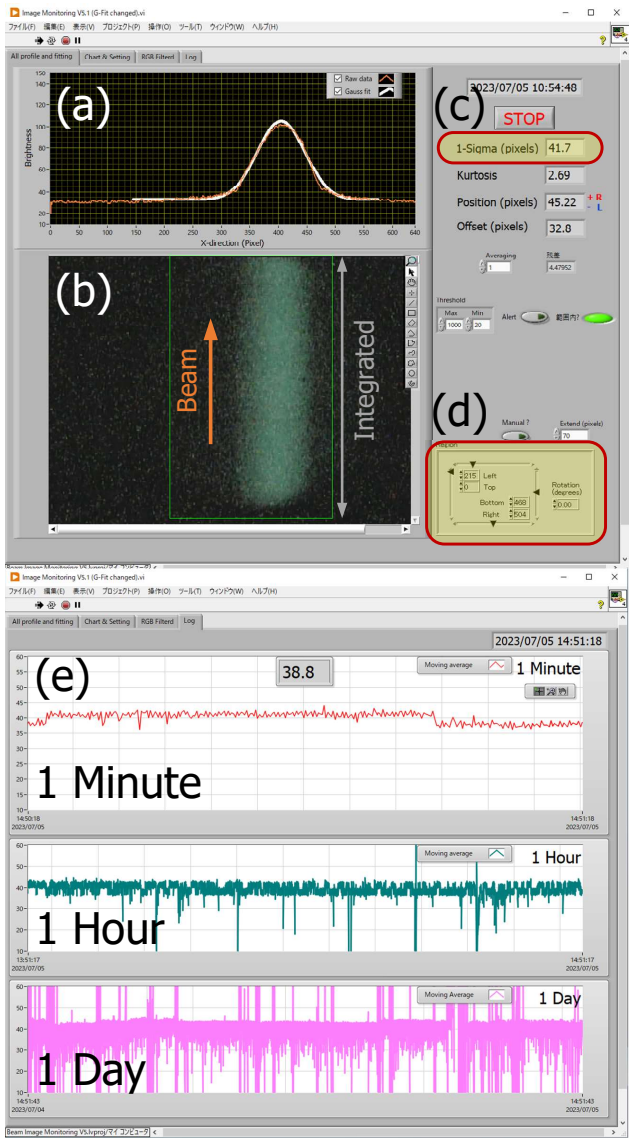


Figure 4: The front panels programmed with LabVIEW. (a) Result of integrating the brightness in the direction of travel of the beam and the result of a Gaussian fit, (b) Image of He gas emission, (c) Value of a Gaussian fit 1σ and the deviation from the center, (d) Setting panel for the fitting region, and (e) Record of the Gaussian fit 1σ.

MEASURED BEAM WIDTH WITH HeLM AND BEAM OPTICS CALCULATIONS USING BEPM

We discuss the HeLM measurements and beam optics calculations by using an example of accelerator operations conducted on 29 June 2022. In the early morning of that day, the experimental user requested that the beam optics be readjusted because the beam width measured using HeLM had decreased from 37 pixels (before the adjustment) to 31 pixels. While we attempted to adequately widen the beam on the target, the beam loss needed to be minimized as much as possible. To this end, we calculated the beam optics and adjusted them using the calculated results. Figure 5 shows the elastic scattering measurement results (red line), the beam width measured by the HeLM (blue line), and the carbon slit current (green line). After the beam optics were adjusted from 10:34 to 11:00, the beam width was improved from 31 to 37 pixels, as shown by the blue line in Fig. 5. The beam transmission efficiency, defined as the ratio of the up-

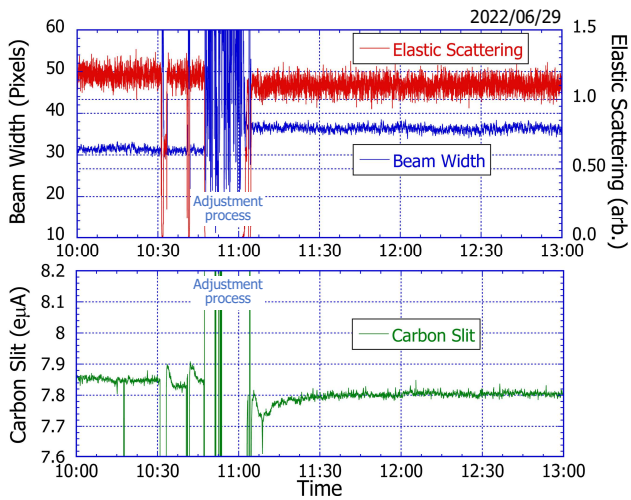


Figure 5: Measured results of elastic scattering (red line), beam width measured by the HeLM (blue line), and carbon slit current (green line).

Content from this work may be used under the terms of the CC-BY-4.0 licence (© 2023). Any distribution of this work must maintain attribution to the author(s), title of the work, publisher, and DOI

ISBN: 978-3-95450-236-3 ISSN: 2673-5350 doi:10.18429/JACoW-IBIC2023-WEP007

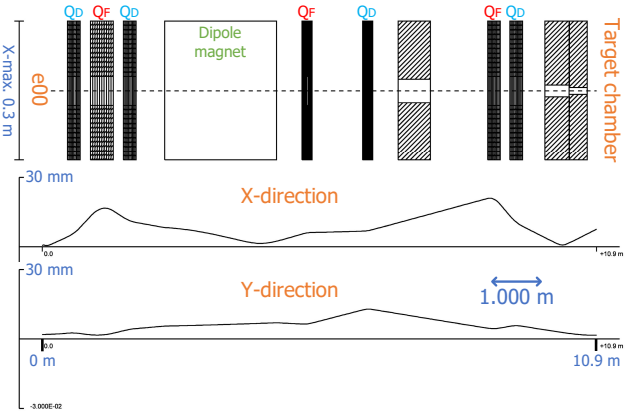


Figure 6: Calculated result of the beam envelope from e00 to the target chamber.

stream beam current to the target one, decreased from 97% to 94%. As shown in Fig. 5, the elastic scattering (red line) and the current of the carbon slit installed just in front of the target (green line) also obviously decreased. The beam current from the carbon slit has a characteristic in which the current increases rapidly just after beam irradiation and then gradually decreases. Therefore, the HeLM, carbon slit current, and elastic scattering measurements are in qualitative agreement.

The calculated results of the beam optics from e00 (see Fig. 1) to the target chamber [5] are shown in Fig. 6. Here, the emittance and Twiss parameters are obtained by the Q-scan method by using a wire scanner installed upstream of SRILAC, and the transfer matrix is calculated from these values to provide optimum conditions at the target. The beam is focused just before the target to increase the spot width, and the beam width measured by the HeLM is fine-tuned to optimize the quadrupole magnet.

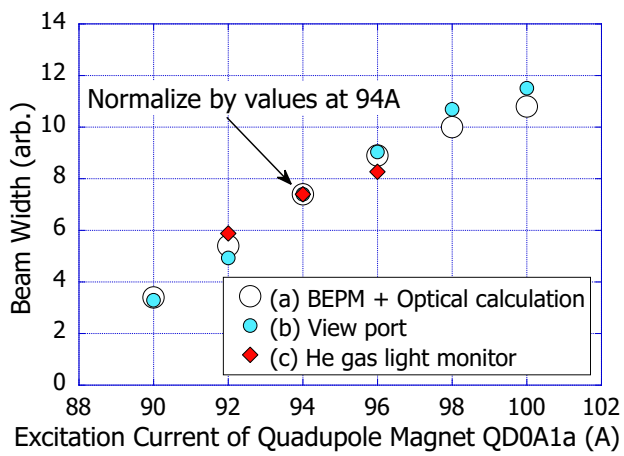


Figure 7: The beam widths obtained by: (a) the beam optical calculation using the quadrupole moments measured by the BEPMs, (b) the target spot on the fluorescent target observed through the view port, and (c) the measurement result taken with the HeLM.

Furthermore, we examined the beam width measurements and the beam optics calculation using the BEPMs [6] by changing the excitation current of the quadrupole magnet located in front of the target chamber. Figure 7 shows the beam widths obtained by (a) the beam optical calculation using the quadrupole moments measured by the BEPMs, (b) the target spot on the fluorescent target observed through the view port, and (c) the measurement result taken with the HeLM. Since these beam widths have different scales, they are all normalized to the excitation current of 94 A. The beam widths analyzed by these methods are in good agreement.

CONCLUSION

In the superheavy element search experiment, the beam profile is obtained with a CCD camera by observing the light emitted when the beam passes through the helium gas in the target chamber. This method has the advantage that the beam profile can be obtained nondestructively and continuously. These measurements are handled through programming in LabVIEW and the analyzed data are integrated into an EPICS control system. Furthermore, a method to estimate the beam envelope has been recently developed by leveraging the measured quadrupole moments with BEPMs, and incorporating calculations of the transfer matrix. The synergistic use of HeLM and BEPM allows us to accurately control the beam size at the Cm target.

ACKNOWLEDGEMENTS

The authors would like to thank Dr. Hiromitsu Haba and Dr. Daiya Kaji for providing detailed information on the superheavy element search experiment, and Dr. Yutaka Watanabe for supplying the CAD data.

REFERENCES

[1] K. Yamada *et al.*, "Successful Beam Commissioning of Heavy-Ion Superconducting Linac at RIKEN", in *Proc. SRF'21*, East Lansing, MI, USA, Jun.-Jul. 2021, pp. 167. doi:10.18429/JACoW-SRF2021-MOOFAV01

[2] H. Sakai *et al.*, "Facility upgrade for superheavy-element research at RIKEN", *Eur. Phys. J. A*, vol. 58, 2022, pp. 1–15. doi:10.1140/epja/s10050-022-00888-3

[3] K. Morita *et al.*, "New Result in the Production and Decay of an Isotope, ^{278}113, of the 113th Element", *J. Phys. Soc. Jpn.*, vol. 81, p. 103201, 2012. doi:10.1143/JPSJ.81.103201

[4] H. Haba *et al.*, "Present status of ^{211}At production at the RIKEN AVF cyclotron", *RIKEN Accel. Prog. Rep.*, vol. 53, 2019, p. 192. https://www.nishina.riken.jp/researcher/APR/APR053/pdf/192.pdf

[5] T. Nishi *et al.*, "Emittance Measurement and Ion Optics Tuning for SRILAC Beamline", in *Proc. of the 17th Annual Meeting of Particle Accelerator Society of Japan*, Sept. 2020, pp. 116–119. https://www.pasj.jp/web_publish/pasj2020/proceedings/PDF/THOO/THOO08.pdf

[6] T. Watanabe *et al.*, "Commissioning of the Beam Energy Position Monitor System for the Superconducting RIKEN Heavy-ion Linac", in *Proc. IBIC'20*, Santos, Brazil, Sep. 2020, pp. 295–302. doi:10.18429/JACoW-IBIC2020-FRAO04

Content from this work may be used under the terms of the CC-BY-4.0 licence (© 2023). Any distribution of this work must maintain attribution to the author(s), title of the work, publisher, and DOI

ISBN: 978-3-95450-236-3 ISSN: 2673-5350 doi:10.18429/JACoW-IBIC2023-WEP011

A PRELIMINARY DESIGN OF BUNCH-BY-BUNCH 3D POSITIONS MEASUREMENT

Ruizhe Wu, Yunkun Zhao, Dongyu Wang, Ping Lu, Leilei Tang, Baogen Sun*
University of Science and Technology of China (USTC),
No. 96, JinZhai Road Baohe District, Hefei, Anhui, China

Abstract

The decrease of beam emittance in the 4^{th} generation light source greatly increases the electron density, thus the wakefields and beam impedance in the storage ring are significantly enhanced, resulting in various beam instabilities. Therefore, it is necessary to observe the transient state of beams using the bunch-by-bunch technique, so as to dig into these instabilities. Here a three-dimensional (3D) positions measurement instrument is designed based on data synchronization module (DSM) to acquire the transverse positions and longitudinal phases of beams in real-time.

INTRODUCTION

Compared with the 3^{th} generation light sources, the 4^{th} generation light sources are generally built with compact MBA structures, so that the horizontal emittance of the beam is reduced by 1 to 2 orders, close to the X-ray diffraction limit. Consequently, the strong nonlinear elements in the MBA structures make the dynamic aperture significantly smaller, causing the beam dynamics to be extremely sensitive to the effects of instabilities, and even affecting the maximum beam current during operation time. Hence, it is essential to observe the beam characteristics on fine time scales using bunch-by-bunch technique, figuring out the instabilities induced by wakefields, and even eliminating these instabilities.

Generally, bunch-by-bunch technique covers bunch length, longitudinal phase, bunch charge, transverse positions and bunch profiles [1–5]. However, it is obvious that these measurements are limited by the number of sampling channels on a single acquisition board, and only one single beam parameter can be obtained, rather than multiple parameters simultaneously. In order to break through the limitation of the number of sampling channels, a bunch-by-bunch 3D positions measurement instrument is designed with DSM [6], as shown in Fig. 1.

The instrument is mainly composed of microwave components and digital logic components, in which the microwave components are divided into signal part and timing part. For the signal part, it duplicates the four-channel signal sensed from the BPM in the storage ring and sends the two duplicated four-channel signals to data acquisition boards. For the timing part, the synchronous signal generated from the storage ring timing system is frequency quadrupled and then divided into two channels to data acquisition boards, between which there is a certain phase difference due to the delay

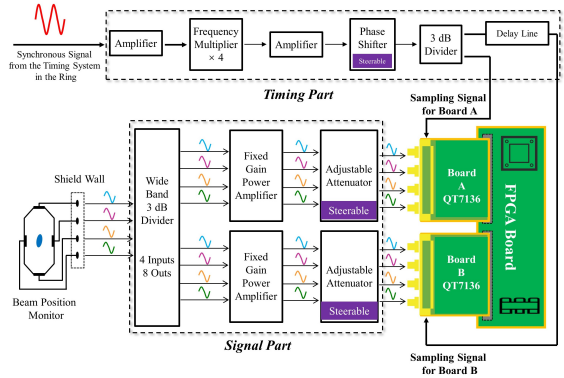


Figure 1: The layout of bunch-by-bunch 3D positions measurement instrument.

line. As for the digital logic components, two four-channel signals are digitized by the acquisition boards, then these digitized signals are synchronized by the DSM in FPGA, and finally the 3D positions of each bunch are calculated. Since these microwave components are at the factory, an evaluation system based on oscilloscope is set up to research the 3D positions measurement processes in the designed instrument.

EVALUATION SYSTEM SETUP

In order to determine the measurement performance in the 3D positions, an oscilloscope-based performance evaluation system was constructed, as shown in Fig. 2. With the help of the low-pass filter, the bandwidth of the oscilloscope is equivalent to that of the acquisition board, so that the data obtained by the oscilloscope and the data acquisition board are consistent. After the acquisition, these data will be sent to the computer for processing, and finally obtain the signals of each bunch during the bunch interval [7]. Finally, the corresponding measurement performance can be obtained by analyzing the signals in the bunch interval.

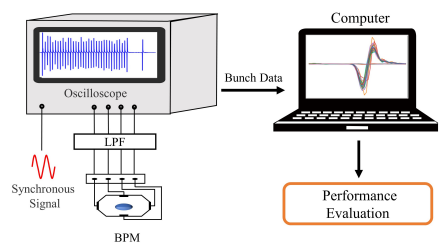


Figure 2: Evaluation system based on oscilloscope.

* bgsun@ustc.edu.cn

Content from this work may be used under the terms of the CC-BY-4.0 licence (© 2023). Any distribution of this work must maintain attribution to the author(s), title of the work, publisher, and DOI

ISBN: 978-3-95450-236-3 ISSN: 2673-5350 doi:10.18429/JACoW-IBIC2023-WEP011

Content from this work may be used under the terms of the CC-BY-4.0 licence (© 2023). Any distribution of this work must maintain attribution to the author(s), title of the work, publisher, and DOI

3D POSITIONS MEASUREMENT

For longitudinal phases of bunches, its measurement formula is shown as Eq. (1) [7]:

$$L = K \cdot V_{OSM} \tag{1}$$

Where coefficient K represents the linearity of the BPM sum signal, which is determined by the amount of charge and the length of the bunch, and V_{OSM} is the BPM sum signal at one sampling point during the bunch interval.

However, this measurement method of longitudinal phases is susceptible to the jitters of the synchronous signals, so that the V_{OSM} obtained has a certain deviation from the actual, for whose detailed information please refer to Ref. [7]. To eliminate the influence of the clock jitters on longitudinal phases, it is necessary to adopt a two-point sampling method as shown in Fig. 3.

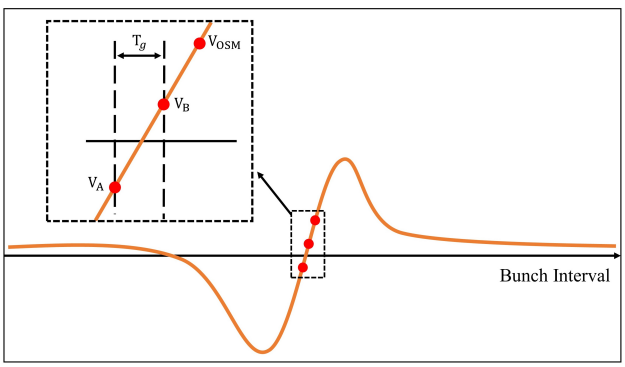


Figure 3: Sampling with two points in the bunch interval.

In the two-point sampling method, T_g is determined by the length of the delay line in the instrument, and the amplitude of the two sampling points V_A and V_B are completely determined by the BPM sum signals collected by the acquisition board A and B. Hence, the factor K in Eq. (1) can be completely determined, as Eq. (2):

$$K = (V_B - V_A) / T_g \tag{2}$$

While the value of V_{OSM} in Eq. (1) can also be determined by V_A and V_B, although the two sampling points corresponding to V_A and V_B have certain clock jitters. For one bunch in a specific filling pattern, the data relations $(V_A, V_B) - V_{OSM}$ can be constructed according to the bunch-by-bunch data collected by the oscilloscope-based evaluation system, as shown in Fig. 4.

In this way, with the data relations $(V_A, V_B) - V_{OSM}$, the vector $V_M(V_A, V_B)$ collected by the instrument in real-time is carried out with multiple vectors $V_D(V_A, V_B)$ in the data relations as shown in Eq. (3), and the corresponding data V_{OSM} is selected as the actual V_{OSM} when the matching coefficient M is the highest one.

$$M = (V_M \cdot V_D) / (|V_M| \cdot |V_D|) \tag{3}$$

Thus, the longitudinal phases L of each bunch can be obtained by two sampling points (V_A, V_B) without the effects of clock jitters. Moreover, it is worth noting that the data relations $(V_A, V_B) - L$ can be directly constructed, then the corresponding longitudinal phase L of the bunch can be directly calculated through Eq. (3), as depicted in Fig. 5. Here the red line shows the actual longitudinal phase of the bunch, while the blue line is the longitudinal phase of the bunch obtained through the data relations $(V_A, V_B) - L$.

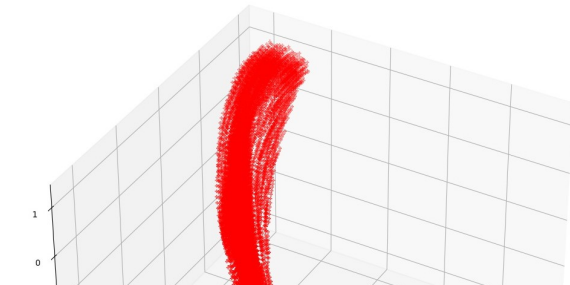


Figure 4: Relations between (V_A, V_B) and V_{OSM}.

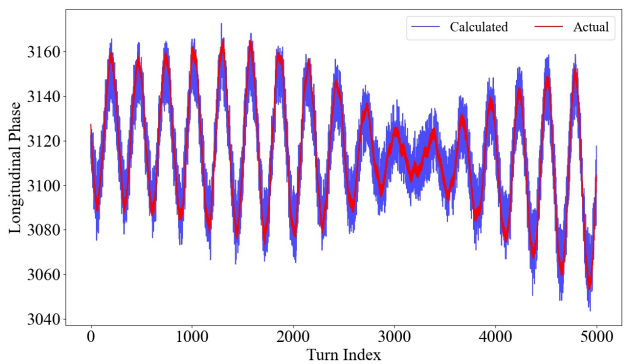


Figure 5: The actual longitudinal phases and the longitudinal phases calculated with relations.

As for the transverse positions of bunches, they are calculated with the $\Delta - \Sigma$ method, but using the four-channel signal whose BPM sum signal is larger between V_A and V_B to ensure the signal-to-noise ratio. The related equations are as follows:

$$\begin{cases} T_{x/y} = K_{x/y} \cdot \left(V_1 - V_{2/4} - V_3 + V_{4/2}\right) \cdot \frac{1}{\sum_{i=1}^{4} V_i} \\ V_i = V_{Ai} \text{ if } V_A > V_B \text{ else } V_{Bi} \end{cases} \tag{4}$$

Wherein: x/y is the transverse position of x-direction or y-direction, $K_{x/y}$ is a constant with unit "mm" depending on the geometry of button BPM, V_i are the digitized four-channel signals from BPM, and the subscript i indicates

ISBN: 978-3-95450-236-3 ISSN: 2673-5350 doi:10.18429/JACoW-IBIC2023-WEP011

the identifier of the four channels. Besides, V_{Ai} and V_{Bi} represent the four-channel signals on sampling points A and B respectively.

DISCUSSION

Using the two-sampling method, the evaluation for the resolution of the transverse positions makes no difference from our previous work [7]. While for the resolution of the longitudinal phases, the error transfer formula is hard to obtain precise results due to the non-formulaic form of the data relations $(V_A, V_B) - V_{OSM}$. In view of this, there are two ways to acquire the actual resolution of the longitudinal phases:

- Construct the formula for $(V_A, V_B) - V_{OSM}$.
- Utilize data dimensional reduction methods.

For the first way, its essence is still the error transfer formula, but the construction is difficult. As for the second way, the longitudinal phases of the bunches obtained through data relations $(V_A, V_B) - V_{OSM}$ are processed for dimensional reduction, and the data variance before and after dimensional reduction is taken as the resolution assessment. However, it has subjective judgment factors in the dimensionality reduction.

Moreover, the data processing flows for 3D positions measurement can be basically determined, as shown in Fig. 6. After these digitized BPM signals are synchronized by the module DSM, the BPM sum signals (V_A, V_B) at two sampling positions in the bunch interval will be sent to the vector matching module to complete the calculation of Eq. (3) to find the most matched data relation $(V_A, V_B) - L$, and the matched L is taken as the longitudinal phase of the bunch. At the same time, the sampling selection module will select the four-channel signal whose BPM sum signal is lager as the input of the $\Delta - \Sigma$ module, which outputs the transverse positions of the bunch.

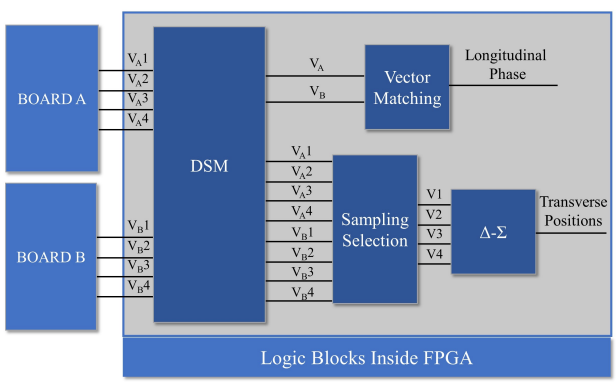


Figure 6: Data processing flows inside the 3D positions measurement device.

It should be noted that the construction of the vector matching module requires a large number of data relations $(V_A, V_B) - L$, in which the machine learning is needed to determine the vector matching parameters of each bunch in the filling pattern. Therefore, it is necessary to collect mass data with the oscilloscope-based evaluation system and then build its corresponding relations before building this bunch-by-bunch 3D positions measurement instrument, otherwise the measurement results will have a deviation. As revealed in Fig. 5, part of the reason why the longitudinal phases of the bunch calculated by vector matching module deviate from the actual longitudinal phases is owe to the insufficient amount of data relations $(V_A, V_B) - L$. But it is not ruled out that these deviations are also caused by inconsistencies of the movements of the bunches in the specific filling modes. Anyway, the two reasons need to be verified later through building sufficient data relations.

CONCLUSION

To design the instrument for observing the 3D positions of bunches in the storage ring, one oscilloscope-based evaluation system is set up to determine the data dealing processes of the 3D positions, and the framework of the logic blocks inside FPGA. However, there is some deviations between the longitudinal phases obtained with the vector matching and the actual longitudinal phases, which is due to the insufficiency of the data relations, or the inconsistency of the movement laws of the bunches in the specific filling mode. More research work is need to verify the two possibles.

REFERENCES

[1] J. Lee, M. H. Chun, G.-J. Kim, D.-C. Shin, D.-T. Kim, and S. Shin, "Bunch-by-bunch position measurement and analysis at PLS-II", *J. Synchrotron Radiat.*, vol. 24, no. 1, pp. 163–167, 2017. doi:10.1107/S1600577516018154

[2] Y.-M. Zhou, *et al.*, "Bunch-by-bunch longitudinal phase monitor at SSRF", *Nucl. Sci. Tech.* vol. 29, no. 113, 2018. doi:10.1007/s41365-018-0445-6

[3] F.-Z. Chen *et al.*, "Touschek lifetime study based on the precise bunch-by-bunch BCM system at SSRF", *Nucl. Sci. Tech.*, vol. 30, no. 144, pp. 1–8, 2019. doi:10.1007/s41365-019-0655-6

[4] A. Drago, *et al.*, "Bunch-by-bunch profile diagnostics in storage rings by infrared array detection", *Meas. Sci. Technol.*, vol. 26, no. 9, pp. 094003, 2015. doi:10.1088/0957-0233/26/9/094003

[5] L.-W. Duan, Y.-B. Leng, R.-X. Yuan, Z.-C. Chen, "Injection transient study using a two-frequency bunch length measurement system at the SSRF", *Nucl. Sci. Tech.*, vol. 28, no. 7, p. 93, 2017. doi:10.1007/s41365-017-0247-2

[6] R. Wu, Y. Zhao, S. Jin, L. Tang, P. Lu, and B. Sun, "Data synchronization module for multi-dimensional bunch-by-bunch measurement in a storage ring" *Rev. Sci. Instrum.*, vol. 93, no. 12, pp. 123301, 2022. doi:10.1063/5.0115976

[7] R. Wu, Y. Zhao, S. Jin, L. Tang, P. Lu, and B. Sun, "A one-time sampling method for the real-time measurement of bunch-by-bunch three-dimensional positions in storage rings", *J. Instrum.*, vol. 17, no. 11, pp. P11001, 2022. doi:10.1088/1748-0221/17/11/P11001

Content from this work may be used under the terms of the CC-BY-4.0 licence (© 2023). Any distribution of this work must maintain attribution to the author(s), title of the work, publisher, and DOI

ISBN: 978-3-95450-236-3 ISSN: 2673-5350 doi:10.18429/JACoW-IBIC2023-WEP013

QUALITY ASSURANCE OF PROTON BEAM PROFILE USING PHOSPHOR SCREEN AND TE-COOLED CMOS CAMERA*

Gwangil Jung†, Young-Seok Hwang, Young Jun Yoon
Korea Atomic Energy Research Institute, Gyeongju-si, Republic of Korea

Abstract

The Korea Multi-Purpose Accelerator Complex (KOMAC) operates a 100 MeV proton linear accelerator, providing a high flux proton beam at the TR103, a general-purpose irradiation facility. Ensuring uniform irradiation of sample with protons is critical, necessitating confirmation of beam profile uniformity through the quality assurance (QA) process. To address this, a real-time and in-situ proton beam profile monitoring system was recently introduced and tested at the TR103. This system includes a P43 phosphor screen and TE-cooled CMOS camera, which captures images of the emitted light from protons with energies of 20, 50, and 100 MeV incident on the screen. Subsequent post-processing, such as background subtraction, image smoothing, geometrical correction, was performed on the image data. The measured beam profiles using the phosphor screen and cooled camera were then compared to those obtained using Gafchromic film™, a widely used dosimeter in radiation measurements. Additionally, the linearity between light output and beam flux was measured to establish a quantitative relationship. This study presents the test results of the proton beam profile measurement using the phosphor screen and TE-cooled CMOS camera, demonstrating its potential as an effective tool for quality assurance in proton beam irradiation experiments at the TR103 facility.

INTRODUCTION

Since 2013, KOMAC has operated a 100 MeV proton linear accelerator, facilitating various proton beam irradiation experiments. To ensure optimal experimental conditions and minimize irradiation errors, a rigorous quality assurance (QA) process for proton beam profiling is essential to achieve uniform proton irradiation within the sample. The uniformity criteria, defined as the difference between the maximum and minimum intensity divided by the mean intensity, must meet a threshold of 10% within the target diameter.

The TR103, a general-purpose irradiation facility at KOMAC, has used film dosimetry for beam profile QA. However, film dosimetry lacks real-time and in-situ monitoring capabilities due to the need for scanning to acquire beam profile data and its susceptibility to saturation under continuous irradiation of high-flux proton. To address these limitations, a recent advancement introduced the use of a P43 phosphor screen and TE-cooled CMOS camera for real-time and in-situ proton beam profile monitoring.

This study aimed to verify the accuracy of the P43 phosphor screen and CMOS camera system and integrated it into the quality assurance process. An experiment was conducted to capture the light response of the phosphor screen.

EXPERIMENTS AND DISCUSSTION

Phosphor Screen and Cooled Camera

Proton irradiation tests were performed at TR103 with a flux of approximately 10^{10} to 10^{11} particle/(cm^2·pulse). The pulsed proton beam was accelerated to energies of 20, 45, and 102 MeV, and its energy was attenuated by 15, 42, and 100 MeV, respectively, as it passed through the beam window and air before reaching the target point. The beam profile monitoring system primarily consisted of a phosphor screen, where light is emitted as protons deposit energy, and a real-time capturing camera. The phosphor screen was positioned 1.5 m away from the beam window, tilted at a 45-degree angle relative to the beam path, while the camera was placed 1 m perpendicular to the screen for real-time imaging of the emitted light (Fig. 1).

The phosphor screen used in this study consisted of a P43 (Gd2o2S :Tb) layer on an Al substrated, providing a detection area of 310 mm × 310 mm and a peak wavelength of 545 nm [1]. With a decay time of 1 ms to 10% and high light efficiency, the phosphor screen proved suitable for real-time light emission detection. The TE-cooled CMOS camera (ASI183MC Pro, ZWO) utilized in the setup had a sensor size of 13.2 mm × 8.8 mm and a thermoelectric cooler capable of cooling sensors down to -10℃ [2]. Figure 2 illustrates the arrangement of the P43 phosphor screen and the camera. To minimize image noise and avoid saturation at high light outputs, the camera

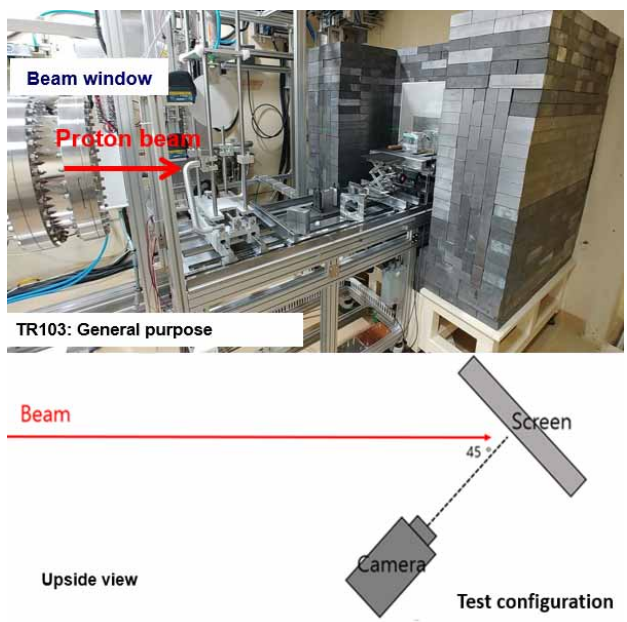


Figure 1: View of general-purpose irradiation facility, TR103 (top) and configuration of device layout (bottom).

Content from this work may be used under the terms of the CC-BY-4.0 licence (© 2023). Any distribution of this work must maintain attribution to the author(s), title of the work, publisher, and DOI

ISBN: 978-3-95450-236-3 ISSN: 2673-5350 doi:10.18429/JACoW-IBIC2023-WEP013

settings were optioptimzed, utilizing the lowest ISO and appropriate exposure time.

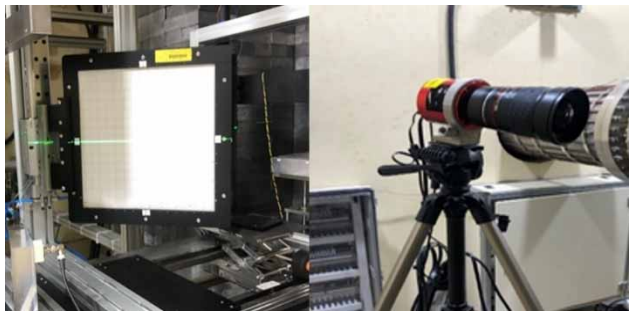


Figure 2: Setup of the P43 phosphor screen.

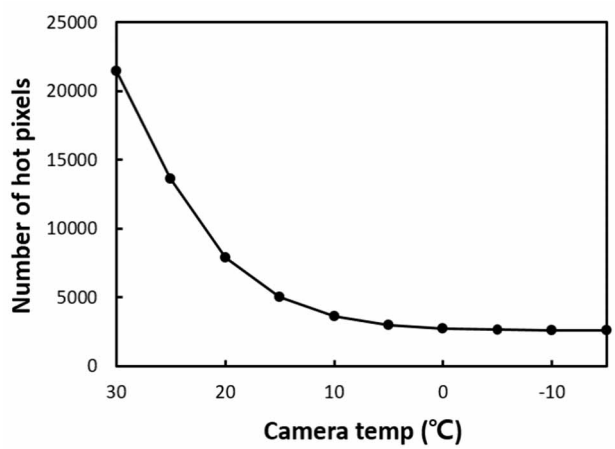


Figure 3: The number of hot pixels as a function of camera temperature.

In general, the presence of hotspots in an image is directly related to the amount of radiation accumulated in the sensor. Cooled cameras demonstrated improved radiation resistance due to the reduction of leakage current in defective sensors with decreasing temperature [3]. To validate the noise reduction effect in the high-radiation setting, an experiment was conducted to measure the number of hot pixels while cooling the pixels decreased accordingly and eventually stabilized at -10 °C, as depicted in Fig. 3.

Image Post-Processing

To enhance the accuracy of beam profile measurements, a series of post-processing steps were employed to approximate the actual beam shape from the raw image data, as illustrated in Fig. 4. Initially, the raw image contained the white screen background and the grid, which are eliminated by subtracting pre-captured background images. Additionally, a Gaussian filter was applied to smooth the image. Considering the 45-degree tilt of the phosphor screen from the beam path, the length ratio of the horizontal axis was adjusted to reconstruct the actual beam shape. To establish X-Y coordination by converting pixels to millimetres, a Region of Interest (ROI) was selected, and the actual length of the ROI was divided by the number of pixels corresponding to that length.

An algorithm was developed to calculate the intensity uniformity within the diameter and identify the position at which the uniformity of a given diameter is minimized. A dedicated software tool was designed to facilitate the selection of beam profile image and streamline the post-processing of image data, as depicted in Fig. 5. These measures collectively contributed to increasing the accuracy and reliability of the beam profile measurements.

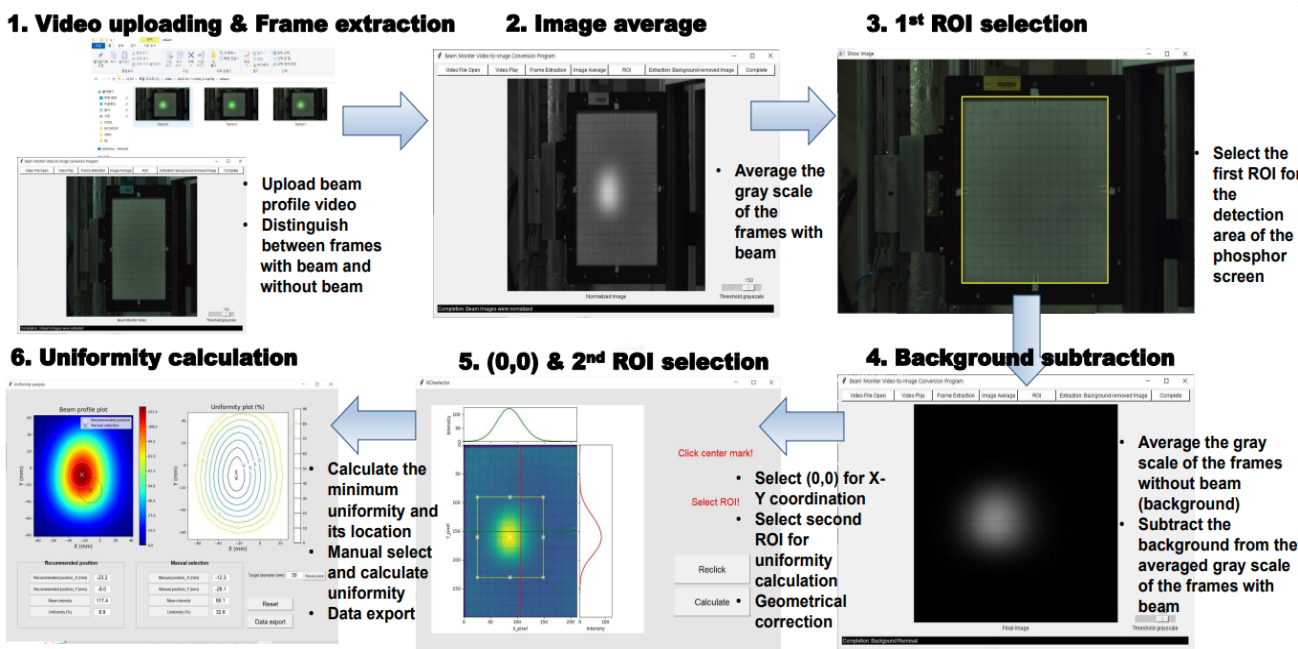


Figure 4: Post-processing of image data using Python.

Content from this work may be used under the terms of the CC-BY-4.0 licence (© 2023). Any distribution of this work must maintain attribution to the author(s), title of the work, publisher, and DOI

ISBN: 978-3-95450-236-3 ISSN: 2673-5350 doi:10.18429/JACoW-IBIC2023-WEP013

Content from this work may be used under the terms of the CC-BY-4.0 licence (© 2023). Any distribution of this work must maintain attribution to the author(s), title of the work, publisher, and DOI

Table 1: Minimum Uniformity, FWHM and Sigma of the Beam Profile Measured by Phosphor Screen and Film for Each Incident Proton Energy

	15 MeV		42 MeV		100 MeV	
	HD-V2	Screen	HD-V2	Screen	HD-V2	Screen
Uniformity in 30 mm-Ø (%)	11.9	9.8	7.5	7.3	6.2	6.5
Uniformity in 50 mm-Ø (%)	31.1	25.6	20.2	19.8	16.1	17.1
FWHM-her (mm)	25.3	28.4	34.5	34.8	36.1	37.1
FWHM-ver (mm)	33.7	34.5	33.6	34.5	38.7	37.1
σ-hor (mm)	21.5	24.2	29.3	29.5	30.4	31.9
σ-ver (mm)	33.7	34.5	34.5	34.5	38.7	37.1

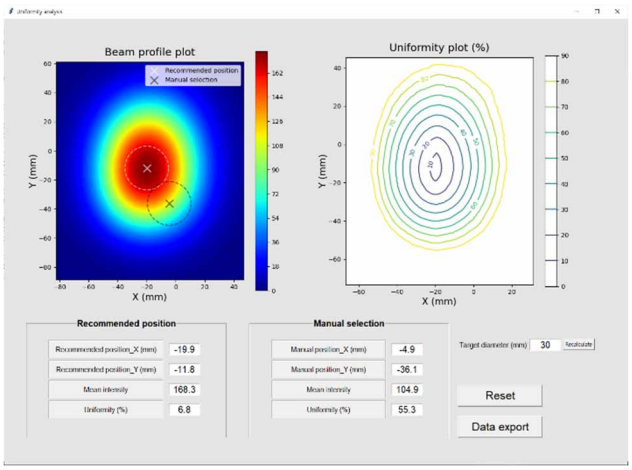


Figure 5: Uniformity calculation result window of beam profile analysis software. Software calculates the uniformity of intensity and find the position at which the uniformity of a given diameter is minimized.

Proton Beam Profile Measurement

To compare the beam profiles obtained from the phosphor screen and film, both were subjected to 5 pulses of proton beam and subsequently normalized based on the maximum intensity value. Figure 6 presents the horizontal and vertical beam profile plots as measured by the phosphor screen. Gaussian function fitting was employed to evaluate the value of sigma and full width at half-maximum (FWHM) for the beam profile data. The minimum

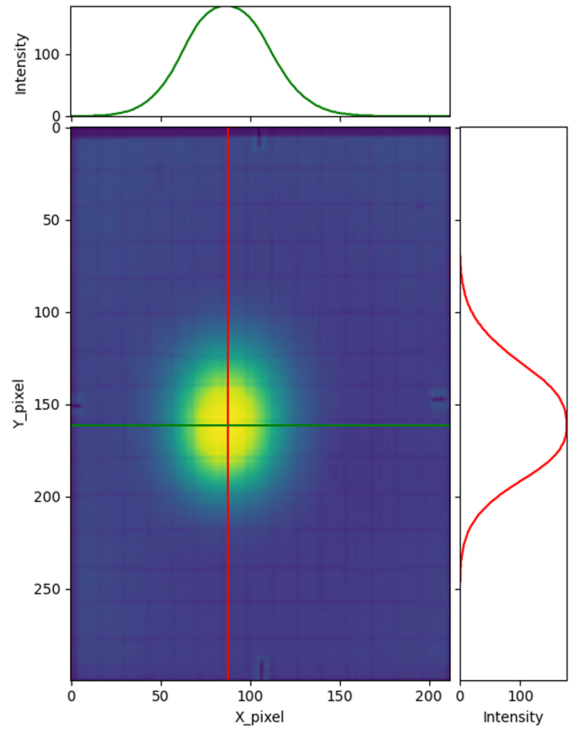


Figure 6: The horizontal and vertical beam profile plots measured by phosphor screen.

uniformity values within the Region of Interest (ROI) for diameters of 30 mm and 50 mm were calculated. Table 1 displays the minimum uniformity, FWHM, and sigma values of the beam profiles measured by the phosphor screen and film for each incident proton energy.

At incident energies of 42 MeV and 100 MeV, both the 1D profiles obtained from the phosphor screen and film display differences of less than 2 mm in both directions, while the uniformity of the 2D profile show differences within 10% for both diameters. In the case of the incident energy of 15 MeV, the 1D profile demonstrates differences of less than 3mm in both directions, and the 2D profiles exhibits differences within 20% for both diameters. These results indicate a good level of agreement and consistency between the beam profile measured using the phosphor screen and film method across various incident proton energies.

A test was conducted to verify the linearity between light output and beam flux. The faraday cup and phosphor screen were utilized simultaneously to measure beam flux and light output as the beam pulse width was increased. The beam fluxes were obtained as a function of light output for each proton energy and then normalized by the maximum value. Figure 7 illustrates the linearity between beam flux and light output for each proton energy. The corresponding R-square values for 100 MeV, 42 MeV, and 15 MeV were found to be 0.995, 0.991 and 0.961, respectively. The results demonstrated a satisfactory linearity between beam flux and light output across the entire range without any signs of saturation. However, it was observed that as the proton energy decreases, the linearity of beam flux and light output diminishes due to the influence of

ISBN: 978-3-95450-236-3 ISSN: 2673-5350 doi:10.18429/JACoW-IBIC2023-WEP013

high linear energy transfer (LET), resulting from the low proton energy, which causes a quenching effect on light intensity [4].

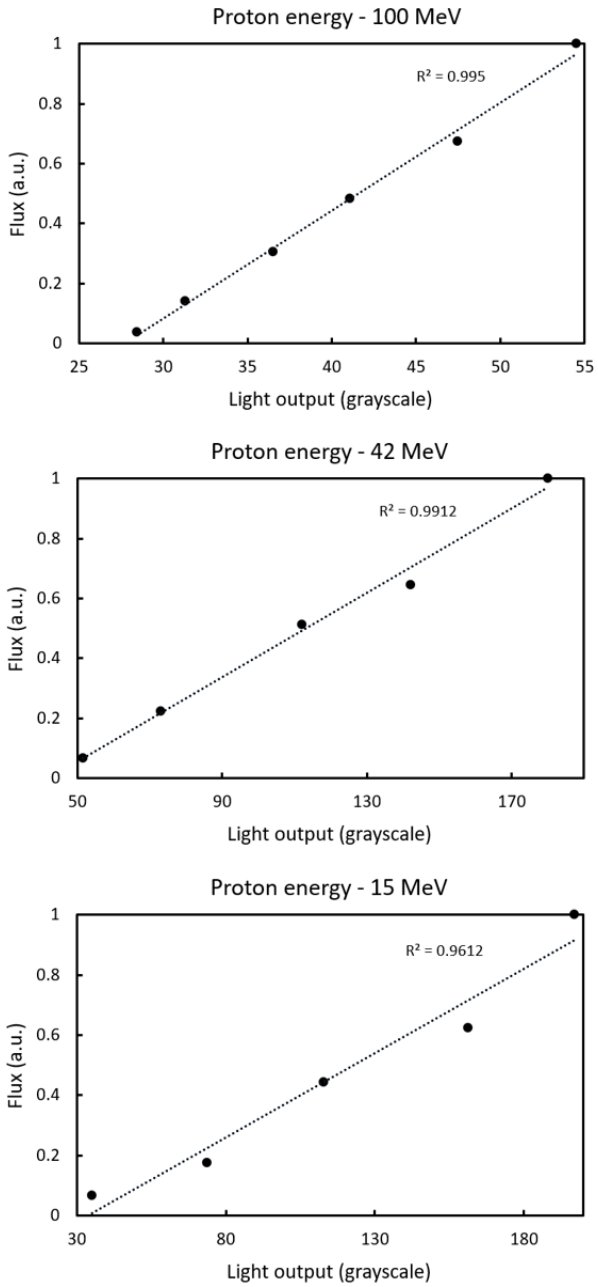


Figure 7: Beam flux as a function of light output for proton energy of 100, 42, 15 MeV.

CONCLUSION

For real-time and in-situ proton beam profile monitoring, the integration of a P43 phosphor screen and a TE-cooled CMOS camera was implemented. To validate the accuracy of this monitoring system and incorporate it into the quality assurance process, an experiment was conducted to capture the light response of the phosphor screen using the CMOS camera. The acquired beam profile data from the phosphor screen were compared with those obtained using gafchromic film. Post-processing of the image data involved background subtraction, image smoothing, geometrical correction, and the selection of Region of Interest (ROI) and X-Y coordination.

Comparison of beam uniformity measured using the phosphor screen and film revealed that incidents with energies of 42 MeV and 100 MeV displayed differences within 10% in both diameters, while the incident energy of 15 MeV exhibited a difference of approximately 20% in both diameters. The linearity between light output and beam flux was found to be excellent, demonstrating a consistent relationship throughout the entire range without any indication of saturation.

Overall, the introduction of this novel beam profile monitoring system is expected to facilitate in-situ quality assurance processes, providing real-time monitoring capabilities and improving the accuracy and reliability of proton beam profiling at the facility.

REFERENCES

[1] http://proxivision.de/product/scintillating-screen/

[2] http://astronomy-imaging-camera.com/product/asi183mc-pro-color/

[3] A. Huber *et al.*, "Response of the imaging camera to hard radiation during JET operation", *Fusion Engineering and Design*, vol. 123, pp. 669-673, 2017.

[4] J. B. Birks, *The Theory and Practice of Scintillation Counting,* Oxford: Pergamon, 1964.

Content from this work may be used under the terms of the CC-BY-4.0 licence (© 2023). Any distribution of this work must maintain attribution to the author(s), title of the work, publisher, and DOI

ISBN: 978-3-95450-236-3 ISSN: 2673-5350 doi:10.18429/JACoW-IBIC2023-WEP014

MEASURING ELECTROMAGNET POLARITY USING MAGNETIC REMANENCE*

K. P. Wootton†, Argonne National Laboratory, Lemont, IL, USA

Abstract

Large accelerator systems typically include many individually powered electromagnets. An important activity prior to commissioning with beam is verifying that the polarity of the installed magnets matches the design lattice. In the present work, we motivate the measurement of magnet polarity in a manner that is electrically safe, by measuring the magnetic remanence of iron yokes of normal conducting electromagnets. This has been used to confirm the polarities of iron-dominated dipole and quadrupole electromagnets at the Linac Extension Area at the Advanced Photon Source.

INTRODUCTION

During installation and commissioning of accelerator systems, a common quality assurance task associated with the installation is ensuring that magnets are connected to power supplies with the correct polarity [1–4]. Magnetic polarity checkout has typically been performed in under administrative controls with magnets energised [5]. We consider that procedures which require workers to approach energised magnets potentially presents an unacceptable electrical safety hazard.

In the present work, we summarise a technique for performing magnet polarity checks using the remnant magnetic field from prior excitation using the connected power supply. Measuring the remnant field with the power supply off obviates the principal safety concern of needing to work adjacent to energised electrical conductors.

BACKGROUND

In many accelerators, the main magnets are powered by unipolar power supplies. Hence, a quality assurance task associated with the installation of a magnet and power supply system is to confirm that the installed magnet polarities match the design polarities of the lattice [6–9]. When powered, electromagnets have the opportunity to present both electrical and magnetic hazards to personnel approaching them [10]. There are different ways of mitigating these hazards, for instance by implementing electrically insulating shielding or shielding that restricts personnel from approaching the magnetic field that the magnet generates. Another way is to switch off the magnet power supply, and Lock-Out-Tag-Out (LOTO) the source of hazardous energy.

METHOD

We tested this procedure using the bending magnets of the booster bypass vertical ramp and the Linac Extension Area (LEA). The steps in the procedure are outlined below.

1. Accelerator enclosure secured.
2. Accelerator magnets energised at its nominal current setpoint for 10 minutes using its connected power supply. This puts the magnet on its hysteresis curve.
3. Accelerator magnets de-energised, leaving only the remnant field in the magnet.
4. Lock-Out-Tag-Out (LOTO) accelerator magnets, and verify zero energy state by Zero Voltage Verification (ZVV). At this point, all LOTO requirements should be complete to enable authorised access to the accelerator enclosure.
5. Lower the accelerator access control system level to authorised access.
6. Enter the accelerator enclosure and approach the unpowered electromagnet.
7. Measure the polarity of the remnant field (without any electrical hazard) using a permanent magnet probe.

RESULTS

Initial Measurement

On the 22nd of August, 2022, Kent Wootton performed magnet polarity checks on booster bypass and LEA magnets. A magnet polarity checker Magnaprobe MKII was used. The north pole of the bar magnet on the magnet probe is coloured red, and the south pole of the magnet is coloured blue. The polarity checker is illustrated in Fig. 1.

The polarity of quadrupoles and vertical bending magnets (skew dipoles) along the booster bypass transport line was measured. We measured the 'top-left' most pole of quadrupoles, and the 'left' pole of skew dipoles. This pole convention is illustrated in Fig. 2.

The probe was held near the poles of the magnets. Photographs illustrating polarity measurements are given in Fig. 3 and Fig. 4. One can see that the experimenter's hand is quite close to the magnet while performing the measurement.

Results of polarity measurements are summarised in Table 1. Magnet polarity measured from remnant field on the 22nd of August, 2022. Magnet types Q_1 correspond to upright quadrupole, and B_2 to skew dipole (vertically deflecting). We deliberately included a couple of quadrupoles from

* Work supported by the U.S. Department of Energy, Office of Science, Office of Basic Energy Sciences, under Contract No. DE-AC02-06CH11357.
† kwootton@anl.gov

Content from this work may be used under the terms of the CC-BY-4.0 licence (© 2023). Any distribution of this work must maintain attribution to the author(s), title of the work, publisher, and DOI

ISBN: 978-3-95450-236-3 ISSN: 2673-5350 doi:10.18429/JACoW-IBIC2023-WEP014



Figure 1: Polarity checker.

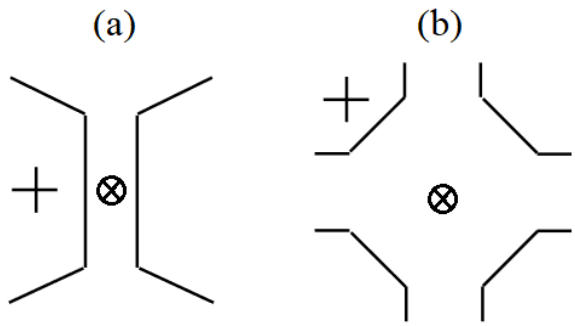


Figure 2: Pole used for measurements, and convention used to express measurement results. (a) Skew dipole, beam direction into the page. The colour of the polarity checker directed towards the left pole is indicated. (b) Normal (upright) quadrupole, beam direction into the page. The colour of the polarity checker directed towards the top-left pole is indicated.



Figure 3: BBBD1. The polarity of the left pole is denoted 'red'. The beam direction in this photograph is from right to left.

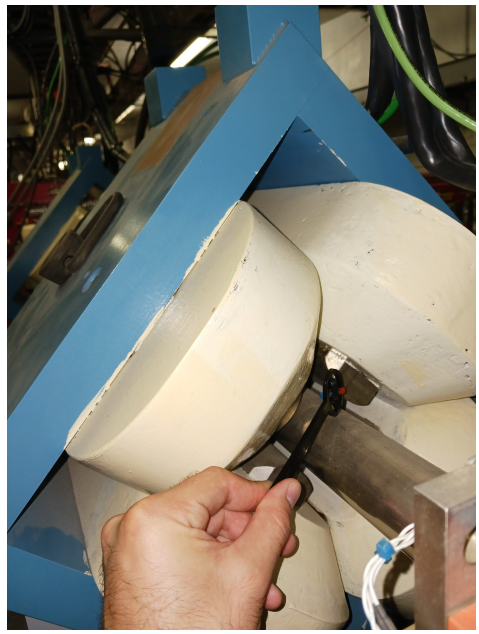


Figure 4: PTB:Q8. The polarity of the top-left pole is denoted 'blue'. The beam direction in this photograph is from right to left.

the PTB line, so that we could associate a known focussing or defocussing polarity with the existing, operational lattice of the accelerator beamline.

We see from the results of polarity measurements in Table 1 that the magnets which had previously been operated in the booster bypass (designations BB and LA) had the correct polarity, while newly installed magnets in the LEA beamline (designation LEA) did not all have the correct polarity. We used this information to correct the polarity of magnets in the LEA beamline.

16th of March, 2023

After correcting the magnet power supply lead polarities of LEA quadrupole magnets, the magnets were re-energised to reverse the remnant field of the magnets. The polarity of a subset of the above magnets (LEA magnets) was re-measured on the 16th of March, 2023. The results are summarised in Table 2. This shows that the polarity of all the quadrupoles has been corrected to match the design lattice.

DISCUSSION

From the perspective of electrical safety, we think this might be the safest way to perform a magnet polarity test. The time required to perform each test was minimal: a few seconds at most per magnet. It took longer to record the result of the measurement than perform the test.

We had expected that remnant field of the magnet may be relatively short-lived. Instead, we found that the remnant magnetisation is comparatively long-lived.

We demonstrated this procedure using magnets as part of the Linac Extension Area beamline. The procedure was

Content from this work may be used under the terms of the CC-BY-4.0 licence (© 2023). Any distribution of this work must maintain attribution to the author(s), title of the work, publisher, and DOI

ISBN: 978-3-95450-236-3 ISSN: 2673-5350 doi:10.18429/JACoW-IBIC2023-WEP014

Content from this work may be used under the terms of the CC-BY-4.0 licence (© 2023). Any distribution of this work must maintain attribution to the author(s), title of the work, publisher, and DOI

Table 1: Initial Magnet Polarity Measurement August 2022

Magnet	Magnet type	Polarity	
		Measured	Correct?
PTB:Q8	Q_1	Blue	Yes
PTB:Q9	Q_1	Red	Yes
BB:QE1	Q_1	Blue	Yes
BB:QE2	Q_1	Red	Yes
BB:Q1	Q_1	Blue	Yes
BB:BM:1-1	B_2	Blue	Yes
BB:BM:1-2	B_2	Blue	Yes
BB:BM:1-3	B_2	Blue	Yes
BB:BD:1	B_2	Red	Yes
BD:Q1	Q_1	Red	Yes
BB:Q2	Q_1	Red	Yes
BB:Q3	Q_1	Blue	Yes
BB:Q4	Q_1	Red	Yes
BB:BM:2-1	B_2	Red	Yes
BB:BM:2-2	B_2	Red	Yes
BB:BM:2-3	B_2	Red	Yes
BB:Q5	Q_1	Blue	Yes
BB:Q6	Q_1	Red	Yes
LA:Q1	Q_1	Blue	Yes
LA:Q2	Q_1	Red	Yes
LEA:Q1	Q_1	Blue	Yes
LEA:Q2	Q_1	Red	Yes
LEA:Q3	Q_1	Red	No
LEA:Q4	Q_1	Red	No
LEA:Q5	Q_1	Blue	No
LEA:Q6	Q_1	Red	No
LEA:Q7	Q_1	Red	Yes
LEA:BD	B_2	Red	Yes

Table 2: Subsequent Magnet Polarity Measurement March 2023

Magnet	Magnet type	Polarity	
		Measured	Correct?
LEA:Q1	Q_1	Blue	Yes
LEA:Q2	Q_1	Red	Yes
LEA:Q3	Q_1	Blue	Yes
LEA:Q4	Q_1	Blue	Yes
LEA:Q5	Q_1	Red	Yes
LEA:Q6	Q_1	Blue	Yes
LEA:Q7	Q_1	Red	Yes
LEA:BD	B_2	Red	Yes

useful in identifying magnets with incorrect power supply polarity, which was corrected.

Alternative schemes such as connecting a small laboratory power supply that is capable of providing current and voltage output so low as to be considered electrically safe was also considered as a different technique. However we consider that such an approach has the potential to introduce new measurement errors, because the supply has to be connected with the correct polarity.

We have tested this method using magnets powered by single unipolar magnet power supplies. Future work could include testing this technique for magnets wound with multiple power supplies (for instance, a quadrupole with additional horizontal and vertical corrector trims). Whether corrector power supplies are able to generate sufficient field to cancel the remnant magnetisation of the main magnetic circuit is probably a detail that depends on the implementation of individual magnet designs.

SUMMARY

We present a step-by-step procedure to test the polarity of magnets installed with their associated power supply off. By exciting the magnet briefly, we propose putting the magnet on its hysteresis curve, and observing the polarity of the excitation using the remnant magnetic field. This procedure allows someone to approach and measure a magnet without electrical hazards.

ACKNOWLEDGEMENTS

The submitted manuscript has been created by UChicago Argonne, LLC, Operator of Argonne National Laboratory ("Argonne"). Argonne, a U.S. Department of Energy Office of Science Laboratory, is operated under Contract No. DE-AC02-06CH11357. The U.S. Government retains for itself, and others acting on its behalf, a paid-up nonexclusive, irrevocable worldwide license in said article to reproduce, prepare derivative works, distribute copies to the public, and perform publicly and display publicly, by or on behalf of the Government. The Department of Energy will provide public access to these results of federally sponsored research in accordance with the DOE Public Access Plan. http://energy.gov/downloads/doe-public-access-plan

REFERENCES

[1] A. Nadji, "Commissioning of an Accelerator: Tools and Management", in *Proc. 11th European Particle Accelerator Conf. (EPAC'08)*, Genoa, Italy, Jun. 2008, paper WEZG02, pp. 1926–1930.

[2] J. Galambos, "Commissioning strategies and methods", CERN, Geneva, Switzerland, Rep. CERN-2013-001, Mar. 2013. doi:10.5170/CERN-2013-001.465

[3] S. M. Liuzzo, N. Carmignani, A. Franchi, T. Perron, K. B. Scheidt, E. Taurel, L. Torino, and S. M. White, "Preparation of the EBS beam commissioning", *J. Phys.: Conf. Ser.*, vol. 1350, pp. 012022, 2019. doi:10.1088/1742-6596/1350/1/012022

ISBN: 978-3-95450-236-3 ISSN: 2673-5350 doi:10.18429/JACoW-IBIC2023-WEP014

[4] S. Tepikian *et al.*, "SNS Ring and Transport System Magnet Acceptance and Installation Preparation", in *Proc. 2003 Particle Accelerator Conf.*, Portland, OR, USA, May 2003, paper WPPE033, pp. 2390–2392. doi:10.1109/PAC.2003.1289130

[5] A. Hillman, private communication, Oct. 2016.

[6] M. Buzio *et al.*, "Checking the Polarity of Superconducting Multipole LHC Magnets", *IEEE Trans. Appl. Supercond.*, vol. 16, no. 2, pp. 1391–1394, June 2006. doi:10.1109/TASC.2005.864490.

[7] L. Bottura, M. Buzio, P. Galbraith, A. Masi, F. Thierry and A. Tikhov, "Design and Implementation of an Automated Polarity Checker for Superconducting Magnets", in *Proc. 2006 IEEE Instrum. Meas. Technol. Conf.*, Sorrento, Italy, 2006, pp. 55–60. doi:10.1109/IMTC.2006.328173

[8] P. F. Tavares *et al.*, "Commissioning of the Max IV Light Source", in *Proc. NAPAC'16*, Chicago, IL, USA, Oct. 2016, paper TUB3IO01, pp. 439–444. doi:10.18429/JACoW-NAPAC2016-TUB3IO01

[9] M. Eriksson *et al.*, "Commissioning of the MAX IV Light Source", in *Proc. IPAC'16*, Busan, Korea, May 2016, pp. 11–15. doi:10.18429/JACoW-IPAC2016-MOYAA01

[10] T. Otto, "Risks and Hazards of Particle Accelerator Technologies", in *Safety for Particle Accelerators*, Springer, Cham, Switzerland, 2021, pp. 5–54. doi:10.1007/978-3-030-57031-6_2

Content from this work may be used under the terms of the CC-BY-4.0 licence (© 2023). Any distribution of this work must maintain attribution to the author(s), title of the work, publisher, and DOI

ISBN: 978-3-95450-236-3 ISSN: 2673-5350 doi:10.18429/JACoW-IBIC2023-WEP015

SYNCHROTRON LIGHT MONITOR FOR THE ADVANCED PHOTON SOURCE BOOSTER SYNCHROTRON*

K. P. Wootton†, W. J. Berg, W. P. Burns III, J. R. Calvey, J. C. Dooling, L. Erwin, A. H. Lumpkin, N. S. Sereno, S. Shoaf, S. G. Wang, Argonne National Laboratory, Lemont, IL, USA

Abstract

A new synchrotron light monitor has been tested for the booster synchrotron of the Advanced Photon Source. Visible light synchrotron radiation is collected by a mirror on a path tangential to the electron beam orbit, and directed to an optical imaging system and camera. This is planned to be a non-intercepting, transverse beam-size monitor even with the higher stored beam charges (~17 nC) needed for the Advanced Photon Source Upgrade. In the present work, we describe the present synchrotron radiation diagnostic layout. An analysis of the synchrotron radiation power on the mirror, the optical layout with components, and features of the control system will be presented.

INTRODUCTION

Synchrotron radiation (SR) presents a significant thermal load on components in electron storage rings. As such, typically absorbers are designed with an inclined profile, and composed of a metallic material such as copper, to conduct heat away from the surface.

The motivation for the present work is to enable accurate measurement of beam properties during high-charge studies of the booster synchrotron for the Advanced Photon Source Upgrade (APS-U) [1, 2]. During those studies, it appears that the support for the mirror that reflects SR out of the vacuum deflects under thermal load from SR [3].

In the present work, we calculate the heat load on the mirror of the booster synchrotron photon monitor at the Advanced Photon Source (APS). We present the details of the mirror design. We summarise stability results using the diagnostic.

BACKGROUND

The beam profile monitors are required to support beam size measurements of the electron beam in the booster. Three photon ports are available for use as synchrotron light photon monitors in the booster [4–7]. Previously, only two ports had been instrumented. Under thermal loading, components of the assembly supporting the mirror in these ports expanded under thermal loading. The expansion was so significant that the image of the beam was deflected off sensors used to measure the beam transverse and longitudinal dimensions [3, 8]. Subsequently, this makes it difficult to routinely measure some properties of the electron beam such as emittance and energy spread.

* Work supported by the U.S. Department of Energy, Office of Science, Office of Basic Energy Sciences, under Contract No. DE-AC02-06CH11357.
† kwootton@anl.gov

To support physics goals of measuring the emittance in the booster, we propose to instrument all three photon monitors. The position of the beam image on the beam profile monitors needs to remain within a small enough displacement from nominal that it does not move off laterally the imaging and diagnostic devices.

SR POWER ON THE MIRROR

For an electron beam, the vertical distribution of SR power $\frac{dP}{d\Omega}$ in units of $\left[\mathrm{W\,mrad^{-2}}\right]$ is calculated by [9]:

$$\frac{dP}{d\Omega} = 5.42E^4BI_b\frac{1}{\left(1+\gamma^2\psi^2\right)^{5/2}}\left[1+\frac{5\gamma^2\psi^2}{7\left(1+\gamma^2\psi^2\right)}\right], \quad (1)$$

where E is in units of [GeV], B is in units of [T], I_b is in units of [A], γ is the Lorentz factor, and ψ is the vertical angle in units of [rad].

The peak power density (on-axis) $\frac{dP}{d\Omega}$ in units of $\left[\mathrm{W\,mrad^{-2}}\right]$ is given by [9]:

$$\frac{dP}{d\Omega} = 5.42E^4BI_b. \quad (2)$$

Integrating over the vertical angle, the power density in the horizontal direction $\frac{dP}{d\Omega}$ in units of $\left[\mathrm{W\,mrad^{-1}}\right]$ is given by [9]:

$$\frac{dP}{d\Omega} = 4.22E^3BI_b. \quad (3)$$

Calculation

We propose to perform a piecewise integration of the SR power, at intervals of 1 ms. Parameters used in the present calculation are summarised in Table 1. These parameters are approximate, and close to the nominal booster ramp [10–12].

Table 1: Booster and Electron Beam Parameters

Parameter	Symbol	Value	Ref.
Booster circumference	C	368 m	[1]
Charge	q	17 nC	[2]
Beam current	I_b	13.9 mA	…
SR source to mirror	d	2.85 m	…
Bending radius	ρ	33.3 m	[13]
Energy at injection	E_i	425 MeV	…
Energy at extraction	E_e	7.1 GeV	…
Ramp time (E_i-E_e)	t_r	0.25 s	…
Booster period	T_B	1.0 s	…
Photon port width	w	60 mm	…
Photon port height	h	37 mm	…

Content from this work may be used under the terms of the CC-BY-4.0 licence (© 2023). Any distribution of this work must maintain attribution to the author(s), title of the work, publisher, and DOI

ISBN: 978-3-95450-236-3 ISSN: 2673-5350 doi:10.18429/JACoW-IBIC2023-WEP015

Results

Figure 1 shows the profile of electron beam energy as a function of time during the ramp, using the parameters given in Table 1. In Fig. 2, we plot the profile of the magnetic field with the time during the ramp.

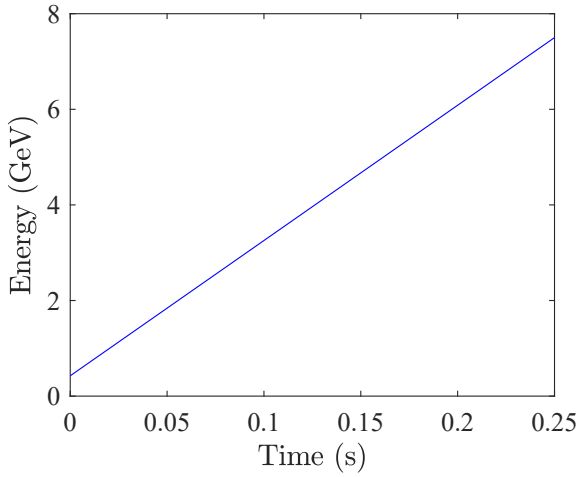


Figure 1: Beam energy as a function of time.

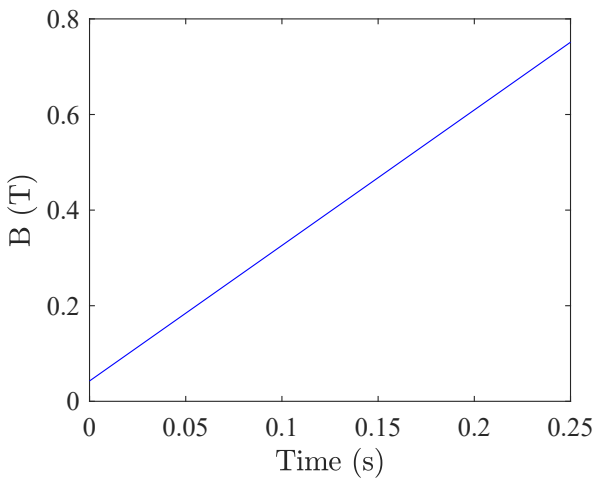


Figure 2: Magnetic field as a function of time.

Using Eq. (1), in Fig. 3 we plot the SR power as a function of both time during the ramp and vertical position at the location of the mirror.

Using Eq. (2), we plot the peak SR power density (on-axis) as a function of time during the booster ramp. We see that the dependence of SR power on the beam energy to the fourth power results in power deposition principally at the highest beam energies in the ramp.

Using Eq. (3), we calculate the SR power integrated over the full vertical fan, as a function of time. This is presented in Fig. 4.

Using the trapezoidal rule, we numerically integrate the power in Fig. 4, which gives 0.783 W mrad^{-1} (per unit horizontal bending angle). We can calculate the horizontal

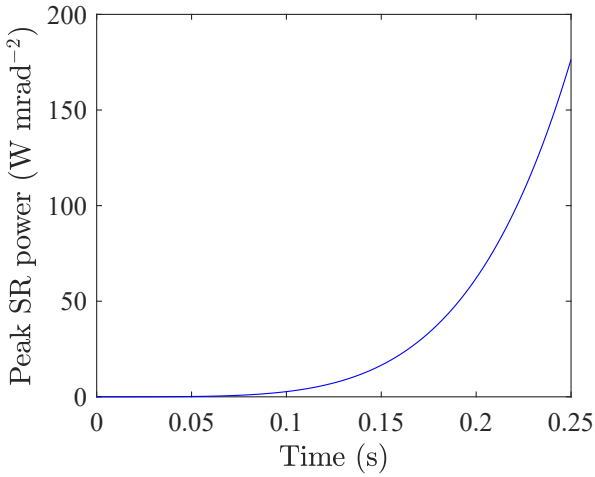


Figure 3: Peak SR power (Eq. (2)) as a function of time during the booster ramp. Essentially, this is equivalent to a line profile through Fig. 5 at vertical position = 0 mm (the orbit plane of the beam).

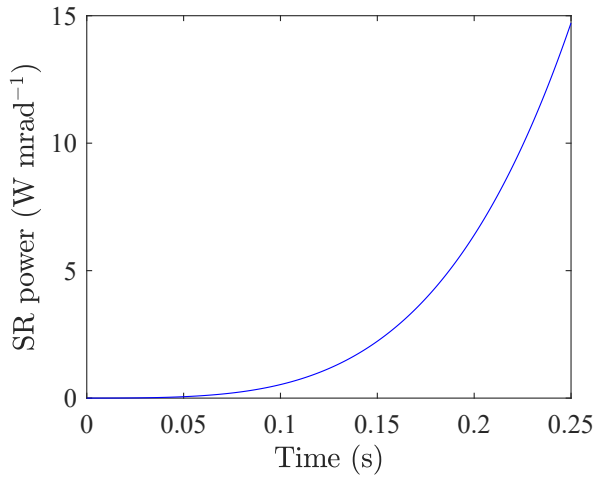


Figure 4: Total SR power on the mirror (Eq. (3)) as a function of time during the booster ramp.

angular size of the photon port as w/d = 21.1 mrad. Hence using the product of the two, we can calculate the total power on the chamber during the ramp to be 16.5 W (across the whole width of the photon port). This is the power that would occur if the booster always had beam (duty factor of 1). However, the duty factor is necessarily reduced, to accommodate ramping of the booster magnets, and stacking in the upstream Particle Accumulator Ring. Hence, we define a duty factor as t_r/T_B = 0.25. Hence the time-averaged SR power across the photon port is 4.1 W.

PROFILE MONITOR LAYOUT

The beam profile monitor optical path and principal components are illustrated schematically in Fig. 6.

Content from this work may be used under the terms of the CC-BY-4.0 licence (© 2023). Any distribution of this work must maintain attribution to the author(s), title of the work, publisher, and DOI

ISBN: 978-3-95450-236-3 ISSN: 2673-5350 doi:10.18429/JACoW-IBIC2023-WEP015

Content from this work may be used under the terms of the CC-BY-4.0 licence (© 2023). Any distribution of this work must maintain attribution to the author(s), title of the work, publisher, and DOI

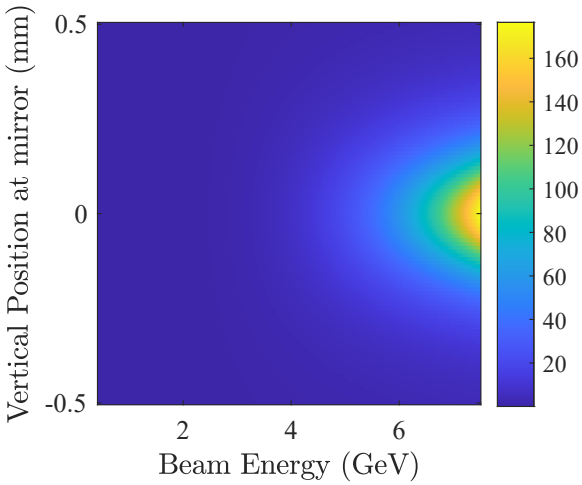


Figure 5: SR power distributed as a function of both time during the ramp and vertical position at the location of the mirror (Eq. (1)).

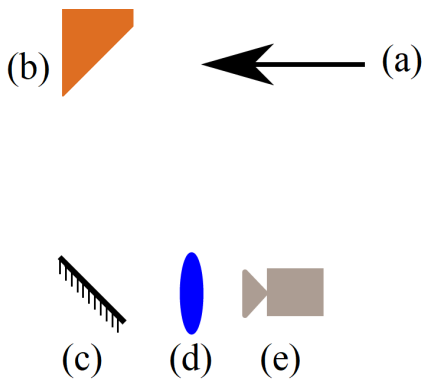


Figure 6: Schematic of beam profile monitor in the booster ring. (a) SR from electron beam. (b) Glidcop mirror. (c) Out-of-vacuum mirror. (d) Motorised zoom-focus lens. (e) Digital camera.

Components of the beam profile monitor are located physically within the booster synchrotron enclosure, which is illustrated in Fig. 7.

Mirror

Since the average SR beam power on the mirror was small (4.1 W), we endeavoured to improve imaging stability using a rigid mirror assembly composed of a bulk material. Glidcop was selected as the mirror substrate material.

The mirror was fabricated and polished in-house. The mirror substrate was cut and then polished using Loose Abrasive Polishing (lapping) to achieve the desired mirror surface finish. The mirror surface was specified as 60-40 scratch-dig, and a flatness error of 1λ. The mirror geometry is illustrated in Fig. 8.

For polishing, lapping was performed in several stages. The Glidcop Mirror and polishing fixture assembly were mounted in a precision vice on an Okamoto surface grinder

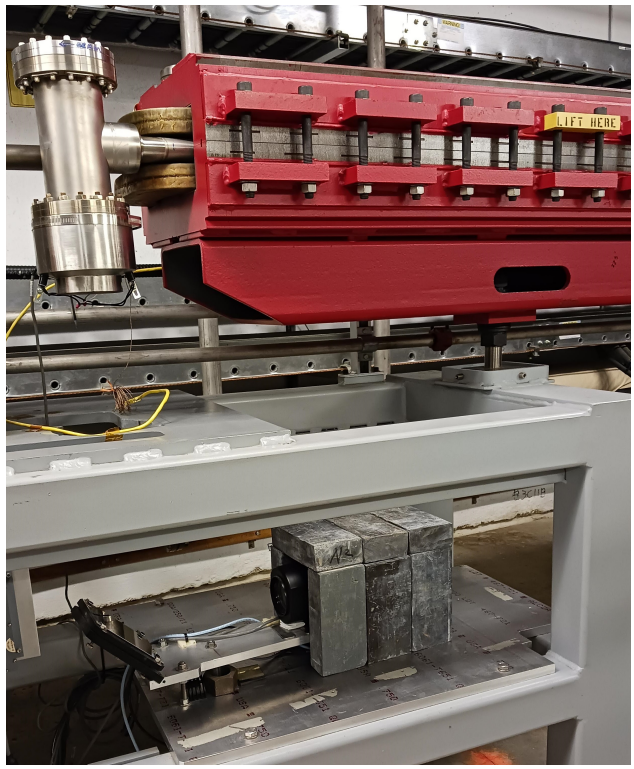


Figure 7: Photograph of beam profile monitor in the booster ring.

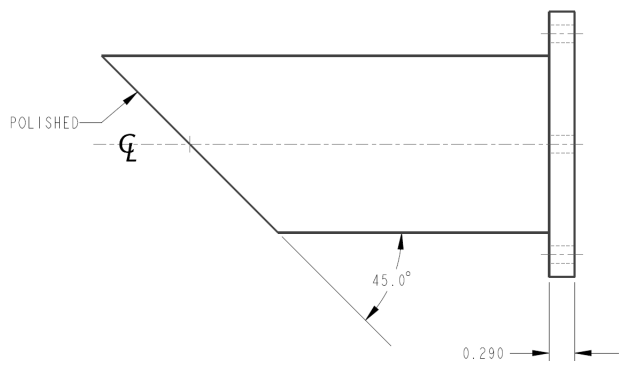


Figure 8: Mirror geometry.

(Fig. 9). The finished polished mirror is illustrated in Fig. 10.

IMAGE STABILITY

The principal goal of this mirror was to improve the image stability under an increased thermal load. We have tested the mirror performance in machine studies. For the existing synchrotron light monitors (denoted 1 & 2), lateral drift in the image position is observed as the mirrors distort under thermal loading from SR [3].

The most demanding beam condition under which we have tested the mirror is a 5 nC beam charge at 2 Hz repetition rate. This represents an average SR power on the mirror of 2.4 W, which is representative compared to the design of 4.1 W. We seek to evaluate the performance of the mirror

ISBN: 978-3-95450-236-3 ISSN: 2673-5350 doi:10.18429/JACoW-IBIC2023-WEP015

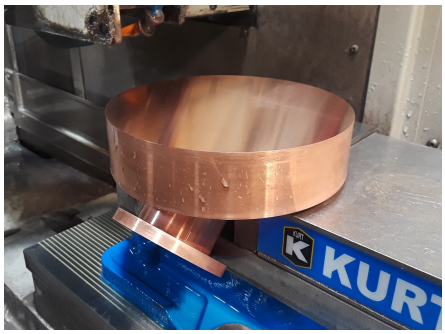


Figure 9: Photograph of the mirror and polishing fixture during machine lapping.

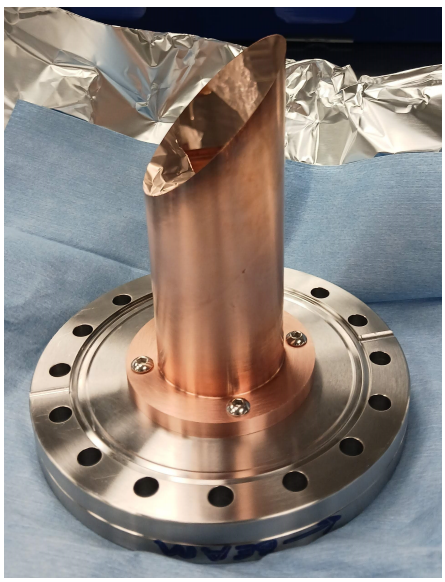


Figure 10: Finished mirror after final polishing.

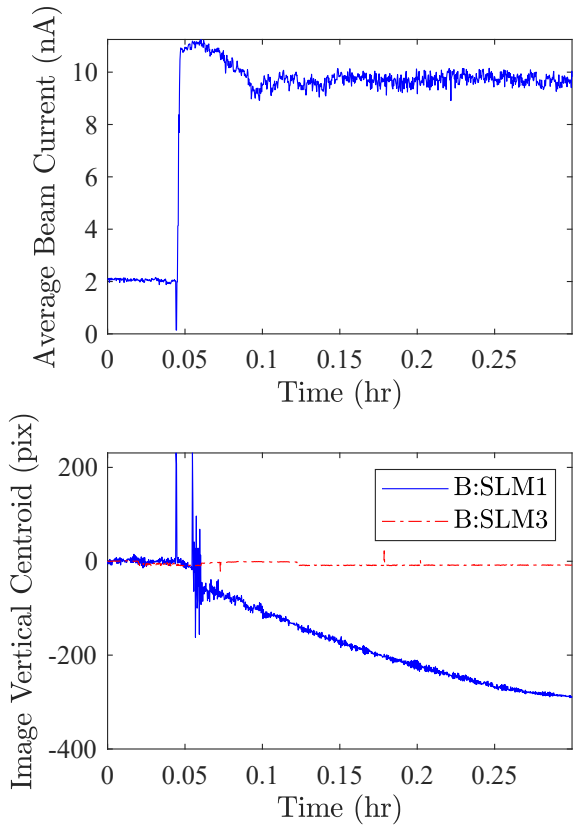


Figure 11: Electron beam image centroid position measured using two synchrotron light monitors. Over a 15 minute period, the centroid position on the old mirror (B:SLM1) drifts significantly, while there is no measurable drift observed for the new mirror design (B:SLM3).

stability under thermal load. We observed the electron beam simultaneously using two synchrotron light monitors: an existing synchrotron light monitor (B:SLM1) and this new monitor using a new mirror (B:SLM3). The motion of the beam image on both monitors is illustrated in Fig. 11.

SUMMARY

We have specified, designed and fabricated a mirror to observe and image visible synchrotron light from the booster synchrotron at the APS. We have calculated the SR power on mirror under anticipated beam conditions for APS-U operations, giving a maximum SR power on the mirror of 4.1 W. The mirror was fabricated and installed in the booster. We have tested the mirror under representative thermal loading and find that the mirror achieves the primary objective of stably transporting the SR power without measurable distortion.

ACKNOWLEDGEMENTS

The submitted manuscript has been created by UChicago Argonne, LLC, Operator of Argonne National Laboratory ("Argonne"). Argonne, a U.S. Department of Energy Office of Science Laboratory, is operated under Contract No. DE-AC02-06CH11357. The U.S. Government retains for itself, and others acting on its behalf, a paid-up nonexclusive, irrevocable worldwide license in said article to reproduce, prepare derivative works, distribute copies to the public, and perform publicly and display publicly, by or on behalf of the Government. The Department of Energy will provide public access to these results of federally sponsored research in accordance with the DOE Public Access Plan. http://energy.gov/downloads/doe-public-access-plan

REFERENCES

[1] J. R. Calvey, M. Borland, K. C. Harkay, R. R. Lindberg, and C. Yao, "Simulations of Booster Injection Efficiency for the APS-Upgrade," in *Proc. NAPAC'16*, Chicago, IL, USA, Oct. 2016, pp. 647–650. doi:10.18429/JACoW-NAPAC2016-WEA1CO03

[2] K.C. Harkay *et al.*, "High-Charge Injector for on-Axis Injection Into A High-Performance Storage Ring Light Source," in *Proc. IPAC'19*, Mel-

Content from this work may be used under the terms of the CC-BY-4.0 licence (© 2023). Any distribution of this work must maintain attribution to the author(s), title of the work, publisher, and DOI

ISBN: 978-3-95450-236-3 ISSN: 2673-5350 doi:10.18429/JACoW-IBIC2023-WEP015

bourne, Australia, May 2019, pp. 3423–3426. doi:10.18429/JACoW-IPAC2019-THYYPLM3

[3] J. C. Dooling, W. Berg, J. R. Calvey, K. C. Harkay, and K. P. Wootton, "Measurements of Bunch Length in the Advanced Photon Source Booster Synchrotron", in *Proc. NAPAC'22*, Albuquerque, NM, USA, Aug. 2022, pp. 394–397. doi:10.18429/JACoW-NAPAC2022-TUPA22

[4] B. Yang, A.H. Lumpkin, "The Planned Photon Diagnostics Beamlines at the Advanced Photon Source", *AIP Conf. Proc.*, vol. 333, no. 1, pp. 252–258, May 1995. doi:10.1063/1.48048

[5] B.X. Yang, A.H. Lumpkin, M. Borland, K. Harkay, and A. Nassiri, "Characterization of Beam Dynamics in the APS Injector Rings Using Time-Resolved Imaging Techniques", in *Proc. PAC'97*, Vancouver, Canada, May 1997, paper 5P040, pp. 2052–2054. https://jacow.org/pac97/papers/pdf/5P040.PDF

[6] A. Lumpkin and B. Yang, "Status of the Synchrotron Radiation Monitors for the APS Facility Rings", in *Proc. PAC'95*, Dallas, TX, USA, May 1995, paper MPQ09, pp. 2470–2472. https://jacow.org/p95/ARTICLES/MPQ/MPQ09.PDF

[7] A. Lumpkin *et al.*, "Initial Diagnostics Commissioning Results for the Advanced Photon Source (APS)", in *Proc. PAC'95*, Dallas, TX, USA, May 1995, paper MPQ10, pp. 2473–2475. https://jacow.org/p95/ARTICLES/MPQ/MPQ10.PDF

[8] J.C. Dooling, J.R. Calvey, K.C. Harkay, private communication, Jan. 2022.

[9] R.P. Walker, "Synchrotron radiation," CAS - CERN Accelerator School: 5th General Accelerator Physics Course (7-18 Sep. 1992, Jyväskylä, Finland), Technical Report CERN-94-01, pp. 437-459, 1994. doi:10.5170/CERN-1994-001.437

[10] S.V. Milton, J.A. Carwardine, "Ramp Tuning of the APS Booster Synchrotron Magnet Power Supplies," in *Proc. PAC'95*, Dallas, TX, USA, May 1995, paper RPQ18, pp. 2708–2710. https://jacow.org/p95/ARTICLES/RPQ/RPQ18.PDF

[11] J.A. Carwardine, S.V. Milton, D.G. McGhee, "Performance of the Ramping Power Supplies for the APS Booster Synchrotron," in *Proc. PAC'95*, Dallas, TX, USA, May 1995, paper RPP03, pp. 1967–1969. https://jacow.org/p95/ARTICLES/RPP/RPP03.PDF

[12] C.-Y. Yao, B. Deriy, G. Feng, H. Shang, and J. Wang, "Upgrade of the APS Booster Synchrotron Magnet Ramp," in *Proc. PAC'11*, New York, NY, USA, Mar.-Apr. 2011, paper TUP190, pp. 1181–1183. https://jacow.org/PAC2011/papers/TUP190.pdf

[13] B. Yang, private communication, Jan. 1998.

Content from this work may be used under the terms of the CC-BY-4.0 licence (© 2023). Any distribution of this work must maintain attribution to the author(s), title of the work, publisher, and DOI

ISBN: 978-3-95450-236-3 ISSN: 2673-5350 doi:10.18429/JACoW-IBIC2023-WEP016

BEAMLINE FOR TIME DOMAIN PHOTON DIAGNOSTICS AT THE ADVANCED PHOTON SOURCE UPGRADE*

K. P. Wootton†, W. Cheng, G. Decker, N. S. Sereno, F. Westferro
Argonne National Laboratory, Lemont, IL, USA

Abstract

Time domain photon diagnostics are proposed for electron beam characterisation and operation of the Advanced Photon Source Upgrade storage ring. In the present work, we present updated status on the time-domain X-ray and visible photon diagnostic beamline for the Advanced Photon Source Upgrade. We outline design influences leading to the proposed beamline layout, in particular long-term maintenance and commonality with other beamlines at the Advanced Photon Source.

INTRODUCTION

The Advanced Photon Source Upgrade (APS-U) project is presently underway, with the goal of increasing the brilliance of photon beams to user beamlines at the Advanced Photon Source (APS) [1–3]. A number of user programs take advantage of the fill pattern for time-resolved X-ray techniques. As these user programs are anticipated to continue during APS-U operations, we are providing temporal photon beam diagnostics for the optimisation and diagnostics of accelerator operations.

In the present work, we present updated status on the time-domain X-ray and visible photon diagnostic beamline at 35-BM for the APS-U. We outline design influences leading to the proposed beamline layout, in particular long-term maintenance and commonality with other beamlines at the APS.

DESIGN INFLUENCES

The beamline layout has matured through the design process, with subtle but notable changes since our previous work on this beamline [4]. In particular, we have made a concerted effort to utilise components standardised across APS-U bending magnet front ends and beamlines to the greatest extent possible.

For the APS, the 35-BM front-end and beamline employed a geometry optimised for providing multiple independent photon beams for diagnostics [5, 6]. The beamline featured three branch lines (X-ray, visible, X-ray) separated horizontally in angle from the bending magnet source. The visible light beamline passed a large vertical angular acceptance of ±2.9 mrad (Fig. 1). Several practical constraints steered us away from adopting the existing 35-BM geometry directly for APS-U.

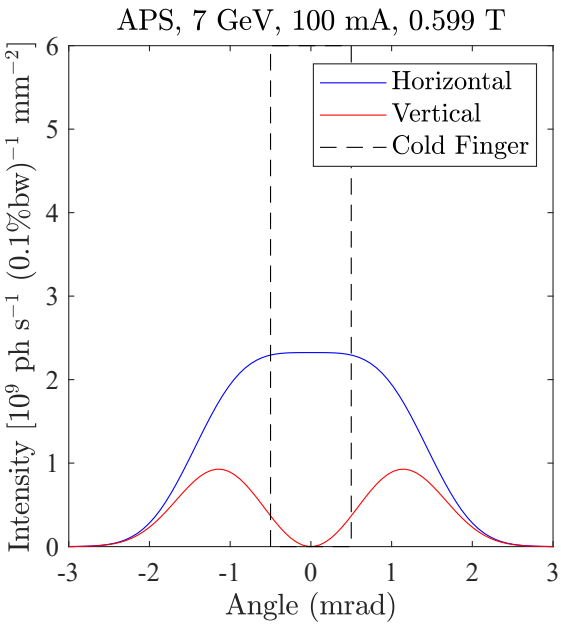


Figure 1: Vertical profile of bending magnet synchrotron radiation accepted by 35-BM for APS storage ring. The cold finger masks synchrotron radiation over the central ±0.5 mrad.

It is envisaged that two diagnostic beamlines will be operated for routine beam diagnostics measurements for APS-U. Transverse beam sizes and emittances will be observed using the 38-AM bending magnet beamline [7–10]. Bunch length and bunch purity will be observed using visible light and X-ray diagnostics at the 35-BM beamline [4]. To meet the long-term need for time-domain diagnostics at 35-BM, a large vertical aperture is not strictly required for either the X-ray or visible light photon diagnostics. Hence rather than creating large vertical opening apertures in many components of the 35-BM front end, we instead start our design from the new bending magnet front end (BMFE) for user APS-U bending magnet beamlines [1]. The opening angle of visible synchrotron radiation and beamline apertures are illustrated in Fig. 2.

The choice to start from the standard user BMFE design affords us opportunities to standardise many beamline components and control equipment. We anticipate that this will be beneficial for long-term maintenance of the beamline.

FRONT END

35-BM has been operational as a diagnostic beamline at APS for many years [5, 6]. We summarise features of the

* Work supported by the U.S. Department of Energy, Office of Science, Office of Basic Energy Sciences, under Contract No. DE-AC02-06CH11357.
† kwootton@anl.gov

Content from this work may be used under the terms of the CC-BY-4.0 licence (© 2023). Any distribution of this work must maintain attribution to the author(s), title of the work, publisher, and DOI

ISBN: 978-3-95450-236-3 ISSN: 2673-5350 doi:10.18429/JACoW-IBIC2023-WEP016

Content from this work may be used under the terms of the CC-BY-4.0 licence (© 2023). Any distribution of this work must maintain attribution to the author(s), title of the work, publisher, and DOI

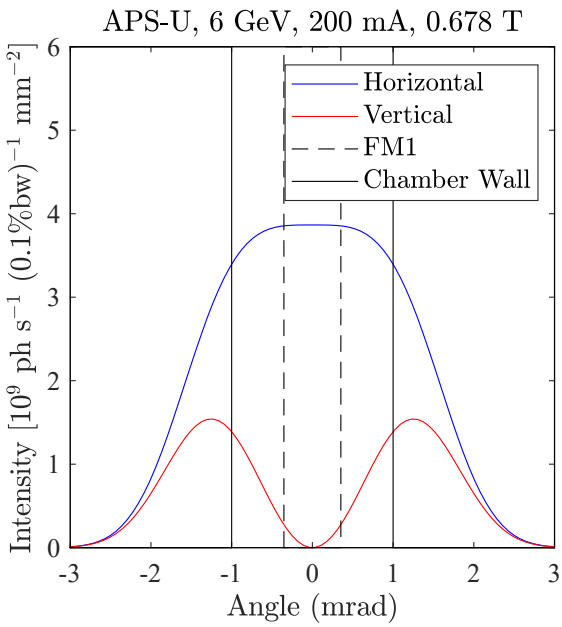


Figure 2: Vertical profile of bending magnet synchrotron radiation accepted by 35-BM for APS-U storage ring. The vacuum chamber wall blocks synchrotron radiation at angles $>\pm 1.0$ mrad. The first fixed mask (FM1) blocks synchrotron radiation at angles $>\pm 0.35$ mrad.

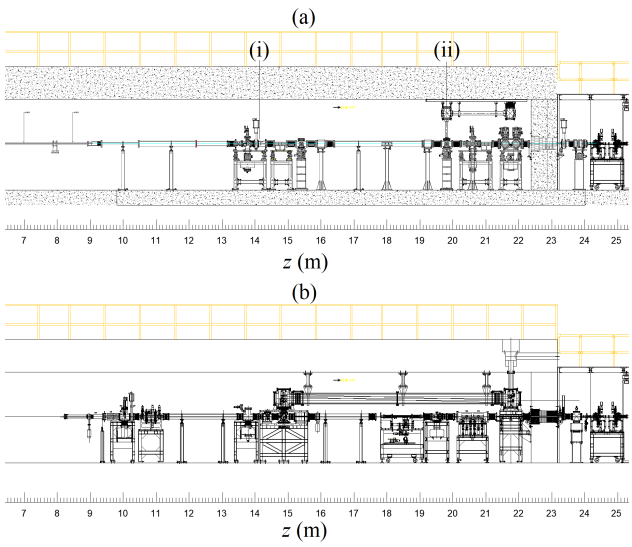


Figure 3: Comparison of 35-BM front ends for APS-U and APS. The horizontal axis z is the distance from the bending magnet source in metres. (a) Front end configuration for APS-U. (i) First Fixed Mask. (ii) Visible Light Mirror. (b) Front end configuration for APS.

front end and beamline layout for APS-U. The beamline front end for APS-U and APS is illustrated in Fig.3.

X-Ray Path

Figure 3 shows the scope of the changes to the front end for 35-BM. The standard BMFE is designed to pass X-rays through the the beamline (and protect the beamline when shutters are closed), so no changes to the standard BMFE are needed to accommodate X-ray beam transport to the shielded enclosures of 35-BM.

Visible Light Path

For visible light, two essential changes are needed to the first fixed mask (FM1) and the visible light mirror. The vertical aperture of FM1 was increased by modifying a completed FM1 assembly using wire-cut electrical discharge machining. This increases the opening angle of synchrotron radiation accepted by the beamline to $\sim\pm 0.35$ mrad. The enlarged machined aperture of FM1 is illustrated in Fig. 4.

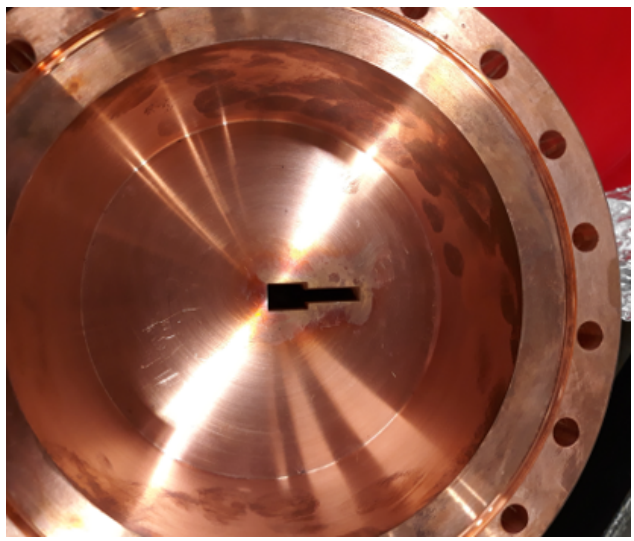


Figure 4: Machining of FM1 vertical aperture to increase the vertical aperture for visible light propagation. The narrower slot (at right) is used to pass X-rays through to the X-ray beamline enclosures. The beam direction in this figure is into the page.

A mirror inclined at 45° was used to reflect visible synchrotron radiation upwards. For APS [Fig. 3(b)], this mirror was at $z \approx 15$ m, while for APS-U [Fig. 3(a)], we position the new mirror at $z \approx 19.8$ m. This location was selected because it replaces the second X-ray Beam Position Monitor (XBPM2) in the standard BFME [1]. A water-cooled and vertically translatable stage for XBPM2 provide the required control for this optical mirror. The visible light mirror is shown installed in its vacuum chamber in Fig. 5.

Thermal analysis of the visible light mirror was performed using finite element analysis. For routine beamline operations, we intend for the mirror to sit below the orbit plane of the ring, intercepting the lower fan of visible light synchrotron radiation in a manner similar to Refs. [11, 12]. Us-

ISBN: 978-3-95450-236-3 ISSN: 2673-5350 doi:10.18429/JACoW-IBIC2023-WEP016



Figure 5: Visible light mirror. The beam direction in this figure is into the page.

ing the translatable vertical stage, the mirror can be moved completely into the beam path to intercept visible light above and below the orbit plane of the ring, however this is anticipated to be used only for dedicated machine studies with very low stored beam current.

Beyond the first mirror, visible light will be transported in air by reflecting the light using planar mirrors to the optical enclosure 35-BM-B. The optical transport is enclosed by stainless steel tubing.

BEAMLINE

The beamline layout on a standard APS sector is illustrated in Fig. 6. From the perspective of the X-ray beamline, the most significant change between the APS and APS-U machine is the lateral offset of 42 mm inboard of the new X-ray source point [1]. As a result, the new beamline centerline is 42 mm inboard of the previous beamline. Fortuitously, 35-BM features a unique shielded X-ray transport passing through the 35-BM-B hutch. The beam transport is actually two separate beam transport tubes, separated horizontally. As a result, we are able to configure the beamline to employ the inboard beam transport with minimal changes to the beamline components. Beamline components are illustrated in profile view in Fig. 7.

OUTLOOK

The principal long-term purpose of the X-ray beamline configuration is to preserve X-ray beam transport from the 35-BM-A through to 35-BM-C hutches, for use with the bunch purity monitor diagnostic [13, 14]. However the beamline can also be used as configured for an X-ray pinhole camera for beam size measurements. Four blades of white-beam slits (z = 24 m) can be closed to form a rectangular pinhole

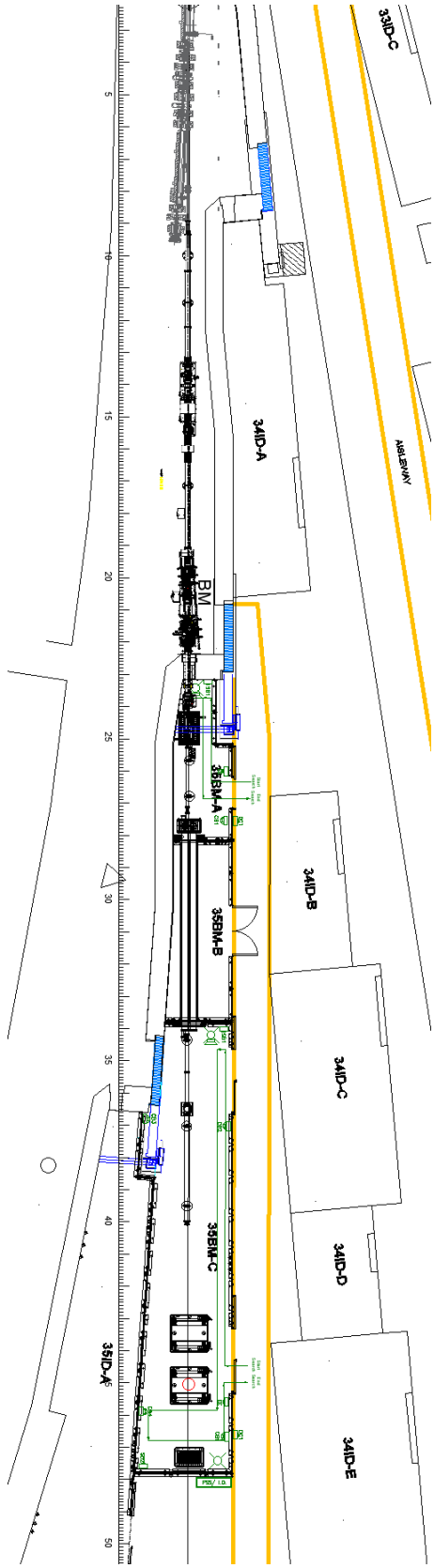


Figure 6: Illustration of 35-BM beamline layout for APS-U operations. The horizontal axis z is the distance from the bending magnet source in metres. The beam direction in this figure is from top to bottom.

Content from this work may be used under the terms of the CC-BY-4.0 licence (© 2023). Any distribution of this work must maintain attribution to the author(s), title of the work, publisher, and DOI

ISBN: 978-3-95450-236-3 ISSN: 2673-5350 doi:10.18429/JACoW-IBIC2023-WEP016

Content from this work may be used under the terms of the CC-BY-4.0 licence (© 2023). Any distribution of this work must maintain attribution to the author(s), title of the work, publisher, and DOI

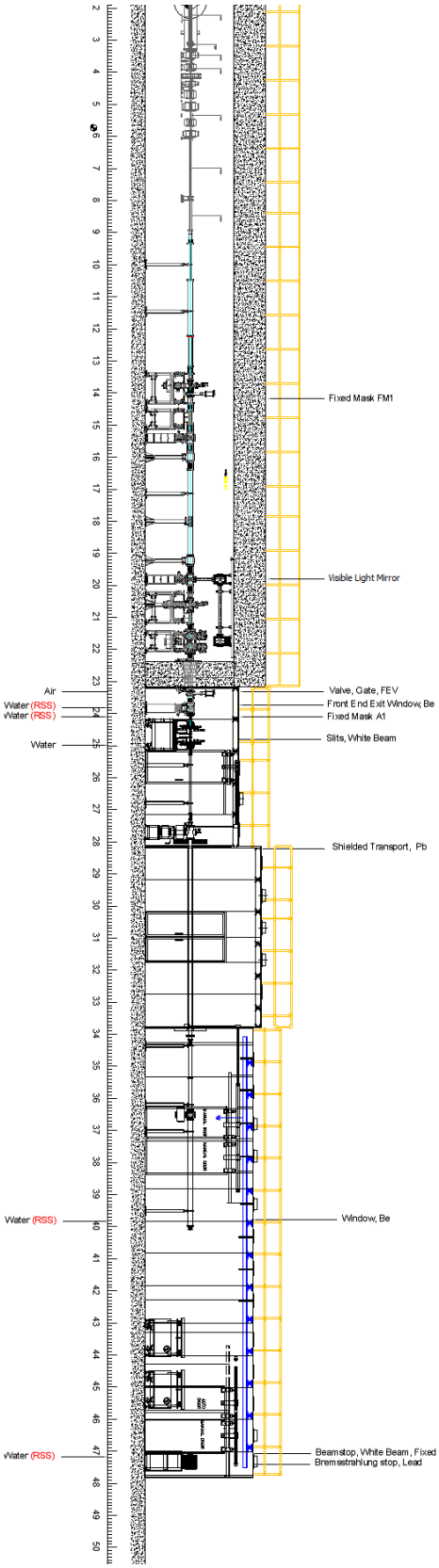


Figure 7: Illustration of 35-BM beamline profile for APS-U operations. The horizontal axis z is the distance from the bending magnet source in metres. The beam direction in this figure is from top to bottom.

aperture. A scintillator and optical microscope can be positioned near the end of the beamline ($z = 45$ m) in order to image the electron beam in the APS-U storage ring with an X-ray pinhole magnification $21/24 = 0.875$. Parameters of the electron beam and pinhole camera in the horizontal plane are summarised in Table 1.

Table 1: Pinhole Camera Parameters

Parameter	Symbol	Value
Beta function	β_x	0.84 m
Emittance	ε_x	42 pm rad
Energy spread	δ	0.156%
Dispersion	η_x	3.67 mm
Beam size (source)	σ_x	8.3 µm
Pinhole magnification	M	0.875
Beam size (scintillator)	Σ_x	7.2 µm

We anticipate that the spatial resolution needed to image an X-ray spot size of Gaussian distribution $\Sigma_x = 7.2$ µm is challenging, but not beyond technical feasibility. We anticipate that few-µm resolution may be achievable by using a 20 µm thick single-crystal scintillator such as Cerium-doped Yttrium Aluminium Garnet imaged by an optical microscope with numerical aperture between 0.4–1.0 [15].

SUMMARY

In the present work, we have presented updated status on the time-domain X-ray and visible photon diagnostic beamline for the Advanced Photon Source Upgrade. We have outlined design influences leading to the proposed beamline layout, in particular long-term maintenance and commonality with other beamlines at the Advanced Photon Source. Beyond its primary use as a time-domain diagnostic, we additionally outline potential use of the beamline to image the electron beam distribution in the horizontal plane.

ACKNOWLEDGEMENTS

The submitted manuscript has been created by UChicago Argonne, LLC, Operator of Argonne National Laboratory ("Argonne"). Argonne, a U.S. Department of Energy Office of Science Laboratory, is operated under Contract No. DE-AC02-06CH11357. The U.S. Government retains for itself, and others acting on its behalf, a paid-up nonexclusive, irrevocable worldwide license in said article to reproduce, prepare derivative works, distribute copies to the public, and perform publicly and display publicly, by or on behalf of the Government. The Department of Energy will provide public access to these results of federally sponsored research in accordance with the DOE Public Access Plan. http://energy.gov/downloads/doe-public-access-plan

REFERENCES

[1] T. E. Fornek, "Advanced Photon Source Upgrade Project Final Design Report", Argonne National Laboratory, Lemont,

ISBN: 978-3-95450-236-3 ISSN: 2673-5350 doi:10.18429/JACoW-IBIC2023-WEP016

IL, USA, Rep. APSU-2.01-RPT-003, May 2019. doi:10.2172/1543138

[2] T. E. Fornek, "Advanced Photon Source Upgrade Project Preliminary Design Report", Argonne National Laboratory, Lemont, IL, USA, Rep. APSU-2.01-RPT-002, Sep. 2017. doi:10.2172/1423830

[3] M. Borland *et al.*, "The Upgrade of the Advanced Photon Source", in *Proc. IPAC'18*, Vancouver, Canada, Apr.-May 2018, pp. 2872–2877. doi:10.18429/JACoW-IPAC2018-THXGBD1

[4] K. P. Wootton, W. X. Cheng, G. Decker, S. H. Lee, N. Sereno, and B. X. Yang, "Time Domain Photon Diagnostics for the Advanced Photon Source Upgrade", in *Proc. IBIC'21*, Pohang, Korea, Sep. 2021, pp. 356–360. doi:10.18429/JACoW-IBIC2021-WEPP02

[5] B. Yang and A. H. Lumpkin, "The Planned Photon Diagnostics Beamlines at the Advanced Photon Source", *AIP Conf. Proc.*, vol. 333, pp. 252–258, 1995. doi:10.1063/1.48048

[6] A. Lumpkin and B. Yang, "Status of the synchrotron radiation monitors for the APS facility rings", in *Proc. PAC'95*, Dallas, TX, USA, May 1995, pp. 2470–2472. https://jacow.org/p95/ARTICLES/MPQ/MPQ09.PDF

[7] B. X. Yang, S. H. Lee, J. W. Morgan, and H. Shang, "High-Energy X-Ray Pinhole Camera for High-Resolution Electron Beam Size Measurements", in *Proc. IBIC'16*, Barcelona, Spain, Sep. 2016, pp. 504–507. doi:10.18429/JACoW-IBIC2016-TUPG66

[8] B. X. Yang and S. H. Lee, "Planned x-ray diffraction diagnostics for APS Upgrade emittance measurements", presented at Topical Workshop on Emittance Measurements for Light Sources and FELs, Barcelona, Spain, Jan. 2018, unpublished.

[9] K. P. Wootton, W. X. Cheng, G. Decker, S. H. Lee, and B. X. Yang, "X-Ray Beam Size Monitor Enclosure for the Advanced Photon Source Upgrade", in *Proc. IBIC'20*, Santos, Brazil, Sep. 2020, pp. 34–36. doi:10.18429/JACoW-IBIC2020-TUPP05

[10] K. P. Wootton *et al.*, "Design of the X-Ray Beam Size Monitor for the Advanced Photon Source Upgrade", in *Proc. IPAC'21*, Campinas, Brazil, May 2021, pp. 956–959. doi:10.18429/JACoW-IPAC2021-MOPAB303

[11] J. C. Bergstrom and J. M. Vogt, "The optical diagnostic beamline at the Canadian Light Source", *Nucl. Instrum. Methods Phys. Res., Sect. A*, vol. 562, pp. 495–512, Jun. 2006. doi:10.1016/j.nima.2006.02.200

[12] M. J. Boland, R. T. Dowd, G. LeBlanc, M. J. Spencer, Y. E. Tan, and A. Walsh, "X-ray and Optical Diagnostic Beamlines at the Australian Synchrotron Storage Ring", in *Proc. EPAC'06*, Edinburgh, UK, Jun. 2006, paper THPLS002, pp. 3263–3265.

[13] W. E. Norum and B. X. Yang, "A Novel FPGA-Based Bunch Purity Monitor System at the APS Storage Ring", in *Proc. PAC'07*, Albuquerque, NM, USA, Jun. 2007, pp. 4384–4386. https://jacow.org/p07/papers/FRPMN115.pdf

[14] B. X. Yang, W. E. Norum, S. E. Shoaf, and J. B. Stevens, "Bunch-by-Bunch Diagnostics at the APS Using Time-Correlated Single-Photon Counting Techniques", in *Proc. BIW'10*, Santa Fe, NM, USA, May 2010, paper TUPSM044, pp. 238–242.

[15] T. Martin, A. Koch, "Recent developments in X-ray imaging with micrometer spatial resolution", *J. Synchrotron Radiat.*, vol. 13, pp. 180–194, Jan. 2006. doi:10.1107/S0909049506000550

Content from this work may be used under the terms of the CC-BY-4.0 licence (© 2023). Any distribution of this work must maintain attribution to the author(s), title of the work, publisher, and DOI

ISBN: 978-3-95450-236-3 ISSN: 2673-5350 doi:10.18429/JACoW-IBIC2023-WEP017

ELECTRON BEAM AT THE ADVANCED PHOTON SOURCE LINAC EXTENSION AREA BEAMLINE*

K. P. Wootton†, W. J. Berg, M. Borland, A. Brill, J. M. Byrd, S. Chitra, J. Collins, J. C. Dooling, J. Edwards, L. Erwin, G. Fystro, T. Grabinski, M. Henry, E. Heyeck, J. Hoyt, R. Keane, S.-H. Lee, J. Lenner, I. Lobach, A. H. Lumpkin, A. Puttkammer, V. Sajaev, N. S. Sereno, Y. Sun, J. Wang, S. G. Wang, A. A. Zholents, Argonne National Laboratory, Lemont, IL, USA

Abstract

The Linac Extension Area has been developed into a beamline area for testing accelerator components and techniques. Beginning commissioning activities in February 2023, we have delivered the first electron beam to the Linac Extension Area at the Advanced Photon Source at 425 MeV. In the present work, we outline the stages of re-commissioning the electron beamline. We summarise measurements of the electron beam transport through the accelerator. We outline scenarios used to verify the adequacy of radiation shielding of the beamline, and measured shielding performance.

INTRODUCTION

The Linac Extension Area (LEA) at the Advanced Photon Source (APS) is a flexible beamline for accelerator component and technique development [1–4]. Hardware installation was completed in 2023, and activities to commission the electron beamline began in 2023.

In the present work, we summarise the progress to date in commissioning the LEA beamline. We outline the features of the LEA beamline. We summarise the stages of re-commissioning. We present measurements of the electron beam using beam diagnostics in the LEA enclosure during stages of commissioning. We outline the beam loss scenarios to be performed for qualifying the enclosure shielding.

LEA BEAMLINE

The LEA beamline lattice is configured to support 'interleaving' operation [5, 6]. Interleaving describes switching between a thermionic cathode radiofrequency electron gun (TCGun) as an electron source for APS storage ring operations, and a photocathode radiofrequency electron gun (PCGun) for LEA operations. We denote the LEA beamline as the section of beamline physically located within the LEA enclosure. The LEA beamline is illustrated in Fig. 1.

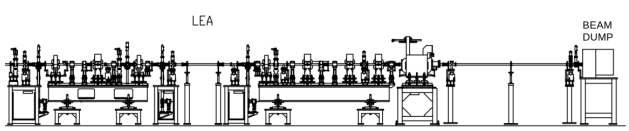


Figure 1: LEA beamline. In this figure the beam direction is from left to right.

As presently installed, the LEA beamline itself occupies ~15 m length within the LEA enclosure, terminating with an electron beam dump. A photograph of the LEA beamline is illustrated in Fig. 2.

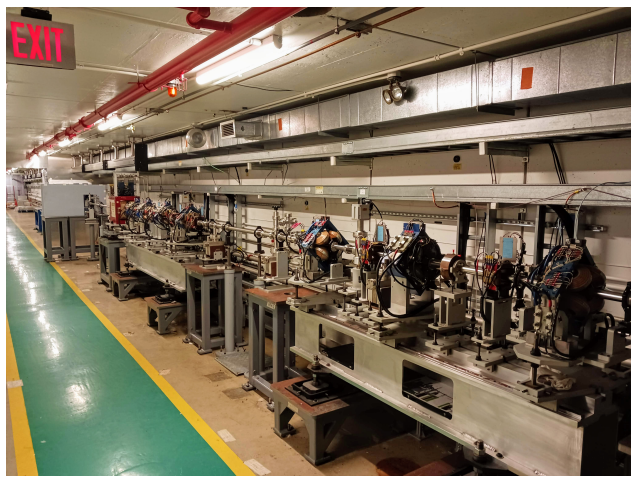


Figure 2: Photograph of the LEA beamline within the LEA enclosure. In this figure the beam direction is from right to left.

The electron beam source for LEA is the APS linac. At present, the APS linac is capable of providing electron beams with energies up to ~450 MeV. The electron beam is transported from the APS linac to the LEA enclosure by several sections of beamline, denoted as the Particle Accumulator Ring bypass (PB), the PAR-to-Booster (PTB), and the Booster Bypass (BB) transport lines. The PAR bypass and PTB have been previously used for electron beam transport, and so for commissioning the LEA beamline, the main activity needed was to establish electron beam transport through the BB and LEA beamlines. The lattice of the booster bypass and LEA beamline for 425 MeV electrons is summarised in Table 1. The magnet types XX:QX correspond to upright quadrupoles, and XX:BX to skew dipoles (vertically deflecting). Numerous horizontal and vertical correctors are also included in the beamlines, but omitted from Table 1 for readability.

STAGES OF COMMISSIONING

The principal consideration in commissioning with the electron beam is that the LEA beamline is located within the LEA enclosure. This enclosure had previously been used for the Low-Energy Undulator Test Line (LEUTL) [7–9], but it

* Work supported by the U.S. Department of Energy, Office of Science, Office of Basic Energy Sciences, under Contract No. DE-AC02-06CH11357.
† kwootton@anl.gov

Content from this work may be used under the terms of the CC-BY-4.0 licence (© 2023). Any distribution of this work must maintain attribution to the author(s), title of the work, publisher, and DOI

ISBN: 978-3-95450-236-3 ISSN: 2673-5350 doi:10.18429/JACoW-IBIC2023-WEP017

Table 1: Booster Bypass, Alcove and LEA Lattice

Element	Position s (m)	Length l (m)	Gradient
BB:QE1	20.872	0.153	4.75 T m^{-1}
BB:QE2	21.399	0.153	-5.95 T m^{-1}
BB:Q1	21.989	0.153	2.55 T m^{-1}
BB:BM:1-1	22.383	0.110	-9.36 mrad
BB:BM:1-2	22.553	0.110	-9.36 mrad
BB:BM:1-3	22.723	0.110	-9.36 mrad
BB:Q2	31.184	0.153	-1.48 T m^{-1}
BB:Q3	40.379	0.153	0.93 T m^{-1}
BB:Q4	49.574	0.153	-1.48 T m^{-1}
BB:BM:2-1	57.993	0.110	9.36 mrad
BB:BM:2-2	58.163	0.110	9.36 mrad
BB:BM:2-3	58.333	0.110	9.36 mrad
BB:Q5	58.769	0.153	2.83 T m^{-1}
BB:Q6	60.642	0.153	-5.17 T m^{-1}
LA:Q1	68.045	0.153	3.05 T m^{-1}
LA:Q2	69.198	0.153	4.21 T m^{-1}
LEA:Q1	74.186	0.100	8.72 T m^{-1}
LEA:Q2	75.190	0.153	-7.61 T m^{-1}
LEA:Q3	76.112	0.100	3.90 T m^{-1}
LEA:Q4	79.053	0.100	9.07 T m^{-1}
LEA:Q5	80.004	0.153	-7.16 T m^{-1}
LEA:Q6	81.004	0.153	7.31 T m^{-1}
LEA:Q7	81.666	0.153	-5.79 T m^{-1}
LEA:BD	82.274	0.500	200 mrad

has been several years since beam was introduced to the enclosure [10]. This motivated the need for a readiness review prior to commissioning the beamline in a staged approach. Commissioning activities performed are broken into two stages: transport to the BB dump, and transport to the LEA beamline. The electron source used for these commissioning tasks was TCGun rather than the nominal PCGun. TCGun is capable of generating the greatest electron beam current and as such represents the principal radiological risk needing experimental validation.

Beam Transport to BB Dump

The BB dump is essentially located at the start of the BB transport line. This allows us to tune up beam transport through the upstream PB and PTB transport lines. Beam transport to the BB dump was established using diagnostics along the beam transport line. The principal diagnostics used in these studies were beam position monitors and beam profile monitors. The principal optimisation needed to establish beam through to the BB dump was transverse steering using corrector magnets.

Beam Transport to LEA

Transporting beam to LEA requires transporting beam through the BB and LEA beamlines. The booster bypass beamline is a vertical chicane rising in elevation by ~1 m over a length of ~40 m. Focussing quadrupoles are included within the lattice. We began beam transport by tuning the vertical bending magnets to optimise electron transport at a beam energy of 425 MeV.

BEAM MEASUREMENTS

The principal diagnostics used for this study included area radiation monitors, handheld portable radiation monitors, electron beam position monitors, beam profile monitors and beam current monitors.

The first signature of electron transport to LEA was observed using area radiation monitors. An area radiation monitor is positioned within the LEA enclosure. This was the first indication that electrons had been successfully transported. Signals were subsequently quickly observed on the beam current monitors and beam position monitors (BPMs) in the LEA enclosure. Signals on the first electron beam position monitor within the LEA enclosure are illustrated in Fig. 3.

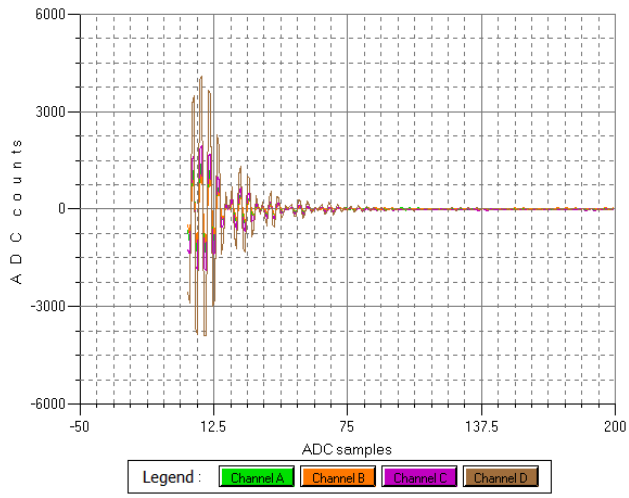


Figure 3: First observation of electron beam in the LEA enclosure measured using signals on the electron BPM.

The electron beam position was observed along the BB and LEA beamlines using all the BPMs in both transport lines. This is illustrated in Fig. 4.

With beam transported through to LEA, we were able to begin tuning up and focussing the electron beam using the beam profile monitor immediately adjacent to the electron beam dump. The visible area of the Cerium-doped Yttrium Aluminium Garnet (Ce:YAG) scintillator is 16 mm diameter. This is illustrated in Fig. 5.

BEAM LOSS SCENARIOS

A critical step in commissioning is validation of the shielding performance. At the APS, the shielding is experimentally validated using beam loss scenarios. Loss scenarios were meant to assess the radiation levels in and around the LEA enclosure under 'normal' and 'off-normal' beam conditions. It was not our intention to evaluate losses in previously commissioned transport beamlines upstream of LEA (PB, PTB, BB).

Content from this work may be used under the terms of the CC-BY-4.0 licence (© 2023). Any distribution of this work must maintain attribution to the author(s), title of the work, publisher, and DOI

ISBN: 978-3-95450-236-3 ISSN: 2673-5350 doi:10.18429/JACoW-IBIC2023-WEP017

Content from this work may be used under the terms of the CC-BY-4.0 licence (© 2023). Any distribution of this work must maintain attribution to the author(s), title of the work, publisher, and DOI

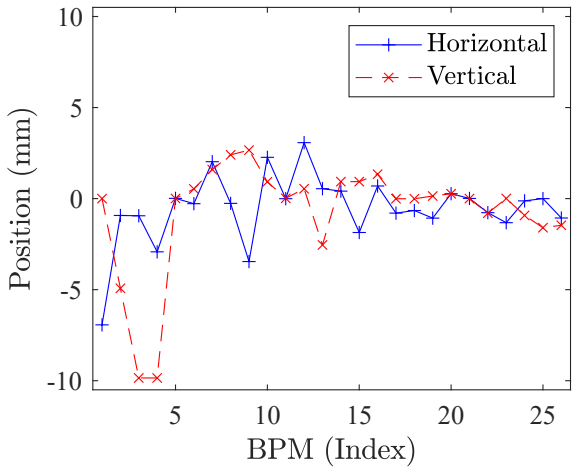


Figure 4: Beam observed using BPMs along booster bypass and LEA. In this figure, the beam trajectory is from left to right. Horizontal and vertical BPM signals are displayed. The horizontal plot axis is BPM index: the BPMs are not equally spaced along the beamline. BPMs 23-26 are the four BPMs in the LEA section of the beamline.

The loss scenarios considered included:

1. No acceleration of beam in the linac (background)
2. Beam to the LEA beam dump (nominal operations)
3. Beam strike on gate valve (GV) 1, GV1.
4. Beam strike on GV3.
5. Steering beam vertically upwards with corrector magnets.
6. Steering beam vertically downwards with corrector magnets.
7. Steering beam horizontally left with corrector magnets.
8. Steering beam horizontally right with corrector magnets.
9. Steering beam vertically upwards with corrector and quadrupole magnets.
10. Steering beam horizontally left with corrector and quadrupole magnets.
11. Steering low-energy beam vertically upwards with corrector and quadrupole magnets.

In developing these scenarios, particular attention was paid to the possibility of oversteering a low energy beam [11]. In this case, the assumed deflection would arise from a large transverse offset of the electron beam from the centerline of multiple quadrupole magnets. The maximum potential angular excursion of an electron beam was determined using simulations in the code ELEGANT [12–14].

In simulation, we considered the possibility of transporting electrons with energy as low as 25 MeV to the LEA enclosure. Using 3D field maps of the quadrupole and corrector magnets, the maximum excursion angle of the electron

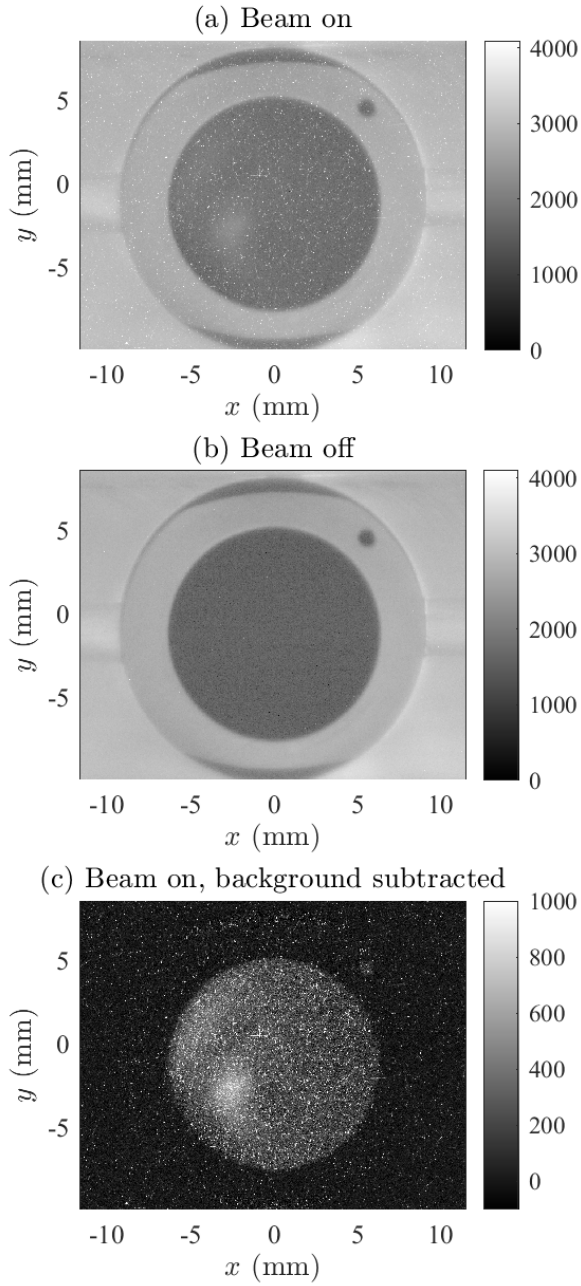


Figure 5: Observing electron beam at Ce:YAG LEA dump beam profile monitor. The top panel shows the image with the electron beam on, the middle panel shows an image with the electron beam off. The lower panel is the difference, showing the electron beam distribution.

ISBN: 978-3-95450-236-3 ISSN: 2673-5350 doi:10.18429/JACoW-IBIC2023-WEP017

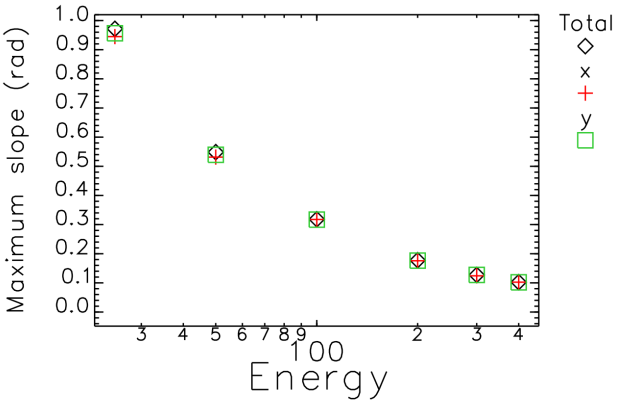


Figure 6: Calculated maximum excursion angle of electron beam at LEA [12].

beam at LEA was calculated over a range of electron beam energies 25–400 MeV. This is illustrated in Fig. 6.

Subsequently, we can use these excursion angles as input to radiological simulations. Radiological simulations of these loss scenarios were performed using MARS [15–18] and FLUKA [19, 20]. We consider several scenarios.

Normal operation of the electron beam transported to the electron beam dump is illustrated in Fig. 7. This simulations was performed assuming a 500 MeV electron beam energy, scaled to a maximum average electron beam current of 40 nA.

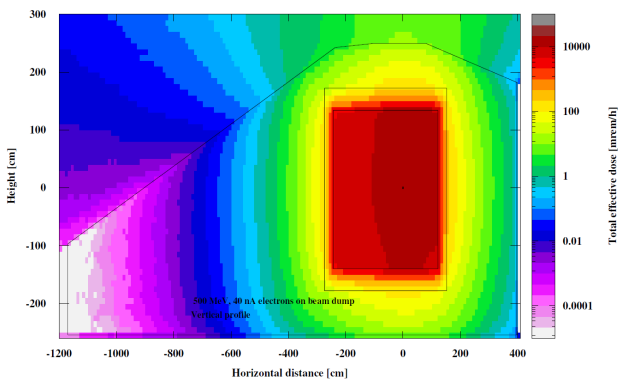


Figure 7: Radiological simulation of electron beam transport to the electron beam dump (Scenario 2) [21]. In this figure, the beam trajectory is into the page.

Maximum possible off-normal steering (vertical excursion) of the electron is illustrated in Fig. 8. This simulations was performed assuming a 300 MeV electron beam energy, scaled to a maximum average electron beam current of 40 nA.

These scenarios were developed to understand the safety consequences of proposed beam conditions. Of particular importance is that the normal operational electron beam current from the PCGun (average 2 nA) is much lower than simulated here for safety.

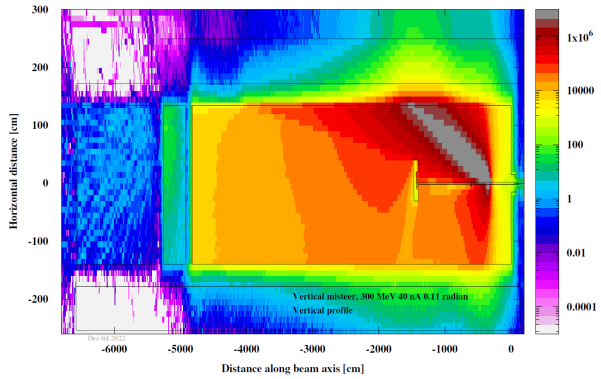


Figure 8: Radiological simulation of maximum possible off-normal electron beam vertical missteer (Scenario 9) [21]. In this figure, the beam trajectory is from right to left.

OUTLOOK

Due to schedule constraints, we were unable to complete measurement of the beam loss scenarios prior to the long shutdown of the APS accelerators to facilitate the start of installation of the Advanced Photon Source Upgrade (APS-U) storage ring. We hope to continue the commissioning process again at a future date.

SUMMARY

We have observed first electron beam to the LEA beamline at the APS. During commissioning activites, diagnostics including radiation monitors, beam position monitors, beam current monitors and beam profile monitors were usefully employed to detect and optimise the electron beam. We developed an extensive set of beam loss scenarios taking advantage of new simulation techniques, and incorporating lessons learned from previous commissioning activities. We began commissioning, but were unable to complete measurement of the beam loss scenarios prior to the long shutdown for APS-U installation.

ACKNOWLEDGEMENTS

We gratefully acknowledge the computing resources provided on Bebop, a high-performance computing cluster operated by the Laboratory Computing Resource Center at Argonne National Laboratory.

The submitted manuscript has been created by UChicago Argonne, LLC, Operator of Argonne National Laboratory ("Argonne"). Argonne, a U.S. Department of Energy Office of Science Laboratory, is operated under Contract No. DE-AC02-06CH11357. The U.S. Government retains for itself, and others acting on its behalf, a paid-up nonexclusive, irrevocable worldwide license in said article to reproduce, prepare derivative works, distribute copies to the public, and perform publicly and display publicly, by or on behalf of the Government. The Department of Energy will provide public access to these results of federally sponsored research in accordance with the DOE Public Access Plan. http://energy.gov/downloads/doe-public-access-plan

Content from this work may be used under the terms of the CC-BY-4.0 licence (© 2023). Any distribution of this work must maintain attribution to the author(s), title of the work, publisher, and DOI

ISBN: 978-3-95450-236-3 ISSN: 2673-5350 doi:10.18429/JACoW-IBIC2023-WEP017

REFERENCES

[1] Y. Sun *et al.*, "APS Linac Interleaving Operation", in *Proc. IPAC'19*, Melbourne, Australia, May 2019, pp. 1161–1163. doi:10.18429/JACoW-IPAC2019-MOPTS119

[2] W. Berg, J. C. Dooling, S. H. Lee, Y. Sun, and A. Zholents, "Development of the Linac Extension Area 450-MeV Electron Test Beam Line at the Advanced Photon Source", in *Proc. IBIC'19*, Malmö, Sweden, Sep. 2019, pp. 219–221. doi:10.18429/JACoW-IBIC2019-MOPP048

[3] K. P. Wootton *et al.*, "The Advanced Photon Source Linac Extension Area Beamline", in *Proc. NAPAC'22*, Albuquerque, NM, USA, Aug. 2022, pp. 430–432. doi:10.18429/JACoW-NAPAC2022-TUPA36

[4] E. A. Nanni *et al.*, "C^3 Demonstration Research and Development Plan", SLAC National Accelerator Laboratory, Menlo Park, CA, USA, Rep. SLAC-PUB-17660, Jul. 2022. doi:10.48550/arXiv.2203.09076

[5] S. Shin, Y. Sun, and A. Zholents, "Interleaving Lattice Design for APS Linac", in *Proc. NAPAC'16*, Chicago, IL, USA, Oct. 2016, pp. 713–715. doi:10.18429/JACoW-NAPAC2016-WEPOA12

[6] S. Shin, Y. Sun, J. Dooling, M. Borland, and A. Zholents, "Interleaving lattice for the Argonne Advanced Photon Source linac", *Phys. Rev. Accel. Beams*, vol. 21, p. 060101, 2018. doi:10.1103/PhysRevAccelBeams.21.060101

[7] M. White *et al.*, "Construction, Commissioning and Operational Experience of the Advanced Photon Source (APS) Linear Accelerator", in *Proc. LINAC'96*, Geneva, Switzerland, Aug. 1996, paper TU301, pp. 315–319. doi:10.5170/CERN-1996-007.315

[8] S. V. Milton, "Advanced Photon Source low-energy undulator test line", in *Proc. SPIE 2988*, San Jose, CA, USA, May 1997, pp. 20–27. doi:10.1117/12.274387

[9] S. V. Milton, J. N. Galayda, and E. Gluskin, "The Advanced Photon Source Low-Energy Undulator Test Line", in *Proc. PAC'97*, Vancouver, Canada, May 1997, paper 3V021, pp. 877–879. https://jacow.org/pac97/papers/pdf/3V021.PDF

[10] R. M. Lill *et al.*, "Design and Performance of the LCLS Cavity BPM System", in *Proc. PAC'07*, Albuquerque, NM, USA, Jun. 2007, paper FRPMN111, pp. 4366–4368. https://jacow.org/p07/papers/FRPMN111.pdf

[11] R. P. Fliller *et al.*, "Results of NSLS-II Linac Commissioning", in *Proc. IPAC'13*, Shanghai, China, May 2013, paper WEPWA083, pp. 2301–2303.

[12] M. Borland, private communication, Dec. 2022.

[13] M. Borland, "elegant: A flexible SDDS-compliant code for accelerator simulation", Argonne National Laboratory, Lemont, IL, USA, Rep. Advanced Photon Source LS-287, Sep. 2000. doi:10.2172/761286

[14] Y. Wang and M. Borland, "Implementation and Performance of Parallelized Elegant", in *Proc. PAC'07*, Albuquerque, NM, USA, Jun. 2007, paper THPAN095, pp. 3444–3446. https://jacow.org/p07/papers/THPAN095.pdf

[15] J. Dooling and A. A. Zholents, private communication, Jul. 2019.

[16] N. V. Mokhov, "The Mars Code System User's Guide Version 13(95)", Fermilab, Batavia, IL, USA, Rep. Fermilab-FN-628, Feb. 1995.

[17] N. V. Mokhov and S. I. Striganov, "MARS15 Overview", *AIP Conf. Proc.*, vol. 896, pp. 50–60, Mar. 2007. doi:10.1063/1.2720456

[18] N. V. Mokhov *et al.*, "MARS15 code developments driven by the intensity frontier needs", *Prog. Nucl. Sci. Technol.*, vol. 4, pp. 496–501, 2014. doi:10.15669/pnst.4.496

[19] C. Ahdida *et al.*, "New Capabilities of the FLUKA Multi-Purpose Code", *Front. Phys.*, vol. 9, p. 788253, Jan. 2022. doi:10.3389/fphy.2021.788253

[20] G. Battistoni *et al.*, "Overview of the FLUKA code", *Ann. Nucl. Energy*, vol. 82, pp. 10-–18, Aug. 2015. doi:10.1016/j.anucene.2014.11.007

[21] S. Chitra, "Radiation Shielding Analysis of LEA", unpublished.

Content from this work may be used under the terms of the CC-BY-4.0 licence (© 2023). Any distribution of this work must maintain attribution to the author(s), title of the work, publisher, and DOI

ISBN: 978-3-95450-236-3 ISSN: 2673-5350 doi:10.18429/JACoW-IBIC2023-WEP018

SIMULATION OF OSCILLATING ARM WIRE MONITOR MECHANICS DRIVEN BY A STEPPER MOTOR

R. Dölling†, Paul Scherrer Institut, Villigen, Switzerland

Abstract

The present oscillating arm wire monitors at HIPA operate with wire speeds of 0.75 m/s. Based on basic dynamic simulations of mechanics and motor, we discuss possible variants of this design using stepper motors in open loop control. The results suggest that 4 m/s can be reached with sufficient position resolution, when using a predefined step sequence customized to the mechanics. This speed should be sufficient to measure the full proton beam current in the injection line.

INTRODUCTION

The majority of profile monitors presently operating in the 0.87 MeV, 72 MeV and 590 MeV beam lines of HIPA are wire monitors using an oscillating monitor arm (MA). A fork at the MA holds the wire, foil, or finger, which is moved transversely through the beam (Fig. 1) [1, 2]. The MA is driven via a con-rod (CR) from a crank wheel (CW), which again is driven via a gear (MG) connected to a brushed DC motor. A bellow at the MA axis of rotation separates the vacuum from the in-air mechanics. Since the bellow needs to bend only ±10°, its lifetime is practically unlimited at the given maximum wire speed of 0.75 m/s. The wire position is determined by a potentiometer attached to the MA, while the home position is indicated by a home switch (HS) actuated by a cam on the CW.

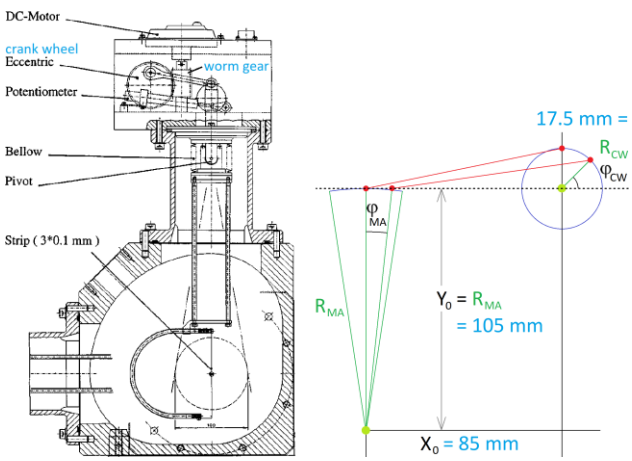


Figure 1: Present MA wire monitor. Wire crosses beam axis at $\varphi_{CW} = 90°$ and 270°. HS not shown. The monitor needs little space in beam direction. Horizontal and vertical MA are only 20 mm apart.

In the 0.87 MeV beam line and a few locations in the 72 MeV beam line, the power density at full proton beam current is too high to let the wire or foil survive at the given speed. Beam induced fluorescence monitors installed in 10 of 32 monitor locations in the 0.87 MeV line allow to measure at full beam current of 10 mA, however, with limited dynamic range. Wire monitors with at least approximately four times higher speed could be an alternative. By using a stepper motor instead of the DC motor, the potentiometer can be eliminated, and the control of the movement is simplified.

In the following we simulate the movement of variants of the present mechanics driven by stepper motors and conclude to wire speed and error of wire position caused by the motor characteristics.

MECHANICS

With the present monitor, the inertia of the 20:1 worm gear and the DC motor is high. We look at three alternatives with stepper motor and the same dimensions of CW-CR-MA connection (Fig. 1, right):

1. Only motor replaced. Worm gear reduction 20:1. The range of unidirectional CW movement is $\varphi_{CW} = 151.2°$ to 568.8°. The long travel allows a softer acceleration. Wire speed 0.75 m/s unchanged.
2. Whole mechanics replaced by a moderately less-inertia variant (Fig. 2c). No potentiometer. Spur gear reduction 3:1. Range $\varphi_{CW} = 151.2°$ to 568.8°. Wire speed 4 m/s.
3. Ditto, but gear reduction 1:1 (direct drive, Fig. 2a) and Range $\varphi_{CW} = 180°$ to 540°.

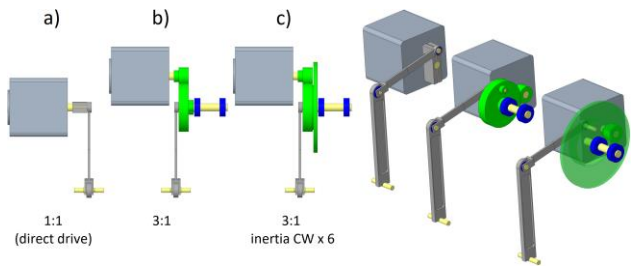


Figure 2: Lower-inertia setups (schematic).

In cases 2, 3, the wire position is determined by counting steps with respect to the HS switching positions. We assume a Baumer precision switch [3], pressed face on by the upper part of the MA. In order not to exceed the specification for the maximum approaching speed, the HS must be positioned not too far from the axis of rotation of the MA. Together with the play of the mechanism, this introduces a wire position error at beam axis of the order of 100 µm. Alternatively, the wire position can be determined by counting steps between the centres of the forward and backward measured beam profiles (if the beam has not shifted in between).

A brake is not needed. The MA is kept in the parking position against gravity by the CR, then in one line with the CW axis. Even the small holding torque of the currentless motor is sufficient for this.

† doelling@protonmail.com, rudolf.doelling@psi.ch

Content from this work may be used under the terms of the CC-BY-4.0 licence (© 2023). Any distribution of this work must maintain attribution to the author(s), title of the work, publisher, and DOI

ISBN: 978-3-95450-236-3 ISSN: 2673-5350 doi:10.18429/JACoW-IBIC2023-WEP018

SIMULATION PROCEDURE

Moments of inertia are estimated for motor, worm or spur MG or direct coupling, CW, CR and the complete MA. The masses of both halves of the CR are assumed to be concentrated in the connection points CW-CR and CR-MA. The actual MA angle is calculated from the CW angle analytically with the simplifying assumption that the connection point between CR and MA moves along the dotted line in Fig. 1 right.

The simulation is split into three runs, each done in time steps of $\Delta t = 0.2$ µs. In the first run, we define the 'preset trajectory' of the whole system by presetting over time one of the three 'input characteristics' a) rotor angular speed ω_{rot_pre}, b) rotor angular acceleration α_{rot_pre}, c) used fraction of pullout-torque $fracD_{pre}$. With the inertias, gear ratios, energy conservation (no losses are assumed in this run) and a preset dependency of pullout-torque on rotor angular speed $D_{pullout_pre}(\omega_{rot})$, from each of the three 'input characteristics' a), b), c), the other two can be derived, together with the rotor angular position φ_{rot_pre} and the actual motor torque D_{pre} over time and many other parameters.

In the second run, the time dependent angular position of stator field and stator current phase $\varphi_{stat_cur_pre}$ is calculated via the phase difference $\varphi_{tooth_pre} = \varphi_{stat_cur_pre} - \varphi_{rot_pre}$, which results from the assumed 'cosine potential' condition $fracD_{pre} = \sin(\varphi_{tooth_pre}\, n_{teeth})$, with n_{teeth} the number of teeth at the rotor. Optionally, $\varphi_{tooth_pre} = 0$ can be used instead in this step ('φ_{tooth_pre} ignored'). However, this lack of adaptation will lead to significant deviations of the resulting trajectory from the 'preset trajectory', especially if these are not smooth as, e.g., the linear ramps often used.

Furthermore, the phase shift $\varphi_{diff_induct_pre}$ between stator voltage $\varphi_{stat_volt_pre}$ and stator current $\varphi_{stat_cur_pre}$ is calculated from the actual change of current, the inductance and resistance of stator coils and 50 m cable, and the available DC voltage (of the actual needed polarity).

(In this way, also the actual motor current could be calculated, which results in a sinusoidal time dependence for high DC voltage or low rotor angular speed, and in triangular time dependence for low DC voltage or high rotor angular speed. Integrating over a half period of same sign results in a charge which depends very similar on angular rotor speed as the pullout-torque given by the manufacturer, however with significant lower DC voltages than specified. We did not use this to calculate $D_{pullout_pre}(\omega_{rot})$, but use the dependency given by the manufacturer.)

With this, we get the angular position of stator voltage $\varphi_{stat_volt_pre}$, i.e., the 'phase' set by the motor driver. It is changed not continuously, but, more realistic, only in full microsteps. To reproduce realistic driver properties, we assume that each microstep needs a minimum time of 2 µs. Further we assume $\varphi_{stat_volt_pre}$ is updated to the actual microstep only in time intervals corresponding to the pulse-width modulation (PWM) frequency $f_{PWM} = 40$ kHz of the driver.

Optionally, all microsteps corresponding to fullstep frequencies below, e.g., $f_{start,fs} = 500$ Hz can be suppressed. This resembles the fullstep start frequency of linear ramps used in many drivers.

The third run starts from the microstep sequence represented by $\varphi_{stat_volt_pre}$. To this, a phase error is added, corresponding to the error of full-step positions due to manufacturing inaccuracies of the teeth of the rotor. The error is statistically distributed to the teeth within boundaries $\varphi_{err_bound} = \pm 0.025°$. It is assumed that the error between one fullstep and the next changes linearly over half a fullstep. An offset is added to all errors to bring the error of the fullstep of the starting position to zero. In general, it is started at rest, hence this position is reached exactly.

φ_{diff_induct} is again calculated as above to get φ_{stat_cur}. From the difference φ_{tooth} to the actual φ_{rot} results the used fraction of pullout-torque $fracD = \sin(\varphi_{tooth}\, n_{teeth})$, and with the actual pullout-torque $k_{weak}\, D_{pullout}(\omega_{rot})$ we derive the torque D. Optionally, with k_{weak} different from 1, here 0.9, we account for the fact that the pullout-torque may differ from the specification.

The difference $d\varphi_{tooth}/dt$ of angular speeds of stator current ω_{stat_cur} and rotor ω_{rot} causes a viscous drag, leading to a torque $D_{loss} = h_{loss}\, d\varphi_{tooth}/dt$, which leads to a damping of eventual oscillations of the rotor angular position in the 'cosine potential' of the teeth (OICP). $h_{loss} = 0.003$ Js/rad^2 is roughly estimated from the damping of oscillations after a single step starting from rest. Optionally, no damping can be assumed. (Microsteps are assumed to instantaneously change φ_{tooth}, not slowed by inductance, which is taken into account only summarily via φ_{diff_induct}. In time steps, where a microstep is executed, this leads to unrealistic large values of D_{loss}, depending on the length of time steps. This cancels out over a microstep and is not critical for the overall trajectory. For a decent plotting, depending parameters are averaged over a microstep or fullstep. Only every 1000th time step is plotted.)

With the inertias, gear ratios, energy conservation and $D_{pullout}(\omega_{rot})$, from the total torque, the change $d\varphi_{rot}/dt$ is calculated, and from this the positions, speeds and kinetic energies of all the other parts and the torques between them, i.e., the 'resulting trajectory' of the system. In this part, an efficiency η_{gear} of the gear between motor and CW can be considered, which is useful in the case of a worm gear. (This option cannot be used together with D_{loss}, since its momentarily unrealistic large values would not cancel out and would cause an unrealistic large overall gear loss.)

In the resulting trajectory, OICP are visible. This is more prominent in the rotor angular speed and acceleration, fracD, and other parameters. The excitation is caused by the 'disturbing conditions' introduced above (printed in blue), but also by not well adapted 'input characteristics', especially if in the second run, φ_{tooth_pre} is ignored.

Further parameters of the trajectory are calculated, as position x_{wire}, speed v_{wire} and acceleration a_{wire} of the wire at the height of the beam, the wire position increment dx_{wire} corresponding to a fullstep, the deviation $x_{wire_dev2pre}$ of wire position against the preset trajectory, and also $x_{wire_dev2pre_corr}$, the same corrected for the predictable part of the effects of PWM and, in case, ignoring φ_{tooth_pre}.

Content from this work may be used under the terms of the CC-BY-4.0 licence (© 2023). Any distribution of this work must maintain attribution to the author(s), title of the work, publisher, and DOI

ISBN: 978-3-95450-236-3 ISSN: 2673-5350 doi:10.18429/JACoW-IBIC2023-WEP018

SIMULATION RESULTS

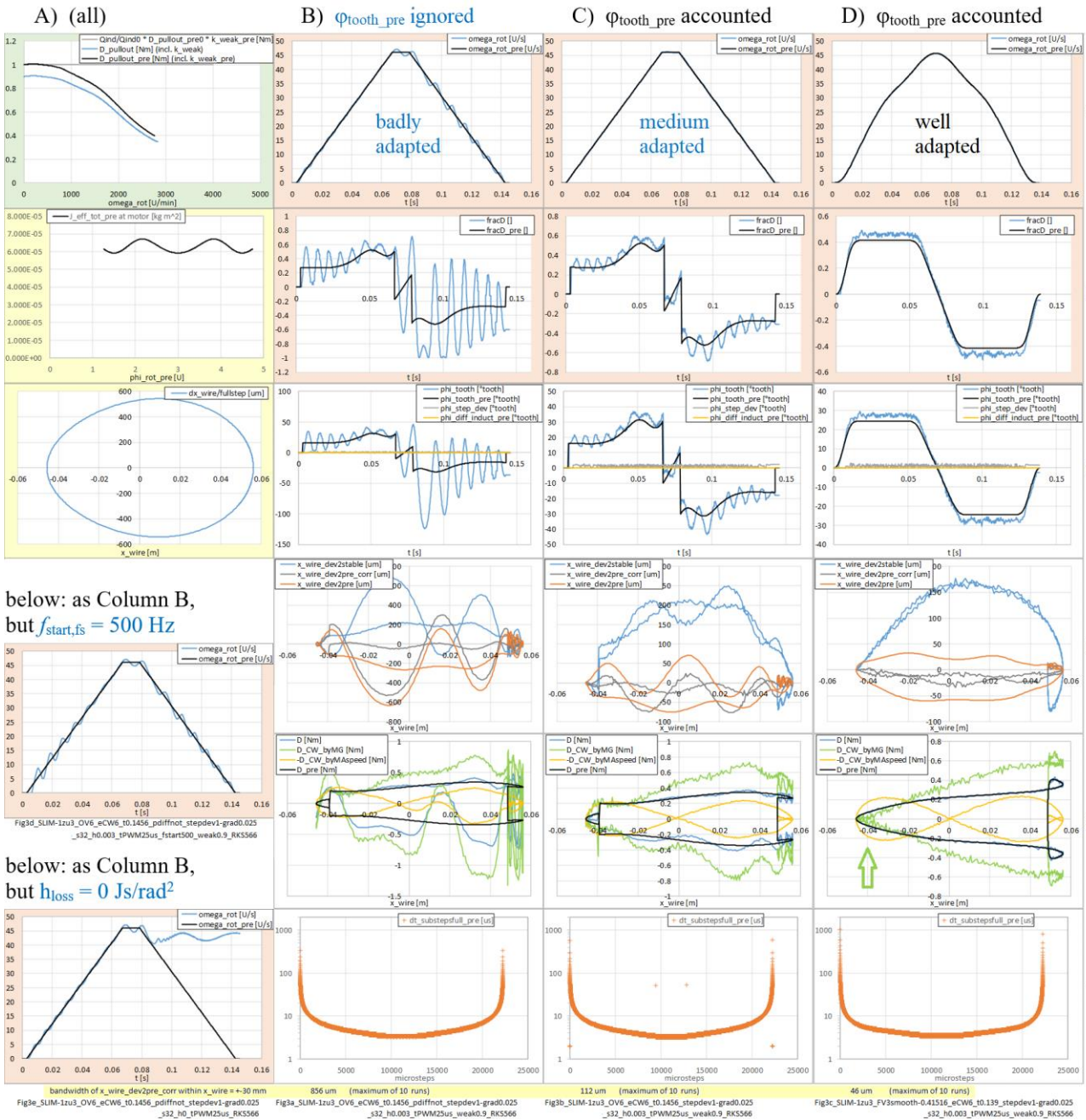


Figure 3: Case 2: Spur gear reduction 3:1, 50 motor teeth, h_{loss} = 0.003 Js/rad², $f_{start,fs}$ = 0 Hz, 6400 microsteps/revolution, φ_{err_bound} = ±0.025°, f_{PWM} = 40 kHz, k_{weak} = 0.9. Column A: a) Pullout-torque characteristic, only used part shown (black: preset trajectory, blue: resulting trajectory), b) total inertia seen by the motor, c) wire position change per fullstep depending on wire position. Column B, C, D: a) Rotor speed over time, b) used fraction of actual pullout-torque, c) phase in 'cosine potential' (grey: deviation due to manufacturing inaccuracies, yellow: due to inductance), d) deviation of wire position (red: to preset trajectory, grey: ditto, corrected, blue: compared to bottom of 'cosine potential'), e) torques of motor and at CW due to MG (green) and MA (yellow). Due to the larger CW inertia (Fig. 2c versus 2b), the torque D_{CW_byMG} of CW to MG changes its sign distant from the beam axis (arrow), thereby minimizing the effect of gear play to the measured profile shape at Column C, D. f) Preset step sequence (time difference between microsteps). At Column C the few adapted microstep intervals at the limits of the ramps are visible. Columns B, C, D present simulations for different input characteristics, ranging from 'badly adapted' to 'well adapted'. The two variants at bottom left illustrate that it depends on details, how 'badly adapted' input characteristics interfere with the eigenfrequency of OICP. This is less critical with 'well adapted' smooth input characteristics.

Content from this work may be used under the terms of the CC-BY-4.0 licence (© 2023). Any distribution of this work must maintain attribution to the author(s), title of the work, publisher, and DOI

ISBN: 978-3-95450-236-3 ISSN: 2673-5350 doi:10.18429/JACoW-IBIC2023-WEP018

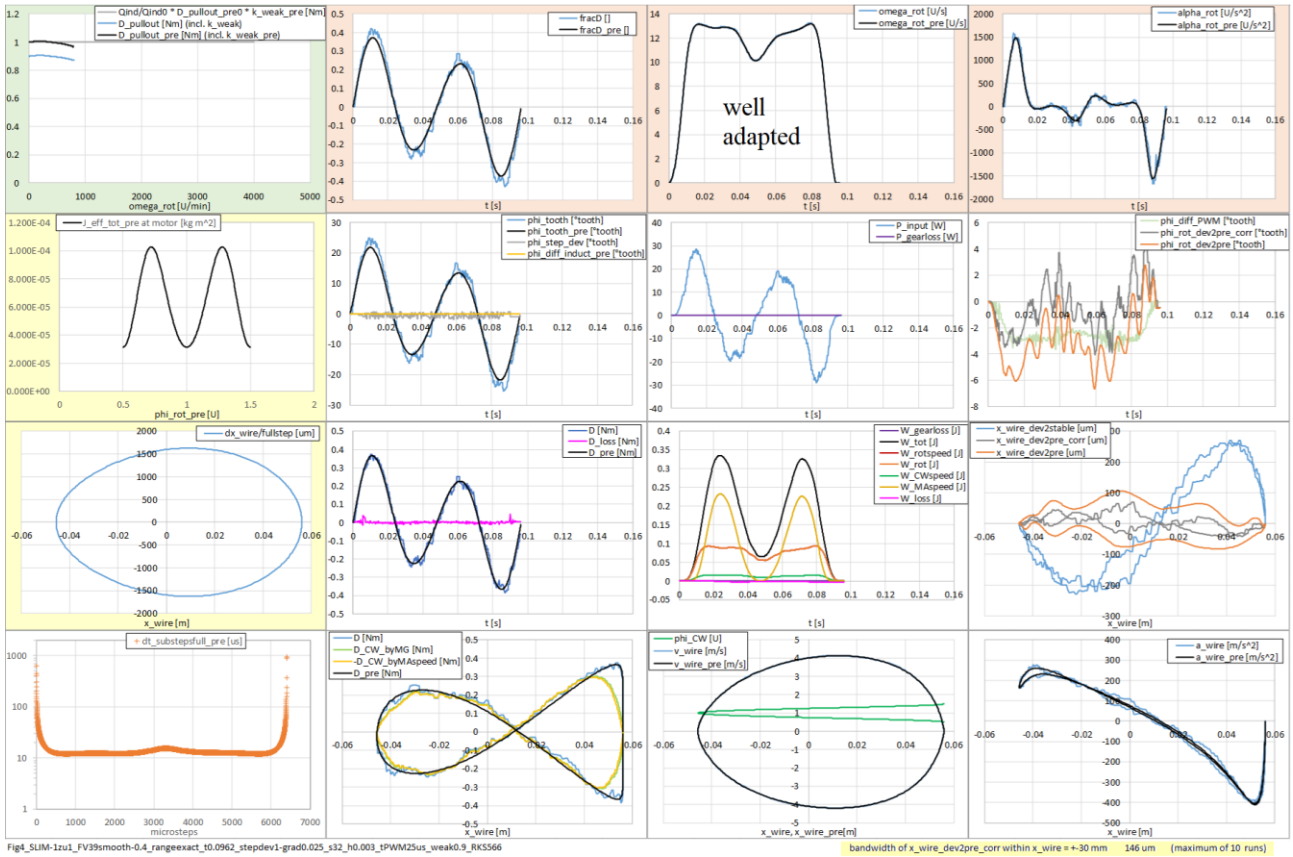


Figure 4: Case 3: Direct drive 1:1. Parameters as in Fig. 3 caption. Additional information compared to Fig. 3: Rotor acceleration, motor power, deviations of rotor phase by PWM (green) and against preset (red) and ditto corrected (grey), energies of parts of the mechanism, wire velocity and CW angular position, wire acceleration.

The example of case 2 (Fig. 3) and further simulations imply that OICP are reduced by (in this order)

- taking into account φ_{tooth_pre}
- providing a (preferentially smooth) input characteristic, not interfering with the eigenfrequency of OICP
- the presence of damping h_{loss} >0 Js/rad^2
- microstepping at least at lower speeds
- small other disturbing conditions
- reduced motor current, if torque is abundant.

Thereby the accuracy of wire movement is improved, and the used fraction of pullout-torque reduced.

With an adapted input characteristic and parameters assumed to be realistic, the simulations suggest that for cases 2 and 3 (Fig. 4), a wire speed of 4 m/s is well in reach. Electronics able to provide a microstep sequence from a look-up table to the step-direction input of a commercial driver is required for this. The predicted accuracy of wire movement, defined as band width of $x_{wire_dev2pre_corr}$, is somewhat better at gear ratio 3:1 (~50 µm) than at 1:1 (~150 µm). With lower wire velocity the accuracy does not improve. Here, a higher gear ratio can provide better accuracy. With 20:1 (case 1) ~3 µm is predicted, which is smaller than the effect of the to be expected mechanical play of the mechanism.

An ultimate limit for maximum wire speed is given by the available motor torque. However, OICP will lead to a loss of synchronisation already at somewhat lower speeds. This is described by the simulation (Fig. 3 bottom left). For quantitative predictions, at least, a more precise determination of h_{loss} is required. Experimental tests are needed to check the predictions of the simulation. A simple test case can be a motor loaded with an additional inertia.

OUTLOOK

A test stand is under preparation [4] to evaluate the performance of monitor setups as the ones discussed here. Furthermore, other aspects, as the lifetime of the bellows, the stiffness of the MA and wire vibrations will be studied.

ACKNOWLEDGEMENTS

Thanks to Oliver Dölling for preparing Fig. 2.

REFERENCES

[1] L. Rezzonico, “Beam diagnostics at SIN”, in *Proc. CYCLOTRONS’86*, Tokyo, Japan, Oct. 1986, paper I5-05, pp. 457-460.

[2] L. Rezzonico, M. Olivo, “Profile measurements of high intensity-low energy ion beams”, *Rev. Sci. Instrum.*, vol. 67, no. 3, pp. 1246-1248, 1996. doi:10.1063/1.1146687

[3] https://www.baumer.com

[4] Stuart Warren, PSI, personal communication.

Content from this work may be used under the terms of the CC-BY-4.0 licence (© 2023). Any distribution of this work must maintain attribution to the author(s), title of the work, publisher, and DOI

ISBN: 978-3-95450-236-3 ISSN: 2673-5350 doi:10.18429/JACoW-IBIC2023-WEP019

STUDY OF SINGLE WIRE SCANNER MONITOR FOR FETS-FFA TEST RING

E. Yamakawa*, D. W. Posthuma de Boer, S. Machida, A. Pertica, A. Letchford
Rutherford Appleton Laboratory, Didcot, United Kingdom
Y. Ishi, T. Uesugi
Kyoto University Institute for Integrated Radiation and Nuclear Science, Osaka, Japan

Abstract

To confirm the use of Fixed Field Alternating gradient accelerator (FFA) as a high power pulsed neutron spallation source, a prototype called FETS-FFA is studied at Rutherford Laboratory (RAL). A single Wire Scanner Monitor (WSM) is planned to be used to measure beam position and beam profile in the ring. One of the concerns of this monitor is the thermal damage on the Carbon Nano Tube (CNT) wire due to high energy deposition of low energy proton beam in FETS-FFA (3–12 MeV). Furthermore, to measure a beam profile during beam acceleration in the ring, a diameter of CNT wire needs to be smaller than the orbit displacements in turns. To confirm whether a single WSM is suitable for FETS-FFA ring, two different beam tests were performed at RAL and at the Institute for Integrated Radiation and Nuclear Science, Kyoto University (KURNS). Both measurements demonstrated that the single WSM is applicable for FETS-FFA ring if the diameter of CNT is smaller than the orbit separation between two consecutive turns. In this paper, the detail of the design study of single WSM as well as the performance tests are presented.

INTRODUCTION

The ISIS-II project [1] is currently considering a 1.25 MW proton driver for a new pulsed spallation neutron source in Europe. A Fixed Field Alternating Gradient (FFA) ring [2, 3] is one option for the main ring of ISIS-II. In order to demonstrate that FFAs can provide the reliability required for user operations in ISIS-II, the small-scale Front End Test Stand and Fixed Field Alternating gradient (FETS-FFA) ring will be built by 2029. The baseline optics of the horizontal excursion FETS-FFA (hFFA) ring were recently finalised, and its main parameters are presented in Table 1.

Based on the planned commissioning scenario, a single WSM will be used to identify the beam profile and the beam position of the injected beam to optimize any injection mismatch with the design orbit and the Twiss parameters. Destructive monitors are extremely useful when a non-destructive monitor cannot detect the beam induced signal in the case of low intensity beam at the beginning of the beam commissioning. According to the measurement of the accelerating multi-turn beam profile in the FETS-FFA ring, the single WSM will be placed on the orbit of a certain beam energy. As the orbit radius changes with beam energy, a single stationary wire can measure the profile by intercepting the beam over several turns during an acceleration cycle.

* emi.yamakawa@stfc.ac.uk

Table 1: Parameters of 4-fold Symmetry FD-spiral FETS-FFA Ring in 2023

Parameter	Value
Beam energy range	3–12 MeV
Bunch intensity	3×10^{11} ppp
Repetition rate	100 Hz (50 pps)
Injection rate	50 Hz
RF frequency bandwidth	2–4 MHz
Harmonic number	2
Normalised Beam Core	10 πmm mrad
Beam Size	±20 mm
Orbit Excursion	600 mm
Vertical Physical Acceptance	±32 mm

As the beam energy changes during a profile measurement, adiabatic damping will cause the transverse beam size to reduce on each successive turn. Furthermore, beam loss due to scattering at the wire might distort the profile during a measurement. To investigate whether the monitor can measure the beam profile in the FETS-FFA ring, a feasibility study of the single WSM is performed in this paper. This will include the relationship between wire thickness and turn separation, as well as predictions for wire heating. Profile measurements made at the FETS Linac and KURNS hFFA ring will then be shown and used to inform conclusions.

FEASIBILITY STUDY

Carbon Nano Tube (CNT) [4–6] wires are used for the single WSM in the FETS-FFA ring owing to their high melting temperature (3000 °C) and high tensile strength (1 GPa).

Wire Thickness

For the case of profile measurement of an accelerating beam over several turns in the FETS-FFA, separation between subsequent transverse profile samples will be fixed by the change in orbit displacement, as illustrated in Fig. 1. This will depend on the RF program and is not expected to be constant throughout an acceleration cycle. To investigate the impact of wire thickness on the measured beam profile, a computer simulation was performed with the vertical excursion FFA (vFFA) lattice [7, 8][1]. In the simulation,

[1] The lattice design of the FETS-FFA ring (Table 1) was changed from the vFFA to the horizontal excursion FFA (hFFA) in 2022. The lattice design of hFFA is different from that of vFFA, however the orbit displacements and the RF program are similar

Content from this work may be used under the terms of the CC-BY-4.0 licence (© 2023). Any distribution of this work must maintain attribution to the author(s), title of the work, publisher, and DOI

ISBN: 978-3-95450-236-3 ISSN: 2673-5350 doi:10.18429/JACoW-IBIC2023-WEP019

Content from this work may be used under the terms of the CC-BY-4.0 licence (© 2023). Any distribution of this work must maintain attribution to the author(s), title of the work, publisher, and DOI

injected particles were generated with a Gaussian distribution and transported using 4×4 transfer matrices with PyTRACK [9]. Although the scattering angle and energy loss of particles at the wire were not taken into account in this calculation, the calculation stopped when a particle hit the wire, assuming 100 % beam-loss due to scatterings. The wire was placed at 3.41 MeV (averaged turn separation of 64.2 µm) and 10.95 MeV (averaged turn separation of 25.3 µm).

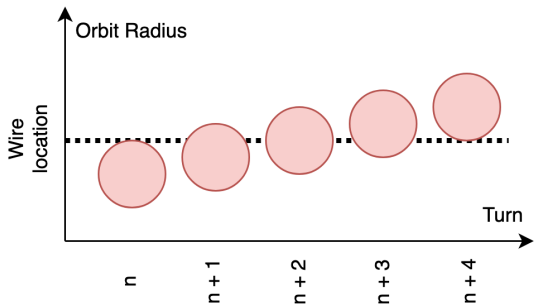


Figure 1: Schematic drawing of the profile measurement of an accelerating beam over several turns (red circles) in the FETS-FFA ring.

Figure 2 shows the computed beam profile measured by wires of differing thicknesses, at around 3 MeV and 12 MeV. In the case of 12 MeV, the beam size measured by each thickness of wire is consistent to the initial beam size of 12.7 mm. On the other hand, in the case of 3 MeV, a distortion can be seen when the wire thickness is larger than ϕ30 µm. Furthermore, the Root Mean Square (RMS) beam size is overestimated compared to the initial beam size of 17.1 mm. This is thought to be caused by the change in particle population throughout the simulation. Whilst the distortion is affected by the assumed loss due to scattering, these results are indicative of a more general relationship between profile accuracy and wire thickness. A beam which intercepts less material will be scattered less, which is particularly significant for the proposed multi-turn profile measurement. Ensuring that the wire thickness is less than the turn separation can help to limit the number of consecutive scattering events, and thus give a more accurate profile. The signal strength from the wire is expected to be proportional to the cross-section of the wire, and affects a Signal to Noise Ratio (SNR) and signal sensitivity of the wire. The thickness of the wire should be chosen with a reasonable balance between the SNR and profile distortion.

Heat Analysis

Temperature rise in the wire is an important consideration for all such interceptive diagnostics, but especially so when measuring the beam profile over multiple turns. The cumulative interaction period will be significantly longer than that of one-pass measurement. A heat analysis has therefore performed by the analytical simulation code [10] which computes a temperature change in the material. According to the vFFA beam parameters and its RF acceleration scheme, the

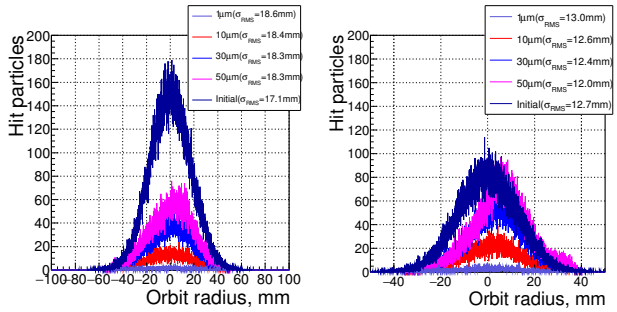


Figure 2: Computed beam profile with several thicknesses of CNTs at around 3 MeV (left) and 12 MeV (right).

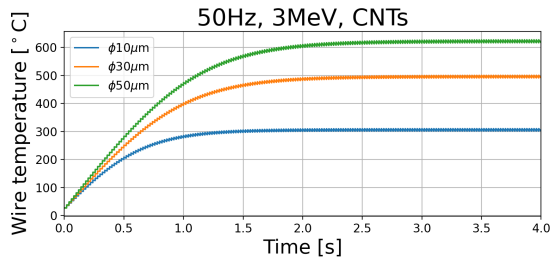


Figure 3: Transient temperature in each CNT wire. A thermal emissivity of CNT in vacuum is estimated to be 0.2 in this simulation.

time duration for the beam orbit to travel over the beam size (2σ=8 mm) is 336 µs with harmonic number 2, corresponding to 0.143 mA of 3×10^{11} ppp, at injection beam energy of 3 MeV. As shown in Fig. 3, the steady temperature on each wire is below the CNT melting temperature.

Heat Test on FETS

To confirm whether a thin CNT wire is applicable with a 3 MeV proton beam, tests were performed with a 3 MeV H^- beam on the FETS Linac [11], using the ISIS single-wire injector profile monitor (SWIP) [12] (Fig. 4). Several diameters of CNT wires: ϕ20, ϕ30, ϕ40 and ϕ50 µm were mounted on the monitor head. The monitor shaft is inclined at 44.5 degrees, and travels nearly 150 mm from the park position.

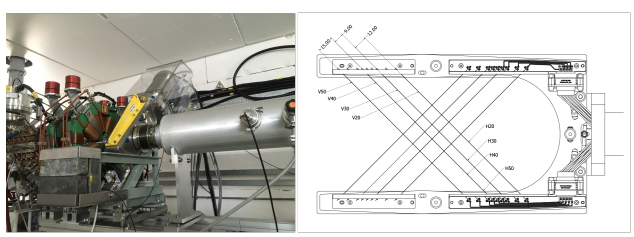


Figure 4: Left: The single WSM on FETS beam line. Right: The monitor head with CNTs. The horizontal wires are upstream of the vertical wires, which are 3 mm apart in the beam direction. The ϕ10 µm CNT was too thin to be mounted on the monitor head.

ISBN: 978-3-95450-236-3 ISSN: 2673-5350 doi:10.18429/JACoW-IBIC2023-WEP019

Figure 5 shows light emission at the wire when interacting with the FETS beam. The smaller the diameter of the wire, the weaker the light emission can be seen at the wire. Based on the beam parameters when the pictures were taken, the steady temperature on the ϕ20 µm is predicted to be beyond 1000 °C, and the ϕ20 µm CNT was not broken after at least 10 minutes of exposure to the FETS beam of 28 mA peak current (3.5E13 ppp with a 200 µs pulse). This is a factor of 1×10^3 and 1×10^2 larger than the peak current of the injection pulse (6×10^9 ppp) and the multi-turn accelerating beam (3×10^{11} ppp) in the FETS-FFA ring. Therefore, the considered thickness of CNTs are not expected to be damaged rapidly by the injection beam in the FETS-FFA ring. However, the heat damage over longer durations should also be analysed in future.

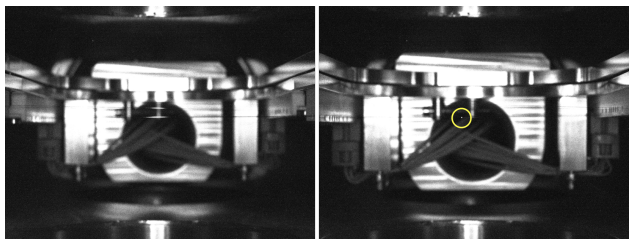


Figure 5: Light emission from the ϕ50 µm (left) and the ϕ20 µm (right, in the circle) CNTs with the 3 MeV FETS H^- beam. The wire was aligned at the centre of the beam pipe when the photo was taken.

Pulse Width Measurement on FETS

The pulse width of the FETS beam was measured by the SWIP. The pulse width is determined by the time window which is above 2 times of standard deviation of the noise level. The noise level is found by computing the RMS within a time window at the end of the data when there is no beam. According to the SRIM [13] simulation, the proton range of 3 MeV is expected to be about 120 µm in a Carbon material (1.4 g/cm^3). Therefore, H^- beam will not be fully stopped at the CNTs mounted on the frame, and the electrons of H^- beam will be directly captured by the wire. The negative charge signal is converted to the voltage signal by the operational amplifier and monitored by the oscilloscope. The gain of amplifier is 1×10^3 V/A with 500 kHz frequency bandwidth.

As shown in Fig. 6, the pulse width measured by each CNT wire is within about 5 % different from the one measured by the CT monitor (210 µm) located at about 535 mm upstream of the SWIP. In the integrated signal within the pulse width, the number of primary H^- particles is degraded by about 18 % when it reaches the downstream wires (vertical profile wires in Fig. 6), that agrees with the PHITS [14] simulation. Although the integrated signal was not proportional to the cross-section of the wires, these data will be useful to predict the signal strength when the required diameter of wire is used in the FETS-FFA ring.

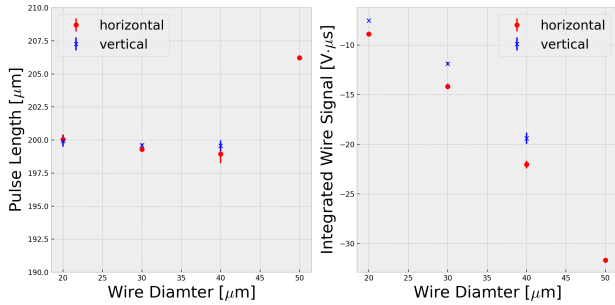


Figure 6: The measured pulse length (left) and the integrated pulse signal (right) of the FETS beam. The error bar is the RMS pulse length and the RMS integrated wire signal over 5 pulses.

BEAM PROFILE MEASUREMENT

Profile Measurement on FETS

The measurement was done by SWIP scanning the wire positions over the beam size. The control units set the wire positions with a stepper motor and acquire the signal at every trigger timing. The control units have a signal amplifier with a gain of 4.7E3 V/A at bandwidth of 50 kHz after low pass filtering. At each monitor step, 10 samples were acquired over 100 ms following a trigger, and averaged before being saved to disk. As shown in Fig. 7 and Table 2, beam profiles were measured by all CNT wires, and all measured horizontal beam sizes are consistent. The vertical beam sizes are not all consistent, which could be due to scattering from the upstream horizontal profile wires. Based on lattice simulations on the FETS, the RMS beam size at the position of the SWIP is about 4–5 mm. Although the distance between adjacent wires is bigger than the expected beam size, the protons generated at the wires will come in the neighbouring wires, decreasing the signal strength and the signal sensitivity.

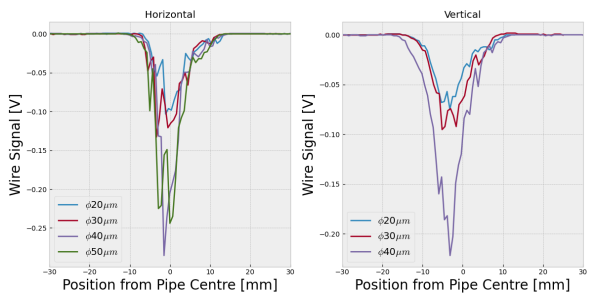


Figure 7: Beam profiles measured by each CNT wire. The scan range was 148.5 mm with a step size of 1 mm. The peak pulse intensity measured by the CT monitor was about 13 mA in this measurement.

Profile Measurement on hFFA

A beam experiment with the single WSM was performed in the hFFA ring at KURNS [15]. The wire position was fixed at the orbit of about 13.5 MeV where the turn separation is about 29 µm. A CNT wire with diameter ϕ10 µm was mounted on the frame as shown in Fig. 8. As the range of 13.5 MeV protons was found to be 1.67 mm in a Carbon

Content from this work may be used under the terms of the CC-BY-4.0 licence (© 2023). Any distribution of this work must maintain attribution to the author(s), title of the work, publisher, and DOI

ISBN: 978-3-95450-236-3 ISSN: 2673-5350 doi:10.18429/JACoW-IBIC2023-WEP019

Table 2: The measured RMS beam size with design values. The errors are RMS of three different beam sizes.

CNT	RMS Beam Size Horizontal [mm]	RMS Beam Size Vertical [mm]
ϕ20 µs	3.5±0.28	4.2±0.04
ϕ30 µs	3.4±0.35	3.8±0.27
ϕ40 µs	3.8±0.77	4.6±0.27
ϕ50 µs	3.8±0.25	N.A.
Design	4-5	4-5

material (1.4 g/cm3) by SRIM simulation, the protons were expected to be fully stopped at the CNT wire. Therefore, secondary electron emissions were read by the signal amplifier with a gain of 1×10^7 V(A) and a cutoff frequency of 4.8 kHz that was wide enough to detect the ≈300 µs beam signal.

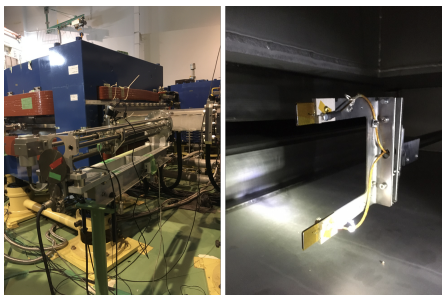


Figure 8: The radial probe (left) and the monitor head of the single WSM with ϕ10 µm CNT wire (right). The monitor head was attached to the radial probe and controlled by the motion control driver.

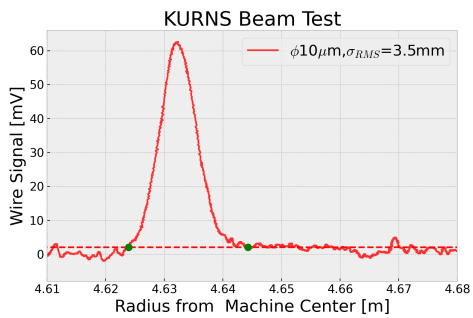


Figure 9: The accelerating multi-turn beam profile measured by a ϕ10 µm CNT wire. The dashed line indicates 2 times of standard deviation of the noise level, computed by the RMS within a time window at the end of the data when there is no beam.

Although the shape of beam profile is similar between the measurement (Fig. 9) and the simulation (Fig. 10) based on the KURNS ring optics and the beam parameters, the measured beam size is smaller than that of design value. The injector (11 MeV H^- Linac) was not stable during the experiment, and the ion source as well as following beam transports were recommissioned prior to the tests. Discrepancies between measurement and expectation could possibly be explained by differences between the actual and design beam emittance.

Stray magnetic fields from the main hFFA magnets is close to 0.05 T near the middle of the straight section where the single WSM was installed. Based on CST tracking simulations [16], some of the secondary electrons generated at the wire will be confined by the magnetic fields and eventually return to the wire, decreasing the signal and resulting in a smaller measured beam size. Profile measurements with a negative bias voltage were planned, but not performed due to time constraints.

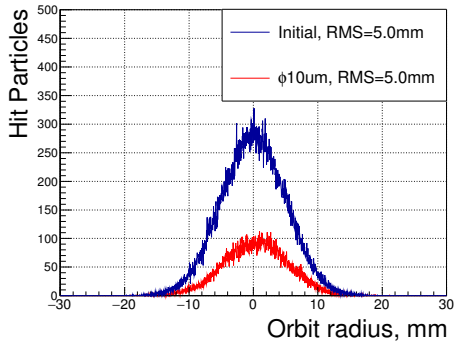


Figure 10: The computed beam profile measured by ϕ10 µm wire. The initial beam is a Gaussian distribution with the design value of beam size (σ=5 mm). The scattering angle and energy loss at the wire are computed by PHITS, which are taken into account in this simulation.

CONCLUSION

The WSM with a single, stationary CNT wire has been developed as a beam profile monitor for the FETS-FFA test ring. Tracking simulations have motivated the study of wires with a small diameter, to minimise scattering over many turns. The durability of these wires has been demonstrated by exposing them to the 3 MeV H^- beam of the FETS Linac. Whilst it has been demonstrated with simulations and measurements that heating of these wires is not expected to produce short-term effects, heat damage over a longer time periods should be also observed in future. It has also been demonstrated with simulations and experimentally, that the single WSM will be able to measure the pulse length and profile of low energy mono-energetic beams as well as the accelerating beam over multiple turns in the FETS-FFA ring. A beam scraper will also be installed in the FETS-FFA ring, and offers an alternative method to measure the beam size of accelerating beams over multiple turns. However, there are challenges in using such monitors when distributions such as hollow beams are possible. As the single WSM will be able to identify the beam profile and the beam size even for a hollow beam, the single WSM will be an invaluable diagnostic for commissioning the FETS-FFA test ring.

ACKNOWLEDGEMENTS

The author wishes to acknowledge the efforts by S. Kellard and A. Chamberlain for the design and manufacture of the single WSM.

Content from this work may be used under the terms of the CC-BY-4.0 licence (© 2023). Any distribution of this work must maintain attribution to the author(s), title of the work, publisher, and DOI

ISBN: 978-3-95450-236-3 ISSN: 2673-5350 doi:10.18429/JACoW-IBIC2023-WEP019

REFERENCES

[1] J.-B. Lagrange *et al.*, "Progress on Design Studies for the ISIS II Upgrade", in *Proc. IPAC'19*, Melbourne, Australia, May 2019, pp. 2075–2078. doi:10.18429/JACoW-IPAC2019-TUPTS068

[2] T. Ohkawa, "Proc. Annual meeting of JPS", 1953, unpublished.

[3] K. R. Symon *et al.*, "Fixed-Field Alternating-Gradient Particle Accelerators", *Phys. Rev.*, vol. 103, pp. 1837–1859, 1956. doi:10.1103/PhysRev.103.1837

[4] HiTaCa by Hitachi Zosen Ltd., https://www.hitachizosen.co.jp/

[5] DexMat, https://store.dexmat.com/

[6] A. Miura, K. Moriya, and T. Miyao, "Application of Carbon Nanotube Wire for Beam Profile Measurement of Negative Hydrogen Ion Beam", in *Proc. IPAC'18*, Vancouver, Canada, Apr.-May 2018, pp. 5022–5025. doi:10.18429/JACoW-IPAC2018-FRXGBD3

[7] J.-B. Lagrange *et al.*, "FETS-FFA Ring Study", in *Proc. IPAC'21*, Campinas, Brazil, May 2021, pp. 1901–1904. doi:10.18429/JACoW-IPAC2021-TUPAB208

[8] S. Machida *et al.*, "Internal Report for FFA Task Report vFFA", 2022, unpublished.

[9] R. Calaga *et al.*, "PYTRACK: self-developed particle transport code", unpublished.

[10] D. W. Posthuma de Boer and A. Pertica, "Thermal Simulations of Wire Profile Monitors in ISIS Extracted Proton Beamline 1", in *Proc. IBIC'16*, Barcelona, Spain, Sep. 2016, pp. 785–787. doi:10.18429/JACoW-IBIC2016-WEPG59

[11] A. P. Letchford, "Upgrades and Developments at the ISIS Linac", in *Proc. LINAC'22*, Liverpool, UK, Aug.-Sep. 2022, pp. 1–6. doi:10.18429/JACoW-LINAC2022-MO1AA01

[12] D. M. Harryman and C. C. Wilcox, "An Upgraded Scanning Wire Beam Profile Monitoring System for the ISIS High Energy Drift Space", in *Proc. IBIC'17*, Grand Rapids, MI, USA, Aug. 2017, pp. 396–400. doi:10.18429/JACoW-IBIC2017-WEPCC18

[13] J. F. Ziegler, M. D. Ziegler and J. P. Biersack, "SRIM - The Stopping and Range of Ions in Matter", *Nucl. Instrum. Methods Phys. Res., Sect. B*, vol. 268, no. 11, pp. 1818-1823, 2020. doi:10.1016/j.nimb.2010.02.091

[14] T. Sato *et al.*, "Features of Particle and Heavy Ion Transport code System (PHITS) version 3.02", *J. Nucl. Sci. Technol.*, vol. 55, no. 6, pp. 684–690, 2018. doi:10.1080/00223131.2017.1419890

[15] Y. Mori *et al.*, "Present Status of FFAG Proton Accelerator at KURRI", in *Proc. IPAC'11*, San Sebastian, Spain, Sep. 2011, paper WEPS077, pp. 2685–2687.

[16] CST Studio Suite: Electromagnetic field simulation software, https://www.3ds.com/products-services/simulia/products/cst-studio-suite/

Content from this work may be used under the terms of the CC-BY-4.0 licence (© 2023). Any distribution of this work must maintain attribution to the author(s), title of the work, publisher, and DOI

ISBN: 978-3-95450-236-3 ISSN: 2673-5350 doi:10.18429/JACoW-IBIC2023-WEP020

PERFORMANCE EVALUATION OF GAGG+ AND TUNGSTEN CARBIDE BLADES IN AN X-RAY PINHOLE CAMERA

S. Burholt*[1], L. Bobb , N. Vitoratou, Diamond Light Source, Didcot, UK

Abstract

At Diamond Light Source two X-ray pinhole cameras are used to measure the transverse profile of the 3 GeV electron beam. The current pinhole assembly is formed using tungsten blades with chemically etched shims to produce a 25 µm x 25 µm aperture and the imager incorporates a 0.2 mm LuAG:Ce scintillator. Tungsten carbide is a machinable high-Z material which at millimetre thicknesses is opaque to X-rays. With a slight change in pinhole design, similar to that already in place at the ESRF, tungsten carbide blades could offer a well-controlled aperture size for the pinhole camera with simpler assembly. Further to this, improvements to the photon yield of scintillators mean that the new scintillator GAGG+ has an almost two-fold increase in yield compared to the current LuAG:Ce scintillator. An evaluation of the tungsten carbide blades and GAGG+ scintillator is presented.

INTRODUCTION

X-ray pinhole cameras are important diagnostic systems used for beam emittance monitoring at synchrotron light sources. Diamond currently uses two X-ray pinhole cameras downstream of two different bending magnets to provide non-invasive transverse beam profile measurements. These two pinhole cameras are referred to as pinhole camera 1 (P1), and pinhole camera 2 (P2). A schematic layout can be seen in Fig. 1. There is another pinhole camera (P3) set up in a similar way to the other pinhole cameras where research and development projects are carried out.

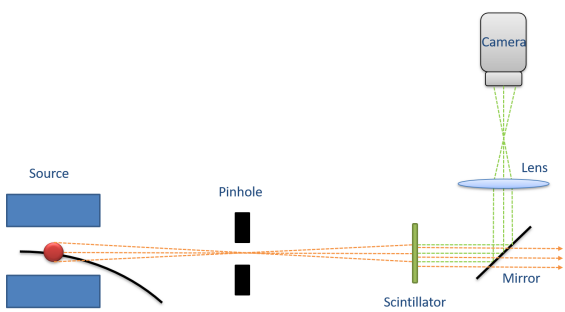


Figure 1: Diamond X-ray pinhole camera layout, including source, pinhole aperture, scintillator, mirror, lens, and camera.

The synchrotron radiation with an energy range of 15 keV to above 60 keV, with a peak around 26 keV, exits vacuum to air through a 1 mm aluminum window. The X-rays then pass through a tungsten pinhole assembly which is formed of 25 µm × 25 µm apertures [1]. This X-ray beam then interacts with a 0.2 mm thick Luttetium aluminium garnet doped with cerium (LuAG:Ce) scintillator screen and is imaged by a CCD camera (Flea 2), allowing for beam profile measurement and fitting.

The 25 µm pinhole aperture is formed from stacks of 25 mm(h) x 1 mm(v) x 5 mm(d) tungsten blades separated by chemically etched shims of the required thickness [2, 3]. There is one stack vertically and one horizontally so that an aperture of 25 µm in both planes is presented to the X-ray beam. This also forms a 10 mm long tunnel, fully attenuating the beam outside of the aperture. A low flow of nitrogen gas is used to reduce metal oxide growth inside the pinhole assembly.

The spatial resolution of a pinhole camera system can be described by the point spread function (PSF). The PSF is assumed to be constant on relatively long timescales for a given system. For a pinhole camera imaging system the overall PSF may be represented as

$$\sigma^2_{PSF} = \sigma^2_{pinhole} + \sigma^2_{camera} \tag{1}$$

with

$$\sigma^2_{pinhole} = \sigma^2_{diffraction} + \sigma^2_{aperture} \tag{2}$$

and

$$\sigma^2_{camera} = \sigma^2_{screen} + \sigma^2_{lens} + \sigma^2_{CCD} \tag{3}$$

where the subscripts denote the sources of the PSF contributions [1]. It is well known that there are many contributions to the point spread function. A significant contribution arises from the pinhole aperture [1].

The pinhole aperture material must be opaque to X-rays. A tungsten blade and shim assembly is currently used due to the opacity of tungsten being a high-z material. Shims are required because tungsten is not readily machinable. Therefore the pinhole apertures must be formed using chemically etched shims between the tungsten blades. Due to this the absolute size of the pinhole aperture differs from the shim thickness and is thus unknown. A few factors can cause this discrepancy including; the deformation from cutting or handling the chemically etched shims, misalignment during assembly, and the pressure of the blade-shim-blade assembly. It is also not trivial to measure the pinhole aperture size due to the 5 mm depth of the tungsten blades and three-dimensional structure of the pinhole assembly.

In order to minimise the PSF contribution from the pinhole aperture it is necessary to be able to control the pinhole aperture size and ensure it is matched to the spectrum of the incident synchrotron radiation. Previously machined molybdenum blades were investigated as an alternative to the tungsten/shim design, however the 5 mm molybdenum

* sam.burholt@diamond.ac.uk

Content from this work may be used under the terms of the CC-BY-4.0 licence (© 2023). Any distribution of this work must maintain attribution to the author(s), title of the work, publisher, and DOI

ISBN: 978-3-95450-236-3 ISSN: 2673-5350 doi:10.18429/JACoW-IBIC2023-WEP020

blade aperture scans showed a non-linear response indicating insufficient opacity to the X-ray beam [2]. LIGA (X-ray lithography) to produce well-defined apertures in a thin 250 µm gold screen has also been studied, however due to the thickness constraints of the LIGA process, images may require background subtraction. LIGA apertures or slits may be more suitable for monochromatic Fresnel diffractometry and/or interferometry [3].

Tungsten carbide is machinable and provides similar opacity to X-rays as tungsten. At the ESRF tungsten carbide blades using a C-D design have been tested [4]. In this paper, similarly machined tungsten carbide blades are evaluated for the pinhole cameras at Diamond.

From Eq. (3) the overall PSF may be reduced by improving the spatial resolution of the scintillator. Gadolinium aluminium gallium garnet doped with cerium (GAGG+) is a relatively new commercially available scintillator and has been studied for diagnostic applications at other facilities [5–7]. This material has an almost two-fold increase in photon yield (@23 °C) of 40 - 60 x 10^3 Ph/MeV vs. 25 x 10^3 Ph/MeV for LuAG:Ce which allows for better imaging of the X-ray beam at low current, and enables shorter exposure times thereby reducing the contribution of jitter within images [8]. In this paper the performance of GAGG+ is also evaluated for the X-ray pinhole cameras at Diamond.

TUNGSTEN CARBIDE BLADES

Tungsten carbide blades have been manufactured in the C-D design used at the ESRF [4] with the aperture being formed from an extrusion (D) and void (C) within the stacked blades, rather than with the traditional shim design, or void/flat assembly. The reason for the C-D design is for ease of manufacture: overall it is better to grind larger steps into the tungsten carbide and combining the C-D blades to form the desired aperture size, than trying to grind the 25 µm aperture exactly.

Two tungsten carbide stacks of matching pairs were manufactured with an aperture size of 25 µm. These two pairs were set up within the normal blade stack as shown with a traditional tungsten aperture using 25 µm chemically etched shims. This formed an overall pinhole stack with a 25 µm tungsten-shim-tungsten aperture and a C-D tungsten carbide aperture which allowed for comparative measurements as shown in Fig. 2. Both blades types were manufactured to have overall dimensions of 5 mm in depth, 1 mm in height, and 20 mm in length.

The tungsten carbide blades were manufactured by Midland Carbide [9] and had aperture specification tolerances of ±1 µm. The blades were manufactured using electro-discharge machining (EDM) to form the overall shape and size then ground and polished to the desired thickness. The stock material was tungsten carbide grade K10, which is the ultra-fine particle size with a material composition of 5.5 % cobalt (Co) and 94.5% tungsten carbide (WC), hardness (HRA) of 92.8, and density of 14.95 g/cm^3 [10].

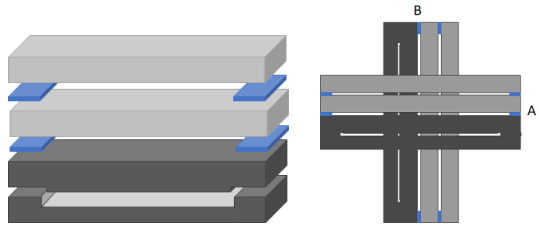


Figure 2: Pinhole blade stack design (left) constructed of tungsten blades (light grey), 25 µm chemically etched shims (blue), and the tungsten carbide C-D design with 25 µm machine gap (dark grey). Stack will be put under pressure when in use to hold all of these as flush as possible. Gaps are not to scale, but to show the C-D design. Total stack formation (right) showing how the apertures are formed from the orthogonal stacks A and B.

Using a back-lit microscope a rough measurement of the pinhole aperture size can be made. With the use of image processing software ImageJ [11] both set of tungsten carbide apertures were measured to be ≈35 µm in size. This is 10 µm larger than the specification.

TUNGSTEN CARBIDE APERTURE INVESTIGATIONS

Aperture Scans

The pinhole assembly is mounted to translation and rotation stages which allow for remote alignment with the beam. This is required because misalignment can cause reduction in the aperture size for the passing synchrotron radiation. Using the rotation stages the angle of the pinhole aperture relative to the incident beam is varied. During this aperture scan the 2D Gaussian fitted beam sizes (σ_x, σ_y), peak intensity and fit error are recorded via the normalisation of these parameters to their maximum and minimum values as a function of angle.

Higher photon flux through the aperture occurs when the aperture is parallel with the X-ray beam. Thus the measured peak intensity reduces from a maximum value as the angle of the aperture becomes misaligned to the beam.

The horizontal rotation scans of the tungsten and tungsten carbide apertures can be seen in Fig. 3. The horizontal rotation of the blades show the expected increase and decrease in the peak intensity around the aligned position, this can also be seen by the consistent horizontal and vertical beam size measurements throughout the scans.

The vertical aperture scans show a similar response for the peak intensity, as seen in Fig. 4, but the tungsten carbide vertical beam size increases as the system becomes aligned to the X-ray beam, whilst the tungsten blades do not.

This response could be attributed to the larger aperture size of the tungsten carbide assembly when compared to the 25 µm tungsten aperture, as it was found to be 35 µm instead of 25 µm via microscope images. To further show this effect a 50 µm tungsten aperture was tested similarly and

Content from this work may be used under the terms of the CC-BY-4.0 licence (© 2023). Any distribution of this work must maintain attribution to the author(s), title of the work, publisher, and DOI

ISBN: 978-3-95450-236-3 ISSN: 2673-5350 doi:10.18429/JACoW-IBIC2023-WEP020

Content from this work may be used under the terms of the CC-BY-4.0 licence (© 2023). Any distribution of this work must maintain attribution to the author(s), title of the work, publisher, and DOI

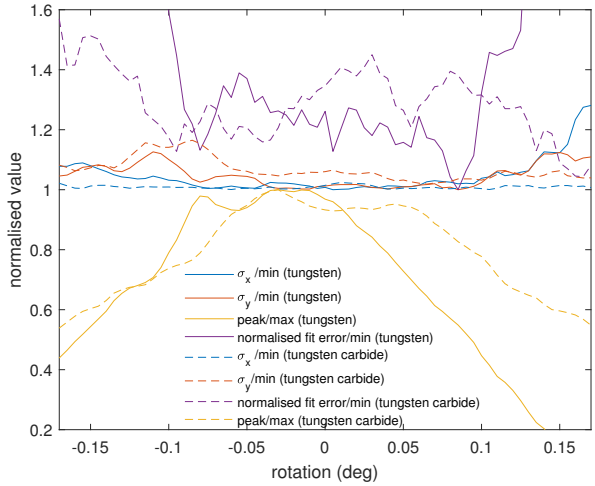


Figure 3: Horizontal rotation scans on pinhole camera 3 of the tungsten aperture (solid lines) and the tungsten carbide aperture (dashed lines).

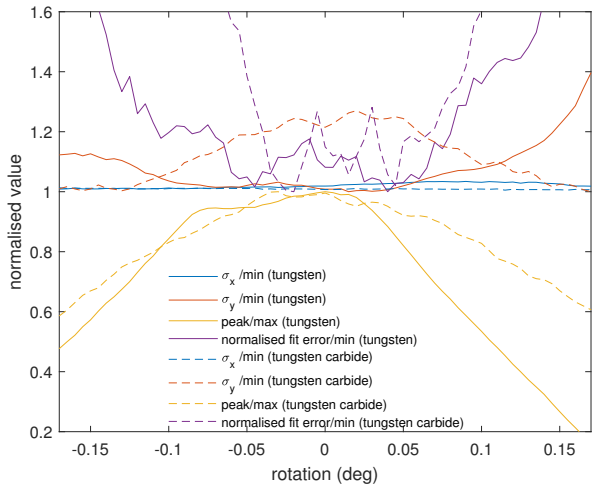


Figure 4: Vertical rotation scans on pinhole camera 3 of the tungsten aperture (solid lines) and the tungsten carbide aperture (dashed lines).

found to have the same response in the fitted vertical beam size (σ_y) and none in the horizontal beam size (σ_x). This shows that the measured beam size of an aperture varies depending on the alignment and size of the aperture due to the PSF contribution. The optimal aperture size for the incident X-ray beam at Diamond is 15 µm [3].

GAGG+ EXPERIMENTS

Modulation Transfer Function Experiments

For these experiments knife-edge images were acquired using a tungsten blade. This blade was placed in front of the scintillator, at a slight angle, to block a portion of the X-ray fan. Knife-edge images are shown in Fig. 5 from which the Edge Spread Function (ESF) is derived. Differentiating

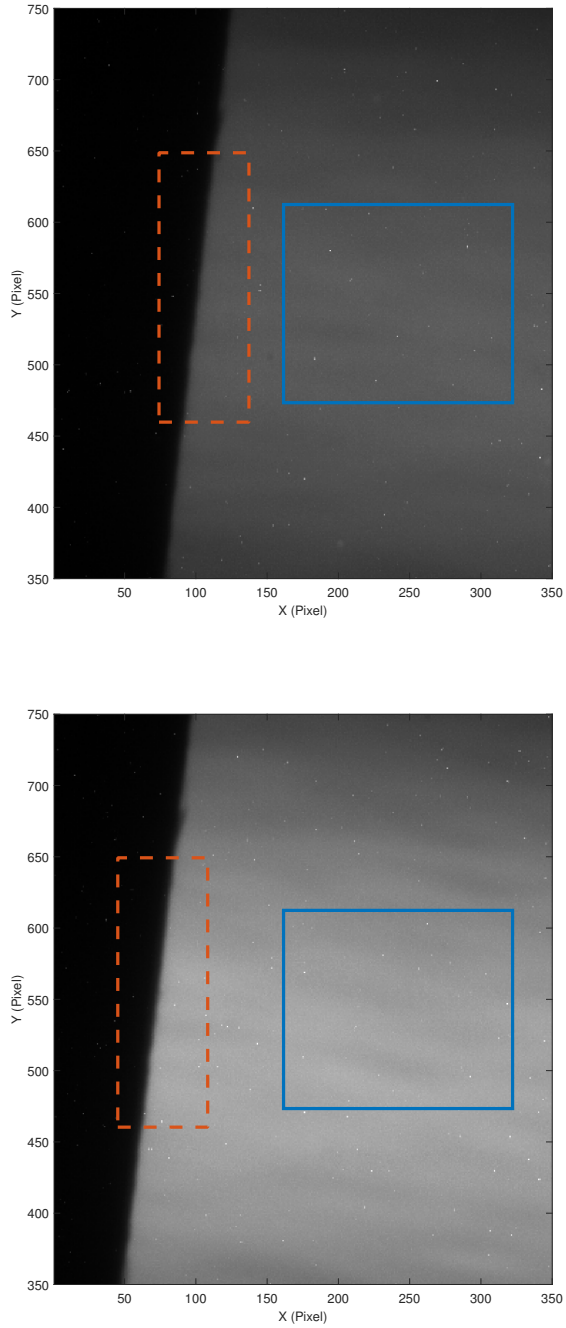


Figure 5: Tungsten blade knife-edge images at the same gain and exposure settings for LuAG:Ce (Top) and GAGG+ (Bottom). ROIs used for knife-edge MTF measurement (dashed orange) and ROIs used for photon yield measurement (solid blue).

the ESF provides the Line Spread Function (LSF) which is analogous to a one-dimensional PSF. Finally the LSF undergoes Fourier Transform to derive the Modulation Transfer Function (MTF) [12–14].

ISBN: 978-3-95450-236-3 ISSN: 2673-5350 doi:10.18429/JACoW-IBIC2023-WEP020

Modulation transfer functions are normally used to investigate the camera lens and camera sensor spatial resolution [13]. The images from the pinhole cameras were taken and processed using QuickMTF which can readily produce the ESF, LSF, and MTF analyses from the region of interest [14].

In order to compare the two scintillators, all aspects of the imaging system (mirror, lens, and camera) remain unchanged. The magnification from the scintillator to the camera sensor is 1.04. The MTF results shown in Table 1 and Fig. 6 have been converted from the image plane (camera sensor) to the object plane (scintillator screen) using the magnification. The MTF10 and MTF50 values in Table 1 have been converted from cycles per pixel to line pairs per mm (lp/mm) using the pixel size of the camera.

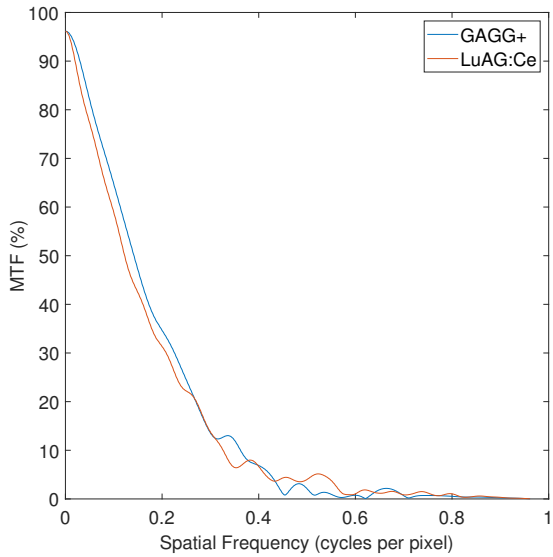


Figure 6: MTF Graph for LuAG:Ce and GAGG+.

Table 1: MTF Results of the Knife-edge Scans of Fig. 6

Value	LuAG:Ce	GAGG+
MTF50 (lp/mm)	27.8	32.0
MTF10 (lp/mm)	70.7	78.6
10 - 90 % rise (pixels)	4.5	3.56

The 10 - 90 % pixel value decreases by one pixel from LuAG:Ce to GAGG+ demonstrating that the edge is sharper. GAGG+ has a slightly increased spatial resolution than LuAG:Ce when referring to the MTF10 and MTF50 values in Table 1, however this increase can be seen to be marginal when compared in Fig. 6. Overall Fig. 6 shows that LuAG:Ce and GAGG+ have similar spatial resolutions.

Photon Yield

A comparison of the photon yield from LuAG:Ce and GAGG+ was undertaken using the ROIs indicated in Fig. 5. The spectral distribution of the emitted synchrotron radiation was consistent for all studies. The intensity per pixel within these ROIs can be seen in Table 2. This shows an increase in the photon yield of 78 % between the current scintillator LuAG:Ce and the new material GAGG+. These results are also in good agreement with the photon yield specifications for the scintillators which predicted a two-fold increase of GAGG+ compared to LuAG:Ce [8].

Table 2: Intensity Results of a ROI of the Knife-edge Images of LuAG:Ce and GAGG+

	LuAG:Ce	GAGG+
Total Intensity (*a.u*)	6.04×10^6	1.07×10^7
Pixels in ROI	68769	68769
Intensity per pixel (*a.u*)	88	157

CONCLUSIONS

This paper investigates whether the use of the new GAGG+ scintillator and tungsten carbide blades could improve the spatial resolution of the X-ray pinhole camera at Diamond Light Source. The microscope images and aperture scans have shown that although specified to 25 µm the new tungsten carbide C-D designed blades have a larger aperture of approximately 35 µm. Aperture scans have shown tungsten carbide is sufficiently opaque to the incident X-ray synchrotron radiation. Although the tungsten carbide aperture shows an increase in vertical beam size during the vertical rotation scan, this can be attributed to its larger aperture size of 35 µm which is less optimal for the given spectrum of synchrotron radiation.

For camera images acquired using the same gain and exposure settings the spatial resolution of GAGG+ and LuAG:Ce has been shown to be almost identical. The expected two-fold increase in photon yield has been largely validated with an 78 % increase in the average intensity per pixel of GAGG+ over LuAG:Ce. This shows that GAGG+ would be a good substitute for LuAG:Ce as it has a higher photon count without any loss in spatial resolution.

REFERENCES

[1] C. Thomas, G. Rehm, I. Martin, and R. Bartolini, "X-Ray Pinhole Camera Resolution and Emittance Measurement", *Phys. Rev. Spec. Top. Accel Beams.*, vol. 13, no. 2, 2010. doi:10.1103/PhysRevSTAB.13.022805

[2] L. M. Bobb, A. F. D. Morgan, and G. Rehm, "Performance Evaluation of Molybdenum Blades in an X-ray Pinhole Camera", in *Proc. IBIC'16*, Barcelona, Spain, Sep. 2016, pp. 795–798. doi:10.18429/JACoW-IBIC2016-WEPG63

[3] N. Vitoratou, L. Bobb, A. Last, and G. Rehm, "X-Ray Pinhole Camera Spatial Resolution Using High Aspect Ratio LIGA Pinhole Apertures", in *Proc. IBIC'22*, Kraków, Poland, Sep. 2022, pp. 71–75. doi:10.18429/JACoW-IBIC2022-MOP18

Content from this work may be used under the terms of the CC-BY-4.0 licence (© 2023). Any distribution of this work must maintain attribution to the author(s), title of the work, publisher, and DOI

ISBN: 978-3-95450-236-3 ISSN: 2673-5350 doi:10.18429/JACoW-IBIC2023-WEP020

[4] F. Ewald, "Emittance diagnostics at ESRF-EBS using the X-ray Pinhole Camera", presented at the ELETTRA 2.0 Workshop on Optical Diagnostics for Low-Emittance Storage Rings, Mar. 2022. https://indico.psi.ch/event/12679/contributions/34867/.

[5] A. I. Novokshonov *et al.*, "Scintillator Nonproportionality Studies at PITZ", in *Proc. IBIC'22*, Kraków, Poland, Sep. 2022, pp. 277–280. doi:10.18429/JACoW-IBIC2022-TUP21

[6] G. Kube, C. Behrens, C. Gerth, B. Schmidt, W. Lauth, and M. Yan, "Inorganic Scintillators for Particle Beam Profile Diagnostics of Highly Brilliant and Highly Energetic Electron Beams", in *Proc. IPAC'12*, New Orleans, LA, USA, May 2012, paper WEOAA02, pp. 2119–2121.

[7] Ch. Wiebers, M. Holz, G. Kube, D. Noelle, G. Priebe, and H.-Ch. Schroeder, "Scintillating Screen Monitors for Transverse Electron Beam Profile Diagnostics at the European XFEL", in *Proc. IBIC'13*, Oxford, UK, Sep. 2013, paper WEPF03, pp. 807–810.

[8] Crytur Company Website, Specific GAGG+ and other materials, https://www.crytur.cz/materials/gagg/.

[9] Midland Carbides Company, https://www.midlandcarbides.co.uk/.

[10] Midland Carbides Company Grades List, https://www.midlandcarbides.co.uk/grade-list

[11] ImageJ, https://imagej.net/ij/.

[12] S. Lutz *et al.*, "Scintillator Evaluation for High-Energy X-Ray Diagnostics", United States, Sep. 2001. doi:10.2172/790063

[13] F. Viallefont-Robinet *et al.*, "Comparison of MTF measurements using edge method: towards reference data set", *Opt. Express*, vol. 26, 2018, pp. 33625-33648. doi:10.1364/OE.26.033625

[14] QuickMTF Program, http://www.quickmtf.com/.

Content from this work may be used under the terms of the CC-BY-4.0 licence (© 2023). Any distribution of this work must maintain attribution to the author(s), title of the work, publisher, and DOI

ISBN: 978-3-95450-236-3 ISSN: 2673-5350 doi:10.18429/JACoW-IBIC2023-WEP021

100 Hz X-RAY BEAM PROFILE MEASUREMENTS FROM A TRANSMISSIVE CVD DIAMOND DETECTOR

C. Bloomer*[1], L. Bobb, Diamond Light Source, Oxfordshire, UK
M.E. Newton, University of Warwick, Coventry, UK
[1]also at University of Warwick, Coventry, UK

Abstract

A non-destructive CVD diamond X-ray beam imaging monitor has been developed for synchrotron beamlines. The device can be permanently installed in the X-ray beam path and is capable of transmissively imaging the beam profile at 100 frames per second. The response of this transmissive detector at this imaging rate is compared to synchronously acquired images using a destructive fluorescent screen. It is shown that beam position, size, and intensity measurements can be obtained with minimal disturbance to the transmitted X-ray beam. This functionality is beneficial to synchrotron beamlines as it enables them to monitor the X-ray beam focal size and position in real-time, during user experiments. This is a key enabling technology that would enable live beam size feedback, keeping the beamline's focusing optics optimised at all times. Ground vibrations (10 Hz - 20 Hz) can cause movement of focusing optics and beamline mirrors, which disturb the X-ray beam and reduce the ultimate quality of the sample-point beam. This instrument can detect this beam motion, enabling the source to be more easily determined and mitigations to be put in place.

INTRODUCTION

Diamond detectors for synchrotron X-ray beamlines are advantageous for a number of reasons. Firstly, diamond is highly transparent to X-rays compared to other detector materials, which enables it to be installed permanently on the beamline in the beam path. Secondly, diamond has favourable thermal properties such high melting point and heat conduction, that enable it to withstand intense X-ray beams from synchrotrons and XFELs. Thirdly, the strong diamond lattice is both physically robust and resistant to mechanical damage, and it is radiation tolerant. Finally, and of particular use for this form of detector, the diamond structure can be modified by fast laser pulses, to 'write' laser conductive wires and electrodes within the bulk diamond [1]. The results presented in this contribution are from a pixellated single-crystal CVD diamond with laser written electrodes. The design of the 10 x 11 pixel detector and initial results from synchrotrons and XFELs are presented in Refs. [2–5], along with discussion of the advantages and disadvantages of diamond for this application.

To briefly summarise the design and operation of this prototype pixellated diamond detector, it builds upon a concept first presented in Ref. [6]. A pattern of 'strip electrodes' on one face of a diamond plate could be sequentially biased, while the subsequent charge reaching a pattern of orthogonal electrodes on the opposite face of the diamond is read out using electrommeters or other sensitive ammeters. Sequentially biasing the 'strip electrodes' enables one row of pixels to the read out at a time. The graphitic wire detector improves upon this design in two respects: firstly, through the use of laser-written graphitic electrodes which are buried under the surface of the diamond plate, protecting them from damage and resulting in a more physically robust detector; and secondly, through a novel lock-in modulated bias technique, illustrated in Fig. 1, whereby all 'bias' electrodes simultaneously have an AC bias applied to them at different frequencies using a programmable multi-channel DAC. The resulting signal currents from each 'measurement' electrode are simultaneously acquired using a multi-channel 20 kS / s acquisition system. A Fourier transform of the signal currents from each measurement electrode is carried out. The Fourier amplitude of the measured signal at a given frequency is proportional to the flux passing through the detector at the intersection between the measurement electrode and the bias electrode modulated by that frequency.

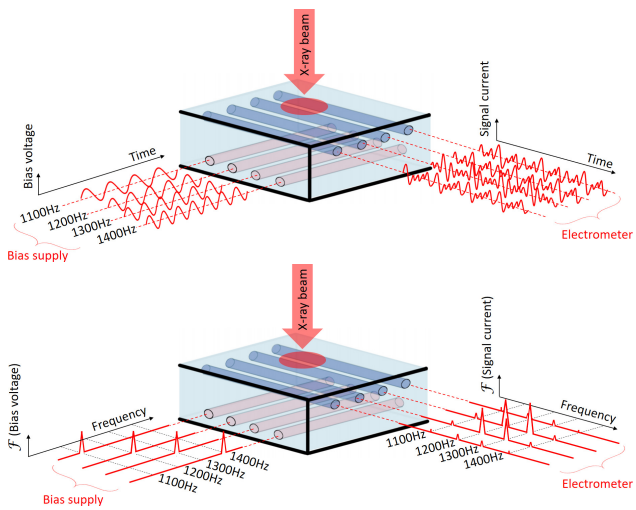


Figure 1: A sketch of the pixel readout scheme, utilising a different modulation frequency applied to each graphitic 'bias' electrode. Top: A time-domain view of the modulation scheme. Bottom: A frequency-domain view, showing how the individual modulation frequencies measured by the electrometer build up a picture of the X-ray beam profile.

* chris.bloomer@diamond.ac.uk

Content from this work may be used under the terms of the CC-BY-4.0 licence (© 2023). Any distribution of this work must maintain attribution to the author(s), title of the work, publisher, and DOI

ISBN: 978-3-95450-236-3 ISSN: 2673-5350 doi:10.18429/JACoW-IBIC2023-WEP021

Content from this work may be used under the terms of the CC-BY-4.0 licence (© 2023). Any distribution of this work must maintain attribution to the author(s), title of the work, publisher, and DOI

OBTAINING 100 FRAME PER SECOND IMAGES

Experiments were carried out on the I18 beamline at Diamond Light Source [7]. A photon energy of 15 keV was selected, providing a collimated photon beam with a flux of up to 3×10^{11} ph / s. The beam size at the detector could be altered from 20 µm up to 250 µm FWHM through the use of adjustable focusing mirrors.

The diamond graphitic wire detector and a traditional fluorescent screen system (a CMOS camera recording the fluorescence from a cerium-doped lutetium-aluminium-garnet, LuAG:Ce, fluorescent screen) were installed together at the focal point, supported on a motion stage which allowed them to be aligned to the incident beam. The transparent graphitic wire detector (15 keV photon absorption < 5 %) was installed ~ 10 mm upstream of the opaque LuAG:Ce fluorescent screen (15 keV photon absorption > 80 %) [3, 8].

Figure 2 presents the sum of the discrete Fourier transform (DFT) from all of the 11 measurement channels, up to 6 kHz, when it was illuminated by a large, 200 µm FWHM. The modulation frequencies used are highlighted. In this image one can see how the 1-dimensional beam profile is determined from the amplitude of the Fourier transform of the modulation frequencies. The individual signal currents obtained from each of the 11 readout channels from the graphitic wire detector beam are presented in Fig. 3. This figure shows the resulting DFT of these signals from a 1 s (top) and 10 ms acquisition period (bottom).

The acquisition goal of 100 frames per second (FPS) was chosen as this would enable any X-ray beam motion arising from the most common 'ground vibration' frequencies at Diamond Light Source, around 10 Hz - 20 Hz, to be clearly measured.

The bias modulation frequencies used were 1.0 kHz, 1.1 kHz, 1.2 kHz, ..., 1.9 kHz. This choice of modulation frequencies has been carefully chosen:

- Firstly, these frequencies easily allows for short acquisition periods of just 10 ms, enabling 100 FPS acquisition of the images. With a 20 kHz sampling rate, a 10 ms acquisition will contain 200 samples. The DFT of these samples will result in each of the modulation frequencies occupying exactly one frequency bin, simplifying the image acquisition. Each frequency bin of the DFT corresponds to one column of pixels on the detector. The bottom plot in Fig. 3 presents the Fourier transform from one 10 ms acquisition to illustrate this.
- Secondly, it ensures that the lowest modulation frequency used, 1.0 kHz is well above the frequency of any *beating* between neighbouring modulation frequencies, observed at 100 Hz, 200 Hz, 300 Hz, etc.
- Lastly, it ensures that higher harmonics of the chosen modulation frequencies will not clash with any of the modulation frequencies themselves: the lowest modulation frequency, 1.0 kHz, has a 2nd harmonic that is above the highest modulation frequency of 1.9 kHz.

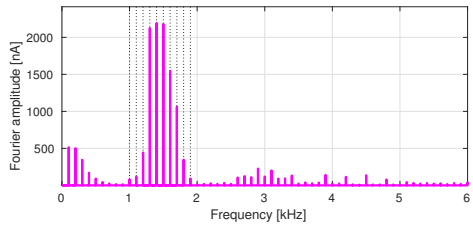


Figure 2: The sum of the individual DFT results from the 11 measurement channels, showing obtained spectra from 1 Hz to 6 kHz calculated from 1 second of data acquired at 20 kHz. These results show the appearance of lower frequency 'beating' and higher frequency harmonics of the main modulation frequencies.

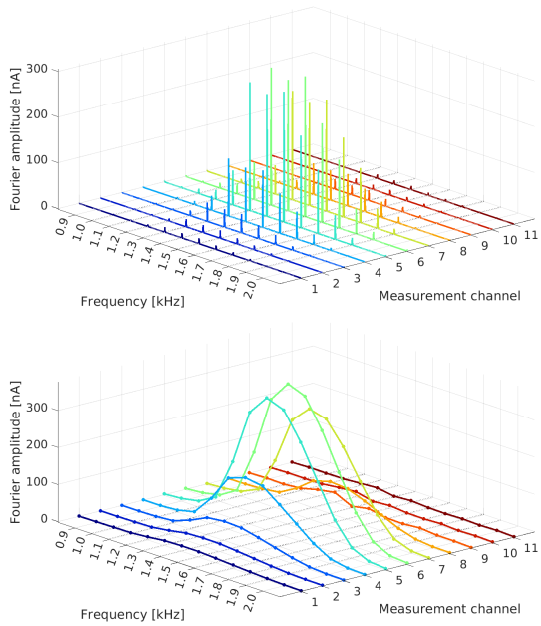


Figure 3: The Fourier transforms from 20 kHz signals acquired from 11 measurement electrodes whilst the X-ray beam is illuminating the detector. These plots just show the DFT amplitudes from 0.9 kHz to 2.0 kHz, around the modulation frequencies used. Top: The Fourier transform of a 1 second long acquisition at 20 kHz signals. Bottom: The Fourier transform of a 10 ms acquisition.

ESTIMATED POINT SPREAD FUNCTION AND IMAGE DECONVOLUTION

By illuminating the detector with as small an X-ray beam as possible an estimate of the 2-dimensional point spread function (PSF) of the detector can be measured. To make this estimate, the beamline optics were used to focus the X-ray beam down to the smallest beamsize achievable at the location of the detector. The resulting beamsize at the detector was measured to be 24 µm x 20 µm FWHM, as measured by two independent means: firstly by direct X-ray camera image, and secondly by knife-edge measurement. This is much smaller than one 50 µm x 50 µm pixel of the graphitic wire detector and is sufficient to make a reasonable estimate of

ISBN: 978-3-95450-236-3 ISSN: 2673-5350 doi:10.18429/JACoW-IBIC2023-WEP021

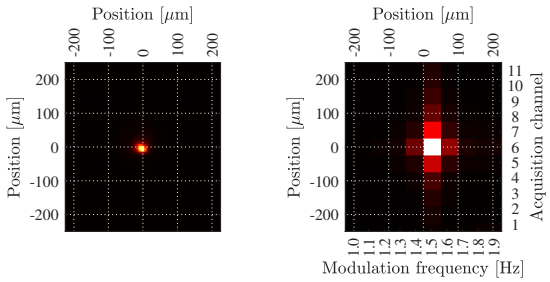


Figure 4: Acquired images of the 24 µm x 20 µm FWHM X-ray beam. Left: The fluorescent screen image of the incident beam profile. Right: The measured estimate of the PSF of the graphitic wire detector, obtained by illuminating the detector with the small incident beam size. Both images depict the same field of view.

the PSF. Under this illumination the obtained 2-dimensional image obtained using both the fluorescent screen monitor and the graphitic wire detector is presented in Fig. 4.

It is clear that there is some 'spread' of the signal across multiple pixels of the graphitic wire detector. Of particular note is that this obtained PSF does not exhibit the radial symmetry that one would anticipate from an ideal detector. There is a vertical spread of the measured beam profile, smearing the 20 µm vertical beam profile across several 50 µm sized pixels. Horizontally there is only a small amount of spread, into only the neighbouring pixels. This asymmetrical response in the vertical and horizontal directions is not entirely unexpected, as the acquisition methods differ in the two axes: each pixel in a horizontal 'row' is defined by a different modulation frequency; each pixel in a vertical vertical column is obtained from a separate measurement channel (as indicated by the axes in Fig. 4). It becomes clear that the frequency of the centre electrode being struck by the incident beam, 1500 Hz in this case, is 'leaking' across the various measurement channels.

As we have obtained a good estimate of the PSF, and confirmed that the PSF is consistent across the face of the graphitic wire detector, image deconvolution algorithms can be introduced to estimate the original beam profile from the detector image. A commonly used method originating from the fields of optics and astronomy is the Richardson-Lucy algorithm [9, 10]. The deconvolution was carried out using MathWorks MATLAB, with the built-in `deconvlucy` function [11]. The default algorithm tuning parameters of the function were used. The results of these reconstructions are presented in Fig. 5.

IMAGING RESULTS

To demonstrate the 100 frame per second (FPS) capabilities of the detector, the motion stage was used to oscillate both the graphitic wire detector and the fluorescent screen back and forth relative to the incident beam. For both detectors, a 2-dimensional Gaussian fit was used to find the beam centroid. The CMOS camera observing the fluorescent screen was configured to acquire data at 100 FPS in free-run mode using an integration period of 1 ms, while the graphitic wire detector signal currents were acquired continuously at 20 kHz and then divided up into 10 ms (100 FPS) chunks for analysis. Acquisition from the two devices was initiated by external hardware trigger. Figure 6 shows the an example of the graphitic wire detector image obtained (after deconvolution using the Richardson-Lucy algorithm) alongside the simultaneously acquired fluorescent screen image, both acquired as part of a 100 FPS sequence. The combined computation time for both the deconvolution and the 2-dimensional Gaussian fit of the graphitic wire detector image using MATLAB was < 4 ms, enabling both to be

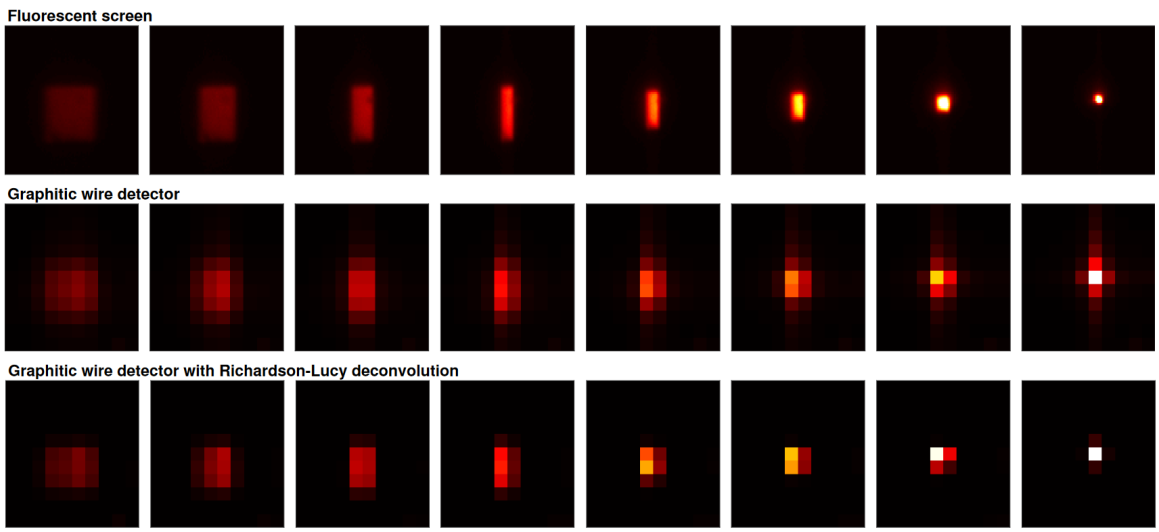


Figure 5: Images obtained of the X-ray beam profile with 10 ms acquisition period during during a beam focusing procedure. Top row: Images obtained from the fluorescent screen. Middle row: Raw images obtained from the graphitic wire detector. Bottom row: The estimated reconstruction of the beam profile obtained using the Richardson-Lucy algorithm.

Content from this work may be used under the terms of the CC-BY-4.0 licence (© 2023). Any distribution of this work must maintain attribution to the author(s), title of the work, publisher, and DOI

ISBN: 978-3-95450-236-3 ISSN: 2673-5350 doi:10.18429/JACoW-IBIC2023-WEP021

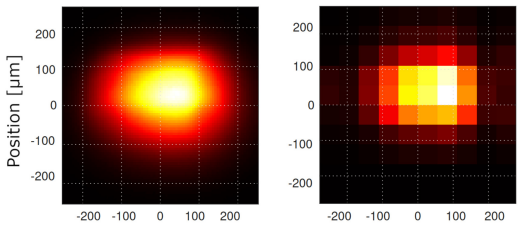


Figure 6: Beam profile images simultaneously acquired using both the the fluorescent screen and CMOS camera (left) and the graphitic wire detector (right). The X, Y measurements shown are units of microns.

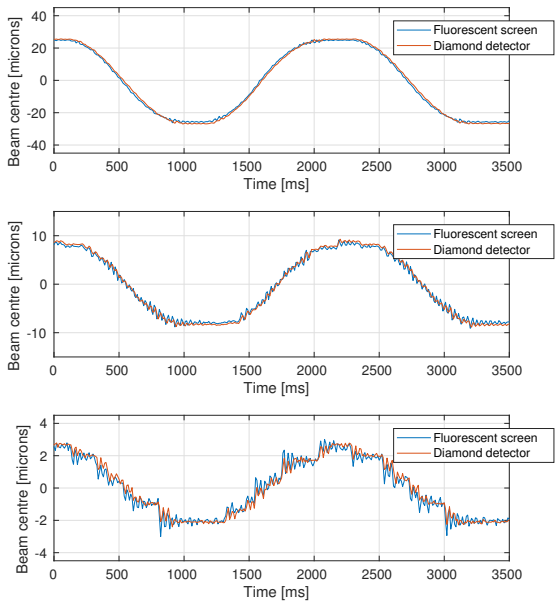


Figure 7: Vertical beam position measurements acquired from 100 FPS image sequences during stepper motor movements of the stage the detector was mounted upon. The motor is requested to move in a sine wave with an amplitude of ± 30 µm (top); ± 10 µm (middle); and ± 3 µm (bottom).

completed in real-time while the following image is being acquired.

Figure 7 shows the measured variation in beam position simultaneously obtained from the 100 FPS images from both the graphitic wire detector and from the fluorescent screen image for a series of 1-dimensional vertical stepper motor sweeps. The first sweep (top) is a ± 30 µm sine wave requested from the motor; the second (middle) is a ± 10 µm motor request; the final motion (bottom) shows the results when a ± 3 µm sine wave was requested. This final sweep was at the limit of the motor's capability, and it is clear from the obtained position measurements that the motor cannot reproduce a smooth sine wave, instead a series of discrete steps is observed, with some settling time and 'rattling' after each step. Both the graphitic wire detector and the fluorescent screen images observe the same effect. The use of 2-dimensional Gaussian fitting enables these motions to be observed on the graphitic wire detector even though they are clearly significantly smaller than the 50 µm pixel size.

CONCLUSIONS

The graphitic wire detector presented in this work is shown to successfully obtain X-ray beam images and beam position measurements. A novel lock-in modulation readout method has been demonstrated, enabling 100 FPS acquisition of 2-dimension X-ray beam profile and centroid measurements. All pixels were acquired simultaneously.

The position measurement results are comparable to that obtained from a traditional fluorescent screen, however the X-ray absorption is significantly less than most fluorescent materials. The graphitic wire detector may be permanently installed in the X-ray beam path, offering significant advantages over fluorescent screens or knife-edge scans which generally cannot be used during user experiments as they intercept too great a portion of the synchrotron flux or block it entirely.

While the PSF of the detector shows 'leakage' into neighbouring pixels and does not exhibit radial symmetry, a software deconvolution approach has been demonstrated to reconstruct the beam profile satisfactorily, and enable submicron beam position measurement.

Possible future developments include both smaller pixel sizes, as the laser writing steps could easily be changed to implement a pixel pitch down to ~ 15 µm, and higher pixel counts, as this experiment was limited by the number of available ADC channels. Using higher sample rate DACs and ADCs would also enable an increase in the frame rate, if required. There are commercially available 32-channel DAC and ADC units capable of 100 kHz output/input which could be used to increase both the pixel count and the acquisition rate.

This detector is beneficial to synchrotron beamlines as it enables scientists and users to monitor the X-ray beam focal size and position in real-time, during user experiments. This functionality would enable live feedback, keeping the beamline focusing optics optimised at all times. It would reduce set-up and commissioning time, as the detector can be permanently installed in the X-ray beam path and beam sizes can be determined without having to temporarily insert destructive monitors into the beam path.

ACKNOWLEDGEMENTS

The authors wish to acknowledge the support of many individuals and groups that aided in this research. The CVD diamond plate used was provided by Element Six. We wish to acknowledge the contributions of P. Salter for the graphitic electrode fabrication, at the University of Oxford. The detector surface metallisation was carried out by B. Green, and the wire bonding by F. Courtney, both at the University of Warwick. We are grateful for the support of G. Cook and K. Ignatyev at Diamond Light Source for their help in carrying out these experiments.

REFERENCES

[1] B. Sun *et al.*, "High conductivity micro-wires in diamond following arbitrary paths", *Appl. Phys. Lett.* , vol. 105, p. 231105,

Content from this work may be used under the terms of the CC-BY-4.0 licence (© 2023). Any distribution of this work must maintain attribution to the author(s), title of the work, publisher, and DOI

ISBN: 978-3-95450-236-3 ISSN: 2673-5350 doi:10.18429/JACoW-IBIC2023-WEP021

2014. doi:10.1063/1.4902998

[2] C. Bloomer *et al.*, "A single-crystal diamond X-ray pixel detector with embedded graphitic electrodes", *J. Synchrotron Radiat.*, vol. 27, pp. 599–607, 2016. doi:10.1107/s160057752000140x

[3] C. Bloomer, L. Bobb, and M. E. Newton, "Single-Crystal Diamond Pixelated Radiation Detector with Buried Graphitic Electrodes", in *Proc. IBIC'21*, Pohang, Korea, Sep. 2021, pp. 158–166. doi:10.18429/JACoW-IBIC2021-TUOA01

[4] C. Bloomer *et al.*, "XFEL Photon Pulse Measurement Using an All-Carbon Diamond Detector", in *Proc. IBIC'22*, Kraków, Poland, Sep. 2022, pp. 416–420. doi:10.18429/JACoW-IBIC2022-WEP15

[5] C. Bloomer, "A Pixelated CVD Diamond Synchrotron Radiation Monitor with Graphitic Electrodes", Ph.D. Thesis, Dept. of Phys., University of Warwick, UK, 2023.

[6] D. Shu *et al.*, "CVD-diamond-based position sensitive photoconductive detector for high-flux X-rays and gamma rays", *Proceedings of the Particle Accelerator Conference*, pp. 2090-2092, 1999. https://jacow.org/p99/PAPERS/WEA90.PDF

[7] J. Mosselmans *et al.*, "I18 - the microfocus spectroscopy beamline at the Diamond Light Source", *J. Synchrotron Radiat.*, vol. 16, pp. 818–824, 2009. doi:10.1107/S0909049509032282

[8] B. L. Henke *et al.*, "X-ray interactions: photoabsorption, scattering, transmission, and reflection at E=50-30000 eV, Z=1-92", *At. Data Nucl. Data Tables*, vol. 54, pp. 181–342, 1993. doi:10.1006/adnd.1993.1013

[9] W.H. Richardson, "Bayesian-based iterative method of image restoration", *J. Opt. Soc. Am.*, vol. 62, 1972. doi:10.1364/josa.62.000055

[10] L.B. Lucy, "An iterative technique for the rectification of observed distributions", *Astron. J.*, vol. 79, 1974. doi:10.1086/111605

[11] Mathworks, "Deblurring Images Using the Lucy-Richardson Algorithm", 2021. https://uk.mathworks.com/help/images/deblurring-images-using-the-lucy-richardson-algorithm.html

Content from this work may be used under the terms of the CC-BY-4.0 licence (© 2023). Any distribution of this work must maintain attribution to the author(s), title of the work, publisher, and DOI

ISBN: 978-3-95450-236-3 ISSN: 2673-5350 doi:10.18429/JACoW-IBIC2023-WEP022

TARGET MULTIWIRE FOR THE FERMILAB BOOSTER NEUTRINO BEAMLINE

R. Prokop†, Fermi National Accelerator Laboratory, Batavia, IL, USA

Abstract

The Booster Neutrino Beamline experiment requested a new secondary electron emission multiwire profile monitor installation. The device had to be durable in high radiation conditions and mounted within a large 10-foot airtight steel fixture for installation near the beam target. Previous iterations of multiwire suffered radiation damage to both the connectors and wires. To ensure accurate horizontal and vertical beam profile measurements, an updated design was proposed, designed, and constructed. The new BNB multiwire utilizes 3 mil diameter gold-plated tungsten sense wires soldered to vertical and horizontal Alumina-96 ceramic planes, 50 wires per plane. Radiation hard Kapton insulated 30-gauge wires carry the output signals. Profiles are readout through charge integrator scanner electronics. This paper will detail the design and functionality of the BNB target multiwire and present relevant beam profile data.

FUNCTION AND APPLICATION

The Booster Neutrino Beamline Multiwire for Horn 5 is a unique secondary emission monitor design at Fermilab utilized specifically for profile measurements of high intensity beam, up close to the experimental target [1]. This specialization calls for high durability and several modifications from the typical multiwire. The goal is to get clean gaussian profile measurements from small diameter wire, using wire/cable that can withstand high radiation environments. Previous iterations of this design used the classic multiwire flat Kapton ribbon cables with zero insertion force connectors glued to the ceramic frames. This is not ideal, as the intense environment of this device causes damage to the connectors. To remedy this problem, small gauge (30-40 AWG) Kapton insulated wire are individually cut to length and wrapped in bundles, soldered to both the frame and readout connectors. This presents many engineering challenges, but also opportunities to improve and craft a very durable and effective multiwire. This project has been a joint effort between the Fermilab Accelerator Directorate Instrumentation, External Beams & Target Systems groups.

The BNB multiwire operates on the principle of secondary electron emission, much the same as all other SEM profile monitors at Fermilab. The particle beam made up of protons strikes the sense wires and knocks off surface electrons from the metal material. This phenomenon leaves a resultant net positive charge on the wires which can be readout as a current through the signal cables. This current is integrated through transimpedance amplifiers in the front-end electronics and digitized as a voltage value to be plotted as a final beam profile measurement. The resultant signal is expected to be proportional to the amount of beam particles striking the wires [2].

Bias planes are comprised of titanium foils, and act to enhance the secondary emission effect by collecting stray electrons. The bias operates at +200 VDC.

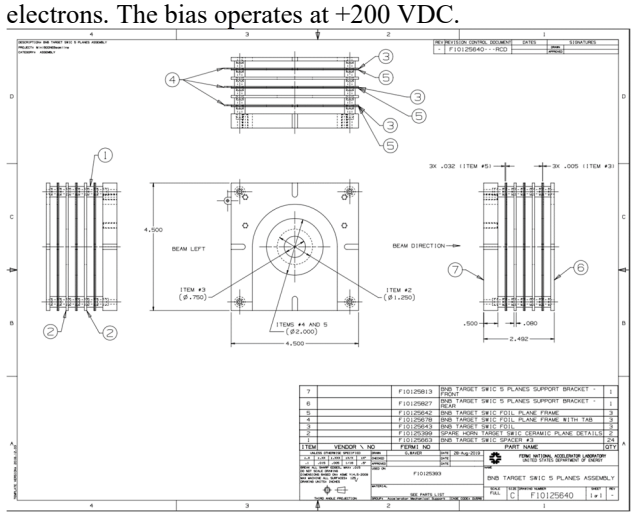


Figure 1: Multiwire assembly drawing.

DESIGN

The BNB Target multiwire is an open air mounted secondary emission monitor designed for the high intensity beam readout. The multiwire assembly as shown in Fig. 1, consists of two ceramic planes, one of vertical orientation and one horizontal. The ceramics are 4.5 x 4.5 inch with a center hole of diameter 1.25 inch. They have 50 pads at 1mm spacing for signal wires, and 100 pads at 0.5 mm spacing for sense wires across the center hole. There are three titanium foils of .005-inch thickness, which act as bias planes to assist in maintaining an electric field for charge deposition on the sense wires. The multiwire assembly is held together by front and back support brackets as well as spacers between the planes. The multiwire mounting assembly is slid into a larger horn mechanical enclosure for insertion close to the target. Discussion of the entire mechanical mounting assembly is beyond the scope of this document.

The signal carrying conductors are fashioned in a similar way to previous the MiniBooNE target multiwire, but without the zero insertion force connectors or Kapton ribbon cables. This new design instead utilizes 100 individual Kapton insulated wires of 0.25 mm diameter for the signal wires, terminated at one end at the pads of the ceramic and at two 50 pin D-Sub connectors on the other end. The use of connectors and epoxy was not ideal for this application, as in previous designs the epoxy wore down and connectors became damaged due to heat and radiation. 0.003-inch diameter AuW wires are soldered pad to pad for the center beam sense wires. AuW wires provide acceptable signal integrity through collected charge, as well as having excel-

* This work was supported by the U.S. Department of Energy under contract DE-AC02-07CH11359
† rprokop@fnal.gov

Content from this work may be used under the terms of the CC-BY-4.0 licence (© 2023). Any distribution of this work must maintain attribution to the author(s), title of the work, publisher, and DOI

ISBN: 978-3-95450-236-3 ISSN: 2673-5350 doi:10.18429/JACoW-IBIC2023-WEP022

lent density and durability with high intensity beam [3]. A small diameter of 3 mil is typical for applications such as this; it limits the amount of material in the beam while also giving ample signal.

Wire Preparation

- The Kapton insulated wires make for a challenge when assembling the multiwire. To account for every sense wire reading, there must be 50 wires per plane, totalling to 100 signal wires. Additionally, there is one high voltage wire which supplies the bias. The signal wires for the multiwire must measure at minimum 10-feet in length. When accounting for some slack, they were cut to ~11 ft. The wires must reach from the multiwire planes to the D-Sub connectors for readout. To achieve a neat and organized bundle of wires, the decision was made to separate the wires into sets of 10. Each plane has five sets of 10 wires, with each set taped together at intervals along the 10-foot length run. The mechanical assembly, shown in Fig. 2, has a 9-foot metal pipe which carries the wire bundles from the wireplane mount to the connectors. There is a slight angular bend at the end of the pipe, which makes the pipe length and wireplane fixture distance approximately 9.5 ft.
- The ends of the Kapton wires are stripped to reveal a few mm length of centre conductor for soldering. It is important to consider the order of the wires when preparing bundles. Each set of 10 wires has a red tick mark on the electrical tape near the first wire. A multimeter was used to check continuity between ends of the wires and ensure that each wire is properly marked on both sides.

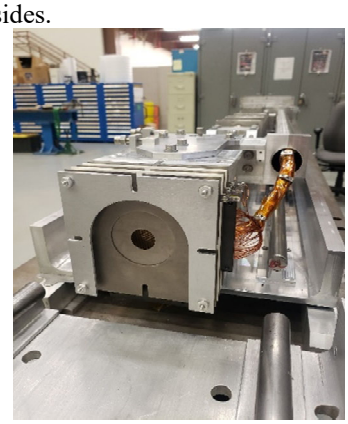


Figure 2. Multiwire assembly completed and mounted.

Soldering Procedure

The soldering of signal wires requires a pre-made wire containing fixture, as a procedure like this has never been attempted before with a multiwire. The signal wires are soldered to pads directly on the ceramic itself, much different than other modern multiwires which have connectors and 50 conductor cables or ribbon cables. The fixture is simply a metal block, with 0.25 mm width slots to sit the wires in. A top block is fastened above the wires to clamp down and secure them in place. This wire fixture is essential for the completion of the multiwire assembly (see Fig. 3).

The central sense wires are soldered with an intricate method by a wireplane specialist at Fermilab. She winds the wires on a transfer plane to get tension and the correct spacing, 0.5 mm in this case. They are aligned to the pads on the ceramic thereafter. Then the wires are temporarily epoxied to tape at the end of the substrate and soldered.

To circumvent damaging the ceramic with high heat, and allow for fast and easier reflow soldering, Alpha CVP-520 low temp solder paste [4] was initially chosen as the bonding agent. This paste has a melting point of 138 °C and an optimum reflow temperature between 150 °C and 190 °C. A soldering iron would work for drag soldering but runs the risk of applying too much focused heat to the ceramic. A heat gun causes far too much spread, with risk of affecting the sense wires or too much airflow. The ideal tool for the job is an adjustable airflow heat wand with changeable tips. Keeping airflow relatively low allows more heat with less risk of paste blowing across the ceramic. A temperature of 190 °C/374 °F provides a fast and effective reflow for the solder paste and bonds the wires efficiently.

The 10-foot bundles were routed through 9-foot pipe to the readout box at MI-8 during the full assembly procedure. The readout cable and connector soldering process involved several days and many hours of stripping and soldering each wire end to the D-Sub connectors bolted to the readout box. A high voltage wire was also connected to the planes and fed to an SHV bulkhead connector.

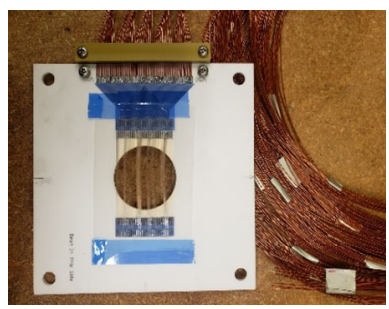


Figure 3: Wireplane with Kapton insulated signal wires.

INSTALLATION AND RESULTS

The multiwire is mounted on a mechanical assembly and aligned with precision instrumentation. This process ensures that the center of the wireplane grids and the center of the beam pipe are within ~1 mm tolerance. Kapton insulated cabling is routed through a 9 ft stainless steel pipe for protection. At the end of the pipe is a welded cap with D-Sub connector feedthroughs and one SHV-5 high voltage connector feedthrough. The signal wires have been carefully soldered individually to each pin and tested for continuity as well as shorts.

The mounting assembly is on rails, and during installation it slides into a larger housing unit. This unit is sealed completely airtight and placed near the beam target. Due to the proximity to the beam target and the high radiation hazard, access to the internals of the unit for repairs or modifications is very difficult and time consuming. All alignment and testing are done to the highest of standards to reduce the risk of failures.

Content from this work may be used under the terms of the CC-BY-4.0 licence (© 2023). Any distribution of this work must maintain attribution to the author(s), title of the work, publisher, and DOI

ISBN: 978-3-95450-236-3 ISSN: 2673-5350 doi:10.18429/JACoW-IBIC2023-WEP022

Content from this work may be used under the terms of the CC-BY-4.0 licence (© 2023). Any distribution of this work must maintain attribution to the author(s), title of the work, publisher, and DOI

Readout Electronics

The BNB target multiwire uses standard Fermilab readout electronics for beam profile monitors. These chassis are called scanners, shown in Fig. 4. A set of boards housing 96 channel analog front end integrator circuits receive the signals from the current carrying cables and integrate them to voltages for digitization. Wire 1 and 50 on the vertical and horizontal wireplanes act as ground wires, tied to chassis ground at the scanner. The modern scanners have ethernet capability, for fast and reliable control and data capture. Every scanner is connected to the Fermilab Accelerator Control Network front end for viewing data and making changes to settings. The Fermilab Controls Department manages these devices and provides Instrumentation with reliable readout electronics.

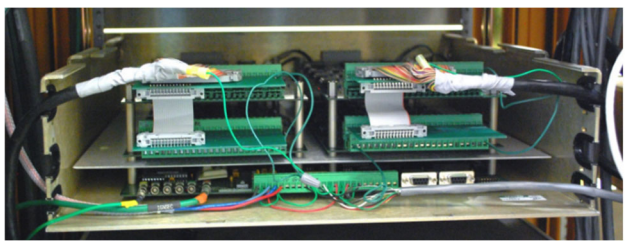


Figure 4: Rear view of scanner electronics.

Profile Data

The data pictured below is not from the BNB target multiwire, as this device is recently installed and has not yet seen beam. The image below shown in Fig. 5 is a screen capture from a similar device, a standard multiwire SEM. This is the horizontal and vertical display showing expected results with a Gaussian fit. The histogram plot has each wire voltage value represented as a blue bar. The center of beam is ideally the center peak of the profile.

The environment which the BNB target multiwire is installed is considered a high radiation area, due to its proximity to the beam target. Exact radiation measurements are not known but are enhanced by secondary beam materials such as neutrons. The beam bunch intensity is approximately 4E12 protons/bunch and the proton rate is around 3E16 protons/hr at a proton beam energy of 8 GeV.



Figure 5: Beam profiles, horizontal and vertical

Future

The readout electronics consist of two flat-to-round signal cables, vertical and horizontal, connected to a Controls Scanner rack-mount chassis. The readout electronics are housed at Main Injector Service Building 12. Testing the device is possible using the common flash test procedure for multiwire profile monitors. This test uses an integrating scanner, high voltage supply, and video monitor to view the charge collection as a histogram of voltages on each wire. Due to the nature of the BNB multiwire and it's very difficult to reach location, as well as nearby hazards, it is challenging to repair. A complete failure or wire replacement would result in the entire assembly's removal and a disassembly of the wireplane fixture.

Another Target multiwire for BNB Horn 4 is coming, and there are lessons learned and proposed modifications the team has come up with. For the signal wire readout cables, there is a ceramic coated small gauge wire produced by a vendor which may be a suitable substitute for the Kapton insulated wire. The ceramic coated wire is highly durable and highly flexible, while maintaining its form. The ceramic coating is extremely small, thin, and porous. The primary challenge when implementing this material will be stripping the coating from the central Copper/Nickel conductor. Using a molten hot solution is one method, but highly hazardous and not ideal for 100 wires. Fermilab engineers who have done research this potential wire type, have proposed a few alternate stripping and mounting methods which will be tested.

CONCLUSION

The BNB target multiwire was a collaborative effort between multiple departments and teams at Fermilab. It overcame numerous challenges during design and assembly. The target systems group expects full operation during the 2023-24 accelerator run, with hopes for quality profile data to follow. The radiation-hard connectors and wire strain relief, as well as the Kapton insulation should provide this multiwire with many years of safe operation within the BNB target enclosure. Lessons learned from this project will be carried over into future installations.

ACKNOWLEDGEMENTS

Thanks to the following past and present Fermilab team members who lent their knowledge, skills, and time to this project. Daniel Schoo, retired Fermilab Electrical Engineer. Gianni Tassotto, retired Fermilab Engineering Physicist. Thomas Kobilarcik, Fermilab Engineering Physicist. George Lolov, Fermilab Mechanical Engineer. Hiep Le, late retired Fermilab Physicist. Stephen Rocos, Fermilab Technician. Wanda Newby, Fermilab Technical Specialist. Paula Lippert, Fermilab Technical Specialist. Cervando Castro, Fermilab Technical Specialist.

REFERENCES

[1] Fermilab, https://ad.fnal.gov/ebd/

[2] G. Tassotto and J. Zagel, "Beam Profile Detectors at the new fermilab injector and associated beamlines", in *Proc. DIPAC'99*, Chester, UK, May 1999, paper PS17, pp. 141-143.

[3] Hsing-yin Chang, Andrew Alvarado, Jaime Marian, "Calculation of secondary electron emission yields from low-energy electron deposition in tungsten surfaces", *Applied Surface Science*, vol. 450, pp. 190-199, 2018. doi:10.1016/j.apsusc.2018.04.155

[4] Alpha, https://www.macdermidalpha.com/assembly-solutions/products/solder-paste/alpha-cvp-520-solder-paste

ISBN: 978-3-95450-236-3 ISSN: 2673-5350 doi:10.18429/JACoW-IBIC2023-WEP023

PROGRESS ON AN ELECTRON BEAM PROFILE MONITOR AT THE FERMILAB MAIN INJECTOR*

R. Thurman-Keup†, T. Folan, M. Mwaniki, S. Sas-Pawlik
Fermi National Accelerator Laboratory, Batavia, IL, USA

Abstract

The current program at Fermilab involves the construction of a new superconducting linear accelerator (LINAC) to replace the existing warm version. The new LINAC, together with other planned improvements, is in support of proton beam intensities in the Main Injector (MI) that will exceed 2 MW. Measuring the transverse profiles of these high intensity beams in a ring requires non-invasive techniques. The MI uses ionization profile monitors as its only profile system. An alternative technique involves measuring the deflection of a probe beam of electrons with a trajectory perpendicular to the proton beam. This type of device was installed in MI and initial studies of it have been previously presented. This paper will present the status and recent studies of the device utilizing different techniques.

INTRODUCTION

Measuring the transverse profile of circulating beam in a proton synchrotron is a challenging endeavor. Historically, thin wires were rapidly swept through the beam and downstream losses recorded as a function of the position of the wire to construct the profile. These were called flying wires [1]. In the Main Injector (MI) at Fermilab, they were removed around 2012 due to wire breakage which was not understood. Since it was already known that wires in the circulating beam might pose a problem at the even higher planned intensities, work had begun on building an electron beam profiler (EBP) to complement the ionization profile monitors that were already installed.

The concept of a probe beam of charged particles to determine a charge distribution has been around since at least the early 1970's [2-4]. Several conceptual and experimental devices have been associated with accelerators around the world [5-9]. An operational device is presently in the accumulator ring at the Spallation Neutron Source at Oak Ridge National Lab [10]. The EBP was constructed and installed in the Main Injector (MI) in 2014 and initial results have been presented previously [11]. This paper presents an update on the status of the EBP.

THEORY

The principle behind the EBP is electromagnetic deflection of the probe beam by the target beam under study (Fig. 1). If one assumes a target beam with $\gamma \gg 1$, no magnetic field, and $\rho \neq f(z)$, then the force on a probe particle is [12]

$$\vec{F}(\vec{r}) \propto \int d^2\vec{r}'\rho(\vec{r}')\frac{(\vec{r}-\vec{r}')}{|\vec{r}-\vec{r}'|^2} \quad (1)$$

and the change in momentum is

$$\Delta\vec{p} = \int_{-\infty}^{\infty} dt\ \vec{F}\big(\vec{r}(t)\big) \quad (2).$$

For small deflections, $\vec{r} \approx \{b, vt\}$, and the change in momentum is

$$\Delta\vec{p} \propto \int_{-\infty}^{\infty} dx' \int_{-\infty}^{\infty} dy'\ \rho(x',y') \cdot \int_{-\infty}^{\infty} dt\ \frac{\{b-x', vt-y'\}}{(b-x')^2+(vt-y')^2}\ , \quad (3)$$

where $\{\}$ indicates a vector. For small deflections, $\vec{p} \approx \{0, p\}$ and the deflection is $\theta \approx \frac{|\Delta\vec{p}|}{|\vec{p}|}$. The integral over time can be written as $\mathrm{sgn}(b - x')$ leading to an equation for the deflection

$$\theta(b) \propto \int_{-\infty}^{\infty} dx' \int_{-\infty}^{\infty} dy'\ \rho(x',y')\ \mathrm{sgn}(b-x')\,, \quad (4)$$

where $\mathrm{sgn}(x) = -1$ for $x < 0$ and $+1$ for $x \geq 0$.

If one takes the derivative of $\theta(b)$ with respect to b, the sgn function becomes $\delta(b - x')$ leading to

$$\frac{d\theta(b)}{db} \propto \int_{-\infty}^{\infty} dy'\ \rho(b,y')\ , \quad (5)$$

which is the profile of the charge distribution of the beam. Thus, for a Gaussian beam, this would be a gaussian distribution and the original deflection angle would be the error function, $\mathrm{erf}(b)$.

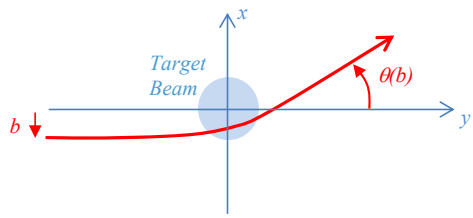


Figure 1: Probe beam deflection (red) for some impact parameter b.

EXPERIMENTAL TECHNIQUE

To obtain $\theta(b)$, one needs to measure the deflection for a range of impact parameters. This can be accomplished by stepping the electron beam through the protons and recording the deflection at each step, or by rapidly sweeping the electron beam through the proton beam (Fig. 2). The latter works without issue provided the sweep time is much smaller than the rms bunch length of the proton beam to

* This manuscript has been authored by Fermi Research Alliance, LLC under Contract No. DE-AC02-07CH11359 with the U.S. Department of Energy, Office of Science, Office of High Energy Physics.
† keup@fnal.gov

Content from this work may be used under the terms of the CC-BY-4.0 licence (© 2023). Any distribution of this work must maintain attribution to the author(s), title of the work, publisher, and DOI

ISBN: 978-3-95450-236-3 ISSN: 2673-5350 doi:10.18429/JACoW-IBIC2023-WEP023

avoid coupling the longitudinal and transverse distributions. In the MI, this condition is not met since the bunch length is only 1-2 ns.

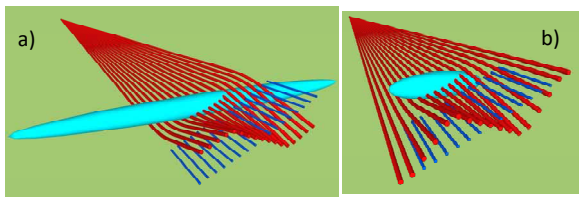


Figure 2: a) Long bunch relative to streak time. b) Short bunch relative to streak time (e.g. MI) leading to bunch-length distortion of deflections.

An alternative method that will be attempted for the MI is a type of raster scan. The beam is swept rapidly along the direction of the proton beam producing an approximate longitudinal distribution (Fig. 3), and slowly transverse to the proton beam. This technique has the potential to allow longitudinal slicing of the transverse profile assuming the longitudinal distribution either remains constant over the series of impact parameter measurements or can be corrected for synchrotron motion.

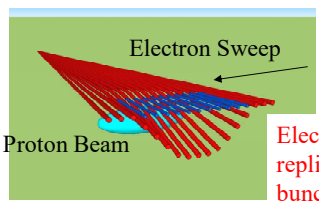


Figure 3: The electron beam is swept along the direction of the proton beam with a sweep time comparable to the proton bunch length. This records the deflection as a function of longitudinal position. A series of these sweeps is collected at different impact parameters to obtain $\theta(b)$.

Simulations of the deflections in this approach are shown in Fig. 4. Here successive sweeps along the proton direction at different impact parameters are displayed in the same image. Each simulated electron produces a Gaussian spot with a rms of 1 mm. The simulation was done for injection parameters of 3 mm horizontal proton beam size, and 2 ns bunch length. One can see that the central deflections may overlap each other.

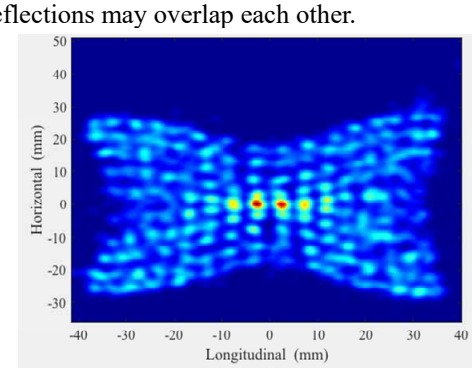


Figure 4: Simulated image of successive electron beam sweeps along the proton beam direction. The sweeps near the center are difficult to separate and may need to be split across multiple camera frames.

Problems such as these must be overcome through, for example, timing shifts or interleaving across multiple camera frames. Before attempting this approach, we have performed a slow diagonal sweep as in Fig. 2 but covering many bunches. The deflections are not as clear, but it is simpler to acquire them.

EXPERIMENTAL DEVICE

The EBP is comprised of an EGH-6210 electron gun from Kimball Physics, followed by a cylindrical, parallel-plate electrostatic deflector, and finally a phosphor screen acting as the beam dump (Fig. 5).

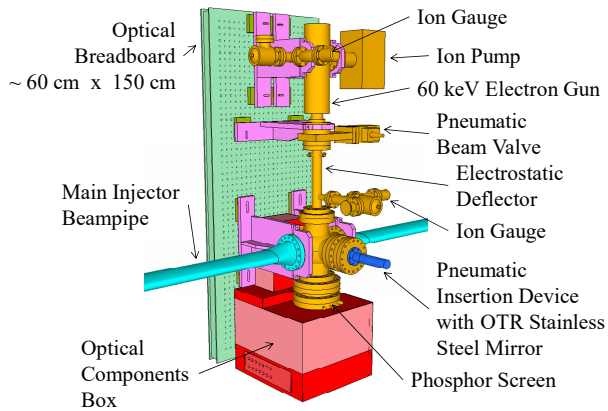


Figure 5: Model of the EBP showing the main components.

The gun is a 60 keV, 6 mA, thermionic gun with a LaB_6 cathode, that can be gated from 2 μs to DC at a 1 kHz rate. The gun contains a focusing solenoid and four independent magnet poles for steering/focusing. The minimum working spot size is <100 μm. The electrostatic deflector (Fig. 6) contains 4 cylindrical plates that are 15 cm long and separated by ~2.5 cm. Following the electrostatic deflector is the intersection with the proton beamline.



Figure 6: Electrostatic deflector showing the curved plates.

After the proton beam intersection, there is a phosphor screen from Beam Imaging Systems. It is composed of P47 (Y_2SiO_5:Ce3+) with an emission wavelength of 400 nm, a decay time of ~60 ns and a quantum yield of 0.055 photons/eV/electron. The phosphor screen has a thin conductive coating with a drain wire attached. The phosphor screen is surrounded by a stainless-steel absorber that is instrumented to function as a faraday cup (Fig. 7).

Content from this work may be used under the terms of the CC-BY-4.0 licence (© 2023). Any distribution of this work must maintain attribution to the author(s), title of the work, publisher, and DOI

ISBN: 978-3-95450-236-3 ISSN: 2673-5350 doi:10.18429/JACoW-IBIC2023-WEP023

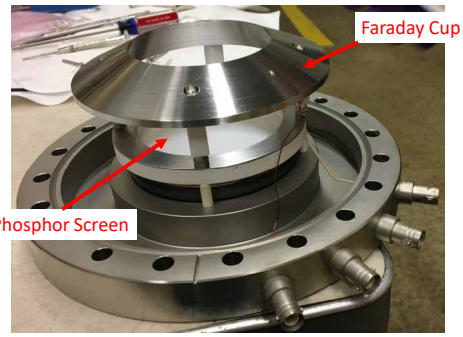


Figure 7: Phosphor screen and angled faraday cup. The faraday cup is intended to be the starting and ending locations for the electron beam during a sweep.

The light from the phosphor traverses a two-lens system plus optional neutral density filters or polarizers before entering a Hamamatsu V6887U-02 gated image intensifier. The output of the intensifier is imaged by a 3710DX12 charge injection device (CID) camera from Spectra-Physics (now Thermo Scientific) which is fiber-optically coupled to the intensifier through a fiber-optic taper to improve light collection (Fig. 8).

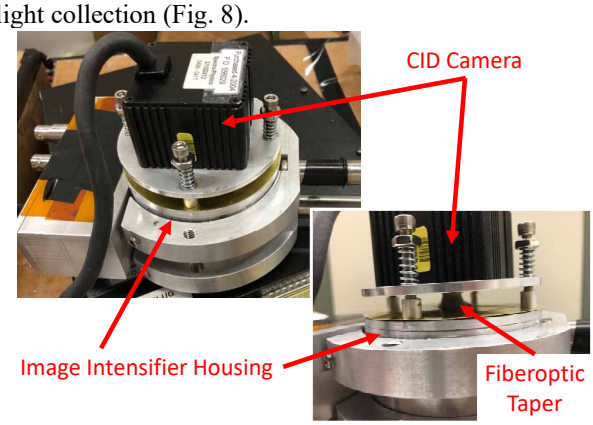


Figure 8: Combination of image intensifier and CID camera coupled together with a fiberoptic taper to map the larger intensifier output to the camera.

Timing for the system is generated by accelerator clock events and requires triggers for camera reset, image acquisition, image intensifier gating, electron gun trigger, fast deflection trigger, and slow deflection trigger. The use and arrangement of the triggers depends on the measurement approach.

MEASUREMENTS

Slow Diagonal Sweep

As stated above, we have performed a slow diagonal sweep utilizing adjacent pairs of deflecting plates to sweep the electron beam diagonally across the proton beam. The sweep is relatively slow such that there are several beam revolutions between deflection measurements (Fig. 9).

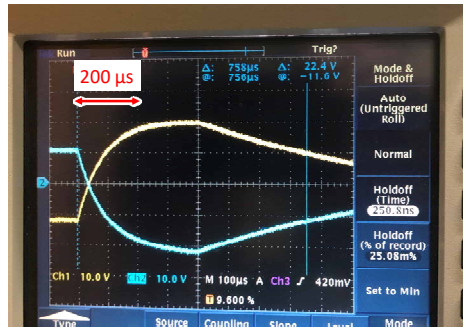


Figure 9: Slow deflection waveforms. The two waveforms are on opposite plates. A MI revolution is 11 µs.

Figure 10 shows images of the sweep both with and without MI beam. These are an average over 10 camera acquisitions. The individual spots are when the image intensifier is gated. A slight enhancement can be seen in the beam image due to the deflections of the electron beam.

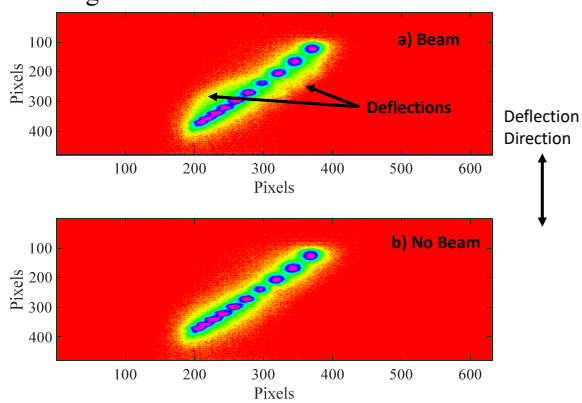


Figure 10: Slow sweep of electron beam. The individual spots are image intensifier gates. A slight enhancement from the electron deflection is visible in (a) where the proton beam is present.

To extract the deflection, we subtract the no-beam image from the beam image (Fig. 11), where the deflections are now more obvious.

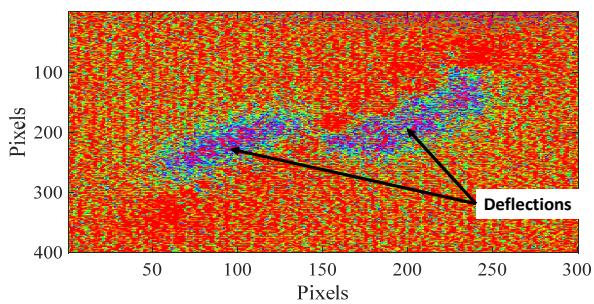


Figure 11: Visible deflections after no-beam image subtraction.

From this image, we find the maximum pixel value in each column. We also find the maximum pixel in each column of Fig. 10b. In Fig. 12, these two curves of maximum pixels are overlayed on the image from Fig. 11.

Content from this work may be used under the terms of the CC-BY-4.0 licence (© 2023). Any distribution of this work must maintain attribution to the author(s), title of the work, publisher, and DOI

ISBN: 978-3-95450-236-3 ISSN: 2673-5350 doi:10.18429/JACoW-IBIC2023-WEP023

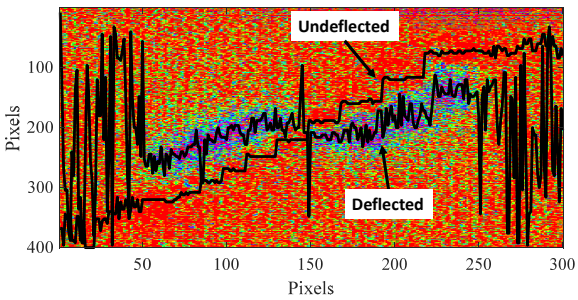


Figure 12: Dark lines show the maximum pixel location for both the deflected electrons and the undeflected electrons.

The undeflected curve shows the step structure of the discrete spots in the original image (Fig. 10b). The difference between these two curves is the deflection distance. We evaluate the average deflection distance for each step region, together with the impact parameter for each step to produce curve (b) in Fig. 13.

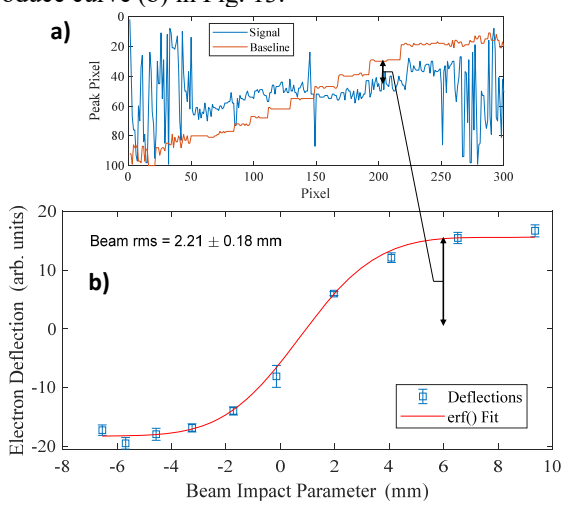


Figure 13: a) The two maximum pixel curves. b) The deflection vs. impact parameter curve generated from (a). The resulting fit sigma is 2.21 mm.

The curve is fit with an error function to extract the underlying gaussian parameters of the proton beam. The sigma of the fit is 2.21 ± 0.18(stat.) mm. This is in reasonable agreement with the same measurement from the ionization profile monitor, 1.71 mm.

It is not clear that using the peak pixel is the best approach, and we may refine this technique in the future.

Fast Sweep

The original goal of the EBP was to perform the fast sweep shown above in Fig. 3. Figure 14 shows a scope trace of the fast deflection waveform. We have made one test of the fast sweep (albeit without an actual measurement) and it is shown in Fig. 15. The size of the sweep line is larger than naively expected. This will make the measurement more difficult as we may not be able to put more than one sweep in a single image.

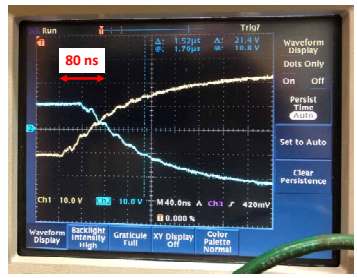


Figure 14: Fast deflection waveforms. A single rf bucket is ~18.8 ns.

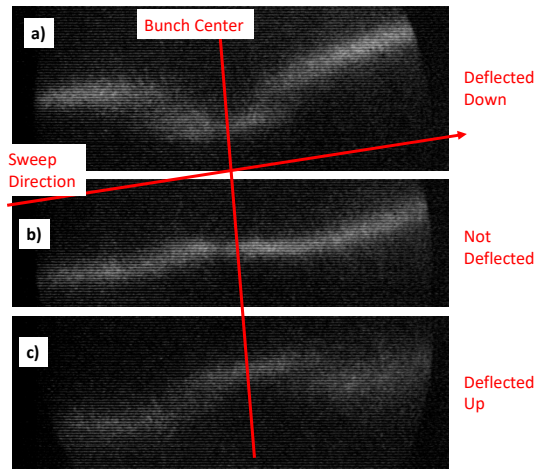


Figure 15: Fast sweep images for the electron beam: a) above the proton beam, b) through the proton beam, and c) below the proton beam.

CONCLUSIONS

We have successfully measured the proton beam profile with a single camera image using a slow sweep method. It is in reasonable agreement with the same measurement from the ionization profile monitor. The fast sweep method has been attempted and some initial traces were shown. More work is required on this approach before we can make a measurement.

REFERENCES

[1] M. Hu *et al.*, "Beam profile measurement with flying wires at the Fermilab Recycler Ring", in *Proc. 21st Particle Accelerator Conf. (PAC'05)*, Knoxville, TN, USA, May 2005, pp. 2182-2184.

[2] Paul D. Goldan, "Collisionless sheath – An experimental investigation", *Phys. Fluids,* vol. 13, pp. 1055-1059, 1970. doi:10.1063/1.1693008

[3] C. H. Stallings, "Electron beam as a method of finding the potential distribution in a cylindrically symmetric plasma", *J. Appl. Phys.*, vol. 42, p. 2831, 1971. doi:10.1063/1.1660634

[4] C. W. Mendel Jr., "Apparatus for measuring rapidly varying electric fields in plasmas", *Rev. Sci. Instrum.*, vol. 46, pp. 847-850, 1975. doi:10.1063/1.1134351

[5] J. Shiloh, M. Lampel and R. Sah, "Electron beam probe for charge neutralization studies of heavy ion beams", *Rev. Sci. Instrum.*, vol. 54, pp. 46-49, 1983. doi:10.1063/1.1137213

Content from this work may be used under the terms of the CC-BY-4.0 licence (© 2023). Any distribution of this work must maintain attribution to the author(s), title of the work, publisher, and DOI

ISBN: 978-3-95450-236-3 ISSN: 2673-5350 doi:10.18429/JACoW-IBIC2023-WEP023

[6] V. Shestak, C.J. Kost, R. Burge, D.B. Steski and S. Kornak, "Electron beam probe for ion beam diagnostics", TRIUMF, Rep. TRI-DN-87-36, 1987.

[7] P. Gross *et al*., "An electron beam probe for ion beam diagnosis", in *Proc. 2nd European Particle Accelerator Conf. (EPAC'90)*, Nice, France, June 1990, pp. 806.

[8] J. Bosser, C. Dimopoulou, A. Feschenko and R. Maccaferri, "Transverse profile monitor using ion probe beams", *Nucl. Instrum. Methods Phys. Res. A,* vol. 484, p. 1, 2002. doi:10.1016/S0168-9002(01)01965-9

[9] P. V. Logatchov *et al*., "Non-destructive singlepass monitor of longitudinal charge distribution in an ultrarelativistic electron bunch", in *Proc. 18th Particle Accelerator Conf. (PAC'99),* New York, NY, USA, March 1999. doi:10.1109/PAC.1999.794408

[10] W. Blokland and S. M. Cousineau, "A Non-Destructive Profile Monitor for High Intensity Beams", in *Proc. 24th Particle Accelerator Conf. (PAC'11)*, New York, NY, USA, Mar.-Apr. 2011, paper WEOCN2, pp. 1438-1442.

[11] R. Thurman-Keup *et al.*, "Commissioning and first results of the electron beam profiler in the Main Injector at Fermilab", in *Proc. 6th Int. Beam Instrumentation Conf. (IBIC'17)*, Grand Rapids, MI, USA, Aug. 2017, paper WE3AB3, pp. 330-334. doi:10.18429/JACoW-IBIC2017-WE3AB3

[12] A. Aleksandrov *et al.*, "Feasibility study of using an electron beam for profile measurements in the SNS accumulator ring", in *Proc. 21st Particle Accelerator Conf. (PAC'05)*, Knoxville, TN, USA, May 2005, pp. 2586-2588. doi:10.1109/PAC.2005.1591191

Content from this work may be used under the terms of the CC-BY-4.0 licence (© 2023). Any distribution of this work must maintain attribution to the author(s), title of the work, publisher, and DOI

ISBN: 978-3-95450-236-3 ISSN: 2673-5350 doi:10.18429/JACoW-IBIC2023-WEP024

A SIMULATION OF THE PHOTOIONIZATION OF H- TOGETHER WITH THE SUBSEQUENT TRACKING OF THE LIBERATED ELECTRONS*

R. Thurman-Keup†, M. El Baz, V. Scarpine
Fermi National Accelerator Laboratory, Batavia, USA

Abstract

The Proton Improvement Plan - II (PIP-II) is a new linear accelerator (LINAC) complex being built at Fermilab. It is based on superconducting radiofrequency cavities and will accelerate H- ions to 800 MeV kinetic energy before injection into the existing Booster ring. Measurements of the profile of the beam along the LINAC must be done by non-intercepting methods due to the superconducting cavities. The method chosen is photoionization of a small number of H- by a focused infrared laser, aka laserwire. The number of ionized electrons is measured as a function of laser position within the H- beam. To aid in the design of the collection mechanism, a simulation was written in MATLAB with input from the commercial electromagnetic simulation, CST. This simulation calculates the number and positions of the liberated electrons and tracks them through the magnetic collection and H- beam fields to the collection point. Results from this simulation for various points along the LINAC will be shown.

INTRODUCTION

Fermilab is in the process of constructing a new superconducting (SC) linear accelerator to replace the existing normal conducting LINAC. This project is called the Proton Improvement Plan - II (PIP-II) [1] and is being built to increase the deliverable beam intensity to the Deep Underground Neutrino Experiment being constructed in South Dakota. Since the LINAC is mostly superconducting, the use of physical wire scanners as beam profilers is not allowed in much of the LINAC due to the risk of a broken wire contaminating the SC cavities. As the beam is composed of H- ions, laserwires [2, 3] were chosen as the profiler. A laserwire functions by photoionization of the extra electron on the H- ion using a focused laser. The binding energy of the extra electron is only 0.7542 eV and can be ionized by a 1064 nm YAG laser. The ionized electrons, which are proportional in number to the local density of H- ions, are collected as the laser is moved through the H- beam, enabling reconstruction of the profile of the beam. Due to the complexity of the system, a simulation was developed to aid in the planning of the laser optics and the electron collection and is presented in this paper.

EXPERIMENTAL DEVICE

The laserwire system for PIP-II is comprised of a source laser that is transported through a pipe from the laser room to the H- beamline (Fig. 1). The pipe is under vacuum to both reduce distortions from air currents and to serve as a safety interlock system. At each measurement location (station), there is an insertable mirror to direct the laser down to the beamline.

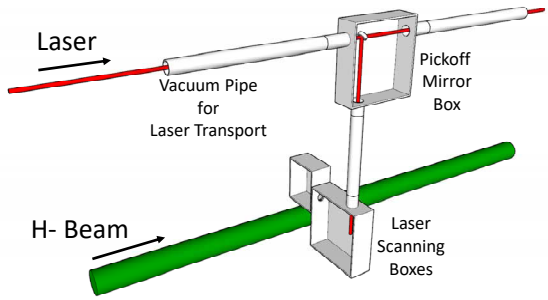


Figure 1: Diagram of laser transport. The laser originates in the laser room and is transported through a vacuum line to the end of the LINAC. At each laserwire, a vertical pipe can direct the laser to the H- beamline.

The optical system at the beamline is comprised of movable stages to scan the laser across the H- beam and to select vertical or horizontal scan mode (Fig. 2).

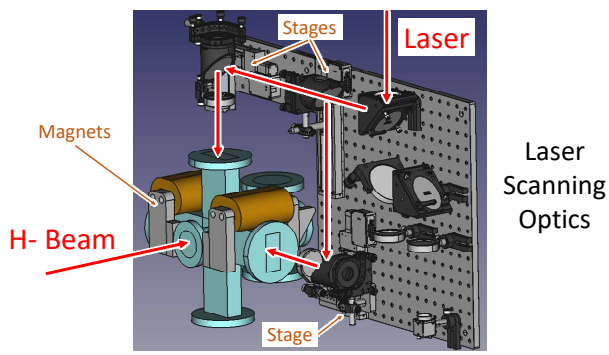


Figure 2: Optics inside the laser scanning box. There are linear stages to pick horizontal or vertical scan, and to do the scans.

There are 12 beamline stations with the locations and beam parameters summarized in Table 1 (plus an additional emittance measuring one after the LINAC). The laserwires are installed just downstream of the location column entry which specifies the cryomodule section and the cryomodule number within that section. The optics within the beamline stations focus the laser from a large incoming rms size of ~5 mm to a focused rms size of <100 μm. The focusing distance will be approximately 300 mm. Once the laser has ionized the H- beam, the electrons are bent vertically upward to a detector which will nominally be a faraday cup (Fig. 3).

* This manuscript has been authored by Fermi Research Alliance, LLC under Contract No. DE-AC02-07CH11359 with the U.S. Department of Energy, Office of Science, Office of High Energy Physics.
† keup@fnal.gov

Content from this work may be used under the terms of the CC-BY-4.0 licence (© 2023). Any distribution of this work must maintain attribution to the author(s), title of the work, publisher, and DOI

ISBN: 978-3-95450-236-3 ISSN: 2673-5350 doi:10.18429/JACoW-IBIC2023-WEP024

SIMULATION

The simulation is comprised of three parts: the calculation of the number of photoionizations and generation of the electrons, the calculation of the electromagnetic fields of the beam and the magnet, and the tracking of the electrons to the detector.

Table 1: Laserwire Locations and Expected Beam Parameters

Laserwire Location	Position [m]	Beam Parameters			
		E_k [MeV]	σ_x [mm]	σ_y [mm]	σ_t [ps]
MEBT	18.7	2.1	2.3	2.3	208
HWR	25.4	10.0	1.3	1.4	33
SSR1 CM #1	31.6	18.6	1.2	1.2	20
SSR2 CM #2	51.5	61.2	1.4	1.5	13
SSR2 CM #4	65.2	106.0	1.3	1.3	13
SSR2 CM #6	78.9	153.9	1.4	1.4	11
LB650 CM #1	93.4	192.2	2.3	2.4	6.7
LB650 CM #3	107.1	267.4	1.8	1.9	5.7
LB650 CM #6	127.6	400.9	1.9	2.0	5.2
LB650 CM #9	148.0	516.5	2.1	1.8	5.0
HB650 CM #2	170.5	652.6	1.8	1.9	4.4
HB650 CM #4	192.9	833.3	1.5	1.9	3.7

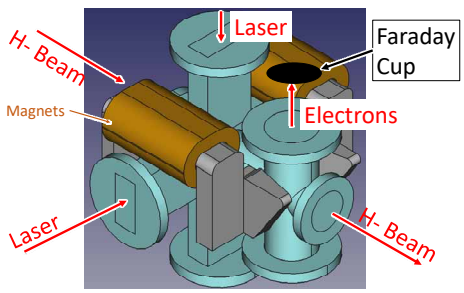


Figure 3: The incoming H- beam is partially ionized by the laser and the electrons are bent vertically by a magnet to a faraday cup. The blue volume is the vacuum chamber.

Photoionization Simulation

Calculation of the number of photoionizations requires the particle densities of both the incoming laser and H- beams, and the cross section for photoionization

$$dn = c\sigma_I \sqrt{\left(|\hat{l} - \vec{\beta}|^2 - |\hat{l} \times \vec{\beta}|^2\right)} I_l I_b \, dtdxdydz \quad (1)$$

Here c is the speed of light, $\hat{l}$ is the laser beam direction, $\vec{\beta}$ is the H- beam velocity vector divided by c, the square root is a Lorentz-transformed relative velocity term [4], I_l and I_b are the laser and H- number densities respectively, and σ_I is the photoionization cross section in the frame of the H- as a function of the laser wavelength Lorentz-transformed to the frame of the H-

$$\tilde{\lambda}_l = \lambda_l \frac{\sqrt{1-\beta^2}}{1 - \hat{l} \cdot \vec{\beta}} \quad (2)$$

where λ_l is the laser wavelength in the lab frame.

For the PIP-II laserwire design, the laser is transverse to the H- beam and as such, the square root term in Eq. (1) and the denominator in Eq. (2) are both equal to 1. The Lorentz-transformed laser wavelength shifts from 1064 nm in the lab frame to 1062 nm in the MEBT and to 883 nm at the end of the LINAC. The cross sections, σ_I, are extracted at the desired wavelengths from a polynomial fit to Table IV in reference [5].

The simulation code is written in MATLAB [6]. It steps through time and calculates the number of ionized electrons on a predefined set of physical mesh points. The simulation utilizes one of two possible numerical mesh arrangements, laser grid or beam grid, depending on the laser and H- beam parameters.

The laser grid approach creates a fixed cylindrical mesh axially aligned with the laser and covering the overlap region of the laser and the H- beam (Fig. 4). The mesh is an elliptic cylinder with radii that scale with the transverse laser size. This keeps the mesh size proportional to the laser width and avoids losing resolution near the laser waist. This works well when the laser intensity is low enough to avoid significant depletion of the H- beam which is not accounted for in this approach.

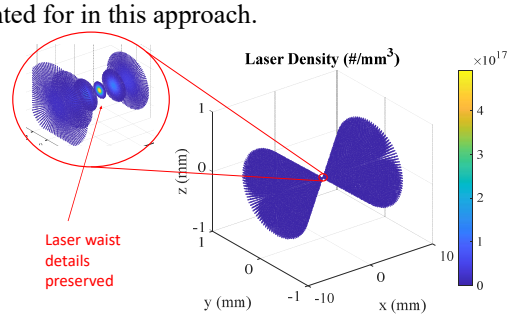


Figure 4: Laser grid version of the mesh points. The mesh spacing scales with the diameter of the laser as it propagates though the H- beam.

The beam grid version is a rectangular fixed mesh covering the physical overlap region of the laser and the H- beam. The simulated time steps have a spacing that is equal to the physical mesh spacing divided by the H- beam velocity. This relationship means that with every time step, the H- beam moves one spatial step, allowing for the fixed mesh to handle depletion of the H- (Fig. 5).

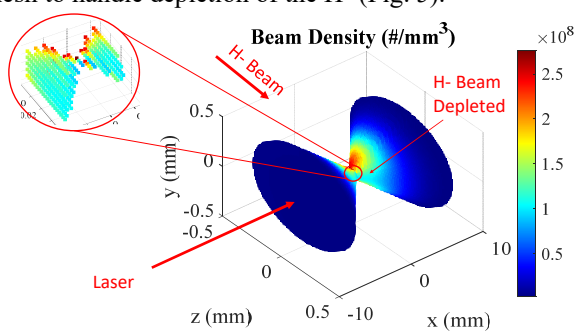


Figure 5: Beam grid version of the mesh points showing the H- beam intensity. Note the depletion of the H- beam as it passes through the laser.

Content from this work may be used under the terms of the CC-BY-4.0 licence (© 2023). Any distribution of this work must maintain attribution to the author(s), title of the work, publisher, and DOI

ISBN: 978-3-95450-236-3 ISSN: 2673-5350 doi:10.18429/JACoW-IBIC2023-WEP024

In both cases, the mesh extent is determined from the space-time interaction region of the laser and H- while the desired number of mesh points is set by the user to avoid loss of details such as the laser waist.

Electrons for tracking are generated from the space-time mesh containing the calculated number of photoionizations. A Poisson distribution is utilized for up to 500 electrons, beyond which a Gaussian approximation is used. The electrons are given momenta based on the 6D phase space specified for the H- beam (Fig. 6).

Electromagnetic Field Calculations

The electromagnetic field calculations involve two separate parts: the fields of the H- beam, and the static fields of both the electron collection magnets and possibly secondary electron containment electrodes.

The beam field calculation is done in MATLAB and uses a single bunch which can have any arbitrary shape and size, but a single fixed velocity. For PIP-II, the H- beam is bunched at a frequency of 162.5 MHz and we use a gaussian shape in all three dimensions. The fields are evaluated on a rectangular mesh containing an inner section with generally closer spacing to resolve the fields within the bunch, and an outer section with larger spacing. The fields at each mesh point are a numerical integration over the bunch charge. This numerical integration requires a mesh of the bunch as well. To reduce numerical errors, the field evaluation mesh spacing is adjusted such that it is an integer multiple of the bunch mesh spacing. The results of the field evaluation are stored for later use by the tracking simulation.

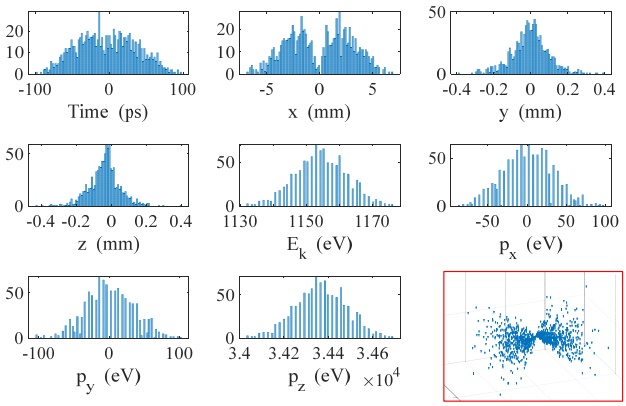


Figure 6: Generated electron distributions. The laser waist can be seen in the *x* position distribution. A 3D distribution of the electron positions is shown in the red box where the laser waist can be seen again.

The static fields are calculated in CST [7] which is a 3D electromagnetic simulation. We designed a magnet with a return yoke to reduce the impact on the H- beam (Fig. 7). In addition, we will also add a small quadrupole magnet for the MEBT laserwire to compensate electron spreading from H- space charge forces. When the electrons strike the faraday cup, they generate secondary electrons that may escape the surface of the faraday cup, altering the collected charge. To avoid this, we may need to install a conductive ring to apply an electrostatic field to keep the secondary electrons from leaving. As with the bunch fields, these electrostatic results are also stored for later use.

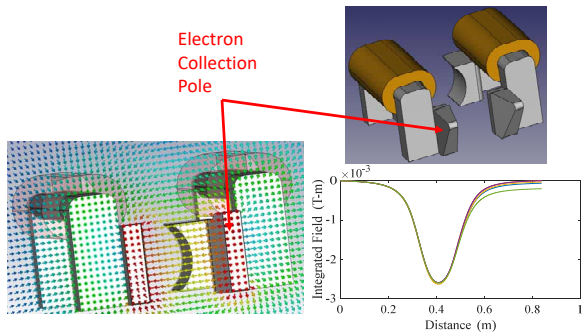


Figure 7: CST calculation of magnetic field of magnets for electron collection. The plot shows transverse magnetic field integrated along H- beam direction for 5 different transverse locations.

Tracking Simulation

The tracking simulation is written in MATLAB and was created originally to track electrons in the electron beam profiler [8] and ionization profile monitors [9]. It tracks the electrons through static fields and the fields of the H- bunches but does not do self-interactions with the other electrons since the effect is generally much smaller than the H- bunches. It uses an adaptive Runge-Kutta method [10] to solve the pseudo-relativistic second-order differential equation of motion

$$\vec{F}(\vec{r},t) = \frac{d\vec{p}}{dt} = m\frac{d(\gamma\vec{v})}{dt}$$
$$\vec{F}(\vec{r},t) = m\gamma\left(\vec{a} + \gamma^2\vec{\beta}(\vec{\beta}\cdot\vec{a})\right) \quad (3)$$

which, when inverted to find $\vec{a}$, is

$$\vec{a} = \frac{d^2\vec{r}}{dt^2} = \frac{1}{\gamma m}(\boldsymbol{I} - \vec{\beta}\vec{\beta}^T)\vec{F}(\vec{r},t) \quad (4)$$

where $\vec{F}(\vec{r},t) = q\left(\vec{E}(\vec{r},t) + \vec{v}\times\vec{B}(\vec{r},t)\right)$, m is the mass of the particle being tracked, $\gamma = 1/\sqrt{1-\beta^2}$ is the Lorentz factor, and $\boldsymbol{I}$ is the identity matrix. We apply the Runge-Kutta method to the second-order differential equation rewritten as coupled first order differential equations

$$\frac{d\vec{v}}{dt} = \frac{1}{\gamma m}(\boldsymbol{I} - \vec{\beta}\vec{\beta}^T)\vec{F}(\vec{r},t)$$
$$\frac{d\vec{r}}{dt} = \vec{v} \quad (5)$$

For each Runge-Kutta time step, the previously stored bunch and static fields are interpolated to find the value at the space-time location of the particle being tracked. For the bunch fields, the field is interpolated to the requested position after adjusting it for the requested time and the velocity of the bunch,

$$\vec{E}|\vec{B}(\vec{r},t) \rightarrow \vec{E}|\vec{B}(\vec{r}+\vec{v}t_m) \quad (6)$$

where $t_m = (t \text{ modulo } t_b)$. The modulo function implements a repetitive bunch structure at the specified bunch spacing, t_b.

Content from this work may be used under the terms of the CC-BY-4.0 licence (© 2023). Any distribution of this work must maintain attribution to the author(s), title of the work, publisher, and DOI

ISBN: 978-3-95450-236-3 ISSN: 2673-5350 doi:10.18429/JACoW-IBIC2023-WEP024

The adaptive part of the algorithm adjusts the step size to keep changes in the momenta, either absolute value or direction, within a range specified by thresholds. If any of the thresholds are exceeded, the step size is adjusted to compensate.

RESULTS

The simulation has been used to design the collection magnet and find optimal laser parameters to avoid wasted laser energy and resolution degradation. Figures 8 and 9 show electron trajectories at two locations: MEBT and HWR. The MEBT location (Fig. 8) shows tracking results with and without a quadrupole field. The extra quadrupole may be necessary in the MEBT to deal with spreading of the electrons due to the space charge of the H- beam.

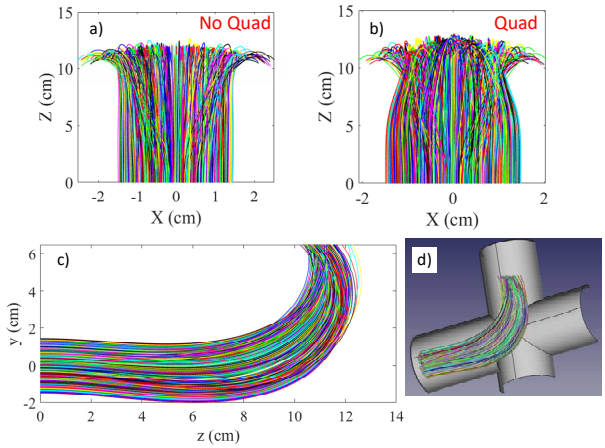


Figure 8: MEBT laserwire; a) and b) are the trajectories looking down from above the beam. They show the difference in final spread between having a quadrupole field and not having a quadrupole field. Plots c) and d) are the trajectories looking from the side of the beam. They first deviate down before bending up which allows more clearance between the electrons and the beampipe.

Figure 9 shows trajectories in the laserwire after the HWR which is the first cryomodule.

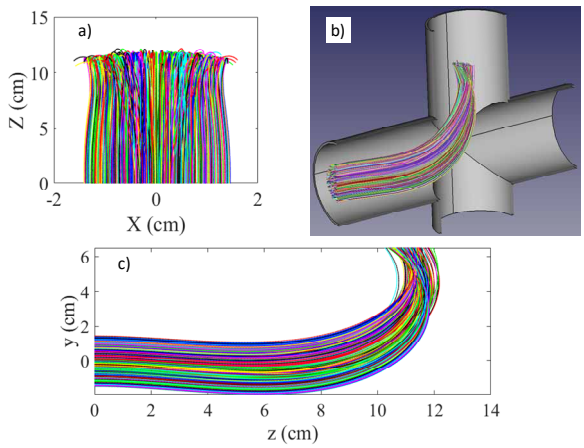


Figure 9: HWR laserwire. Plot a) is the trajectories looking down from above the beam. b) and c) are the trajectories looking from the side of the beam.

The containment of the electrons is better at this location since the electrons have higher energy and are less susceptible to H- space charge forces. The initial deflection down in all of these is driven by the positioning of the two magnet yokes where the first corrector yoke is closer to the laser interaction region. This effect helps to increase the clearance between the electrons and the corner of the beampipes.

Studies were also done to evaluate the photoionization rates for different length laser pulses, laser arrival time jitter, and H- temporal bunch lengths (Fig. 10). These results will help to determine the optimal laser properties to maximize signal and resolution while minimizing unused laser energy which has detrimental effects on the vacuum windows. For instance, from the plots, we can see that laser pulses with a length of 20 or 30 ps have good photoionization but small variation with jitter.

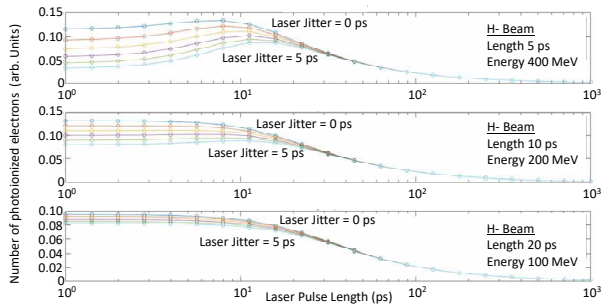


Figure 10: Study of the effect of laser jitter on the number of photoionized electrons using the simulation at 3 different H- beam energies.

This simulation was also recently used in an analysis of a novel bunch length measurement at the Spallation Neutron Source at Oak Ridge National Lab [11].

CONCLUSIONS

This laserwire simulation has proven to be useful for a number of analyses pertaining to laserwires. From magnet designs and laser parameter choices to measurement analyses. We foresee even more uses as we proceed to build and commission the PIP-II laserwire systems.

REFERENCES

[1] V. Lebedev *et al.*, "The PIP-II conceptual design report", FNAL, Batavia, IL, USA, Rep. FERMILAB-DESIGN-2017-01, Mar 2017. doi:10.2172/1346823

[2] Y. Liu *et al.*, "Laser based diagnostics for measuring H- beam parameters", in *Proc. 24th Particle Accelerator Conf. (PAC'11)*, New York, NY, USA, Mar.-Apr. 2011, paper WEOCN1, pp. 1433-1437. https://jacow.org/PAC2011/papers/weocn1.pdf

[3] V. Scarpine *et al.*, "Beam profile measurements utilizing an amplitude modulated pulsed fiber laser at PIP2IT", in *Proc. 10th Int. Beam Instrumentation Conf. (IBIC'21)*, Korea, Sept 2021, paper TUPP25. doi:10.18429/JACoW-IBIC2021-TUPP25

[4] L.D. Landau and E.M. Lifshitz, *The Classical Theory of Fields*. Oxford, England: Pergamon Press, pp. 34-36, 1975.

Content from this work may be used under the terms of the CC-BY-4.0 licence (© 2023). Any distribution of this work must maintain attribution to the author(s), title of the work, publisher, and DOI

ISBN: 978-3-95450-236-3 ISSN: 2673-5350 doi:10.18429/JACoW-IBIC2023-WEP024

[5] J.T. Broad and W.P. Reinhardt, "One- and two-electron photoejection from H−: A multichannel J-matrix calculation", *Phys. Rev. A*, vol. 14, p. 2159, 1976. doi:10.1103/PhysRevA.14.2159

[6] MathWorks, https://www.mathworks.com

[7] Dassault Systemes – Simulia, https://www.3ds.com

[8] R. Thurman-Keup *et al.*, "Commissioning and First Results of the Electron Beam Profiler in the Main Injector at Fermilab", in *Proc. 6th Int. Beam Instrumentation Conf. (IBIC'17)*, Grand Rapids, MI, USA, Aug. 2017, paper WE3AB3, pp. 330-334. doi:10.18429/JACoW-IBIC2017-WE3AB3

[9] J.R. Zagel *et al.*, "Third Generation Residual Gas Ionization Profile Monitors at Fermilab", in *Proc. 3rd Int. Beam Instrumentation Conf. (IBIC'14)*, Monterey, CA, USA, Sep. 2014, paper TUPD04, pp. 408-411. https://jacow.org/IBIC2014/papers/tupd04.pdf

[10] Runge-Kutta Methods, https://en.wikipedia.org/wiki/Runge%E2%80%93Kutta_methodsp

[11] Y. Liu *et al.*, "Longitudinal bunch profile measurement of operational H- beam using laser wire and virtual slit", *Phys. Rev. Accel. Beams*, vol. 26, p. 042801, 2023. doi:10.1103/PhysRevAccelBeams.26.042801

Content from this work may be used under the terms of the CC-BY-4.0 licence (© 2023). Any distribution of this work must maintain attribution to the author(s), title of the work, publisher, and DOI

ISBN: 978-3-95450-236-3 ISSN: 2673-5350 doi:10.18429/JACoW-IBIC2023-WEP025

A STUDY OF THE GAIN OF MICROCHANNEL PLATES IN THE IONIZATION PROFILE MONITORS AT FERMILAB*

R. Thurman-Keup†, D. Slimmer, C. Lundberg, J.R. Zagel
Fermi National Accelerator Laboratory, Batavia, USA

Abstract

One of the on-going issues with the use of microchannel plates (MCP) in the ionization profile monitors (IPM) at Fermilab is the significant decrease in gain over time. There are several possible issues that can cause this. Historically, the assumption has been that this is aging, where the secondary emission yield (SEY) of the pore surface changes after some amount of extracted charge. Recent literature searches have brought to light the possibility that this is an initial 'scrubbing' effect whereby adsorbed gasses are removed from the MCP pores by the removal of charge from the MCP. This paper discusses the results of studies conducted on the IPMs in the Main Injector at Fermilab.

INTRODUCTION

Ionization profile monitors (IPM) are used in many accelerator laboratories around the world [1-7]. They have been used in nearly all the synchrotrons built at Fermilab, and presently are used in the Main Injector (MI), Recycler Ring (RR), and Booster synchrotron [8], with another one being planned for the Integral Optics Test Accelerator (IOTA). All Fermilab IPMs, as well as many of those at other laboratories, utilize one or more microchannel plates (MCP) for signal amplification. Historically we have found that the gain of the MCP decreases over time (Fig. 1) and have attributed it to the well-known fact that they age with current extracted from them [9]. Thus, we have periodically replaced them.

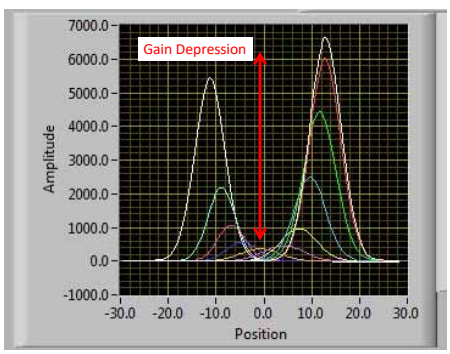


Figure 1: Scan of MCP plate across beam showing gain depression where beam is normally positioned.

Recently, more in-depth investigations have revealed that the decrease in the gain is much more consistent with conditioning, or 'scrubbing', of the MCPs, and not aging. Literature searches have rediscovered the fact that a decrease in gain with conditioning is a known property of MCPs [10,11]. Our own historical IPM data and a recent dedicated test show results which are much more consistent with what one expects from conditioning. In this paper, we summarize our current understanding of the behavior of the MCPs in our IPMs.

EXPERIMENTAL DEVICE

IPMs are devices which utilize the ionization of residual gas to measure the transverse profile of the beam. Figure 2 is a diagram of the present Fermilab IPMs. When the beam passes through the IPM, it ionizes the residual gas. The IPM collects the ionization products using an electrostatic field to accelerate them to the MCP.

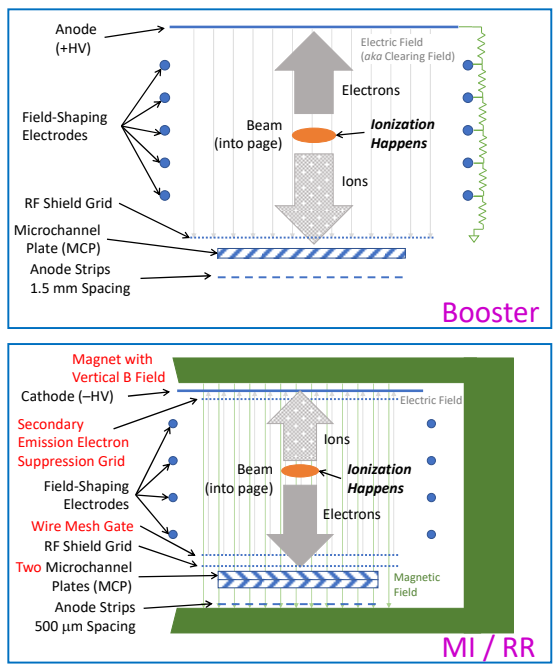


Figure 2: Diagrams of Booster and MI/RR IPMs.

The MCP is a thin plate with microscopic holes (aka pores) through it, each of which acts as a charge multiplier, much like a photomultiplier tube (PMT) (Fig. 3) [12,13].

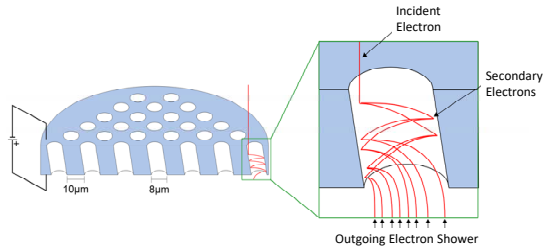


Figure 3: Schematic of MCP functional behavior showing amplification by electron avalanche.

* This manuscript has been authored by Fermi Research Alliance, LLC under Contract No. DE-AC02-07CH11359 with the U.S. Department of Energy, Office of Science, Office of High Energy Physics.
† keup@fnal.gov

Content from this work may be used under the terms of the CC-BY-4.0 licence (© 2023). Any distribution of this work must maintain attribution to the author(s), title of the work, publisher, and DOI

ISBN: 978-3-95450-236-3 ISSN: 2673-5350 doi:10.18429/JACoW-IBIC2023-WEP025

Content from this work may be used under the terms of the CC-BY-4.0 licence (© 2023). Any distribution of this work must maintain attribution to the author(s), title of the work, publisher, and DOI

The output electrons from the MCP are collected via thin conductive strips which function as the anode in the multiplication chain. This current is converted to a voltage by a preamp and digitized. The digitized signals from the IPM are processed by a LabVIEW program that generates gaussian profile fits to the data. The IPMs collect data on request. The high voltage is turned on and data is collected for a single injection-extraction cycle which is usually less than one second.

There are two IPM versions at Fermilab (as shown in Fig. 2): magnetic and electrostatic. The magnetic version, used in MI and RR, collects electrons, and has both an electric field to accelerate the electrons and a magnetic field to constrain their trajectories. Without the magnetic field, the electrons would be moved transversely by the beam space charge and not maintain the position where the ionization occurred. These IPMs are also installed on motorized stages such that the MCP can be moved relative to the beam. The electrostatic version, used in Booster, collects ions, and has no magnetic field since the ions are heavy and not dramatically affected by the beam space charge. These are bolted to the beampipe and cannot be moved relative to the beam.

PRIOR MCP LITERATURE

MCPs have been used since at least the early 1970's for image intensification [14]. A mathematical model of MCPs was developed in reference [11]. In addition to the model, the paper also showed the measured gain of an MCP at various stages in the preparation: initial, after vacuum bake, after scrub, and after final seal-in. The gain decrease from after vacuum bake to after scrub was a factor of 3. Scrubbing refers to the initial phase of operation of the MCP, where the electrons act to ionize adsorbed gases and remove them from the surfaces of the pores. Since these gases are additional contributors of secondary emission electrons, the gain is higher with them than without them. One approach to this conditioning is to illuminate the MCP with ultraviolet radiation until the gain stabilizes [10]. Whether or not the MCP can be exposed to atmosphere after conditioning without losing the benefits of the conditioning is not yet entirely clear to us [15,16]. Ideally the scrubbing would happen after installation of the MCP in vacuum. The use of MCPs in satellites encounters similar gain issues as we do with the IPMs [17-19]. When used in a spectrometer, spectral lines are placed at defined positions on the MCP. As it is apparently impractical [16] to keep a satellite MCP under vacuum, the initial operation of it in space causes the brighter lines to scrub faster resulting in a non-uniform gain, just as the beam in an accelerator is always located at the same location and produces a dip in the gain. Reference [20] discusses gain issues impacting MCP-based PMTs used in the PANDA experiment at FAIR. They also consider the new atomic layer deposition technique for MCPs. The lifetime of a MCP is generally stated in units of C/cm^2 of extracted charge and is usually understood to be > 1 C/cm^2. Conditioning of the MCP requires much less than that, typically less than 0.1 C/cm^2 [9,19,21].

IPM DATA

The present versions of the IPMs were installed in the MI and RR in 2014, and the Booster in 2017. All the data collected since then is available for analysis and is what is used to assess the behavior of the MCPs.

Historical Booster IPM Data

The MCPs in the Booster IPMs were not changed until 2022, providing 5 years of MCP gain data. Two things simplify the analysis of Booster IPM data: each IPM has only one MCP, and the Booster operation is always the same. Figure 4 shows a typical IPM signal for a Booster cycle.

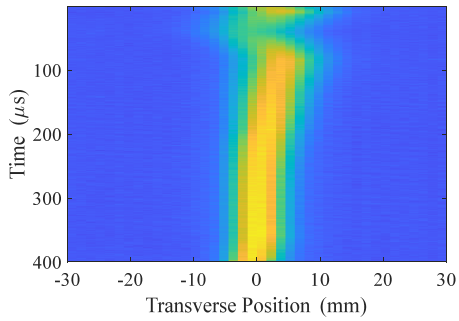


Figure 4: Booster cycle from injection (top) to extraction (bottom).

The goal of the analysis is to measure the relative gain of the MCP over time, ideally as a function of extracted charge. To determine the gain, one must scale the signal to the beam intensity, and adjust for the voltage setting of the MCP. The beam intensity is recorded for each acquisition. In addition, there were occasional measurements made at a series of voltage settings, which are used to determine the gain vs. voltage curve (Figs. 5 and 6).

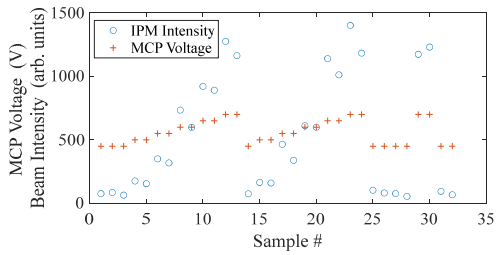


Figure 5: Collection of 32 acquisitions with varied MCP voltage. From this we extract a voltage gain curve.

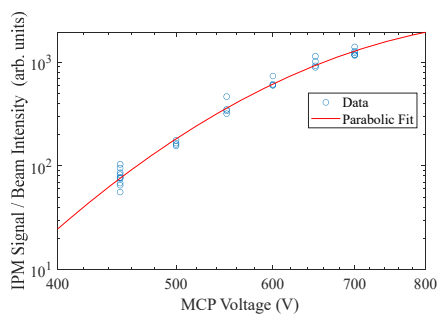


Figure 6: MCP voltage vs. gain curve with parabolic fit. This fit is used to normalize the IPM data to extract the MCP gain.

ISBN: 978-3-95450-236-3 ISSN: 2673-5350 doi:10.18429/JACoW-IBIC2023-WEP025

Figure 7 shows the distribution of IPM acquisitions as a function of time. We calculated the MCP gain from this data by scaling it by the beam intensity and by the voltage gain of Fig. 6. The resulting MCP gain is shown in Fig. 8 as a function of time.

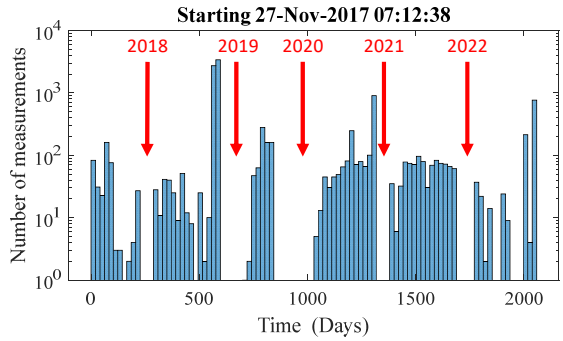


Figure 7: The red arrows indicate maintenance periods which are usually July – October.

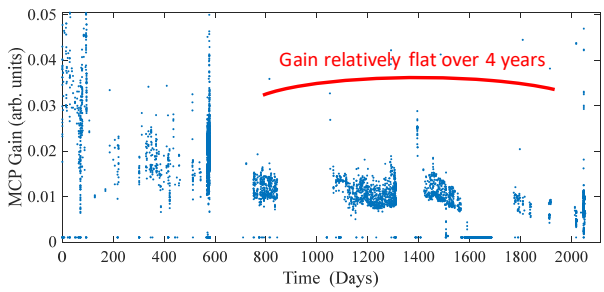


Figure 8: Relative MCP gain as a function of time. The gain has been relatively flat for the last 4 years.

From this plot, it would appear that the MCP gain decreased after initial installation but has been relatively flat after that. This is a behavior consistent with initial conditioning, and not aging. One thing that the reader might notice is the slight decrease over the last 600 days or so. It was discovered late in the writing of this paper that scaling the IPM signal by the measured beam intensity is not entirely accurate. As one can see in the Fig. 9, there is a clear non-linear relationship even after scaling, and, in addition, there are isolated regions, all of which must still be investigated. The non-linear relationship is in part responsible for the decrease in the last 200 days where the beam intensity was much less for most of the acquisitions. Despite this behavior, we don't see a dramatic decrease in the apparent gain of the MCP over recent time.

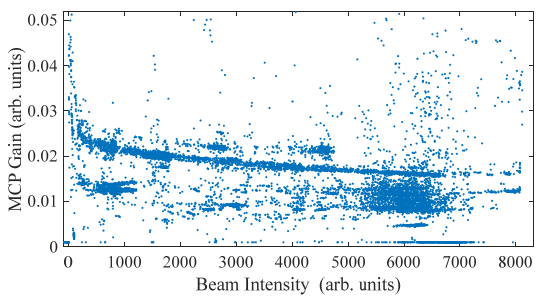


Figure 9: Relationship between MCP response and beam intensity after correcting the MCP response for the beam intensity and voltage.

Since the MCP should age with extracted charge, we calculate the extracted charge for an acquisition as $Q = ITD$, where I is the average current from the MCP during the acquisition, T is the time the high voltage is on (~3 seconds), and D is the Booster duty cycle (~50%). Figure 10 shows the integral of the extracted charge vs. time. At present, the total extracted charge is a little over 4 mC/cm^2, which is not yet near the level where aging would be a concern.

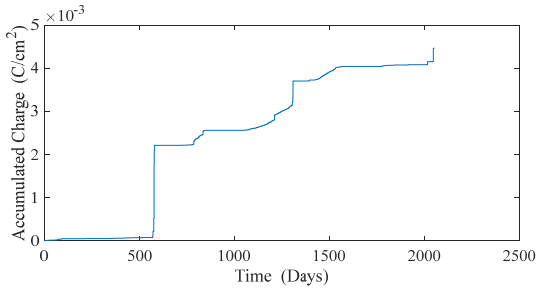


Figure 10: Integral of the extracted charge as a function of time.

MI Dedicated Experiment

Recently, one of the MI IPMs was run continuously to measure the behavior of the gain. Since these IPMs can be moved, the MCP was moved to a new region of the plate, and then run repeatedly for a period of ~5 days. Figure 11 shows the typical MI IPM signals where one can see that the MCP has been positioned to the side of the beam.

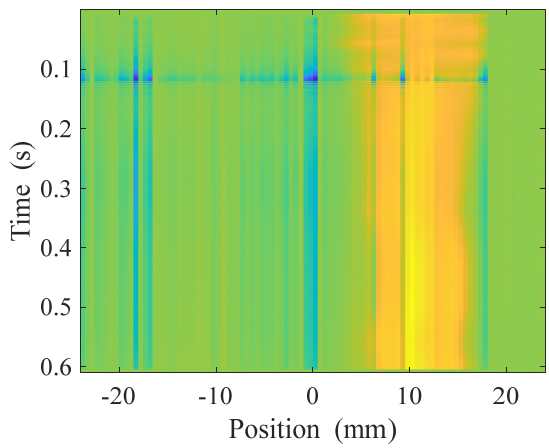


Figure 11: MI cycle from injection (top) to extraction (bottom). Some channels have obvious problems (blue).

Figure 12 shows the raw IPM integrated signals and the beam intensities. During the 5 days, the voltage was periodically adjusted to keep the signals at similar levels. The processing corrected for the beam intensity and accounted for the changes in voltage by scaling the data in each voltage region to match at the boundaries. Figure 13 shows this gain as a function of acquisition number, time, and integrated charge out of the MCP. Here as well, the change in gain is consistent with scrubbing, not with aging. One additional thing to note is that since the MI/RR IPMs have a pair of MCPs, the scrubbing is mostly affecting the second MCP which has much higher current draw. As such the

Content from this work may be used under the terms of the CC-BY-4.0 licence (© 2023). Any distribution of this work must maintain attribution to the author(s), title of the work, publisher, and DOI

ISBN: 978-3-95450-236-3 ISSN: 2673-5350 doi:10.18429/JACoW-IBIC2023-WEP025

gain will continue to decrease with time albeit much more slowly.

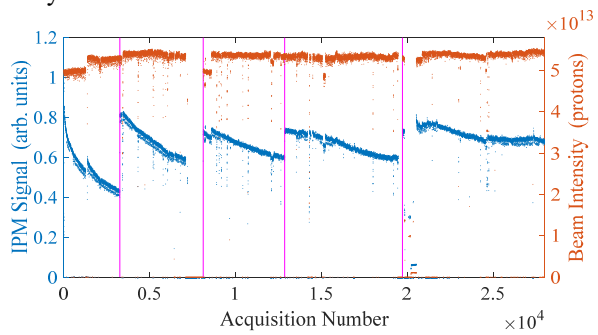


Figure 12: MI IPM signal (blue) and beam intensity (red). The magenta vertical lines indicate when the MCP voltage was changed.

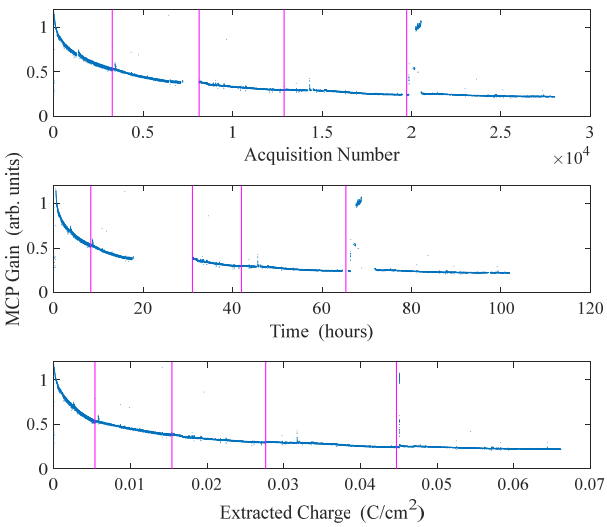


Figure 13: Integral of the extracted charge as functions of acquisition number, time, and extracted charge from the MCP.

CONCLUSIONS

Both previous literature and the studies done with the IPMs indicate that aging is not the cause of the decrease in gain seen in our IPMs. The implication is that the MCPs do not need to be replaced as often as they have been in the past. Instead, our attention now focuses on the problem of *in situ* conditioning of the MCP or periodic calibration of the gain of the MCP.

As stated earlier, the MI and RR MCP devices are mounted on motorized stages and therefore can be moved. They can be slowly moved across the beam to allow the scrubbing to uniformly condition the MCP and avoid uneven gains. The same technique could also be used to calibrate the gain as a function of position, which may be a more useful approach since the gain will continue to decrease with use.

In the Booster, there is no way to easily change the relative position of the beam on the MCP other than to move the beam itself. However, if one lowers the electrostatic field, the ions will spread out transversely due to space charge and more uniformly cover the MCP. This may offer a way to initially scrub the MCP.

REFERENCES

[1] K. Satou, "Development of a gated IPM system for J-PARC MR", in *Proc. 8th Int. Beam Instrumentation Conf. (IBIC'19)*, Malmö, Sweden, Sep. 2019, pp. 343-346. doi:10.18429/JACoW-IBIC2019-TUPP020

[2] H.S. Sandberg *et al.*, "Commissioning of Timepix3 based beam gas ionisation profile monitors for the CERN Proton Synchrotron", in *Proc. 10th Int. Beam Instrumentation Conf. (IBIC'21)*, Pohang, Rep. of Korea, May 2021, pp. 172-175. doi:10.18429/JACoW-IBIC2021-TUOA05

[3] A. Jansson *et al.*, "IPM measurements in the Tevatron", in *Proc. 22nd Particle Accelerator Conf. (PAC'07)*, Albuquerque, NM, USA, June 2007, pp. 3883-3885. doi:10.1109/PAC.2007.4440026

[4] M. Sachwitz, A. Hofmann, S. Pauliuk, K. I. Tiedtke, and H. Wabnitz, "Ionisation Profile Monitor to Determine Spatial and Angular Stability of FEL Radiation of FLASH", in *Proc. EPAC'08,* Genoa, Italy, Jun. 2008, paper TUPC090, pp. 1266-1268.

[5] R. Connolly, J. Fite, S. Jao, S. Tepikian, and C. Trabocchi, "Residual-gas-ionization beam profile monitors in RHIC", in *Proc. 14th Beam Instrumentation Workshop (BIW'10)*, Santa Fe, NM, USA, May 2010, pp. 116-118.

[6] K. Wittenburg, "Experience with the residual gas ionisation beam profile monitors at the DESY proton accelerators", in *Proc. 3rd European Particle Accelerator Conf. (EPAC'92)*, Berlin, Germany, Mar. 1992, pp.1133-1135.

[7] F. Benedetti *et al.*, "Design and development of ionization profile monitor for the cryogenic sections of the ESS linac", *EPJ Web Conf.*, vol. 225, p. 01009, 2020. doi:10.1051/epjconf/202022501009

[8] J.R. Zagel *et al.*, "Third generation residual gas ionization profile monitors at Fermilab", in *Proc. 3rd International Beam Instrumentation Conference (IBIC'14)*, Monterey, CA, USA, Sep. 2014, paper TUPD04, pp. 408–411.

[9] B.R. Sandel, A. Lyle Broadfoot and D. E. Shemansky, "Microchannel plate life tests", *Appl. Opt.*, vol. 16, no. 5, 1977, pp. 1435-1437. doi:10.1364/AO.16.001435

[10] O.H.W. Siegmund, "Preconditioning of microchannel plate stacks", *Proc. SPIE 1072, Image Intensification*, April 1989, pp. 111-118. doi:10.1117/12.952545

[11] E.H. Eberhardt, "Gain model for microchannel plates", *Appl. Opt.*, vol. 18, no. 9, May 1979, pp. 1418-1423. doi:10.1364/AO.18.001418

[12] J.L. Wiza, "Microchannel plate detectors", *Nucl. Instrum. Methods*, vol. 162, 1979, pp. 587-601. doi:10.1016/0029-554X(79)90734-1

[13] T. Gys, "Micro-channel plates and vacuum detectors", *Nucl. Instrum. Methods Phys. Res., Sect. A*, vol. 787, July 2015, pp. 254-260. doi:10.1016/j.nima.2014.12.044

[14] J. M. Grant, "Noise problems in continuous channel electron multipliers", in *Proc. NASA ERDL Image Intensifier Symposium*, vol. 9. Fort Belvoir, VA, USA, p. 63, 1961. doi:10.1088/0022-3735/9/5/001

[15] J.P. Rager and J.F. Renaud, "The use of a microchannel electron multiplier in spectroscopic instrumentation, involving frequent vacuum breaking", *Rev. Sci. Instrum.*, vol. 45, no. 7, July 1974, pp. 922-926. doi:10.1063/1.1686769

Content from this work may be used under the terms of the CC-BY-4.0 licence (© 2023). Any distribution of this work must maintain attribution to the author(s), title of the work, publisher, and DOI

ISBN: 978-3-95450-236-3 ISSN: 2673-5350 doi:10.18429/JACoW-IBIC2023-WEP025

[16] A. Chumikov, V. Cheptsov and N. Managadze, "Microchannel plate detector gain decrease through storage under environmental conditions", *IEEE Trans. Instrum. Meas.*, vol. 72, pp. 1-8, 2023. doi:10.1109/TIM.2023.3265633

[17] N. Griffiths, S. Airieau and O. Siegmund, "In-flight performance of the SUMER microchannel plate detectors", *Proc. SPIE 3445, EUV, X-Ray, and Gamma-Ray Instrumentation for Astronomy IX*, Nov. 1998, pp. 566-577. doi:10.1117/12.330312

[18] J. De Keyser *et al.*, "Position-dependent microchannel plate gain correction in Rosetta's ROSINA/DFMS mass spectrometer", *Int. J. Mass Spectrom.*, vol. 446, p. 116232, 2019. doi:10.1016/j.ijms.2019.116232

[19] R.F. Malina and K.R. Coburn, "Comparative lifetesting results for microchannel plates in windowless EUV photon detectors", *IEEE Trans. Nucl. Sci.*, vol. 31, no. 1, Feb. 1984, pp. 404-407. doi:10.1109/TNS.1984.4333287

[20] A. Lehmann *et al.*, "Recent developments with microchannel-plate PMTs", *Nucl. Instrum. Methods Phys. Res., Sect. A*, vol. 876, pp. 42-47, 2017. doi:10.1016/j.nima.2016.12.06

[21] G.W. Fraser, J.F. Pearson and J.E. Lees, "Evaluation of long life (L^2) microchannel plates for x-ray photon counting", *IEEE Trans. Nucl. Sci.*, vol. 35, no. 1, pp. 529-533, Feb. 1988. doi:10.1109/23.12779

Content from this work may be used under the terms of the CC-BY-4.0 licence (© 2023). Any distribution of this work must maintain attribution to the author(s), title of the work, publisher, and DOI

ISBN: 978-3-95450-236-3 ISSN: 2673-5350 doi:10.18429/JACoW-IBIC2023-WEP027

STATUS OF GAS SHEET MONITOR FOR PROFILE MEASUREMENTS AT FRIB*

A. Lokey†, S. Lidia
Facility for Rare Isotope Beams, Michigan State University, East Lansing, MI, USA

Abstract

We report on the status of work on a non-invasive profile monitor under development for use at the Facility for Rare Isotope Beams (FRIB), a heavy-ion LINAC which produces high-intensity, multi-charge state beams. The measurement will be made by collecting photons generated at the interaction point of the beam and a collimated molecular gas curtain. These photons will be collected with an intensified camera system, generating a two-dimensional image and allowing for measurements of profile, beam halo, and other properties more prevalent at specific locations of interest, such as charge state spread after folding segment bends. Included will be ongoing design specifications, simulation results, and discussion of measurement techniques for acquiring signal from the device.

INTRODUCTION

A non-invasive profile measurement device using nitrogen gas fluorescence is in development for use in the Facility for Rare Isotope Beams (FRIB), a high-intensity heavy ion facility which can provide beams of a variety of different ion species and charge states.

By using a non-interceptive method, it is possible to sample the state of the beam during operation, providing information about the spread of the charge states at points of interest, such as after bending magnets in the folding LINAC sections of FRIB. This method also allows the state of the beam to be measured in both transverse directions at once [1].

One way to accomplish this is by creating an ultra-thin, rarefied gas curtain and collecting the photons released in the interaction between the beam and the working gas. This is known as beam-induced fluorescence (BIF) and has the advantage of being a simpler system design than similar ionization-based monitors, which require an electrode to sweep the electrons or ions into the detector and a magnet to steer them to the correct location to be collected. Additionally, BIF monitors have greater time resolution, since the time for the interaction particles to travel to the detector is negligible [2]. By introducing only a small amount of gas to the system, both pumping requirements and interaction effects like scattering and charge stripping are reduced [3].

Assuming the gas sheet is uniform and thin, photons collected can then be correlated to the profile of the beam with some degree of accuracy. This technique has been used successfully with protons and lighter ions at other facilities [1,3-5].

* This material is based upon work supported by the U.S Department of Energy, Office of Science, Office of Nuclear Physics and used resources of the Facility for Rare Isotope Beams (FRIB), which is a DOE Office of Science User Facility, under Award Number DE-SC0000661
† lokey@frib.msu.edu

SYSTEM OVERVIEW AND REQUIREMENTS

The beamline device is divided into three sections:(i) the gas generating chamber; (ii) the main interaction chamber; and (iii) the optics system. Within the gas generating section, nitrogen gas is pumped into a reservoir which feeds into a thin rectangular cavity. Molecules of nitrogen are emitted from a slit at the front of the cavity and are further collimated into sheet by a slit placed between the generating and main chambers as shown in Figure 1.

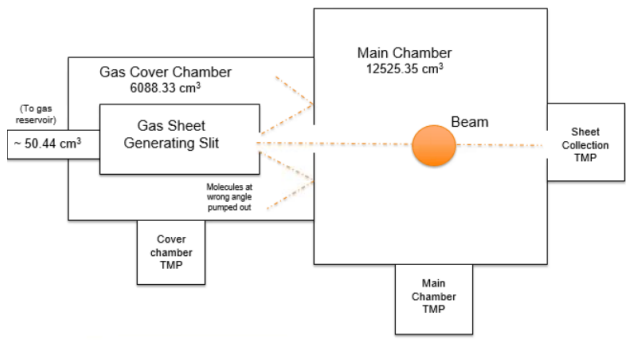


Figure 1: Overview of device layout.

Considerations

Although rarefied, gas generated from the monitor will require significant pumping to prevent contamination and protect the rest of the high vacuum system and this must be accounted for in appropriately sizing of the pumps.

For the measurement to correlate with the beam profile, the sheet must be thin and uniform, positioned at a 45-degree angle to the incident beam with the detector perpendicular to the point of interaction. Careful alignment must be performed to ensure that the angle of interaction is correct [6].

Signals generated by the interaction will be of relatively low intensity. The fluorescence interaction generates a small signal compared to ionization monitors due to fluorescence cross sections being lower than ionization cross sections. To assist with collection and reduce scattering from reflection, the interior of the main chamber will be blackened and an intensified camera array will be used to amplify the incoming signal. Light is gathered by the camera system at a small solid angle, and relatively few photons, are released in the interaction. For example, using a residual-type BIF, Tsang et al. noted a production of 7 photons per 3×10^8 ion Uranium bunch with hydrogen as the working gas [7]. Photon production is expected to be higher with use of a collimated sheet, as well as nitrogen as the working gas since it has a greater fluorescence cross

Content from this work may be used under the terms of the CC-BY-4.0 licence (© 2023). Any distribution of this work must maintain attribution to the author(s), title of the work, publisher, and DOI

ISBN: 978-3-95450-236-3 ISSN: 2673-5350 doi:10.18429/JACoW-IBIC2023-WEP027

section. However, additional amplification and noise reduction techniques will still be needed the optics system [1,2].

The ratio of the mean free path of the nitrogen molecules is significantly larger than the length scale of the generator, which puts the gas in the desired free molecular flow regime. This is represented by the Knudsen number, characterized by the mean free path of the molecule, λ, over the characteristic length of the system, l, see Eq. (1). The system is in molecular flow at a Knudsen ratio greater than 10.

$$K_n = \frac{\lambda}{l} \quad (1)$$

The mean free path of the molecules in the generator slit is approximately 704 mm, making the Knudsen number 7040. To achieve this, the generating slit will need to be machined to a depth of 0.1 mm, which could pose challenging due to tolerances at that scale.

DESIGN OF MECHANICAL SYSTEM

To facilitate manufacturing, the gas sheet generating slit will be formed from a half-cylindrical slug machined on one side to the required depth and capped with a flat top connected to the reservoir and gas injection. The generating slit will be secured to the gas cover and attached to a rotatable CF flange to allow for alignment of the cover slit with the collimator and interaction point. A SOLIDWORKS model is shown in Figure 2.

The gas sheet generator has dimensions of length 100 mm by width 100 mm with a depth of 0.1 mm. The slit widens to 110 mm at its exit to widen the area of the gas curtain, shown in Figure 2.

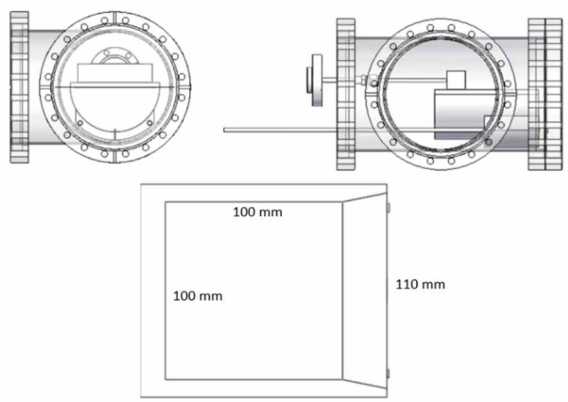


Figure 2: SOLIDWORKS model of sheet generator prepared for MolFlow+ simulation.

The collimator is to be located 10 mm from the exit of the gas sheet generator and sized slightly larger at 0.3 mm and 160 mm. The width of the collimating slit is determined such that approximately 10% of the gas molecules exiting the gas sheet generator enter the main chamber, or molecules that deviate from a path about 0.4 radians from the x-z plane.

For both the main chamber and gas cover sheet, off-the-shelf components will be used. The cover chamber will be manufactured using a vacuum nipple modified to hold the gas sheet generating slit in place, for alignment with the collimator and interaction point.

Three turbomolecular pumps will be used to prevent the buildup of gas in the system, one placed in the gas cover before the collimating slit to remove excess nitrogen emitted from the generator at undesirable angles, one in the main chamber of the device to maintain high vacuum, and one at the exit of the main chamber to collect the gas sheet.

SIMULATION

The device was initially modeled using simplified geometry as reported in [8], using MolFlow+, a Monte Carlo gas dynamics simulation software [9].

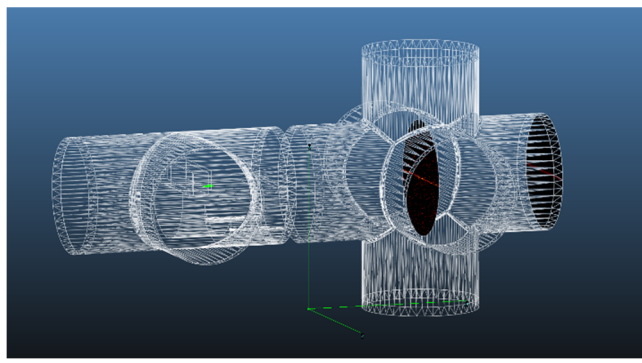


Figure 3: Molflow+ simulation set up.

Simulations were updated to include more complex geometry, as well as consideration for distance of the gas sheet generator opening to the collimating slit. Figure 3 shows the prepared volume of the model in MolFlow+, while Figure 4 shows a close-up of the pressure distribution at the gas sheet exit point of the model.

The gas is introduced on one of the reservoir chamber faces with a cosine desorption and outgassing rate of 0.001 mbar-liter/s.

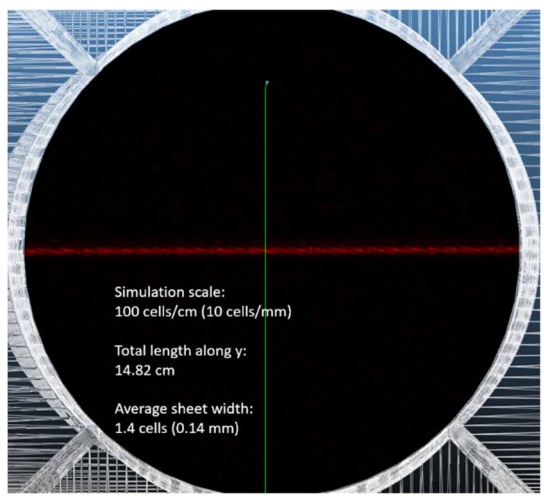


Figure 4: Width of the sheet at removal as seen along the x-y plane.

The interaction point is placed at the center point of the main chamber, and the gas sheet generator is positioned without the angle to facilitate measurement of the sheet width.

Content from this work may be used under the terms of the CC-BY-4.0 licence (© 2023). Any distribution of this work must maintain attribution to the author(s), title of the work, publisher, and DOI

ISBN: 978-3-95450-236-3 ISSN: 2673-5350 doi:10.18429/JACoW-IBIC2023-WEP027

The width of the sheet at the center point of the main chamber was found to be 0.14 mm (see Figure 4).

MEASUREMENT

The proposed design for signal acquisition involves positioning an intensified camera perpendicular to the interaction point. For bench testing to determine uniformity of sheet thickness and density, a hot-cathode gauge on a movable platform will be positioned in place of the camera system.

Photons will be produced in the range of 390 to 470 nm [1]. After validation of the gas sheet, the hot-cathode gauge will be replaced with an intensified camera with sensitivity in this range. Future work will include design of the optics platform and system specifications.

Use in Beam Halo Measurements

Additional functionality can be added to this device to allow for monitoring beam halo. Since profile image generated is two-dimensional, a coronagraph modification to the optics could be made to block the core of the beam when halo measurements are desired. This technique is adapted from optical coronograph devices used to view the halo of the sun and would be done by adding a movable occulting disk, an additional field lens and Lyot stop to mitigate diffraction effects caused by masking the core. This technique has been previous deployed in beam halo monitors with good results [10].

CONCLUSION

Work continues on the design of a molecular dynamics-based gas-sheet monitor to be used with high-intensity heavy ions beams generated at FRIB. This paper presented an update on the design work performed. Future work will include further specifications on the optics system and bench testing of the initial mechanical design.

ACKOWLEDGEMENTS

Special thanks to S. Rodriguez, B. Ewert, and S. Szustkowski for assistance and guidance with this work.

REFERENCES

[1] I. Yamada *et al*., "High-intensity beam profile measurement using a gas sheet monitor by beam induced fluorescence detection", *Phys. Rev. Accel. Beams*, vol. 24, no. 4, p. 042801, Apr. 2021. doi:10.1103/PhysRevAccel-Beams.24.042801

[2] F. Becker, "Beam Induced Fluorescence Monitors", in *Proc. DIPAC'11*, Hamburg, Germany, May 2011, paper WEOD01, pp. 575-579.

[3] J. Kamiya *et al.,* "Evaluation of 2-D Transverse Beam Profile Monitor Using Gas Sheet at J-PARC LINAC", *J. Phys: Conf. S.*, vol. 1350, p. 012149, 2019. doi:10.1088/1742-6596/1350/1/012149

[4] S. Szustkowski, B. T. Freemire, S. Chattopadhyay, and D.J. Crawford, "Development of a Gas Sheet Beam Profile Monitor for IOTA", in *Proc. IPAC'18,* Vancouver, Canada, Apr.-May 2018, pp. 2326-2329. doi:10.18429/JACoW-IPAC2018-WEPAL065

[5] N. Ogiwara *et al.*, "A Non-destructive Profile Monitor Using a Gas Sheet", in *Proc. IPAC'16*, Busan, Korea, May 2016, pp. 2102-2104. doi:10.18429/JACoW-IPAC2016-WEOBB03

[6] C.P. Welsch, "Non-destructive Beam Profile Monitors", in *Proc. IPAC'17*, Copenhagen, Denmark, May 2017, pp. 1234-1239. doi:10.18429/JACoW-IPAC2017-TUXB1

[7] T. Tsang, D. Gassner, and M. Minty, "Residual gas fluorescence monitor for relativistic heavy ions at RHIC," *Phys. Rev. ST Accel. Beams*, vol. 16, p. 102802, 2013.

[8] A. Lokey and S. M. Lidia, "Design Study for Non-Intercepting Gas-Sheet Profile Monitor at FRIB", in *Proc. NA-PAC'22,* Albuquerque, NM, USA, Aug. 2022, pp. 229-231. doi:10.18429/JACoW-NAPAC2022-MOPA80

[9] Molflow+, https://molflow.web.cern.ch/

[10] A. Goldblatt, E. Bravin, T.M. Mitsuhashi, F. Roncarolo, and G. Trad, "Design and Performance of Coronagraph for Beam Halo Measurements in the LHC", in *Proc. IBIC'16,* Barcelona, Spain, Sep. 2016, pp. 254-257. doi:10.18429/JACoW-IBIC2016-MOPG74

Content from this work may be used under the terms of the CC-BY-4.0 licence (© 2023). Any distribution of this work must maintain attribution to the author(s), title of the work, publisher, and DOI

ISBN: 978-3-95450-236-3 ISSN: 2673-5350 doi:10.18429/JACoW-IBIC2023-WEP028

LANSCE HIGH DENSITY EMITTANCE INSTRUMENTATION SYSTEM*

L. Montoya†, S. Baily, S. Johnson, H. Leffler, H. Watkins, D. Zimmermann
Los Alamos National Laboratory, Los Alamos, NM, USA

Abstract

The Los Alamos Neutron Science Center (LANSCE) is currently upgrading the existing emittance stations with a high-density instrumentation system for emittance measurements in the low energy beam transport region. Emittance measurements were obtained using obsolete legacy equipment. For motion control a switching station with a mechanical mux to switch actuators was used. This caused a single point of failure for all emittance stations and is becoming increasingly unreliable. For data acquisition, two sets of signal conditioning and digitizers were employed and had to be shared between 7 emittance stations. Physical cable swapping was necessary when taking measurements from station to station. A system was developed using dedicated Quad Actuator Controller (QAC) chassis, capable of driving four (4) actuators, and dedicated data acquisition (DAQ) chassis capable of signal conditioning and digitizing up to 80 channels simultaneously. Details of the system development are presented.

INTRODUCTION

Emittance diagnostics have long been operating using aging instrumentation with limited spares available with the need to be upgraded with modern electronics to avoid obsolescence and increase reliability of measurements.

The emittance instrumentation upgrade aims to extend the lifetime and capability of beam diagnostic equipment by replacing antiquated systems that are now in obsolescence with modern equipment and to improve operational efficiency and performance with the ability to automate previously labor-intensive tasks to initialize measurements on the legacy system. The reliability of the equipment would be greatly improved as the National Instruments (NI) compact Reconfigurable Input/Output (cRIO) controllers are inherently more robust than the legacy equipment and reduces the amount of potential failure and is more easily maintained as components in each chassis are readily available off the shelf.

SYSTEM LOCATION AND OVERVIEW

Locations

There are 11 emittance stations in the H- dome, Low Energy Beam Transport (LEBT), and Transition Region (TR) which corresponds to 44 unique devices associated with the upgrade. Locations upgraded during the 2023 outage are shown in green, and planned upgrades to be completed during the 2024 outage are shown in yellow in Fig. 1.

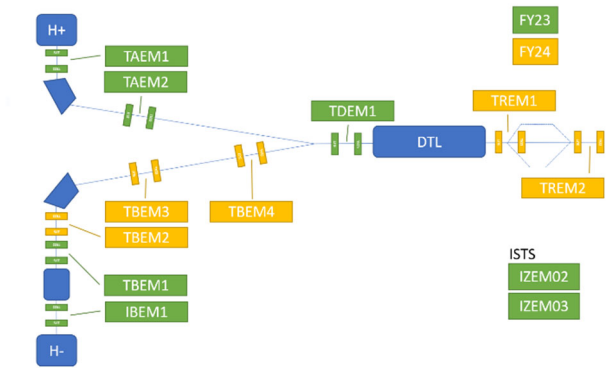


Figure 1: Emittance location map.

System Overview

Emittance stations are beam interceptive devices, thus are comprised of actuators in both horizontal and vertical axes with sensor payloads at the head of each device. Emittance measurements provide necessary information to tune the beam by providing beam parameters such as beam position, shape, angle, and intensity in both transverse and longitudinal planes through the beam pulse.

CONTROLLER HARDWARE

Using recently developed Quad Actuator Controllers (QAC) and Data Acquisition (DAQ) instrumentation chassis, the existing system is to be completely replaced and condensed with increased density of electronics [1]. The hardware diagram of the emittance system is shown on Fig. 2.

The QAC chassis will provide actuator control for a single emittance station, driving vertical and horizontal slits and collectors. In doing so, the legacy actuator switching station will be retired, removing it as a single point of failure in the system. Each emittance station was deployed a dedicated DAQ chassis removing the need to rely on the Sample and Hold chassis and shared digitizers used for all emittance measurements [2]. Both horizontal and vertical collectors in the emittance station are wired in parallel such that excitation of one axis can be read at a time and allow for a single 80 channel DAQ to read in 76 sensor inputs from the collector.

* This work was supported by the U.S. Department of Energy through the Los Alamos National Laboratory. Los Alamos National Laboratory is operated by Triad National Security, LLC, for the National Nuclear Security Administration of U.S. Department of Energy (Contract No. 89233218CNA000001).
† lucasm@lanl.gov. LA-UR-23-30153

Content from this work may be used under the terms of the CC-BY-4.0 licence (© 2023). Any distribution of this work must maintain attribution to the author(s), title of the work, publisher, and DOI

ISBN: 978-3-95450-236-3 ISSN: 2673-5350 doi:10.18429/JACoW-IBIC2023-WEP028

Content from this work may be used under the terms of the CC-BY-4.0 licence (© 2023). Any distribution of this work must maintain attribution to the author(s), title of the work, publisher, and DOI

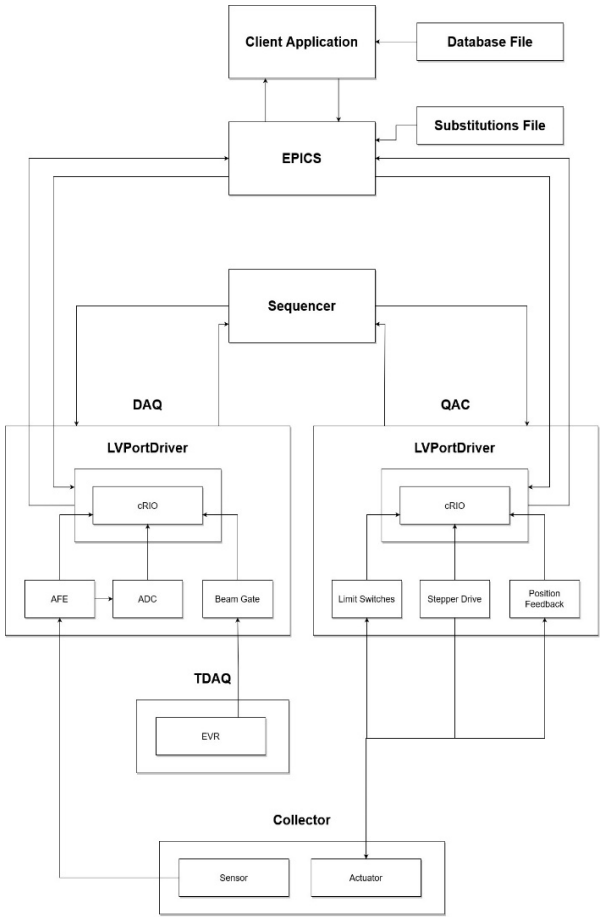


Figure 2: Emittance hardware block diagram.

The DAQ maintains acquisition capabilities as developed on the Isotope Production Facility emittance upgrade project from which it was initially developed [3]. Live waveform data can be observed as shown in Fig. 3 where a collector can effectively be utilized as a harp device.

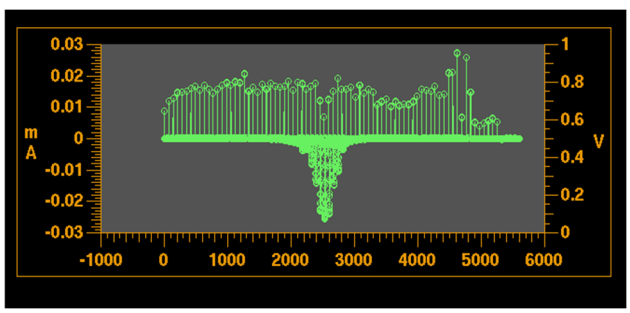


Figure 3: DAQ emittance waveform.

BEAM MEASUREMENT RESULTS

Emittance measurements were taken using chopped and un-chopped beam in the LEBT using both H+ and H- beams. Figure 4 shows IBEM01 horizontal emittance scan on the cRIO system with similar measurements being produced from previous years confirming the viability of the system and allowing for a total replacement of all legacy hardware.

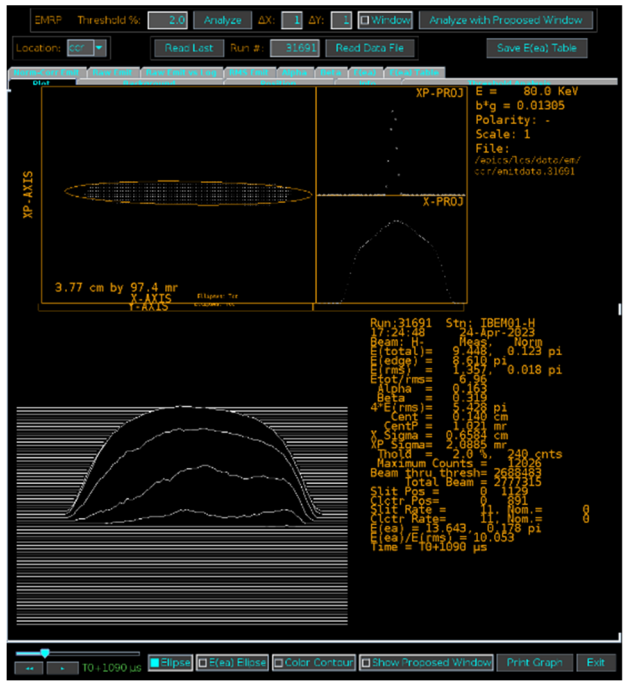


Figure 4: IBEM01 horizontal emittance scan.

CONCLUSION

With a successful commissioning of the emittance stations, work is planned to complete the remaining stations and upgrade harp devices using the QAC and DAQ platform. With all LANSCE beam interceptive devices on the same platform, diagnostics will become easier to maintain with fewer hardware types to learn and have spares more readily available.

REFERENCES

[1] L. Montoya, *et al.*, "LANSCE QAC/DAQ Wire Scanner Instrumentation Upgrade," presented at IBIC'23, Saskatoon, Canada, Sep. 2023, paper WEP029, this conference.

[2] D. Baros, J. D. Sedillo, and H. A. Watkins, "Bridging the Gap; Updating LANSCE Digitizers", in *Proc. IBIC'16*, Barcelona, Spain, Sep. 2016, pp. 822-824. doi:10.18429/JACoW-IBIC2016-WEPG74

[3] J. D. Sedillo, D. Baros, J. F. O, L. Rybarcyk, R. A. Valicenti, and H. A. Watkins, "LANSCE Isotope Production Facility Emittance Measurement System", in *Proc. IBIC'16*, Barcelona, Spain, Sep. 2016, pp. 548-550. doi:10.18429/JACoW-IBIC2016-TUPG79

ISBN: 978-3-95450-236-3 ISSN: 2673-5350 doi:10.18429/JACoW-IBIC2023-WEP029

LANSCE QAC/DAQ WIRE SCANNER INSTRUMENTATION UPGRADE*

L. Montoya†, S. Johnson, H. Watkins, D. Zimmermann
Los Alamos National Laboratory, Los Alamos, NM, USA

Abstract

High density instrumentation has been developed to upgrade wire scanner beam diagnostic capability in all areas downstream of the Coupled Cavity (CCL) LINAC (Linear Accelerator). Transverse beam profile measurements were originally obtained using legacy electronics known as Computer Automated Measurement and Control (CAMAC) crates. CAMAC has become obsolete, and a new wire scanner diagnostic system was developed as a replacement. With high wire scanner device density located in each area, instrumentation was developed to meet that need along with the ability to interface with legacy open-loop controlled actuators and be forward compatible with upgraded closed-loop systems. A high-density system was developed using a Quad Actuator Controller (QAC) and Data Acquisition (DAQ) chassis that pair together using a sequencer when taking measurements. Software improvements were also made, allowing for full waveform functionality that was previously unavailable. Deployment of 52 wire scanner locations in 2022 increased device availability and functionality across the facility. Hardware and software design details along with results from accelerator beam measurements are presented.

INTRODUCTION

Legacy diagnostic instrumentation used at the Los Alamos Neutron Science Center (LANSCE) have become obsolete with no readily available spares for CAMAC systems. Because of the density of devices downstream of the CCL a high-density solution was needed.

A new wire scanner instrumentation system has been developed and implemented by the LANSCE controls hardware team to replace CAMAC and interface with legacy devices. Software was developed to interface the old devices with the new hardware, primarily the embedded and client software.

SYSTEM OVERVIEW

Wire scanners are electro-mechanical beam interceptive devices that provide cross-sectional beam profile measurements that describe beam shape and position. A wire scanner system consists of an actuator to drive the sense wires across the beam, and data acquisition to obtain the waveform data from the current induced by the proton beam impinging on the wire. The wire scanner hardware architecture diagram is shown in Fig. 1.

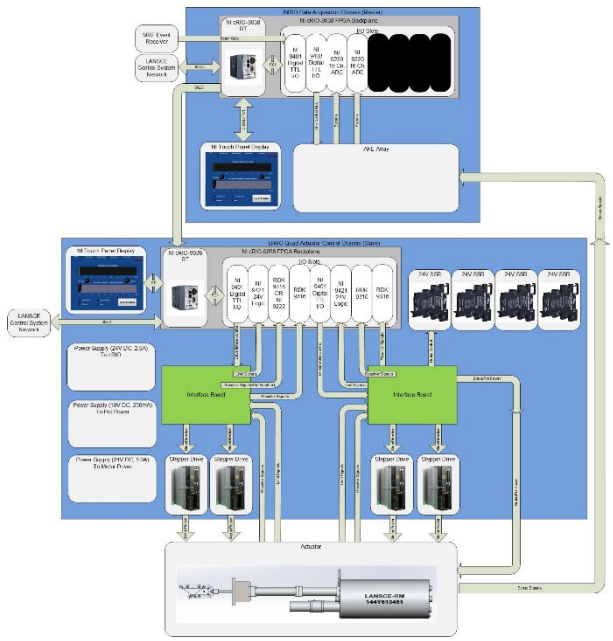


Figure 1: Wire scanner hardware diagram.

CONTROLLER HARDWARE

The electronic hardware consists primarily of two separate chassis, each controlled using a National Instruments (NI) 9038 compact Reconfigurable Input/Output (cRIO) packaged in 4U rack mountable enclosures configured as input output controllers (IOC). The QAC chassis controls the wire scanner actuators, and the DAQ chassis is used for data acquisition from the beam induced current on the wire.

Quad Actuator Controller

The QAC chassis was designed to control up to four stepper motor actuators, two actuators simultaneous. The chassis is compatible with both open loop and closed loop motion control to be forward compatible with potential actuator upgrades to resolver position closed loop control as was done on the LANSCE risk mitigation project [1].

Within the cRIO controller on the QAC is housed NI I/O modules, and serve as the interface between the wire scanner actuator and the cRIO and perform the functions as follows:

- NI 9401 digital I/O for stepper motor and brake control
- NI 9421 sinking digital input for limit switch indication
- NI 9222 voltage input potentiometer position feedback, for open loop control
- RDK 9316 resolver to digital converter, for closed loop only

* This work was supported by the U.S. Department of Energy through the Los Alamos National Laboratory. Los Alamos National Laboratory is operated by Triad National Security, LLC, for the National Nuclear Security Administration of U.S. Department of Energy (Contract No. 89233218CNA000001).
† lucasm@lanl.gov. LA-UR-23-30151

Content from this work may be used under the terms of the CC-BY-4.0 licence (© 2023). Any distribution of this work must maintain attribution to the author(s), title of the work, publisher, and DOI

ISBN: 978-3-95450-236-3 ISSN: 2673-5350 doi:10.18429/JACoW-IBIC2023-WEP029

Content from this work may be used under the terms of the CC-BY-4.0 licence (© 2023). Any distribution of this work must maintain attribution to the author(s), title of the work, publisher, and DOI

In addition to the cRIO, the QAC chassis consists of four stepper motor drivers, four solid state relays for electrically released brake, two signal distribution boards, a touch display, 10V potentiometer power supply and 24V power supplies for the cRIO and actuator power. The QAC chassis is shown in Fig. 2.



Figure 2: QAC chassis.

Data Acquisition

The DAQ chassis is capable of 32 channel, 100 kS/channel, simultaneous waveform acquisition (10µs resolution) with a compact Peripheral Component Interconnect backplane with two high density 16 channel each, gain adjustable, 2 kΩ input impedance Analog Front End (AFE) conditioning card capable of reading from 270 µA down to 3 µA current levels [2]. The NI I/O modules installed into the cRIO consist of an NI 9403 for AFE gain setting, two NI 9220 digitizers, and an NI 9401 digital I/O for beam gate input. The DAQ chassis is expandable from 32 channels to 80 by adding AFE cards and 9220 digitizer modules depending on the area device density.

Sequencer

A sequencer was implemented as a soft IOC to coordinate motion and data acquisition between the QAC and DAQ hardware during a scan. The sequencer also sets all scan parameters for the measurement. When in scan mode the sequencer initiates the scan, awaits a beam gate trigger, and acquires the waveform for that beam pulse, commands the next actuator position and repeats until a scan is completed.

BEAM MEASUREMENT RESULTS

Beam profile measurements were taken using Long Bunch Enable Gate beam, set to 4 Hz rep rate with 150 µs beam length. As shown in Fig. 3, a Gaussian profile was obtained.

The full waveform can be seen in Fig. 4 for the same scan taken in Fig. 3. Each trace is a waveform from a separate beam pulse as the wire scanned across the beam.

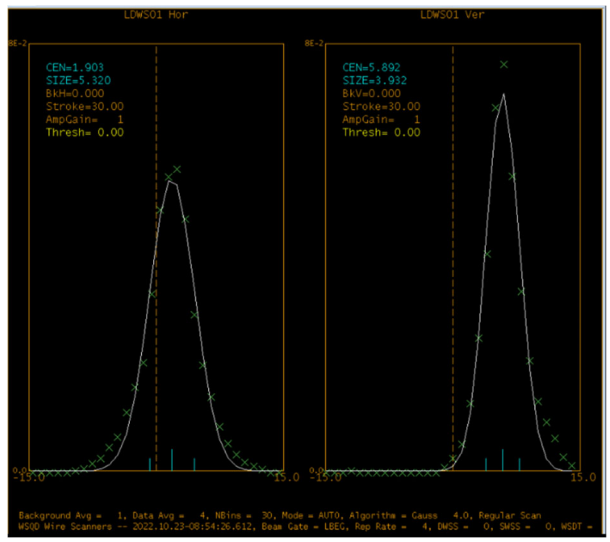


Figure 3: Vertical and Horizontal Axis Beam Profiles.

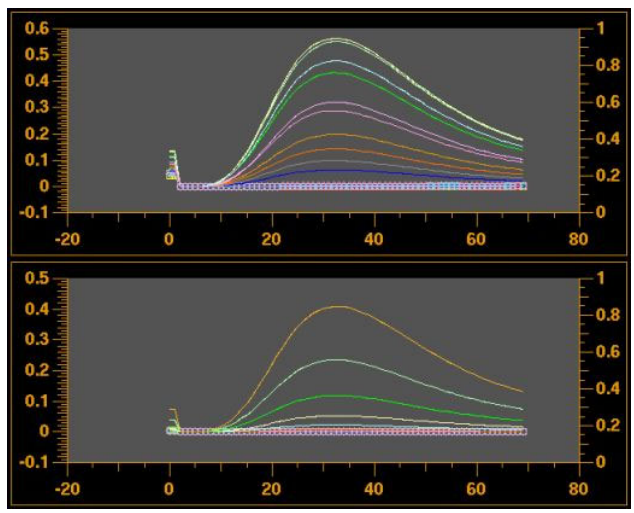


Figure 4: Vertical and horizontal axis waveform.

Challenges

The challenge encountered during development was insufficient gain on the 2K AFE in obtaining data from Micro Pulse Enable Gate (MPEG) beam. To mitigate the lack of gain, legacy transimpedance amplifiers were used in a dual stage amplification in conjunction with the 2K AFE which was sufficient in providing the amplification needed to obtain beam profile waveforms.

A transimpedance AFE was implemented to accommodate the wider gain range and allow for dependence on legacy amplifiers to no longer be needed. [3]

CONCLUSION

All 52 wire scanner locations have been successfully upgraded with each device tested and validated with beam, providing beam profile measurements for each location this past run cycle during the 2022 calendar year.

ISBN: 978-3-95450-236-3 ISSN: 2673-5350 doi:10.18429/JACoW-IBIC2023-WEP029

REFERENCES

[1] J. D. Sedillo, J. D. Gilpatrick, F. Gonzales, V. Kutac, D. Martinez, and M. E. Gruchalla, "First Test Results of the New LANSCE Wire Scanner", in *Proc. PAC'11*, New York, NY, USA, Mar.-Apr. 2011, paper MOP236, pp. 554-556.

[2] J. D. Sedillo *et al,* "LANSCE Isotope Production Facility Emittance Measurement System", in *Proc. IBIC'16*, Barcelona, Spain, Sep. 2016, pp. 548-550. doi:10.18429/JACoW-IBIC2016-TUPG79

[3] D. Rai, *et al.,* "Implementation of Transimpedance Analog Front End Card for Los Alamos Neutron Science Center Accelerator Wire Scanners," presented at IBIC2023, Saskatoon, Canada, September 2023, paper WEP042, this conference.

Content from this work may be used under the terms of the CC-BY-4.0 licence (© 2023). Any distribution of this work must maintain attribution to the author(s), title of the work, publisher, and DOI

ISBN: 978-3-95450-236-3 ISSN: 2673-5350 doi:10.18429/JACoW-IBIC2023-WEP030

FIRST RESULTS FOR A 50 MeV BEAM INDUNCED FLUORESCENCE MONITOR FOR BEAM PROFILE MEASUREMENTS

G. Rosenthal, J.I. Anderson, A. Cao, E. Cramer, T. Gordon, K. Kuhn, O. Vazquez, J. Lopez
S. Lynam, J. Ringuette, L. Szeto, J. Zhou, Nusano, Salt Lake City, UT, USA
E. Dorman, R. Emery, B. Smith, University of Washington Medical Center, Seattle, WA, USA

Abstract

Nusano is developing a 50 MeV alpha ($^4He^{++}$) particle accelerator (The Nusano accelerator can also accelerate $^2H^+$, $^3He^{++}$, $^6Li^{3+}$, $^7Li^{3+}$, and a few other heavier ions), primarily to produce medical radionuclides. The accelerator produces an average current of 3 mA_e with 20 mA_e average macro pulse current. This results in an average beam power of 75 kW, and an average beam power within the macro pulse of 500 kW. The beam profile at the exit of the DTL is approximately Gaussian with a radius (FWHM) of about 3 mm. Designing diagnostics for this beam is challenging, as diagnostics that intercept beam will receive a very high heat load. A BIFM (Beam Induced Fluorescence Monitor) is being developed to measure beam profiles. Nitrogen gas is leaked into the beamline. Excitation of the nitrogen by beam particles is captured using an image intensifier. The signal generated is directly proportional to the beam current. A prototype system has been constructed and tested on a lower intensity alpha beam. First results indicate we can measure beam profile to a 100 µm accuracy. Production system is currently being designed.

EXPERIMENTAL SYSTEM

The 50 MeV alpha particle accelerator Nusano is developing will be commissioned in 2025. The 47.3 MeV at the University of Washington Medical Cyclotron Facility was used as a test facility to evaluate the BIFM (Beam Induced Fluorescence Monitor) intended to be installed on the beamline. The cyclotron provides 20-40 µA_e alpha beam, which is a good model for the Nusano beam.

The experimental apparatus is shown in Figure 1, consists of a vacuum chamber that the beam passes through. In the chamber the beam particles interact with nitrogen leaked into the chamber and photons are generated by decay in excited nitrogen. The light exits the chamber through a window and is directed by lenses and mirrors into an image intensified camera (Photonis iNocturn HI-QE Blue). Since the light emitted is directly proportional to the density of nitrogen and the beam current, by analyzing the images generated the beam distribution can be measured. A calibrated PMT is also provided to measure light intensity received by the camera.

Control of the nitrogen pressure is critical to correct operation of the BIFM. The experimental system allowed for both pulse and CW nitrogen flow, but the data presented here is entirely based on CW flow. One of the key goals of the project was to determine the ideal nitrogen pressure for the system. The system also includes vacuum chokes that allow the pressure in the measurement chamber to be about an order of magnitude higher than the pressure in the surrounding vacuum system.

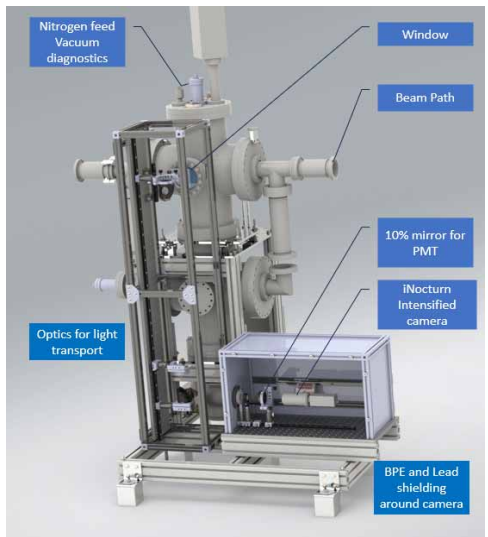


Figure 1: CAD drawing of experimental system.

RESULTS

A basic raw data image is show in Figure 2. The beam is the horizontal strip shown in the blue outline. The crescent shape, and the three dots (red outline), are compound reflections of light generated by ionization of background gas in the cold cathode pressure gauge.

In order to understand the resolution of the BIFM a picture was taken with a test pattern located at the beam position. Combining this with the data averaged across the beam part of the image indicates a spatial resolution on the order of 100 µm (see Figure 3).



Figure 2: Basic image show the beam induced fluorescence (show in the blue box). The crescent shape, and the three dots (red box), are a compound reflection from the cold cathode pressure gauge.

Content from this work may be used under the terms of the CC-BY-4.0 licence (© 2023). Any distribution of this work must maintain attribution to the author(s), title of the work, publisher, and DOI

ISBN: 978-3-95450-236-3 ISSN: 2673-5350 doi:10.18429/JACoW-IBIC2023-WEP030

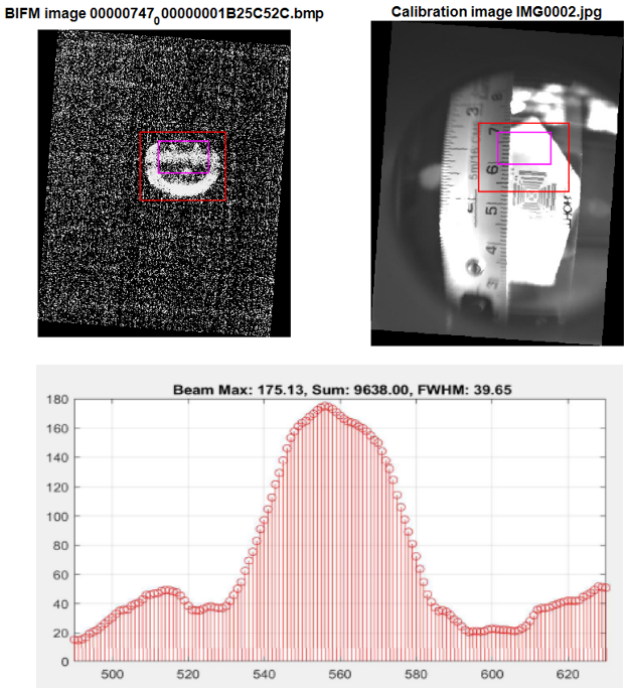
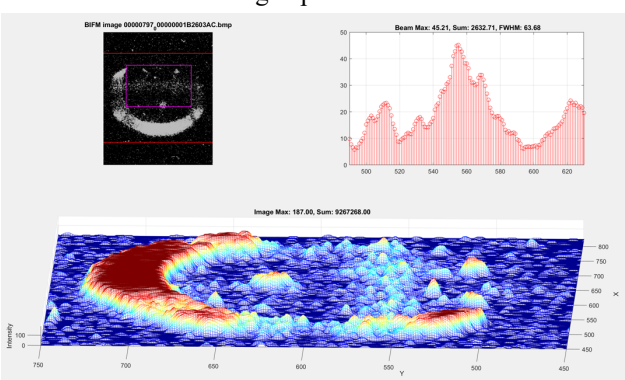


Figure 3: Spatial resolution of the BIFM. The upper left shows a beam induced image. The upper right is the calibration image. Note the blue and red boxes represent matching areas. The lower image indicates the averaged data from pixels in the beam box.

Variation with Nitrogen Pressure

Varying the nitrogen pressure varies the intensity of received light (Figure 4). The received beam signal is proportional to the nitrogen pressure. The light from the cold cathode gauge is not because it saturates the detector at the highest pressures.

Pulsing the nitrogen gas feed, to reduce the load on the rest of the vacuum system, was considered but the data tends to indicate that Nusano can probably operate the BIFMs with a CW nitrogen pressure.



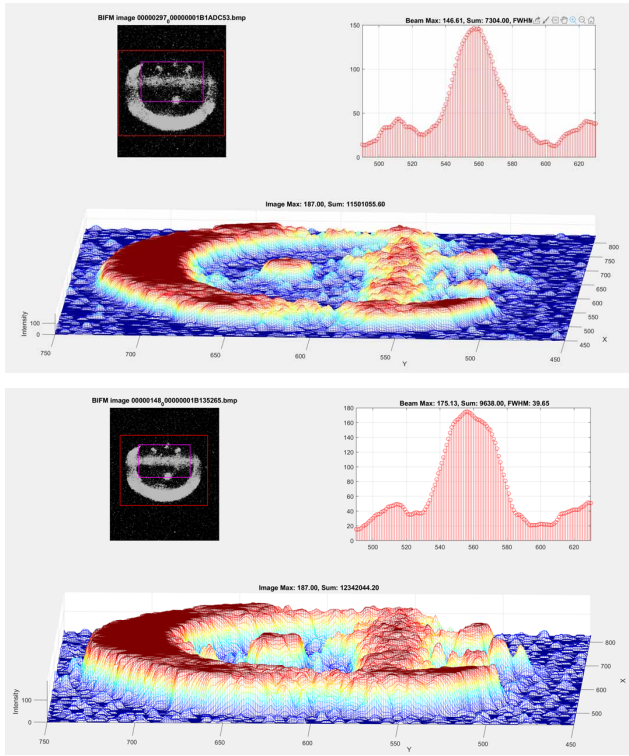


Figure 4: Variation of signal with nitrogen pressure. The upper data is at 2×10^{-5} torr, middle data is at 5×10^{-5} torr, and the lower data is at 7×10^{-5} torr.

Variation with Beam Position

As a test of system performance, the beam was steered up and down and BIFM was used to track the beam position (Figure 5). The beam centroid moves about 4.5 mm, which is consistent with the beam optics and limits placed by the collimators.

The beam profile is consistent with a wire scanner diagnostic. Direct comparison is difficult because the wire scanner is limited to a much smaller beam current than was used for the BIFM experiments.

UW / Nusano Comparison

The UW experiments were conducted primarily with 22 μA_e beam current. Clearly sufficient light was generated for the single layer MCP intensifier to form images (averaging several hundred images was necessary to generate good statistical data). Nusano will operate with 20 mA_e beam current, so 1000 times as many photons would be generated for the same nitrogen pressure. Nusano will reduce the nitrogen pressure to 5×10^{-7} torr resulting in a reduction in the number of photons by a factor of 100. This still results in Nusano generating 10 times the light seen in these experiments. This low nitrogen pressure should allow Nusano to operate the BIFMs with a CW gas flow, simplifying the diagnostics.

We are also evaluating the possibility of operating with the lower gain camera and using a puffed gas system.

Content from this work may be used under the terms of the CC-BY-4.0 licence (© 2023). Any distribution of this work must maintain attribution to the author(s), title of the work, publisher, and DOI

ISBN: 978-3-95450-236-3 ISSN: 2673-5350 doi:10.18429/JACoW-IBIC2023-WEP030

Content from this work may be used under the terms of the CC-BY-4.0 licence (© 2023). Any distribution of this work must maintain attribution to the author(s), title of the work, publisher, and DOI

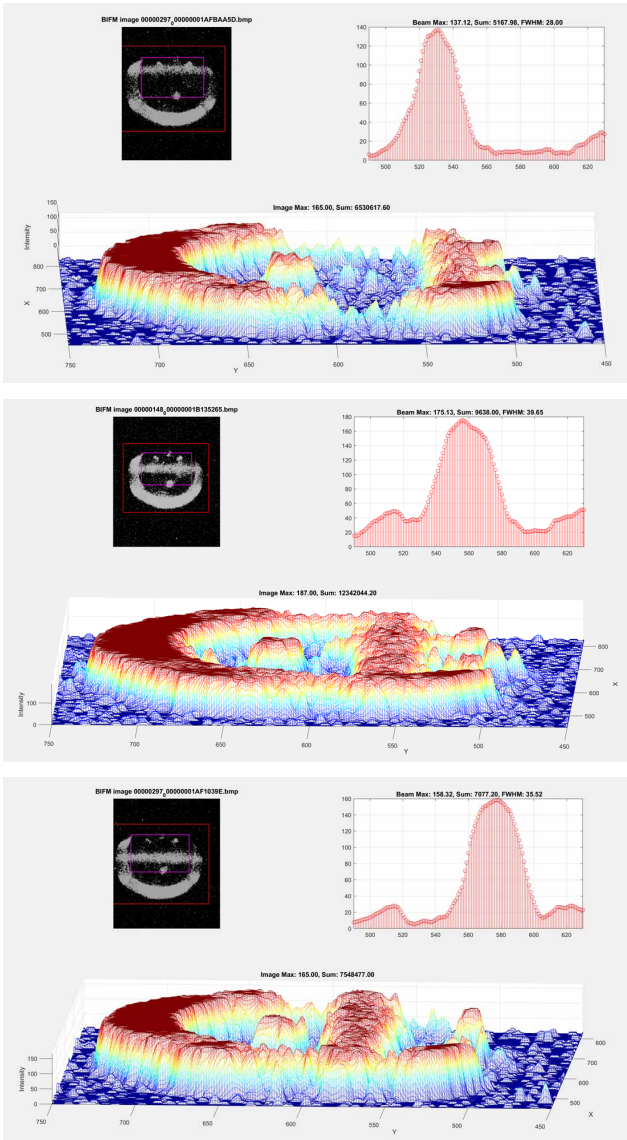


Figure 5: Beam steering. The beam centroid was moved up and down and the position followed on the BIFM. The centroid travel is about 4.5 mm, which is consistent with beam optics and collimators.

RADIATION DAMGE

The long optical path and shielding are to reduce the radiation dose on sensitive electronic such as the camera. Nusan's beam line will be exposed to high radiation dose. Up to 25,000 mrem/hour on the switchyard floor, and more than order of magnitude higher at beam height. This dose is primarily from neutrons (~90%) and gammas (~10%). The UW facility also has a high dose of neutrons from their neutron treatment beam.

Images taken before and after operation of the neutron beam (Figure 6) clearly show an increase in the number of dead pixels as well as a reduced sensitivity.

The experimental setup had limited shield due to space constraints on the beamline.

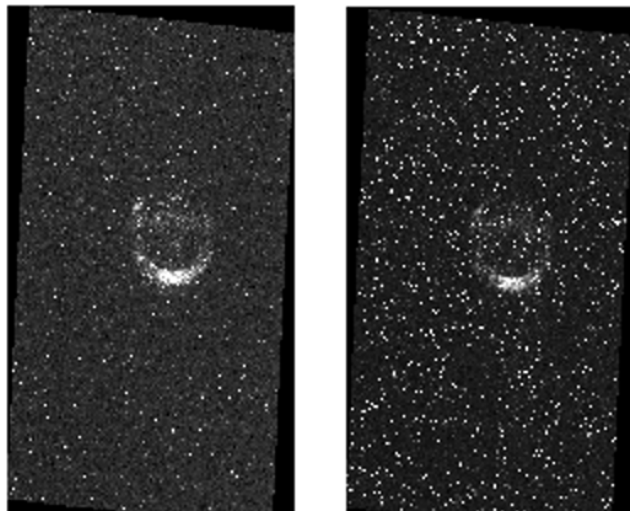


Figure 6: Neutron damage, primarily to the camera system. The image on the left was taken at the end of the first day of operation. The image on the right was taken after the neutron treatment beam had been running for an entire day.

NEXT STEPS

The camera settings were not optimal at the UW experiments. Several pixels were saturated. The gain can be turned down on the camera or we could change the image size. For example, increasing the image size on the camara by a factor of two, in both directions, would decrease the brightness and increase the spatial resolution to 50 µm.

The camera showed some radiation damage so shielding around the camera will have to be increased. The limited shielding at UW was mostly a function of space constraints.

We had several problems with small light leaks into the darkened optics boxes. These will be redesigned to reduce light leaks and make them easier to work with.

The cold cathode vacuum gauge generated significant light problems. This will be relocated, and reflective surfaces darkened.

CONCLUSIONS

The first test of the Nusano BIFM was very successful. All project goals were achieved and then some. An improved version of the system is being designed and constructed. Emphasis is on a system that can be deployed and maintained along the beamline. Nusano will eventually deploy 35 BIFM systems along the beamline. Some are for specific diagnostics or tuning applications, but many are expected to be part of routine operations.

ISBN: 978-3-95450-236-3 ISSN: 2673-5350 doi:10.18429/JACoW-IBIC2023-WEP031

IMAGE ACQUISITION SYSTEM FOR THE INJECTION DUMP AT THE SPALLATION NEUTRON SOURCE*

W. Blokland†, N. Evans, A. Oguz, and D. Willis
Oak Ridge National Laboratory, Oak Ridge, TN, USA

Abstract

We describe the Image Acquisition system for the Injection Dump. This system visualizes the different beamlets, on the vacuum window after the H- beam is stripped of its electrons by two stripper foils. One beamlet is from H- with its electrons stripped by the first foil and the second beamlet has its final electron stripped by the second foil. We used the PXI platform to implement the data-acquisition including timing decoder. We describe the hardware and software for the system. We use a standard non-radhard GigE camera to acquire the image from the luminescent coating on the dump vacuum window. To lower the radiation damage to the camera, we shield it with stainless steel blocks. We present radiation measurements before and after shielding. We also show the radiation damage over time to estimate the camera's lifetime.

INTRODUCTION

The Ring Injection Dump (RID) needs diagnostics to properly steer two waste beam species, leftover from the charge exchanging injection scheme, to the dump. The Proton Power Upgrade (PPU) upgrades the magnets in the injection region and confirmation is needed of the new trajectories.

The two waste species are referred to as "H^0 beam" (partially stripped H^- beam) and "H^- beam" (the beam that misses the primary foil) see Fig. 1. The width of the beam is up to 20 cm with vertical size slightly smaller. Both species end up as H+ after passing through a secondary stripping foil.

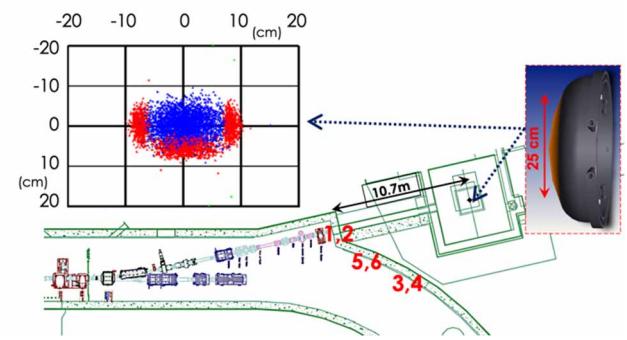


Figure 1: The Ring Injection Dump line along with the calculated projection of beam particles on dump window.

To visualize the waste species on the injection dump window, it has been coated with a luminescent coating made of Al2O3:Cr, similar to the SNS target. An optical system transfers the light to a camera, see Ref. [1]. The requirements include an absolution position accuracy of 10 mm, both horizontal and vertical, and to survive an 16-hour study period to confirm the particles' trajectories. The intention was to install the window with the coating right before the measurement but changes in schedule resulted in installing the coating window but not the optical system. Hence no results with actual beam will be presented in this paper. The coating luminescence will have been reduced due to radiation damage while running beam without the having an optical system but experience with the SNS target coatings indicates that enough luminescence remains to perform the required measurements once the optical system has been installed. The optics are described in Ref. [1].

CAMERA SETUP

The system is based on non-radhard GigE cameras because radhard cameras are expensive or do not have the right features. To use non-radhard cameras we tested the radiation doses during full power beam conditions at different locations, see also Ref. [2]. The results are repeated in Table 1. The odd locations are at ground level and the even locations at about 1.5 m (above the beam plane). Location ES (Electron Scanner) is in a straight section of the ring and is listed as a control reference. Cameras in those locations easily survive multiple years of beam runtime (5000 Hrs/year). We used CERN HiRadMat results from Ref. [3] to convert from dose to Time-to-Death and Time-to-Significant-Event (crash). The calculation confirms that cameras at the ES location can survive for a long time. The results in the table show that locations further from the injection dump beamline have lower doses. However, locations 1 and 2 simplify the optical system and location 1 allows for the system to be installed on the floor. Unfortunately, this location has the highest dose rates, thus we will use shielding to reduce the dose.

Table 1: Camera Locations, Doses, and Expected Time to Death and Significant Event (SE) at 1.4 MW Beam Power

Location	Total (Gy/MWHr)	Time to Death (Hrs)	Time to SE (Hrs)
1	0.29	285	0.91
2	0.24	339	1.09
3	0.04	2246	7.20
4	0.05	1797	5.76
5	0.08	998	3.20
6	0.08	998	3.20
ES	0.0032	25674	82.29

* SNS is managed by UT-Battelle, LLC, under contract DE-AC05-00OR22725 for the U.S. Department of Energy
† blokland@ornl.gov

Content from this work may be used under the terms of the CC-BY-4.0 licence (© 2023). Any distribution of this work must maintain attribution to the author(s), title of the work, publisher, and DOI

ISBN: 978-3-95450-236-3 ISSN: 2673-5350 doi:10.18429/JACoW-IBIC2023-WEP031

Content from this work may be used under the terms of the CC-BY-4.0 licence (© 2023). Any distribution of this work must maintain attribution to the author(s), title of the work, publisher, and DOI

We investigated shielding blocks of tungsten and stainless steel. While tungsten is more effective as a radiation shield, it was also a factor of three more expensive, so we chose stainless steel, still at a cost of ~$50k. We also avoided requiring lifting equipment for installation by using smaller blocks that can be moved by hand, including blocks with handles to allow for easy camera replacement. The configuration and blocks are shown in Fig. 2. The shielding was calculated to shield by a factor of around 30, we measured almost a factor of 40 lower dose, but this was at ground level, while in the final installation the camera will be slightly higher. This brings the estimated Time-to-Death to ~11,000 hrs and the Time-to-Significant-Event (SE) to almost 40 hrs. These are very reasonable numbers, our typical beam runtime is 5000 hrs/year, and will allow the system to be maintained and used for many years with minimal replacement cost for the non-radhard camera.

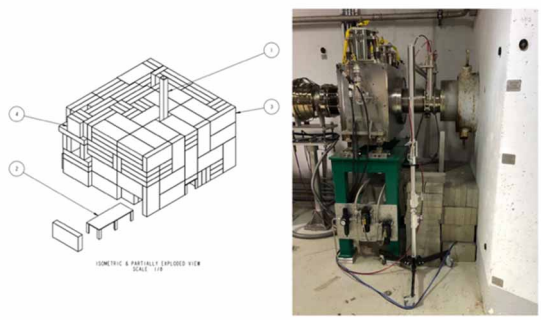


Figure 2: The shielding blocks to protect the camera.

The shielding was installed without the optics to perform testing of the non-radhard camera in place. The camera was a FLIR Blackfly 23S6M-C Mono camera with the Sony IMX249 sensor. The camera was in place for about a year and survived but had to be rebooted multiple times. Figure 3 shows the camera being inserted into the shielding blocks.



Figure 3: The camera inserted into the shielding blocks arrangement.

After 1800 MWhrs of production beam exposure the camera image was checked, see Fig. 4. It shows that we can expect to provide details on the beamlets even after full production beam at 1.4 MW after 50 days.

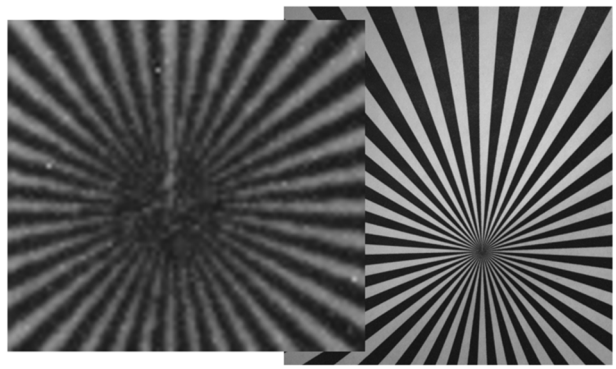


Figure 4: The Camera image after 1800 MWHrs of exposure at 1.4 MW at 1 GeV. Left a close-up of the test image center.

ACQUISITION SYSTEM

The imaging system's requirements are:

- Survive a 16-hour study to document the new beamline's behavior,
- provide position resolution of < 4 mm, and
- interface with the EPICS controls system.

The camera test showed that the system can survive for much longer than needed for the study. The optics have been tested in the lab and has a resolution of 0.2 mm. We estimate the position accuracy to be 2 mm depending on the actual signal-to-noise in the field which depends on how the coating has aged. The acquisition platform is PXI with LabVIEW. The system is shown in Fig. 5.



Figure 5: System Hardware.

The PXIe-840 computer runs Windows OS and connects the control network and the camera through separate ethernet interfaces. The power to the camera is controlled by a PXIe-4112 module to be able to reboot the camera after a crash (Significant Event). To decode the accelerator timing systems, we use a SNS Timing Adaptor board to transmit the timing signals over the PXIe bus to the FPGA board, a PXIe-7971, for decoding of beam triggers and information such as timestamps. To satisfy the position accuracy requirement, we put fiducial markers on the coating of the injection dump window, see Fig. 6. A high intensity lamp, powered through the BK Precision 1687B power supply, makes the fiducials visible for calibration before there is beam on the window.

ISBN: 978-3-95450-236-3 ISSN: 2673-5350 doi:10.18429/JACoW-IBIC2023-WEP031



Figure 6: Fiducial markers on the vacuum window.

Software

The software program acquires the image from the camera and provides intensity projections both horizontal and vertical as well as the centroid of the image. Different overlays can be added to the image. A circle that is matched to the edge of the coated area and a crosshair that the user can align with a blob in the image. The LabVIEW program interface is shown in Fig. 7.

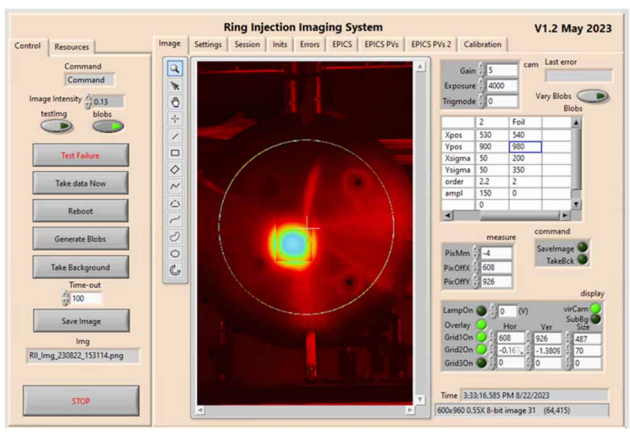


Figure 7: LabVIEW program.

Additional features in the program are to display two generated 2D gaussians to mimic the beamlets, and the stripper foil effect to test the program. Background images can be taken and subtracted from the acquired images.

The LabVIEW program, besides performing the data acquisition and analysis, also functions as an expert screen while a CS-Studio interface is available for use in the control room. We use a SNS LabVIEW native Channel Access (CA) server to interface with the EPICS based control system. The LabVIEW program uses a library on top of this CA Server to generate Extensible Display Manager (EDM) and Control System (CS) Studio files of the published Process Variables (PVs). These files give you a head start with

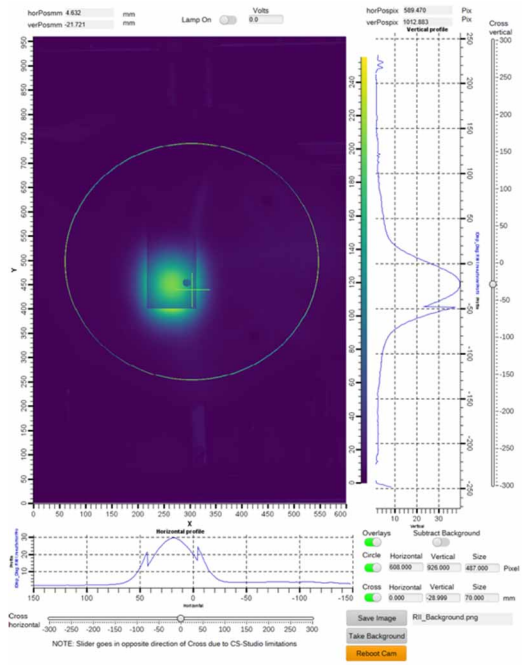


Figure 8: CS-Studio screen.

implementing the operator screens. The CS-Studio screen for the Injection Imaging System is shown in Fig. 8.

CONCLUSION

An image acquisition system has been created for the injection dump to visualize the waste beam from the stripping foil. A non-radhard camera is used but shielded to provide months of operation based on measurements and reference data. The system integrates with the SNS EPICS-based controls system to provide data to studiers in the control room. Unfortunately, the installation of the optics system was delayed due to problems with the installation of the coated vacuum window and no field measurements have yet been taken.

ACKNOWLEDGEMENTS

The authors wish to thank Melissa Harvey for her work on the shielding.

The authors are grateful for support from the Neutron Sciences Directorate at ORNL in the investigation of this work. This research used resources at the Spallation Neutron Source, a DOE Office of Science User Facility operated by the Oak Ridge National Laboratory. This manuscript has been authored by UT-Battelle, LLC, under Contract No. DE-AC05-00OR22725 with the US Department of Energy (DOE). The US government retains and the publisher, by accepting the article for publication, acknowledges that the US government retains a nonexclusive, paid-up, irrevocable, worldwide license to publish or reproduce the published form of this manuscript, or allow others to do so, for US government purposes. DOE will provide public access to these results of federally sponsored research in accordance with the DOE Public Access Plan [4].

Content from this work may be used under the terms of the CC-BY-4.0 licence (© 2023). Any distribution of this work must maintain attribution to the author(s), title of the work, publisher, and DOI

ISBN: 978-3-95450-236-3 ISSN: 2673-5350 doi:10.18429/JACoW-IBIC2023-WEP031

REFERENCES

[1] A. Rakhman, D. Willis, D. Aikens, J. Mason, W. Blokland, N. Evans, *et al.*, "Off-axis, Reflective Schmidt Telescope Design for Proton Beam Imaging System*," in *OSA Optical Design and Fabrication 2021*, Nov. 2021, paper 120781K.

[2] W. Blokland and A. R. Oguz, "Feasibility Study of a Non-Rad Camera for the SNS* Ring Injection Dump Imaging System", presented at the IBIC'20, Santos, Brazil, Sep. 2020, paper THPP32, unpublished.

[3] S. Burger, "Scintillation Screens and Optical Technology for transverse Profile Measurements", Presentation at ARIES-ADA Topical Workshop, Krakow, Poland, Apr. 2019.

[4] Department of Energy Public Access Plan, https://www.energy.gov/sites/prod/files/2014/08/f18/DOE_Public_Access%20Plan_FINAL.pdf.

Content from this work may be used under the terms of the CC-BY-4.0 licence (© 2023). Any distribution of this work must maintain attribution to the author(s), title of the work, publisher, and DOI

ISBN: 978-3-95450-236-3 ISSN: 2673-5350 doi:10.18429/JACoW-IBIC2023-WEP033

A Schottky Tune Meter for the Fermilab Mu2E Delivery Ring*

V. Scarpine†, B. Fellenz, A. Semenov, D. Slimmer
Fermi National Accelerator Laboratory, Batavia, IL, USA

Abstract

The Mu2E experiment will measure the ratio of the rate of the neutrinoless, coherent conversion of muons into electrons as a measure of Charged Lepton Flavor Violation. As part of the Mu2E experiment, a proton storage ring, called the Delivery Ring, will utilize resonant extraction to slow-spill protons to the experiment. To regulate and optimize the Delivery Ring resonant extraction process, a fast tune measurement scheme will be required. This Mu2E tune meter will measure the average tune and the tune spectrum, in multiple time slices, through the entire resonant extraction cycle of nominally 43 msec. The Mu2E tune meter system utilizes vertical and horizontal 21.4 MHz Schottky detector resonant pickups, taken from the decommissioned Tevatron, high-gain amplifiers and digital down-conversion FPGA logic for its signal processing. This paper will present the design of this Schottky tune meter as well as tune measurements from the Mu2E delivery ring.

MU2E SLOW SPILL

The Mu2E experiment will search for the charged-lepton flavor violating process $\mu^- N \rightarrow e^- N$ [1]. Mu2E proposes to measure the ratio of the rate of the neutrino-less, coherent conversion of muons into electrons in the field of a nucleus, relative to the rate of ordinary muon capture on the nucleus. This requires the resonant extraction of a stream of pulsed beam, comprised of short micro-bunches (pulses) from the Delivery Ring (DR) to the Mu2e target [2].

Mu2e uses 8 kW of 8 GeV protons extracted from the Fermilab Booster. Figure 1 show a table of key DR beam parameters. Once 1e12 protons are injected into the DR, beam is then slow extracted to the Muon proton target at the DR revolution frequency of 590.08 kHz over a nominally 43 ms spill period. Between each spill period, there is 5 ms reset period, in which there is no extraction. After the 8th spill, there is no beam in DR for 1.02 s. Figure 2 shows the Mu2E DR intensity timeline for eight slow spills.

By exciting two families of the harmonic sextupoles in the DR, the third integer slow-spill resonant extraction condition is established [3]. Figure 3 shows the modelled change in the DR tune along a single slow spill along with expected data points from this tune meter system.

MU2E TUNE METER SYSTEM

The Mu2E tune meter system, shown in figure 4, consists of 21.4 MHz inductively resonated stripline pickups, low noise RF amplifiers, bandpass filters and a high-speed FPGA-based DAQ board.

Parameter	Value	Units
MI Cycle time	1.333	sec
Number of spills per MI cycle	8	
Duration of each spill	34-54	msec
Number of protons per micro-pulse	$(3.0\text{-}5.0)\times10^7$	protons
Maximum DR Beam Intensity	1.0×10^{12}	protons
Reset Time Gap between spills	5	msec
Operation point (Qx/Qy)	9.650/9.735	
DR revolution frequency	590.018	kHz

Figure 1: Mu2E delivery ring beam parameters.

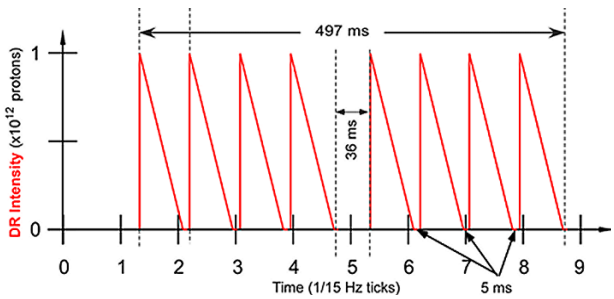


Figure 2: Mu2E slow spill beam timeline.

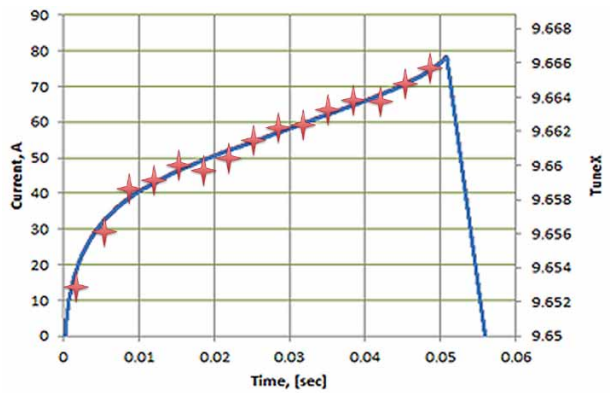


Figure 3: Expected tune along slow spill.

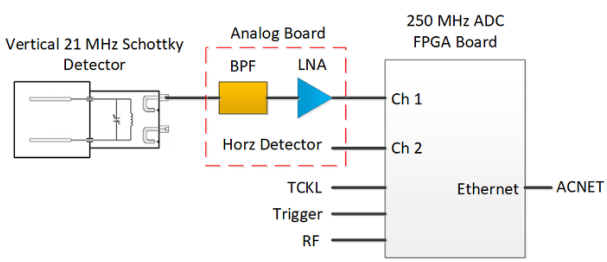


Figure 4: Mu2E tune meter system.

* This work was supported by the U.S. Department of Energy under contract No. DE-AC02-07CH11359.
† Scarpine@fnal.gov

Content from this work may be used under the terms of the CC-BY-4.0 licence (© 2023). Any distribution of this work must maintain attribution to the author(s), title of the work, publisher, and DOI

ISBN: 978-3-95450-236-3 ISSN: 2673-5350 doi:10.18429/JACoW-IBIC2023-WEP033

Content from this work may be used under the terms of the CC-BY-4.0 licence (© 2023). Any distribution of this work must maintain attribution to the author(s), title of the work, publisher, and DOI

The system requires low noise RF amplifiers with +80db gain. Crystal bandpass filters are used to suppress the revolution harmonics of the DR. A high-speed FPGA-based DAQ board to use for the digital signal processing.

21.4 MHz Schottky Pickups

Inductively resonated, balanced stripline pickups were used to observe tunes in the now decommissioned Tevatron accelerator [4]. These 21.4 MHz Schottky resonant pickups are now being reused for the Mu2E DR. The Schottky detectors are 1 m striplines consisting of two copper bars which can be moved by stepper motors to change the sensitivity. Its resonant frequency can also be tuned by using the variable capacitor Cv. Presently these detectors are tuned to resonate around 21.4 MHz with a loaded QL = 370 [5]. Two of the Schottky detectors, one vertical and one horizontal, were installed in the Mu2E DR. Figure 5 shows photos of the vertical Schottky pickup.

The DR revolution frequency is 590.018 kHz. The 21.4 MHz resonate frequency of these Schottky detectors then requires us to look for the DR tune lines between the 36th and 37th harmonics of the DR revolution frequency. Figure 6 shows the vertical and horizontal tunes lines between the 36th and 37th harmonics. This figure also shows the frequency responses of both vertical and horizontal Schottky detectors, tuned to optimized sensitivity to their respective tune lines, as well as the bandpass filter widths.

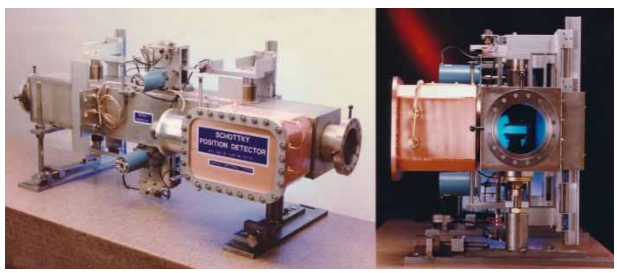


Figure 5: 21.4 MHz resonant Schottky pickups.

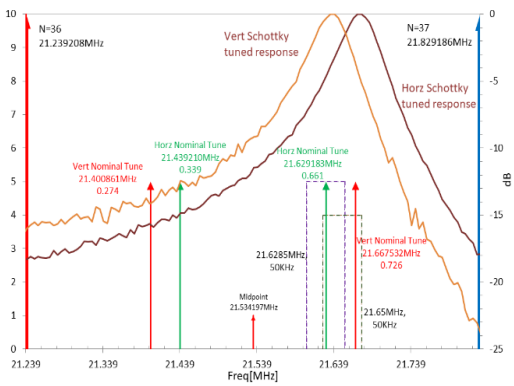


Figure 6: Schottky pickup response and tune spectrum at 21.4 MHz.

Digital Signal Processing

The Mu2E tune meter systems uses a high-speed FPGA VME board that was originally designed as part of a digital damper system for proton storage rings. This board consists of four 16-bit, 250MSPS ADCs, four 16-bit 250MSPS DACs and a Cyclone V FPGA. The present tune meter system utilizes two of the ADC channels for the vertical and horizontal Schottky signals. The FPGA logic digitally down converts the tunes at the 36th harmonic down to baseband. The down converted data is then either analyzed in the FPGA to generate FFT spectrums or else is offloaded to a local computer to further analysis. Figure 7 shows a block diagram of the FPGA logic for down conversion.

The signal processing analysis can time slice the down converted data to generate FFTs along the slow spill. The system can select the number of time slices and whether to average the time sliced FFT across many slow spills to help reduce noise fluctuations in the FFT spectrum.

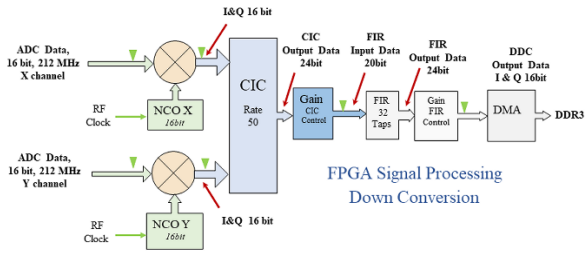


Figure 7: Block diagram of tune digital signal processing.

INITIAL RESULTS

The Mu2E tune meter system has been tested during initial commissioning of the Mu2E DR. Initial tune measurements were made with a spectrum analyzer in place of our FPGA board. This allowed for us to confirm the analog portion of the tune meter with a slower system. Figure 8 show the vertical tune line, along with the bandpass filter width, for ~5e10 protons coasting in the DR.

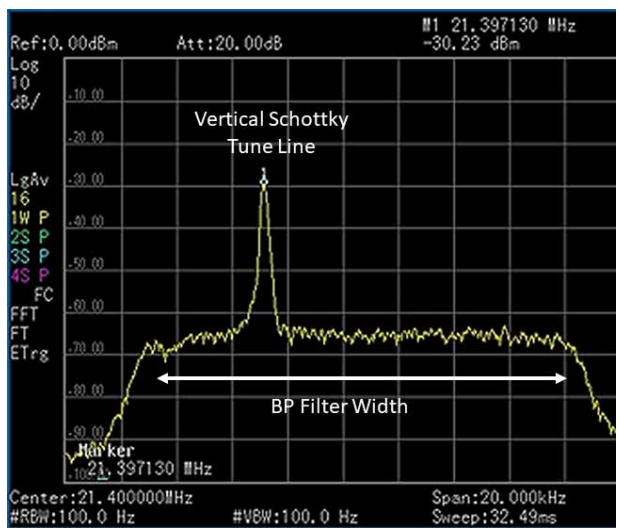


Figure 8: Coasting DR tune taken with spectrum analyzer.

After initial measurements, the spectrum analyzer was replaced with our digital FPGA board. We tested the board operation with millisecond time slices. Figure 9 shows a

ISBN: 978-3-95450-236-3 ISSN: 2673-5350 doi:10.18429/JACoW-IBIC2023-WEP033

preliminary measure of the tune spectrum at injection of ~1e11 protons into the DR. This shows the potential of measuring the tune along the slow spill at a few millisecond resolution.

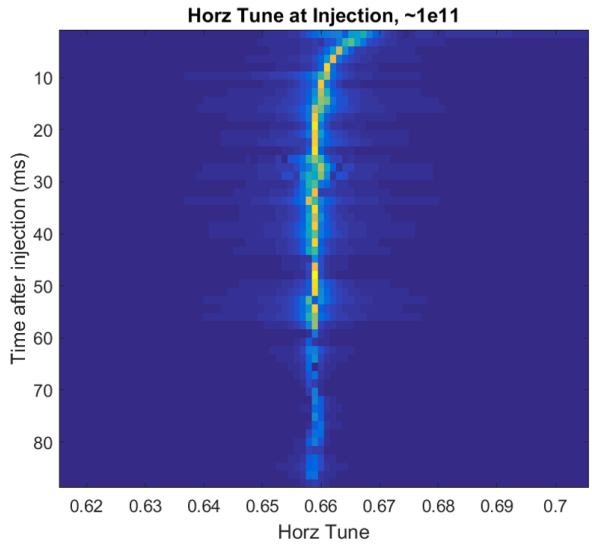


Figure 9: Preliminary DR tune measurements with Mu2E tune meter at beam injection.

CONCLUSION

A Schottky digital tune monitor system, based on 21.4 MHz resonant stripline pickups, has been design, installed and tested in the MU2E DR. Initial tune measurements show that beam tunes can be measured during the proposed Mu2E slow spill time at the time resolution of a few milliseconds. Future beam measurements will focus on measuring these tunes during a slow spill over the full dynamic intensity range in the DR.

ACKNOWLEDGEMENTS

We would like to acknowledge the Fermilab Mu2E accelerator team, Jerry Annala, Dean Still, George Deinlein, Dave Vander Meulen, Brian Drendel and Steve Werkema for their knowledge and beam studies support.

REFERENCES

[1] R. Bernstein, The Mu2e Experiment, *Frontiers in Physics,* vol. 7, 2019 7 doi:10.3389/fphy.2019.00001

[2] A. Ibrahim *et al.*, “Preliminary Design of Mu2E Spill Regulation System (SRS)”, in *Proc. IBIC’19*, Malmo, Sweden, Sep. 2019, paper MOPP033

[3] V. Nagaslaev *et al*. The Mu2e Experiment, *Phys. Rev. Accelerators and Beams*, vol. 22, p. 043501, 2019.

[4] D. Martin *et al.*, “A Schottky Receiver for Non-Perturbative Tune Monitoring in the Tevatron”, in *Proc. 13th Particle Accelerator Conf. (PAC'89),* Chicago, IL, USA, Mar. 1989, pp. 1483-1486.

[5] C.Y. Tan, P. Lebrun, and X. L. Zhang, “Tune Measurement Methods of the Tevatron”, in *Proc. 20th Particle Accelerator Conf. (PAC'03),* Portland, OR, USA, May 2003, paper WPPG052, pp. xx-xx.

Content from this work may be used under the terms of the CC-BY-4.0 licence (© 2023). Any distribution of this work must maintain attribution to the author(s), title of the work, publisher, and DOI

ISBN: 978-3-95450-236-3 ISSN: 2673-5350 doi:10.18429/JACoW-IBIC2023-WEP034

EFFECT OF LONGITUDINAL BEAM-COUPLING IMPEDANCE ON THE SCHOTTKY SPECTRUM OF BUNCHED BEAMS

C. Lannoy[1,*], D. Alves, K. Lasocha, N. Mounet, CERN, Geneva, Switzerland
T. Pieloni, EPFL, Lausanne, Switzerland
[1]also at EPFL, Lausanne, Switzerland

Abstract

Schottky spectra can be strongly affected by collective effects, in particular those arising from beam-coupling impedance when a large number of bunch charges are involved. In such conditions, the direct interpretation of the measured spectra becomes difficult, which prevents the extraction of beam and machine parameters in the same way as is usually done for lower bunch charges. Since no theory is yet directly applicable to predict the impact of impedance on such spectra, we use here time-domain, macro-particle simulations and apply a semi-analytical method to compute the Schottky spectrum for various machine and beam conditions, such as the ones found at the Large Hadron Collider. A simple longitudinal resonator-like impedance model is introduced in the simulations and its effect studied in different configurations, allowing preliminary interpretations of the impact of longitudinal impedance on Schottky spectra.

INTRODUCTION

Theoretical reconstructions of Schottky spectra, such as the matrix formalism proposed in [1, 2], or the Monte Carlo approach used in [3, 4], are based on the assumption that the synchrotron frequency distribution is known. Under certain conditions, one can derive an analytical relation between the amplitude of the synchrotron oscillation and its frequency (see below) allowing these methods to reconstruct the Schottky spectrum from the synchrotron amplitude distribution. However, this relation has to be modified when external forces, such as the one coming from beam-coupling impedance, affect the longitudinal dynamics.

This study will briefly present the available theory relating the amplitude of the synchrotron oscillation to its frequency, as well as a commonly adopted approximation. The second section will deal with the additional external forces coming from impedance, extending the theory presented in [5] to the case of a non-linear radio frequency (RF) bucket. Finally, we will apply the developed theory to the particular case of a longitudinal broad-band resonator, and will benchmark it against macro-particle simulations performed with PyHEADTAIL [4, 6, 7], in the case of a proton bunch in the Large Hadron Collider (LHC).

Synchrotron Oscillation

For an impedance-free environment, the equation of motion for the RF phase ϕ [1] of a given particle is [8, Eq. (9.51)]:

$$\frac{d^2\phi}{dt^2} + \Omega_0^2 \sin\phi = 0, \tag{1}$$

assuming that the synchronous phase ϕ_s is such that $\sin\phi_s$ is small enough to be neglected (i.e. no acceleration or energy loss compensation). The nominal synchrotron frequency[2] reads

$$\Omega_0^2 = \omega_0^2 \frac{-\eta h e \widehat{V}}{2\pi E_0 \beta^2} \cos\phi_s, \tag{2}$$

where e is the elementary charge, and where the relevant machine parameters are: the revolution frequency ω_0, the slippage factor η, the amplitude of the RF voltage $\widehat{V}$, the rf harmonic number h, the relativistic factor β, and the reference energy E_0. Note that by convention η is positive above transition, such that η and $\cos\phi_s$ always have opposite sign.

Equation (1) is similar to the non-linear pendulum equation, hence the synchrotron frequency Ω_s of the particle can be written [9]

$$\Omega_s(\widehat{\phi}) = \frac{\pi}{2\mathcal{K}\left[\sin\left(\frac{\widehat{\phi}}{2}\right)\right]}\Omega_0, \tag{3}$$

where $\widehat{\phi}$ is the RF phase amplitude of the synchrotron oscillation and $\mathcal{K}$ is the complete elliptic integral of the first kind [10, Eq. (8.112.1)].

Equation (1) can also be approximated by replacing the sine function with its Maclaurin series expansion up to the third order, which yields

$$\frac{d^2\phi}{dt^2} + \Omega_0^2 \left(\phi - \frac{\phi^3}{6}\right) + \mathcal{O}(\phi^5) = 0. \tag{4}$$

This last equation has been studied in [9], and an approximation of the oscillation frequency is given by

$$\Omega_s(\widehat{\phi}) = \Omega_0 \left(1 - \frac{\widehat{\phi}^2}{16}\right). \tag{5}$$

Figure 1 illustrates how the exact solution from Eq. (3) compares with the approximation from Eq. (5). The amplitude distribution corresponding to a Gaussian bunch profile of standard deviation $\sigma = 31$ ns is also shown in order to compare the most populated region with the zone where the

[1] Above transition ϕ has to be taken as the difference between the RF phase of the particle and π.
[2] By nominal synchrotron frequency, we mean the limit of the synchrotron frequency for synchrotron amplitudes approaching zero.

* christophe.lannoy@cern.ch

Content from this work may be used under the terms of the CC-BY-4.0 licence (© 2023). Any distribution of this work must maintain attribution to the author(s), title of the work, publisher, and DOI

ISBN: 978-3-95450-236-3 ISSN: 2673-5350 doi:10.18429/JACoW-IBIC2023-WEP034

approximation is valid. As can be seen, the approximation holds for an amplitude $\widehat{\phi} \lesssim 0.8\pi$, which is the region where the vast majority of the particles are. Noting that $\phi = h\omega_0\tau$,

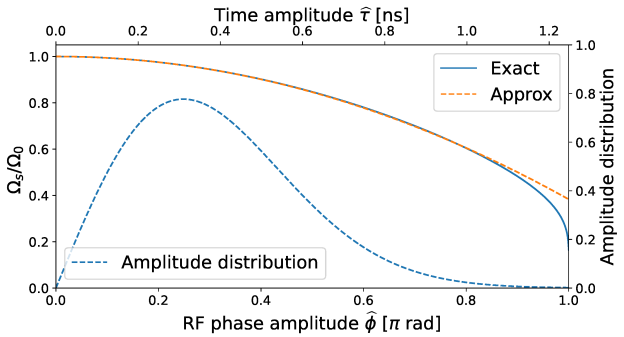


Figure 1: Comparison between the exact and approximate expressions of the synchrotron frequency as a function of the oscillation amplitude. The distribution of amplitudes for a Gaussian bunch is also shown.

with τ the arrival time difference between a given particle and the synchronous particle, we can also express the amplitude of the synchrotron oscillation in terms of the time amplitude defined by

$$\widehat{\tau} \equiv \widehat{\phi}/h\omega_0. \tag{6}$$

THEORETICAL DESCRIPTION

In this section, we investigate the influence of impedance on the longitudinal dynamics of a particle and, more specifically, how it can affect its oscillation frequency. A given force F_i acting longitudinally on the particle will impact the phase dynamics with

$$F_i = \frac{dp}{dt} = \frac{d(p_0+\delta p)}{dt} = \frac{d(\delta p)}{dt} = \frac{p_0}{\eta}\ddot{\tau} = \frac{p_0}{\eta h\omega_0}\ddot{\phi}, \tag{7}$$

where we used the fact that p_0 is constant, the definition of the slippage factor, and Eq. (6). The equation of motion with an additional external force is given by combining Eqs. (1) and (7), which yields

$$\ddot{\phi} + \Omega_0^2 \sin\phi = \frac{\eta h\omega_0}{p_0} F_i(t). \tag{8}$$

Impedance Force

In this study, we will focus on the force arising from the longitudinal beam-coupling impedance, which is given by [11, Eq. (4.18)]

$$\begin{aligned} F_{Imp}(t) &= e\left[\vec{E} + \vec{\beta}c \times \vec{B}\right]_{\parallel}\left(t, z = \beta c\tau(t)\right) \\ &= -\frac{Ne^2}{2\pi C}\int_{-\infty}^{\infty} Z_{\parallel}(\omega)\widehat{\Lambda}(\omega)e^{j\frac{\omega z}{\beta c}}d\omega, \end{aligned} \tag{9}$$

where C stands for the circumference of the accelerator, N for the number of particles in the bunch, $Z_{\parallel}(\omega)$ for the longitudinal impedance, and $\widehat{\Lambda}(\omega)$ for the beam spectrum normalised by the bunch intensity. The force has to be taken at the current position of the particle, i.e. at a distance $z = \beta c\tau$ behind the synchronous particle. Note that the bunch spectrum $\widehat{\lambda}(\omega)$ of [11, Eq. (4.18)], has been replaced by the beam spectrum $\widehat{\Lambda}(\omega)$ in order to take into account the possible multi-turn wake (this approach is equivalent to adding the forces coming from different turns).

The beam spectrum is the Fourier transform of the beam profile. For a single bunch in a circular accelerator, the latter can be expressed as the convolution of the bunch profile $\lambda(t)$ with a Dirac comb of the revolution period T_0. Using the convolution theorem, the beam spectrum can be written

$$\begin{aligned} \widehat{\Lambda}(\omega) &= \mathscr{F}\{\lambda(t) * \text{Ш}_{T_0}(t)\} \\ &= \mathscr{F}\{\lambda(t)\}\,\mathscr{F}\{\text{Ш}_{T_0}(t)\} \\ &= \widehat{\lambda}(\omega)\omega_0\text{Ш}_{\omega_0}(\omega), \end{aligned} \tag{10}$$

where $*$ stands for the convolution operation and where the Dirac comb of period T_0 is defined as follows

$$\text{Ш}_{T_0}(t) = \sum_{p=-\infty}^{\infty}\delta(t - pT_0).$$

Substituting Eq. (10) in Eq. (9) , we have

$$\begin{aligned} F_{Imp}(t) &= \frac{-Ie}{C}\sum_{p=-\infty}^{\infty}\int_{-\infty}^{\infty} Z_{\parallel}(\omega)\widehat{\lambda}(\omega)e^{j\frac{\omega z}{\beta c}}\delta(\omega - p\omega_0)d\omega \\ &= \frac{-Ie}{C}\sum_{p=-\infty}^{\infty} Z_{\parallel}(p)\widehat{\lambda}(p)e^{jp\omega_0\tau(t)}, \end{aligned} \tag{11}$$

where we used the compact notation $Z_{\parallel}(p) \equiv Z_{\parallel}(p\omega_0)$, $\widehat{\lambda}(p) \equiv \widehat{\lambda}(p\omega_0)$, and the average current $I \equiv Ne\frac{\omega_0}{2\pi}$.

General Equation of Motion

Combining Eqs. (2), (6), (8), and (11) yields

$$\ddot{\phi} + \Omega_0^2 \sin\phi = \Omega_0^2\frac{I}{\widehat{V}\cos\phi_s}\sum_{p=-\infty}^{\infty} Z_{\parallel}(p)\widehat{\lambda}(p)e^{j\frac{p}{h}\phi}. \tag{12}$$

By expanding the sine and exponential functions into their Maclaurin series

$$\sin\phi = \sum_{n=0}^{\infty}\frac{(-1)^n}{(2n+1)!}\phi^{2n+1}, \quad e^{j\frac{p}{h}\phi} = \sum_{n=0}^{\infty}\frac{1}{n!}\left(\frac{jp}{h}\right)^n\phi^n,$$

Eq. (12) can be written in the compact form

$$\ddot{\phi} + \Omega_0^2\sum_{n=0}^{\infty} S_n\phi^n = 0, \tag{13}$$

with the coefficients S_n defined by

$$S_n = \begin{cases} -Z_n & : n \text{ even}, \\ \frac{j^{n-1}}{n!} - Z_n & : n \text{ odd}, \end{cases} \tag{14}$$

and

$$\begin{aligned} Z_n &= \frac{I}{\widehat{V}\cos\phi_s}\sum_{p=-\infty}^{\infty} Z_{\parallel}(p)\widehat{\lambda}(p)\frac{1}{n!}\left(\frac{jp}{h}\right)^n \\ &= \frac{Ij^n}{\widehat{V}\cos\phi_s\, n!h^n}\sum_{p=-\infty}^{\infty}\widehat{\lambda}(p)p^n \times \begin{cases} Re[Z_{\parallel}(p)] & : n \text{ even}, \\ j\,Im[Z_{\parallel}(p)] & : n \text{ odd}. \end{cases} \end{aligned}$$

Content from this work may be used under the terms of the CC-BY-4.0 licence (© 2023). Any distribution of this work must maintain attribution to the author(s), title of the work, publisher, and DOI

ISBN: 978-3-95450-236-3 ISSN: 2673-5350 doi:10.18429/JACoW-IBIC2023-WEP034

In the last equality, we used the fact that $\widehat{\lambda}(p)$, $Re\left[Z_\parallel(p)\right]$, and $Im\left[Z_\parallel(p)\right]$ are respectively even, even, and odd functions.

The idea behind the expansion performed above is that, for small oscillation amplitudes, only the first order terms can be kept. The shift of the nominal synchrotron frequency is given by S_1 while the non-linear terms will be responsible for an amplitude dependent synchrotron frequency shift.

Broad-Band Resonator

We will now apply Eq. (13) to the particular case of a broad-band resonator described by the following function

$$Z_\parallel^{BB}(\omega) = \frac{R_\parallel}{1 - jQ\left(\frac{\omega_r}{\omega} - \frac{\omega}{\omega_r}\right)},$$

where $R_\parallel$ is the shunt impedance, ω_r the angular cut-off frequency, and Q the quality factor. The values we will use for these parameters are shown in Table 1 and correspond to a first estimate of the broad-band part of the LHC impedance [12, p. 71].

The even terms in Eq. (13) are responsible for the synchronous phase shift and we assume that, in the particular case of a broad-band resonator, their contribution can be neglected. Expanding Eq. (13) up to the third order gives

$$\ddot{\phi} + \Omega_0^2\,(S_1\phi + S_3\phi^3) + \mathcal{O}(\phi^5) = 0, \qquad (15)$$

which is similar to Eq. (4) where the factors 1 and $-\frac{1}{6}$ have been generalised to the arbitrary coefficients S_1 and S_3. In this case, the approximate synchrotron frequency is given by

$$\Omega_s(\widehat{\phi}) = \Omega_0\sqrt{S_1}\left(1 + \frac{3S_3}{8S_1}\widehat{\phi}^2\right), \qquad (16)$$

as can be seen by substituting the function $\phi(t) = \sqrt{A}\Phi(t)$ (with A an arbitrary number) in Eq. (4) and identifying the coefficients.

SIMULATION

The simulation aims at reproducing the typical conditions of an LHC proton fill at injection. The method used to reconstruct the Schottky spectrum from the macro-particle simulation is presented in [4] and the simulation parameters are summarised in Table 1.

Table 1: PyHEADTAIL Simulation Parameters

Intensity	1.5×10^{11} protons per bunch
Energy per proton	450 GeV
Slippage factor	3.436×10^{-4}
RF harmonic	35640
RF voltage	4 MV
LHC circumference	26.659 km
Bunch length (RMS)	$\sigma = 0.31$ ns
Broad-band resonator	
Shunt impedance	$R_\parallel = 31.1\,\mathrm{k}\Omega$
Cut-off frequency	$\omega_r = 2\pi \times 5$ GHz
Quality factor	$Q = 1$

Figure 2 presents an overall view (upper plot) of the simulated longitudinal Schottky spectrum together with a detailed view of two regions (lower plots). It can be observed that the broad-band resonator induces a shift of the nominal synchrotron frequency (all the satellites moving toward the central one). This shift is due to the term S_1 and the new nominal synchrotron frequency is $\Omega_0\sqrt{S_1}$. The broad-band resonator will reduce the nominal synchrotron frequency for

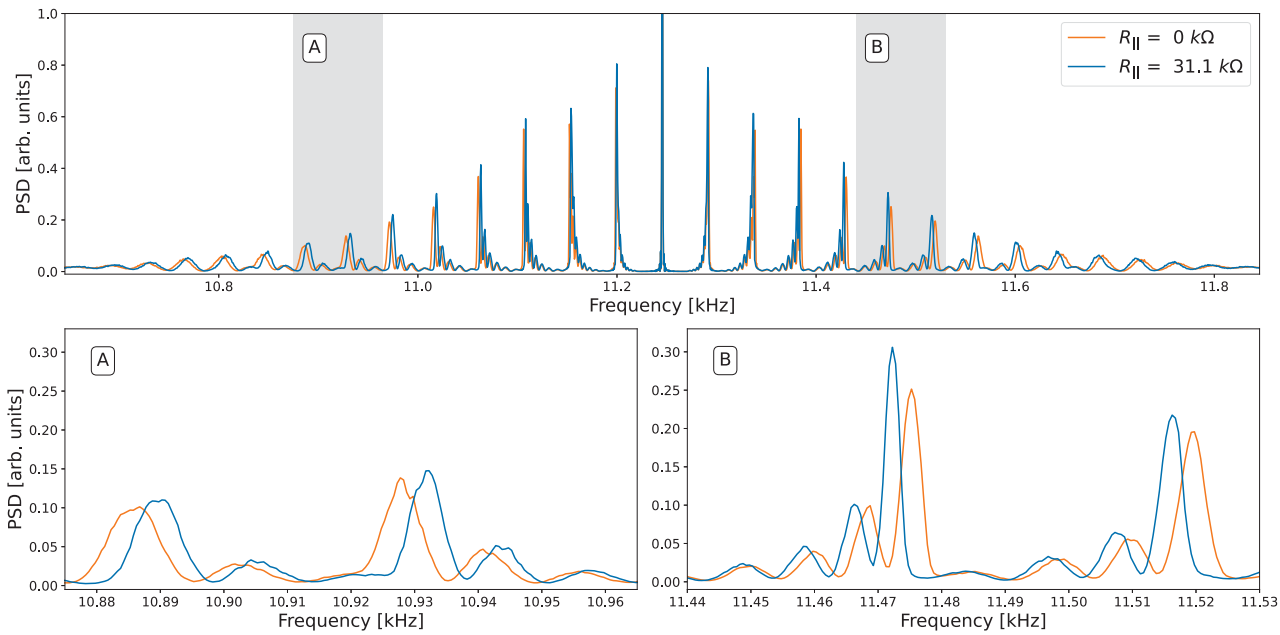


Figure 2: Simulated longitudinal Schottky spectra with (blue) and without (orange) an LHC-like broad-band resonator.

Content from this work may be used under the terms of the CC-BY-4.0 licence (© 2023). Any distribution of this work must maintain attribution to the author(s), title of the work, publisher, and DOI

ISBN: 978-3-95450-236-3 ISSN: 2673-5350 doi:10.18429/JACoW-IBIC2023-WEP034

a machine operating above transition, as can be seen from Eq. (14) (the opposite happens below transition). One can also observe in Fig. 2 an amplitude-dependent synchrotron frequency shift, as the alterations in the satellite shapes can not be explained by a simple linear transformation involving shifting and scaling of the original form. This effect is due to the higher order terms $S_{2n+1},\ n \geq 1$ in Eq. (13).

Figure 3 compares the macro-particle simulation with the theoretical matrix formalism of Ref. [1], where the relation between synchrotron amplitudes and frequencies has been adapted, replacing Eq. (5) by Eq. (16) to take into account the effect of impedance. The dashed red line corresponds to the matrix formalism where only the first order term of the impedance contribution has been kept (i.e. $Z_1 \neq 0$ and $Z_3 = 0$, which corresponds to $S_1 = 1 - Z_1$ and $S_3 = -1/6$ in Eq. (16)). As can be seen, the nominal synchrotron frequency shift is well reproduced by the theory, while the shift for non-zero amplitude particles, requires higher order terms (Z_n).

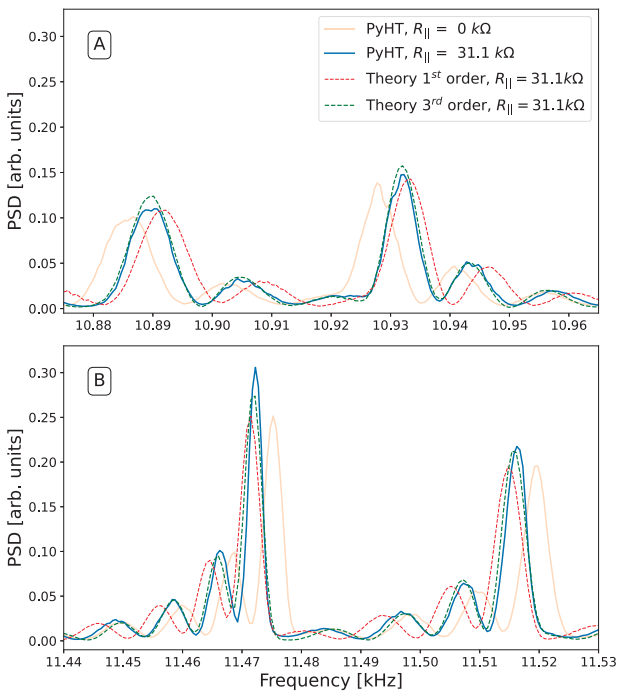


Figure 3: Comparison of the macro-particle simulation (blue) against the adapted matrix formalism, with Eq. (16) including impedance terms Z_n up to the first (red) and third (green) order. The A-B labels correspond to the shaded regions of Fig. 2.

The dashed green line also includes the third order term of the impedance contribution (i.e. $Z_1 \neq 0$ and $Z_3 \neq 0$, which corresponds to $S_1 = 1 - Z_1$ and $S_3 = -1/6 - Z_3$). With the third order impedance term, the theory is in good agreement with the simulation.

One can also probe the validity of Eq. (16) by directly extracting the relation $\Omega_s(\widehat{\phi})$ from the macro-particle simulation. This was done in Fig. 4 where each black dot corresponds to the synchrotron amplitude and frequency of a given macro-particle. As before, one can observe that the nominal synchrotron frequency shift is well reproduced by the first order term Z_1, while the shift for larger amplitude particles is correct with the third order theory, up to a certain amplitude $\widehat{\phi} \sim 1.25$ rad. In order to extend the region where Eq. (16) is valid, one would need to take into account the fifth order term S_5, in the equation of motion. However, this is not crucial since the majority of the particles are well described, as can be seen from the amplitude distribution.

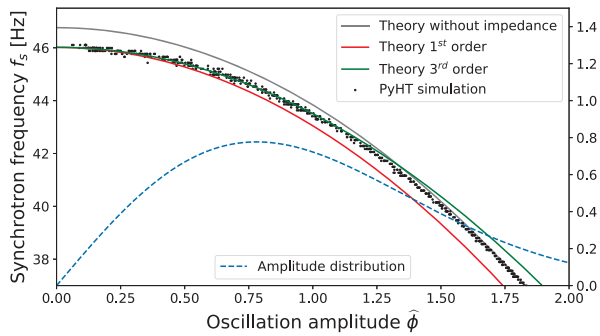


Figure 4: Comparison of Eq. (16) including impedance terms Z_n up to the first (red) and third (green) order, against macro-particle simulation (black dots).

CONCLUSION

The aim of this work was to explore the effects of longitudinal impedance on the Schottky spectrum. We first derived a longitudinal equation of motion including the forces coming from any impedance $Z(\omega)$. The particular case of a broad-band resonator was then studied in more detail and the relation between synchrotron amplitude and frequency was generalised to this situation, allowing existing theoretical reconstruction methods of Schottky spectra to include impedance effects. The developed theory was shown to be in good agreement with macro-particle simulations, by correctly reproducing the amplitude-dependent synchrotron tune shift.

REFERENCES

[1] K. Lasocha and D. Alves, "Estimation of longitudinal bunch characteristics in the LHC using Schottky-based diagnostics," *Phys. Rev. Accel. Beams*, vol. 23, no. 6, p. 062 803, 2020. doi:10.1103/PhysRevAccelBeams.23.062803

[2] K. Lasocha and D. Alves, "Estimation of transverse bunch characteristics in the lhc using schottky-based diagnostics," *Phys. Rev. Accel. Beams*, vol. 25, no. 6, p. 062 801, 2022. doi:10.1103/PhysRevAccelBeams.25.062801

Content from this work may be used under the terms of the CC-BY-4.0 licence (© 2023). Any distribution of this work must maintain attribution to the author(s), title of the work, publisher, and DOI

ISBN: 978-3-95450-236-3 ISSN: 2673-5350 doi:10.18429/JACoW-IBIC2023-WEP034

[3] M. Betz, O. R. Jones, T. Lefevre, and M. Wendt, "Bunched-beam Schottky monitoring in the LHC," *Nucl. Instrum. Methods Phys. Res., A*, vol. 874, pp. 113–126, 2017. doi:10.1016/j.nima.2017.08.045

[4] C. Lannoy, D. Alves, N. Mounet, and T. Pieloni, "LHC Schottky Spectrum from Macro-Particle Simulations," in *Proc. IBIC'22*, Kraków, Poland, 2022, pp. 308–312. doi:10.18429/JACoW-IBIC2022-TUP34

[5] J. L. Laclare, "Bunched beam coherent instabilities," 1987. doi:10.5170/CERN-1987-003-V-1.264

[6] PyHEADTAIL code repository. https://github.com/PyCOMPLETE

[7] K. S. B. Li *et al.*, "Code Development for Collective Effects," in *Proc. HB'16*, Malmö, Sweden, Jul. 2016, pp. 362–367. doi:10.18429/JACoW-HB2016-WEAM3X01

[8] H. Wiedemann, *Particle accelerator physics*, 4th ed. Springer, 2015. doi:10.1007/978-3-319-18317-6

[9] Z. Szabó, "On the analytical methods approximating the time period of the nonlinear physical pendulum," *Periodica Polytechnica Mechanical Engineering*, vol. 48, no. 1, pp. 73–82, 2004. https://pp.bme.hu/me/article/view/1358

[10] I. Gradshteyn and I. Ryzhik, *Table of Integrals, Series, and Products*. 2007. http://fisica.ciens.ucv.ve/~svincenz/TISPISGIMR.pdf

[11] G. Stupakov, R. Lindberg, and B. Podobedov, "Wakefields and collective beam instabilities," in 2023. https://www.slac.stanford.edu/~stupakov/uspas23/2023-01-20/2022-12-07-LECTURES.pdf

[12] N. Mounet, "The LHC Transverse Coupled-Bunch Instability," Presented 2012, Ph.D. dissertation, 2012. doi:10.5075/epfl-thesis-5305

Content from this work may be used under the terms of the CC-BY-4.0 licence (© 2023). Any distribution of this work must maintain attribution to the author(s), title of the work, publisher, and DOI

ISBN: 978-3-95450-236-3 ISSN: 2673-5350 doi:10.18429/JACoW-IBIC2023-WEP035

STATISTICAL PROPERTIES OF SCHOTTKY SPECTRA

C. Lannoy[1,*], D. Alves, K. Lasocha, N. Mounet, CERN, Geneva, Switzerland
T. Pieloni, EPFL, Lausanne, Switzerland
[1]also at EPFL, Lausanne, Switzerland

Abstract

Schottky signals are used for non-invasive beam diagnostics as they contain information on various beam and machine parameters. The instantaneous Schottky signal is, however, only a single realisation of a random process, implicitly depending on the discrete distribution of synchrotron and betatron amplitudes and phases among the particles. To estimate the expected value of the Schottky power spectrum, and reveal the inner structure of the Bessel satellites described by the theory, the averaging of instantaneous Schottky spectra is required. This study describes this procedure quantitatively by analysing the statistical properties of the Schottky signals, including the expected value and variance of Schottky power spectra. Furthermore, we investigate how these quantities evolve with the number of particles in the bunch, the observed harmonic of the revolution frequency, the distribution of synchrotron oscillation amplitudes, and the bunch profile. The theoretical findings are compared against macro-particle simulations as well as Monte Carlo computations.

INTRODUCTION

The Large Hadron Collider (LHC) Schottky system provides a single spectrum every second, based on the signal acquired over approximately the last 16 000 revolutions. Notably, consecutive spectra exhibit significant dissimilarity, requiring the aggregation of numerous spectra to attain the mean value. This study aims at exploring the inherent variability of consecutive instantaneous Schottky spectra and at characterising their statistical properties.

The LHC Schottky monitors measure the power spectral density (PSD) of a signal (intensity for the longitudinal spectrum, or dipole moment for the transverse one). For a random process $X(t)$, the PSD is defined in general by [1, Eq. (10.9)]

$$P(\omega) = \lim_{T\to\infty} \frac{1}{2T}|X_T(\omega)|^2, \tag{1}$$

where $X_T(\omega)$ is the Fourier transform of the truncated process

$$X_T(\omega) = \int_{-T}^{T} X(t)e^{-j\omega t}dt.$$

In these proceeding we will first investigate the statistical properties of the longitudinal spectrum, before elaborating on the transverse one. Then we will compare our results with simulations and the available measurements, and finally present our conclusions.

* christophe.lannoy@cern.ch

LONGITUDINAL SCHOTTKY SPECTRA

As shown in the literature [2–5], the intensity signal $i(t)$ of a bunch consisting of N particles can be written

$$i(t) = qf_0 \sum_{i=1}^{N} \sum_{n,p=-\infty}^{\infty} J_p(n\omega_0\widehat{\tau_i})\, e^{j(n\omega_0 t + p\Omega_{s_i} t + p\varphi_{s_i})}, \tag{2}$$

where J_p is the Bessel function of the first kind of order p, q the charge of the particle, $f_0 = \omega_0/2\pi$ the revolution frequency, and $\widehat{\tau_i}$, Ω_{s_i}, and φ_{s_i}, respectively, the synchrotron time amplitude[1], frequency, and initial phase of particle i. The summations over n and p are related to the revolution frequency harmonic and the Bessel satellite number p.

Equation (2) is a deterministic signal entirely defined by a set of N amplitudes $\widehat{\tau}_i$ and N phases φ_{s_i} (the synchrotron frequencies Ω_{s_i} can be determined from the synchrotron amplitudes as in [6, 7]). To examine the statistical properties of the Schottky spectra, we define the corresponding random process $I(t)$ of the intensity signal $i(t)$

$$I(t) = qf_0 \sum_{i,n,p} J_p(n\omega_0\widehat{T}_i)\, e^{j(n\omega_0 t + p\Omega_{s_i} t + p\Phi_{s_i})}, \tag{3}$$

where the summation bounds have been omitted for readability. The random variables $\widehat{T}_i$ and Φ_{s_i} describe respectively, the synchrotron time amplitude and initial phase for particle i. Equation (2) can be seen as one realisation of the random process defined by Eq. (3).

In the following, Φ_{s_i} is assumed to follow a uniform distribution on $[0, 2\pi]$, while $\widehat{T}_i$ is described by various probability density functions $g(\widehat{\tau})$, such as the Rice distribution as in [7]

$$g(\widehat{\tau}) = \frac{\widehat{\tau}}{\sigma^2} e^{-\frac{\widehat{\tau}^2}{2\sigma^2} - \frac{b^2}{2}} I_0(\widehat{\tau}b/\sigma),$$

or a distribution corresponding to a Gaussian bunch profile

$$g(\widehat{\tau}) = \frac{\widehat{\tau}}{\sigma^2} e^{-\frac{\widehat{\tau}^2}{2\sigma^2}},$$

in order to assess the impact of different bunch profiles.

Applying the PSD definition from Eq. (1) to Eq. (3) yields [8]

$$P(\omega) = q^2 f_0^2 \sum_{\substack{i,n,p \\ i',p'}} J_p(n\omega_0\widehat{T}_i) J_{p'}(n\omega_0\widehat{T_{i'}}) e^{j(p\Phi_{s_i} - p'\Phi_{s_{i'}})} \times 2\pi\delta\left(n\omega_0 + p\Omega_{s_i} - \omega\right)\delta_K\left(p\Omega_{s_i} - p'\Omega_{s_{i'}}\right), \tag{4}$$

[1] By time amplitude, we mean the maximum time arrival difference between a given particle and the synchronous particle

Content from this work may be used under the terms of the CC-BY-4.0 licence (© 2023). Any distribution of this work must maintain attribution to the author(s), title of the work, publisher, and DOI

ISBN: 978-3-95450-236-3 ISSN: 2673-5350 doi:10.18429/JACoW-IBIC2023-WEP035

Content from this work may be used under the terms of the CC-BY-4.0 licence (© 2023). Any distribution of this work must maintain attribution to the author(s), title of the work, publisher, and DOI

where δ is the Dirac delta distribution and with

$$\delta_K(x) = \lim_{T\to\infty} \frac{\sin(xT)}{xT} = \begin{cases} 1, & \text{if } x = 0, \\ 0, & \text{otherwise.} \end{cases}$$

Central Satellite

The power (i.e. the integrated PSD) of the central satellite $p = 0$, at a given harmonic $n = n_h$ can be deduced from Eq. (4) and is given by

$$\begin{aligned} P_{(0)} &= q^2 f_0^2 \sum_{i=1}^{N}\sum_{i'=1}^{N} J_0(n_h\omega_0\widehat{T_i}) J_0(n_h\omega_0\widehat{T_{i'}}) \\ &= q^2 f_0^2 \left(\sum_{i=1}^{N} Z_i\right)^2, \end{aligned} \tag{5}$$

where we defined the random variables

$$Z_i = J_0(n_h\omega_0\widehat{T_i}), \qquad \forall i \in [1, N], \tag{6}$$

In the following we derive the expected power and variance of the central satellite.

Expected Power Using the linearity of the expectation and the fact that the expected value of a product is the product of the expected values for independent random variables, we have

$$\begin{aligned} \frac{E(P_{(0)})}{q^2 f_0^2} &= E\left(\sum_{i=1}^{N}\sum_{j=1}^{N} Z_i Z_j\right) \\ &= \sum_{i=1}^{N} E(Z_i^2) + \sum_{i=1}^{N}\sum_{\substack{j=1 \\ j\neq i}}^{N} E(Z_i)E(Z_j) \\ &= N\beta + N(N-1)\alpha^2, \end{aligned} \tag{7}$$

where we defined the notations

$$\alpha = E(Z_i), \qquad \beta = E(Z_i^2), \tag{8}$$

for the first and second moments of Z_i. These are independent of i since all the particles have the same synchrotron amplitude distribution. Note that if $\alpha \approx 0$, the dominant term of the expected value of the power for the central satellite, scales as N rather than N^2.

Variance The variance can be expressed as

$$Var\left(P_{(0)}\right) = E\left(P_{(0)}^2\right) - \left(E(P_{(0)})\right)^2, \tag{9}$$

where the second term is the square of the average power calculated in Eq. (7). From the multinomial theorem, the first term can be expanded using

$$E\left[\left(\sum_{i=1}^{N} Z_i\right)^4\right] = \sum_{\substack{k_1+k_2+\ldots+k_N=4 \\ k_1,k_2,\ldots,k_N\geq 0}} \frac{4!}{k_1!k_2!\ldots k_N!} E\left[\prod_{i=1}^{N} Z_i^{k_i}\right], \tag{10}$$

where the sum is taken over all combinations of non-negative integer indices k_1 through k_N.

Substituting Eqs. (7) and (10) in Eq. (9), we obtain the variance of the power for the central satellite [8]

$$\begin{aligned} \frac{Var\left(P_{(0)}\right)}{q^4 f_0^4} &= N\delta + (4N^2 - 4N)\gamma\alpha + (2N^2 - 3N)\beta^2 \\ &+ (4N^3 - 16N^2 + 12N)\beta\alpha^2 + (-4N^3 + 10N^2 - 6N)\alpha^4, \end{aligned} \tag{11}$$

where γ and δ represent the third and fourth moments of Z_i.

It is worth noting that Eq. (5) is formally identical to the squared distance of a one-dimensional random walk of N steps of variable length Z_i. By reducing Eq. (5) to the particular case of unit steps, we have $\alpha = \gamma = 0$, $\beta = \delta = 1$, and we find the same expression for the mean and variance as in the one-dimensional random walk of unit steps [9].

Non-Central Satellites

For non-central satellites (i.e. $p \neq 0$), we extend the notation introduced in Eq. (6) to different order p of the Bessel function

$$Z_{i,(p)} = J_p(n_h\omega_0\widehat{T_i}), \qquad \forall i \in [1, N].$$

Similarly, we also define the following moments of $Z_{i,(p)}$

$$\beta_{(p)} = E(Z_{i,(p)}^2), \qquad \delta_{(p)} = E(Z_{i,(p)}^4). \tag{12}$$

The power contained in a given satellite p, can be derived from Eq. (4) and is given by [8]

$$\begin{aligned} P_{(p)} &= q^2 f_0^2 \sum_{i,i'} J_p(n_h\omega_0\widehat{T_i}) J_p(n_h\omega_0\widehat{T_{i'}}) e^{jp(\Phi_{s_i} - \Phi_{s_{i'}})} \\ &= q^2 f_0^2 \left|\sum_i Z_{i,(p)} e^{jp\Phi_{s_i}}\right|^2. \end{aligned} \tag{13}$$

By assuming that $\widehat{T_i}$ and Φ_{s_i} are independent random variables, one can show that the expected value and variance[2] for non-central satellites are respectively given by [8]

$$\begin{aligned} E(P_{(p)}) &= q^2 f_0^2\, N\beta_{(p)}, \\ Var(P_{(p)}) &= q^4 f_0^4 \left(N\delta_{(p)} + (N^2 - 2N)\beta_{(p)}^2\right). \end{aligned}$$

Note that Eq. (13) is formally identical to the squared distance of a two-dimensional random walk of N steps of variable length $Z_{i,(p)}$ and directions $p\Phi_{s_i}$. By reducing Eq. (13) to the particular case of unit steps, we have $\beta_{(p)} = \delta_{(p)} = 1$, and we find the same expression for the mean and variance as in the two-dimensional random walk of unit steps [10].

Figure 1 illustrates the coefficient of variation (CV), defined for both central ($p = 0$) and non-central satellites as

$$CV_{(p)} = \frac{\sqrt{Var(P_{(p)})}}{E(P_{(p)})}.$$

As can be seen, for typical LHC conditions, CV is $\sqrt{2}$ for the central satellite and 1 for non-central satellites.

[2] The variance was derived under the assumption of a linear RF bucket.

ISBN: 978-3-95450-236-3 ISSN: 2673-5350 doi:10.18429/JACoW-IBIC2023-WEP035

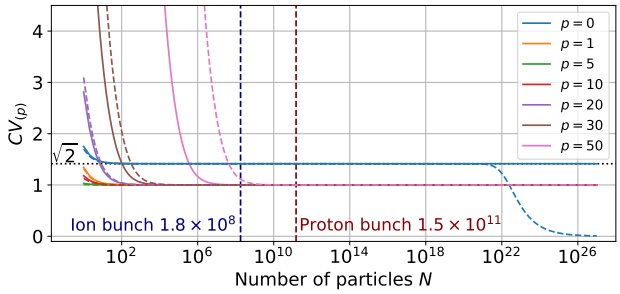


Figure 1: CV of the longitudinal satellites around the harmonic $n_h = 427\,725$ for a Rice amplitude distribution (dashed lines, $\sigma_r = 0.22$ ns and $b_r = 1.306$) and a Gaussian bunch profile (solid lines, $\sigma_g = 0.31$ ns).

TRANSVERSE SCHOTTKY SPECTRA

The transverse Schottky spectrum is given by the power spectral density of the dipole moment signal. By assuming that chromaticity $Q\xi$ is the only source of betatron frequency spread, the corresponding random process of the dipole moment can be written [2, 5]

$$D(t) = \sum_{(\pm)} \sum_{i=1}^{N} \sum_{n,p=-\infty}^{\infty} \frac{\widehat{X}_i q f_0}{2} J_p\left(\chi^{\pm}_{\widehat{T}_i, n\mp Q_I}\right) \times e^{j\left(t[(n\pm Q_F)\omega_0 + p\Omega_{s_i}] \pm \Phi_{\beta_i} + p\Phi_{s_i}\right)},$$

where the nominal tune is decomposed into its integer and fractional part $Q = Q_I + Q_F$ and with

$$\chi^{\pm}_{\widehat{T}_i, n} = \left(n \pm \frac{Q\xi}{\eta}\right)\omega_0 \widehat{T}_i.$$

In the above equations, η is the slippage factor, and $\widehat{X}_i$, Φ_{β_i} are respectively, the random variable of the amplitude, and the initial phase of the betatron motion of particle i. The summation over $\pm$ corresponds to the upper and lower transverse sidebands of the Schottky spectrum.

The PSD of the dipole moment can then be computed with Eq. (1), and the mean and variance of the power for a given satellite p around the Schottky harmonic $n = n_h$ can be derived, leading to the following expressions [8]:

$$E(P^{\pm}_{(p)}) = \frac{N q^2 f_0^2 \widehat{x_2}}{4} \beta^{\pm}_{(p)}, \tag{14}$$

$$Var\left(P^{\pm}_{(p)}\right) = \frac{q^4 f_0^4}{16}\left(N\widehat{x_4}\delta^{\pm}_{(p)} + (N^2 - 2N)\widehat{x_2}^2 (\beta^{\pm}_{(p)})^2\right),$$

with $\widehat{x_2}$ and $\widehat{x_4}$, the second and fourth moments of $\widehat{X}_i$, and where we extended the notations introduced previously with

$$\beta^{\pm}_{(p)} = E\left[J_p^2\left(\chi^{\pm}_{\widehat{T}_i, n_h\mp Q_I}\right)\right], \quad \delta(p)^{\pm} = E\left[J_p^4\left(\chi^{\pm}_{\widehat{T}_i, n_h\mp Q_I}\right)\right].$$

In contrast to the longitudinal spectrum, these expressions are also valid for the central transverse satellites due to the additional betatron phase appearing in the dipole moment. The CVs behave similarly to those of the longitudinal satellites, approaching 1 as N becomes sufficiently large (including the central satellites).

Figure 2 illustrates how the power of different Bessel satellites, as given by Eq. (14), are impacted by the harmonic number and the chromaticity on each sideband. It can be observed that as the harmonic number increases, the power of lower order satellites decreases, while the opposite occurs for higher order satellites. The effect of chromaticity can also be observed, resulting in a higher and narrower upper band compared to the lower band.

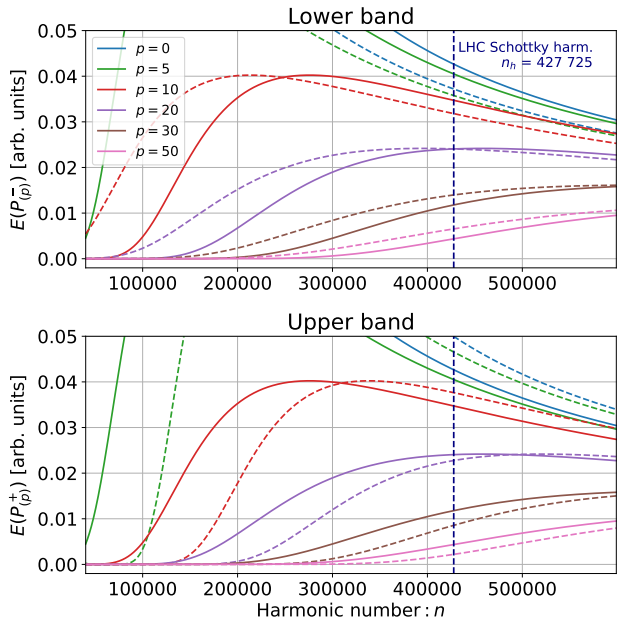


Figure 2: Harmonic scan of the expected powers of the transverse Bessel satellites for a Gaussian bunch profile ($\sigma_g = 0.31$ ns). The solid lines correspond to a zero chromaticity $Q\xi = 0$ while the dashed lines correspond to $Q\xi = 20$.

SIMULATIONS AND MEASUREMENTS

The theoretical equations derived in this study are compared against macro-particle and Monte-Carlo simulations of a realistic LHC ion fill in Fig. 3. The macro-particle simulations has been performed using PyHEADTAIL [11, 12] and the method used to retrieve the Schottky spectra from the tracking simulations is presented in [13]. The procedure of the Monte-Carlo simulation is described in [13, 14]. Both simulation techniques show a good agreement with the theoretical predictions and a clear convergence to a CV of $\sqrt{2}$ and 1 can be observed.

It should be noted that the previously developed theory is studying the mean and variance over different random draws of the bunches (phases and amplitudes of synchrotron and betatron motions), while in the real machine, there is a unique instance of the bunch. However, due to various non-linearities present in reality, the relative initial phases of synchrotron and betatron motions are drifting with time.

Content from this work may be used under the terms of the CC-BY-4.0 licence (© 2023). Any distribution of this work must maintain attribution to the author(s), title of the work, publisher, and DOI

ISBN: 978-3-95450-236-3 ISSN: 2673-5350 doi:10.18429/JACoW-IBIC2023-WEP035

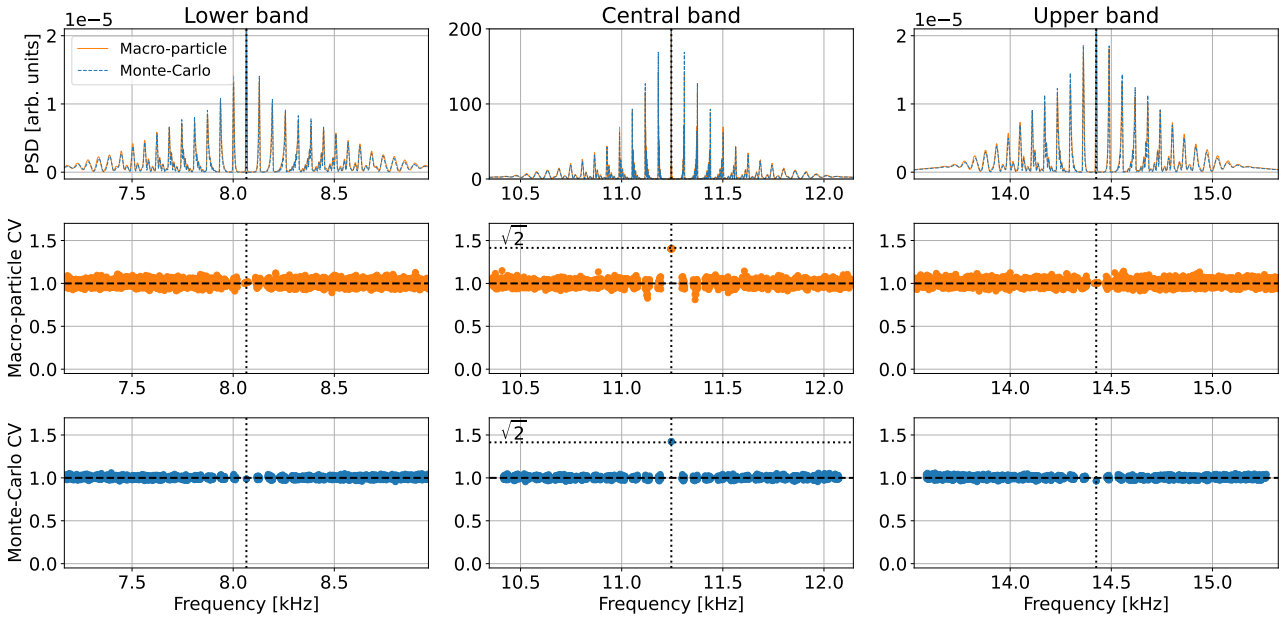


Figure 3: Macro-particle and Monte-Carlo simulations of a Schottky spectrum. The average spectrum and CV are based on 1000 random draws of the bunch for the macro-particle simulation, and 5000 random draws for the Monte-Carlo simulation.

After a given period, this unpredictable drift is equivalent to drawing new random phases, making the averaging over successive instantaneous Schottky spectra equivalent to the averaging over different random draws of the bunch. The same conclusion can not be drawn for the longitudinal central satellite, since the synchrotron phases do not appear in Eq. (5). Figure 4 presents an experimental measurement from the LHC Schottky monitors. The CV for the transverse sidebands and the non-central ($|p| > 2$) longitudinal satellites agree with the theory. No conclusion can be drawn for the central ($p = 0$) longitudinal satellite for the reason given above. The CVs for $p = \pm 1$ and ± 2 longitudinal satellites deviate from the predictions, which suggests that these satellites are subject to effects beyond the adopted theory of Schottky spectra and should not be used for diagnostics.

CONCLUSION

The aim of this study was to quantify the statistical properties of Schottky spectra and reveal the dependencies on particle count, harmonic number, and oscillation amplitude distribution. Our analysis demonstrated the convergence of the coefficient of variation to specific, non-zero values, for different Bessel satellites. This highlights the importance of averaging instantaneous Schottky spectra to access the mean spectrum described by existing theories. Our findings were validated through simulations and data from the LHC Schottky monitors and while transverse and non-central longitudinal satellites exhibit consistent convergence in the experimental data, the behaviour of the central longitudinal satellite still requires further investigation.

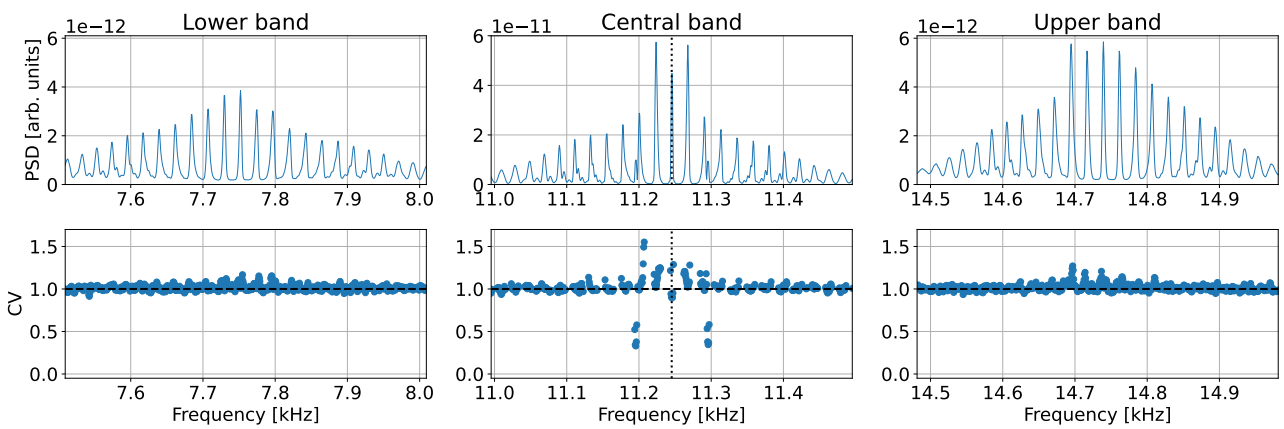


Figure 4: Experimental LHC Schottky spectrum taking during fill 8412 from '2022-11-18 17:44:00' to '2022-11-18 18:17:00'. Upper plots: average of 1980 instantaneous Schottky spectra. Lower plots: CV of the PSD.

Content from this work may be used under the terms of the CC-BY-4.0 licence (© 2023). Any distribution of this work must maintain attribution to the author(s), title of the work, publisher, and DOI

ISBN: 978-3-95450-236-3 ISSN: 2673-5350 doi:10.18429/JACoW-IBIC2023-WEP035

REFERENCES

[1] S. L. Miller and D. Childers, *Probability and Random Processes (Second Edition)*. Academic Press, 2012. doi:10.1016/B978-0-12-386981-4.50013-8

[2] D. Boussard, "Schottky noise and beam transfer function diagnostics," p. 42, 1986. doi:10.5170/CERN-1987-003-V-2.416

[3] S. Chattopadhyay, "Some fundamental aspects of fluctuations and coherence in charged-particle beams in storage rings," *AIP Conference Proceedings*, vol. 127, no. 1, pp. 467–623, 1985. doi:10.1063/1.35175

[4] J. L. Laclare, "Bunched beam coherent instabilities," 1987. doi:10.5170/CERN-1987-003-V-1.264

[5] K. Lasocha, "Non-Invasive Beam Diagnostics with Schottky Signals and Cherenkov Diffraction Radiation," PhD thesis, Jagiellonian University, Kraków, Poland, 2022. https://cds.cern.ch/record/2846538

[6] D. Alves and K. Lasocha, "Kalman filter-based longitudinal phase-space reconstruction method for hadron machines," *Phys. Rev. Accel. Beams*, vol. 24, no. 9, p. 072 801, 2021. doi:10.1103/PhysRevAccelBeams.24.072801

[7] K. Lasocha and D. Alves, "Estimation of longitudinal bunch characteristics in the LHC using Schottky-based diagnostics," *Phys. Rev. Accel. Beams*, vol. 23, no. 6, p. 062 803, 2020. doi:10.1103/PhysRevAccelBeams.23.062803

[8] C. Lannoy, "Statistical properties of Schottky spectra," CERN note, in preparation.

[9] Random Walk–1-Dimensional. https://mathworld.wolfram.com/RandomWalk1-Dimensional.html

[10] J. M. Borwein, D. Nuyens, A. Straub, and J. Wan, "Some arithmetic properties of short random walk integrals," *The Ramanujan Journal*, vol. 26, no. 1, pp. 109–132, 2011. doi:10.1007/s11139-011-9325-y

[11] PyHEADTAIL code repository. https://github.com/PyCOMPLETE

[12] K. S. B. Li *et al.*, "Code development for collective effects," in *Proc. HB'16, Malmö, Sweden*, 2016, pp. 362–367. doi:10.18429/JACoW-HB2016-WEAM3X01

[13] C. Lannoy, D. Alves, N. Mounet, and T. Pieloni, "LHC Schottky Spectrum from Macro-Particle Simulations," in *Proc. IBIC'22*, Kraków, Poland, 2022, pp. 308–312. doi:10.18429/JACoW-IBIC2022-TUP34

[14] M. Betz, O. R. Jones, T. Lefevre, and M. Wendt, "Bunched-beam Schottky monitoring in the LHC," *Nucl. Instrum. Methods Phys. Res., A*, vol. 874, no. 14, pp. 113–126, 2017. doi:10.1016/j.nima.2017.08.045

Content from this work may be used under the terms of the CC-BY-4.0 licence (© 2023). Any distribution of this work must maintain attribution to the author(s), title of the work, publisher, and DOI

ISBN: 978-3-95450-236-3 ISSN: 2673-5350 doi:10.18429/JACoW-IBIC2023-WEP036

STUDY OF NON-DESTRUCTIVE BPM-BASED ENERGY MEASUREMENT OF THE CANADIAN LIGHT SOURCE LINAC

H. Shaker*, D. Bertwistle, E.J. Ericson[1], Y. Sigari[1], E. Soltan[2]
Canadian Light Source, Saskatoon, Canada
[1]also at the University of Saskatchewan, Department of Physics and Engineering Physics
[2]also at the University of Saskatchewan, Department of Computer Science

Abstract

There is a plan in the Canadian Light Source (CLS) to replace the current Linac with a new one from Research Instruments GmbH in mid-2024. The first straight section of LTB (Linac-To-Booster) was upgraded to have two BPMs (Beam Position Monitors) with a 4.75 m drift between them and two phosphor screens were replaced by YAG screens. A new BPM and a YAG-based screen station upgraded the following 90-degree achromat beamline. These upgrades help us to measure the current and future Linac beam parameters, including the beam twiss parameters, energy, and energy spread. In this paper, we discussed how we could use these three BPMs for non-destructive energy measurement, which will be a part of the active energy correction system.

INTRODUCTION

Canadian Light Source's current electron linear accelerator will be replaced with a new one by Research Instruments GmbH in mid-2024 [1, 2]. As part of the project, the beam diagnostic systems in the LTB were upgraded. Figure 1 shows the layout of LTB and where the current diagnostic components were upgraded or new components added. A new BPM, BPM2, added by pairing with the BPM1, measures the transversal position and momentum of the electron beam in the BPM2 location. There is a long drift between these two BPMs and one Steerer (ST0003-05), just 26.22 cm before that, and its effect is negligible compared to a pure drift as calculated. VSC0003-01 and VSC0003-03 phosphor screens were replaced by one inch round YAG screens, and the camera was upgraded to a digital one. This helps us to measure twiss parameters. Also, they can be used to calibrate BPMs. A new VSC0003-06 screen was installed in the achromat beamline to measure energy and energy spread destructively and be used as a reference to calibrate the BPM3. An online non-destructive method for the energy measurement is required for the energy monitoring by operators and potentially to use in an active energy correction system, which uses a script which implement a negative feedback system to change the phase of the Linac accelerating section to keep the energy constant. For this purpose, a new BPM, SLM0003-03 (BPM3), was installed in the achromat beamline just before the new screen station and after the slit. The slit will be upgraded, as part of the project, for the beam profile scanning and energy filtering. When we combine these three BPMs together, as we suggest, we can measure the energy non-destructively. The first two are to measure the transverse position and momentum of the beam just before entering the achromat beamline in the location of the BPM2. Then, using the transfer matrix between the BPM2 and the BPM3 and the location of the beam read by the BPM3, we can find the energy of the electron beam.

TRANSFER MATRIX & NORMALIZED X

The position of the beam at BPM3, SLM0003-03, is a function of the beam energy and the beam position and momentum at the BPM2 location. Here we defined a new parameter, normalized horizontal position, or normalized x, which is just a function of energy. To calculate that, we should know the transversal position and momentum of the beam in the BPM2 location. We can measure x_1 and x_2 and Eq. (1) shows how we can calculate x_2' by knowing the drift length between them, which is 4.7518 m.

$$\begin{Bmatrix} x_2 \\ x_2' \end{Bmatrix} = \begin{Bmatrix} 1 & D \\ 0 & 1 \end{Bmatrix} \begin{Bmatrix} x_1 \\ x_1' \end{Bmatrix} \Rightarrow x_2' = (x_2 - x_1)/D \qquad (1)$$

Equation (2) shows the position and momentum at the BPM3 location, knowing the transfer matrix and the position and momentum at the BPM2 location. We used a 3x3 transfer matrix which included the horizontal information and dispersion. Because of using linear elements, the vertical components are decoupled.

$$\begin{Bmatrix} x_3 \\ x_3' \\ \Delta p/p \end{Bmatrix} = M \begin{Bmatrix} x_2 \\ x_2' \\ \Delta p/p \end{Bmatrix} \qquad (2)$$

Now we can define the normalized x which is equal to $\Delta p/p$ as you can see in Eq. (3) and it is a function of horizontal beam position in three BPMs, the drift length between BPM1 and BPM2 and the first row of the transfer matrix between the BPM2 and BPM3.

$$\begin{aligned} &x_3 = M_{11} * x_2 + M_{12} * x_2' + M_{13} * \Delta p/p = \\ &M_{11} * x_2 + M_{12} * (x_2 - x_1)/D + M_{13} * \Delta p/p \Rightarrow \\ &x_n \equiv \left[x_3 - M_{11} * x_2 - M_{12} * (x_2 - x_1)/D\right]/M_{13} = \Delta p/p \end{aligned} \qquad (3)$$

The BPM2 to BPM3 transfer matrix can be calculated by knowing the elements between two BPMs.

$$M = M_{D4} * M_{QF2} * M_{D3} * M_B * M_{D2} * M_{QF1} * M_{D1} \qquad (4)$$

* hamed.shaker@lightsource.ca

Content from this work may be used under the terms of the CC-BY-4.0 licence (© 2023). Any distribution of this work must maintain attribution to the author(s), title of the work, publisher, and DOI

ISBN: 978-3-95450-236-3 ISSN: 2673-5350 doi:10.18429/JACoW-IBIC2023-WEP036

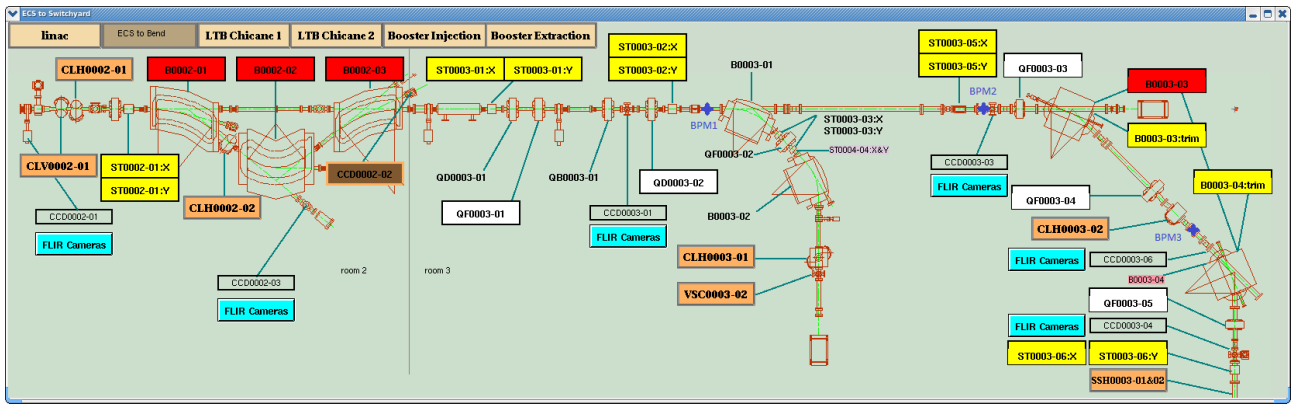


Figure 1: The LTB layout with BPMs positions, BPM1 (SLM0003-02), BPM2(SLM0003-01), BPM3(SLM0003-03) and screens (VSC0003-01, VSC0003-03, VSC0003-06).

M_{D1-4} is a drift transfer matrix and D_{1-4} = 0.6849, 0.45775, 1.54695, 0.7328 m is the drift length. M_B is a sector dipole transfer matrix, ϕ is the dipole angle and R is its radius. $\phi = 45°$ and R = 850 mm in our case. $M_{QF1,2}$ is a focusing quadrupole transfer matrix, $\mu = \sqrt{k}$ which k is the quadrupole focusing strength and L is the quadrupole length. Both quadrupole length is 166.1 mm. $k = 0.2148I\ 1/\mathrm{m}^2$ [3] and the first and second quadrupole coil current is 9.14 A and 28.35 A, respectively. Equations (5)–(7) show the transfer matrix for a drift, sector dipole and a focusing quadrupole, respectively [4].

$$M_{D1-4} = \begin{Bmatrix} 1 & D_{1-4} & 0 \\ 0 & 1 & 0 \\ 0 & 0 & 1 \end{Bmatrix} \tag{5}$$

$$M_B = \begin{Bmatrix} cos(\phi) & Rsin(\phi) & R(1-cos(\phi)) \\ -sin(\phi)/R & cos(\phi) & sin(\phi) \\ 0 & 0 & 1 \end{Bmatrix} \tag{6}$$

$$M_{QF} = \begin{Bmatrix} cos(\mu L) & sin(\mu L)/\mu & 0 \\ -\mu sin(\mu L) & cos(\mu L) & 0 \\ 0 & 0 & 1 \end{Bmatrix} \tag{7}$$

Now we can calculate the total transfer matrix, using the mentioned current parameters. It is easy to recalculate it or it is part of the script to calculate energy and to do the energy correction using different currents for quadrupoles. Equation (8) shows the BPM2-BPM3 transfer matrix when the achromat beamline middle quadrupole, QF0003-04, is ON and in its nominal value. It is also practical for offline measurement to turn this quadrupole off for a better energy and energy spread measurement resolution. Equation (9) shows the transfer matrix when this quadrupole is off.

$$M_{ON} = \begin{Bmatrix} -0.9643 & -0.2553\ \mathrm{m} & 0.8533\ \mathrm{m} \\ 0.1700\ (1/\mathrm{m}) & -0.9920 & -0.6720 \\ 0 & 0 & 1 \end{Bmatrix} \tag{8}$$

$$M_{OFF} = \begin{Bmatrix} -1.8485 & 0.1918\ \mathrm{m} & 1.9784\ \mathrm{m} \\ -0.9149\ (1/\mathrm{m}) & -0.4460 & 0.7071 \\ 0 & 0 & 1 \end{Bmatrix} \tag{9}$$

Now we can rewrite Eq. (3) using the M_{ON} transfer matrix, which shows how we can calculate the normalized x based on the current parameters.

$$x_n \equiv \frac{x_3 + 0.9643 * x_2 + 0.2553\ \mathrm{m} * \frac{(x_2 - x_1)}{4.7518\ \mathrm{m}}}{0.8533\ \mathrm{m}} = \Delta p/p \tag{10}$$

BPM CALIBRATION

We must calibrate BPMs and do alignment corrections based on the mechanical LTB coordinates survey [5] before implementing them in Eq. (10). We will start with the BPM2. As shown in Fig. 1, there is the VSC0003-03 screen, 294.7 mm after the BPM2. We use it as a reference since it was grided, and we can directly see the beam profile dimension and position. There is a positive axial offset of 1.62 mm for BPM2 compared to this screen, as measured mechanically during the LTB survey. We should consider the offset and the drift to add to the measured position with the BPM to find equivalent positions. We will use the BPM1 measured position to correct this drift to calculate x_2' using Eq. (1). Also, the small effect of the ST0003-05X steerer that was 262.2 mm before the BPM2 was calculated to correct the x_2' at the BPM2 location. Figure 2 shows the result. The scanning was done using the ST0003-02X steerer. We should also consider the negative axial offset of 0.835 mm for BPM2 compared to BPM1. Then, we can use the following equation for BPM1-3 to find the horizontal position based on the BPM x measurement.

$$\begin{cases} x_1 = 2.59 x_{BPM1} + 4.46\ \mathrm{mm} \\ x_2 = 2.59 x_{BPM2} + 3.62\ \mathrm{mm} \\ x_3 = 2.53 x_{BPM3} - 11.53\ \mathrm{mm} \end{cases} \tag{11}$$

Content from this work may be used under the terms of the CC-BY-4.0 licence (© 2023). Any distribution of this work must maintain attribution to the author(s), title of the work, publisher, and DOI

ISBN: 978-3-95450-236-3 ISSN: 2673-5350 doi:10.18429/JACoW-IBIC2023-WEP036

Content from this work may be used under the terms of the CC-BY-4.0 licence (© 2023). Any distribution of this work must maintain attribution to the author(s), title of the work, publisher, and DOI

We assumed BPM1 following the same calibration slope. Measurement of the VSC0003-01 screen behind the BPM1 confirms that roughly. Also, the beam goes through a very small horizontal spanning in the BPM1, and then a slight slope change is negligible. The result of the BPM3 calibration also confirms this assumption since all these three BPMs are similar.

Now, we should go to calibrate BPM3. For the BPM3, we used the data of the VSC0003-06 screen by scanning the ST0003-02X steerer and considered the drift and alignment between the screen and the BPM. The data was taken when the achromat beamline quadrupole was off for a better resolution. To correct the drift effect, we need to know the x_3'. For that, we are using Eq. (9). The negative axial offset of 0.644 mm for BPM3 compared to VSC0003-06 was also considered. Figure 3 shows the calibration result. It shows almost the same calibration factor of BPM1 and BPM2 but a negative polarity compared to them, Eq. (11).

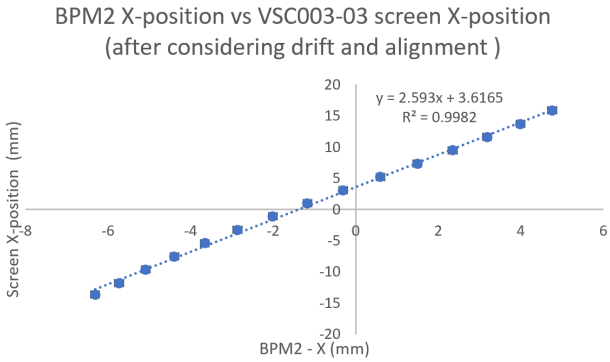


Figure 2: BPM2 calibration result.

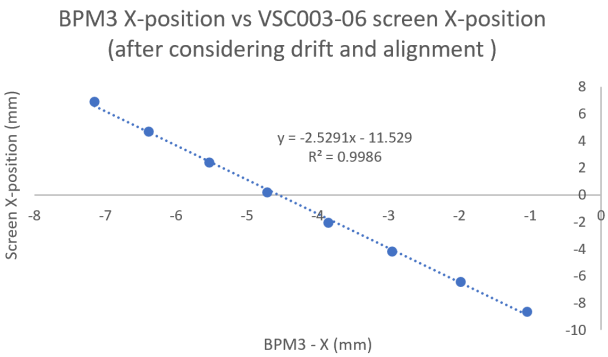


Figure 3: BPM3 calibration result.

ENERGY MEASUREMENT RESULT

Now, we have the tool to start energy measurement. First, we checked the model by scanning the ST0003-02X steerer without changing the beam energy. The VSC0003-06 shows horizontal displacement of the beam profile, which we know comes from the beam's horizontal position and momentum on the BPM2 location, not from the energy variation. Measuring BPM1-3 horizontal data and using Eqs. (10) and (11), we see the result in Fig. 4. Energy variation is about 0.07 %, below 0.1 %, which is the pulse-to-pulse energy jittering of the current and the new Linac. The non-zero average energy is arbitrary and depends on how we select the nominal energy, which is about 250 MeV. It shows our model works well. Now, we can measure the energy by scanning the last accelerating structure phase. The last accelerating section is operating off-crest as a tool to correct the total beam energy of the Linac. Figure 5 shows the result. The energy changes linearly around the nominal phase (~ 110.3°), but we saw some non-linearity below ~ 104°. Although the energy correction script operates in the linear part, further study for non-linear behaviour could be helpful.

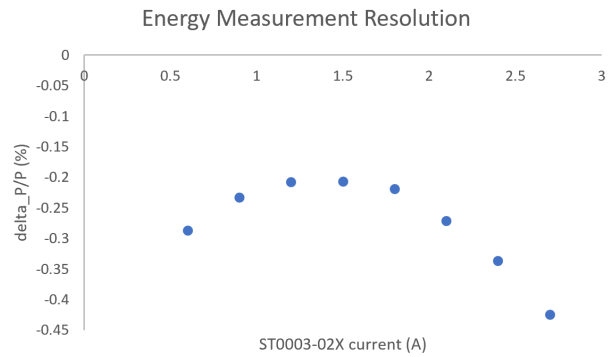


Figure 4: Energy measurement resolution, 0.07%.

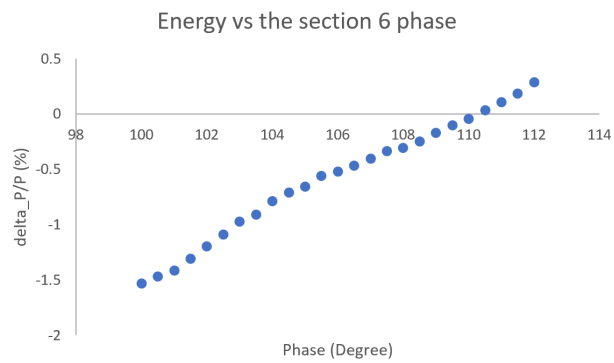


Figure 5: Energy measurement by scanning the last accelerating section phase.

CONCLUSION

The proposed BPM-based non-destructive energy measurement method shows a good resolution which is below the machine energy jittering. Based on this method, we prepared a script to measure and correct the Linac total energy. This script will be used for the new Linac, and operators can monitor the long-term operation of the Linac. Further non-linear studies will be helpful for more accurate energy measurements.

ISBN: 978-3-95450-236-3 ISSN: 2673-5350 doi:10.18429/JACoW-IBIC2023-WEP036

REFERENCES

[1] "CLS Linac Final Design Report", CLS, Saskatoon, Canada, Internal CLS-RI document, Mar. 2023.

[2] M. Boland *et al.*, "Design of a new S-band 250 MeV electron linac with RF SLED compression for the CLS", in *Proc. IPAC'23*, Venice, Italy, May 2023. doi:1018429/JACoW-IPAC2023-TUPL108

[3] C. Baribeau, "Magnetic Measurements of LTB Quadrupole", CLS, Saskatoon, Canada, CLS internal report, Mar. 2023.

[4] K. Wille, *The Physics of Particle Accelerators, An Introduction*, Oxford University Press Inc., 2000.

[5] A. Janis, "LTB Diagnostic Survey Coordinates", CLS, Saskatoon, Canada, CLS internal report, Apr. 2023.

Content from this work may be used under the terms of the CC-BY-4.0 licence (© 2023). Any distribution of this work must maintain attribution to the author(s), title of the work, publisher, and DOI

ISBN: 978-3-95450-236-3 ISSN: 2673-5350 doi:10.18429/JACoW-IBIC2023-WEP042

IMPLEMENTATION OF TRANSIMPEDANCE ANALOG FRONT – END CARD FOR LOS ALAMOS NEUTRON SCIENCE CENTER ACCELERATOR WIRE SCANNERS *

D. Rai†, H. Leffler, S.A. Baily, D. Zimmermann, L. Montoya,
L. Kennel, D. Martinez, J. Duran, A. Braido
Los Alamos National Laboratory, Los Alamos, NM, USA

Abstract

The Los Alamos Neutron Science Center's (LANSCE) Accelerator Operations and Technology division - Instrumentation and Controls (AOT-IC) team executed a project that implemented a new Analog Front-End (AFE) card for their wire scanner's Data Acquisition (DAQ) system. The AFE accommodates the signal amplification and noise reduction needed to acquire essential measurement data required for beam diagnostics for LANSCE accelerator. Wire Scanners are electro-mechanical beam interceptive devices that provide cross-sectional beam profile measurement data fitted to a Gaussian distribution that is then extrapolated to provide beam shape and position. The beam shape and position information allow the operator to adjust parameters such as acceleration, steering, and focus to provide optimized beam delivery to targets. The project included software and hardware implementation that eliminated the dependency on legacy systems and consolidated various AFE designs for diagnostics systems into a single design with 11 gain settings ranging from 100 nA to 40 mA at 10 V full scale to accommodate its future applications on other diagnostics systems.

BACKGROUND

The LANSCE facility utilizes various beam diagnostics devices for operators to adjust beam parameters such as acceleration, steering, and focus to provide efficient and effective beams to all five experimental areas. Wire scanners are interceptive beam diagnostics devices with a mechanical actuator assembly and a single or pair of Silicon Carbide (SiC) or Tungsten (W) wires (sensor) mounted vertically and/or horizontally to the sensor fork mount as shown in Fig. 1.

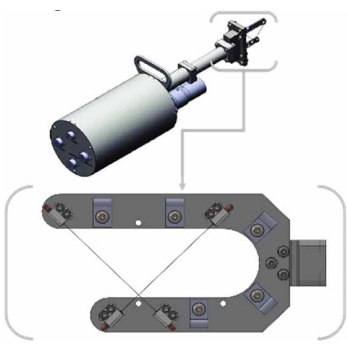


Figure 1: Wire Scanner and Sensor Fork Assembly.

When the beam impinges on the wires, current resulting from the emitted secondary emission yield is deposited on the wire; this current is proportional to the beam current [1]. Since the wire's position is scanned in the beam pipe, the wire scanner provides the transverse vertical and horizontal profile measurements with a Gaussian fit, as shown in Fig. 2.

The data from the wire scanner is obtained by hardware and software implementation of the QAC (Quad Actuator Controller) DAQ, National Instruments – CompactRIO (cRIO) Systems. The QAC DAQ cRIO system controls movement and acquires data. The user interface JAVA program analyzes and displays the result of the received scan data [2]. The AFE card is the component of the DAQ that acquires beam-impinged secondary electron current flow from the wires. The AFE is a compact Peripheral Component Interconnect (cPCI) form factor card supporting 16 channels, assuming one channel for each axis, supporting eight wire scanners per card.

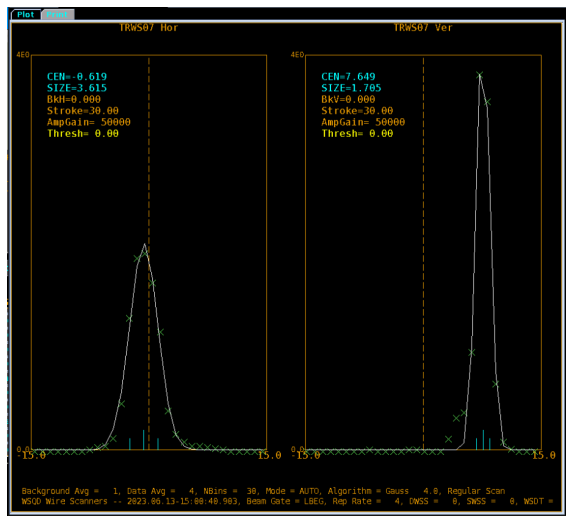


Figure 2: LBEG (Long Bunch Enabled Gate) Beam scan of TRWS07 Wire Scanners.

During the implementation of the QACDAQ system for wire scanner systems in the transition region and downstream areas, the LANSCE Harp AFE was used. The LANSCE Harp AFE full scale range is from 3 µA to 270 µA and was not sensitive enough for typical Wire scanner application [3]. As shown in Table 1, LBEG is a higher current beam with 50 times greater macro pulse average current and 100 times greater charge per pulse than MPEG (Micro Pulse Enabled Gate) [4]. Therefore, the LANSCE Harp AFE was adequate in performing wire scanner scans of the LBEG beam but not for MPEG.

* This work was supported by the U.S. Department of Energy through the Los Alamos National Laboratory. Los Alamos National Laboratory is operated by Triad National Security, LLC, for the National Nuclear Security Administration of U.S. Department of Energy (Contract No. 89233218CNA000001). † drai@lanl.gov, LA-UR-23-30149

Content from this work may be used under the terms of the CC-BY-4.0 licence (© 2023). Any distribution of this work must maintain attribution to the author(s), title of the work, publisher, and DOI

ISBN: 978-3-95450-236-3 ISSN: 2673-5350 doi:10.18429/JACoW-IBIC2023-WEP042

Table 1: LBEG and MPEG Comparison

Descriptions	LBEG	MPEG
Pulse Spacing	358 ns	1800 ns
Pulse Duration	290 ns	20 ns
Pulses Per Macro Pulse (625us)	~1746	~347
Average Current	100 µA	2.0 µA
Charge/Pulse	5.0 µC	.05 µC
Protons/Pulse	$3.1x10^{13}$	$3.1x10^{11}$

NEW DESIGN

Design Requirements

Table 2: Design Requirements

ID	Requirement
1	Same Form and Fit as the LANSCE Harp AFE with 16 input channels
2	LBEG and MPEG beam scans capable
3	+/-50 VDC Bias Input Capability
4	Gain selection options for user optimization which cover expected beam currents
5	Protected Input
6	Greater than +/-5 VDC Full Scale Output

Dynamic Range

The dynamic range for expected induced current had to be determined to design a new AFE. Induced sensor current measurements of strategic wire scanner locations were performed for LBEG and MPEG beam during beam development time using an off-the-shelf Thorlabs, PDA200C - Benchtop Photodiode Amplifier [5]. We determined the range of induced current for the wire scanners to be between 300 nA and 10 µA, giving us a better understanding of potential gain ranges for the new AFE design.

Bandwidth

At LANSCE, two-beam pulse widths are used: a pulse width of 625 µs (1.6 kHz) is typically used for the production beam with repetition rate of 120 Hz, and 150 µs (6.6 kHz) is generally used during beam tuning efforts with repetition rate of 4 Hz.

Design Approach

It was necessary to use an amplifier scheme that accepts current to amplify low current signal accurately and stably from the wire scanner wires to a usable voltage level. Transimpedance amplifier (TIA) circuit design is typically used to convert and amplify low current output of sensors such as Photodiodes to a proportional output voltage. With the successful use of the Thorlabs, PDA200C - Benchtop Photodiode Amplifier during testing under nominal beam delivery conditions, we gained assurance of the effectiveness of the TIA design approach.

The TIA circuit in Fig. 3 presents near 0 voltage and impedance to the current source, maximizing signal transfer from a high-impedance current signal source. Due to this characteristic and with a known voltage output requirement of +/- 10 V and the desired current range for each gain stage shown in Table 3, the values of feedback resistors, Rf, can be calculated using Eq. (1).

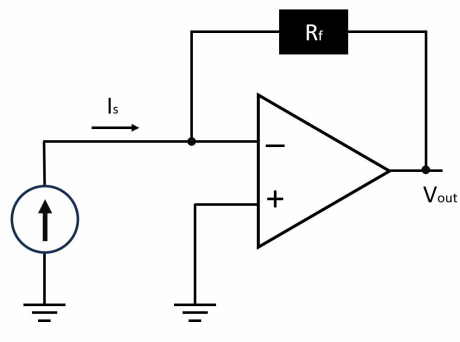


Figure 3: TIA Circuit

Table 3: New AFE Gain Stages

Gain#	I_{Min}	I_{Max}	V_{Min}	V_{Max}	f_p
0	0	100 nA	-10 V	+10 V	1.6 kHz
1	0	500 nA	-10 V	+10 V	1.6 kHz
2	0	2.5 µA	-10 V	+10 V	1.6 kHz
3	0	12.5 µA	-10 V	+10 V	1.6 kHz
4	0	10 µA	-10 V	+10 V	6.6 kHz
5	0	50 µA	-10 V	+10 V	6.6 kHz
6	0	250 µA	-10 V	+10 V	6.6 kHz
7	0	1.25 mA	-10 V	+10 V	6.6 kHz
8	0	5 mA	-10 V	+10 V	6.6 kHz
9	0	20 mA	-10 V	+10 V	6.6 kHz
10	0	40 mA	-10 V	+10 V	6.6 kHz

$$V_{Out} = -I_{in}R_f \text{ or } R_f = \left|\frac{V_{out}}{-I_{in}}\right| \quad (1)$$

At higher input frequencies, f_p, it is important to ensure the feedback network doesn't interact with the open loop gain of the op-amp to cause instability. Without compensation, a frequency causes a gain of 0 dB and complete phase reversal to the input, causing positive feedback. Even a tiny input capacitance results in stability issues. Parasitic capacitance in the circuit is unavoidable; therefore, adding a feedback capacitor, C_f, in parallel with a feedback resistor, R_f, as shown in Fig. 4, is crucial for compensating these undesired effects [6].

Content from this work may be used under the terms of the CC-BY-4.0 licence (© 2023). Any distribution of this work must maintain attribution to the author(s), title of the work, publisher, and DOI

ISBN: 978-3-95450-236-3 ISSN: 2673-5350 doi:10.18429/JACoW-IBIC2023-WEP042

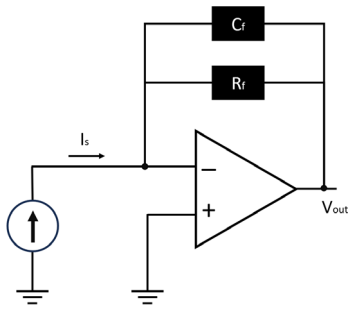


Figure 4: TIA Circuit Layout with Feedback Capacitor.

Figure 5 shows the transient response of how an uncompensated TIA circuit is marginally stable with substantial ringing, causing the output to overshoot. On the other hand, Fig. 6 represents a compensated TIA transient response, which is stable with a clean step response.

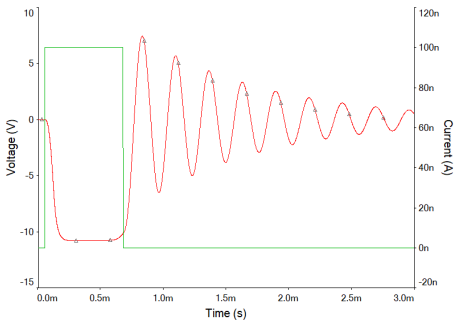


Figure 5: Transient Response of Uncompensated TIA.

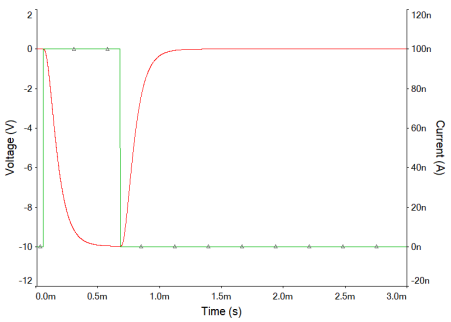


Figure 6: Transient Response of Compensated TIA.

Equation 2 can be used to calculate C_f, using the computed value for R_f and f_p given in Table 3 for each gain stage. Lastly, to ensure that the Gain Bandwidth Product (GBWP) of the op-amp is sufficient for each gain stage configuration, Eq. (3) can be used. C_{in} in Eq. (3) is the total input capacitance, which includes the capacitance for the input cable and sensor along with amplifier common mode and differential mode capacitance. The calculated GBWP (right-side) must be less than the GBWP of the op-amp; otherwise, it will lead to instability and a non-linear response of the TIA output [7].

$$C_f \leq \frac{1}{2\pi f_p R_f} \quad (2)$$

$$GBWP > \frac{C_{in}}{2\pi * R_f * C_f 2} \quad (3)$$

Design Challenges

The design's main challenge was finding an operational amplifier (op-amp) with low bias current and high GBWP to meet the gain and bandwidth requirements of all the gain stages listed in Table 3. We narrowed our selection to the Texas Instruments, THS4631- High-Speed FET-Input Operational Amplifier based on performance, cost, and availability. It was the only op-amp available with GBWP over 200 MHz that supported +/-12 VDC dual input supply rail that was available at the time of the development.

Final Design Discussion

Figure 5 shows the simulation result for Gain 0, which required the highest gain of 100 M, and the transient response is stable and has a clean step response when excited with 100 nA. Figure 7 shows the final fabricated assembly and Fig. 8 shows the final single-channel layout of the TIA circuit of the new AFE design. The design includes 11 selectable gains divided between seven high and four low bandwidths, shown in Table 3.



Figure 7: New TIA AFE Assembly.

The gain stages 0 to 3 for low bandwidth and gain stages 5 to 10 for high bandwidth are designed to have 20% overlap higher to lower gain stage to ensure continuity between gain stages. This overlap helps in the case of a user experiencing saturated voltage output at selected scan gain selection, then lowering the gain still provides overlap to better capture the signal within an acceptable range.

During beam development, we had issues with unknown transient voltage damaging the TIA inside the Thorlabs, PDA200C - Benchtop Photodiode Amplifier. Hence, to make the design robust, we added a dual diode, D1, as shown in Fig. 8, to protect the amplifier from overvoltage. The current limiting resistor, R26, is also placed at the non-inverting input of the amplifier, as shown in Fig. 8.

A low pass filter with a 6.6 kHz corner is added to improve noise attenuation. Gain stages 8, 9, and 10 were added later to accommodate other beam diagnostics systems using the same QAC DAQ system.

Even though the dynamic range for the sensor current was between 300 nA and 10 µA, we added gain 0 covering the 0-100 nA current range to have the capability to measure lower current for additional diagnostics purposes.

Content from this work may be used under the terms of the CC-BY-4.0 licence (© 2023). Any distribution of this work must maintain attribution to the author(s), title of the work, publisher, and DOI

ISBN: 978-3-95450-236-3 ISSN: 2673-5350 doi:10.18429/JACoW-IBIC2023-WEP042

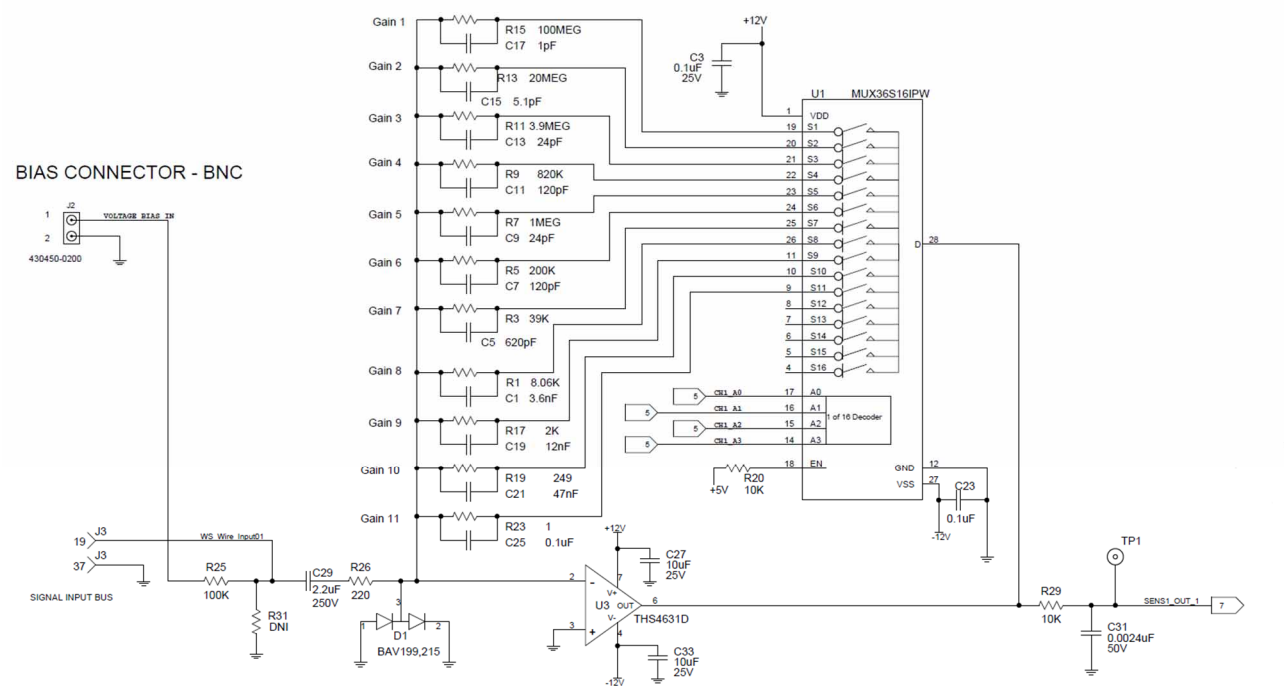


Figure 8: Single Channel Layout of New Transimpedance AFE.

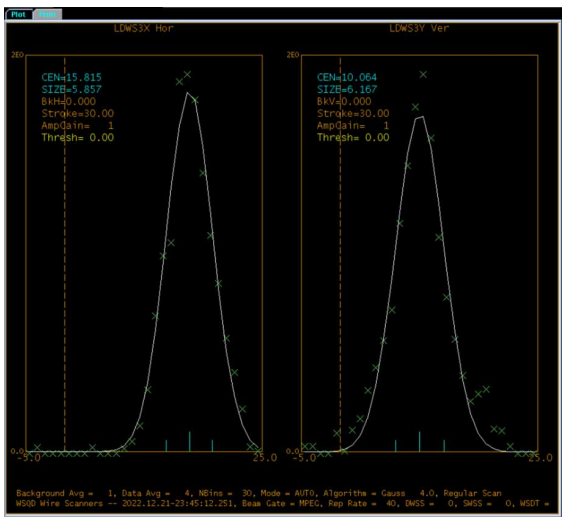


Figure 9: MPEG Beam scan of LDWS3X and LDWS3Y Wire Scanners.

CONCLUSION

During the V&V (Verification and Validation) of the new AFE, hardware and software implementation it showed that the new Transimpedance AFE design for the DAQ system meets all the design requirements listed in Table 1. Figure 2 and Fig. 9 show successful wire scanner scans with LBEG and MPEG beam taken during beam development time, respectively. Both scans show a good Gaussian fit with a clear beam center and size for horizontal and vertical axes providing essential data for beam tuning. The new design has adequately addressed design and functional limitations of the LANSCE Harp AFE providing a dynamic gain range to measure the induced sensor current with accuracy and stability.

Also, with additional gain stages out to 40 mA full scale, future efforts can be made to convert all diagnostics systems to the new Transimpedance AFE, streamlining and reducing the life-cycle management cost of maintaining configuration. Additional opportunities exist to use the same design scheme for other DAQ systems but in a different form and fit.

REFERENCES

[1] E. Sternglass, "Theory of Secondary Electron Emission by High-Speed Ions," *Phys. Rev.*, vol. 108, no. 1, Oct. 1957. doi:10.1103/PhysRev.108.1

[2] L. Montoya, "LANSCE QAC/DAQ Wire Scanner Instrumentation Upgrade," presented at the 12th Int. Beam Instrumentation Conf. (IBIC'23), Saskatoon, Canada, September 2023, paper WEP029, this conference.

[3] J. Sedillo *et al.*, "LANSCE Isotope Production Facility Emittance Measurement System," in *Proc. IBIC'16*, Barcelona, Spain, Feb. 2017. pp. 548-550. doi:10.18429/JACOW-IBIC2016-TUPG79

[4] B. White, "AOT-OPS Accelerator Pulse Structure," unpublished.

[5] Thorlabs, https://www.thorlabs.com/thorproduct.cfm?partnumber=PDA200C

[6] UltimateElectronics, Op-Amp Transimpedance Amplifier https://ultimateelectronicsbook.com/op-amp-transimpedance-amplifier/

[7] Texas Instruments, Transimpedance Amplifiers (TIA): Choosing the Best Amplifier for the Job https://www.tij.co.jp/jp/lit/an/snoa942a/snoa942a.pdf

Content from this work may be used under the terms of the CC-BY-4.0 licence (© 2023). Any distribution of this work must maintain attribution to the author(s), title of the work, publisher, and DOI

ISBN: 978-3-95450-236-3 ISSN: 2673-5350 doi:10.18429/JACoW-IBIC2023-WEP043

UPGRADE OF THE ELBE TIMING SYSTEM

M. Kuntzsch, A. Schwarz, K. Zenker, M. Justus
Helmholtz-Zentrum Dresden-Rossendorf, Dresden, Germany
Z. Oven, L. Perusko, L. Krmpotic, U. Legat, U. Rojec, Cosylab, Ljubljana, Slovenia

Abstract

The ELBE center for high power radiation sources is operating an electron linear accelerator to generate various secondary radiation like neutrons, positrons, intense THz and IR pulses and Bremsstrahlung. The legacy timing system has been modified and extend over the past two decades to enable new experiments. Part of this system is using obsolete parts which makes the maintenance more complex and the heterogenous structure requires a major revision of the timing signal generation and distribution at ELBE.

A new timing system based on the Micro Research Finland hardware platform is being adapted to be used at ELBE. It will enable parallel operation of two electron sources and subsequent kickers to serve multiple end stations at a time. The hardware enables low jitter emission of timing patterns and a long term drift compensation of the distribution network. In spring 2023 the development of the software has been accomplished, which included the mapping of operation modes and different complex beam patterns onto the capabilities of the commercial MRF platform. The system generates complex beam patterns from single pulse, to macro pulse and 26 MHz continuous wave (CW) operation, including special triggers for diagnostics and machine subsystems.

REQUIREMENTS

The requirements for the new timing system have been derived mainly from the features of the old timing system and feature requests from the ELBE user community. Timing signal receivers as well as operators expect a particular composition of different signals, that have to be delivered by the new timing system.

Even though ELBE is a CW machine, a macro pulser is used to generate pulsed, low current beams. This mode is mainly used for beam tuning in order to allow a safe operation of destructive diagnostics like view screens. The macro pulser setting defines in turn also the timing for diagnostic triggers for the low level radio frequency (LLRF) controllers, cameras and loss monitors. If in operation, the macro pulser chops the beam into short bursts using magnetic steerer coils. The inductance of the coils combined with the capabilities of the driver unit define the rising and falling slope of the macro pulse train. At ELBE slew rates are on the 10 µs scale and define the shortest opening time of 100 µs. The minimal period is derived from the maximum camera sampling time of 10 ms. So, the period can be set to multiples of 10 ms up to many minutes period.

Biological experiments at ELBE require a very complex trigger pattern in order to adjust the applied dose and its structure to a sample with high accuracy. At the same time the background radiation needs to be reduced which means to suppress dark current from the injector section.

For this application a dedicated single pulser system needs to be in place, which allows for patterns with single bunch resolution, periods up to minutes and a possibility to combine the gun pulse emission with a macro pulse gate to suppress dark current. These features are required for both thermionic injector and superconducting radiofrequency (SRF) gun that are available at ELBE.

Table 1 summarizes the main pulser modes of the timing system and their parameter range. In detail, the requirements are much more complex, the edge cases and error handling makes the implementation a complex development. The complete specification has been written into a design documents which serves as a reference for the implementation process.

Table 1: Main Pulser Modes and Their Parameter Ranges

	Unit	Min	Max
Electron Bunch Rate	Hz	0.03	26e6
Macro Pulser Period	s	10e-3	33864
Macro Pulser Duty Cycle	s	100e-6	33864
Single Pulser Period	s	115.5e-9	33864
Single Pulser Duration	s	38.5e-9	33864

SYSTEM DESCRIPTION

Hardware

For the implementation at ELBE different systems have been evaluated and after a comprehensive feasibility study a European Tender has been awarded to COSYLAB to set up the new ELBE timing system. As hardware platform the Micro Research Finland Oy (MRF) timing modules have been selected [1].

The latest revision of the MRF hardware is available for MicroTCA standard, which is becoming more and more popular in accelerator community and found its application for new beam diagnostic systems and LLRF systems at ELBE.

The system consists of event master modules (EVM) that are generating and send a continuous stream of events which are received by event receiver modules (EVR). EVRs are located in different sections around the accelerator and generate physical trigger signals based on the event stream. EVMs and EVRs are connected over optical fibers, forming a hierarchic structure which allows for a high flexibility and the possibility to extend the system with ease.

Each EVR has four fixed TTL outputs on the front panel and provides two slots for universal IO modules, each housing two physical outputs. There are universal IO modules for different logic levels, electrical and optical outputs

Content from this work may be used under the terms of the CC-BY-4.0 licence (© 2023). Any distribution of this work must maintain attribution to the author(s), title of the work, publisher, and DOI

ISBN: 978-3-95450-236-3 ISSN: 2673-5350 doi:10.18429/JACoW-IBIC2023-WEP043

and special outputs that allow for a fine delay with picosecond precision. Standard modules can delay output signals with the precision of an event clock cycle. In addition a dedicated rear transition module can be attached to the EVR, providing five additional slots for universal IO modules. A fully equipped EVR can in turn deliver 18 output signals to connected timing clients. Timing clients in the same MicroTCA crate can be triggered through the differential backplane trigger bus.

The interconnections between EVMs and EVRs are subject to timing drifts due to changing environmental conditions. The system offers an active drift stabilization, minimizing the residual instability to < 10 ps peak-peak.

The event clock rate can be selected from 50 MHz to 166.6 MHz, and has been defined to 130 MHz at ELBE. This is a ten times the nominal ELBE bunch repetition rate of 13 MHz and one tenth of the accelerator cavity frequency of 1.3 GHz. This event clock rate defines the minimum spacing between to events to 7.7 ns.

At ELBE one EVM is set up per injector, allowing for independent operation in separate beamlines and combined emission into the ELBE accelerator. For machine timing receivers like beam diagnostics LLRF MicroTCA EVRs are applied. For users that do not use MicroTCA hardware we provide PCIe based receiver modules, which is more cost effective.

Software

While the hardware could be used from stock, the Software needed to be tailored to the requirements of ELBE. The base implementation is done using EPICS and EPICS mrfioc2 module [2]. This offers access to all features of the timing system, diagnostic functionality and basic graphical user interfaces (GUI).

The logical mapping of the ELBE machine structure to software is a complex process. It reflects the operation of two injectors in parallel, different beamline sections and beam modes. The above-mentioned beam modes, macro pulse, single pulse and CW are realized as sequences of events, combined with prescalers in order to generate bunch triggers, triggers for LLRF, macro pulser, kicker and diagnostics. The sequences are being built by a algorithm, that translates the user defined parameters into the correct EVM and EVR settings. This complex algorithm, the handling of edge cases and error handling is the major effort needed for the system integration.

The graphical user interfaces are designed using Phoebus [3]. In the course of the design process it has been extended and offers now a simple way to control the operation modes of the timing system, parameter checks, error handling and status information of all hardware components (Fig. 1).

The Phoebus Interface is mainly used for system test and commissioning. Currently a interface for the ELBE SCADA system WinCC is developed which will make the timing system a part of the operator panels used for the machine control.

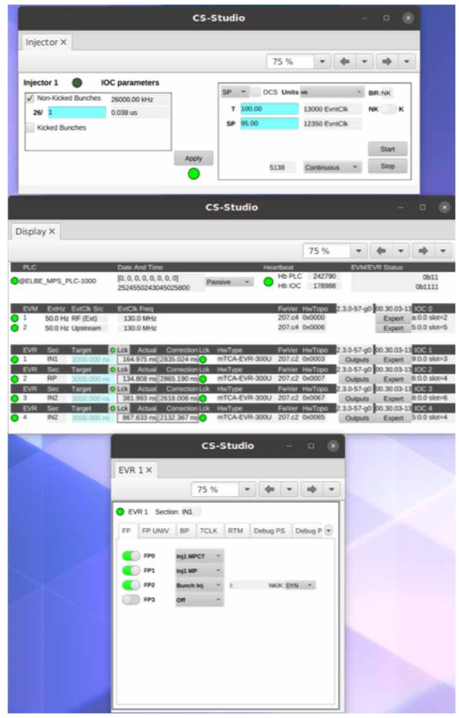


Figure 1: ELBE Timing System Phoebus GUIs to control injectors, EVR outputs and a status panel of all EVMs and EVRs

All machine parameters are checked by a master programmable logic controller (PLC) which acts as the main instance for machine protection. User commands and status signals from the timing system are processed and interlock signals are generated accordingly.

WORK IN PROGRESS

In spring 2023 the development of the software has been accomplished, which included the mapping of operation mode and different complex beam patterns onto the capabilities of the commercial platform. Figure 2 shows the setup used for the intensive on-site software tests.

In parallel, machine development shifts have been used to test all components at the ELBE accelerator. Especially the machine protection system functionality and parameter transfer between timing hardware and MPS PLC has been tested thoroughly to ensure safe operation of the system.

In a next step the complete transition from the legacy system to the new timing system will be made. While all old timing system generators will be replaced by MRF hardware in one step, the old timing distribution system can be replaced stepwise. The whole process means a major change to the operation of the ELBE accelerator and needs to be planned in great detail in order to ensure a seamless transition und not to lose time devoted to user operation.

Content from this work may be used under the terms of the CC-BY-4.0 licence (© 2023). Any distribution of this work must maintain attribution to the author(s), title of the work, publisher, and DOI

ISBN: 978-3-95450-236-3 ISSN: 2673-5350 doi:10.18429/JACoW-IBIC2023-WEP043



Figure 2: Timing System Test Setup.

CONCLUSION

A new flexible timing system has been developed for the ELBE accelerator. The system will replace many hardware components which are generating timing signals for ELBE and unify the timing pattern generation as well as the distribution in one modular system.

The software development has been finalized in spring 2023, dedicated machine development shifts have been used to implement and test the interface to the machine protection.

In a final step the legacy hardware will be replaced by MRF components and the new timing system will be the only source of clock signals for the ELBE operation.

REFERENCES

[1] Micro Research Finlad Oy, http://www.mrf.fi
[2] EPICS mrfioc2, https://github.com/epics-modules/mrfioc2/
[3] SNS Controls CS-Studio, https://controlssoftware.sns.ornl.gov/css_phoebus/

Content from this work may be used under the terms of the CC-BY-4.0 licence (© 2023). Any distribution of this work must maintain attribution to the author(s), title of the work, publisher, and DOI

ISBN: 978-3-95450-236-3 ISSN: 2673-5350 doi:10.18429/JACoW-IBIC2023-WEP046

PROGRESS ON DISTRIBUTED IMAGE ANALYSIS FROM DIGITAL CAMERAS AT ELSA USING THE RABBITMQ MESSAGE BROKER

M. Switka*, K. Desch, T. Gereons, S. Kronenberg, D. Proft, A. Spreitzer
Physikalisches Institut, University of Bonn, Germany

Abstract

In the course of modernization of camera based imaging and image analysis for accelerator hardware and beam control at the ELSA facility, a distributed image processing approach was implemented, called `FGrabbit`. We utilize the RabbitMQ message broker to share the high data throughput from image acquisition, processing, analysis (e.g. profile fit), display and storage between different work stations to achieve an optimum efficacy of the involved hardware. Recalibration of already deployed beam profile monitors using machine vision algorithms allow us to perform qualitative beam photometry measurements to obtain beam sizes and dynamics with good precision. We describe the robustness of the calibration, image acquisition and processing and present the architecture and applications, such as the programming- and web-interface for machine operators and developers.

INTRODUCTION

The ELSA facility [1] deploys around 50 optical beam monitors based on luminescence screens (Chromox or OTR) and synchrotron radiation. The previous installation of cameras with analogue video signal output provided mediocre beam analysis capability due to limited signal quality and the lack of comprehensive camera control. To obtain qualitative beam data from photometry we modernize hardware and software of the optical monitors, primarily utilizing Ethernet-capable digital cameras controlled with non-commercial camera drivers and open source machine vision libraries for image calibration. The`FGrabbit` framework was created [2] to provide resource-optimized camera control, data handling and computing power based on the `RabbitMQ` message broker for distributed analysis. A Gigabit Ethernet (GigE) network between PoE-capable switches links processing computers and image generating devices, such as GenIcam [3] compatible digital cameras, other digitizers or image generating programs. A graphical user interface allows access to the `FGrabbit` framework from the accelerator control system or the facility website and provides comprehensive device and image control.

ARCHITECTURE

The architecture of the `FGrabbit` framework is depicted in Fig. 1. All peripheral devices (cameras, computers) participating in the `FGrabbit` framework communicate through a GigE network, separated from the ELSA control system, but accessible through a gateway computer. As camera control and readout can be achieved through various drivers. We favor the `Aravis` [4] driver in combination with GenICam [3] compatible digital cameras. Streams from other drivers (e.g. Video4linux [1]), VNC[2] servers or image generating programs may also be used as input for the `FGrabbit` framework. Comprehensive image calibration can be applied via the OpenCV computer vision library [5] to account for beam profile distortions resulting from tilted screens (extrinsic properties) or lens imperfections of the imaging system (intrinsic properties). Calibrated images are typically cropped to a useful area of interest (AOI) and ideally visualize an undistorted transverse cross section of an observed beam with correct pixel to millimeter scaling. The calibrated images are typically reduced in size, allowing to economically stream images from multiple cameras through the GigE network. The data load from imaging and image analysis is handled by the `RabbitMQ` message broker. Computing power (e.g. for computational expensive 2D profile fits) is distributed to multiple standard computers within the network. A QT-based [6] graphical user interface

[1] https://www.kernel.org/doc/html/v4.8/media/v4l-drivers/
[2] virtual network computing

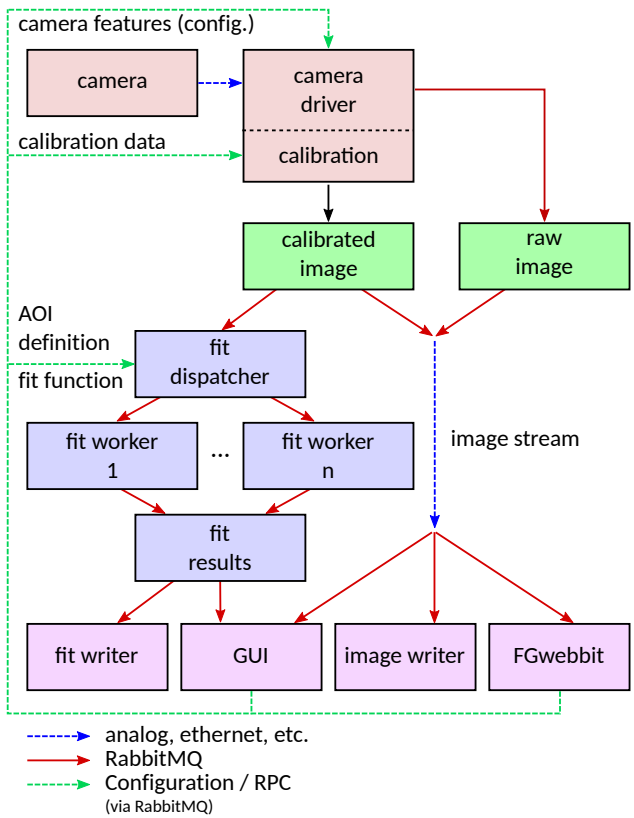


Figure 1: Architecture of the `FGrabbit` framework.

* switka@physik.uni-bonn.de

Content from this work may be used under the terms of the CC-BY-4.0 licence (© 2023). Any distribution of this work must maintain attribution to the author(s), title of the work, publisher, and DOI

ISBN: 978-3-95450-236-3 ISSN: 2673-5350 doi:10.18429/JACoW-IBIC2023-WEP046

(GUI) allows full-scale user interaction. A web interface allows down-scaled interaction from anywhere via the ELSA website[3].

Performance

A `RabbitMQ` message is limited to 128 MB, defining the limit for the streamable image size. While the cumulative streaming data rate is limited by the network bandwidth, the computationally expensive fit calculations are outsourced to an arbitrary amount of computers participating in the net- and framework. Computation and network load is conveniently monitored via the `RabbitMQ` analysis interface. Using standard desktop computers we achieve repetition rates up to 10 Hz of display and beam analysis on a sufficiently large AOI (2D data fit on a hundreds by hundreds large pixel grid).

MEASUREMENT PRECISION

Image Calibration

Beam images taken from e.g. Chromox screens suffer from projection and optical imaging errors which can be classified as intrinsic and extrinsic properties[4]. To obtain a projection-free image without optical errors, a 3×3 projection matrix P can be applied to the uncalibrated image

$$P = K \cdot M, \quad M = H \cdot \vec{t}\,, \tag{1}$$

where K denotes to the intrinsic and M to the extrinsic properties of the individual setup. M is calculated from a rotation matrix H and a translation vector $\vec{t}$. The main influence to the extrinsic uncertainties are image distortions due to the observation perspective, e.g. a screen under a tilt angle of typically 45°. This can be resolved by using a homography matrix as rotation matrix. The matrix entries can be computed from an image taken with a regular pattern of known dimensions (checkerboard or circular patterns consisting of $m \times n$ corners or circles, respectively). Such a calibration image can be temporally installed on the surface of a screen, as demonstrated in Fig. 2. A calibration pattern printed on cardboard with a regular laser printer usually suffices the required image quality. For the calibration we use an OpenCV [5] approach as depicted in Fig. 3. Therewith, a raw image is captured on which an OpenCV detector function finds the position of the corners of the checkerboard (or centers of circles, resp., compare with circular calibration patterns in Appendix). The obtained coordinates are then optimized by performing an additional search for the position using sub-pixel accuracy. Then a coordinate grid that matches the shape of the used pattern is created with a predefined step range. By mapping the found image coordinates into the real world grid the homography matrix can be calculated.

Measurement Error

The radial displacement of the transformed positions to the expected grid is classified as the calibration error. To minimize statistical fluctuations a sequence of n images is recorded to obtain an averaged radial error, as visualized in Fig. 2 c). Intrinsic properties, such as radial or tangential distortions introduced by the camera lens may be represented by

$$\begin{aligned} x_{\text{dist,rad}} &= x(1 + k_1 r^2 + k_2 r^4 + k_3 r^6) \\ y_{\text{dist,rad}} &= y(1 + k_1 r^2 + k_2 r^4 + k_3 r^6) \\ x_{\text{dist,tan}} &= x + \left(2p_1 xz + p_2(r^2 + 2x^2)\right) \\ y_{\text{dist,tan}} &= y + \left(p_1(r^2 + 2y^2) + 2p_2 xy\right)\,, \end{aligned}$$

with distortion coefficients $(k_1, k_2, k_3, p_1, p_2)$. OpenCV functions allow to determine these coefficients and to undistort the respective image. The distortion coefficients are obtained from taking multiple pictures of a regular pattern from multiple angles[5]. We find that intrinsic distortions play a neglectable role with usage of industry standard photographic objectives (e.g. $f = 16$ mm) for our monitor setups.

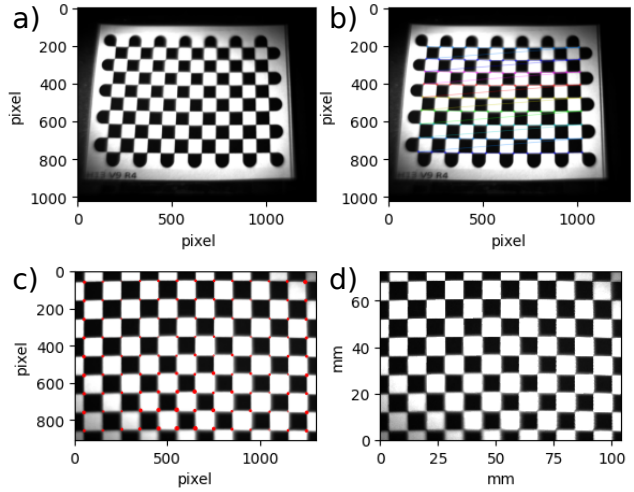


Figure 2: Image calibration using a printed checkerboard pattern on a tilted screen and OpenCV [5] transformation functions: a) original image, b) recognized pattern, c) image after homography transformation including precision errors (red circles), d) scaled and calibrated image.

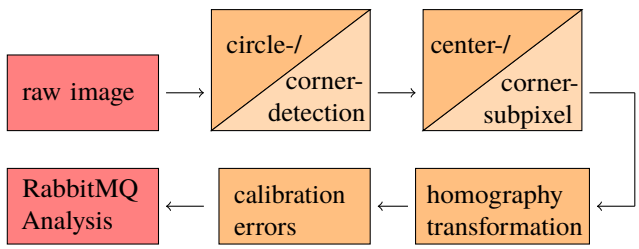


Figure 3: Schematic sketch of the calibration chain. The chain is divided into RabbitMQ framework (red) and OpenCV tasks (orange). The chain can be applied to circular patterns (dark-orange) and checkerboard patterns (light-orange).

[3] https://www-elsa.physik.uni-bonn.de
[4] compare e.g. with https://docs.opencv.org/4.x/
[5] For details see https://docs.opencv.org/4.x/dc/dbb/tutorial_py_calibration.html

Content from this work may be used under the terms of the CC-BY-4.0 licence (© 2023). Any distribution of this work must maintain attribution to the author(s), title of the work, publisher, and DOI

ISBN: 978-3-95450-236-3 ISSN: 2673-5350 doi:10.18429/JACoW-IBIC2023-WEP046

The calibration error determined from the deviation from the keypoint grid can be interpolated to every pixel, for example using radial basis functions[6], as shown in Fig. 4. Thereon, non-linear weighted fit algorithms can be applied to take local uncertainties into account. For this purpose the GNU scientific library (GSL) [7] back-end of the in-house developed fit library is used. For the unweighted case the common function to be minimized is

$$\Phi(x) = \frac{1}{2}\|f(x)\|^2 = \frac{1}{2}\sum_{i=1}^{n} f_i(x_1, \ldots, x_p)^2,$$

where f is the residual function, n the number of data points (e.g. the number of pixels of the captured image) and p is the number of parameters or the dimension of the fit function. In the weighted case this formula is expanded to

$$\Phi(x) = \frac{1}{2}\sum_{i=1}^{n} w_i \cdot f_i(x_1, \ldots, x_p)^2, \qquad (2)$$

where an individual weight w_i is added for each individual data point. These weights can be utilized for various purposes or represent different effects. Using the obtained inverse calibration variances as weights allows us to suppress potential errors introduced by the calibration process. Furthermore, this allows to mask areas on the screens that exhibit altered behavior to achieve a better fit result. In Fig. 4 a profile captured on a calibrated screen as well as the weighted fit to this data is shown. The inverse variance of the calibration was used as weight, resulting in a profile parameter deviation of up to 2 % comparing weighted and unweighted case.

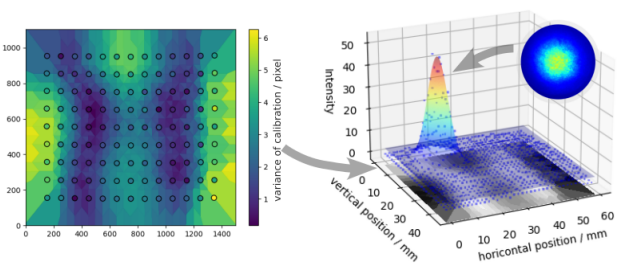


Figure 4: The variance of an exemplary screen calibration with circled nodes and in-between interpolation (left) and a beam profile image on a calibrated screen analyzed with a weighted fit algorithm (right).

FGRABBIT INTERFACES

While RPC[7] commands allow for automated settings and application of the `FGrabbit` framework, the graphical user interfaces provide practical user interaction and monitoring capability.

Operator GUI

A QT-based [6] graphical user interface allows for convenient control of camera and imaging settings (Fig. 5). The numerous available camera settings are listed and manipulatable, as shown in Fig. 6. Favorite settings can be marked and made available for the main menu. A detail view of the image analysis gives the operator fast and comprehensive feedback of fit parameters and fit quality.

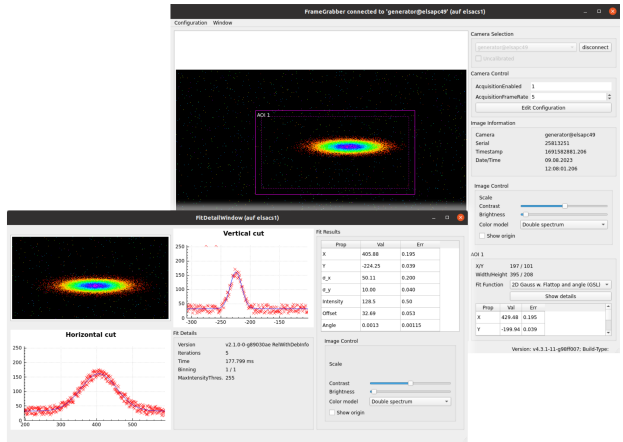


Figure 5: `FGrabbit` graphical user interface with detail view on profile analysis.

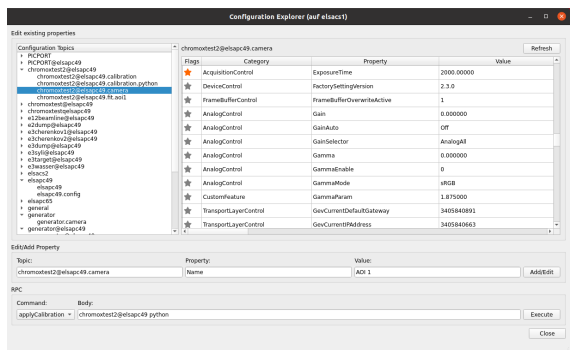


Figure 6: `FGrabbit` configuration explorer listing all properties of the digital cameras obtained by the Aravis [4] driver.

FGwebbit

In addition to the Operator GUI a slimmed down Interface is accessible via an in-house developed web application, called `FGwebbit`. It provides platform independent access to `FGrabbit` combined with flexible availability via internet and intranet. The responsive architecture (Fig. 7) enables control and views optimized for handheld devices when working on experiments or maintenance tasks in confined spaces. The simplified user interface provides access to live views of multiple camera streams simultaneously. The user interface is complemented by a modular card for each camera. Within a camera card, favorite settings of the attached device are directly available. An expert menu contains all available device parameters for detailed adjustments, accompanied by tooltips for the available settings. Each client can adjust the compression, frame rate, color model and preference for calibrated or uncalibrated data. These settings are saved

[6] e.g. using Python SciPy RBFInterpolator
[7] remote procedure call

Content from this work may be used under the terms of the CC-BY-4.0 licence (© 2023). Any distribution of this work must maintain attribution to the author(s), title of the work, publisher, and DOI

ISBN: 978-3-95450-236-3 ISSN: 2673-5350 doi:10.18429/JACoW-IBIC2023-WEP046

and applied only for that particular client, allowing for an optimized application e.g. for mobile use with limited data availability. The web application is prepared to host a global overview of the state of the FGrabbit systems, summarizing the status of all associated nodes and devices. Furthermore, the application provides space for the documentation of the FGrabbit framework and interfaces.

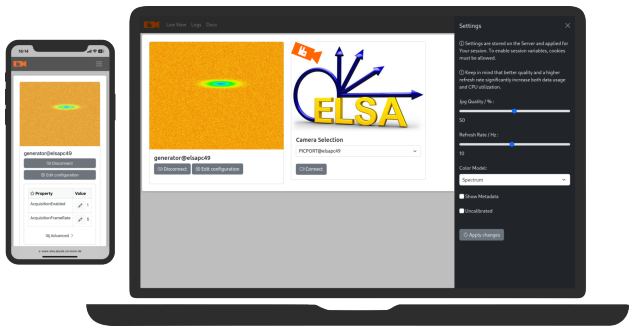


Figure 7: Responsive behavior of the FGwebbit interface and active session settings menu.

The FGwebbit backend extends the FGrabbit Python interface [2] and uses the lightweight Python web framework Flask. To reduce network traffic and data usage in mobile or low bandwidth environments, the live camera feeds are served as compressed JPEG streams. The OpenCV library [5] is used for compression and color model application. Further streamlining is achieved by smart handling of TCP connections to the underlying FGrabbit framework. Multiple clients and simultaneous streams from or to the same camera device are detected and clustered into a single open TCP connection. This alone significantly improves connection times for additional clients and reduces server load. Unused TCP connections are closed after a predefined timeout, freeing up system resources. For modern design and easy responsive implementation the popular Bootstrap frontend toolkit is used, resulting in familiar design elements and usability concepts for FGwebbit.

CONCLUSION

Screen calibration for extrinsic properties is the key advantage for beam photometry with monitors installed in environments typical for accelerator beamlines. Calibration errors may be used to improve measurement accuracy using weighted data fit algorithms. The performance of the FGrabbit framework is continuously tested and has shown to be robust and scalable. Minor software development is yet carried out to improve usability for long-term accelerator operations.

APPENDIX

Circular Calibration Pattern

Circular calibration patterns are generally more robust (successful) than checkerboard patterns, e.g. when illumination is non-ideal, as shown in Fig. 8.

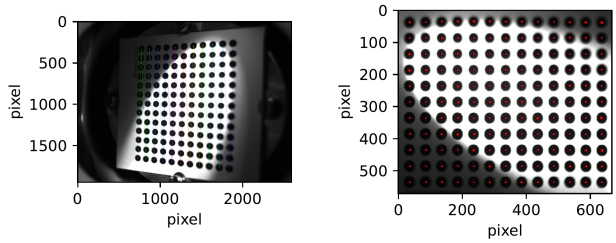


Figure 8: Screen with confined illumination and recognized pattern (left). Calibrated image using circular patterns including precision errors (right).

Virtual Calibration Pattern

Screens with sufficient markings for reference can be calibrated with a virtual pattern, e.g. created with a drawing tool and fed to the calibration algorithm, as shown in Fig. 9.

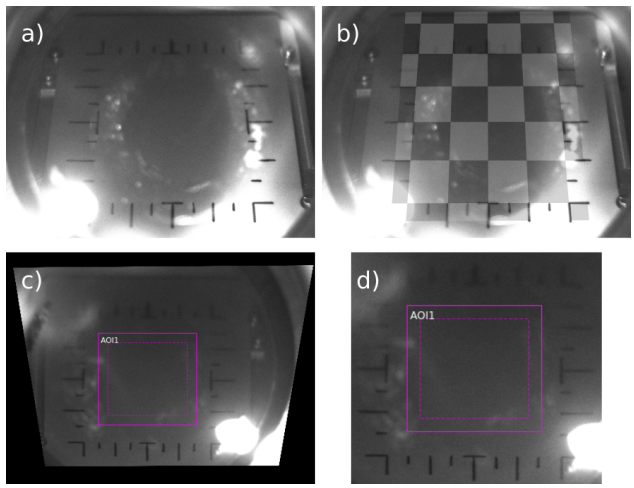


Figure 9: a) Sufficient visible markings may be used to create a b) virtual pattern for c) & d) image calibration.

REFERENCES

[1] W. Hillert *et al.*, "Beam and spin dynamics in the fast ramping storage ring ELSA", *EPJ Web Conf.*, vol. 134, p. 05002, Jan. 2017. doi:10.1051/epjconf/201713405002

[2] D. Proft *et al.*, "Beam profile monitoring and distributed analyis using the RabbitMQ message broker", in *Proc. IBIC'22*, Kraków, Poland, Sept. 2022, pp. 140–143. doi:10.18429/JACoW-IBIC2022-MOP38

[3] European Machine Vision Association, "GenICam Standard", https://www.emva.org/standards-technology/genicam/

[4] A vision library for genicam based cameras, https://github.com/AravisProject/aravis

[5] G. Bradski,"The OpenCV Library", *Dr. Dobb's Journal of Software Tools*, 2000.

[6] The Qt Company, https://www.qt.io/

[7] M. Galassi *et al.*, *GNU Scientific Library Reference Manual*, 3rd ed., ISBN 0954612078, https://www.gnu.org/software/gsl/

Content from this work may be used under the terms of the CC-BY-4.0 licence (© 2023). Any distribution of this work must maintain attribution to the author(s), title of the work, publisher, and DOI

ISBN: 978-3-95450-236-3 ISSN: 2673-5350 doi:10.18429/JACoW-IBIC2023-TH1I01

LCLS-II TIMING SYSTEM AND SYNCHRONOUS BUNCH DATA ACQUISITION*

C.B. Mattison, K. Kim, P. Krejcik, M. Weaver, M. Zelazny
SLAC National Laboratory, CA USA

Abstract

The new timing system for the LCLS-II SC linac and FEL meets the challenging requirements for delivering multiple interleaved timing patterns to several different destinations at rates up to 1 MHz. The timing patterns also carry information on bunch charge and beam energy to prevent inadvertent selection of beam dumps beyond their rated beam power. Beamline instruments are equipped with a timing receiver that performs bunch-by-bunch synchronous data acquisition based on the timing pattern for that location. Data is buffered in on-board memory for up to 10^6 machine pulses (1 s at 1 MHz). The large data volume can be locally processed and analysed before transmission to clients on the network. Commissioning and experience with the new system will be presented

INTRODUCTION

The LCLS-II Timing System developed at SLAC is the first timing system able to provide programmable timing patterns with variable rates from 1 Hz to 1 MHz with interleaved bunches to multiple destinations. The LCLS-II Timing System provides the triggers for the timing receivers along the 4 km beamline that are used to trigger hardware pulsed devices (kickers, Klystrons) and diagnostic devices (BPMS, cameras, wire scanners etc) as well as providing soft triggers for the data acquisition.

The LCLS-I and LCLS-II timing systems are physically decoupled: two separate dedicated fiber networks. The Timing pattern is generated upstream in the LINAC with a Timing Pattern Generator (TPG) and is then distributed to the Timing Pattern Receivers (TPR) at the device level. In shared areas, between LCLS-I and LCLS-II, the TPRs are capable to select the timing source to trigger on.

The SLAC accelerator complex provides multiple sources and destinations options to the machine operators.

The complexity of programming the LCLS-II timing pattern is ultimately resolved in the Timing Pattern Generator Graphical User Interface (TPGGUI). The LCLS-II project is currently under commissioning and it is the scope of this paper to describe the components that made the LCLS-II Timing System successful as well as discuss the commissioning experience with this new cutting-edge system.

TIMING PATTERN GENERATOR

The LCLS-II Timing System is composed of the master source, phase reference distribution, timing pattern generator, and timing pattern receiver units.

* Work supported by the U.S. Department of Energy under contract number DE-AC02-76SF00515.

The LCLS-II master source generates the 1300 MHz and 185.7 MHz (1300 MHz/7) phase reference signals with small jitters, phase locked together. The transmission of the 1300 MHz phase reference to LLRF has tight requirements on the stability and jitter of the timing signal over a large distance.

The LCLS-II Requirements parameters are listed in Table 1 below:

Table 1: LCLS-II Timing System Parameters

Timing Attribute	Value
Phase Reference (Linac RF)	1300 MHz
Clock (Gun RF = Linac RF/7)	185.71 MHz
Nominal Beam Rate (Clock/200)	0.92857 MHz
Fiducial Resync Freq (Clock/2600)	0.07143 MHz
Fiducial (Power Line Phase)	360 Hz
Stability - Standard (fiber)	0.4 ns
Stability – Phase reference line (PRL)	1 fs/sec, 1 ps/day
Jitter – Standard (fiber)	30 ps
Jitter – PRL (50 Hz to 5 kHz)	0.005° or 10.7 fs

The Timing Pattern Generator (TPG) runs on an FPGA in an ATCA crate. The TPG publishes the timing pattern over a dedicated fiber network. A timing pattern is a collection of timing frames and contains unique information about a beam pulse (Table 2). The timing frame is time stamped by the TPG and tagged with a unique pulse ID for post-data acquisition processing, allowing cross-correlation of signals between multiple devices.

The timing pattern frame in Fig. 1 shows how the timing pattern frame is encapsulated within control characters that allow additional data streams to be serialized onto the link. This configuration allows control transmissions of differing domains that firmware outside of that domain are not required to parse. The entire 1 MHz frame is validated by 32-bit CRC calculation [1].



Figure 1: Timing pattern frame (visual).

The timing frame is manipulated by the firmware and software. The software, hosted on the EPICS control system, can send information to the firmware by programming the sequence engines, which can then update the pulse timing frame content providing useful information such as the beam destination.

Content from this work may be used under the terms of the CC-BY-4.0 licence (© 2023). Any distribution of this work must maintain attribution to the author(s), title of the work, publisher, and DOI

ISBN: 978-3-95450-236-3 ISSN: 2673-5350 doi:10.18429/JACoW-IBIC2023-TH1I01

Content from this work may be used under the terms of the CC-BY-4.0 licence (© 2023). Any distribution of this work must maintain attribution to the author(s), title of the work, publisher, and DOI

Table 2: Timing Pattern Frame

Field	Size	Description
Pulse ID	64	Unique, monotonic., increments at base rate
Time Stamp	64	Time since 1990 epoch., increments at programmed step size
Fixed Rates	10	Fixed rate markers 0-9; one bit for each
ACRates	6	Power line synchronized markers 0-5, one bit for each
Time Slot	3	360 Hz time 1-6 persistent. Computed from TS1 input
Beam Request	1	Beam is requested from the injector
Destination	4	Beam destinations
Charge Inj.	16	Bunch charge
Beam Energy	4×16	Beam energy at 4 locations
BSA Control	4×64	For each buffer, initialize, average, acquire, finalize
ControlSeq[0:17]	288	16b control step data for each of 18 sequences
+ others		

The main sequence engines used for generating the timing patterns in the firmware were developed at SLAC:

- Beam-Engines: used to schedule the beam patterns to request beam to a specific destination published on the timing frame.
- Allow-Engines: hosts the allowed sequences given the pattern running on the beam engine. And through the Allow-Table, which selects the appropriate allowed sequence to run, provides the handshake between Machine Protection System (MPS)/Timing.
- Experimental/Control Engines: Manipulates the tail, 288 control bits, of the timing frame to support multi-destination beam, beam synchronous acquisitions, experiment requirements.

The Fixed Rate Markers

The Fixed Rate markers are set by the firmware and are the base rate reference used to define all beam patterns.

The Fixed Rate markers are computed by dividing the 185 MHz reference clock by 1, 13, 91, 910, 9 100, 91 000, 910 000, LSB to MSB.

The frames are then tagged accordingly to the appropriate spacing between fixed rate markers, but all timing frames are tagged as 1 MHz frames. This results in overlap of all the markers at 1 Hz.

The AC Rate Compatibility Requirement

The Event Generator, used on the LCLS-I accelerator operates at a maximum frequency of 120 Hz.

The LCLS-II project had to embrace the challenge to increase the trigger rate by up to 104 times higher frequency but still provide the capability to provide AC rates synchronized to the power line. This requirement is essential for some of the pulsed-power devices like Klystrons (XTCAV and STCAV). The triggering system for these devices needs to be synchronized to the AC Power line phase zero-crossings (timeslots) up to 120 Hz in order to minimize power supply ripple and jitter to the beam.

TIMING FIBER DISTRIBUTION

The LCLS-II Timing System hardware is completely decoupled from LCLS-I Timing System. The timing Pattern Generator (TPG) sends Timing Frames to each Timing Pattern Receiver (TPR) over a dedicated fiber network at 1 MHz.

The timing fiber distribution starts in Sector 2 where the TPG is located and is patched through passive and active fanouts. The active fanouts, developed at SLAC, provide the required drift compensation to resolve the challenge of signal stability over this long fiber network. The timing fiber distribution extends through the 4 km accelerator complex which is subject to large variations in temperature (Fig. 2).

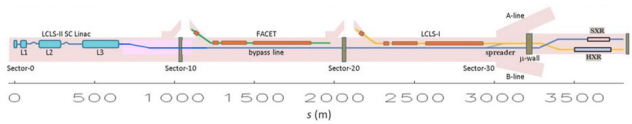


Figure 2: SLAC Accelerator Complex in meters.

The Active Fanouts are placed at three strategic locations along the linac to provide drift compensation. The first Active Fanout is in Sector 2 where it receives a signal directly from the TPG and distributes it to nearby passive fanouts plus the next Active Fanout in Sector 20. The Active Fanout in Sector 20 is like the one in Sector 2 where it feeds nearby passive fanouts plus the next Active Fanout in B005 (Fig. 3). The passive fanouts distribute the timing pattern to the final receivers.

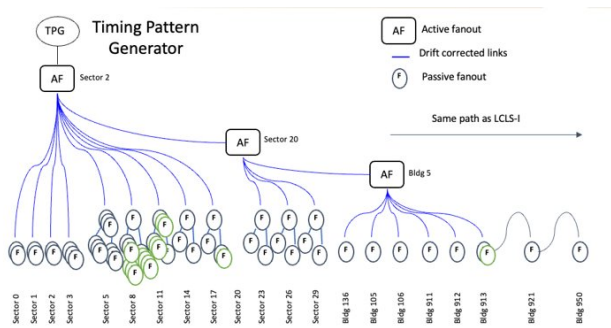


Figure 3: Timing fiber distribution.

Figure 4 shows the signal drift on 6 channels measured at the Sector 20 Active Fanout.

ISBN: 978-3-95450-236-3 ISSN: 2673-5350 doi:10.18429/JACoW-IBIC2023-TH1I01

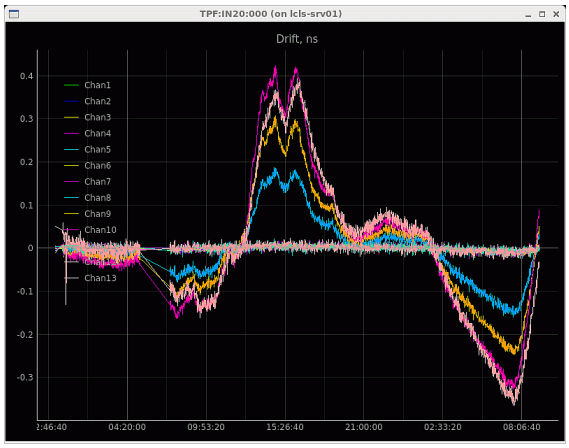


Figure 4: Signal drift on 6 channels measured at the Sector 20 Active Fanout. On the y axes the signal drift (1 ns) over time (about 12 h).

BEAM SYNCHRONOUS ACQUISITION

LCLS-II is a single-pass machine which requires that diagnostic devices be able to read out the same pulse throughout the machine on a bunch-by-bunch basis. The Superconducting Beam Synchronous Acquisition (SC BSA) provides data buffers time stamped by the SC Timing System (Timing Pattern Generator – TPG). An acquisition can be set with data filtering to satisfy user needs for each beam destination. The data is released in data buffers containing up to 20,000 data points. Each data point can be averaged over up to 8191 beam pulses. This feature is very useful for acquisition running at a very high rate such as 1 MHz.

There are five regions, or beam destinations, of interests in the LINAC: the diagnostic line (SC_DIAG0), the Beam Switch Yard Dump (SC_BSYD), the Hard X-ray beam line (SC_HXR), the Soft X-ray Line (SC_SXR) and the LINAC area beyond the diagnostic line. For each of these regions the system provides permanent, continuous data acquisition at the following rates:

- 1 Hz, for data archive,
- 10 Hz, for accelerator control room displays,
- 100 Hz, for physics applications.

This gives a total of 15 continuously running BSA buffers. In addition, there are 29 user-configurable BSA buffers and four, 1 second deep, fault buffers for the Machine Protection System (MPS).

The LCLS-II Timing System also provides the Beam Synchronous Scaler Service (BSSS) which provides real-time pulse-by-pulse scaler data at rates up to 100 Hz for control room displays.

COMMISSIONING BEAM PATTERNS

The LCLS-II timing system is very flexible and can be programmed with a wide variety of bunch patterns. However, for the initial commissioning, we required a set of preconfigured patterns that would allow us to commission each of the subsystems such as the BPMs, beam loss monitors, MPS, LLRF (Low-Level RF), and other diagnostics.

The patterns that satisfy these requirements are defined as Standard Patterns and are listed in Fig. 5.

FIXED RATE Patterns	AC RATE Patterns	Burst Spacing	Burst bunch(es)
0Hz	0Hz	2-20	100
Single shot	1Hz	9	2;5;10;20;50;100
1Hz	10Hz	1,2	1;2-21;50;100;200;500;1000;2000
10Hz	30Hz	10000	2
50Hz	60Hz		
100Hz	110Hz		
1KHz	119Hz		
10KHz	120Hz		
100KHz			
496KHz			
930KHz			

Figure 5: Standard Patterns for Commissioning.

The standard timing patterns are available for the four SC final destinations: SC_DIAG0, SC_BSYD, SC_HXR and SC_SXR. The beamline map (Fig. 6) below shows in blue the diagnostic line, used for emittance studies; in green the path to the BSYD dump; in yellow to the Soft X-ray Line Dump, and in Green to the Hard X-ray Line Dump.

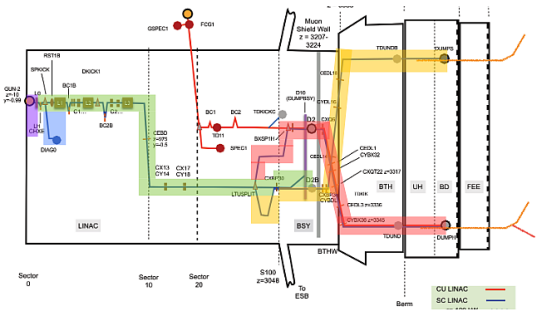


Figure 6: Beamline paths and destinations for LCLS-II.

Depending on the machine mode, the operator can request beam pulses going to different destinations and some of them are compatible with each other. The compatibility of these destinations is described by a lookup table of the machine modes.

The standard patterns can then be combined to generate Complex Patterns allowing multiple destinations request beam at the same time. The Complex Patterns are distinguished in:

- Pulse Stealing: all pulses with beam land on the Fixed Rate Markers distributed as part of the timing pattern. In case of multiple destination requesting beam, destination priority will determine beam pulses assignment.
- Interleaved Patterns: each destination is assigned an offset from the closest fixed rate marker to the requested beam rate.
- Bunch Train: user defined interval between beam patterns

Interleaved Patterns

Interleaved Patterns are patterns where the beam is requested for two destinations, but its request is placed on a fixed offset in respect to a rate marker coming out of the timing pattern. The offset is unique to that destination to ensure no overlap.

Content from this work may be used under the terms of the CC-BY-4.0 licence (© 2023). Any distribution of this work must maintain attribution to the author(s), title of the work, publisher, and DOI

ISBN: 978-3-95450-236-3 ISSN: 2673-5350 doi:10.18429/JACoW-IBIC2023-TH1I01

Content from this work may be used under the terms of the CC-BY-4.0 licence (© 2023). Any distribution of this work must maintain attribution to the author(s), title of the work, publisher, and DOI

The subharmonic frequency that allows the two LINAC (LCLS-I and LCLS-II) to be phase-locked together is 71.5 kHz. Between two fixed rate pulses at 71.5 kHz there are 13 empty pulses. The offset of empty pulses from a Fixed Rate marker, per destination, is then selected to be one of the prime numbers <13, such as: 3 empty pulses for SC_DIAG0, 5 for SC_HXR and 7 for SC_SXR. Following this logic, we are then able to schedule independent beam requests for multiple destinations.

TPG Graphical User Interface

The Timing Pattern Generator Graphical User Interface (TPGGUI) is python-based code that allows expert operators and physicists to program new timing patterns to satisfy additional pattern requirements. The interface provides a preview of possible conflict between destinations requesting the same beam pulse. The conflicts are highlighted by a yellow triangle (Fig. 7).



Figure 7: TPGGUI showing conflict on beam pulse requested by two destinations on the same bucket.

COMMISSIONING EXPERIENCE

SC_DIAG0 and SC_BSYD in Pulse Stealing Mode

In this commissioning example shown in Fig. 8, a requested pattern of 100 Hz to DIAG0 and 10 Hz to BSYD will actually result in 90 Hz to DIAG0 and 10 Hz to BSYD (Fig. 9). This example shows that in pulse stealing mode any beam pulse overlap in beam request is "stolen" by the higher priority destination, in this case SC_BSYD. It is noted that the beam pulses are equally spaced along the pattern.

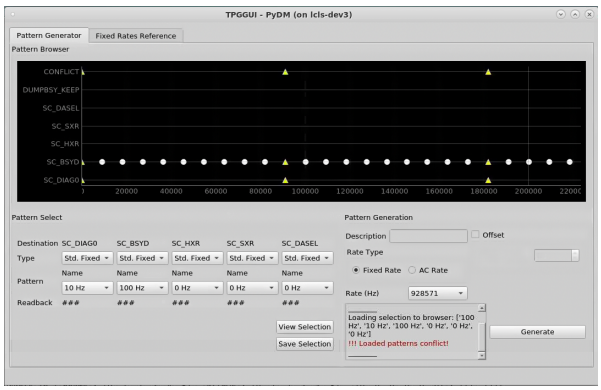


Figure 8: TPGGUI showing conflict on beam pulse requested by SC_DIAG0 and SC_BSYD in pulse stealing mode.



Figure 9: Beam pulses collected in the SC_DIAG0 and SC_BSYD areas corresponding to the pattern shown in Fig. 8.

SC_DIAG0 and SC_BSYD in Interleaved Mode

In this second example shown in Fig. 10, the requested rate is the same as in the previous example but the beam pulses for SC_DIAG0 are now requested with an offset of 3 pulses from the Fixed Rate Marker at 100 Hz. Now the scheduled pattern does produce a 100 Hz beam as requested to DIAG0 and 10 Hz beam to BSYD with the difference that the interval between beam pulses is no longer equally spaced (Fig. 11). However, during commissioning, this did not create any problems for the average RF load.

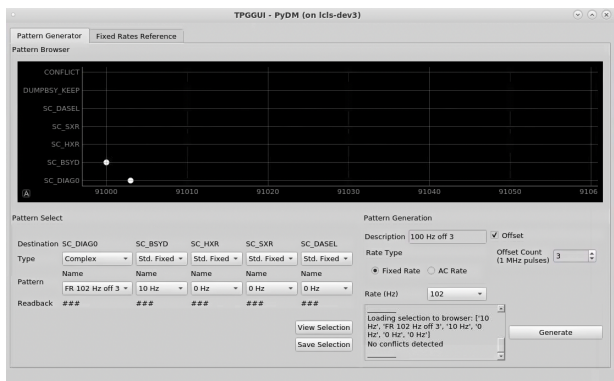


Figure 10: TPGGUI showing beam request with offset pulses between SC_DIAG0 and SC_BSYD.

SC_HXR and SC_SXR in Interleaved Mode

In the third example shown in Fig. 12, the requested rate is 1 Hz to SC_HXR and 1 Hz to SC_SXR. This succeeds because the beam requested to SC_HXR is offset by 5 pulses from the 1 Hz rate marker (Fig. 13). In the situation where an offset is not selected for one of the two destinations, then only the higher priority destination would receive beam pulses.

All of these offsets and rules need to be communicated in the timing pattern in order to trigger devices at rates lower

ISBN: 978-3-95450-236-3 ISSN: 2673-5350 doi:10.18429/JACoW-IBIC2023-TH1I01



Figure 11: Beam pulses collected in the SC_DIAG0 and SC_BSYD areas corresponding to the pattern shown in Fig. 10.

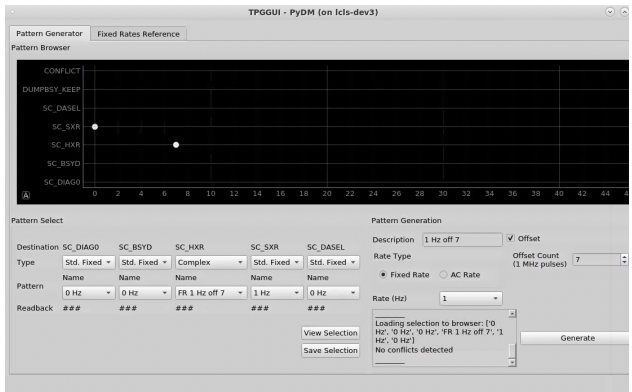


Figure 12: TPGGUI showing beam request on offset pulses between SC_HXR and SC_SXR.

than beam rate as well. For this reason, selecting a fixed offset per destination increases the stability and reliability of the pattern generation.

CONCLUSION

During LCLS-II Project commissioning we were able to satisfy all operation requirements and provide patterns flexible enough to run beam to multiple destinations at the same time. The interleaved pattern concept of dedicated offset associated with a destination allows a more stable configuration for also triggering devices and data acquisition at rates lower rate than the beam rate.

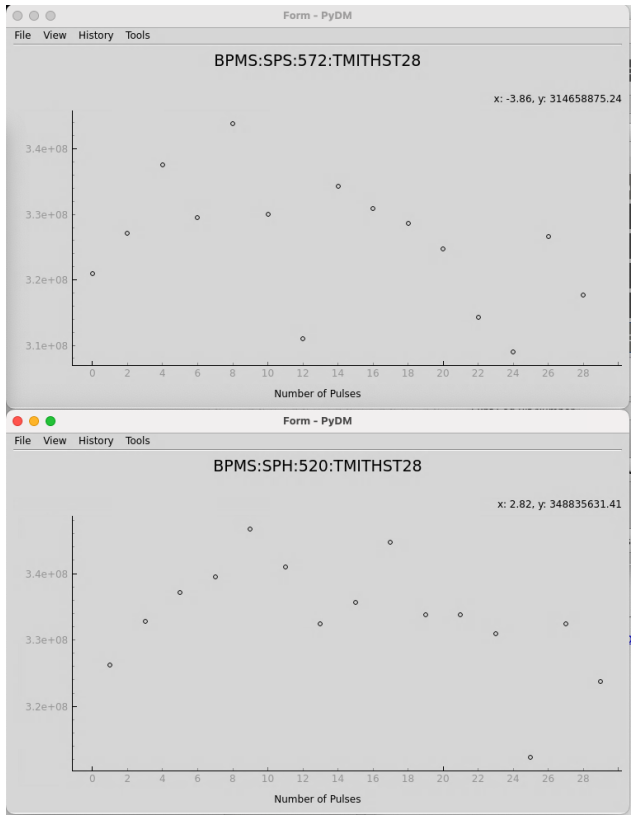


Figure 13: Beam pulses collected in the SC_HXR and SC_SXR areas at 1 Hz corresponding to the pattern shown in Fig. 12.

ACKNOWLEDGEMENTS

Acknowledgement to the timing team, physicists, operation and machine protection system team for all the support and the great teamwork. The LCLS-II timing system is the product of the great collaboration between those three groups. Work supported by the U.S. Department of Energy under contract number DE-AC02-76SF00515.

REFERENCES

[1] LCLS-II Timing System Engineering Specifications, https://docs.slac.stanford.edu/sites/pub/Publications/LCLS-II_Timing_System_Engineering_Specifications.pdf

Content from this work may be used under the terms of the CC-BY-4.0 licence (© 2023). Any distribution of this work must maintain attribution to the author(s), title of the work, publisher, and DOI

ISBN: 978-3-95450-236-3 ISSN: 2673-5350 doi:10.18429/JACoW-IBIC2023-TH1I02

NOVEL CAVITY BPM ELECTRONICS FOR SHINE BASED ON RF DIRECT SAMPLING AND PROCESSING*

L.W. Lai†, R. Meng, Y.M. Zhou, S.S. Cao, J. Chen, X.Q. Liu
SSRF, Shanghai Advanced Research Institute, Chinese Academy of Sciences, Shanghai, China

Abstract

A RF direct sampling beam signal processor has been developed in SSRF. It mainly consists of four channels RF direct sampling ADCs and a SoC FPGA. The ADC is 9 GHz bandwidth and 2.6 GHz sampling rate. A prototype of RF module contains band pass filter, low noise amplifier and step attenuator has been designed for SHINE cavity BPM system. Then a novel cavity BPM electronic including the processor and the RF module has been built for SHINE. The performance of the electronic has been analyzed and evaluated in lab. The amplitude relative error is 2.0×10^{-4} which is better than the required 1×10^{-3} on cavity BPM system. The phase error is 14 fs, also better than the requirement of RF BAM system. The algorithm and implementation in FPGA have been introduced.

INTRODUCTION

Shanghai Hgh repetitioN rate XFEL and Extreme light facility (SHINE) is a 3 km long hard X-ray FEL facility built 30 m underground in Shanghai. The designed beam repetition rate is 1 MHz. The project was initiated at the end of 2018, and to be completed at 2027. The SHINE was built adjacent to the campus of Shanghai Synchrotron Radiation Facility (SSRF) and Shanghai Soft X-ray FEL(SXFEL). Three types of BPMs are used in different sections: stripline BPMs are used in injector and sections between cryomodules, cold button BPMs are installed inside the cryomodules of the super conducting LINAC, and cavity BPMs are used in beam distribution lines and FEL sections.

Two types of cavity BPMs are designed for SHINE. A Φ35mm cavity BPM is designed for the distribution lines, which center frequency is 3520.87 MHz, and the required resolution 1 μm at 100 pC, and the dynamic range is ±1 mm. While a Φ8 mm cavity BPM is designed for the FEL sections, which center frequency is 5254.2 MHz, and the required resolution 200 nm at 100 pC, and the dynamic range is ±100 μm. It means the relative resolution of the cavity BPM electronics should better than 0.1%.

The cavity BPM generates signals with different modes when electron beam passing through. The amplitude of TM_{010} mode signal is proportional to beam charge, and the TM_{110} mode signal is proportional to both beam charge and beam position. The signals are narrow bandwidth at high frequency with high Signal to Noise Ratio (SNR), normally at several GHz.

BPM electronics use independent RF front-end modules and digital signal processors. Different RF front-end modules will be designed to meet the signal characteristics requirements of different BPM types. A generic beam signal processor platform has been developed for beam diagnostic system. Three types of electronic structures can be used to process the high frequency cavity BPM signal. First is the heterodyne, it down converts the signal to intermediate frequency (always at tens of MHz) for digitizing. It is proven trusted and high performance, and widely used, like LCLS I, LCLS-II, SXFEL, *et al.* But it is complicate and large physical size. The long chain RF components, especially Local Oscillator (LO) synthesizer and mixing modules introduce extra noise, and fragile to environment temperature humidity. Second is direct sampling the high frequency signal with ADC. The hardware is the simplest, most flexible, it is practical at L, S, C band right now. Because of the limitation of ADC bandwidth and effective number of bits, no large-scale application now adays. Third is direct-convert the signal to base band, or we say zero intermediate frequency in two quadrature channels. This structure lowers the requirement to low-pass filters and ADCs, simplifies the digital signal processing. European-XFEL made excellent work with this structure. The challenges of this structure including I/Q balance, local oscillator leakage, the interference from low frequency noise, also need one more ADC.

In SXFEL, the cavity BPM signal is down converted from about 4680 MHz to 30 MHz, and then digitized and processed with a self-developed signal processor (DBPM) [1]. The DBPM in a one stand-alone processor with a FPGA carrier board, an ADCs board and an ARM board. The ADC board has four input channels, the maximum sampling rate is 125 MHz, resolution is 16 bits, and bandwidth is 650 MHz. The ADC running at 119 MHz external clock synchronizing to RF. A XILINX Virtex5 FPGA is used as the core component on the carrier board. Except for the DBPM, a RF front-end is install besides the pickup in tunnel, a LO synthesizer and a down-conversion module are installed in the cabinet of electronic hall with DBPM. Obviously, the install space is quite large and cost is high.

In SHINE, the cavity BPM electronic cabinets are near the pickups in tunnel. The RF module integrates RF front-end module, LO synthesizer, and down conversion module into a 1U chassis. The signal is down-converted to 54 MHz, then sampled and processed with a generic beam diagnostic processor. The processor is stand-alone 1U height, including a XILINX Soc FPGA carrier board, a high-speed

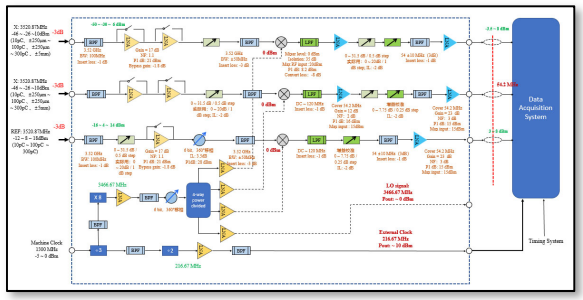
*Work supported by The National Science Foundation of China (Grant No.12175293). Youth Innovation Promotion Association, CAS (Grant No. 2019290)
†Corresponding author: lailw@sari.ac.cn

Content from this work may be used under the terms of the CC-BY-4.0 licence (© 2023). Any distribution of this work must maintain attribution to the author(s), title of the work, publisher, and DOI

ISBN: 978-3-95450-236-3 ISSN: 2673-5350 doi:10.18429/JACoW-IBIC2023-TH1I02

ADC board and White Rabbit timing board connected through two FMC interfaces. The ADC's maximum sampling rate is 1GHz, bandwidth is 2 GHz, and resolution is 14 bits [2-4].

Figure 1(a) is the block diagram of the cavity BPM electronic in SHINE, Fig. 1(b) is the picture of the beam signal processor.



(a)



(b)

Figure 1: Block diagram of Cavity BPM electronic (a) and picture of generic processor (b) for SHINE.

RF DIRECT SAMPLING ELECTRONICS

From the block diagram of the Fig. 1(a), we can see complicate RF chains. Mainly because of the heterodyne structure. RF Direct sampling Electronic (RFDE) shows obvious benefits compared to it. First, RFDE have no need of different LO synthesizers and down conversions for different types of cavity BPM in heterodyne structure, only need bandpass filter (BPF), low noise amplifier (LNA), and adjustable attenuator, which reduces the design difficulties and improve the maintenances efficiency. Second, less analog components improve the system sensitivity and stability. Third, smaller system size reduce power consumption and save budgets.

RFDE has long been pursued in accelerator. Since 2008, there have LLRF system, bunch feedback system, high speed digitizer, and BAM have used RF direct sampling electronics. We can summarize them into two categories. One is ADC boards sampling rate lower than 1 GHz, bandwidth smaller than 2.5 GHz. The other is XILINX RFSoC demo boards with multi number high speed ADCs and DACs. We tried the RFDE with an oscilloscope in 2017 [5]. No application in cavity BPM online signal processing yet.

The digital signal processing system mainly includes two parts: sampling and digital signal processing. Currently, varieties of ADCs with sampling rate to several GHz and bandwidths to about 10 GHz appeared. Then the CBPM signal in L/S/C band can be digitized directly. The ADCs based on JESD204B serial interface standard supports 12.5 Gbps data transmit speed between ADCs and FPGA, which makes real-time data transmission and processing in FPGA possible. Nowadays, powerful FPGA contains hard ARM cores, rich peripheral interfaces and massive logic resources have been widely used, which can realise real-time complex signal processing algorithms.

RFDE FOR SHINE CAVITY BPM

We developed a RFDE processor for SHINE. The processor is specified in Table 1. The processor is designed as a 1U height standalone, consists of a FPGA carrier board and an ADC daughter board connected through FMC connector. Another FMC connector is reserved for a White Rabbit timing board.

Table 1: RFDE Processor Specifications

Parameter	Value
Channels	4
Bandwidth	9 GHz
ADC bits	14
Max ADC rate	2.6 GHz
FPGA	Xilinx ZCU15EG
Clock	External
Trigger	Ext./Self/Period
SFP	2 UDP, 2Aurora
Interlock	Lemo
PL DDR4	2 GB
GPIO	12
Software	Arm-Linux/EPICS

Figure 2 shows the pictures of the processor. The ADC board is designed in large size for better performance.



Figure 2: Picture of RFDE processor.

We build a protype of RF module to evaluate the possibility of RFDE. Each channel includes a band pass filter, a low noise amplifier, and a 10 dB step attenuator. The block diagram and the picture are show in Fig. 3. The connections between components are removable for easy testing.

Content from this work may be used under the terms of the CC-BY-4.0 licence (© 2023). Any distribution of this work must maintain attribution to the author(s), title of the work, publisher, and DOI

ISBN: 978-3-95450-236-3 ISSN: 2673-5350 doi:10.18429/JACoW-IBIC2023-TH1I02

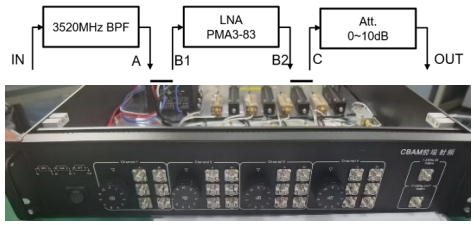


Figure 3: RFDE RF module.

With the developed processor and the RF module, a RFDE for cavity BPM system is built. The overall function is depicted in Fig. 4. Compared to the heterodyne structure in Fig. 1, RFDE system is much simpler.

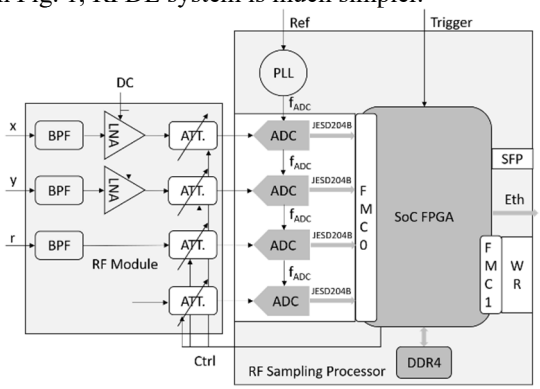


Figure 4: Overview of RFDE for SHINE cavity BPM.

SYSTEM PERFORMANCE ANALYZING

One of the main concerns with RFDE is whether it can meet the requirement of cavity BPM system. Noise figure (NF) is always used to evaluate the performance of an electronic. It's a measure of the noise added by the device (degradation of the SNR from input to output). The definition F and NF are listed below:

$$F = \frac{S_i/N_i}{S_o/N_o} \quad (1)$$

$$NF = 10 * log_{10}(F) \quad (2)$$

Where $S_{i/o}$ and $N_{i/o}$ are the signal and noise of the input and output respectively.

The NF of the cascaded devices chain can be calculated with NF and the gain (G) of each device. The NF and G parameter can be found in the datasheet of LNA. For passive devices, such as mixer, filter, and attenuator, the NF is not listed. The NF can be approximated with insert loss. There is no NF parameter listed in ADC datasheet, the calculation is a bit complicate. Equation (3) is the definition of NF_{ADC}.

$$NF_{ADC} = 10 \cdot \log\left(1000 \cdot \frac{(V_{PP})^2}{8 \cdot Z_{IN}}\right) + 174dBm - SNR_{ADC} - 10 \cdot \log\left(\frac{F_S}{2}\right) \quad (3)$$

Where F_S is the sampling frequency. The NF_{ADC} of RFDE processor and SHINE generic processor is 30.1 dB and 25.4 dB respectively.

Except for the NF of the hardware, extra digital signal processing gain can be obtained from filtering out the 1.6 MHz cavity BPM signal from the Nyquist zone. The formula is:

$$Processing\ Gain = 10 \cdot \log\left(\frac{F_S}{2B}\right) \quad (4)$$

Where B is the bandwidth of the cavity BPM signal. The processing gain of RFDE processor and SHINE generic processor is 24.3 dB and 29 dB respectively.

After getting above information, the SNR of RFDE and SHINE heterodyne structure is 85 dB and 87.2 dB respectively when the SNR of cavity BPM signal is 72 dB, the relative error of them is 7×10^{-5} and 5×10^{-5} respectively. They show similar performance and both far better than the requirements.

RFDE PERFORMANCE EVALUATION

Processor B using 16 bits ADCs and Xilinx FPGA XCZU9EG. LMK04832 is used to provide low jitter clock for ADC and the system. Figure 4 is the PCB of the processor. The ADC board is wider than the FMC standard. Lab test conditions were the same as the processor A test, but the sampling clock was multiplied to 833 MHz.

A lab test platform in Fig. 5 was built to evaluate the RFDE performance. A vector signal source generates a decay RF signal to simulate the cavity BPM signal and a 1.3 GHz signal divided as clock source. An external trigger from trigger divider is input.

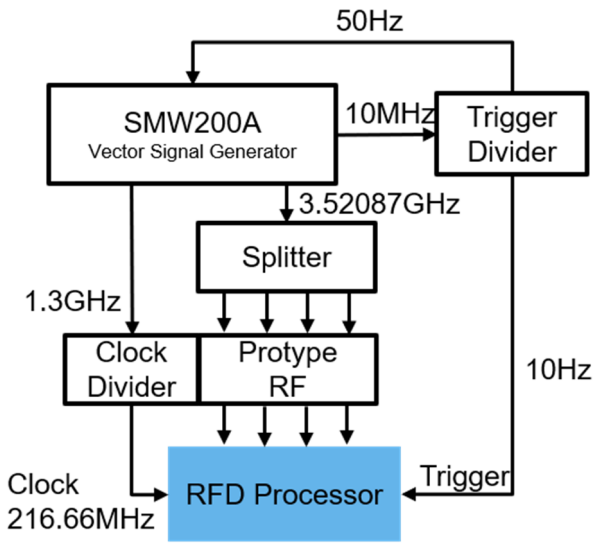
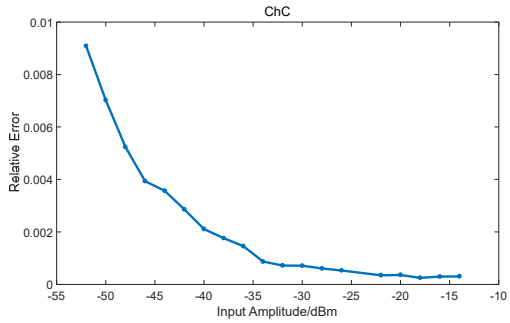


Figure 5: Block diagram of lab test platform.

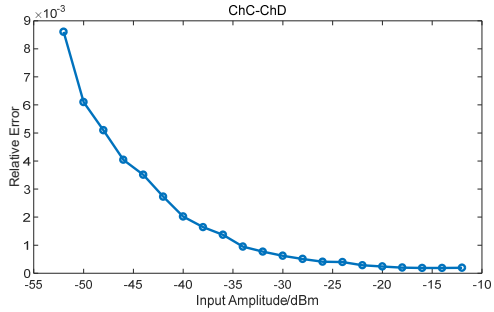
The channel input signal amplitude changed from -52 dBm to -14 dBm. Figure 6 is test results. The best relative error of one channel is 2.6×10^{-4}, which contains signal source jitter. The best relative error between two channels is 2.0×10^{-4}, this is better than the required 1.0×10^{-3}.



(a)

Content from this work may be used under the terms of the CC-BY-4.0 licence (© 2023). Any distribution of this work must maintain attribution to the author(s), title of the work, publisher, and DOI

ISBN: 978-3-95450-236-3 ISSN: 2673-5350 doi:10.18429/JACoW-IBIC2023-TH1I02



(b)

Figure 6: The relative amplitude error of one channel (a) and the value between two channels (b).

There are RF cavity BAMs in LINAC of SHINE designed the same frequency with Φ35 mm CBPM. Figure 7 is the relative phase error between two channels. The best phase RMS jitter is 14 fs, which is better than the required 25 fs resolution.

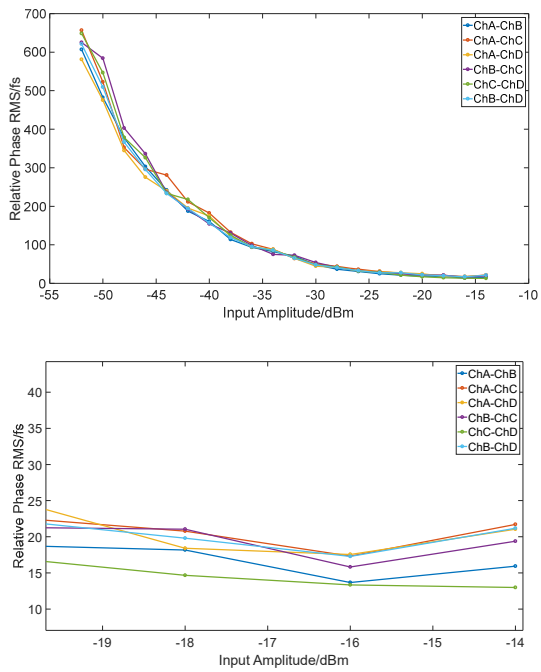
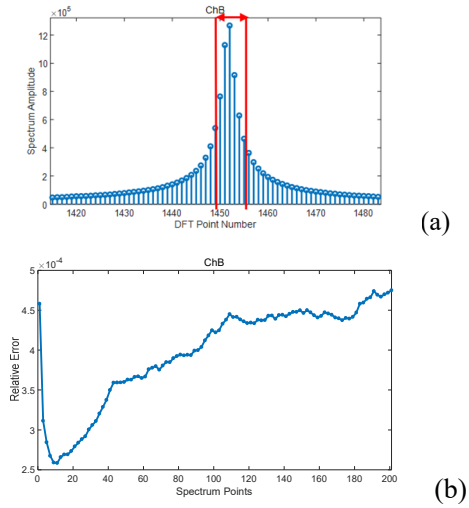


Figure 7: The relative phase error between two channels.

We investigated three cavity BPM signal processing algorithms to evaluate the performance and implementation. First is the fix point Goertzel-DFT algorithm. Figure 8(a) shows the calculated DFT points. The number of used points around peak influence the calculated relative error. Figure 8(b) shows the relative error of peak point is 4.5×10^{-4}, 3 points is 3.1×10^{-4}, 5 points is 2.8×10^{-4}, the best value is 2.6×10^{-4}. Second is Digital Down Conversion (DDC) algorithm. Third is Hilbert algorithm. All three algorithms can get the best result of relative error at 2.6×10^{-4}. We choose to implement Goertzel-DFT in FPGA, because the calculation point is fixed and 3 points DFT calculation is good enough.



(a)

(b)

Figure 8: Goertzel-DFT algorithm (a) and the relative error change with DFT points (b).

We implemented 3 points DFT algorithm in FPGA. About 35% CLB and 7.5% DSP were costed.

CONCLUSION

A RFDE has been built for SHINE cavity BPM signal processing, including a prototype RF module and a RF direct sampling processor. The RF module contains only BPF, LNA and step attenuator, which is much simpler compared to the heterodyne structure. The processor supports sampling 9 GHz signal at 2.6 GHz, and calculate 1 MHz rate beam position in real-time. The system performance is 2.0×10^{-4}, which is better than the requirement of SHINE.

Compared to the electronics 10 years ago, same budget today can afford much higher performance electronics. The cost saved from RF module can support the RF direct sampling ADCs. It's time to consider large-scale application of RFDE in beam diagnostics.

REFERENCES

[1] L. W. Lai *et al.*, "Beam Instrumentation System for Shanghai Soft X-ray FEL Test Facility", in *Proc. IBIC'20*, Santos, Brazil, Sep. 2020, pp. 17-20. doi:10.18429/JACoW-IBIC2020-MOAO05

[2] L. W. Lai and Y. B. Leng, "High-Speed Beam Signal Processor for SHINE", in *Proc. IBIC'19*, Malmö, Sweden, Sep. 2019, pp. 283-284. doi:10.18429/JACoW-IBIC2019-TUPP004

[3] L. W. Lai, F. Z. Chen, Y. B. Leng, J. Wan, T. Wu, and Y. M. Zhou, "Status of Digital BPM Signal Processor for SHINE", in *Proc. IPAC'21*, Campinas, Brazil, May 2021, pp. 3430-3433. doi:10.18429/JACoW-IPAC2021-WEPAB322

[4] X. Yang, L. W. Lai, Y. B. Leng, J. Wan, W. M. Zhou, and Y.M. Zhou, "Tests of Digital BPM Signal Processors for SHINE", in *Proc. IBIC'21*, Pohang, Korea, Sep. 2021, pp. 443-445. doi:10.18429/JACoW-IBIC2021-WEPP32

[5] L. W. Lai *et al.*, "The Application of Direct RF Sampling System on Cavity BPM Signal Processing", in *Proc. IBIC'17*, Grand Rapids, MI, USA, Aug. 2017, pp. 278-280. doi:10.18429/JACoW-IBIC2017-TUPWC01

Content from this work may be used under the terms of the CC-BY-4.0 licence (© 2023). Any distribution of this work must maintain attribution to the author(s), title of the work, publisher, and DOI

ISBN: 978-3-95450-236-3 ISSN: 2673-5350 doi:10.18429/JACoW-IBIC2023-TH2C03

ANALYSIS OF THE TRANSVERSE SCHOTTKY SIGNALS IN THE LHC

K. Lasocha*, D. Alves, CERN, Geneva, Switzerland

Abstract

Schottky-based diagnostics are remarkably useful tools for the non-invasive monitoring of hadron beam and machine characteristics such as the betatron tune and the chromaticity. In this contribution recent developments in the analysis of the transverse Schottky signals measured at the Large Hadron Collider will be reported. A fitting-based technique, where the measured spectra are iteratively compared with theoretical predictions, will be presented and benchmarked with respect to the previously known methods and alternative diagnostic.

INTRODUCTION

Schottky signals are the fluctuations of macroscopic beam characteristics, such as intensity or dipole moment, due to the discrete nature of the particle ensemble. They were first measured at the CERN's Intersecting Storage Ring in the early 1970s [1] and immediately used to provide information on momentum spread and betatron tune, as well as the rate of growth of betatron amplitudes at tune values close to resonant lines. Notably, it was the observation of Schottky signals what convinced Simon van der Meer to persue the implementation of his eminent concept of stochastic cooling [2].

Since then, the Schottky signal analysis has become a standard diagnostic technique for both coasting and bunched hadron beams, used among others in Tevatron [3], RHIC [4], SIS18 [5], CSR [6], ELENA [7] and LHC [8]. The basic theory of Schottky signals of coasting beams [9] has been enriched by studies on the Schottky spectrum deformation due to space charge, impedance and collective effects present in dense cooled beams [10, 11].

The case of Schottky signals of bunched beams is much less understood. The theory describing such signals is more complex, as it also has to take into account the particles' synchrotron motion. Some main principles can be found in Refs. [12, 13], as well as the effect of space-charge [14], but the knowledge on the impact of impedance, octupole magnets or beam-beam effects on Schottky spectra is so far very limited.

In addition, bunching introduces a finite degree of correlation in the motion of individual particles. In steady-state conditions, thanks to the filamentation associated with the betatron and synchrotron motion of particles, this correlation (also known as coherent motion) has a limited impact on the observed Schottky spectrum. Nevertheless, in certain conditions coherent effects are not negligible, yet very difficult to describe quantitatively.

* kacper.lasocha@cern.ch

In this contribution we shall recall the theory of the transverse Schottky spectra of bunched beams. Using experimental Schottky spectra measured during the ongoing LHC Run3 (2022-2026), we will address the issues of how and when the theory can be used to derive parameters such as the betatron tune and chromaticity. We shall also apply a fitting-based technique, proposed in [15, 16], which can be used to derive transverse beam characteristics from the spectrum, even in the presence of coherent components.

THEORY

Let us consider first the Power Spectral Density (PSD) of a transverse Schottky signal originating from a single particle. Around every harmonic h of the revolution frequency ω_0, the PSD consists of two bands, described by the following expression

$$P_T^{\pm}(\omega, \widehat{\tau}, \Omega_{s_0}, Q, Q\xi) =$$

$$= \hat{a} \sum_{p=-\infty}^{\infty} J_p^2 \left(\chi^{\pm}_{\widehat{\tau}, h\mp Q_I} \right) \delta[\omega - (h \pm Q_F)\omega_0 - p\Omega_s(\widehat{\tau})], \quad (1)$$

where Q_I and Q_F denote respectively the integer and fractional part of the betatron tune Q, $Q\xi$ is the chromaticity, $\widehat{\tau}$ is the time amplitude of synchrotron motion, $\Omega_s(\widehat{\tau})$ is the amplitude-dependent synchrotron frequency and $\hat{a}$ is a constant proportional to the squared amplitude of the betatron motion at the pick-up location. The argument of the Bessel function is given by

$$\chi^{\pm}_{\widehat{\tau}_i, n} = \left(n\widehat{\tau_i} \pm \frac{\widehat{Q_i}}{\Omega_{s_i}} \right) \omega_0 = (n\eta \pm Q\xi) \frac{\omega_0 \hat{p}}{\Omega_{s_i} p_0}, \quad (2)$$

with η denoting the slip factor and $\hat{p}$ the amplitude of momentum oscillations around the nominal value p_0. We assume that particles perform harmonic synchrotron motion, with the synchrotron frequency given by the theory of the mathematical pendulum [17]:

$$\Omega_s = \frac{\pi}{2\mathscr{K}\left[\sin\left(\frac{h_{RF}\omega_0\widehat{\tau}}{2}\right)\right]} \Omega_{s_0}, \quad (3)$$

where Ω_{s_0} is the nominal, limit synchrotron frequency, $h_{RF}\omega_0\widehat{\tau}$ is the the RF phase amplitude of synchrotron oscillations and $\mathscr{K}([0,1]) \to [\pi/2, \infty]$ denotes the complete elliptic integral of the first kind [18, p. 590].

In the absence of coherent components which, in the case of the transverse Schottky spectrum is equivalent to having a uniform distribution of both betatron and synchrotron oscillation phases, the total multiparticle PSD is given simply

Content from this work may be used under the terms of the CC-BY-4.0 licence (© 2023). Any distribution of this work must maintain attribution to the author(s), title of the work, publisher, and DOI

ISBN: 978-3-95450-236-3 ISSN: 2673-5350 doi:10.18429/JACoW-IBIC2023-TH2C03

by the sum of individual PSDs

$$P_T^{\pm}(\omega, \Omega_{s_0}, Q, Q\xi) = \sum_{i=1}^{N} P_T^{\pm}(\omega, \widehat{\tau_i}, \Omega_{s_0}, Q, Q\xi). \quad (4)$$

As we can see, given a set of parameters Ω_{s_0}, Q and $Q\xi$, the Schottky spectrum can be fully determined by the distribution of synchrotron amplitudes $\widehat{\tau_i}$ within a given bunch. In [15] we also showed that, in the absence of coherent motion, one can also use the longitudinal bunch profile or the distribution of synchrotron frequencies to determine the distribution of synchrotron amplitudes.

An example theoretical transverse Schottky spectrum is shown in Fig. 1. Two sidebands, located around the frequencies $(h \pm Q_F)\omega_0$, consist of a series of *Bessel satellites*. The distance between consecutive satellites is given by the synchrotron frequency. Individual satellites have a finite width, which reflects the spread in synchrotron frequencies among the particles. For non-zero chromaticity, the upper (right) and lower (left) sidebands are different, what is a result of a different argument of the Bessel functions, Eq. (2).

One has to keep in mind, that the observed Schottky signal is an intrinsically random process and in each time instance one can observe only its single realization [19]. Meanwhile the theory presented here describes the expected value, i.e. the ensemble average, of the spectrum.

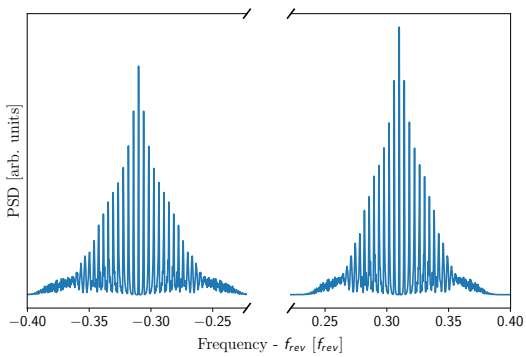


Figure 1: Theoretical transverse Schottky spectrum.

Assuming a discrete macroscopic distribution of synchrotron amplitudes $g(\widehat{\tau}_i)$ for an apriori chosen grid of synchrotron amplitudes $\widehat{\tau}_1, \ldots, \widehat{\tau}_m$, the DFT (Discrete Fourier Transform) of the total transverse Schottky signal at frequencies $\omega_1, \ldots, \omega_n$ can be expressed in a form of a matrix equation (Eq. (5)), where single particle $P_{DFT}^{T,\pm}$s can be calculated directly from Eq. (1), taking into the account the sampling frequency, period and the windowing function. The vector $\mathscr{A}$ denotes the discrete synchrotron amplitude distribution, while $\mathscr{S}_{DFT}$ is the DFT of the total Schottky signal. The number of considered amplitudes $\widehat{\tau_1}, \ldots, \widehat{\tau_n}$ has to be chosen as a trade-off between the time-complexity and discretisation error. In our studies we have used 50 amplitudes uniformly distributed over the whole RF bucket.

SCHOTTKY SIGNALS IN THE LHC

The LHC Schottky Monitor consists of four pairs of approximately 1 m waveguides, one for each of the 2 beams and the 2 planes, sensitive to the beam field within a band of approximately 400 MHz around 4.8 GHz. An electronic gating system allows one to isolate the signal coming from a single bunch. The coupled signal is then sequentially filtered and down-mixed, so that the final digitized Schottky signal consists of a narrow (approximately 14 kHz wide) band, originally located around the 427725^{th} harmonic of the revolution frequency, but mixed down to the 1^{st} harmonic.

The sampling rate, locked to the RF frequency to avoid discrepancies during the energy ramp, is kept equal to $4\times f_{rev}$. The spectra are calculated every second using the last $2^{16} = 65536$ samples, which results in a frequency resolution of approximately 0.69 Hz, and the expected value of the spectrum is estimated by performing a moving average of the last 100 spectra on a bin-by-bin basis.

The typical Schottky spectrum measured by the LHC Schottky monitor, in the absence of any coherent effects, consists of three bands: two transverse bands described by Eq. (4) plus the central longitudinal band. Although by design the strong longitudinal signal should not be seen by the monitor, imperfections of the common mode rejection make this signal visible and available for the diagnostic purposes, as discussed in Ref. [15].

The particle species accelerated in the LHC are either protons or Pb^{82+} ions. For the purpose of Schottky signals analysis, ion beams are significantly more favorable. Ion bunches consist of a lower number of particles, but each having a higher individual charge, they are therefore less likely to produce coherent effects in the spectrum. In addition, the higher transverse emittance of ion bunches increases the measured dipole moment, and therefore intensifies the transverse Schottky signal.

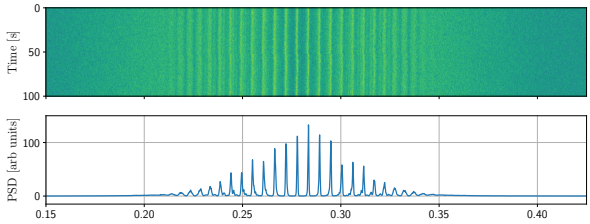
In Fig. 2 one can observe spectrograms and averaged spectra during typical stages of the ion beam operation. For ilustrative purposes only the upper transverse sideband is shown.

Figure 2 a) presents an unperturbed spectrum during steady conditions. Such a spectrum reliably reflect the theory discussed in the previous section, and can be easily analyzed. Spectra in Fig. 2 b) and c) were measured under conditions which introduced a local deformation of the averaged spectrum. The majority of the spectrum is however not affected, and can be matched with the theoretical description. The spectrogram shown in Fig. 2 d) is an example of a variety of transient effects, including different types of beam beam parameters change. Inevitably under these non-stationary conditions, and while the spectrogram is understandable, information is lost in the averaging process and the time averaged spectrum becomes very complex to analyse. Finally, Fig. 2 e) shows the spectrogram and average Schottky spectrum measured while the current in the octupole magnets is being ramped up. In this case individual Bessel satellites smear into wider bands (and eventually disappear for

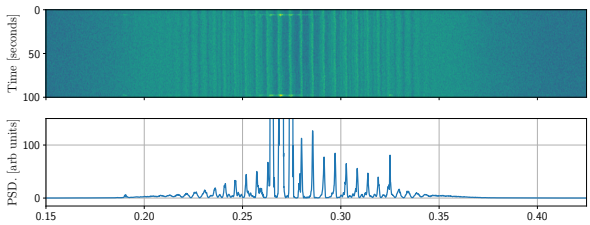
Content from this work may be used under the terms of the CC-BY-4.0 licence (© 2023). Any distribution of this work must maintain attribution to the author(s), title of the work, publisher, and DOI

ISBN: 978-3-95450-236-3 ISSN: 2673-5350 doi:10.18429/JACoW-IBIC2023-TH2C03

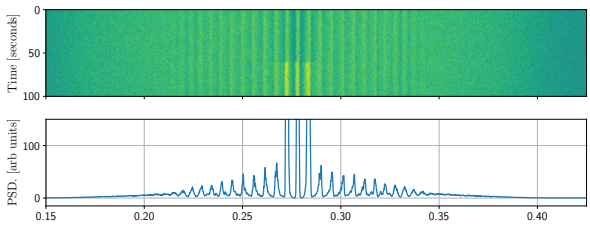
$$\underbrace{\begin{bmatrix} P^{T,\pm}_{DFT}(\omega_1,\widehat{\tau_1},\Omega_{s_0},Q,Q\xi) & \cdots & P^{T,\pm}_{DFT}(\omega_1,\widehat{\tau_n},\Omega_{s_0},Q,Q\xi) \\ P^{T,\pm}_{DFT}(\omega_2,\widehat{\tau_1},\Omega_{s_0},Q,Q\xi) & \cdots & P^{T,\pm}_{DFT}(\omega_2,\widehat{\tau_n},\Omega_{s_0},Q,Q\xi) \\ \vdots & \ddots & \vdots \\ P^{T,\pm}_{DFT}(\omega_m,\widehat{\tau_1},\Omega_{s_0},Q,Q\xi) & \cdots & P^{T,\pm}_{DFT}(\omega_m,\widehat{\tau_n},\Omega_{s_0},Q,Q\xi) \end{bmatrix}}_{\mathscr{M}(\Omega_{s_0},Q,Q\xi))} \cdot \underbrace{\begin{bmatrix} \tilde{g}(\widehat{\tau_1}) \\ \tilde{g}(\widehat{\tau_2}) \\ \vdots \\ \tilde{g}(\widehat{\tau_n}) \end{bmatrix}}_{\mathscr{A}} = \underbrace{\begin{bmatrix} P^{T,\pm}_{DFT}(\omega_1) \\ P^{T,\pm}_{DFT}(\omega_2) \\ \vdots \\ P^{T,\pm}_{DFT}(\omega_m) \end{bmatrix}}_{\mathscr{S}_{DFT}}, \tag{5}$$



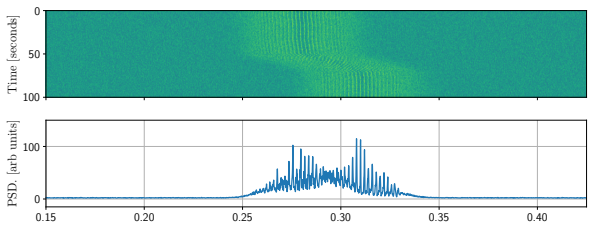
(a) Stable conditions



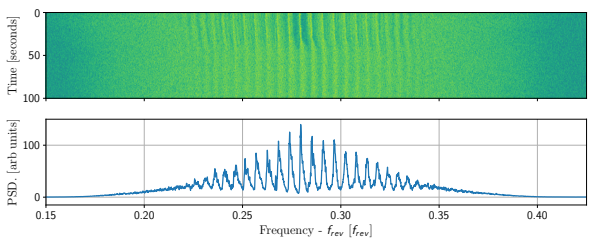
(b) Coupling measurement



(c) Collimator movement



(d) Tune shift



(e) Octupole ramp

Figure 2: Examples of upper sidebands of Schottky spectrograms and averaged spectra of ion beam. All, apart from (d), measured at the injection energy.

high enough octupole strength), corresponding to the tune spread induced by the octupoles. The authors of this contribution are not aware of any theoretical result explaining how transverse beam characteristics can be derived in such cases.

ANALYSIS

Of the various parameters that can be estimated from transverse Schottky spectra, some of the most important include the fractional betatron tune Q_F and the chromaticity $Q\xi$. Examining Eq. (1), one sees that the transverse sidebands are symmetric with respect to the frequencies $(h \pm Q_F)\omega_0$. The frequency bin corresponding to the tune value can then be determined as the one which minimizes the following expression:

$$C_{MD}(k) = \sum_{i=1}^{i=N} \left| P^{\pm}_T(\omega_{k-i}) - P^{\pm}_T(\omega_{k+i}) \right|. \tag{6}$$

If a higher tune resolution is desired, values in between the frequency bins can be interpolated.

In order to estimate chromaticity, it can be proven [16] that, for LHC conditions and RMS widths of the lower and upper transverse sidebands equal to Δf_- and Δf_+ respectively, the chromacity is given by

$$Q\xi = -\eta \left(n \frac{\Delta f_- - \Delta f_+}{\Delta f_- + \Delta f_+} - Q_I \right). \tag{7}$$

Application of Eqs. (6) and (7) requires stationary beam conditions and negligible coherent effects. In the case of the LHC, this is mostly achievable during Pb^{82+} ion runs. In Fig. 3 one can see the tune and chromaticity at flattop during LHC fill 8413, estimated using these formulas. The effect of octupole magnets is neglected here, what couldn't be done at injection energy due to the lower magnetic rigidity and higher transverse size of the beam. The resolution of the measured chromaticity is below the 3 units, the value required at flattop energy by the LHC design report [20].

During less favorable conditions, when spurious components are present in the spectrum as in Fig. 2 b) and c), a different approach has to be taken. A key observation is that Eq. (5) remains valid after removing an arbitrary number of rows from both matrix $\mathscr{M}$ and vector $\mathscr{S}_{DFT}$. If an unwanted component is present at frequency bins $\omega_i, \ldots, \omega_j$, these can be simply excluded from Eq. (5) forming new matrix $\tilde{\mathscr{M}}$ and vector $\tilde{\mathscr{S}}_{DFT}$. Then, the values of Q and $Q\xi$ can be obtained by minimizing the cost function:

$$C_T(\Omega_{s_0},\mathscr{A},Q,Q\xi) = |\tilde{\mathscr{M}}(\Omega_{s_0},Q,Q\xi)\cdot\mathscr{A} - \tilde{\mathscr{S}}_{exp}|^2, \tag{8}$$

Content from this work may be used under the terms of the CC-BY-4.0 licence (© 2023). Any distribution of this work must maintain attribution to the author(s), title of the work, publisher, and DOI

ISBN: 978-3-95450-236-3 ISSN: 2673-5350 doi:10.18429/JACoW-IBIC2023-TH2C03

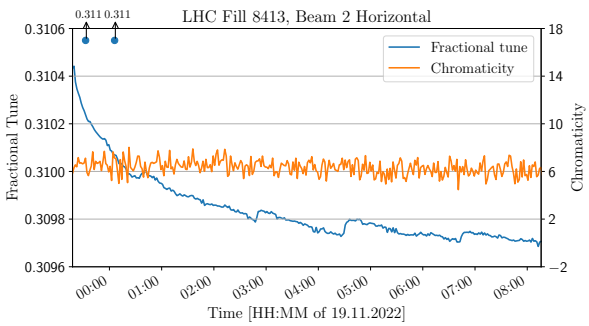


Figure 3: Q and $Q\xi$, estimated in stable beam conditions using Eqs. (6) and (7). Two tune outliers marked with dots.

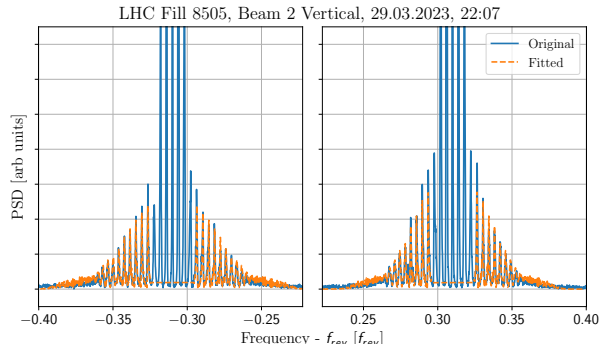


Figure 4: Measured and fitted transverse sidebands. The central part of each sideband was excluded from the analysis.

where $\mathscr{S}_{exp}$ is the experimentally measured Schottky spectrum and $|\cdot|$ denotes the standard Euclidean norm. Similarly, the betatron tune can also be obtained by modifying Eq. (6) in a way where only frequency bins which do not contain coherent components are included in the sum, and the results is then scaled by the number of elements in the sum.

In addition, it is also possible to estimate Ω_{s_0} and $\mathscr{A}$, apriori, either from the longitudinal part of the spectrum as shown in [15], or by measuring using other instruments. At the LHC, the synchrotron amplitude distributions can be calculated from measured longitudinal bunch profiles [15, 21], while the nominal synchrotron frequency is possible to derive either from the peak detected Schottky system [22] or calculated based on the knowledge of the voltage in the RF cavities. The cost function given by Eq. (8) can be minimized using optimization routines, such as L-BFGS-B [23] or differential evolution algorithms [24]. Both approaches have been successfully used in Refs. [15, 16]. This approach has been used on transverse proton spectra acquired shortly after the restart of the LHC in 2023 (fill 8505), at injection energy. As can be seen in Fig. 4, the central satellites are significantly enhanced, which suggests the presence of residual coherence in the particles' synchro-betatron motion. To eliminate their impact on the analysis, the central frequency bins have been excluded. The betatron tune was calculated using Eq. (6), modified as explained previously, while the nominal synchrotron frequency was determined based on the RF voltage and corrected using the Schottky spectra in an independent analysis of the longitudinal part of the spectrum. The minimization of Eq. (8), using the differential evolution algorithm from SciPy library, required finding only three distinct parameters, under the assumption that $\mathscr{A}$ follows the Rice distribution [25]. The obtained fit, that is $\tilde{\mathscr{M}} \cdot \mathscr{A}$ for optimal parameters, is compared with the experimental spectrum in Fig. 4, while estimated values of the betatron tune and chromaticity are presented in Fig. 5. As a reference for comparison, both the chromaticity estimated with the invasive RF-modulation technique [26] is shown as the dashed black line, as well as the chromaticity calculated using Eq. (7).

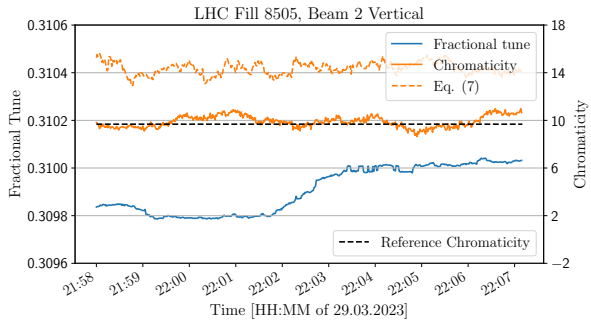


Figure 5: Q and $Q\xi$, estimated in the presence of coherent components, using modifed Eq. (6) and spectra fitting.

CONCLUSION

In this contribution we presented results and discussed some of the challenges associated with the analysis of the Schottky spectra at the LHC. We have demonstrated how a new fitting technique can help to overcome problems with the analysis of spectra containing strong localized components.

The online implementation of the Schottky spectrum analysis is in the final stage of development and is planned to be validated during the LHC ion campaing during the fall of 2023. In parallel, studies are ongoing in order to better understand the spectra, for example including the effect of octupole magnets and beam coupling impedance [27].

The future steps towards further understanding of Schottky spectra and improvement of the beam diagnostic procedures should focus on the developing the theory of Schottky signals which includes the effect of octupole magnets. Very beneficial would also be to investigate the possibilities of using image recognition techniques to analyze 2D Schottky spectrograms.

REFERENCES

[1] J. Borer *et al.*, "Non-destructive diagnostics of coasting beams with Schottky noise", in *Proc. 9th International Conference on High-energy Accelerators*, Stanford, CA, USA, May 1974, pp. 53–56.

[2] S. van der Meer, "Stochastic damping of betatron oscillations in the ISR", CERN, Geneva, Switzerland, Rep. CERN-ISR-

Content from this work may be used under the terms of the CC-BY-4.0 licence (© 2023). Any distribution of this work must maintain attribution to the author(s), title of the work, publisher, and DOI

ISBN: 978-3-95450-236-3 ISSN: 2673-5350 doi:10.18429/JACoW-IBIC2023-TH2C03

PO-72-31, 1972.

[3] A. Jansson, P. Lebrun, and R. Pasquinelli, "Experience with the 1.7 GHz Schottky Pick-ups in the Tevatron", in *Proc. EPAC'04*, Lucerne, Switzerland, Jul. 2004, paper THPLT135, pp. 2777–2779.

[4] A. Sukhanov, K. A. Brown, C. W. Dawson, J. P. Jamilkowski, A. Marusic, and J. Morris, "Processing of the Schottky Signals at RHIC", in *Proc. ICALEPCS'17*, Barcelona, Spain, Oct. 2017, pp. 1327–1329. doi:10.18429/JACoW-ICALEPCS2017-THMPA08

[5] R. Singh *et al.*, "Interpretation of transverse tune spectra in a heavy-ion synchrotron at high intensities", *Phys. Rev. ST Accel. Beams*, vol. 16, no. 3, pp. 034201, 2013. doi:10.1103/PhysRevSTAB.16.034201

[6] Wu, J. *et al.*, "Performance of the resonant Schottky pickup at CSRe", *Nucl. Instrum. Methods Phys. Res., Sect. B*, vol. 317, pp. 623–628, 2013. doi:10.1016/j.nimb.2013.08.017

[7] L. Soby *et al.*, "Elena Orbit and Schottky Measurement Systems", in *Proc. IPAC'15*, Richmond, VA, USA, May 2015, pp. 1061–1064. doi:10.18429/JACoW-IPAC2015-MOPTY056

[8] M. Betz *et al.*, "Bunched-beam Schottky monitoring in the LHC", *Nucl. Instrum. Methods Phys. Res., Sect. A*, vol. 874, pp. 113–126, 2017. doi:10.1016/j.nima.2017.08.045

[9] S. van der Meer, "Diagnostics with Schottky noise", in *Proc. 3rd Joint US-CERN School on Particle Accelerators*, Anacapri, Italy, Oct. 1988, pp. 423-433.

[10] S. Paret *et al.*, "Transverse Schottky and beam transfer function measurements in space charge affected coasting ion beams", *Phys. Rev. ST Accel. Beams*, vol. 13, no. 2, pp. 022802, 2010. doi:10.1103/PhysRevSTAB.13.022802

[11] L. J. Mao *et al.*, "A Characteristics Study for Cold Ion Beam Momentum Spread at HIRFL-CSR", in *Proc. IPAC'10*, Kyoto, Japan, May 2010, paper TUPD012, pp. 1946–1948.

[12] D. Boussard, "Schottky noise and beam transfer function diagnostics," in *Proc. CERN Accelerator School: Advanced Accelerator Physics course*, pp.749-782, 1995. doi:10.5170/CERN-1995-006.749

[13] S. Chattopadhyay, "Some fundamental aspects of fluctuations and coherence in charged-particle beams in storage rings", CERN, Geneva, Switzerland, 1984. doi:10.5170/CERN-1984-011

[14] O. Boine-Frankenheim and V. Kornilov, "Transverse Schottky noise spectrum for bunches with space charge". *Phys. Rev. ST Accel. Beams*, vol. 12, no. 11, pp. 114201, 2009. doi:10.1103/PhysRevSTAB.12.114201

[15] K. Lasocha and D. Alves, "Estimation of longitudinal bunch characteristics in the LHC using Schottky-based diagnostics", *Phys. Rev. Accel. Beams*, vol. 23, no. 6, pp. 062803, 2020. doi:10.1103/PhysRevAccelBeams.23.062803

[16] K. Lasocha and D. Alves, "Estimation of transverse bunch characteristics in the LHC using Schottky-based diagnostics", *Phys. Rev. Accel. Beams*, vol. 25, no. 6, pp. 062801, 2022. doi:10.1103/PhysRevAccelBeams.25.062801

[17] K. Ochs, "A comprehensive analytical solution of the nonlinear pendulum", *Eur. J. Phys.*, vol. 32, no. 2, p. 479, 2011. doi:10.1088/0143-0807/32/2/019

[18] M. Abramowitz and I. A. Stegun, *Handbook of Mathematical Functions with Formulas, Graphs, and Mathematical Tables*, 9th ed, Dover, 1964. doi:10.1119/1.15378

[19] C. Lannoy *et al.* "Statistical Properties of Schottky Spectra", in *Proc. IBIC'23*, Saskatoon, Canada, Sep. 2023, paper WEP035, this conference.

[20] O. S. Brüning *et al.*, *LHC Design Report*, CERN Yellow Reports: Monographs, CERN, Geneva, Switzerland, 2004. doi:10.5170/CERN-2004-003-V-1

[21] J. Jõul, "Software development for a high-speed digitizer to provide online access to longitudinal bunch profiles in the Large Hadron Collider", Master Thesis, Tartu University, 2023.

[22] E. N. Shaposhnikova, T. Bohl, and T. P. R. Linnecar, "Longitudinal Peak Detected Schottky Spectrum", in *Proc. HB'10*, Morschach, Switzerland, Sep.-Oct. 2010, paper TUO1C04, pp. 363–367.

[23] R. Byrd *et al.*, "A limited memory algorithm for bound constrained optimization", *SIAM J. Sci. Comput.*, vol. 16, no. 5, pp. 1190-1208, 1995. doi:10.1137/0916069

[24] R. Storn and K. Price, "Differential evolution - a simple and efficient heuristic for global optimization over continuous spaces", *J. Global Optim.*, vol. 11, pp. 341–-359, 1997. doi:10.1023/A:1008202821328

[25] A. Abdi *et al.*, "On the estimation of the K parameter for the Rice fading distribution", *IEEE Commun. Lett.*, vol. 5, no. 3, pp. 92–94, 2001. doi:10.1109/4234.913150

[26] O. S. Brüning , W. Höfle, R. Jones, T. Linnecar, and H. Schmickler, "Chromaticity Measurements via RF Phase Modulation and Continuous Tune Tracking", in *Proc. EPAC'02*, Paris, France, Jun. 2002, paper THPRI061, pp. 1852–1854.

[27] C. Lannoy *et al.* "Effect of Longitudinal Beam-Coupling Impedance on the Schottky Spectrum of Bunched Beams", in *Proc. IBIC'23*, Saskatoon, Canada, Sep. 2023, paper WEP034, this conference.

Content from this work may be used under the terms of the CC-BY-4.0 licence (© 2023). Any distribution of this work must maintain attribution to the author(s), title of the work, publisher, and DOI

ISBN: 978-3-95450-236-3 ISSN: 2673-5350 doi:10.18429/JACoW-IBIC2023

List of Authors

Bold papercodes indicate primary authors; ~~strike through/black~~ papercodes indicate **no submission received**

— A —

Abbon, P. WEP001
Abbott, M.G. MO2I02, MOP041
Ackermann, W. TUP012
Adachi, T. WEP007
Ady, M. WE3I01
Akbari, M. ~~WEP044~~, ~~WEP045~~
Aleksandrov, A.V. ~~**TH2I01**~~
Alves, D. MOP009, WEP034, WEP035, TH2C03
Anderson, J.I. WEP030
Andre, T. ~~MOP015~~
Arnold, J.M.S. TU3C02
Arnold, M. MOP038, TUP009
Austin, M.R. TU3C02

— B —

Bacha, B. ~~MOP012~~
Baeta Neves Diniz Santos, P.H. **TUP046**
Bai, M. TUP006
Baily, S.A. WEP028, WEP042
Balakrishnan, N. TUP005
Banerjee, S. **MOP041**
Bardorfer, A. MO3C04, MOP013, ~~MOP021~~
Baribeau, C.K. MOP037
Baričevič, B. MOP013
Barkley, W.C. MOP011
Baron, R.A. TU1I02, TUP038
Bassi, G. ~~MOP012~~
Batten, T. ~~**MO1I00**~~, ~~MO1I01~~, MO3C05, ~~**MO3I06**~~, ~~**TU3I06**~~, ~~**TH2I05**~~
Beauregard, R. ~~MO1I01~~, ~~**WE2T01**~~
Bellon, J.R. ~~MOP012~~
Belloni, F. WEP001
Belohrad, D. **TUP044**
Bence, A. MO2C04
Bénédetti, F. WEP001
Berg, W. TUP028, WEP015, WEP017
Bergman, E.C. TU1I02
Berlioz, J.R. TU3C02
Bertwistle, A. WEP036
Bianchini Mattison, C. **TH1I01**
Bielawski, S. ~~TUP008~~, ~~TUP013~~
Biernat, J.B. MOP008
Bisou, J. MO2C04
Blednykh, A. ~~MOP012~~
Blokland, W. ~~MO2I01~~, **WEP031**
Bloomer, C. MOP031, **WEP021**
Bobb, L. MO2I02, MOP031, MOP032, MOP041, WEP020, WEP021
Boccardi, A. MOP009
Böhme, C. **MOP001**
Bogataj, L. MO3C04, ~~MOP021~~
Bohler, D.K. ~~**TUP030**~~
Boland, M.J. MOP036
Bolzon, B. WEP001
Bonnes, U. MOP038
Borland, M. TUP028, WEP017
Boutachkov, P. TUP004, TUP035
Braido, A.J. WEP042
Brauch, A. MOP038, **TUP009**
Bree, M. **MO3C05**
Brill, A.R. MO2C03, TUP027, WEP017
Brionnet, B. WEP007
Bronès, R. **MO2C04**
Brown, G.W. TUP005
Brubach, J.B. ~~TUP008~~
Bruker, M.W. **TUP031**
Buchanan, E. **WE3C03**
Bulut, S. TU1C03
Bundesmann, J. MOP002
Burholt, S.B. **WEP020**
Burns III, W.P. WEP015
Byrd, J.M. WEP017

— C —

Calvey, J.R. TUP028, WEP015
Cao, A. WEP030
Cao, J.S. ~~MOP003~~, ~~MOP024~~, MOP026
Cao, S.S. ~~WEP038~~, TH1I02
Caracappa, A. TUP041
Cargnelutti, M. MO3C04, ~~MOP021~~
Carwardine, J. MO2C03
Cauchon, G. WEP002
Cenede, J. WE3C03
Cerv, M. MOP013
Chaikovska, I. ~~**MO1I02**~~
Chauvin, N. WEP001
Chen, F.Z. ~~WEP038~~
Chen, J. ~~**WEP038**~~, TH1I02
Cheng, W.X. WEP016
Chevrot, M. WEP002
Chin, E.P. TUP005
Chirpaz-Cerbat, D. WEP001
Chitra, S. WEP017
Christian, G.B. MO2I02
Chung, M. WE3C02
Churchman, A.R. WE3I01
Clapp, A.J. **MOP032**
Cobau, W.G. TUP005
Collins, J.T. WEP017
Combet, M. WEP001
Cook, G. MOP032
Cook, N.M. TUP028
Cooke, D.A. TUP023
Craievich, P. MOP010
Cramer, E. WEP030

Content from this work may be used under the terms of the CC-BY-4.0 licence (© 2023). Any distribution of this work must maintain attribution to the author(s), title of the work, publisher, and DOI

ISBN: 978-3-95450-236-3 ISSN: 2673-5350 doi:10.18429/JACoW-IBIC2023

Content from this work may be used under the terms of the CC-BY-4.0 licence (© 2023). Any distribution of this work must maintain attribution to the author(s), title of the work, publisher, and DOI

Crescimbeni, L. **TUP034**, TUP036
Crivelli, D. MOP031
Curcio, A. MOP007, MOP008
Czuba, K. TUP038
Czwalinna, M.K. TUP012, ~~TUP013~~

— D —

Danneil, C. TUP041
Datzmann, G. MOP002
De Gersem, H. TUP011, TUP012
Decker, G. WEP016
Degen, C.M. WE2C03
Demazeux, Q. ~~TUP013~~
Denker, A. MOP002
DeSanto, L. WE2C03
Desch, K. WEP046
Deschamps, S. WE3C03
Desmons, M.J. WEP001
Devauchelle, W. WE3C03
Dewa, H. MOP022
Ditter, R. MO3C03
Dittwald, A. MOP002
Dölling, R. **WEP018**
Dolenc Kittelmann, I. **TUP004**, WEP001
Dollinger, G. MOP002
Donegani, E.M. TU1I02
Dong, Q.Y. MOP004
Dooling, J.C. **TUP027**, **TUP028**, WEP015, WEP017
Dorman, E.F. WEP030
Drees, K.A. ~~MOP012~~
Du, Y.Y. ~~MOP003~~, ~~**MOP024**~~, MOP026
Duffy, A.M. MOP037
Duhme, H.T. MO3C04, MOP019, ~~MOP021~~, MOP039
Duncan, S. MO2I02
Dupuy, B. TUP045
Duran, J.I. TUP029, WEP042
Dusatko, J.E. TUP005
Dutine, M. MOP038, TUP009
Duvillaret, L. TUP022

— E —

Edwards, J.N. WEP017
Effinger, E. TUP004
El Baz, M. WEP024
Emery, J. TUP044
Emery, L. MO2C03, TUP028
Emery, R.C. WEP030
Enders, J. TUP009
Ericson, E.J. WEP036
Erwin, L. WEP015, WEP017
Esteban Felipe, J.C. TUP044
Evain, C. ~~TUP008~~, ~~TUP013~~
Evans, N.J. WEP031

— F —

Fan, K. ~~MOP029~~, ~~TUP019~~
Fan, Z. WEP002
Fellenz, B.J. WEP033
Fisher, A.S. TU3I01, **TUP005**, **TUP006**, TUP042
Folan, T.V. WEP023
Forck, P. WE3I01
Fortunati, R.F. MOP010
Frassier, A. WE3C03
Freitag, M. TUP012
Freyermuth, P. **TUP045**
Frosio, T. TUP006
Fujita, T. MOP022
Fystro, G.I. WEP017

— G —

Gabourin, S. TUP038
Galatyuk, T. MOP018
Gamba, D. TUP045
Gassner, D.M. ~~**MOP012**~~, WE2C03
Gauthier, Y. WEP001
Geißler, R.N. WE2C02
Gereons, T.J. WEP046
Gevorgyan, A.A. WEP001
Giovannozzi, M. TU3C03
Goldblatt, A. TUP044
Gordon, T. WEP030
Gorokhova, E.I. TUP035
Grabinski, T. WEP017
Grames, J.M. TUP031
Grannan, A.M. TUP028
Grewe, R. MOP038, TUP009
Grishin, V. TU1I02, TUP004
Guerrero, A. TUP044
Guo, J. TUP031

— H —

Ha, K. TUP041
Haedar, H.H. ~~WEP044~~, ~~WEP045~~
Hafeez, S.H. ~~MOP012~~, WE2C03
Hahn, G. MOP030, ~~**WE1I01**~~, WE3C02
Haider, D.M. TUP034, TUP036
Halama, A.J. MOP001
Hamelin, T. WEP001
Hanlet, P.M. TU3C02
Harkay, K.C. TUP028, TUP041
Hassanzadegan, H. TU1I02, **TUP038**
Hatanaka, K. WEP006
Hatch, C.D. MOP011
Hazelwood, K.J. TU3C02
He, J. ~~MOP003~~, MOP026
Henry, M.J. WEP017
Herbst, R.T. TU3I01
Hermes, P.D. **TU3C03**
Hetzel, C. ~~MOP012~~
Heyeck, E.E. WEP017
Hiller, N. ~~**TU2T01**~~
Holmes, D. ~~MOP012~~
Hosoda, N. MOP022

ISBN: 978-3-95450-236-3 ISSN: 2673-5350 doi:10.18429/JACoW-IBIC2023

Houghton, C.E. **MOP031**
Hoyt, J.E. WEP017
Hu, J.YC. TU3C02
Huang, C. TUP042
Huang, J.Y. MOP030
Huang, L.T. MOP004
Huang, W.L. TU3C05, **TUP014**
Hubert, N. ~~MO1I02~~, MO2C04, WEP002
Hulsart, R.L. ~~MOP012~~, WE2C03
Hwang, J.-G. ~~WE1I01~~
Hwang, Y.S. WEP013

— I —

Ibrahim, M.A. **TU3C02**
Iida, N. ~~TH2C02~~
Ikeda, H. TUP002, WEP005
Imai, N. WEP006
Inacker, P. ~~MOP012~~
Ischebeck, R. MOP010
Ishi, Y. WEP019
Ismaili, E. MOP010

— J —

Jabłoński, S. **MOP039**
Jackson, S. MOP009
Jacobson, B.T. TUP005
Jamet, C. ~~**MOP015**~~
Jamilkowski, J.P. WE2C03
Jang, S.W. **MOP030**
Jatczak, P.K. TUP038
Jiang, J. TU3C02
Johnson, S.M. WEP028, WEP029
Jürgensen, L.E. MOP038, TUP009
Jung, G.I. **WEP013**
Jung, P.M. TUP007
Juranič, P.N. MOP010
Justus, M. WEP043

— K —

Kallakuri, P.S. **MO2C03**
Kamakura, K. WEP006
Kamerdzhiev, V. MOP001
Kamigaito, O. WEP007
Kamoshida, A. WEP007
Kaneko, K. WEP007
Kang, H.-S. TUP021
Karataev, P. MOP032
Kato, S.K. ~~TH2C02~~
Kaya, U. TU1C03
Keane, R.T. **TUP041**, WEP017
Kearney, J.N.G. WE3C03
Kedych, V. MOP018
Keil, B. **MO3C03**
Kempf, I. **MO2I02**, MOP041
Kennel, L.S. WEP042
Kerstiens, E.L. MOP033
Khaleghi, A. ~~**WEP044**~~, ~~**WEP045**~~
Kim, C. MOP030, ~~WE1I01~~
Kim, D. MOP030, ~~WE1I01~~
Kim, E.-S. ~~TUP043~~
Kim, G. MOP030, TUP021
Kim, G.D. ~~TUP043~~
Kim, G.D. ~~TUP020~~
Kim, K.H. TH1I01
Kis, M. MOP018
Kittelmann, I.D. **TU1I02**
Kiy, S. **TUP007**
Klaproth, S. **TUP011**
Klopf, J.M. WE1C03
Kocevar, H. TU1I02, TUP038, WEP001
Koch, G.K. MOP001
Kotaka, Y. **WEP006**
Kourkafas, G. MOP002
Koyama, R. WEP007
Krejcik, P. TU3I01, ~~TUP030~~, TH1I01
Krmpotić, L. WEP043
Kronenberg, S. WEP046
Krouptchenkov, I. MOP019
Krüger, W. MOP018
Kube, G. **MO3C04**, ~~MOP021~~
Kubsky, S. WEP002
Kuhn, K. WEP030
Kuklev, N. TUP027
Kuntzsch, M. TUP012, WE1C03, **WEP043**
Kurfürst, C. MOP013
Kwon, J.W. ~~**TUP020**~~, ~~TUP043~~
Kwon, S. TUP005

— L —

Labat, M. ~~TUP008~~, WEP002
Lahonde-Hamdoun, C. WEP001
Lai, L.W. **TH1I02**
Laihem, K. MOP001
Lamaack, J.L. MO3C04, ~~**MOP021**~~
Lannoy, C. **WEP034**, **WEP035**
Larsen, R.G. WE3C03
Łasocha, K. MOP007, WEP034, WEP035, **TH2C03**
Laxdal, R.E. ~~**MO1I01**~~
Le Parquier, M. ~~TUP008~~
Leban, P. MO3C04, MOP013, ~~MOP021~~
Ledezma Vazquez, O.O. WEP030
Lee, D.W. TUP028
Lee, S.H. WEP017
Lee, Y. TUP028
Lefèvre, T. ~~MO3I02~~, **MOP009**, TUP022
Leffler, H.L. WEP028, WEP042
Legallois, P. ~~MOP015~~
Legat, U. WEP043
Legou, Ph. WEP001
Leloir, S. ~~MOP015~~
Leng, Y.B. ~~MOP006~~, ~~TUP018~~, ~~WEP038~~, ~~WEP039~~
Lenner, J. WEP017
Lensch, T. MOP019, **TU3I04**, TUP037

Content from this work may be used under the terms of the CC-BY-4.0 licence (© 2023). Any distribution of this work must maintain attribution to the author(s), title of the work, publisher, and DOI

ISBN: 978-3-95450-236-3 ISSN: 2673-5350 doi:10.18429/JACoW-IBIC2023

Content from this work may be used under the terms of the CC-BY-4.0 licence (© 2023). Any distribution of this work must maintain attribution to the author(s), title of the work, publisher, and DOI

Lernevall, A.T. TUP004
Leseigneur, O. WEP001
Letchford, A.P. WEP019
Li, F. TU3C05, ~~**WEP009**~~
Li, J.Q. ~~**MOP029**~~
Li, L.X.F. ~~TUP019~~
Liang, Y. ~~MOP006~~
Lidia, S.M. WEP027
Lim, E.H. ~~TUP020~~, ~~**TUP043**~~
Lin, L.F. ~~WEP037~~
Lindberg, R.R. TUP028
Lipka, D. MOP019, TU3I04, **TUP037**
Littleton, S.T. **TUP042**
Liu, B. TU2C03
Liu, C. ~~MOP012~~
Liu, F. ~~MOP003~~
Liu, H. TU3C02
Liu, M.Y. TU3C05, TUP014
Liu, Q.R. TU3C05, TUP014
Liu, X.Q. TH1I02
Liu, X.Y. ~~MOP003~~, TUP014
Liu, Y. ~~**MO2I01**~~
Liu, Z. ~~TUP019~~
Liu, Z. ~~MOP003~~, ~~MOP024~~
Lobach, I. TUP027, WEP017
Lokey, A. **WEP027**
Lopez, J. WEP030
Lorbeer, B. **MOP019**
Lu, P. ~~MOP006~~, ~~TUP016~~, WEP011
Lu, Y.H. ~~MOP003~~
Lumpkin, A.H. TUP027, WEP015, WEP017
Lundberg, C.E. WEP025
Luo, Q. MOP004, ~~MOP006~~
Lutman, A.A. ~~TUP030~~
Lynam, S. WEP030

— M —

Ma, H.Z. ~~MOP003~~
Machida, S. WEP019
Maesaka, H. **MOP022**
Mahmoudi, K. ~~WEP044~~, ~~WEP045~~
Manceron, L. ~~TUP008~~
Mansten, E. ~~**WE1I02**~~
Marcellini, F. MO3C03, MOP010
Mariette, Y. WEP001
Marinkovic, G.M. MO3C03
Marroncle, J. **WEP001**
Marsic, N. TUP036
Martin Nieto, M. TUP044
Martinez, D. MOP011, WEP042
Masaki, M. MOP022
Mavrič, U. MOP039
Mazzoni, S. TUP022, TUP023, WE3I01
Mead, J. TUP041, WE2C03
Melton, J.E. MOP031
Memik, S. TU3C02
Meng, R. TH1I02
Mernick, K. WE2C03
Michnoff, R.J. ~~MOP012~~, **WE2C03**
Micolon, F. ~~MOP012~~
Milas, N. TU1I02
Milton, E.B. ~~**TUP040**~~
Min, C.-K. TUP021
Minty, M.G. ~~MOP012~~
Mitrevski, J. TU3C02
Mitsuhashi, T.M. **WEP005**
Mitsuka, G. **TU1I01**, TUP002, WEP005, ~~**TH2C02**~~
Miyamoto, R. TU1I02
Mock, J.A. **TU3I01**, TUP005
Mohammednezhad, M. TU1I02, TUP038
Mols, J.-Ph. WEP001
Montag, C. ~~MOP012~~
Montanari, C.E. TU3C03
Montoya, L.S. **WEP028**, **WEP029**, WEP042
Morales Vigo, S. TU3C03
Morimoto, K.M. WEP007
Mostafanezhad, I.S. TUP006
Mounet, N. WEP034, WEP035
Moutardier, A. **WEP002**
Mun, G. TUP021
Murari, J.F.J. TUP038
Musson, J. TUP031
Mwaniki, M.W. WEP023
Myalski, S. MOP013

— N —

Na, N.Y. ~~**WEP037**~~
Nadot, V. WEP001
Nagaslaev, V.P. TU3C02
Nakaye, Y. ~~**WEP047**~~
Narayan, G. WE2C03
Narayanan, A. TU3C02
Natsui, T. ~~TH2C02~~
Navrotski, G. TUP028
Nazer, T.A. TUP012
Neubauer, J. MOP002
Neumann, Re. TU3I04, TUP037
Newton, M.E. WEP021
Nicklaus, D.J. TU3C02
Nie, X.J. TUP014
Niedermayer, P.J. **WE2C02**
Nilen, F. TU1I02
Nishi, T. WEP007
Noll, D. TU1I02
Novokhatski, A. ~~TUP030~~

— O —

Oblak, M.O. MO3C04, ~~MOP021~~
Oddo, P. WE2C03
Oguz, A.R. WEP031
Ohnishi, J. WEP006
Orlandi, G.L. MOP010, **TUP026**
Ortega Ruiz, I. WE3C03
Oublaid, M. WEP001

ISBN: 978-3-95450-236-3 ISSN: 2673-5350 doi:10.18429/JACoW-IBIC2023

Oven, Ž. WEP043
Overstreet, S.A. TUP031

— P —

Pablo, M.H. TUP031
Padrazo, D. ~~**MO3I01**~~, ~~MOP012~~, TUP041
Paglovec, P. MO3C04, MOP013, ~~MOP021~~
Panaś, R. **MOP007**, MOP008
Paniccia, M.C. ~~MOP012~~, WE2C03
Pannell, F.E. TUP023
Park, G.-T. TUP031
Park, J. TUP005
Patel, H. MOP031
Pavinato, S. TUP038
Pédeau, D. MO2C04
Penirschke, A. TUP010, TUP011, TUP012, WE1C03
Perreu, G. WEP001
Pertica, A. WEP019
Perusko, L. WEP043
Pfeiffer, S. MOP039
Pichon, G. MO2C04
Pieloni, T. WEP034, WEP035
Pietralla, N. MOP038, TUP009
Pietraszko, J. MOP018
Pigula, J. TUP005
Pinayev, I. ~~MOP012~~, **MOP043**, **MOP044**, **MOP045**, **MOP046**
Planche, T. TUP007
Plawski, T.E. TUP031
Poelker, M. TUP031
Pomaro, J.A. ~~MOP012~~, WE2C03
Popieul, F. WEP001
Porsuk, D. TU1C03
Posthuma de Boer, D.W. WEP019
Potier de courcy, C. ~~MOP015~~
Pottin, B. WEP001
Pradhan, G. TU3C02
Pramberger, A.C. ~~MOP012~~, WE2C03
Preu, S. TUP010, WE1C03
Proft, D. WEP046
Prokop, R.M. **WEP022**
Ptitsyn, V. ~~MOP012~~
Purtschert, J. MO3C03
Puttkammer, A. WEP017

— Q —

Qiu, R.Y. **TU3C05**

— R —

Rai, D. MOP011, **WEP042**
Rakic, M. TU3C03
Ramakrishnan, T. **TUP029**
Ranjbar, V.H. ~~MOP012~~
Ratti, A. TUP006
Raubenheimer, T.O. TUP042
Redaelli, S. TU3C03
Rehm, G. MO2I02
Rehman, M.A. TU3C05
Reimers, K. MOP001
Reindl, J. **MOP002**
Reiter, A. TUP034
Renta, J.C. WE2C03
Repič, B. MO3C04, ~~MOP021~~
Repovž, M. MOP013
Riedel, S.M. TUP028
Rimmer, R.A. TUP031
Ringuette, J.B. WEP030
Rizzi, M. MO3C03
Roberts, B.F. TUP031
Rodnyi, P. TUP035
Rodriguez, E. TUP005
Roggli, M. MO3C03
Rojec, U. WEP043
Roncarolo, F. MOP009, TUP044
Rosengren, K.E. TU1I02, TUP038
Rosenthal, G.B. **WEP030**
Rossi, A. WE3I01
Rost, A. **MOP018**
Rotter, B. TUP006
Roussel, E. ~~TUP008~~, ~~TUP013~~
Rousseti, A. MOP002
Roy, P. ~~TUP008~~
Rudolph, J.I.D. TUP005

— S —

Saadat, S. **MOP036**
Saewert, A.L. TU3C02
Saifulin, M. **TUP035**
Sajaev, V. TUP028, WEP017
Sakemi, Y. WEP006
Salvachúa, B. TU3C03
Sameed, M. WE3I01
Sanchez, D. TUP005
Sangroula, M.P. ~~MOP012~~
Sapozhnikov, L. TU3I01, TUP005
Sas-Pawlik, S.G. WEP023
Satoh, M. ~~TH2C02~~
Satou, K. **MOP023**
Sauce, Y. WEP001
Scarpine, V.E. WEP024, **WEP033**
Schaer, M. MOP010
Scheible, B.E.J. **TUP012**
Schlarb, H. MOP039, TUP012
Schließmann, F. MOP038, TUP009
Schlögelhofer, A. **TUP022**
Schlott, V. ~~TU2T01~~
Schmelz, M. TUP034, TUP036
Schmid, F. TUP034, TUP036
Schmidt-Föhre, F. MO3C04, ~~MOP021~~
Schmitzer, C. MOP013
Schneider, D. **MOP038**, TUP009
Schneider, G. WE3I01
Schupbach, B.A. TU3C02
Schwarz, A. WEP043

Content from this work may be used under the terms of the CC-BY-4.0 licence (© 2023). Any distribution of this work must maintain attribution to the author(s), title of the work, publisher, and DOI

ISBN: 978-3-95450-236-3 ISSN: 2673-5350 doi:10.18429/JACoW-IBIC2023

Content from this work may be used under the terms of the CC-BY-4.0 licence (© 2023). Any distribution of this work must maintain attribution to the author(s), title of the work, publisher, and DOI

Schwickert, M. TUP034, TUP036
Schwindling, J. WEP001
Scola, L. WEP001
Sedláček, O. **WE3I01**
Seiya, K. TU3C02
Semenov, A. WEP033
Senée, F. WEP001
Senes, E. ~~**MO3I02**~~, TUP022, **TUP023**
Senger, A. MOP018
Sequeiro, C.C. WE3I01
Sereno, N. MO2C03, TUP027, TUP028, TUP041, WEP015, WEP016, WEP017
Serin, N.O. TU1C03
Severino, F. WE2C03
Shaker, H. **WEP036**
Shea, T.J. TU1I02, TUP038
Shelbaya, O. TUP007
Shi, R. TU3C02
Shin, B.K. MOP030, **WE3C02**
Shin, D.C. MOP030, **TUP021**
Shoaf, S.E. WEP015
Shuping, A.M. TU3C02
Sidorowski, K. WE3I01
Sieber, T. TUP034, **TUP036**
Simakov, E.I. MOP011
Singh, R. TUP011, WE2C02
Škabar, M. MOP013
Slimmer, D. WEP025, WEP033
Smedley, J. TUP006
Smith, B. WEP030
Soltan, E. WEP036
Song, D. MOP030
Song, W.J. MOP030, ~~WE1I01~~
Song, Y. ~~TUP019~~
Speirs, D. TUP031
Spreitzer, A. WEP046
Steffen, B. ~~**TUP013**~~
Steinhilber, G. MOP038
Stephan, D. MO3C03
Stevens, C.W. MO3C05
Stevens, J.B. TUP028
Stöhlker, T. TUP034, TUP036
Stolz, R. TUP034, TUP036
Storey, J.W. MOP009
Stringer, O. WE3I01
Sui, Y.F. ~~MOP003~~, ~~MOP024~~, MOP026, TUP014
Sun, B.G. ~~**MOP006**~~, ~~TUP016~~, WEP011
Sun, Y. TUP027, WEP017
Sun, Y.P. TUP028
Sung, C.K. WE3C02
Suwada, T. **TU2I02**
Switka, M.T. **WEP046**
Szeto, L. WEP030
Szwaj, C. ~~**TUP008**~~, ~~TUP013~~

— T —

Takano, S. MOP022
Tan, J. TUP036
Tan, Z.X. TU3C05
Tang, L.L. ~~MOP006~~, ~~TUP016~~, WEP011
Tang, X.H. **MOP026**
Tarkeshian, R. TU1I02, WEP001
Thaufelder, J. MOP018
Thieberger, P. ~~MOP012~~
Thieme, M. TU3C02
Thomas, C.A. TU1I02, WEP001
Thomasset, M. WEP002
Thorin, S. ~~WE1I02~~
Thurman-Keup, R.M. TU3C02, **WEP023**, **WEP024**, **WEP025**
Tian, W. ~~**TH1C03**~~
Tobiyama, M. **TUP002**
Toyama, T. MOP023
Tran, N.V. TU3C02
Trautmann, C. TUP035
Tsai, C.-Y. ~~TUP019~~
Türemen, G. **TU1C03**
Turner, M. TUP023
Tuske, O. WEP001
Tympel, V. TUP034, TUP036
Tzvetkov, S. WEP001

— U —

Uchiyama, A. WEP007
Udrea, S. WE3I01
Ünal, M.T. MOP008
Uesugi, T. WEP019
Ulrich-Pur, F. MOP018

— V —

Vallis, N. **MOP010**
Veness, R. MOP009, WE3I01
Venevtsev, I.D. TUP035
Verzilov, V.V. TUP007
Viganò, W. TUP004
Vilcins, S. TUP012
Vitoratou, N. WEP020
Vogt, J.M. MO3C05

— W —

Walasek-Höhne, B. TUP035
Walker, A.D. **MOP033**
Wang, A.X. ~~MOP003~~, ~~MOP006~~
Wang, D.Y. WEP011
Wang, E. ~~MOP012~~
Wang, H. TUP031
Wang, HS. ~~**TUP018**~~
Wang, J. WEP017
Wang, J. ~~MOP006~~, ~~**TUP016**~~
Wang, J. ~~MOP029~~
Wang, J.G. **TU2C03**
Wang, L. ~~MOP003~~
Wang, Q. **MOP004**

ISBN: 978-3-95450-236-3 ISSN: 2673-5350 doi:10.18429/JACoW-IBIC2023

Wang, S.G. WEP015, WEP017
Wang, X. MO3C03
Wang, Y.Y. ~~WEP037~~
Watanabe, T. **WEP007**
Watkins, H.A. **MOP011**, TUP029, WEP028, WEP029
Wawrzyniak, A.I. MOP007, **MOP008**
Weaver, M. TH1I01
Webber-Date, A. WE3I01
Wei, S.J. ~~MOP003~~, ~~MOP024~~
Welch, J.J. TUP005
Welsch, C.P. WE3I01
Werner, M. MOP019, TU3I04, TUP037
Westferro, F. WEP016
Wiechecki, J.J. MOP008
Willeke, F.J. ~~MOP012~~
Willis, W.D. WEP031
Wilson, C.M. TUP031
Wing, M. TUP023
Wittenburg, K. MO3C04, ~~MOP021~~
Wolf, M. **MOP013**
Woo, H.J. ~~TUP020~~, ~~TUP043~~
Wootton, K.P. TUP028, **WEP014**, **WEP015**, **WEP016**, **WEP017**
Wu, J. TUP006
Wu, R.Z. **WEP011**
Wu, W. TU2C03
Wurtz, W.A. **MOP037**

— X —

Xie, H.M. ~~**WEP012**~~
Xu, C. TU3C02
Xu, T.G. ~~MOP003~~
Xu, Y. ~~**TUP019**~~
Xu, Zh.H. TU3C05

— Y —

Yadav, R. **TUP010**, **WE1C03**
Yamada, S. MOP023
Yamaguchi, H. WEP006
Yamakawa, E. **WEP019**
Yang, R.J. TU3C05
Yang, T. TU3C05
Yang, X. ~~**WEP039**~~, ~~TUP018~~
Yang, Y.L. ~~WEP037~~
Ye, Q. ~~MOP003~~, ~~MOP024~~
Yeltepe, E. TU1C03
Yoon, Y.J. WEP013
Yousefi Sigari, Y. WEP036
Yu, L. ~~MOP003~~
Yu, T. ~~**MOP028**~~
Yue, J.H. ~~**MOP003**~~, ~~MOP024~~, MOP026, ~~**TH2I04**~~

— Z —

Zagel, J.R. WEP025
Zakosarenko, V. TUP034, TUP036
Zamantzas, C. MOP009, TUP004
Zelazny, S. TH1I01
Zeng, L. TU3C05
Zeng, R. TUP038
Zenker, K. WEP043
Zennaro, R. MOP010
Zevi Della Porta, G. TUP023
Zhang, H.D. WE3I01
Zhang, S. TUP031
Zhang, W. ~~MOP003~~
Zhang, Z.S. ~~WEP037~~
Zhao, Y. ~~MOP003~~
Zhao, Y.K. ~~TUP016~~, WEP011
Zhao, Z.L. ~~WEP037~~
Zholents, A. WEP017
Zhou, J. WEP030
Zhou, T.Y. ~~MOP006~~, ~~TUP016~~
Zhou, Y.M. ~~WEP039~~, TH1I02, ~~TUP018~~
Zhou, Z.R. ~~MOP006~~
Zhou, Z.R. ~~TUP016~~
Zhu, D.C. ~~MOP003~~
Zhu, G. ~~WEP037~~
Zimmermann, D.D. WEP028, WEP029, WEP042
Zykova, M. MOP010

Content from this work may be used under the terms of the CC-BY-4.0 licence (© 2023). Any distribution of this work must maintain attribution to the author(s), title of the work, publisher, and DOI

ISBN: 978-3-95450-236-3 ISSN: 2673-5350 doi:10.18429/JACoW-IBIC2023

Institutes List

Content from this work may be used under the terms of the CC-BY-4.0 licence (© 2023). Any distribution of this work must maintain attribution to the author(s), title of the work, publisher, and DOI

ANL
Lemont, Illinois, USA
- Berg, W.
- Borland, M.
- Brill, A.R.
- Burns III, W.P.
- Byrd, J.M.
- Calvey, J.R.
- Carwardine, J.
- Cheng, W.X.
- Chitra, S.
- Collins, J.T.
- Decker, G.
- Dooling, J.C.
- Edwards, J.N.
- Emery, L.
- Erwin, L.
- Fystro, G.I.
- Grabinski, T.
- Grannan, A.M.
- Harkay, K.C.
- Henry, M.J.
- Heyeck, E.E.
- Hoyt, J.E.
- Kallakuri, P.S.
- Keane, R.T.
- Kuklev, N.
- Lee, S.H.
- Lee, Y.
- Lenner, J.
- Lindberg, R.R.
- Lobach, I.
- Lumpkin, A.H.
- Navrotski, G.
- Puttkammer, A.
- Sajaev, V.
- Sereno, N.
- Shoaf, S.E.
- Stevens, J.B.
- Sun, Y.P.
- Sun, Y.
- Wang, J.
- Wang, S.G.
- Westferro, F.
- Wootton, K.P.
- Zholents, A.

BHT
Berlin, Germany
- Denker, A.

BNL
Upton, New York, USA
- Bacha, B.
- Bassi, G.
- Caracappa, A.
- Danneil, C.
- Degen, C.M.
- DeSanto, L.
- Drees, K.A.
- Gassner, D.M.
- Ha, K.
- Hafeez, S.H.
- Holmes, D.
- Hulsart, R.L.
- Inacker, P.
- Jamilkowski, J.P.
- Liu, C.
- Mead, J.
- Mernick, K.
- Michnoff, R.J.
- Minty, M.G.
- Narayan, G.
- Oddo, P.
- Padrazo, D.
- Paniccia, M.C.
- Pinayev, I.
- Pomaro, J.A.
- Pramberger, A.C.
- Renta, J.C.
- Sangroula, M.P.
- Severino, F.
- Thieberger, P.
- Wang, E.
- Willeke, F.J.

Brookhaven National Laboratory (BNL), Electron-Ion Collider
Upton, New York, USA
- Bellon, J.R.
- Blednykh, A.
- Gassner, D.M.
- Hetzel, C.
- Micolon, F.
- Montag, C.
- Ptitsyn, V.
- Ranjbar, V.H.

CEA-DRF-IRFU
France
- Abbon, P.
- Belloni, F.
- Bénédetti, F.
- Hamelin, T.
- Marroncle, J.
- Mols, J.-Ph.
- Scola, L.

CEA-IRFU
Gif-sur-Yvette, France
- Bolzon, B.
- Chauvin, N.
- Chirpaz-Cerbat, D.
- Combet, M.
- Desmons, M.J.
- Gauthier, Y.
- Lahonde-Hamdoun, C.
- Legou, Ph.
- Leseigneur, O.
- Mariette, Y.
- Nadot, V.

ISBN: 978-3-95450-236-3 ISSN: 2673-5350 doi:10.18429/JACoW-IBIC2023

- Oublaid, M.
- Perreu, G.
- Popieul, F.
- Pottin, B.
- Sauce, Y.
- Schwindling, J.
- Senée, F.
- Tuske, O.
- Tzvetkov, S.

CERN
Meyrin, Switzerland
- Alves, D.
- Boccardi, A.
- Cenede, J.
- Churchman, A.R.
- Deschamps, S.
- Devauchelle, W.
- Dupuy, B.
- Effinger, E.
- Emery, J.
- Esteban Felipe, J.C.
- Frassier, A.
- Freyermuth, P.
- Gamba, D.
- Giovannozzi, M.
- Goldblatt, A.
- Guerrero, A.
- Hermes, P.D.
- Jackson, S.
- Kearney, J.N.G.
- Lannoy, C.
- Larsen, R.G.
- Łasocha, K.
- Lefèvre, T.
- Lernevall, A.T.
- Martin Nieto, M.
- Mazzoni, S.
- Montanari, C.E.
- Morales Vigo, S.
- Mounet, N.
- Ortega Ruiz, I.
- Redaelli, S.
- Roncarolo, F.
- Rossi, A.
- Salvachúa, B.
- Schlögelhofer, A.
- Schneider, G.
- Sedláček, O.
- Senes, E.
- Sequeiro, C.C.
- Sidorowski, K.
- Storey, J.W.
- Tan, J.
- Turner, M.
- Veness, R.
- Viganò, W.
- Zamantzas, C.
- Zevi Della Porta, G.

CLS
Saskatoon, Saskatchewan, Canada
- Baribeau, C.K.
- Batten, T.
- Beauregard, R.
- Bertwistle, A.
- Boland, M.J.
- Bree, M.
- Duffy, A.M.
- Ericson, E.J.
- Saadat, S.
- Shaker, H.
- Stevens, C.W.
- Vogt, J.M.
- Wurtz, W.A.
- Yousefi Sigari, Y.

CNS
Saitama, Japan
- Imai, N.
- Kamakura, K.
- Kotaka, Y.
- Sakemi, Y.
- Yamaguchi, H.

Cockcroft Institute
Warrington, Cheshire, United Kingdom
- Sedláček, O.
- Stringer, O.
- Welsch, C.P.
- Zhang, H.D.

Cockcroft Institute, University of Liverpool
Liverpool, United Kingdom
- Webber-Date, A.

Cosylab
Ljubljana, Slovenia
- Krmpotić, L.
- Legat, U.
- Oven, Ž.
- Perusko, L.
- Rojec, U.

Datzmann Interact & Innovate GmbH
München, Germany
- Datzmann, G.

DESY
Hamburg, Germany
- Czwalinna, M.K.
- Duhme, H.T.
- Jabłoński, S.
- Krouptchenkov, I.
- Kube, G.
- Lamaack, J.L.
- Lensch, T.
- Lipka, D.
- Lorbeer, B.
- Mavrič, U.
- Nazer, T.A.
- Neumann, Re.
- Pfeiffer, S.
- Schlarb, H.
- Schmidt-Föhre, F.

Content from this work may be used under the terms of the CC-BY-4.0 licence (© 2023). Any distribution of this work must maintain attribution to the author(s), title of the work, publisher, and DOI

ISBN: 978-3-95450-236-3 ISSN: 2673-5350 doi:10.18429/JACoW-IBIC2023

Content from this work may be used under the terms of the CC-BY-4.0 licence (© 2023). Any distribution of this work must maintain attribution to the author(s), title of the work, publisher, and DOI

- Steffen, B.
- Vilcins, S.
- Werner, M.
- Wittenburg, K.

DICP
Dalian, Liaoning, People's Republic of China
- Dong, Q.Y.
- Huang, L.T.
- Wang, Q.

DLS
Oxfordshire, United Kingdom
- Abbott, M.G.
- Banerjee, S.
- Bloomer, C.
- Bobb, L.
- Burholt, S.B.
- Christian, G.B.
- Cook, G.
- Crivelli, D.
- Houghton, C.E.
- Kempf, I.
- Melton, J.E.
- Patel, H.
- Vitoratou, N.

EBG MedAustron
Wr. Neustadt, Austria
- Cerv, M.
- Kurfürst, C.
- Myalski, S.
- Repovž, M.
- Schmitzer, C.
- Wolf, M.

Electrodynamic
Albuquerque, New Mexico, USA
- Pablo, M.H.
- Roberts, B.F.
- Speirs, D.

ELSA
Bonn, Germany
- Desch, K.
- Gereons, T.J.
- Kronenberg, S.
- Proft, D.
- Spreitzer, A.
- Switka, M.T.

EPFL
Lausanne, Switzerland
- Lannoy, C.
- Pieloni, T.
- Rakic, M.

ESS
Lund, Sweden
- Baron, R.A.
- Bergman, E.C.
- Dolenc Kittelmann, I.
- Donegani, E.M.
- Gabourin, S.
- Gevorgyan, A.A.
- Grishin, V.
- Hassanzadegan, H.
- Kittelmann, I.D.
- Kocevar, H.
- Milas, N.
- Miyamoto, R.
- Mohammednezhad, M.
- Murari, J.F.J.
- Nilen, F.
- Noll, D.
- Pavinato, S.
- Rosengren, K.E.
- Shea, T.J.
- Tarkeshian, R.
- Thomas, C.A.
- Zeng, R.

European Organization for Nuclear Research (CERN)
Geneva, Switzerland
- Ady, M.
- Belohrad, D.
- Buchanan, E.
- Mazzoni, S.
- Sameed, M.

FAIR
Darmstadt, Germany
- Rost, A.
- Senger, A.

Fermilab
Batavia, Illinois, USA
- Arnold, J.M.S.
- Austin, M.R.
- Berlioz, J.R.
- El Baz, M.
- Fellenz, B.J.
- Folan, T.V.
- Hanlet, P.M.
- Hazelwood, K.J.
- Ibrahim, M.A.
- Lundberg, C.E.
- Milton, E.B.
- Mitrevski, J.
- Mwaniki, M.W.
- Nagaslaev, V.P.
- Narayanan, A.
- Nicklaus, D.J.
- Pradhan, G.
- Prokop, R.M.
- Saewert, A.L.
- Sas-Pawlik, S.G.
- Scarpine, V.E.
- Schupbach, B.A.
- Seiya, K.
- Semenov, A.
- Slimmer, D.
- Thurman-Keup, R.M.
- Tran, N.V.
- Zagel, J.R.

ISBN: 978-3-95450-236-3 ISSN: 2673-5350 doi:10.18429/JACoW-IBIC2023

FRIB
East Lansing, Michigan, USA
- Lidia, S.M.
- Lokey, A.

FSU Jena
Jena, Germany
- Schmid, F.
- Tympel, V.

FZJ
Jülich, Germany
- Böhme, C.

GANIL
Caen, France
- Andre, T.
- Jamet, C.
- Legallois, P.
- Leloir, S.
- Potier de courcy, C.

GOI
St Petersburg, Russia
- Gorokhova, E.I.

GSI
Darmstadt, Germany
- Boutachkov, P.
- Crescimbeni, L.
- Forck, P.
- Galatyuk, T.
- Geißler, R.N.
- Haider, D.M.
- Halama, A.J.
- Kamerdzhiev, V.
- Kis, M.
- Koch, G.K.
- Laihem, K.
- Niedermayer, P.J.
- Pietraszko, J.
- Reimers, K.
- Reiter, A.
- Saifulin, M.
- Schwickert, M.
- Sieber, T.
- Singh, R.
- Stöhlker, T.
- Thaufelder, J.
- Trautmann, C.
- Udrea, S.
- Ulrich-Pur, F.
- Walasek-Höhne, B.

HIJ
Jena, Germany
- Stöhlker, T.
- Tympel, V.

HUST
Hubei, People's Republic of China
- Fan, K.
- Li, J.Q.
- Liu, Z.
- Song, Y.
- Tsai, C.-Y.
- Wang, J.
- Xu, Y.

HZB
Berlin, Germany
- Bundesmann, J.
- Denker, A.
- Dittwald, A.
- Hwang, J.-G.
- Kourkafas, G.
- Rehm, G.

HZDR
Dresden, Germany
- Freitag, M.
- Justus, M.
- Klopf, J.M.
- Kuntzsch, M.
- Schwarz, A.
- Zenker, K.

I-Tech
Solkan, Slovenia
- Bardorfer, A.
- Baričevič, B.
- Bogataj, L.
- Cargnelutti, M.
- Leban, P.
- Oblak, M.O.
- Paglovec, P.
- Repič, B.
- Škabar, M.

IASF
Shenzhen, Guangdong, People's Republic of China
- Yu, T.

IBS
Daejeon, Republic of Korea
- Kim, G.D.
- Kwon, J.W.
- Woo, H.J.

IHEP
Beijing, People's Republic of China
- Cao, J.S.
- Du, Y.Y.
- He, J.
- Liu, F.
- Liu, M.Y.
- Liu, X.Y.
- Liu, Z.
- Lu, Y.H.
- Ma, H.Z.
- Sui, Y.F.
- Tang, X.H.
- Wang, L.
- Wei, S.J.
- Xu, T.G.
- Ye, Q.
- Yu, L.
- Yue, J.H.

Content from this work may be used under the terms of the CC-BY-4.0 licence (© 2023). Any distribution of this work must maintain attribution to the author(s), title of the work, publisher, and DOI

ISBN: 978-3-95450-236-3 ISSN: 2673-5350 doi:10.18429/JACoW-IBIC2023

Content from this work may be used under the terms of the CC-BY-4.0 licence (© 2023). Any distribution of this work must maintain attribution to the author(s), title of the work, publisher, and DOI

- Zeng, L.
- Zhang, W.
- Zhao, Y.
- Zhu, D.C.

IHEP CSNS
Guangdong Province, People's Republic of China
- Huang, W.L.
- Li, F.
- Nie, X.J.
- Qiu, R.Y.
- Rehman, M.A.
- Tan, Z.X.
- Xu, Zh.H.
- Yang, R.J.
- Yang, T.

IKIU
Qazvin, Iran
- Haedar, H.H.
- Mahmoudi, K.

ILSF
Tehran, Iran
- Akbari, M.
- Khaleghi, A.

IMP, TU Darmstadt
Darmstadt, Germany
- Preu, S.
- Yadav, R.

IMP/CAS
Lanzhou, People's Republic of China
- Tian, W.
- Wang, Y.Y.
- Xie, H.M.
- Yang, Y.L.
- Zhao, Z.L.
- Zhu, G.

IOQ
Jena, Germany
- Stöhlker, T.

IPHT
Jena, Germany
- Schmelz, M.
- Stolz, R.
- Zakosarenko, V.

JAI
Egham, Surrey, United Kingdom
- Karataev, P.

JASRI
Hyogo, Japan
- Dewa, H.
- Fujita, T.
- Hosoda, N.
- Maesaka, H.
- Masaki, M.
- Takano, S.

JLab
Newport News, Virginia, USA
- Bruker, M.W.
- Grames, J.M.
- Guo, J.
- Musson, J.
- Overstreet, S.A.
- Park, G.-T.
- Plawski, T.E.
- Poelker, M.
- Rimmer, R.A.
- Wang, H.
- Wilson, C.M.
- Zhang, S.

KAPTEOS
Sainte-Helene-du-Lac, France
- Duvillaret, L.

KEK
Ibaraki, Japan
- Iida, N.
- Ikeda, H.
- Kato, S.K.
- Mitsuhashi, T.M.
- Mitsuka, G.
- Natsui, T.
- Satoh, M.
- Satou, K.
- Suwada, T.
- Tobiyama, M.
- Toyama, T.
- Yamada, S.

KOMAC, KAERI
Gyeongju, Republic of Korea
- Hwang, Y.S.
- Yoon, Y.J.

Korea Atomic Energy Research Institute (KAERI)
Daejeon, Republic of Korea
- Jung, G.I.

Korea University Sejong Campus
Sejong, Republic of Korea
- Kim, E.-S.
- Lim, E.H.

Kyoto University, Institute for Integrated Radiation and Nuclear Science
Osaka, Japan
- Uesugi, T.

Kyoto University, Research Reactor Institute
Osaka, Japan
- Ishi, Y.

LANL
Los Alamos, New Mexico, USA
- Baily, S.A.
- Barkley, W.C.
- Braido, A.J.
- Duran, J.I.
- Hatch, C.D.

ISBN: 978-3-95450-236-3 ISSN: 2673-5350 doi:10.18429/JACoW-IBIC2023

- Johnson, S.M.
- Kennel, L.S.
- Kerstiens, E.L.
- Leffler, H.L.
- Martinez, D.
- Montoya, L.S.
- Rai, D.
- Ramakrishnan, T.
- Simakov, E.I.
- Walker, A.D.
- Watkins, H.A.
- Zimmermann, D.D.

LNF-INFN
Frascati, Italy
- Curcio, A.

MAX IV Laboratory, Lund University
Lund, Sweden
- Mansten, E.
- Thorin, S.

Nalu Scientific, LLC
Honolulu, USA
- Mostafanezhad, I.S.
- Rotter, B.

National Instruments Japan Corporation
Mlnato-ku, Tokyo, Japan
- Kamoshida, A.

Northwestern University
EVANSTON, USA
- Hu, J.YC.
- Jiang, J.
- Liu, H.
- Memik, S.
- Shi, R.
- Shuping, A.M.
- Thieme, M.
- Xu, C.

NSRC SOLARIS
Kraków, Poland
- Biernat, J.B.
- Panaś, R.
- Wawrzyniak, A.I.
- Wiechecki, J.J.
- Ünal, M.T.

Nusano
Valencia, CA, USA
- Anderson, J.I.
- Cao, A.
- Cramer, E.
- Gordon, T.
- Kuhn, K.
- Ledezma Vazquez, O.O.
- Lopez, J.
- Lynam, S.
- Ringuette, J.B.
- Rosenthal, G.B.
- Szeto, L.
- Zhou, J.

ORNL
Oak Ridge, Tennessee, USA
- Aleksandrov, A.V.
- Blokland, W.
- Liu, Y.

ORNL RAD
Oak Ridge, Tennessee, USA
- Evans, N.J.
- Oguz, A.R.
- Willis, W.D.

PAL
Pohang, Republic of Korea
- Hahn, G.
- Huang, J.Y.
- Jang, S.W.
- Kang, H.-S.
- Kim, C.
- Kim, D.
- Kim, G.
- Min, C.-K.
- Mun, G.
- Shin, B.K.
- Shin, D.C.
- Song, D.

PhLAM/CERCLA
Villeneuve d'Ascq Cedex, France
- Evain, C.
- Le Parquier, M.
- Roussel, E.

PhLAM/CERLA
Villeneuve d'Ascq, France
- Bielawski, S.
- Demazeux, Q.
- Evain, C.
- Roussel, E.
- Szwaj, C.

POSTECH
Pohang, Republic of Korea
- Song, W.J.

Private Address
Wuhan, People's Republic of China
- Li, L.X.F.

PSI
Villigen PSI, Switzerland
- Baeta Neves Diniz Santos, P.H.
- Craievich, P.
- Ditter, R.
- Dölling, R.
- Fortunati, R.F.
- Hiller, N.
- Ischebeck, R.
- Ismaili, E.
- Juranič, P.N.
- Keil, B.
- Marcellini, F.
- Marinkovic, G.M.

Content from this work may be used under the terms of the CC-BY-4.0 licence (© 2023). Any distribution of this work must maintain attribution to the author(s), title of the work, publisher, and DOI

ISBN: 978-3-95450-236-3 ISSN: 2673-5350 doi:10.18429/JACoW-IBIC2023

Content from this work may be used under the terms of the CC-BY-4.0 licence (© 2023). Any distribution of this work must maintain attribution to the author(s), title of the work, publisher, and DOI

- Orlandi, G.L.
- Purtschert, J.
- Rizzi, M.
- Roggli, M.
- Schaer, M.
- Schlott, V.
- Stephan, D.
- Vallis, N.
- Wang, X.
- Zennaro, R.
- Zykova, M.

RadiaSoft LLC
Boulder, Colorado, USA
- Cook, N.M.

RCNP
Osaka, Japan
- Hatanaka, K.

Rejected
Tanzania
- Nakaye, Y.

RIKEN
Saitama, Japan
- Adachi, T.
- Brionnet, B.
- Morimoto, K.M.

RIKEN Nishina Center
Wako, Japan
- Kamigaito, O.
- Nishi, T.
- Ohnishi, J.
- Uchiyama, A.
- Watanabe, T.

RIKEN SPring-8 Center
Hyogo, Japan
- Hosoda, N.
- Maesaka, H.
- Takano, S.

Royal Holloway, University of London
Surrey, United Kingdom
- Clapp, A.J.

SARI-CAS
Pudong, Shanghai, People's Republic of China
- Cao, S.S.
- Lai, L.W.
- Liu, B.
- Liu, X.Q.
- Wang, J.G.
- Wu, W.
- Zhou, Y.M.

SCNU
Guangzhou, People's Republic of China
- Lin, L.F.
- Na, N.Y.
- Zhang, Z.S.

SHI Accelerator Service Ltd.
Tokyo, Japan
- Kaneko, K.
- Koyama, R.

SINAP
Shanghai, People's Republic of China
- Meng, R.
- Yang, X.

SLAC
Menlo Park, California, USA
- Bai, M.
- Balakrishnan, N.
- Bianchini Mattison, C.
- Bohler, D.K.
- Brown, G.W.
- Chin, E.P.
- Cobau, W.G.
- Dusatko, J.E.
- Fisher, A.S.
- Frosio, T.
- Herbst, R.T.
- Huang, C.
- Jacobson, B.T.
- Kim, K.H.
- Krejcik, P.
- Kwon, S.
- Lutman, A.A.
- Mock, J.A.
- Novokhatski, A.
- Park, J.
- Pigula, J.
- Ratti, A.
- Raubenheimer, T.O.
- Rodriguez, E.
- Rudolph, J.I.D.
- Sanchez, D.
- Sapozhnikov, L.
- Smedley, J.
- Weaver, M.
- Welch, J.J.
- Wu, J.
- Zelazny, S.

SOLEIL
Gif-sur-Yvette, France
- Bence, A.
- Bisou, J.
- Bronès, R.
- Brubach, J.B.
- Cauchon, G.
- Chevrot, M.
- Fan, Z.
- Hubert, N.
- Kubsky, S.
- Labat, M.
- Manceron, L.
- Moutardier, A.
- Pédeau, D.
- Pichon, G.
- Roy, P.
- Thomasset, M.

ISBN: 978-3-95450-236-3 ISSN: 2673-5350 doi:10.18429/JACoW-IBIC2023

SPbPU
St. Petersburg, Russia
- Rodnyi, P.
- Venevtsev, I.D.

SSRF
Shanghai, People's Republic of China
- Chen, F.Z.
- Chen, J.
- Wang, H.S.
- Zhou, Y.M.

Stanford University
Stanford, California, USA
- Littleton, S.T.

STFC/RAL
Chilton, Didcot, Oxon, United Kingdom
- Letchford, A.P.

STFC/RAL/ISIS
Chilton, Didcot, Oxon, United Kingdom
- Machida, S.
- Pertica, A.
- Posthuma de Boer, D.W.
- Yamakawa, E.

Supracon AG
Jena, Germany
- Zakosarenko, V.

TEMF, TU Darmstadt
Darmstadt, Germany
- Ackermann, W.
- De Gersem, H.
- Haider, D.M.
- Marsic, N.

TENMAK-NUKEN
Ankara, Turkey
- Bulut, S.
- Kaya, U.
- Porsuk, D.
- Serin, N.O.
- Türemen, G.
- Yeltepe, E.

The University of Liverpool
Liverpool, United Kingdom
- Sedláček, O.
- Stringer, O.
- Welsch, C.P.
- Zhang, H.D.

THM
Friedberg, Germany
- Klaproth, S.
- Penirschke, A.
- Scheible, B.E.J.

TRIUMF
Vancouver, Canada
- Jung, P.M.
- Kiy, S.
- Laxdal, R.E.
- Planche, T.
- Shelbaya, O.
- Verzilov, V.V.

TU Darmstadt
Darmstadt, Germany
- Arnold, M.
- Bonnes, U.
- Brauch, A.
- Dutine, M.
- Enders, J.
- Galatyuk, T.
- Grewe, R.
- Jürgensen, L.E.
- Kedych, V.
- Krüger, W.
- Pietralla, N.
- Schließmann, F.
- Schneider, D.
- Steinhilber, G.
- Trautmann, C.

TU Vienna
Wien, Austria
- Schlögelhofer, A.

UCAS
Beijing, People's Republic of China
- Liu, Q.R.
- Yang, X.

UCL
London, United Kingdom
- Cooke, D.A.
- Pannell, F.E.
- Wing, M.

UCSC
Santa Cruz, California, USA
- Lee, D.W.
- Riedel, S.M.

UNIST
Ulsan, Republic of Korea
- Chung, M.
- Sung, C.K.

Universität der Bundeswehr Muenchen
Neubiberg, Germany
- Datzmann, G.
- Dollinger, G.
- Neubauer, J.
- Reindl, J.
- Rousseti, A.

University of Hamburg
Hamburg, Germany
- Lamaack, J.L.

University of Oxford
Oxford, United Kingdom
- Duncan, S.
- Kempf, I.

Content from this work may be used under the terms of the CC-BY-4.0 licence (© 2023). Any distribution of this work must maintain attribution to the author(s), title of the work, publisher, and DOI

ISBN: 978-3-95450-236-3 ISSN: 2673-5350 doi:10.18429/JACoW-IBIC2023

Content from this work may be used under the terms of the CC-BY-4.0 licence (© 2023). Any distribution of this work must maintain attribution to the author(s), title of the work, publisher, and DOI

University of Saskatchewan
Saskatoon, Canada
- Boland, M.J.
- Soltan, E.
- Yousefi Sigari, Y.

University of Warwick
Coventry, United Kingdom
- Newton, M.E.

University of Washington Medical Center
Seattle, Washington, USA
- Dorman, E.F.
- Emery, R.C.
- Smith, B.

Université Paris-Saclay, CNRS/IN2P3, IJCLab
Orsay, France
- Chaikovska, I.

USTC/NSRL
Hefei, Anhui, People's Republic of China
- Leng, Y.B.
- Liang, Y.
- Lu, P.
- Luo, Q.
- Sun, B.G.
- Tang, L.L.
- Wang, A.X.
- Wang, D.Y.
- Wang, J.
- Wu, R.Z.
- Zhao, Y.K.
- Zhou, T.Y.
- Zhou, Z.R.

Warsaw University of Technology, Institute of Electronic Systems
Warsaw, Poland
- Czuba, K.
- Jatczak, P.K.

ISBN: 978-3-95450-236-3 ISSN: 2673-5350 doi:10.18429/JACoW-IBIC2023

Participants List

— A —

Alcorta, Martin
TRIUMF, Vancouver, Canada

Aleksandrov, Alexander V.
ORNL, Oakridge, TN, USA

— B —

Baeta Neves Diniz Santos, Pedro H.
PSI, Villigen, Switzerland

Banerjee, Shohan
DLS, Harwell, UK

Baribeau, Cameron K.
CLS, Saskatoon, Canada

Batten, Tonia
CLS, Saskatoon, Canada

Bayle, Hervé
BERGOZ
Saint Genis Pouilly, France

Beauregard, David
CLS, Saskatoon, Canada

Bechtold, Alexander
NTG, Gelnhausen, Germany

Belohrad, David
CERN, Geneva, Switzerland

Bianchini Mattison, Carolina
SLAC, Stanford, CA, USA

Bielawski, Serge
PhLAM/CERLA
Villeneuve d'Ascq, France

Bobb, Lorraine
DLS, Harwell, UK

Boehme, Christian
FZJ, Jülich, Germany

Brauch, Adrian
TU Darmstadt, Darmstadt, Germany

Bree, Michael
CLS, Saskatoon, Canada

Bronès, Romain
SOLEIL, Gif-sur-Yvette, France

Bruker, Max W.
JLab, Newport News, VA, USA

Buchanan, Emma
CERN, Geneva, Switzerland

— C —

Cargnelutti, Manuel
I-Tech, Solkan, Slovenia

Chaikovska, Iryna
CNRS/IN2P3, IJCLa, Orsay, France

Clapp, Alec J.
University of London, London, UK

Crescimbeni, Lorenzo
GSI, Darmstadt, Germany

Cunningham, Justin G. J.
D-Pace, Nelson, Canada

— D —

Dehnel, Morgan P.
D-Pace, Nelson, Canada

Delaviere, Tom
BERGOZ
Saint Genis Pouilly, France

Dölling, Rudolf
PSI, Villigen, Switzerland

Dooling, Jeffrey C.
ANL, Argonne, IL, USA

Du, Yaoyao
IHEP, Beijing, China

Dupuy, Laurent
BERGOZ
Saint Genis Pouilly, France

— E —

Enke, Sascha
MedAustron, Wien, Austria

— F —

Fisher, Alan S.
SLAC, Stanford, CA, USA

Forck, Peter
GSI, Darmstadt, Germany

Freyermuth, Pierre
CERN, Geneva, Switzerland

— G —

Gassner, David
BNL, Upton, NY, USA

Grishin, Viatcheslav
ESS, Lund, Sweden

— H —

Hahn, Garam
PAL, Pohang, Korea

Hassanzadegan, Hooman
ESS, Lund, Sweden

He, Jun
IHEP, Beijing, China

Hermes, Pascal D.
CERN, Geneva, Switzerland

Hiller, Nicole
PSI, Villigen, Switzerland

Hoehl, Arne
PTB, Berlin, Germany

Hrovatin, Rok
Cosylab, Ljubljana, Slovenia

Huang, Weiling
IHEP CSNS, Guangdong, China

Hubert, Nicolas
SOLEIL, Gif-sur-Yvette, France

— I —

Ibrahim, Michelle A
Fermilab, Batavia, IL, USA

Content from this work may be used under the terms of the CC-BY-4.0 licence (© 2023). Any distribution of this work must maintain attribution to the author(s), title of the work, publisher, and DOI

ISBN: 978-3-95450-236-3 ISSN: 2673-5350 doi:10.18429/JACoW-IBIC2023

Content from this work may be used under the terms of the CC-BY-4.0 licence (© 2023). Any distribution of this work must maintain attribution to the author(s), title of the work, publisher, and DOI

— J —

Jablonski, Szymon
DESY, Hamburg, Germany

Jang, Si-Won
PAL, Pohang, Korea

Javed, Wahhaj
CLS, Saskatoon, Canada

Jordan, Kevin
Kevin Jordan PE
Newport News, VA, USA

Jung, Gwangil
KAERI, Daejeon, Korea

— K —

Kallakuri, Pavana S.
ANL, Argonne, IL, USA

Kato, Shinnosuke
KEK, Tsukuba, Japan

Keane, Robert
ANL, Argonne, IL, USA

Keil, Boris
PSI, Villigen, Switzerland

Kempf, Idris
DLS, Harwell, UK

Kittelmann, Irena D.
ESS, Lund, Sweden

Kiy, Spencer
TRIUMF, Vancouver, Canada

Klaproth, Stephan
THM, Friedberg, Germany

Kotaka, Yasuteru
CNS, Saitama, Japan

Krejcik, Patrick
SLAC, Stanford, CA, USA

Kržič, Tina
Cosylab, Ljubljana, Slovenia

Kube, Gero
DESY, Hamburg, Germany

Kuntzsch, Michael
HZDR
Dresden-Rossendorf, Germany

Kwon, Jangwon
IBS, Daejeon, Korea

— L —

Lavieville, Thomas
PANTECHNIK, Bayeux, France

Lai, Longwei
SARI-CAS, Shanghai, China

Lamaack, Jonas Leon
DESY, Hamburg, Germany

Lannoy, Christophe
CERN, Geneva, Switzerland

Lasocha, Kacper
CERN, Geneva, Switzerland

Laxdal, Robert E.
TRIUMF, Vancouver, Canada

Leban, Peter
I-Tech, Solkan, Slovenia

Lefevre, Thibaut
CERN, Geneva, Switzerland

Leng, Yongbin
USTC/NSRL, Hefei, China

Lensch, Timmy
DESY, Hamburg, Germany

Li, Fang
IHEP CSNS, Guangdong, China

Lidia, Steven M.
FRIB, East Lansing, MI, USA

Lim, Eunhoon
Korea University, Sejong, Korea

Liu, Yun
ORNL, Oakridge, TN, USA

Lokey, Aubrey
FRIB, East Lansing, MI, USA

Lorbeer, Bastian
DESY, Hamburg, Germany

— M —

Maesaka, Hirokazu
RIKEN SPring-8, Hyogo, Japan

Mansten, Erik
MAX IV, Lund, Sweden

Marroncle, Jacques
CEA-DRF-IRFU
Gif-sur-Yvette, France

Michnoff, Robert
BNL, Upton, NY, USA

Milton, Evan
Fermilab, Batavia, IL, USA

Mitsuka, Gaku
KEK, Tsukuba, Japan

Mock, Jeremy A.
SLAC, Stanford, CA, USA

Montoya, Lucas S.
LANL, Los Alamos, NM, USA

Moutardier, Alexandre
SOLEIL, Gif-sur-Yvette, France

— N —

Nakaye, Yasukazu
Rigaku Americas Corporation
The Woodlands, TX, USA

Niedermayer, Philipp
GSI, Darmstadt, Germany

— O —

Orlandi, Gian Luca
PSI, Villigen, Switzerland

Ortega Ruiz, Inaki
CERN, Geneva, Switzerland

ISBN: 978-3-95450-236-3 ISSN: 2673-5350 doi:10.18429/JACoW-IBIC2023

— P —

Pirotte, Christian
JEMA, Louvain-la-Neuve, Belgium

Padrazo, Danny
BNL, Upton, NY, USA

Panaś, Roman
NSRC SOLARIS, Kraków, Poland

Penirschke, Andreas
THM, Friedberg, Germany

Pinayev, Igor
BNL, Upton, NY, USA

Prokop, Richard Michael
Fermilab, Batavia, IL, USA

— R —

Raguenes, Arnaud L. A.
PANTECHNIK, Bayeux, France

Rai, Deepak
LANL, Los Alamos, NM, USA

Reindl, Judith
Uni. der Bundeswehr
München, Germany

Richter, Brian
GMW Associates
San Carlos, CA, USA

Rosenthal, Glenn
Alpha Source
Los Angeles, CA, USA

Rost, Adrian
FAIR, Darmstadt, Germany

— S —

Saadat, Shervin
CLS, Saskatoon, Canada

Saifulin, Maxim
GSI, Darmstadt, Germany

Satou, Kenichirou
KEK, Tsukuba, Japan

Scarpine, Victor
Fermilab, Batavia, IL, USA

Scheible, Bernhard E. J.
THM, Friedberg, Germany

Schloegelhofer, Andreas
CERN, Geneva, Switzerland

Schneider, Dominic
TU Darmstadt, Darmstadt, Germany

Sedlacek, Ondrej
CERN, Geneva, Switzerland

Senes, Eugenio
CERN, Geneva, Switzerland

Shaker, Seyd Hamed
CLS, Saskatoon, Canada

Shin, Bokkyun
PAL, Pohang, Korea

Shin, DongCheol
PAL, Pohang, Korea

Sieber, Thomas
GSI, Darmstadt, Germany

Smith, Michael B.
CLS, Saskatoon, Canada

Steffen, Bernd
DESY, Hamburg, Germany

Sung, Chang-Kyu
UNIST, Ulsan, Korea

Suwada, Tsuyoshi
KEK, Tsukuba, Japan

Switka, Michael T.
ELSA, Bonn, Germany

— T —

Tang, Xuhui
IHEP, Beijing, China

Teytelman, Dmitry
Dimtel, San Jose, CA, USA

Thiebaux, Christophe
LLR, Paris, France

Thurman-Keup, Randy M.
Fermilab, Batavia, IL, USA

Tian, Wang
IMP/CAS, Lanzhou, China

Tobiyama, Makoto
KEK, Tsukuba, Japan

Touzain, Etienne
BERGOZ
Saint Genis Pouilly, France

Trumper, Nathanael
UHV Design, Lewes, UK

Türemen, Görkem
TENMAK-NUKEN
Ankara, Türkiye

— V —

Vallis, Nicolas
EPFL, Lausanne, Switzerland

Vezeau, Nigel
Mevex, Stittsville, Canada

— W —

Walker, Aaron D.
LANL, Los Alamos, NM, USA

Wang, Hongshuang
SSRF, Shanghai, China

Wang, Jinguo
SARI-CAS, Shanghai, China

Wang, Qian
DICP, Dalian, China

Watanabe, Tamaki
RIKEN, Wako, Japan

Watkins, Heath A.
LANL, Los Alamos, NM, USA

Wawrzyniak, Adriana I.
NSRC SOLARIS, Kraków, Poland

Wittenburg, Kay
DESY, Hamburg, Germany

Wootton, Kent P.
ANL, Argonne, IL, USA

Wu, Ruizhe
USTC/NSRL, Hefei, China

Wurtz, Ward A.
CLS, Saskatoon, Canada

— Y —

Yadav, Rahul
IMP TU Darmstadt
Darmstadt, Germany

Yang, Xing
SINAP, Shanghai, China

Yue, Junhui
IHEP, Beijing, China

Content from this work may be used under the terms of the CC-BY-4.0 licence (© 2023). Any distribution of this work must maintain attribution to the author(s), title of the work, publisher, and DOI

ISBN: 978-3-95450-236-3 ISSN: 2673-5350 doi:10.18429/JACoW-IBIC2023

SPONSORS

Content from this work may be used under the terms of the CC-BY-4.0 licence (© 2023). Any distribution of this work must maintain attribution to the author(s), title of the work, publisher, and DOI

ISBN: 978-3-95450-236-3 ISSN: 2673-5350 doi:10.18429/JACoW-IBIC2023

Exhibitors

Bergoz Instrumentation
Email: info@bergoz.com
Phone: +33 450 42 66 4

Instrumentation Technologies
Email: info@i-tech.si
Phone: +38 653 35 26 00

Dimtel, Inc.
Email: info@dimtel.com
Phone: +16 508 62 81 47

UHV Design Ltd
Email: sales@uhvdesign.com
Phone: +44 (0)132 38 11 188

GMW Associates
email: sales@gmw.com
Phone 1-650-802-8292

CAEN ELS s.r.l.
Phone: +390403756610
www,caenels.com

NORCADA
email: info@norcada.com
www.norcada.com

PANTECHNIK
email: contact@pantechnik.com
pantechnik.com

Neue Technologien GmbH & Co. KG
email: Info@NTG.de
www.ntg.de

Busch Vacuum Technics Inc.
https://www.buschvacuum.com/

Content from this work may be used under the terms of the CC-BY-4.0 licence (© 2023). Any distribution of this work must maintain attribution to the author(s), title of the work, publisher, and DOI